THE ROLE OF NATURAL PRODUCTS IN CHRONIC INFLAMMATION

EDITED BY: Zhaocheng Ma, Dahui Liu and Hongzhi Du
PUBLISHED IN: Frontiers in Pharmacology



frontiers Research Topics

Frontiers eBook Copyright Statement

The copyright in the text of individual articles in this eBook is the property of their respective authors or their respective institutions or funders. The copyright in graphics and images within each article may be subject to copyright of other parties. In both cases this is subject to a license granted to Frontiers.

The compilation of articles constituting this eBook is the property of Frontiers.

Each article within this eBook, and the eBook itself, are published under the most recent version of the Creative Commons CC-BY licence. The version current at the date of publication of this eBook is CC-BY 4.0. If the CC-BY licence is updated, the licence granted by Frontiers is automatically updated to the new version.

When exercising any right under the CC-BY licence, Frontiers must be attributed as the original publisher of the article or eBook, as applicable.

Authors have the responsibility of ensuring that any graphics or other materials which are the property of others may be included in the CC-BY licence, but this should be checked before relying on the CC-BY licence to reproduce those materials. Any copyright notices relating to those materials must be complied with.

Copyright and source acknowledgement notices may not be removed and must be displayed in any copy, derivative work or partial copy which includes the elements in question.

All copyright, and all rights therein, are protected by national and international copyright laws. The above represents a summary only. For further information please read Frontiers' Conditions for Website Use and Copyright Statement, and the applicable CC-BY licence.

ISSN 1664-8714
ISBN 978-2-88976-208-8
DOI 10.3389/978-2-88976-208-8

About Frontiers

Frontiers is more than just an open-access publisher of scholarly articles: it is a pioneering approach to the world of academia, radically improving the way scholarly research is managed. The grand vision of Frontiers is a world where all people have an equal opportunity to seek, share and generate knowledge. Frontiers provides immediate and permanent online open access to all its publications, but this alone is not enough to realize our grand goals.

Frontiers Journal Series

The Frontiers Journal Series is a multi-tier and interdisciplinary set of open-access, online journals, promising a paradigm shift from the current review, selection and dissemination processes in academic publishing. All Frontiers journals are driven by researchers for researchers; therefore, they constitute a service to the scholarly community. At the same time, the Frontiers Journal Series operates on a revolutionary invention, the tiered publishing system, initially addressing specific communities of scholars, and gradually climbing up to broader public understanding, thus serving the interests of the lay society, too.

Dedication to Quality

Each Frontiers article is a landmark of the highest quality, thanks to genuinely collaborative interactions between authors and review editors, who include some of the world's best academicians. Research must be certified by peers before entering a stream of knowledge that may eventually reach the public - and shape society; therefore, Frontiers only applies the most rigorous and unbiased reviews.
Frontiers revolutionizes research publishing by freely delivering the most outstanding research, evaluated with no bias from both the academic and social point of view. By applying the most advanced information technologies, Frontiers is catapulting scholarly publishing into a new generation.

What are Frontiers Research Topics?

Frontiers Research Topics are very popular trademarks of the Frontiers Journals Series: they are collections of at least ten articles, all centered on a particular subject. With their unique mix of varied contributions from Original Research to Review Articles, Frontiers Research Topics unify the most influential researchers, the latest key findings and historical advances in a hot research area! Find out more on how to host your own Frontiers Research Topic or contribute to one as an author by contacting the Frontiers Editorial Office: frontiersin.org/about/contact

THE ROLE OF NATURAL PRODUCTS IN CHRONIC INFLAMMATION

Topic Editors:
Zhaocheng Ma, Huazhong Agricultural University, China
Dahui Liu, Hubei University of Chinese Medicine, China
Hongzhi Du, Hubei University of Chinese Medicine, China

Citation: Ma, Z., Liu, D., Du, H., eds. (2022). The Role of Natural Products in Chronic Inflammation. Lausanne: Frontiers Media SA. doi: 10.3389/978-2-88976-208-8

Table of Contents

06 ***Editorial: The Role of Natural Products in Chronic Inflammation***
Wenjun Deng, Hongzhi Du, Dahui Liu and Zhaocheng Ma

09 **Bacteroides Fragilis *Polysaccharide A Ameliorates Abnormal Voriconazole Metabolism Accompanied With the Inhibition of TLR4/NF-κB Pathway***
Xiaokang Wang, Chunxiao Ye, Tianrong Xun, Liqian Mo, Yong Tong, Wensi Ni, Suping Huang, Bin Liu, Xia Zhan and Xixiao Yang

22 ***Hydroxytyrosol Acetate Inhibits Vascular Endothelial Cell Pyroptosis via the HDAC11 Signaling Pathway in Atherosclerosis***
Feng Yao, Zhen Jin, Xiaohan Lv, Zihan Zheng, Hongqian Gao, Ying Deng, Yizhen Liu, Lifang Chen, Weirong Wang, Jianyu He, Jianli Gu and Rong Lin

34 ***Combined Oral and Topical Application of Pumpkin (*Cucurbita pepo *L.) Alleviates Contact Dermatitis Associated With Depression Through Downregulation Pro-Inflammatory Cytokines***
Maha Jameal Balgoon, Maryam H. Al-Zahrani, Soad Al Jaouni and Nasra Ayuob

47 ***New Polyketides With Anti-Inflammatory Activity From the Fungus* Aspergillus rugulosa**
Qianqian Xu, Yuben Qiao, Zijun Zhang, Yanfang Deng, Tianqi Chen, Li Tao, Qiaoxin Xu, Junjun Liu, Weiguang Sun, Ying Ye, Yuanyuan Lu, Changxing Qi and Yonghui Zhang

60 ***Bazi Bushen Capsule Alleviates Post-Menopausal Atherosclerosis via GPER1-Dependent Anti-Inflammatory and Anti-Apoptotic Effects***
Dan Huang, Xindong Wang, Yunhong Zhu, Juexiao Gong, Junqing Liang, Yanfei Song, Yiyan Zhang, Linsheng Liu and Cong Wei

72 ***Corrigendum: Bazi Bushen Capsule Alleviates Post-Menopausal Atherosclerosis* via *GPER1-Dependent Anti-Inflammatory and Anti-Apoptotic Effects***
Dan Huang, Xindong Wang, Yunhong Zhu, Juexiao Gong, Junqing Liang, Yanfei Song, Yiyan Zhang, Linsheng Liu and Cong Wei

74 ***Tomatidine Suppresses the Destructive Behaviors of Fibroblast-Like Synoviocytes and Ameliorates Type II Collagen-Induced Arthritis in Rats***
Xiaolu Yu, Junnan Zhou, Fuli Zhao, Xuan Liu, Yuhang Mao, Li Diao, Chuanjun Wen and Mei Liu

88 ***Huangbai Liniment Ameliorates Skin Inflammation in Atopic Dermatitis***
Ting Zheng, Miao Fan, Yunbo Wei, Jinhong Feng, Pengcheng Zhou, Xin Sun, Anqi Xue, Cheng Xue Qin and Di Yu

101 ***Ferulic Acid Ameliorates Hepatic Inflammation and Fibrotic Liver Injury by Inhibiting PTP1B Activity and Subsequent Promoting AMPK Phosphorylation***
Jianzhi Wu, Xiaoyong Xue, Guifang Fan, Yiqing Gu, Fei Zhou, Qi Zheng, Runping Liu, Yajing Li, Boning Ma, Shuo Li, Guangrui Huang, Lin Ma and Xiaojiaoyang Li

117 ***Hesperetin Exhibits Anti-Inflammatory Effects on Chondrocytes via the AMPK Pathway to Attenuate Anterior Cruciate Ligament Transection-Induced Osteoarthritis***
Jiaqin Wu, Yuna Qian, Cheng Chen, Fan Feng, Lianhong Pan, Li Yang and Chunli Wang

128 ***Berberine Alleviates Non-alcoholic Steatohepatitis Through Modulating Gut Microbiota Mediated Intestinal FXR Activation***
Xiangbing Shu, Meng Li, Ying Cao, Chunlin Li, Wenjun Zhou, Guang Ji and Li Zhang

141 ***Protective Effects of Lentinan Against Lipopolysaccharide-Induced Mastitis in Mice***
Huifang Yin, Guanhong Xue, Ailing Dai and Haichong Wu

150 ***Betulin Alleviates the Inflammatory Response in Mouse Chondrocytes and Ameliorates Osteoarthritis via AKT/Nrf2/HO-1/NF-κB Axis***
Chenghao Ren, Jie Jin, Wei Hu, Qi Chen, Jian Yang, Yaosen Wu, Yifei Zhou, Liaojun Sun, Weiyang Gao, Xiaolei Zhang and Naifeng Tian

164 ***Saikosaponin D Attenuates Pancreatic Injury Through Suppressing the Apoptosis of Acinar Cell via Modulation of the MAPK Signaling Pathway***
Caixia Li, Lihua Cui, Lanqiu Zhang, Lei Yang, Yuzhen Zhuo, Jialin Cui, Naiqiang Cui and Shukun Zhang

175 ***Exploring Multifunctional Bioactive Components From* Podophyllum sinense *Using Multi-Target Ultrafiltration***
Huixia Feng, Guilin Chen, Yongli Zhang and Mingquan Guo

191 ***Total C-21 Steroidal Glycosides From* Baishouwu *Ameliorate Hepatic and Renal Fibrosis by Regulating IL-1β/MyD88 Inflammation Signaling***
Tingting Qin, Mingliang Wang, Ting Zhang, Yingyu Wang, Yunyun Zhang, Muhammad Hasnat, Zirui Zhuang, Yongfang Ding and Yunru Peng

206 ***Metabolomics Study of Guizhi Fuling Capsules in Rats With Cold Coagulation Dysmenorrhea***
Yu Zhang, Na Su, Weiyi Liu, Qingqing Wang, Jianguo Sun and Ying Peng

217 **Euphorbia *Factor L2 ameliorates the Progression of K/BxN Serum-Induced Arthritis by Blocking TLR7 Mediated IRAK4/IKKβ/IRF5 and NF-kB Signaling Pathways***
Jing Tang, Xiaolan Cheng, Shiyu Yi, Yuanyuan Zhang, Zhigang Tang, Yutong Zhong, Qiuping Zhang, Bin Pan and Yubin Luo

232 ***Yi Shen Juan Bi Pill Regulates the Bone Immune Microenvironment* via *the JAK2/STAT3 Signaling Pathway* in Vitro**
Ya Xia, Danping Fan, Xiaoya Li, Xiangchen Lu, Qinbin Ye, Xiaoyu Xi, Qiong Wang, Hongyan Zhao and Cheng Xiao

245 ***Puerarin Alleviates Depression-Like Behavior Induced by High-Fat Diet Combined With Chronic Unpredictable Mild Stress* via *Repairing TLR4-Induced Inflammatory Damages and Phospholipid Metabolism Disorders***
Li-Na Gao, Maocai Yan, Lirun Zhou, Jian'an Wang, Chunmei Sai, Yingjie Fu, Yang Liu and Lin Ding

259 ***Shugan Hewei Decoction Alleviates Cecum Mucosal Injury and Improves Depressive- and Anxiety-Like Behaviors in Chronic Stress Model Rats by Regulating Cecal Microbiota and Inhibiting NLRP3 Inflammasome***
Yingying Yue, Yu Chen, Hao Liu, Lesi Xu, Xian Zhou, Hao Ming, Xin Chen, Miaoqi Chen, Yunya Lin, Lin Liu, Yingqian Zhao and Songlin Liu

278 ***Amelioration of AOM/DSS-Induced Murine Colitis-Associated Cancer by Evodiamine Intervention is Primarily Associated With Gut Microbiota-Metabolism-Inflammatory Signaling Axis***
Mengxia Wang, Biqiang Zhou, Weihong Cong, Miao Zhang, Ziwen Li, Yan Li, Shaoyu Liang, Keji Chen, Depo Yang and Zhengzhi Wu

296 ***Bilobalide Exerts Anti-Inflammatory Effects on Chondrocytes Through the AMPK/SIRT1/mTOR Pathway to Attenuate ACLT-Induced Post-Traumatic Osteoarthritis in Rats***
Tianwen Ma, Liangyu Lv, Yue Yu, Lina Jia, Xiaopeng Song, XinYu Xu, Ting Li, Xuanbo Sheng, Haoran Wang, Jiantao Zhang and Li Gao

310 ***Notoginsenoside R1 (NG-R1) Promoted Lymphatic Drainage Function to Ameliorating Rheumatoid Arthritis in TNF-Tg Mice by Suppressing NF-κB Signaling Pathway***
Danli Jiao, Yang Liu, Tong Hou, Hao Xu, Xiaoyun Wang, Qi Shi, Yongjun Wang, Qiujuan Xing and Qianqian Liang

frontiers | Frontiers in Pharmacology

EDITORIAL
published: 29 April 2022
doi: 10.3389/fphar.2022.901538

Editorial: The Role of Natural Products in Chronic Inflammation

Wenjun Deng[1], *Hongzhi Du*[2], *Dahui Liu*[2] *and Zhaocheng Ma*[1]*

[1]Key Laboratory of Horticultural Plant Biology (Ministry of Education), College of Horticulture and Forestry, Huazhong Agricultural University, Wuhan, China, [2]College of Pharmacy, Hubei University of Traditional Chinese Medicine, Wuhan, China

Keywords: natural products, chronic inflammation, inflammation-related diseases, anti-inflammatory, target, signaling pathway

Editorial on the Research Topic

The Role of Natural Products in Chronic Inflammation

Inflammation including acute and chronic inflammation is the body's defense response to external stimuli, such as pathogens, irritants, or infections. Inflammation is usually beneficial to the body. However, repeated stimulation of harmful substances or ineffective regulation of acute inflammation can lead to chronic inflammation (Ma et al., 2021). Persistent inflammatory responses may lead to chronic inflammation-related diseases such as cardiovascular, neurodegenerative, and inflammatory bowel disease (Hussain et al., 2020). In addition, chronic inflammation is also involved in the physiological and pathological processes of various diseases, such as atherosclerosis (AS), rheumatoid arthritis (RA), depression, obesity, gout, Alzheimer's disease, and cancer (Bai et al., 2021). Currently, steroidal and non-steroidal anti-inflammatory drugs (NSAIDs) with anti-inflammatory, analgesic and other curative effects, are the most commonly used classical treatments for inflammation in clinical practice. However, long-term use of these drugs can cause kinds of adverse reactions (Borquaye et al., 2017), such as gastrointestinal damages (gastric ulcers, bleeding, etc.), liver and kidney dysfunction, and skin diseases (Bai et al., 2021). While rational drug use, drugs with higher safety should be used as much as possible. Therefore, finding natural plant compounds without toxic side effects and good curative effects to replace traditional anti-inflammatory drugs is an urgent issue to be solved in the clinical treatment of inflammation-related diseases.

Natural products have more pharmacological activities and low toxicity properties, which can serve as potential resources for the development of natural anti-inflammatory drugs. Although some severe symptoms of chronic conditions are difficult to be treat with natural products, which are more effective for relieving light pain in the early stage of these disease. Current studies have found that natural products with anti-inflammatory activity include polysaccharides, flavonoids, polyphenols, alkaloids, terpenes, natural pigments, plant volatile oils, quinones, and other compounds (Wu et al., 2021). In recent years, great progress has been made in the development and resolution mechanisms of chronic inflammation-related diseases, and the use of natural products to alleviate inflammatory diseases. We are committed to exploring the anti-inflammatory mechanism and action targets of natural anti-inflammatory components in the context of chronic inflammation, establishing a rapid screening and identification method of natural products, and a technical system for mining action targets, to develop natural products with strong anti-inflammatory activity and no side effects, that can replace traditional anti-inflammatory drugs.

In this Research Topic, the role of natural polysaccharides, alkaloids, terpenes polyphenols in inflammation-related diseases are discussed. Wang et al. reported for the first time the role of *Bacteroides fragilis* polysaccharide A (PSA) in the LPS-induced abnormal hepatic metabolism of voriconazole (VRC). They showed that PSA improved the abnormal metabolism of VRC by

OPEN ACCESS

Edited by:
Javier Echeverria,
University of Santiago, Chile

Reviewed by:
Guido Iaccarino,
University of Naples Federico II, Italy

***Correspondence:**
Zhaocheng Ma
mzhaocheng@mail.hzau.edu.cn

Specialty section:
This article was submitted to Ethnopharmacology, a section of the journal Frontiers in Pharmacology

Received: *22 March 2022*
Accepted: *11 April 2022*
Published: *29 April 2022*

Citation:
Deng W, Du H, Liu D and Ma Z (2022) Editorial: The Role of Natural Products in Chronic Inflammation. Front. Pharmacol. 13:901538. doi: 10.3389/fphar.2022.901538

inhibiting the TLR4-mediated NF-κB signaling pathway, and they also discussed the possibility of PSA as a clinical adjuvant therapy. Yin et al. found that lentinan, a plant polysaccharide extracted from *Lentinus edodes*, exerted an anti-inflammatory effect by inhibiting the activation of the Wnt/β-catenin pathway. Flavonoids are a major anti-inflammatory natural product that is widely used in the treatment of various chronic inflammatory diseases. Wu et al.found that the anti-inflammatory effect of hesperetin could effectively prevent cartilage degradation, suggesting that hesperetin may be a potential natural product for the treatment of osteoarthritis (OA). Alkaloids are one of the most important functional compounds in Chinese herbal medicine with significant biological activity. Yu et al. found that tomatidine with anti-inflammatory, antitumor and immunomodulatory activities, inhibited the destructive behaviors of fibroblast-like synoviocytes and ameliorated RA in rats. Another interesting study performed by Wang et al. analyzed the effect of evodiamine (EVO) on inflammation and cancer from the perspective of colitis-associated cancer (CAC), and they found that EVO may be a new drug to prevent CAC through regulating gut microbiota metabolites. Terpenes including monoterpenes, sesquiterpenes, diterpenoids, etc., are major sources for the study of natural products and the development of new drugs. Betulin, a natural triterpene extracted from birch bark, could be used to treat OA. Ren et al. found that betulin can ameliorate OA by reducing inflammation through the AKT/Nrf2/HO-1/NF-κB signaling pathway. In addition, Ma et al. described the sesquiterpene compound bilobalide as a unique component in *Ginkgo biloba* L. extract with strong anti-inflammatory activity. From their findings, bilobalide was found to be a potential natural therapeutic drug for OA. Polyphenols are widely found in plant foods and have antioxidant and anti-inflammatory activities. Yao et al. identified HDAC11 protein as the target of the natural polyphenolic compound hydroxytyrosol acetate (HF-AC) in olive oil through molecular docking and drug affinity responsive target stability. This study provided a new insight into chronic inflammation-induced atherosclerosis treatment strategy.

Additionally, some medicinal plant extracts and classic traditional Chinese medicine formulas are also used for the development of anti-inflammatory drugs. Medicinal plant extracts have complex components and high medicinal value. Feng et al. used the screening method of multi-target affinity ultrafiltration combined with HPLC-MS to quickly screen out the multi-target bioactive components from *Podophyllum sinense*, which provided an effective method for mining new multi-target drugs from natural products. In terms of natural extracts, Balgoon et al. compared the effects of topical and oral administration of pumpkin extract (PE) with betamethasone-treated groups and found that PE could be used as an alternative or supplementary method for the treatment of contact dermatitis associated with depression. Classic traditional Chinese medicine formulas are another effective method for the clinical treatment of chronic diseases. Xu et al. explored the role of Huangbai liniment (HB) in the treatment of skin inflammation in Atopic dermatitis (AD). The results showed that HB can significantly reduce the expression of pro-inflammatory factors and effectively relieve skin inflammation in AD patients by restoring the T cell immune balance. It provided a research basis for HB to develop new AD treatments in the future. Yue et al. explored the therapeutic effect of Shu Gan He Wei decoction (SHD) on depression, anxiety and cecal mucosal injury in chronic stress model rats. It provided a new therapeutic method for the clinical treatment of TCM regulation of inflammation-related diseases. Also, Xia et al.studied the effect of Yi Shen Juan Bi pill on the homeostasis of the bone immune microenvironment in RA.

Natural products are critical in new drug development due to their broad chemical and functional diversity. The authors of this Research Topic have tried to establish a system for rapid screening and identification of bioactive components and looked for natural products that can replace NASIDs. In summary, the articles in this Research Topic provide new discoveries that natural products can be used to treat chronic inflammation-related diseases and offer useful information for the development of natural products and their derivatives. To expand the wide application of natural products in the treatment of chronic inflammatory diseases, it is necessary to further explore bioactive components with multiple targets and multiple pharmacological activities. And it needs to improve the purity and effectiveness of natural products through separation technology. However, the development of natural products is currently only at the *in vitro* experimental stage, and randomized clinical trials are needed to evaluate the safety and efficacy of natural products for inflammation-related diseases under specific conditions. More importantly, how to improve the safety and efficacy of natural products in the treatment of diseases.

AUTHOR CONTRIBUTIONS

WD: drafting manuscript. WD, HD, DL, and ZM: revision, editing, and final approval. All authors contributed to the work and approved it for publication.

ACKNOWLEDGMENTS

We would like to thank the authors, editors, and reviewers who contributed to this Research Topic. We thank the project Innovation Team and Talents Cultivation Program of National Administration of Traditional Chinese Medicine (ZYYCXTD-D-202005).

REFERENCES

Bai, R., Yao, C., Zhong, Z., Ge, J., Bai, Z., Ye, X., et al. (2021). Discovery of Natural Anti-inflammatory Alkaloids: Potential Leads for the Drug Discovery for the Treatment of Inflammation. *Eur. J. Med. Chem.* 213, 113165. doi:10.1016/j.ejmech.2021.113165

Borquaye, L. S., Darko, G., Laryea, M. K., Roberts, V., Boateng, R., Gasu, E. N., et al. (2017). Anti-Inflammatory Activities of Extracts From Oliva sp., Patella Rustica, and *Littorina littorea* Collected From Ghana's Coastal Shorelines. *Cogent Biol.* 3, 1364063. doi:10.1080/23312025.2017.1364063

Hussain, T., Murtaza, G., Yang, H., Kalhoro, M. S., and Kalhoro, D. H. (2020). Exploiting Anti-inflammation Effects of Flavonoids in Chronic Inflammatory Diseases. *Curr. Pharm. Des.* 26, 2610–2619. doi:10.2174/1381612826666200408101550

Ma, Z., Du, B., Li, J., Yang, Y., and Zhu, F. (2021). An Insight Into Anti-Inflammatory Activities and Inflammation Related Diseases of Anthocyanins: A Review of Both *In Vivo* and *In Vitro* Investigations. *Int. J. Mol. Sci.* 22, 11076. doi:10.3390/ijms222011076

Wu, S., Pang, Y., He, Y., Zhang, X., Peng, L., Guo, J., et al. (2021). A Comprehensive Review of Natural Products Against Atopic Dermatitis: Flavonoids, Alkaloids, Terpenes, Glycosides and Other Compounds. *Biomed. Pharmacother.* 140, 111741. doi:10.1016/j.biopha.2021.111741

Conflict of Interest: The authors declare that the research was conducted in the absence of any commercial or financial relationships that could be construed as a potential conflict of interest.

Publisher's Note: All claims expressed in this article are solely those of the authors and do not necessarily represent those of their affiliated organizations, or those of the publisher, the editors and the reviewers. Any product that may be evaluated in this article, or claim that may be made by its manufacturer, is not guaranteed or endorsed by the publisher.

Copyright © 2022 Deng, Du, Liu and Ma. This is an open-access article distributed under the terms of the Creative Commons Attribution License (CC BY). The use, distribution or reproduction in other forums is permitted, provided the original author(s) and the copyright owner(s) are credited and that the original publication in this journal is cited, in accordance with accepted academic practice. No use, distribution or reproduction is permitted which does not comply with these terms.

frontiers in Pharmacology

ORIGINAL RESEARCH
published: 15 April 2021
doi: 10.3389/fphar.2021.663325

Bacteroides Fragilis Polysaccharide A Ameliorates Abnormal Voriconazole Metabolism Accompanied With the Inhibition of TLR4/NF-κB Pathway

Xiaokang Wang[1,2,3†‡], *Chunxiao Ye*[1,2‡], *Tianrong Xun*[1], *Liqian Mo*[4], *Yong Tong*[5], *Wensi Ni*[6], *Suping Huang*[7], *Bin Liu*[1,2], *Xia Zhan*[1,2] *and Xixiao Yang*[1,2,4*]

[1]*Department of Pharmacy, Shenzhen Hospital, Southern Medical University, Shenzhen, China,* [2]*School of Traditional Chinese Medicine, Southern Medical University, Guangzhou, China,* [3]*Department of Pharmacy, Shenzhen Longhua District Central Hospital, Shenzhen, China,* [4]*Department of Pharmacy, Nanfang Hospital, Southern Medical University, Guangzhou, China,* [5]*Department of Hematology, Shenzhen Hospital, Southern Medical University, Shenzhen, China,* [6]*Department of Pediatric, Shenzhen University General Hospital, Shenzhen, China,* [7]*Department of Intensive Care Unit, Shenzhen Longhua District Central Hospital, Shenzhen, China*

The antifungal agent voriconazole (VRC) exhibits extreme inter-individual and intra-individual variation in terms of its clinical efficacy and toxicity. Inflammation, as reflected by C-reactive protein (CRP) concentrations, significantly affects the metabolic ratio and trough concentrations of voriconazole. *Bacteroides fragilis* (*B. fragilis*) is an important component of the human intestinal microbiota. Clinical data have shown that *B. fragilis* abundance is comparatively higher in patients not presenting with adverse drug reactions, and inflammatory cytokine (IL-1β) levels are negatively correlated with *B. fragilis* abundance. *B. fragilis* natural product capsular polysaccharide A (PSA) prevents various inflammatory disorders. We tested the hypothesis that PSA ameliorates abnormal voriconazole metabolism by inhibiting inflammation. Germ-free animals were administered PSA intragastrically for 5 days after lipopolysaccharide (LPS) stimulation. Their blood and liver tissues were collected to measure VRC concentrations. PSA administration dramatically improved the resolution phase of LPS-induced hepatic VRC metabolism and inflammatory factor secretion. It reversed inflammatory lesions and alleviated hepatic pro-inflammatory factor secretion. Both *in vitro* and *in vivo* data demonstrate that PSA reversed LPS-induced IL-1β secretion, downregulated the TLR4/NF-κB signaling pathway and upregulated CYP2C19 and P-gp. To the best of our knowledge, this study is the first to show that PSA from the probiotic *B. fragilis* ameliorates abnormal voriconazole metabolism by inhibiting TLR4-mediated NF-κB transcription and regulating drug metabolizing enzyme and transporter expression. Thus, PSA could serve as a clinical adjunct therapy.

Keywords: voriconazole, abnormal metabolism, polysaccharide A, TLR4 (toll-like receptor 4), hepatic inflammation

OPEN ACCESS

Edited by:
Hongzhi Du,
Hubei University of Chinese Medicine, China

Reviewed by:
Jiahui Chen,
Harvard Medical School, United States
Long Wu,
University of Maryland, Baltimore, United States

****Correspondence:***
Xixiao Yang
yaxx@smu.edu.cn

†ORCID:
Xiaokang Wang
orcid.org/0000-0002-4325-9907
‡These authors have contributed equally to this work

Specialty section:
This article was submitted to Inflammation Pharmacology, a section of the journal Frontiers in Pharmacology

Received: *02 February 2021*
Accepted: *15 March 2021*
Published: *15 April 2021*

Citation:
Wang X, Ye C, Xun T, Mo L, Tong Y, Ni W, Huang S, Liu B, Zhan X and Yang X (2021) Bacteroides Fragilis *Polysaccharide A Ameliorates Abnormal Voriconazole Metabolism Accompanied With the Inhibition of TLR4/NF-κB Pathway. Front. Pharmacol. 12:663325. doi: 10.3389/fphar.2021.663325*

INTRODUCTION

The liver maintains homeostasis and plays important roles in host defense and drug metabolism. Gut microbiota modulate the injury response in certain organs that are remote from the gastrointestinal tract, such as the liver (Gong et al., 2019). Intestinal blood accounts for 70% of the total hepatic blood supply. Gut microbiota composition affects hepatic cellular function (Adolph et al., 2018). Alteration of gut microbiota composition or target bacteria modifies the toxicity profile of certain drugs (Sivan et al., 2015; Taylor et al., 2019). Elucidating the physiological, chemical and microbial factors that determine the contributions of the microbiome to drug metabolism could help explain intra- and inter-individual variability in drug exposure and provide opportunities for personalized medicine (Zimmermann et al., 2019).

The fungal infection rates in immunocompromised patients with acute myeloid leukemia (AML) may be in the range of 8–12% (Hicks et al., 2020). Prophylactic administration of the antifungal agent VRC, reduces the incidence of invasive fungal infections. The pharmacokinetics of VRC are nonlinear and highly variable. Changes in trough concentrations (C_{min}) are associated with genetic factors, drug interactions and pathophysiological parameters, such as age or hepatic function. Pharmacogenetics is a key component of precision medicine (Hicks et al., 2020), however, alterations in disease status can result in inter- and intra-individual drug exposure variability and many adverse drug reactions (ADRs) such as hepatotoxicity, loss of visual acuity, and neuropathies (Pascual et al., 2012). Inflammation is reflected by CRP concentrations and affects drug metabolic enzymes and transporters (DMETs) (Stanke-Labesque et al., 2020). It may also contribute to the pharmacokinetic variability of VRC. During infection or inflammation, several drug-metabolizing enzymes in the liver are downregulated (Morgan, 2009; Keller et al., 2016; Veringa et al., 2017). Consequently, VRC overexposure can occur in type two diabetes, non-alcoholic fatty–liver disease and hematopathies (Stanke-Labesque et al., 2020). However, there have been limited studies of VRC pharmacology based on patients' inflammatory state and few have formulated or tested anti-inflammatory agents to improve hepatic DMETs.

Pro-inflammatory cytokines such as IL-6, IL-1β and TNF-α evoke major recombination in hepatic gene expression and induce the synthesis of acute phase proteins such as CRP. Toll-like receptors (TLRs) recognize patterns and are expressed in monocytes, macrophages, hepatocytes, and other cells (Kawai and Akira, 2010). As adjuvant, TLRs agonists can launch a strong immune response to assist cancer radiotherapy and bio-chemotherapy.

B. fragilis is a strict anaerobe in the human gut microbiome. Its natural product capsular PSA prevents certain sterile PNS and CNS inflammatory disorders (Mazmanian et al., 2008; Ramakrishna et al., 2019). PSA is a unique zwitterionic polysaccharide and an immunogenic capsule component of the non-toxin-producing *B. fragilis* (NTBF) strain NCTC9343. It is a unique T-cell-dependent antigen that mediates $CD4^+$ T-cell proliferation and induces secretion of the immunosuppressive cytokine IL-10 in regulatory T cells. IL-10 is a potent anti-inflammatory cytokine that restrains pathogenic inflammation in the gut, brain and lungs (Lee and Mazmanian, 2010; Shen et al., 2012). A recent biodiversity study showed a clear relationship between NTBF and the immune system and this association implies its potential use as a probiotic (Sun et al., 2019). Therefore, we infer that NTBF may inhibit the inflammatory environment in the liver and the entire body by promoting interactions between microorganisms and hosts and ameliorating abnormal VRC metabolism in inflammatory disease.

MATERIALS AND METHODS

Study Population

The study procedures were approved by the Ethics Committee of Shenzhen Hospital of Southern Medical University (No. NYSZYYEC20180017), and were performed in accordance with the Helsinki Declaration. Subjects were selected from patients seen in the Hematology Department of Shenzhen Hospital, Southern Medical University who were diagnosed with AML and required VRC for antifungal prophylaxis. AML was diagnosed according to the criteria of the National Comprehensive Cancer Network (NCCN) Guidelines for Acute Myeloid Leukemia (Tallman et al., 2019). All adult patients were tested for the CYP2C19 genotype before being grouped. Patients who were being administered "3 + 7" chemotherapy (3 days daunorubicin plus 7 days continuous cytarabine infusion) were screened for enrollment. Sixty-five patients with the CYP2C19 genotype who were normal metabolizers signed informed-consent forms before participating in this study.

The course of VRC treatment lasted ≥ 5 days. Each patient was administered two doses a day in strict accordance with drug-label instructions. The exclusion criteria were as follows: patients 1) who were pregnant within the past year or who were administered antibiotics or probiotics within the past 2 months; 2) who were <16 year old; 3) for whom combination chemotherapy was contraindicated because of renal/hepatic or cardiac insufficiency; 4) administered combinations of patent CYP2C19 or CYP3A4 modulators such as rifampicin, ritonavir, carbamazepine, long-acting barbiturates, or macrolide antibiotics; 5) who presented with hypokalaemia (serum potassium < 3.5 mmol/L) or those undergoing haemodialysis or peritoneal dialysis; 6) who presented with visual impairment; 7) who presented with hepatopathy; and 8) who presented with poor compliance to their medications according to electronic medical records.

Clinical Data and Patient Blood Sample Collection

Clinical information was collected and ADRs were recorded in an earlier study (Wang et al., 2020). A 5 ml sodium -heparin tube was used for blood sample collection. CRP and TNF-α concentrations were used as indices of inflammation and were routinely measured in discarded blood samples. Serum total bilirubin (TB > 26 μmol/L), aspartate transaminase (AST > 40 IU/L), and alanine transaminase (ALT > 50 IU/L) were

quantitated to diagnose hepatotoxicity during VRC treatment. The metabolic ratio was determined as follows:

$$\text{Metabolic ratio} = \frac{\text{C (Voriconazole N - oxide)}}{\text{C (Voriconazole)}} \times 100\,\%$$

Liquid Chromatography-Tandem Mass Spectrometry Analysis

Lipid LC-MS/MS was conducted as previously described (Wang et al., 2020). A Waters UPLC-TOF-MS (Waters ACQUITY UPLC™ System Tandem Waters LCT Premier XE TOF-MS; Waters Corp., Milford, MA, United States) was usedto determine plasma VRC and VRC N-oxide.

Microbial Diversity Analysis

Human stool samples were collected from patients in the haematology department of Shenzhen Hospital, Southern Medical University. Faeces were collected in labelled stool tubes, flash-frozen, and stored at −80°C.

Microbial DNA was extracted from all fecal samples using an E. Z.N.A.® DNA kit (Omega Bio-Tek, Norcross, GA, United States) according to the manufacturer's instructions. The V3 - V4 hypervariable region of the bacterial 16S rRNA gene was amplified by thermal cycling PCR with 338F_806R primers. All primers are listed in **Supplementary Table S1**. The purified amplification products were mixed in equimolar ratios and subjected to paired-end sequencing (2 × 300) on the Illumina MiSeq platform (Illumina, San Diego, CA, United States) according to standard methods. The original FASTQ files were demultiplexed, quality filtered with Trimmomatic, and flash merged. The RDP classifier algorithm (http://rdp.cme.msu.edu/) was used to classify each 16S rRNA gene sequence in the SILVA (SSU123) 16S rRNA database.

To investigate the roles of gut microbiota in adverse reaction development and modulation in patients, we analysed metagenomic sequence data extracted from the NCBI Sequencing Read Archive database using faecal samples from individuals with and without adverse reactions. DNA extraction and quality control were performed as previously described (Taur et al., 2012). Covaris M220 (Covaris Inc., Woburn, MA, United States) was used to cut, the extracted DNA fragments into 400-bp sections. The latter were then used to construct a double-terminal library. NEXTFLEX Rapid DNA-Seq (PerkinElmer, Waltham, MA, United States) was used to build a pair of terminal libraries. The joint containing the hybridisation site of the complete sequencing primer was connected to the blunt end of the fragment. A NovaSeq kit (Illumina, San Diego, CA, United States) was used on the Illumina NovaSeq platform to perform paired-end sequencing according to the manufacturer's instructions (www.illlighta.com).

MATERIALS

LPS and TAK-242 were purchased from MCE (Monmouth Junction, NJ, United States). Enzyme-linked immunosorbent assay (ELISA) kits were purchased from Group, Inc (Rosemont, IL, United States). Primary antibodies against P-gp were obtained from Cell Signaling Technology (Danvers, MA, United States). His-H3 was procured from Affinity Biosciences (Cincinnati, OH, United States). Other antibodies were acquired from Invitrogen (Carlsbad, CA, United States).

Animal Model and Treatments

Male Sprague-Dawley rats (180–220 g) and male C57BL/10J mice were purchased from Southern Medical University. They were housed in ventilated boxes, in a protected temperature- and humidity-controlled room, with a 12 h on/off light cycle. The animals had *ad libitum* food and water to access. Animal care was conducted in strict accordance with the China and Nanfang Hospital policies for animal health and well-being and the animals were euthanized by CO_2 asphyxiation at the end of the experiments (No. NFYY-2020–73).

Germ-free mice were prepared by administering vancomycin (100 mg/kg), neomycin sulphate (200 mg/kg), metronidazole (200 mg/kg), and ampicillin (200 mg/kg) intragastrically once daily for 5 days.

The rats and mice were randomly assigned to control (CON), lipopolysaccharide (LPS), LPS + germ free, LPS + germ free + PSA ($n = 6$, respectively) groups. In the CON group, physiological saline (2 ml/kg) was continuously infused *via* the jugular vein. In the LPS group, LPS in saline was continuously infused *via* the jugular artery at a dose of 2 mg/kg bodyweight per hour. In the LPS + PSA group, PSA was diluted with sterile phosphate-buffered saline (PBS; vehicle) and infused *via* the jugular vein (2 ml/kg), starting 10 min before the LPS infusion. All of the germ-free animals were kept under sterile conditions, and received sterile nutrition and water. After 3 days of treatment, the animals were humanely euthanized by CO_2 asphyxiation.

Voriconazole Metabolism *In Vivo*

Blood and liver tissues were collected in heparinized test tubes at 0, 0.5, 2 and 12 h after VRC administration. Plasma was separated by centrifugation at 13,000 rpm for 10 min. VRC concentrations were determined by lipid LC-MS/MS.

Polysaccharide A Purification

B. fragilis strain NCTC9343 was obtained from the American Type Culture Collection (Manassas, VA, United States). PSA purification was performed by Fenghai Biotechnology Co., Ltd. (Hangzhou, China) according to the method described previously (Ramakrishna et al., 2019). Bacteria were resuspended in 1:1 v/v water: phenol and centrifuged into fragments at 70°C. The aqueous phase was collected, extracted with ether, and dialyzed against water overnight. PSA was then digested twice with DNA and RNA enzymes and analyzed using 1H NMR (**Supplementary Figure S2**). Fractions containing PSA alone were collected, freeze-dried and stored at −80°C until use.

Histologic Analysis

Isolated liver tissue was fixed in 10% (v/v) buffered formalin, embedded in paraffin, and sliced into 5 mm thick sections. The degree of liver impairment was assessed by H&E staining. The hepatic parameters were inflammation, coagulation, and lipid

accumulation. For the immunohistochemical (IHC) analysis, monoclonal IL-1β antibody (1:1,000) was used.

Primary Hepatocytes and Treatments

In brief, liver samples were immediately moved to a 10 cm sterile Petri dish and minced, then hepatocytes were collected using a large-bore pipette, filtered through a 70 μm membrane to remove tissue fragments, and transferred to sterile 10 cm cell-culture dishes. Primary hepatocytes were cultured in cold Dulbecco's Modified Eagle's Medium (DMEM), and seeded in 6 cm dishes containing DMEM supplemented with 10% fetal bovine serum. Cells were maintained at 37°C and 5% CO_2 in a humidified atmosphere. Primary hepatocytes were incubated with LPS (0.5 μg/mL) for 12 h to obtain inflammation. For PSA treatment, the cells were treated with 10 μg/ml for 2 h before LPS stimulation.

For the experiments studying the effects of inhibitor on TLR4/NF-κB induced IL-1β secretion, the cells were prestimulated with TAK-242 (1 μM) and added to the cell culture for 30 min at 2 h before stimulation with LPS.

Primary hepatocytes were seeded in 24-well plates. TLR4 specific siRNA (siTLR4) and its negative control siRNA (siNC) were purchased from RiboBio Co., Ltd. (Guangzhou, China). More effective single siRNAs were used for further experiments as follows: siTLR4#1: CTACTACCTCGATGA TATT; siTLR4#2: GGAAACTTGGAAAAGTTTG. Non-specific negative control siRNAs were also designed (sense strand: 5′-UUCUCCGAACGUGUCACG-3′ and anti-sense strand: 5′-ACGUGACACGUUCGGAGAATT-3′). Lipofectamine 3,000 transfection reagent (Invitrogen, United States) was used for co-transfection with 40 nM siTLR4#2 and siNC according to the manufacturer's recommendations. After 48 h, the cells were collected and subjected to subsequent experimentation.

Gene Expression Analysis

TRIzol reagent was used for total RNA isolation, and reverse transcription was performed using reverse transcriptase. Hepatic TLR2, TLR4, and TLR9 expression was quantified by RT-PCR.

Cytokine Detection by Enzyme-Linked Immunosorbent Assay and Luminex Analysis

Serum and supernatant levels of IL-1β and IFN-γ were analyzed using ELISA kits (Nanjing Jiancheng Bioengineering Institute, Nanjing, China) according to the instructions of the manufacturer. IL-2, IL-6, IL-10, TNF-α and CXCL8 in serum were quantified by Luminex xMAP technology on an LX200 instrument (Luminex Corp., Austin, TX).

Western Blotting Analysis

Protein extracts from whole cell and liver tissue samples were separated on SDS-PAGE gels and transferred onto polyvinylidene fluoride (PVDF) membranes (Millipore, Massachusetts, MA, United States). Total hepatic protein extraction was conducted using the radioimmunoprecipitation assay (RIPA) method. The membrane was sealed with 5% (w/v) skim milk in TBST buffer for 1 h and incubated at 4°C for 12 h with primary antibody diluted with 5% (w/v) skim milk TBST followed by secondary antibody coupled with horseradish peroxidase incubated with 5% (w/v) skim milk-TBST for 1 h. Antigen expression was observed using an enhanced chemiluminescence kit. The following primary antibodies were used: anti-P-gp (1:1,000), anti-CYP2C19 (1:1,000), anti-IL-1β (1:2,000), anti-NF-κB-p65 (1:50,000), anti-TLR4 (1:1,000), anti-MyD88 (1:1,000), anti-NF-κB (1:1,000), anti-GAPDH (1:10,000), anti-His-H3 (1:6,000), anti-TRAF6 (1:1,000) and anti-IL-1β-p17 (1:1,000).

Statistical Analysis

Data were analyzed using GraphPad Prism version 8.0. One-way analysis of variance (ANOVA) and t-tests were used to compare differences among treatment means. Linear regression analysis was performed using the loss minimization (LM) function in R 3.5.3 (R Core Team, Vienna, Austria). Data are presented as means ± standard deviation (SD). All statistical tests were two-sided and differences were considered statistically significant at $p < 0.05$.

RESULTS

Demographic information is shown in **Supplementary Table S2**.

The Metabolic Ability of Voriconazole Decreased During Inflammation

Sixty-five VRC trough concentrations were included in the analysis. There was a significant positive linear correlation between levels of the inflammatory marker CRP and VRC Cssmin ($R^2 = 0.45$; $p < 0.001$), **Figure 1B**. CRP levels were significantly positively correlated with AST ($R^2 = 0.56$; $p < 0.001$) (**Figure 1D**) and total bilirubin ($R^2 = 0.48$; $p < 0.001$) (**Figure 1E**).

To explore the ability of CRP to metabolize VRC in liver, we quantified nitrogen oxides metabolized by VRC, calculated the metabolic capacity, and established the correlation between CRP and metabolic ability. **Figure 1C** shows all calculated metabolic ratios and indicates that they decreased with increasing CRP concentration. CRP levels were significantly correlated with metabolic ratios ($R^2 = 0.53$; $p < 0.001$).

Based on the correlation between inflammation and ADR detailed above, we also analyzed the correlations between key inflammatory cytokines and *B. fragilis* in the two groups. We found that ADR were associated with higher levels of IL-1β in peripheral blood (**Figure 2A**).

Bacteroides Fragilis Abundance Was Higher in Patients Without Adverse Reactions

Alterations in patients' microbial community structure and diversity may be associated with chemotherapy efficacy and toxicity (Jia et al., 2008). To determine whether gut microbial community diversity was altered in the AML individuals susceptible to ADRs, we evaluated **α**-diversity in the feces of

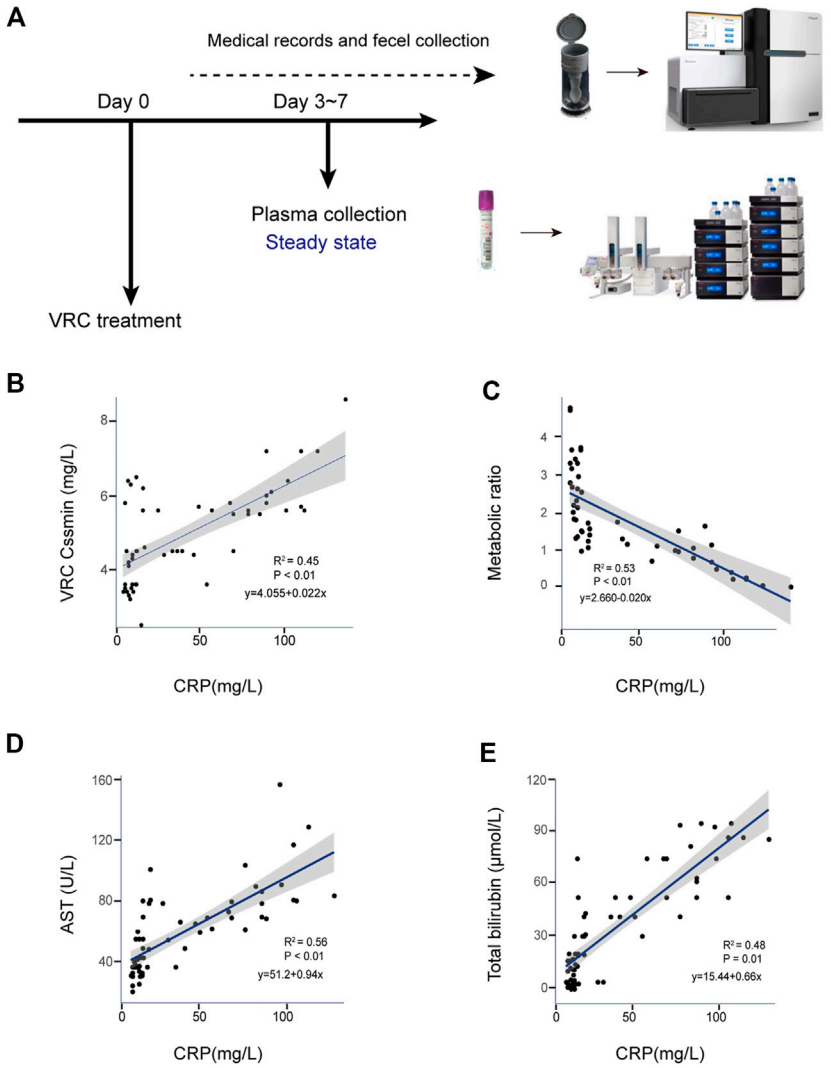


FIGURE 1 | Correlation between CRP and adverse reactions in clinical voriconazole administration. **(A)** Schematic of sample collection process. **(B)** Scatterplot of VRC Cssmin *vs.* CRP concentration (mg/L). **(C)** Scatterplot of VRC metabolic ability *vs.* CRP concentration (mg/L). **(D,E)** Correlation between the CRP and liver function parameters possibly induced by voriconazole in peripheral blood. Each graph presents a trend line, regression equations, R-squared values (R^2) and *p*-values of the regression model are shown on the figures (n = 65).

nonADR and ADR patients using an inverse Simpson index, which is an overall diversity parameter (**Figure 2B**). Gut microbial abundance among groups was compared using a Wilcoxon rank sum test. At the phylum level, the abundance of *Bacteroides* was significantly lower in ADR patients than in nonADR patients (p = 0.025; **Figure 2B**).

Samples were randomly selected from each group and the relative differences in their genus-level *Bacteroides* abundance were analyzed. The heat map in **Figure 2C** shows that *Bacteroides* abundance was significantly higher in nonADR patients than in ADR patients. Variable importance in projection (VIP) scores for gut microbiota showed that *B. fragilis* contributed significantly to the group separation (**Figure 2D**). Identified reads of bacteria in the 16S rDNA data extracted from these fecal samples are presented in **Figure 2E**. Significant *B. fragilis* enrichment was found in the fecal samples obtained from AML patients presenting with no adverse reactions.

Based on the correlation between inflammation and ADRs outlined above, we also analyzed the correlations between key inflammatory cytokines and *B. fragilis* in the two groups. Of interest, IL-1β levels were negatively correlated with relative *B. fragilis* abundance (R^2 = 0.58; p < 0.001) (**Figure 2F**). This finding, accords with the results presented in **Figure 2A**.

Bacteroides Fragilis Polysaccharide a Treatment Ameliorated Abnormal Hepatic Voriconazole Metabolism

We began by determining the appropriate dose of PSA for the animals (**Figure 3**). Based on the experimental analysis shown in

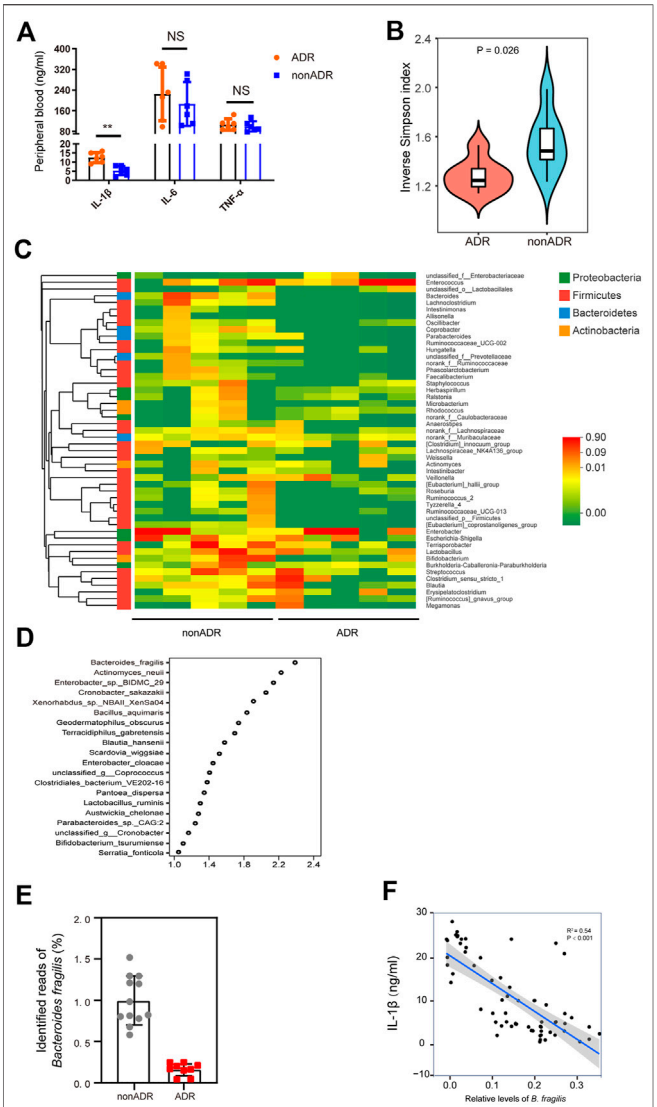


FIGURE 2 | Profiling of the gut microbiota and pro-inflammatory cytokines in individuals with AML. **(A)** Pro-inflammatory cytokine concentrations were determined in peripheral blood (n = 6, respectively). **(B)** Alpha diversity, measured by the inverse Simpson index (n = 6, respectively). **(C)** Community heatmap analysis at genus level (n = 5, respectively). **(D)** VIP scores of PLS-DA. VIP scores ranked discriminating power of various taxa between nonADR and ADR groups. Taxon with VIP score of > 1 was considered important in discrimination. **(E)** Identified reads of *B. fragilis* in ADR and nonADR patients. **(F)** Scatterplots of IL-1β levels in periheral blood *vs.* relative levels of *B. fragilis*. R^2 and p-values of the regression model are shown on the figures.

Figures 3A,**B**, we set the dose for mice at 100 μg/kg, and that for rats at 50 μg/kg. Mouse survival analysis showed that PSA (100 μg/kg) significantly prolonged the survival times in the of LPS-induced model (**Figure 3C**).

In the rat experiment, we verified that metabolism of VRC was abnormal in the inflammatory-model animals. The VRC metabolism drug-time curves for each group are shown in **Figure 4A**, which shows that VRC AUC and plasma disposal ability were significantly increased in the LPS-treated rats, as well as other pharmacokinetic (PK) parameters (**Figure 4B**), implying that inflammation increased the risk of VRC induced adverse reactions. PSA treatment significantly improved VRC AUC and other PK parameters.

In the mouse experiment, we monitored the dose-time relation of voriconazole in the liver and serum and again found that PSA alleviated the abnormal metabolism of voriconazole in the inflammatory-model animals (**Figures 4C,D**). PSA significantly reduced the peak concentration of voriconazole within 2 h. At 12 h, the concentrations of voriconazole in the liver and serum were significantly reduced (p < 0.05). These

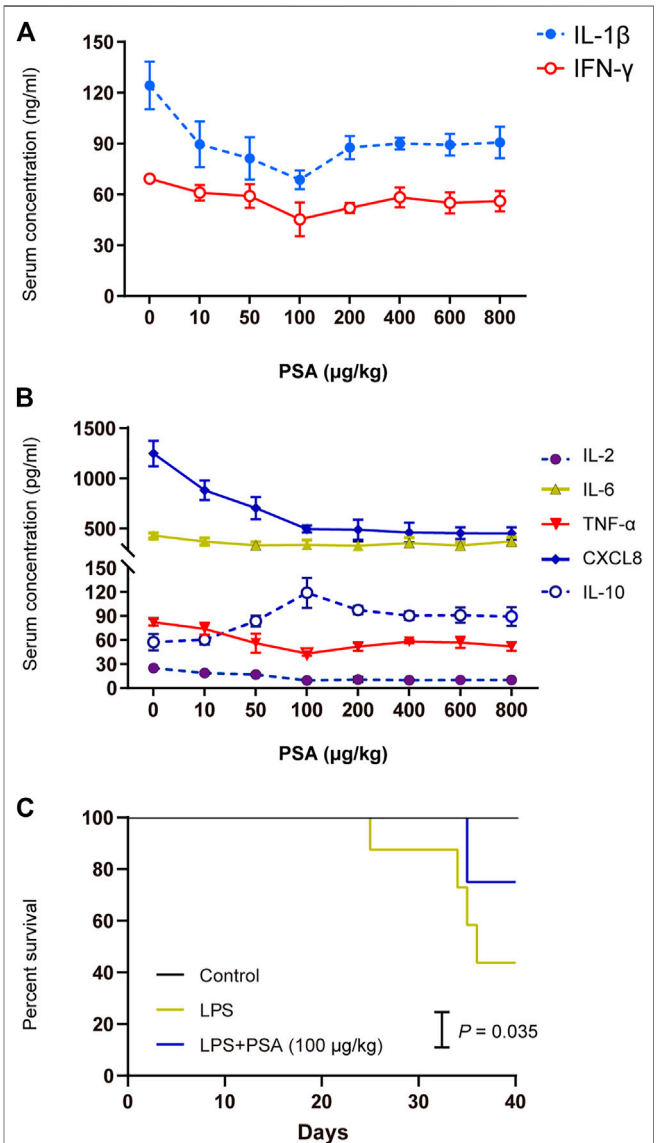
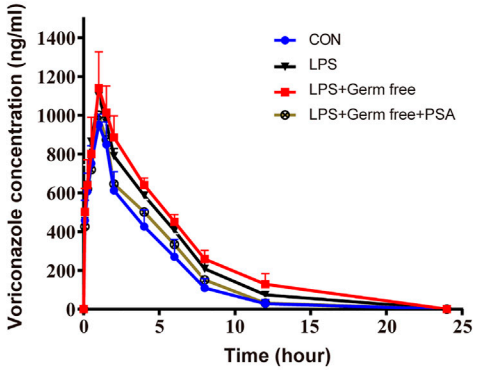


FIGURE 3 | Concentration screening over the effect of PSA on animal models. **(A,B)** Screening assay was performed at eight PSA concentrations (0, 10, 50, 100, 200,400, 600 and 800 μg/kg) in animals (n = 5, respectively). Optimum PSA concentration selection based on the levels of proinflammatory cytokines. **(C)** Kaplan-Meier survival curve analysis with PSA (100 μg/kg).

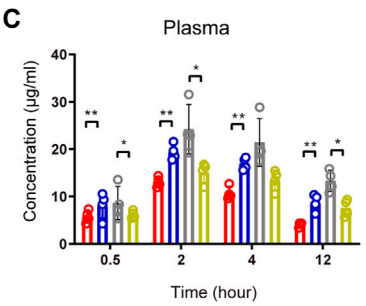
A



B

Parameter	CON	LPS	LPS+Germ free	LPS+Germ free+PSA
AUC (0-t) (mg/L·h)	3912.13±660.426	5288.33±400.407*(a)	5897.65±507.147***(b)	4383.35±291.197**(c)
AUC (0-∞) (mg/L·h)	4008.041±653.076	5631.411±554.411*(a)	6623.194±646.355*(b)	4514.652±193.915**(c)
MRT (0-t) (h)	3.238±0.308	3.727±0.284	3.999±0.187	3.504±0.251**(c)
MRT (0-∞) (h)	3.535±0.513	4.375±0.541	5.376±0.978	3.808±0.665*(c)
$t_{1/2}$ (h)	1.961±0.68	2.825±0.444*(a)	3.642±0.58*(b)	1.978±0.888**(c)
C_{max} (mg/L)	960±54.314	1098±87.006*(a)	1140±186.949	1000±90.909*(c)

C



D

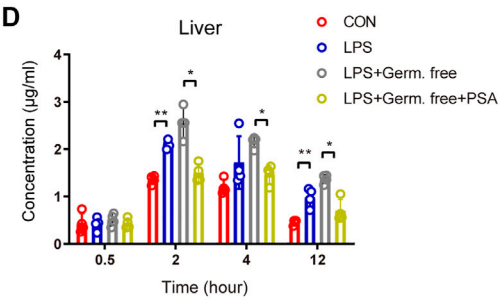


FIGURE 4 | VRC metabolism by LPS with or without PSA treated rats and mice. **(A)** VRC plasma kinetics in individual rats ($n = 5$, respectively). **(B)** Pharmacokinetic (PK) parameters in rats. **(C)** VRC blood concentrations in individual mice ($n = 5$, respectively). **(D)** VRC liver tissue concentrations in individual mice. The PK parameters were calculated according to the noncompartmental PK calculated by DAS 2.0 software. Tmax, maximum time corresponding to Cmax; AUC (0-∞), area under the curve from 0 to ∞; MRT, Mean residence time; t1/2, half-life; Cmax, maximum concentration; Rats receiving a single dose of VRC, 10 mg/kg; Mice receiving a single dose of VRC, 10 mg/kg. (a) LPS *vs.* CON; (b) LPS + Germ free *vs.* LPS; (c) LPS + Germ free + PSA *vs.* LPS + Germ free. Unpaired *t* test, $^{*}p < 0.05$, $^{**}p < 0.01$, $^{***}p < 0.001$.

results imply that PSA was beneficial in reducing the residual amounts of voriconazole during metabolic clearance *in vivo*.

PSA administration also reversed VRC-induced hepatotoxicity in the inflammatory-model animals (**Figures 4A–C**). Levels of AST, ALT and TB were significantly lower in the PSA-treated group than in the LPS-treated group.

Polysaccharide A Reversed Hepatic Inflammatory Lesions

PSA is the main functional molecule produced by *B. fragilis*. It has a zwitterionic structure consisting of repeating oligosaccharide units comprising sugars with free amino and carboxyl groups. It is vital to the biological activity of bacteria (**Supplementary Figure S1**). To determine the optimal cellular and molecular concentrations required for an immune response to PSA *in vivo*, the effects of purified PSA on IL-1β and IFN-γ levels in mice were assessed. At 0–100 μg/kg, PSA decreased IL-1β and IFN-γ levels. At > 100 μg/kg, however, PSA was no longer inhibitive (**Figure 3A**). We selected a concentration of 100 μg/kg PSA for the mouse gastric-perfusion experiment.

After continuous intragastric PSA administration, the livers of the mice were excised for pathological examination. Continuous intragastric PSA administration significantly improved the inflammatory response and reduced the edematous liver tissue degeneration induced by LPS (**Figure 5E**). We then performed IHC experiments on the liver tissue and found that the IL-1β secretion in the PSA treated group did not differ from that in the normal control (CON) group, but was lower than that in the group with inflammation induced by LPS (**Figure 5D**).

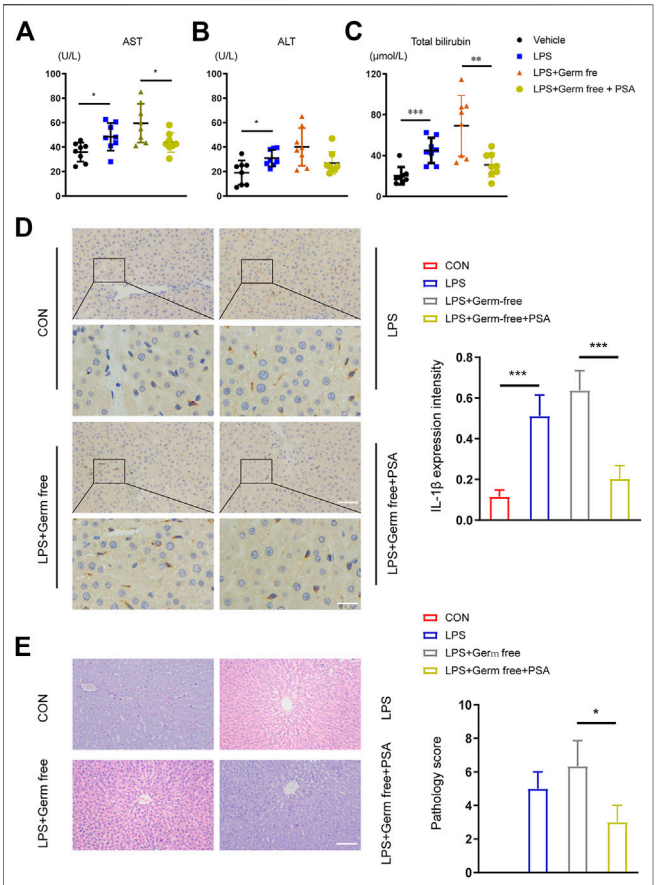


FIGURE 5 | Hepatic function and histological analysis of the livers after intravenous administration of LPS with or without PSA in mice. **(A–C)** Plasma chemistry profile analyses of aspartate transaminase (AST) **(A)** alanine transaminase (ALT) **(B)** and total bilirubin **(C)** after VRC treated 5 days **(D)** Left: Immunohistochemical (IHC) detection of hepatic IL-1β (200 × upper and 400 × down), Right: IL-1β expression intensity in different treated groups were analyzed **(E)** Left: Photomicrographs of stained with H&E (200×). Right: Semiquantitative pathology scores of liver tissues. *$p < 0.05$, **$p < 0.01$, ***$p < 0.001$; Unpaired *t* test.

Polysaccharide A Inhibits the Secretion of IL-1β Through the TLR4 Signaling Pathway

To confirm the foregoing results *in vivo*, we used western blotting to measure hepatic inflammasome suppression and drug enzyme and transporter protein upregulation in response to PSA treatment. Here, we specifically analyzed IL-1β, voriconazole metabolic enzyme (CYP2C19) and transporter (P-gp). Following PSA administration, the mRNA expression levels of IL-1β decreased in a dose-dependent manner, and this was reversed at a PSA concentration of 10 μg/ml, the proteins were immunostained in primary hepatocytes (**Figure 6C**). As expected, LPS stimulation induced significant IL-1β-17 protein secretion (**Figures 6C–E**). CYP2C19 and P-gp expression were down-regulated after LPS treatment. Remarkably, the western blot analysis showed that PSA treatment significantly reduced IL-1β protein expression, whereas that of CYP2C19 and P-gp significantly increased (**Figures 6F,G**).

To elucidate the mechanisms involved, we analyzed toll-like receptors TLR gene expression in primary hepatocytes and found that PSA upregulated TLR4 significantly after LPS stimulation (**Figure 6B**). Inhibition of the hepatic inflammatory response by PSA may be associated with down-regulation of the TLR4 signaling pathway. We therefore used TAK-242 to disrupt TLR4 signaling in primary hepatocytes. When TLR4 signaling was blocked in primary hepatocytes stimulated by LPS, there was a significant ($p < 0.001$) decrease in MyD88 and IL-1β protein levels (**Figures 6K,L**); to a lesser extent, NF-κB levels were also reduced (**Figure 6I**). Of note, a similar observation was made in PSA-treated primary hepatocytes: TLR4, MyD88, IL-1β and NF-κB-p65 were significantly decreased ($p < 0.05$). This may indicate that PSA can play a similar role to that of TAK-242 targeting the same target.

Polysaccharide A Up Regulates Expression of Hepatic CYP2C19 and P-gp by Inhibiting the TLR4/NF-κB Signaling Pathway

To investigate the potential role of PSA in the TLR4 signaling pathway, lentivirus encoding siRNA against TLR4 (siTLR4) was used to selectively reduce TLR4 gene expression in primary hepatocytes. Scramble siRNA was used as a control (siNC) (**Figures 7A,B**).

There were no significant differences in the expression of CYP2C19 or P-gp between the LPS + siTLR4 and LPS + siTLR4+PSA groups (**Figures 7C,I,J**). PSA did not further increase expression of these proteins when TLR4 was silenced. These results imply that PSA affects the NF-κB signaling pathway *via* TLR4.

Comparatively, PSA reduced the relative protein levels of the main molecules in the TLR4/NF-κB signaling pathway. Infecting cells with siTLR4 and exposing them to LPS significantly decreased expression of MyD88, TRAF6 and NF-κB, three key proteins downstream of TLR4 (**Figures 7C,E–G**). Similarly, under the same conditions, MyD88, TRAF6 and NF-κB expression did not significantly decrease in response to PSA alone. More importantly, PSA did not further increase IL-1β expression when TLR4 was silenced. These findings suggested that PSA may affect IL-1β expression *via* the TLR4/NF-κB signaling pathway, thus regulating the expression of metabolic enzymes.

DISCUSSION

The aim of this study was to determine whether the immunomodulatory molecule, PSA, from intestinal *B. fragilis* mitigates individual differences in VRC metabolism among patients with inflammation by regulating hepatic metabolic enzyme activity. Analysis of correlations between CRP and abnormal VRC metabolism in clinical cases revealed that hepatotoxicity and weak VRC metabolic ability significantly increased with CRP levels. Metagenome sequence analysis revealed that high *B. fragilis* abundance was strongly related to the inhibition of pro-inflammatory cytokines such as IL-1β. We

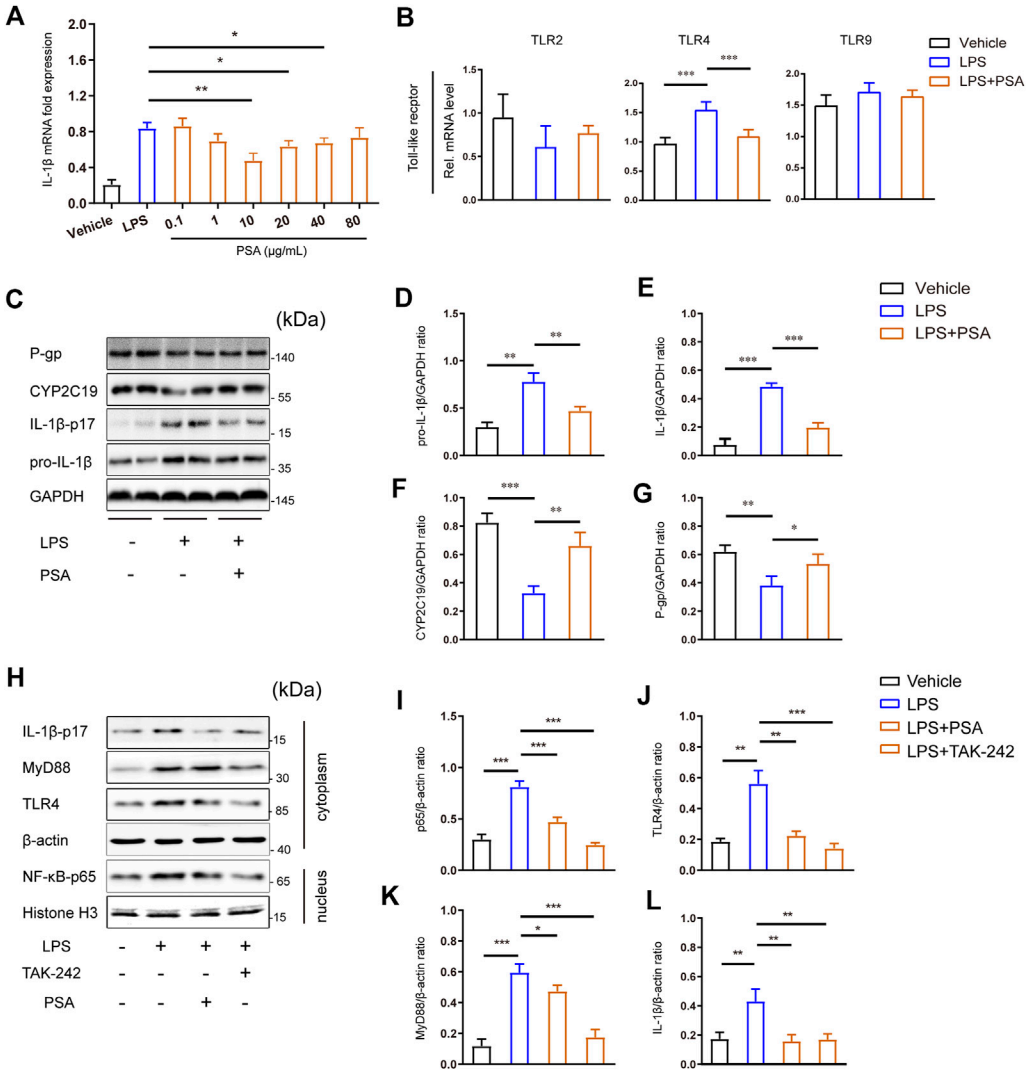


FIGURE 6 | PSA inhibits the secretion of IL-1β may through TLR4 signal pathway. **(A)** Optimum PSA concentration selection based on the mRNA expression levels of IL-1β. **(B)** mRNA levels of key toll-like recepters in the liver (n = 6–12). **(C–G)** Immunblots **(C)** and densitometric analysis of pro-IL-1β **(D)**, IL-1β-p17 **(E)**, CYP2C19 **(F)** and P-gp **(G)** in liver tissue homogenates treated with the vehicle, LPS and LPS + PSA. **(G–K)**, Immunblots **(H)** of key proteins of TLR4 signal transduction and densitometric analysis of these proteins **(I–L)** in primary hepatocyte treated with the vehicle, LPS, LPS + PSA and LPS + TAK-242. Western blot results are representative of three independent experiments. *p < 0.05, **p < 0.01, ***p < 0.001, Unpaired t test.

established a sterile inflammatory disease model to elucidate the mechanism by which *B. fragilis* natural product capsular (PSA) alleviates abnormal VRC metabolism in an inflammatory environment. Molecular studies showed that PSA downregulated the LPS-induced IL-1β expression by inhibiting the TLR4/NF-kB signaling pathway. The former would alter the enzymatic expression of P-450 isoform (CYP2C19), as well as regulate drug transporters such as hepatic P-glycoprotein, ultimately affecting VRC metabolism. **Figure 8** shows the major modes of action identified in this study.

Gene polymorphism may reflect differences in susceptibility to drug treatment between individuals (Mangal et al., 2018; Zhuo et al., 2020). Here, there was still inter-individual variability in VRC concentrations and hepatotoxicity even among patients of the same metabolic type. In the past 2 decades, studies on the effects of treatment-related gastrointestinal changes, protein-binding changes, drug-drug interactions and even food intake on voriconazole metabolism have been reported (Purkins et al., 2003; Hope et al., 2013; Yuan et al., 2020). While it has been shown that these physiological characteristics affect individual differences in response to voriconazole, the influence of inflammatory responses (*eg.*, CRP, IL-6) in combination with these physiological characteristics on the course of disease has not been investigated. Furthermore, there has been no report on the effect of "3 + 7" therapy on voriconazole metabolism, or the effects of daunorubicin and cytarabine on voriconazole metabolism. On the other hand, one study found that intake of whole grains, fiber and healthy fats reduced systemic

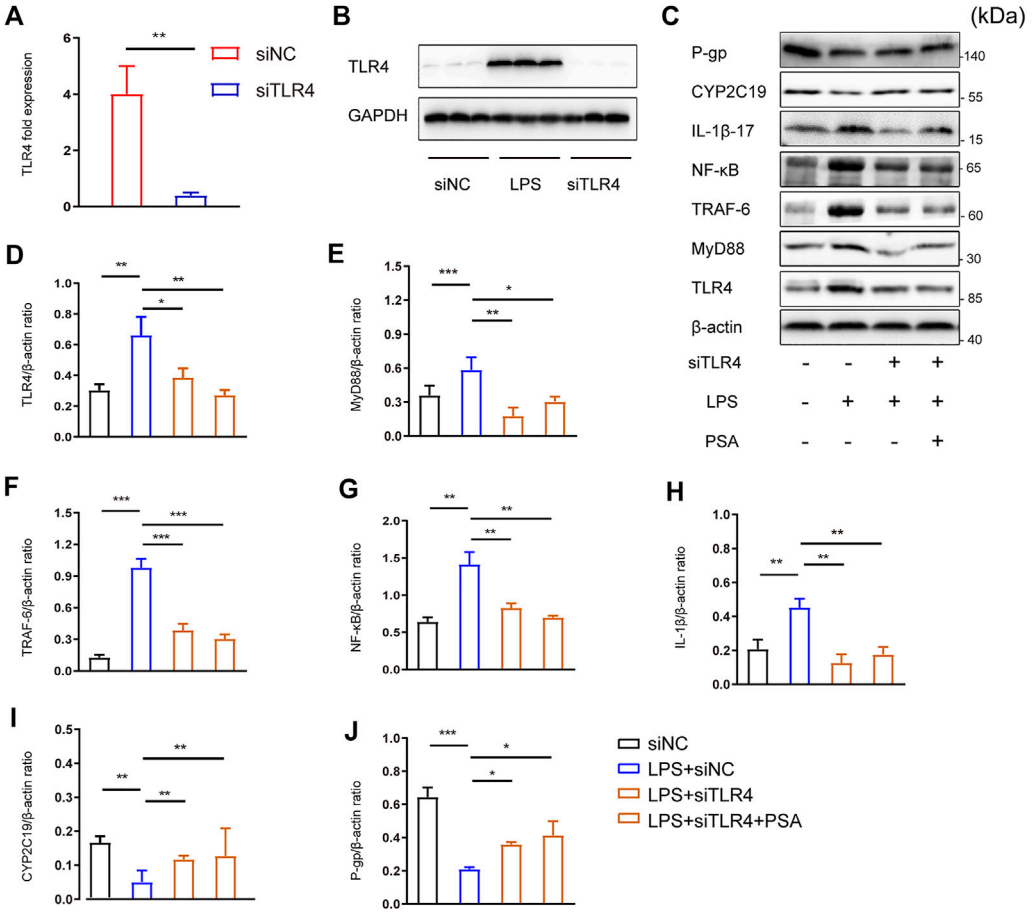


FIGURE 7 | PSA up-regulates the expression of hepatic CYP2C19 and P-gp by inhibiting TLR4/NF-κB signal pathway. **(A,B)** RT-PCR and Western blot analyses were used to evaluate the efficiency of TLR4 knock-down by siRNA (**$p < 0.01$) **(C–H)** Immunblots **(C)** and densitometric analysis of TLR4 **(D)**, MyD88 **(E)**, TRAF6 **(F)**, NF-κB **(G)** and IL-1β **(H)** in primary hepatocytes treated with the vehicle, LPS, LPS + siTLR4 and LPS + PSA **(C,I–J)**, Immunblots **(C)** and densitometric analysis of CYP2C19 **(I)**, and P-gp **(J)** in primary hepatocytes. Western blot results represent three independent experiments. *$p < 0.05$, **$p < 0.01$, ***$p < 0.001$, *t*-test.

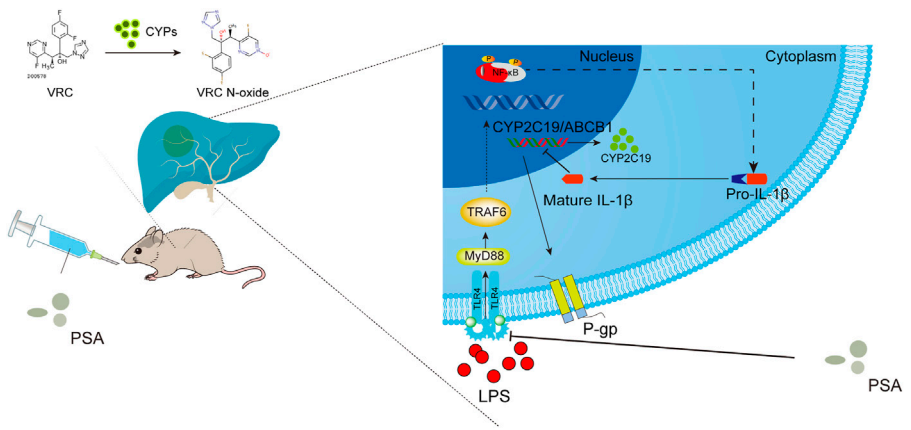


FIGURE 8 | Schematic illustration of PSA regulatory mechanism of VRC metabolism. PSA inhibits the TLR4/NF-κB axis signal transduction pathway induced by LPS, suppressed the secretion of mature IL-1β in the cytoplasm, promotes the expression of liver drug metabolic enzyme (CYP2C19) and transporter (P-gp and its protein coding gene ABCB1), and finally improves the metabolic ability of voriconazole.

inflammation, and therefore represents a promising treatment for a deleterious inflammatory response (Bujtor et al., 2021). A high-quality diet may also alleviate the metabolic disorders associated with voriconazole. Therefore, patients with unconventional or unhealthy eating habits were excluded from this study. Although a prospective study reported that voriconazole metabolism is affected by severe inflammation (Veringa et al., 2017), the present study is the first to report clinical analysis samples from AML patients taking VRC. This has clarified the influences of CRP on individual differences observed in VRC concentrations, furthermore, we focused on a single disease (AML) and a specific treatment ("3 + 7") to develop a microbiome-based therapy.

The liver promotes C-reactive protein production in hepatocytes by excreting circulating triglycerides and free fatty acids and triggering the release of cytokines which play key roles in inflammation (Zhong et al., 2020). The observed diminution in VRC metabolism during inflammation may be explained by the concomitant synthesis of hub targets of the active compounds, namely TNF-α, IL-1β and IL-6 which in turn, alter the expression of specific transcription factors such as NF-κB, leading to a vicious circle of inflammatory response (Zhou et al., 2020). Our results support the concept that disruption of metabolic capacity is accompanied by an increased in liver damage due to inflammation, CRP levels increased with the VRC exposure level. We found that patients prone to ADRs had significantly lower *B. fragilis* abundance than those who were not susceptible to them. Whole-metagenome sequence analysis also showed that *B. fragilis* abundance was negatively correlated with the levels of pro-inflammatory cytokines such as IL-1β. Hence, *B. fragilis* has a beneficial immunomodulatory effect on hosts undergoing VRC therapy. The results of this study are consistent with the concept that *B. fragilis* strongly reverses host susceptibility to inflammatory diseases (Sun et al., 2019).

Clinical findings need to be verified by basic experiments. We developed a sterile inflammatory disease model to elucidate the regulatory events responsible for the regulation of DMET gene expression by PSA. A recent study showed that oral PSA induced intestinal regulatory cells and prevented pro-inflammatory activity (Mazmanian et al., 2008; Ramakrishna et al., 2019). It was also shown to alleviate respiratory tract inflammations, encephalitis, and colitis (Sun et al., 2019). Here, we explored whether PSA would alleviate VRC hepatotoxicity in sterile inflammatory model. As expected, *B. fragilis* natural product ameliorated hepatic lesions and mitigated VRC hepatotoxicity. In the experiment using primary hepatocytes, we found that PSA significantly down-regulated the mRNA expression of TLR4 in toll-like receptor induced by LPS stimulation. Moreover, as shown in **Figure 6C**, with the decrease in IL-1β secretory protein in the PSA treated group, expression of CYP2C19 and P-gp increased. We speculate that *B. fragilis* PSA improves abnormal hepatic VRC metabolism induced by TLR4, which may trigger inflammatory cytokine production.

Notably, IL-1β is a central mediator of innate immunity and inflammation. TLRs induce activation of the NF-κB/MAP kinase (MAPK) signaling pathway, which leads to the transcription of genes encoding inflammatory cytokines (IL-1β and TNF-α), chemokines, cyclooxygenase-2, and inducible NO synthase (Stanke-Labesque et al., 2020). Accumulating evidence indicates that production of IL-1β is closely correlated with TLR4 (Jiménez-Dalmaroni et al., 2016; Phongsisay, 2016). IL-1β is a pleiotropic cytokine with multiple roles in various physiological and pathological conditions (Jesus and Goldbach-Mansky, 2014). We propose that to intervene in LPS-induced abnormal hepatic VRC metabolism, it is desirable to target IL-1β. Administered PSA suppresses TLR-mediated NF-κB activation in the nucleus, by extension, inhibiting IL-1β secretion. **Figure 6H** shows that the expression of IL-1β decreased significantly when the TLR4 signaling pathway was blocked. Of note, compared with the TLR4 signal inhibitor TAK-242, PSA had the same effect on IL-1β inhibition. This further simplies that IL-1β is a downstream inflammatory cytokine in the TLR4/NF-κB signaling pathway.

Moreover, we examined the effect of TLR4 silencing on LPS-induced metabolic inhibition and the prospective molecular mechanisms. Our *in vitro* results indicate that TLR4 deficiency abrogated the increases in LPS-induced TLR4 and TRAF6 expression. Subsequently, TLR4 deficiency attenuated LPS-mediated changes in the proinflammatory cytokine IL-1β. Finally, TLR4 deficiency increased the expression of metabolic enzyme and transporter genes in primary hepatocytes. Similarly, in the siTLR4+PSA group, cellular levels of these proteins were the same as those in the siTLR4 group. These data imply that the inhibitory effect of PSA on inflammation is similar to that of TLR4/NF-κB signal transduction, ultimately inhibiting the secretion of the downstream inflammatory factor IL-1β and promoting the expression of hepatic drug metabolic enzymes.

Nevertheless, the present study had several limitations. First, as PSA is an amphoteric macromolecular compound, it must have some impact on intestinal immune regulation. It has been reported that binding to $TLR2^{+}$ pDC and macrophages, causes tissue-specific regulatory T cells to secrete IL-10 after orally administered PSA (Shen et al., 2012; Dasgupta et al., 2014). Therefore, other correlations between intestinal and hepatic cellular immunity need to be elucidated. Second, to the best of our knowledge, this study is the first to verify the therapeutic action of PSA on hepatocytes' inflammatory response *in vivo*. Hence, the efficacy of PSA should also be validated in other diseases models such as in animal models of AML. Further studies are also warranted to determine whether gut bacteria such as *B. fragilis* that are associated with abnormal hepatic metabolism play roles in immune dysfunction and liver inflammation in the AML pathogenesis.

The present study demonstrated that PSA up-regulates the expression of hepatocellular CYP2C19 and P-gp *via* TLR4-mediated NF-κB transcription and IL-1β expression. Our findings imply that, monitoring of the abundance of *B. fragilis* in feces during voriconazole treatment is recommended during and after severe inflammation, to reduce the risk of adverse reactions to voriconazole.

DATA AVAILABILITY STATEMENT

The datasets generated for this study are available on request to the corresponding authors. The sequencing data in our study has been uploaded in the BioProject: PRJNA707356.

ETHICS STATEMENT

The studies involving human participants were reviewed and approved by the Ethical Committee of Shenzhen Hospital of Southern Medical University (No. NYSZYYEC20180017). The animal study was reviewed and approved by the China and Nanfang Hospital polocies for health and well-being (No. NFYY-2020-73).

AUTHOR CONTRIBUTIONS

XY and LM designed the whole research study. XW and CY performed research. TX, YT, WN, SH, BL, and XZ collated the data and carried out data analyses. XW contributed to drafting the manuscript. CY and LM reviewed and revised the manuscript. All authors have read and approved the final submitted manuscript.

FUNDING

This work was supported by research grants from the National Nature Science Foundation of China (No. 81573681 and No. 81603373), Shenzhen Foundation of Science and Technology (No. JCYJ20170307143952713 and No. JCYJ20190814112205770), Shenzhen Longhua District Science and Technology Innovation Fund Projects (No. 2020036).

ACKNOWLEDGMENTS

Director Zhiqiang Sun and nurses in the Department of Hematology, Shenzhen Hospital, Southern Medical University assist the sample collection of patients. We would like to give our sincere gratitude to all the researchers participating in the whole experimental study and also appreciate all the reviewers for their helpful comments on this paper.

SUPPLEMENTARY MATERIAL

The Supplementary Material for this article can be found online at: https://www.frontiersin.org/articles/10.3389/fphar.2021.663325/full#supplementary-material.

REFERENCES

Adolph, T. E., Grander, C., Moschen, A. R., and Tilg, H. (2018). Liver-microbiome axis in health and disease. *Trends Immunol.* 39, 712–723. doi:10.1016/j.it.2018.05.002

Bujtor, M., Turner, A., Torres, S., Esteban-Gonzalo, L., Pariante, C., and Borsini, A. (2021). Associations of dietary intake on biological markers of inflammation in children and adolescents: a systematic review. *Nutrients* 13, 356–384. doi:10.3390/nu13020356

Dasgupta, S., Erturk-Hasdemir, D., Ochoa-Reparaz, J., Reinecker, H.-C., and Kasper, D. L. (2014). Plasmacytoid dendritic cells mediate anti-inflammatory responses to a gut commensal molecule via both innate and adaptive mechanisms. *Cell Host Microbe.* 15, 413–423. doi:10.1016/j.chom.2014.03.006

Gong, S., Yan, Z., Liu, Z., Niu, M., Fang, H., Li, N., et al. (2019). Intestinal microbiota mediates the susceptibility to polymicrobial sepsis-induced liver injury by granisetron generation in mice. *Hepatology* 69, 1751–1767. doi:10.1002/hep.30361

Hicks, J. K., Quilitz, R. E., Komrokji, R. S., Kubal, T. E., Lancet, J. E., Pasikhova, Y., et al. (2020). Prospective CYP2C19 -guided voriconazole prophylaxis in patients with neutropenic acute myeloid leukemia reduces the incidence of subtherapeutic antifungal plasma concentrations. *Clin. Pharmacol. Ther.* 107, 563–570. doi:10.1002/cpt.1641

Hope, W. W., Vanguilder, M., Donnelly, J. P., Blijlevens, N. M. A., Brüggemann, R. J. M., Jelliffe, R. W., et al. (2013). Software for dosage individualization of voriconazole for immunocompromised patients. *Antimicrob. Agents Chemother.* 57, 1888–1894. doi:10.1128/aac.02025-12

Jesus, A. A., and Goldbach-Mansky, R. (2014). IL-1 blockade in autoinflammatory syndromes. *Annu. Rev. Med.* 65, 223–244. doi:10.1146/annurev-med-061512-150641

Jia, W., Li, H., Zhao, L., and Nicholson, J. K. (2008). Gut microbiota: a potential new territory for drug targeting. *Nat. Rev. Drug Discov.* 7, 123–129. doi:10.1038/nrd2505

Jiménez-Dalmaroni, M. J., Gerswhin, M. E., and Adamopoulos, I. E. (2016). The critical role of toll-like receptors - from microbial recognition to autoimmunity: a comprehensive review. *Autoimmun. Rev.* 15, 1–8. doi:10.1016/j.autrev.2015.08.009

Kawai, T., and Akira, S. (2010). The role of pattern-recognition receptors in innate immunity: update on Toll-like receptors. *Nat. Immunol.* 11, 373–384. doi:10.1038/ni.1863

Keller, R., Klein, M., Thomas, M., Dräger, A., Metzger, U., Templin, M., et al. (2016). Coordinating role of RXRα in downregulating hepatic detoxification during inflammation revealed by fuzzy-logic modeling. *PLoS Comput. Biol.* 12, e1004431. doi:10.1371/journal.pcbi.1004431

Lee, Y. K., and Mazmanian, S. K. (2010). Has the microbiota played a critical role in the evolution of the adaptive immune system?. *Science* 330, 1768–1773. doi:10.1126/science.1195568

Mangal, N., Hamadeh, I. S., Arwood, M. J., Cavallari, L. H., Samant, T. S., Klinker, K. P., et al. (2018). Optimization of voriconazole therapy for the treatment of invasive fungal infections in adults. *Clin. Pharmacol. Ther.* 104, 957–965. doi:10.1002/cpt.1012

Mazmanian, S. K., Round, J. L., and Kasper, D. L. (2008). A microbial symbiosis factor prevents intestinal inflammatory disease. *Nature* 453, 620–625. doi:10.1038/nature07008

Morgan, E. (2009). Impact of infectious and inflammatory disease on cytochrome P450-mediated drug metabolism and pharmacokinetics. *Clin. Pharmacol. Ther.* 85, 434–438. doi:10.1038/clpt.2008.302

Pascual, A., Csajka, C., Buclin, T., Bolay, S., Bille, J., Calandra, T., et al. (2012). Challenging recommended oral and intravenous voriconazole doses for improved efficacy and safety: population pharmacokinetics-based analysis of adult patients with invasive fungal infections. *Clin. Infect. Dis.* 55, 381–390. doi:10.1093/cid/cis437

Phongsisay, V. (2016). The immunobiology of Campylobacter jejuni: innate immunity and autoimmune diseases. *Immunobiology* 221, 535–543. doi:10.1016/j.imbio.2015.12.005

Purkins, L., Wood, N., Kleinermans, D., Greenhalgh, K., and Nichols, D. (2003). Effect of food on the pharmacokinetics of multiple-dose oral voriconazole. *Br. J. Clin. Pharmacol.* 56, 17–23. doi:10.1046/j.1365-2125.2003.01994.x

Ramakrishna, C., Kujawski, M., Chu, H., Li, L., Mazmanian, S., and Cantin, E. (2019). Bacteroides fragilis polysaccharide A induces IL-10 secreting B and

T cells that prevent viral encephalitis. *Nat. Commun.* 10, 2153. doi:10.1038/s41467-019-09884-6

Shen, Y., Torchia, M. L. G., Lawson, G. W., Karp, C. L., Ashwell, J. D., and Mazmanian, S. K. (2012). Outer membrane vesicles of a human commensal mediate immune regulation and disease protection. *Cell Host Microbe.* 12, 509–520. doi:10.1016/j.chom.2012.08.004

Sivan, A., Corrales, L., Hubert, N., Williams, J. B., Aquino-Michaels, K., Earley, Z. M., et al. (2015). Commensal Bifidobacterium promotes antitumor immunity and facilitates anti-PD-L1 efficacy. *Science* 350, 1084–1089. doi:10.1126/science.aac4255

Stanke-Labesque, F., Gautier-Veyret, E., Chhun, S., and Guilhaumou, R. (2020). Inflammation is a major regulator of drug metabolizing enzymes and transporters: consequences for the personalization of drug treatment. *Pharmacol. Ther.* 215, 107627. doi:10.1016/j.pharmthera.2020.107627

Sun, F., Zhang, Q., Zhao, J., Zhang, H., Zhai, Q., and Chen, W. (2019). A potential species of next-generation probiotics? The dark and light sides of Bacteroides fragilis in health. *Food Res. Int.* 126, 108590. doi:10.1016/j.foodres.2019.108590

Tallman, M. S., Wang, E. S., Altman, J. K., Appelbaum, F. R., Bhatt, V. R., Bixby, D., et al. (2019). Acute myeloid leukemia, version 3.2019, NCCN clinical practice guidelines in oncology. *J. Natl. Compr. Canc. Ne.* 17, 721–749. doi:10.6004/jnccn.2019.0028

Taur, Y., Xavier, J. B., Lipuma, L., Ubeda, C., Goldberg, J., Gobourne, A., et al. (2012). Intestinal domination and the risk of bacteremia in patients undergoing allogeneic hematopoietic stem cell transplantation. *Clin. Infect. Dis.* 55, 905–914. doi:10.1093/cid/cis580

Taylor, M., Flannigan, K., Rahim, H., Mohamud, A., Lewis, I., Hirota, S., et al. (2019). Vancomycin relieves mycophenolate mofetil-induced gastrointestinal toxicity by eliminating gut bacterial β-glucuronidase activity. *Sci. Adv.* 5, eaax2358. doi:10.1126/sciadv.aax2358

Veringa, A., Ter Avest, M., Span, L. F. R., van den Heuvel, E. R., Touw, D. J., Zijlstra, J. G., et al. (2017). Voriconazole metabolism is influenced by severe inflammation: a prospective study. *J. Antimicrob. Chemother.* 72, 261–267. doi:10.1093/jac/dkw349

Wang, X., Zhao, J., Wen, T., Liao, X., and Luo, B. (2020). Predictive value of FMO3 variants on plasma disposition and adverse reactions of oral voriconazole in febrile neutropenia. *Pharmacology* 106 (3-4), 202–210. doi:10.1159/000510327

Yuan, Z., Qiao, C., Yang, Z., Yu, L., Sun, L., Qian, Y., et al. (2020). The impact of plasma protein binding characteristics and unbound concentration of voriconazole on its adverse drug reactions. *Front. Pharmacol.* 11, 505–515. doi:10.3389/fphar.2020.00505

Zhong, W., Gummesson, A., Tebani, A., Karlsson, M., Hong, M., Schwenk, J., et al. (2020). Whole-genome sequence association analysis of blood proteins in a longitudinal wellness cohort. *Genome Med.* 12, 53–68. doi:10.1186/s13073-020-00755-0

Zhou, S., Ai, Z., Li, W., You, P., Wu, C., Li, L., et al. (2020). Deciphering the pharmacological mechanisms of taohe-chengqi decoction extract against renal fibrosis through integrating Network pharmacology and experimental validation in vitro and in vivo. *Front. Pharmacol.* 11, 425–442. 10.3389/fphar.2020.00425]

Zhuo, Z., Zhou, C., Fang, Y., Zhu, J., Lu, H., Zhou, H., et al. (2020). Correlation between the genetic variants of base excision repair (BER) pathway genes and neuroblastoma susceptibility in eastern Chinese children. *Cancer Commun.* 40, 641–646. doi:10.1002/cac2.12088

Zimmermann, M., Zimmermann-Kogadeeva, M., Wegmann, R., and Goodman, A. (2019). Separating host and microbiome contributions to drug pharmacokinetics and toxicity. *Science* 363, 1–16. doi:10.1126/science.aat9931

Conflict of Interest: The authors declare that the research was conducted in the absence of any commercial or financial relationships that could be construed as a potential conflict of interest.

Copyright © 2021 Wang, Ye, Xun, Mo, Tong, Ni, Huang, Liu, Zhan and Yang. This is an open-access article distributed under the terms of the Creative Commons Attribution License (CC BY). The use, distribution or reproduction in other forums is permitted, provided the original author(s) and the copyright owner(s) are credited and that the original publication in this journal is cited, in accordance with accepted academic practice. No use, distribution or reproduction is permitted which does not comply with these terms.

frontiers in Pharmacology

ORIGINAL RESEARCH
published: 23 April 2021
doi: 10.3389/fphar.2021.656272

Hydroxytyrosol Acetate Inhibits Vascular Endothelial Cell Pyroptosis via the HDAC11 Signaling Pathway in Atherosclerosis

Feng Yao[1†], Zhen Jin[2†], Xiaohan Lv[2], Zihan Zheng[2], Hongqian Gao[2], Ying Deng[2], Yizhen Liu[2], Lifang Chen[3,4], Weirong Wang[3], Jianyu He[2], Jianli Gu[2,5] and Rong Lin[2]**

[1]School of Pharmacy, Xi'an Jiaotong University Health Science Center, Xi'an, China, [2]Department of Pharmacology, Xi'an Jiaotong University Health Science Center, Xi'an, China, [3]Department of Medical Laboratory Animal Science, Xi'an Jiaotong University Health Science Center, Xi'an, China, [4]Department of Pathology, Xi'an Jiaotong University Health Science Center, Xi'an, China, [5]Xi'an NO.3 Hospital, Xi'an, China

OPEN ACCESS

Edited by:
Zhaocheng Ma,
Huazhong Agricultural University, China

Reviewed by:
Cinzia Parolini,
University of Milan, Italy
Hartmut Kuhn,
Charité–Universitätsmedizin Berlin, Germany

***Correspondence:**
Rong Lin
linrong@xjtu.edu.cn
Jianli Gu
gjllz45@163.com

[†]These authors have contributed equally to this work

Specialty section:
This article was submitted to Inflammation Pharmacology, a section of the journal Frontiers in Pharmacology

Received: 20 January 2021
Accepted: 23 March 2021
Published: 23 April 2021

Citation:
Yao F, Jin Z, Lv X, Zheng Z, Gao H, Deng Y, Liu Y, Chen L, Wang W, He J, Gu J and Lin R (2021) Hydroxytyrosol Acetate Inhibits Vascular Endothelial Cell Pyroptosis via the HDAC11 Signaling Pathway in Atherosclerosis. Front. Pharmacol. 12:656272. doi: 10.3389/fphar.2021.656272

Hydroxytyrosol acetate (HT-AC), a natural polyphenolic compound in olive oil, exerts an anti-inflammatory effect in cardiovascular diseases (CVDs). Pyroptosis is a newly discovered form of programmed inflammatory cell death and is suggested to be involved in the atherosclerosis (AS) process. However, the effect of HT-AC on vascular endothelial cell pyroptosis remains unknown. Thus, we aimed to investigate the effect of HT-AC on vascular endothelial cell pyroptosis in AS and related signaling pathways. *In vivo* studies showed that HT-AC alleviated the formation of atherosclerotic lesions and inhibited pyroptosis in the aortic intima of ApoE$^{-/-}$ mice fed a high-fat diet (HFD) for 12 weeks. *In vitro*, we found that HT-AC treatment of human umbilical vein endothelial cells (HUVECs) alleviated tumor necrosis factor-alpha (TNF-α)-induced pyroptosis by decreasing the number of PI positive cells, decreasing the enhanced protein expressions of activated caspase-1 and gasdermin D (GSDMD), as well as by decreasing the release of pro-inflammatory interleukin (IL)-1β and IL-6. Besides, HT-AC down-regulated HDAC11 expression in the aortic intima of HFD-fed ApoE$^{-/-}$ mice and TNF-α-stimulated HUVECs. To determine the underlying mechanism of action, molecular docking and drug affinity responsive target stability (DARTS) were utilized to identify whether HDAC11 protein is a target of HT-AC. The molecular docking result showed good compatibility between HT-AC and HDAC11. DARTS study's result showed that HDAC11 protein may be a target of HT-AC. Further study demonstrated that knockdown of HDAC11 augmented the inhibition of HT-AC on pyroptosis in TNF-α-stimulated HUVECs. These findings indicate that HT-AC might prevent vascular endothelial pyroptosis through down-regulation of HDAC11 related signaling pathway in AS.

Keywords: hydroxytyrosol acetate, atherosclerosis, HDAC11, pyroptosis, vascular endothelial cells

INTRODUCTION

Atherosclerosis (AS) is a chronic inflammatory disease that is initiated by endothelial dysfunction and structural alterations and involves chronic inflammation of the vascular wall (Weber and Noels, 2011). Previous studies have shown that endothelial cell death is a crucial and initial stage in the process of AS (Wu et al., 2018; Xing et al., 2020). Pyroptosis is a newly discovered form of programmed inflammatory cell death differing from apoptosis and necrosis and suggested to be involved in AS process, which features gasdermin family mediated pore formation on the plasma membrane as well as the release of pro-inflammatory intracellular contents including interleukin (IL)-1β, IL-18 and High Mobility Group Box 1 (HMGB1) (Jia et al., 2019; Wang et al., 2020). Thus, the inhibition of endothelial cell death especially pyroptosis is of great significance to prevent AS. Hydroxytyrosol acetate (HT-AC) is the polyphenolic compound, which is present in the olive oil of the fruit and leaf of the olive (Lisete-Torres et al., 2012). Olive oil phenolic compounds can be used to prevent and treat cardiovascular diseases (CVDs) (Bulotta et al., 2014). Accumulating evidence indicates that HT-AC has antioxidant (Gordon et al., 2001), antiplatelet aggregating (González-Correa et al., 2008), and anti-inflammatory activities (Rosillo et al., 2015). In our previous study, we demonstrated that HT-AC had an anti-inflammatory effect in hypercholesterolemic mice and tumor necrosis factor-alpha (TNF-α)-stimulated human umbilical vein endothelial cells (HUVECs) (Yao et al., 2019). However, the underlying mechanism of HT-AC on inflammation is still under investigation. Since pyroptosis is involved in the inflammatory process of AS (Chang et al., 2013), we hypothesize that HT-AC might play a role in inflammation by regulating pyroptosis in endothelial cells. Thereby, we conducted this study to prove it.

Histone deacetylase 11 (HDAC11) is a class IV histone deacetylase, which is one of the most recently identified members of the HDAC family (Nutsford et al., 2019). HDAC11 has been shown to play a role in a variety of diseases including kidney ischemia and reperfusion (I/R) injury (Kim et al., 2013), cancer (Yue et al., 2020) and CVDs (Fan et al., 2018; Yuan et al., 2018). A study showed that HDAC11 knockout ($HDAC11^{-/-}$) attenuated apoptosis, oxidative stress and inflammation in the heart of fructose-fed mice (Fan et al., 2018). Another study demonstrated that HDAC11 compromised the vascular endothelial barrier function by suppressing the expression of Ve-cadherin (Zhang and Ge, 2017). Besides, it has been reported that treatment of the HDAC11 inhibitor attenuated vascular injury in mice (Zhou et al., 2017). These studies suggested that HDAC11 was involved in CVDs. However, whether the regulation of HT-AC on the vascular endothelial cell pyroptosis is mediated by HDAC11 remains unknown.

Therefore, in the present study, we first determined the effects of HT-AC on the formation of atherosclerotic lesions and pyroptosis in the aortic intima of high-fat diet (HFD)-fed $ApoE^{-/-}$ mice for 12 weeks. Then, we examined the effect of HT-AC on pyroptosis in TNF-α-stimulated HUVECs and whether this effect of HT-AC was mediated by HDAC11 to elucidate its antiatherogenic mechanism.

MATERIALS AND METHODS

Materials

HT-AC (purity>98%) was purchased from APP-Chem Bio (Xi'an, China). Oil Red O staining kit and propidium iodide (PI) solution were purchased from Solarbio (Beijing, China). Mouse TNF-α and IL-1β enzyme-linked immunosorbent assay (ELISA) kit and human IL-6 ELISA kit were products of TBhealthcare (Foshan, China). TNF-α was obtained from PeproTech (Rocky Hill, New Jersey, United States of America). A CCK8 assay kit was obtained from biosharp (Hefei, China). Human IL-1β ELISA, lactate dehydrogenase (LDH) cytotoxicity assay kit, caspase-1 activity assay kit, 4′, 6-diamidino-2-phenylindole (DAPI), and Hoechchst 33342 staining solution for live cells were purchased from Beyotime (Haimen, China). Pro-caspase-1 and cleaved caspase-1 (caspase-1 p20) antibodies were obtained from Wanleibio (Shenyang, China). Antibodies against HDAC11 and CD31 were ordered from Abcam (Cambridge, Massachusetts, United States of America). Gasdermin D (GSDMD) antibody, cleaved GSDMD (Asp275) (GSDMD-N) rabbit mAb, mouse anti-β-actin, goat anti-mouse and anti-rabbit IgG-HRP antibodies, and goat anti-rabbit IgG (H + L) were purchased from Cell Signaling Technology Inc. (Beverly, Massachusetts, United States of America). Protease inhibitor cocktail and pronase were products of Roche (Mannheim, Germany). The Bradford protein assay kit was obtained from Pierce (Rockford, Illinois, United States of America). Lipofectamine 2000 transfection reagent and TRIzol reagent were purchased from Invitrogen (Carlsbad, California, United States of America). All-in-One cDNA Synthesis SuperMix and 2 × SYBR qPCR Master Mix were purchased from Bimake (Houston, Texas, United States of America). Fetal bovine serum (FBS) was obtained from Gibco (Grand Island, New York, United States of America). All these reagents were of analytical grade unless otherwise specified.

Animals and Establishment of Atherosclerosis Model

$ApoE^{-/-}$ mice in the C57/BL6 background were purchased from The Jackson Laboratory (Bar Harbor, ME). Eight-week-old male $ApoE^{-/-}$ mice were housed in a SPF facility (12 h light/dark cycle). The mice were randomly divided into four groups (ten animals each): the normal diet (ND) group, the normal diet group treated with HT-AC (ND + HT-AC), the HFD group, and the HFD group treated with HT-AC (HFD + HT-AC). The animals of the HFD group were maintained on diet with a Western diet consisting of 21% fat and 0.15% cholesterol (Huafukang, Beijing, China) for 12 weeks to induce atherosclerosis. HT-AC was dissolved in sterile saline, then mice were gavaged with HT-AC at a dosage of 20 mg/kg/day for 12 weeks. After 12 weeks of treatment, all mice were fasted overnight (12 h), and then

anesthetized with intraperitoneal 50 mg/kg of sodium pentobarbital and sacrificed.

Immunohistology of Atherosclerotic Lesions

The aortic root along with the basal portion of the heart was fixed with 4% paraformaldehyde, followed by embedding in optimum cutting temperature (OCT) compound (SAKURA, United States of America), and was then cut cross-sectionally into 7 μm-thick sections. Hematoxylin and eosin (H&E) staining and Oil red O staining were performed to show atherosclerotic lesions of the aortic root and the lipid deposition of atherosclerotic lesions. Besides, immunostaining was performed on the aortic root for the expressions of cleaved caspase-1 and HDAC11. CD31 was used as an endothelial marker. Images were captured using a fluorescence microscope (Olympus TL4, Japan).

Cell Culture and Treatment

A human umbilical vein endothelial cell line (CRL-1730 cells) was obtained from the American Type Culture Collection (ATCC, Manassas, United States of America). In brief, HUVECs were grown in DMEM/F-12 medium supplemented with 10% FBS and 100 U/ml penicillin-streptomycin in a humidified atmosphere of 5% CO_2 at 37°C. When cells were grown to confluence, the culture medium was replaced with a serum-free medium for 24 h of incubation prior to experimental use. To determine whether HT-AC inhibited endothelial cell pyroptosis, cells were pretreated with different concentrations of HT-AC (25, 50 and 100 μmol/L) for 1 h and then incubated with TNF-α (40 ng/ml) for 12 h. To further detect whether the effect of HT-AC on pyroptosis was mediated by HDAC11, HDAC11 small interfering RNA (siRNA) was used. HDAC11 siRNA and negative control (NC) siRNA were chemically synthesized by Shanghai GenePharma Corporation (SGC, China). HUVECs were transfected with HDAC11 siRNA or NC siRNA using Lipofectamine 2000 according to the manufacturer's instructions. After 48 h, cells were pretreated with HT-AC (50 μmol/L) for 1 h and then incubated with TNF-α (40 ng/ml) for 12 h. HT-AC was dissolved in sterile saline.

Western Blotting

Total protein was extracted from the snap-frozen thoracic aorta of mice (20–30 mg) and HUVECs with RIPA lysis buffer containing protease inhibitor cocktail. The protein concentrations were determined by using the Bradford protein assay kit. Equal amounts of protein lysates were separated by SDS-PAGE gels and transferred to polyvinylidene difluoride membranes followed by a block with 5% skimmed milk at room temperature for 2–3 h. Subsequently, the membranes were incubated with primary antibodies against pro-caspase-1 (diluted 1:1,000), cleaved caspase-1 (diluted 1:1,000), GSDMD (diluted 1:1,000), GSDMD-N (diluted 1:1,000), HDAC11 (diluted 1:200) or β-actin (diluted 1:5,000) at 4°C overnight. After washing three times with tris-buffered saline and Tween 20 (TBST), the membranes were incubated with goat anti-rabbit IgG-HRP antibody (diluted 1:5,000) or goat anti-mouse IgG-HRP antibody (diluted 1:5,000) for 1–2 h. Then the membranes were washed three times with TBST and the enhanced chemiluminescent substrate was used for detection. The intensity of protein bands was analyzed by Lane 1D software (Sage Creation Science Co., China).

Cytokine Analysis by ELISA

Blood samples were obtained by penetrating the retro-orbital sinus in mice, and the serum was separated by centrifugation at 3,000 rpm for 15 min at 4°C. All samples were stored at −80°C until analysis. According to the manufacturer's instructions, concentrations of TNF-α and IL-1β in the serum of $ApoE^{-/-}$ mice and concentrations of IL-1β and IL-6 in cellular supernatant of HUVECs were detected by ELISA assay.

Cell Viability Assay

The cell viability was determined by a CCK8 assay. HUVECs were seeded in 96-well plates in complete medium and treated with different concentrations of HT-AC (12.5, 25, 50, 100 and 200 μmol/L) for 13 h, subsequently treated with 10 μl CCK8 reagent for 4 h. And then absorbance measurements were taken at 450 nm using a microplate reader (Thermo Fisher, United States of America).

Caspase-1 Activity Analysis

HUVECs were seeded onto a 6-well microplate with three replicate wells for each condition and cultured overnight to allow cells to attach. After the indicated treatments, cells were collected and caspase-1 activity was assayed using the caspase-1 activity assay kit according to the manufacturer's instructions.

Measurement of LDH Release

HUVECs were plated in 48-well plates. Cell supernatants were collected and cellular debris was removed by centrifugation at 1,500 rpm for 5 min. Supernatant LDH levels were measured using the cytotoxicity detection LDH kit according to the manufacturer's instruction.

Hoechst 33342/PI Fluorescent Staining

Double-fluorescent staining with Hoechst 33342 and PI was used to assess the formation of membrane pores during pyroptosis. The cells were stained with Hoechst 33342 staining solution for live cells and 2 μg/ml PI for 20 min in a humidified atmosphere of 5% CO_2 at 37°C. Then the cells were washed three times with PBS. The fluorescence of Hoechst 33,342 was detected by a fluorescence microscope (Olympus TL4, Japan) at the excitation wavelength of 346 nm and the emission wavelength of 460 nm, and the fluorescence of PI was detected at the excitation wavelength of 535 nm and the emission wavelength of 615 nm.

Immunofluorescence

The HUVECs were fixed with 4% paraformaldehyde for 30 min, subsequently permeabilized with 0.3% Triton X-100 for an additional 30 min, and then blocked with normal goat serum for 1 h at room temperature. To determine the effect of HT-AC on HDAC11 expression and localization, the samples were

incubated with anti-HDAC11 antibody (diluted 1:100) overnight at 4°C, followed by incubation with a goat anti-rabbit IgG (H + L) antibody (diluted 1:200) for 2 h at room temperature. Nuclei were stained with DAPI (1 μg/ml) dye and observed by a fluorescence microscope (Olympus TL4, Japan).

RNA Extraction and Real-Time PCR

RNA was extracted from the thoracic aorta of mice and cultured HUVECs using TRIzol reagent. RNA quality and integrity were detected using a NanoDrop ND1000 and determined via the A260/A280 ratio. And then the RNA was reversely transcripted to cDNA using All-in-One cDNA Synthesis SuperMix following the manufacturer's instructions. Quantitative real-time PCR was performed with 2 × SYBR Green qPCR Master Mix by StepOnePlus™ Real-Time PCR System (Thermo Fisher, Massachusetts, United States of America). Relative changes in mRNA levels were analyzed by the ΔΔCT method using GAPDH as a control. The sequences of primer pairs are as follows:

Mouse HDAC11: forward 5′-GCCCTGGATCTGCTCCAACTAC-3′,
reverse 5′-AACTGGTGACTCTGGCATCCTC-3';
Mouse GAPDH: forward 5′-TGTGTCCGTCGTGGATCTGA-3′,
reverse 5′-TTGCTGTTGAAGTCGCAGGAG-3';
Human HDAC11: forward 5′-GATGTCTACAACCGCCACATCTACC-3′,
reverse 5′- CCTGCATTGTATACCACCACGTC-3';
Human GAPDH: forward 5′-GGAGCGAGATCCCTCCAAAAT-3′,
reverse 5′-GGCTGTTGTCATACTTCTCATGG-3'.

HDAC11 Protein Homology Modeling and Molecular Docking

The amino acid sequence of HDAC11 was retrieved from the protein database of NCBI (NP_079103.2). The crystal structure of human HDAC11 was built and validated using a fully automated protein structure homology-modeling tool at the Swiss-Model server (http://swissmodel.expasy.org). It has been shown that a good quality model would be expected to have over 90% in the most favored regions (Laskowski et al., 1996). The Surflex-Dock module of SYBYL X-2.0 (Tripos Inc., Saint Louis, MO, United States of America) was performed for the docking calculations with default parameters.

Drug Affinity Responsive Target Stability (DARTS) Analysis

Here, DARTS methods were used to identify whether HDAC11 protein is a target of HT-AC. Total protein was extracted from HUVECs with M-PER reagent (Thermo Scientific) containing a 1× protease inhibitor cocktail. The protein concentration of cell lysate was determined by using the Bradford protein assay kit. Then cell lysate was divided into identical aliquots of 50 μl, which was incubated with different concentrations of HT-AC (10, 100 and 1,000 μmol/L) or sterile saline for 2 h at 4°C. After incubation with the HT-AC is complete, each sample added 2 μl pronase solutions at different mass ratios of pronase to protein (1:100, 1:500, 1:1,000, 1:2,500 and 1:5,000). Then each sample was incubated with pronase for 20 min at room temperature, and each digestion reaction was stopped by adding 2 μl of 20 × protease inhibitor cocktail on ice for 10 min. Then the samples were subjected to SDS–PAGE for coomassie staining and Western blotting. Anti-HDAC11 (diluted 1:200) and anti-β-actin (diluted 1:5,000) antibodies were used as the primary antibodies.

Statistical Analysis

All quantitative data are presented as the mean ± SEM from three independent experiments. Statistical analysis was undertaken using GraphPad Prism (GraphPad Software, La Jolla, CA, United States of America). Multiple comparisons were assessed by one-way analysis of variance. Statistical significance was ascribed to a p value <0.05.

RESULTS

HT-AC Attenuated the Formation of Atherosclerotic Lesions in ApoE$^{-/-}$ Mice

To examine the possible impact of HT-AC on AS, we performed H&E and Oil Red O staining in histological sections of the aortic sinus of the ApoE$^{-/-}$ mice. Our results showed that severe atherosclerosis was successfully induced in our model, while 12 weeks of HT-AC treatment decreased the lipid deposition(**Figure 1A**) and plaque formation in ApoE$^{-/-}$ mice fed with HFD (**Figures 1B,C**). By comparison, no significant changes were noticed in the mice treated with ND. These results suggested that HT-AC attenuated the formation of atherosclerotic lesions in HFD-fed ApoE$^{-/-}$ mice.

HT-AC Inhibited Pyroptosis in the Aortic Intima of HFD-Fed ApoE$^{-/-}$ Mice

Compared with the ND group, immunofluorescent double staining of the aortic sinus of cleaved caspase-1 and CD31 (an endothelial cell marker) revealed that caspase-1 activation (cleaved caspase-1 intensity) was significantly increased in the HFD group, while HT-AC significantly suppressed such an increase (**Figure 2A**). Western blotting results further showed that the protein expressions of cleaved caspase-1, GSDMD and GSDMD-N in the thoracic aorta of HFD-fed ApoE$^{-/-}$ mice were significantly increased as compared with the ND group, while HT-AC significantly suppressed the enhanced protein expressions of cleaved caspase-1, GSDMD and GSDMD-N (**Figures 2B-E**). In addition, concentrations of TNF-α and IL-1β in the serum of HFD-fed ApoE$^{-/-}$ mice were significantly increased as compared with the ND group, while HT-AC significantly suppressed concentrations of TNF-α and IL-1β in the serum of HFD-fed ApoE$^{-/-}$mice (**Figures 2F,G**). Our findings suggested that HT-AC suppressed pyroptosis in the aortic intima of HFD-fed ApoE$^{-/-}$ mice.

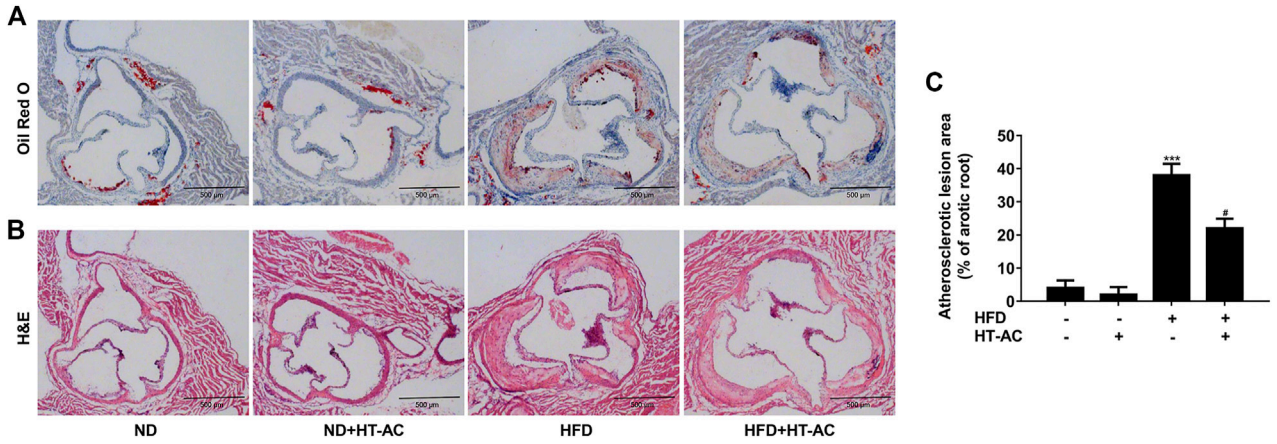


FIGURE 1 | HT-AC attenuated the formation of atherosclerotic lesions in ApoE$^{-/-}$ mice. ApoE$^{-/-}$ mice with ND or HFD with or without HT-AC treatment (20 mg/kg/day) for 12 weeks **(A)** Representative images showing the lipid deposition of aortic root sections with Oil red O staining, ×100 **(B)** Representative images showing the atherosclerotic lesions of aortic root sections with H&E staining, ×100. Scale bar indicates 500 μm **(C)** The atherosclerotic lesion area of aortic root sections was analyzed. ***$p < 0.001$ vs. ND group; $^{\#}p < 0.05$ vs. HFD group. Results are expressed as mean ± SEM ($n = 10$).

HT-AC Inhibited TNF-α-Induced Pyroptosis in HUVECs

The cell viability was measured after incubation with various concentrations of HT-AC (12.5, 25, 50, 100 and 200 μmol/L) for 13 h using the CCK8 assay. Consistent with our previous report, we found that there was no significant difference in the cell viability of HT-AC groups for different concentrations as compared with the control group (**Figure 3A**). To further investigate the effect of HT-AC on pyroptosis, the HUVECs were pretreated with different concentrations of HT-AC (25, 50 and 100 μmol/L) for 1 h and then stimulated with TNF-α (40 ng/ml) for 12 h. We found that TNF-α increased the protein expressions of activated caspase-1 and caspase-1 activity. However, HT-AC significantly decreased the protein expressions of activated caspase-1 and caspase-1 activity compared with the TNF-α group (**Figures 3B-D**). HT-AC also significantly decreased the protein expressions of GSDMD (**Figure 3E**) and GSDMD-N (**Figure 3F**) compared with the TNF-α group. Moreover, HT-AC significantly suppressed TNF-α-induced the release of pro-inflammatory IL-1β (**Figure 3G**) and IL-6 (**Figure 3H**). We further found that HT-AC significantly decreased TNF-α-induced pore formation and membrane rupture by decreasing the release of LDH (**Figure 3I**) and the number of PI positive cells (**Figure 3J**).

HT-AC Down-Regulated HDAC11 Expression in the Aortic Intima of HFD-Fed ApoE$^{-/-}$ Mice and TNF-α-Stimulated HUVECs

To investigate the effect of HT-AC on HDAC11 expression, we examined the expression of HDAC11 in the aortic intima of ApoE$^{-/-}$ mice by immunofluorescent double staining of the aortic sinus of HDAC11 and CD31. The results showed that HDAC11 protein expression in the aortic intima of HFD-fed ApoE$^{-/-}$ mice were increased as compared with the ND group, while treatment with HT-AC decreased HDAC11 protein expression (**Figure 4A**). We further examined the expression of HDAC11 in the aorta of ApoE$^{-/-}$ mice by Western blotting and quantitative real-time PCR. We found that HDAC11 protein and mRNA expressions in the aorta of HFD-fed ApoE$^{-/-}$ mice were significantly increased as compared with the ND group, while HT-AC significantly decreased HDAC11 protein and mRNA expressions compared with the HFD group (**Figures 4B,C**).

To further confirm whether the HDAC11 signaling pathway was involved in the regulatory effect of HT-AC on pyroptosis, HUVECs were pretreated with HT-AC for 1 h and then stimulated with TNF-α (40 ng/ml) for 12 h. The expression of HDAC11 was determined by immunofluorescence, Western blotting and quantitative real-time PCR. The results showed that HT-AC decreased HDAC11 protein and mRNA expressions compared with the TNF-α group (**Figures 4D-F**).

HT-AC May Target HDAC11

Given our findings that HT-AC down-regulated HDAC11 expression in the aortic intima of HFD-fed ApoE$^{-/-}$ mice and TNF-stimulated HUVECs, we explored the possibility of whether HT-AC targets HDAC11. Here, we evaluated the ability of HT-AC to bind to the HDAC11 ligand-binding domain to activate HDAC11 by molecular docking. The three-dimensional structure of human HDAC11 was built by homology-modeling (**Figure 5A**). Ramachandran plot analysis showed that the amino acid residue of the HDAC11 model had 91.27% in the most favored regions (**Figure 5B**). The molecular docking result showed good compatibility between HT-AC and HDAC11, indicating that HT-AC might act through HDAC11 (**Figures 5C,D**). DARTS methods were used to identify the potential molecular targets of HT-AC. We added pronase solutions at different mass ratios of pronase to protein (1:100, 1:500, 1:1,000, 1:2,500 and 1:5,000) to the experiment, the results showed that the 1:1,000 pronase to protein mass ratio was most suitable (**Figure 5E**). Further analysis revealed one visible differential band between HT-AC-treated HUVECs and the control group about 35–48 kDa molecular weight (**Figure 5F**). We also

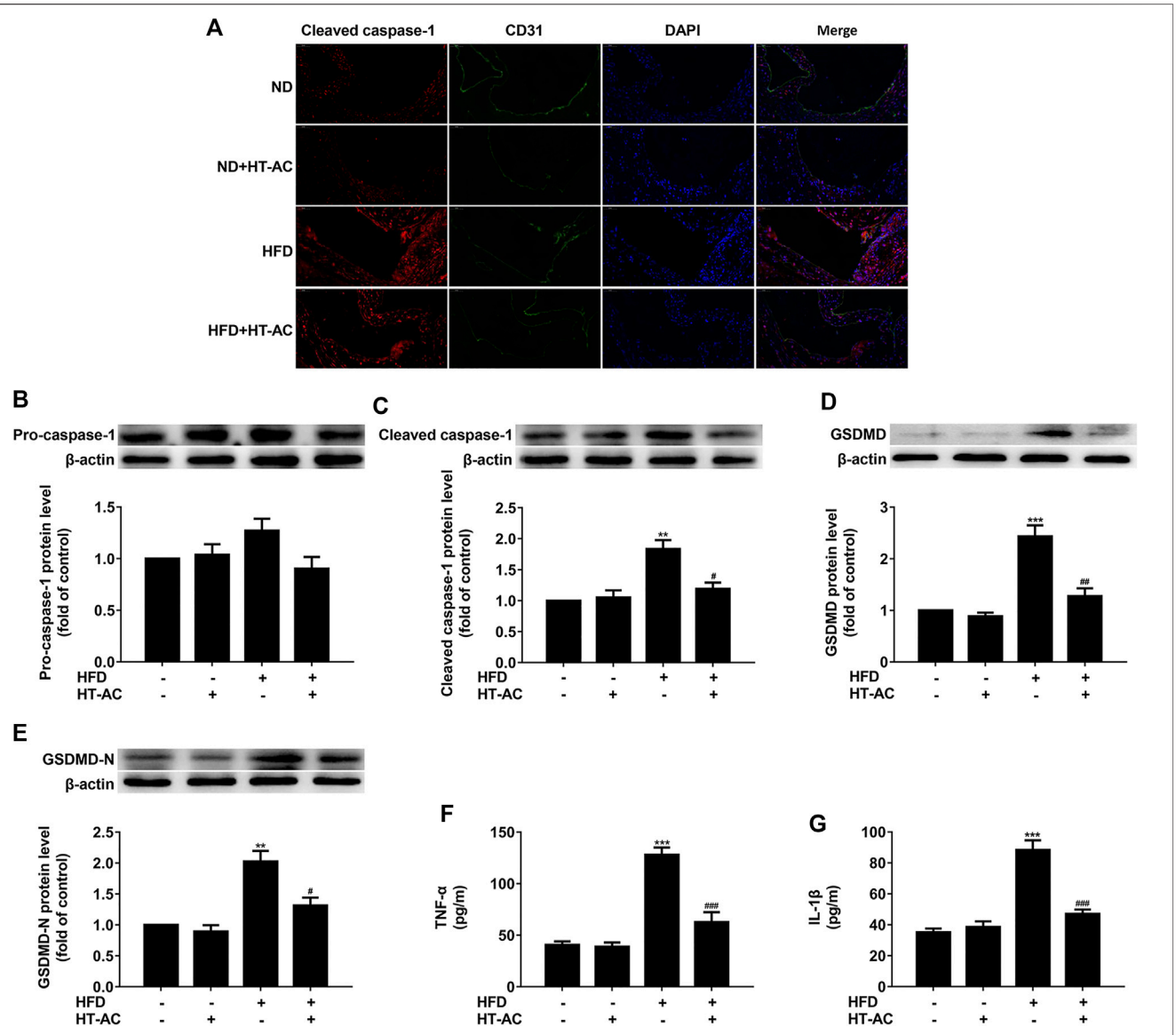


FIGURE 2 | HT-AC inhibited pyroptosis in the aortic intima of HFD-fed ApoE$^{-/-}$ mice **(A)** Frozen sections of aortic root were stained for activated caspase-1 (cleaved caspase-1) (stained in red). The nuclei were stained blue with DAPI. CD31 (stained in green) was used as an endothelial marker. Scale bar indicates 50 μm **(B–E)** The protein expressions of pro-caspase-1, cleaved caspase-1, GSDMD and GSDMD-N were determined by Western blotting **(F,G)** The concentrations of TNF-α and IL-1β in the serum were determined by ELISA. $^{**}p < 0.01$, $^{***}p < 0.001$ vs. ND group; $^{\#}p < 0.05$, $^{\#\#}p < 0.01$, $^{\#\#\#}p < 0.001$ vs. HFD group. Results are expressed as mean ± SEM (n = 10).

examined the protein expression of HDAC11 in HUVECs after treatment with HT-AC by Western blotting. Our results showed that various concentrations of HT-AC (10, 100 and 1,000 μmol/L) treatment of HUVECs prevented enzymatic digestion of HDAC11 protein compared with vehicle-treated pronase (**Figure 5G**).

HT-AC Inhibited Pyroptosis Through HDAC11 in TNF-α-Induced HUVECs

Given our findings that HT-AC down-regulated HDAC11 expression and HT-AC might target HDAC11, we further explored the possibility of whether the inhibitory effect of HT-AC on pyroptosis is related to HDAC11. HUVECs were transfected with HDAC11 siRNA or NC siRNA for 48 h, and then the protein expression of HDAC11 was examined by Western blotting. HDAC11 protein expression was significantly declined and the knockdown efficiency of HDAC11 was 63% (**Figure 6A**). Then the HUVECs transfected with HDAC11 siRNA were pretreated with HT-AC (50 μmol/L) before stimulation with TNF-α (40 ng/ml). The protein expressions of pro-caspase-1, cleaved caspase-1 were detected by Western blotting, and caspase-1 activity was assayed using the caspase-1 activity assay kit. The results showed that knockdown of HDAC11 increased the inhibitory effects of

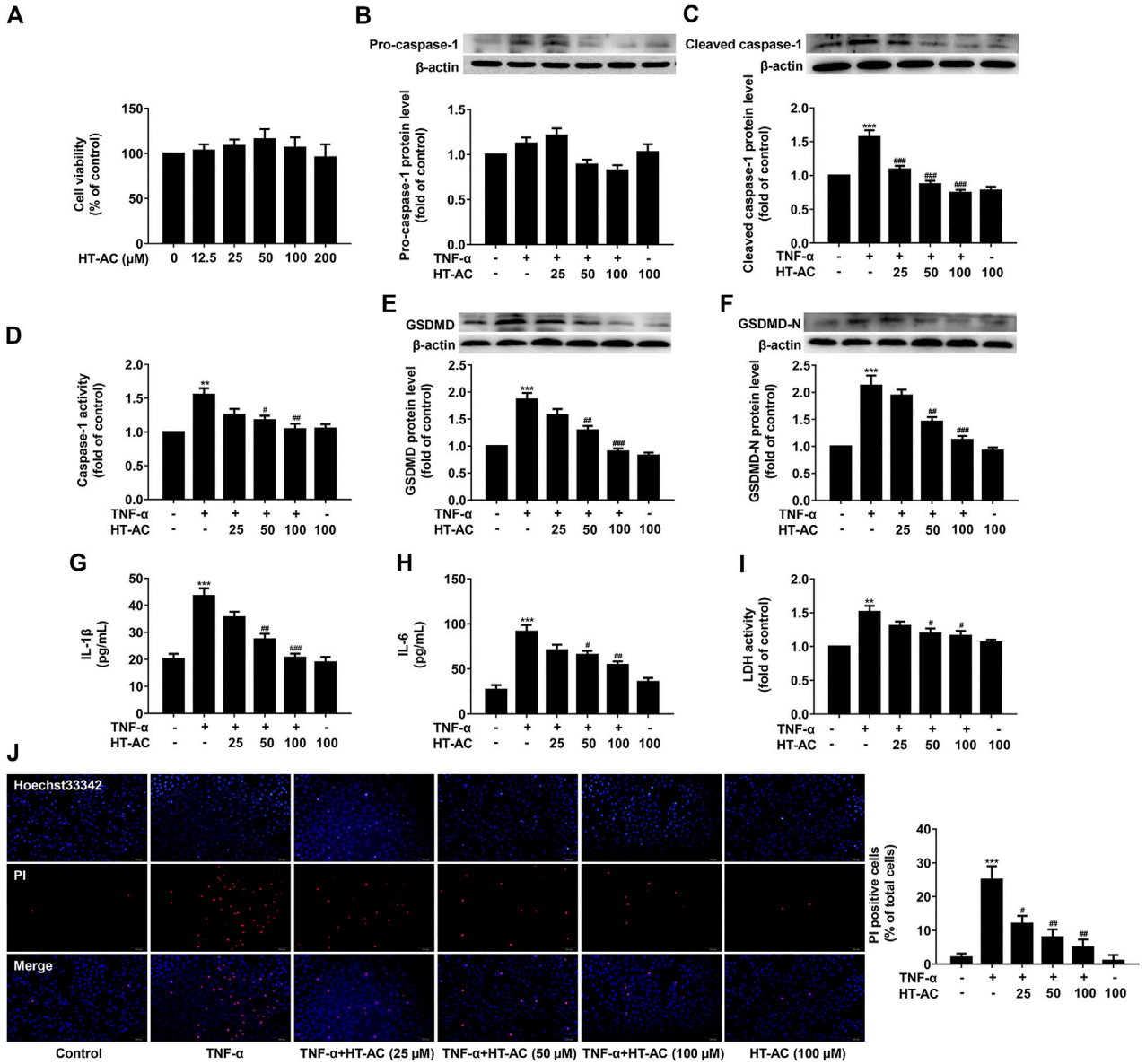


FIGURE 3 | HT-AC inhibited pyroptosis in TNF-stimulated HUVECs **(A)** The cell viability was measured after incubation with various concentrations of HT-AC (12.5, 25, 50, 100 and 200 μmol/L) for 13 h using the CCK8 assay. The HUVECs were treated with different concentrations of HT-AC (25, 50 and 100 μmol/L) for 1 h, and then stimulated with TNF-α (40 ng/ml) for 12 h **(B,C)** The protein expressions of pro-caspase-1 and cleaved caspase-1 were determined by Western blotting **(D)** Caspase-1 activity was assayed using the caspase-1 activity assay kit **(E,F)** The protein expressions of GSDMD and GSDMD-N were determined by Western blotting **(G,H)** The concentrations of IL-1β and IL-6 in cellular supernatant of HUVECs were detected by ELISA assay **(I)** The LDH release was evaluated with a cytotoxicity detection LDH kit **(J)** Double-fluorescent staining with PI (red) and Hoechst 33,342 (blue) was used to assess the formation of membrane pores during pyroptosis, ×200. Scale bar indicates 100 μm $^{**}p < 0.01$, $^{***}p < 0.001$ vs. control group; $^{\#}p < 0.05$, $^{\#\#}p < 0.01$, $^{\#\#\#}p < 0.001$ vs. TNF-α group. Results are expressed as mean ± SEM ($n = 3$).

HT-AC on cleaved caspase-1 protein expression and caspase-1 activity in TNF-stimulated HUVECs (**Figures 6B-D**). In addition, knockdown of HDAC11 increased the inhibitory effects of HT-AC on the protein expressions of GSDMD and GSDMD-N in TNF-stimulated HUVECs (**Figures 6E,F**). Our results further showed that knockdown of HDAC11 increased the inhibitory effects of HT-AC on the cellular supernatant concentrations of IL-1β (**Figure 6G**), IL-6 (**Figure 6H**) and LDH (**Figure 6I**), and the number of PI positive staining cells (**Figure 6J**) in TNF-stimulated HUVECs. Taken together, our findings suggested that the modulatory effect of HT-AC on pyroptosis is partly mediated by HDAC11 in TNF-α-stimulated HUVECs.

DISCUSSION

HT-AC is present in the olive oil of the fruit and leaf of the olive. In the past few years, the beneficial effects of HT-AC have been

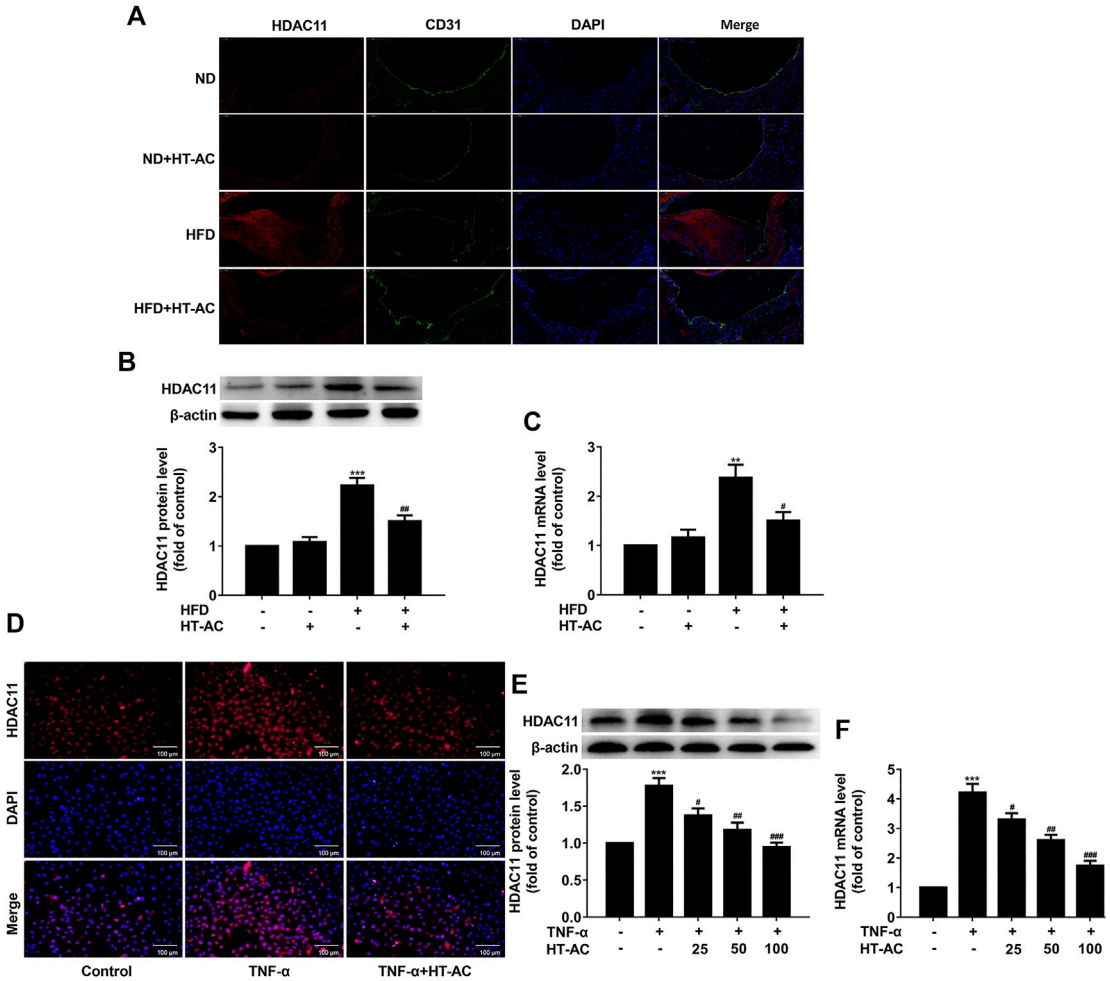


FIGURE 4 | HT-AC down-regulated HDAC11 expression **(A)** The expression of HDAC11 in the aortic intima of ApoE$^{-/-}$ mice by immunofluorescent double staining of the aortic sinus of HDAC11 and CD31. Scale bar indicates 50 μm **(B,C)** The expression of HDAC11 in the aorta of ApoE$^{-/-}$ mice was determined by Western blotting and quantitative real-time PCR. $^{**}p < 0.01$, $^{***}p < 0.001$ vs. ND group; $^{\#}p < 0.05$, $^{\#\#}p < 0.01$ vs. HFD group. Results are expressed as mean ± SEM (n = 10) **(D)** The expression and localization of HDAC11 in TNF-α-stimulated HUVECs were determined by immunofluorescence, ×200. Scale bar indicates 100 μm **(E,F)** The expression of HDAC11 in TNF-α-stimulated HUVECs was determined by Western blotting and quantitative real-time PCR. $^{***}p < 0.001$ vs. control group; $^{\#}p < 0.05$, $^{\#\#}p < 0.01$, $^{\#\#\#}p < 0.001$ vs. TNF-α group. Results are expressed as mean ± SEM ($n = 3$).

demonstrated such as antioxidant (Gordon et al., 2001), antiplatelet aggregating (González-Correa et al., 2008), and anti-inflammatory effects (Rosillo et al., 2015) in CVDs. Herein, we demonstrated that HT-AC attenuated the formation of atherosclerotic lesions and inhibit pyroptosis in the aortic intima of HFD-fed ApoE$^{-/-}$ mice, and HT-AC inhibited pyroptosis in TNF-α-stimulated HUVECs. We demonstrated that HT-AC might play a role in inflammation by regulating pyroptosis in endothelial cells to prevent and treat AS. Importantly, our results showed that HT-AC might prevent pyroptosis in vascular endothelial cells via down-regulation of HDAC11 related signaling pathway.

The studies have demonstrated that HT-AC exerted anti-inflammatory effects in CVDs (Tabernero et al., 2014; Rosillo et al., 2015). In the present study, we observed that HT-AC attenuated the formation of atherosclerotic lesions in HFD-fed ApoE$^{-/-}$ mice. Previous studies have shown that treatment with salidroside (Xing et al., 2020) or Melatonin (Zhang et al., 2018) decreases atherosclerosis plaque formation in the aorta of HFD-fed ApoE$^{-/-}$ mice via inhibiting endothelial cell pyroptosis. Pyroptosis is accompanied by the release of a large number of pro-inflammatory factors (Chang et al., 2013). It has been reported that dietary HT-AC inhibited TNF-α and IL-1β levels in the plasma of cholesterol-rich diet-induced hypercholesterolemic rats (Tabernero et al., 2014). Our previous study found that HT-AC inhibited TNF-α and IL-1β levels in the serum of hypercholesterolemic mice (Yao et al., 2019). In the present study, we observed that HT-AC inhibited pro-inflammatory TNF-α and IL-1β levels in the serum of HFD-fed ApoE$^{-/-}$ mice. Several studies have provided evidence that pyroptosis is involved in the inflammatory process of AS (Chang et al., 2013). GSDMD N-terminal segment, the central effector

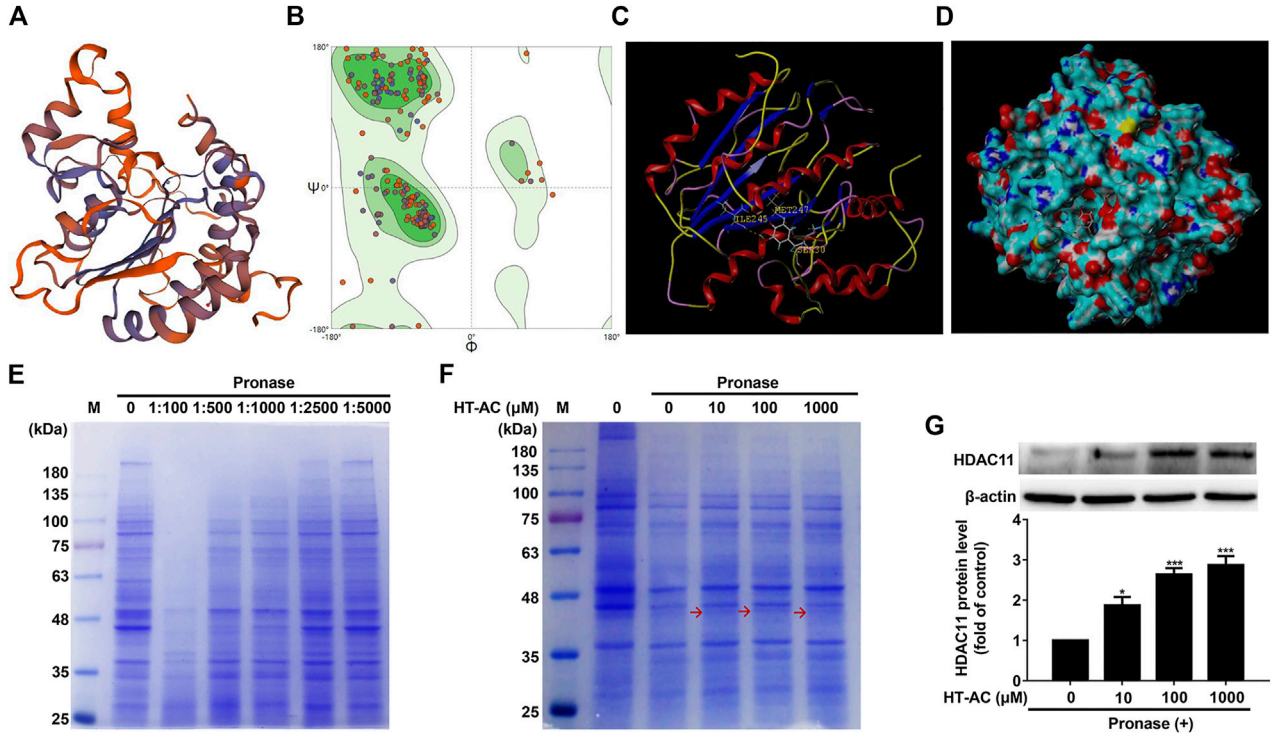


FIGURE 5 | HT-AC may target HDAC11 **(A)** Schematic SWISS-MODEL model of human HDAC11 **(B)** Ramachandran plot analysis of the three-dimensional structure of human HDAC11. The green, light green, and light blue regions represent the "most favored", "additional allowed" and "generously allowed" regions that amino acid residue fall regions, respectively **(C,D)** The ability of HT-AC to bind to the HDAC11 ligand-binding domain by molecular docking **(E)** Cell lysates were subjected to pronase digestion at various mass ratios of pronase to protein (1:100, 1:500, 1:1,000, 1:2,500 and 1:5,000) and coomassie staining **(F)** After treatment with HT-AC (10, 100 and 1,000 μmol/L) for 2 h at 4°C, cell lysates were subjected to pronase digestion at the 1:1,000 pronase to protein mass ratio and coomassie staining **(G)** The protein expression of HDAC11 was examined by Western blotting in HUVECs following HT-AC treatment. $^{*}p < 0.05$ and $^{***}p < 0.001$ vs. control group. Results are expressed as mean ± SEM ($n = 3$).

molecule and executor protein, executes pyroptosis by promoting the formation of membrane pores (Liu H. et al., 2020). In the present study, GSDMD N-terminal segment was remarkably inhibited by HT-AC in the aorta of HFD-fed ApoE$^{-/-}$ mice. GSDMD N-terminal segment is the cleavage product of activated caspase-1 (Liu Z. et al., 2020). We found that HT-AC treatment significantly suppressed the protein expression of activated caspase-1 in the aortic intima of HFD-fed ApoE$^{-/-}$ mice. Combined with the above results, beneficial effects of HT-AC in the prevention and reversal of AS may be dependent on the regulation of activated caspase-1 and GSDMD signaling pathway. It has been well-known that TNF-α induces endothelial cell inflammatory injury, apoptosis and endothelial dysfunction (Jain et al., 2007). It has been indicated that TNF-α induced caspase-1 expression in A549 cells (Jain et al., 2007), and induced activation of caspase-1 in 3T3-L1 cells (Furuoka et al., 2016). During pyroptosis, GSDMD cleavage was dependent on caspase-1 activation, which promoted the formation of membrane pores and cell lysis as well as the release of pro-inflammatory intracellular contents (Opdenbosch and Lamkanfi, 2019; Liu Z. et al., 2020). In the present study, we observed that HT-AC treatment of HUVECs alleviated TNF-α-induced pyroptosis by decreasing the number of PI positive cells, decreasing the enhanced protein expression of activated caspase-1 and gasdermin D, as well as by decreasing the release of pro-inflammatory IL-1β and IL-6. These results suggested that HT-AC may play an anti-atherosclerosis role by inhibiting the pyroptosis of endothelial cells.

Histone deacetylase enzymes regulate diverse biological function, including gene expression, rendering them potential targets for intervention in a number of diseases (Moreno-Yruela et al., 2018). Among the human zinc-dependent histone deacetylase enzymes, the most recently discovered member, HDAC11, has been shown to play a role in CVDs through promoting apoptosis, oxidative stress and inflammation (Zhou et al., 2017; Fan et al., 2018). A study showed that peritoneal injection of a small-molecule HDAC11 inhibitor significantly attenuated the formation of neointima after carotid artery ligation in Sprague–Dawley rats (Fan et al., 2018). Another study showed that HDAC inhibitor Trichostatin A mitigated the inflammation-induced pyroptosis and apoptosis during endotoxemia-induced acute lung injury (Samanta et al., 2018). Our present study revealed that treatment with HT-AC decreased HDAC11 protein expression in aortic intima, and suppressed HDAC11 protein and mRNA expressions in the aorta of HFD-fed ApoE$^{-/-}$ mice. In addition, it has been reported that TNF-α can upregulate

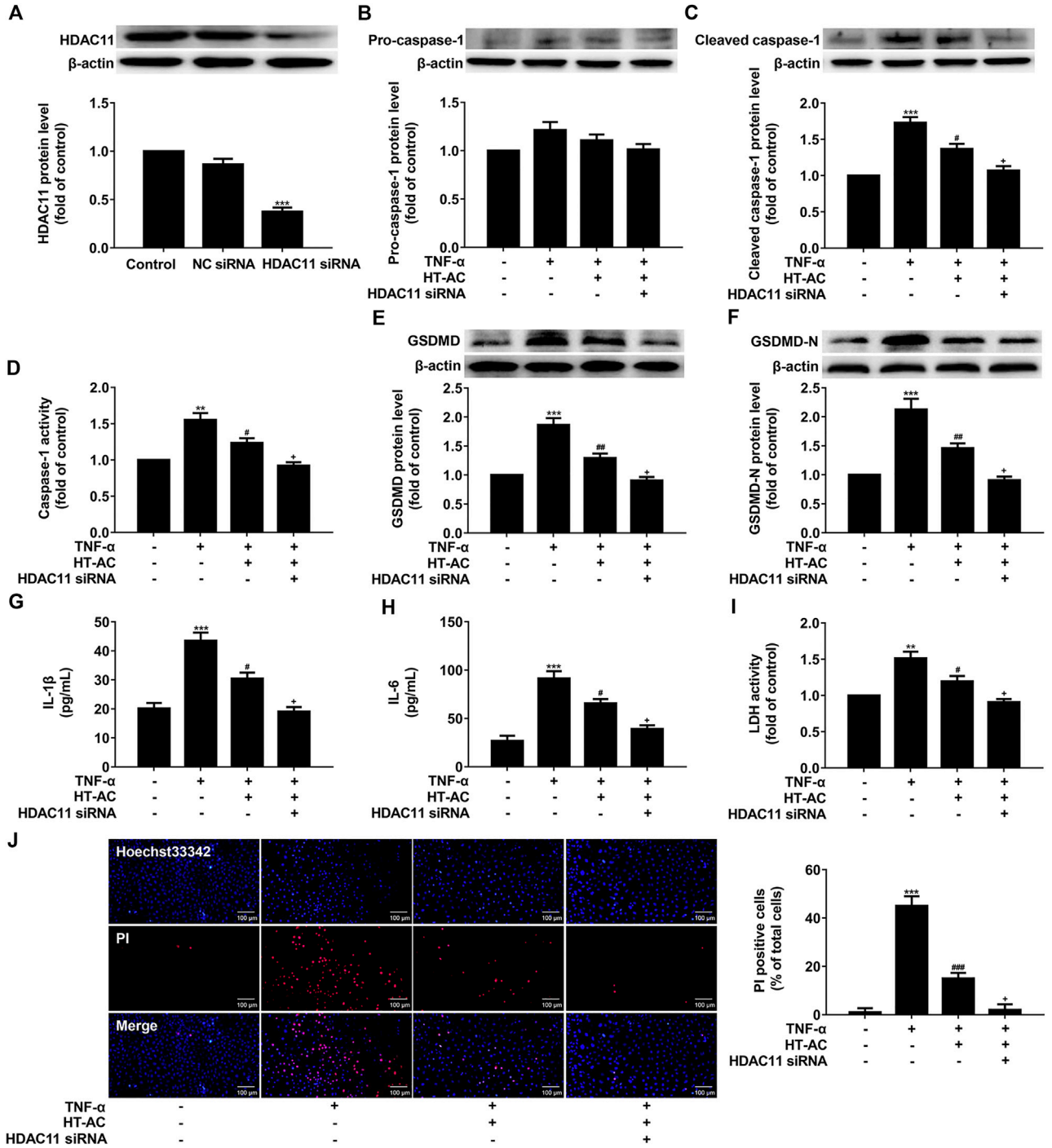


FIGURE 6 | HT-AC inhibited pyroptosis through HDAC11 in TNF-α-induced HUVECs. HUVECs were transfected with HDAC11 siRNA or NC siRNA for 48 h **(A)** The expression of HDAC11 was determined by Western blotting. The HUVECs transfected with HDAC11 siRNA or NC siRNA were pretreated with HT-AC before stimulation with TNF-α **(B,C)** The protein expressions of pro-caspase-1 and cleaved caspase-1 were determined by Western blotting **(D)** Caspase-1 activity was assayed using the caspase-1 activity assay kit **(E,F)** The protein expressions of GSDMD and GSDMD-N were determined by Western blotting **(G,H)** The concentrations of IL-1β and IL-6 in cellular supernatant of HUVECs were detected by ELISA assay **(I)** The LDH release was evaluated with a cytotoxicity detection LDH kit **(J)** Double-fluorescent staining with PI (red) and Hoechst 33,342 (blue) was used to assess the formation of membrane pores during pyroptosis, ×200. Scale bar indicates 100 μm $^{**}p < 0.01$, $^{***}p < 0.001$ vs. control group; $^{\#}p < 0.05$, $^{\#\#}p < 0.01$, $^{\#\#\#}p < 0.001$ vs. TNF-α group; $^{+}p < 0.05$ vs. TNF-α+HT-AC group. Results are expressed as mean ± SEM ($n = 3$).

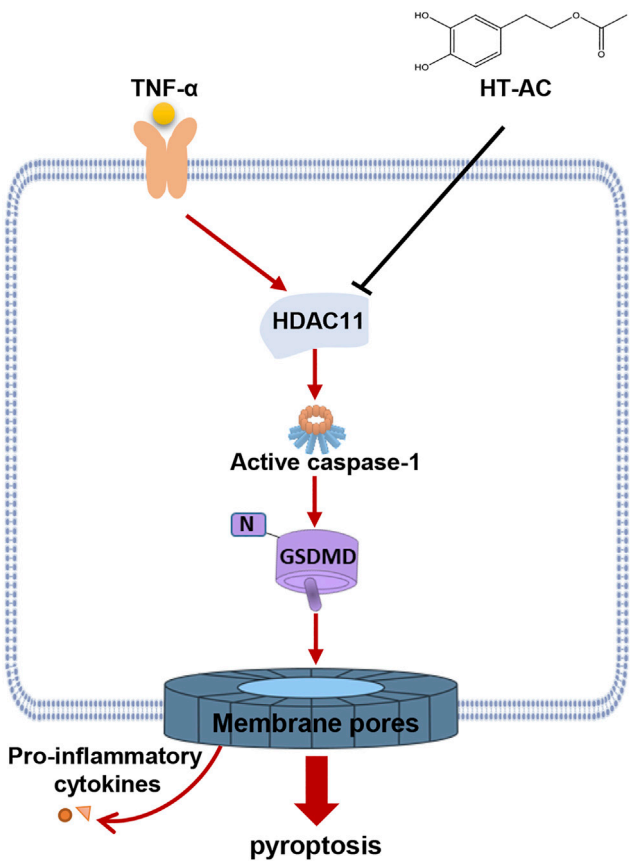


FIGURE 7 | Schematic illustration of the signaling pathway involved in the effect of HT-AC on pyroptosis in HUVECs.

the expression of HDAC11 in B cells in a dose-dependent manner (Shao et al., 2018). Our study also indicated that TNF-α can upregulate the protein and mRNA expressions of HDAC11 in HUVECs, while HT-AC decreased HDAC11 protein and mRNA expressions in TNF-α-stimulated HUVECs. Therefore, we further investigated the possibility of whether HT-AC targets HDAC11. The molecular docking result showed good compatibility between HT-AC and HDAC11. DARTS has been used for the identification of ligand targets by identifying the alterations in proteolytic sensitivity that occur after the binding of ligand and receptor (Gong et al., 2013; Pai et al., 2015). In our present study, the DARTS result showed that various concentrations of HT-AC (10, 100 and 1,000 μmol/L) treatment of HUVECs prevented enzymatic digestion of HDAC11 protein compared with vehicle-treated pronase. However, the differential band about 35–48 kDa molecular weight is very weak and there is no evidence that this band originated from HDAC11. To further elucidate this question, liquid chromatography-mass spectrometry (LC-MS) analysis will be conducted to confirm the binding between HT-AC and HDAC11 in our laboratory. In addition, whether the activities of HDAC11 are inhibited by HT-AC were not further analyzed in the present study. Moreover, these data do not exclude the possibility of other potential targets (Yang et al., 2017). Therefore, the molecular docking and DARTS analysis indicated that HT-AC may bind to HDAC11. In addition, Stammler D *et al.* revealed that treatment of HDACi increased lipopolysaccharide-mediated secretion of IL-1β via a caspase-1-independent mechanism (Stammler et al., 2015). Our research found that knockdown of HDAC11 with siRNA increased the inhibitory effects of HT-AC on pyroptosis in TNF-α-stimulated HUVECs. Therefore, HT-AC may exert the modulatory effect on pyroptosis partly through the HDAC11-mediated signaling pathway.

In conclusion, HT-AC *in vivo* attenuated the formation of atherosclerotic lesions and pyroptosis in the aortic intima of HFD-fed ApoE$^{-/-}$ mice. *In vitro*, we found that HT-AC treatment of HUVECs alleviated TNF-α-induced pyroptosis. Moreover, HT-AC might prevent pyroptosis in vascular endothelial cells via down-regulation of HDAC11 related signaling pathway (summarized in **Figure 7**). These findings provide a novel mechanism to the beneficial effects of HT-AC in the prevention and reversal of AS.

DATA AVAILABILITY STATEMENT

The raw data supporting the conclusions of this article will be made available by the authors, without undue reservation.

ETHICS STATEMENT

The animal care and study were reviewed and approved by the Animal Care and Use Committee of Xi'an Jiaotong University and conformed to the Guide for the Care and Use of Laboratory Animals published by the U.S. National Institutes of Health (NIH Publication No. 85-23, revised 1996).

AUTHOR CONTRIBUTIONS

All authors contributed significantly to this project. RL, and JG designed the research; FY, ZJ and XL performed the research; ZZ, HG and LC analyzed the data; YD, and YL performed molecular docking; FY wrote the paper; WW, and JH revised paper.

FUNDING

This study was supported by the National Natural Science Foundation of China (Grants 81970369 and 81770459).

ACKNOWLEDGMENTS

The authors wish to thank Prof. Jie Zhang (School of Medicine, Xi'an Jiaotong University) for excellent technical support with the molecular docking study.

REFERENCES

Bulotta, S., Celano, M., Lepore, S. M., Montalcini, T., Pujia, A., and Russo, D. (2014). Beneficial effects of the olive oil phenolic components oleuropein and hydroxytyrosol: focus on protection against cardiovascular and metabolic diseases. *J. Transl. Med.* 12, 219. doi:10.1186/s12967-014-0219-9

Chang, W., Lin, J., Dong, J., and Li, D. (2013). Pyroptosis: an inflammatory cell death implicates in atherosclerosis. *Med. Hypotheses* 81, 484–486. doi:10.1016/j.mehy.2013.06.016

Fan, X. D., Wan, L. L., Duan, M., and Lu, S. (2018). HDAC11 deletion reduces fructose-induced cardiac dyslipidemia, apoptosis and inflammation by attenuating oxidative stress injury. *Biochem. Biophys. Res. Commun.* 503, 444–451. doi:10.1016/j.bbrc.2018.04.090

Furuoka, M., Ozaki, K. I., Sadatomi, D., Mamiya, S., Yonezawa, T., Tanimura, S., et al. (2016). TNF-α induces caspase-1 activation independently of simultaneously induced NLRP3 in 3T3-L1 cells. *J. Cell. Physiol.* 231, 2761–2767. doi:10.1002/jcp.25385

Gong, F., Peng, X., Sang, Y., Qiu, M., Luo, C., He, Z., et al. (2013). Dichloroacetate induces protective autophagy in LoVo cells: involvement of cathepsin D/thioredoxin-like protein 1 and Akt-mTOR-mediated signaling. *Cell Death Dis.* 4, e913. doi:10.1038/cddis.2013.438

González-Correa, J. A., Navas, M. D., Muñoz-Marín, J., Trujillo, M., Fernández-Bolaños, J., and de la Cruz, J. P. (2008). Effects of hydroxytyrosol and hydroxytyrosol acetate administration to rats on platelet function compared to acetylsalicylic acid. *J. Agric. Food Chem.* 56, 7872–7876. doi:10.1021/jf801502z

Gordon, M. H., Paiva-Martins, F., and Almeida, M. (2001). Antioxidant activity of hydroxytyrosol acetate compared with that of other olive oil polyphenols. *J. Agric. Food Chem.* 49, 2480–2485. doi:10.1021/jf000537w

Jain, N., Sudhakar, C., and Swarup, G. (2007). Tumor necrosis factor-α-induced caspase-1 gene expression. *FEBS J.* 274, 4396–4407. doi:10.1111/j.1742-4658.2007.05969.x

Jia, C., Chen, H., Zhang, J., Zhou, K., Zhuge, Y., Niu, C., et al. (2019). Role of pyroptosis in cardiovascular diseases. *Int. Immunopharmacol.* 67, 311–318. doi:10.1016/j.intimp.2018.12.028

Kim, J. I., Jung, K. J., Jang, H. S., and Park, K. M. (2013). Gender-specific role of HDAC11 in kidney ischemia- and reperfusion-induced PAI-1 expression and injury. *Am. J. Physiol.-Renal Physiol.* 305, F61–F70. doi:10.1152/ajprenal.00015.2013

Laskowski, R., Rullmann, J. A., MacArthur, M., Kaptein, R., and Thornton, J. (1996). AQUA and PROCHECK-NMR: programs for checking the quality of protein structures solved by NMR. *J. Biomol. NMR* 8, 477–486. doi:10.1007/BF00228148

Lisete-Torres, P., Losada-Barreiro, S., Albuquerque, H., Sánchez-Paz, V., Paiva-Martins, F., and Bravo-Díaz, C. (2012). Distribution of hydroxytyrosol and hydroxytyrosol acetate in olive oil emulsions and their antioxidant efficiency. *J. Agric. Food Chem.* 60, 7318–7325. doi:10.1021/jf301998s

Liu, H., Tang, D., Zhou, X., Yang, X., and Chen, A. F. (2020). PhospholipaseCγ1/calcium-dependent membranous localization of Gsdmd-N drives endothelial pyroptosis, contributing to lipopolysaccharide-induced fatal outcome. *Am. J. Physiology-Heart Circulatory Physiol.* 319, H1482–H1495. doi:10.1152/ajpheart.00731.2019

Liu, Z., Wang, C., Yang, J., Chen, Y., Zhou, B., Abbott, D. W., et al. (2020). Caspase-1 engages full-length gasdermin D through two distinct interfaces that mediate caspase recruitment and substrate cleavage. *Immunity* 53, 106–114.e5. doi:10.1016/j.immuni.2020.06.007

Moreno-Yruela, C., Galleano, I., Madsen, A. S., and Olsen, C. A. (2018). Histone deacetylase 11 is an ε-N-myristoyllysine hydrolase. *Cell Chem. Biol.* 25, 849–856.e8. doi:10.1016/j.chembiol.2018.04.007

Nutsford, A. N., Galvin, H. D., Ahmed, F., and Husain, M. (2019). The Class IV human deacetylase, HDAC11, exhibits anti-influenza A virus properties via its involvement in host innate antiviral response. *Cell Microbiol.* 21, e12989. doi:10.1111/cmi.12989

Opdenbosch, N. V., and Lamkanfi, M. (2019). Caspases in cell death, inflammation, and disease. *Immunity* 50, 1352–1364. doi:10.1016/j.immuni.2019.05.020

Pai, M. Y., Lomenick, B., Hwang, H., Schiestl, R., McBride, W., Loo, J. A., et al. (2015). Drug affinity responsive target stability (DARTS) for small-molecule target identification. *Methods Mol. Biol.* 1263, 287–298. doi:10.1007/978-1-4939-2269-7_22

Rosillo, M. A., Sánchez-Hidalgo, M., González-Benjumea, A., Fernández-Bolaños, J. G., Lubberts, E., and Alarcón-de-la-Lastra, C. (2015). Preventive effects of dietary hydroxytyrosol acetate, an extra virgin olive oil polyphenol in murine collagen-induced arthritis. *Mol. Nutr. Food Res.* 59, 2537–2546. doi:10.1002/mnfr.201500304

Samanta, S., Zhou, Z., Rajasingh, S., Panda, A., Sampath, V., and Rajasingh, J. (2018). DNMT and HDAC inhibitors together abrogate endotoxemia mediated macrophage death by STAT3-JMJD3 signaling. *Int. J. Biochem. Cel Biol.* 102, 117–127. doi:10.1016/j.biocel.2018.07.002

Shao, J. B., Luo, X. Q., Wu, Y. J., Li, M. G., Hong, J. Y., Mo, L. H., et al. (2018). Histone deacetylase 11 inhibits interleukin 10 in B cells of subjects with allergic rhinitis. *Int. Forum Allergy Rhinol.* 8, 1274–1283. doi:10.1002/alr.22171

Stammler, D., Eigenbrod, T., Menz, S., Frick, J. S., Sweet, M. J., Shakespear, M. R., et al. (2015). Inhibition of histone deacetylases permits lipopolysaccharide-mediated secretion of bioactive IL-1 via a caspase-1-independent mechanism. *J. Immunol.* 195, 5421–5431. doi:10.4049/jimmunol.1501195

Tabernero, M., Sarriá, B., Largo, C., Martínez-López, S., Madrona, A., Espartero, J. L., et al. (2014). Comparative evaluation of the metabolic effects of hydroxytyrosol and its lipophilic derivatives (hydroxytyrosyl acetate and ethyl hydroxytyrosyl ether) in hypercholesterolemic rats. *Food Funct.* 5, 1556–1563. doi:10.1039/c3fo60677e

Wang, Q., Wu, J., Zeng, Y., Chen, K., Wang, C., Yang, S., et al. (2020). Pyroptosis: a pro-inflammatory type of cell death in cardiovascular disease. *Clin. Chim. Acta* 510, 62–72. doi:10.1016/j.cca.2020.06.044

Weber, C., and Noels, H. (2011). Atherosclerosis: current pathogenesis and therapeutic options. *Nat. Med.* 17, 1410–1422. doi:10.1038/nm.2538

Wu, X., Zhang, H., Qi, W., Zhang, Y., Li, J., Li, Z., et al. (2018). Nicotine promotes atherosclerosis via ROS-NLRP3-mediated endothelial cell pyroptosis. *Cel Death Dis* 9, 171. doi:10.1038/s41419-017-0257-3

Xing, S. S., Yang, J., Li, W. J., Li, J., Chen, L., Yang, Y. T., et al. (2020). Salidroside decreases atherosclerosis plaque formation via inhibiting endothelial cell pyroptosis. *Inflammation* 43, 433–440. doi:10.1007/s10753-019-01106-x

Yang, Z., Kuboyama, T., and Tohda, C. (2017). A systematic strategy for discovering a therapeutic drug for alzheimer's disease and its target molecule. *Front. Pharmacol.* 8, 340. doi:10.3389/fphar.2017.00340

Yao, F., Yang, G., Xian, Y., Wang, G., Zheng, Z., Jin, Z., et al. (2019). The protective effect of hydroxytyrosol acetate against inflammation of vascular endothelial cells partly through the SIRT6-mediated PKM2 signaling pathway. *Food Funct.* 10, 5789–5803. doi:10.1039/c9fo00586b

Yuan, L., Chen, X., Cheng, L., Rao, M., Chen, K., Zhang, N., et al. (2018). HDAC11 regulates interleukin-13 expression in CD4+ T cells in the heart. *J. Mol. Cell Cardiol.* 122, 1–10. doi:10.1016/j.yjmcc.2018.07.253

Yue, L., Sharma, V., Horvat, N. P., Akuffo, A. A., Beatty, M. S., Murdun, C., et al. (2020). HDAC11 deficiency disrupts oncogene-induced hematopoiesis in myeloproliferative neoplasms. *Blood* 135, 191–207. doi:10.1182/blood.2019895326

Zhang, R., and Ge, J. (2017). Proteinase-activated receptor-2 modulates ve-cadherin expression to affect human vascular endothelial barrier function. *J. Cel. Biochem.* 118, 4587–4593. doi:10.1002/jcb.26123

Zhang, Y., Liu, X., Bai, X., Lin, Y., Li, Z., Fu, J., et al. (2018). Melatonin prevents endothelial cell pyroptosis via regulation of long noncoding RNA MEG3/miR-223/NLRP3 axis. *J. Pineal Res.* 64, e12449. doi:10.1111/jpi.12449

Zhou, B., Zeng, S., Li, N., Yu, L., Yang, G., Yang, Y., et al. (2017). Angiogenic factor with G patch and FHA domains 1 is a novel regulator of vascular injury. *Arterioscler Thromb. Vasc. Biol.* 37, 675–684. doi:10.1161/ATVBAHA.117.308992

Conflict of Interest: The authors declare that the research was conducted in the absence of any commercial or financial relationships that could be construed as a potential conflict of interest.

Copyright © 2021 Yao, Jin, Lv, Zheng, Gao, Deng, Liu, Chen, Wang, He, Gu and Lin. This is an open-access article distributed under the terms of the Creative Commons Attribution License (CC BY). The use, distribution or reproduction in other forums is permitted, provided the original author(s) and the copyright owner(s) are credited and that the original publication in this journal is cited, in accordance with accepted academic practice. No use, distribution or reproduction is permitted which does not comply with these terms.

frontiers in Pharmacology

ORIGINAL RESEARCH
published: 10 May 2021
doi: 10.3389/fphar.2021.663417

Combined Oral and Topical Application of Pumpkin (*Cucurbita pepo* L.) Alleviates Contact Dermatitis Associated With Depression Through Downregulation Pro-Inflammatory Cytokines

Maha Jameal Balgoon[1], *Maryam H. Al-Zahrani*[1], *Soad Al Jaouni*[2] *and Nasra Ayuob*[3]*

[1]*Department of Biochemistry, Faculty of Science, King Abdulaziz University, Jeddah, Saudi Arabia,* [2]*Department of Hematology/Pediatric Oncology and Yousef Abdullatif Jameel Chair of Prophetic Medical Applications (YAJCPMA), Faculty of Medicine, King Abdulaziz University, Jeddah, Saudi Arabia,* [3]*Department of Medical Histology, Faculty of Medicine, Damietta University, Damietta, Egypt*

OPEN ACCESS

Edited by:
Karl Tsim,
Hong Kong University of Science and Technology, Hong Kong

Reviewed by:
Suzana Guimaraes Leitao,
Federal University of Rio de Janeiro, Brazil
Xinmin Liu,
Chinese Academy of Medical Sciences and Peking Union Medical College, China

***Correspondence:**
Nasra Ayuob
nasraayuob@gmail.com
nasraayuob@du.edu.eg

Specialty section:
This article was submitted to Ethnopharmacology, a section of the journal Frontiers in Pharmacology

Received: *05 February 2021*
Accepted: *07 April 2021*
Published: *10 May 2021*

Citation:
*Balgoon MJ, Al-Zahrani MH, Jaouni SA and Ayuob N (2021) Combined Oral and Topical Application of Pumpkin (*Cucurbita pepo *L.) Alleviates Contact Dermatitis Associated With Depression Through Downregulation Pro-Inflammatory Cytokines. Front. Pharmacol. 12:663417. doi: 10.3389/fphar.2021.663417*

Background: Depression and contact dermatitis (CD) are considered relatively common health problems that are linked with psychological stress. The antioxidant, anti-inflammatory, and antidepressant activities of pumpkin were previously reported.

Objectives: This study aimed to evaluate the efficacy of the combined topical and oral application of pumpkin fruit (*Cucurbita pepo* L.) extract (PE) in relieving CD associated with chronic stress–induced depression and compare it to the topical pumpkin extract alone and to the standard treatment.

Materials and Methods: Forty male albino rats were exposed to chronic unpredictable mild stress (CUMS) for 4 weeks for induction of depression and then exposed to (1-fluoro-2, 4-dinitrofluorobenzene, DNFB) for 2 weeks for induction of CD. Those rats were assigned into 4 groups (n = 10 each); untreated, betamethasone-treated, PE-treated and pumpkin extract cream, and oral-treated groups. Treatments were continued for 2 weeks. All groups were compared to the negative control group (n = 10). Depression was behaviorally and biochemically confirmed. Serum and mRNA levels of pro-inflammatory cytokines, such as TNF-α, IL-6, COX-2, and iNOS, were assessed. Oxidant/antioxidant profile was assessed in the serum and skin. Histopathological and immunohistochemical assessments of affected skin samples were performed.

Results: Pumpkin extract, used in this study, included a large amount of oleic acid (about 56%). The combined topical and oral administration of PE significantly reduced inflammatory and oxidative changes induced by CD and depression compared to the CD standard treatment and to the topical PE alone. PE significantly alleviated CD signs and the histopathological score (p < 0.001) mostly through the downregulation of pro-inflammatory cytokines and the upregulation of antioxidants.

Conclusion: Pumpkin extract, applied topically and orally, could be an alternative and/or complementary approach for treating contact dermatitis associated with depression. Further studies on volunteer patients of contact dermatitis are recommended.

Keywords: skin, inflammation, CD4, CD68, COX2, iNOS, antioxidants, oleic acid

INTRODUCTION

Depression is a common illness worldwide as more than 264 million people are suffering from it. Depressed persons suffer greatly and function poorly at work, at school, and in the family. There is a link between depression and physical health (WHO, 2020). The Lancet Psychiatry Commission concluded that patients with depression are at a higher risk for premature mortality and morbidity due to their unhealthy food choices, adverse effects of some offered treatments, and the effects of its symptoms (Firth et al., 2019).

The prevalence of contact dermatitis (CD, one of the skin inflammatory diseases, was described to be 10–40%, in general population; Ozgur et al. (2018). The occupational CD was reported to represent 70–90% of all occupational skin diseases and was described to deteriorate the functional capacity and the quality of life of the patient (Malik and English, 2015). Some studies have reported that psychological stress acts as a precipitating factor in triggering or worsening various skin diseases, including atopic contact dermatitis (Picardi et al., 2005; Amano et al., 2008). On the other hand, some biological and social studies support the causal effect of atopic CD on depression (Choi et al., 2018). CD was described to be linked to allergy and was proved to be associated with inflammatory factors (Thyssen et al., 2014). IL-6 and TNF-α have been reported to be elevated in mice showing behavioral despair and in patients with depression (Numakawa et al., 2014; Taraz et al., 2015). In a recent study conducted on depressed patients, the pro-inflammatory cytokine IL-6 was increased and TNF-α was correlated with psychological and cognitive fatigue (Pedraz-Petrozzi et al., 2020). Therefore, treatments with anti-inflammatory effect might be effective for treating CD and depression.

Recently, *Cucurbita* genus has received a great interest as it has been used in folk medicine in many countries for the treatment of gastrointestinal diseases and other clinical conditions (Salehi et al., 2019). Ethnopharmacological studies showed that pumpkin seeds were used to improve the erysipelas skin contamination (Yang et al., 2000). In addition, *Cucurbita pepo* L was used in some countries for treating burns and wounds (Ejaz et al., 2014), acne, dermatitis, and ecchymosis (Rigat et al., 2015). Traditional medicines, mainly Ayurvedic systems and Chinese medicine, have used different parts of the plant, including flesh of the fruits and seeds (Perez Gutierrez, 2016).

Pumpkin was described to have many health benefits, such as antioxidant, anti-inflammatory, and anti-fatigue (Wang et al., 2012; Nawirska-Olszańska et al., 2013). The effect of pumpkin on the central nervous system specifically was previously described, as the consumption of pumpkin seed oil (PSO) showed an efficacy in relieving the symptoms of ischemic stroke after ischemia-reperfusion (Shiri et al., 2016). In addition, pumpkin seed extracts were reported to produce antidepressant effects in rats comparable to that of imipramine, an antidepressant drug (George and Nazni, 2012). Sweetme Sweet Pumpkin (SPP) and *Cucurbita moschata* Duch. also showed an antidepressant effect in forced swimming test (FST)-induced depression comparable to that of fluoxetine, a classical antidepressant (Kim et al., 2016). They added that SPP and *Cucurbita moschata* Duch. increased brain tissue levels of the brain-derived neurotropic factor (BDNF), whereas they reduced the level of inflammatory cytokine (Kim et al., 2016). In a relatively recent review, pumpkin was described to have an antidepressant food score of 46%, indicating its antidepressant potential (LaChance and Ramsey, 2018). Recently, Dotto and Chacha (2020) endorsed conducting more animal and clinical trial–based researches in order to confirm the ameliorative effect of pumpkin seed on depression.

Regarding the effect of pumpkin on the skin, it was described that *Cucurbita pepo* L. seed oil even in small proportions significantly benefits the skin by increasing collagen synthesis and providing adequate photoprotection (Narendhirakannan and Hannah, 2013). Adding to that, *Cucurbita pepo* L. seeds' oil has been described to be effective in enhancing healing of cutaneous diseases (Bardaa et al., 2016) and burns due to antioxidant and antibacterial activity (Bahramsoltani et al., 2017). Not only that, Bora et al., (2019) reported that the formulation including pumpkin seed oil and melatonin showed augmented anti-inflammatory effects occur in UV radiation–related sunburn along with the downregulation of inflammatory cytokines.

Putting together these studies, pumpkin fruit extract was hypothesized to improve both CD and depressive status due to its anti-inflammatory and antidepressive effects, respectively. This study aimed to evaluate the efficacy of the combined topical and oral application of *Cucurbita pepo* L. fruit extract in relieving CD associated with depression compared to topical pumpkin extract as well as the standard CD treatment.

MATERIALS AND METHODS

This study was approved by the Biomedical Research Ethics Committee at the Faculty of Medicine, King Abdulaziz University, Jeddah, KSA (reference number 45-20).

Chemicals

Betamethasone valerate (BETA) was purchased from EPICO (19th of Ramadan City, Egypt) and used to treat the positive control group for pharmacological validation of the pumpkin extract (PE) cream. It was used at a dose of 75 µg (thinly and gently paint) using a specific brush twice a day for two weeks.

Fresh pumpkin (*Cucurbita pepo* L.) fruits were obtained from the local market at Jeddah, Saudi Arabia (voucher specimen:

AQJ_123). It was identified in the King Abdulaziz University herbarium using specimens of herbarium, flora of KSA (Chaudhary, 2001). Voucher specimen was deposited in the herbarium, and the identification was verified by a botanist (Dr Faten Filimban, a certified plant taxonomist at Division of Botany, Department of Biology at King Abdulaziz University).

Extraction of pumpkin was done according to Wang et al. (2012). First, the seeds were removed, and the raw fruits with skin were cut with a slicer, dried in a freeze dryer (FD5508; ILShinBase Co., Ltd., Korea), and crushed by grinding using an electrical machine. The obtained powder was passed through a 40-mesh sieve to get the fine powder to be stored in an airtight container.

The dried powder of pumpkin (50 g) was mixed with 450 ml of 80% ethanol at 37 C temperature for 1 day, left in shaker machine (JSSI-100T; JS Research Inc., Compact Shaking Incubator., Korea) for 1 day, and filtered with cotton and filter paper at the next day. This extraction process was repeated twice, and the excess solvent was evaporated under reduced pressure using a rotary vacuum evaporator (HS-2005S; HAHNSHIN Scientific Co., Ltd., Korea) to give an ethanol extract. It was left at fume hood for extra evaporation of ethanol, and then the extract was dried in freeze-dryer machine (FD5508; ILShinBase Co., Ltd., Korea). Pumpkin extract was stored in a suitable container till use after being diluted with hot distilled water in a dilution of 2:1 in an ultrasonication bath (Elmasonic S, lma Schmidbauer GmbHm Singen, Germany) and was administrated at a dose of 100 mg/kg by gavage once daily for two weeks (Wang et al., 2012).

Analysis of the PE

The chemical composition of PE was analyzed using trace gas chromatography GC-TSQ Evo 8000 mass spectrometer (Thermo Scientific, Austin, TX, United States) with a direct capillary column TG-5MS (30 m × 0.25 mm × 0.25 μm film thickness). The column oven temperature was initially held at 50°C, then increased by 5°C/min and held at 250 °C for 2 min, and increased to the final temperature of 300°C by 25°C/min and held for 2 min. The injector and MS transfer line temperatures were kept at 270 and 260°C, respectively; helium was used as a carrier gas at a constant flow rate of 1 ml/min. The solvent delay was 4 min, and diluted samples of 3 μL were injected automatically using an Autosampler AS1300 coupled with GC in the splitless mode in the PTV injector. EI mass spectra were collected at 70 eV ionization voltages over the range of m/z 50–650 in full scan mode. The ion source temperature was set at 250°C. The components were identified by comparison of their mass spectra with those of WILEY 09 and NIST 14 mass spectral database that is used in identification and study the chemical composition of unknown components in any extract (Wiley, 2006; Mikaia et al., 2014).

Analysis had been done in the qualitative type using Thermo Scientific™ Xcalibur™ 2.2 software, and all values were reported in relative percentage (Abd El-Kareem et al., 2016).

Preparation of PE Cream

Simple ethanolic PE was formulated into cream as was previously described by Chen et al. (2016) with a modification. Oils used by Chen et al. were replaced by olive oil.

The PE cream was stored in a suitable container till the time of use at the dose (0.52 μL/mm^2) reported by Bardaa et al. (2016), who used extracted oils of *Cucurbita pepo* L. for treating second-degree burns in rats.

Experimental Design

Fifty male albino rats weighing 30–40 g were obtained from animal house of the King Fahd Medical Research Center (KFMRC) and left to acclimatize in the laboratory condition. Weights of the rats at the start of the experiment were ranged from 150 to 200 g. They were housed in plastic cages in an air-conditioned room at 22 ± 1°C and offered the standard animal chow and water *ad libitum*. Ten rats, which were left unexposed to neither stress nor CD, were assigned as the negative control group (control). The other forty rats were subjected to a CUMS procedure as they were exposed to different types of stressors at different times during the day for 4 weeks in order to prevent habituation to the stressors. The CUMS procedure was fully described in previous works (Ayuob et al., 2018).

Induction of Skin Contact Dermatitis

A rectangular area (3 × 2 cm) on the dorsal surface of the rats was marked, and hair over this area was carefully shaved with an electrical shaving machine. Contact dermatitis was induced in the shaved area in all rats exposed to CUMS according to Simonetta and Bourgeois (2011). Briefly, rats were sensitized by painting 50 μL of 1-fluoro-2,4-dinitrofluorobenzene (DNFB) (0.1%, v/v) in acetone:olive oil 4:1 (AOO) onto the shaved dorsum of each animal for three consecutive days. Four days after sensitization, each rat was challenged by painting 30 μL of DNFB (0.2%, v/v) in AOO onto the dorsum every two days for 15 days. The painted areas were observed for signs of skin irritation for two weeks. These rats were then divided into 4 groups (n = 10 each). The positive control group was treated with the vehicle AOO. The CD + BETA group was topically treated with betamethasone cream, while the CD + PE group was topically treated with PE cream. CD + PE cream and the oral group were topically treated with PE cream and orally treated with PE. Topical treatments were performed using a special paint brush twice a day for two weeks.

Behavioral Changes

In order to confirm the effect of CUMS, the forced swim test (FST) and elevated plus maize (EPM) were conducted for all rats after 4 weeks. Regarding FST, it was conducted according to Yankelevitch-Yahav et al. (2015). During this test, the rat was left to swim in a glassy cylindrical container with 15 cm depth of water at 25 ± 2 C. The rat was observed for 6 min by a technician blind to the experiment groups. The total time, in seconds, spent by the rat without mobility during the 6 min was determined. Immobility was defined as "the cessation of limb movement, except for the minor movement necessary to keep the rat afloat."

Regarding the elevated plus maze (EPM) test, it was performed according to Carobrez and Bertoglio (2005). The number of closed arm entries during 6 min and time spent by each mouse inside the open and closed arms were recorded in seconds.

Serum Levels of Corticosterone and Pro-Inflammatory Cytokines

Blood samples were obtained for biochemical assessment from the intra-orbital sinus after completing the 4 weeks of exposure to CUMS and from the heart at the end of the experiment. Centrifugation was performed at 3,000 rpm for 15 min at 4 C to obtain the serum from the blood samples and was kept at −18°C. The corticosterone level was assessed to confirm induction of depression using enzyme-linked immunosorbent assay (ELISA) kits (ALPCO Diagnostics, Orangeburg, NY, United States) according to the manufacturer's instructions.

Tumor necrosis factor-α (TNF-α) and interleukin-6 (IL-6) (Quantikine R&D system, United States) kits were measured in the serum using ELISA according to the manufacturer's instruction. The optical density of each sample was determined in duplicate with a microplate ELISA reader set to 450 nm.

Pro-Inflammatory Cytokines in the Skin

To assess the anti-inflammatory effect of treatment, the levels of cytokines such as TNF-α, IL-6, cyclooxygenase-2 (COX-2), and inducible nitric oxide synthase (iNOS) were measured in the skin. Samples of the affected skin were obtained and kept at −80°C for assessment of protein and gene expression. These frozen samples were homogenized and then centrifuged for 10 min at 5,000 g. The supernatant was used for ELISA (Thermo Fisher, Vienna, Austria) to assess the levels of cytokines.

Oxidant/Antioxidant Profile in the Skin and Serum

Malonaldehyde (MDA) was used for the estimation of damage by reactive oxygen species (H_2O_2). The level of MDA was measured spectrophotometrically at 535 nm using the thiobarbituric acid reactive substance (TBARS) Assay Kit (Biodiagnostic; Egypt) according to the method described by Gamal et al. (2018).

In order to determine the superoxide dismutase (SOD) activity, nitroblue tetrazolium (NBT) was used. SOD Assay Kit (Biodiagnostic; Egypt) allowed very convenient SOD assaying through reduction of NBT to insoluble blue formazan. The method described by Packer (2002) was used.

Glutathione peroxidase (GPX) Kit (Randox Labs, Crumlin, United Kingdom) was used to assess GPX. To quantify catalase (CAT) activity, a calibration curve was generated for the assay using kits (Biodiagnostic; Egypt). The method used was described by Gamal et al. (2018).

Quantitative Real-Time Polymerase Reaction

Total RNA extraction was done from the tissue samples using the TriFast™ reagent (PeqLab, Germany, Cat No.: 30–2010) according to the provided manufacturer's protocol. The concentration of the purified RNA was estimated by NanoDrop 2000c Spectrophotometer (Thermo Scientific, United States). The extracted RNA from each sample was reverse-transcribed using the SensiFAST™ cDNA Synthesis Kit for qRT-PCR (Bioline United States Inc., United States, Cat No.: BIO-65053), following the manufacturer's instruction. The synthesized cDNA was stored at −80°C until utilization for qRT-PCR.

The qRT-PCR reactions were performed using the SensiFAST™ SYBR Lo-ROX Kit (Bioline United States Inc., United States, Cat No.: BIO-94002) on the Applied Biosystems 7500 real-time PCR detection system (Life technology, United States). Gene-specific primers for rat-GAPDH internal control, rat-TNF-α, rat-IL-6, rat-iNOS, and rat-COX2 were designed using *Primer3 software* (*v.0.4.0*), while their specificity was checked using NCBI/Primer-BLAST program. The primers were purchased from Willowfort™ (United Kingdom) and the forward and the reverse primer sequences for the studied genes are presented in **Supplementary Material S1**. The PCR mixture was prepared as follows: 10 μL SensiFAST™ SYBR Lo-ROX Mix, 0.8 μL forward primers, 0.8 μL reverse primer, 2 μL template cDNA, and 6.4 μL nuclease-free water. The reaction mix was transferred to thermal cycler that was previously programmed to an initial hold at 95°C for 2 min followed by 40 cycles of 95°C for 15 s and then 60°C for 30 s. A negative control reaction containing no template was run in each experiment.

Melting curve analysis was carried out to prove specificity of PCR products, and the Ct value for each reaction was obtained from amplification plots. The relative quantification for each gene expression in the tissue samples was calculated using the comparative threshold (ΔΔCt) method with the GAPDH as the internal control gene. For overall fold change, it was calculated and linearized by the $2^{-\Delta\Delta Ct}$ arithmetic formula.

Histological Techniques

At the end of the experiment, rats were anesthetized with 4% isoflurane (SEDICO Pharmaceuticals Company, Cairo, Egypt) in 100% oxygen and then euthanized by cervical dislocation. The chest wall was opened, and blood was obtained rapidly from the heart. Skin samples (2 × 2 mm) were immediately and gently dissected out and fixed in 10% neutral buffered formalin to be further processed for obtaining paraffin blocks. Paraffin sections at 4-μm thickness were prepared and stained with hematoxylin and eosin (Hand E) and Masson's trichrome stain.

Another set of paraffin sections, at same thickness, was immunohistochemically stained using the streptavidin–biotin–peroxidase technique. Anti-CD68 antibodies (Biocare Medical, Pachieco, United States, at a dilution 1/100), Anti CD4 (Biocare Medical, Pachieco, United States, at a dilution 1/100), and anti-COX-2 (Biocare Medical, Pachieco, United States, at a dilution 1/100) were utilized in this study. CD68 and CD4 were used for detection of macrophages and T lymphocytes, respectively. The primary antibody was omitted while the secondary antibody IgG was added during staining of some slides to act as negative control slides. The nuclei were counterstained with hematoxylin. Brown cytoplasmic staining was considered positive reaction in the three antibodies. Olympus Microscope BX-51 (Olympus, Germany) connected to a digital camera and a computer was used for

TABLE 1 | Component of *Cucurbita pepo* L. extract identified using gas chromatography and mass spectrometer (GC-MS) analysis.

SN	Name of the compound	Molecular formula	Molecular weights	Retention time (in min)	Relative percentage (%)	NIST match factor Mikaia et al. (2014)	Activity
1.	Hexadecanoic acid, methyl Ester (palmitic acid methyl ester)	$C_{17}H_{34}O_2$	270	21.50	3.02	839	Anti-inflammatory action through inhibition of the cyclooxygenase II enzyme Hema et al. (2011). Antioxidant, hypocholesterolemic, lubricant, and antiandrogenic Duke (1992)
2.	Hexadecanoic acid (palmitic acid)	$C_{16}H_{32}O_2$	256	22.61	8.90	821	Anti-inflammatory through inhibition of phospholipase A2 Aparna et al. (2012). Antioxidant, hypocholesterolemic, lubricant, and antiandrogenic Duke (1992)
3.	9-Octadecenoic ACID (Z)-	$C_{18}H_{34}O_2$	256	22.82	4.40	894	—
4.	10-Octadecenoic acid, methyl ester	$C_{19}H_{36}O_2$	296	24.13	4.82	804	Antibacterial, antifungal, and antioxidant Asghar and Choudahry (2011)
5.	Butyl 9,12,15-octadecatrienoate	$C_{22}H_{38}O_2$	334	24.73	1.60	743	No activity reported
6.	9-Octadecenoic acid (oleic acid)	$C_{18}H_{34}O_2$	282	25.14	56.59	901	Anti-inflammatory actions through peroxisome proliferator–activated receptor gamma (PPAR-γ) activation Song et al. (2019)
7.	9,12-Octadecadienoic acid (Z,Z) (linolenic acid)	$C_{18}H_{32}O_2$	280	25.42	3.52	855	Anti-inflammatory, hypocholesterolemic, antiandrogenic, antihistaminic, and anti-eczemic Duke (1992)
8.	*cis*-13-Octadecenoic acid (linoleic acid)	$C_{18}H_{34}O_2$	282	26.01	1.75	796	Anti-inflammatory, antiandrogenic, antileukotriene—D4, hypocholesterolemic, and flavor Duke (1992)
9.	9-Octadecenoic acid (Z)-, anhydride (oleic anhydride)	$C_{36}H_{66}O_3$	546	28.98	3.60	800	Anti-inflammatory Song et al. (2019)
10.	Linoleic acid ethyl ester (ethyl linoleate)	$C_{20}H_{36}O_2$	308	29.21	1.08	782	No activity reported
11.	Stigmast-5-en-3-ol	$C_{29}H_{50}O$	414	35.65	3.08	725	Decrease endothelial leukocyte and platelet adhesion Duke (1992), Kikuchi et al. (2015)
12.	Betulin	$C_{30}H_{50}O_2$	442	40.49	2.35	644	Anti-inflammatory and antitumor effect Jonnalagadda et al. (2017), Kikuchi et al. (2015)

photographing the histological sections. Image-Pro Plus Analysis Software (Media cybernetics, United States) was used for semi-quantitative analysis of antibody immunoreactivity. The area percentage of immunoexpression of $CD68^-$, CD4, and COX-2, used as an indicator of the extension of the reaction, was assessed in 30 fields using a × 40 objective lens and × 10 ocular lens. Epidermal thickness was measured in at least five fields in each slide, and the mean was calculated for each animal.

The histopathological scores of contact dermatitis were assessed using the scoring system previously described by Wang et al. (2015). This scoring system includes two parameters: infiltration of inflammatory cells (Grade 0, no changes; Grade one, few infiltrations; Grade 2, moderate infiltrations; and Grade 3, extensive infiltrations) and cuticulate *epidermis* (Grade 0, no changes; Grade 1, minor keratinization in epidermal tissue; Grade 2, obvious epidermal keratinization; and Grade 3, severe keratinization in epidermal tissue).

Statistical Analysis

Statistical Package of Social Science Program (SPSS, SPSS Inc., Chicago, Illinois, United States) version 20 was used to analyze the raw data. Results were presented in the form of mean ± standard deviation (SD). The F-test (one-way analysis of variance) was used to compare the studied groups followed by the *post hoc* Bonferroni test to compare each two groups and avoid repeated comparisons. Significance was considered when $p < 0.05$.

RESULTS

Compounds Detected in PE Using GC-MS

The constituents of PE, used in this study, mainly include oleic acid (about 56%), palmitic acid (about 8.9%), linolenic acid (3.5%), and linoleic acid (2.8%) beside many other compounds (**Table 1**). Some compounds of PE with anti-inflammatory effects were detected in this study such as oleic acid, palmitic acid, linolenic acid, betulin, and linoleic acid, while others have antimicrobial and antibacterial effects as 10-octadecenoic acid. Some compounds with antihistaminic and anti-eczemic effects were also detected like linolenic acid and linoleic acid, besides those with antioxidant effects as palmitic acid.

Confirmation of Depressive Status

After 4 weeks of exposing rats to CUMS, the development of depression-like behavior was confirmed through assessment of

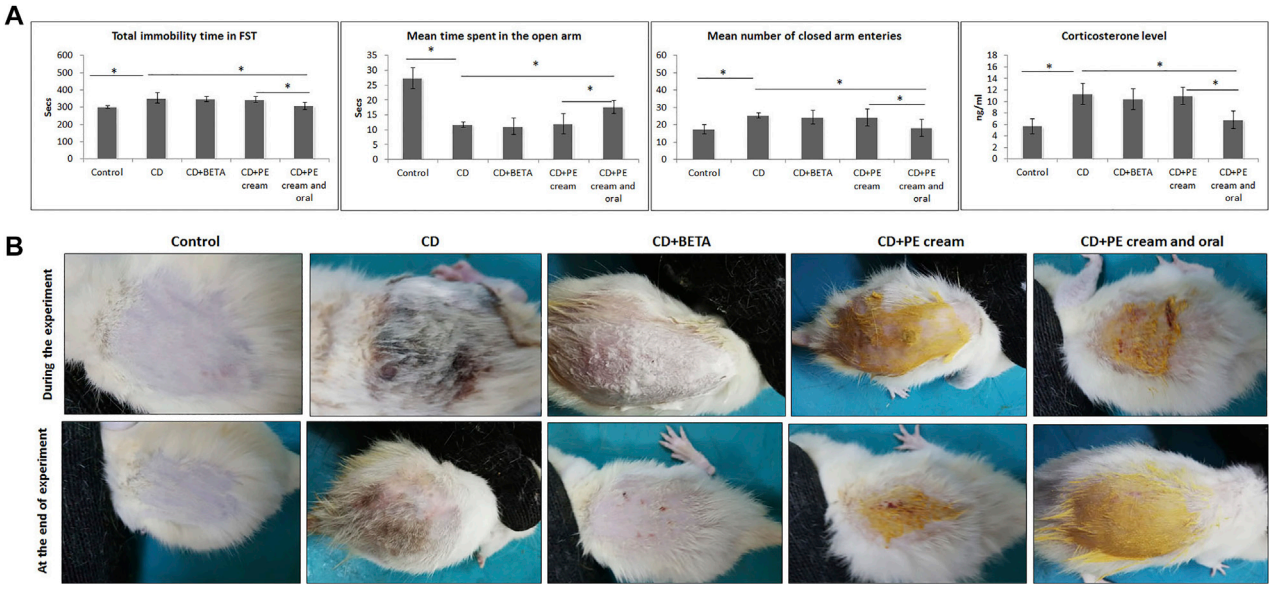


FIGURE 1 | (A): Confirmation of the depressive status in rats after exposure to CUMS through assessing of immobility time in FST, the EPM test, and the corticosterone level in the serum. **(B)**: Pumpkin extract affects the DNFB-induced dermatitis in rats morphologically as it improves the signs of contact dermatitis. CD: contact dermatitis, BETA: Betaderm, and PE: pumpkin extract. Data are presented as the mean ± SD, $n = 10$. Comparison between groups was done using the one-way ANOVA test followed by the Bonferroni *post hoc* test. FST: forced swimming test and EPM: elevated plus maize test.

the behavioral changes and serum corticosterone level. A significant ($p < 0.001$) increase in the mean immobility time during FST was recorded in all CUMS-exposed rats compared to the control. Although no significant difference in the immobility time was recorded in either BETA-treated ($p = 0.44$) or PE cream–treated ($p = 0.33$) groups, a significant decrease ($p < 0.001$) was recorded in the group treated with topical and oral PE compared to the untreated and PE cream–treated groups (**Figure 1A**).

The EPM revealed a significant decrease ($p < 0.001$) in the time spent by CUMS-exposed rats in the open arm as well as a significant increase ($p < 0.001$) in the number of closed arm entries compared to the control.

Although no significant difference in both parameters was recorded in either BETA- or PE cream–treated groups, the group treated with topical and oral PE showed a significant increase ($p < 0.001$) in the time spent in the open arm as well as a significant decrease ($p = 0.002$, $p = 0.01$) in the number of closed arm entries compared to the untreated and PE cream–treated groups, respectively.

Administration of FLU and Pump significantly increased ($p < 0.001$) the time spent in the open arm compared to the CUMS group.

Also, the number of closed arm entries was significantly increased ($p < 0.001$) after CUMS exposure in comparison to the control group, while administration of FLU ($p < 0.001$) and Pump ($p = 0.001$) significantly decreased it in comparison to the CUMS group.

Regarding the serum corticosterone level, it showed a significant ($p < 0.001$) increase in the CUMS-exposed rats. Neither BETA nor PE cream significantly affected ($p = 0.34$, $p = 0.78$) the serum corticosterone level, respectively, while the group treated with topical and oral PE showed a significant reduction ($p < 0.001$) compared to the untreated as well as the PE-treated group (**Figure 1B**).

Morphologic Appearance of Contact Dermatitis

Painting of the dorsal skin of rats with DNFB for two weeks resulted in the appearance of signs of CD that included hardness, dryness, and scaling. Application of BETA, and topical and oral PE for two weeks progressively improved these changes compared to the untreated group (**Figure 1B**).

Anti-Inflammatory Effect of PE

To assess the anti-inflammatory effect of PE, pro-inflammatory cytokine levels were measured. It was found that serum TNF-α and IL-6 levels were significantly increased ($p < 0.001$) in the untreated CD group compared to the control, while their levels showed no significant difference in either BETA-treated ($p = 0.44$, $p = 0.08$) or PE-treated ($p = 0.26$, $p = 0.06$) groups. On the other hand, serum TNF-α and IL-6 significantly reduced ($p < 0.001$) in the group treated with topical and oral PE compared to both untreated CD and PE-treated groups (**Figure 2A**).

Levels of IL-6, iNOS, COX-2, and TNF-α showed a significant increase ($p < 0.001$) in the skin of the untreated CD group compared to the control, while they showed a significant reduction in the BETA-treated group ($p < 0.001$, $p = 0.02$, $p = 0.03$, $p = 0.03$), PE-treated group ($p < 0.001$, $p = 0.03$, $p = 0.02$, $p < 0.001$), and group treated with topical and

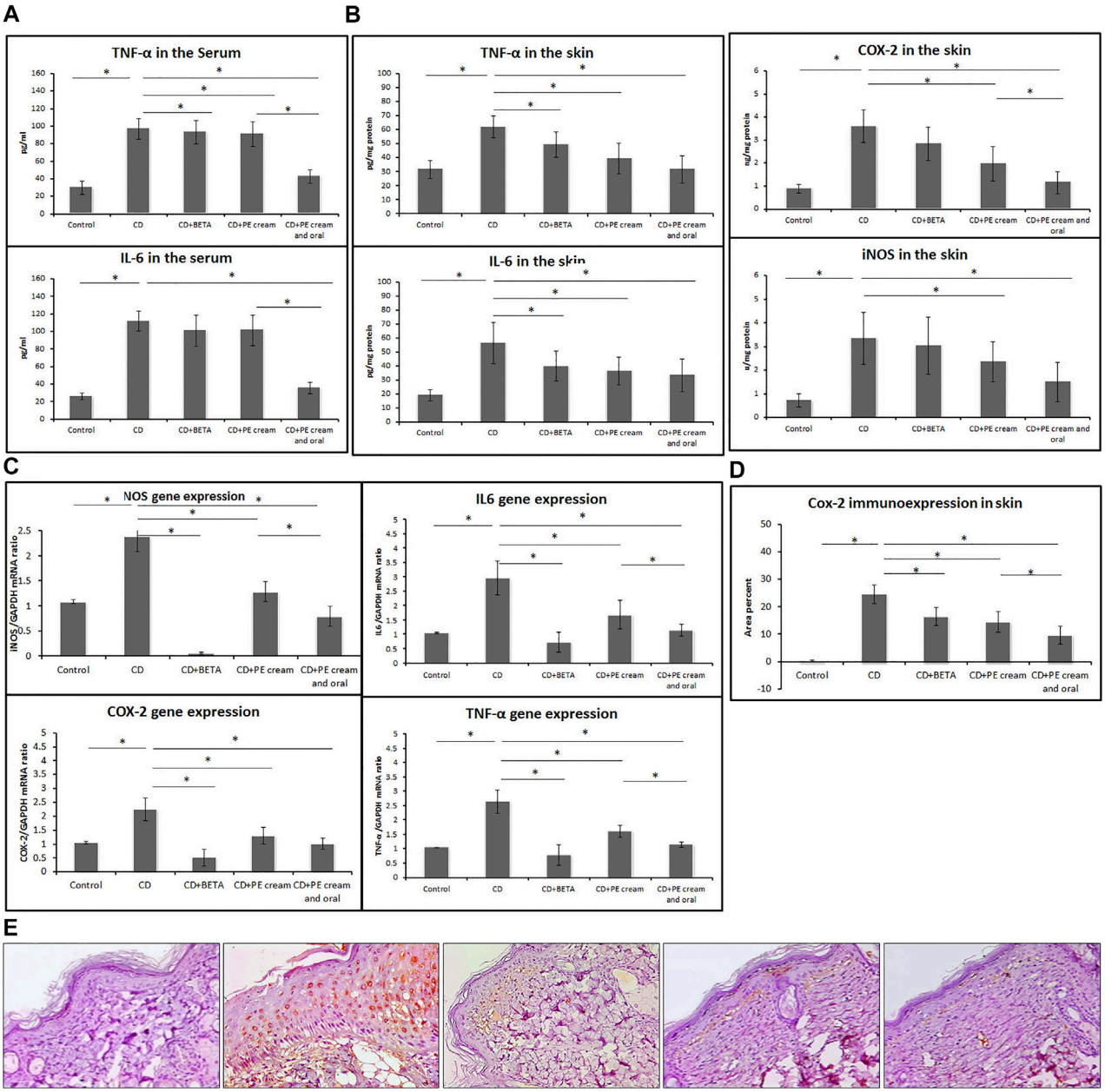


FIGURE 2 | Pumpkin extract attenuates the pro-inflammatory cytokine secretion in DNFB-induced contact dermatitis. Levels of IL-6 and TNF-α in the serum **(A)** and in skin **(B)** were assessed using ELISA. The levels of mRNA of IL-6, iNOS, COX-2, and TNF-α **(C)** were assessed in the skin using qRT-PCR. Cox-2 immunoexpression **(D,E)** in the skin was assessed immunohistochemically. CD: contact dermatitis, BETA: Betaderm, and PE: pumpkin extract. Data are presented as the mean ± SD, n = 10. Comparison between groups was done using the one-way ANOVA test followed by the Bonferroni *post hoc* test.

oral PE ($p < 0.001$), respectively, compared to the untreated CD group (**Figure 2B**).

The mean expression of mRNA of IL-6, iNOS, COX-2, and TNF-α in the skin, assessed using qRT-PCR, was significantly upregulated ($p < 0.001$) in the untreated CD group, while it was downregulated in the BETA-treated group ($p < 0.001$), PE-treated group ($p < 0.001$), and group treated with topical and oral PE ($p < 0.001$) compared to the untreated CD group, respectively (**Figure 2C**).

Immunoexpression of COX-2 in the skin showed a significant upregulation ($p < 0.001$) in the untreated CD group, while it showed a significant downregulation ($p < 0.001$) in all treated groups compared to the untreated CD group. In addition, COX-2 immunoexpression was significantly downregulated ($p = 0.001$) in PE- and topical and oral PE-treated groups compared to the groups treated with PE cream only **Figures 2D,E**.

TABLE 2 | Effect of *Cucurbita pepo L.* on the oxidant/antioxidant profile in the serum and skin.

	Control	CD	CD + BETA	CD + PE cream	CD + PE cream and oral
MDA in skin (nm/mg protein)	1.66 ± 0.22	2.91 ± 0.68 P1 < 0.001	2.53 ± 0.69 P2 = 0.12	2.30 ± 0.51 P2 = 0.01 P3 = 0.34	1.79 ± 0.38 P2 < 0.001 P4 = 0.003
SOD in skin (μ/mg protein)	4.11 ± 1	1.74 ± 0.67 P1 < 0.001	2.51 ± 1.2 P2 = 0.08	2.65 ± 1.02 P2 = 0.04 P3 = 0.74	3.62 ± 1.35 P2<0.001 P4 = 0.03
GPX in skin (nmol/mg protein)	58.93 ± 5.2	35.7 ± 12.5 P1 < 0.001	41.83 ± 9.2 P2 = 0.12	46.02 ± 9.1 P2 = 0.01 P3 = 0.28	52.8 ± 9.2 P2 < 0.001 P3 = 0.09
CAT in skin (μ/mg protein)	116.7 ± 10.1	88.9 ± 17.6 P1 < 0.001	97.4 ± 18.3 P2 = 0.18	103.58 ± 13.8 P2 = 0.02 P3 = 0.32	111.4 ± 12.1 P2 = 0.001 P4 = 0.21
MDA in serum (nmoL/ml)	1.35 ± 0.14	1.73 ± 0.5 P1 = 0.06	1.74 ± 0.34 P2 = 0.98	1.64 ± 0.41 P2 = 0.65 P3 = 0.63	1.30 ± 0.19 P2 = 0.03 P4 = 0.09
SOD in serum (μ/ml)	18.9 ± 2.9	9.9 ± 2.1 P1 < 0.001	8.95 ± 2.6 P2 = 0.47	9.10 ± 1.8 P2 = 0.33 P3 = 0.80	13.9 ± 3.6 P2 = 0.004 P4 < 0.001
GPX in serum (μ/ml)	58.6 ± 7.8	37.5 ± 4.9 P1 < 0.001	35.16 ± 5.9 P2 = 0.47	33.35 ± 6.6 P2 = 0.20 P3 = 0.57	47.9 ± 6.9 P2 = 0.003 P4 < 0.001
CAT in serum (μ/L)	0.41 ± 0.09	0.27 ± 0.08 P1 = 0.001	0.23 ± 0.04 P2 = 0.39	0.19 ± 0.06 P2 = 0.08 P3 = 0.36	0.37 ± 0.09 P2 = 0.02 P4 < 0.001

One-way analysis of variance (Kvetnansky et al., 2003) was used to compare the studied groups followed by post hoc *test with the least significant difference. Results were presented in the form of mean ± standard deviation (SD). Significance was considered when* p < *0.05.*
P1, significance vs. the control.
P2, significance vs. the CD.
P3, significance vs. the CD + BETA.
P4, significance vs. the CD + PE cream.

Antioxidant Effect of PE

Contact dermatitis was associated with a significant increase ($p < 0.001$) in MDA in the skin as well as an insignificant ($p = 0.06$) increase in its level in the serum. Although topical treatment with DETA did not significantly reduce the MDA level in the skin, PE applied either topically ($p = 0.01$) or combined with oral PE ($p < 0.001$) could significantly reduce it compared to the untreated CD group. Regarding the MDA level in the serum, it was significantly reduced ($p = 0.03$) only in the topical and oral PE-treated group (**Table 2**).

Contact dermatitis was found to be accompanied with a significant reduction in SOD ($p < 0.001$), GPX ($p < 0.001$), and CAT ($p < 0.001$, $p = 0.002$) in the skin and serum, respectively, compared to the control. Although the DETA-treated group did not show a significant change in SOD, GPX, and CAT levels in either the skin or serum, the PE-treated group showed a significant increase ($p = 0.04$, $p = 0.01$, $p = 0.02$) in the skin but not in the serum. The group treated with topical and oral PE showed a significant increase in SOD ($p < 0.001$, $p = 0.004$), GPX ($p < 0.001$, $p = 0.003$), and CAT ($p = 0.001$, $p = 0.02$) levels in both the skin and serum, respectively (**Table 2**).

Histopathological Alternations Associated With CD

Histopathological assessment revealed an intact skin structure of the control group, while the CD group showed epidermal hyperplasia, vacuolation of keratinocytes, edema in the superficial dermis, inflammatory cell infiltrate, increased capillaries, and hemorrhages in some areas. A significant increase ($p < 0.001$) in the epidermal thickness, histopathological score of CD, and the area percent of Masson's trichrome–stained dense collagen fibers was recorded in the CD group compared to the control (**Figure 3**).

Pumpkin extract administered as a topical cream alone or combined with oral PE markedly improved CD-associated histopathological changes. BETA-treated ($p < 0.001$), PE cream–treated ($p < 0.001$), and topical and oral PE-treated ($p < 0.001$) groups showed a significant decrease in epidermal thickness and the histopathological score of CD compared to the untreated CD group. A significant decrease in the area percent of Masson-stained dense collagen fibers was recorded in BETA-treated ($p = 0.01$), PE-treated ($p < 0.001$), and topical and oral PE-treated ($p = 0.01$) groups (**Figure 3**).

Inflammatory cell infiltrate observed in the superficial dermis was specified and quantified immunohistochemically and found to include mainly CD68-positive macrophages and CD4-positive T lymphocytes. It was noticed that DNFB-induced CD associated with upregulation of CD68 and CD4 immunoexpression compared to the control. On the other hand, CD68 and CD4 immunoexpression was significantly downregulated in BETA-treated ($p = 0.002$, $p < 0.001$), PE-treated ($p < 0.001$), and topical

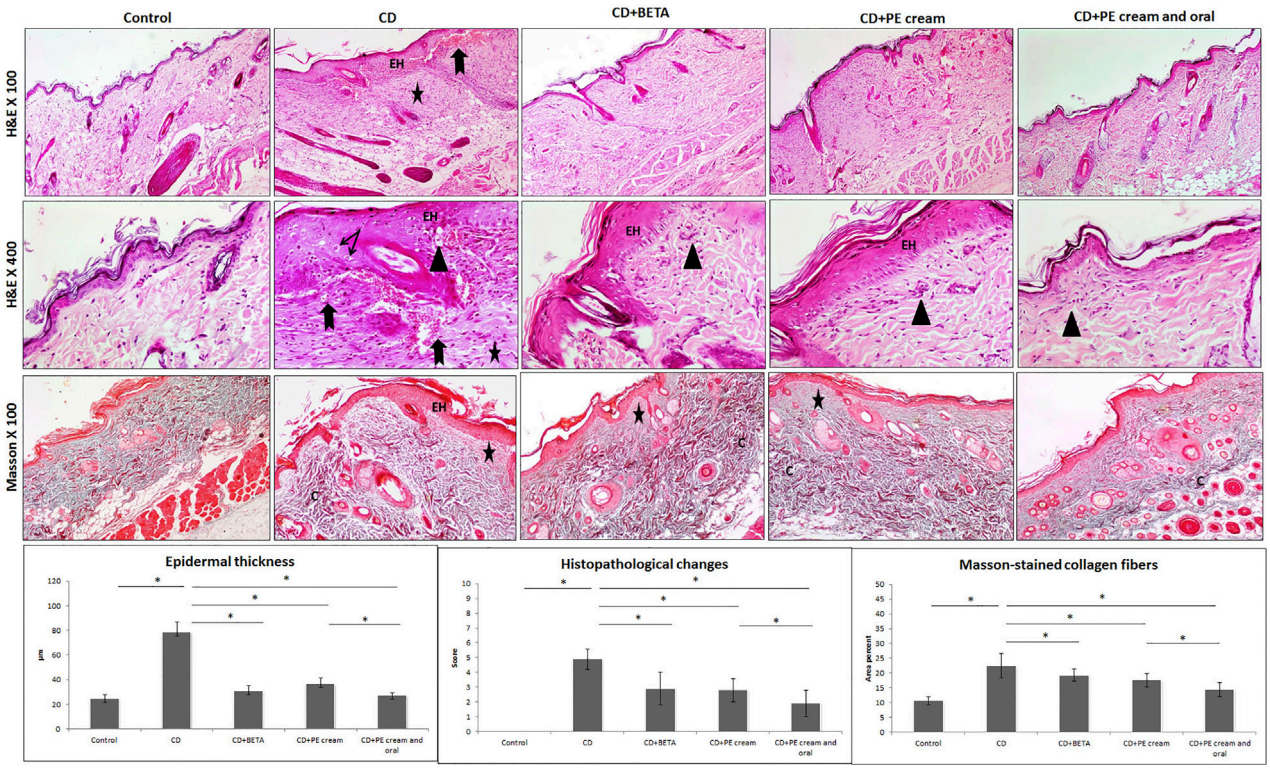


FIGURE 3 | Pumpkin extract affects the DNFB-induced dermatitis in rats histologically. The histological changes in contact dermatitis (CD) group includes epidermal hyperplasia (EH), edema in superficial dermis (star), vacuolation of keratinocytes (arrow), inflammatory cell infiltrate (arrow head) and increased capillaries and hemorrhages (bifid arrow) as well as increased dense collagen fibers (C) in the dermis. The histological changes are improved in the treated groups (H&E and Masson stain). Data are presented as the mean ±SD, n= 10. Comparison between groups was done using One way ANOVA test followed by Bonferroni post *hoc* test

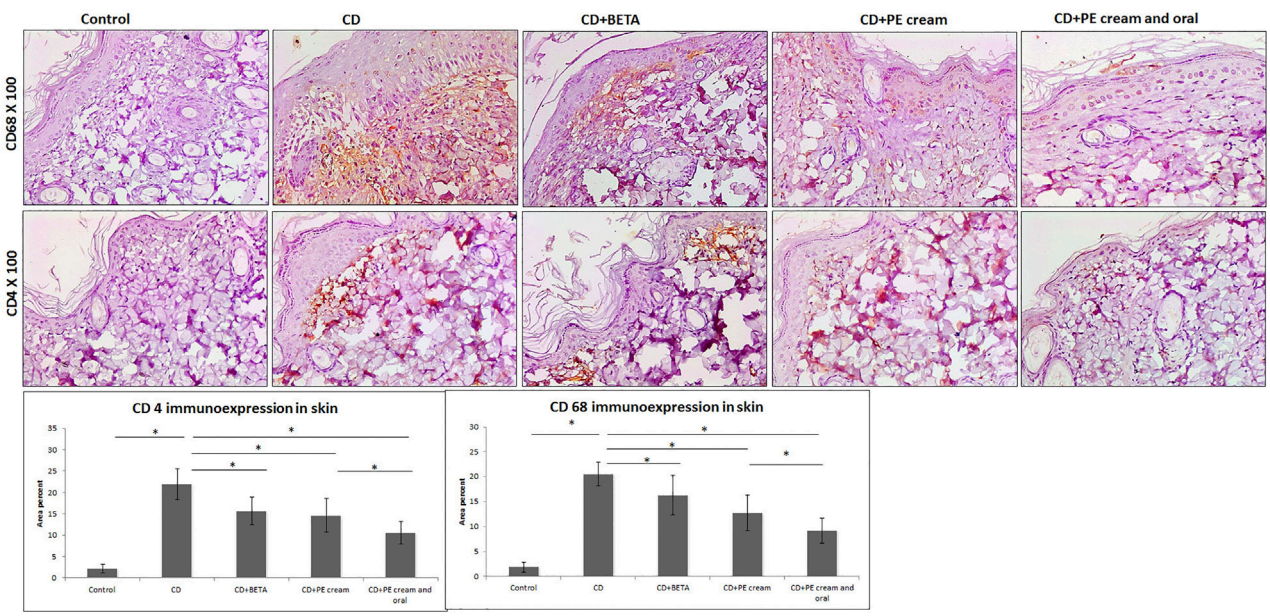


FIGURE 4 | Pumpkin extract attenuates the inflammatory infiltrate in DNFB-induced contact dermatitis. CD68 and CD4 immunoexpression is downregulated as shown by immunohistochemistry. CD: contact dermatitis, BETA: Betaderm, and PE: pumpkin extract. Data are presented as the mean ± SD, *n* = 10. Comparison between groups was done using the one-way ANOVA test followed by the Bonferroni *post hoc* test.

and oral PE-treated groups, compared to the untreated CD group, respectively (**Figure 4**).

DISCUSSION

Stress influences the nature of some skin inflammatory diseases, such as psoriasis and allergic contact dermatitis (Buske-Kirschbaum et al., 2006). Stressful life situations were found to be related to the onset of symptoms in 16% of chronic urticaria cases (Malhotra and Mehta, 2008). This study was conducted to investigate the ability of combined topical and oral application of pumpkin fruit extract to biochemically and histopathologically improve CD in depressed rats.

The effect of chronic stress with the subsequent depression-like behavior on CD was not previously addressed in the experimental models. Among the well-established experimental models of human CD is DNFB-induced contact hypersensitivity in mice (Thomas et al., 1999). Chronic unpredictable mild stress (CUMS) procedure is considered a robust animal model for depression, which expressively contribute to the understanding of the mechanisms implicated in depression and the development of novel antidepressant drugs (Antoniuk et al., 2019). Therefore, these two models of depression and CD were adopted in this study. In the current study, exposure to CUMS successfully induced depression-like behavior as evidenced by the significant increase in the serum corticosterone level and prolongation in immobility time during the FST, and was confirmed by the EPM test. The latter was described as an important tool in the study of neurobiological signaling pathways involved in depression (Nestler et al., 2002). It is sensitive to all available antidepressant drugs commonly used to test the antidepressant effect of new drugs (Jeong et al., 2015).

iNOS, COX-2, and TNF-α are inflammatory mediators involved in the regulation of inflammatory reactions, including those of the skin, such as CD (Laouini et al., 2005; Orita et al., 2011; Danso et al., 2014). Both TNF-α and IL-6 were reported to be involved in the pathogenesis of depression (Taraz et al., 2015; Pedraz-Petrozzi et al., 2020). Hence, these cytokines were assessed, in this study, in order to investigate the anti-inflammatory effect of PE.

DNFB-induced CD was associated, in this study, with increased inflammatory cytokines TNF-α and IL-6 in the serum as well as IL-6, iNOS, COX-2, and TNF-α, at protein and mRNS levels, in the skin. These findings were in accordance with those reported by Kaur et al. (2014) in patients with acute and subacute allergic dermatitis as well as those reported by Qu et al. (2019) in rat model of contact dermatitis. Increased level of TNF- originated from the activated macrophages, T cells, and keratinocytes, and their release into the circulation in cutaneous inflammatory conditions was previously reported (Kerstan et al., 2011). In accordance with that, the number of macrophages, T cells, and keratinocytes was found to be increased in the dermis and epidermis of rats with CD, in this study. Although the inflammatory response plays a chief role in the protection of the host as well as in tissue repair, it can also damage the normal skin tissue (Cha et al., 2016). Based on that, inhibition of pro-inflammatory cytokine expression was described to improve dermatitis as it protects from extended adaptive immunity (Chang et al., 2018). Another reason for increased TNF-α and IL-6 in the serum in this study was the occurrence of CUMS-induced depression as they have been reported to be elevated in patients with depression and mice showing behavioral despair (Numakawa et al., 2014; Taraz et al., 2015).

In this study, topical application of PE extract to the areas affected with CD resulted in marked improvement of hardness, dryness, and scaling in a comparable degree to those animals treated with Betaderm cream, the standard treatment of CD. This morphological improvement was associated with a significant reduction in the inflammatory cytokines such as TNF-α and IL-6 in the serum as well as IL-6, iNOS, COX-2, and TNF-α in the skin. These findings were in agreement with those of Kim et al. (2016), who reported that SSP significantly reduced the protein levels of TNF-α and IL-6 in the serum of depressed animals. Regarding the effect on the skin, Bora et al. (2019) reported an enhancement in anti-inflammatory effects following the administration of PSO and melatonin formulation to UV radiation–induced sunburn evident by reduced inflammatory cytokines. Analysis of the PE compounds, conducted in this study, revealed the presence of many compounds with anti-inflammatory effect, for example, oleic acid, palmitic acid, and linolenic acid as well as some compounds with antihistaminic and anti-eczemic effects, for example linolenic acid and linoleic acid, besides those with antioxidant effect like palmitic acid. These compounds were behind the improving effect induced by PE in depressed rats with CD.

Disturbed oxidant/antioxidant profile manifested by increased MDA and decreased SOD, GPX, and CAT in the skin and serum was observed in DNFB-induced CD in this study. Similar findings were reported by Kaur et al. (2014) in patients with restricted allergic contact dermatitis. Disturbance in oxidant/antioxidant profile in CD was attributed to the consumption of radical-scavenging antioxidants as a result of increased free radical amounts (Serefhanoglu et al., 2009). The PE cream–treated group showed a significant improvement in antioxidant status in the skin, while the BETA-treated group did not show any improvement in this parameter. In addition, the group treated with topical and oral PE showed a significant improvement in the antioxidant profile in the skin and serum as well, and this might explain the marked improvement observed morphologically and histologically in this group.

The antioxidant properties of pumpkin fruit extract and seed oil were previously reported (Xia et al., 2003; Azizah et al., 2009; Bahramsoltani et al., 2017). It was said that natural products with antioxidant, anti-fatigue, and anti-inflammatory effects also exert an antidepressant-like effect (Jeong et al., 2015). All these previous activities were proved in pumpkin. Not only that, the antidepressant-like effect of pumpkin was previously reported by Kim et al. (2016), who found that oral SSP significantly reduced the immobility time in FST, increased the levels of brain-derived neurotropic factor (BDNF), and decreased the levels of IL-6 and TNF-α. Therefore, pumpkin was chosen, in this study, to relieve the combined manifestation of contact dermatitis with depression.

The morphological and histopathological alternations observed in CD in this study were in accordance with those

observed by Zhou et al. (2016) in dinitrochlorobenzene-induced allergic CD in BALB/c mice (Alshathly and Alqahtani, 2017) in benzene-induced skin irritation in rats and (Qu et al., 2019) in oxazolone-induced CD in mice. Significant upregulation of Cox-2 immunoexpression in CD was among the findings recorded in this study and previous studies (Chang et al., 2018).

It was previously documented that T lymphocytes and macrophages have crucial roles in skin inflammatory diseases such as contact dermatitis and psoriasis (Qu et al., 2019); therefore, they were investigated in this study. Skin keratinocytes act as a potent source of pro-inflammatory cytokines and chemokines. Therefore, a particular dialog between keratinocytes and activated immune cells initiates and maintains the T cell–mediated immune responses in inflammatory lesions (Pivarcsi et al., 2005). T cells in the skin tissue were reported to sensitize and elicit a hypersensitive inflammation reaction (Pasparakis et al., 2014). These cellular events explained what was observed in the CD group in this study, which included keratinocyte hyperplasia, the overexpression of pro-inflammatory cytokines, the upregulated immunoexpression of CD4-positive T lymphocytes, and CD68-positive macrophages.

Pumpkin extract administered both topically and orally, in this study, markedly improved CD-associated histological changes in a comparable degree to that of BETA cream. CD68 and CD4 immunoexpression was significantly downregulated in BETA- and PE-treated groups, which implied reduced hypersensitivity reaction (Luo et al., 2014). No previous studies were found to describe the effect of pumpkin extract on CD associated with depression or chronic stress. The effect of caffeic acid (3,4-dihydroxycinnamic acid, CA), one of the six phenolic acids detected in pumpkin (*Cucurbita maxima*), on 12-O-tetradecanoyl-phorbol-13-acetate CD was previously studied (Zhang et al., 2014). They found that CA has anti-inflammatory activities in both acute and chronic contact dermatitis models through blocking of mRNA and protein synthesis of the cytokines, such as TNF-α, IL-6, and IL-1β, and neutrophil-mediated myeloperoxidase activity (Zhang et al., 2014).

Oleic and palmitic acids represent the main constituents of pumpkin fruit extract, utilized in this study. These findings are in partial agreement with those of Kim et al. (2012), Bardaa et al. (2016), and Bora et al. (2019). Both oleic and palmitic acids were reported to possess antioxidant, antidiabetic, and antiatherogenic effects (Cho et al., 2010). The link between depression and oleic acid was previously reported in the literature. Oleic, palmitic, and linoleic acids were described to be downregulated in depression (Conklin et al., 2010; Martín et al., 2010). Oleic acid in specific was reported to inhibit the production of Aβ peptide and amyloid plaque Alzheimer disease-type neuropathology both *in vitro* and *vivo* (Amtul et al., 2011). More recently, oleic acid–mediated neuroprotection might be attributable to its anti-inflammatory actions through peroxisome proliferator–activated receptor gamma (PPAR-γ) activation (Song et al., 2019). Regarding hexadecanoic acid (palmitic acid), it was described as an inhibitor of phospholipase A (2), and therefore considered as an anti-inflammatory compound (Aparna et al., 2012).

The improvement in CD as well as CUMS-induced depression, observed in the PE-treated group morphologically and behaviorally and were evident biochemically and histopathologically, is attributed mainly to the anti-inflammatory and antioxidant effects of pumpkin compounds that were detected in this study. Getie et al. (2002) reported that the antioxidant effect of any drug prevents cell damage, promotes DNA synthesis, increases vascularity, increases the strength of collagen fibers, and improves the viability of collagen fibrils.

In conclusion, topical application of pumpkin extract when combined with the oral administration was superior to the topical application alone in attenuating inflammation and oxidative changes induced by contact dermatitis associated with chronic stress–induced depression. These results imply that pumpkin can alleviate symptoms of contact dermatitis and depression through the downregulation of pro-inflammatory cytokines and enhancing the antioxidant status. Therefore, pumpkin extract, applied topically and orally, could be an alternative and/or complementary approach in contact dermatitis associated with depression-like behavior. Further studies to test this effect on volunteer patients of contact dermatitis are recommended.

DATA AVAILABILITY STATEMENT

The original contributions presented in the study are included in the article/**Supplementary Material**; further inquiries can be directed to the corresponding author

ETHICS STATEMENT

The animal study was reviewed and approved by the Biomedical Research Ethics Committee at the Faculty of Medicine, King Abdulaziz University, Jeddah, KSA.

AUTHOR CONTRIBUTIONS

All authors listed have made a substantial, direct, and intellectual contribution to the work and approved it for publication.

FUNDING

This research work was funded by institutional fund projects under grant no. IFPHI-237-247-2020; therefore, authors gratefully acknowledge technical and financial support from the Ministry of Education and King Abdulaziz University, DSR, Jeddah, Saudi Arabia.

SUPPLEMENTARY MATERIAL

The Supplementary Material for this article can be found online at: https://www.frontiersin.org/articles/10.3389/fphar.2021.663417/full#supplementary-material.

REFERENCES

Abd El-Kareem, M. S. M. A., Rabbih, M. A. E. F., Selim, E. T. M., Elsherbiny, E. A. E.-M., and El-Khateeb, A. Y. (2016). Application of GC/EIMS in Combination with Semi-empirical Calculations for Identification and Investigation of Some Volatile Components in Basil Essential Oil. *Ijamsc* 04, 14–25. doi:10.4236/ijamsc.2016.41002

Alshathly, M., and Alqahtani, M. (2017). Ameliorating Effect of achillea Fragrantissima against Benzene-Induced Skin Irritation: Histological Study. *Adv. Pharm. Ethnomed* 5, 1–7. doi:10.17582/journal.ape/2017/5.1.1.7

Amano, H., Negishi, I., Akiyama, H., and Ishikawa, O. (2008). Psychological Stress Can Trigger Atopic Dermatitis in NC/Nga Mice: an Inhibitory Effect of Corticotropin-Releasing Factor. *Neuropsychopharmacol* 33, 566–573. doi:10.1038/sj.npp.1301435

Amtul, Z., Westaway, D., Cechetto, D. F., and Rozmahel, R. F. (2011). Oleic Acid Ameliorates Amyloidosis in Cellular and Mouse Models of Alzheimer's Disease. *Brain Pathol.* 21, 321–329. doi:10.1111/j.1750-3639.2010.00449.x

Antoniuk, S., Bijata, M., Ponimaskin, E., and Wlodarczyk, J. (2019). Chronic Unpredictable Mild Stress for Modeling Depression in Rodents: Meta-Analysis of Model Reliability. *Neurosci. Biobehavioral Rev.* 99, 101–116. doi:10.1016/j.neubiorev.2018.12.002

Aparna, V., Dileep, K. V., Mandal, P. K., Karthe, P., Sadasivan, C., and Haridas, M. (2012). Anti-Inflammatory Property of N-Hexadecanoic Acid: Structural Evidence and Kinetic Assessment. *Chem. Biol. Drug Des.* 80, 434–439. doi:10.1111/j.1747-0285.2012.01418.x

Asghar, S. F., and Choudahry, M. (2011). Gas Chromatography-Mass Spectrometry (GC-MS) Analysis of Petroleum Ether Extract (Oil) and Bio-Assays of Crude Extract of Iris Germanica. *Int. J. Genet. Mol. Biol.* 3, 95–100.

Ayuob, N. N., El Wahab, M. G. A., Ali, S. S., and Abdel-Tawab, H. S. (2018). Ocimum Basilicum Improve Chronic Stress-Induced Neurodegenerative Changes in Mice hippocampus. *Metab. Brain Dis.* 33, 795–804. doi:10.1007/s11011-017-0173-3

Azizah, A., Wee, K., Azizah, O., and Azizah, M. (2009). Effect of Boiling and Stir Frying on Total Phenolics, Carotenoids and Radical Scavenging Activity of Pumpkin (Cucurbita Moschato). *Int. Food Res. J.* 16, 45–51.

Bahramsoltani, R., Farzaei, M. H., Abdolghaffari, A. H., Rahimi, R., Samadi, N., Heidari, M., et al. (2017). Evaluation of Phytochemicals, Antioxidant and Burn Wound Healing Activities of Cucurbita Moschata Duchesne Fruit Peel. *Iran J. Basic Med. Sci.* 20, 798–805. doi:10.22038/IJBMS.2017.9015

Bardaa, S., Halima, N. B., Aloui, F., Mansour, R. B., Jabeur, H., Bouaziz, M., et al. (2016). Oil from Pumpkin (Cucurbita Pepo L.) Seeds: Evaluation of its Functional Properties on Wound Healing in Rats. *Lipids Health Dis.* 15, 1–12. doi:10.1186/s12944-016-0237-0

Bora, N. S., Mazumder, B., Mandal, S., Patowary, P., Goyary, D., Chattopadhyay, P., et al. (2019). Amelioration of UV Radiation-Induced Photoaging by a Combinational Sunscreen Formulation via Aversion of Oxidative Collagen Degradation and Promotion of TGF-β-Smad-Mediated Collagen Production. *Eur. J. Pharm. Sci.* 127, 261–275. doi:10.1016/j.ejps.2018.11.004

Buske-Kirschbaum, A., Ebrecht, M., Kern, S., and Hellhammer, D. H. (2006). Endocrine Stress Responses in TH1-Mediated Chronic Inflammatory Skin Disease (Psoriasis Vulgaris)-Do They Parallel Stress-Induced Endocrine Changes in TH2-Mediated Inflammatory Dermatoses (Atopic Dermatitis)? *Psychoneuroendocrinology* 31, 439–446. doi:10.1016/j.psyneuen.2005.10.006

Carobrez, A. P., and Bertoglio, L. J. (2005). Ethological and Temporal Analyses of Anxiety-like Behavior: the Elevated Plus-Maze Model 20 Years on. *Neurosci. Biobehavioral Rev.* 29, 1193–1205. doi:10.1016/j.neubiorev.2005.04.017

Cha, H.-Y., Ahn, S.-H., Cheon, J.-H., Park, I.-S., Kim, J.-T., and Kim, K. (2016). Hataedock Treatment Has Preventive Therapeutic Effects in Atopic Dermatitis-Induced NC/Nga Mice under High-Fat Diet Conditions. *Evidence-Based Complement. Altern. Med.* 2016, 1739760. doi:10.1155/2016/1739760

Chang, T.-M., Yang, T.-Y., Niu, Y.-L., and Huang, H.-C. (2018). The Extract of D. Dasycarpus Ameliorates Oxazolone-Induced Skin Damage in Mice by Anti-inflammatory and Antioxidant Mechanisms. *Antioxidants* 7, 77. doi:10.3390/antiox7060077

Chaudhary, S. (2001). *Flora of the Kingdom of Saudi Arabia: Illustrated Riyadh: Ministry of Agriculture and Water*. Riyadh, Saudi Arabia: National Herbarium, National Agriculture and Water Research Center

Chen, M. X., Alexander, K. S., and Baki, G. (2016). Formulation and Evaluation of Antibacterial Creams and Gels Containing Metal Ions for Topical Application. *J. Pharm. (Cairo)* 2016, 5754349. doi:10.1155/2016/5754349

Cho, K.-H., Hong, J.-H., and Lee, K.-T. (2010). Monoacylglycerol (MAG)-oleic Acid Has Stronger Antioxidant, Anti-atherosclerotic, and Protein Glycation Inhibitory Activities Than MAG-Palmitic Acid. *J. Med. Food* 13, 99–107. doi:10.1089/jmf.2009.1024

Choi, H. M., Kim, D., Lee, W., and Kim, H. (2018). Estimating Causal Associations of Atopic Dermatitis with Depression Using the Propensity Score Method: An Analysis of Korea Community Health Survey Data, 2010-2013. *Epidemiology and health* 40, e2018059. doi:10.4178/epih.e2018059

Conklin, S. M., Runyan, C. A., Leonard, S., Reddy, R. D., Muldoon, M. F., and Yao, J. K. (2010). Age-related Changes of N-3 and N-6 Polyunsaturated Fatty Acids in the Anterior Cingulate Cortex of Individuals with Major Depressive Disorder. *Prostaglandins, Leukot. Essent. Fatty Acids* 82, 111–119. doi:10.1016/j.plefa.2009.12.002

Danso, M. O., Van Drongelen, V., Mulder, A., Van Esch, J., Scott, H., Van Smeden, J., et al. (2014). TNF-α and Th2 Cytokines Induce Atopic Dermatitis-like Features on Epidermal Differentiation Proteins and Stratum Corneum Lipids in Human Skin Equivalents. *J. Invest. Dermatol.* 134, 1941–1950. doi:10.1038/jid.2014.83

Dotto, J. M., and Chacha, J. S. (2020). The Potential of Pumpkin Seeds as a Functional Food Ingredient: A Review. *Scientific Afr.* 10, e00575. doi:10.1016/j.sciaf.2020.e00575

Duke, J. A. (1992). Handbook of Phytochemical Constituents of GRAS Herbs and Other Economic Plants. Boca Raton: FL: CRC Press. Available at: https://phytochem.nal.usda.gov/phytochem/search.[Online]

Ejaz, R., Ashfaq, U. A., and Idrees, S. (2014). Antimicrobial Potential of Pakistani Medicinal Plants against Multi-Drug Resistance *Staphylococcus aureus*. *J. Coast Life Med.* 2, 714–720. doi:10.12980/JCLM.2.201414B1

Firth, J., Siddiqi, N., Koyanagi, A., Siskind, D., Rosenbaum, S., Galletly, C., et al. (2019). The Lancet Psychiatry Commission: A Blueprint for Protecting Physical Health in People with Mental Illness. *Lancet Psychiatry* 6, 675–712. [Online]. [Accessed 8 6]. 10.1016/S2215-0366(19)30132-4

Gamal, M., Moawad, J., Rashed, L., Morcos, M. A., and Sharawy, N. (2018). Possible Involvement of Tetrahydrobiopterin in the Disturbance of Redox Homeostasis in Sepsis - Induced Brain Dysfunction. *Brain Res.* 1685, 19–28. doi:10.1016/j.brainres.2018.02.008

George, S., and Nazni, P. (2012). Antidepressive Activity of Processed Pumpkin (Cucurbita Maxima) Seeds on Rats. *Int. J. Pharm. Med. Bio. Sc* 1, 225–231.

Getie, M., Gebre-Mariam, T., Rietz, R., and Neubert, R. (2002). Evaluation of the Release Profiles of Flavonoids from Topical Formulations of the Crude Extract of the Leaves of Dodonea Viscosa (Sapindaceae). *Pharmazie* 57, 320–322.

Hema, R., Kumaravel, S., and Alagusundaram, K. (2011). GC/MS Determination of Bioactive Components of Murraya Koenigii. *J. Am. Sci.* 7, 80–83.

Jonnalagadda, S. C., Suman, P., Morgan, D. C., and Seay, J. N. (2017). Chapter 2—Recent Developments on the Synthesis and Applications of Betulin and Betulinic Acid Derivatives as Therapeutic Agents. *Stud. Nat. Prod. Chem.* 53, 45–84. doi:10.1016/B978-0-444-63930-1.00002-8

Jeong, H.-J., Kim, J.-H., Kim, N.-R., Yoou, M.-S., Nam, S.-Y., Kim, K.-Y., et al. (2015). Antidepressant Effect of Stillen. *Arch. Pharm. Res.,* 38, 1223–1231. doi:10.1007/s12272-014-0472-8

Kaur, S., Zilmer, K., Leping, V., and Zilmer, M. (2014). *Allergic Contact Dermatitis Is Associated with Significant Oxidative stressDermatology Research and Practice*. 2014, 10.1155/2014/415638

Kerstan, A., Brocker, E.-B., and Trautmann, A. (2011). Decisive Role of Tumor Necrosis Factor-α for Spongiosis Formation in Acute Eczematous Dermatitis. *Arch. Dermatol. Res.* 303, 651–658. doi:10.1007/s00403-011-1149-5

Kikuchi, T., Ando, H., Maekawa, K.-i., Arie, H., Yamada, T., and Tanaka, R. (2015). Two New Ent -kaurane-type Diterpene Glycosides from Zucchini (Cucurbita Pepo L.) Seeds. *Fitoterapia* 107, 69–76. doi:10.1016/j.fitote.2015.09.019

Kim, M. Y., Kim, E. J., Kim, Y.-N., Choi, C., and Lee, B.-H. (2012). Comparison of the Chemical Compositions and Nutritive Values of Various Pumpkin (Cucurbitaceae) Species and Parts. *Nutr. Res. Pract.* 6, 21–27. doi:10.4162/nrp.2011.5.6.21

Kim, N.-R., Kim, H.-Y., Kim, M.-H., Kim, H.-M., and Jeong, H.-J. (2016). Improvement of Depressive Behavior by Sweetme Sweet Pumpkin and its Active Compound, β-carotene. *Life Sci.* 147, 39–45. doi:10.1016/j.lfs.2016.01.036

Kim, S. C., Suman, P., Morgan, D. C., and Seay, J. N. (2017). "Chapter 2 - Recent Developments on the Synthesis and Applications of Betulin and Betulinic Acid

Derivatives as Therapeutic Agents," in *Studies in Natural Products Chemistry*. Editor R. ATTA UR (Elsevier).

Kvetnansky, R., Rusnak, M., Dronjak, S., Krizanova, O., and Sabban, E. L. (2003). Effect of Novel Stressors on Tyrosine Hydroxylase Gene Expression in the Adrenal Medulla of Repeatedly Immobilized Rats. *Neurochem. Res.* 28, 625–630. doi:10.1023/a:1022846012174

Lachance, L. R., and Ramsey, D. (2018). Antidepressant Foods: An Evidence-Based Nutrient Profiling System for Depression. *Wjp* 8, 97–104. doi:10.5498/wjp.v8.i3.97

Laouini, D., Elkhal, A., Yalcindag, A., Kawamoto, S., Oettgen, H., and Geha, R. S. (2005). COX-2 Inhibition Enhances the TH2 Immune Response to Epicutaneous Sensitization. *J. Allergy Clin. Immunol.* 116, 390–396. doi:10.1016/j.jaci.2005.03.042

Luo, M., Zhang, Z., Li, H., Qiao, S., Liu, Z., Fu, L., et al. (2014). Multi-scale Optical Imaging of the Delayed Type Hypersensitivity Reaction Attenuated by Rapamycin. *Theranostics* 4, 201–214. doi:10.7150/thno.7570

Macdougall, C. E., Wood, E. G., Solomou, A., Scagliotti, V., Taketo, M. M., Gaston-Massuet, C., et al. (2019). Constitutive Activation of β-Catenin in Conventional Dendritic Cells Increases the Insulin Reserve to Ameliorate the Development of Type 2 Diabetes in Mice. *Diabetes* 68, 1473–1484. doi:10.2337/db18-1243

Malhotra, S., and Mehta, V. (2008). Role of Stressful Life Events in Induction or Exacerbation of Psoriasis and Chronic Urticaria. *Indian J. Dermatol. Venereol. Leprol.* 74, 594. doi:10.4103/0378-6323.45100

Malik, M., and English, J. (2015). Irritant Hand Dermatitis in Health Care Workers: Table 1. *Occmed* 65, 474–476. doi:10.1093/occmed/kqv067

Martín, V., Fabelo, N., Santpere, G., Puig, B., Marín, R., Ferrer, I., et al. (2010). Lipid Alterations in Lipid Rafts from Alzheimer's Disease Human Brain Cortex. *Jad* 19, 489–502. doi:10.3233/jad-2010-1242

Mikaia, A., Ei, P. E. W. V., Ei, V. Z., Ei, D. Z., Ei, O. D. S., Neta, P., et al. (2014). NIST Standard Reference Database 1A. Standard Reference Data. Gaithersburg, MD, USA: NIST. https://www.nist.gov/srd/nist-standard-reference-database-1a

Narendhirakannan, R. T., and Hannah, M. A. C. (2013). Oxidative Stress and Skin Cancer: an Overview. *Ind. J. Clin. Biochem.* 28, 110–115. doi:10.1007/s12291-012-0278-8

Nawirska-Olszańska, A., Kita, A., Biesiada, A., SOKoŁ-Łętowska, A., and Kucharska, A. Z. (2013). Characteristics of Antioxidant Activity and Composition of Pumpkin Seed Oils in 12 Cultivars. *Food Chem.* 139, 155–161.

Nestler, E. J., Barrot, M., Dileone, R. J., Eisch, A. J., Gold, S. J., and Monteggia, L. M. (2002). Neurobiology of Depression. *Neuron* 34, 13–25. doi:10.1016/s0896-6273(02)00653-0

Numakawa, T., Richards, M., Nakajima, S., Adachi, N., Furuta, M., Odaka, H., et al. (2014). The Role of Brain-Derived Neurotrophic Factor in Comorbid Depression: Possible Linkage with Steroid Hormones, Cytokines, and Nutrition. *Front. Psychiatry* 5, 136. doi:10.3389/fpsyt.2014.00136

Orita, K., Hiramoto, K., Kobayashi, H., Ishii, M., Sekiyama, A., and Inoue, M. (2011). Inducible Nitric Oxide Synthase (iNOS) and α-melanocyte-stimulating Hormones of iNOS Origin Play Important Roles in the Allergic Reactions of Atopic Dermatitis in Mice. *Exp. Dermatol.* 20, 911–914. doi:10.1111/j.1600-0625.2011.01360.x

Ozgur, E., Demıral, Y., and Cımrın, A. (2018). *714 Occupational Contact Dermatitis*. London, United Kingdom: BMJ Publishing Group Ltd.. doi:10.1136/oemed-2018-icohabstracts.147

Packer, L. (2002). *Superoxide Dismutase*. Amsterdam, Netherlands: Elsevier.

Pasparakis, M., Haase, I., and Nestle, F. O. (2014). Mechanisms Regulating Skin Immunity and Inflammation. *Nat. Rev. Immunol.* 14, 289–301. doi:10.1038/nri3646

Pedraz-Petrozzi, B., Neumann, E., and Sammer, G. (2020). Pro-inflammatory Markers and Fatigue in Patients with Depression: A Case-Control Study. *Scientific Rep.* 10, 1–12. doi:10.1038/s41598-020-66532-6

Perez Gutierrez, R. M. (2016). Review of Cucurbita Pepo (Pumpkin) its Phytochemistry and Pharmacology. *Med. Chem.* 6, 012–021. doi:10.4172/2161-0444.1000316

Picardi, A., Mazzotti, E., Gaetano, P., Cattaruzza, M. S., Baliva, G., Melchi, C. F., et al. (2005). Stress, Social Support, Emotional Regulation, and Exacerbation of Diffuse Plaque Psoriasis. *Psychosomatics* 46, 556–564. doi:10.1176/appi.psy.46.6.556

Pivarcsi, A., Nagy, I., and Kemeny, L. (2005). Innate Immunity in the Skin: How Keratinocytes Fight against Pathogens. *Cir* 1, 29–42. doi:10.2174/1573395052952941

Qu, R., Chen, X., Hu, J., Fu, Y., Peng, J., Li, Y., et al. (2019). Ghrelin Protects against Contact Dermatitis and Psoriasiform Skin Inflammation by Antagonizing TNF-A/nf-Kb Signaling Pathways. *Scientific Rep.* 9, 1–14. doi:10.1038/s41598-018-38174-2

Rigat, M., Vallès, J., D'Ambrosio, U., Gras, A., Iglésias, J., and Garnatje, T. (2015). Plants with Topical Uses in the Ripollès District (Pyrenees, Catalonia, Iberian Peninsula): Ethnobotanical Survey and Pharmacological Validation in the Literature. *J. Ethnopharmacology* 164, 162–179. doi:10.1016/j.jep.2015.01.055

Salehi, B., Capanoglu, E., Adrar, N., Catalkaya, G., Shaheen, S., Jaffer, M., et al. (2019). plants: A Key Emphasis to its Pharmacological Potential. *Molecules*, 24, 1854. doi:10.3390/molecules24101854

Serefhanoglu, K., Taskin, A., Turan, H., Timurkaynak, F. E., Arslan, H., and Erel, O. (2009). Evaluation of Oxidative Status in Patients with Brucellosis. *Braz. J. Infect. Dis.* 13, 249–251. doi:10.1590/s1413-86702009000400001

Shiri, E., Rahnema, M., and Bigdeli, M. (2016). The Effect of Pumpkin Seed Oil (Cucurbita Moschata) on the Permeability of the Blood-Brain Barrier and on Brain Edema in Stroke Animal Model.*J. North Khorasan Univ. Med. Sci.* 8 (2), 301–311. doi:10.18869/acadpub.jnkums.8.2.301

Simonetta, F., and Bourgeois, C. (2011). *Animal Models of Contact Dermatitis*. Contact Dermatitis. Editor S. R. Young, 23–38.

Song, J., Kim, Y.-S., Lee, D. H., Lee, S. H., Park, H. J., Lee, D., et al. (2019). Neuroprotective Effects of Oleic Acid in Rodent Models of Cerebral Ischaemia. *Scientific Rep.* 9, 1–13. doi:10.1038/s41598-019-47057-z

Taraz, M., Taraz, S., and Dashti-Khavidaki, S. (2015). Association between Depression and Inflammatory/anti-Inflammatory Cytokines in Chronic Kidney Disease and End-Stage Renal Disease Patients: A Review of Literature. *Hemodial Int.* 19, 11–22. doi:10.1111/hdi.12200

Thomas, J. A., Allen, J. L., Tsen, M., Dubnicoff, T., Danao, J., Liao, X. C., et al. (1999). Impaired Cytokine Signaling in Mice Lacking the IL-1 Receptor-Associated Kinase. *J. Immunol.* 163, 978–984.

Thyssen, J. P., Mcfadden, J. P., and Kimber, I. (2014). The Multiple Factors Affecting the Association between Atopic Dermatitis and Contact Sensitization. *Allergy* 69, 28–36. doi:10.1111/all.12358

Wang, C., Yuan, J., Wu, H.-X., Chang, Y., Wang, Q.-T., Wu, Y.-J., et al. (2015). Total Glucosides of Paeony Inhibit the Inflammatory Responses of Mice with Allergic Contact Dermatitis by Restoring the Balanced Secretion of Pro-/anti-inflammatory Cytokines. *Int. Immunopharmacology* 24, 325–334. doi:10.1016/j.intimp.2014.12.026

Wang, S.-Y., Huang, W.-C., Liu, C.-C., Wang, M.-F., Ho, C.-S., Huang, W.-P., et al. (2012). Pumpkin (Cucurbita Moschata) Fruit Extract Improves Physical Fatigue and Exercise Performance in Mice. *Molecules* 17, 11864–11876. doi:10.3390/molecules171011864

WHO (2020). Available at: https://www.who.int/news-room/fact-sheets/detail/depression. (Accessed January 12, 2021)

Wiley, J. (2006). *Wiley Registry of Mass Spectral Data*. Hoboken, NJ: John Wiley.

Xia, H. C., Li, F., Li, Z., and Zhang, Z. C. (2003). Purification and Characterization of Moschatin, a Novel Type I Ribosome-Inactivating Protein from the Mature Seeds of Pumpkin (Cucurbita Moschata), and Preparation of its Immunotoxin against Human Melanoma Cells. *Cell Res* 13, 369–374. doi:10.1038/sj.cr.7290182

Yang, B., Yang, S., and Chen, S. (2000). A Preliminary Study on the Cultivating Technique of Cucurbita Pepo Cv Dayangua. *Spec. Econ. Amin. Plant* 3, 28

Yankelevitch-Yahav, R., Franko, M., Huly, A., and Doron, R. (2015). The Forced Swim Test as a Model of Depressive-like Behavior. *JoVE (Journal of Visualized Experiments)*, e52587. doi:10.3791/52587

Zhang, M., Zhou, J., Wang, L., Li, B., Guo, J., Guan, X., et al. (2014). Caffeic Acid Reduces Cutaneous Tumor Necrosis Factor Alpha (TNF-α), IL-6 and IL-1β Levels and Ameliorates Skin Edema in Acute and Chronic Model of Cutaneous Inflammation in Mice. *Biol. Pharm. Bull.* 37, 347–354. doi:10.1248/bpb.b13-00459

Zhou, P., Yang, X., Jia, X., Yu, J., Asenso, J., Xiao, F., et al. (2016). Effect of 6′-acetylpaeoniflorin on Dinitrochlorobenzene-Induced Allergic Contact Dermatitis in BALB/c Mice. *Immunol. Res.* 64, 857–868. doi:10.1007/s12026-016-8788-8

Conflict of Interest: The authors declare that the research was conducted in the absence of any commercial or financial relationships that could be construed as a potential conflict of interest.

Copyright © 2021 Balgoon, Al-Zahrani, Jaouni and Ayuob. This is an open-access article distributed under the terms of the Creative Commons Attribution License (CC BY). The use, distribution or reproduction in other forums is permitted, provided the original author(s) and the copyright owner(s) are credited and that the original publication in this journal is cited, in accordance with accepted academic practice. No use, distribution or reproduction is permitted which does not comply with these terms.

frontiers in Pharmacology

ORIGINAL RESEARCH
published: 21 June 2021
doi: 10.3389/fphar.2021.700573

New Polyketides With Anti-Inflammatory Activity From the Fungus *Aspergillus rugulosa*

Qianqian Xu[1†], Yuben Qiao[1†], Zijun Zhang[1†], Yanfang Deng[1], Tianqi Chen[1], Li Tao[2], Qiaoxin Xu[1], Junjun Liu[1], Weiguang Sun[1], Ying Ye[1], Yuanyuan Lu[3], Changxing Qi[1]* and Yonghui Zhang[1]**

[1]Hubei Key Laboratory of Natural Medicinal Chemistry and Resource Evaluation, School of Pharmacy, Tongji Medical College, Huazhong University of Science and Technology, Wuhan, China, [2]Ezhou Central Hospital, Ezhou, China, [3]Maternal and Child Health Hospital of Hubei Province, Tongji Medical College, Huazhong University of Science and Technology, Wuhan, China

OPEN ACCESS

Edited by:
Hongzhi Du,
Hubei University of Chinese Medicine, China

Reviewed by:
Ni Fan,
The University of Hong Kong, Hong Kong, SAR China
Ghulam Jilany Khan,
University of Central Punjab, Pakistan

***Correspondence:**
Yonghui Zhang
zhangyh@mails.tjmu.edu.cn
Changxing Qi
qichangxing@hust.edu.cn
Yuanyuan Lu
Luyuanyuan@hust.edu.cn

[†]These authors contributed equally to this work.

Specialty section:
This article was submitted to Inflammation Pharmacology, a section of the journal Frontiers in Pharmacology

Received: 26 April 2021
Accepted: 26 May 2021
Published: 21 June 2021

Citation:
Xu Q, Qiao Y, Zhang Z, Deng Y, Chen T, Tao L, Xu Q, Liu J, Sun W, Ye Y, Lu Y, Qi C and Zhang Y (2021) New Polyketides With Anti-Inflammatory Activity From the Fungus Aspergillus rugulosa. Front. Pharmacol. 12:700573. doi: 10.3389/fphar.2021.700573

Two new polyketide compounds, asperulosins A and B (**1**–**2**), and one new prenylated small molecule, asperulosin C (**3**), along with nine known compounds (**4**–**12**), were isolated and identified from a fungus *Aspergillus rugulosa*. Their structures were extensively elucidated *via* HRESIMS, 1D, and 2D NMR analysis. The absolute configurations of the new compounds were determined by the comparison of their electronic circular dichroism (ECD), calculated ECD spectra, and the detailed discussion with those in previous reports. Structurally, compounds **1** and **2** belonged to the polyketide family and were from different origins. Compound **2** was constructed by five continuous quaternary carbon atoms, which occur rarely in natural products. All of the isolates were evaluated for anti-inflammatory activity against the production of nitric oxide (NO) in lipopolysaccharide (LPS)-induced RAW264.7 cells. Among those, compounds **1** and **5** showed a significant inhibitory effect on NO production with IC_{50} values of 1.49 ± 0.31 and 3.41 ± 0.85 μM, respectively. Additionally, compounds **1** and **5** markedly increased the secretion of anti-inflammatory cytokine IL10 while suppressing the secretion of pro-inflammatory cytokines IL6, TNF-α, IFN-γ, MCP-1, and IL12. Besides, **1** and **5** inhibited the transcription level of pro-inflammatory macrophage markers IL6, IL1β, and TNF-α while remarkably elevating the anti-inflammatory factor IL10 and M2 macrophage markers ARG1 and CD206. Moreover, **1** and **5** restrained the expression and nuclear translocation of NF-κB, as well as its downstream signaling proteins COX-2 and iNOS. All these results suggest that **1** and **5** have potential as anti-inflammatory agents, with better or comparable activities than those of the positive control, dexamethasone.

Keywords: ***Aspergillus rugulosa*, polyketides, anti-inflammatory, molecular docking, immunofluorescence**

INTRODUCTION

Small molecular polyketide compounds have been considered commercially valuable for their wide range of functions, structural diversity, and outstanding pharmaceutical activities (González-Medina et al., 2017; Newman and Cragg, 2020). For instance, lovastatin, daunomycin, and tetracycline are all small molecular polyketides (Herkommer et al., 2014; Van Wagoner et al., 2014). Natural polyketides are biosynthesized by consecutive decarboxylative condensations of short-chain acyl-CoAs by fungi,

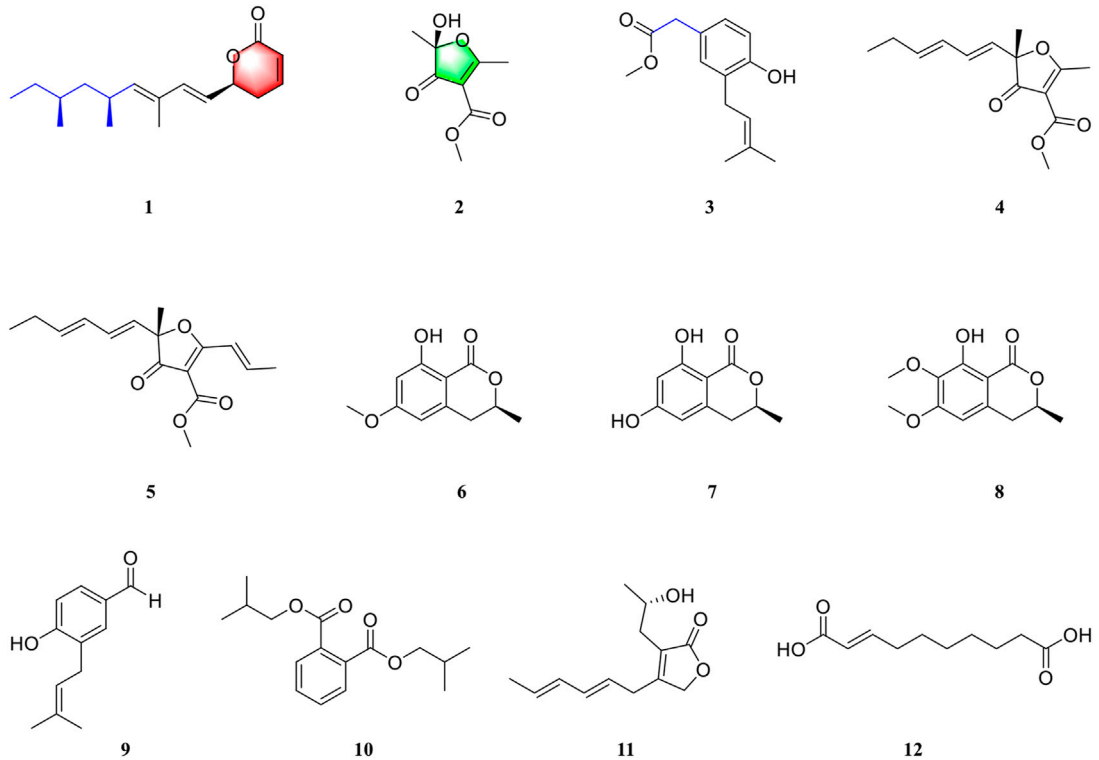


FIGURE 1 | Structures of compounds **1**–**12**.

bacteria, and plants (Hertweck, 2009). Consequently, bioactive polyketides have roused extensive scientific interest in the fields of chemistry and pharmacology in recent years (Lacoske and Theodorakis, 2015).

Inflammation is a defensive response to fight infections such as microbial infection, chemical stimuli, and toxins (Medzhitov, 2010). However, recent studies have shown that uncontrolled chronic inflammation is associated with multiple diseases, including rheumatoid arthritis, metabolic syndrome, diabetes, and cancer (Okamoto et al., 2007). Overproduction of pro-inflammatory factors including nitric oxide (NO) and cyclooxygenase-2 (COX-2) and cytokines such as tumor necrosis factor-α (TNF-α) and interleukin-6 (IL-6) impulses the inflammatory response (Lee et al., 2016). Furthermore, the activation of the transcription factor nuclear factor-kappa B (NF-κB) accelerates the immune response *via* the transcriptional activation of the pro-inflammatory factors and cytokines mentioned above (Alvarez-Suarez et al., 2017).

Our group focuses on the discovery and development of novel bioactive secondary metabolites from the *Aspergillus* species in recent years. Representative research studies include asperflavipine A (Zhu et al., 2017), epicochalasines A and B (Zhu et al., 2016), asperterpenes A and B (Qi et al., 2016), asperpyridone A (Qiao et al., 2019), and terreuspyridine (Li et al., 2020). Moreover, we recently found that large-scale culture can approach many more natural products with novel skeletons (Hu et al., 2021). As part of the program mentioned above, we performed a chemical investigation on a polyketide-producing fungus, *Aspergillus rugulosa* (Ballantine et al., 1969; Cacho et al., 2012). As a result, we isolated and identified two new polyketides, asperulosins A and B (**1**–**2**), and one new prenylated small molecule, asperulosin C (**3**), along with nine known compounds (**4**–**12**). These compounds were determined as (–)-gregatin B (**4**) (Burghart-Stoll and Brückner, 2012), aspertetronin A (**5**) (Burghart-Stoll and Brückner et al., 2012), angelicoin B (**6**) (Elsebai et al., 2018), (*R*)-6-hydroxymellein (**7**) (Islam et al., 2007), dimethoxymellein (**8**) (Choudhary et al., 2004), 4-hydroxy-3-(3-methylbut-2-enyl) benzaldehyde (**9**) (Vu et al., 2016), diisobutyl phthalate (**10**) (Zhang et al., 2003), 3-(2-hydroxypropyl)-4-(hexa-2*E*,4*E*-dien-6-yl) furan-2(5*H*)-one (**11**) (Almassi et al., 1991), and trans-2-decenedioic acid (**12**) (Kwok et al., 1992) by detailed comparison of their NMR data and specific rotations with those of previous literatures. Herein, the details of the isolation, structural elucidation, and biological evaluations of the isolates (**Figure 1**) are described.

MATERIALS AND METHODS

General

Optical rotation, UV, and IR data were recorded on a PerkinElmer 341 instrument, a Varian Cary 50 instrument, and a Bruker Vertex 70 instrument with KBr pellets, respectively. ECD data were measured using a JASCO-810 CD spectrometer. The high-resolution electrospray ionization mass

spectra (HRESIMS) were recorded by using the positive ion mode on a Thermo Fisher LC-LTQ-Orbitrap XL instrument. One- and two-dimensional NMR data were recorded on a Bruker AM-400 instrument, with the reference of ^{1}H and ^{13}C NMR chemical shifts of the solvent peaks for methanol-d_4 (δ_H 3.31 and δ_C 49.0) and $CHCl_3$-d (δ_H 7.26 and δ_C 77.0). Semi-preparative HPLC was conducted on a Dionex HPLC system equipped with an Ultimate 3,000 pump (Thermo Fisher Scientific, Germany), an Ultimate 3,000 autosampler injector, and an Ultimate 3,000 diode array detector (DAD) controlled by Chromeleon software (version 6.80), using a reverse-phased C18 column (5 μm, 10 × 250 mm, Welch Ultimate XB-C18). Column chromatography (CC) was carried out by using silica gel (80–120, 100–200, 200–300 mesh, Qingdao Marine Chemical, Inc., Qingdao, People's Republic of China), Lichroprep RP-C_{18} gel (40–63 μm, Merck, Darmstadt, Germany), and Sephadex LH-20 (GE Healthcare Bio-Sciences AB, Sweden). Silica gel 60 F_{254} was used for the TLC (thin-layer chromatography) detection, and spots were visualized by spraying heated silica gel plates with 5% H_2SO_4 in EtOH.

Fungal Material

The fungus *Aspergillus rugulosa* was purchased from the China General Microbiological Culture Collection Center (CGMCC, no. 3.6395). The fungal sample was deposited in the culture collection of Tongji Medical College, Huazhong University of Science and Technology.

Fermentation, Extraction, and Purification

The experimental stain was incubated in potato dextrose agar (PDA) medium at 28 °C for 4 days to prepare the seed cultures, which was then transferred into 500-ml Erlenmeyer flasks, each containing 200 g rice (total 20 kg). After being cultivated for 21 days, the medium was extracted with 95% aqueous EtOH five times at room temperature. Afterward, the solvent was removed under reduced pressure to yield a total residue, which was then suspended in water and partitioned repeatedly with EtOAc. The EtOAc extract (130.4 g) was chromatographed by silica gel CC (80–120 mesh), using an increasing gradient of petroleum ether–ethyl acetate (100:0–0:100) to afford six fractions (A–F).

Fraction C (16.5 g) was fractioned by silica gel CC (200–300 mesh), using an increasing gradient of petroleum ether–ethyl acetate (20:1–10:1) to afford ten subfractions (C1–C10). Subfraction C4 (375 mg) was chromatographed on Sephadex LH-20 eluted with CH_2Cl_2–MeOH (1:1, v/v) to yield three fractions (C4.1–C4.3). Fraction C4.2 was purified by using semi-preparative HPLC eluted with MeCN–H_2O (82:18, v/v, 2.0 ml/min) to afford compound **1** (t_R 15.2 min, 4.6 mg). Fraction C4.3 was purified by using semi-preparative HPLC (MeCN–H_2O, 77:23, v/v, 2.0 ml/min) to yield compound **5** (t_R 15.8 min, 5.4 mg). Compound **9** (t_R 17.1 min, 3.0 mg) was purified by semi-preparative HPLC (MeCN–H_2O, 52:48, v/v, 2.0 ml/min) from fraction C4.1. Subfraction C5 was chromatographed on Sephadex LH-20 eluted with CH_2Cl_2–MeOH (1:1, v/v) to yield five fractions (C5.1–C5.5). Fraction C5.2 was purified by using semi-preparative HPLC (MeOH–H_2O, 80:20, v/v, 2.0 ml/min) to yield compound **10** (t_R 31.3 min, 18.2 mg). Fraction C5.3 was chromatographed using the RP-C_{18} column with MeOH–H_2O (from 35:65 to 100:0, v/v) to afford ten subfractions (C5.3.1–C5.3.10). Compound **3** (t_R 25.1 min, 5.0 mg) was purified by semi-preparative HPLC (MeCN–H_2O, 58:42, v/v, 2.0 ml/min) from fraction C5.3.2. Compound **2** (t_R 9.3 min, 4.9 mg) was purified by semi-preparative HPLC (MeCN–H_2O, 30:70, v/v, 2.0 ml/min) from fraction C5.3.4. Compound **11** (t_R 41.3 min, 66.0 mg) was purified by semi-preparative HPLC (MeOH–H_2O, 55:45, v/v, 2.0 ml/min) from fraction C5.3.5. Compound **4** (t_R 14.0 min, 55.6 mg) was purified by semi-preparative HPLC (MeOH–H_2O, 79:21, v/v, 2.0 ml/min) from C5.3.6. Compound **12** (t_R 31.3 min, 3.5 mg) was purified by semi-preparative HPLC (MeOH–H_2O, 75:45, v/v, 2.0 ml/min) from fraction C5.3.8.

Fraction E (1.4 g) was fractioned by silica gel CC (200–300 mesh), using an increasing gradient of petroleum ether–ethyl acetate (10:1–1:1) to afford five subfractions (E1–E5). Subfraction E4 (417 mg) was chromatographed using the RP-C_{18} column with MeOH–H_2O (from 30:70 to 90:10, v/v) to afford eight subfractions (E4.1–E4.8). Compound **6** (t_R 19.2 min, 9.1 mg) was purified by semi-preparative HPLC (MeCN–H_2O, 33:67, v/v, 2.0 ml/min) from fraction E4.3. Fraction E4.2 was purified by using semi-preparative HPLC (MeCN–H_2O, 28:72, v/v, 2.0 ml/min) to afford compound **7** (t_R 16.3 min, 3.4 mg). Compound **8** (t_R 15.5 min, 16.4 mg) was purified by semi-preparative HPLC (MeCN–H_2O, 47:53, v/v, 2.0 ml/min) from fraction E4.6.

Spectroscopic Data

Compound **1**: colorless oil; (α)25 D: +2.0 (*c* 0.1, MeOH); UV (MeOH) λ_{max} (log ε) = 233 (3.34) nm; IR ν_{max} = 2,962, 1,725, 1,384, 1,345, 1,246, 1,028, 1,024, 818 cm^{-1}; ECD (*c* 0.1, MeOH) $\Delta\varepsilon_{202}$—6.3, $\Delta\varepsilon_{236}$ + 0.20, $\Delta\varepsilon_{258}$—1.15; molecular formula $C_{17}H_{26}O_2$; HRESIMS *m/z* 285.1837 $(M + Na)^+$ (calcd for $C_{17}H_{26}O_2Na$, 285.1830); for ^{1}H and ^{13}C NMR data, see **Table 1**.

Compound **2**: white powders; (α)25 D: 52.2 (*c* 0.1, MeOH); IR ν_{max} = 3,425, 1,732, 1,649, 1,579, 1,447, 1,205, 1,009 cm^{-1}; ECD (*c* 0.1, MeOH) $\Delta\varepsilon_{214}$ + 8.37, $\Delta\varepsilon_{241}$ − 2.62, $\Delta\varepsilon_{268}$ + 3.78; HRESIMS *m/z* 209.0404 $(M + Na)^+$ (calcd for $C_8H_{10}O_5Na$, 209.0426); for ^{1}H and ^{13}C NMR data, see **Table 1**.

Compound **3**: white powders; UV (MeOH) λ_{max} (log ε) = 202 (4.16), 279 (4.01) nm; IR ν_{max} = 3,429, 1,720, 1,613, 1,588, 1,438, 1,265, 1,018 cm^{-1}; molecular formula $C_{14}H_{18}O_3$, HRESIMS *m/z* 257.1155 $(M + Na)^+$ (calcd for $C_{14}H_{18}O_3Na$, 257.1154); for ^{1}H and ^{13}C NMR data, see **Table 1**.

Compound **4** [(−) gregatin B]: Colorless oil; (α)25 D = −178.0 (MeOH); ^{1}H-NMR (400 MHz, $CDCl_3$) δ_H: 0.98 (3H, t, J = 7.5 Hz, H_3-6″), 1.52 (3H, s, H_3-2), 2.09 (2H, q, J = 7.5 Hz, H_2-5″), 2.64 (3H, s, H_3-6), 3.82 (3H, s, OCH_3-1′), 5.53 (1H, d, J = 15.5 Hz, H-1″), 5.81 (1H, dt, J = 15.5, 6.5 Hz, H-4″), 5.96 (1H, m, H-3″), and 6.27 (1H, dd, J = 15.5, 10.3 Hz, H-2″).

Compound **5** (aspertetronin A): Colorless oil; ^{1}H-NMR (400 MHz, $CDCl_3$) δ_H: 0.98 (3H, t, J = 7.5 Hz, H_3-6′), 1.54 (3H, s, H_3-7′), 2.07 (2H, m, H_2-5′), 3.83 (3H, s, OCH_3-1‴), 5.56 (1H, d, J = 15.5 Hz, H-1′), 5.80 (1H, dt, J = 15.5, 6.5 Hz, H-4′), 5.96 (1H, m, H-3′), 6.26 (1H, dd, J = 15.5, 10.3 Hz, H-2′), 7.21 (1H, m, H-2″), and 7.33 (1H, m, H-1″). ^{13}C-NMR (100 MHz,

TABLE 1 | ^{1}H (400 MHz) and ^{13}C NMR (100 MHz) data for compounds **1**–**3** (δ in ppm, J in Hz).

No.	1 (in $CDCl_3$)		No.	2 (in methanol-d_4)		No.	3 (in $CDCl_3$)	
	δ_H (J in Hz)	δ_C, type		δ_H (J in Hz)	δ_C, type		δ_H (J in Hz)	δ_C, type
1	—	164.1 C	1	—	197.7 C	1	—	153.5 C
2	6.06 dt (9.8, 1.8)	121.6 CH	2	—	107.7 C	2	—	127.0 C
3	6.89 dt (9.8, 4.3)	144.7 CH	3	—	198.3 C	3	7.00 overlap	130.8 CH
4	2.47 m	30.1 CH_2	4	—	164.4 C	4	—	126.0 C
5	4.97 ddd (15.0, 7.4, 0.8)	78.6 CH	5	—	106.4 C	5	6.74 dd (8.8, 7.9)	115.8 CH
6	5.61 dd (15.7, 6.8)	122.2 CH	6	1.49 s	21.8 CH_3	6	7.02 overlap	128.2 CH
7	6.34 d (15.7)	138.9 CH	7	2.60 s	18.3 CH_3	7	3.53 s	40.4 CH_2
8	—	130.7 C	8	3.78 s	51.6 CH_3	8	—	172.5 C
9	5.29 d (9.8)	142.4 CH	—	—	—	9	3.33 br d (7.4)	29.8 CH_2
10	2.59 m	30.3 CH	—	—	—	10	5.30 tq (7.3, 2.8)	121.6 CH
11α	1.27 overlap	44.7 CH_2	—	—	—	11	—	134.8 CH
11β	1.09 overlap		—	—	—	12	1.77 s	17.9 CH_3
12	1.25 overlap	32.2 CH	—	—	—	13	1.77 s	25.8 CH_3
13α	1.27 overlap	30.0 CH_2	—	—	—	14	3.69 s	52.0 CH_3
13β	1.13 overlap		—	—	—	—	—	—
14	0.85 d (7.1)	11.3 CH_3	—	—	—	—	—	—
15	1.75 d (0.8)	12.5 CH_3	—	—	—	—	—	—
16	0.94 d (6.7)	21.4 CH_3	—	—	—	—	—	—
17	0.81 d (6.5)	19.1 CH_3	—	—	—	—	—	—

$CDCl_3$) δ_C: 13.3 (C-6′), 19.4 (C-3″), 22.5 (C-7′), 26.7 (C-5′), 51.6 (OCH_3-1‴), 90.4 (C-5), 103.7 (C-3), 120.8 (C-1″), 126.1 (C-1′), 127.7 (C-3′), 131.5 (C-2′), 139.3 (C-4′), 144.8 (C-2″), 163.9 (C-1‴), 185.2 (C-2), and 197.0 (C-4).

Compound **6** (angelicoin B): White amorphous powder; ^{1}H-NMR (400 MHz, $CDCl_3$) δ_H: 1.47 (3H, d, J = 6.3 Hz, CH_3-3), 2.82 (2H, br d, J = 7.3 Hz, H_2-4), 3.78 (3H, s, OMe-6), 3.90 (3H, s, OMe-7), 4.63 (1H, m, H-3), 6.21 (1H, d, J = 2.2 Hz, H-5), 6.31 (1H, d, J = 2.3 Hz, H-7), and 11.2 (1H, s, OH-8). ^{13}C-NMR (100 MHz, $CDCl_3$) δ_C: 20.6 (C-9), 34.7 (C-4), 55.4 (OMe-6), 75.4 (C-3), 99.3 (C-7), 101.4 (C-8a), 106.0 (C-5), 140.9 (C-4a), 164.3 (C-8), 165.6 (C-6), and 169.8 (C-1).

Compound **7** [(*R*)-6-hydroxymellein]: White amorphous powder; ^{1}H-NMR (400 MHz, MeOH-d_4) δ_H: 1.46 (3H, d, J = 6.3 Hz, CH_3-3), 2.82 (1H, dd, J = 16.4, 11.0 Hz, H-4a), 2.91 (1H, dd, J = 16.4, 3.7 Hz, H-4b), 4.66 (1H, m, H-3), 6.19 (1H, d, J = 2.3 Hz, H-5), and 6.21 (1H, d, J = 2.3 Hz, H-7). ^{13}C-NMR (100 MHz, MeOH-d_4) δ_C: 20.9 (C-9), 35.5 (C-4), 71.2 (C-3), 101.3 (C-7), 102.2 (C-8a), 107.9 (C-5), 143.5 (C-4a), 165.7 (C-8), 166.5 (C-6), and 171.7 (C-1).

Compound **8** [(–)-(3*R*)-6,7-Dimethoxymellein]: Colorless crystalline solid; ^{1}H-NMR (400 MHz, $CDCl_3$) δ_H: 1.51 (3H, d, J = 6.3 Hz, H_3-9), 2.86 (2H, m, H_2-4), 3.87 (3H, s, OMe-6), 3.90 (3H, s, OMe-7), 4.66 (1H, m, H-3), 6.28 (1H, s, H-5), and 11.1 (1H, s, OH-8). ^{13}C-NMR (100 MHz, $CDCl_3$) δ_C: 20.6 (C-9), 34.6 (C-4), 56.1 (OMe-6), 60.7 (OMe-7), 75.8 (C-3), 102.0 (C-5), 102.8 (C-8a), 135.4 (C-7), 156.1 (C-8), 158.4 (C-6), and 169.8 (C-1).

Compound **9** [4-hydroxy-3-(3-methylbut-2-enyl) benzaldehyde]: Colorless oil; ^{1}H-NMR (400 MHz, MeOH-d_4) δ_H: 1.72 (3H, s, H_3-4′), 1.76 (3H, s, H_3-5′), 3.33 (2H, overlap, H_2-1′), 5.34 (1H, ddq, J = 8.9, 5.9, 1.5 Hz, H-2′), 6.89 (1H, d, J = 8.2 Hz, H-5), 7.60 (1H, dd, J = 8.2, 2.3 Hz, H-6), 7.62 (1H, d, J = 2.3 Hz, H-2), and 9.72 (1H, s, CHO). ^{13}C-NMR (100 MHz, MeOH-d_4) δ_C: 17.8 (C-4′), 25.9 (C-5′), 28.9 (C-1′), 116.0 (C-2, C-5), 122.9 (C-2′), 130.2 (C-3), 130.4 (C-1), 131.4 (C-5), 132.3 (C-6), 134.1 (C-3′), 163.0 (C-4), and 193.2 (C-7).

Compound **10** (diisobutyl phthalate): Colorless viscous liquid; ^{1}H-NMR (400 MHz, MeOH-d_4) δ_H: 0.99 (12H, d, J = 6.7 Hz, 4 × CH_3), 2.03 (2H, dp, J = 13.4, 6.7 Hz), 4.07 (4H, d, J = 6.5 Hz), 7.62 (2H, dd, J = 5.7, 3.3 Hz), and 7.73 (2H, dd, J = 5.7, 3.3 Hz). ^{13}C-NMR (100 MHz, MeOH-d_4) δ_C: 19.5, 29.0, 72.9, 129.9, 132.3, 133.6, and 169.2.

Compound **11** [3-(2-hydroxypropyl)-4-(hexa-2*E*,4*E*-dien-6-yl) furan-2(5*H*)-one]: Colorless oil; ^{1}H-NMR (400 MHz, MeOH-d_4) δ_H: 1.18 (3H, d, J = 6.2 Hz, H_3-3″), 1.73 (3H, br d, J = 6.8 Hz, H_3-1′), 2.40 (2H, m, H_2-1″), 3.28 (2H, d, J = 7.1 Hz, H_2-6′), 3.96 (1H, m, H-2″), 4.75 (2H, s, H_2-5), 5.55 (1H, dt, J = 14.0, 7.1 Hz, H-5′), 5.68 (1H, dq, J = 13.7, 6.8 Hz, H-2′), 6.05 (1H, m, H-3′), and 6.15 (1H, m, H-4′). ^{13}C-NMR (100 MHz, MeOH-d_4) δ_C: 18.1 (C-1′), 23.3 (C-3″), 31.2 (C-6′), 34.1 (C-1″), 67.0 (C-2″), 73.2 (C-5), 124.8 (C-5′), 125.6 (C-4), 130.1 (C-2′), 132.1 (C-3′), 135.1 (C-4′), 164.3 (C-3), and 177.7 (C-2).

Compound **12** (*trans*-2-decenedioic acid): Colorless oil; ^{1}H-NMR (400 MHz, MeOH-d_4) δ_H: 1.36 (2H, m, H_2-5), 1.36 (2H, m, H_2-6), 1.48 (2H, m, H_2-7), 1.60 (2H, m, H_2-8), 2.22 (2H, m, H_2-4), 2.28 (2H, m, H_2-9), 5.80 (1H, d, J = 15.6 Hz, H-2), and 6.94 (1H, dt, J = 15.5, 7.0 Hz, H-3). ^{13}C-NMR (100 MHz, MeOH-d_4) δ_C: 26.0 (C-8′), 29.1 (C-7), 29.9 (C-5), 30.0 (C-6), 33.0 (C-4), 35.0 (C-9), 122.7 (C-2), 150.9 (C-3), 170.3 (C-1), and 177.7 (C-10).

Cell Culture and Administration

Mouse macrophage-like cell line RAW 264.7 was cultured at 37 °C in a 5% CO_2 environment in DMEM (Hyclone, United States) supplemented with 10% fetal calf serum (Gibico, United States), the antibiotics of penicillin/streptomycin (100 units/ml) (Invitrogen, United States), and 1.5% horse serum. LPS (1 μg/ml) was used to activate

RAW264.7 cells. Dexamethasone (DEX) was used as the positive control.

Measurement of Nitric Oxide (NO) and Cytotoxic Assay

RAW 264.7 cells (5×10^4 cells/ml) were seeded in 96-well plates in 100 μl culture. After preincubation for 24 h, the seeded cells were treated with tested compounds ranging from 40 to 5 μM for 1 h, followed by stimulation with LPS (1 μg/ml) for another 24 h. The production of NO was determined with Griess reagent. Cell culture supernatants (50 μl) were mixed with 100 μl Griess reagent (1% sulfanilamide/0.1% naphthylethylene diamine dihydrochloride/2% phosphoric acid) in a 96-well plate for 10 min at room temperature. Then, the optical density was measured at 510 nm using a microplate reader (Thermo Fisher Scientific, United States). After 24 h of treatment with tested compounds, 10 μl of CCK-8 solution was added to each well, and the cells were incubated for a further 2 h, followed by the detection of absorbance at 450 nm.

Cytokine Production Bioassay

Cells were treated as described above. After 24 h of treatment, the secretion level of cytokines IL6, IL10, MCP-1, IFN-γ, TNF-α, and IL12 in the culture supernatant was detected using an Ms Inflammation Cytometric Bead Array (CBA) kit (BD Pharmingen, United States) according to the manufacturer's protocol.

Quantitative Real Time Polymerase Chain Reaction Tests

RNA was isolated from RAW264.7 cells treated with the tested compounds (Invitrogen, Thermo Fisher Scientific, United States) according to the manufacturer's recommendations. Total RNA was reverse-transcribed into cDNA using a transcription kit (ABP, United States). Quantitative RT-PCR (qRT-PCR) was performed using SYBR Green qPCR Mix (ABP, United States) with 0.2-μM forward and reverse primers in a final volume of 10 μl, and detection was performed using ABI QuantStudio 5 (Thermo Fisher Scientific, United States). The resulting cDNA was amplified by incubating at 95 °C for 5 min, 40 cycles of denaturation at 95 °C for 10 s, annealing at 55–60 °C for 20 s, and extension at 72 °C for 30 s. Values were exhibited relative to β-actin. The corresponding primer sequences are listed in **Supplementary Table S1**.

Western Blot Analysis

Total proteins from the RAW264.7 cells were lysed in radioimmunoprecipitation assay (RIPA, Beyotime, China) buffer, and 30 μg total proteins were used for each blot. The samples were separated by SDS-PAGE and transferred onto a nitrocellulose filter (NC, Millipore, United States) membrane by electro-blotting. The membranes were blocked for 1 h and then incubated overnight with 1:1,000 dilutions of anti-TLR4, anti-iNOS, anti-COX2, and anti–NF-κB p65 (Cell Signaling Technology, United States). After incubation with the secondary antibody anti-mouse IgG (H + L) (DyLight™ 800, Cell Signaling Technology, United States) at 1:15,000 dilutions, the membranes were imaged using a LiCor Odyssey scanner (LI-COR, United States). Protein expressions were normalized using β-actin as the reference (Cell Signaling Technology, United States) in the same sample.

Immunofluorescence

The cell-seeded glass cover slips were fixed with 4% cold paraformaldehyde for 15 min and permeabilized with 0.1% Triton X-100 for 30 min. Then, the cover slips were blocked with 5% BSA for 1 h and incubated with a primary antibody specific to the NF-κB p65 subunit (Cell Signaling Technology, United States) overnight at 4°C, followed by a secondary antibody labeled with Alexa Fluor-594 (1:5,000) for 1 h at room temperature, protected from light. After being stained with DAPI (5 μg/ml in PBS) for 30 min at 37 °C, the cover slips were washed and sealed. Images were obtained using an OLYMPUS IX73 fluorescence microscope (Olympus, Tokyo, Japan) with excitation/emission wavelengths of 590 nm/617 nm for Alexa Fluor-594 and 360 nm/450 nm for DAPI, respectively.

Molecular Docking

The virtual docking was carried out in the Surflex-Dock module of FlexX/Sybyl software, which belongs to a fast docking method that allows sufficient flexibility of ligands and keeps the target protein rigid. Molecules were built using Chemdraw software and further optimized at the molecular, mechanical, and semiempirical level using Open Babel GUI. The crystallographic ligands were extracted from the active site, and the designed ligands were modeled. All the hydrogen atoms were added to define the correct ionization and tautomeric states, and the carboxylate, phosphonate, and sulfonate groups were considered in their charged form. In the docking calculation, the default FlexX scoring function was applied for exhaustive searching, solid body optimizing, and interaction scoring. Finally, the ligands with the lowest energy and the most optimum orientation were chosen.

Statistical Analysis

All experiments were conducted in biological triplicate. All data are displayed as the mean ± standard error of the mean (SEM). Differences were evaluated by the Student's *t*-test using GraphPad Prism software (GraphPad Prism version 5.01 for Windows, San Diego, CA). Differences with $^{*}p$ and $^{\#}p < 0.05$ were considered statistically significant.

RESULTS

Structure Elucidation

Compound **1** was isolated as colorless oil. The molecular formula $C_{17}H_{26}O_2$ was deduced from the HRESIMS data (**Supplementary Figure S7**) at *m/z* 285.1837 $(M + Na)^+$ (calcd for $C_{17}H_{26}O_2Na$, 285.1830), referring to five degrees of unsaturation. The ^{13}C NMR and DEPT spectroscopic data (**Table 1**; **Supplementary Figure S2**) of **1** revealed 17 carbon resonances that were attributed to

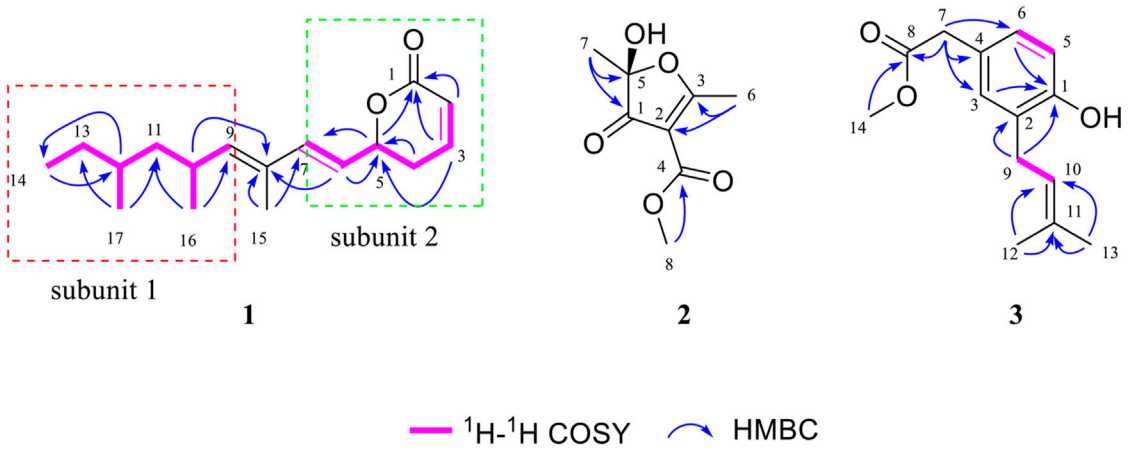


FIGURE 2 | Selected ^{1}H–^{1}H COSY and HMBC correlations of **1**–**3**.

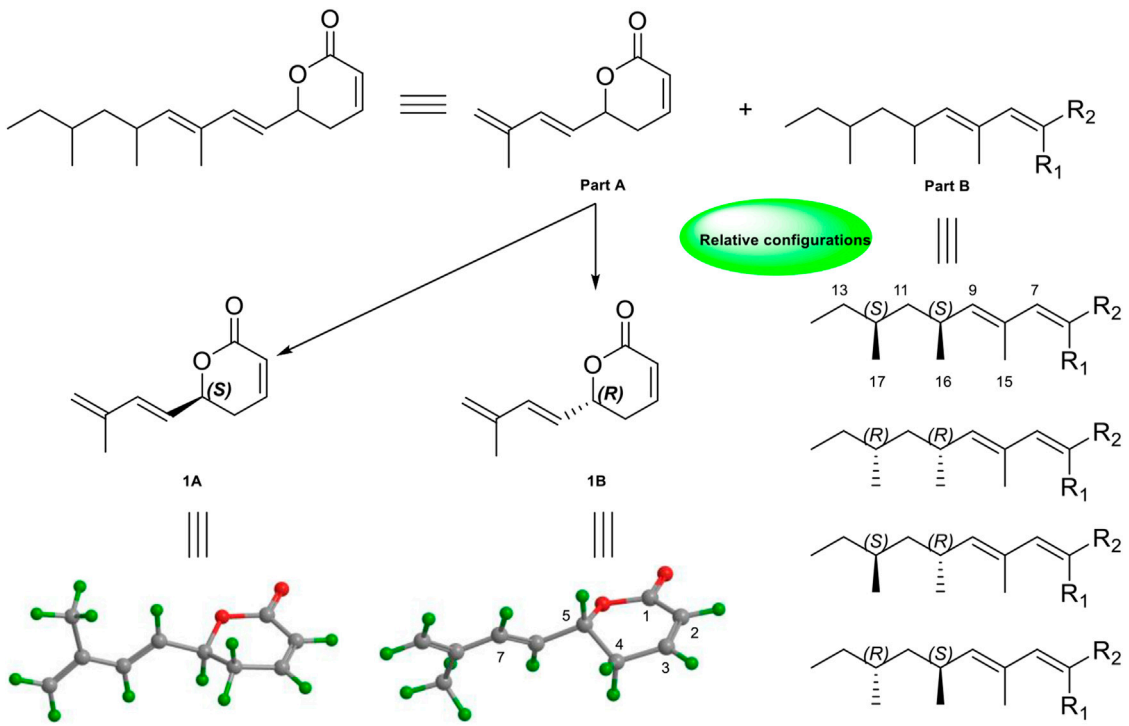


FIGURE 3 | Key NOESY correlations and relative configurations of compound **1.**

four methyls at δ_C 11.3 (C-14), 12.5 (C-15), 21.4 (C-16), and 19.1 (C-17), three sp^3 methylenes at δ_C 30.1 (C-4), 44.7 (C-11), and 30.0 (C-13), five olefinic methines at δ_C 121.6 (C-2), 144.7 (C-3), 122.2 (C-6), 138.7 (C-7), and 142.4 (C-9), three sp^3 methines at δ_C 78.6 (C-5), 30.3 (C-10), and 32.2 (C-12), one olefinic quaternary carbon at δ_C 130.7 (C-8), and one ester carbonyl at δ_C 164.1 (C-1). The ^{1}H NMR spectrum (**Table 1**; **Supplementary Figure S1**) of **1** showed diagnostic signals for four methyls, three sp^3 methylenes, five olefinic methines, and three sp^3 methines, which were attributed to the corresponding carbon atoms with the help of the HSQC spectrum. One carbonyl group and six olefinic carbon atoms, accounting for 4 out of 5 degrees of unsaturation, indicated that **1** possessed a monocyclic ring system. The key ^{1}H–^{1}H COSY spin–spin coupling system (**Figure 2**; **Supplementary Figure S5**) of H-9/H-10/H$_2$-11/H-12/H$_2$-13/H$_3$-14, H$_3$-16/H-10, and H$_3$-17/H-12 in **1** indicated the direct carbon–carbon connectivity of C-9/C-10/C-11/C-12/C-13/C-14, C-16/C-10, and C-17/C-12. Subunit 1 was deduced and

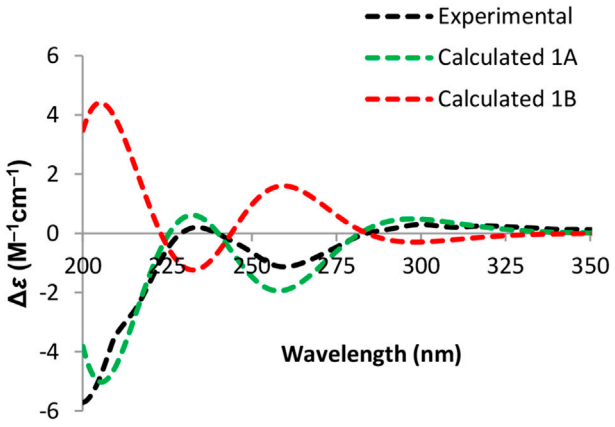


FIGURE 4 | Experimental and calculated ECD spectra of **part A**.

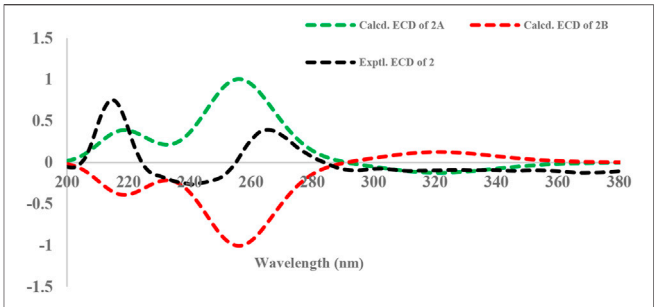


FIGURE 5 | Experimental and calculated ECD spectra of **2.**

confirmed by the key HMBC correlations (**Figure 2**; **Supplementary Figure S4**) from H_3-16 to C-9 and C-11, from H_3-17 to C-11 and C-13, from H_3-14 to C-12, and from H-12 to C-14. In the same manner, the direct carbon–carbon connectivity of C-2/C-3/C-4/C-5/C-6/C-7 was elucidated. The obvious HMBC correlations from H-2 (δ_H 6.06 dt J = 9.8, 1.8 Hz), H-3 (δ_H 6.89 dt J = 9.8, 4.3 Hz), and H-5 (4.97 ddd J = 15.0, 7.4, 0.8 Hz) to C-1 (δ_C 164.1) and from H-3 and H_2-4 (δ_H 2.47 m) to C-5 (δ_C 78.6) showed the presence of lactone groups in subunit 2. The construction of subunits 1 and 2 was connected by an olefinic quaternary carbon atom (δ_C 130.7, C-8), which was deduced from the key HMBC cross peaks (**Figure 2**) of H-6/C-8, H-10/C-8, H_3-15/C-8, and H_3-15/C-7. Thus, the planar structure of **1** was determined (**Figure 2**).

Due to the presence of side chains in **1**, its relative configuration was determined with difficulty. In order to search for evidence for the configurational elucidation, we disassembled the structure of **1** into parts A and B (**Figure 3**). The configurations of **1A** (5*S*) and **1B** (5*R*) were calculated *via* the time-dependent density functional theory (TDDFT) method at the B3LYP/6-311++G** level with PCM in MeOH (Qiao et al., 2016; Qiao et al., 2019). In this case, the experimental curve displayed a good accordance behavior with the calculated ECD of **1A** and showed an absolutely reverse curve to that of enantiomer **1B** (**Figure 4**). Thus, the absolute configuration of part A was elucidated as 5*S*. Raffaele Riccio and co-workers (Bifulco et al., 2007) reported a useful method for the determination of relative configuration in organic compounds. In the rule, 16β is determined as the chemical shift of C-15 at less or more than 12.0 ppm (**Table 2**). Accordingly, the 16β of **1** was established because of the chemical shift of C-15 at δ_C 12.5 ppm. Moreover, the chemical shifts of C-13 (δ_C 30.0), C-16 (δ_C 21.4), and C-17 (δ_C 19.1), located in the intervals of 30.0–30.5, 21.0–21.6, and 18.9–19.2 ppm, respectively, showed the agreement with the configurations of 16β and 17β (**Table 2**). The discussions mentioned above enable us to elucidate the absolute configuration of **1** as 5*S*, 16*S*, and 17*S*. Using the search network SciFinder (https://scifinder.cas.org), compound **1** was determined as a unique linear chain compound with an α, β-unsaturated monocyclic lactone structure originating from the polyketide family.

Compound **2** was obtained as a white, amorphous powder and showed a molecular formula of $C_8H_{10}O_5$, on the basis of its HRESIMS analysis (**Supplementary Figure S14**) at *m/z* 209.0404 $(M + Na)^+$ (calcd for $C_8H_{10}O_5Na$, 209.0426), requiring four degrees of unsaturation. The IR spectrum (**Supplementary Figure S15**) of **2** exhibited characterized absorption bands for hydroxy groups (3,425 cm^{-1}) and ester/lactone carbonyl groups (1732 cm^{-1}). The ^1H NMR spectrum (**Table 1**; **Supplementary Figure S10**) of **2** showed two sp^3 methyls [(δ_H 1.49, s, CH_3-6) and (δ_H 2.60, s, CH_3-7)] and one methoxy group at δ_H 3.78 (s, CH_3-8) signals. The ^{13}C NMR data (**Table 1**; **Supplementary Figure S11**) of **2** were attributed to one carbonyl group (δ_C 197.7, C-1), one lactone carbonyl group (δ_C 164.4, C-4), two sp^2 quaternary carbons (δ_C 107.7, C-2 and δ_C 198.3, C-3), and one hemiacetal carbon atom at δ_C 106.4 (C-5). The key HMBC correlations (**Supplementary Figure S13**) from H_3-6 to C-2 and C-3, from H_3-7 to C-1 and C-5, and from the methoxy proton (δ_H 3.78) to C-4, coupled with the molecular degrees of unsaturation, deduced the planar structure of **2**, as shown in **Figure 2**.

To determine the absolute configuration of C-5, the time-dependent density functional theory (TDDFT) method at the B3LYP/6-311++G** level with PCM in MeOH was performed for **2A** (5*S*) and **2B** (5*R*). The calculated ECD spectrum of **2A**

TABLE 2 | Previously reported rule for the identification of relative configurations in side chain compounds (Bifulco et al., 2007).

Position	16α, 17α	16α, 17β	16β,17α	16β,17β
Chemical shift (ppm)	C13, 30.0–31.0 C15 < 12.0 C16, 21.0–21.6 C17 < 18.5	C13, 29.0–29.3 C15 < 12.0 C16, 20.2–20.5 C17, 19.0–19.6	C13, 28.9–29.5 C15 > 12.0 C16, 20.5–20.8 C17, 19.0–19.6	C13, 30.0–30.5 C15 > 12.0 C16, 21.0–21.6 C17, 18.9–19.2

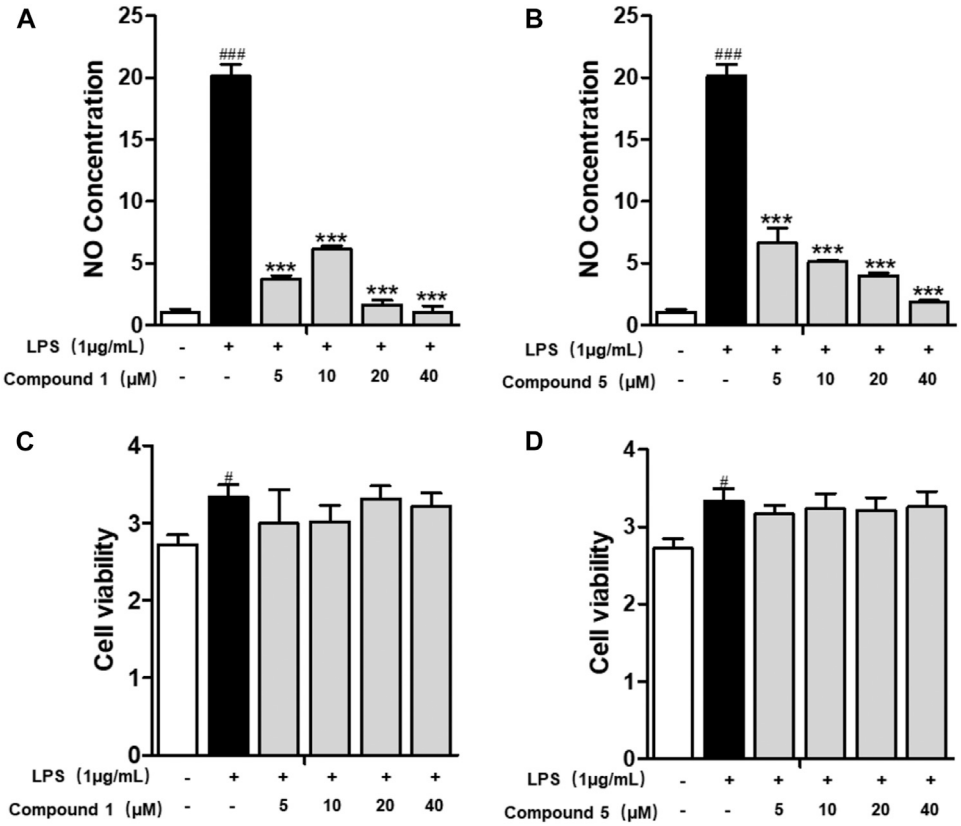


FIGURE 6 | Compounds **1** and **5** exert significant anti-inflammatory effect on RAW264.7 macrophage cells. Effects of **1** and **5** on the NO production **(A, B)** and cell viability **(C, D)** of LPS-induced RAW264.7. Cells were treated with various concentrations of **1** and **5** ranging from 5, 10, 20, and 40 μM. Data were presented as the mean ± SEM (n = 4). #p < 0.05, ###p < 0.001 vs. control, ***p < 0.001 vs. model.

matched well with that of the experimental ECD (**Figure 5**), indicating that the absolute configuration of **2** was elucidated as 5*S*.

Compound **3** was obtained as a white, amorphous powder, and the molecular formula $C_{14}H_{18}O_3$ was established according to HRESIMS (**Supplementary Figure S21**) *m/z* 257.1155 $(M + Na)^+$ (calcd for $C_{14}H_{18}O_3Na$, 257.1154), requiring six degrees of unsaturation. The ^1H NMR and ^{13}C NMR spectra (**Table 1**; **Supplementary Figures S16, S17**) exhibited signals indicating the presence of a 1,2,4-trisubsituted phenyl group with the NMR data C-1 (δ_C 153.5), C-2 (δ_C 127.0), CH-3 (δ_H 7.00 overlap, δ_C 130.8), C-4 (δ_C 126.0), CH-5 (δ_H 6.74 dd, J = 8.8, 7.9 Hz, δ_C 115.8), and CH-6 (δ_H 7.02 overlap, δ_C 128.2). The key ^1H–^1H COSY spin–spin coupling system (**Figure 2**; **Supplementary Figure S20**) of H_2-9/H-10 and the HMBC (**Supplementary Figure S19**) correlations from H_3-12 and H_3-13 to C-10 and C-11 (**Figure 2**) indicated the presence of a classical isopentenyl group. Additionally, the key HMBC correlations from H_2-9 to C-1 and C-2 and from H-3 and H-6 to C-1 indicated the isopentenyl group locating at C-2. In turn, the HMBC correlations from H_3-14 and H_2-7 to C-8 and from H_2-7 to C-3, C-4, and C-6 constructed a methyl acetate group connected to the phenyl group locating at C-4. Moreover, the chemical shift of C-1 (δ_C 153.5), coupled with HRESIMS, indicated a hydroxyl group locating at C-1. The chemical structure was thus elucidated as shown in **Figure 1**.

TABLE 3 | Inhibitory activity against LPS-induced NO production of **1**–**12**.

No.	IC_{50} (μM)	No.	IC_{50} (μM)
	NO production		NO production
1	**1.49 ± 0.31**	**7**	>40
2	>40	**8**	>40
3	>40	**9**	>40
4	>40	**10**	>40
5	**3.41 ± 0.85**	**11**	>40
6	>40	**12**	>40
DEX[a]	6.68 ± 0.58	—	—

[a]*DEX was used as the positive control.*

One and Five Suppressed LPS-Induced Nitric Oxide Production

All of the isolates were evaluated for anti-inflammatory activity against the production of NO in RAW264.7 stimulated by LPS. Among the isolates evaluated, compounds **1** and **5** showed a significant inhibitory effect on NO production, with IC_{50} values of 1.49 ± 0.31 and 3.41 ± 0.85 μM, respectively, while the others exhibited no obviously inhibitory activities, with IC_{50} values up to over 40 μM (**Figures 6A,B**; **Table 3**). Besides, the cytotoxicity assay exhibited that no apparent toxicities were observed at different

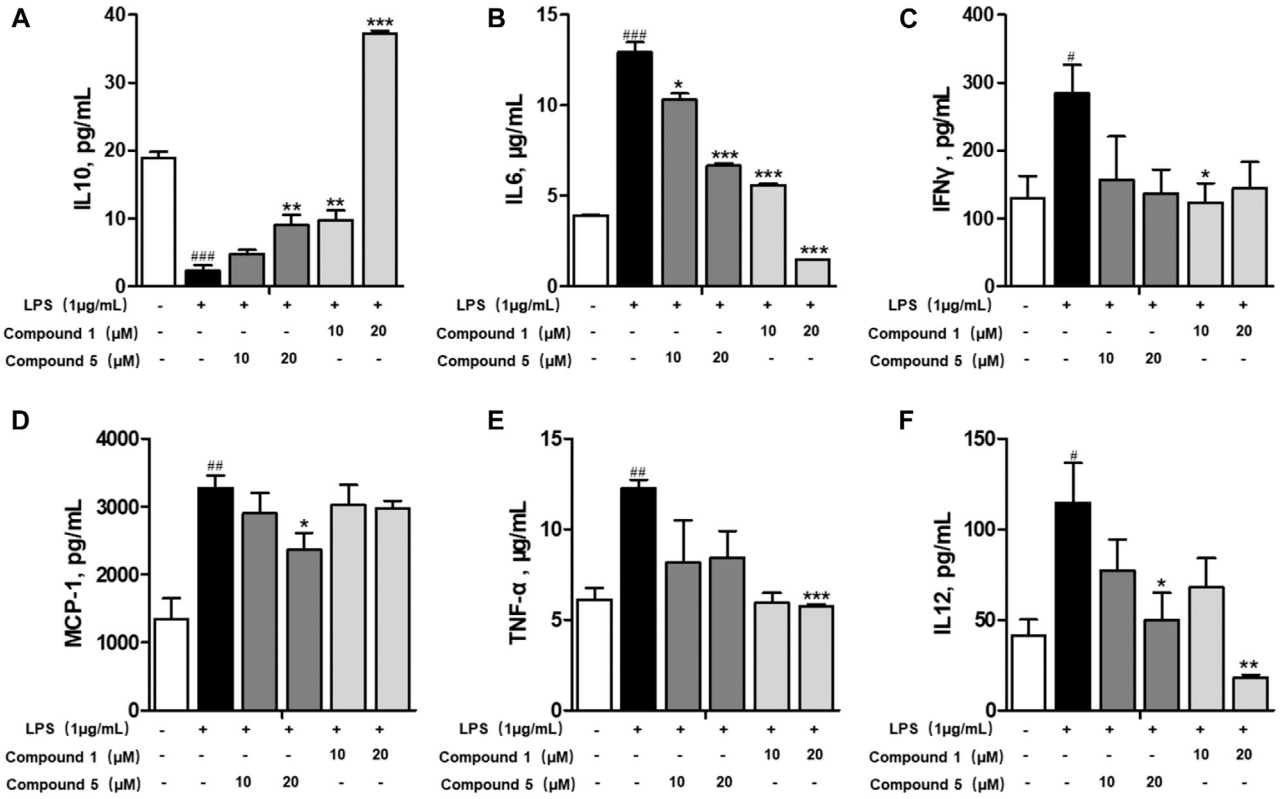


FIGURE 7 | Effects of **1** and **5** on the production of cytokines by LPS-induced RAW264.7 cells. The level of IL10 **(A)**, IL6 **(B)**, IFNγ **(C)**, MCP-1 **(D)**, TNF-α **(E)**, and IL12 **(F)** produced by LPS-stimulated RAW264.7 cells treated with **1** or **5**. Data were presented as the mean ± SEM ($n = 3$). $^{\#}p < 0.05$, $^{\#\#}p < 0.01$, $^{\#\#\#}p < 0.001$ vs. control, $^{*}p < 0.05$, $^{**}p < 0.01$, $^{***}p < 0.001$ vs. model.

concentrations of **1** and **5** (**Figures 6C,D**). These results suggest that **1** and **5** have potential as *in vitro* anti-inflammatory agents, with better or comparable activities than those of the positive control, dexamethasone (DEX).

One and Five Exerted Potent Anti-Inflammatory Effect by Restraining the M1 Macrophage Polarization Induced by LPS

Macrophages play an important role in multiple immune responses. Research studies have clarified two major macrophages, including classically activated or inflammatory (M1) and alternatively activated or anti-inflammatory (M2) macrophages (Wang et al., 2019). M1 macrophages can be stimulated by LPS, and then, they secrete high levels of pro-inflammatory cytokine factors, such as NO, COX-2, IL6, IL1β, and TNF-α. Meanwhile, M2 macrophages can be activated by IL-4 or IL-13, characterized by the high-level secretion of IL10, arginase-1 (ARG1), and the mannose receptor, C type 1 (MRC1/CD206) (Kong et al., 2019). Hence, we first detected the secretion of cytokines from the cell culture supernatant of administrated RAW264.7 cells. Our results demonstrated that **1** and **5** both elevated the level of immunoregulatory cytokine IL10 while decreasing pro-inflammatory cytokines IL6, TNF-α, IFN-γ, MCP-1, and IL12 (**Figures 7A–F**). These findings prompted us to conclude that both **1** and **5** can suppress the induction of M1 macrophages by LPS. As well, our qRT-PCR results exhibited that **1** and **5** significantly inhibited the transcription level of pro-inflammation M1 markers IL6, IL1β, and TNF-α (**Figures 8A–D**) while remarkably increasing the expression of IL10 and the anti-inflammation M2 markers ARG1 and CD206 (**Figures 8E,F**). Altogether, our results revealed that both **1** and **5** can have a potent anti-inflammatory effect by preventing the M1 macrophage polarization induced by LPS.

One and Five Inhibit the Nuclear Translocation of Nuclear Factor-Kappa B p65

LPS can bind to and activate cell membrane receptor toll-like receptor 4 (TLR4), thus producing a large number of NF-κB through MyD88-dependent pathways, thereby promoting M1 macrophage polarization (Ostareck and Ostareck-Lederer, 2019). We also found that both **1** and **5** can significantly depress the transcription level of inflammatory factors iNOS and COX-2 (**Figures 9A,B**). Meanwhile, only compound **1** can notably inhibit the protein expression of iNOS and NF-κB p65 (**Figure 9D**), while **5** exerts slight inhibition on the protein

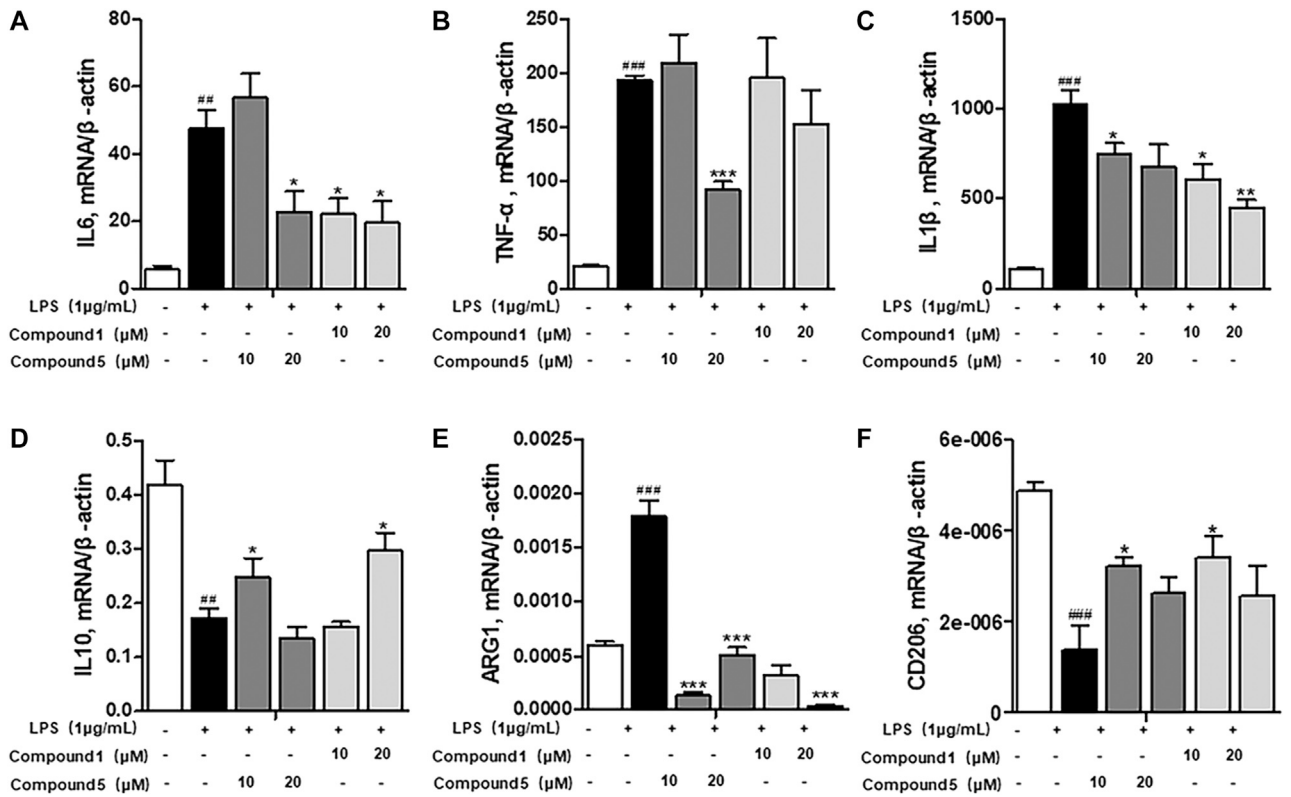


FIGURE 8 | Influences of **1** and **5** on the transcription level of macrophage markers. The expression of inflammatory markers IL6 **(A)**, TNF-α **(B)**, and IL1β **(C)** and immunomodulatory markers IL10 **(D)**, ARG1 **(E)**, and CD206 **(F)** in **1-** or **5**-administrated RAW264.7 cells activated by LPS. Data were presented as the mean ± SEM (n = 3). $^{\#\#}p < 0.01$, $^{\#\#\#}p < 0.001$ vs. control, $^{*}p < 0.05$, $^{**}p < 0.01$, $^{***}p < 0.001$ vs. model.

expression of COX-2 and NF-κB p65 (**Figure 9D**). NF-κB p65 is a pivotal transcriptional factor in the macrophage activation progress, which can activate and translocate into the nucleus to regulate the transcription of COX-2 and iNOS (Emam et al., 2021). We also found that both **1** and **5** can inhibit the nuclear translocation of NF-κB p65 (**Figure 9C**). On this basis, compounds **1** and **5** were subjected to molecular docking to NF-κB p65 (PDB ID of protein receptor: 1OY3) to gain a better understanding of the hypothetical mechanism. As a result, **1** can virtually bind to NF-κB p65 through hydrogen bonds to the binding sites Asn139 and Arg73, active residues shown in **Figure 9E**, with an affinity of −6.98 kcal/mol. In comparison, **5** binds to NF-κB p65 through hydrogen bonds to the binding sites Arg246 and Lys221, active residues shown in **Figure 9F**, with an affinity of −5.78 kcal/mol. Hence, we speculate that **1** can preferably bind to and inhibit NF-κB p65 to exert the anti-inflammatory effect.

DISCUSSION

To the best of our knowledge, there are very little research data on the secondary metabolites of *Aspergillus rugulosa*. Aiming to discover new chemical constituents and their pharmacological activities, we explored the secondary metabolites of this fungus. In conclusion, two new polyketide compounds, asperulosins A and B (**1**–**2**), and one new prenylated small molecule, asperulosin C (**3**), along with nine known compounds (**4**–**12**), were isolated and identified from the fungus *Aspergillus rugulosa*. Remarkably, compound **1** was determined as a unique linear chain compound with an α,β-unsaturated monocyclic lactone structure originating from the polyketide family. Compound **2** was constructed by five continuous quaternary carbon atoms, which occur rarely in natural products. Except for compound **5**, the others were first isolated from the fungus *Aspergillus rugulosa*.

Macrophages play an important role in the immune system. They can be stimulated by LPS, and then, they secrete multiple pro-inflammatory factors, such as NO, COX-2, IL6, IL1β, and TNF-α (Duarte et al., 2014). Excessive NO can induce DNA damage, apoptosis, and oxidative stress, thereby amplifying the inflammatory response (Gu et al., 2020). Accordingly, all of the isolates were evaluated for anti-inflammatory activity against the production of NO in RAW264.7 stimulated by LPS. Among them, polyketide compounds **1** and **5** showed a significant inhibitory effect on NO production, with IC_{50} values of 1.49 ± 0.31 and 3.41 ± 0.85 μM, respectively. Moreover, our results uncovered that **1** and **5** can also elevate the level of immunoregulatory cytokine IL10 while decreasing pro-inflammatory cytokines IL6, TNF-α, IFN-γ, MCP-1, and IL12. As well, **1** and **5** significantly inhibited the transcription level of pro-inflammation M1 markers IL6, IL1β, and TNF-α while

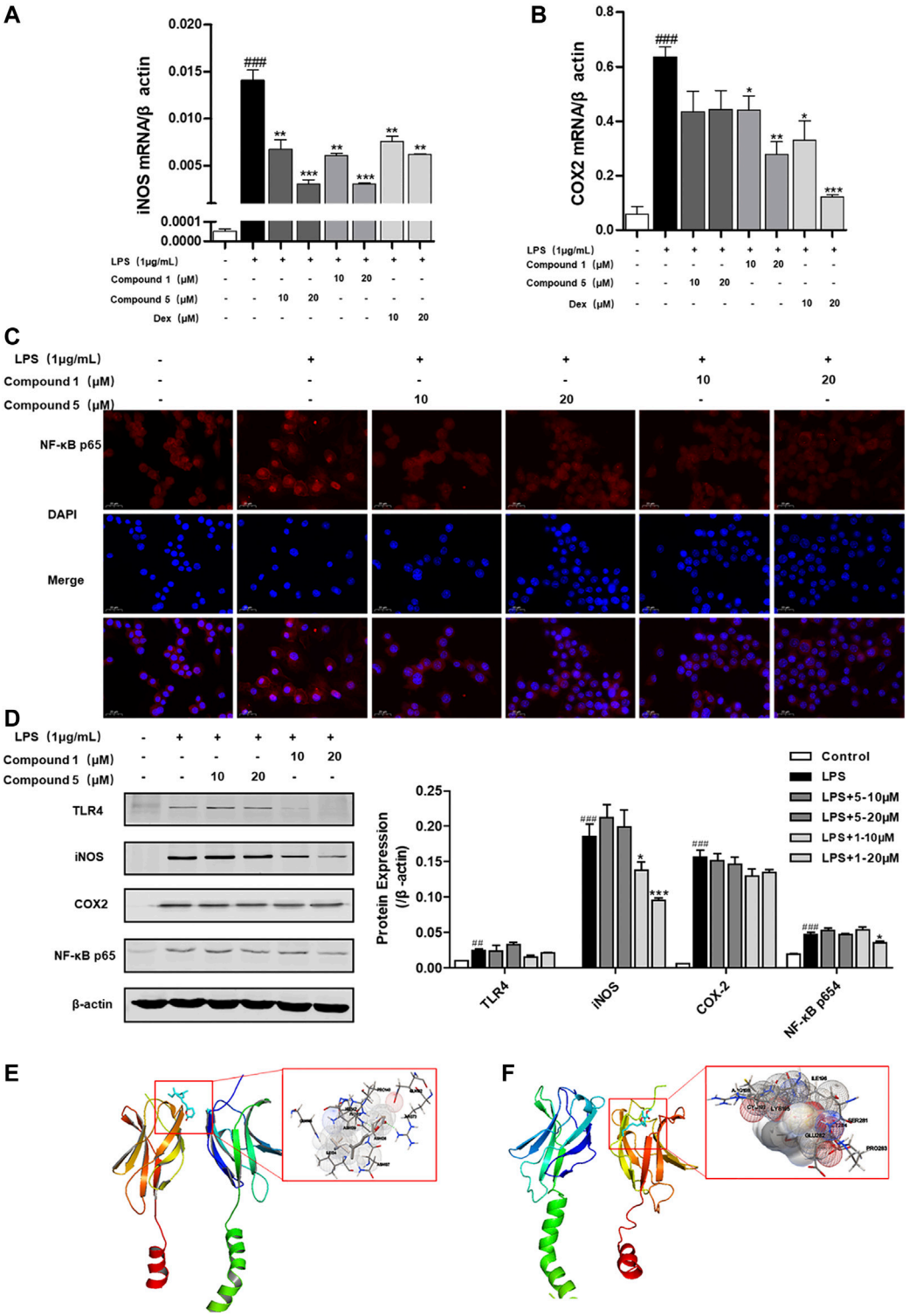


FIGURE 9 | 1 and **5** inhibit the nuclear translocation of NF-κB p65 to exert anti-inflammation effect. Effects of **1** and **5** on the transcription level of inflammatory factors iNOS **(A)** and COX-2 **(B)** in LPS-induced RAW 264.7 cells. Dexamethasone (Dex) was used as a positive control. Data were presented as the mean ± SEM ($n = 3$). $^{###}p < 0.001$ vs. control, $^{*}p < 0.05$, $^{**}p < 0.01$, $^{***}p < 0.001$ vs. model. **(C)** Effects of **1** and **5** on the expression of NF-κB p65 in LPS-treated RAW264.7 cells by immunofluorescence (scale bar = 20 μm). **(D)** Protein expression of TLR4, iNOS, COX-2, and NF-κB p65 in RAW264.7 cells stimulated with LPS. $^{##}p < 0.01$, $^{###}p < 0.001$ vs. control, $^{*}p < 0.05$, $^{**}p < 0.01$, $^{***}p < 0.001$ vs. model. *In silico* analysis of the interactions between NF-κB p65 and **1 (E)** and **5 (F)**, respectively.

remarkably increasing the expression of IL10 and the anti-inflammation M2 markers ARG1 and CD206. These results suggest that **1** and **5** could be considered as a basis for the synthesis of novel anti-inflammatory drugs.

NF-κB is a transcription factor that regulates the gene expression of inflammation, cell growth, proliferation, and immune response (Khan et al., 2020). NF-κB is composed of the p65 and p50 subunits. LPS can stimulate and activate the transcription activity of NF-κB p65 by promoting its translocation into the nucleus (Christian et al., 2016). Our results demonstrate that both **1** and **5** can obviously prevent the expression of NF-κB p65 in the nucleus and suppress the transcription of COX-2 and iNOS. However, **1** exerts more potent inhibition activity on the protein expression of TLR4, iNOS, and NF-κB p65 than **5**. These results are consistent with the NO inhibition IC_{50} value. Hence, we presume that **1** can suppress the expression and the nuclear translocation of NF-κB p65 to induce stronger anti-inflammatory activity than that of **5**.

In conclusion, both **1** and **5** can suppress immune response in LPS-induced RAW264.7 cells by blocking the NF-κB pathway and decreasing the production of COX-2 and iNOS. Finally, compounds **1** and **5** exhibited potential anti-inflammatory activities *in vitro* that were comparable to those of the positive control, DEX.

DATA AVAILABILITY STATEMENT

The original contributions presented in the study are included in the article/**Supplementary Material**; further inquiries can be directed to the corresponding authors.

AUTHOR CONTRIBUTIONS

YZ, CQ, and YL designed and funded the study; QX, YQ, and ZZ performed the experiments and obtained and analyzed the data; YD, TC, and LT did the statistical analysis. QX participated in the purification of the compounds; JL performed the ECD calculations; and WS and YY provided some suggestions on the structural elucidation and pharmacological bioactivities evaluation. All authors discussed the results and wrote the manuscript.

FUNDING

This work was financially supported by the Program for Changjiang Scholars of the Ministry of Education of the People's Republic of China (No. T2016088), the National Natural Science Foundation for Distinguished Young Scholars (No. 81725021), the National Science and Technology Project of China (No. 2018ZX09201001-001-003), Innovative Research Groups of the National Natural Science Foundation of China (No. 81721005), the National Natural Science Foundation of China (No. 82003633), the Academic Frontier Youth Team of HUST (2017QYTD19), the Integrated Innovative Team for the Major Human Diseases Program of Tongji Medical College (HUST), the Hubei Province Postdoctoral Innovation Research Fund to YQ (2020), and the Open Foundation of the Hubei Key Laboratory of Wudang Local Chinese Medicine Research (No. WDCM2019004).

ACKNOWLEDGMENTS

We acknowledge the Analytical and Testing Center at HUST for ECD, UV, and IR analyses.

SUPPLEMENTARY MATERIAL

The Supplementary Material for this article can be found online at: https://www.frontiersin.org/articles/10.3389/fphar.2021.700573/full#supplementary-material

REFERENCES

Almassi, F., Ghisalberti, E. L., Narbey, M. J., and Sivasithamparam, K. (1991). New Antibiotics from Strains of Trichoderma harzianum. *J. Nat. Prod.* 54, 396–402. doi:10.1021/np50074a008

Alvarez-Suarez, J. M., Carrillo-Perdomo, E., Aller, A., Giampieri, F., Gasparrini, M., González-Pérez, L., et al. (2017). Anti-inflammatory Effect of Capuli Cherry against LPS-Induced Cytotoxic Damage in RAW 264.7 Macrophages. *Food Chem. Toxicol.* 102, 46–52. doi:10.1016/j.fct.2017.01.024

Ballantine, J. A., Ferrito, V., Hassall, C. H., and Jones, V. I. P. (1969). Aspertetronin A and B, Two Novel Tetronic Acid Derivatives Produced by a Blocked Mutant of Aspergillus rugulosus. *J. Chem. Soc. C*, 56–61. doi:10.1039/J39690000056

Bifulco, G., Dambruoso, P., Gomez-Paloma, L., and Riccio, R. (2007). Determination of Relative Configuration in Organic Compounds by NMR Spectroscopy and Computational Methods. *Chem. Rev.* 107, 3744–3779. doi:10.1021/cr030733c

Burghart-Stoll, H., and Brückner, R. (2012). Total Syntheses of the Gregatins A-D and Aspertetronin A: Structure Revisions of These Compounds and of Aspertetronin B, Together with Plausible Structure Revisions of Gregatin E, Cyclogregatin, Graminin A, the Penicilliols A and B, and the Huaspenones A. *Eur. J. Org. Chem.* 2012, 3978–4017. doi:10.1002/ejoc.201200207

Cacho, R. A., Jiang, W., Chooi, Y.-H., Walsh, C. T., and Tang, Y. (2012). Identification and Characterization of the Echinocandin B Biosynthetic Gene Cluster from Emericella rugulosa NRRL 11440. *J. Am. Chem. Soc.* 134, 16781–16790. doi:10.1021/ja307220z

Choudhary, M. I., Musharraf, S. G., Mukhmoor, T., Shaheen, F., Ali, S., and Rahman, A.-u. (2004). Isolation of Bioactive Compounds from Aspergillus terreus. *Naturforsch. B* 59, 324–328. doi:10.1515/znb-2004-0315

Christian, F., Smith, E., and Carmody, R. (2016). The Regulation of NF-Kb Subunits by Phosphorylation. *Cells* 5, 12. doi:10.3390/cells5010012

Duarte, J., Francisco, V., and Perez-Vizcaino, F. (2014). Modulation of Nitric Oxide by Flavonoids. *Food Funct.* 5, 1653–1668. doi:10.1039/c4fo00144c

Elsebai, M. F., Ghabbour, H. A., Legrave, N., Fontaine-Vive, F., and Mehiri, M. (2018). New Bioactive Chlorinated Cyclopentene Derivatives from the marine-derived Fungus Phoma Sp. *Med. Chem. Res.* 27, 1885–1892. doi:10.1007/s00044-018-2201-1

Emam, S. H., Sonousi, A., Osman, E. O., Hwang, D., Kim, G.-D., and Hassan, R. A. (2021). Design and Synthesis of Methoxyphenyl- and Coumarin-Based Chalcone Derivatives as Anti-inflammatory Agents by Inhibition of NO Production and Down-Regulation of NF-Kb in LPS-Induced RAW264.7 Macrophage Cells. *Bioorg. Chem.* 107, 104630. doi:10.1016/j.bioorg.2021.104630

González-Medina, M., Owen, J. R., El-Elimat, T., Pearce, C. J., Oberlies, N. H., Figueroa, M., et al. (2017). Scaffold Diversity of Fungal Metabolites. *Front. Pharmacol.* 8, 180. doi:10.3389/fphar.2017.00180

Gu, I., Brownmiller, C., Stebbins, N. B., Mauromoustakos, A., Howard, L., and Lee, S.-O. (2020). Berry Phenolic and Volatile Extracts Inhibit Pro-inflammatory Cytokine Secretion in LPS-Stimulated RAW264.7 Cells through Suppression of NF-Kb Signaling Pathway. *Antioxidants* 9, 871. doi:10.3390/antiox9090871

Herkommer, D., Schmalzbauer, B., and Menche, D. (2014). Sequential Catalysis for Stereoselective Synthesis of Complex Polyketides. *Nat. Prod. Rep.* 31, 456–467. doi:10.1039/C3NP70093C

Hertweck, C. (2009). The Biosynthetic Logic of Polyketide Diversity. *Angew. Chem. Int. Ed.* 48, 4688–4716. doi:10.1002/anie.200806121

Hu, Z., Ye, Y., and Zhang, Y. (2021). Large-scale Culture as a Complementary and Practical Method for Discovering Natural Products with Novel Skeletons. *Nat. Prod. Rep.* doi:10.1039/D0NP00069H

Islam, M. S., Ishigami, K., and Watanabe, H. (2007). Synthesis of (−)-mellein, (+)-ramulosin, and Related Natural Products. *Tetrahedron.* 63, 1074–1079. doi:10.1016/j.tet.2006.11.068

Khan, H., Ullah, H., Castilho, P. C. M. F., Gomila, A. S., D'Onofrio, G., Filosa, R., et al. (2020). Targeting NF-Kb Signaling Pathway in Cancer by Dietary Polyphenols. *Crit. Rev. Food Sci. Nutr.* 60, 2790–2800. doi:10.1080/10408398.2019.1661827

Kwok, O. C. H., Plattner, R., Weisleder, D., and Wicklow, D. T. (1992). A Nematicidal Toxin fromPleurotus Ostreatus NRRL 3526. *J. Chem. Ecol.* 18, 127–136. doi:10.1007/BF00993748

Lacoske, M. H., and Theodorakis, E. A. (2015). Spirotetronate Polyketides as Leads in Drug Discovery. *J. Nat. Prod.* 78, 562–575. doi:10.1021/np500757w

Lee, W.-S., Shin, J.-S., Jang, D. S., and Lee, K.-T. (2016). Cnidilide, an Alkylphthalide Isolated from the Roots of Cnidium Officinale, Suppresses LPS-Induced NO, PGE 2, IL-1β, IL-6 and TNF-α Production by AP-1 and NF-Kb Inactivation in RAW 264.7 Macrophages. *Int. Immunopharmacology* 40, 146–155. doi:10.1016/j.intimp.2016.08.021

Li, H., Feng, W., Li, X., Kang, X., Yan, S., Chao, M., et al. (2020). Terreuspyridine: An Unexpected Pyridine-Fused Meroterpenoid Alkaloid with a Tetracyclic 6/6/6/6 Skeleton from Aspergillus terreus. *Org. Lett.* 22, 7041–7046. doi:10.1021/acs.orglett.0c02641

Medzhitov, R. (2010). Inflammation 2010: New Adventures of an Old Flame. *Cell* 140, 771–776. doi:10.1016/j.cell.2010.03.006

Newman, D. J., and Cragg, G. M. (2020). Natural Products as Sources of New Drugs over the Nearly Four Decades from 01/1981 to 09/2019. *J. Nat. Prod.* 83, 770–803. doi:10.1021/acs.jnatprod.9b01285

Okamoto, T., Sanda, T., and Asamitsu, K. (2007). NF-κB Signaling and Carcinogenesis. *Cpd*, 13, 447–462. doi:10.2174/138161207780162944

Ostareck, D. H., and Ostareck-Lederer, A. (2019). RNA-binding Proteins in the Control of LPS-Induced Macrophage Response. *Front. Genet.* 10. doi:10.3389/fgene.2019.00031

Qi, C., Bao, J., Wang, J., Zhu, H., Xue, Y., Wang, X., et al. (2016). Asperterpenes A and B, Two Unprecedented Meroterpenoids from Aspergillus terreus with BACE1 Inhibitory Activities. *Chem. Sci.* 7, 6563–6572. doi:10.1039/C6SC02464E

Qiao, Y., Xu, Q., Feng, W., Tao, L., Li, X.-N., Liu, J., et al. (2019). Asperpyridone A: An Unusual Pyridone Alkaloid Exerts Hypoglycemic Activity through the Insulin Signaling Pathway. *J. Nat. Prod.* 82 (10), 2925–2930. doi:10.1021/acs.jnatprod.9b00188

Qiao, Y., Xu, Q., Hu, Z., Li, X.-N., Xiang, M., Liu, J., et al. (2016). Diterpenoids of the Cassane Type from caesalpinia Decapetala. *J. Nat. Prod.* 79 (12), 3134–3142. doi:10.1021/acs.jnatprod.6b00910

Van Wagoner, R. M., Satake, M., and Wright, J. L. C. (2014). Polyketide Biosynthesis in Dinoflagellates: what Makes it Different?. *Nat. Prod. Rep.* 31, 1101–1137. doi:10.1039/C4NP00016A

Vu, M., Herfindal, L., Juvik, O. J., Vedeler, A., Haavik, S., and Fossen, T. (2016). Toxic Aromatic Compounds from Fruits of Narthecium Ossifragum L. *Phytochemistry* 132, 76–85. doi:10.1016/j.phytochem.2016.09.010

Wang, Y., Smith, W., Hao, D., He, B., and Kong, L. (2019). M1 and M2 Macrophage Polarization and Potentially Therapeutic Naturally Occurring Compounds. *Int. Immunopharmacology* 70, 459–466. doi:10.1016/j.intimp.2019.02.050

Zhang, W., Lou, H.-X., Li, G.-Y., and Wu, H.-M. (2003). A New Triterpenoid fromEntodon Okamuraebroth. *J. Asian Nat. Prod. Res.* 5, 189–195. doi:10.1080/1028602031000082016

Zhu, H., Chen, C., Tong, Q., Li, X.-N., Yang, J., Xue, Y., et al. (2016). Epicochalasines A and B: Two Bioactive Merocytochalasans Bearing Caged Epicoccine Dimer Units from Aspergillus flavipes. *Angew. Chem. Int. Ed.* 55, 3486–3490. doi:10.1002/anie.201511315

Zhu, H., Chen, C., Tong, Q., Yang, J., Wei, G., Xue, Y., et al. (2017). Asperflavipine A: A Cytochalasan Heterotetramer Uniquely Defined by a Highly Complex Tetradecacyclic Ring System from Aspergillus flavipes QCS12. *Angew. Chem. Int. Ed.* 56, 5242–5246. doi:10.1002/anie.201701125

Conflict of Interest: The authors declare that the research was conducted in the absence of any commercial or financial relationships that could be construed as a potential conflict of interest.

Copyright © 2021 Xu, Qiao, Zhang, Deng, Chen, Tao, Xu, Liu, Sun, Ye, Lu, Qi and Zhang. This is an open-access article distributed under the terms of the Creative Commons Attribution License (CC BY). The use, distribution or reproduction in other forums is permitted, provided the original author(s) and the copyright owner(s) are credited and that the original publication in this journal is cited, in accordance with accepted academic practice. No use, distribution or reproduction is permitted which does not comply with these terms.

frontiers in Pharmacology

ORIGINAL RESEARCH
published: 25 June 2021
doi: 10.3389/fphar.2021.658998

Bazi Bushen Capsule Alleviates Post-Menopausal Atherosclerosis via GPER1-Dependent Anti-Inflammatory and Anti-Apoptotic Effects

Dan Huang[1,2†], Xindong Wang[1,2†], Yunhong Zhu[1,2], Juexiao Gong[1,2], Junqing Liang[3], Yanfei Song[3], Yiyan Zhang[1,2], Linsheng Liu[4] and Cong Wei[3]**

[1]Affiliated Hospital of Integrated Traditional Chinese and Western Medicine, Nanjing University of Chinese Medicine, Nanjing, China, [2]Jiangsu Province Academy of Traditional Chinese Medicine, Nanjing, China, [3]National Key Laboratory of Collateral Disease Research and Innovative Chinese Medicine, Shijiazhuang, China, [4]Department of Clinical Pharmacology, The First Affiliated Hospital of Soochow University, Suzhou, China

OPEN ACCESS

Edited by:
Hongzhi Du,
Hubei University of Chinese Medicine, China

Reviewed by:
Mingming Chen,
China Pharmaceutical University, China
Kang Xu,
Hubei University of Chinese Medicine, China

***Correspondence:**
Linsheng Liu
linsheng_liu@126.com
Cong Wei
weicong@yiling.cn

[†]*These authors have contributed equally to this work*

Specialty section:
This article was submitted to Ethnopharmacology, a section of the journal Frontiers in Pharmacology

Received: *26 January 2021*
Accepted: *07 June 2021*
Published: *25 June 2021*

Citation:
Huang D, Wang X, Zhu Y, Gong J, Liang J, Song Y, Zhang Y, Liu L and Wei C (2021) Bazi Bushen Capsule Alleviates Post-Menopausal Atherosclerosis via GPER1-Dependent Anti-Inflammatory and Anti-Apoptotic Effects. Front. Pharmacol. 12:658998. doi: 10.3389/fphar.2021.658998

Bazi Bushen capsule (BZBS), as a Chinese medicine used to relieve fatigue, has been proven effective for the treatment of atherogenesis through antilipid effects. To investigate the potential mechanism of BZBS in the anti-atherosclerotic effect, Ovx/ApoE$^{-/-}$ mice were applied to investigate the anti-atherosclerotic efficiency and potential mechanism of BZBS. Therapeutic effect was evaluated based on the number of CD68^{+} and CD3^{+} cells, the level of intercellular adhesion molecule-1 (ICAM-1) and vascular cell adhesion molecule-1 (VCAM-1), and the ratio of cleaved caspase-3/caspase-3, as well as increasing ratio of Bcl2/Bax. Human umbilical vein endothelial cells (HUVECs) were chosen to evaluate the role of GPER1. Treatment with BZBS reduced lipid deposition by reducing the numbers of CD68^{+} and CD3^{+} cells, the level of ICAM-1 and VCAM-1, and the ratio of cleaved caspase-3/caspase-3, and increasing the ratio of Bcl2/Bax as compared with the control group. In si-GPER1-treated HUVECs, the anti-apoptotic effect of BZBS was decreased. This study revealed that BZBS exhibited a clear effect against atherogenesis *via* GPER1-dependent anti-inflammatory and anti-apoptotic mechanisms. We believe that this manuscript is informative and useful for researchers pursuing the related alleviation of post-menopausal AS *via* anti-inflammatory and anti-apoptotic mechanisms.

Keywords: atherosclerosis, bazi bushen capsule, lipid profile, inflammation, apoptosis, GPER1 antagonist

INTRODUCTION

Atherosclerosis (AS) is the basis of cardiovascular diseases (Gaziano et al., 2010; Libby et al., 2011), and cardiovascular diseases are the leading cause of death in women worldwide. Endogenous estrogen has a protective effect against AS in pre-menopausal women. However, in post-menopausal (PM) women, due to the lack of estrogen, the morbidity and mortality associated with AS are greatly increased (Barton, 2013). Despite strong vasculoprotective effects, exogenous estrogen has many side

Abbreviations: AS, atherosclerosis; BZBS, bazi bushen capsule; CMC, carboxymethylcellulose; ECs, endothelial cells; GPER1, G-protein-coupled estrogen receptor 1; NF-κB, nuclear factor kappa B; Ovx, ovariectomy; PEs, phytoestrogens; PM, post-menopausal

TABLE 1 | The ratio of the plants present in the preparation of BZBS.

Plants	Amount in application (ratio)
Cuscuta chinensis Lam. [Convolvulaceae; Cuscutae semen]	250
Lycium barbarum L. [Solanaceae; Lycii cortex]	138
Schisandra chinensis (Turcz.) Baill. [Schisandraceae; Schisandrae chinensis fructus]	46
Cnidium monnieri (L.) Cusson [Apiaceae; Cnidii fructus]	35
Rosa laevigata Michx. [Rosaceae; Rosae laevigatae fructus]	35
Rubus chingii Hu [Rosaceae; Rubi fructus]	35
Allium tuberosum Rottler ex Spreng. [Amaryllidaceae; Allii tuberosi semen]	35
Toosendan fructus [Meliaceae; Fuctus Toosendan]	23
Epimedium brevicornu Maxim. [Berberidaceae; Epimedii folium]	70
Morindae officinalis radix [Rubiaceae; Radix Morindae Offcinalis]	35
Cistanche deserticola Ma [Orobanchaceae; Cistanches herba]	35
Rehmannia root [Orobanchaceae; Radix Rehmanniae Recens]	46
Cyathula officinalis K.C.Kuan [Amaranthaceae; Cyathulae radix]	35
Panax ginseng C.A.Mey. [Araliaceae; Ginseng radix et rhizoma]	25
Cervus nippon Temminck [Cervidae; Cervi Cornu Pantotrichum]	16
Hippocampus Kelloggi [Syngnathidae; Hippocampus]	21

effects such as thrombosis and tumorigenesis (Schenck-Gustafsson et al., 2011), and clinical treatment of women with estrogen replacement therapy may prevent subclinical AS but has no benefit on cardiovascular disease risk after menopause and later in life (Mcgowan and pottern, 2000; Schenck-Gustafsson et al., 2011). Therefore, estrogen supplementation in PM women for primary and secondary prevention of cardiovascular disease is controversial.

Phytoestrogens (PEs) are a class of non-steroidal compounds that naturally occur in plants, fruits, and vegetables. PEs have structures and molecular weights similar to those of endogenous estrogen, and have estrogen-like effects without estrogen-like side effects (Poluzzi et al., 2014). Many traditional Chinese medicines contain PEs (Zhao et al., 2017; Liang et al., 2019; Yang et al., 2019), which provides new options for PM women looking for safe and effective anti-atherosclerotic drugs. *Bazi Bushen capsule* (BZBS; an eight-seed kidney-tonifying capsule) was used to relieve fatigue with a compound formula composed of 16 kinds of traditional Chinese medicines (**Table 1**) BZBS has been proven to improves lipid metabolism (Huang et al., 2020). Fingerprint analysis of BZBS revealed that it contained a variety of PEs, including flavones, coumarins, lignans, and the terpenoid catalpol (Huang et al., 2020).

Estrogen and PEs perform various physiological functions by binding to the corresponding estrogen receptors (Prossnitz and Arterburn, 2015; Rexrode, 2018). The classical estrogen nuclear receptors ERα and ERβ mediate genomic effects by regulating the transcription of specific target genes (Meyer et al., 2011). As a membrane estrogen receptor, the G protein-coupled oestrogen receptor 1 (GPER1) has a rapid nongenomic effect mediated by the second messenger system (Revankar et al., 2005; Meyer et al., 2011). The pathogenesis of AS is complex. Endothelial cells (ECs) inflammation and inflammation-induced endothelial apoptosis are triggers for the occurrence and development of AS (Madhur et al., 2011; Herrero-Fernandez et al., 2019). Moreover, the PM state is characterized by generalized inflammatory activation. Estrogen exerts potent vasculoprotective effects that are partly mediated by inhibiting inflammation and apoptosis (Barton, 2013). GPER1 is expressed in many organs of the body including the arteries (Reslan et al., 2013). In PM mice, GPER1 deficiency exacerbates AS, an effect that is associated with significant vascular inflammation. Administration of G1, a highly selective GPER1 agonist, led to a pronounced decrease in vascular inflammation accompanied by attenuated atherosclerotic plaque formation (Meyer et al., 2014).

In the current study, we aimed to investigate the potential mechanism of BZBS on AS. We investigated the effects of BZBS in an animal model of PM AS ovariectomized (Ovx) ApoE$^{-/-}$ mice. After demonstrating that BZBS has anti-inflammatory and anti-apoptotic effects, we performed an *in vitro* study to assess the underlying mechanism. Our results revealed that these effects are dependent on the GPER1-mediated inhibition of anti-inflammatory and anti-apoptotic mechanisms.

MATERIALS AND METHODS

Chemicals and Reagents

BZBS capsules were provided by Shijiazhuang Yiling Pharmaceutical Co., Ltd. (Lot: A1801001, Shijiazhuang, China). A BZBS suspension in 0.5% sodium carboxymethylcellulose (CMC) was administered to mice *via* intragastric injection. BZBS was weighed and dissolved in serum-free Ham's F-12K medium. G1 was provided by ApexBio (Houston, TX, United States). As previously described, G1 was dissolved in absolute ethanol to prepare a stock solution of 20 μg/ml and stored in a -20°C freezer. The G1 working solution was diluted 10 times with solvent, and each mouse was injected subcutaneously with 0.2 μg G1 per day (Dennis et al., 2009). The high-fat diet was purchased from Research Diets, Inc. (PE-free, 1.25% cholesterol, 40 kcal% fat, and 0.5% cholic acid, New Brunswick, NJ, United States).

TABLE 2 | Treatment protocol of mice.

Treatment Regimen	Mice	Diet	Dosage in mouse (administration route)	Treatment Days
Control	C57BL/6J	Normal	0.5% CMC-Na (ig)	12 weeks
Model	ApoE$^{-/-}$	High-fat	0.5% CMC-Na (ig)	
G1	ApoE$^{-/-}$	High-fat	0.2 μg/d G1 (sc)	
HD-BZ	ApoE$^{-/-}$	High-fat	2.8 g/kg/d (ig)	
LD-BZ	ApoE$^{-/-}$	High-fat	1.4 g/kg/d (ig)	

Animal Experiments and Sample Preparation

Fifty C57BL/6J mice and sixty female homozygous ApoE$^{-/-}$ mice (18–22 g) were obtained from GemPharmatech Co., Ltd. (Nanjing, China). The animals were acclimated for three-days with a 12 h light-dark cycle with water and food *ad libitum*. The experiments were approved by the Ethics Commission of Animal Care of the Hebei Yiling Chinese Medicine Research Institute under approval number N2018050 (20180711).

Surgical menopause (Ovx/ApoE$^{-/-}$ mice) were induced by ovary ligation and bilateral ovariectomy under sterile conditions, whereas the C57BL/6J mice (control group, $n = 15$) only underwent sham surgery (needle threading). After recovering for 7 days, the ApoE$^{-/-}$ mice were randomly assigned to four groups ($n = 15$) as described in **Table 2**. The first group served as the model group, and these animals received a high-fat diet with intragastric (i.g.) injection of the vehicle (0.5% CMC-Na). In the three experimental groups, the G1 group was treated with 0.2 μg/day G1 and high-fat diet, while the low-dose BZBS (1.4 g/kg/day, LD-BZ) group and the high-dose BZBS (2.8 g/kg/day, HD-BZ) groups were treated with BZBS and high-fat diet for 12 weeks.

Cell Experiments

Human umbilical vein endothelial cells (HUVECs) were cultured in Ham's F-12K medium supplemented with 100 μg/ml heparin, 50 μg/ml endothelial cell growth supplement (ECGS), 10% foetal bovine serum (FBS), and 1% penicillin-streptomycin (P/S) (Procell Life Science & Technology Co., Ltd., Wuhan, China) at 37°C in 5% CO_2. Cells at passages 3–7 were used in subsequent experiments. HUVECs were seeded at a density of 1×10^5 cells per well into 35-mm dishes. After 24 h, the cells were transfected with 50 nM *GPER1* siRNA (CCGACCUGUACUUCAUCAATT and UUGAUGAAGUACAGGUCGGTT; GenePharma, Shanghai, China) in Gibco Opti-MEM I reduced serum medium with Invitrogen Lipofectamine RNAiMAX transfection reagent. Scrambled siRNA without sequence homology to any known human gene served as the negative control (NC). GPER1 protein levels were measured 40 h post-transfection to evaluate the knockdown efficiency. To establish an oxidized low-density lipoprotein (Ox-LDL)-induced apoptosis model and assess the protective effect of BZBS, we pretreated transfected HUVECs with 400 μg/ml BZBS in serum-free EC basal medium. The pretreatment started 8 h after transfection, lasted for 12 h and was followed by incubation with Ox-LDL (120 μg/ml, 24 h).

Serum Analysis

The levels of intercellular adhesion molecule-1 (ICAM-1) and vascular cell adhesion molecule-1 (VCAM-1) were quantified by an enzyme-linked immunosorbent assay (ELISA) kit (CUSABIO, Wuhan, China).

Quantification of Atherosclerotic Lesions

For en face quantification of AS, part of the aorta from the descending aorta to the iliac bifurcation was excised, carefully cleaned to remove adherent fat and connective tissue, and mounted en face with oil red O staining solution. To observe atherosclerotic plaques under a microscope, the hearts and proximal aortae were removed, and cross-sections (8 μm serial sections) of the aortic root were stained with haematoxylin-eosin (H&E) and oil red O. Neutral lipids were stained with oil red O. Four cross-sections were analysed from each mouse. Quantification was performed using Image-Pro Plus 6.0 software (Meyer Instruments, Houston, TX, United States).

TUNEL Apoptosis Assay

TUNEL (terminal deoxynucleotidyl transferase dUTP nick end labelling) apoptosis assays were performed with the *In Situ* Cell Death Detection Kit, Fluorescein (Roche, Mannheim, Germany). Cells grow on cover slips were fixed by 4% paraformaldehyde. Proteinase K working solution was then applied to cover the cells and incubated at 37°C for 25 min. Permeabilization working solution was added to the cover slips, and incubated at room temperature for 20 min. TDT enzyme, dUTP and buffer from the TUNEL kit were mixed at the ratio of 1:5:50 according to the number of slices. After 3% BSA blocking, rabbit polyclonal antibody to CD31 (1:100; Abcam) and goat anti-rabbit IgG (1:100; Abcam, red fluorescence) were used to confirm ECs. The cells were then incubated with a DAPI solution at room temperature for 10 min. Images were obtained using a ZEISS laser scanning confocal microscope.

Immunofluorescence, Quantitative Real-Time PCR analysis, Western Blot Analysis, and Annexin V-FITC/Propidium Iodide Apoptosis Assay

The complete details of immunofluorescence, quantitative real-time PCR analysis, Western blot analysis, and Annexin V-FITC/propidium iodide (PI) apoptosis assay are provided in the **Supplementary Material**.

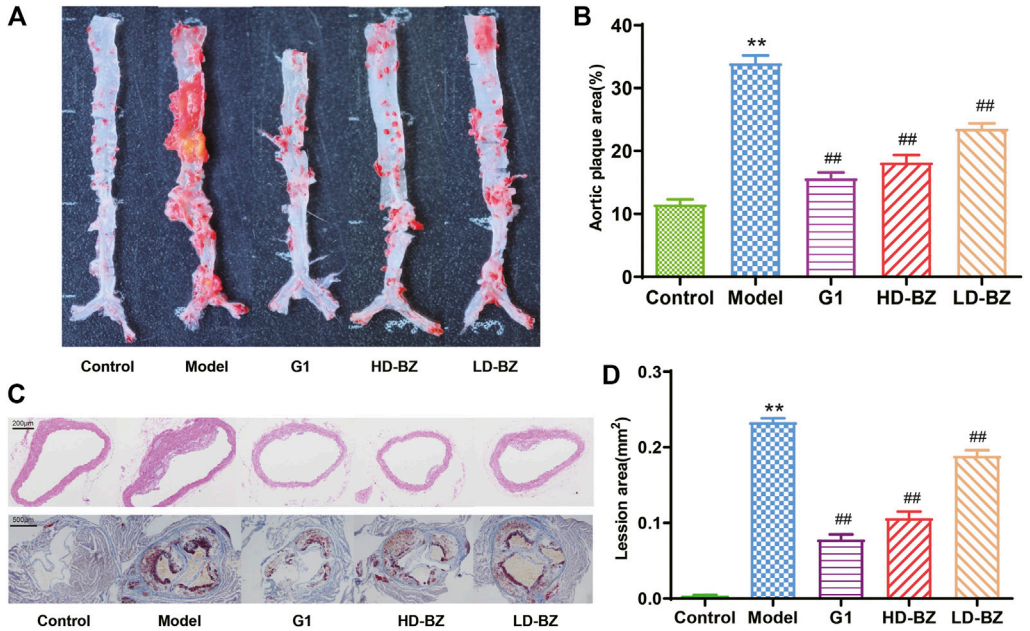


FIGURE 1 | Effects of BZBS on atherosclerotic plaque formation in Ovx/ApoE$^{-/-}$ mice. **(A)**En face staining of aortas with oil red O. **(B)** Quantification of the plaque area as measured in A. **(C)** Light microscopy images (40×) of aortic roots stained with H&E and oil red O. **(D)** Quantification of the lesion areas as measured in C. $^{**}p < 0.01$ vs. the control group; $^{\#\#}p < 0.01$ vs. the model group (n = 4–6).

Statistical Analysis

Correlation analysis was performed using IBM SPSS 20.0 software. Statistical analysis was performed by one-way ANOVA. Differences with p-values < 0.05 were considered statistically significant. All results are presented as mean ± SE.

RESULTS

Bazi Bushen Capsule Treatment Hindered the Development of AS in Ovx/ApoE$^{-/-}$ Mice

Both the macroscopic observation of the aortas (**Figures 1A,B**) and the microscopic images of the aortic roots (**Figures 1C,D**) revealed that lipid deposition was most severe in the model group. Treatment with G1 or BZBS reduced lipid deposition, as the lesions in the corresponding groups (G1, HD-BZ, and LD-BZ) were narrower than those of the model group (**Figures 1A–D**). En face analysis of the aortas revealed 29, 26, and 17% reduction in plaque area in the G1, HD-BZ, and LD-BZ groups, respectively, compared with that of the model group (**Figures 1A,B**), indicating that BZBS has a therapeutic effect against AS induced by estrogen deficiency and a high fat diet. These results support the idea that BZBS exhibits a protective effect against AS.

Bazi Bushen Capsule Treatment Inhibited the Accumulation of Inflammatory Cells in Ovx/ApoE$^{-/-}$ Mice

AS is known to involve an ongoing inflammatory response, with macrophages and T cells playing key roles in the onset and development of this condition (Hansson and Hermansson, 2011). Immunofluorescence analysis of atherosclerotic lesion areas in aortic arches revealed that surgically-induced menopause resulted in a marked accumulation of CD68^{+} cells (macrophages) and CD3^{+} cells (T cells) (**Figure 2A–C**). However, inflammatory cell infiltration in the G1 group and both BZBS groups was significantly reduced (**Figure 2A–C**). The NF-κB pathway serves as a critical mediator of inflammatory responses by activating the transcription of several pro-inflammatory genes (Taylor and Cummins, 2009). We observed that the p-IκBα/IκBα and p-p65/p65 ratios in the aortas of the model group were significantly higher than those of the control group. G1 and BZBS treatment significantly reduced these ratios, bringing them closer to those of the control group (**Figures 2D,E**). Activation of the NF-κB pathway can lead to the expression of the adhesion proteins VCAM-1 and ICAM-1 (Sun et al., 2020b). The mRNA and protein levels of these adhesion molecules were also assessed. Compared with the control mice, the expression levels of VCAM-1 and ICAM-1 were higher not only in the serum (protein level) but also in the aorta (RNA level) in the high fat diet-fed PM mice. G1 and BZBS reduced the expression of VCAM-1 and ICAM-1 (**Figures 2F,G**).

Bazi Bushen Capsule Treatment Inhibited Apoptosis in Ovx/ApoE$^{-/-}$ Mice

Inflammation often causes apoptosis. TUNEL apoptosis assays showed that there were significantly fewer apoptotic ECs in the atherosclerotic plaques of the BZBS groups than in those of the model group (**Figure 3A**). Model mice had markedly lower expression levels (at both the mRNA and protein levels) of the

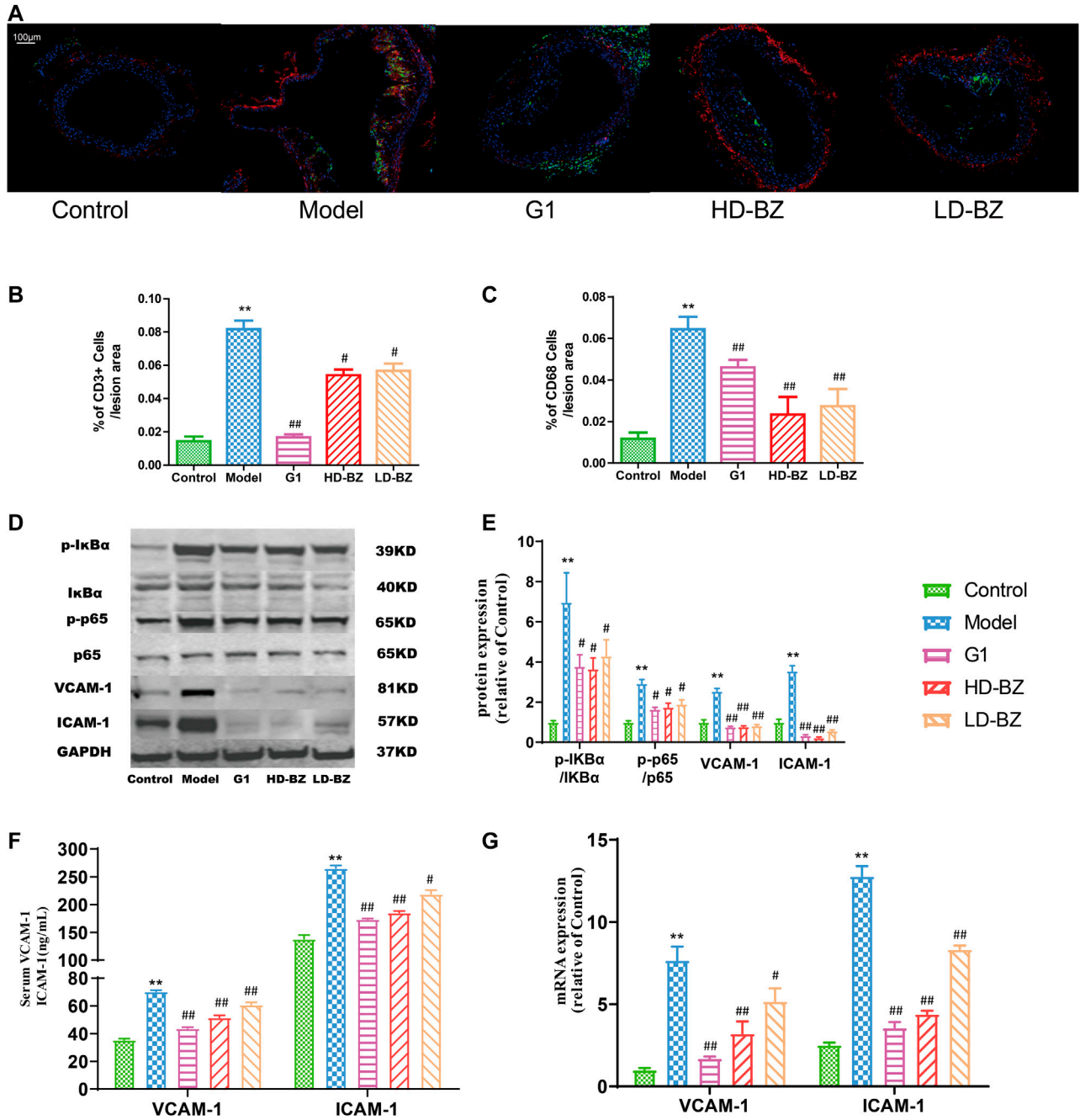


FIGURE 2 | Effect of BZBS on the accumulation of inflammatory cells and adhesion molecule expression mediated by transactivation of NF-κB signalling in Ovx/ApoE^{-}/-mice. **(A)** Immunofluorescence was used to quantify CD68^{+} cells (macrophages, green) and CD3^{+} cells (T cells, red) in the aortic arch. **(B)** %of CD3^{+} cells/lesion area. **(C)** %of CD68^{+} cells/lesion area. **(D)** Western blots of phospho-IκBα (Ser36), IκBα, phospho-p65, p65, VCAM-1, ICAM-1, and GAPDH. **(E)** Graph showing quantification results of the bands in D, using GAPDH as an internal reference protein. **(F)** Graph showing the levels of VCAM-1 and ICAM-1 as determined by ELISA. **(G)** Graph showing the levels of *VCAM-1* and *ICAM-1* mRNA as determined by quantitative real-time PCR analysis; *GAPDH* was used as an internal reference gene. $^{**}p < 0.01$ vs. the control group; $^{\#}p < 0.05$, $^{\#\#}p < 0.01$ vs. the model group (n = 4–6).

anti-apoptotic gene, *Bcl-2*, than control mice, whereas the opposite result was observed for the pro-apoptotic gene, *Bax*. However, G1 and BZBS attenuated the effects of ovariectomy on both genes, increasing *Bcl-2* expression and reducing *Bax* expression (**Figures 3B–D**). We also assessed another apoptotic index, the ratio of cleaved caspase-3 to caspase-3. As shown in **Figures 3C,D**, mice in the model group had higher ratios than control mice, whereas G1 or BZBS treatment reduced the ratio. In other words, BZBS reduced estrogen deficiency-induced apoptosis by regulating Bcl-2, Bax and cleaved caspase-3.

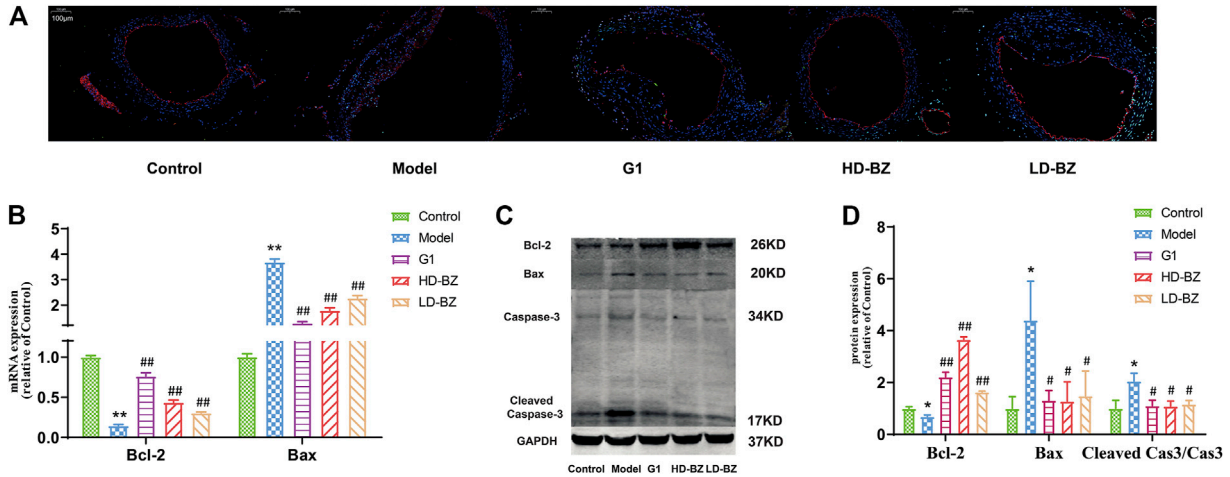


FIGURE 3 | Effect of BZBS on endothelial cell apoptosis in Ovx/ApoE$^{-/-}$mice. **(A)** Images from the TUNEL apoptosis assay were used to quantify apoptotic ECs in aortic arch atherosclerotic plaques in mice. **(B)** *Bcl2* and *Bax* mRNA levels were determined by quantitative real-time PCR analysis. *GAPDH* was used as an internal reference gene. **(C)** Western blots showing Bcl2, Bax, and caspase-3 analytes. **(D)** Graph showing the values derived from the quantification of the bands shown in C; GAPDH was used as an internal reference protein. The data are presented as the mean ± SD. $^{*}p < 0.05$, $^{**}p < 0.01$ vs. the control group; $^{\#}p < 0.05$, $^{\#\#}p < 0.01$ vs. the model group (n = 4–6).

G-Protein-Coupled Estrogen Receptor 1 is a Key Mediator of Bazi Bushen Capsule-Induced Endothelial Protection

Selective *GPER1* activation can inhibit postmenopausal AS (Jing et al., 2017). To determine whether GPER1 mediates the endothelial-protective effect of BZBS, GPER1 expression was knocked down in HUVECs by transfection with GPER1-specific siRNA (**Figures 4A,B**). Apoptosis was induced with 120 μg/ml Ox-LDL. At this concentration, more than half of the cells remained viable (60.04 ± 3.35%, **Supplementary Figure S1A**). As shown in **Supplementary Figure S1B**, BZBS increased cell viability, with the increase being most prominent at 400 μg/ml BZBS. As other kinds of vascular cells such as smooth muscle cells were also included in aortic arch atherosclerotic plaques, **Figure 3** does not represent the complete results for endothelial cells. Here a similar result was observed with respect to the effect of BZBS on HUVECs.

After the GPER1 gene was knocked down, Bcl2, Bax, cleaved caspase-3 and caspase-3 were almost unchanged between the si-GPER1-control and si-NC-control groups. The Bcl2/Bax ratio decreased slightly (−20.8%, $p = 0.088$) and the cleaved caspase-3/caspase-3 ratio increased slightly (19.6%, $p = 0.158$) in the si-GPER1-control group, but the differences were not significant. These results indicate that silencing GPER1 in unstimulated HUVECs may slightly induce apoptosis. Interestingly, after stimulation with Ox-LDL, the Bcl2/Bax ratio in both model groups decreased compared with that in each control group, while the cleaved caspase-3/caspase-3 ratio was significantly increased. BZBS improved these ratios to some extent in the si-GPER1-BZBS group but had a reduced effect compared to that in the si-NC-BZBS group (BZBS upregulated Bcl2/Bax 85.9% in the si-NC group vs. 33.2% in the si-GPER1 group and downregulated cleaved caspase-3/caspase-3 44.8% in the si-NC group vs. 12.0% in the si-GPER1 group; **Figures 4C,D**). TUNEL and Annexin V-FITC/PI assays also showed that the apoptotic rates in the si-GPER1-control groups were generally higher than those in the corresponding si-NC-control groups (**Figures 4E–H**). Ox-LDL induced more apoptosis in the si-GPER1 group than in the control group, and the anti-apoptotic effect of BZBS was weaker in si-GPER1 cells than in control cells, suggesting that GPER1 plays a key role in protecting ECs (**Figures 4E–H**). Although there was no significant difference among the groups in early apoptosis (**Supplementary Figure S2A**), the same result was found in late apoptosis (**Supplementary Figure S2B**).

DISCUSSION

The accumulation of lipids in the arterial walls induces AS (Salvayre et al., 2016; Suciu et al., 2018). Sex hormone levels after menopause are associated with increased AS risk in women later in life (Zhao et al., 2018). PEs have been shown to prevent the development of atherosclerotic lesions via lipid metabolism pathways (Chen et al., 2018), and we demonstrated that BZBS contains 11 unique PEs, and improve fatty acid metabolism in high-fat diet-fed, surgically-induced menopausal ApoE$^{-/-}$ mice by reducing serum lipid levels (Huang et al., 2020). Although the mouse model used is quite complex, it also successfully simulated the clinically severe hyperlipidemia state after menopause. This animal model is widely used in the hyperlipidemia model of postmenopausal women (Meng et al., 2021b; Sun et al., 2020a). In this study, we aimed to investigate the potential mechanism of BZBS on AS. Lipid deposition was higher after high-fat diet-feeding and spaying ovariotomy. Treatment with BZBS reduced lipid deposition, and BZBS exhibited a clear effect against atherogenesis *via* GPER1-dependent anti-inflammatory and

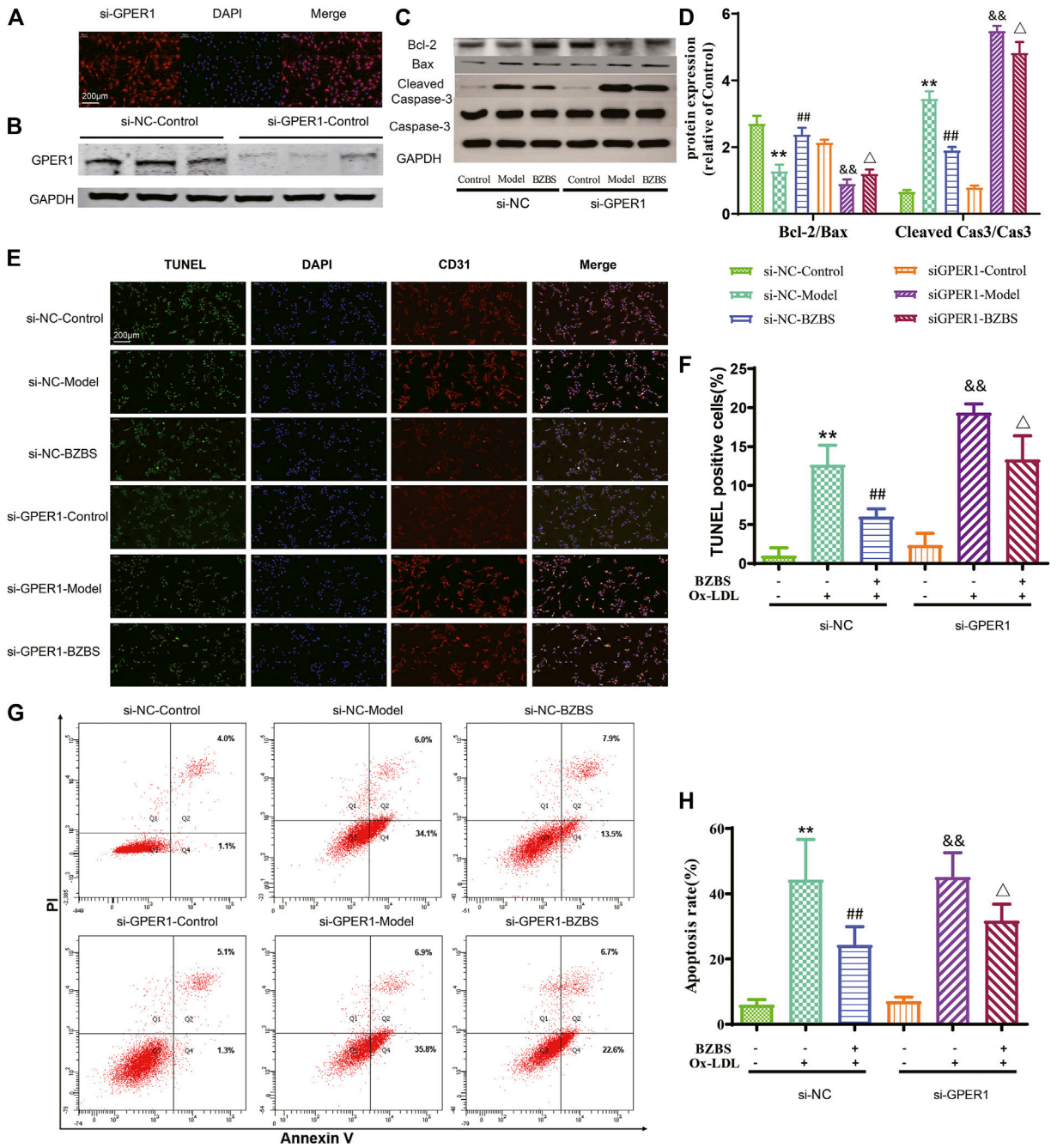


FIGURE 4 | Effect of BZBS on the apoptosis of Ox-LDL-induced HUVECs with GPER1 deficiency. **(A,B)** GPER1 protein levels were measured 40 h posttransfection to evaluate knockdown efficiency. **(C,D)** Western blots showing Bcl2, Bax, and caspase-3 proteins. **(E,F)** Annexin V-FITC/propidium iodide (PI) **(G,H)** was used to measure the apoptotic rates in the various groups of Ox-LDL-treated HUVECs. The data are presented as the mean ± SD. $^{**}p < 0.01$ vs. the si-NC control group; $^{\#\#}p < 0.01$ vs. the si-NC model group; $^{\&\&}p < 0.01$ vs. the si-GPER1 control group; $^{\triangle}p < 0.05$ vs. the si-GPER1 model group ($n = 3$).

anti-apoptotic mechanisms, which revealed that BZBS exhibited a protective effect against AS.

AS is a chronic inflammatory disease, and lipid metabolism mediates AS-related inflammation (Zhu et al., 2018; Wu et al., 2020). In atherosclerotic lesions, macrophages, T lymphocytes, B-lymphocytes, dendritic cells, ECs, and resident immune cells are activated and accumulate, manifesting inflammatory effects (Pyka-Fosciak et al., 2013). Our immunofluorescence analysis demonstrated that BZBS treatment reduced the accumulation of $CD68^+$ macrophages and $CD3^+$ T cells. Inflammation-activated ECs release pro-inflammatory mediators, including chemokines, pro-inflammatory cytokines, and adhesion molecules (Song et al.,

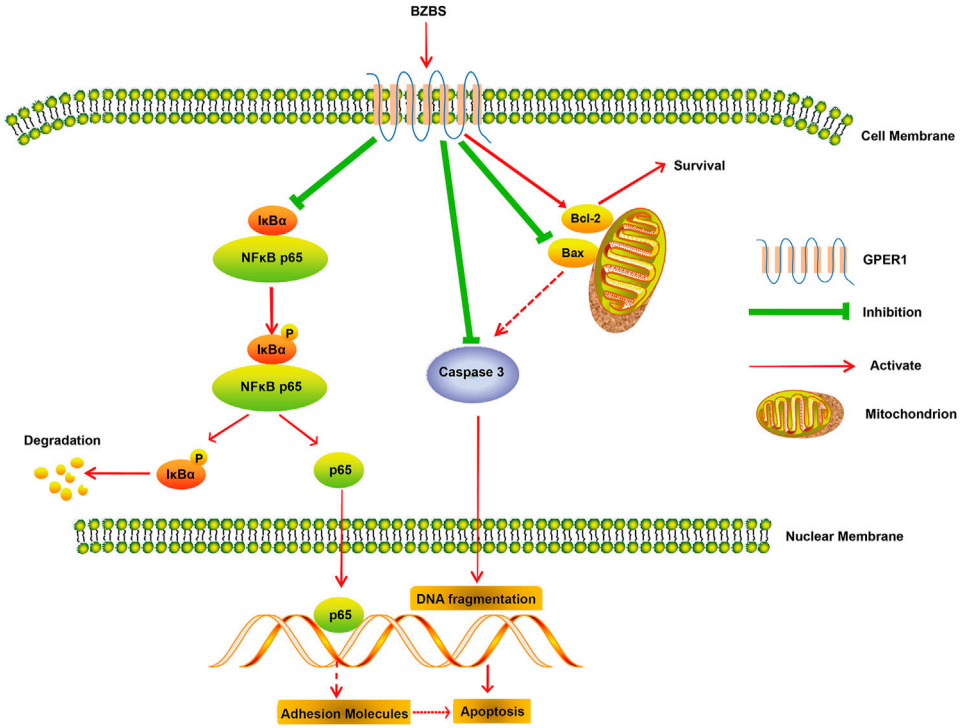


FIGURE 5 | Mechanism by which BZBS inhibits endothelial cell apoptosis through GPER1 mediated regulation.

2016). ECs are the main target of estrogen-mediated vascular protection (Sun et al., 2020a). Estrogen acts as an anti-inflammatory agent by reducing the expression of adhesion proteins via inhibition of the NF-κB pathway (Zhang et al., 2003; Knowlton and Lee, 2012). In this study, the data revealed that BZBS treatment may block the NF-κB signalling pathway, thereby reducing the secretion of adhesion molecules VCAM-1 and ICAM-1 (**Figures 2**, **5**), indicating an anti-inflammatory effect.

EC apoptosis occurs throughout the early stages of AS, and is an important characteristic of this condition (Hort et al., 2014). NF-κB regulates the expression of genes associated with EC apoptosis (Cao et al., 2016). Bcl-2 family members are either anti-apoptotic, such as Bcl-xl and Bcl-2, or pro-apoptotic, such as Bad, Bak, and Bax. The latter proteins are associated with mitochondrial permeability transition pore (MPTP) regulation and the release of cytochrome c (Cyt-c), a critical mitochondrial death factor, resulting in the activation of caspase-9 and caspase-3 and, ultimately, apoptosis (Solesio et al., 2013). Caspase-3 is considered the final executor, as it is indispensable for apoptotic chromatin condensation and DNA fragmentation (Lu et al., 2010). Our data indicated that BZBS markedly inhibited apoptosis, as shown by the upregulation of the anti-apoptotic protein Bcl-2, downregulation of pro-apoptotic Bax, and decreased expression and activity of caspase-3 (**Figures 3**, **5**). This finding was confirmed by immunofluorescence analysis.

As a transmembrane protein, GPER1 contains 375 amino acids and belongs to the G-protein-coupled receptor family. As such, its peptide chain starts with an extracellular N-terminus, traverses the membrane seven times, and ends with an intracellular C-terminus that contains the binding site of a guanosine-binding protein (G protein) (Meyer et al., 2011). Upon binding to estrogen, GPER1 activates several intracellular signal transduction pathways, such as the NF-κB (Du et al., 2018) and caspase-3 signalling pathways (Jiang et al., 2019), decreases the Bax/Bcl-2 ratio (He et al., 2018) and exerts protective effects by inhibiting NF-κB-mediated inflammation and caspase-3- mediated apoptosis. It is well known that PEs exhibit estrogenic activity. The pharmacological effects of some PEs were sensitized by activating GPER1 (Du et al., 2018; Ariyani et al., 2019). In our previous study, 11 unique PEs were identified in BZBS (the relative levels of 11 unique PEs are shown in **Table 3**, and **Figure 6**). G1 was selected as a GPER1 agonist because G1 is devoid of uterotrophic activity, similarly to PEs (Meyer et al., 2014). Indeed, our previous study revealed that BZBS did not prevent uterine atrophy in Ovx/ApoE$^{-/-}$ mice (Huang et al., 2020). In Ox-LDL-stimulated HUVECs, the Bcl2/Bax ratio decreased compared with that of the control group, while the cleaved caspase-3/caspase-3 ratio was increased significantly after the GPER1 gene was knocked down (**Figures 4**, **5**). TUNEL and Annexin V-FITC/PI assays also showed increased Ox-LDL-mediated apoptosis in the si-GPER1 group, and the anti-apoptotic effect of BZBS was reduced in si-GPER1 cells, suggesting that BZBS exerted a protective effect on ECs (**Figure 5**) via GPER1-dependent anti-inflammatory and anti-apoptotic mechanisms. In this study, results showed that BSBZ and G1 (GPER agonist) reduce apoptosis in HUVECs through activated GPER, which is contrary to previous observation that

TABLE 3 | Precision test of relative area.

Peak	RT (time)	Relative Area					Mean	SD	RSD%
		Test 1	Test 2	Test 3	Test 4	Test 5			
1	3.52	0.40	0.41	0.41	0.40	0.41	0.40	0.00	0.44
2	3.72	0.90	0.91	0.89	0.91	0.91	0.90	0.01	1.09
3	4.15	1.71	1.69	1.65	1.66	1.69	1.68	0.02	1.43
4	4.93	0.40	0.41	0.41	0.41	0.40	0.41	0.00	1.13
5	6.3	6.84	6.91	6.90	6.86	6.84	6.87	0.03	0.45
6	6.8	0.21	0.21	0.21	0.21	0.21	0.21	0.00	1.62
7	7.12	1.33	1.33	1.37	1.31	1.35	1.34	0.02	1.66
8	8.24	0.43	0.42	0.42	0.42	0.42	0.42	0.01	1.49
9	8.74	0.85	0.85	0.85	0.85	0.85	0.85	0.00	0.34
10	9.88	1.26	1.29	1.24	1.26	1.25	1.26	0.02	1.53
11	12.67	6.71	6.62	6.73	6.70	6.68	6.69	0.04	0.59
12	13.16	2.96	2.94	2.96	2.91	2.86	2.92	0.04	1.41
13[a]	14.02	4.91	4.99	4.93	4.96	4.97	4.95	0.03	0.60
14[a]	14.47	1.17	1.16	1.21	1.16	1.16	1.17	0.02	1.88
15	14.73	1.03	1.03	1.04	1.02	1.03	1.03	0.01	0.82
16	15.33	0.45	0.45	0.46	0.45	0.45	0.45	0.00	0.34
17[a]	15.71	1.09	1.11	1.10	1.10	1.10	1.10	0.01	0.56
18	16.43	3.35	3.43	3.35	3.36	3.30	3.36	0.05	1.44
19	16.82	0.42	0.43	0.43	0.43	0.42	0.42	0.00	0.73
20	17.85	2.74	2.76	2.66	2.68	2.72	2.71	0.04	1.54
21	21.2	1.07	1.08	1.12	1.07	1.08	1.08	0.02	1.77
22[a]	27.92	1.75	1.74	1.75	1.72	1.78	1.75	0.02	1.16
23	28.52	6.50	6.54	6.59	6.43	6.50	6.51	0.06	0.94
24[a]	29.31	3.98	3.89	3.85	3.81	3.81	3.87	0.07	1.80
25	29.64	19.31	18.73	18.96	19.40	19.31	19.14	0.29	1.50
26	34.71	0.16	0.17	0.16	0.16	0.16	0.16	0.00	1.89
27	35.07	1.69	1.77	1.72	1.70	1.70	1.72	0.03	1.89
28	35.71	1.32	1.36	1.36	1.34	1.34	1.35	0.02	1.15
29[a]	35.93	0.37	0.37	0.37	0.37	0.36	0.37	0.00	1.28
30	36.5	2.45	2.44	2.51	2.50	2.48	2.47	0.03	1.27
31[a]	37.09	3.15	3.19	3.25	3.21	3.19	3.20	0.03	1.07
32[a]	38.05	6.68	6.74	6.63	6.66	6.73	6.69	0.05	0.73
33	39.02	0.42	0.43	0.42	0.42	0.42	0.42	0.00	1.03
34	39.71	0.66	0.65	0.67	0.66	0.66	0.66	0.01	0.87
35	40.17	2.05	2.09	2.11	2.05	2.04	2.07	0.03	1.36
36[a]	41.49	3.53	3.58	3.49	3.59	3.54	3.55	0.04	1.10
37[a]	43.31	2.55	2.59	2.58	2.51	2.61	2.57	0.04	1.43
38	44.75	0.67	0.65	0.66	0.67	0.66	0.66	0.01	1.54
39[a]	45.18	2.53	2.65	2.64	2.67	2.62	2.62	0.05	2.04

[a]*Phytoestrogens 13. Isoquercitrin; 14. Hyperoside; 17. Verbascoside; 22. Epimedins A; 24. Icariin; 29. Baohuoside* I*; 31. Imperatorin; 32. Osthole; 36. Catalpol; 37. Deoxyschizandrin; 39.Schisandrin B.*

GPER activation stimulates cell apoptosis (Gros et al., 2013; Feldman et al., 2014): we speculate that the *in vivo* situation is likely very different from the *in vitro* observation (Ding et al., 2009). In addition, the research objects of previous observation are vascular smooth muscle cells. The object of this study is vascular endothelial cells. Some literature studies have shown that the effect of E2 and GPER on endothelial cells is to inhibit apoptosis, while is to promote apoptosis on smooth muscle cells (Kassi et al., 2015; Jing et al., 2017; Wei et al., 2020). In our research, we also found that BSBZ and G1 (GPER agonist) reduce the apoptosis in HUVECs through activated GPER.

However, this study also has some limitations. First, BZBS is a complex molecular mixture, and not all of the contents are completely known. Second, the specific PEs that play major roles have not been determined. Cell membrane chromatography is a very efficient method and was developed to identify bioactive compounds from TCMs (Sun et al., 2020b), this method can be used to characterize the 11 phytoestrogens in BZBS with respect to anti-atherosclerosis effects. Third, GPER1 overexpression was not considered. Fourth, the effects of AS progression through other pathways require further study, such as classic estrogen receptors (ERα, ERβ and several splice variants). We deduced that BZBS can reduce vascular endothelial cell pyroptosis through ERα-mediated activation of autophagy or the following regulation of the expressions of SREBPs and SIRT1 to improve atherosclerosis in post-menopausal stage (Chen, et al., 2020; Meng et al., 2021a). Finally, for extracts already used in humans, it is critical to have a dose–response curve in the experimental set up that includes the usual dose in humans (Heinrich et al., 2020). Current dose usage in our study (1.4 and 2.8 mg/kg/d) was slightly higher than the clinical equivalent dose in mice

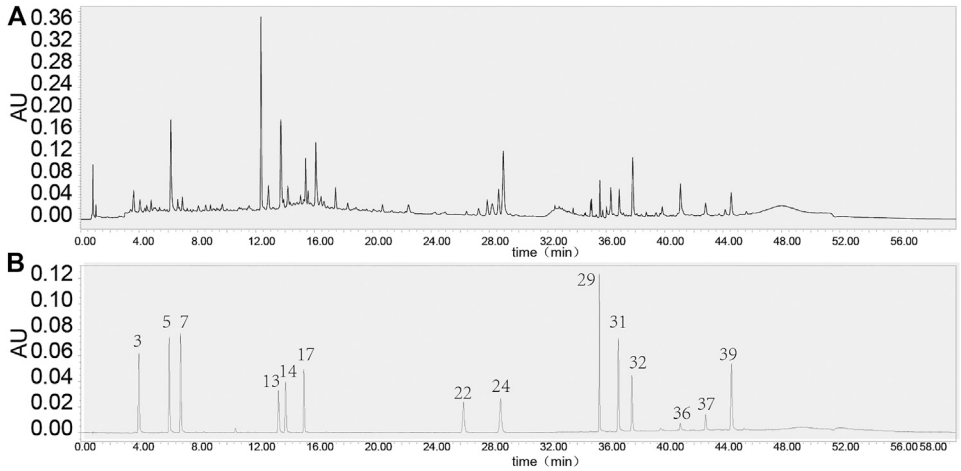


FIGURE 6 | UPLC of BZBS **(A)** and Reference substance [**(B)**, mixed reference substance]. The BZBS detection method is shown as a Supplementary method. Compound 13. Isoquercitrin; compound 14. Hyperoside; compound 17. Verbascoside; compound 22. Epimedins A; compound 24. Icariin; compound 29. Baohuoside I; compound 31. Imperatorin; compound 32. Osthole; compound 36. Catalpol; compound 37. Deoxyschizandrin; 39.Schisandrin B.

(0.7 mg/kg/d). Although the dose is not grossly excessive, the lower dose studies will be needed.

CONCLUSION

In this study, we revealed that BZBS treatment reduced lipid deposition, inhibited inflammatory molecule expression, protected against apoptosis, and decreased atherosclerotic lesion formation in high-fat diet-fed, surgically-induced menopausal mice. We further indicated that the underlying mechanism of these anti-inflammatory and anti-apoptotic effects was mediated by the GPER1 pathway. Our findings indicate that BZBS may prevent AS in postmenopausal women.

DATA AVAILABILITY STATEMENT

The original contributions presented in the study are included in the article/**Supplementary Material**, further inquiries can be directed to the corresponding authors.

ETHICS STATEMENT

The animal study was reviewed and approved by the Ethics Commission of Animal Care of the Hebei Yiling Chinese Medicine Research Institute under approval number N2018050 (20180711). Written informed consent was obtained from the owners for the participation of their animals in this study.

AUTHOR CONTRIBUTIONS

DH, LL, and CW designed the study; DH, XW, Y Zhu, JG, JL, YS, and Y Zhang performed the experiments and collected and analysed data; LL and DH wrote the manuscript.

FUNDING

This work was supported by the National Key Research and Development Program-Modernization of Traditional Chinese Medicine (2017YFC1700501); and the National Natural Science Foundation of China (81973766).

SUPPLEMENTARY MATERIAL

The Supplementary Material for this article can be found online at: https://www.frontiersin.org/articles/10.3389/fphar.2021.658998/full#supplementary-material

REFERENCES

Ariyani, W., Miyazaki, W., and Koibuchi, N. (2019). A Novel Mechanism of S-Equol Action in Neurons and Astrocytes: The Possible Involvement of GPR30/GPER1. *Int. J. Mol. Sci.* 20, 5178. doi:10.3390/ijms20205178

Barton, M. (2013). Cholesterol and Atherosclerosis. *Curr. Opin. Lipidol.* 24, 214–220. doi:10.1097/MOL.0b013e3283613a94

Cao, W., Hu, C., Wu, L., Xu, L., and Jiang, W. (2016). Rosmarinic Acid Inhibits Inflammation and Angiogenesis of Hepatocellular Carcinoma by Suppression of NF-κB Signaling in H22 Tumor-Bearing Mice. *J. Pharmacol. Sci.* 132, 131–137. doi:10.1016/j.jphs.2016.09.003

Chen, J., Yue, J., Liu, Y., Liu, J., Jiao, K., Teng, M., et al. (2018). Blocking of STAT-3/SREBP1-Mediated Glucose-Lipid Metabolism Is Involved in Dietary Phytoestrogen-Inhibited Ovariectomized-Induced Body Weight Gain in Rats. *J. Nutr. Biochem.* 61, 17–23. doi:10.1016/j.jnutbio.2018.06.009

Chen, Q., Chao, Y., Zhang, W., Zhang, Y., Bi, Y., Fu, Y., et al. (2020). Activation of Estrogen Receptor α (ERα) Is Required for Alisol B23-Acetate to Prevent post-menopausal Atherosclerosis and Reduced Lipid Accumulation. *Life Sci.* 258, 118030. doi:10.1016/j.lfs.2020.118030

Dennis, M. K., Burai, R., Ramesh, C., Petrie, W. K., Alcon, S. N., Nayak, T. K., et al. (2009). *In Vivo* effects of a GPR30 Antagonist. *Nat. Chem. Biol.* 5, 421–427. doi:10.1038/nchembio.168

Ding, Q., Gros, R., Limbird, L. E., Chorazyczewski, J., and Feldman, R. D. (2009). Estradiol-mediated ERK Phosphorylation and Apoptosis in Vascular Smooth Muscle Cells Requires GPR 30. *Am. J. Physiology-Cell Physiol.* 297, C1178–C1187. doi:10.1152/ajpcell.00185.2009

Du, Z.-R., Feng, X.-Q., Li, N., Qu, J.-X., Feng, L., Chen, L., et al. (2018). G Protein-Coupled Estrogen Receptor Is Involved in the Anti-inflammatory Effects of Genistein in Microglia. *Phytomedicine* 43, 11–20. doi:10.1016/j.phymed.2018.03.039

Feldman, R. D., Gros, R., Ding, Q., Hussain, Y., Ban, M. R., McIntyre, A. D., et al. (2014). A Common Hypofunctional Genetic Variant of GPER Is Associated with Increased Blood Pressure in Women. *Br. J. Clin. Pharmacol.* 78, 1441–1452. doi:10.1111/bcp.12471

Gaziano, T. A., Bitton, A., Anand, S., Abrahams-Gessel, S., and Murphy, A. (2010). Growing Epidemic of Coronary Heart Disease in Low- and Middle-Income Countries. *Curr. Probl. Cardiol.* 35, 72–115. doi:10.1016/j.cpcardiol.2009.10.002

Gros, R., Ding, Q., Liu, B., Chorazyczewski, J., and Feldman, R. D. (2013). Aldosterone Mediates its Rapid Effects in Vascular Endothelial Cells through GPER Activation. *Am. J. Physiology-Cell Physiol.* 304, C532–C540. doi:10.1152/ajpcell.00203.2012

Hansson, G. K., and Hermansson, A. (2011). The Immune System in Atherosclerosis. *Nat. Immunol.* 12, 204–212. doi:10.1038/ni.2001

He, S., Li, J., Bao, H., Wang, M., Wang, X., Huang, X., et al. (2018). G Protein coupled Estrogen receptor/miR148a/human Leukocyte antigenG Signaling Pathway Mediates Cell Apoptosis of Ovarian Endometriosis. *Mol. Med. Rep.* 18, 1141–1148. doi:10.3892/mmr.2018.9039

Heinrich, M., Appendino, G., Efferth, T., Fürst, R., Izzo, A. A., Kayser, O., et al. (2020). Best Practice in Research - Overcoming Common Challenges in Phytopharmacological Research. *J. Ethnopharmacology* 246, 112230. doi:10.1016/j.jep.2019.112230

Herrero-Fernandez, B., Gomez-Bris, R., Somovilla-Crespo, B., and Gonzalez-Granado, J. M. (2019). Immunobiology of Atherosclerosis: A Complex Net of Interactions. *Int. J. Mol. Sci.* 20, 5293. doi:10.3390/ijms20215293

Hort, M. A., Straliotto, M. R., de Oliveira, J., Amoêdo, N. D., da Rocha, J. B. T., Galina, A., et al. (2014). Diphenyl Diselenide Protects Endothelial Cells against Oxidized Low Density Lipoprotein-Induced Injury: Involvement of Mitochondrial Function. *Biochimie* 105, 172–181. doi:10.1016/j.biochi.2014.07.004

Huang, D., Hu, H., Chang, L., Liu, S., Liang, J., Song, Y., et al. (2020). Chinese Medicine Bazi Bushen Capsule Improves Lipid Metabolism in Ovariectomized Female ApoE−/− Mice. *Ann. Palliat. Med.* 9, 1073–1083. doi:10.21037/apm-20-906

Jiang, M., Ma, X., Zhao, Q., Li, Y., Xing, Y., Deng, Q., et al. (2019). The Neuroprotective Effects of Novel Estrogen Receptor GPER1 in Mouse Retinal Ganglion Cell Degeneration. *Exp. Eye Res.* 189, 107826. doi:10.1016/j.exer.2019.107826

Jing, Y., Cai, D., Chen, Q., Xiong, Q., Hu, T., Yao, Y., et al. (2017). Liuwei Dihuang Soft Capsules Attenuates Endothelial Cell Apoptosis to Prevent Atherosclerosis through GPR30-Mediated Regulation in Ovariectomized ApoE-Deficient Mice. *J. Ethnopharmacol.* 208, 185–198. doi:10.1016/j.jep.2017.06.052

Kassi, E., Spilioti, E., Nasiri-Ansari, N., Adamopoulos, C., Moutsatsou, P., Papapanagiotou, A., et al. (2015). Vascular Inflammation and Atherosclerosis: The Role of Estrogen Receptors. *Curr. Med. Chem.* 22, 2651–2665. doi:10.2174/0929867322666150608093607

Knowlton, A. A., and Lee, A. R. (2012). Estrogen and the Cardiovascular System. *Pharmacol. Ther.* 135, 54–70. doi:10.1016/j.pharmthera.2012.03.007

Liang, C., Zhou, A., Sui, C., and Huang, Z. (2019). The Effect of Formononetin on the Proliferation and Migration of Human Umbilical Vein Endothelial Cells and its Mechanism. *Biomed. Pharmacother.* 111, 86–90. doi:10.1016/j.biopha.2018.12.049

Libby, P., Ridker, P. M., and Hansson, G. K. (2011). Progress and Challenges in Translating the Biology of Atherosclerosis. *Nature* 473, 317–325. doi:10.1038/nature10146

Lu, W.-C., Chen, C.-J., Hsu, H.-C., Hsu, H.-L., and Chen, L. (2010). The Adaptor Protein SH2B1β Reduces Hydrogen Peroxide-Induced Cell Death in PC12 Cells and Hippocampal Neurons. *J. Mol. Signal* 5, 17. doi:10.1186/1750-2187-5-17

Madhur, M. S., Funt, S. A., Li, L., Vinh, A., Chen, W., Lob, H. E., et al. (2011). Role of Interleukin 17 in Inflammation, Atherosclerosis, and Vascular Function in Apolipoprotein E-Deficient Mice. *Arterioscler Thromb. Vasc. Biol.* 31, 1565–1572. doi:10.1161/ATVBAHA.111.227629

Mcgowan, J. A., and Pottern, L. (2000). Commentary on the Women's Health Initiative. *Maturitas* 34, 109–112. doi:10.1016/s0378-5122(99)00109-7

Meng, Q., Li, Y., Ji, T., Chao, Y., Li, J., Fu, Y., et al. (2021a). Estrogen Prevent Atherosclerosis by Attenuating Endothelial Cell Pyroptosis via Activation of Estrogen Receptor α-mediated Autophagy. *J. Adv. Res.* 28, 149–164. doi:10.1016/j.jare.2020.08.010

Meng, Q., Ma, M., Zhang, W., Bi, Y., Cheng, P., Yu, X., et al. (2021b). The Gut Microbiota during the Progression of Atherosclerosis in the Perimenopausal Period Shows Specific Compositional Changes and Significant Correlations with Circulating Lipid Metabolites. *Gut Microbes* 13, 1–27. doi:10.1080/19490976.2021.1880220

Meyer, M. R., Clegg, D. J., Prossnitz, E. R., and Barton, M. (2011). Obesity, Insulin Resistance and Diabetes: Sex Differences and Role of Oestrogen Receptors. *Acta Physiol. (Oxf).* 203, 259–269. doi:10.1111/j.1748-1716.2010.02237.x

Meyer, M. R., Fredette, N. C., Howard, T. A., Hu, C., Ramesh, C., Daniel, C., et al. (2014). G Protein-Coupled Estrogen Receptor Protects from Atherosclerosis. *Sci. Rep.* 4, 7564. doi:10.1038/srep07564

Poluzzi, E., Piccinni, C., Raschi, E., Rampa, A., Recanatini, M., and De Ponti, F. (2014). Phytoestrogens in Postmenopause: the State of the Art from a Chemical, Pharmacological and Regulatory Perspective. *Curr. Med. Chem.* 21, 417–436. doi:10.2174/09298673113206660297

Prossnitz, E. R., and Arterburn, J. B. (2015). International Union of Basic and Clinical Pharmacology. XCVII. G Protein-Coupled Estrogen Receptor and Its Pharmacologic Modulators. *Pharmacol. Rev.* 67, 505–540. doi:10.1124/pr.114.009712

Pyka-Fosciak, G., Jawien, J., Gajda, M., Jasek, E., and Litwin, J. A. (2013). Effect of Nebivolol Treatment on Atherosclerotic Plaque Components in apoE-Knockout Mice. *J. Physiol. Pharmacol.* 64, 745–750.

Reslan, O. M., Yin, Z., do Nascimento, G. R. A., and Khalil, R. A. (2013). Subtype-specific Estrogen Receptor-Mediated Vasodilator Activity in the Cephalic, Thoracic, and Abdominal Vasculature of Female Rat. *J. Cardiovasc. Pharmacol.* 62, 26–40. doi:10.1097/FJC.0b013e31828bc88a

Revankar, C. M., Cimino, D. F., Sklar, L. A., Arterburn, J. B., and Prossnitz, E. R. (2005). A Transmembrane Intracellular Estrogen Receptor Mediates Rapid Cell Signaling. *Science* 307, 1625–1630. doi:10.1126/science.1106943

Rexrode, K. (2018). Sex Differences in Sex Hormones, Carotid Atherosclerosis, and Stroke. *Circ. Res.* 122, 17–19. doi:10.1161/CIRCRESAHA.117.312336

Salvayre, R., Negre-Salvayre, A., and Camaré, C. (2016). Oxidative Theory of Atherosclerosis and Antioxidants. *Biochimie* 125, 281–296. doi:10.1016/j.biochi.2015.12.014

Schenck-Gustafsson, K., Brincat, M., Erel, C. T., Gambacciani, M., Lambrinoudaki, I., Moen, M. H., et al. (2011). EMAS Position Statement: Managing the Menopause in the Context of Coronary Heart Disease. *Maturitas* 68, 94–97. doi:10.1016/j.maturitas.2010.10.005

Solesio, M. E., Saez-Atienzar, S., Jordan, J., and Galindo, M. F. (2013). 3-Nitropropionic Acid Induces Autophagy by Forming Mitochondrial Permeability Transition Pores rather Than Activatiing the Mitochondrial Fission Pathway. *Br. J. Pharmacol.* 168, 63–75. doi:10.1111/j.1476-5381.2012.01994.x

Song, L., Kang, C., Sun, Y., Huang, W., Liu, W., and Qian, Z. (2016). Crocetin Inhibits Lipopolysaccharide-Induced Inflammatory Response in Human Umbilical Vein Endothelial Cells. *Cell Physiol. Biochem.* 40, 443–452. doi:10.1159/000452559

Suciu, C. F., Prete, M., Ruscitti, P., Favoino, E., Giacomelli, R., and Perosa, F. (2018). Oxidized Low Density Lipoproteins: The Bridge between Atherosclerosis and Autoimmunity. Possible Implications in Accelerated Atherosclerosis and for Immune Intervention in Autoimmune Rheumatic Disorders. *Autoimmun. Rev.* 17, 366–375. doi:10.1016/j.autrev.2017.11.028

Sun, B., Yang, D., Yin, Y.-z., and Xiao, J. (2020a). Estrogenic and Anti-inflammatory Effects of Pseudoprotodioscin in Atherosclerosis-Prone Mice: Insights into Endothelial Cells and Perivascular Adipose Tissues. *Eur. J. Pharmacol.* 869, 172887. doi:10.1016/j.ejphar.2019.172887

Sun, X., Wu, A., Kwan Law, B. Y., Liu, C., Zeng, W., Ling Qiu, A. C., et al. (2020b). The Active Components Derived from Penthorum Chinense Pursh Protect against Oxidative-Stress-Induced Vascular Injury via Autophagy Induction. *Free Radic. Biol. Med.* 146, 160–180. doi:10.1016/j.freeradbiomed.2019.10.417

Taylor, C. T., and Cummins, E. P. (2009). The Role of NF-κB in Hypoxia-Induced Gene Expression. *Ann. N. Y Acad. Sci.* 1177, 178–184. doi:10.1111/j.1749-6632.2009.05024.x

Wei, Y., Yuan, P., Zhang, Q., Fu, Y., Hou, Y., Gao, L., et al. (2020). Acacetin Improves Endothelial Dysfunction and Aortic Fibrosis in Insulin-Resistant SHR Rats by Estrogen Receptors. *Mol. Biol. Rep.* 47, 6899–6918. doi:10.1007/s11033-020-05746-3

Wu, H. M., Ni, X. X., Xu, Q. Y., Wang, Q., Li, X. Y., and Hua, J. (2020). Regulation of Lipid-induced Macrophage Polarization through Modulating Peroxisome Proliferator-activated Receptor-gamma Activity Affects Hepatic Lipid Metabolism via a Toll-like Receptor 4/NF-κB Signaling Pathway. *J. Gastroenterol. Hepatol.* 35, 1998–2008. doi:10.1111/jgh.15025

Yang, Q., Wang, C., Jin, Y., Ma, X., Xie, T., Wang, J., et al. (2019). Disocin Prevents Postmenopausal Atherosclerosis in Ovariectomized LDLR-/- Mice through a PGC-1α/ERα Pathway Leading to Promotion of Autophagy and Inhibition of Oxidative Stress, Inflammation and Apoptosis. *Pharmacol. Res.* 148, 104414. doi:10.1016/j.phrs.2019.104414

Zhang, W.-J., Hufnagl, P., Binder, B., and Wojta, J. (2003). Antiinflammatory Activity of Astragaloside IV Is Mediated by Inhibition of NF-κB Activation and Adhesion Molecule Expression. *Thromb. Haemost.* 90, 904–914. doi:10.1160/TH03-03-0136

Zhao, D., Guallar, E., Ouyang, P., Subramanya, V., Vaidya, D., Ndumele, C. E., et al. (2018). Endogenous Sex Hormones and Incident Cardiovascular Disease in Post-Menopausal Women. *J. Am. Coll. Cardiol.* 71, 2555–2566. doi:10.1016/j.jacc.2018.01.083

Zhao, Y., Zheng, H. X., Xu, Y., and Lin, N. (2017). Research Progress in Phytoestrogens of Traditional Chinese Medicine. *Zhongguo Zhong Yao Za Zhi* 42, 3474–3487. doi:10.19540/j.cnki.cjcmm.2017.0135

Zhu, Y., Xian, X., Wang, Z., Bi, Y., Chen, Q., Han, X., et al. (2018). Research Progress on the Relationship between Atherosclerosis and Inflammation. *Biomolecules* 8, 80. doi:10.3390/biom8030080

Conflict of Interest: The authors declare that the research was conducted in the absence of any commercial or financial relationships that could be construed as a potential conflict of interest.

Copyright © 2021 Huang, Wang, Zhu, Gong, Liang, Song, Zhang, Liu and Wei. This is an open-access article distributed under the terms of the Creative Commons Attribution License (CC BY). The use, distribution or reproduction in other forums is permitted, provided the original author(s) and the copyright owner(s) are credited and that the original publication in this journal is cited, in accordance with accepted academic practice. No use, distribution or reproduction is permitted which does not comply with these terms.

frontiers in Pharmacology

CORRECTION
published: 04 October 2021
doi: 10.3389/fphar.2021.774792

Corrigendum: Bazi Bushen Capsule Alleviates Post-Menopausal Atherosclerosis *via* GPER1-Dependent Anti-Inflammatory and Anti-Apoptotic Effects

Dan Huang[1,2†], Xindong Wang[1,2†], Yunhong Zhu[1,2], Juexiao Gong[1,2], Junqing Liang[3], Yanfei Song[3], Yiyan Zhang[1,2], Linsheng Liu[4] and Cong Wei[3]**

[1]Affiliated Hospital of Integrated Traditional Chinese and Western Medicine, Nanjing University of Chinese Medicine, Nanjing, China, [2]Jiangsu Province Academy of Traditional Chinese Medicine, Nanjing, China, [3]National Key Laboratory of Collateral Disease Research and Innovative Chinese Medicine, Shijiazhuang, China, [4]Department of Clinical Pharmacology, The First Affiliated Hospital of Soochow University, Suzhou, China

Keywords: atherosclerosis, bazi bushen capsule, lipid profile, inflammation, GPER1 antagonist, apoptosis

OPEN ACCESS

Edited and reviewed by:
Hongzhi Du,
Hubei University of Chinese Medicine, China

****Correspondence:***
Linsheng Liu
linsheng_liu@126.com
Cong Wei
weicong@yiling.cn

[†]These authors have contributed equally to this work

Specialty section:
This article was submitted to Ethnopharmacology, a section of the journal Frontiers in Pharmacology

Received: *13 September 2021*
Accepted: *17 September 2021*
Published: *04 October 2021*

Citation:
Huang D, Wang X, Zhu Y, Gong J, Liang J, Song Y, Zhang Y, Liu L and Wei C (2021) Corrigendum: Bazi Bushen Capsule Alleviates Post-Menopausal Atherosclerosis via GPER1-Dependent Anti-Inflammatory and Anti-Apoptotic Effects. Front. Pharmacol. 12:774792. doi: 10.3389/fphar.2021.774792

A Corrigendum on

Bazi Bushen Capsule Alleviates Post-Menopausal Atherosclerosis via GPER1-Dependent Anti-Inflammatory and Anti-Apoptotic Effects

by Huang, D., Wang, X., Zhu, Y., Gong, J., Liang, J., Song, Y., Zhang, Y., Liu, L., and Wei, C. (2021). Bazi Bushen Capsule Alleviates Post-Menopausal Atherosclerosis via GPER1-Dependent Anti-Inflammatory and Anti-Apoptotic Effects. Front. Pharmacol. 12:658,998. doi:10.3389/fphar.2021.658998

In the original article, there was a mistake in **Table 1** as published. BZBS is a post-marketing drug, and there is an error in the components of BZBS and ratio amounts in application (Li et al., 2021). The corrected **Table 1** appears below.

The authors apologize for this error and state that this does not change the scientific conclusions of the article in any way. The original article has been updated.

REFERENCE

Li, L., Chen, B., An, T., Zhang, H., Xia, B., Li, R., et al. (2021). BaZiBuShen Alleviates Altered Testicular Morphology and Spermatogenesis and Modulates Sirt6/P53 and Sirt6/NF-Kb Pathways in Aging Mice Induced by D-Galactose and NaNO2. *J. Ethnopharmacol* 271, 113810. doi:10.1016/j.jep.2021.113810

Publisher's Note: All claims expressed in this article are solely those of the authors and do not necessarily represent those of their affiliated organizations, or those of the publisher, the editors and the reviewers. Any product that may be evaluated in this article, or claim that may be made by its manufacturer, is not guaranteed or endorsed by the publisher.

Copyright © 2021 Huang, Wang, Zhu, Gong, Liang, Song, Zhang, Liu and Wei. This is an open-access article distributed under the terms of the Creative Commons Attribution License (CC BY). The use, distribution or reproduction in other forums is permitted, provided the original author(s) and the copyright owner(s) are credited and that the original publication in this journal is cited, in accordance with accepted academic practice. No use, distribution or reproduction is permitted which does not comply with these terms.

TABLE 1 | The ratio of the plants present in the preparation of BZBS.

Plants	Amount in application (ratio)
Cuscuta chinensis Lam. [Convolvulaceae; Cuscutae semen]	250
Lycium barbarum L. [Solanaceae; Lycii cortex]	138
Schisandra chinensis (Turcz.) Baill. [Schisandraceae; Schisandrae chinensis fructus]	46
Cnidium monnieri (L.) Cusson [Apiaceae; Cnidii fructus]	35
Rosa laevigata Michx. [Rosaceae; Rosae laevigatae fructus]	35
Rubus chingii Hu [Rosaceae; Rubi fructus]	35
Allium tuberosum Rottler ex Spreng. [Amaryllidaceae; Allii tuberosi semen]	35
Toosendan fructus [Meliaceae; Fuctus Toosendan]	23
Epimedium brevicornu Maxim. [Berberidaceae; Epimedii folium]	70
Morindae officinalis radix [Rubiaceae; Radix Morindae Offcinalis]	35
Cistanche deserticola Ma [Orobanchaceae; Cistanches herba]	35
Rehmannia root [Orobanchaceae; Radix Rehmanniae Recens]	46
Cyathula officinalis K.C.Kuan [Amaranthaceae; Cyathulae radix]	35
Panax ginseng C.A.Mey. [Araliaceae; Ginseng radix et rhizoma]	25
Cervus nippon Temminck [Cervidae; Cervi Cornu Pantotrichum]	16
Hippocampus Kelloggi [Syngnathidae; Hippocampus]	21

frontiers in Pharmacology

ORIGINAL RESEARCH
published: 26 August 2021
doi: 10.3389/fphar.2021.670707

Tomatidine Suppresses the Destructive Behaviors of Fibroblast-Like Synoviocytes and Ameliorates Type II Collagen-Induced Arthritis in Rats

Xiaolu Yu, Junnan Zhou, Fuli Zhao, Xuan Liu, Yuhang Mao, Li Diao, Chuanjun Wen and Mei Liu**

Jiangsu Key Laboratory for Molecular and Medical Biotechnology, College of Life Sciences, Nanjing Normal University, Nanjing, China

OPEN ACCESS

Edited by:
Zhaocheng Ma, Huazhong Agricultural University, China

Reviewed by:
Zhongshi Zhou, Hubei University of Chinese Medicine, China
Xian-Tao Zeng, Zhongnan Hospital, Wuhan University, China

***Correspondence:**
Chuanjun Wen
wenchuanjun@hotmail.com
Mei Liu
meiliunj@163.com

Specialty section:
This article was submitted to Ethnopharmacology, a section of the journal Frontiers in Pharmacology

Received: 22 February 2021
Accepted: 12 August 2021
Published: 26 August 2021

Citation:
Yu X, Zhou J, Zhao F, Liu X, Mao Y, Diao L, Wen C and Liu M (2021) Tomatidine Suppresses the Destructive Behaviors of Fibroblast-Like Synoviocytes and Ameliorates Type II Collagen-Induced Arthritis in Rats. Front. Pharmacol. 12:670707. doi: 10.3389/fphar.2021.670707

Fibroblast-like synoviocytes (FLSs) are the prominent non-immune cells in synovium and play a pivotal role in rheumatoid arthritis (RA) pathogenesis. Searching for natural compounds that may suppress the pathological phenotypes of FLSs is important for the development of RA treatment. Tomatidine (Td), a steroidal alkaloid derived from the solanaceae family, has been reported to have anti-inflammatory, anti-tumor and immunomodulatory effects. However, its effect on RA remains unknown. Here, we examined the inhibitory effect of Td on TNFα-induced arthritic FLSs, and subsequently investigated its therapeutic effect on collagen-induced arthritis (CIA) rats. Our results revealed that Td significantly inhibited TNFα-induced proliferation and migration of arthritic FLSs. In addition, we found that Td treatment could efficaciously ameliorate synovial inflammation and joint destruction of rats with CIA. Both *in vitro* and *in vivo* studies showed that Td significantly suppressed the production of pro-inflammatory cytokines including IL-1β, IL-6 and TNFα, and downregulated the expression of MMP-9 and RANKL. Further molecular mechanism studies revealed that the inhibitory effect of Td on RA might attribute to the decreased activations of MAPKs (ERK and JNK) and NF-κB. These findings provide evidence that Td has the potential to be developed into a complementary or alternative agent for RA therapy.

Keywords: tomatidine, rheumatoid arthritis, fibroblast-like synoviocytes, collagen-induced arthritis, MAPK, NF-κB

INTRODUCTION

Rheumatoid arthritis (RA) is a chronic autoimmune inflammatory disorder characterized byinflammation of the synovium and destruction of bone tissue (Ath and Denton, 1991; Athanasou, 1996; Danks et al., 2002). Although RA pathogenesis remains incompletely understood, many cell types such as fibroblast-like synoviocytes (FLSs), macrophages, osteoclasts and lymphocytes have been demonstrated to be involved (Gravallese, 2002; Ma and Pope, 2005; Skapenko et al., 2005). As

Abbreviations: Td, tomatidine; RA, rheumatoid arthritis; TNFα, tumor necrosis factor alpha; FLSs, fibroblast-like synoviocytes; CIA, collagen-induced arthritis; IL-1β, Interleukin-1β; IL-6, Interleukin-6; RANKL, receptor activator of nuclear factor κB ligand; MMP-9, matrix metallopeptidase nine; MAPK, mitogen-activated protein kinase; ERK, extracellular signal-regulated kinase; JNK, c-Jun N-terminal kinases; NF-κB, nuclear factor of kappaB.

the important effector cells in this disease, FLSs exhibit tumor-like characteristics such as overproliferation, aggressive migration and invasion, and apoptosis-resistance (Neidhart et al., 2003; Mor et al., 2005; Noss and Brenner, 2008; Bartok and Firestein, 2010; Lahoti et al., 2014). These over-activated FLSs can produce multiple pro-inflammatory cytokines which promote the formation of pannus and the destruction of cartilage and bone (Firestein, 2003). In addition, the pathogenic properties of FLSs have been demonstrated to tightly correlate with histological and radiographic damage in RA animal models and patients (Lange et al., 2005; Laragione et al., 2008). Therefore, FLS-targeted therapy represents an attractive complementary approach to immune-directed therapies in RA.

Many current drugs used for RA therapy have relatively limited effectiveness and unwanted side effects. Therefore, botanical medicines as alternative remedies have become increasingly popular as they are believed to be safe, efficacious and have over a thousand years' history in treating patients. Furthermore, analysis of patents on anti-RA therapies issued in China revealed that traditional Chinese Medicine may provide substantial new information for anti-RA drug development (Yuan et al., 2015). Tomatidine (Td) is a natural steroidal alkaloid that isolated from the Solanaceae plants such as tomatoes, potatoes and eggplants (Lange et al., 2005; Laragione et al., 2008). Steroidal alkaloids are known to be essentially nitrogen analogues of steroid saponins such as diosgenin, which is a precursor of steroidal hormones and anti-inflammatory steroids. Nowadays, Td has received increasing attention for its confirmed pharmacological safety and a variety of biologic activities, including cardioprotective, antioxidative, anti-inflammatory, anticancer, anti-osteoporosis, and immuno-regulatory effects, as well as its ability to inhibit muscle atrophy (Chiu and Lin, 2008; Friedman et al., 2009; Lee et al., 2011; Shieh et al., 2011; Yan et al., 2013; Hu et al., 2019; Jeon and Kim, 2019). For example, Chiu and Lin found that Td effectively inhibited the expressions of COX2 and iNOS by suppressing NF-κB and JNK pathways in LPS-stimulated mouse macrophage cells (Chiu and Lin, 2008). Meanwhile, Td was demonstrated to regulate the function of the immune system through stimulating potent antigen-specific humoral and cellular immune responses (Lee et al., 2004). In addition, Td could effectively inhibit the proliferation and invasion of tumor cells, and promote the cell apoptosis (Friedman et al., 2009; Lee et al., 2011; Shieh et al., 2011). More importantly, Hu et al. found that Td suppressed osteoclast formation and mitigated estrogen deficiency-induced bone mass loss (Hu et al., 2019). Given the reported pharmacological functions of Td and the clinical and pathological features of RA, we hypothesized that Td might represent a novel treatment for RA. Thus, we here investigated the therapeutic effect of Td on cultured arthritic FLSs and type II collagen-induced arthritis (CIA) in rats, and subsequently explored their underlying mechanisms.

MATERIALS AND METHODS

Reagents

Td ($C_{27}H_{45}NO_2$, purity ≥ 98%) was obtained from MedchemExpress (Shanghai, China). Lyophilized native chicken type II collagen (CII) was purchased from Chengdu Herbpurify Co., Ltd. (Chengdu, Sichuan, China). Methotrexate (MTX) was from Shanghai Sine Pharmaceutical Co., Ltd. (Shanghai, China). Commercial kits for measurement of alanine aminotransferase (ALT) and aspartate aminotransferase (AST) were from Jiancheng Institute of Biotechnology (Nanjing, Jiangsu, China). IL-1β, IL-6 and TNFα ELISA kits were purchased from SenBeiJia Biological Technology Co., Ltd. (Nanjing, Jiangsu, China). Dulbecco's modified Eagle's medium (DMEM) was purchased from Gibco (Gibco BRL, Grand Island, NY, United States). Fetal bovine serum (FBS) was purchased from Invigentech (Sydney, Australia). Recombinant tumor necrosis factor alpha (TNFα) was purchased from Peprotech (PeproTech, Rocky Hill, NJ, United States). MTS reagents, Triton-X 100, DAPI solution and Freund's complete adjuvant (CFA) were purchased from Sigma-Aldrich (St Louis, MO, United States). 5-Ethynyl-2′-deoxyuridine (EdU) was obtained from Guangzhou RiBo Bio Co., Ltd. (Guangzhou, Guangdong, China). Annexin V-FITC apoptosis detection kit was from KeyGEN Biotech Co., Ltd. (Nanjing, Jiangsu, China). TRIzol reagent was from Invitrogen Life Technologies (Carlsbad, CA, United States). Primary antibodies targeting phosphorylated extracellular signal-regulated kinase 1/2 (p-ERK1/2), phosphorylated c-Jun N-terminal kinases (p-JNK), phosphorylated p38 (p-p38), phosphorylated inhibitor of NF-κB (p-IκBα), total ERK, total JNK, total p38, IκBα, p65, MMP-2, MMP-9 and glyceraldehyde-3-phosphate dehydrogenase (GAPDH) were purchased from CST (Cell Signaling Technology, Inc., Beverly, MA, United States). Anti-RANKL antibody was obtained from Proteintech (Proteintech Group, Inc., Chicago, United States).

Isolation and Culture of Arthritic Fibroblast-Like Synoviocytes

Arthritic FLS cells were isolated and cultured as previously reported (Liu Z. et al., 2018). Briefly, the synovial tissues were dissected from the knees of the vehicle-treated CIA rats, minced and incubated with 0.25% trypsase and 0.4% collagenase. Arthritic FLS cells were collected and cultured in DMEM supplemented with 10% FBS, 100 $U{\cdot}mL^{-1}$ penicillin and 100 $\mu g{\cdot}mL^{-1}$ streptomycin at 37°C in 5% CO_2. Cells from passages three to nine were used for all *in vitro* experiments.

Cell Viability Assay

Arthritic FLS cells were seeded into 96-well plates and cultured for 48 h with complete DMEM containing varying concentrations of Td (0, 2.5, 5, 10, 20, 40, 80 μM). MTS/PMS mixture was added and cells were incubated for another 4 h. The absorbance at 490 nm was measured using a microplate reader (Model 680, BioRAD, Hercules, CA, United States). The effect of Td on cell viability was expressed as percent cell viability with vehicle treated control cells set at 100%. GraphPad Prism (version 5.0c; San Diego, CA) was used to calculate the half maximal inhibitory concentration (IC_{50}).

Ethynyl-2′-deoxyuridine Incorporation Assay

Arthritic FLS cells were incubated with Td (5 μM) for 6 h and then stimulated with or without TNFα (50 ng·mL^{-1}) for 24 h. EdU (10 μM) was added to measure the newly synthesized DNA and Hoechst 33342 was used to counterstain cell nuclei. The cell proliferation rate was calculated as the proportion of nucleated cells incorporating EdU in five high-power fields per well.

Wound-Healing Assay

Wound-healing assay was carried out as our previous descriptions (Liu et al., 2018b; Qiu et al., 2018). In brief, arthritic FLSs were seeded into 12-well plates and cultured to 80% confluency. A linear scratch was created using a sterile 200 ul pipette tip. After washing the suspended cell debris with PBS, arthritic FLSs were treated with different concentrations of Td (0, 2.5, 5 and 10 μM) for 1 h and then stimulated with TNFα (50 ng·mL^{-1}) for 24 h. The cell migration area was measured by comparing the remaining cell-free area in the identical fields using Image J software (National Institutes of Health, Bethesda, MD, United States).

Apoptosis Assay

Arthritic FLS cells were seeded into 6-well plates and incubated with varying concentrations of Td (0, 2.5, 5 and 10 μM) for 24 h. Cells were then harvested for staining with annexin V and propidium iodide (PI) solution. The cells were detected by a flow cytometer (Beckman Coulter, CA, United States) and the apoptotic cell percentage was analyzed using Cell Quest Software (FACScan; Becton Dickinson, Franklin Lakes, NJ, United States).

Cytokine and MMP Analysis in Cultured Arthritic Fibroblast-Like Synoviocytes

Arthritic FLS cells were incubated with varying concentrations of Td (0, 2.5, 5 and 10 μM) for 1 h and then stimulated with TNFα (50 ng·mL^{-1}) for 24 h. The cells were harvested for real-time polymerase chain reaction (PCR) assay or Western blot analysis. The culture supernatants were collected for ELISA assay.

For real-time PCR assay, the total RNA was extracted using TRIzol reagent and subjected to cDNA synthesis according to the manufacturer's instructions. Real-time PCR was performed using a SYBR Green PCR Kit (Vazyme Biotech) and run in Mastercycler ep realplex two systems (Eppendorf, Hamburg, Germany). The primer pairs for *IL-1β*, *IL-6*, *TNFα*, *MMP-2*, *MMP-9*, *RANKL* and *β-actin* were used as the previous descriptions (Ueland et al., 2005; Liu et al., 2018b). The expression of each target gene was normalized to the transcription level of *β-actin* gene.

For Western blot assay, the cells were lysed and the protein levels of MMP-2, MMP-9 and RANKL were examined by Western blot as described below.

For ELISA assay, the culture supernatants were centrifuged at 2000 rpm for 20 min to remove the particulate matter. The pro-inflammatory cytokines IL-1β, IL-6 and TNFα were determined using cytokine-specific ELISA kits according to the manufacturer's instructions.

Collagen-Induced Arthritis

A total of 30 female Wistar rats (170–180 g, about 6–8 weeks) were purchased from Beijing Vital River Laboratory Animal Technology Co., Ltd. (Beijing, China). All of the rats were housed under specific pathogen-free (SPF) conditions (22°C, 12 h/12 h light/dark, 50–55% humidity) and given free access to food and water. All the animal experiments were approved by the Experimental Committee of Nanjing Normal University (#2020065, approved date July 15, 2020).

The CIA model was induced as previously described (Liu et al., 2018a; Liu et al., 2018b; Qiu et al., 2018). Briefly, the rats were intradermally injected with 1 mg native chicken CII emulsified in Freund's complete adjuvant. Seven days later, the rats were subcutaneously boosted with half the amount of CII emulsified in Freund's incomplete adjuvant. The normal control rats were immunized with saline (n = 6). All the immunized rats developed CIA (clinical score ≥2) after a mean (±SD) interval of 14 ± 1 days. Rats with CIA were randomly divided into four groups as two Td-treated groups, MTX-treated group and vehicle-treated group (n = 6 per group). The MTX-treated group was administrated with MTX (3 mg·kg^{-1} body weight) every 3 days (according to clinical usage). The Td-treated groups were intraperitoneally injected with different doses of Td (5 and 15 mg·kg^{-1} body weight, respectively) and the vehicle-treated group was injected with 0.9% saline every day for a 14-day period. The doses of Td were determined according to the previous reports (Fujiwara et al., 2012; Dyle et al., 2014; Hu et al., 2019) with modification from our preliminary experiments. Clinical arthritic scores were evaluated using a scoring system of 0–4 for each limb: 0 = no swelling; 1 = swelling and/or redness of one to two interphalangeal joints; 2 = involvement of three to four interphalangeal joints or one larger joint; 3 = more than four joints red/swollen; 4 = severe arthritis of an entire paw. The reported arthritis score for each rat was the sum of the two hind paws. The volumes of the hind paws were measured using a volume displacement plethysmometer (YLS-7A, Facility Station of Shandong Academy of Medical Science, Shandong, China). Arthritis scoring and paw volume measurements were performed by two independent observers in a blinded manner. After a 14-days treatment, serum was collected for measurement of pro-inflammatory cytokines, ALT and AST. Joint tissues were harvested for radiographic and histopathological evaluation, cytokine and MMP analysis, and signaling pathway detection. In addition, we weighed the main organs including heart, liver, kidney, spleen and thymus, and calculated the organ coefficients, as our previous report (Liu et al., 2013). Also, the change in body weight of each individual CIA rat was calculated as the following formula: change in body weight = [(body weight of day 14 arthritis/body weight of day 1 arthritis)−1] *100%.

Radiographic Evaluation

The left hind paws were separated, fixed and exposed under X-ray (MX-20; Faxitron X-ray Corporation, Wheeling, IL, United States). Bone destruction was evaluated using a scoring system of 0–3, as the previous report (Cai et al., 2007). The radiological evaluation was carried out by two independent observers in a blinded manner.

Histopathological Assessment

After X-ray examination, the left ankle joints were decalcified in 12% ethylenediaminetetraacetic acid (EDTA) and then embedded in paraffin. Sections with a thickness of 4 μm were stained with haematoxylin and eosin (H&E). Pathological changes in inflammation, pannus formation, synovial hyperplasia, cartilage destruction and bone erosion were scored using a semi-quantitative scale, as our previous descriptions (Liu et al., 2018a; Liu et al., 2018b; Qiu et al., 2018). Histopathological analysis was recorded by two independent observers in a blinded manner.

Cytokine and MMP Analysis in Collagen-Induced Arthritis Rats

Serum was collected by centrifugation (5000 rpm for 15 min) and stored at −80°C until analysis. The levels of IL-1β, IL-6 and TNFα were measured using ELISA kits according to the standard method. In addition, serum ALT and AST were detected using commercial kits following the protocol of manufacturer's instructions.

The right hind paws of rats were removed and homogenized, as our previous report (Liu et al., 2018a; Liu et al., 2018b; Qiu et al., 2018). The homogenates were used to detect the protein levels of IL-1β, IL-6, TNFα and MMP-9, RANKL by ELISA and Western blot, respectively. In addition, the phosphorylation changes of MAPKs (ERK, JNK and p38) and the protein level of IκBα were examined by Western blot.

Western Blot Analysis

Arthritic cells or joint tissues were homogenized in radioimmunoprecipitation assay buffer and the supernatants containing proteins were collected by centrifugation. Protein was separated by sodium dodecyl sulphate–polyacrylamide gelelectrophoresis (SDS-PAGE) and then transferred to nitrocellulose membranes. The membranes were incubated with various kinds of primary antibodies including p-JNK, JNK, p-ERK, ERK, p-p38, p38, p-IκBα, IκBα, MMP-2, MMP-9, RANKL and GAPDH. The immunoreactivity was visualized using enhanced chemiluminescence reagents (Labgic Technology) according to the manufacturer's instructions. Three independent experiments were performed and the intensity of each band was analyzed using ImageJ software.

Confocal Microscopy for NF-κB Localization

Arthritic FLS cells were seeded on sterile cover slips in a 24-well plate and cultured overnight at 37°C. Following serum starvation, the cells were treated with Td (10 μM) for 4 h, and then stimulated with TNFα (50 ng·mL^{-1}) for 30 min. After washing with PBS, the cells were fixed by methanol and permeabilized by 0.5% Triton-X 100. The arthritic FLS cells were blocked with 10% goat serum and then incubated with NF-κB p65 antibody. DAPI solution were used to stain cell nuclear. The nuclear translocation of p65 was imaged using a Nikon A1R resonance scanning confocal microscope with spectral detector (Nikon, Tokyo, Japan).

Statistical Analysis

All data were expressed as the mean ± SD of results obtained from three or more experiments. Multiple comparisons were performed using one-way analysis of variance (ANOVA), followed by Tukey's p*ost hoc* analysis. Comparisons between two groups were made using Student's *t*-test. $P < 0.05$ was considered statistically significant.

RESULTS

Tomatidine Suppressed TNFα-Induced Proliferation and Migration of Arthritic FLSs

Arthritic FLSs are the main effector cells of RA. Inhibiting the over-activated properties of FLSs has become a potential approach to RA therapies. In this study, we firstly used an MTS assay to quantify the potential cytotoxicity of Td on FLSs. As shown in **Figure 1B**, up to 20 μM for 2 days treatment, arthritic FLSs did not show a significant decline in cell viability. And the calculated IC_{50} was 34.31 μM (**Figure 1C**). In the subsequent *in vitro* experiments, concentrations of Td used did not exceed 10 μM. We here investigated the effects of Td on TNFα-induced proliferation, migration and apoptosis in arthritic FLSs. The EdU assay showed that TNFα stimulation could dramatically enhance FLS's proliferative potential, however, this enhancement was significantly suppressed by 5 μM Td (**Figures 1D,E**). The wound healing assay demonstrated that Td at doses of 2.5–10 μM could significantly and dose-dependently inhibit the migration rate of arthritic FLSs (**Figures 1F,G**). Since Td was able to induce apoptosis in several tumor cells (Song et al., 2018), we analyzed the apoptosis-inducing effect of Td on arthritic FLSs. As shown in **Figure 1H**, the given doses of Td had little effect on the apoptotic rate of arthritic FLSs, suggesting that the suppression of Td on proliferation and migration was not due to its apoptosis-inducing action.

Tomatidine Decreased the Production of Cytokines and MMP-9 in TNFα-Stimulated Arthritic FLSs

It is well known that RA is an immune-driven inflammation disease and manifests as cartilage and bone erosion occurs the later stage of the disease. Efforts should be made to inhibit the expressions of pro-inflammatory cytokines as well as genes involved cartilage and bone destruction in RA treatment. Our studies revealed that TNFα stimulation could dramatically upregulate the mRNA levels of pro-inflammatory cytokines including *IL-1β*, *IL-6* and *TNFα*. However, these upregulations were significantly inhibited by Td treatment (**Figure 2A**). Consistent with the real-time PCR data, ELISA assay showed that the protein levels of IL-1β, IL-6 and TNFα were also decreased by Td (**Figure 2B**), which further confirmed the anti-inflammatory action of Td. Rheumatoid FLSs contribute to the degradation of connective tissue by secreting substantial amounts of MMPs, which results in the breakdown of cartilage destruction. In this study, the data of real-time PCR and Western blot both demonstrated that Td had

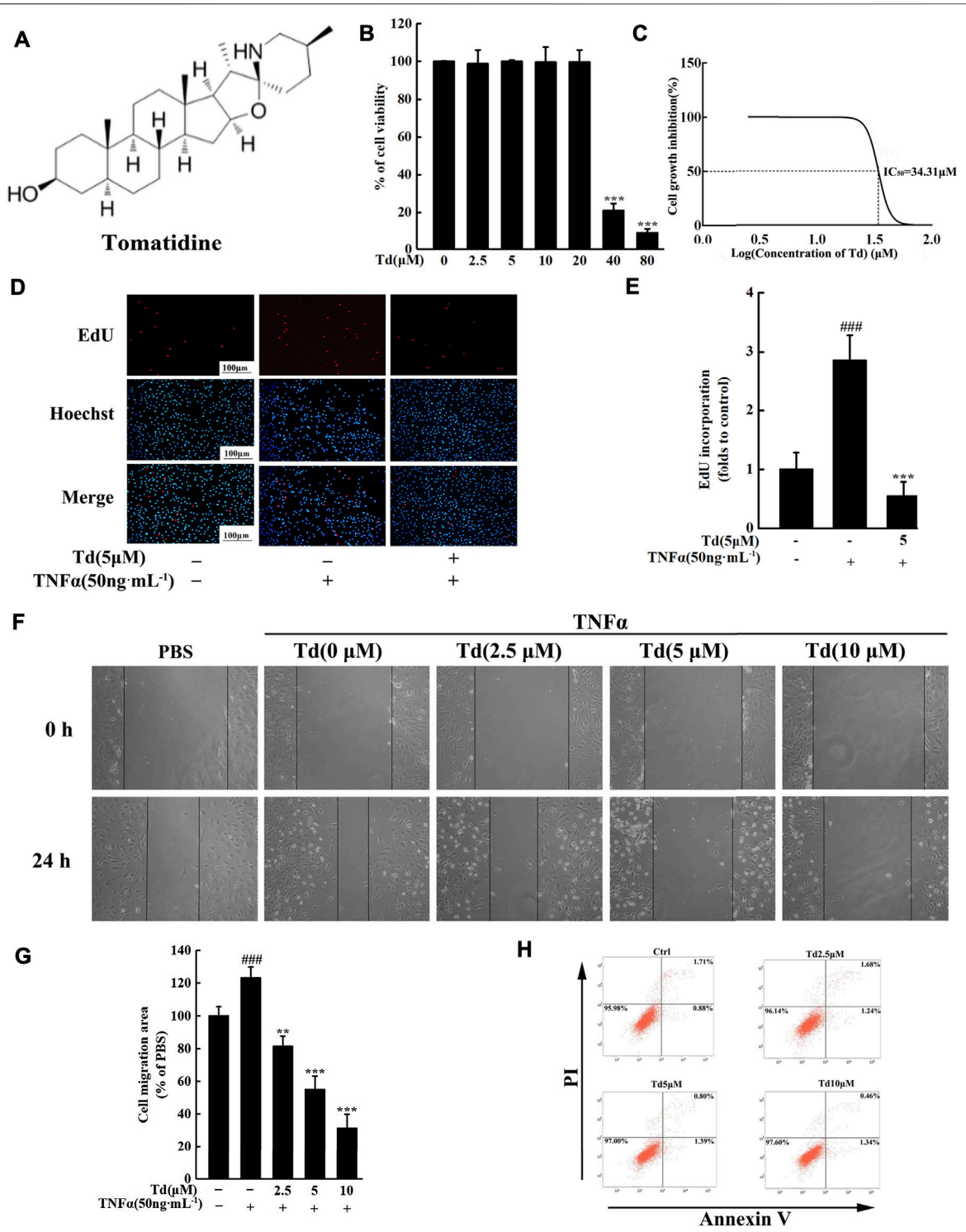


FIGURE 1 | Td attenuated TNFα-induced proliferation and migration of arthritic FLS *in vitro*. **(A)** The chemical structure of Td. **(B,C)** The viability of Td-treated arthritic FLSs was quantified using an MTS assay and the IC_{50} was calculated. **(D,E)** The EdU assay showed that Td (5 μM) significantly inhibited TNFα-induced proliferation of arthritic FLSs. $^{###}P < 0.001$ versus TNFα-untreated, Td-untreated cells; $^{***}P < 0.001$ versus TNFα-treated, Td-untreated cells. **(F,G)** Td dose-dependently reduced TNFα-induced migration of arthritic FLSs. Serum-starved cells were treated with various doses of Td (0, 2.5, 5 and 10 μM) for 1 h and then incubated with TNFα (50 ng·mL^{-1}) for 24 h. The cell migration rate was measured by a wound-healing assay. $^{###}P < 0.001$ versus TNFα-untreated, Td-untreated cells; $^{**}P < 0.01$ and $^{***}P < 0.001$ versus TNFα-treated, Td-untreated cells. **(H)** After treating with varying doses of Td (0, 2.5, 5, and 10 μM) for 24 h, the arthritic FLSs were stained with Annexin V-FITC and propidium iodide (PI). Flow cytometry was used to detect the percentage of apoptosis cells within each population.

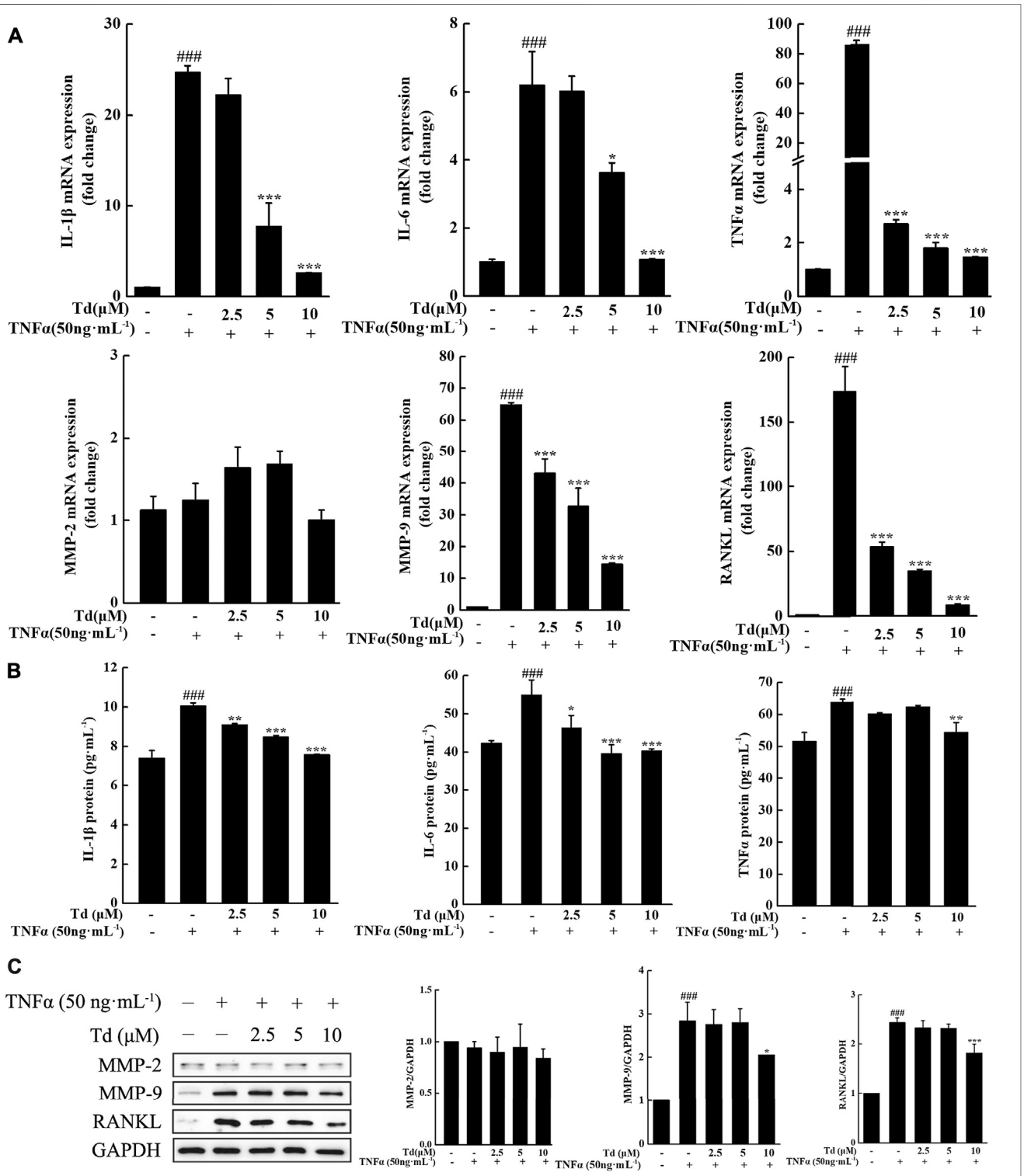


FIGURE 2 | Td decreased the production of proinflammatory cytokines, RANKL and MMP-9 in TNFα-induced arthritic FLSs. Arthritic FLSs were treated with various doses of Td (0, 2.5, 5 and 10 μM) for 1 h and then incubated with TNFα (50 ng·mL^{-1}) for 24 h. The cells were harvested for real-time polymerase chain reaction (PCR) assay or Western blot analysis. The culture supernatants were collected for ELISA assay. **(A)** The total RNA was extracted and real-time PCR was performed to measure the transcripts of *IL-1β*, *IL-6*, *TNFα*, *MMP-2*, *MMP-9* and *RANKL*. The mRNA levels of these genes were normalized to *β-actin* and represented as fold change over the TNFα-untreated, Td-untreated cells. $n = 3$, $^{###}P < 0.001$ versus TNFα-untreated, Td-untreated cells; $^{*}P < 0.05$ and $^{***}P < 0.001$ versus TNFα-treated, Td-untreated cells. **(B)** The culture supernatants were collected and ELISA was performed to detect the protein levels of IL-1β, IL-6, TNFα. $n = 3$, $^{###}P < 0.001$ versus TNFα-untreated, Td-untreated cells; $^{*}P < 0.05$, $^{**}P < 0.01$ and $^{***}P < 0.001$ versus TNFα-treated, Td-untreated cells. **(C)** Western blot was performed to examine the protein expressions of MMP-2, MMP-9 and RANKL. Relative expression was determined by densitometric analysis using ImageJ software. $n = 3$, $^{###}P < 0.001$ versus TNFα-untreated, Td-untreated cells; $^{*}P < 0.05$ and $^{***}P < 0.001$ versus TNFα-treated, Td-untreated cells.

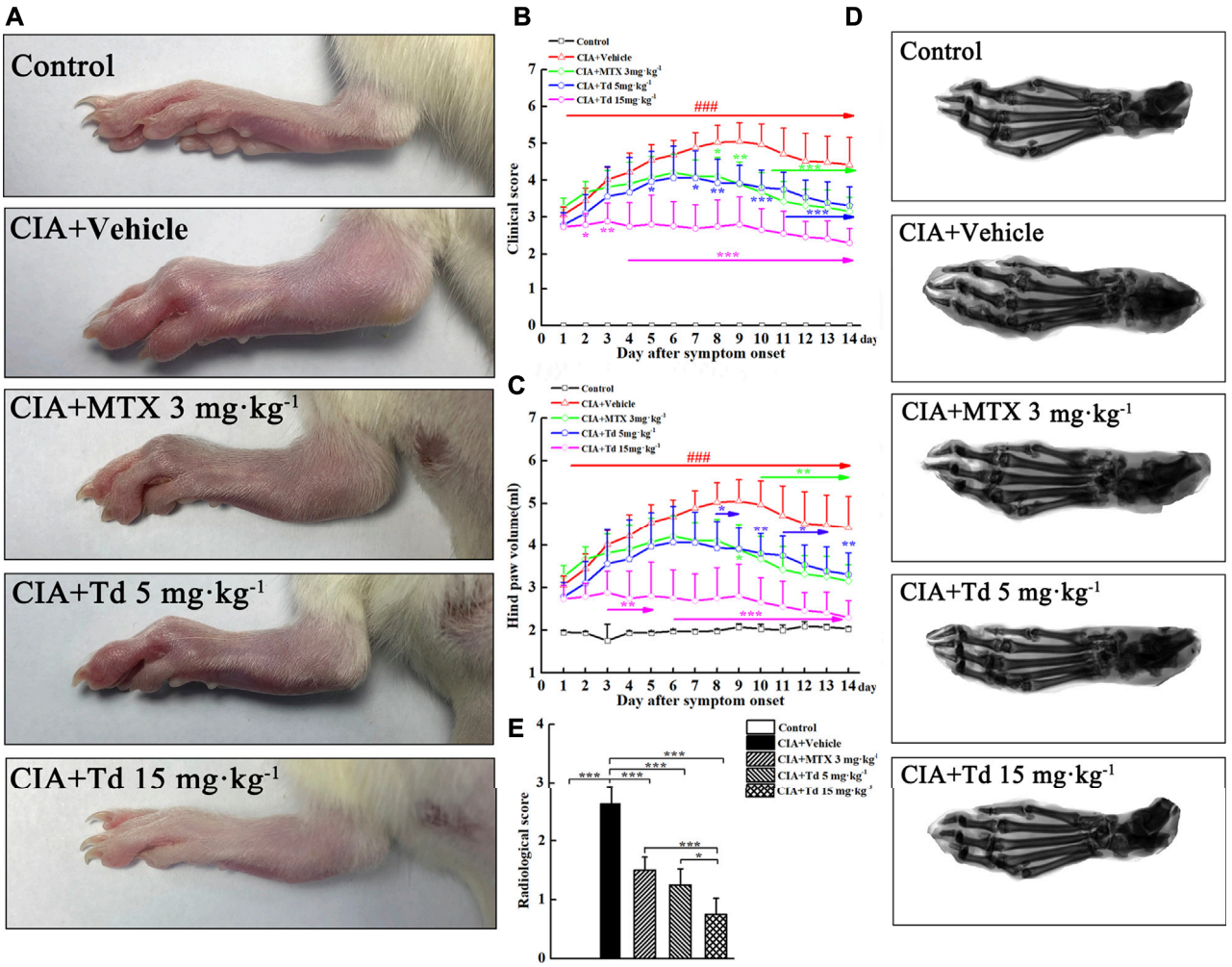


FIGURE 3 | Td significantly suppressed synovial inflammation and bone destruction in CIA rats. **(A)** Representative photographs of the hind paws of CIA rats obtained from different groups. Clinical score **(B)** and hind paw volume **(C)** were inhibited by Td or MTX. $n = 6$, $^{###}P < 0.001$ versus the normal control rats; $^{*}P < 0.05$, $^{**}P < 0.01$ and $^{***}P < 0.001$ versus the vehicle-treated CIA rats. **(D)** Representative radiographs of the hind paws of CIA rats obtained from different groups. **(E)** Radiological scores were calculated as described in Materials and Methods section. $n = 6$, $^{*}P < 0.05$ and $^{***}P < 0.001$.

no obvious effect on the expression of MMP-2 but distinctively inhibited MMP-9 production (**Figures 2A,C**). RANKL has been regarded as the strongest inducer in osteoclast differentiation and activity (Yasuda et al., 1998; Kobayashi et al., 2000; Liu et al., 2018a). In our study, RANKL was significantly suppressed by Td at both the mRNA and protein levels (**Figures 2A,C**), indicating that Td might play an important protective role in bone destruction.

Tomatidine Attenuated the Severity of Arthritis in CIA Rats

To assess the anti-arthritic effect of Td, a CIA model in Wistar rats was used. When the CIA model was firmly established (clinical score ≥2), Td with different doses or vehicle was intraperitoneally administrated once a day and continued for 14 days. As shown in **Figure 3A**, arthritis symptoms such as swelling and erythema were obviously observed in the vehicle-treated CIA rats, while Td or MTX treatment significantly attenuated the severity of the disease. Compared to MTX or 5 mg·kg^{-1} of Td which significantly suppressed the development of CIA, 15 mg·kg^{-1} of Td showed a stronger protective action as assessed by clinical score and paw swelling (**Figures 3B,C**).

Tomatidine Suppressed Synovial Inflammation and Bone Destruction in CIA Rats

To further confirm the therapeutic effect of Td, radiographic and histopathological assessments were performed on the rat hind paws. The X-ray images showed that the typical RA changes, such as joint destruction and joint space narrowing, appeared in the vehicle-treated CIA rats without exception (**Figure 3D**). However, these destructions were significantly improved in

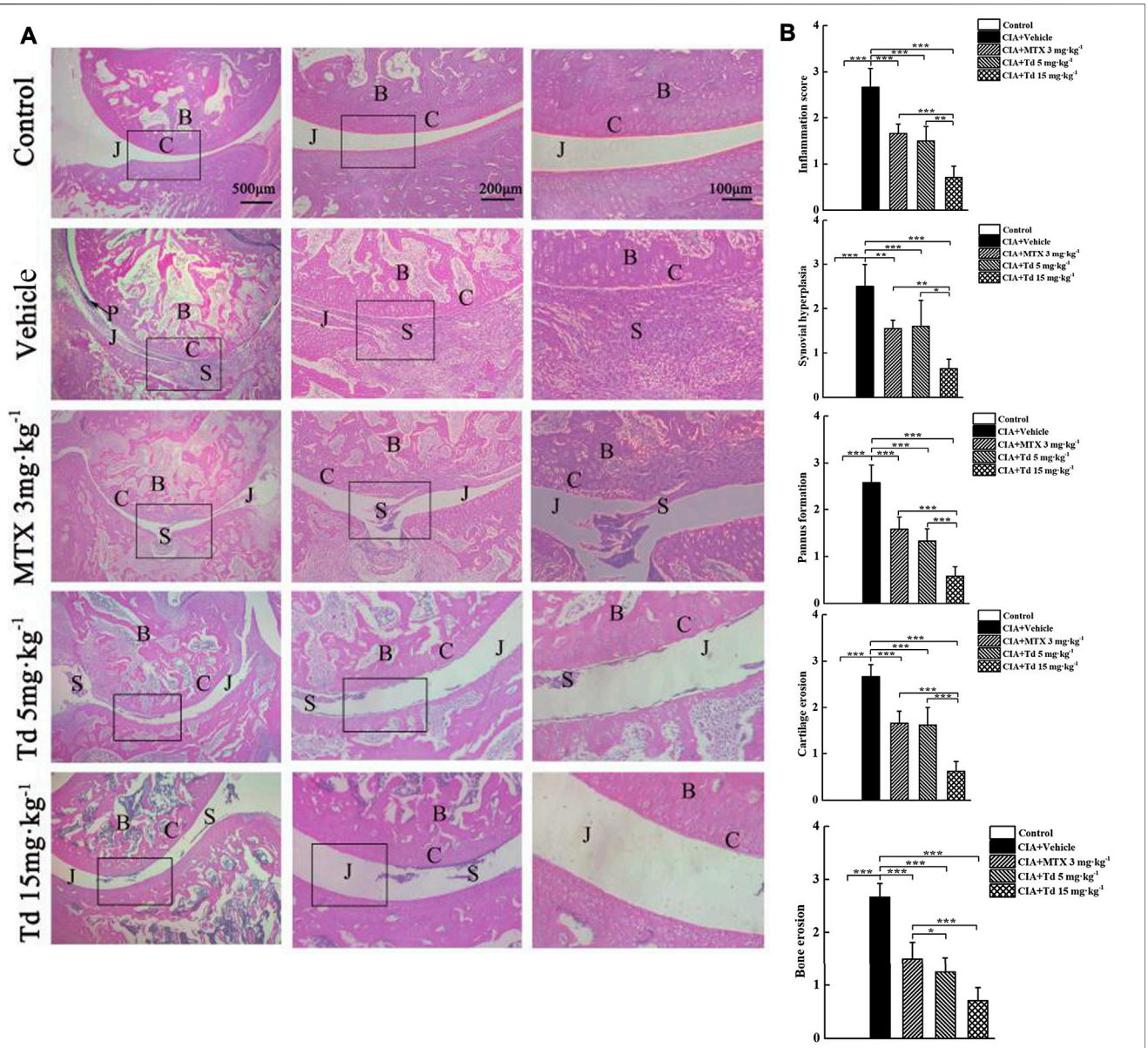


FIGURE 4 | Effects of Td on histologic changes in CIA rats. **(A)** Representative H&E images of ankle joints obtained from different groups. **(B)** Histological scores were calculated as described in Materials and Methods section. $n = 6$, $^{*}P < 0.05$, $^{**}P < 0.01$ and $^{***}P < 0.001$. B, bone; C, cartilage; J, joint space; P, pannus; S, synovium.

MTX- or Td-treated groups. Furthermore, this improvement was more obvious in the high-dose Td group (**Figure 3E**). In line with the data of radiographic scoring and the clinical scoring, H&E staining and histopathological assessment showed that Td significantly attenuated the pathological characteristics of CIA rats including inflammatory cell infiltration, synovial hyperplasia, pannus formation, cartilage erosion, and bone erosion, which further demonstrated the inhibitory effect of Td on RA (**Figures 4A,B**).

To evaluate the potential adverse effect of Td on CIA rats, a preliminary study was carried out to analyze the weight loss, organ indexes and serum markers of liver injury (ALT and AST). As shown in **Table 1**, compared to the normal control, the vehicle-treated CIA rats showed a significant weight loss. However, this weight loss was significantly suppressed by Td treatment. Except that the kidney index was decreased by Td, the other organ indexes as well as serum ALT and AST have no significant differences between the Td-treated groups and the vehicle-treated CIA group, further supporting that the given doses of Td used in this study had no significant side effects.

Tomatidine Decreased Synthesis of Cytokines and MMP-9 in CIA Rats

We have demonstrated that, in primary arthritic FLSs, Td could inhibit the expressions of multiple pro-inflammatory

TABLE 1 | Effects of Td on organ indexes and serum ALT and AST in rats with collagen-induced arthritis.

Parameters	Control	Vehicle	MTX (3 mg·kg^{-1})	Td (5 mg·kg^{-1})	Td (15 mg·kg^{-1})
Body weight gain (%)	27.29 ± 5.98	–5.11 ± 1.35$^{###}$	7.86 ± 2.47***	7.72 ± 2.44***	12.68 ± 3.66***
Index of heart (%)	0.34 ± 0.02	0.42 ± 0.03$^{###}$	0.41 ± 0.05	0.37 ± 0.04	0.40 ± 0.01
Index of liver (%)	3.82 ± 0.25	4.76 ± 0.53$^{##}$	3.88 ± 0.32**	4.38 ± 0.25	4.20 ± 0.55
Index of kidney (%)	0.39 ± 0.03	0.54 ± 0.06$^{###}$	0.49 ± 0.04	0.44 ± 0.04***	0.45 ± 0.04***
Index of spleen (%)	0.25 ± 0.02	0.41 ± 0.06$^{###}$	0.32 ± 0.05	0.37 ± 0.07	0.32 ± 0.06
Index of thymus (%)	0.26 ± 0.04	0.27 ± 0.06	0.23 ± 0.05	0.22 ± 0.06	0.29 ± 0.05
AST (U/L)	25.78 ± 5.81	23.90 ± 2.62	24.31 ± 2.00	24.62 ± 1.73	25.46 ± 0.92
ALT (U/L)	26.90 ± 0.48	27.72 ± 2.60	26.13 ± 0.48	25.38 ± 1.57	25.12 ± 1.65

Rats were intraperitoneally injected with Td (5 and 15 mg·kg^{-1}) or 0.9% saline daily for up to 14 days. The MTX-treated group was intraperitoneally injected with MTX (3 mg·kg^{-1}) every 3 days according to clinical usage. Data were expressed as mean ± SD; n = 6, $^{##}$P < *0.01 and* $^{###}$P < *0.001 versus the normal control (age-matched rats);* **P < *0.01 and* ***P <*0.001 versus the vehicle-treated CIA rats. ALT, alanine aminotransferase; AST, aspartate aminotransferase.*

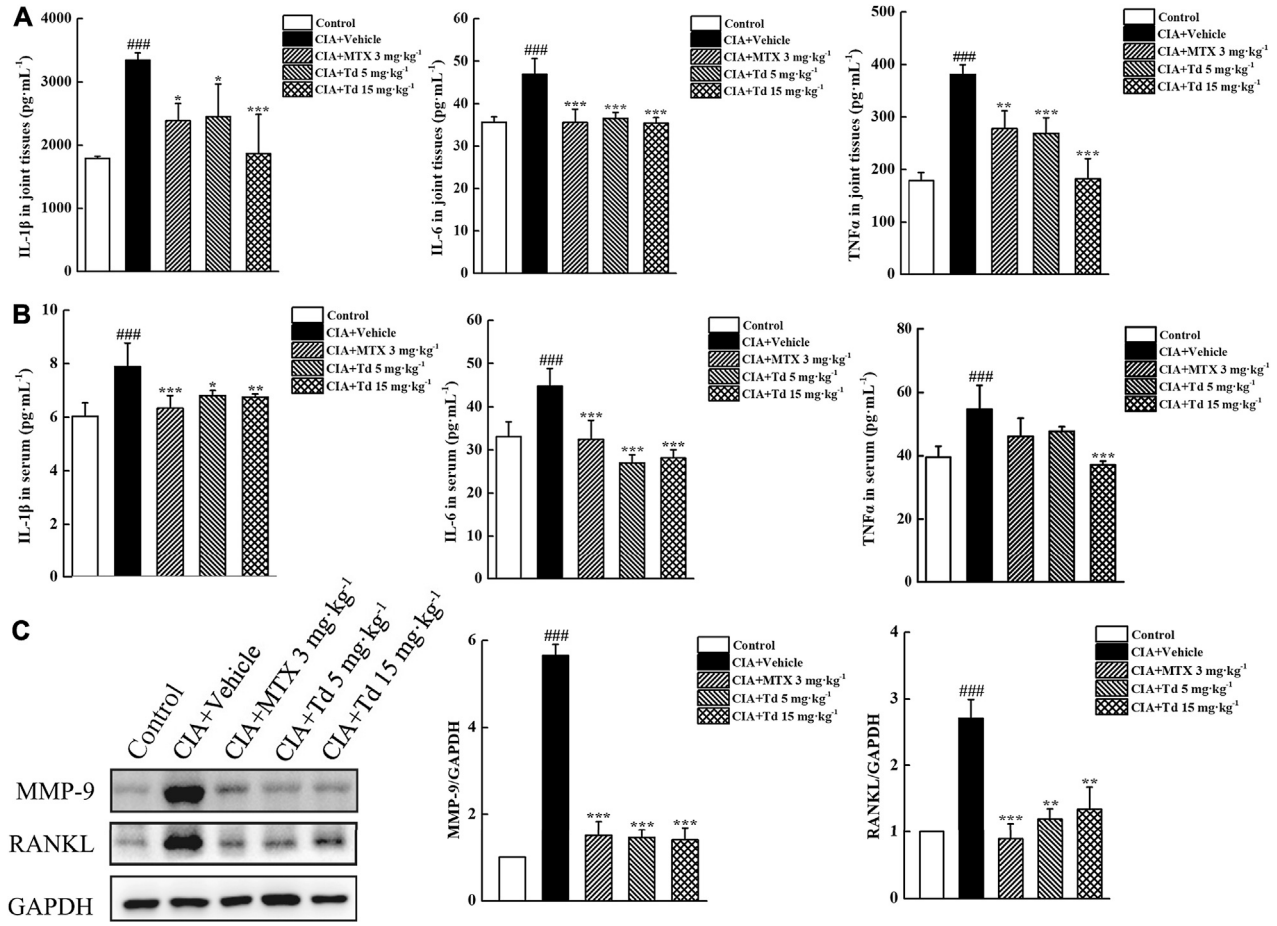


FIGURE 5 | Td decreased synthesis of proinflammatory cytokines, MMP-9 and RANKL in CIA rats. **(A,B)** ELISA was performed to measure the protein levels of IL-1β, IL-6 and TNFα in serum and joint tissues of rats. *n* = 6, $^{###}P < 0.001$ versus the normal control rats; $^{*}P < 0.01$, $^{**}P < 0.05$ and $^{***}P < 0.001$ versus the vehicle-treated group. **(C)** Western blot was performed to examine the protein expression of MMP-9 and RANKL in joint tissues of rats. Relative expression was determined by densitometric analysis using ImageJ software. *n* = 6, $^{###}P < 0.001$ versus the normal control rats; $^{**}P < 0.01$ and $^{***}P < 0.001$ versus the vehicle-treated group.

cytokines. To further confirm the *in vitro* results, serum and joint tissues of each group were collected and the protein expressions of IL-1β, IL-6 and TNFα were examined using ELISA. As shown in **Figures 5A,B**, the local and systemic levels of IL-1β, IL-6 and TNFα in the Td-treated groups were much lower than those in the vehicle-treated group. In addition, compared with the vehicle-treated rats, those treated with Td had significantly decreased production of MMP-9 and RANKL (**Figure 5C**), which further confirmed the data from arthritic FLSs.

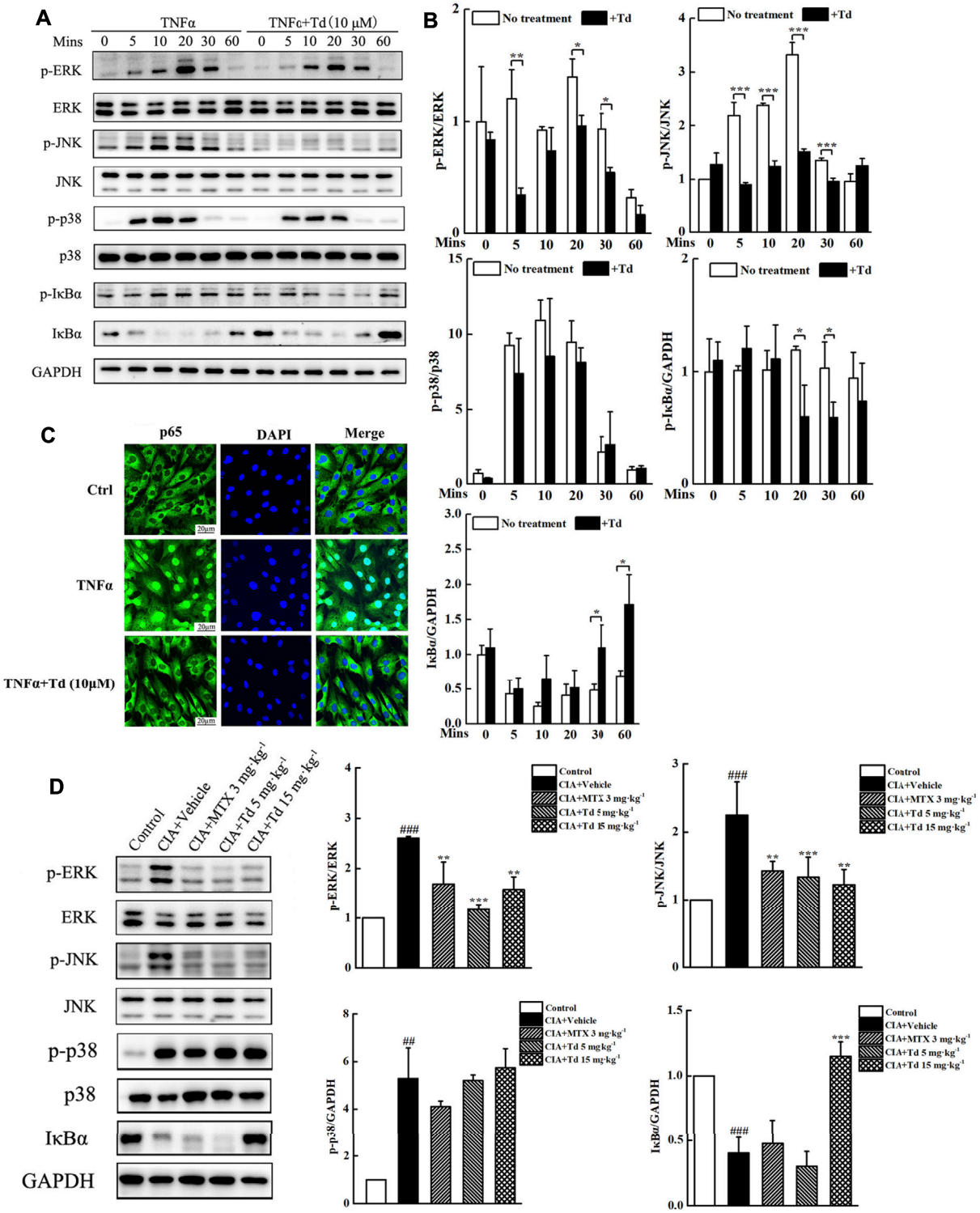


FIGURE 6 | Td suppressed TNFα-induced MAPKs and NF-κB activations. **(A)** Arthritic FLSs were treated with or without Td (10 μM) for 4 h, and then incubated with TNFα (50 ng·mL^{-1}) for 0, 5, 10, 20, 30 and 60 mins. Western blot was probed for p-ERK1/2, total ERK1/2, p-JNK1/2, total JNK1/2, p-p38, total p38, p-IκBα, IκBα and GAPDH. **(B)** The ratios of p-ERK/ERK, p-JNK/JNK, p-p38/p38, p-IκBα/GAPDH and IκBα/GAPDH were analyzed using ImageJ software. $^{*}P < 0.05$, $^{**}P < 0.01$ and $^{***}P < 0.001$ versus TNFα-treated, Td-untreated cells. **(C)** Arthritic FLSs were seeded at a density of 2×10^4/well in 24-well plates and cultured overnight. Following pre-treatment with or without Td (10 μM) for 4 h, and the cells were incubated with TNFα (50 ng·mL^{-1}) for 30 min. The localization of p65 was fixed, stained, and visualized by immunofluorescence analysis. **(D)** The right hind paws were collected and joint tissue homogenates were used to measure the protein levels and phosphorylations of MAPK members (ERK, JNK and p38). Additionally, the protein level of IκBα was also detected. Relative expression was determined by densitometric analysis using ImageJ software. $n = 6$, $^{\#\#}P < 0.01$ and $^{\#\#\#}P < 0.001$ versus the normal control rats; $^{**}P < 0.01$ and $^{***}P < 0.001$ versus the vehicle-treated group.

Tomatidine Inhibited TNFα-Induced MAPKs (ERK and JNK) and NF-κB Activations

To reveal the mechanisms through which Td plays an inhibitory action on CIA model and arthritic FLS cells, we used immunoblotting to examine the activations of MAPKs and NF-κB, which play vital roles in RA pathogenesis. In cultured primary arthritic FLSs, TNFα stimulation could rapidly increase the phosphorylation levels of the MAPK family members (ERK, JNK and p38) (**Figures 6A,B**). Td treatment significantly suppressed TNFα-induced phosphorylations of ERK and JNK but without effect on p38 (**Figures 6A,B**). In addition, TNFα stimulation initiated phosphorylation and degradation of IκBα. When the cells were treated with Td (10 μM), IκBα phosphorylation and degradation were both significantly suppressed (**Figures 6A,B**). It is well known that IκB degradation can liberate NF-κB p65 protein into the nucleus and trigger its downstream target gene expression (Makarov, 2001). Thus, we used immunofluorescence microscopy to detect the effect of Td on p65 nuclear translocation. As shown in **Figure 6C**, TNFα incubation for 30 min clearly promoted NF-κB p65 translocation from the cytoplasm to the nuclei. However, this translocation process was substantially blocked when the cell was treated with 10 μM Td, as evidenced by the cytoplasmic retention of p65 proteins (**Figure 6C**).

To confirm the *in vitro* results, we isolated the protein from the joint tissues of each group and examined the activations of MAPKs and NF-κB using Western blot. As expected, Td had no obvious influence on p38 phosphorylation. However Td significantly decreased the phosphorylation levels of ERK and JNK compared with the vehicle-treated group (**Figure 6D**). Additionally, the degradation of IκBα was also suppressed by high-dose Td treatment (**Figure 6D**).

DISCUSSION

Td, a steroidal alkaloid derived from the solanaceae family, has been reported to possess antioxidative, anti-inflammatory, anti-tumor, immunomodulatory and anti-osteoclastic properties (Lee et al., 2004; Chiu and Lin, 2008; Yan et al., 2013; Jeon and Kim, 2019). Based on the evidence, we reasoned that Td might exert a protective role in RA development. Indeed, this study demonstrated that Td could suppress synovial inflammatory and bone destruction through inhibiting the pathogenic behaviors of arthritic FLSs.

As the prominent cell type in synovium, FLSs play an indispensable role in establishing the complex three-dimensional synovial lining architecture. In inflamed RA synovium, FLS cells acquire and sustain uniquely aggressive properties including increasing proliferative and invasive capacity, escaping contacting inhibition and resisting apoptosis (Neidhart et al., 2003; Lahoti et al., 2014). These over-activated FLSs can autonomously drive and maintain joint inflammation through secretion of multiple pro-inflammatory mediators, directly invade and destroy articular cartilage through producing matrix metalloproteinases (MMPs), and promote bone erosion through synthesis of osteoclast differentiation factor RANKL (Takayanagi et al., 2000; Kim et al., 2009). Hence, inhibiting the pathogenic properties of FLSs may be a promising strategy for RA treatment. In this study, the *in vitro* and *in vivo* experiments provided rigorous demonstrations that Td could attenuate FLS's destructive phenotypes. The EdU assay showed that Td significantly inhibited the proliferative potential of primary arthritic FLSs. In line with the *in vitro* data, the histopathological results showed that both low dose and high dose of Td could significantly suppress synovial hyperplasia in CIA rats. In addition, Td could dose-dependently reduce the migration rate of arthritic FLSs. The histopathological scores also demonstrated that the pannus formation in CIA rats was significantly suppressed by Td. MMPs, especially the members of MMP-2 and MMP-9, are well known to exert a critical role in ECM breakdown and tissues degradation (Gruber et al., 1996; Tchetverikov et al., 2004). MMP-2 is constitutively expressed in an inactive form in various cell types without being affected by pro-inflammatory mediators (Konttinen et al., 1999). However, MMP-9 is inducible by inflammatory cytokines, indicating a close relationship with synovial inflammation (Giannelli et al., 2004). In this study, Td had little effect on the production of MMP-2, however, it significantly suppressed synthesis of MMP-9. This finding was consistent with our *in vivo* results, which showed a protective effect of Td on cartilage erosion. In addition to MMP-9, Td also inhibited the expressions of IL-1β, IL-6 and TNFα at both the mRNA and protein levels, indicating that Td could suppress synovial inflammation. Indeed, the *in vivo* data showed that Td significantly attenuated inflammatory cell infiltration and inflammation response. Notably, RANKL, an essential inducer of osteoclastogenesis, was significantly down-regulated by Td. Consistent with this result, the radiographic evaluation and the histopathological analysis both verified that Td at the dosages of 5 $mg \cdot kg^{-1}$ and 15 $mg \cdot kg^{-1}$ effectively protected against bone destruction in CIA rats. The previous study reported that Td could directly inhibited osteoclast formation through modulating multiple TRAF6-mediated pathways (Hu et al., 2019). Therefore, we speculated that Td's anti-bone erosive action might attribute to its direct inhibition on osteoclastogenesis, and an indirect inhibitory effect through decreasing RANKL expression in arthritic FLSs.

Having demonstrated that Td exerted an inhibitory action on CIA rats and arthritic FLSs, we further analyzed the possibly involved molecular mechanisms. MAPKs are well known to play essential roles in regulating multiple cellular events such as cell migration, proliferation and secretion of proinflammatory cytokines (Herlaar and Brown, 1999; Han and Sun, 2007; Bogoyevitch et al., 2010). In the over-activated RA FLSs, the three MAPK kinases (ERK, JNK and p38) showed significantly up-regulated

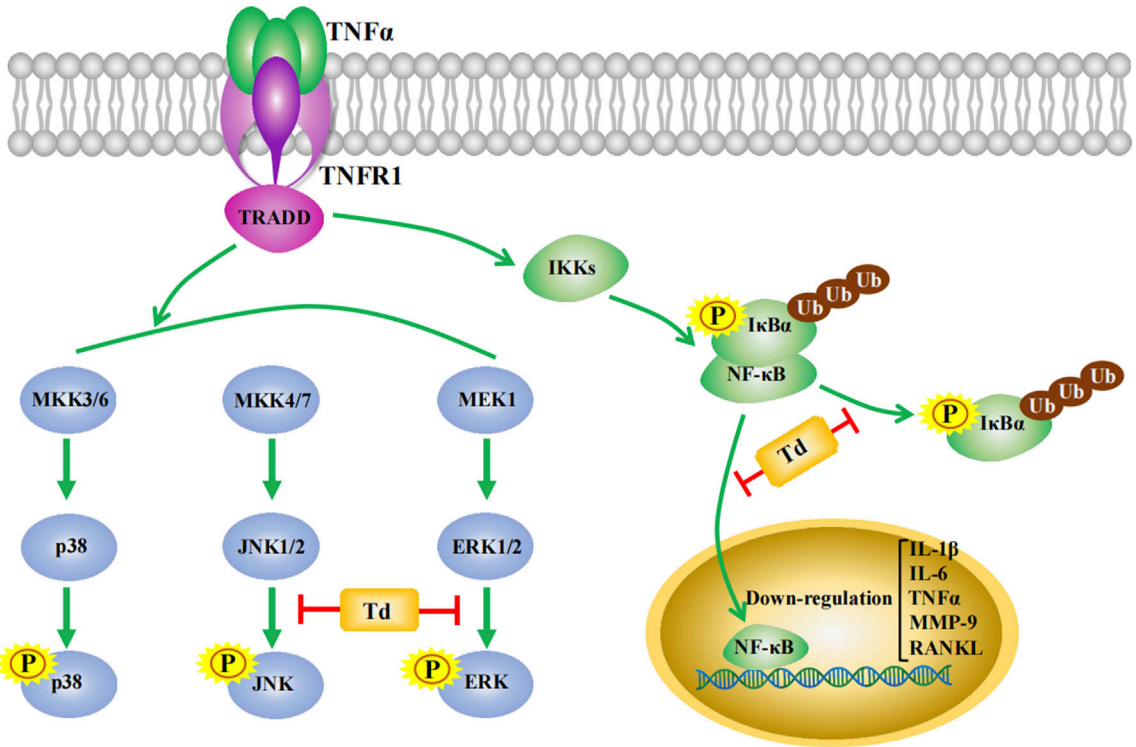


FIGURE 7 | Schematic summarizing of the mechanism by which Td relieved the destructive behaviors of FLSs and prevented the development of CIA. In TNFα-stimulated FLSs and CIA rat model, MAPK and NF-κB signaling pathways were activated. Td treatment significantly inhibited phosphorylations of ERK and JNK. Also, NF-κB activation was suppressed *via* decreasing IκBα phosphorylation and degradation, and thereby inhibiting the nuclear translocation of the p65 subunit of NF-κB. Accordingly, NF-κB target genes including *IL-1β*, *IL-6*, *TNFα, MMP-9* and *RANKL* were downregulated.

phosphorylation and activation. Therefore, the blockage of their activations may offer promising benefits to RA treatment (Thompson and Lyons, 2005; Senolt et al., 2009). In arthritic FLSs, we found that Td had little effect on the phosphorylation of p38 but significantly attenuated TNFa-induced phosphorylation of ERK and JNK. A similar result was observed in the CIA rat model, which further confirmed the inhibition of Td on ERK and JNK pathways. Besides, Td also suppressed the activation of NF-κB, as evidenced by the downregulations of IκBα phosphorylation and degradation, and thereby inhibition of p65 nuclear translocation. These results were further demonstrated by the real-time PCR data that Td significantly inhibited the transcripts of NF-κB target genes including *IL-1β*, *IL-6*, *TNFα*, *MMP-9* and *RANKL*. Taken together, these data indicated that Td might play an inhibitory action on RA via multiple targets (**Figure 7**), and further studies are needed to clarify its direct binding sites.

In summary, we here demonstrated for the first time that Td could inhibit the pathological properties of arthritic FLSs *in vitro* and protect against CIA *in vivo*. This inhibitory effect of Td on RA might attribute to the decreased activations of MAPKs (ERK and JNK) and NF-κB. Td has the potential to become a complementary or alternative medicine for RA therapy.

DATA AVAILABILITY STATEMENT

The raw data supporting the conclusion of this article will be made available by the authors, without undue reservation, to any qualified researcher.

ETHICS STATEMENT

The animal study was reviewed and approved by the Experimental Committee of Nanjing Normal University.

AUTHOR CONTRIBUTIONS

ML and CW conceived and designed the experiments. XY, JZ, FZ, XL, YM, and LD performed the experiments. ML, CW, and XY analyzed the data. ML and XY wrote the manuscript.

FUNDING

This study was supported by National Natural Science Foundation of China (Grant No. 31870895; 32071165; 31171135) and the Priority Academic Program Development of Jiangsu Higher Education Institutions (PAPD).

REFERENCES

Ath, A. J. F., and Denton, J. (1991). *Atlas of Synovial Fluid Cytopathology*. Springer Netherlands.

Athanasou, N. A. (1996). Cellular Biology of Bone-Resorbing Cells. *J. Bone Jt. Surg Am* 78 (7), 1096–1112. Epub 1996/07/01PubMed PMID: 8698729. doi:10.2106/00004623-199607000-00016

Bartok, B., and Firestein, G. S. (2010). Fibroblast-like Synoviocytes: Key Effector Cells in Rheumatoid Arthritis. *Immunol. Rev.* 233 (1), 233–255. Epub 2010/03/03PubMed PMID: 20193003; PubMed Central PMCID: PMCPMC2913689. doi:10.1111/j.0105-2896.2009.00859.x

Bogoyevitch, M. A., Ngoei, K. R., Zhao, T. T., Yeap, Y. Y., and Ng, D. C. (2010). c-Jun N-Terminal Kinase (JNK) Signaling: Recent Advances and Challenges. *Biochim. Biophys. Acta* 1804 (3), 463–475. Epub 2009/11/11PubMed PMID: 19900593. doi:10.1016/j.bbapap.2009.11.002

Cai, X., Zhou, H., Wong, Y. F., Xie, Y., Liu, Z. Q., Jiang, Z. H., et al. (2007). Suppression of the Onset and Progression of Collagen-Induced Arthritis in Rats by QFGJS, a Preparation from an Anti-arthritic Chinese Herbal Formula. *J. Ethnopharmacol* 110 (1), 39–48. Epub 2006/10/20PubMed PMID: 17049776. doi:10.1016/j.jep.2006.09.008

Chiu, F. L., and Lin, J. K. (2008). Tomatidine Inhibits iNOS and COX-2 through Suppression of NF-kappaB and JNK Pathways in LPS-Stimulated Mouse Macrophages. *FEBS Lett.* 582 (16), 2407–2412. Epub 2008/06/12PubMed PMID: 18544347. doi:10.1016/j.febslet.2008.05.049

Danks, L., Sabokbar, A., Gundle, R., and Athanasou, N. A. (2002). Synovial Macrophage-Osteoclast Differentiation in Inflammatory Arthritis. *Ann. Rheum. Dis.* 61 (10), 916–921. Epub 2002/09/14PubMed PMID: 12228163; PubMed Central PMCID: PMCPMC1753924. doi:10.1136/ard.61.10.916

Dyle, M. C., Ebert, S. M., Cook, D. P., Kunkel, S. D., Fox, D. K., Bongers, K. S., et al. (2014). Systems-based Discovery of Tomatidine as a Natural Small Molecule Inhibitor of Skeletal Muscle Atrophy. *J. Biol. Chem.* 289 (21), 14913–14924. Epub 2014/04/11PubMed PMID: 24719321; PubMed Central PMCID: PMCPMC4031541. doi:10.1074/jbc.M114.556241

Firestein, G. S. (2003). Evolving Concepts of Rheumatoid Arthritis. *Nature* 423 (6937), 356–361. Epub 2003/05/16PubMed PMID: 12748655. doi:10.1038/nature01661

Friedman, M., Levin, C. E., Lee, S. U., Kim, H. J., Lee, I. S., Byun, J. O., et al. (2009). Tomatine-containing green Tomato Extracts Inhibit Growth of Human Breast, colon, Liver, and Stomach Cancer Cells. *J. Agric. Food Chem.* 57 (13), 5727–5733. Epub 2009/06/12PubMed PMID: 19514731. doi:10.1021/jf900364j

Fujiwara, Y., Kiyota, N., Tsurushima, K., Yoshitomi, M., Horlad, H., Ikeda, T., et al. (2012). Tomatidine, a Tomato Sapogenol, Ameliorates Hyperlipidemia and Atherosclerosis in apoE-Deficient Mice by Inhibiting Acyl-CoA:cholesterol Acyl-Transferase (ACAT). *J. Agric. Food Chem.* 60 (10), 2472–2479. Epub 2012/01/10PubMed PMID: 22224814. doi:10.1021/jf204197r

Giannelli, G., Erriquez, R., Iannone, F., Marinosci, F., Lapadula, G., and Antonaci, S. (2004). MMP-2, MMP-9, TIMP-1 and TIMP-2 Levels in Patients with Rheumatoid Arthritis and Psoriatic Arthritis. *Clin. Exp. Rheumatol.* 22 (3), 335–338. Epub 2004/05/18. PubMed PMID: 15144129.

Gravallese, E. M. (2002). Bone Destruction in Arthritis. *Ann. Rheum. Dis.* 61 Suppl 2 (Suppl. 2Suppl 2), ii84–6. Epub 2002/10/16PubMed PMID: 12379632; PubMed Central PMCID: PMCPMC1766721. doi:10.1136/ard.61.suppl_2.ii84

Gruber, B. L., Sorbi, D., French, D. L., Marchese, M. J., Nuovo, G. J., Kew, R. R., et al. (1996). Markedly Elevated Serum MMP-9 (Gelatinase B) Levels in Rheumatoid Arthritis: a Potentially Useful Laboratory Marker. *Clin. Immunol. Immunopathol* 78 (2), 161–171. Epub 1996/02/01PubMed PMID: 8625558. doi:10.1006/clin.1996.0025

Han, J., and Sun, P. (2007). The Pathways to Tumor Suppression via Route P38. *Trends Biochem. Sci.* 32 (8), 364–371. Epub 2007/07/13PubMed PMID: 17624785. doi:10.1016/j.tibs.2007.06.007

Herlaar, E., and Brown, Z. (1999). p38 MAPK Signalling Cascades in Inflammatory Disease. *Mol. Med. Today* 5 (10), 439–447. Epub 1999/09/28PubMed PMID: 10498912. doi:10.1016/s1357-4310(99)01544-0

Hu, B., Sun, X., Yang, Y., Ying, Z., Meng, J., Zhou, C., et al. (2019). Tomatidine Suppresses Osteoclastogenesis and Mitigates Estrogen Deficiency-Induced Bone Mass Loss by Modulating TRAF6-Mediated Signaling. *FASEB J.* 33 (2), 2574–2586. Epub 2018/10/05PubMed PMID: 30285579. doi:10.1096/fj.201800920R

Jeon, S., and Kim, M. M. (2019). Tomatidine Inhibits Cell Invasion through the Negative Modulation of Gelatinase and Inactivation of P38 and ERK. *Chem. Biol. Interact* 313, 108826, 2019. Epub 2019/09/24PubMed PMID: 31545954. doi:10.1016/j.cbi.2019.108826

Kim, K. W., Cho, M. L., Oh, H. J., Kim, H. R., Kang, C. M., Heo, Y. M., et al. (2009). TLR-3 Enhances Osteoclastogenesis through Upregulation of RANKL Expression from Fibroblast-like Synoviocytes in Patients with Rheumatoid Arthritis. *Immunol. Lett.* 124 (1), 9–17. Epub 2009/05/19PubMed PMID: 19446344. doi:10.1016/j.imlet.2009.02.006

Kobayashi, K., Takahashi, N., Jimi, E., Udagawa, N., Takami, M., Kotake, S., et al. (2000). Tumor Necrosis Factor Alpha Stimulates Osteoclast Differentiation by a Mechanism Independent of the ODF/RANKL-RANK Interaction. *J. Exp. Med.* 191 (2), 275–286. Epub 2000/01/19PubMed PMID: 10637272; PubMed Central PMCID: PMCPMC2195746. doi:10.1084/jem.191.2.275

Konttinen, Y. T., Ainola, M., Valleala, H., Ma, J., Ida, H., Mandelin, J., et al. (1999). Analysis of 16 Different Matrix Metalloproteinases (MMP-1 to MMP-20) in the Synovial Membrane: Different Profiles in Trauma and Rheumatoid Arthritis. *Ann. Rheum. Dis.* 58 (11), 691–697. Epub 1999/10/26PubMed PMID: 10531073; PubMed Central PMCID: PMCPMC1752794. doi:10.1136/ard.58.11.691

Lahoti, T. S., Hughes, J. M., Kusnadi, A., John, K., Zhu, B., Murray, I. A., et al. (2014). Aryl Hydrocarbon Receptor Antagonism Attenuates Growth Factor Expression, Proliferation, and Migration in Fibroblast-like Synoviocytes from Patients with Rheumatoid Arthritis. *J. Pharmacol. Exp. Ther.* 348 (2), 236–245. Epub 2013/12/07PubMed PMID: 24309559; PubMed Central PMCID: PMCPMC3912548. doi:10.1124/jpet.113.209726

Lange, F., Bajtner, E., Rintisch, C., Nandakumar, K. S., Sack, U., and Holmdahl, R. (2005). Methotrexate Ameliorates T Cell Dependent Autoimmune Arthritis and Encephalomyelitis but Not Antibody Induced or Fibroblast Induced Arthritis. *Ann. Rheum. Dis.* 64 (4), 599–605. Epub 2004/09/04PubMed PMID: 15345503; PubMed Central PMCID: PMCPMC1755430. doi:10.1136/ard.2004.026120

Laragione, T., Brenner, M., Mello, A., Symons, M., and Gulko, P. S. (2008). The Arthritis Severity Locus Cia5d Is a Novel Genetic Regulator of the Invasive Properties of Synovial Fibroblasts. *Arthritis Rheum.* 58 (8), 2296–2306. Epub 2008/08/01PubMed PMID: 18668563; PubMed Central PMCID: PMCPMC2714698. doi:10.1002/art.23610

Lee, K. R., Kozukue, N., Han, J. S., Park, J. H., Chang, E. Y., Baek, E. J., et al. (2004). Glycoalkaloids and Metabolites Inhibit the Growth of Human colon (HT29) and Liver (HepG2) Cancer Cells. *J. Agric. Food Chem.* 52 (10), 2832–2839. Epub 2004/05/13PubMed PMID: 15137822. doi:10.1021/jf030526d

Lee, S. T., Wong, P. F., Cheah, S. C., and Mustafa, M. R. (2011). Alpha-tomatine Induces Apoptosis and Inhibits Nuclear Factor-Kappa B Activation on Human Prostatic Adenocarcinoma PC-3 Cells. *PloS one* 6 (4), e18915, 2011 . Epub 2011/05/05PubMed PMID: 21541327; PubMed Central PMCID: PMCPMC3082542. doi:10.1371/journal.pone.0018915

Liu, C., Zhang, Y., Kong, X., Zhu, L., Pang, J., Xu, Y., et al. (2013). Triptolide Prevents Bone Destruction in the Collagen-Induced Arthritis Model of Rheumatoid Arthritis by Targeting RANKL/RANK/OPG Signal Pathway. *Evidence-Based Complement. Altern. Med.*, 2013, 1–12. Epub 2013/04/11PubMed PMID: 23573139; PubMed Central PMCID: PMCPMC3610373. doi:10.1155/2013/626038

Liu, M., Zhou, X., Zhou, L., Liu, Z., Yuan, J., Cheng, J., et al. (2018). Carnosic Acid Inhibits Inflammation Response and Joint Destruction on Osteoclasts, Fibroblast-like Synoviocytes, and Collagen-Induced Arthritis Rats. *J. Cel Physiol* 233 (8), 6291–6303. Epub 2018/03/10PubMed PMID: 29521424. doi:10.1002/jcp.26517

Liu, Z., Zhou, L., Ma, X., Sun, S., Qiu, H., Li, H., et al. (2018). Inhibitory Effects of Tubeimoside I on Synoviocytes and Collagen-Induced Arthritis in Rats. *J. Cel Physiol* 233 (11), 8740–8753. Epub 2018/05/16PubMed PMID: 29761884. doi:10.1002/jcp.26754

Ma, Y., and Pope, R. M. (2005). The Role of Macrophages in Rheumatoid Arthritis. *Curr. Pharm. Des.* 11 (5), 569–580. Epub 2005/02/22PubMed PMID: 15720276. doi:10.2174/1381612053381927

Makarov, S. S. (2001). NF-kappa B in Rheumatoid Arthritis: a Pivotal Regulator of Inflammation, Hyperplasia, and Tissue Destruction. *Arthritis Res.* 3 (4),

200–206. Epub 2001/07/05PubMed PMID: 11438035; PubMed Central PMCID: PMCPMC128895. doi:10.1186/ar300

Mor, A., Abramson, S. B., and Pillinger, M. H. (2005). The Fibroblast-like Synovial Cell in Rheumatoid Arthritis: a Key Player in Inflammation and Joint Destruction. *Clin. Immunol.* 115 (2), 118–128. Epub 2005/05/12PubMed PMID: 15885632. doi:10.1016/j.clim.2004.12.009

Neidhart, M., Seemayer, C. A., Hummel, K. M., Michel, B. A., Gay, R. E., and Gay, S. (2003). Functional Characterization of Adherent Synovial Fluid Cells in Rheumatoid Arthritis: Destructive Potential *In Vitro* and *In Vivo*. *Arthritis Rheum.* 48 (7), 1873–1880. Epub 2003/07/09PubMed PMID: 12847681. doi:10.1002/art.11166

Noss, E. H., and Brenner, M. B. (2008). The Role and Therapeutic Implications of Fibroblast-like Synoviocytes in Inflammation and Cartilage Erosion in Rheumatoid Arthritis. *Immunol. Rev.* 223, 252–270. Epub 2008/07/11PubMed PMID: 18613841. doi:10.1111/j.1600-065X.2008.00648.x

Qiu, H., Sun, S., Ma, X., Cui, C., Chen, G., Liu, Z., et al. (2018). Jatrorrhizine Hydrochloride Suppresses Proliferation, Migration, and Secretion of Synoviocytes *In Vitro* and Ameliorates Rat Models of Rheumatoid Arthritis *In Vivo*. *Int. J. Mol. Sci.* 19 (5). PubMed PMID: 29783696; PubMed Central PMCID: PMCPMC5983572. doi:10.3390/ijms19051514Epub 2018/05/23

Senolt, L., Vencovský, J., Pavelka, K., Ospelt, C., and Gay, S. (2009). Prospective New Biological Therapies for Rheumatoid Arthritis. *Autoimmun. Rev.* 9 (2), 102–107. Epub 2009/03/31PubMed PMID: 19328245. doi:10.1016/j.autrev.2009.03.010

Shieh, J. M., Cheng, T. H., Shi, M. D., Wu, P. F., Chen, Y., Ko, S. C., et al. (2011). α-Tomatine Suppresses Invasion and Migration of Human Non-small Cell Lung Cancer NCI-H460 Cells through Inactivating FAK/PI3K/Akt Signaling Pathway and Reducing Binding Activity of NF-Kb. *Cell Biochem. Biophys.* 60 (3), 297–310. Epub 2011/01/26PubMed PMID: 21264526. doi:10.1007/s12013-011-9152-1

Skapenko, A., Leipe, J., Lipsky, P. E., and Schulze-Koops, H. (2005). The Role of the T Cell in Autoimmune Inflammation. *Arthritis Res. Ther.* 7 Suppl 2 (Suppl. 2Suppl 2), S4–S14. Epub 2005/04/19PubMed PMID: 15833146; PubMed Central PMCID: PMCPMC2833981. doi:10.1186/ar1703

Song, S. E., Shin, S. K., Cho, H. W., Im, S. S., Bae, J. H., Woo, S. M., et al. (2018). Tomatidine Inhibits Tumor Necrosis Factor-α-Induced Apoptosis in C2C12 Myoblasts via Ameliorating Endoplasmic Reticulum Stress. *Mol. Cel. Biochem.* 444 (1-2), 17–25. Epub 2017/12/03PubMed PMID: 29196971. doi:10.1007/s11010-017-3226-3

Takayanagi, H., Iizuka, H., Juji, T., Nakagawa, T., Yamamoto, A., Miyazaki, T., et al. (2000). Involvement of Receptor Activator of Nuclear Factor kappaB Ligand/osteoclast Differentiation Factor in Osteoclastogenesis from Synoviocytes in Rheumatoid Arthritis. *Arthritis Rheum.* 43 (2), 259–269. Epub 2000/02/29PubMed PMID: 10693864. doi:10.1002/1529-013110.1002/1529-0131(200002)43:2<259::AID-ANR4>3.0.CO;2-W

Tchetverikov, I., Ronday, H. K., Van El, B., Kiers, G. H., Verzijl, N., TeKoppele, J. M., et al. (2004). MMP Profile in Paired Serum and Synovial Fluid Samples of Patients with Rheumatoid Arthritis. *Ann. Rheum. Dis.* 63 (7), 881–883. Epub 2004/06/15PubMed PMID: 15194590; PubMed Central PMCID: PMCPMC1755080. doi:10.1136/ard.2003.013243

Thompson, N., and Lyons, J. (2005). Recent Progress in Targeting the Raf/MEK/ERK Pathway with Inhibitors in Cancer Drug Discovery. *Curr. Opin. Pharmacol.* 5 (4), 350–356. Epub 2005/06/16PubMed PMID: 15955734. doi:10.1016/j.coph.2005.04.007

Ueland, T., Yndestad, A., Øie, E., Florholmen, G., Halvorsen, B., Frøland, S. S., et al. (2005). Dysregulated Osteoprotegerin/RANK Ligand/RANK axis in Clinical and Experimental Heart Failure. *Circulation* 111 (19), 2461–2468. Epub 2005/05/11PubMed PMID: 15883214. doi:10.1161/01.Cir.0000165119.62099.14

Yan, K. H., Lee, L. M., Yan, S. H., Huang, H. C., Li, C. C., Lin, H. T., et al. (2013). Tomatidine Inhibits Invasion of Human Lung Adenocarcinoma Cell A549 by Reducing Matrix Metalloproteinases Expression. *Chem. Biol. Interact* 203 (3), 580–587. Epub 2013/04/10PubMed PMID: 23566884. doi:10.1016/j.cbi.2013.03.016

Yasuda, H., Shima, N., Nakagawa, N., Yamaguchi, K., Kinosaki, M., Mochizuki, S., et al. (1998). Osteoclast Differentiation Factor Is a Ligand for Osteoprotegerin/osteoclastogenesis-Inhibitory Factor and Is Identical to TRANCE/RANKL. *Proc. Natl. Acad. Sci. U S A.* 95 (7), 3597–3602. Epub 1998/05/09PubMed PMID: 9520411; PubMed Central PMCID: PMCPMC19881. doi:10.1073/pnas.95.7.3597

Yuan, H. Y., Zhang, X. L., Zhang, X. H., Meng, L., and Wei, J. F. (2015). Analysis of Patents on Anti-rheumatoid Arthritis Therapies Issued in China. *Expert Opin. Ther. Pat* 25 (8), 909–930. Epub 2015/06/13PubMed PMID: 26066366. doi:10.1517/13543776.2015.1044972

Conflict of Interest: The authors declare that the research was conducted in the absence of any commercial or financial relationships that could be construed as a potential conflict of interest.

Publisher's Note: All claims expressed in this article are solely those of the authors and do not necessarily represent those of their affiliated organizations, or those of the publisher, the editors and the reviewers. Any product that may be evaluated in this article, or claim that may be made by its manufacturer, is not guaranteed or endorsed by the publisher.

Copyright © 2021 Yu, Zhou, Zhao, Liu, Mao, Diao, Wen and Liu. This is an open-access article distributed under the terms of the Creative Commons Attribution License (CC BY). The use, distribution or reproduction in other forums is permitted, provided the original author(s) and the copyright owner(s) are credited and that the original publication in this journal is cited, in accordance with accepted academic practice. No use, distribution or reproduction is permitted which does not comply with these terms.

frontiers in Pharmacology

ORIGINAL RESEARCH
published: 31 August 2021
doi: 10.3389/fphar.2021.726035

Huangbai Liniment Ameliorates Skin Inflammation in Atopic Dermatitis

Ting Zheng[1,2], Miao Fan[3], Yunbo Wei[1,2], Jinhong Feng[1,2], Pengcheng Zhou[4], Xin Sun[5], Anqi Xue[1,2], Cheng Xue Qin[3,6,7] and Di Yu[1,4]*

[1]Shandong Analysis and Test Center, Laboratory of Immunology for Environment and Health, Qilu University of Technology (Shandong Academy of Sciences), Jinan, China, [2]School of Pharmaceutical Sciences, Qilu University of Technology (Shandong Academy of Sciences), Jinan, China, [3]School of Pharmaceutical Science, Shandong University, Jinan, China, [4]The University of Queensland Diamantina Institute, Translational Research Institute, Brisbane, QLD, Australia, [5]School of Food Science and Engineering, Qilu University of Technology (Shandong Academy of Sciences), Jinan, China, [6]Qilu Hospital, Cheeloo College of Medicine, Shandong University, Jinan, China, [7]Drug Discovery Biology, Monash Institute of Pharmaceutical Sciences, Monash University, Melbourne, VIC, Australia

Atopic dermatitis (AD), also known as atopic eczema, is one of the most common skin diseases and is characterized by allergic skin inflammation, redness, and itchiness and is associated with a hyperactivated type 2 immune response. The leading causes of AD include an imbalance in the immune system, genetic predisposition, or environmental factors, making the development of effective pharmacotherapies complex. Steroids are widely used to treat AD; however, they provide limited efficacy in the long term and can lead to adverse effects. Thus, novel treatments that offer durable efficacy and fewer side effects are urgently needed. Here, we investigated the therapeutic potential of Huangbai Liniment (HB), a traditional Chinese medicine, using an experimental AD mouse model, following our clinical observations of AD patients. In both AD patient and the mouse disease model, HB significantly improved the disease condition. Specifically, patients who received HB treatment on local skin lesions (3–4 times/day) showed improved resolution of inflammation. Using the 1-Chloro-2,4-dinitrobenzene (DNCB)-induced AD model in BALB/c mice, we observed that HB profoundly alleviated severe skin inflammation and relieved the itching. The dermatopathological results showed markedly reversed skin inflammation with decreased epidermal thickness and overall cellularity. Correspondingly, HB treatment largely decreased the mRNA expression of proinflammatory cytokines, including IL-1β, TNF-α, IL-17, IL-4, and IL-13, associated with declined gene expression of IL-33, ST2, and GATA3, which are connected to the type 2 immune response. In addition, HB restored immune tolerance by promoting regulatory T (T_{REG}) cells and inhibiting the generation of T_H1, T_H2, and T_H17 cells *in vitro* and in the DNCB-induced AD mouse model. For the first time, we demonstrate that HB markedly mitigates skin inflammation in AD patients and the DNCB-induced AD mouse model by reinvigorating the T cell immune balance, shedding light on the future development and application of novel HB-based therapeutics for AD.

Keywords: atopic dermatitis, huangbai liniment (HB), CD4 T cells, regulatory T (treg) cell, immunomodulation

OPEN ACCESS

Edited by:
Zhaocheng Ma,
Huazhong Agricultural University, China

Reviewed by:
Masanori Fujii,
Kyoto Pharmaceutical University, Japan
Marc Christophe Karam,
University of Balamand, Lebanon

****Correspondence:***
Ting Zheng
ting081226@hotmail.com

Specialty section:
This article was submitted to Inflammation Pharmacology, a section of the journal Frontiers in Pharmacology

Received: *16 June 2021*
Accepted: *19 August 2021*
Published: *31 August 2021*

Citation:
Zheng T, Fan M, Wei Y, Feng J, Zhou P, Sun X, Xue A, Qin CX and Yu D (2021) Huangbai Liniment Ameliorates Skin Inflammation in Atopic Dermatitis. Front. Pharmacol. 12:726035. doi: 10.3389/fphar.2021.726035

INTRODUCTION

As the physical barrier of the host, the skin is the organ where dynamic environmental-host interactions occur to drive the host's defense against stimuli, including microbial antigens and environmental chemicals, while abnormities in this response can lead to atopic reactions (Weidinger and Novak, 2016). Atopic dermatitis (AD), also known as atopic eczema, is a chronic allergic inflammatory skin disease that affects millions of people worldwide. Patients with AD exhibit mild to severe symptoms and often display eczematous lesions, erythema, pruritus, and skin inflammation (Leung et al., 2004; Weidinger and Novak, 2016). A proportion of AD patients also show comorbidities, including food allergies, asthma, allergic rhinitis, and other immune-mediated inflammatory diseases (Weidinger and Novak, 2016). A key pathophysiological mechanism of AD is the inappropriate immune response to antigens in the skin, which results in abnormalities of the epidermal structure and function and serious skin inflammation (Leung et al., 2004; Biedermann et al., 2015; Weidinger and Novak, 2016). Immune cells largely contribute to the development and regulation of AD, where the imbalance of CD4 T helper cell subsets is considered to be one of the major causes of the disease (Biedermann et al., 2015). Therefore, targeting the immune system imbalance is a promising approach to treat AD patients (Leung et al., 2004; Kim et al., 2019).

CD4 T helper cells play a vital role in the pathogenesis of AD. Emerging studies have shown that increased frequencies of T_H1, T_H2, T_H17, and T_H22 together with an excessive accumulation of inflammatory cytokines indispensably contribute to the onset of AD (Grewe et al., 1998; Weidinger and Novak, 2016). Specifically, the type 2 immune response and enhanced IgE response to allergens are the major factors that induce AD (Grewe et al., 1998; Weidinger and Novak, 2016). Antigen-primed T_H2 cells and their associated cytokines, including IL-4, IL-5, and IL-13 induce immune dysfunction and subsequently damage cutaneous tissue integrity, leading to AD initiation (Suárez-Fariñas et al., 2011; Dainichi et al., 2018). In chronic lesions of AD, both T_H2 and T_H1 cells induce further cellular infiltration, while T_H17 and T_H22 cells play important roles in acute lesions (Nograles et al., 2009; Gittler et al., 2012). It is thus critical to inhibit the excess of these pro-AD T cell subsets to improve AD in patients. Regulatory T (T_{REG}) cells regulate inflammation by substantially inhibiting proinflammatory T cells (Lei et al., 2015). By producing IL-10 and TGF-β, T_{REG} cells induce immune tolerance suppressing the severity of AD (Biedermann et al., 2015). Moreover, T_{REG} effector memory cells are reported to display the highest suppressive function (Rostaher et al., 2018; Looman et al., 2020). Furthermore, T_H2-cytokine-producing type 2 innate lymphoid cells are also found in AD lesions and contribute to IL-17 dependent inflammation (Imai et al., 2013).

Although significant progress has been made in understanding AD pathogenesis, the lack of durable and well-tolerated treatments has led to significant health and economic burdens in managing AD in patients. Immunosuppressive drugs, such as steroids, are most commonly used to treat AD; however, side effects include severe immunosuppression, increased risk of opportunistic infection, and osteoporosis (Nguyen et al., 2019). Thus, novel therapeutics that can provide long-term benefits and are well tolerated in AD patients are urgently needed.

Emerging studies have demonstrated that traditional Chinese medicine provides desirable therapeutic effects in inflammatory diseases. Huangbai Liniment (HB) is a standardized medicinal product clinically prescribed for use in dermatology and wound management (Liu et al., 2020; Zhang et al., 2020). It is a compound traditional Chinese medicine that includes forsythia, honeysuckle, phellodendron, dandelion, and centipede. In clinical trials, HB has been reported to exert profound anti-inflammatory effects during wound healing in several chronic inflammatory diseases, such as diabetic foot ulcers (Liu et al., 2020; Zhang et al., 2020), ulcerative colitis (Xiao et al., 2009), and traumatic infection (Li-yun, 2016). Mechanistically, experimental and clinical data indicate that HB accelerates diabetic wound healing via activation of Nrf2 and its downstream antioxidant genes (Zhang et al., 2020). Although the protective effects of HB are reported in many mucosal damage and inflammatory diseases in clinical therapy, the therapeutic effects and mechanism of HB in ameliorating dermatitis remains unclear. In this study, we investigated the therapeutic potential of HB in controlling inflammatory dermatoses in a DNCB-induced AD mouse model following clinical observations in AD patients and found that HB markedly alleviated skin inflammation and reinvigorated T_{REG}-induced immune balance in AD.

MATERIALS AND METHODS

Patient

Using the Hanifin and Rajka AD diagnostic guidelines and the eczema area and severity index (EASI) AD guidelines as standard, patient was selected from the diagnostic clinic of Dongzhimen Hospital for AD diagnosis. AD patient had no history or family history of allergic disease. Patient had not received steroid or immunosuppressive therapy and had no history of parasitic infection 2 weeks before the examination. The study design was approved by the Ethics committee of Beijing University of Chinese Medicine (NO. ECSL-BDY-2012-45-01). Written informed consent was obtained from patient included in the study.

Animals

All experimental 6–8 week-old BALB/c female mice were purchased from Vital River Laboratories (VRL, Beijing, China), and maintained at the Shandong Analysis and Test Center at a controlled temperature of 23 ˚C ± 2˚C, and a humidity of 50 ± 10%. All animal work was in accordance with protocols approved by the Animal Experimentation Ethics committee of Shandong Analysis and Test Center (NO. ECAESDATC-2018-010) and followed the ARRIVE (Animal Research: Reporting of *In Vivo* Experiments) guidelines.

Reagents

The HB (lot number: 18010111) used in this study was supplied by Shandong Hanfang Pharmaceutical Co., Ltd (Chinese medicine character: Z10950097). Hydrocortisone butyrate cream and 2, 4-Dinitrochlorobenzene (DNCB) were purchased from Jinyao Medical & Pharmaceutical Company Ltd. and Shanghai Chemical Reagent Company Ltd., respectively. The mouse antibodies against specific antigens used in flow cytometry analysis were purchased from BD Biosciences (San Jose, CA, United States) or BioLegend (San Diego, CA, United States). Recombinant murine IL-1β, IL-2, IL-4, IL-6, TGF-β, and IL-12 were purchased from PeproTech (Rocky Hill, NJ, United States). All other reagents were purchased from Sigma-Aldrich (St. Louis, MO, United States).

Experimental 1-Chloro-2,4-Dinitrobenzene-Induced AD Mouse Model

For induction of AD-like skin lesions in an experimental mouse model, mice were topically sensitized with 100 μl of 1% DNCB, diluted in a 4:1 mixture of acetone and olive oil, on shaved dorsal skin three times a week. From day five, mice were challenged with 0.4% DNCB on the dorsal skin (100 μl) and right ear (10 μl) every 3 days. The HB or hydrocortisone was applied by hydropathic compress on treatment group mice twice a day for 20 days (400 μl/day), and the control animals received the same volume of phosphate-buffered saline (PBS). At the end of the model construction, ear thickness measurements were performed with dial calipers as previously described (KimKim et al., 2013; Kim et al., 2014). For behavioral assessments, mice were acclimated to the recording cage and then evaluated for their scratching behavior. Total numbers of scratching bout per 10 min were record manually by an assessor who was blind to the experimental design. One scratching bout was defined as one instance of lifting the forepaw from the floor, scratching, and returning the paw to the floor or placing the paw around the animal's mouth (Oetjen et al., 2017). The severity of dermatitis was evaluated according to symptoms, including scaling, erythema, erosion, and edema. Each symptom was scored as 0 (no symptom), 1 (mild), 2 (moderate), or 3 (severe). After 20 days, at the end of the DNCB treatment, murine ear skin tissues and dorsal skin tissues were fixed in 4% paraformaldehyde (PFA) and subjected to histopathological analysis and other related experiments. Representative data are from one of three independent experiments ($n \geq 5$ in each group).

Skin Histology

Dorsal skin tissues were fully fixed with 4% paraformaldehyde at the endpoint before embedding in paraffin, sectioning, and staining with hematoxylin and eosin (H&E). Morphological evaluation of inflammatory infiltrates, and structural alterations were determined at a magnification of ×200 or ×50. To score the skin histopathology, inflammatory cell infiltration, epidermal thickness, and hair follicles were assessed blind-based using a five-point grading system and evaluated by blind scoring from 1 to 5, resulting in an average pathology score for each section. The infiltrated cells and the thickness of the epidermis or dermis were measured. Five randomized fields were counted for each section slide and calculated from five animals. All histology results were measured by blind evaluation.

Quantitative Real-Time Polymerase Chain Reaction

Total RNA was purified from skin tissue using TRIzol reagent (Invitrogen), and cDNA was synthesized from a total of 5 μg of RNA using RevertAid First Strand cDNA Synthesis Kit (Thermo Scientific) and amplified using qPCR according to the manufacturer's instructions. All qPCRs were run on the Roche real-time system using SYBR Green Master Mix (Roche) and normalized with β-Actin. The sequences of the primers used for qPCR are shown in **Table 1**.

In vitro Polarization

Naïve $CD4^+$ T cells were sorted from the spleens of healthy female 8 week-old BALB/c mice using a flow cytometer (BD FACS Aria III, BD Biosciences). The purity of the naïve $CD4^+$ T cells was >98%. Sorted naïve $CD4^+$ T cells (50,000 cells per well) were cultured in a 96-well culture plate pre-coated with anti-CD3 (5 μg/ml) and anti-CD28 (5 μg/ml) and polarized under T_H1 (IL-2 20 ng/ml, anti-IL-4 10 μg/ml and IL-12 20 ng/ml), T_H2 (IL-2 20 ng/ml, anti-IFN-γ 10 μg/ml, anti-IL-12 10 μg/ml, and IL-4 20 ng/ml), T_H17 (IL-2 20 ng/ml, IL-6 50 ng/ml, TGF-β 1ng/ml, IL-1β 10 ng/ml, anti-IL-4 10 μg/ml, and anti-IFN-γ 10 μg/ml), or T_{REG} cell (IL-2 20 ng/ml and TGF-β 2 ng/ml) differentiation conditions with or without 1/1000 H B for 4 days.

MTT Assay

Sorted naïve $CD4^+$ T cells were cultured with 20 ng/ml IL-2 with or without 1/1000 HB for 2 days, MTT solution was then added, and the sorted cells were incubated in the dark. After a 6 h incubation, solubilization buffer (10% SDS in 0.01 M HCl) was added, and the cells were cultured overnight. Cell proliferation was measured at an OD value of 570 nm.

Flow Cytometry

Mouse splenocytes were stained with Fc-receptor blocking antibodies (clone 2.4G2, 1:100 dilution, BD Biosciences) for 10 min on ice to block non-specific staining. For surface staining, cells were washed once with PBS containing 2% heat-inactivated fetal bovine serum (FBS, Gibco) and stained in an appropriately diluted antibody solution for 40 min at 4 C. Dead cells were excluded after staining with 7-amino-actinomycin D (7-AAD, BioLegend). For intracellular staining of cytokines, PMA and ionomycin stimulated cells were washed once after surface staining and permeabilized using Cytofix/Cytoperm (BD Biosciences) for 40 min on ice. The antibodies were diluted in Perm/Wash Buffer (BD), and

TABLE 1 | Sequences of qPCR primers.

Gene	Forward (5′-3′)	Reverse (5′-3′)	Size
IL-1β	TGCCACCTTTTGACAGTGATG	ATGTGCTGCTGCGAGATTTG	136 bp
IL-4	TCAACCCCCAGCTAGTTGTC	TCTGTGGTGTTCTTCGTTGC	184 bp
IL-10	CCAGTACAGCCGGGAAGACA	CAGCTGGTCCTTTGTTTGAAAGA	121 bp
IL-13	CAGCATGGTATGGAGTGTGG	AGGCTGGAGACCGTAGTGG	153 bp
IL-33	CTACTGCATGAGACTCCGTTCTG	AGAATCCCGTGGATAGGCAGAG	136 bp
IFN-γ	GCGTCATTGAATCACACCTG	TGAGCTCATTGAATGCTTGG	129 bp
TNF-α	GCTGAGCTCAAACCCTGGTA	CGGACTCCGCAAAGTCTAAG	118 bp
GATA3	CAGCTCTGGACTCTTCCCAC	GTTCACACACTCCCTGCCTT	112 bp
RORγt	TGAGGCCATTCAGTATGTGG	CTTCCATTGCTCCTGCTTTC	104 bp
β-actin	TGACAGGATGCAGAAGGAGA	CGCTCAGGAGGAGCAATG	75 bp

TABLE 2 | Antibodies for FACS staining of mouse cells.

Antibody	Parameter	Clone	Vendor
CD44	FITC	IM7	BD
RORγt	PE	Q31-378	BD
IFN-γ	PE-CF 594	XMG1.2	BD
GATA3	PE-CF 594	L50-823	BD
CD4	PE-Cy7	RM4-5	BD
Foxp3	Alexa Fluor® 647	MF23	BD
IL-17A	Alexa Fluor® 647	TC11-18H10.1	BioLegend
CD3	Alexa Fluor® 700	17A2	BioLegend
CD45	APC-Cy7	30-F11	BD
CD45R/B220	APC-Cy7	RA3-6B2	BD
CD62L	BV421	MEL-14	BD
IL-4	BV421	11B11	BD
ST2	BV421	DIH9	BioLegend
Ki67	BV605	16A8	BioLegend
CD127	BV605	A7R34	BioLegend
CD8α	BV605	53–6.7	BD
CD25	BV650	3C7	BD
7-AAD	—	—	BioLegend

stained in an appropriately diluted antibody solution for 1 h at 4 C. For intranuclear staining of transcription factors, cells were washed once after surface staining and permeabilized using Foxp3/Transcription Factor Staining Buffer Set (eBioscience) for 40 min on ice. The specific antibodies were diluted in Fixation/Permeabilization buffer (eBioscience) and incubated for 1 h at 4 C. Data were collected on a BD FACS Aria III flow cytometer (BD Biosciences) and analyzed using FlowJo (BD Biosciences) software. Antibody information is presented in **Table 2**.

Statistical Analysis

All data are expressed as Standard Error of the Mean (SEM) and are representative of three independent experiments. In the heatmap diagram, Z-score is measured in terms of standard deviations from the mean. The z-score is calculated by subtracting the population mean from the raw score, then dividing the difference by the population standard deviation. Groups were compared using unpaired Student's *t*-tests and one-way analysis of variance (ANOVA). Differences were considered to be statistically significant at $p < 0.05$.

RESULTS

Huangbai Liniment Ameliorates Dermatitis in AD Patient and a 1-Chloro-2,4-Dinitrobenzene-Induced AD Mouse Model

HB is a common dermatological medicinal product clinically prescribed to treat allergic contact dermatitis and eczema (Li and Gong, 2014; Yao and Zhao, 2014); however, its mechanism remains unclear. To evaluate the clinical efficacy and safety of HB in the treatment of AD, we locally applied hydropathic compresses of HB on lesioned skin of an AD patient. The AD patient presented with features of skin inflammation, including pruritus, erythema exudativum, and a mixed dermal inflammatory infiltrate around the head and neck region. The EASI score was around 13, and the lesion area was approximately 30–40% (**Table 3**). Several treatments had previously failed, and the patient had not received steroid or immunosuppressive therapy. The hydropathic compress of HB was administered to the lesioned skin region of the patient 3 times a day for 15 days. After the treatment, the AD patient showed marked improvement in AD clinical characteristics, including lessened random redness and limited itch symptoms (**Figure 1A**). These findings suggested that HB could be beneficial to patients with chronic skin inflammation who might be resistant to conventional treatments.

To investigate the underlying mechanism of HB on AD, a DNCB-induced AD mouse model was used (**Figure 1B**). Following DNCB treatment, the ears of the mice became red and swollen, and the dorsal skin showed severe erosion, erythema, and dryness. A variety of skin inflammation parameters and pathology were compared at the endpoint of the DNCB-induced AD mouse model. Interestingly, we found these atopic skin lesions were markedly attenuated by HB and 10-fold concentrated HB. The efficiency of HB was comparable with hydrocortisone, a common steroid medicine, which is widely used in the treatment of different dermatitis types (**Figure 1C**). Consistent with the photographic images of the skin lesions of the AD patient, the dorsal skin of the mice had obviously relieved edema, redness, and erosion following HB treatment (**Figure 1D**). HB also suppressed scratching behavior due to defused itching and skin lesions in the DNCB-induced AD mouse model group (**Figure 1E**, **Supplementary Figure S1A**) and ear

TABLE 3 | Baseline and clinical characteristics of patient with AD.

Characteristics	Patient
Age (years)	52
Gender	Male
Disease severity	EASI score:13
Lesion Area	Head and neck, 30–40%
Signs and symptoms	
Eczema	Significant redness; score 3
Infiltration/ papule	Infiltration occurred; score 3
Scales	Local mild desquamation, mainly fine scales; score 1
Exudation/crust	Extensive dermal edema; score 3
Pruritus	Frequent itching and scratching, affecting life and sleep, unbearable; score 3
Erosion	None; score 0
Family history	None

thickness was also significantly thinner than in the DNCB-induced AD mouse model group (**Figure 1F**, **Supplementary Figure S1B**). Together, these results demonstrate that HB profoundly ameliorated the clinical symptoms of AD in mice.

Huangbai Liniment Improves Symptoms of AD Through the Inhibition of Local Inflammatory Cytokines and Allergic Reactions

The improvements in the atopic symptoms of mice in the DNCB-induced AD mouse model group following HB and conventional hydrocortisone treatments were confirmed by morphological analysis of H&E-stained sections from damaged dorsal skin at the endpoint (**Figure 2A**). The DNCB-induced AD mouse model group exhibited the typical microscopic characteristics of dermatitis, such as hyperkeratosis, thickened epidermal tissue, and immune cell infiltration. However, in skin tissue from HB and 10-fold concentrated HB treated mice, the epidermal and dermal tissues were markedly thinner than tissue from untreated mice. Furthermore, the infiltration of inflammatory cells was also significantly reduced by HB treatment (**Figures 2B–E**). Accordingly, the pathology score, mRNA expression of inflammation, and the type 2 cytokine-related genes, including IL-1β, TNF-α, IL-17A, IFN-γ, IL-4, IL-13, and IL-33, were largely downregulated by HB treatment. In contrast, HB increased the expression of anti-inflammatory cytokine IL-10 (**Figure 2F**). Moreover, the mRNA expression of T_H2 and T_H17 classical transcription factors, GATA3 and RORγt, were suppressed in HB-treated mice compared with untreated mice (**Figures 2F,G**). Collectively, these data suggest that HB improves AD and largely rescues the excessive expression of cytokines critical for skin inflammation and the atopic response.

Huangbai Liniment Relieves Skin Inflammation by Modulating the Immune Balance of T_H17/T_{REG} Cells

To clarify the underlying mechanism of HB-based immunomodulation, we analyzed mouse splenocytes in different treatment groups using multi-color flow cytometry to characterize the phenotype of $CD4^+$ T cell subsets in DNCB-induced skin inflammation. We established gating strategies based on the key cytokines produced by each cell type to evaluate the different $CD4^+$ T cell subsets (**Figure 3A**). Intriguingly, we found altered frequencies of $CD4^+$ T cells in the different groups. Specifically, HB treatment reduced the frequency of $CD4^+$ T cells that were substantially reduced in the DNCB-induced AD mouse model group (**Figure 3B**), while no difference was observed in the frequencies of $CD8^+$ T cells (**Figure 3C**), which led to an increased CD4/CD8 ratio in the DNCB-induced AD mouse model group after HB treatment (**Figure 3D**). Furthermore, using the gating strategy of naïve ($CD25^-CD62L^+CD44low$), effector memory ($CD25^-CD62LlowCD44^+$), T_{REG} cells ($CD25^+Foxp3^+$) $CD4^+$T cells (**Figure 3A**), we noted a comparable frequency of naïve CD4 T cells (**Figure 3E**), but a significant reduction in effector memory CD4 T cells in HB-treated mice compared with untreated mice (**Figure 3F**). T_{REG} cells have been shown to control excessive T cell responses in inflammation, atopic responses, and AD-like inflammation (Ou et al., 2004; Fyhrquist et al., 2012). Interestingly, we also noticed that HB increased the frequency of T_{REG} cells in the DNCB-induced AD mouse model group, which partially constituted the underlying mechanisms of HB-induced improvement of skin inflammation in our DNCB-induced AD mouse model (**Figure 3H**).

Effector $CD4^+$ T cells are known to contribute to the pathology of AD. T_H1, T_H2, and T_H17 are examined by gating on $CD25^-CD4^+CD44^+$ T cells and through the expression of their signature cytokines (T_H1: IFN-γ^+CD44^+; T_H2: IL-4^+CD44^+; T_H17: IL-$17A^+CD44^+$). We found that HB treatment reduced the frequency of T_H17 and slightly suppressed the T_H1 subset in the DNCB-induced AD mouse model group (**Figures 3I,K**). Comparable frequencies were observed for T_H2 cells in untreated and HB-treated mice (**Figure 3J**). T_H17/T_{REG} imbalance is widely reported in autoimmune, inflammatory, and allergic diseases (Ma et al., 2014). We next analyzed the percentage of T_H17 and T_{REG} cells in different mouse groups. The ratio of T_H17/T_{REG} was compared between untreated and HB-treated mice, and a significant reduction in the ratio was noticed in HB-treated mice (**Figure 3L**). Taken together, we reveal that HB treatment plays an important role in controlling AD-like inflammation by potentiating T_{REG} cells while reducing T_H17 cells *in vivo*.

Huangbai Liniment Directly Promotes T_{REG} Cells and Inhibits Effector T Cell Subsets *in vitro*

To further evaluate whether HB can directly affect the differentiation of different T cell subsets, we *in vitro* polarized purified naïve $CD4^+$ T cells into T_H1, T_H2, T_H17, and T_{REG} cells and added HB to the cell culture (**Figure 4A**). Based on the cell survival data, HB did not affect the survival of naive $CD4^+$ T cells

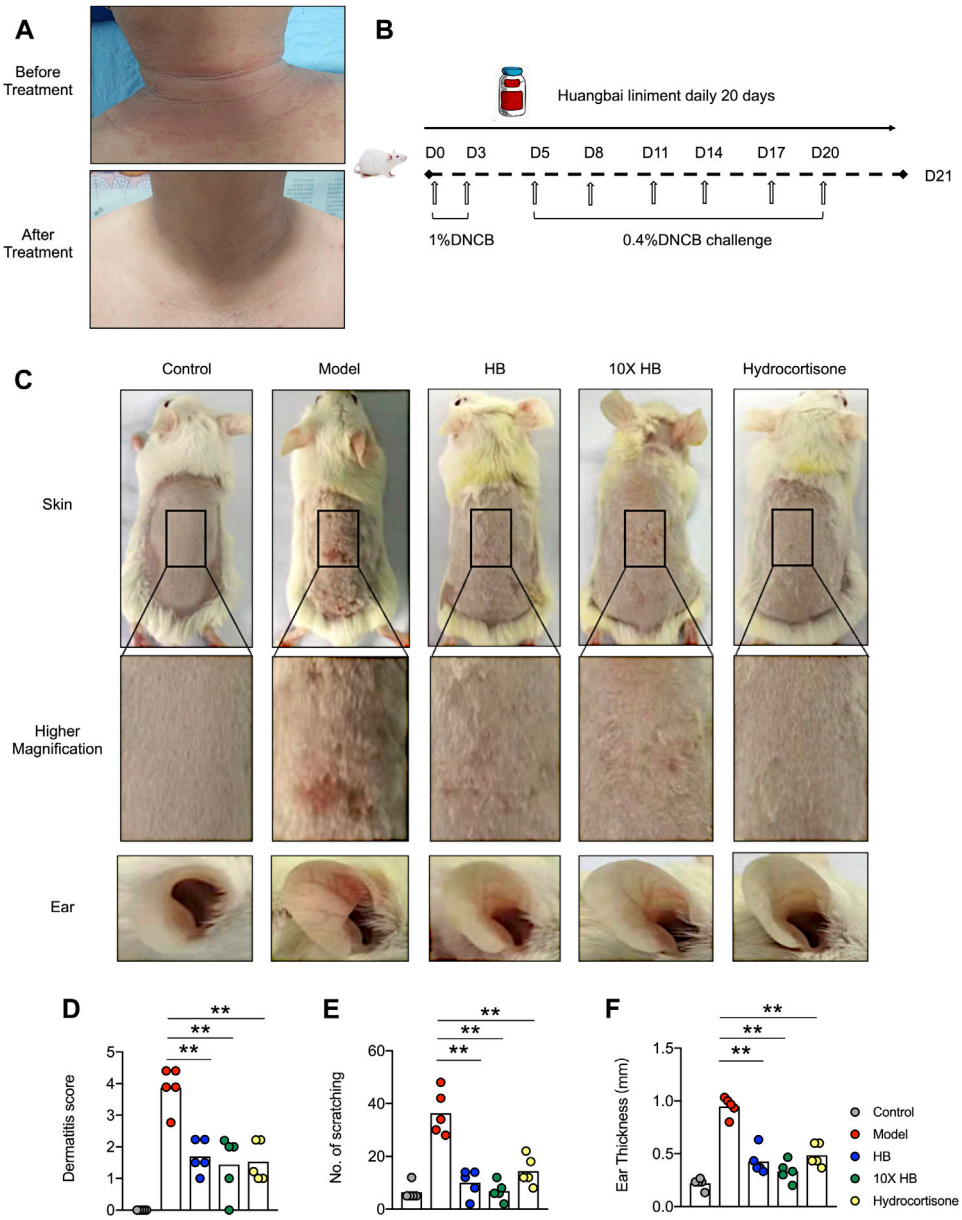


FIGURE 1 | HB ameliorates the symptoms of AD in clinical AD patient and mice. **(A)** HB was topically applied to a patient with AD 3 times a day for a continuous 15 days. Representative image of dermatitis on the patient before and after treatment with HB. After HB application, the eczema on the skin of the AD patient's neck was obviously ameliorated and the skin condition altered. **(B)** Schematic for (C–F). Mice were sensitized with 1% DNCB on dorsal skin at days 0 and 3 and then challenged with 0.4% DNCB on the dorsum of ears at 3 day intervals from days 5 to 20. HB, 10X HB (a 10-fold concentration of HB), hydrocortisone, or PBS was topically applied daily to the dorsal skin of the DNCB-induced mice. **(C)** Representative images of dorsal skins and ears in each group. The severity of AD was evaluated, and statistics are shown in **(D)**. **(E,F)** The amount of scratching and ear thicknesses were recorded at the endpoint, and statistics are shown. Each dot represents one mouse from one of three independent experiments, and bars indicate mean values. Statistical significance was determined by one-way ANOVA, $^{*}p < 0.05$, $^{**}p < 0.01$.

when cultured in T_H0 conditions for 48 h (**Figure 4B**). In line with the *in vivo* data, we found that HB directly suppressed the generation of T_H1, T_H2, and T_H17 cells and promoted T_{REG} differentiation in cell culture with altered cell proliferation indicated by Ki67 (**Figures 4C–F**). This mechanistic evidence indicates that HB directly promotes T_{REG} cells while largely inhibiting the generation of T_H1 and T_H17 cells.

DISCUSSION

AD is a chronic relapsing inflammatory skin disease characterized by an impaired immune response (Auriemma et al., 2013). The relapsing and persistent itch triggers a self-perpetuating itch-scratch cycle, which can have a significant impact on the patient's quality of life, and effective treatments are limited (Oetjen et al., 2017). HB

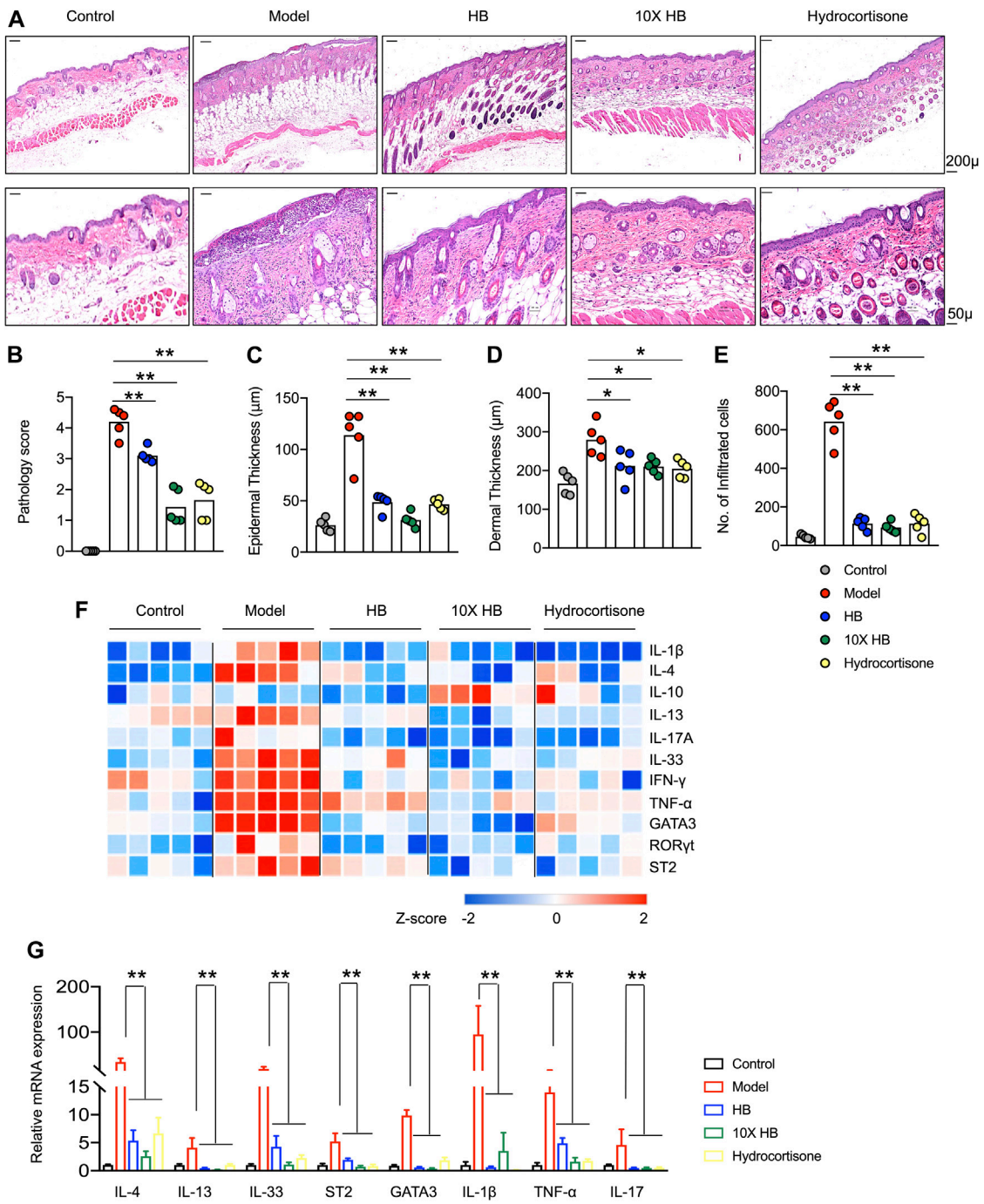


FIGURE 2 | HB reduces AD-like skin inflammation and the type 2 immune response induced by DNCB in mice. Mice were sensitized with 1% DNCB on dorsal skin at days 0 and 3 and then challenged with 0.4% DNCB on the dorsum of both ears at 3 day intervals from days 5 to 20. HB, 10X HB (a 10-fold concentration of HB), hydrocortisone, or PBS was topically applied daily to the dorsal skin of these DNCB-induced mice. **(A)** Histopathology of mouse dorsal skin tissue was evaluated by H&E staining (scale bars, 50 or 200 μM). Representative images in each group are shown. Pathology scores were blindly evaluated, and statistics are shown in **(B)**. **(C–E)** ImagePro10 software was used to measure and calculate epidermal thickness **(C)**, dermal thickness **(D)**, and number of infiltrated cells **(E)**. **(F)** Gene expression in skin tissue from five individual mice in each group, measured by qPCR and shown in a heatmap. Blue represents low expression, and red represents high expression of each inflammatory gene compared between three groups, with Row Z-Score (–2–2). **(G)** Type 2 cytokines and transcription factors in skin tissues were measured by qPCR. Each dot represents one mouse from one of three independent experiments, and bars indicate mean values. Statistical significance was determined by one-way ANOVA, $^{*}p < 0.05$, $^{**}p < 0.01$.

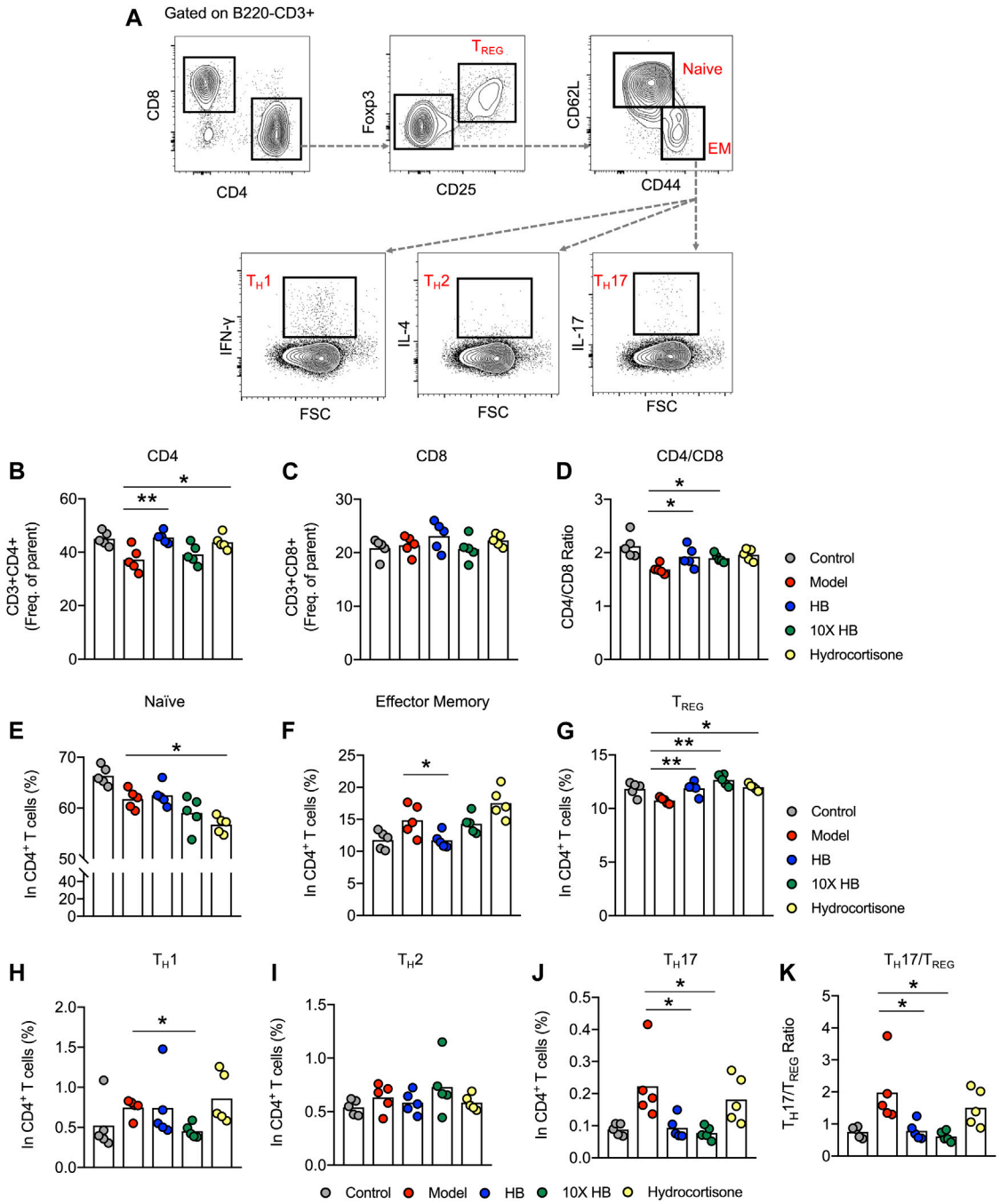


FIGURE 3 | HB relieves skin inflammation by downregulation of the T_H17/T_{REG} ratio. Mice were sensitized with 1% DNCB on dorsal skin at days 0 and 3, and then challenged with 0.4% DNCB on the dorsum of both ears at 3 day intervals from days 5 to 20. HB, 10X HB (a 10-fold concentration of HB), hydrocortisone, or PBS, was topically applied daily to the dorsal skin of the DNCB-induced mice. Splenocytes of AD model mice treated with PBS, HB, 10X HB, and hydrocortisone were isolated and stained using immunofluorescence antibodies. **(A)** Gating strategy for different T cell subsets. **(B,C)** Statistical analysis of the frequencies of $B220^{-}CD3^{+}CD4^{+}$ T cells **(B)** and $B220^{-}CD3^{+}CD8^{+}$ T cells **(C)** in different groups. **(D)** CD4/CD8 ratio. **(E–J)** Statistical analysis showing the differences in the frequencies of naïve **(E)** and effector memory **(F)** CD4 T cells and T_{REG} **(G)**, T_H1 **(H)**, T_H2 **(I)**, and T_H17 **(J)** cells. **(K)** The T_H17/T_{REG} ratio was calculated to show the differences in different groups. Each dot represents one mouse from one of three independent experiments, and bars indicate mean values. Statistical significance was determined by one-way ANOVA, $^{*}p < 0.05$, $^{**}p < 0.01$.

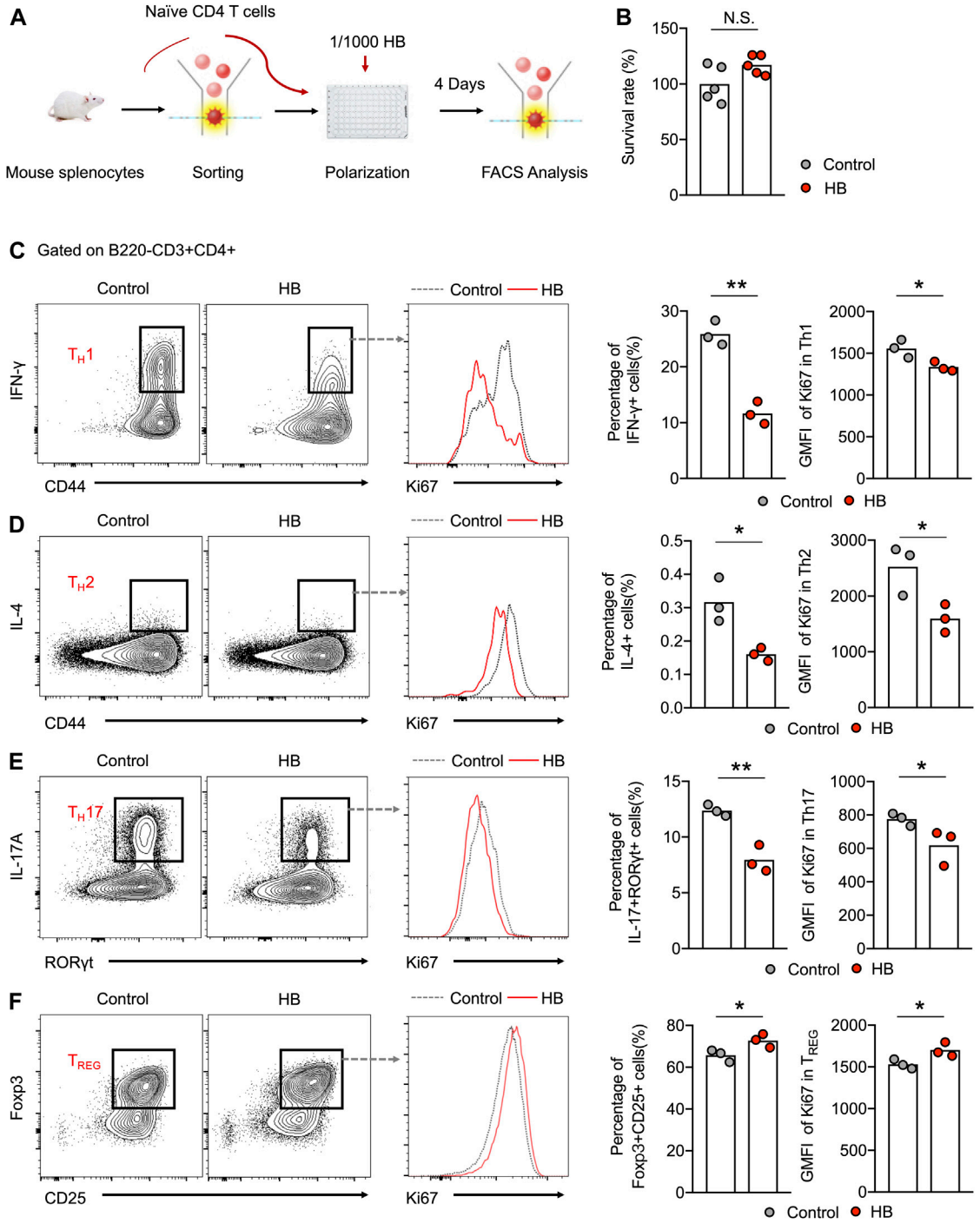


FIGURE 4 | HB directly potentiates regulatory T cell activation and depresses inflammatory cells *in vitro*. **(A)** Schematic *in vitro* experiments. Naïve CD4 T cells, derived from mouse splenocytes, were sorted by flow cytometry and polarized under different culture conditions with or without 1/1000 HB for 4 days. **(B)** Survival analysis of HB for naïve CD4 cells was performed using an MTT assay after 48 h of culture with or without 1/1000 H B. **(C–F)** Representative FACS plots and statistical analysis of *in vitro* polarized T_H1 **(C)**, T_H2 **(D)**, T_H17 **(E)**, and T_{REG} **(F)** cells with or without HB treatment. Histogram plots and statistical analysis indicated the changes in Ki67 in different CD4 subsets after HB treatment. Each dot represents one mouse from one of three independent experiments, and bars indicate mean values. Statistical significance was determined by Student's *t*-test, $^*p < 0.05$, $^{**}p < 0.01$.

was reported to have therapeutic effects on different types of inflammation in patients, especially in those patients with eczema (Li and Gong, 2014; Yao and Zhao, 2014; Li-yun, 2016). However, it is unknown whether HB could be used to treat skin inflammation, such as AD, and if so, what are the underlying mechanisms of HB-mediated anti-inflammatory effects. In this study, we first examined the therapeutic potential of HB in a patient with AD and found that HB profoundly mitigated skin inflammation in the patient. Further, we investigated the therapeutic effects of HB on DNCB-induced AD in mice and examined its immune-modulative effects on $CD4^+$ T cell subsets. In mice with DNCB-induced AD, HB markedly alleviated skin inflammation and inhibited proinflammatory immune responses mediated by Th1 and Th17 cells. This evidence suggests that HB effectively mitigates skin inflammation in mice with DNCB-induced AD by restoring the balance of the $CD4^+$ T cell response. Our study also provides insights for the future development and application of HB-based immune-modulation of AD.

Type 2 cytokines, such as IL-4, IL-5, and IL-13 coordinate inflammatory and atopic responses in AD (Bieber, 2010). In our study, we found that HB markedly suppressed mRNA expression of IL-4, IL-13, and the transcription factor GATA3 known to drive immune cells to produce a type 2 immune response in dermatitis skin tissue. IL-33 and its receptor ST2 are strongly associated with the development of AD disease triggered by allergen exposure, irritants, scratching, and the bacterial and viral infections seen in this condition (Savinko et al., 2012). We noticed that that HB inhibits DNCB-induced IL-33 and ST2 mRNA levels in dermatitis skin tissue. Because ST2 is also expressed on innate lymphoid cells, such as ILC2 cells that are known to synergize with T_H2 cells to induce type 2 inflammation (Artis and Spits, 2015; Eberl et al., 2015; Zhou et al., 2021), it will be interesting in future studies to know whether HB could directly regulate ILC2s to control skin inflammation in AD mouse models and patients. IFN-γ mRNA and protein were highly expressed in eczematous skin in the vast percentage of AD patients (Leung et al., 2011; Weidinger and Novak, 2016). More importantly, the *in situ* expression of IFN-γ decreased with the successful treatment of AD patients (Grewe et al., 1998). We also found that HB could largely reduce the mRNA expression of IFN-γ in skin tissue from mice with DNCB-induced AD. Together, our data indicate that HB suppresses the overall production of inflammatory cytokines in the skin of mice with DNCB-induced AD-like inflammation.

An imbalanced immune response is one of the major causes of AD. An excessive accumulation of activated T lymphocytes in the skin drives severe inflammation and induces destruction of the skin tissue integrity. Several effector subsets of CD4 T cells have been identified as potent regulators of AD pathogenesis, including T_H1, T_H2, T_H17, and T_{REG} cells (Grewe et al., 1998; Martel et al., 2016). We found that HB treatment restored the CD4/CD8 T cell ratio in mice with DNCB-induced AD-like inflammation. Our data also suggested that DNCB-induced AD-like inflammation in mice was associated with reduced naïve cells and increased effector memory $CD4^+$ T cells, and this imbalance was largely rescued after HB treatment. Activated T_H2 cells prominently mediated the development of AD-like skin inflammation, manifesting as enhanced IgE-mediated sensitization and eosinophil infiltration (Bieber, 2010). Other effector T cell subsets, such as proinflammatory cells T_H1, T_H9, T_H17, and T_H22, produced a large number of proinflammatory cytokines, including IFN-γ, IL-9, IL-17, and IL-22, driving the development of AD. This promotion of effector $CD4^+$ T cells was often associated with a decline in the presence of T_{REG} cells that are essential for immune tolerance and control of inflammation in AD (Auriemma et al., 2013). Our study further revealed that HB could potentiate T_{REG} cells while suppressing other effector $CD4^+$ T cell subsets both *in vivo* and *in vitro*, which at least partially constituted the mechanisms of HB-mediated improvement in AD.

Th17 cells are critical for the development of AD (Koga et al., 2008). The frequency of IL-17-producing $CD4^+$T cells in AD patients is increased and associated with AD severity (Esaki et al., 2016). In addition, IL-17 was reported to trigger the production of IL-4 by T_H2 cells (Milovanovic et al., 2010). Mice lacking IL-17A exhibited reduced dermatitis together with less IL-4 and IgE production (Milovanovic et al., 2010). In line with these reports, our study showed that the frequency of Th17 cells was drastically reduced by HB *in vitro* and *in vivo*. The local expression of Th17-related cytokines and transcription factors were also shown to be suppressed by qPCR. These findings support the notion that HB directly regulates the differentiation of T_H17 cells, could have immune-modulative effects in other inflammatory diseases and might be beneficial in controlling lesioned skin of sclerosis (Ahmed et al., 2019) or psoriasis, which are largely IL-17-driven diseases (Noda et al., 2015).

Interestingly, T_H17 and T follicular helper (T_{FH}) cells produce IL-21, which promotes T_H17 cell differentiation (Ouyang et al., 2008; Gong et al., 2019), and IL-21 is increased in AD lesions in humans and mice (Jin et al., 2009). Moreover, IL-21 suppresses the production of IgE and possesses anti-inflammatory effects (Ozaki et al., 2002). The administration of IL-21 not only reduces the frequency of T_H2 cells but also suppresses the secretion of T_H2-associated cytokines, such as IL-4, IL-5, and IL-13 (Lin et al., 2015). Additionally, T_{FH} cells predominantly produce IL-2, IL-4 and IL-21 in B cell follicles and closely regulate antibody class-switching in severe inflammatory and allergic diseases, including AD, asthma, and COVID-19-induced airway inflammation (Yao et al., 2018; Crotty, 2019; Gong et al., 2019; Papillion et al., 2019; Yao et al., 2019; Zhou et al., 2019; Gong et al., 2020). Further, circulating T_{FH} cells are associated with disease severity in children with AD (Gong et al., 2019; Marschall et al., 2021). These accumulating findings indicate the importance of T_{FH} cells in the context of AD and other inflammatory diseases. It is thus of interest to know whether HB treatment also regulates T_{FH} cells in the context of AD in the DNCB-induced AD mouse model and patients.

In contrast to the reduction in proinflammatory $CD4^+$ T cell subsets, HB enhanced T_{REG} cells *in vivo* and *in vitro*. In addition to the T_H1/T_H2 paradigm, the imbalance of T_{REG} and T_H17 cells is another cardinal mechanism in AD pathogenesis (Ma et al., 2014). Our data importantly showed that HB potently restored this imbalance in mice with DNCB-induced AD. Future studies should further demonstrate the potential molecular insights

underlying HB-mediated direct regulation of T_{REG} cells and other effector $CD4^+$ T cell subsets, including but not limited to transcriptional regulation, epigenetic changes, and metabolic alterations.

In summary, our findings indicate that HB treatment improves AD in patients and can ameliorate skin inflammation in mice with DNCB-induced AD. HB profoundly reduced the expression of proinflammatory cytokines, including IL-1β, IL-4, IFN-γ, IL-13, and IL-17, and increased the expression of anti-inflammatory cytokine IL-10. Furthermore, we demonstrated that HB reduced skin inflammation and inhibited T_H17 cells while promoting T_{REG} cells. In line with *in vivo* data, HB directly inhibited T_H1, T_H2, and T_H17 differentiation and promoted T_{REG} polarization *in vitro*. Altogether, this study provides mechanistic insights into HB-mediated amelioration of AD through the restoration of $CD4^+$ T cells and sheds light on the broad use of HB in treating inflammatory diseases.

DATA AVAILABILITY STATEMENT

The raw data supporting the conclusions of this article will be made available by the authors, without undue reservation.

ETHICS STATEMENT

The studies involving human participants were reviewed and approved by the Ethics committee of Beijing University of Chinese Medicine (NO. ECSL-BDY-2012-45-01). The patients/participants provided their written informed consent to participate in this study. The animal study was reviewed and approved by the Animal Experimentation Ethics committee of Shandong Analysis and Test Center (NO. ECAESDATC-2018-010). Written informed consent was obtained from the individual(s) for the publication of any potentially identifiable images or data included in this article.

AUTHOR CONTRIBUTIONS

TZ conceived and oversaw the study. TZ and PZ designed the experiments. TZ, MF, and AX performed the experiments. TZ, YW, JF, PZ, and XS analyzed the data. CQ and DY participated in scientific discussions. TZ and PZ wrote the manuscript and prepared the figures. PZ revised the manuscript. TZ led the submission.

FUNDING

This project was supported by the National Natural Science Foundation of China (81970759, 82101920, 81803539), Key Technology Research and Development Program of Shandong (2018YYSP022).

ACKNOWLEDGMENTS

We thank Xuding Sun and Jizhen Zhao from Shandong Hanfang Pharmaceutical Co. Ltd. for supplying Huangbai Liniment.

SUPPLEMENTARY MATERIAL

The Supplementary Material for this article can be found online at: https://www.frontiersin.org/articles/10.3389/fphar.2021.726035/full#supplementary-material

REFERENCES

Ahmed, S., Misra, D. P., and Agarwal, V. (2019). Interleukin-17 Pathways in Systemic Sclerosis-Associated Fibrosis. *Rheumatol. Int.* 39 (7), 1135–1143. doi:10.1007/s00296-019-04317-5

Artis, D., and Spits, H. (2015). The Biology of Innate Lymphoid Cells. *Nature* 517 (7534), 293–301. doi:10.1038/nature14189

Auriemma, M., Vianale, G., Amerio, P., and Reale, M. (2013). Cytokines and T Cells in Atopic Dermatitis. *Eur. Cytokine Netw.* 24 (1), 37–44. doi:10.1684/ecn.2013.0333

Bieber, T. (2010). Atopic Dermatitis. *Ann. Dermatol.* 22 (2), 125–137. doi:10.5021/ad.2010.22.2.125

Biedermann, T., Skabytska, Y., Kaesler, S., and Volz, T. (2015). Regulation of T Cell Immunity in Atopic Dermatitis by Microbes: The Yin and Yang of Cutaneous Inflammation. *Front. Immunol.* 6, 353. doi:10.3389/fimmu.2015.00353

Crotty, S. (2019). T Follicular Helper Cell Biology: a Decade of Discovery and Diseases. *Immunity* 50 (5), 1132–1148. doi:10.1016/j.immuni.2019.04.011

Dainichi, T., Kitoh, A., Otsuka, A., Nakajima, S., Nomura, T., Kaplan, D. H., et al. (2018). The Epithelial Immune Microenvironment (EIME) in Atopic Dermatitis and Psoriasis. *Nat. Immunol.* 19 (12), 1286–1298. doi:10.1038/s41590-018-0256-2

Eberl, G., Colonna, M., Di Santo, J. P., and McKenzie, A. N. (2015). Innate Lymphoid Cells. Innate Lymphoid Cells: a New Paradigm in Immunology. *Science* 348 (6237), aaa6566. doi:10.1126/science.aaa6566

Esaki, H., Brunner, P. M., Renert-Yuval, Y., Czarnowicki, T., Huynh, T., Tran, G., et al. (2016). Early-onset Pediatric Atopic Dermatitis Is TH2 but Also TH17 Polarized in Skin. *J. Allergy Clin. Immunol.* 138 (6), 1639–1651. doi:10.1016/j.jaci.2016.07.013

Fyhrquist, N., Lehtimäki, S., Lahl, K., Savinko, T., Lappeteläinen, A. M., Sparwasser, T., et al. (2012). Foxp3+ Cells Control Th2 Responses in a Murine Model of Atopic Dermatitis. *J. Invest. Dermatol.* 132 (6), 1672–1680. doi:10.1038/jid.2012.40

Gittler, J. K., Shemer, A., Suárez-Fariñas, M., Fuentes-Duculan, J., Gulewicz, K. J., Wang, C. Q., et al. (2012). Progressive Activation of T(H)2/T(H)22 Cytokines and Selective Epidermal Proteins Characterizes Acute and Chronic Atopic Dermatitis. *J. Allergy Clin. Immunol.* 130 (6), 1344–1354. doi:10.1016/j.jaci.2012.07.012

Gong, F., Zheng, T., Zhou, P., et al. (2019). T Follicular Helper Cell Subsets and the Associated Cytokine IL-21 in the Pathogenesis and Therapy of Asthma. *Front. Immunol.* 10, 2918. doi:10.3389/fimmu.2019.02918

Gong, F., Dai, Y., Zheng, T., Cheng, L., Zhao, D., and Wang, H. (2020). Peripheral CD4+ T Cell Subsets and Antibody Response in COVID-19 Convalescent Individuals. *J. Clin. Invest.* 130 (12), 6588–6599. doi:10.1172/JCI141054

Grewe, M., Schopf, E., Bruijnzeel-Koomen, C. A., Thepen, T., Langeveld-Wildschut, A. G., Ruzicka, T., et al. (1998). A Role for Th1 and Th2 Cells

in the Immunopathogenesis of Atopic Dermatitis. *Immunol. Today* 19 (8), 359–361. doi:10.1016/s0167-5699(98)01285-7

Imai, Y., Yasuda, K., Sakaguchi, Y., Haneda, T., Mizutani, H., Yoshimoto, T., et al. (2013). Skin-specific Expression of IL-33 Activates Group 2 Innate Lymphoid Cells and Elicits Atopic Dermatitis-like Inflammation in Mice. *Proc. Natl. Acad. Sci. U S A.* 110 (34), 13921–13926. doi:10.1073/pnas.1307321110

Jin, H., Oyoshi, M. K., Le, Y., Bianchi, T., Koduru, S., Mathias, C. B., et al. (2009). IL-21R Is Essential for Epicutaneous Sensitization and Allergic Skin Inflammation in Humans and Mice. *J. Clin. Invest.* 119 (1), 47–60. doi:10.1172/JCI32310

Li, H., and Gong, H. (2014). Clinical Study of Fufang Huangbai Liquid in Treating Acute and Sub-acute Aczema. *J. Nanjing University TCM* 30 (5), 492–494.

Kim, B. S., Wang, K., Siracusa, M. C., Saenz, S. A., Brestoff, J. R., Monticelli, L. A., et al. (2014). Basophils Promote Innate Lymphoid Cell Responses in Inflamed Skin. *J. Immunol.* 193 (7), 3717–3725. doi:10.4049/jimmunol.1401307

Kim, I. S., Lee, S. H., Kwon, Y. M., Adhikari, B., Kim, J. A., Yu, D. Y., et al. (2019). Oral Administration of β-Glucan and Lactobacillus Plantarum Alleviates Atopic Dermatitis-like Symptoms. *J. Microbiol. Biotechnol.* 29 (11), 1693–1706. doi:10.4014/jmb.1907.07011

KimKim, B. S., Siracusa, M. C., Siracusa, S. A., Noti, M., Monticelli, L. A., Sonnenberg, G. F., et al. (2013). TSLP Elicits IL-33-independent Innate Lymphoid Cell Responses to Promote Skin Inflammation. *Sci. Transl Med.* 5 (170), 170ra16. doi:10.1126/scitranslmed.3005374

Koga, C., Kabashima, K., Shiraishi, N., Kobayashi, M., and Tokura, Y. (2008). Possible Pathogenic Role of Th17 Cells for Atopic Dermatitis. *J. Invest. Dermatol.* 128 (11), 2625–2630. doi:10.1038/jid.2008.111

Lei, H., Schmidt-Bleek, K., Dienelt, A., Reinke, P., and Volk, H. D. (2015). Regulatory T Cell-Mediated Anti-inflammatory Effects Promote Successful Tissue Repair in Both Indirect and Direct Manners. *Front. Pharmacol.* 6, 184. doi:10.3389/fphar.2015.00184

Leung, D. Y., Boguniewicz, M., Howell, M. D., Nomura, I., and Hamid, Q. A. (2004). New Insights into Atopic Dermatitis. *J. Clin. Invest.* 113 (5), 651–657. doi:10.1172/JCI21060

Leung, D. Y., Gao, P. S., Grigoryev, D. N., Rafaels, N. M., Streib, J. E., Howell, M. D., et al. (2011). Human Atopic Dermatitis Complicated by Eczema Herpeticum Is Associated with Abnormalities in IFN-γ Response. *J. Allergy Clin. Immunol.* 127 (4), 965–5. doi:10.1016/j.jaci.2011.02.010

Li-yun, X. X. (2016). Clinical Efficacy of Compound Fluid of Cortex Phellodendri in the Treatment of Traumatic Infections. *Chin. J. New Drugs* 25 (20), 2349–2352.

Lin, P. Y., Jen, H. Y., Chiang, B. L., Sheu, F., and Chuang, Y. H. (2015). Interleukin-21 Suppresses the Differentiation and Functions of T Helper 2 Cells. *Immunology* 144 (4), 668–676. doi:10.1111/imm.12419

Liu, Y., Li, Y., Du, Y., Huang, T., and Zhu, C. (2020). Multicenter Clinical Trials Analyzing Efficacy and Safety of Topical Cortex Phellodendri Compound Fluid in Treatment of Diabetic Foot Ulcers. *Med. Sci. Monit.* 26, e923424. doi:10.12659/MSM.923424

Looman, K. I. M., van Meel, E. R., Grosserichter-Wagener, C., Vissers, F. J. M., Klingenberg, J. H., de Jong, N. W., et al. (2020). Associations of Th2, Th17, Treg Cells, and IgA+ Memory B Cells with Atopic Disease in Children: The Generation R Study. *Allergy* 75 (1), 178–187. doi:10.1111/all.14010

Ma, L., Xue, H. B., Guan, X. H., Shu, C. M., Wang, F., Zhang, J. H., et al. (2014). The Imbalance of Th17 Cells and CD4(+) CD25(high) Foxp3(+) Treg Cells in Patients with Atopic Dermatitis. *J. Eur. Acad. Dermatol. Venereol.* 28 (8), 1079–1086. doi:10.1111/jdv.12288

Marschall, P., Wei, R., Segaud, J., Yao, W., Hener, P., German, B. F., et al. (2021). Dual function of Langerhans cells in skin TSLP-promoted TFH differentiation in mouse atopic dermatitis. *J Allergy Clin. Immunol.* 147 (5), 1778–1794. doi:10.1016/j.jaci.2020.10.006

Martel, B. C., Dyring-Andersen, B., Skov, L., Thestrup-Pedersen, K., Skov, S., Skak, K., et al. (2016). Different Cytokine Profiles of Skin-Derived T Cell Cultures from Patients with Atopic Dermatitis and Psoriasis. *Inflamm. Res.* 65 (4), 265–272. doi:10.1007/s00011-015-0912-z

Milovanovic, M., Drozdenko, G., Weise, C., Babina, M., and Worm, M. (2010). Interleukin-17A Promotes IgE Production in Human B Cells. *J. Invest. Dermatol.* 130 (11), 2621–2628. doi:10.1038/jid.2010.175

Nguyen, H. L., Anderson, K. R., and Tollefson, M. M. (2019). New and Emerging Therapies for Pediatric Atopic Dermatitis. *Paediatr. Drugs* 21 (4), 239–260. doi:10.1007/s40272-019-00342-w

Noda, S., Suárez-Fariñas, M., Ungar, B., Kim, S. J., de Guzman Strong, C., Xu, H., et al. (2015). The Asian Atopic Dermatitis Phenotype Combines Features of Atopic Dermatitis and Psoriasis with Increased TH17 Polarization. *J. Allergy Clin. Immunol.* 136 (5), 1254–1264. doi:10.1016/j.jaci.2015.08.015

Nograles, K. E., Zaba, L. C., Shemer, A., Fuentes-Duculan, J., Cardinale, I., Kikuchi, T., et al. (2009). IL-22-producing "T22" T Cells Account for Upregulated IL-22 in Atopic Dermatitis Despite Reduced IL-17-producing TH17 T Cells. *J. Allergy Clin. Immunol.* 123 (6), 1244–e2. doi:10.1016/j.jaci.2009.03.041

Oetjen, L. K., Mack, M. R., Feng, J., Whelan, T. M., Niu, H., Guo, C. J., et al. (2017). Sensory Neurons Co-opt Classical Immune Signaling Pathways to Mediate Chronic Itch. *Cell* 171 (1), 217–e13. doi:10.1016/j.cell.2017.08.006

Ou, L. S., Goleva, E., Hall, C., and Leung, D. Y. (2004). T Regulatory Cells in Atopic Dermatitis and Subversion of Their Activity by Superantigens. *J. Allergy Clin. Immunol.* 113 (4), 756–763. doi:10.1016/j.jaci.2004.01.772

Ouyang, W., Kolls, J. K., and Zheng, Y. (2008). The Biological Functions of T Helper 17 Cell Effector Cytokines in Inflammation. *Immunity* 28 (4), 454–467. doi:10.1016/j.immuni.2008.03.004

Ozaki, K., Spolski, R., Feng, C. G., Qi, C. F., Cheng, J., Sher, A., et al. (2002). A Critical Role for IL-21 in Regulating Immunoglobulin Production. *Science* 298 (5598), 1630–1634. doi:10.1126/science.1077002

Papillion, A., Powell, M. D., Chisolm, D. A., Bachus, H., Fuller, M. J., Weinmann, A. S., et al. (2019). Inhibition of IL-2 Responsiveness by IL-6 Is Required for the Generation of GC-TFH Cells. *Sci. Immunol.* 4 (39). doi:10.1126/sciimmunol.aaw7636

Rostaher, A., Fischer, N. M., Urwyler, A., and Favrot, C. (2018). Circulating CD4(+)CD25(+)Foxp3(+) T Regulatory Cell Levels in an Experimental Model of Canine Atopic Dermatitis. *Vet. Dermatol.* 29 (6), 511–e171. doi:10.1111/vde.12693

Savinko, T., Matikainen, S., Saarialho-Kere, U., Lehto, M., Wang, G., Lehtimäki, S., et al. (2012). IL-33 and ST2 in Atopic Dermatitis: Expression Profiles and Modulation by Triggering Factors. *J. Invest. Dermatol.* 132 (5), 1392–1400. doi:10.1038/jid.2011.446

Suárez-Fariñas, M., Tintle, S. J., Shemer, A., Chiricozzi, A., Nograles, K., Cardinale, I., et al. (2011). Nonlesional Atopic Dermatitis Skin Is Characterized by Broad Terminal Differentiation Defects and Variable Immune Abnormalities. *J. Allergy Clin. Immunol.* 127 (4), 954–964 e14. doi:10.1016/j.jaci.2010.12.1124

Weidinger, S., and Novak, N. (2016). Atopic Dermatitis. *Lancet* 387 (10023), 1109–1122. doi:10.1016/S0140-6736(15)00149-X

Xiao, J., He, W., Li, J., and Xia, B. (2009). Investigation on Therapeutic Mechanism of Compound Huangbai Solution in TNBS-Induced Colitis in Rats. *Gastroenterology* 14 (8), 473–477. doi:10.3969/j.issn.1008-7125.2009.08.007

Yao, J., and Zhao, X. (2014). Advance in Clinical Application of Compound Phellodendron Liquid. *Chin. J. New Drugs* 23 (3), 308–337.

Yao, Y., Chen, C. L., Wang, N., Wang, Z. C., Ma, J., Zhu, R. F., et al. (2018). Correlation of Allergen-specific T Follicular Helper Cell Counts with Specific IgE Levels and Efficacy of Allergen Immunotherapy. *J. Allergy Clin. Immunol.* 142 (1), 321–e10. doi:10.1016/j.jaci.2018.03.008

Yao, Y., Wang, Z. C., Wang, N., Zhou, P. C., Chen, C. L., Song, J., et al. (2019). Allergen Immunotherapy Improves Defective Follicular Regulatory T Cells in Patients with Allergic Rhinitis. *J. Allergy Clin. Immunol.* 144 (1), 118–128. doi:10.1016/j.jaci.2019.02.008

Zhang, J., Zhou, R., Xiang, C., Jia, Q., Wu, H., and Yang, H. (2020). Huangbai Liniment Accelerated Wound Healing by Activating Nrf2 Signaling in Diabetes. *Oxid Med. Cel Longev* 2020, 4951820. doi:10.1155/2020/4951820

Zhou, P., Liang, K., and Yu, D. (2019). Germinal center TFH Cells: T(w)o Be or Not T(w)o Be, IL-6 Is the Answer. *Sci. Immunol.* 4 (39). doi:10.1126/sciimmunol.aay7668

Zhou, P., Zheng, T., Li, Y., Zhang, X., Feng, J., Wei, Y., et al. (2021). Chlorinated Flame-Retardant Dechlorane 602 Potentiates Type 2 Innate Lymphoid Cells and Exacerbates Airway Inflammation. *Environ. Sci. Technol.* 55 (2), 1099–1109. doi:10.1021/acs.est.0c03758

Conflict of Interest: The authors disclose that this project is partially funded by Shandong Hanfang Pharmaceutical Co. Ltd., who also provided Huangbai Liniment (Chinese Medicine Character: Z910950097) for this research. The authors promise that the authenticity and conclusions of this study are not affected by the funding source. CQ was also a paid consultant for Shandong Hanfang Pharmaceutical Co. Ltd.

Publisher's Note: All claims expressed in this article are solely those of the authors and do not necessarily represent those of their affiliated organizations, or those of the publisher, the editors and the reviewers. Any product that may be evaluated in this article, or claim that may be made by its manufacturer, is not guaranteed or endorsed by the publisher.

Copyright © 2021 Zheng, Fan, Wei, Feng, Zhou, Sun, Xue, Qin and Yu. This is an open-access article distributed under the terms of the Creative Commons Attribution License (CC BY). The use, distribution or reproduction in other forums is permitted, provided the original author(s) and the copyright owner(s) are credited and that the original publication in this journal is cited, in accordance with accepted academic practice. No use, distribution or reproduction is permitted which does not comply with these terms.

frontiers in Pharmacology

ORIGINAL RESEARCH
published: 08 September 2021
doi: 10.3389/fphar.2021.754976

Ferulic Acid Ameliorates Hepatic Inflammation and Fibrotic Liver Injury by Inhibiting PTP1B Activity and Subsequent Promoting AMPK Phosphorylation

*Jianzhi Wu[1†], Xiaoyong Xue[1†], Guifang Fan[2], Yiqing Gu[2], Fei Zhou[1], Qi Zheng[2], Runping Liu[2], Yajing Li[1], Boning Ma[1], Shuo Li[2], Guangrui Huang[1], Lin Ma[1] and Xiaojiaoyang Li[1]**

[1]School of Life Sciences, Beijing University of Chinese Medicine, Beijing, China, [2]School of Chinese Materia Medica, Beijing University of Chinese Medicine, Beijing, China

OPEN ACCESS

Edited by:
Dahui Liu,
Hubei University of Chinese Medicine, China

Reviewed by:
Tianhao Zhou,
Indiana University Bloomington, United States
Yun Zhang,
Biology Institute of Shandong Academy of Sciences, China

***Correspondence:**
Xiaojiaoyang Li
xiaojiaoyang.li@bucm.edu.cn

[†]These authors have contributed equally to this work

Specialty section:
This article was submitted to Inflammation Pharmacology, a section of the journal Frontiers in Pharmacology

Received: 07 August 2021
Accepted: 27 August 2021
Published: 08 September 2021

Citation:
Wu J, Xue X, Fan G, Gu Y, Zhou F, Zheng Q, Liu R, Li Y, Ma B, Li S, Huang G, Ma L and Li X (2021) Ferulic Acid Ameliorates Hepatic Inflammation and Fibrotic Liver Injury by Inhibiting PTP1B Activity and Subsequent Promoting AMPK Phosphorylation. Front. Pharmacol. 12:754976. doi: 10.3389/fphar.2021.754976

Chronic inflammation in response to persistent exogenous stimuli or damage results in liver fibrosis, which subsequently progresses into malignant liver diseases with high morbidity and mortality. Ferulic acid (FA) is a phenolic acid widely isolated from abundant plants and exhibits multiple biological activities including anti-oxidant, anti-inflammation and enhancement of immune responses. Adenosine monophosphate-activated protein kinase (AMPK) functions as a critical energy sensor and is regulated through the phosphorylation of liver kinases like LKB1 or dephosphorylation by protein tyrosine phosphatases (PTPs). However, the role of FA in carbon tetrachloride (CCl_4)-induced chronic inflammation and liver fibrosis and AMPK activation has not been elucidated. Here we reported that FA ameliorated CCl_4-induced inflammation and fibrotic liver damage in mice as indicated by reduced levels of serum liver function enzyme activities and decreased expression of genes and proteins associated with fibrogenesis. Additionally, FA inhibited hepatic oxidative stress, macrophage activation and HSC activation via AMPK phosphorylation in different liver cells. Mechanically, without the participation of LKB1, FA-induced anti-inflammatory and anti-fibrotic effects were abrogated by a specific AMPK inhibitor, compound C. Combining with the results of molecular docking, surface plasmon resonance and co-immunoprecipitation assays, we further demonstrated that FA directly bound to and inhibited PTP1B, an enzyme responsible for dephosphorylating key protein kinases, and eventually leading to the phosphorylation of AMPK. In summary, our results indicated that FA alleviated oxidative stress, hepatic inflammation and fibrotic response in livers through PTP1B-AMPK signaling pathways. Taken together, we provide novel insights into the potential of FA as a natural product-derived therapeutic agent for the treatment of fibrotic liver injury.

Keywords: ferulic acid, AMPK, PTP1B, oxidative stress, inflammation, liver fibrosis

Abbreviations: ALT, alanine aminotransferase; AST, aspartate aminotransferase; CC, compound C; CCl4, carbon tetrachloride; COL1, collagen 1; FN, fibronectin; TGF-β, transforming growth factor-beta; LPS, lipopolysaccharide; MPH, mouse primary hepatocyte; FA, ferulic acid; MF, methyl ferulate; PTP1B, protein tyrosine phosphatase 1B; AMPK, adenosine monophosphate-activated protein kinase; LKB1, liver kinase B1; ERK1/2, extracellular-signal-regulated protein kinase 1/2; HSC, hepatic stellate cell; ECM, extracellular matrix; SPR, surface plasmon resonance; α-SMA, alpha-smooth muscle actin; NOX2, nicotinamide adenine dinucleotide phosphate oxidase-2; NF-κB, nuclear factor kappa B; SMAD, small mothers against decapentaplegic.

INTRODUCTION

Liver fibrosis is a dynamic process leading to inflammatory cascades, excessive deposition of extracellular matrix (ECM) and the formation of fibrous scars. With persistent inflammatory stimuli or exogenous damage, liver fibrosis is becoming a leading cause of cirrhosis and hepatocellular carcinoma with high morbidity and mortality (Kisseleva, 2017). Underlying etiologies in fibrotic liver injury comprise but not limited to viral infection, alcoholic or nonalcoholic steatohepatitis, oxidative stress and exogenous noxious stimuli (Parola and Pinzani, 2019). Meanwhile, liver fibrosis is not a single-target disease and its progression is attributed to the highly active crosstalk between several liver cell types, including hepatocytes, macrophages and hepatic stellate cells (HSCs). Although liver fibrosis is theoretically reversible, numerous attempts have failed due to a narrow therapeutic window, limited therapeutic efficacy or undesired severe adverse effects.

Adenosine monophosphate-activated protein kinase (AMPK), an obligate heterotrimer composed of three subunits (α, β, and γ), is regarded as a critical cellular energy sensor that controls energy expenditure and storage. Besides the reduced adenosine triphosphate (ATP)/adenosine diphosphate (ADP) ratio caused by any cellular stress (Li et al., 2015), the phosphorylation of extracellular-signal-regulated protein kinase 1/2 (ERK1/2) and liver kinase B1 (LKB1) are the major upstream signal cascades of AMPK activation (Li et al., 2017). It has long been conceived that AMPK is critical for maintaining normal hepatic physiological functions and its activity is decreased during several liver diseases. The activation of AMPKα1 upregulated cyclin A2 transcription, promoted hepatocyte proliferation and eventually restored the liver mass after partial hepatectomy (Merlen et al., 2014). On the other side, once the activation of AMPK was decreased, pro-apoptotic caspase-6 cleaved Bid to induce cytochrome c release that led to hepatocyte damage and fibrotic liver injury (Zhao et al., 2020). Most recently, Qian Lin et al. constructed liver-specific AMPK knockout mice and investigated the specific role of phosphorylated AMPK in fibrotic steatohepatitis. The hepatic depletion of AMPK completely disrupted hepatic lipid metabolism, triggered inflammatory response and aggregated liver fibrosis in a western diet-induced liver steatotic mouse model (Lin et al., 2020). Collectively, considering the vital role that AMPK plays in the progression of fibrotic liver injury, the identification of novel drugs targeting AMPK is urgently needed.

Mechanisms involved in AMPK activation include activating upstream kinases of AMPK or inactivating dephosphorylated kinases that control the activation of AMPK. The aberrant interplay between protein-tyrosine phosphatases (PTPs), responsible for protein dephosphorylation, and tyrosine kinases affects the function of multiple proteins, disrupts the normal liver function and impacts the progression of chronic liver diseases (Rubio et al., 2020). PTP1B is one of the most critical members of PTPs family and expresses in multiple hepatic cells. Studies revealed that PTP1B has become an effective target for the therapeutic intervention of hepatic injury and lipid metabolism disorders (Mobasher et al., 2013; Hu et al., 2021). Recently, researches concerning the role of PTP1B in fibrotic liver injury have stepped into a new stage. Specific liver-knockout of PTP1B protected mice from chronic alcohol plus binge-induced oxidative stress, liver fibrosis and inflammation *via* the inhibition of nuclear factor kappa B (NF-κB) and reduction of nicotinamide adenine dinucleotide phosphate oxidase 2 (NOX2) and NOX4 expression (Hsu et al., 2020). Consistent with prior findings, PTP1B overexpression notably hindered the inactivation of HSC-T6 cells, as manifested by restoring the levels of collagen 1 (COL1) and alpha-smooth muscle actin (α-SMA) (Chen et al., 2016). However, whether hepatic PTP1B influences hepatic inflammation and liver fibrosis through the phosphorylation of AMPK and potential PTP1B inhibitors are suitable for treating fibrotic liver injury remain to be identified.

Ferulic acid (3-methoxy-4-hydroxycinnamic acid, FA) is a phenolic acid widely distributed in abundant grains, vegetables and plants such as *Angelicae Sinensis Radix*, *Ligusticum Chuanxiong Rhizoma* and *Cimicifuga racemose* (Oliveira et al., 2019). It also exhibits a broad spectrum of biological activities, including repairing mitochondrial dysfunction (Luo et al., 2020), anti-oxidant (Xie et al., 2020), enhancement of immune function (Kohno et al., 2020) and preventing epithelial-mesenchymal transition (Ali et al., 2021). Several recent studies further provided evidence for the hepatoprotective effects of FA. Administration of FA improved lipid metabolism and hepatic inflammation in apolipoprotein E-deficient mice fed with high fat diet (HFD) by upregulating AMPKα and downregulating lipogenic genes (Gu et al., 2021). FA also offered significant therapeutic benefits for oxidative stress and liver injury depending on its ability to activate Nrf2/HO-1 and PPARγ pathways (Mahmoud et al., 2020). In addition, FA significantly alleviated septic liver injury through the GSK-3β/NF-κB/CREB pathway both *in vivo* and *in vivo* (Cao et al., 2021). Moreover, it could prevent acetaminophen-induced inflammatory response in livers through the inhibition of TLR4/NF-κB signalings (Yuan et al., 2016). Up to now, relevant studies only preliminarily verified the protective effects of FA using western diet- or toxins-induced mouse models but was still lack of in-depth investigation on mechanism (Mu et al., 2018; Gu et al., 2021). Therefore, the protective effects of FA against fibrotic liver injury and the potential mechanisms involved need to be clarified and is the purpose of this study.

In the current study, we inspected the effects of FA on carbon tetrachloride (CCl_4)-induced fibrotic mouse model and in different drugs-stimulated liver cells. Our findings indicated that FA prevented all histological alterations, suppressed hepatic oxidative stress, inflammatory response, macrophage activation and HSC activation by phosphorylating AMPK. We also demonstrated that FA directly bound to PTP1B, suppressed its enzyme activity rather than its expression and subsequently contributed to AMPK activation.

MATERIALS AND METHODS

Materials

FA and methyl ferulate (MF) were purchased from Innochem Technology Co., Ltd. (Beijing, China). Compound C (CC) was

purchased from Selleck Chemicals (Shanghai, China). CCl_4 and all cell culture supplemental components were purchased from Sigma-Aldrich (St. Louis, United States). HiScript III RT SuperMix cDNA reverse transcription Kits (R323-01) and AceQ^{TM} Universal SYBR qPCR Master Mix (Q511-02) were obtained from Vazyme Biotech (Nanjing, China). Antibodies against p-ERK1/2 (sc-7383), ERK1 (sc-271269), ERK2 (sc-81457), LKB1 (sc-32245) were purchased from Santa Cruz Biotechnology (Santa Cruz, United States). Antibodies against p-AMPK (ab23875), AMPK (ab131512) and p-LKB1 (ab63473) were from Abcam (Cambridge, United States). Antibodies against ALB (4929S), β-actin (4970S) and normal rabbit IgG (2729S) were obtained from Cell Signaling Technology (Danvers, United States). Antibodies against PTP1B (11334-1-AP) and FIBRONENCTIN (FN) (15613-1-AP) were purchased from Proteintech Group, Inc (Rosemont, United States). Goat anti-rabbit IgG-HRP (abs20040) and goat anti-mouse IgG-HRP (abs20039) were obtained from Absin Bioscience (Shanghai, China). Protein A/G-PLUS agarose beads (sc-2003) was purchased from Santa Cruz Biotechnology (Santa Cruz, United States).

Isolation and Culture of Mouse Primary Hepatocytes

Mouse primary hepatocytes (MPHs) were isolated according to a method of two-step collagenase digestion and seeded into collagen pre-coated cell dishes as previously described (Li et al., 2018). After 4 h attachment, MPHs were cultured with William's E medium supplemented with penicillin G (100 U/ml), streptomycin (100 μg/ml), dexamethasone (0.1 μM) and thyroxine (0.1 μM) for further experiments.

Cell Culture and Treatment

RAW 264.7 cells and LX-2 cells were obtained from ATCC and cultured with Dulbecco's modified Eagle medium (DMEM) supplemented with penicillin G (100 U/ml), streptomycin (100 μg/ml) and 10% fetal bovine serum (FBS) in the atmosphere of 5% CO_2 at 37°C. After seeded, RAW 264.7 cells were treated with FA or MF (both 100 μM) for 0.5, 1, 2, 4 and 6 h for the time course experiment or treated with FA or MF (both 50, 100, and 200 μM) for 24 h. LX-2 cells and MPHs were either treated with FA or MF (25 μM) at different time points or treated with FA or MF (both 12.5, 25 and 50 μM) for 24 h. To explore the anti-fibrotic effects of FA, LX-2 cells were pretreated with FA (25 μM) for 1 h and then treated with transforming growth factor-beta (TGF-β) (5 ng/ml) for another 2 h or 24 h. To examine the anti-inflammatory activity of FA, RAW 264.7 cells were administrated with 100 μM FA for 1 h, followed by 100 ng/ml lipopolysaccharide (LPS) treatment for another 4 h. For the AMPK inhibition study, after 10 μM CC-pretreated, MPHs, RAW 264.7 cells and LX-2 cells were treated with different dosages of FA. To investigate the hepatoprotective effects of FA, MPHs were pretreated with 25 μM FA for 1 h and then treated with 10 mM CCl_4 for another 24 h.

Animal Studies

C57BL/6J mice (22–24 g, male and female, SPF grade) were purchased from SIBEIFU Biotechnology Co, Ltd (Beijing, China). Mice were housed in a homoiothermic and sterile condition of 12-h light/dark cycles and fed standard chow and tap water at libitum. After 1 week acclimatization, mice were divided into five experimental groups (n = 6): 1) control group; 2) CCl_4 group; 3) CCl_4 + FA (low dose) group; 4) CCl_4+ FA (medium dose) group; 5) CCl_4+ FA (high dose) group. To chronically induce liver fibrosis, mice were received 1 ml/kg CCl_4 by gavage twice a week for 8 weeks in groups (2–5) or were orally treated with the same volume of vehicle solution (olive oil) in group (1). To investigate the anti-fibrotic effects of FA, groups (3–5) were orally administrated with FA at different dosages (25, 50 and 100 mg/kg) for 4 weeks after 4 weeks of CCl_4 administration. After treatment, mice were weighed, anesthetized with isoflurane and sacrificed to collect blood and livers. All animal studies and procedures were approved by the Institutional Animal Care and Use Committee of Beijing University of Chinese Medicine and were carried out in accordance with all guidelines and regulations.

PTP1B Activity Assay

The activity of PTP1B was determined by measuring the free phosphate released from PTP1B substrate using the commercially available PTP1B Assay kit 539736) from Merck Millipore (Darmstadt, Germany). Different concentrations of FA and MF or the equal volume of assay buffer solution (as a negative control) were prepared and added in a 96-well plate, followed by incubation with PTP1B enzyme dilution and warmed substrate for 40 min at 30°C. After incubating wells for the desired duration, reactions were terminated with Red Reagent. The absorbance was measured at 620 nm wavelength by xMark™ Microplate Absorbance Spectrophotometer. The activity of PTP1B enzyme in different wells was calculated by the conversion of absorbance to phosphate concentration with the phosphate standard curve as follows.

$$\%\ Activity = \frac{\left[\text{FA or MF sample } \left(\text{nmol } po_4^{2-}\right) - \text{“}time\ 0\text{”} \left(\text{nmol } po_4^{2-}\right)\right]}{\left[\text{Assay buffer } \left(\text{nmol } po_4^{2-}\right) - \text{“}time\ 0\text{”} \left(\text{nmol } po_4^{2-}\right)\right]} \times 100\% \quad (1)$$

Histopathology, Masson's Trichrome Staining and Immunohistochemistry

After immobilized with 4% formaldehyde, 4.5-μm paraffin sections were prepared and further stained with hematoxylin and eosin (H&E) and Masson's Trichrome as previously described (Li et al., 2017). Cell damage and inflammatory infiltration in histological changes were determined by evaluating the degree of hepatic injury. H&E scoring was performed as previously described (Wu et al., 2021). Quantification of collagen deposition (the percentage of blue collagen area relative to the total staining area) in Masson's Trichrome staining was conducted using ImageJ software. For IHC staining, paraffin sections were rehydrated, antigen retrieval by EDTA and blocked endogenous peroxidases with 0.3% H_2O_2. After blocked with BSA reagent supplemented with 10% goat serum, slides were incubated with primary antibody against FN (dilution, 1:100) at 4°C overnight, washed and incubated with

goat anti-mouse/rabbit IgG HRP polymer secondary antibody (ZSGB-BIO, Beijing, China). The images of staining sections were obtained by Aperio Versa (Leica, Wetzlar, Germany).

Immunofluorescence Staining

After treatment, cells were rinsed with phosphate-buffered saline (PBS) buffer, fixed in 3.7% formaldehyde, blocked and permeabilized with 1% PBS-BSA with 0.1% Triton-X-100, followed by incubation with primary antibody against ALB (dilution, 1:500) in a wet chamber at 4°C overnight. Later, cells were incubated with Alexa Fluor® 594 Goat anti-rat secondary antibody (dilution, 1:1,000) and then counterstained with DAPI. Immunofluorescence images were captured by Olympus FV3000 confocal laser scanning microscopy (Tokyo, Japan).

Measurement of Intracellular ROS

A ROS assay kit (S0033S, Jiancheng Bioengineering Institute, Nanjing, China) with DCFH-DA as a fluorescent probe was used to determine the relative ROS levels in MPHs. After treatment, MPHs were washed with PBS and incubated with the 10 μmol/L of DCFH-DA probe in dark at 37°C for 30 min. After discarding the unreacted probes and washing twice with PBS, the fluorescent intensity of oxidized product was determined at 525 nm. Immunofluorescence images were captured by Olympus FV3000 confocal laser scanning microscopy (Tokyo, Japan).

Molecular Docking Study

In silicon docking studies was performed using SYBYL-X 2.0 software (Tripos Inc, St. Louis, MO). The 3D structures of the compound FA and MF were downloaded from the ZINC database. The crystal structures of PTP1B (PDB ID:4I8N) in complex with an inhibitor of compound A [(4-{(2s)-2-(1,3-benzoxazol-2-yl)-2-[(4-fluorophenyl)sulfamoyl]ethyl}phenyl) amino](oxo)acetic acid and AMPK (PDB ID:6BX6) in complex with an inhibitor of compound B, SBI-0206965 were downloaded from RCSB protein data bank. The PTP1B and AMPK were optimized for molecular docking as follows. After removing the inhibitors and all of the water molecules and adding H atoms, side-chain amides were fixed and then prepared with the protein preparation module using default parameters. Furthermore, compound A, FA and MF were docked with the prepared PTP1B crystal structure, and compound B and FA were docked with AMPK by undertaking the Surflex-Dock (SFXC) docking mode. Meanwhile, the original inhibitors of compound A and compound B were respectively used to compare the interaction between residues and dispositions when PTP1B and AMPK were docked. Docking results were analyzed and visualized using SYBYL-X 2.0 software and Molecular Operating Environment software (Chemical Computing Group ULC, Canada).

Co-immunoprecipitation Study

Protein A/G-PLUS agarose beads were incubated with PTP1B antibody or IgG in IP lysis buffer at 4°C overnight. The next day, agarose beads were centrifuged and resuspended three times with IP buffer. After washing with ice-PBS, the cell pellet was gently lysed and centrifuged to collect the lysate for the following experiment. After pre-cleared by incubation with protein A/G-PLUS agarose beads for 1 h, cell lysate was incubated with PTP1B antibody- or lgG-coated beads on a 4°C rotator overnight. After washed four times with IP buffer, the immunoprecipitated beads were denatured with 4x laemmli sample buffer (1610747, Bio-Rad) at 100°C, followed by western blot analysis to determine the binding capacity of PTP1B and p-AMPK or t-AMPK.

Surface Plasmon Resonance Assay

The surface plasmon resonance (SPR) assay was conducted at 25°C using Biacore T200 SPR sensor (Biacore, GE Healthcare) with control software version 3.0. Briefly, a CM5 chip (carboxymethylated dextran surface) in Biacore PBS-EP running buffer was first activated following a standard EDC/NHS method. PTP1B protein was prepared in NaAc buffer (pH 4.5) to a final concentration of 20 μg/ml and was then injected into the channel of analysis instrument for 420 s followed by a 7 min injection of 1 M of ethanolamine buffer (pH 8.5) to block the residual active groups. For each sample analysis, another reference channel without the conjugated protein was also activated and blocked to eliminate non-specific binding to the surface of CM5 chip. Next, FA solution was diluted into different concentrations and injected into the analysis channel at a flow rate of 30 μL/min. The binding time of proteins and ligands was 420 s and the natural dissociation time was 420 s. All data were analyzed using Biacore T200 software.

Statistical Analysis

All experimental data were expressed as mean ± SEM and repeated at least three times. One-way ANOVA was employed to compare the differences between multiple groups using GraphPad Prism 8 (Graph-Pad, San Diego, CA). p value ≤ 0.05 was considered statistically significant.

RESULTS

FA Significantly Prevents Liver Fibrosis in CCl_4-Induced Mouse Model

To reveal the potential protective effects and detailed mechanisms of FA on liver fibrosis progression, C57BL/6J mice were first orally administered with CCl_4 for 4 weeks to induce chronic inflammation and liver fibrosis followed by treatment with different doses of FA (25, 50 and 100 mg/kg) or vehicle control for additional 4 weeks in addition to continuous gavage of CCl_4 (**Figure 1A**). The significant increased ratios of liver or spleen weight over body weight caused by CCl_4 were slightly decreased after FA treatment (**Supplementary Figure S1A**). Notably, serum biochemistry assays showed that CCl_4 significantly increased the serum levels of alanine transaminase (ALT) and aspartate transaminase (AST), which were all markedly reversed by FA administration (**Figure 1B**). We further determined whether FA protected liver fibrosis through the suppression of hepatic oxidative stress. As expected, the hepatic content of malondialdehyde (MDA) in

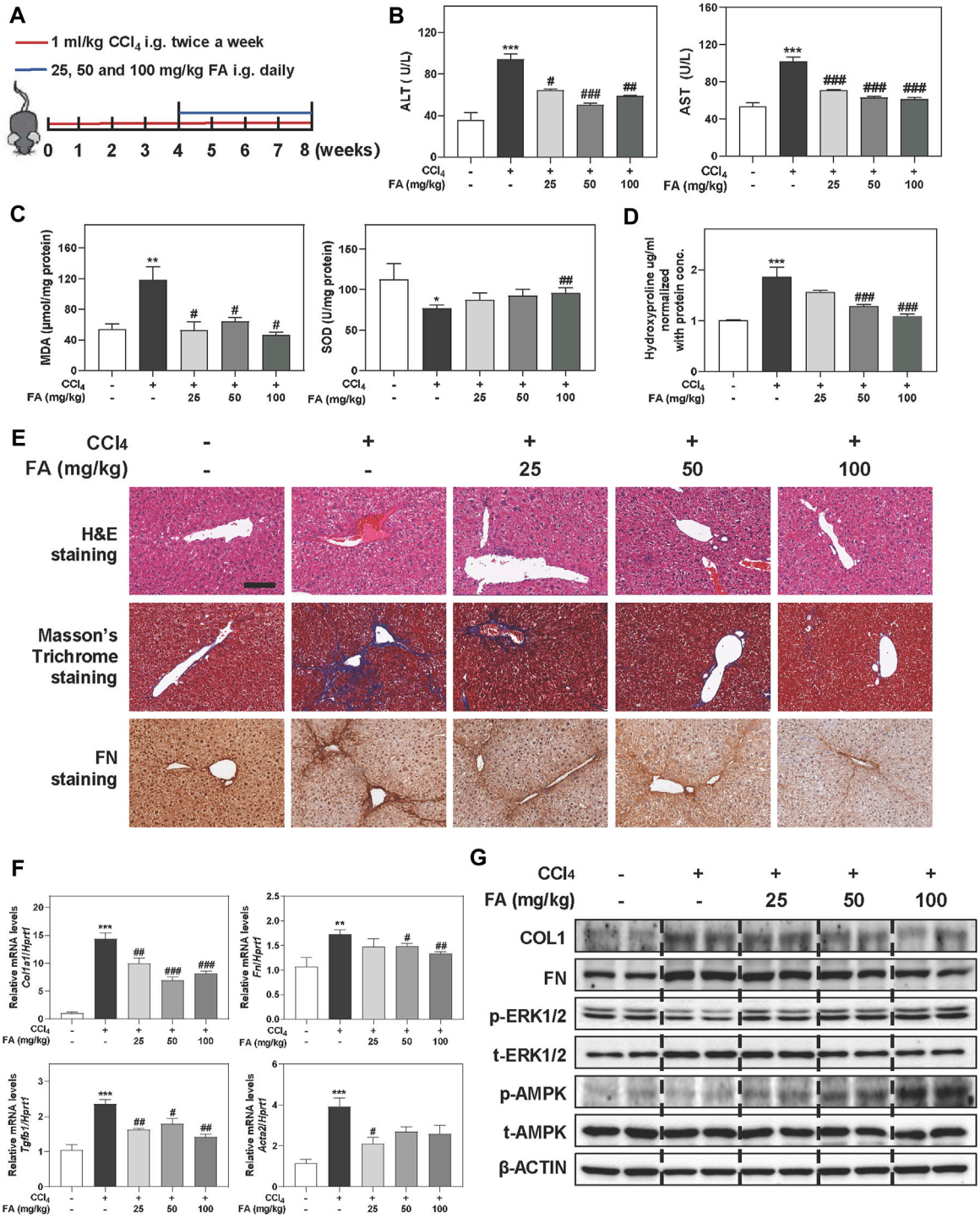


FIGURE 1 | FA alleviates CCl4-induced fibrotic injury in mice. Mice were received with CCl_4 (1 ml/kg) and different dosages (25, 50, and 100 mg/kg) of FA by gavage. **(A)** Schematic diagram of *in vivo* experiments that linked FA with anti-fibrotic therapies. **(B)** ALT and AST levels in serum. **(C)** MDA and SOD levels in livers. **(D)** Measurement of the liver hydroxyproline. **(E)** Representative images of H & E, Masson's Trichrome and FN staining. Scale bar = 100 μm. **(F)** Relative mRNA levels of Col1a1, Fn, Tgfb1 and Acta2 were determined by qPCR and normalized using Hprt1 as an internal control. **(G)** Representative immunoblots against COL1, FN, p-ERK1/2, t-ERK1/2, p-AMPK, t-AMPK and β-ACTIN were shown. Statistical significance: $^{*}p < 0.05$, $^{**}p < 0.01$, $^{***}p < 0.001$, compared with control group; $^{\#}p < 0.05$, $^{\#\#}p < 0.01$, $^{\#\#\#}p < 0.001$, compared with CCl_4 group. One-way ANOVA with Tukey's post-hoc tests ($n = 6$).

CCl_4-treated group was markedly increased than that in control group (**Figure 1C**, left panel), while superoxide dismutase (SOD) level was decreased in livers (**Figure 1C**, right panel). Interestingly, FA significantly downregulated MDA level and only high dose of FA upregulated the SOD level in livers (**Figure 1C**). Consistently, biochemical quantification of hepatic collagen revealed readily detectable collagen deposition in CCl_4 treated mice but decreased when treated with FA (**Figure 1D**). As shown in **Figure 1E** and **Supplementary Figure S1B**, H & E and Masson's Trichrome staining depicted that FA significantly prevented the CCl_4-caused fibrotic responses as indicated by reduced ballooning changes of hepatocytes and area of inflammation infiltration and collagenous fibers in the liver. Immunohistochemistry staining of FN, a specific marker of liver fibrosis, indicated that FN was upregulated in CCl_4 groups and downregulated after FA treatment. QPCR and western blot analysis further confirmed that CCl_4-induced the upregulation of COL1 and FN were significantly inhibited by FA (**Figures 1F,G** and **Supplementary Figure S1C**). TGF-β, a principal pro-fibrotic factor, promoted the expression of Acta2 and other fibrotic indicators through small mothers against decapentaplegic (SMAD) pathways. As shown in **Figure 1F**, FA-induced recovery from CCl_4 injury was accompanied with the downregulation of pro-fibrogenic mRNA encoding for Tgfb1 and Acta2. Previous studies reported that AMPK activation improved hepatic inflammation and fibrosis even after the onset of liver fibrosis associated-steatohepatitis (Zhao et al., 2020). To further investigate whether the protective effect of FA on liver fibrosis was relevant to AMPK phosphorylation, we determined the protein expression of phosphorylated AMPK and its upstream kinases, ERK1/2 and LKB1. As shown in **Figure 1G** and **Supplementary Figure S1D**, the phosphorylation of AMPK and ERK1/2, but not LKB1, was significantly increased after FA treatment compared with CCl_4 group.

FA Activates AMPK and Alleviates CCl_4-Induced Oxidative Stress in Hepatocytes

It is well known that oxidative stress is particularly relevant to liver fibrosis progression. Given the hepatoprotective and anti-fibrotic effects of FA *in vivo* experiments, we next examined whether FA attenuated oxidative hepatic injury in MPHs treated with CCl_4. First, CCK-8 assay showed that FA below 100 μM didn't cause any cytotoxicity in MPHs (**Figure 2A**). Therefore, 12.5, 25 and 50 μM of FA were used for dose-dependent experiments and 25 μM of FA was used for following *in vitro* assays. As shown in **Figure 2B**, consistent with the results *in vivo*, CCl_4 treatment markedly increased the hepatic level of MDA, which was significantly inhibited by FA at medium and high doses. In addition, 25 and 50 μM FA were able to significantly reverse the decrease of SOD caused by CCl_4 administration. Immunofluorescent images further showed that the expression of ALB, a marker of hepatocyte function, had a significant increase in FA treated groups compared with CCl_4 group (**Figure 2C**). Of note, FA significantly induced the activation of AMPK and ERK1/2 after 2 h treatment and peaked at 4 h (**Figure 2D**, left panel and **Supplementary Figure S2A**). Additionally, medium and high doses of FA rapidly and significantly induced AMPK phosphorylation at 2 h but didn't affect the expressions of ERK1/2 and LKB1 (**Figure 2D**, right panel and **Supplementary Figures S2B,C**). Considering that AMPK activation attenuated NOX2-induced excessive ROS generation and oxidative stress (**Figure 2E**) (Rodriguez et al., 2020), we measured the NOX2 expression after FA and CCl_4 treatment with or without the presence of AMPK inhibitor, CC. As shown in **Figure 2F** and **Supplementary Figure S2D**, the protein levels of NOX2 were significantly decreased after FA treatment compared with CCl_4 group. Although co-treatment of FA and CCl_4 barely affected the phosphorylation of LKB1 and ERK1/2 compared with CCl_4 treatment alone, FA significantly increased the phosphorylation of AMPK. In addition, FA treatment significantly decreased the ROS production in MPHs caused by CCl_4 (**Figure 2G**). Next, we examined whether the inhibition of AMPK activation had any influence on FA-induced hepatoprotective effects. In agreement with our hypothesis, pretreatment of MPHs with CC (2 μM) not only completely inhibited FA-induced AMPK activation but also reversed FA-induced downregulation of NOX2, while the levels of p-ERK1/2 and p-LKB1 were not changed (**Figure 2H**, left panel and **Supplementary Figure S2E**). Interestingly, the level of NOX2 was significantly decreased and the levels of p-AMPK was increased after FA treatment compared with CCl_4-treated group, which was blocked by CC administration. Again, no significant change of ERK1/2 and LKB1 expression was observed (**Figure 2H**, right panel and **Supplementary Figure S2F**).

FA Activates AMPK and Relieves LPS-Induced Inflammation in Macrophages

In addition to oxidative stress response, another key driver responsible for liver fibrosis is macrophage activation-associated inflammatory response, which promotes us to investigate the anti-inflammatory effects of FA both *in vivo* and *in vitro*. As shown in **Figure 3A**, hepatic mRNA expressions of interleukin-1 beta (Il1b) and macrophage markers including F4/80 and Cd11b were significantly increased after CCl4 treatment compared to control group, which were reversed by FA treatment. Furthermore, pro-inflammatory gene transcript levels of chemokine (C-C motif) ligand 2 (Ccl2) and tumor necrosis factor alpha (Tnfa) in the livers of CCl4-treated mice were markedly reduced post FA administration (**Supplementary Figure S3A**). Based on the observations *in vivo*, we next sought to determine the *in vitro* consequence of FA on RAW cells induced by LPS. Results showed that FA didn't affect cell viability up to 200 μM (**Figure 3B**). After LPS intervention for 4 h, several inflammatory-related genes expression were significantly upregulated, such as inducible nitric oxide synthase (Inos), Tnf-a, Ccl2, and Il6, which were downregulated by FA treatment except for Il1b (**Figure 3C**). As depicted in **Figure 3D** and **Supplementary Figures S3B,C**, administration of FA significantly induced the phosphorylation of AMPK as well as p-ERK1/2 after 2 h treatment and peaked at

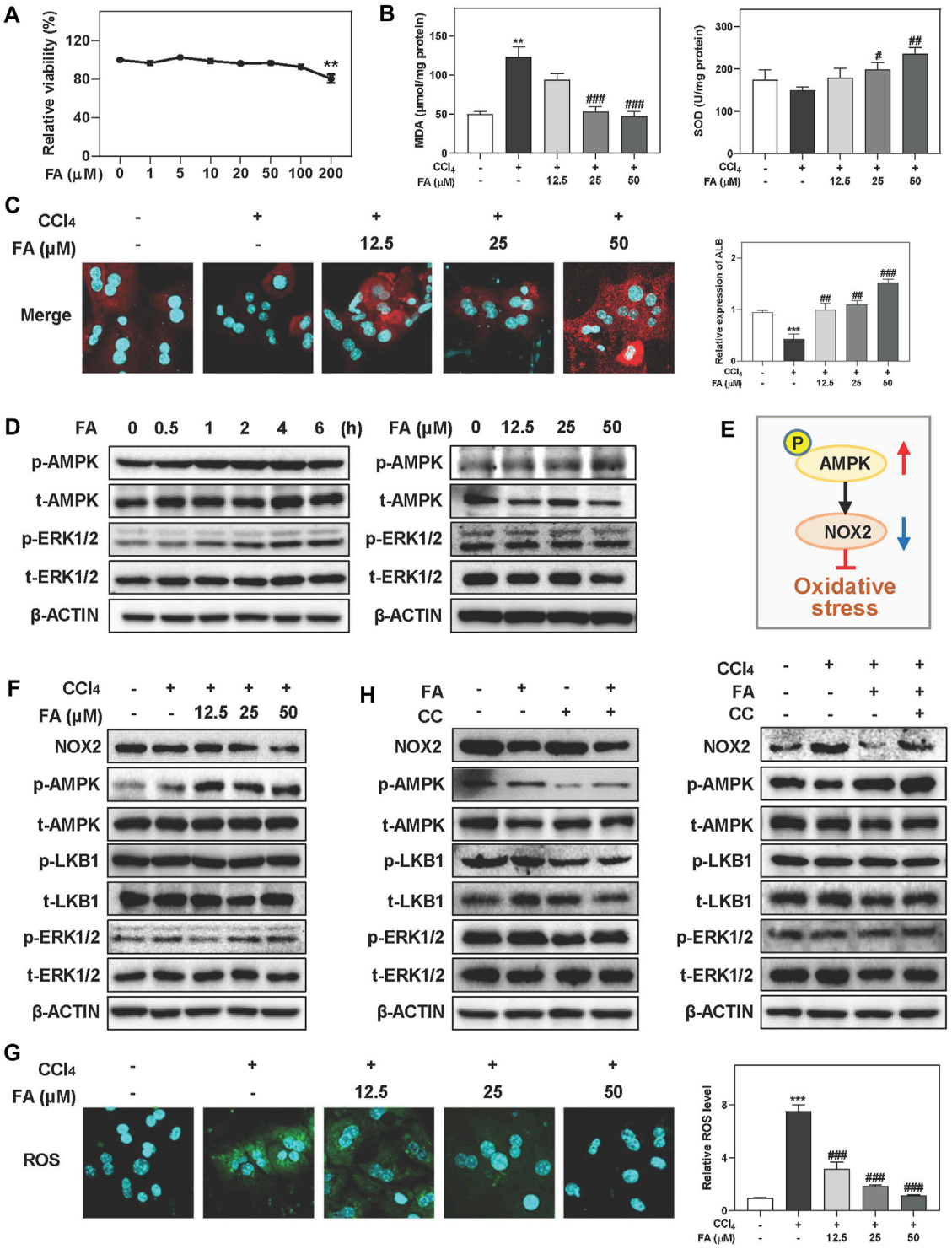


FIGURE 2 | FA improves CCl4-induced oxidative stress and hepatic injury in MPHs. **(A)** A CCK-8 assay. **(B, C, F and G)** MPHs were pre-treated with FA at different concentrations for 1 h and then treated with CCl_4 (10 mM) for another 24 h **(B)** MDA and SOD levels in MPHs. **(C)** Representative images of immunofluorescent staining of ALB in MPHs. **(D)** MPHs were treated with 25 μM FA at different time points or different concentrations of FA for 24 h. **(E)** The pathway of AMPK and NOX2 involved in oxidative stress. **(G)** Representative images of ROS immunofluorescent staining in MPHs. **(H)** After pre-treated with CC (2 μM) or FA (25 μM) or both, MPHs were administrated with CCl_4 (10 mM) for another 2 h or 24 h **(D, F and H)** Representative immunoblots against p-AMPK, t-AMPK, p-LKB1, t-LKB1, p-ERK1/2, t-ERK1/2, NOX2 and β-ACTIN were shown. Statistical significance: $^{**}p < 0.01$, $^{***}p < 0.001$, compared with control group; $^{\#}p < 0.05$, $^{\#\#}p < 0.01$, $^{\#\#\#}p < 0.001$, compared with CCl_4 group. One-way ANOVA with Tukey's post-hoc tests ($n = 3$).

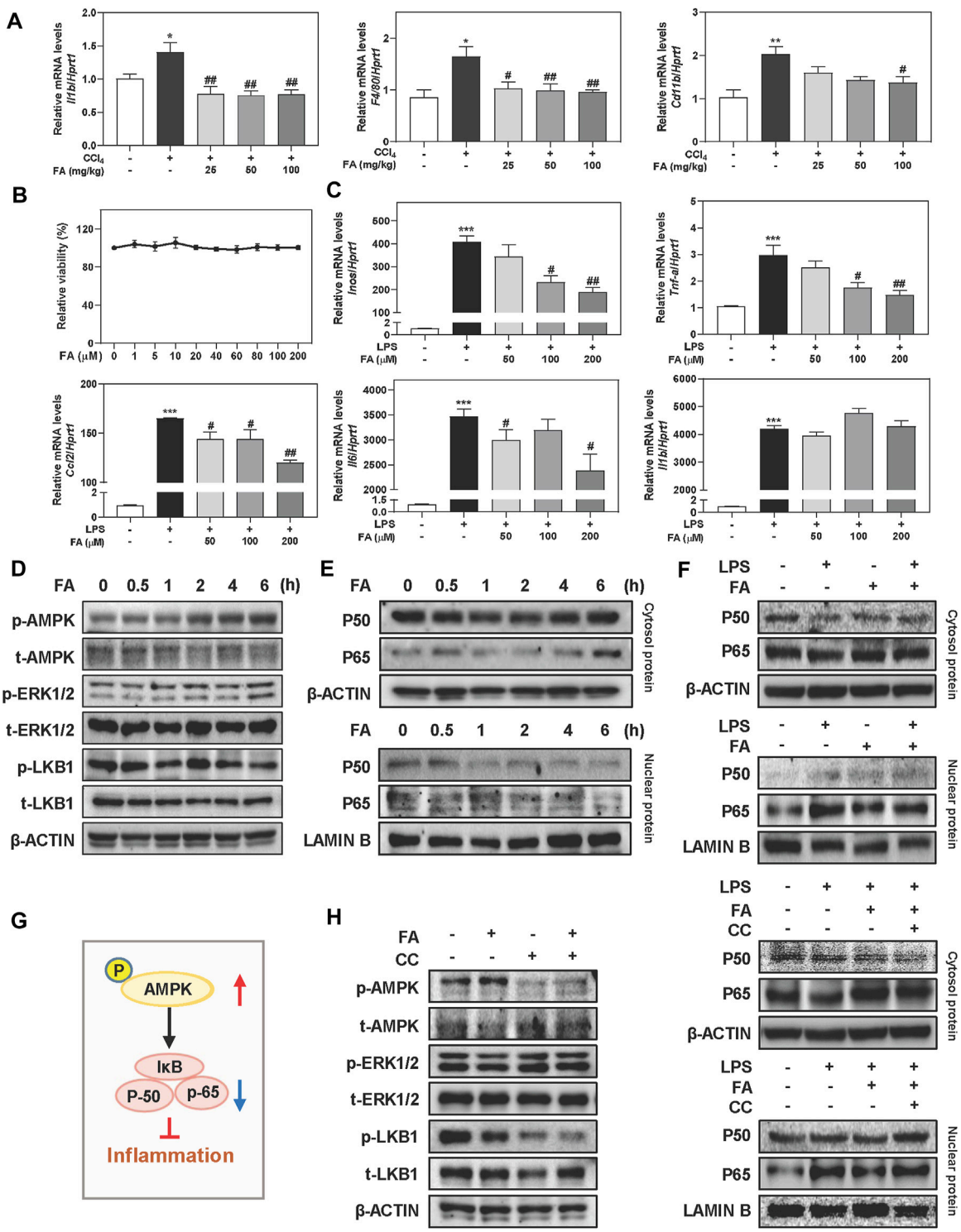


FIGURE 3 | FA suppresses LPS-induced macrophage activation in RAW cells. **(A)** Relative hepatic mRNA levels of Il1b, F4/80 and Cd11b were determined by qPCR and normalized using Hprt1 as an internal control in mice. **(B)** A CCK-8 assay. **(C)** RAW cells were pre-treated with FA at different concentrations for 1 h and then treated with LPS (100 ng/ml) for another 4 h. **(D, E)** RAW cells were treated with 100 μM FA at different time points. **(F, H)** After treated with CC (10 μM) or FA (100 μM) or both, RAW cells were administrated with LPS for another 4 h. **(G)** The pathway of AMPK and NF-κB involved in inflammation. **(D-F and H)** Representative immunoblots against p-AMPK, t-AMPK, p-ERK1/2, t-ERK1/2, p-LKB1, t-LKB1, P50, P65, β-ACTIN and LAMIN B were shown. Statistical significance: $^{*}p < 0.05$, $^{***}p < 0.01$, $^{***}p < 0.001$, compared with control group; $^{\#}p < 0.05$, $^{\#\#}p < 0.01$, compared with LPS group. One-way ANOVA with Tukey's post-hoc tests ($n = 3$).

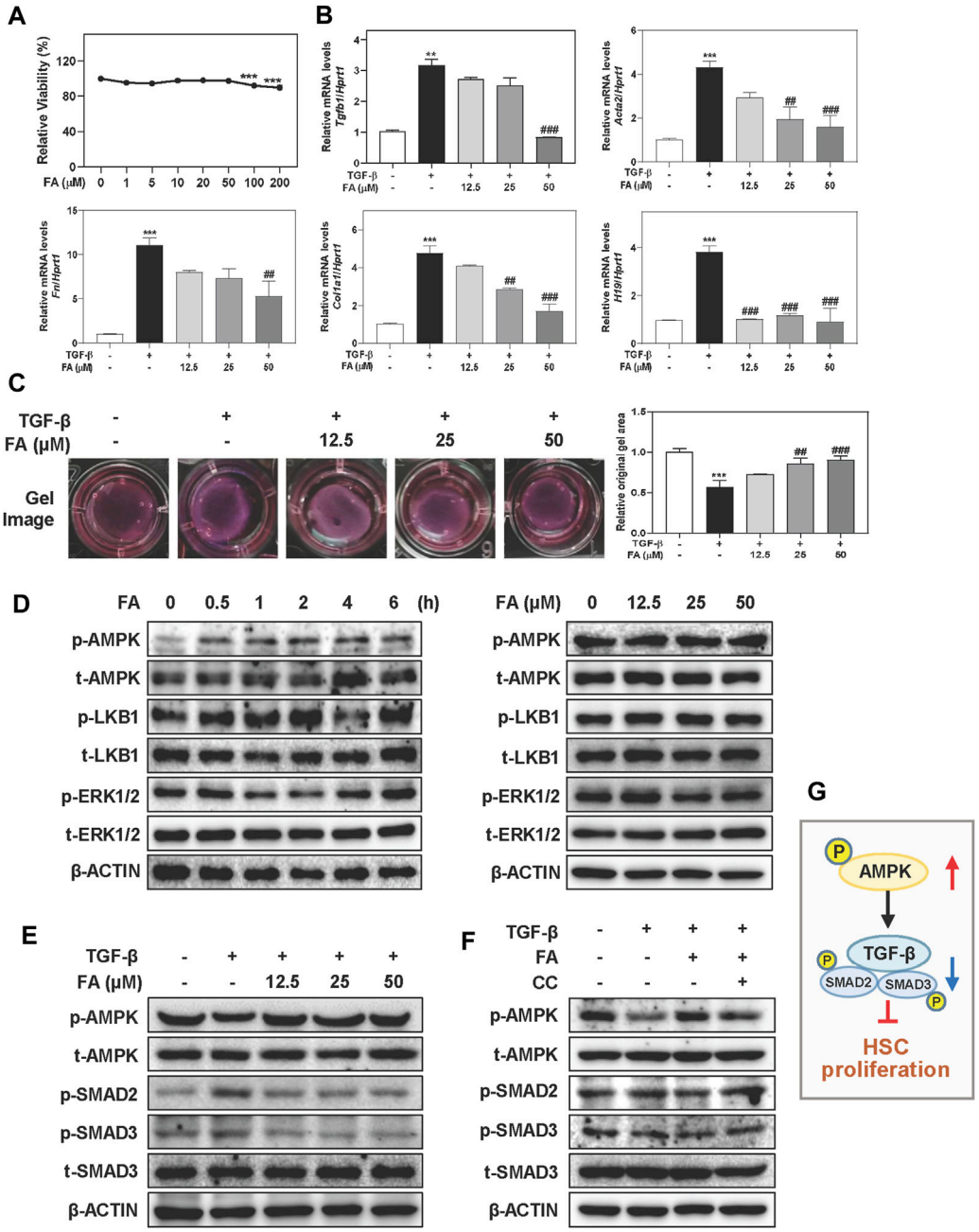


FIGURE 4 | FA attenuates TGF-β-induced HSC activation and fibrotic responses in LX-2 cells. **(A)** A CCK-8 assay. After pre-treated with FA at different concentrations for 1 h, LX-2 cells were treated with TGF-β (5 ng/ml) for another 24 h **(B and C)** or 6 h **(E)**. **(B)** Relative mRNA levels of Tgfb1, Acta2, Fn, Col1a1 and H19 were determined by qPCR and normalized using *Hprt1* as an internal control. **(C)** Representative collagen gel images from three independent experiments were shown. **(D)** LX-2 cells were treated with 25 μM FA at different time points or different concentrations of FA for 24 h. **(F)** After treated with CC (2 μM) or FA (25 μM) or both, LX-2 cells were administrated with TGF-β for another 6 h **(D-F)** Representative immunoblots against p-AMPK, t-AMPK, p-LKB1, t-LKB1, p-SMAD2, p-SMAD3, t-SMAD3, p-ERK1/2, t-ERK1/2 and β-ACTIN were shown. **(G)** The pathway of AMPK, TGF-β and SMADs involved in HSC proliferation. Statistical significance: $^{**}p < 0.01$, $^{***}p < 0.001$, compared with control group; $^{\#\#}p < 0.01$, $^{\#\#\#}p < 0.001$, compared with TGF-β group. One-way ANOVA with Tukey's post-hoc tests ($n = 3$).

6 h, but didn't affect or even slightly decrease the expression of p-LKB1. The activation of NF-κB was crucial in the process of hepatic inflammation by translocating its subunits (P50 and P65) from cytoplasm to nucleus and promoting the release of cytokines (Catrysse and van Loo, 2017). As expected, FA promoted the translocation of P50 and P65 from nucleus to cytoplasm in a time-dependent manner (**Figure 3E** and **Supplementary Figure S3D**). In addition, FA was able to markedly decrease the LPS-induced nuclear translocation of P50 and P65 (**Figure 3F** and **Supplementary Figure S3E**). We further determined if FA-

induced activation of AMPK was correlated to the inhibition of NF-κB nuclear translocation (**Figure 3G**). As shown in **Figure 3H**, left panel and **Supplementary Figure S3F**, FA-induced AMPK phosphorylation was completely blocked by CC (10 μM). Co-treatment with FA and CC significantly decreased the phosphorylation of LKB1 but not affect ERK1/2 level. Furthermore, with the presence of CC, FA was unable to prevent the nuclear translocation caused by LPS (**Figure 3H**, right panel and **Supplementary Figure S3G**). These findings indicated that FA inhibited inflammatory responses through the activation of AMPK and subsequent inhibition of NF-κB in macrophages.

FA Activates AMPK and Alleviates TGF-β-Induced Fibrotic Response in HSCs

In order to explore whether FA prevented the activation of HSCs, main ECM-producing cells in livers, through the phosphorylation of AMPK, we incubated LX-2 cells, a human HSC cell line, with TGF-β and increasing concentrations of FA *in vitro*. As shown in **Figure 4A**, we conducted CCK-8 assay and selected 12.5, 25 and 50 μM of FA for dose-dependent experiments and 25 μM of FA for other *in vitro* studies. 50 μM of FA significantly downregulated the mRNA levels of genes associated with HSC activation like Tgfb1 and Fn compared to TGF-β group. In addition, the mRNA levels of Acta2 and Col1a1 were dramatically increased in TGF-β-treated group, which were significantly reduced after FA treatment at medium and high doses (**Figure 4B**). We recently reported that the aberrant expression of long noncoding RNA (lncRNA) H19 was responsible for HSC activation and liver fibrosis progression in multiple mouse models (Wang et al., 2021). As shown in **Figure 4B**, TGF-β-induced upregulation of H19 was significantly reversed by FA in LX-2 cells. According to the results of gel contraction analysis, the relative original gel area in TGF-β treated group was significantly reduced due to a strong contraction force compared to control group, which was markedly reversed by FA treatment at 25 and 50 μM (**Figure 4C**). Meanwhile, the effects of FA alone were not statistically significant (**Supplementary Figure S4A**). As shown in **Figure 4D**, left panel and **Supplementary Figure S4B**, although FA did not affect LKB1 expression, it caused a time-dependent increase of p-AMPK phosphorylation at 0.5 h and peaked at 2 h in LX-2 cells. Interestingly, with the presence of FA, p-ERK1/2 was slightly decreased from 1 to 2 h while was continually increased after 4 h. Consistent with the results above, FA also markedly activated the phosphorylation of AMPK without affecting the levels of p-LKB1 and p-ERK1/2 in LX-2 cells (**Figure 4D**, right panel and **Supplementary Figure S4C**). Given the strong influence of FA on AMPK activation, we further explored whether FA prevented HSC activation by regulating AMPK and its related SMAD2/3 signaling. As shown in **Figure 4E** and **Supplementary Figure S4D**, FA reversed the downregulation of phosphorylated AMPK and suppressed the phosphorylation of p-SMAD2 and p-SMAD3 caused by TGF-β administration. Notably, CC significantly inhibited FA-induced upregulation of AMPK, accompanied by a robust increase of p-SMAD2 and p-SMAD3 except for LKB1 (**Figure 4F** and **Supplementary Figures S4E,F**). These results confirmed that the anti-fibrotic effects of FA depended on AMPK activation and its downstream SMAD2/3 pathways (**Figure 4G**).

PTP1B is Required for FA-Mediated Phosphorylation of AMPK

Based on the reported above, we demonstrated that FA was able to upregulate the phosphorylation of AMPK in different liver cells without affecting LKB1 phosphorylation. Given that PTP1B deficiency contributed to oxidative stress and hepatic lipid disorders, we also examined the mRNA and protein levels of PTP1B after FA treatment. Interestingly, FA had no effect on PTP1B expression in hepatocytes, macrophages as well as HSCs, with or without the presence of different model drugs (**Supplementary Figures S5A–E**). Lines of evidence indicated that PTP1B dephosphorylated multiple protein kinases and caused the modulation of multiple signaling pathways (Niu et al., 2020). Given that the regulatory effects of PTP1B on AMPK activation were not only affected by its expression but also relied on its phosphatase activity, FA might mediate AMPK phosphorylation through the regulation of PTP1B activity. To test this hypothesis, we first examined whether FA directly bound to PTP1B using molecular docking and SPR assays. Molecular docking was used to construct a virtual FA-PTP1B structure model. As shown in **Figures 5A,B**, the receptor and ligand of PTP1B were prepared and the bonding mode was predicted by the Surflex-Dock program. The total score of PTP1B towards FA was 7.5695 and towards its inhibitor, compound A, was 12.3564. Correspondingly, PTP1B interacted with FA by forming the hydrogen bonds with catalytically active sites, Arg221, Ser216 and Ala217, and interacted with compound A by forming the hydrogen bonds with Arg221, Ser216, Ala217, Gly220, Ile219 and Asp48. Comparing the binding sites of PTP1B with FA or compound A, we pointed out that Arg221 might become the most critical residue responsible for the interaction between PTP1B and FA. Consistent with our hypothesis, FA might have a moderate binding affinity with PTP1B and act as a potential antagonist of PTP1B. Additionally, SPR is one of the most prominent optical biosensor technologies and was used to gain further insight into the binding affinity of PTP1B to FA (**Figure 5C**). As expected, binding of FA to PTP1B was dose-dependent, exhibiting a association-dissociation process (**Figure 5D**). The response units at equilibrium were plotted against FA concentrations and the dissociation constant (KD) was calculated by non-linear regression. As shown in **Figure 5E**, PTP1B directly bound to FA with a KD value of 3.474 μM.

The Chemical Structure of FA is Crucial for AMPK Phosphorylation

Guided by the results that FA had a strong binding ability with PTP1B (**Figure 5**) but not AMPK (**Supplementary Figure S5F**), we further examined whether FA regulated AMPK phosphorylation by affecting the enzyme activity of PTP1B. As

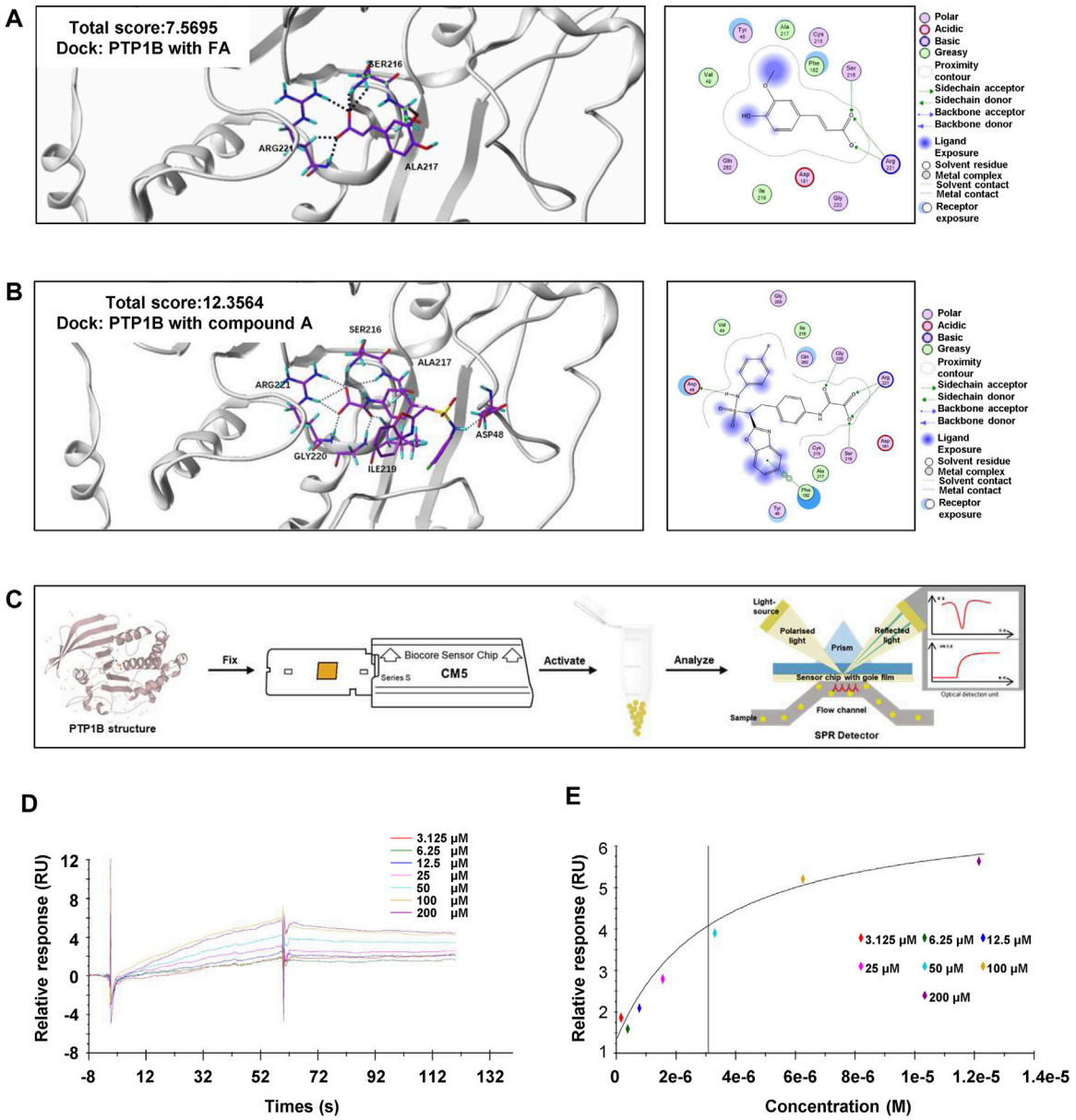


FIGURE 5 | FA directly binds to PTP1B. **(A)** Representative images for the binding mode of FA and PTP1B with the crystal structure of PTP1B (PDB ID: Ser216, Arg221, Ala217). **(B)** Representative images for the binding mode of compound A and PTP1B with the crystal structure of PTP1B (PDB ID: Arg221, Ser216, Ala217, Gly220, Ile219 and Asp48). **(C)** The process flow diagram of SPR. **(D)** The concentration gradient binding curves of protein PTP1B with FA (3.125, 6.25, 12.5, 25, 50, 100 and 200 μM). **(E)** The representative binding curve of FA binding to PTP1B. All the experiments were conducted three independent times.

shown in **Figure 6A**, FA rapidly inhibited the activity of PTP1B more than 50% in a dose-dependent manner, suggesting that it might behave as a potential inhibitor of PTP1B. In addition, co-immunoprecipitation assay was employed to test whether and how FA regulated the interaction between PTP1B and AMPK. In support of our hypothesis, the interaction between PTP1B and AMPK was weakened after FA treatment, possibly because FA competitively occupied the catalytic domain of PTP1B, which was also the binding site for phosphorylated AMPK (**Figure 6B**).

Combined with the above results, we further speculated that the inhibitory effect of FA on PTP1B might be related to the predicted binding mode, especially the formation of hydrogen bond between -COOH on FA and Arg221 and Ser216 of PTP1B. MF is a methyl ester of FA (Cheng et al., 2019). The only difference between FA and MF was a -COOH group in the side chain of FA while a -COOCH3 in the same position of MF (**Figure 6C**). Interestingly, MF had a low predicted binding score and the critical hydrogen bond between -OH with Arg221

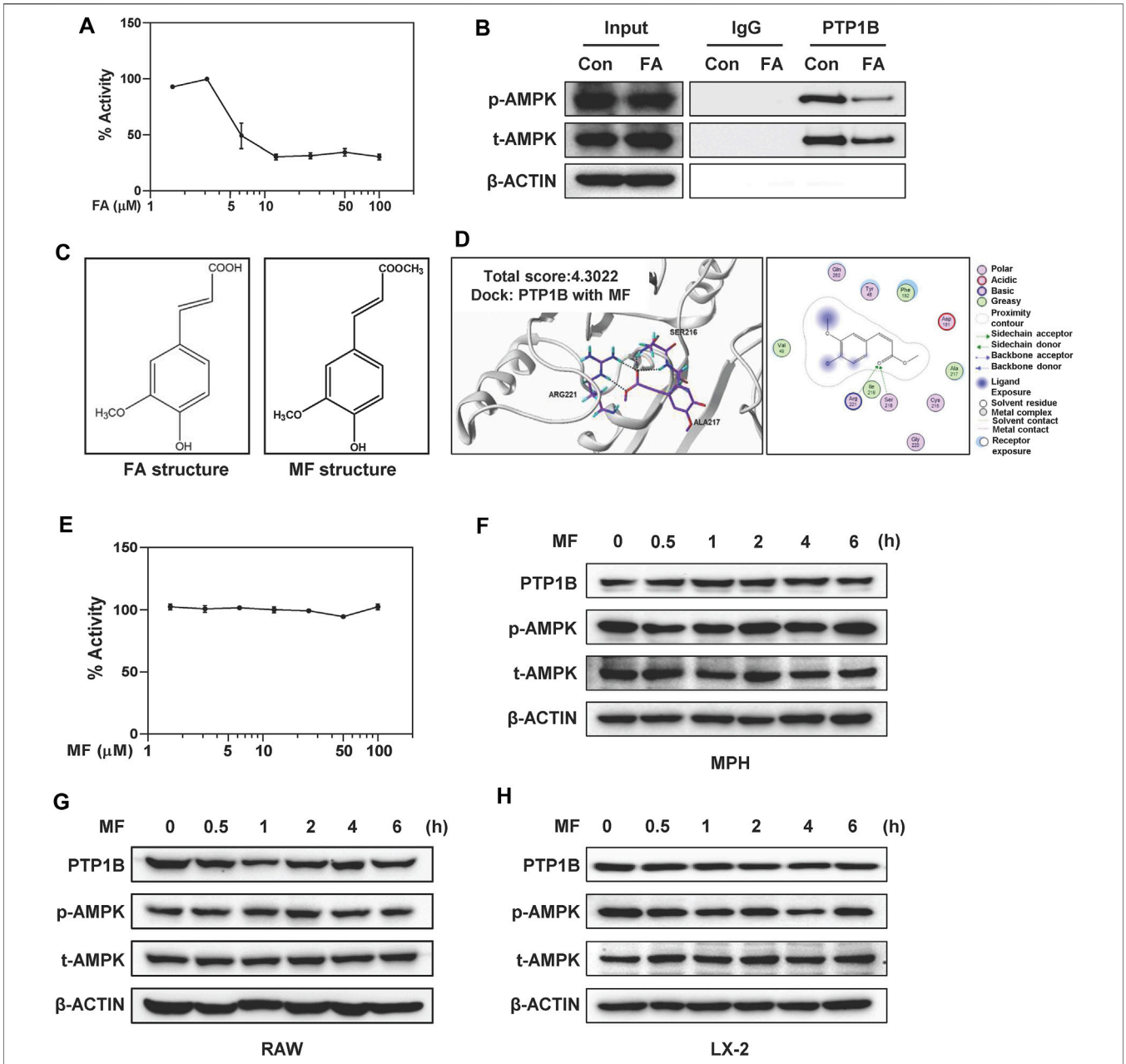


FIGURE 6 | FA directly inhibits PTP1B activity but MF doesn't affect PTP1B and AMPK signalings in different liver cells. **(A)** Inhibition of the catalytic activity of PTP1B by FA was shown. **(B)** LX-2 cells were treated with 25 μM FA for 24 h. Immunoprecipitation using monoclonal anti-PTP1B or IgG, followed by western blot analysis using rabbit polyclonal anti-p-AMPK and t-AMPK. 10% input was prepared as a positive control and ß-ACTIN was used as a loading control. **(C)** Chemical structures of FA and MF. **(D)** Representative images for the binding mode of MF and PTP1B. **(E)** Inhibition of the catalytic activity of PTP1B by MF was shown. **(F and H)** MPHs, LX-2 cells and **(G)** RAW cells were treated with 25 or 100 μM MF at different time points. **(F-H)** Representative immunoblots against p-AMPK, t-AMPK, PTP1B and ß-ACTIN were shown. One-way ANOVA with Tukey's post-hoc tests (n = 3).

was missing (**Figure 6D**). In supporting of molecular docking results, MF had minimal effects on the enzymatic activities of PTP1B at as high as 100 μM (**Figure 6E**). Furthermore, time- and dose-course analyses by western blot revealed that MF didn't affect the phosphorylation of AMPK as well as the expression of PTP1B in MPHs, RAW cells and LX-2 cells, respectively (**Figures 6F–H** and **Supplementary Figures S6A–F**).

DISCUSSION

Liver fibrosis results from multiple pathogenic factors such as oxidative stress, persistent inflammation and lipid disorders and is characterized by the net accumulation of ECM, leading to a serious threat to human health. Indeed, although several anti-fibrotic drugs are in development, high research and development

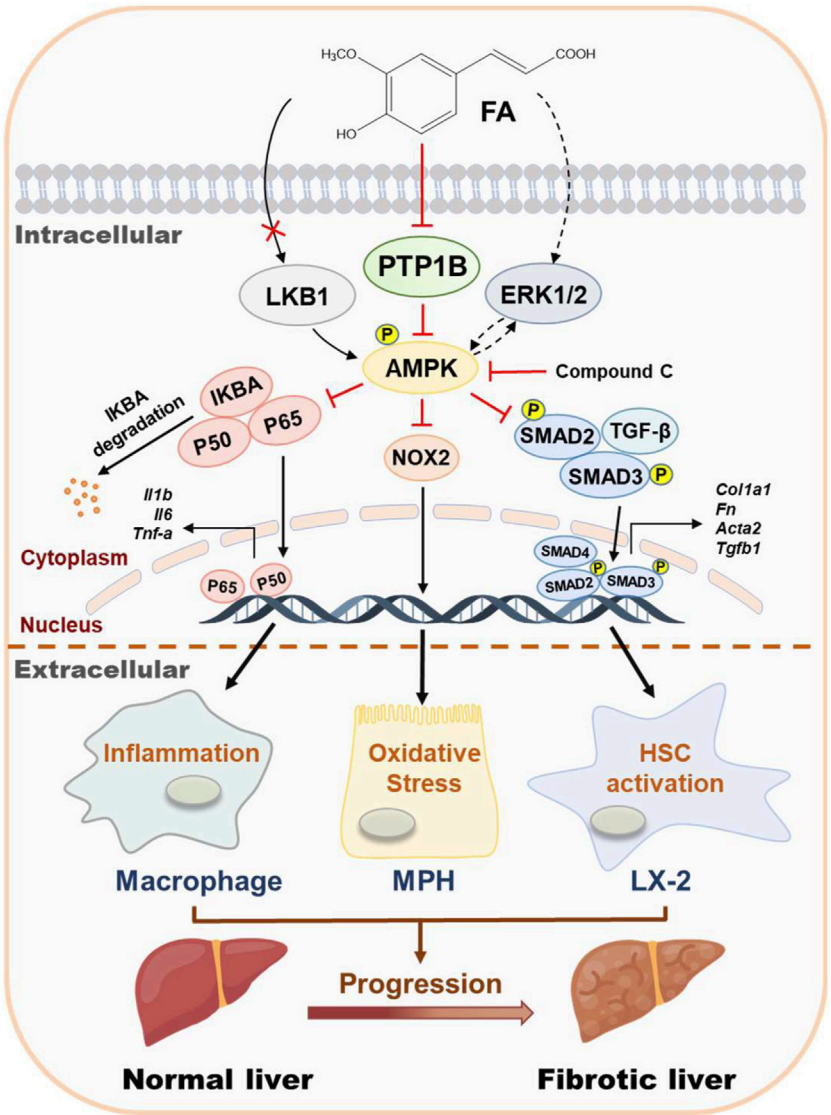


FIGURE 7 | Schematic diagram of the proposed mechanisms underlying the protective effects of FA on oxidative stress, inflammation in macrophages and HSC activation during liver fibrosis. FA ameliorated CCl_4-induced oxidative stress in hepatocytes, relieved LPS-induced inflammation in macrophages and alleviated TGF-β-induced fibrotic response in HSCs. The potential mechanism was that FA directly bound to and inhibited the activity of PTP1B, eventually leading to the phosphorylation of AMPK.

costs and the risk of side effects restrict their clinical applications. In the past decades, natural products are reported to possess novel biological activities, thus making them a rich source of lead compounds for new drug discovery for the treatment of chronic liver diseases. FA, one of the natural representative phenolic acids, has provided opportunities for the treatment of acute or chronic diseases. FA exerts a broad spectrum of biological activities, including ameliorating inflammation, preventing microbial invasion and alleviating lipid droplets deposition, which may be related to antioxidant or antifibrosis but systemic pharmacological evaluation and clear underlying mechanism are still missing. The current study reported that FA markedly protected against pathological changes and liver fibrosis caused by CCl_4 in mice. It also inhibited hepatic oxidative stress, inflammation in macrophages and HSC activation at the cellular level. Mechanically, our data suggested that the beneficial effects of FA were due to its activation of AMPK by directly binding to PTP1B and further inhibiting PTP1B activity (**Figure 7**). Therefore, a better understanding of the protective mechanisms of FA may yield important insights into the treatment of liver fibrosis and advanced complications.

AMPK, as a pivotal player in maintaining cellular energy homeostasis, is reported to regulate multiple metabolic processes. Previous articles indicated that the loss of AMPK activation significantly aggravated liver inflammation and lipid disorders in mouse fibrotic models (Lin et al., 2020; Zhao et al.,

2020). In addition, the protective functions of AMPK phosphorylation are also highlighted recently, including preventing oxidative stress and attenuating alcoholic liver disease progression (Lu et al., 2021). Although AMPK activation is also documented to suppress the expression of bile acid transporters in hepatocytes and further be responsible for estrogen-induced cholestasis, which may result from the sustained over-activation of AMPK (Li et al., 2017), loss of AMPK promotes steatosis development in mice without affecting normal physiological functions (Boudaba et al., 2018; Zhao et al., 2020). Thus, AMPK activation may serve as a reversal point of fibrotic liver damage. If so, pharmaceutical interventions that activate AMPK in livers may represent potential approaches to treat hepatic fibrosis. Here, we reported that FA strikingly protected against oxidative stress and fibrotic responses both *in vivo* and *in vitro* by facilitating AMPK phosphorylation (**Figures 1–4**).

CCl_4 is a multicellular injury model and the consequences it induced are similar to the clinical pathological phenotype of liver fibrosis. Hepatocytes, which account for 60% of the total liver cells and 80% of the liver volume, are the primary source of sensing "danger signals" in liver fibrosis. Under pathological processes, damaged hepatocytes release damage-associated molecular patterns (DAMPs), stimulate the liver-resident macrophages to release pro-inflammatory cytokines/chemokines and result in the recruitment of macrophages that promote HSC survival and activation (Cha et al., 2018; Hirsova et al., 2016). Activated AMPK in hepatocytes not only suppressed the apoptosis of hepatocytes and NOX2-derived ROS production (Rodriguez et al., 2020) but also inhibited the production of endothelial pro-inflammatory cytokines (Hawley et al., 2016). The current work provided evidence that FA exerted excellent anti-oxidant effects and protected hepatocyte injury through AMPK activation and subsequent NOX2 inhibition (**Figure 2**), indicating that the protective effects of FA against oxidative stress on hepatocytes might further reduce the release of cytokines/chemokines and macrophage activation. On the other side, sensitized hepatocytes respond to the release of inflammatory cytokines and further result in hepatic damage and progression of hepatocyte steatosis (Nagy et al., 2016; Zhang et al., 2019). Meanwhile, the activation of AMPK is reported to block NF-κB translocation from the cytosol to the nucleus in activated macrophages (Zhai et al., 2018). Except for the role of FA alone in preventing the nuclear translocation and activation of NF-κB, we further reported that FA reduced the release of inflammatory cytokines in LPS-stimulated RAW cells through the inhibition of NF-κB translocation (**Figure 3**). In addition, AMPK activation was reported to antagonize TGF-β-induced SMAD3 activation and fibrogenic response in HSCs by directly targeting transcriptional coactivator p300, and finally, improve hepatocellular dysfunction in the liver (Lim et al., 2012). Our results further suggested that FA directly activated AMPK phosphorylation and inhibited HSC activation through TGF-β/SMADs pathway (**Figure 4**). These results indicated that FA protected hepatocytes from the "second hit" by suppressing inflammatory reactions in macrophages and preventing HSC activation. Furthermore, CC completely inhibited AMPK activation and abrogated FA-induced hepatoprotective effects in different liver cells, suggesting an indispensable role of AMPK activation underlying the therapeutic effects of FA.

Our results indicate that the FA-induced activation of AMPK is not related to LKB1 but regulated by an alternative mechanism. Similar to AMPK, emerging proofs suggest that PTP1B participates in the course of metabolic and fibrotic liver diseases (Zhang et al., 2015). Deficiency of PTP1B is also reported to effectively restore the dampened phosphorylation of AMPK and hyperactivate phosphorylation of mTOR and Raptor in mice fed with HFD (Kandadi et al., 2015; Xu et al., 2019). Considering the low expressions of NF-κB and NOX2 and inhibited inflammation in liver-specific PTP1B knockout mice (Hsu et al., 2020), we speculated whether these changes are related to AMPK activation in livers and our hypothesis remains to be identified in the future. In the current study, we found that FA relived hepatic fibrosis by, at least partly, directly binding to and acting as a PTP1B antagonist, which further confirmed our hypothesis that the binding ability between FA and AMPK was weaker than that between FA with PTP1B (**Figure 5**). In support of molecular docking and SPR studies, we further showed that although no significant change of PTP1B expression was detected, its enzyme activity was significantly inhibited after FA administration (**Figure 6**). Collectively, our study provided critical evidence that FA alleviated fibrotic liver injury through AMPK phosphorylation, which was relied on the inhibition of PTP1B activity.

There are several critical amino acid residues (Arg221, Ala217, Asp 48, Asp181, Gly183, Gly220, Lys116, Phe182 and Tyr46) of PTP1B were found to directly interact with potential inhibitors isolated from natural products (Jung et al., 2017; Sharma et al., 2020; Hu et al., 2021). Notably, Arg221 exerts an important function in optimizing salt bridge interactions with the phosphate bound to the catalytic site and stabilizing the phosphoryl-enzyme intermediator (Niu et al., 2020). Here we reported that Arg221 might play a vital role in the inhibition of PTP1B by FA. Our molecular docking results revealed that the MF did not fully occupy the positions of Arg221 and might lead to a low binding ability of MF to PTP1B. In order to explore whether the differences in PTP1B inhibition might be related to the structural differences, we compared PTP1B activities after FA and MF treatments, respectively. Although MF was able to attenuate HSC activation and liver fibrosis by inhibiting TGF-β1/SMADs and NOX4/ROS signaling pathways (Cheng et al., 2019), there was no alteration of PTP1B activity observed after MF administration. Additionally, one of the unavoidable ways to generate FA is through the ester hydrolyzation of MF (Mathew and Abraham, 2004). Interestingly, MF took a longer time than FA to slightly increase the phosphorylation of AMPK (**Figure 6**). This phenomenon may be because MF is able to be metabolized into FA and subsequently inhibit PTP1B activity to activate AMPK. These results encourage that FA and its derivatives with similar

structures may provide a possible opportunity for the development of potential PTP1B inhibitors to treat fibrotic liver injury.

In conclusion, our findings indicated that FA exhibited therapeutic effects against fibrotic liver injury both *in vivo* and *in vitro* by effectively inhibiting hepatic oxidative stress, inflammation and HSC activation. Importantly, we clarified that the anti-fibrotic effect of FA was primarily attributed to the inhibition of PTP1B activity and subsequent AMPK phosphorylation. Collectively, as illustrated in **Figure 7**, the hepatoprotective effects of FA and underlying complicated mechanisms by which FA activates AMPK are emphasized and vital evidence inspiring the development of FA-based innovative drug candidates for the treatment of liver fibrosis and related complications is provided.

DATA AVAILABILITY STATEMENT

The original contributions presented in the study are included in the article/**Supplementary Material**, further inquiries can be directed to the corresponding author.

ETHICS STATEMENT

The animal study was reviewed and approved by the animal study was reviewed and approved by the Animal Ethic Committee of Beijing University of Chinese Medicine.

AUTHOR CONTRIBUTIONS

XL designed the research. JW, XX, YG, QZ, YL, and SL performed and analyzed the research. JW, XX, RL, and FZ wrote the manuscript. GF, BM, GH, and LM revised the figures.

FUNDING

This work was supported by grants from Beijing Nova Program of Science and Technology (Grant NO. Z191100001119088 to XL); National Natural Science Foundation of China (Grant NO. 82004045 to XL); Beijing Municipal Science and Technology Commission (Grant NO. 7212174 to XL); Young Talents Promotion Project of China Association of Traditional Chinese Medicine (Grant NO. 2020-QNRC2-01 to XL); Beijing Nova Program of Science and Technology (Grant NO. Z201100006820025 to RL); National innovation team of Traditional Chinese Medicine (Subproject to XL). We thank National Center for Protein Sciences at Peking University in Beijing, China, for the assistance with SPR measurement and Dr. Hui Li for helping with the sample preparation.

SUPPLEMENTARY MATERIAL

The Supplementary Material for this article can be found online at: https://www.frontiersin.org/articles/10.3389/fphar.2021.754976/full#supplementary-material

REFERENCES

Ali, S. A., Saifi, M. A., Pulivendala, G., Godugu, C., and Talla, V. (2021). Ferulic Acid Ameliorates the Progression of Pulmonary Fibrosis via Inhibition of TGF-B/smad Signalling. *Food Chem. Toxicol.* 149, 111980. doi:10.1016/j.fct.2021.111980

Boudaba, N., Marion, A., Huet, C., Pierre, R., Viollet, B., and Foretz, M. (2018). AMPK Re-activation Suppresses Hepatic Steatosis but its Downregulation Does Not Promote Fatty Liver Development. *EBioMedicine* 28, 194–209. doi:10.1016/j.ebiom.2018.01.008

Cao, L., Li, Z., Yang, Z., Wang, M., Zhang, W., Ren, Y., et al. (2021). Ferulic Acid Positively Modulates the Inflammatory Response to Septic Liver Injury through the GSK-3β/NF-κB/CREB Pathway. *Life Sci.* 277, 119584. doi:10.1016/j.lfs.2021.119584

Catrysse, L., and van Loo, G. (2017). Inflammation and the Metabolic Syndrome: The Tissue-specific Functions of NF-κB. *Trends Cel Biol* 27 (6), 417–429. doi:10.1016/j.tcb.2017.01.006

Cha, J. Y., Kim, D. H., and Chun, K. H. (2018). The Role of Hepatic Macrophages in Nonalcoholic Fatty Liver Disease and Nonalcoholic Steatohepatitis. *Lab. Anim. Res.* 34 (4), 133–139. doi:10.5625/lar.2018.34.4.133

Chen, P. J., Cai, S. P., Yang, Y., Li, W. X., Huang, C., Meng, X. M., et al. (2016). PTP1B Confers Liver Fibrosis by Regulating the Activation of Hepatic Stellate Cells. *Toxicol. Appl. Pharmacol.* 292, 8–18. doi:10.1016/j.taap.2015.12.021

Cheng, Q., Li, C., Yang, C. F., Zhong, Y. J., Wu, D., Shi, L., et al. (2019). Methyl Ferulic Acid Attenuates Liver Fibrosis and Hepatic Stellate Cell Activation through the TGF-β1/Smad and NOX4/ROS Pathways. *Chem. Biol. Interact* 299, 131–139. doi:10.1016/j.cbi.2018.12.006

Gu, Y., Zhang, Y., Li, M., Huang, Z., Jiang, J., Chen, Y., et al. (2021). Ferulic Acid Ameliorates Atherosclerotic Injury by Modulating Gut Microbiota and Lipid Metabolism. *Front. Pharmacol.* 12, 621339. doi:10.3389/fphar.2021.621339

Hawley, S. A., Ford, R. J., Smith, B. K., Gowans, G. J., Mancini, S. J., Pitt, R. D., et al. (2016). The Na+/Glucose Cotransporter Inhibitor Canagliflozin Activates AMPK by Inhibiting Mitochondrial Function and Increasing Cellular AMP Levels. *Diabetes* 65 (9), 2784–2794. doi:10.2337/db16-0058

Hirsova, P., Ibrahim, S. H., Krishnan, A., Verma, V. K., Bronk, S. F., Werneburg, N. W., et al. (2016). Lipid-Induced Signaling Causes Release of Inflammatory Extracellular Vesicles from Hepatocytes. *Gastroenterology* 150 (4), 956–967. doi:10.1053/j.gastro.2015.12.037

Hsu, M. F., Koike, S., Mello, A., Nagy, L. E., and Haj, F. G. (2020). Hepatic Protein-Tyrosine Phosphatase 1B Disruption and Pharmacological Inhibition Attenuate Ethanol-Induced Oxidative Stress and Ameliorate Alcoholic Liver Disease in Mice. *Redox Biol.* 36, 101658. doi:10.1016/j.redox.2020.101658

Hu, Y., Li, J., Chang, A. K., Li, Y., Tao, X., Liu, W., et al. (2021). Screening and Tissue Distribution of Protein Tyrosine Phosphatase 1B Inhibitors in Mice Following Oral Administration of Garcinia Mangostana L. Ethanolic Extract. *Food Chem.* 357, 129759. doi:10.1016/j.foodchem.2021.129759

Jung, H. A., Ali, M. Y., Bhakta, H. K., Min, B. S., and Choi, J. S. (2017). Prunin Is a Highly Potent Flavonoid from Prunus Davidiana Stems that Inhibits Protein Tyrosine Phosphatase 1B and Stimulates Glucose Uptake in Insulin-Resistant HepG2 Cells. *Arch. Pharm. Res.* 40 (1), 37–48. doi:10.1007/s12272-016-0852-3

Kandadi, M. R., Panzhinskiy, E., Roe, N. D., Nair, S., Hu, D., and Sun, A. (2015). Deletion of Protein Tyrosine Phosphatase 1B Rescues against Myocardial Anomalies in High Fat Diet-Induced Obesity: Role of AMPK-dependent Autophagy. *Biochim. Biophys. Acta* 1852 (2), 299–309. doi:10.1016/j.bbadis.2014.07.004

Kisseleva, T. (2017). The Origin of Fibrogenic Myofibroblasts in Fibrotic Liver. *Hepatology* 65 (3), 1039–1043. doi:10.1002/hep.28948

Kohno, M., Musashi, K., Ikeda, H. O., Horibe, T., Matsumoto, A., and Kawakami, K. (2020). Oral Administration of Ferulic Acid or Ethyl Ferulate Attenuates Retinal Damage in Sodium Iodate-Induced Retinal Degeneration Mice. *Sci. Rep.* 10 (1), 8688. doi:10.1038/s41598-020-65673-y

Li, X., Liu, R., Huang, Z., Gurley, E. C., Wang, X., Wang, J., et al. (2018). Cholangiocyte-derived Exosomal Long Noncoding RNA H19 Promotes Cholestatic Liver Injury in Mouse and Humans. *Hepatology* 68 (2), 599–615. doi:10.1002/hep.29838

Li, X., Liu, R., Luo, L., Yu, L., Chen, X., Sun, L., et al. (2017). Role of AMP-Activated Protein Kinase α1 in 17α-Ethinylestradiol-Induced Cholestasis in Rats. *Arch. Toxicol.* 91 (1), 481–494. doi:10.1007/s00204-016-1697-8

Li, X., Wang, L., Zhou, X. E., Ke, J., de Waal, P. W., Gu, X., et al. (2015). Structural Basis of AMPK Regulation by Adenine Nucleotides and Glycogen. *Cell Res* 25 (1), 50–66. doi:10.1038/cr.2014.150

Lim, J. Y., Oh, M. A., Kim, W. H., Sohn, H. Y., and Park, S. I. (2012). AMP-activated Protein Kinase Inhibits TGF-β-Induced Fibrogenic Responses of Hepatic Stellate Cells by Targeting Transcriptional Coactivator P300. *J. Cel Physiol* 227 (3), 1081–1089. doi:10.1002/jcp.22824

Lin, Q., Huang, Z., Cai, G., Fan, X., Yan, X., Liu, Z., et al. (2021). Activating Adenosine Monophosphate-Activated Protein Kinase Mediates Fibroblast Growth Factor 1 Protection from Nonalcoholic Fatty Liver Disease in Mice. *Hepatology* 73, 2206–2222. doi:10.1002/hep.31568

Lu, X., Xuan, W., Li, J., Yao, H., Huang, C., and Li, J. (2021). AMPK Protects against Alcohol-Induced Liver Injury through UQCRC2 to Up-Regulate Mitophagy. *Autophagy*, 1–22. doi:10.1080/15548627.2021.1886829

Luo, C., Zhang, Y., Guo, H., Han, X., Ren, J., and Liu, J. (2020). Ferulic Acid Attenuates Hypoxia/Reoxygenation Injury by Suppressing Mitophagy through the PINK1/Parkin Signaling Pathway in H9c2 Cells. *Front. Pharmacol.* 11, 103. doi:10.3389/fphar.2020.00103

Mahmoud, A. M., Hussein, O. E., Hozayen, W. G., Bin-Jumah, M., and Abd El-Twab, S. M. (2020). Ferulic Acid Prevents Oxidative Stress, Inflammation, and Liver Injury via Upregulation of Nrf2/HO-1 Signaling in Methotrexate-Induced Rats. *Environ. Sci. Pollut. Res. Int.* 27 (8), 7910–7921. doi:10.1007/s11356-019-07532-6

Mathew, S., and Abraham, T. E. (2004). Ferulic Acid: an Antioxidant Found Naturally in Plant Cell walls and Feruloyl Esterases Involved in its Release and Their Applications. *Crit. Rev. Biotechnol.* 24 (2-3), 59–83. doi:10.1080/07388550490491467

Merlen, G., Gentric, G., Celton-Morizur, S., Foretz, M., Guidotti, J. E., Fauveau, V., et al. (2014). AMPKα1 Controls Hepatocyte Proliferation Independently of Energy Balance by Regulating Cyclin A2 Expression. *J. Hepatol.* 60 (1), 152–159. doi:10.1016/j.jhep.2013.08.025

Mobasher, M. A., González-Rodriguez, A., Santamaría, B., Ramos, S., Martín, M. Á., Goya, L., et al. (2013). Protein Tyrosine Phosphatase 1B Modulates GSK3β/Nrf2 and IGFIR Signaling Pathways in Acetaminophen-Induced Hepatotoxicity. *Cell Death Dis* 4, e626. doi:10.1038/cddis.2013.150

Mu, M., Zuo, S., Wu, R. M., Deng, K. S., Lu, S., Zhu, J. J., et al. (2018). Ferulic Acid Attenuates Liver Fibrosis and Hepatic Stellate Cell Activation via Inhibition of TGF-β/Smad Signaling Pathway. *Drug Des. Devel Ther.* 12, 4107–4115. doi:10.2147/DDDT.S186726

Nagy, L. E., Ding, W. X., Cresci, G., Saikia, P., and Shah, V. H. (2016). Linking Pathogenic Mechanisms of Alcoholic Liver Disease with Clinical Phenotypes. *Gastroenterology* 150 (8), 1756–1768. doi:10.1053/j.gastro.2016.02.035

Niu, S. L., Tong, Z. F., Zhang, Y., Liu, T. L., Tian, C. L., Zhang, D. X., et al. (2020). Novel Protein Tyrosine Phosphatase 1B Inhibitor-Geranylated Flavonoid from Mulberry Leaves Ameliorates Insulin Resistance. *J. Agric. Food Chem.* 68 (31), 8223–8231. doi:10.1021/acs.jafc.0c02720

Oliveira, D. M., Mota, T. R., Oliva, B., Segato, F., Marchiosi, R., Ferrarese-Filho, O., et al. (2019). Feruloyl Esterases: Biocatalysts to Overcome Biomass Recalcitrance and for the Production of Bioactive Compounds. *Bioresour. Technol.* 278, 408–423. doi:10.1016/j.biortech.2019.01.064

Parola, M., and Pinzani, M. (2019). Liver Fibrosis: Pathophysiology, Pathogenetic Targets and Clinical Issues. *Mol. Aspects Med.* 65, 37–55. doi:10.1016/j.mam.2018.09.002

Rodríguez, C., Contreras, C., Sáenz-Medina, J., Muñoz, M., Corbacho, C., Carballido, J., et al. (2020). Activation of the AMP-Related Kinase (AMPK) Induces Renal Vasodilatation and Downregulates Nox-Derived Reactive Oxygen Species (ROS) Generation. *Redox Biol.* 34, 101575. doi:10.1016/j.redox.2020.101575

Rubio, C., Puerto, M., García-Rodríquez, J. J., Lu, V. B., García-Martínez, I., Alén, R., et al. (2020). Impact of Global PTP1B Deficiency on the Gut Barrier Permeability during NASH in Mice. *Mol. Metab.* 35, 100954. doi:10.1016/j.molmet.2020.01.018

Sharma, B., Xie, L., Yang, F., Wang, W., Zhou, Q., Xiang, M., et al. (2020). Recent advance on PTP1B Inhibitors and Their Biomedical Applications. *Eur. J. Med. Chem.* 199, 112376. doi:10.1016/j.ejmech.2020.112376

Wang, Y., Hylemon, P. B., and Zhou, H. (2021). Long Non-coding RNA H19: A Key Player in Liver Diseases. *Hepatology*. doi:10.1002/hep.31765

Wu, J.-Z., Li, Y.-J., Huang, G.-R., Xu, B., Zhou, F., Liu, R.-P., et al. (2021). Mechanisms Exploration of Angelicae Sinensis Radix and Ligusticum Chuanxiong Rhizoma Herb-Pair for Liver Fibrosis Prevention Based on Network Pharmacology and Experimental Pharmacologylogy. *Chin. J. Nat. Medicines* 19 (4), 241–254. doi:10.1016/S1875-5364(21)60026-2

Xie, K., Jin, B., Zhu, H., Zhou, P., Du, L., and Jin, X. (2020). Ferulic Acid (FA) Protects Human Retinal Pigment Epithelial Cells from H2 O2 -induced Oxidative Injuries. *J. Cel Mol Med* 24 (22), 13454–13462. doi:10.1111/jcmm.15970

Xu, Q., Wu, N., Li, X., Guo, C., Li, C., Jiang, B., et al. (2019). Inhibition of PTP1B Blocks Pancreatic Cancer Progression by Targeting the PKM2/AMPK/mTOC1 Pathway. *Cel Death Dis* 10 (12), 874. doi:10.1038/s41419-019-2073-4

Yuan, J., Ge, K., Mu, J., Rong, J., Zhang, L., Wang, B., et al. (2016). Ferulic Acid Attenuated Acetaminophen-Induced Hepatotoxicity Though Down-Regulating the Cytochrome P 2E1 and Inhibiting Toll-like Receptor 4 Signaling-Mediated Inflammation in Mice. *Am. J. Transl Res.* 8 (10), 4205–4214.

Zhai, C., Shi, W., Feng, W., Zhu, Y., Wang, J., Li, S., et al. (2018). Activation of AMPK Prevents Monocrotaline-Induced Pulmonary Arterial Hypertension by Suppression of NF-κB-Mediated Autophagy Activation. *Life Sci.* 208, 87–95. doi:10.1016/j.lfs.2018.07.018

Zhang, X., Fan, L., Wu, J., Xu, H., Leung, W. Y., Fu, K., et al. (2019). Macrophage P38α Promotes Nutritional Steatohepatitis through M1 Polarization. *J. Hepatol.* 71 (1), 163–174. doi:10.1016/j.jhep.2019.03.014

Zhang, Z. Y., Dodd, G. T., and Tiganis, T. (2015). Protein Tyrosine Phosphatases in Hypothalamic Insulin and Leptin Signaling. *Trends Pharmacol. Sci.* 36 (10), 661–674. doi:10.1016/j.tips.2015.07.003

Zhao, P., Sun, X., Chaggan, C., Liao, Z., In Wong, K., He, F., et al. (2020). An AMPK-Caspase-6 axis Controls Liver Damage in Nonalcoholic Steatohepatitis. *Science* 367 (6478), 652–660. doi:10.1126/science.aay0542

Conflict of Interest: The authors declare that the research was conducted in the absence of any commercial or financial relationships that could be construed as a potential conflict of interest.

Publisher's Note: All claims expressed in this article are solely those of the authors and do not necessarily represent those of their affiliated organizations, or those of the publisher, the editors and the reviewers. Any product that may be evaluated in this article, or claim that may be made by its manufacturer, is not guaranteed or endorsed by the publisher.

Copyright © 2021 Wu, Xue, Fan, Gu, Zhou, Zheng, Liu, Li, Ma, Li, Huang, Ma and Li. This is an open-access article distributed under the terms of the Creative Commons Attribution License (CC BY). The use, distribution or reproduction in other forums is permitted, provided the original author(s) and the copyright owner(s) are credited and that the original publication in this journal is cited, in accordance with accepted academic practice. No use, distribution or reproduction is permitted which does not comply with these terms.

frontiers in Pharmacology

ORIGINAL RESEARCH
published: 16 September 2021
doi: 10.3389/fphar.2021.735087

Hesperetin Exhibits Anti-Inflammatory Effects on Chondrocytes via the AMPK Pathway to Attenuate Anterior Cruciate Ligament Transection-Induced Osteoarthritis

Jiaqin Wu[1], Yuna Qian[2], Cheng Chen[3], Fan Feng[1], Lianhong Pan[1], Li Yang[1]* and Chunli Wang[1]**

[1]National Innovation and Attracting Talents "111" Base, Key Laboratory of Biorheological Science and Technology, Ministry of Education, College of Bioengineering, Chongqing University, Chongqing, China, [2]Engineering Research Center of Clinical Functional Materials and Diagnosis and Treatment Devices of Zhejiang Province, Wenzhou Institute, University of Chinese Academy of Sciences, Wenzhou, China, [3]Department of Orthopaedics, The First Affiliated Hospital of Chongqing Medical University, Chongqing, China

OPEN ACCESS

Edited and Reviewed by:
Hongzhi Du,
Hubei University of Chinese Medicine, China

***Correspondence:**
Yuna Qian
qianyn@wiucas.ac.cn
Li Yang
yanglibme@cqu.edu.cn
Chunli Wang
lilywang@cqu.edu.cn

Specialty section:
This article was submitted to Ethnopharmacology, a section of the journal Frontiers in Pharmacology

Received: 02 July 2021
Accepted: 20 August 2021
Published: 16 September 2021

Citation:
Wu J, Qian Y, Chen C, Feng F, Pan L, Yang L and Wang C (2021) Hesperetin Exhibits Anti-Inflammatory Effects on Chondrocytes via the AMPK Pathway to Attenuate Anterior Cruciate Ligament Transection-Induced Osteoarthritis. Front. Pharmacol. 12:735087. doi: 10.3389/fphar.2021.735087

This study aimed to determine whether hesperetin (HPT) has chondroprotective effects against the TNF-α-induced inflammatory response of chondrocytes and related mechanisms and clarify the impact of HPT on osteoarthritis (OA) induced by anterior cruciate ligament transection (ACLT). Under tumor necrosis factor-α (TNF-α) stimulation, rat chondrocytes were treated with or without HPT. The CCK-8 assay was used to detect viability and cytotoxicity. RT-qPCR and Western blot were used to examine the expression of aggrecan, collagen type II, and inflammatory and proliferative genes/proteins in chondrocytes. Flow cytometry was used to check the cell cycle to determine whether HPT protects chondrocytes against the inhibitory effect of TNF-α on chondrocyte proliferation. In addition, RNA sequencing was used to discover possible molecular targets and pathways and then validate these pathways with specific protein phosphorylation levels. Finally, immunofluorescence staining was used to examine the phosphorylation of the AMP-activated protein kinase (AMPK) pathway. The results showed that HPT restored the upregulation of interleukin 1β (IL-1β), PTGS2, and MMP-13 induced by TNF-α. In addition, HPT reversed the degradation of the extracellular matrix of chondrocytes induced by TNF-α. HPT also reversed the inhibitory effect of TNF-α on chondrocyte proliferation. RNA sequencing revealed 549 differentially expressed genes (DEGs), of which 105 were upregulated and 444 were downregulated, suggesting the potential importance of the AMPK pathway. Progressive analysis showed that HPT mediated the repair of TNF-α-induced chondrocyte damage through the AMPK signaling pathway. Thus, local treatment of HPT can improve OA induced by ACLT. These findings indicated that HPT has significant protective and anti-inflammatory effects on chondrocytes through the AMPK signaling pathway, effectively preventing cartilage degradation. Given the various beneficial effects of HPT, it can be used as a potential natural drug to treat OA.

Keywords: osteoarthritis, inflammation, cartilage degeneration, hesperetin, AMPK

INTRODUCTION

Osteoarthritis (OA) is a connective tissue degenerative disease and frequently associated with joint inflammation and substantial pain, possibly debilitating the affected patient (Dieppe and Lohmander, 2005; Neogi, 2013; Glyn-Jones et al., 2015; Lin et al., 2016; Wang et al., 2020a). It is characterized by the loss of the articular cartilage and subchondral bone reactive hyperplasia due to repeated inflammatory responses (Chen et al., 2017). Growing evidence indicates that the inflammatory response induced by elevated levels of proinflammatory cytokines, including tumor necrosis factor- (TNF-) α and interleukin- (IL-) 1β, plays a critical role in the pathogenesis of OA (Robinson et al., 2016; Wang and He, 2018). Although osteoarthritis is an epidemic, the drugs for this condition are far from ideal (Wang et al., 2015; Zhu et al., 2018). Currently available therapeutic strategies for OA include injectable glucocorticoid compounds and nonsteroidal anti-inflammatory drugs (NSAIDs) (Deyle et al., 2020; Kolasinski et al., 2020). However, these drugs only offer symptomatic relief, with no effect on disease modification or progression. Therefore, it is imperative to seek effective medicines to prevent OA.

TNF-α is a key inflammatory factor, with a leading role in the inflammatory process. Several studies have demonstrated that TNF-α downregulates the synthesis of major extracellular matrix (ECM) components by inhibiting the anabolic activities of chondrocytes (Saklatvala, 1986). It has been reported that inflammatory cytokines exert a destructive effect on cartilage by inhibiting the anabolic activities of chondrocytes (Zhao et al., 2015) and activated chondrocytes to produce matrix metalloproteinases (MMPs), especially MMP-13 (a key regulator of cartilage destruction) (Gonzalez-Rey et al., 2006). TNF-α activates the NF-κB signaling pathway in various medical conditions, which in turn further facilitates the proinflammatory function of TNF-α (Hayden and Ghosh, 2014). Apart from their destructive effects, inflammatory cytokines also tend to induce apoptosis in chondrocytes (Hosseinzadeh et al., 2016). Moreover, recent data suggest that TNF-α is involved in cartilage degeneration in OA (Hosseinzadeh et al., 2016).

With rapid advances in natural products research, active ingredients in natural products have demonstrated their therapeutic effects, with fewer side effects in clinical practice. Hesperetin (HPT), a natural flavonoid from the *Citrus L.* plant in the *Rutaceae* family, has diverse pharmacological capacities, including anti-inflammatory and antioxidative properties (Parhiz et al., 2015). HPT has widely been used to prevent and treat various chronic inflammatory conditions (Chen et al., 2019; Muhammad et al., 2019; Wang et al., 2020c). Although HPT is known to significantly inhibit IL-1β-induced inflammatory responses in human chondrocytes during osteoarthritis (Lin et al., 2020), it remains unknown whether exogenously applied HPT is capable of reversing TNF-α-induced abnormal expression of genes and proteins to prevent the degradation of articular cartilages induced by ACLT transection injury. Moreover, the specific molecular mechanism of this effect is still unknown.

This study investigated whether HPT has chondroprotective effects against the inflammatory responses of chondrocytes induced by TNF-α and the related mechanisms. First, an *in vitro* OA model of chondrocytes (with TNF-α induction) was prepared to assess the inhibitory effects of HPT on the inflammation caused by abnormal gene/protein phenotypic changes. To further unravel the underlying molecular mechanisms, high throughput RNA sequencing quantification was used to analyze mRNA-level changes induced by TNF-α with or without HPT treatment in global chondrocytes. Finally, the AMPK signaling pathway was demonstrated to relieve OA, which could be inhibited by HPT treatment.

MATERIALS AND METHODS

Cell Culture

Rat chondrocytes were isolated and cultured as described in a previous study (Wang et al., 2019; Xu et al., 2019). Sprague Dawley (SD) rat knee cartilage tissues were cut into small pieces and digested with 2 mg/ml collagenase type II (Sigma, United States) for 4–6 h. The undigested tissues were removed, and the isolated cells were seeded in DMEM/F12 (1:1) medium (Gibco, United States) containing 10% fetal bovine serum (FBS) (Gibco, United States). Cells from the second or third passages were used in cell experiments. Animal experiments for this study were approved by the Institutional Review Board (IRB) of Chongqing University.

Hesperetin and TNF-α Treatment

Hesperetin (HPT) and dexamethasone (DEX) were purchased from Selleck (Selleck Chemicals, United States) and then dissolved in DMSO as a 10 mM stock solution. Rat chondrocytes were treated with HPT at different concentrations (1, 5, 10, 20, 50, and 100 μM); DMSO was used as a control. Meanwhile, exposure to 10 μM HPT was implemented at different time intervals (1, 2, 3, 4, and 5 days). Morphology caused by HPT at different concentrations (1, 5, 10, 20, 50, and 100 μM) was detected by microscopy (Olympus, Japan). In addition, 10 ng/ml of TNF-α alone (the TNF-α-treated group) or TNF-α plus HPT at 10 μM (TNF-α + HPT-treated group) or TNF-α plus DEX at 10 μM (TNF-α + DEX-treated group) was used for treating chondrocytes for 48 h (TNF-α and HPT or TNF-α and DEX were added in the same order). All the experiments were performed in triplicate independently.

Cell Viability Assay

Cell Counting Kit 8 (CCK-8) (Beyotime, China) was used to investigate cell viability and cytotoxicity. Chondrocytes were seeded at a density of 1,000 cells/well in a 96-well plate and tested for toxicity for 1–5 days with different concentrations of HPT. DMSO was used as a control. At designated time intervals, the cells were incubated with 10% CCK-8 reagent at 37°C for 2–4 h. After incubation, the corresponding absorbance was measured with a microplate reader at a wavelength of 490 nm.

The data were analyzed with GraphPad 8.0. All the experiments were performed in triplicate independently.

RT-qPCR Analysis

Chondrocytes were treated with TNF-α alone or TNF-α plus HPT and then harvested for the qRT-PCR assay. DMSO was used as control. Each sample was harvested using TRIzol reagent, and RNA was isolated. Total RNA was reverse transcribed into cDNA using the RevertAid First Strand cDNA Synthesis Kit (Thermo Fisher Scientific). Then, the cDNA was used as template to perform real-time polymerase chain reaction (PCR) on a StepOne Plus thermal cycler (Applied Biosystems). Primers were designed by NCBI primer blast and synthesized using Invitrogen. Data were analyzed according to the $2-\Delta\Delta ct$ method.

Western Blotting

Rat chondrocytes were lysed by RIPA lysis buffer to extract the total protein which was separated by SDS-PAGE gel electrophoresis and transferred to PVDF (polyvinylidene fluoride) membrane (0.2 μm; BioRad). After 1 h blocking with 5% skimmed milk, the membrane was incubated with primary antibody ACAN (Abcam, ab36861), COL2A (Santa Cruz, sc-7763), IL-1β (Proteintech, 66,737-1-lg), IL-6 (Zen Bio, 347023), MMP-13 (Zen Bio, 511755), PTGS2 (Zen Bio, 383967), Bcl-2 (Zen Bio, 381702), CDK1 (Abcam,ab18), Cyclin D1 (Zen Bio, 382442), p-AMPKα1 (Zen Bio, 310044), AMPKα (Zen Bio, 380431), and GAPDH (Zen Bio, 384404) antibodies overnight at 4°C. After washing 3 times with 1×TBST, the membrane was incubated with horseradish peroxidase-labeled secondary antibody (goat anti-rabbit/mouse IgG, 1:5,000) at room temperature for 1 h. Finally, target protein was visualized by the ECL Western Detection Kit (Thermo Fisher Scientific, United States) and quantified by ImageJ software.

Cell Cycle Flow Cytometric Analysis

Flow cytometry was used to determine the effect of HPT on the chondrocyte cycle. After being treated with TNF-α alone or TNF-α plus HPT, the chondrocytes were harvested and washed, followed by fixation using 70% alcohol at 4°C overnight. After washing the cells with PBS, they were treated with ribonuclease RNase A and incubated with propidium iodide (PI) for the cell cycle analysis on a BD FACSVerse™ flow cytometer (BD Bioscience, San Jose, CA).

RNA Sequencing

RNA sequencing was performed on chondrocytes in different treatments to determine the changes in their mRNA expression profiles. RNA extraction kit (Thermo Fisher Scientific, Waltham, MA) was used to extract total RNA from each group of cells. Send the obtained RNA sample to BGI Co., Ltd., Shenzhen, China, and perform RNA-seq operation on BGISEQ-500. The R language program was used to further analyze the sequencing results to find differential genes in the chip expression profile. Then, use the R program to perform the gene ontology (GO) biological function enrichment analysis and genome encyclopedia (KEGG) signal pathway enrichment analysis. All samples were repeated three times.

Immunostaining Assays

The chondrocytes were seeded on coverslips coated with 0.01% poly L-lysine. After treatment, the cells were fixed in 4% paraformaldehyde for 30 min, followed by rinsing with PBS and permeating with 0.1% Triton X-100 on ice for 5 min. Then, the cells were blocked with a blocking solution at 37°C for 1 h and then incubated with the primary antibody p-AMPKα1 (Zen Bio, 310044) at 4°C overnight and with a fluorescently labeled secondary antibody (concentration 1:200) at 37°C for 1 h, respectively. After counterstaining with DAPI, the samples were imaged and captured under a fluorescence microscope (Olympus, Japan).

Animal Model

The animal experiments were carried out following the protocol approved by the Animal Care and Use Committee of Chongqing University. The OA model was achieved by anterior cruciate ligament transection (ACLT) in SD rats, as described in our previous study (Wang et al., 2020a; Xu et al., 2021). There are 24 rats randomly assigned to four groups: healthy, OA (normal saline group), DEX, and HPT groups. Four weeks after ACLT surgery, 0.5 mg/kg DEX was injected into the knee joint in the DEX group, and 10 mM HPT was injected into the knee joint in the HPT group. Four weeks after drug treatment, all the rats were sacrificed by carbon dioxide anesthesia, then cervical dislocation, and articular cartilage samples were collected for microscopic evaluations. Six samples were collected in each group.

Histological Analysis

The samples of the OA animal model were collected 8 weeks after ACLT. First, the knee joints of the rats were fixed in 4% paraformaldehyde for 2 days. Subsequently, they were decalcified in 10% EDTA solution for 2 months, dehydrated with a concentration gradient of alcohol, embedded in paraffin, and cut into 10 μm thick paraffin sections. All specimens were stained with hematoxylin and eosin (H&E) and safranin-O fast green. H&E staining was used to observe changes in the surface of articular cartilage, cartilage levels, and the number and morphology of cartilage cells. In addition, the histological immunofluorescent staining for p-AMPKα1 (Zen Bio, 310044) was performed to verify HPT exhibits the effect *in vivo* on regulating the AMPK pathway. In the microscopic examination, the histological score was scored according to the histological evaluation performed in the previous study (Xu et al., 2019; Wang et al., 2020b). The (SD) score of each group was the content of cartilage matrix captured from the safranin-O-positive staining area by ImageJ software. In short, we selected the ROI of the red area of the cartilage matrix in each group, and then, calculate the intensity value of the algorithm built into the ImageJ software for further statistical analysis. The statistical analysis is based on the mean ± SD.

Statistical Analysis

SPSS 22.0 software package was used to perform statistical processing. One-way analysis of variance was used to determine significant differences between groups. The experimental data were expressed as mean ± SD (mean ± SEM), and $p < 0.05$ was considered statistically significant.

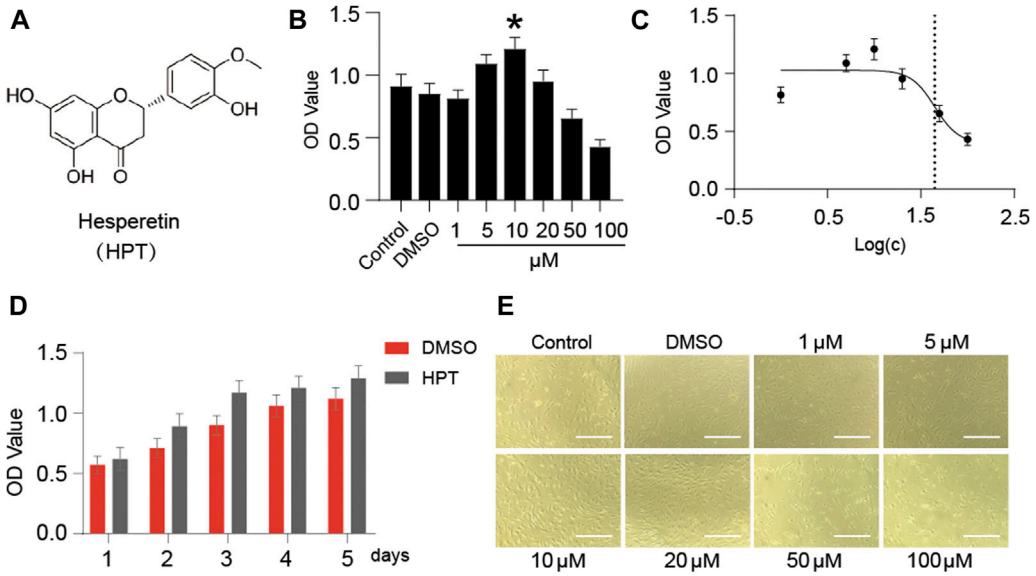


FIGURE 1 | Cytotoxicity of HPT-treated chondrocytes. **(A)** The molecular structure of HPT. **(B)** Different concentrations (1, 5, 10, 20, 50, and 100 μM) of HPT were cultured for 48 h, with $^*p < 0.05$ as a significant difference. **(C)** The IC50 of HPT to chondrocytes, and the concentration is transferred to Log(c). **(D)** HPT treated 10 μM and controlled the cell proliferation curve for 5 days. **(E)** Photographs of cells cultured with different concentrations (1, 5, 10, 20, 50, and 100 μM) of HPT for 48 h.

RESULTS

Cytotoxicity of HPT to Chondrocytes

Figure 1A presents the chemical structure of HPT. CCK-8 assay was used to investigate the cytotoxic effects of HPT on SD rat chondrocytes. The results showed no apparent cytotoxic effects of HPT on chondrocytes at concentrations of 0–20 μM; however, it had cytotoxic effects at concentrations ≥50 μM (**Figure 1B**). In addition, HPT promoted the proliferation of chondrocytes slightly at 10 μM concentration. Therefore, 10 μM HPT was the concentration selected for further studies. We further investigated the cell proliferation rate after treatment with 10 μM HPT for 5 days. Compared with the control group (DMSO), supplementation with 10 μM HPT increased cell proliferation (**Figure 1D**). There was no change in the morphology of chondrocytes after treatment with 1–20 μM HPT; however, chondrocytes exposed to 50 and 100 μM HPT showed significant morphological changes, and cell counts decreased in a dose-dependent pattern as well (**Figure 1E**).

HPT Recoveries TNF-α-Induced Abnormal Gene and Protein Expression

Chondrocytes are generally very sensitive to TNF-α, which reduces the aggrecan and collagen type II synthesis and promotes the development of OA. To investigate the protective function of HPT in TNF-α-treated chondrocytes, we examined the effect of HPT on aggrecan and collagen type II using the Western blotting analysis and RT-PCR. Moreover, we then examined the impact of HPT on TNF-α-induced production of IL-1β, IL-6, MMP13, and PTGS2 in chondrocytes. The cells were treated with 10 μM HPT and 10 ng/ml of TNF-α for 48 h. Compared with the control group, TNF-α significantly increased mRNA levels of IL-1β, IL-6, MMP-13, and PTGS2 and inhibited ACAN and COL2A gene expression ($^*p < 0.05$; TNF-α vs. control), while HPT recovered these gene levels ($\#p < 0.05$; TNF-α + HPT vs. TNF-α) (**Figures 2A–F**). Like gene expression results, HPT restored TNF-α-induced downregulation of COL2A and ACAN and reversed TNF-α-induced IL-1β, IL-6, MMP-13, and PTGS2 protein production (**Figures 2G,H**). Moreover, DEX also restored TNF-α-induced downregulation of COL2A and reversed TNF-α-induced IL-1β, IL-6, and MMP-13 protein production (**Figures 2I,J**). Finally, 20 and 30 μM HPT also restored TNF-α-induced downregulation of COL2A and reversed TNF-α-induced IL-1β and MMP-13 protein production (**Figures 2K,L**). These findings indicated that HPT could activate cartilaginous ECM synthesis and suppress the associated TNF-α-induced expression of inflammatory genes.

Effects of HPT on TNF-α-Induced Expression of Proliferative Gene/Protein

The qRT-PCR and Western blotting were used to investigate the gene and protein expression of Bcl-2, CDK1, and Cyclin D1. The results showed that TNF-α significantly decreased Bcl-2, CDK1, and Cyclin D1 mRNA levels ($^*p < 0.05$; TNF-α vs. control), while HPT recovered these gene levels ($\#p < 0.05$; TNF-α + HPT vs. TNF-α) (**Figures 3A–C**). Similar to the transcription level, the decreased Bcl-2, CDK1, and Cyclin D1 levels induced by TNF-α were restored to the control group level in the group with TNF-α + HPT ($^*p < 0.05$, TNF-α vs. control; $\#p < 0.05$, TNF-α + HPT vs. TNF-α) (**Figures 3D,E**).

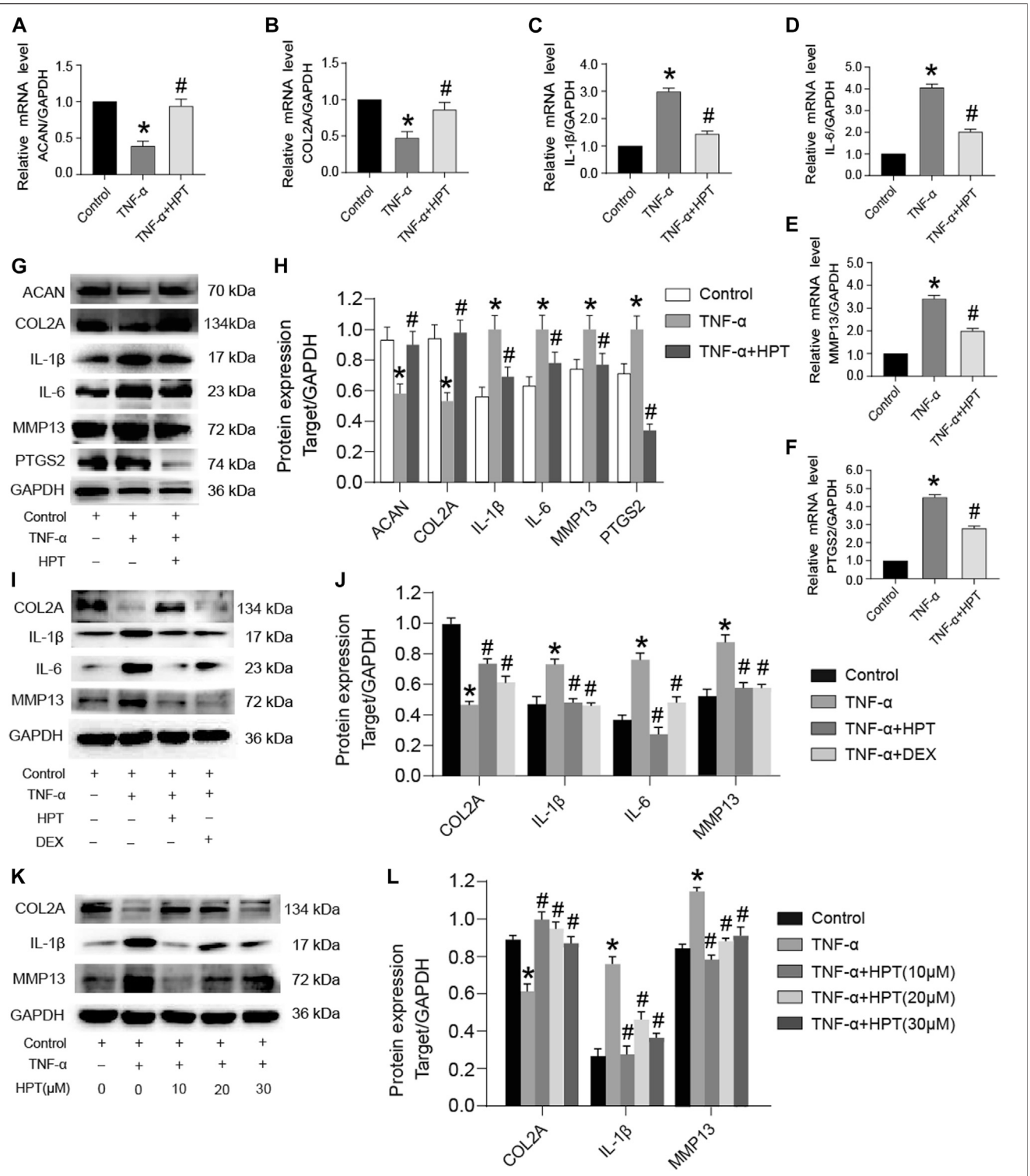


FIGURE 2 | HPT recovered TNF-α-induced abnormal expression of genes and proteins. **(A–F)** After stimulated chondrocytes with TNF-α and then treated them with or without 10 μM HPT for 48 h, the mRNA expression levels of ACAN, COL2A, IL-1β, IL-6, MMP-13, and PTGS2. **(G, H)** After stimulated chondrocytes with TNF-α and then treated them with or without 10 μM HPT for 48 h, the protein expression levels of IL-1β, IL-6, PTGS2 and (cartilage matrix markers) COL2A, ACAN, MMP13. **(I, J)** After stimulated chondrocytes with TNF-α and then treated them with/without 10 μM HPT or DEX for 48 h, the protein expression levels of IL-1β, IL-6, and (cartilage matrix markers) COL2A and MMP13. **(K, L)** After stimulated chondrocytes with TNF-α and then treated them with or without 10, 20, and 30 μM HPT for 48 h, the protein expression levels of IL-1β and (cartilage matrix markers) COL2A and MMP13. According to the intensity of semiquantitative IOD through the ImageJ software, $^{*}p < 0.05$ was considered as a significant difference from the control group; $\#p < 0.05$ was considered as a significant difference from TNF-α.

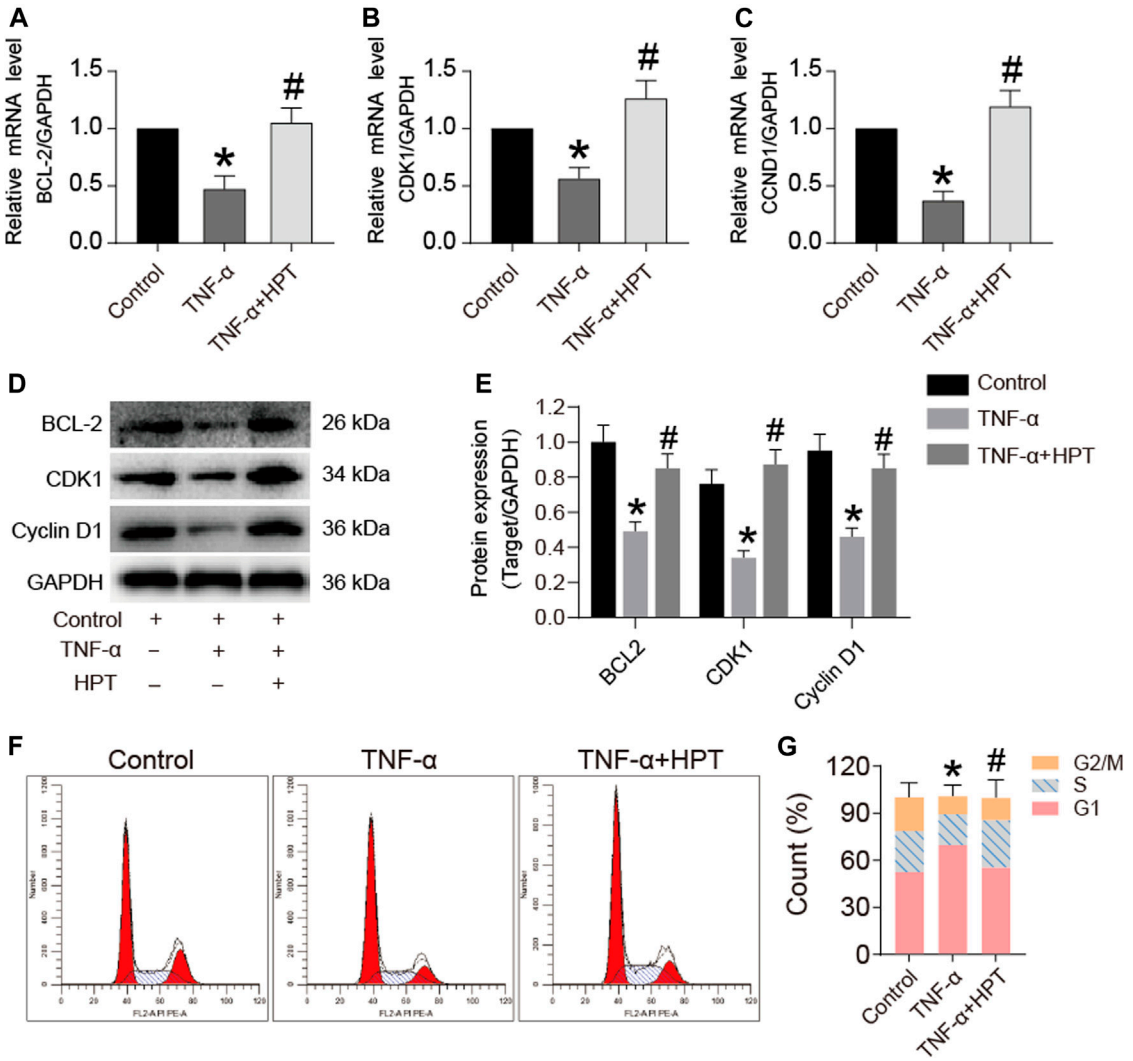


FIGURE 3 | The effect of HPT on the cell cycle of chondrocytes induced by TNF-α. **(A–E)** The expression levels of apoptosis and cycle-related genes and proteins after stimulated chondrocytes with TNF-α and then treated them with or without 10 μM HPT for 48 h. *$P < 0.05$ was considered as a significant difference from the control group; #$p < 0.05$ was considered as a significant difference from TNF-α. **(F, G)** Flow cytometry used to detect the effect of HPT on the chondrocytes cycle. Counted the percentages of the G2/M phase, s phase, and G1 phase, make statistical comparisons. There are three replicates for each concentration point. *$P < 0.05$ was considered as a significant difference from the control group; #$p < 0.05$ was considered as a significant difference from TNF-α.

We further investigated the cell cycle to determine whether HPT protects chondrocytes against the inhibitory effect of TNF-α on the proliferation of chondrocytes by flow cytometry. The results showed significant decreases in the S phase following TNF-α treatment (*$p < 0.05$; TNF-α vs. control), while the percentages of chondrocytes in the S phase were restored to the control group level in the group with TNF-α + HPT (#$p < 0.05$; TNF-α + HPT vs. TNF-α) (**Figures 3F,G**).

DEGs Identification and Pathway Enrichment Analysis

The RNA-seq experiments were performed in cells affected by TNF-α induction with or without HPT treatment to further investigate the protective and anti-inflammatory mechanism of HPT in TNF-α-induced chondrocytes. The results demonstrated that compared with the TNF-α group, there were many differentially expressed genes (DEGs) in chondrocytes treated with TNF-α and 10 μM HPT, of which 105 genes were upregulated and 444 genes were downregulated (**Figure 4A**). Furthermore, GO functional annotations were made on the identified DEGs, which were highly involved in cell processing, biological regulation, metabolic processes, and biological process regulation (**Figure 4B**). Furthermore, the KEGG signaling pathway enrichment analysis indicated that these DEGs were highly enriched in functions related to the longevity-regulating pathway, regulation of lipolysis in adipocytes, insulin signaling pathway, AMPK signaling pathway, and glucagon signaling pathway (**Figure 4C**).

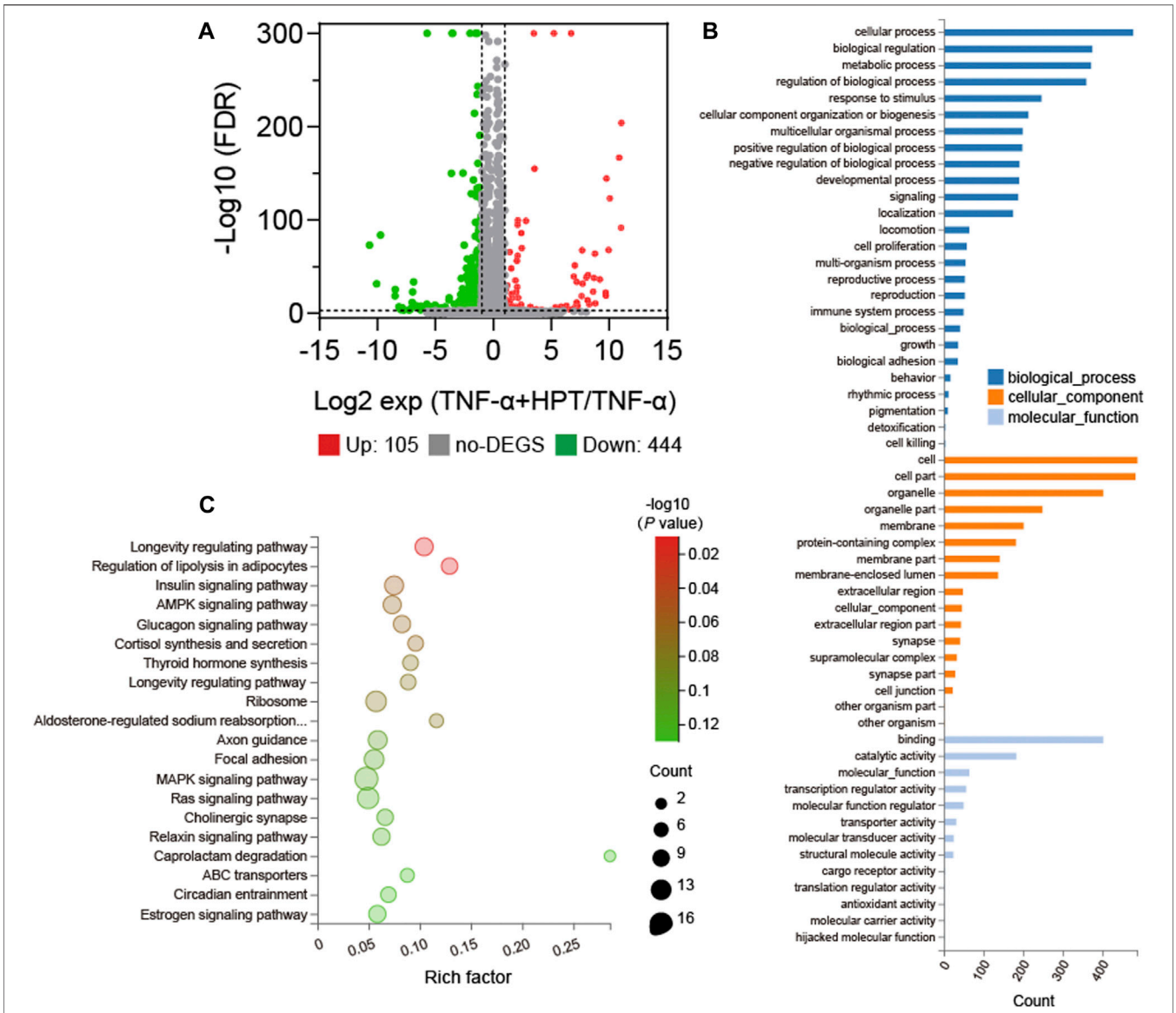


FIGURE 4 | Gene expression profile with or without 10 μM HPT treatment. **(A)** Volcano map of differentially expressed genes (DEGs) in HPT and control (upregulation: 105; downregulation: 444), FC (fold change) > 1 was considered as a positive DEGs. **(B)** GO enrichment those common choices for DEGs including biological processes (blue), cellular components (orange), and molecular functions (light blue). **(C)** Enrichment bubble chart based on the KEGG enrichment analysis. A larger *p* value indicates a higher degree of enrichment.

HPT Relieves TNF-α-Induced Inflammation of Chondrocytes through the AMPK Signaling Pathway

Based on the results of highly enriched signaling pathways, we selected AMPK signaling pathways for further analyses. Western blot analysis showed that TNF-α induction suppressed the phosphorylated-/total-AMPKα1 (p/t-AMPKα1) ratios; however, the phosphorylation of AMPKα1 increased after HPT supplementation (**Figures 5A,B**) (*p < 0.05). Furthermore, immunofluorescence staining with p-AMPKα1 was performed, which further supported the Western blot results (**Figure 5C**), indicating that HPT plays a key role in the activation of AMPK phosphorylation in chondrocytes. To determine the role of the AMPK signaling pathway in HPT-induced alleviation of inflammation, we examined the effect of HPT on TNF-α-induced inflammation with or without compound C, a selective AMPK inhibitor. Inhibition of AMPK activation by compound C abolished the HPT-induced decrease in IL-1β and MMP-13 levels (**Figures 5D–F**) ($^{a}p < 0.05$). In addition, it also diminished the upregulation of p-AMPKα1 and COL2A expression by HPT treatment (**Figures 5D,G,H**) ($^{a}p < 0.05$). These data suggested that HPT relieves TNF-α-induced inflammation of chondrocytes through the AMPK signaling pathway.

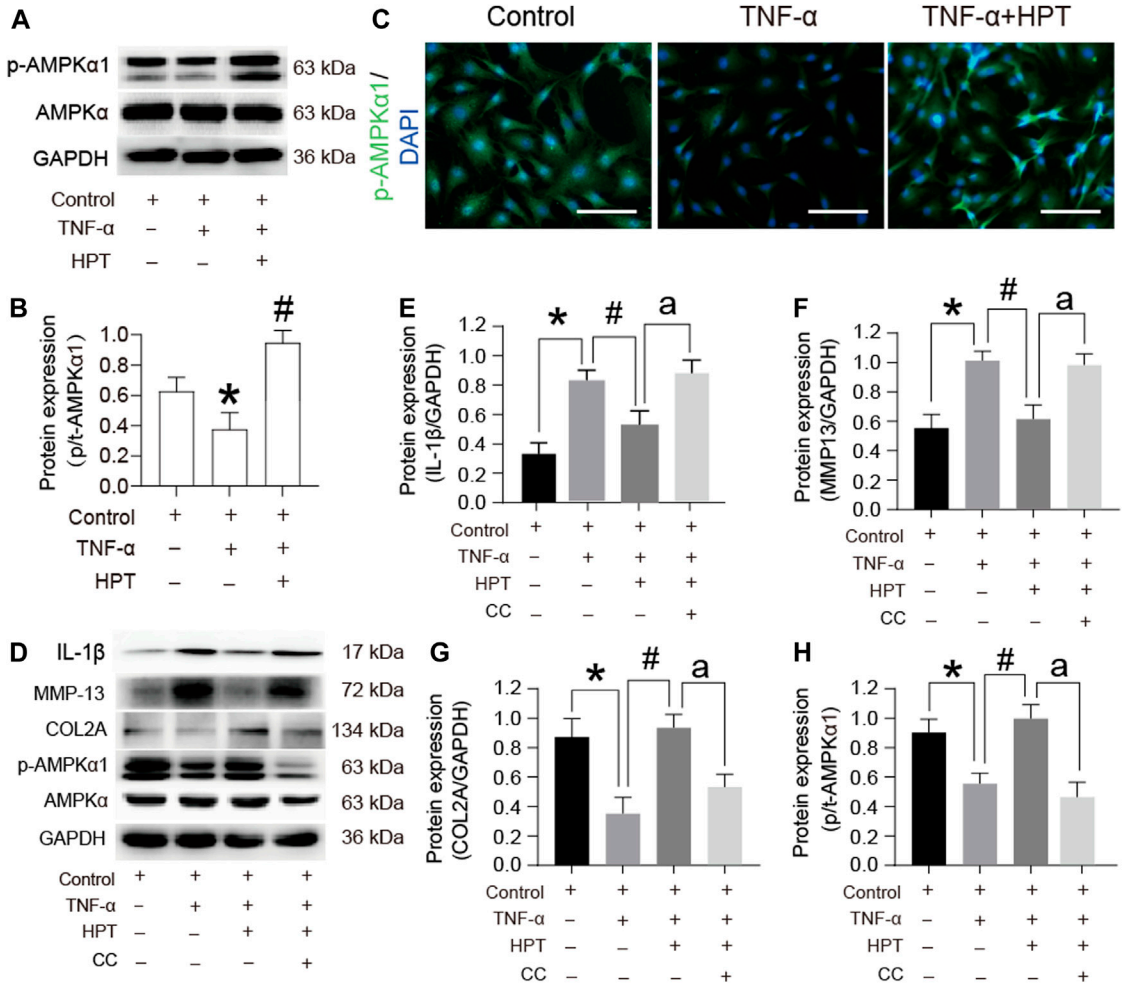


FIGURE 5 | AMPK signaling pathway participates in the protective effect of HPT on TNF-α-stimulated rat chondrocytes. **(A, B)** Protein expression profile of p-AMPKα1 cultured under TNF-α conditions with or without HPT. **(C)** Immunofluorescence of p-AMPKα1 in chondrocytes treated with TNF-α and/or HPT. **(D–H)** Protein expression profile of IL-1β, MMP13, COL2A, and p-AMPKα1 cultured under the condition of HPT with or without and TNF-α with or without CC. For statistical analysis, $^{*}p < 0.05$ was considered as a significant difference from the control group; $\#p < 0.05$ was considered as a significant difference from TNF-α. $^{a}P < 0.05$ was considered as a significant difference from TNF-α + HPT.

HPT Prevents Cartilage Degradation in the Rat Model

ACLT was used to establish the rat OA model. Healthy rats served as a control group. HPT was locally injected into the joint cavity 4 weeks after ACLT surgery. As shown in **Figure 6**, the articular cartilage had a regular shape in the healthy group. The articular cartilage morphology in the OA group was uneven, with reduced cartilage thickness compared with the healthy group. The articular cartilage in the HPT group was more regular, with significantly higher cartilage thickness compared with the OA group. The cartilage matrix of the OA group was significantly thinner than that of the healthy group ($^{*}p < 0.05$). HPT treatment significantly changed this situation ($\#p < 0.05$). In addition, compared with the healthy group, the histological score of the OA group was significantly different ($^{*}p < 0.05$); however, DEX and HPT treatment significantly improved cartilage degeneration, and the histological score was significantly different from that of the OA group ($\#p < 0.05$), indicating that HPT treatment successfully inhibited cartilage degeneration. In addition, the expression of p-AMPKα1 was measured *in vivo* by immunofluorescent staining (**Figure 6**). The result showed that TNF-α induction suppressed the phosphorylation of AMPKα1; however, the phosphorylation level of AMPKα1 was recovered after DEX and HPT supplementation.

DISCUSSION

OA is a chronic disease with low-grade inflammation (Haseeb and Haqqi, 2013; Bartels et al., 2016). Thus, inhibition of

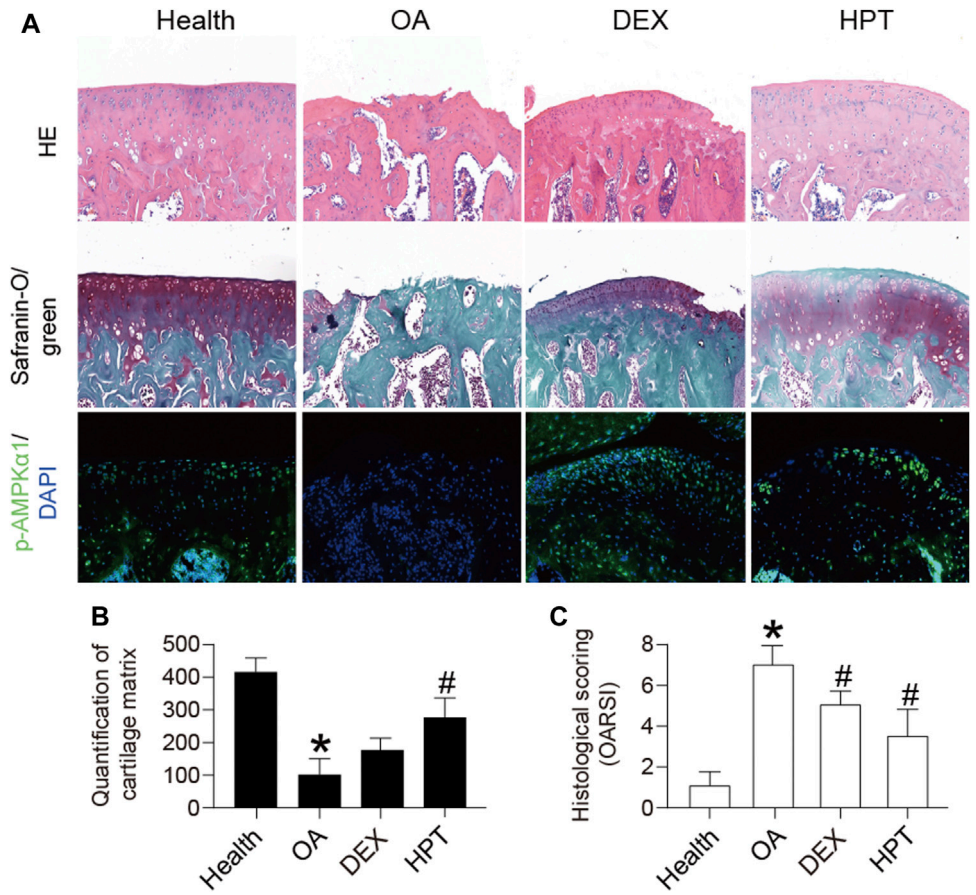


FIGURE 6 | Histological analysis of knee cartilage after HPT treatment (H&E, safranin-O/green, and IF), magnified 100 times. For statistical analysis, $^{*}p < 0.05$ was considered statistically significant compared with healthy; $\#p < 0.05$ was considered statistically significant with OA. DEX, dexamethasone as positive control.

inflammation is considered a strategy to delay the progression of OA (Robinson et al., 2016). However, there is currently no medication available to cure OA or decelerate its progression. Recently, an increasing number of natural compounds have caused concerns as ideal drugs for OA due to their anti-inflammatory activities and limited side effects (Wang et al., 2020a). Thus, a drug, like HPT, with an anti-inflammatory function that delays the structural progression of the disease, represents a novel class of drugs to treat OA.

Growing evidence indicates that HPT positively affects anti-inflammatory reactions (Spagnuolo et al., 2018; Khan et al., 2020). Inflammatory mediators, such as TNF-α, IL-1β, and IL-6, can induce metabolic factors such as PTGS2 and MMPs, leading to articular cartilage degeneration (Oliviero et al., 2020). It has been reported that HPT exerts marked anti-inflammatory effects in mice with neurodegeneration (Ikram et al., 2019) and postmyocardial infarction (Wang et al., 2017). It has also been reported that HPT can significantly inhibit IL-1β-induced inflammatory response in human chondrocytes in osteoarthritis (Lin et al., 2020). In this study, HPT activated cartilaginous ECM synthesis and suppressed the associated TNF-α-induced expression of inflammatory genes. Furthermore, HPT at 10 μM concentration promoted the proliferation of chondrocytes slightly. The RT-qPCR, Western blotting, and flow cytometry results also showed that HPT reversed the inhibitory effect of TNF-α on chondrocyte proliferation. It also has been reported that HPT can protect HK-2 cells by reducing the apoptosis induced by cisplatin (Chen et al., 2019). The above finding shows that HPT can protect chondrocytes. However, the related signaling pathways and molecular mechanisms of HPT in chondrocytes remain unclear.

HPT can inhibit inflammatory responses in lipopolysaccharide-induced RAW 264.7 cells via the inhibition of the NF-κB pathway and activation of the Nrf2/HO-1 pathway (Ren et al., 2016). Researchers found that HPT inhibits IL-1β-induced inflammation in human OA chondrocytes by suppressing NF-κB and initiating the Nrf2/HO-1 pathway (Lin et al., 2020). However, the RNA-seq experiment was used to investigate the protective and anti-inflammatory mechanisms of HPT in TNF-α-induced chondrocytes in the present study. Enrichment analysis of the KEGG signaling pathway showed that important DEGs are highly enriched in the longevity regulating pathway, regulation of lipolysis in adipocytes, insulin signaling pathway, AMPK signaling pathway, and glucagon signaling pathway, among which activating the AMPK signaling pathway can slow down the development and progression of OA (Li et al., 2020). AMPK is the main regulator of

energy balance and metabolism. Decreased AMPK activity can be assessed by AMPK-catalyzed phosphorylation of a specific threonine in the α subunit (AMPKα1) (Stein et al., 2000). Therefore, we evaluated the phosphorylation level of AMPKα1 in chondrocytes and showed that TNF-α reduced the phosphorylation level of AMPKα1. Immunofluorescence staining also confirmed this finding, which is consistent with previous studies demonstrating that decreased phosphorylation of AMPKα1 is also seen in chondrocytes in response to TNF-α (Terkeltaub et al., 2011). Furthermore, flavonoids have always been considered natural AMPK agonists, and many of their pharmacological activities depend on the activation of AMPK (Gentile et al., 2018). The present study showed that HPT plays a key role in the activation of AMPK phosphorylation in chondrocytes.

We examined the effect of HPT on TNF-α-induced inflammation with or without compound C, a selective AMPK inhibitor, to determine the role of the AMPK signaling pathway in HPT-induced alleviation of inflammation. Further verification experiments showed that HPT relieves TNF-α-induced inflammation of chondrocytes through the AMPK signaling pathway. It has also been demonstrated that AMPKα1 deficiency in chondrocytes accelerates the development of both injury-induced and age-related spontaneous OA in mice (Zhou et al., 2017). Furthermore, it is well known that the activation of AMPK can inhibit the inflammatory response by inhibiting the function of the NF-κB signaling pathway (Salminen et al., 2011). Therefore, we speculate that HPT can be regulated through the AMPK signaling pathway to protect chondrocytes.

This study established an ACLT rat model and locally administered HPT treatment to further determine the therapeutic effect of HPT on OA. The ACLT-induced OA model we established is very similar to human osteoarthritis, and our previous studies have been reported (Wang et al., 2020a). It has also been reported that the ACLT model accompanied the activation of TNF-α (Xie et al., 2018). Besides, restabilization of joint instability by ACLT may suppress inflammatory cytokines (TNF-α), thereby delaying the progression of OA (Murata et al., 2017). Previous studies have also demonstrated that HPT can inhibit the development of OA induced by the DMM model (Lin et al., 2020). Our research results showed that HPT treatment could significantly inhibit the inflammatory response of the ACLT-induced OA model. Furthermore, HPT treatment could delay the progression of articular cartilage degeneration, and the cartilage defects in the rat knee joint were significantly restored, with increased cartilage thickness. Furthermore, the *in vivo* study provided evidence that HPT prevented the occurrence and development of OA by reducing cartilage degradation, delaying cartilage surface erosion, and maintaining chondrocyte formation. In conclusion, this study suggests that HPT might be used as a potential therapeutic agent for OA.

DATA AVAILABILITY STATEMENT

The datasets presented in this study can be found in online repositories. The names of the repository/repositories and accession number(s) can be found in the following: NCBI BioProject PRJNA755303.

ETHICS STATEMENT

Animal experiments for this study were approved by the Institutional Review Board (IRB) of Chongqing University.

AUTHOR CONTRIBUTIONS

LY and CW conceived and designed the experiments. JW, LP, and FF performed the experiments. JW and YQ analyzed the data and prepared figures. CC wrote the manuscript. All the authors read and approved the final manuscript.

FUNDING

This work was supported by the National Natural Science Foundation of China (11902058 and 11832008), Innovation and Attracting Talents Program for College and University ("111" Project) (Grant No. B06023), Visiting Scholar Foundation of Key Laboratory of Biorheological Science and Technology (Chongqing University), Ministry of Education (Grant number: CQKLBST-2018-005), and Postdoctoral Fund of the Natural Science Foundation of Chongqing Science and Technology Bureau (grant number: cstc2019jcyj-bshX0059).

REFERENCES

Bartels, E. M., Juhl, C. B., Christensen, R., Hagen, K. B., Danneskiold-Samsøe, B., Dagfinrud, H., et al. (2016). Aquatic Exercise for the Treatment of Knee and Hip Osteoarthritis. *Cochrane Database Syst. Rev.* 3, CD005523. doi:10.1002/14651858.CD005523.pub3

Chen, D., Shen, J., Zhao, W., Wang, T., Han, L., Hamilton, J. L., et al. (2017). Osteoarthritis: toward a Comprehensive Understanding of Pathological Mechanism. *Bone Res.* 5, 16044. doi:10.1038/boneres.2016.44

Chen, X., Wei, W., Li, Y., Huang, J., and Ci, X. (2019). Hesperetin Relieves Cisplatin-Induced Acute Kidney Injury by Mitigating Oxidative Stress, Inflammation and Apoptosis. *Chem. Biol. Interact* 308, 269–278. doi:10.1016/j.cbi.2019.05.040

Deyle, G. D., Allen, C. S., Allison, S. C., Gill, N. W., Hando, B. R., Petersen, E. J., et al. (2020). Physical Therapy versus Glucocorticoid Injection for Osteoarthritis of the Knee. *N. Engl. J. Med.* 382 (15), 1420–1429. doi:10.1056/NEJMoa1905877

Dieppe, P. A., and Lohmander, L. S. (2005). Pathogenesis and Management of Pain in Osteoarthritis. *Lancet* 365 (9463), 965–973. doi:10.1016/S0140-6736(05)71086-2

Gentile, D., Fornai, M., Pellegrini, C., Colucci, R., Blandizzi, C., and Antonioli, L. (2018). Dietary Flavonoids as a Potential Intervention to Improve Redox Balance in Obesity and Related Co-morbidities: a Review. *Nutr. Res. Rev.* 31 (2), 239–247. doi:10.1017/S0954422418000082

Glyn-Jones, S., Palmer, A. J., Agricola, R., Price, A. J., Vincent, T. L., Weinans, H., et al. (2015). Osteoarthritis. *Lancet* 386 (9991), 376–387. doi:10.1016/S0140-6736(14)60802-3

Gonzalez-Rey, E., Varela, N., Sheibanie, A. F., Chorny, A., Ganea, D., and Delgado, M. (2006). Cortistatin, an Antiinflammatory Peptide with Therapeutic Action

in Inflammatory Bowel Disease. *Proc. Natl. Acad. Sci. U S A.* 103 (11), 4228–4233. doi:10.1073/pnas.0508997103

Haseeb, A., and Haqqi, T. M. (2013). Immunopathogenesis of Osteoarthritis. *Clin. Immunol.* 146 (3), 185–196. doi:10.1016/j.clim.2012.12.011

Hayden, M. S., and Ghosh, S. (2014). Regulation of NF-Kb by TNF Family Cytokines. *Semin. Immunol.* 26 (3), 253–266. doi:10.1016/j.smim.2014.05.004

Hosseinzadeh, A., Kamrava, S. K., Joghataei, M. T., Darabi, R., Shakeri-Zadeh, A., Shahriari, M., et al. (2016). Apoptosis Signaling Pathways in Osteoarthritis and Possible Protective Role of Melatonin. *J. Pineal Res.* 61 (4), 411–425. doi:10.1111/jpi.12362

Ikram, M., Muhammad, T., Rehman, S. U., Khan, A., Jo, M. G., Ali, T., et al. (2019). Hesperetin Confers Neuroprotection by Regulating Nrf2/TLR4/NF-Kb Signaling in an Aβ Mouse Model. *Mol. Neurobiol.* 56 (9), 6293–6309. doi:10.1007/s12035-019-1512-7

Khan, A., Ikram, M., Hahm, J. R., and Kim, M. O. (2020). Antioxidant and Anti-inflammatory Effects of Citrus Flavonoid Hesperetin: Special Focus on Neurological Disorders. *Antioxidants (Basel)* 9 (7), 609. doi:10.3390/antiox9070609

Kolasinski, S. L., Neogi, T., Hochberg, M. C., Oatis, C., Guyatt, G., Block, J., et al. (2020). 2019 American College of Rheumatology/Arthritis Foundation Guideline for the Management of Osteoarthritis of the Hand, Hip, and Knee. *Arthritis Care Res. (Hoboken)* 72 (2), 149–162. doi:10.1002/art.4114210.1002/acr.24131

Li, J., Zhang, B., Liu, W. X., Lu, K., Pan, H., Wang, T., et al. (2020). Metformin Limits Osteoarthritis Development and Progression through Activation of AMPK Signalling. *Ann. Rheum. Dis.* 79 (5), 635–645. doi:10.1136/annrheumdis-2019-216713

Lin, X., Huang, K., Zhu, G., Huang, Z., Qin, A., and Fan, S. (2016). The Effects of Acupuncture on Chronic Knee Pain Due to Osteoarthritis: A Meta-Analysis. *J. Bone Jt. Surg Am* 98 (18), 1578–1585. doi:10.2106/JBJS.15.00620

Lin, Z., Fu, C., Yan, Z., Wu, Y., Zhan, J., Lou, Z., et al. (2020). The Protective Effect of Hesperetin in Osteoarthritis: an *In Vitro* and *In Vivo* Study. *Food Funct.* 11 (3), 2654–2666. doi:10.1039/c9fo02552a

Muhammad, T., Ikram, M., Ullah, R., Rehman, S. U., and Kim, M. O. (2019). Hesperetin, a Citrus Flavonoid, Attenuates LPS-Induced Neuroinflammation, Apoptosis and Memory Impairments by Modulating TLR4/NF-Kb Signaling. *Nutrients* 11 (3), 648. doi:10.3390/nu11030648

Murata, K., Kanemura, N., Kokubun, T., Fujino, T., Morishita, Y., Onitsuka, K., et al. (2017). Controlling Joint Instability Delays the Degeneration of Articular Cartilage in a Rat Model. *Osteoarthritis Cartilage* 25 (2), 297–308. doi:10.1016/j.joca.2016.10.011

Neogi, T. (2013). The Epidemiology and Impact of Pain in Osteoarthritis. *Osteoarthritis Cartilage* 21 (9), 1145–1153. doi:10.1016/j.joca.2013.03.018

Oliviero, F., Ramonda, R., Scanu, A., Galozzi, P., Favero, M., and Punzi, L. (2020). Levels of Inflammatory Cytokines and Metalloproteinases Are Increased in Knee Synovial Fluid of Patients with Concomitant Erosive Hand Osteoarthritis. *Clin. Exp. Rheumatol.* 38 (4), 800.

Parhiz, H., Roohbakhsh, A., Soltani, F., Rezaee, R., and Iranshahi, M. (2015). Antioxidant and Anti-inflammatory Properties of the Citrus Flavonoids Hesperidin and Hesperetin: an Updated Review of Their Molecular Mechanisms and Experimental Models. *Phytother Res.* 29 (3), 323–331. doi:10.1002/ptr.5256

Ren, H., Hao, J., Liu, T., Zhang, D., Lv, H., Song, E., et al. (2016). Hesperetin Suppresses Inflammatory Responses in Lipopolysaccharide-Induced RAW 264.7 Cells via the Inhibition of NF-Kb and Activation of Nrf2/HO-1 Pathways. *Inflammation* 39 (3), 964–973. doi:10.1007/s10753-016-0311-9

Robinson, W. H., Lepus, C. M., Wang, Q., Raghu, H., Mao, R., Lindstrom, T. M., et al. (2016). Low-grade Inflammation as a Key Mediator of the Pathogenesis of Osteoarthritis. *Nat. Rev. Rheumatol.* 12 (10), 580–592. doi:10.1038/nrrheum.2016.136

Saklatvala, J. (1986). Tumour Necrosis Factor Alpha Stimulates Resorption and Inhibits Synthesis of Proteoglycan in Cartilage. *Nature* 322 (6079), 547–549. doi:10.1038/322547a0

Salminen, A., Hyttinen, J. M., and Kaarniranta, K. (2011). AMP-activated Protein Kinase Inhibits NF-Kb Signaling and Inflammation: Impact on Healthspan and Lifespan. *J. Mol. Med. (Berl)* 89 (7), 667–676. doi:10.1007/s00109-011-0748-0

Spagnuolo, C., Moccia, S., and Russo, G. L. (2018). Anti-inflammatory Effects of Flavonoids in Neurodegenerative Disorders. *Eur. J. Med. Chem.* 153, 105–115. doi:10.1016/j.ejmech.2017.09.001

Stein, S. C., Woods, A., Jones, N. A., Davison, M. D., and Carling, D. (2000). The Regulation of AMP-Activated Protein Kinase by Phosphorylation. *Biochem. J.* 345 Pt 3, 437–443. doi:10.1042/bj3450437

Terkeltaub, R., Yang, B., Lotz, M., and Liu-Bryan, R. (2011). Chondrocyte AMP-Activated Protein Kinase Activity Suppresses Matrix Degradation Responses to Proinflammatory Cytokines Interleukin-1β and Tumor Necrosis Factor α. *Arthritis Rheum.* 63 (7), 1928–1937. doi:10.1002/art.30333

Wang, B., Li, L., Jin, P., Li, M., and Li, J. (2017). Hesperetin Protects against Inflammatory Response and Cardiac Fibrosis in Postmyocardial Infarction Mice by Inhibiting Nuclear Factor κB Signaling Pathway. *Exp. Ther. Med.* 14 (3), 2255–2260. doi:10.3892/etm.2017.4729

Wang, C., Al-Ani, M. K., Sha, Y., Chi, Q., Dong, N., Yang, L., et al. (2019). Psoralen Protects Chondrocytes, Exhibits Anti-inflammatory Effects on Synoviocytes, and Attenuates Monosodium Iodoacetate-Induced Osteoarthritis. *Int. J. Biol. Sci.* 15 (1), 229–238. doi:10.7150/ijbs.28830

Wang, C., Gao, Y., Zhang, Z., Chen, C., Chi, Q., Xu, K., et al. (2020a). Ursolic Acid Protects Chondrocytes, Exhibits Anti-inflammatory Properties via Regulation of the NF-Kb/nlrp3 Inflammasome Pathway and Ameliorates Osteoarthritis. *Biomed. Pharmacother.* 130, 110568. doi:10.1016/j.biopha.2020.110568

Wang, C., Gao, Y., Zhang, Z., Chi, Q., Liu, Y., Yang, L., et al. (2020b). Safflower Yellow Alleviates Osteoarthritis and Prevents Inflammation by Inhibiting PGE2 Release and Regulating NF-Kb/sirt1/AMPK Signaling Pathways. *Phytomedicine* 78, 153305. doi:10.1016/j.phymed.2020.153305

Wang, K., Xu, J., Hunter, D. J., and Ding, C. (2015). Investigational Drugs for the Treatment of Osteoarthritis. *Expert Opin. Investig. Drugs* 24 (12), 1539–1556. doi:10.1517/13543784.2015.1091880

Wang, S. W., Wang, W., Sheng, H., Bai, Y. F., Weng, Y. Y., Fan, X. Y., et al. (2020c). Hesperetin, a SIRT1 Activator, Inhibits Hepatic Inflammation via AMPK/CREB Pathway. *Int. Immunopharmacol* 89 (Pt B), 107036. doi:10.1016/j.intimp.2020.107036

Wang, T., and He, C. (2018). Pro-inflammatory Cytokines: The Link between Obesity and Osteoarthritis. *Cytokine Growth Factor. Rev.* 44, 38–50. doi:10.1016/j.cytogfr.2018.10.002

Xie, J., Zhang, D., Lin, Y., Yuan, Q., and Zhou, X. (2018). Anterior Cruciate Ligament Transection-Induced Cellular and Extracellular Events in Menisci: Implications for Osteoarthritis. *Am. J. Sports Med.* 46 (5), 1185–1198. doi:10.1177/0363546518756087

Xu, K., Gao, Y., Yang, L., Liu, Y., and Wang, C. (2021). Magnolin Exhibits Anti-inflammatory Effects on Chondrocytes via the NF-Kb Pathway for Attenuating Anterior Cruciate Ligament Transection-Induced Osteoarthritis. *Connect. Tissue Res.* 62 (4), 475–484. doi:10.1080/03008207.2020.1778679

Xu, K., Sha, Y., Wang, S., Chi, Q., Liu, Y., Wang, C., et al. (2019). Effects of Bakuchiol on Chondrocyte Proliferation via the PI3K-Akt and ERK1/2 Pathways Mediated by the Estrogen Receptor for Promotion of the Regeneration of Knee Articular Cartilage Defects. *Cell Prolif* 52 (5), e12666. doi:10.1111/cpr.12666

Zhao, Y. P., Liu, B., Tian, Q. Y., Wei, J. L., Richbourgh, B., and Liu, C. J. (2015). Progranulin Protects against Osteoarthritis through Interacting with TNF-α and β-Catenin Signalling. *Ann. Rheum. Dis.* 74 (12), 2244–2253. doi:10.1136/annrheumdis-2014-205779

Zhou, S., Lu, W., Chen, L., Ge, Q., Chen, D., Xu, Z., et al. (2017). AMPK Deficiency in Chondrocytes Accelerated the Progression of Instability-Induced and Ageing-Associated Osteoarthritis in Adult Mice. *Sci. Rep.* 7, 43245. doi:10.1038/srep43245

Zhu, Z., Li, J., Ruan, G., Wang, G., Huang, C., and Ding, C. (2018). Investigational Drugs for the Treatment of Osteoarthritis, an Update on Recent Developments. *Expert Opin. Investig. Drugs* 27 (11), 881–900. doi:10.1080/13543784.2018.1539075

Conflict of Interest: The authors declare that the research was conducted in the absence of any commercial or financial relationships that could be construed as a potential conflict of interest.

Publisher's Note: All claims expressed in this article are solely those of the authors and do not necessarily represent those of their affiliated organizations or those of the publisher, the editors, and the reviewers. Any product that may be evaluated in this article, or claim that may be made by its manufacturer, is not guaranteed or endorsed by the publisher.

Copyright © 2021 Wu, Qian, Chen, Feng, Pan, Yang and Wang. This is an open-access article distributed under the terms of the Creative Commons Attribution License (CC BY). The use, distribution or reproduction in other forums is permitted, provided the original author(s) and the copyright owner(s) are credited and that the original publication in this journal is cited, in accordance with accepted academic practice. No use, distribution or reproduction is permitted which does not comply with these terms.

frontiers in Pharmacology

ORIGINAL RESEARCH
published: 17 September 2021
doi: 10.3389/fphar.2021.750826

Berberine Alleviates Non-alcoholic Steatohepatitis Through Modulating Gut Microbiota Mediated Intestinal FXR Activation

Xiangbing Shu[1,2†], *Meng Li*[1†], *Ying Cao*[1], *Chunlin Li*[1], *Wenjun Zhou*[1], *Guang Ji*[1*] and *Li Zhang*[1*]

[1]Institute of Digestive Diseases, Longhua Hospital, Shanghai University of Traditional Chinese Medicine, Shanghai, China, [2]Department of Geratology, Baoshan Branch of Shuguang Hospital, Shanghai University of Traditional Chinese Medicine, Shanghai, China

OPEN ACCESS

Edited by:
Zhaocheng Ma,
Huazhong Agricultural University, China

Reviewed by:
Vijay Omprakash Kothari,
Nirma University, India
Yongsheng Chen,
Jinan University, China

***Correspondence:**
Guang Ji
jiliver@vip.sina.com
Li Zhang
zhangli.hl@163.com

†These authors share first authorship

Specialty section:
This article was submitted to Ethnopharmacology, a section of the journal Frontiers in Pharmacology

Received: 31 July 2021
Accepted: 06 September 2021
Published: 17 September 2021

Citation:
Shu X, Li M, Cao Y, Li C, Zhou W, Ji G and Zhang L (2021) Berberine Alleviates Non-alcoholic Steatohepatitis Through Modulating Gut Microbiota Mediated Intestinal FXR Activation. Front. Pharmacol. 12:750826. doi: 10.3389/fphar.2021.750826

Berberine is a natural plant alkaloid isolated from a diverse range of genera, it obtains anti-inflammatory, anti-obesity, and hepatoprotective properties, and is a promising agent for non-alcoholic steatohepatitis (NASH). Farnesoid X receptor (FXR) is a bile acid receptor and a drug target for NASH, however, the underlying mechanisms of berberine on regulating FXR are still unknown. In the present study, we feed mice with a 12-week high-fat diet with interval dextran sulfate sodium (0.5% in drinking water) diet to induce NASH, and treat the mice with berberine (100 mg/kg per day) *via* oral gavage for additional 4 weeks. We demonstrate that administration of berberine alleviates steatosis and infiltration of inflammatory cells in the liver of NASH mice. We apply 16S ribosomal DNA sequencing to screen the structure of gut microbiota, and ultra-performance liquid chromatography-tandem mass spectrometry analysis to determine the bile acid profiles. The results show that berberine modulates gut dysbiosis, and specifically increases the relative abundance of *Clostridiales*, *Lactobacillaceae,* and *Bacteroidale*. Berberine modulated microbiomes are associated with bile acid de-conjugation and transformation, which are consistent with the altered bile acid species (e.g., deoxycholic acid, ursodeoxycholic acid) upon berberine treatment. BA species that respond to berberine treatment are known FXR agonists, thus we performed quantitative Real Time-PCR and western blot to examine the FXR pathway, and find that berberine up-regulates intestinal FXR and fibroblast growth factor 15 (FGF15) expression, and the secretion of FGF15 further inhibits lipogenesis and nuclear factor-κB activation in the liver. Whereas the beneficial effects of berberine are blunted in FXR knockout mice. Our results reveal that berberine alleviates NASH by modulating the interplay of gut microbiota and bile acid metabolism, as well as the subsequent intestinal FXR activation.

Keywords: berberine, non-alcoholic steatohepatitis (NASH), gut microbiota, bile acids, farnesoid X receptor (FXR)

INTRODUCTION

Nonalcoholic fatty liver disease (NAFLD) is becoming a world epidemic currently, the histopathologic spectrum of NAFLD includes simple steatosis, nonalcoholic steatohepatitis (NASH), fibrosis, and hepatocellular carcinoma (Pataky et al., 2016). Although simple steatosis is considered to be benign, the presence of inflammation and injury in NASH usually indicates the liver injury (Takaki et al., 2014), and approximately 30% of NASH patients could eventually develop into cirrhosis or hepatocellular carcinoma (Adams et al., 2005; Ekstedt et al., 2006). Dietary management and lifestyle modification are the first-line recommendations for NASH treatment, however, many patients are difficult to maintain the pattern for a prolonged period of time, making pharmaceutical therapy in urgent need. Since the mechanisms of NASH are profound and are only partially understood, there are no approved drugs in the NASH field.

Berberine (BBR) is a natural product that is principally isolated from herbs such as *Coptis chinensis* Franch. [Ranunculaceae], *Phellodendron chinense* C.K.Schneid. [Rutaceae], *Hydrastis canadensis* L. [Ranunculaceae], *Berberis aquifolium* Pursh [Berberidaceae], and *Berberis vulgaris* L. [Berberidaceae] (Neag et al., 2018). BBR is initially used as an anti-microbial agent for infective diarrhea. Since the 1980s, BBR has been reported to be beneficial for metabolic disorders such as type 2 diabetes (Yin et al., 2008; Lan et al., 2015; Belwal et al., 2020), dyslipidemia (Guo et al., 2019), NAFLD/NASH (Zhou et al., 2019) among others. However, the effects of BBR contrast with its low bioavailability, thus gut microbiota, as well as microbiota-derived metabolites, are proposed as the critical mechanisms for BBR (Zhang et al., 2020). The reciprocal interaction of bile acids (BAs) and gut microbiota has long been recognized. BAs undergo enterohepatic circulation several times per day, the primary BAs that are produced in the liver can convert to secondary BAs by the action of microbiomes, whereas the anti-microbial properties of BAs determine the growth of certain microbial species. BA receptor farnesoid X receptor (FXR) is a promising drug target for NASH, and FXR agonists are currently tested in clinical trials for NASH (Gonzalez et al., 2016; Schmidt et al., 2017). While the unwanted side effects of exogenous FXR agonists are difficult to avoid, endogenous FXR activation might be an alternative choice. Studies proposed that BBR administration decreased the enrichment of *Clostridium*, and inhibited the deconjugation of primary BA, e.g., taurine conjugated cholic acid (TCA), which activated intestinal FXR in physiologically healthy and obese mice (Sun et al., 2017; Tian et al., 2019). However, whether the regulation of BBR on gut microbiota and BA metabolism activates intestinal FXR in NASH is still unknown.

In the present study, we show that BBR administration potently improves hepatic steatosis and reduces infiltration of inflammatory cells in the liver of NASH mice. Applying 16S ribosomal DNA (16SrDNA)-based microbiota analysis and BA profiling, we demonstrate that BBR treatment remodels the structure of gut microbiota and alters the composition of BA species in NASH mice. The increase of certain BA species, e.g., deoxycholic acid (DCA), chenodeoxycholic acid (CDCA) in the intestine might activate FXR-fibroblast growth factor 15 (FGF15) axis, and further suppresses lipogenesis and inflammation in the liver. We also demonstrate that the beneficial effects of BBR are abolished in FXR knock-out mice. These findings thus suggest that intestinal FXR activation is one of the underlying mechanisms of BBR on NASH mice.

MATERIALS AND METHODS

Chemicals and Reagents

Berberine hydrochloride was purchased from Shanghai Source Leaf Biological Technology Co., Ltd. (Shanghai, China), the purity of BBR is ≥98%. Oil red O reagent, high-performance liquid chromatography grade formic acid and ammonium acetate, and BA standards including cholic acid (CA), CDCA, DCA, ursodeoxycholic acid (UDCA), α, β and ω muricholic acids (MCA), tauroursodeoxycholic acid (TUDCA), taurochenodeoxycholic acid (TCDCA), tauro α-muricholic acid (TαMCA), tauro β-muricholic acid (TβMCA), tauro ω-muricholic acid (TωMCA), TCA, and taurodeoxycholic acid (TDCA) were obtained from Sigma-Aldrich (St. Louis, Mo, United States) and the purity of the above reagents was higher than 98%.

Animals

Male C57BL/6J mice (6–8 weeks old, 22 ± 2 g) were purchased from SLAC Laboratory Animal Co., Ltd. (Shanghai, China). Male FXR knockout ($FXR^{-/-}$) mice on a C57BL/6J background were given as a present by Prof. Li Yang from Shanghai University of Traditional Chinese medicine. After 1-week acclimatization, the mice were fed with chow diet (normal control group, $n = 8$) or high-fat diet (HFD, 60% of calories derived from fat, Research Diets, NJ, United States) supplemented with 1% dextran sulfate sodium (DSS) in drinking water periodically (7-day DSS administration followed by a 10-day interval). After 12 weeks of the diet, the HFD-DSS fed C57BL/6J mice were then randomly divided into NASH group (vehicle control, continuously supply of HFD-DSS, $n = 8$) and BBR-treated group (with HFD-DSS and BBR treatment, $n = 8$). The LD50 of BBR is 713.58 mg/kg in mice, and the present study applied the routine dosage of 100 mg/kg/d to the NASH mice. BBR was suspended in 0.5% carboxymethyl cellulose sodium solution (CMC-Na) and administered to the mice by gavage (0.1 ml/10 g body weight) once a day for 4 weeks, the normal control and vehicle control (NASH) mice were given an equal volume of 0.5% CMC-Na solution. For HFD-DSS fed $FXR^{-/-}$mice, BBR and vehicle treatment were the same as C57BL/6J mice. All animals were maintained under controlled temperature (25°C ± 2°C) and humidity (60 ± 5%) at a 12 h light-dark cycle, and access to food and water *ad libitum*. Food consumption and body weight were recorded weekly. The animal experiments were all approved by the Animal Experiment Ethics Committee of Shanghai University of Traditional Chinese Medicine.

Serum and Liver Biochemical Parameters Analysis

At the end of the experiment, all animals were fasted for 12 h, anesthetized intraperitoneally with 2% pentobarbital sodium, and

TABLE 1 | Primers used for mRNA analysis.

Genes	Gene function	Forward primer	Reverse primer
GAPDH	Internal control	GTGCCGCCTGGAGAAACC	GGTGGAAGAGTGGGAGTTGC
FXR	BA receptor	CGGCTGTCAGGATTTGTGC	GAAGCCCAGGTTGGAATAGTAAG
SHP	Form heterodimer with FXR	AACCTGCCGTCCTTCTGC	GAGCCTCAGCCACCTCGA
FGF15	Feedback inhibition of BA synthesis	GATCCACTCTTTCTCTACGGCTG	CGTTCGTTTTGGTCCTCCTC
FGFR4	FGF15 receptor	CTGTATGGGCTAATGAGGGAGTG	TCAGGCGGAGGTCAAGGTAC
CYP7A1	BA synthesis enzyme	TTCAAGACCGCACATAAAGCC	GAGATGCCCAGAGGATCACG
CYP8B1	BA synthesis enzyme	CTCGGGTGTTTCCAAGTGC	GGGCTTCAGGCGATAGAGG
SREBP1	Transcription of lipogenesis	AGTCCAGCCTTTGAGGATAGCC	CCGTAGCATCAGAGGGAGTGAG
ACC	Key enzyme in fatty acid synthesis	CCACAGAACTTACAAGGCACG	GAATTGTGAGGGTCGGCG
FASN	Key enzyme in fatty acid synthesis	GTCAACAACCATAGGCGATTTC	GCACCCTGACCCAGAATACC
SCD1	Key enzyme in fatty acid synthesis	GACCTGAAAGCCGAGAAGC	ATGAAGCACATCAGCAGGAGG
TNF-α	Inflammatory cytokine	ACGTGGAACTGGCAGAAGAG	GGTTGTCTTTGAGATCCATGC
IL-6	Inflammatory cytokine	AAATGATGGATGCTACCAAACTG	CTCTGGCTTTGTCTTTCTTGTTATC

sacrificed. To obtain the serum samples, blood was collected and centrifugated at 4°C, 3,000 rpm for 15 min. Serum lipid profiles including triglyceride (TG), total cholesterol (TC), low-density lipoprotein cholesterol (LDL-c), and serum enzymes as indicators of liver damage such as alanine transaminase (ALT) and aspartate transaminase (AST) were analyzed using the Hitachi full-automatic system.

For measurement of hepatic TG content, liver tissues were rapidly excised and rinsed with precooled normal saline, the same portion of liver samples were cut and homogenized with 10 volumes of ice-cold ethanol in a homogenizer. The homogenate was extracted overnight at 4°C and centrifuged at 4°C, 3,000 rpm for 15 min. The organic layer was removed and the content of TG and TC were measured using commercial kits from Nanjing Jiancheng Bioengineering Institute (Nanjing, China) according to the manufacturer's instruction.

Liver Histopathologic Evaluation

Liver histological changes were examined according to the previously described method (Li Q. et al., 2020). Briefly, for hematoxylin and eosin (H&E) staining, liver tissues were fixed in 10% formalin solution for 24 h, dehydrated, paraffin-embedded, sectioned to ~5 μm thickness, and stained with H&E reagent (Kohypath, Shanghai, China). For Oil Red O (ORO) staining, frozen liver tissues were embedded in Tissue-Tek OCT Compound (Sakura, Tokyo, Japan), cut into ~8 μm frozen sections, and stained with ORO reagent (Sigma, St. Louis, MO, United States). Images were captured under a Nikon Eclipse 50i microscope (Nikon, Tokyo, Japan) with a magnification of 200×.

Fecal 16S rDNA Analysis

Fecal samples were collected from the cecum of the mice, and total DNA in feces was isolated using the Qiagen QIAmp® Fast DNA Stool Mini Kit (Qiagen, CA, United States) according to the recommended protocol. The extracted DNA from each sample was used as a template to amplify the V3-V4 region of bacterial 16S rDNA genes of distinct regions was carried out by PCR, and then further gel-purified and quantified. Purified amplicons were pooled in equimolar and sequenced on the Illumina MiSeq™ platform (paired-end) by Majorbio Bio-Pharm Technology Co. Ltd. (Shanghai, China). The raw sequencing reads were generated and quality-filtered by QIIME version 1.9.1 with optimized parameters and analyzed using Mothur version 1.33.0 (http://www.mothur.org/), UPARSE version 7.1 (http://drive5.com/uparse/) and R version 3.6.1 (http://www.R-project.org/). The raw data of 16S rDNA was deposited at https://www.ncbi.nlm.nih.gov/Traces/study/?acc=PRJNA753953.

Bile Acids Profiling Analysis Using Ultra-Performance Liquid Chromatography Tandem-Mass Spectrometry

Serum, liver, and fecal samples were collected, and the BAs were extracted and quantified by ultra-performance liquid chromatography tandem-mass spectrometry (UPLC/MS) according to our previous research (Li Q. et al., 2020).

Western Blot Analysis

Liver tissues were lysed with radioimmunoprecipitation assay lysis buffer (Beyotime Institute of Biotechnology, Shanghai, China) with protease and phosphatase inhibitors (Roche, Indiana, United States). The prepared protein was separated by 12% SDS-PAGE, transferred to polyvinylidene difluoride membranes (Millipore, Temecula, CA, United States), and incubated with the primary antibody and secondary antibody, respectively. Anti-FXR, anti-FGF15, and anti-small heterodimer partner (SHP) were obtained from Abcam (Cambridge, United Kingdom), anti-cholesterol 7-alpha hydroxy-lase (CYP7A1) and anti-cytochrome P450, family 8, subfamily B, polypeptide 1 (CYP8B1) were purchased from Santa Cruz Biotechnology (Texas, CA, United States), anti-nuclear factor-κB (NF-κB) p65 and anti-NF-κB P-p65 were purchase from Cell Signaling Technology (Beverly, MA, United States). As an internal control, β-actin was purchased from HuaBio (Hangzhou, China). Anti-rabbit IgG and anti-mouse IgG was obtained from Cell Signaling Technology (Beverly, MA, United States). The bands were visualized by ECL chemiluminescence detection kit (Millipore, MA, United States), and quantified

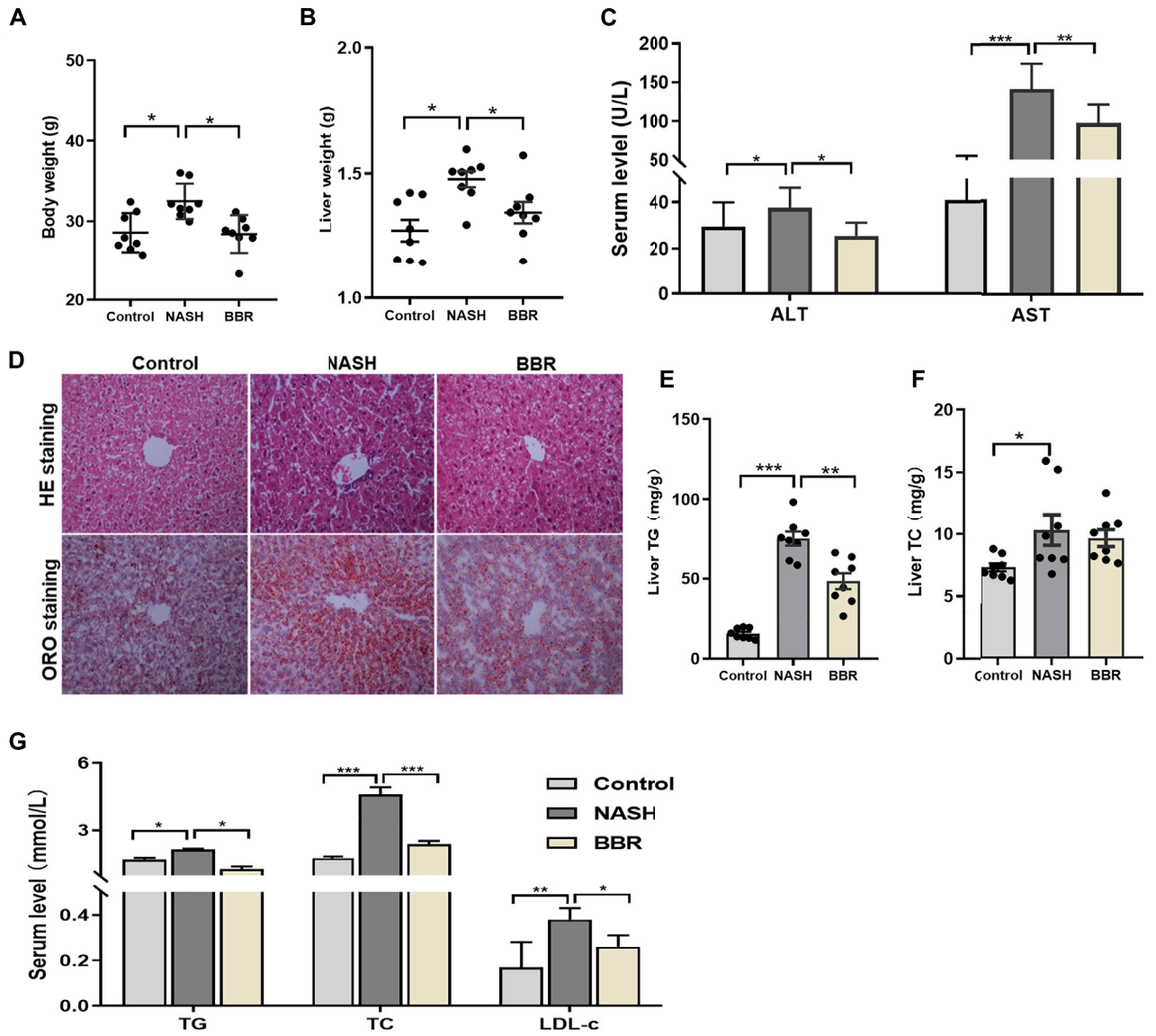


FIGURE 1 | Effects of BBR on HFD-DSS induced NASH mice. **(A)** Body weight; **(B)** Liver weight; **(C)** Serum ALT and AST levels; **(D)** Representative H&E and ORO staining images of liver sections (magnification 200×); **(E,F)** Liver TG and TC content; **(G)** Serum TG, TC and LDL-c levels. Data are expressed as mean ± SEM, eight animals are allocated for each group. $^{*}p < 0.05$, $^{**}p < 0.01$; $^{***}p < 0.001$ between groups.

using the Tanon 5200 Chemiluminescent Imaging System (Tanon Science & Technology Inc., Shanghai, China).

Quantitative Real Time-PCR Analysis

Quantitative Real Time-PCR (RT-qPCR) was conducted as described previously (Li Q. et al., 2020). Briefly, total RNA was extracted from liver and intestinal tissues using TRIzol reagent (Thermo Fisher Scientific, United States), reversely transcribed into cDNA by reverse transcription kits (Promega, Madison, WI, United States), and subjected to PCR on a StepOne Applied PCR system (Applied Biosystems, Carlsbad, CA, United States) using PowerUp SYBR Green Master Mix (TOYOBO, Osaka, Japan). The relative gene expression was normalized to glyceraldehyde-3-phosphate dehydrogenase (GAPDH) using a $2^{-\Delta\Delta Ct}$ method. The gene function and primer sequences were listed in **Table 1**.

Statistical Analysis

The quantitative data were presented with mean ± SEM and analyzed by one-way analysis of variance (ANOVA) and unpaired two-tailed Student's *t*-test using SPSS 18.0 statistical software (Chicago, IL, United States) and GraphPad Prism version 8.0 (San Diego, CA, United States). $p < 0.05$ was considered statistically different.

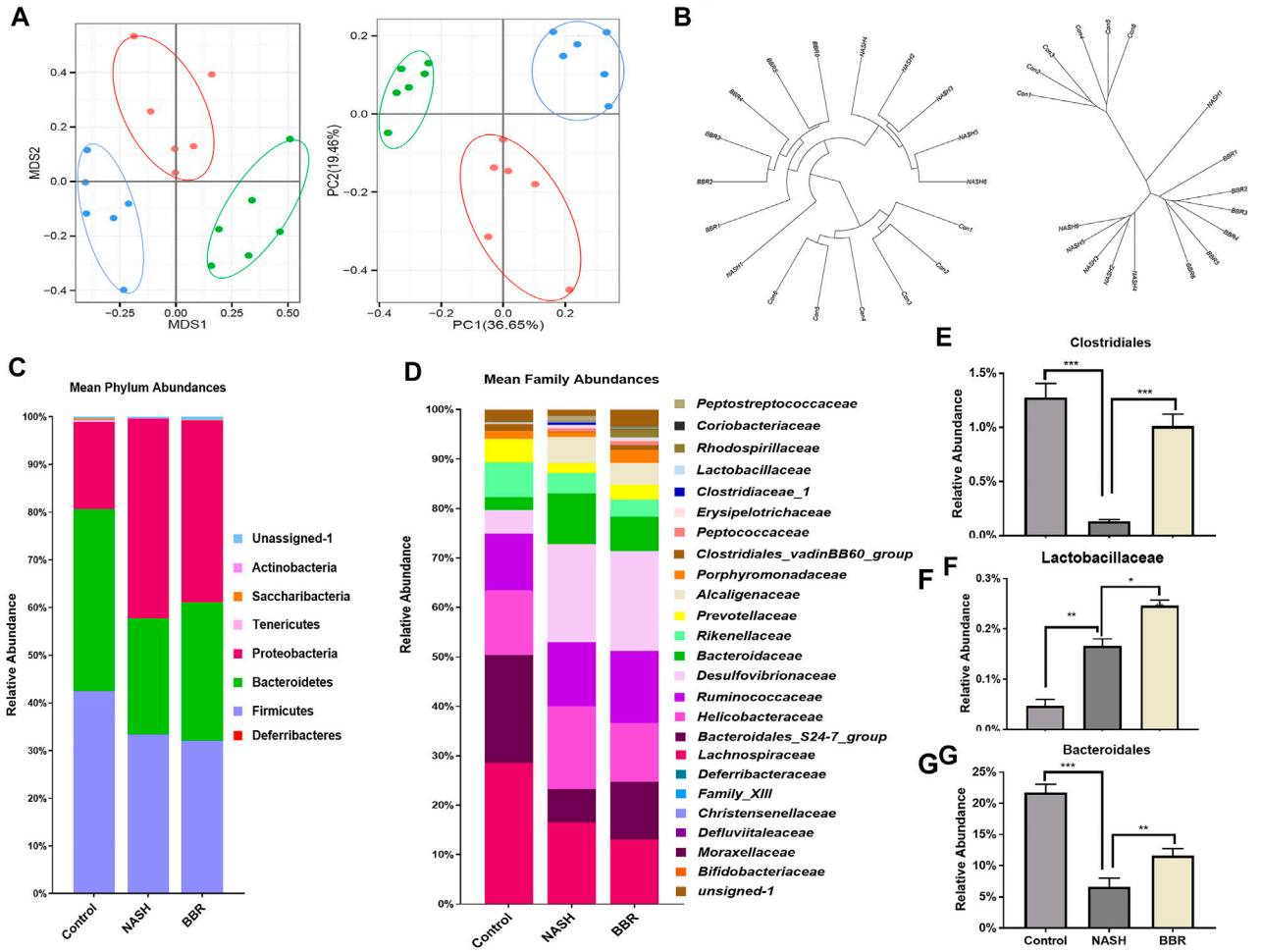


FIGURE 2 | BBR reshapes gut microbiota in NASH mice. **(A)** PCoA analysis based on the unweighted UniFrac analysis of OTUs; **(B)** Bray-Curtis distance analysis of OTUs; **(C)** Mean phylum abundance of OTUs; **(D)** Mean family abundance of OTUs; **(E–G)** The relative abundance of *Clostridiales*, *Lactobacillaceae* and *Bacteroidaies*. Data are expressed as mean ± SEM of six animals per group. *$p < 0.05$, **$p < 0.01$; ***$p < 0.001$ between groups.

RESULTS

Berberine Alleviates Non-Alcoholic Steatohepatitis in HFD-DSS Induced Mice

To address the effects of BBR on NASH, we used HFD-DSS induced NASH model. The treatment of DSS is shown to increase portal liposaccharide (LPS) level and therefore exacerbates the progression of NASH (Gabele et al., 2011; Achiwa et al., 2016). Mice fed with HFD-DSS demonstrated a typical NASH phenotype as evidenced by increased body weight and liver weight, obvious hepatic steatosis and inflammation, as well as increased liver TG content. During the 4-week treatment, all the mice were well-groomed, alert, active and showed good condition. The stool color of BBR-treated mice was a little bit yellow due to the drug administration. BBR treatment significantly reduced body weight and liver weight by 10 and 8%, respectively (**Figures 1A,B**), improved hepatic steatosis and inflammation (**Figures 1C,D**), and reduced liver TG content by approximately 30% (**Figure 1E**). The serum levels of AST and ALT in NASH mice were significantly increased, and BBR treatment could decrease the serum ALT and AST levels by 30% each (**Figure 1C**). Assembly, serum TG, TC, and LDL-c levels were increased in NASH mice, and BBR treatment partially restored these parameters (**Figure 1F**). These results implied that BBR exhibits robust efficacy against NASH in HFD-DSS fed mice.

Berberine Reshaped Gut Microbiota in Non-Alcoholic Steatohepatitis Mice

Gut dysbiosis is associated with the pathogenesis of NASH, and modulating gut microbiota is reported to contribute to the efficacy of BBR in various diseases. Here we analyzed the overall structural changes of gut microbiota in response to BBR by 16S rDNA sequencing. A total of 3,274 operational

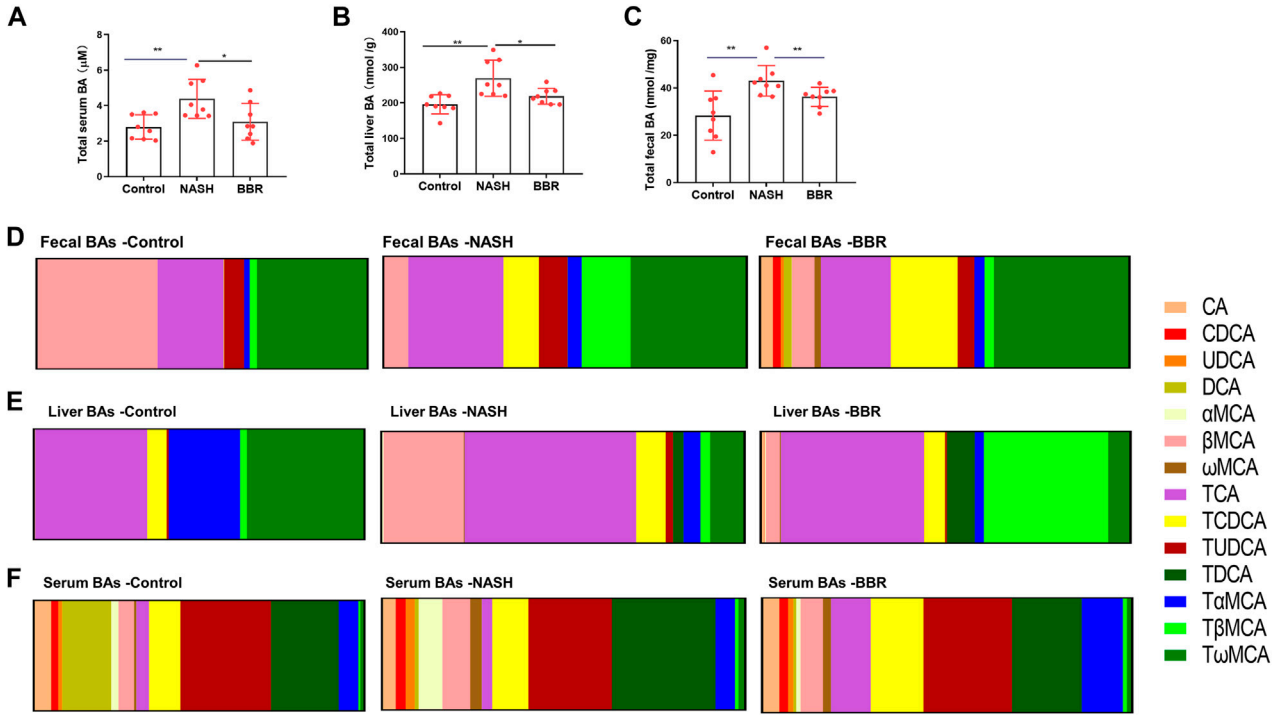


FIGURE 3 | BBR alters BA profiles in NASH mice. The total BA levels in the **(A)** liver, **(B)** serum and **(C)** feces. The ratio of BA species of **(A)** feces, **(B)** liver and **(C)** serum in control, NASH and BBR-treated mice. Data are presented as mean ± SEM (n = 8 per group). *p < 0.05, **p < 0.01 between groups.

taxonomic units (OTUs) were captured. UniFrac distance-based principal coordinate analysis (PCoA) (**Figure 2A**) and Bray-Curtis distance (**Figure 2B**) analysis revealed distinct clustering of microbe communities among control mice, NASH mice, as well as BBR treated mice. To assess the overall composition of the bacterial community in different groups, we analyzed the degree of bacterial taxonomic similarity at the phylum level. Compared to control mice, NASH mice displayed a higher Firmicutes-to-Bacteroidetes ratio due to the significant decrease in the relative abundance of Bacteroidetes, whereas BBR treatment increased the relative abundance of Bacteroidetes (**Figure 2C**). At the family level, BBR treatment significantly increased the relative abundance of *Clostridiales*, *Lactobacillaceae*, and *Bacteroidale* (**Figures 2D–G**). Assembly, these increased bacteria are participating in bile salt hydrolase (BSH) activity and secondary BA production, suggesting that BBR reshapes gut microbiota and might affect BA profiles in NASH mice.

Berberine Altered Bile Acids Profiles in Non-Alcoholic Steatohepatitis Mice

The interaction of gut microbiota and BA metabolism has been reported in NASH development and progression (Sydor et al., 2020). Enriched BSH producing microbiomes upon BBR treatment indicated that the BA profiles might alter accordingly. BBR treatment decreased the total BA levels in the liver (**Figure 3A**) and serum (**Figure 3B**) and increased the content of fecal BAs (**Figure 3C**). BA profiling (**Supplementary Tables S1–S3**) showed that fecal CDCA, UDCA, DCA, and MCA of NASH mice were all significantly increased in response to BBR treatment, whereas the conjugated BAs in feces were unchanged (TDCA, TCA, TωMCA) or decreased (TβMCA) upon BBR treatment (**Figure 3D**). BBR remarkably decreased the percentage of liver βMCA and TβMCA (**Figure 3E**), but had no obvious effects on serum BA profiles (**Figure 3F**). These results suggest that BBR promotes intestinal unconjugated and secondary BA production in NASH mice.

Berberine Activated Intestinal Farnesoid X Receptor Signaling

Certain BA species (e.g., DCA, UDCA) that are mediated by BBR are known FXR agonists, so we next investigated the protein expression of intestinal FXR in mice. The protein expression of intestinal FXR showed a 50% decrease in NASH mice, and BBR treatment could reverse the decrease of FXR expression (**Figures 4A,B**, **Supplementary Figure S1**). Up-regulation of intestinal FXR promotes the production of FGF15 in epithelium cells, and BBR-treatment prevented the decrease of intestinal FGF15 levels in NASH mice. Intestine-derived FGF15 may enter the liver through the portal vein, and the liver FGF15 expression was also significantly increased upon BBR treatment. We also detected the mRNA expression of liver FXR, SHP, and FGFR4, but did not find any statistical difference between NASH mice and BBR treated mice (**Figure 4C**). FGF15 is a suppressor of BA synthesis, and CYP7A1 and CYP8B1 are the main enzymes of BA synthesis that could convert cholesterol into CA,

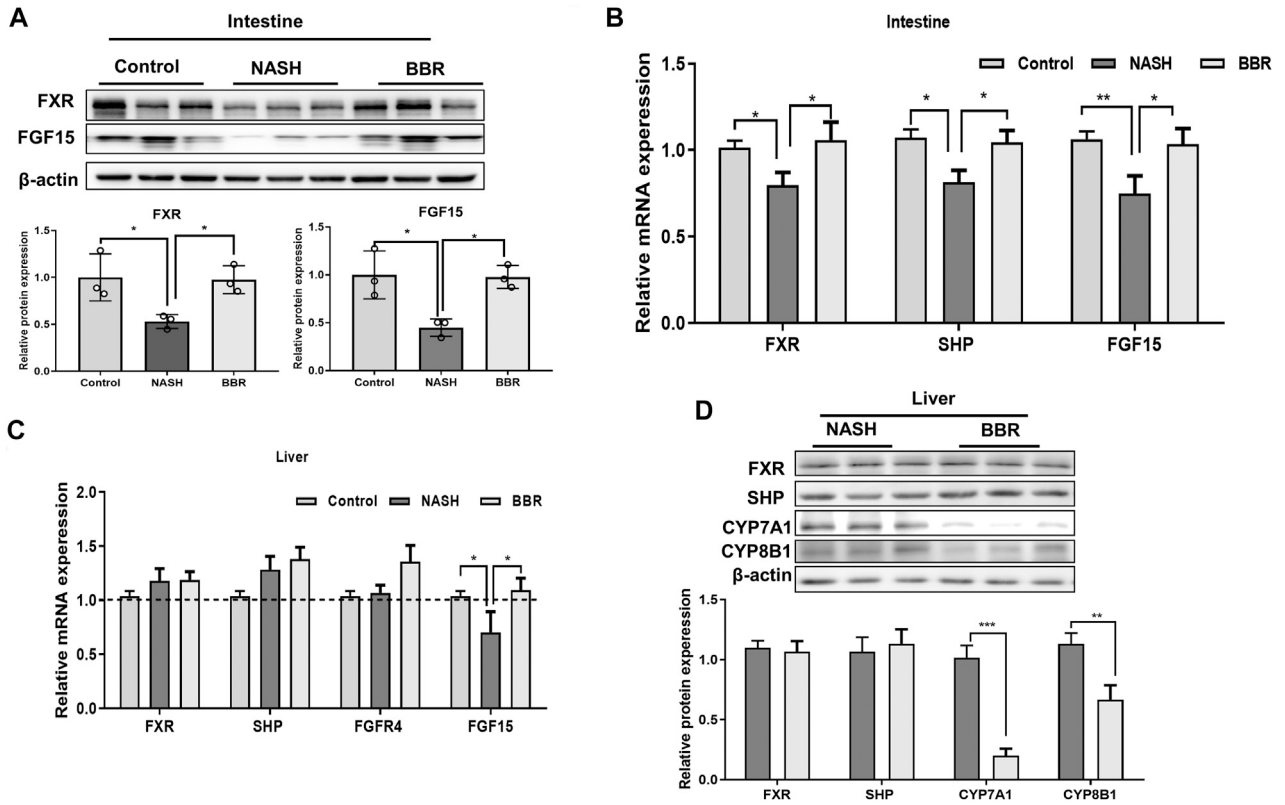


FIGURE 4 | BBR regulates FXR signaling in NASH mice. **(A)** The protein expression of intestinal FXR and FGF15, and **(B)** the mRNA expression of FXR, SHP and FGF15. **(C)** Liver mRNA expression of FXR, SHP, FGFR4 and FGF15. **(D)** The protein expression of FXR, SHP, CYP7A1 and CYP8B1 between NASH mice and BBR treated mice. Data are presented as mean ± SEM (n = 3 per group). *p < 0.05, **p < 0.01, ***p < 0.001 between groups.

CDCA, and β-MCA. We found that the protein expression of CYP7A1 and CYP8B1 of BBR treated mice were all significantly decreased in comparison to untreated NASH mice, whereas the expression of liver FXR and SHP was not statistically different between BBR treated mice and untreated NASH mice (**Figure 4D**; **Supplementary Figure S2**). These results indicate that the activation of intestinal but not liver FXR inhibits the BA synthesis.

Berberine Suppressed Liver Inflammation

To confirm the effect of BBR on intestinal FXR activation and FGF15 secretion, we detected the downstream lipogenesis genes in the liver, and found that BBR treatment significantly decreased the mRNA expression of sterol-regulatory element-binding protein 1 (SREBP1), acetyl-CoA carboxylase (ACC), fatty acid synthase (FASN), and stearoyl-CoA desaturase-1 (SCD1) in NASH mice (**Figure 5A**), suggesting the suppression of *de novo* lipogenesis upon BBR treatment. In addition, BBR treatment decreased the ratio of phosphorylated p65 to total p65 (**Figure 5B**; **Supplementary Figure S3**), indicating the suppression of NF-κB activation in the liver. Accordingly, the mRNA expression of inflammatory cytokines tumor necrosis factor alpha (TNF-α) (**Figure 5C**) and interleukin-6 (IL-6) (**Figure 5D**) was also decreased in BBR treated mice. These results indicate that BBR suppresses lipogenesis and inflammatory pathways *via* intestinal FXR activation.

The Effect of Berberine was Abolished in FXR$^{-/-}$ Mice

To confirm the effect of BBR on FXR, we conducted experiments on FXR$^{-/-}$ mice. The results showed that BBR treatment has no effect on body weight and liver weight in FXR$^{-/-}$ mice (**Figure 6A**). The serum levels of ALT and AST were also comparable between BBR treated and untreated FXR$^{-/-}$ mice (**Figure 6B**). FXR$^{-/-}$ mice demonstrated obvious hepatic steatosis and inflammatory cell infiltration in the liver, whereas the effects of BBR on improving hepatic steatosis were negligible in FXR$^{-/-}$ mice (**Figures 6C,D**). Consistently, the serum levels of TG, TC, and LDL-c, as well as the mRNA expressions of TNF-α and IL-6 were not statistically different between BBR treated and untreated FXR$^{-/-}$ mice (**Figures 6E,F**). These results suggest that the beneficial effects of BBR are abolished in FXR$^{-/-}$ mice.

DISCUSSION

The lipid-lowering and anti-inflammatory effects of BBR are of clinical value in treating NASH. In this study, we found that BBR treatment significantly improves hepatic steatosis and inflammation, as well as dyslipidemia in NASH mice, and beneficial effects are associated with the regulation of gut

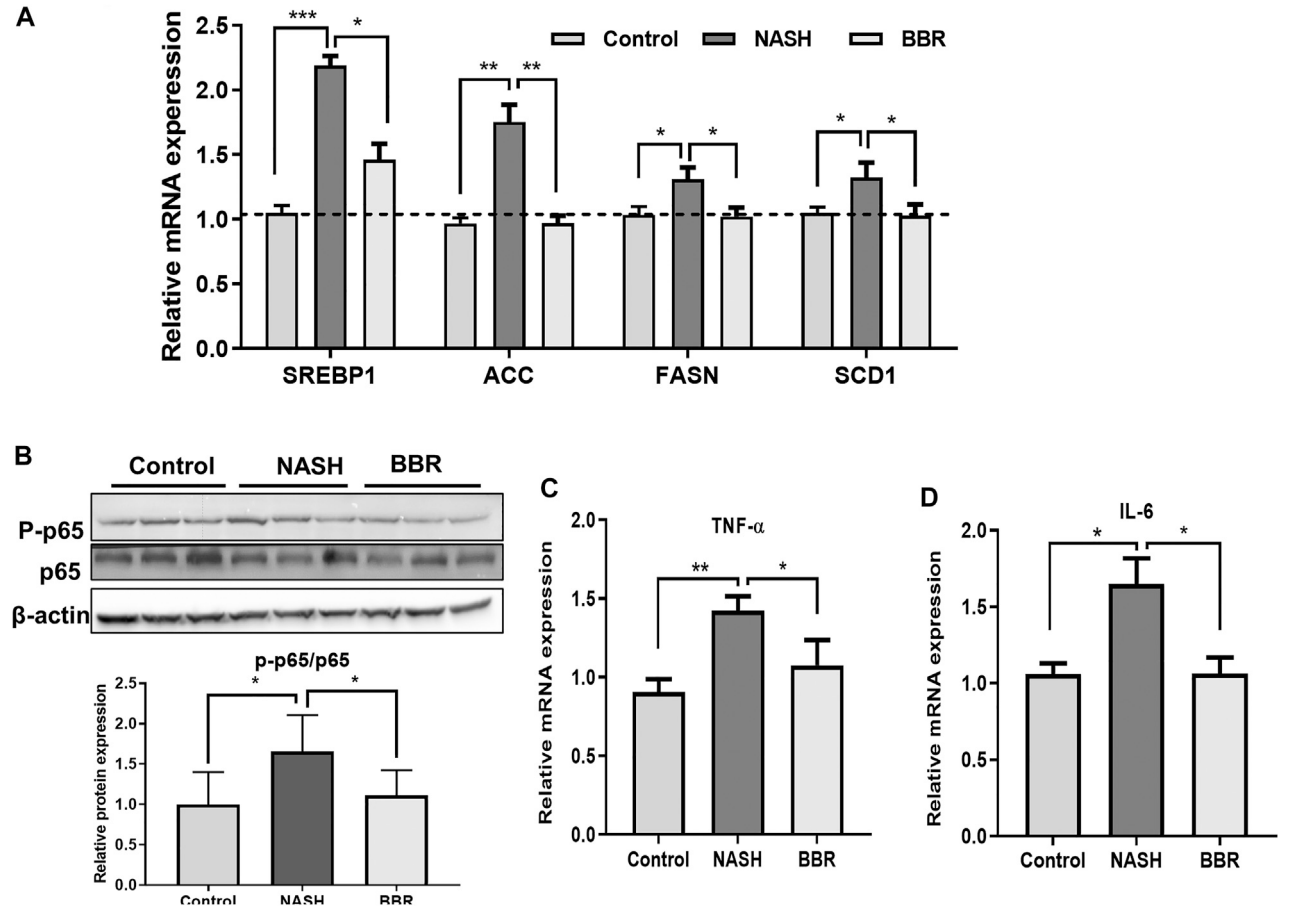


FIGURE 5 | BBR suppresses liver inflammation in NASH mice. **(A)** The mRNA expression of SREBP1c, ACC, FASN and SCD1 in the liver; **(B)** The protein expression of p65 and P-p65 in the liver; **(C,D)** The mRNA expression of TNF-α and IL-6 in the liver. Data are presented as mean ± SEM ($n = 3$ per group). $^{*}p < 0.05$, $^{**}p < 0.01$; $^{***}p < 0.001$ between groups.

microbiota and BA metabolism, which further activate intestinal FXR and promote FGF15 secretion. These data reveal that intestinal FXR activation might contribute to the improvement of BBR on NASH (**Figure 7**).

NAFLD is considered to be the hepatic manifestation of the metabolic syndrome, and the pathogenesis of the progressive form NASH is elusive, arising a series of hypotheses, and of them, the "multi-parallel- hits" theory is the most popular one (Younossi, 2008). The theory emphasizes the pathological factors of the liver, and also from peripheral tissues (adipose, gut, etc.). Considering the characteristics of the distribution and excretion of active metabolites in the BBR pharmacokinetics study, as well as the contribution of gut-derived endotoxins to NASH development, we adopted HFD-DSS induced NASH mouse model. Studies revealed that DSS could increase portal LPS level and exaggerate the development of NASH, suggesting that the alteration of the gut environment is a potential risk for NASH (Gabele et al., 2011; Achiwa et al., 2016).

BBR is a kind of benzylisoquinoline alkaloids and reported to reshape gut microbiota in NASH patients and animals. A randomized, parallel controlled, open-label clinical trial has been conducted to evaluate the effects of BBR on NAFLD, and the 16-week BBR treatment (0.5 g, PO, *tid*) has shown better improvement in reducing body weight and serum lipid profile in comparison to pioglitazone (15 mg, PO, *qd*) in NAFLD patients (Yan et al., 2015). In mildly overweight patients with NAFLD, 1-month BBR intervention reduces body weight and improves insulin resistance (Wu et al., 2019). Under physiological conditions, administration of BBR to C57BL/6 mice is reported to decrease Firmicutes-to-Bactrodetes ratio, enrich *Bacteroides* and decrease secondary BAs (DCA, LCA, etc.) in the liver and serum of the mice (Guo et al., 2016). It is reported that Firmicutes-to-Bacteroidetes ratio increase is a typical feature of obese mice (Gu et al., 2019) and humans (Monga Kravetz et al., 2020), whereas weight loss is often accompanied by a higher abundance of Bacteroidetes. In our study, NASH mice showed increased Firmicutes-to-Bactrodetes ratio as the relative abundance of Firmicutes increased and Bacteroidetes decreased, whereas BBR treatment reversed the ratio. At the family level, BBR treatment enriched the abundance of Bacteroidetes, which is actively involved in the BSH activity. BSH catalyzes the hydrolysis of the amino group from the

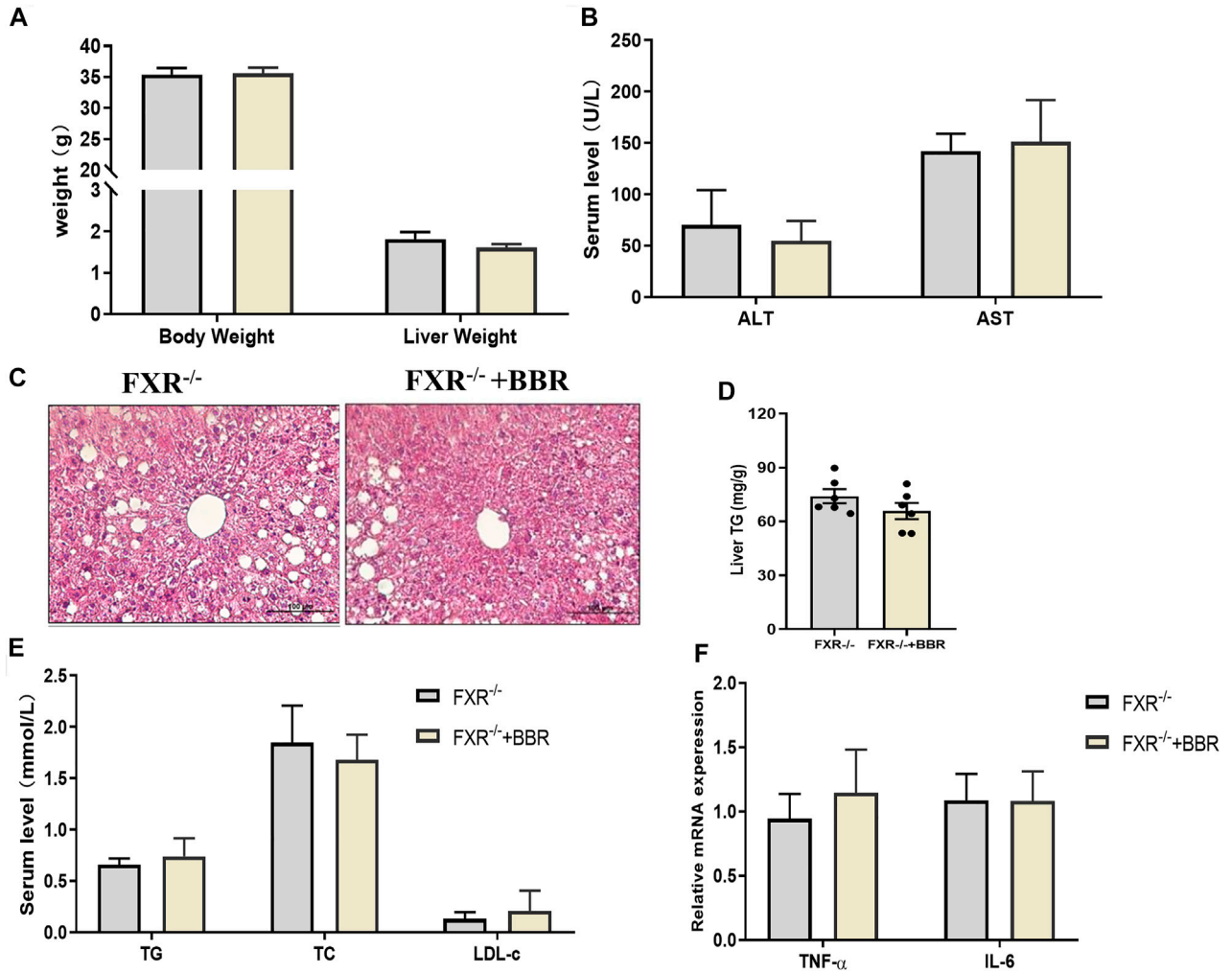


FIGURE 6 | The effect of BBR on FXR$^{-/-}$ mice. **(A)** The body weight and liver weight. **(B)** Serum ALT and AST levels. **(C)** Representative H&E staining images of liver sections (magnification 200×). **(D)** Liver TG content. **(E)** Serum TG, TC and LDL-c levels. **(F)** The mRNA expression of TNF-α and IL-6 in the liver. Data are presented as mean ± SEM (n = 6 per group).

conjugated BAs to produce unconjugated BAs, which is a prerequisite for the subsequent secondary BA production (Enright et al., 2017). BSH-producing microbiomes such as *Bacteroides*, *Clostridium*, *Lactobacillus*, *Bifidobacterium*, *Listeria*, *Eubacterium*, *Escherichia*, *Eggerthella*, *Peptostreptococcus*, and *Ruminococcus* have been reported to be involved in BA conversion (Urdaneta and Casadesus, 2017; Jia et al., 2018). *Lactobacillus* that over-expressing BSH induces reduced cholesterol absorption and accelerated cholesterol transportation, which counters hypercholesterolemia in high-cholesterol-diet animals (Wang et al., 2019). Clinical investigation revealed that the abundance of intestinal *Bacteroides fragilis* and *Bacteroides dorei* is decreased in NASH patients compared with healthy controls (Zhang et al., 2019).

Previous studies suggest that LDL receptors, adenosine 5′-monophosphate-activated protein kinase, as well as glucokinase are involved in the actions of BBR. Due to the low bioavailability of BBR, recent studies have been concerned more about the function of BBR on the intestinal FXR. Short-term BBR exposure reduces *Clostridium* cluster XIVa and IV, and activates the intestinal FXR due to the accumulation of TCA, indicating that BBR alters BA metabolism and activates FXR signaling through directly modulating gut bacteria (Tian et al., 2019). In HFD-induced obese mice, the lipid-lowering effect, as well as the anti-obesity potential of BBR, are associated with the increase of serum TCA level and the intestinal FXR activation, however, BBR fails to prevent HFD-induced obesity in intestine-specific FXR knockout mice (Sun et al., 2017). Here we identified the altered BA species (DCA, UDCA) that in response to BBR treatment in NASH mice. Although not as efficient as CDCA in activating FXR, the DCA and UDCA species are also the confirmed FXR agonists (Li et al., 2016; Zaufel et al., 2021). In addition, TβMCA is a known antagonist of FXR in rodents (Li et al., 2013), consistently, we found that fecal TβMCA in BBR-treated mice was decreased, indicating the intestinal FXR activation might be the critical mechanism underlying the efficacy of BBR on NASH.

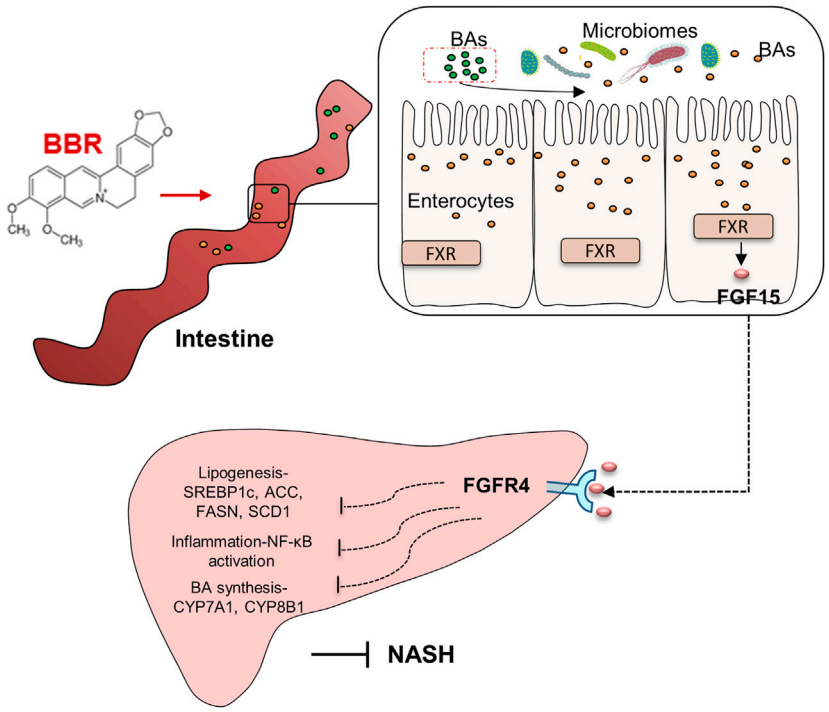


FIGURE 7 | Graphic summary of the study.

Animal studies demonstrated that FXR activation could reduce hepatic BA levels and protect the liver against BA toxicity (Kim et al., 2015; Li et al., 2021). FXR agonists have been proved to be effective in treating diet-induced NAFLD/NASH (Gonzalez et al., 2016; Schmidt et al., 2017; Li J. et al., 2020). In addition, FXR inhibition or knockout could promote lipid accumulation or exacerbate the NASH progression in animals. While the activation of FXR is beneficial for NAFLD/NASH patients, side effects are difficult to avoid for long-term treatment. Studies found that the selective intestinal FXR agonist fexaramine could improve obesity-related metabolic dysfunctions, and activate G protein-coupled bile acid receptor 1/Glucagon-like peptide-1 signaling to improve insulin sensitivity and increase adipose tissue browning (Jiang et al., 2015). These reports implicated that intestinal FXR activation might be a better choice for NAFLD. Actually, activation of intestinal FXR promotes FGF15 (rodents)/19 (human) production, and the secreted FGF15/19 protein can enter the liver via the portal vein. The receptors of FGFs are widely expressed in the liver, intestine, adipose, and brain. It is found that the FGF19 level in humans is directly associated with uncoupled protein1 expression in subcutaneous adipose tissue, whereas supplementation of FGF15 or FGF19 induces white adipose browning in mice (Moron-Ros et al., 2021). The FGF19 analog NGM282 is reported to reduce liver fat content in patients with NASH (Harrison et al., 2018). In the present study, we found that the intestinal FXR activation mediated FGF15 is increased in NASH mice upon BBR treatment, and the binding of FGF15 with liver-specific receptor FGFR4 may contribute to the anti-steatosis and anti-inflammatory properties of BBR. We also analyzed the FXR expression in the liver, but BBR treatment showed no obvious effect on liver FXR expression. Thus, the inhibition of BA synthesis enzymes (CYP7A1 and CYP8B1), might attribute to intestinal FXR activation.

In summary, our study highlighted the mechanisms of BBR on modulating gut microbiota and BA metabolism, and the subsequent activation of intestinal FXR in promoting FGF15 production to alleviate NASH in mice. Our study identified the activation of intestinal FXR, which is associated with gut microbiota and BA metabolism, as a potential target for BBR treatment. However, since this is a single dose study using a pretty high dose BBR in mice, the scientific interpretability is not strong enough. In addition, as the exact regulation of FXR in different metabolic disorders is still elusive, further studies are in need to clarify the exact mechanisms.

DATA AVAILABILITY STATEMENT

The original contributions presented in the study are publicly available. This data can be found here: National Center for Biotechnology Information (NCBI) BioProject database under accession number PRJNA753953.

ETHICS STATEMENT

The animal study was reviewed and approved by the animal experiments were all approved by the Animal Experiment Ethics

Committee of Shanghai University of Traditional Chinese Medicine.

AUTHOR CONTRIBUTIONS

LZ and GJ designed the project. XS, ML, YC, CL, and WZ carried out experiments, collected the samples. LZ, XS, and ML interpreted the data, drafted and edited the manuscript, GJ supervised the process, and critically revised the manuscript. All data were generated in-house, and the authors all have read and approved the final version of the manuscript before submission.

FUNDING

The work was supported by grants from the National Natural Science Foundation of China (Nos. 81774084 and 81804020). The funders had no role in study design, data collection and analysis, decision to publish, or preparation of the manuscript.

SUPPLEMENTARY MATERIAL

The Supplementary Material for this article can be found online at: https://www.frontiersin.org/articles/10.3389/fphar.2021.750826/full#supplementary-material

REFERENCES

Achiwa, K., Ishigami, M., Ishizu, Y., Kuzuya, T., Honda, T., Hayashi, K., et al. (2016). DSS Colitis Promotes Tumorigenesis and Fibrogenesis in a Choline-Deficient High-Fat Diet-Induced NASH Mouse Model. *Biochem. Biophys. Res. Commun.* 470 (1), 15–21. doi:10.1016/j.bbrc.2015.12.012

Adams, L. A., Lymp, J. F., St Sauver, J., Sanderson, S. O., Lindor, K. D., Feldstein, A., et al. (2005). The Natural History of Nonalcoholic Fatty Liver Disease: a Population-Based Cohort Study. *Gastroenterology* 129 (1), 113–121. doi:10.1053/j.gastro.2005.04.014

Belwal, T., Bisht, A., Devkota, H. P., Ullah, H., Khan, H., Pandey, A., et al. (2020). Phytopharmacology and Clinical Updates of Berberis Species against Diabetes and Other Metabolic Diseases. *Front. Pharmacol.* 11, 41. doi:10.3389/fphar.2020.00041

Ekstedt, M., Franzén, L. E., Mathiesen, U. L., Thorelius, L., Holmqvist, M., Bodemar, G., et al. (2006). Long-term Follow-Up of Patients with NAFLD and Elevated Liver Enzymes. *Hepatology* 44 (4), 865–873. doi:10.1002/hep.21327

Enright, E. F., Joyce, S. A., Gahan, C. G., and Griffin, B. T. (2017). Impact of Gut Microbiota-Mediated Bile Acid Metabolism on the Solubilization Capacity of Bile Salt Micelles and Drug Solubility. *Mol. Pharm.* 14 (4), 1251–1263. doi:10.1021/acs.molpharmaceut.6b01155

Gäbele, E., Dostert, K., Hofmann, C., Wiest, R., Schölmerich, J., Hellerbrand, C., et al. (2011). DSS Induced Colitis Increases portal LPS Levels and Enhances Hepatic Inflammation and Fibrogenesis in Experimental NASH. *J. Hepatol.* 55 (6), 1391–1399. doi:10.1016/j.jhep.2011.02.035

Gonzalez, F. J., Jiang, C., and Patterson, A. D. (2016). An Intestinal Microbiota-Farnesoid X Receptor Axis Modulates Metabolic Disease. *Gastroenterology* 151 (5), 845–859. doi:10.1053/j.gastro.2016.08.057

Gu, Y., Liu, C., Zheng, N., Jia, W., Zhang, W., and Li, H. (2019). Metabolic and Gut Microbial Characterization of Obesity-Prone Mice under a High-FaDiet. *J. Proteome Res.* 18 (4), 1703–1714. doi:10.1021/acs.jproteome.8b00945

Guo, H. H., Feng, C. L., Zhang, W. X., Luo, Z. G., Zhang, H. J., Zhang, T. T., et al. (2019). Liver-target Nanotechnology Facilitates Berberine to Ameliorate Cardio-Metabolic Diseases. *Nat. Commun.* 10 (1), 1981. doi:10.1038/s41467-019-09852-0

Guo, Y., Zhang, Y., Huang, W., Selwyn, F. P., and Klaassen, C. D. (2016). Dose-response Effect of Berberine on Bile Acid Profile and Gut Microbiota in Mice. *BMC Complement. Altern. Med.* 16 (1), 394. doi:10.1186/s12906-016-1367-7

Harrison, S. A., Rinella, M. E., Abdelmalek, M. F., Trotter, J. F., Paredes, A. H., Arnold, H. L., et al. (2018). NGM282 for Treatment of Non-alcoholic Steatohepatitis: a Multicentre, Randomised, Double-Blind, Placebo-Controlled, Phase 2 Trial. *Lancet* 391 (10126), 1174–1185. doi:10.1016/S0140-6736(18)30474-4

Jia, W., and Rajani, C. (2018). The Influence of Gut Microbial Metabolism on the Development and Progression of Non-alcoholic Fatty Liver Disease. *Adv. Exp. Med. Biol.* 1061, 95–110. doi:10.1007/978-981-10-8684-7_8

Jiang, C., Xie, C., Lv, Y., Li, J., Krausz, K. W., Shi, J., et al. (2015). Intestine-selective Farnesoid X Receptor Inhibition Improves Obesity-Related Metabolic Dysfunction. *Nat. Commun.* 6, 10166. doi:10.1038/ncomms10166

Kim, Y. C., Fang, S., Byun, S., Seok, S., Kemper, B., and Kemper, J. K. (2015). Farnesoid X Receptor-Induced Lysine-specific Histone Demethylase Reduces Hepatic Bile Acid Levels and Protects the Liver against Bile Acid Toxicity. *Hepatology* 62 (1), 220–231. doi:10.1002/hep.27677

Lan, J., Zhao, Y., Dong, F., Yan, Z., Zheng, W., Fan, J., et al. (2015). Meta-analysis of the Effect and Safety of Berberine in the Treatment of Type 2 Diabetes Mellitus, Hyperlipemia and Hypertension. *J. Ethnopharmacol* 161, 69–81. doi:10.1016/j.jep.2014.09.049

Li, F., Jiang, C., Krausz, K. W., Li, Y., Albert, I., Hao, H., et al. (2013). Microbiome Remodelling Leads to Inhibition of Intestinal Farnesoid X Receptor Signalling and Decreased Obesity. *Nat. Commun.* 4, 2384. doi:10.1038/ncomms3384

Li, J., Liu, C., Zhou, Z., Dou, B., Huang, J., Huang, L., et al. (2021). Isotschimgine Alleviates Nonalcoholic Steatohepatitis and Fibrosis via FXR Agonism in Mice. *Phytother Res.* 35 (6), 3351–3364. doi:10.1002/ptr.7055

Li, J., Liu, M., Li, Y., Sun, D. D., Shu, Z., Tan, Q., et al. (2020a). Discovery and Optimization of Non-bile Acid FXR Agonists as Preclinical Candidates for the Treatment of Nonalcoholic Steatohepatitis. *J. Med. Chem.* 63 (21), 12748–12772. doi:10.1021/acs.jmedchem.0c01065

Li, Q., Li, M., Li, F., Zhou, W., Dang, Y., Zhang, L., et al. (2020b). Qiang-Gan Formula Extract Improves Non-alcoholic Steatohepatitis via Regulating Bile Acid Metabolism and Gut Microbiota in Mice. *J. Ethnopharmacol* 258, 112896. doi:10.1016/j.jep.2020.112896

Li, X., Yuan, Z., Liu, R., Hassan, H. M., Yang, H., Sun, R., et al. (2016). UDCA and CDCA Alleviate 17α-Ethinylestradiol-Induced Cholestasis through PKA-AMPK Pathways in Rats. *Toxicol. Appl. Pharmacol.* 311, 12–25. doi:10.1016/j.taap.2016.10.011

Monga Kravetz, A., Testerman, T., Galuppo, B., Graf, J., Pierpont, B., Siebel, S., et al. (2020). Effect of Gut Microbiota and PNPLA3 Rs738409 Variant on Nonalcoholic Fatty Liver Disease (NAFLD) in Obese Youth. *J. Clin. Endocrinol. Metab.* 105 (10), dgaa382. doi:10.1210/clinem/dgaa382

Morón-Ros, S., Uriarte, I., Berasain, C., Avila, M. A., Sabater-Masdeu, M., Moreno-Navarrete, J. M., et al. (2021). FGF15/19 Is Required for Adipose Tissue Plasticity in Response to Thermogenic Adaptations. *Mol. Metab.* 43, 101113. doi:10.1016/j.molmet.2020.101113

Neag, M. A., Mocan, A., Echeverría, J., Pop, R. M., Bocsan, C. I., Crişan, G., et al. (2018). Berberine: Botanical Occurrence, Traditional Uses, Extraction Methods, and Relevance in Cardiovascular, Metabolic, Hepatic, and Renal Disorders. *Front. Pharmacol.* 9, 557. doi:10.3389/fphar.2018.00557

Pataky, Z., Genton, L., Spahr, L., Lazarevic, V., Terraz, S., Gaïa, N., et al. (2016). Impact of Hypocaloric Hyperproteic Diet on Gut Microbiota in Overweight or Obese Patients with Nonalcoholic Fatty Liver Disease: A Pilot Study. *Dig. Dis. Sci.* 61 (9), 2721–2731. doi:10.1007/s10620-016-4179-1

Schmidt, J., Rotter, M., Weiser, T., Wittmann, S., Weizel, L., Kaiser, A., et al. (2017). A Dual Modulator of Farnesoid X Receptor and Soluble Epoxide Hydrolase to Counter Nonalcoholic Steatohepatitis. *J. Med. Chem.* 60 (18), 7703–7724. doi:10.1021/acs.jmedchem.7b00398

Sun, R., Yang, N., Kong, B., Cao, B., Feng, D., Yu, X., et al. (2017). Orally Administered Berberine Modulates Hepatic Lipid Metabolism by Altering

Microbial Bile Acid Metabolism and the Intestinal FXR Signaling Pathway. *Mol. Pharmacol.* 91 (2), 110–122. doi:10.1124/mol.116.106617

Sydor, S., Best, J., Messerschmidt, I., Manka, P., Vilchez-Vargas, R., Brodesser, S., et al. (2020). Altered Microbiota Diversity and Bile Acid Signaling in Cirrhotic and Noncirrhotic NASH-HCC. *Clin. Transl. Gastroenterol.* 11 (3), e00131. doi:10.14309/ctg.0000000000000131

Takaki, A., Kawai, D., and Yamamoto, K. (2014). Molecular Mechanisms and New Treatment Strategies for Non-alcoholic Steatohepatitis (NASH). *Int. J. Mol. Sci.* 15 (5), 7352–7379. doi:10.3390/ijms15057352

Tian, Y., Cai, J., Gui, W., Nichols, R. G., Koo, I., Zhang, J., et al. (2019). Berberine Directly Affects the Gut Microbiota to Promote Intestinal Farnesoid X Receptor Activation. *Drug Metab. Dispos* 47 (2), 86–93. doi:10.1124/dmd.118.083691

Urdaneta, V., and Casadesus, J. (2017). Interactions between Bacteria and Bile Salts in the Gastrointestinal and Hepatobiliary Tracts. *Front. Med. (Lausanne)* 4, 163. doi:10.3389/fmed.2017.00163

Wang, G., Huang, W., Xia, Y., Xiong, Z., and Ai, L. (2019). Cholesterol-lowering Potentials of Lactobacillus Strain Overexpression of Bile Salt Hydrolase on High Cholesterol Diet-Induced Hypercholesterolemic Mice. *Food Funct.* 10 (3), 1684–1695. doi:10.1039/c8fo02181c

Wu, L., Xia, M., Duan, Y., Zhang, L., Jiang, H., Hu, X., et al. (2019). Berberine Promotes the Recruitment and Activation of Brown Adipose Tissue in Mice and Humans. *Cell Death Dis* 10 (6), 468. doi:10.1038/s41419-019-1706-y

Yan, H. M., Xia, M. F., Wang, Y., Chang, X. X., Yao, X. Z., Rao, S. X., et al. (2015). Efficacy of Berberine in Patients with Non-alcoholic Fatty Liver Disease. *PLoS One* 10 (8), e0134172. doi:10.1371/journal.pone.0134172

Yin, J., Xing, H., and Ye, J. (2008). Efficacy of Berberine in Patients with Type 2 Diabetes Mellitus. *Metabolism* 57 (5), 712–717. doi:10.1016/j.metabol.2008.01.013

Younossi, Z. M. (2008). Review Article: Current Management of Non-alcoholic Fatty Liver Disease and Non-alcoholic Steatohepatitis. *Aliment. Pharmacol. Ther.* 28 (1), 2–12. doi:10.1111/j.1365-2036.2008.03710.x

Zaufel, A., van de Wiel, S. M. W., Yin, L., Fauler, G., Chien, D., Dong, X., et al. (2021). Secondary (iso)BAs Cooperate with Endogenous Ligands to Activate FXR under Physiological and Pathological Conditions. *Biochim. Biophys. Acta Mol. Basis Dis.* 1867 (8), 166153. doi:10.1016/j.bbadis.2021.166153

Zhang, Y., Gu, Y., Ren, H., Wang, S., Zhong, H., Zhao, X., et al. (2020). Gut Microbiome-Related Effects of Berberine and Probiotics on Type 2 Diabetes (The PREMOTE Study). *Nat. Commun.* 11 (1), 5015. doi:10.1038/s41467-020-18414-8

Zhang, Y., Xu, J., Wang, X., Ren, X., and Liu, Y. (2019). Changes of Intestinal Bacterial Microbiota in Coronary Heart Disease Complicated with Nonalcoholic Fatty Liver Disease. *BMC Genomics* 20 (1), 862. doi:10.1186/s12864-019-6251-7

Zhou, F., Zhou, J., Wang, W., Zhang, X. J., Ji, Y. X., Zhang, P., et al. (2019). Unexpected Rapid Increase in the Burden of NAFLD in China from 2008 to 2018: A Systematic Review and Meta-Analysis. *Hepatology* 70 (4), 1119–1133. doi:10.1002/hep.30702

Conflict of Interest: The authors declare that the research was conducted in the absence of any commercial or financial relationships that could be construed as a potential conflict of interest.

Publisher's Note: All claims expressed in this article are solely those of the authors and do not necessarily represent those of their affiliated organizations, or those of the publisher, the editors and the reviewers. Any product that may be evaluated in this article, or claim that may be made by its manufacturer, is not guaranteed or endorsed by the publisher.

Copyright © 2021 Shu, Li, Cao, Li, Zhou, Ji and Zhang. This is an open-access article distributed under the terms of the Creative Commons Attribution License (CC BY). The use, distribution or reproduction in other forums is permitted, provided the original author(s) and the copyright owner(s) are credited and that the original publication in this journal is cited, in accordance with accepted academic practice. No use, distribution or reproduction is permitted which does not comply with these terms.

GLOSSARY

ACC acetyl-CoA carboxylase
ALT alanine transaminase
AST aspartate transaminase
BAs bile acids
BBR berberine
BSH bile salt hydrolase
CA cholic acid
CDCA chenodeoxycholic acid
CMC-Na carboxymethyl cellulose sodium solution
CYP7A1 cytochrome P450 7A1
CYP8B1 cytochrome P450, family 8, subfamily B, polypeptide 1
DCA deoxycholic acid
DSS dextran sulfate sodium
FASN fatty acid synthase
FGF15 fibroblast growth factor 15
FGFR4 fibroblast growth factor receptor
FXR farnesoid X receptor
GAPDH glyceraldehyde-3-phosphate dehydrogenase
H&E hematoxylin and eosin staining
HFD high-fat diet
IL-6 interleukin 6
LDL-c low-density lipoprotein cholesterol
LPS liposaccharide
MCA muricholic acids
NAFLD nonalcoholic fatty liver disease
NASH nonalcoholic steatohepatitis
NF-κB nuclear factor-κB
ORO oil red O
OTUs operational taxonomic units
PCoA UniFrac distance-based principal coordinate analysis
RT-qPCR quantitative real time-PCR
SCD1 stearoyl-CoA desaturase
SHP small heterodimer partner
SREBP1 sterol regulatory element binding protein 1
TC total cholesterol
TCA taurine conjugated cholic acid
TCDCA taurochenodeoxycholic acid
TDCA taurodeoxycholic acid
TG triglyceride
TNF-α tumour necrosis factor alpha
TUDCA tauroursodeoxycholic acid
UPLC/MS ultra-performance liquid chromatography tandem-mass spectrometry
16SrDNA 16S ribosomal DNA

frontiers in Pharmacology

ORIGINAL RESEARCH
published: 24 September 2021
doi: 10.3389/fphar.2021.755768

Protective Effects of Lentinan Against Lipopolysaccharide-Induced Mastitis in Mice

Huifang Yin[1,2,3], *Guanhong Xue*[4], *Ailing Dai*[1,2,3] *and Haichong Wu*[2,3,4]*

[1]College of Life Sciences of Longyan University, Longyan, China, [2]Fujian Provincial Key Laboratory for the Prevention and Control of Animal Infectious Diseases and Biotechnology, Longyan, China, [3]Key Laboratory of Preventive Veterinary Medicine and Biotechnology, Longyan University, Longyan, China, [4]Department of Veterinary Medicine, College of Animal Sciences, Zhejiang University, Hangzhou, China

Mastitis is a worldwide production disease in dairy cows, which mainly affects milk yield, causing huge economic losses to dairy farmers. Lentinan is a kind of polysaccharide extracted from *Lentinus edodes*, which has no toxicity and possesses various pharmacological activities including antibacterial and immunomodulatory effects. Therefore, the anti-inflammatory function of lentinan on LPS-stimulated mastitis was carried out, and the mechanism involved was explored. *In vivo*, lentinan greatly reduced LPS-stimulated pathological injury, myeloperoxidase (MPO) activity, and the proinflammatory factor production (TNF-α and IL-1β) in mice. Further study was performed to determine the activation of the Wnt/β-catenin pathway during LPS stimulation. These results suggested that LPS-induced activation of the Wnt/β-catenin pathway was suppressed by lentinan administration. *In vitro*, we observed that the mouse mammary epithelial cell (mMEC) viability was not affected by lentinan treatment. As expected, LPS increased the TNF-α and IL-1β protein secretion and the activation of the Wnt/β-catenin pathway that was inhibited by lentinan administration in a dose-dependent manner in mMECs. Conclusively, lentinan exerts the anti-inflammatory function in LPS-stimulated mastitis *via* inhibiting the activation of the Wnt/β-catenin pathway. Thus, the results of our study also gave an insight that lentinan may serve as a potential treatment for mastitis.

Keywords: lentinan, mastitis, LPS, inflammation, Wnt/β-catenin pathway

OPEN ACCESS

Edited by:
Zhaocheng Ma,
Huazhong Agricultural University, China

Reviewed by:
Shuai Guo,
Huazhong Agricultural University, China
Yunhe Fu,
Jilin University, China

***Correspondence:**
Haichong Wu
haichongwu@zju.edu.cn

Specialty section:
This article was submitted to Inflammation Pharmacology, a section of the journal Frontiers in Pharmacology

Received: *09 August 2021*
Accepted: *06 September 2021*
Published: *24 September 2021*

Citation:
Yin H, Xue G, Dai A and Wu H (2021) Protective Effects of Lentinan Against Lipopolysaccharide-Induced Mastitis in Mice. Front. Pharmacol. 12:755768. doi: 10.3389/fphar.2021.755768

INTRODUCTION

Mastitis, one of the most prevalent diseases in dairy cows, is mainly characterized by the inflammation of the mammary gland with major economic, hygienic, and welfare implications (Wu et al., 2016; Dai et al., 2019; Puggioni et al., 2019). There are abundant pathogenic microorganisms that can cause mastitis, such as Gram-negative bacteria *Escherichia coli* (Zadoks et al., 2011; Jiang et al., 2018). *Escherichia coli* inflicts widespread infection in humans and is one of the most common causative pathogens in bovine mastitis (Filioussis et al., 2020).

Lipopolysaccharide (LPS, which is also called the endotoxin), a main constituent of the Gram-negative bacterial cell wall, has been often used to mimic *E. coli*-infected mastitis *in vivo* as well as in cultured mammary epithelial cells (Chen et al., 2018; Kusebauch et al., 2018). When the components of pathogens (for example LPS) or their pathogen-associated molecular patterns are recognized by

the innate immune system, multiple signaling pathways will be initiated to eradicate infection and protect the host against pathogens (Stokes et al., 2015; Iida et al., 2018; Kumar, 2019). Increasing evidence has revealed that the Wnt/β-catenin signaling pathway is involved in several inflammatory diseases (Mu et al., 2020; Quandt et al., 2021; Zhou et al., 2021). Therefore, pharmacological inhibition or interference of the Wnt/β-catenin pathway may be an effective strategy for treatment of several inflammatory diseases.

At present, antibiotics are the major drugs for the treatment of mastitis, but the emergence of antibiotic resistance has brought great trouble, threatened the health of humans and animals, and even caused the possibility of zoonotic bacteria entering the food chain (Doehring and Sundrum, 2019; Meade et al., 2019). Lentinan, a plant polysaccharide extracted from the mushroom, has harmless and few side effects on the human body (Wang X. et al., 2019; Zhang and Zhao, 2019). Although lentinan has been reported to possess various pharmacological activities such as anticancer, antibacterial, antiviral, and antioxidant effects (Nishitani et al., 2013; Wang X. et al., 2019; Hou et al., 2020), the potential protective mechanisms of lentinan on LPS-induced mastitis remain to be explored.

We hypothesized that lentinan alleviated LPS-induced mastitis by interfering with the activation of the Wnt/β-catenin pathway, which may also be a potential target for treatment of bovine mastitis and other inflammatory diseases. In the present research, the LPS-induced mouse mastitis was used to evaluate whether lentinan could protect the LPS-stimulated mastitis and explain its therapeutic mechanisms.

MATERIALS AND METHODS

Reagents

Lentinan was obtained from Shanghai Yuanye Biotechnology Co., Ltd., and dissolved with DMSO to prepare a final concentration of 100 mg/ml. When lentinan is used, it is diluted to the experimental concentrations (DMSO<0.1%). LPS was purchased from Sigma Chemical CO (St. Louis, United States). A mouse myeloperoxidase (MPO) ELISA kit was obtained from MultiSciences (Lianke) Biotech Co., Ltd (Zhejiang, China).

Animal Treatment and Experimental Groups

Mice were purchased from the Laboratory Animal Center of Zhejiang University (Hangzhou, China). Ninety BALB/c female mice (8 week old) were used in this experiment. Food and water were available *ad libitum*. The mice were kept in separate cages for a 12 h dark light cycle under controlled temperature (24°C ± 1°C) and 60% humidity for 1 week before the research. All experimental procedures and protocols were approved by the Institutional Animal Care and Use Committee in Zhejiang University.

The mice were randomly classified into six groups, each comprising fifteen mice: Control group, LPS group, lentinan (5, 10, and 20 mg/kg) + LPS groups, and dexamethasone group (5 mg/kg). The mastitis model was carried out as described previously by us (Xingxing et al., 2018). In brief, 100 μl of LPS (1 mg/ml) was infused into two abdominal mammary glands (R4 and L4) in mice under anesthesia with pentobarbital. Mice received an intraperitoneal injection (ip) of different lentinan concentrations (5, 10, and 20 mg/kg) or dexamethasone after 1 h of LPS or saline ip treatment. After 24 h, the mice were sacrificed by CO_2 inhalation at the same time. The mouse mammary tissues were collected and stored at −80°C until being analyzed.

Histopathologic Evaluation of the Mammary Tissues

The mouse mammary gland tissues were excised and fixed in 10% formalin for subsequent histopathological analysis. In brief, tissues were dehydrated with different concentrations of alcohol, paraffin-embedded sections were prepared at a 4-μm thickness, and hematoxylin and eosin (H and E) staining was then performed to observe the morphology changes with an optical microscope (Olympus, Japan).

Myeloperoxidase (MPO) Analysis

MPO activity in mammary gland tissue was detected in tissue homogenates prepared as described above using the ELISA kit following the instruction book of the producer. In addition, mammary tissues were fixed in 4% paraformaldehyde, embedded in paraffin, sectioned, and then incubated with the MPO antibody (Servicebio, China). Immunopositive cells were counted, and positive cells in mammary gland tissue sections were quantified to the tissue area.

Cell Culture and Treatment

Epithelial cells from the mammary gland tissue of lactating mice were cultured as described previously (Wu et al., 2017). The mouse mammary epithelial cells (mMECs) were cultured in DMEM containing 10% FBS, 100 U/mL penicillin–streptomycin, and 10 μg/ml insulin in a 5% CO_2 incubator. The cells were pretreated with different concentrations of lentinan (5, 10, and 20 μg/ml) or dexamethasone for 1 h before LPS challenge.

Cell Biological Examination and MTT Assay

The cells were fixed with paraformaldehyde at room temperature for 15 min and then washed three times with PBS in a twelve-well plate. Next, the cells were sealed with 10% normal goat serum at room temperature for 1 , followed by incubation with the primary antibody CK-18 at 4°C for 12 h. The cells were then incubated with the fluorescent-labeled secondary antibody (Bioss, China) for 45 min at room temperature and washed three times in PBS. Finally, DAPI was used to stain the cell nuclei, which were then observed using a laser scanning confocal microscope (Leica, Germany).

The mMEC viability was evaluated by the 3-[4,5-dimethylthiazol-2-yl]-2,5 diphenyl tetrazolium bromide (MTT) experiment. Cells (1×10^5 cell/mL) were cultured in 96-well plates for 6 hours. The cells were stimulated with lentinan (5, 10, and 20 μg/ml) for 24 h. Next, the MTT (5 mg/ml) agent was added in

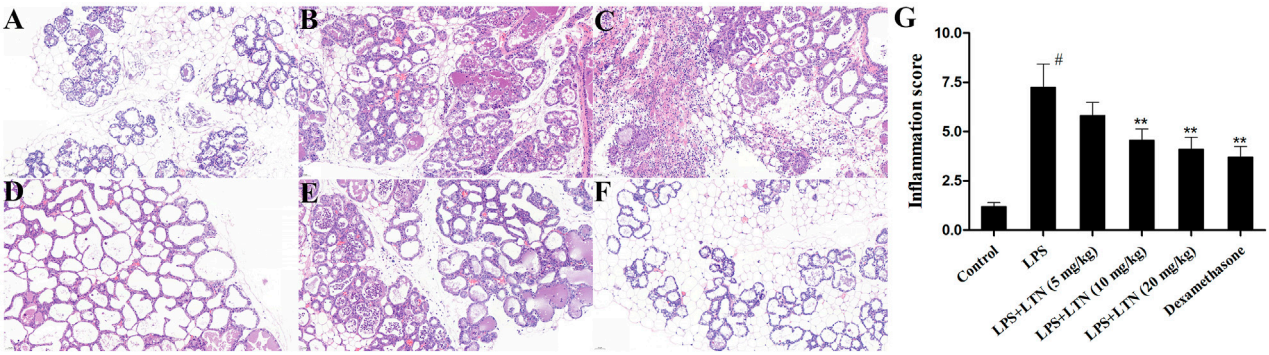


FIGURE 1 | Effects of lentinan on LPS-stimulated histopathological changes. Histopathological changes in mammary gland tissues (H and E). **(A)** Control group, **(B)** LPS group, **(C–E)** lentinan (5, 10, and 20 mg/kg) groups, **(F)** dexamethasone group, and **(G)** histopathological grade score. The blue arrow indicates the mammary gland tissue lesion area. All data are represented as the mean ± S.E.M. of three replicates. $^{\#}p < 0.05$ vs the control group. $^{*}p < 0.05$ vs. the LPS group. $^{**}p < 0.01$ compared with the LPS group. $^{***}p < 0.01$ compared with the LPS group.

mMECs for 4 h, and 100 μl of DMSO per well was added. The optical density (OD) at 570 nm was read with a microplate reader (Thermo, United States).

Immunofluorescence Staining

Immunofluorescence staining assay of the mouse mammary tissue and mMECs was carried out. Briefly, the mouse mammary tissues or cells were fixed in 10% formalin, and tissues were embedded in paraffin. The tissue or cell slice was permeated with PBS appending Triton X-100 (0.3%, Sigma, United States) and 10% BSA. The tissue or cell slice was hatched for 12 h at 4°C with a special antibody for Wnt3a and β-catenin (Servicebio, China) and a Cy3 secondary antibody. Then, Wnt3a and β-catenin proteins were determined and immobilized using mounting media supplemented with DAPI. Finally, all of the slices were observed with fluorescence microscopy.

Cytokine Assay

The cytokine secretion after LPS challenge was assessed with the ELISA kit in the mouse mammary tissues and mMECs. The tissues were homogenized in ice-cold PBS and then centrifugation at 10,000 rpm, 4°C for 15 min. Harvested tissue and cell supernate to detect the production of cytokines (IL-1β and TNF-α) using the ELISA kit following the instruction book of the producer. Finally, the optical density (OD) at 450 nm is read with a microplate reader.

Western Blot Assay

The total protein of mMECs was obtained by the lysis solution containing the phosphatase repressor. The BCA kit was used to determine the protein concentration. Then, samples with the same amount of protein were applied to 10% SDS-PAGE gel electrophoresis and then transferred to the PVDF membrane. After being placed in the 5% skim milk, the membrane was washed three times and incubated with the corresponding primary antibody at 4°C for 12 h. Next, the membrane was incubated with the secondary antibody at room temperature for 1 hour. The protein band density was detected using a chemiluminescence system.

Statistical Analysis

SPSS software was used for data analysis. Statistical data were expressed as the mean ± S.E.M. of three individual experiments. Data were analyzed by Student's *t*-test or one-way analysis of variance (ANOVA). $p \leq 0.05$ was deemed a statistically significant difference.

RESULTS

Effects of Lentinan on LPS-Induced Histopathological Changes

The histological analysis was used to evaluate the mouse mammary tissue damage. Histological analysis showed that the mammary tissue of the control group was intact without histopathological changes (**Figure 1A**). In the LPS group, the injury of mouse mammary tissue was obvious, and inflammatory cell infiltration was extensive and hyperemia (**Figure 1B**). However, the extensive inflammatory cell infiltration and hyperemia were relieved, and the tissue structure was relatively complete in lentinan or dexamethasone treatment (**Figures 1C–F**). Moreover, in order to further verify the degree of tissue damage, the histopathological changes of the mouse mammary gland were evaluated according to the number of infiltrated inflammatory cells. As described in the literature, the pathological grade was scored according to 0–5 (Xingxing et al., 2018). As expected, the result was consistent with pathological sections (**Figure 1G**).

Effects of Lentinan on Myeloperoxidase Activity

MPO is an enzyme in neutrophils, and its activity is related to neutrophil infiltration (Lin et al., 2020). As displayed in **Figure 2A**, compared with the control group, the MPO activity was obviously enhanced in LPS challenge. Lentinan treatment reduced MPO activity in a dose-dependent manner,

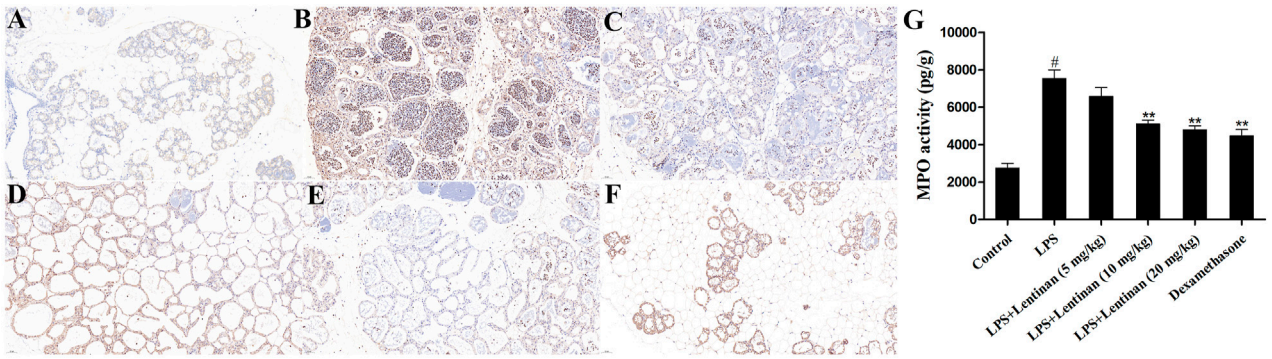


FIGURE 2 | Effects of lentinan on MPO activity. **(A,B)** MPO activity assay in lentinan-treated mMECs. All data are represented as the mean ± S.E.M. of three replicates. *$p < 0.05$ vs. the LPS group. **$p < 0.01$ compared with the LPS group. ***$p < 0.01$ compared with the LPS group.

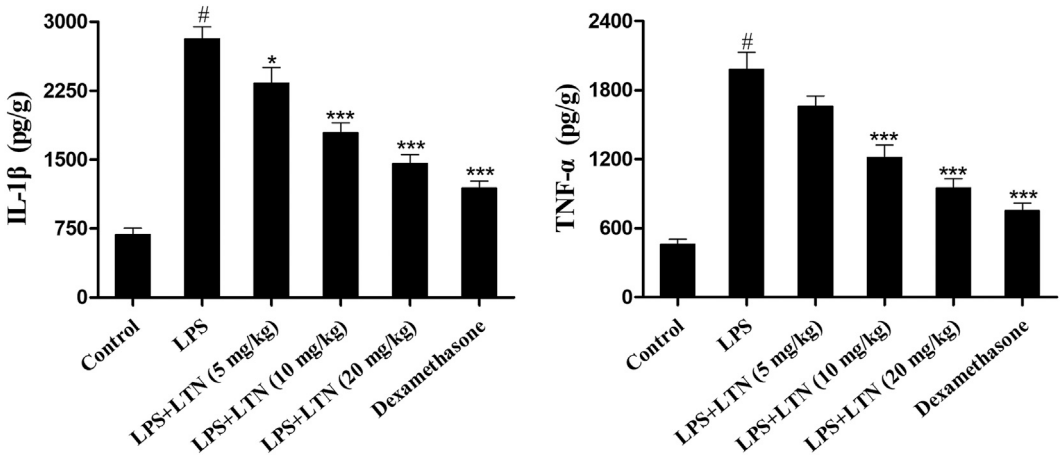


FIGURE 3 | Lentinan inhibited the secretion of proinflammatory factors. The expression of TNF-α and IL-1β in LPS-stimulated mouse mastitis was detected using ELISA kits. All data are represented as the mean ± S.E.M. of three replicates. *$p < 0.05$ vs the LPS group. **$p < 0.01$ compared with the LPS group. ***$p < 0.01$ compared with the LPS group.

especially at high concentration. In order to further verify the effect of Lentinan on MPO activity, the immunofluorescence technique was performed. As expected, LPS-enhanced MPO activity was decreased by lentinan or dexamethasone treatment (**Figure 2B**).

Lentinan Inhibited the Secretion of Proinflammatory Factors

The secretion of proinflammatory factors in mouse mammary tissues was detected using ELISA kits. The result of ELISA assay displayed that LPS markedly promoted the production of TNF-α and IL-1β. In contrast, lentinan or dexamethasone treatment substantially decreased the levels of TNF-α and IL-1β (**Figure 3**). These abovementioned results suggested that lentinan significantly inhibited the secretion of proinflammatory factors in LPS-induced mastitis at a concentration of 20 mg/kg. Thus, this concentration of lentinan was used to study the protective mechanism of LPS-induced mastitis.

Effects of Lentinan on the Activation of the Wnt/β-Catenin Pathway

The Wnt/β-catenin signaling pathway is an evolutionarily conserved mechanism that is fundamentally vital for inflammation-related diseases (Guan et al., 2021). We evaluated whether lentinan alleviated the LPS-induced inflammatory response by suppressing the Wnt/β-catenin pathway. The result of immunofluorescence assay displayed that LPS treatment significantly enhanced the activation of the Wnt/β-catenin signaling pathway that was reduced by lentinan treatment (**Figure 4**).

Cell Biological Detection

CK-18 is commonly used to identify the integrity of epithelial cells. Thus, mMECs were pretreated with the blue fluorescent pigment to identify the cell nucleus and CK-18 labeled with the green fluorescent pigment to show the cell integrity. The result is displayed in **Figure 5**.

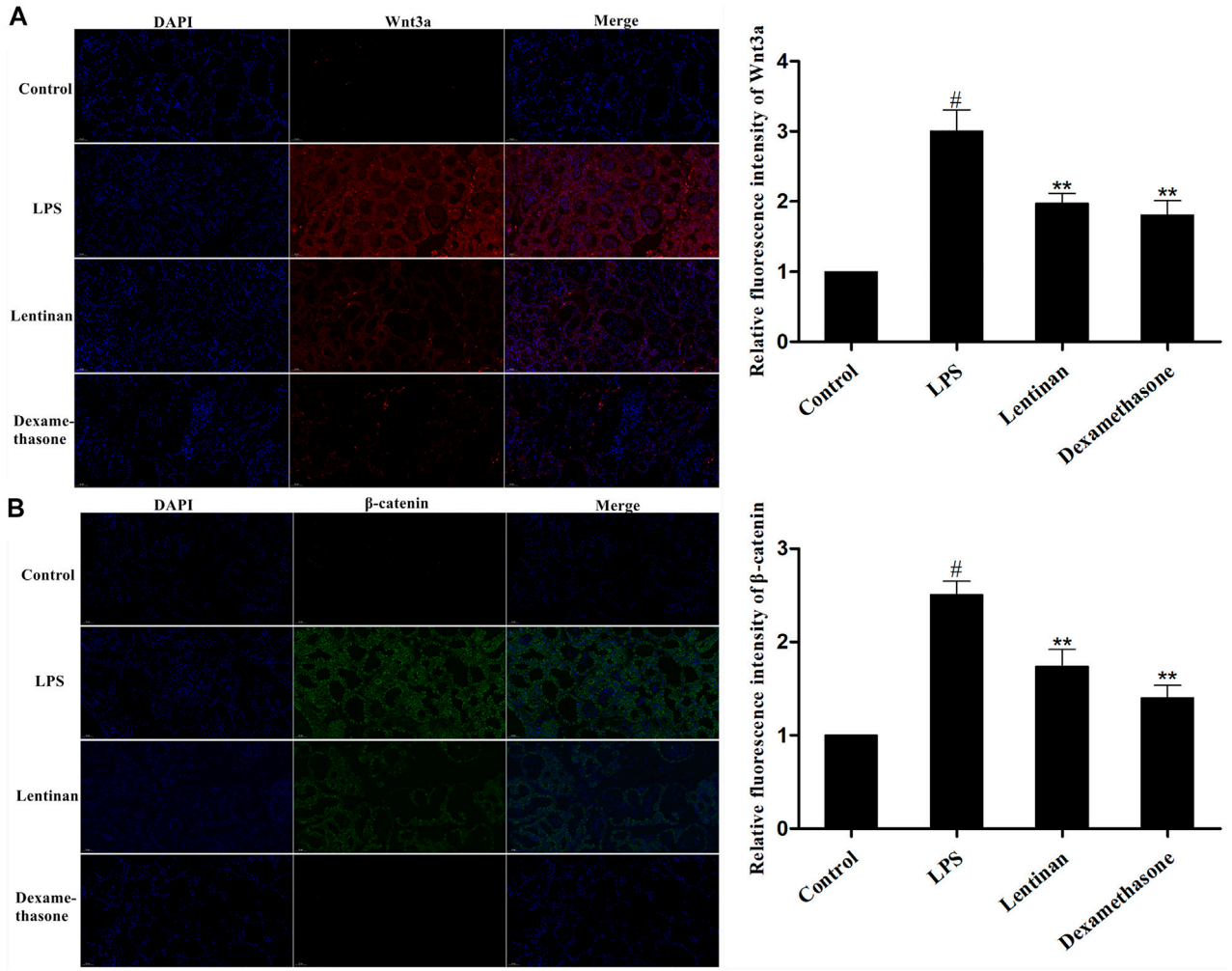


FIGURE 4 | Effects of lentinan on the activation of the Wnt/β-catenin pathway. The activation of the Wnt/β-catenin pathway in LPS-stimulated mouse mastitis was determined by immunofluorescence assay. All data are represented as the mean ± S.E.M. of three replicates.

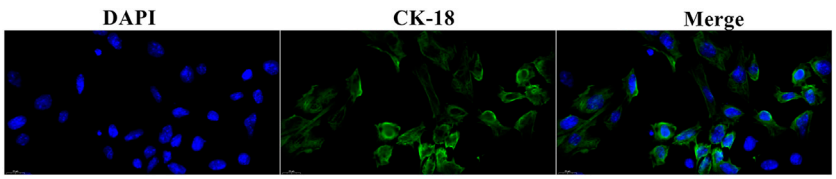


FIGURE 5 | Cell biological detection. The nucleus was dyed blue. The cytoplasm was dyed green by CK-18.

Effects of Lentinan on Inflammatory Response of Mouse Mammary Epithelial Cells

First, the potential cytotoxicity of lentinan on mMECs was detected by MTT experiment. As shown in **Figure 6A**, the cell viability was not affected by lentinan treatment. To investigate the effects of lentinan on inflammatory response in LPS-stimulated mMECs, the TNF-α and IL-1β protein levels were detected using the ELISA kit. As displayed in **Figure 6B**, LPS increased TNF-α and IL-1β secretion that was inhibited by lentinan or dexamethasone administration.

Effects of Lentinan on the Activation of the Wnt/β-Catenin Pathway in mMECs

The activation of the Wnt/β-catenin signaling pathway in LPS-stimulated mMECs was also determined by immunofluorescence assay. The result showed that LPS challenge greatly enhanced the activation of the Wnt/β-catenin pathway, but that was reduced by

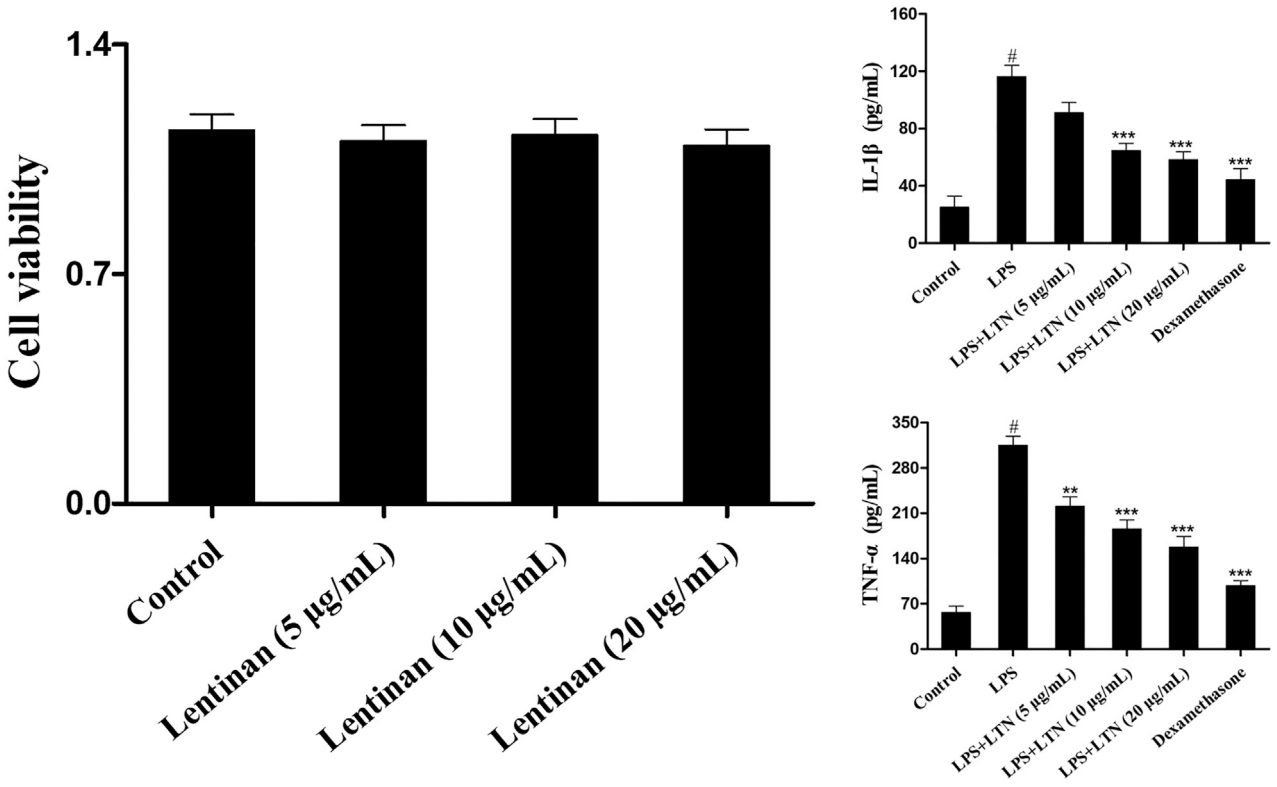


FIGURE 6 | Effects of lentinan on inflammatory response of LPS-induced mouse mammary epithelial cells. **(A)** The potential cytotoxicity of lentinan (5, 10, and 20 μg/ml) on mMECs was detected by MTT experiment. **(B)** The TNF-α and IL-1β protein levels were detected using the ELISA kit in LPS-stimulated mMECs. All data are represented as the mean ± S.E.M. of three replicates. $^{*}p < 0.05$ vs. the LPS group. $^{**}p < 0.01$ compared with the LPS group. $^{***}p < 0.01$ compared with the LPS group.

lentinan treatment or dexamethasone administration (**Figures 7A,B**). In order to confirm the effect of lentinan on the Wnt/β-catenin pathway activation, western blot was performed in mMECs. Consistent with the results in **Figure 7C**, the downstream factors in the Wnt/β-catenin pathway, Wnt3α, and *β*-catenin were activated upon LPS challenge, while lentinan or dexamethasone administration downregulated the Wnt3α and *β*-catenin protein expression.

DISCUSSION

Mastitis is a worldwide production disease of dairy cattle, which mainly affects milk yield, causing huge economic losses to dairy farmers (Krishnamoorthy et al., 2021). It is well known that inflammation is harmful to the breast, but the effect of mastitis on parts other than the breast is not obvious until researchers began to pay attention to environmental pathogens (Ruegg, 2017). The main pathogen causing mastitis in dairy cows is *Escherichia coli* (Shao et al., 2015). At present, antibacterial agents are still the main treatment and prevention of mastitis in most dairy farms (Stevens et al., 2016). However, consumers and public health authorities are increasingly concerned about the use of antibiotics to balance animal health and the development of antimicrobial resistance on farms (Ruegg, 2017; Nobrega et al., 2020). Lentinan is a kind of polysaccharide extracted from *Lentinus edodes*, which has no toxicity and possesses various pharmacological activities such as anticancer, antibacterial, and antiviral effects (Antonelli et al., 2020; Lv et al., 2020; Zi et al., 2020). Thus, the anti-inflammatory function of lentinan on LPS-stimulated mastitis was carried out, and the mechanism involved was explored.

In the present research, LPS challenge significantly enhanced the LPS-induced inflammatory injury that was lightened by lentinan treatment. Additionally, as the first line of defense against microorganisms, epithelial cells are cleared by producing a series of immune reactions (Shin et al., 2010). Therefore, the effect of lentinan on LPS-stimulated mouse mammary epithelial cells (mMECs) was also determined. The MTT test showed that the dose of lentinan used in the study had no cytotoxicity, which was consistent with the results of other studies (Guangming et al., 2018; Zhang and Zhao, 2019). Although inflammatory factors can produce adaptive behavioral response and promote energy conservation to fight infection or recover from injury, excessive proinflammatory factors (such as TNF-α and IL-1β) will cause damage to the body and cause inflammation-related diseases (Wang J. et al., 2019). We found that LPS induced the overproduction of proinflammatory factors that were suppressed by lentinan treatment.

There is increasing evidence that in many activated signaling pathways, the Wnt/β-catenin pathway plays vital role in the process of bacterial infection (Umar, 2012; Li et al., 2021). The proinflammatory stimulation of bacterial infection is a necessary condition for activating the Wnt/β-catenin pathway (Silva-García et al., 2014). For instance,

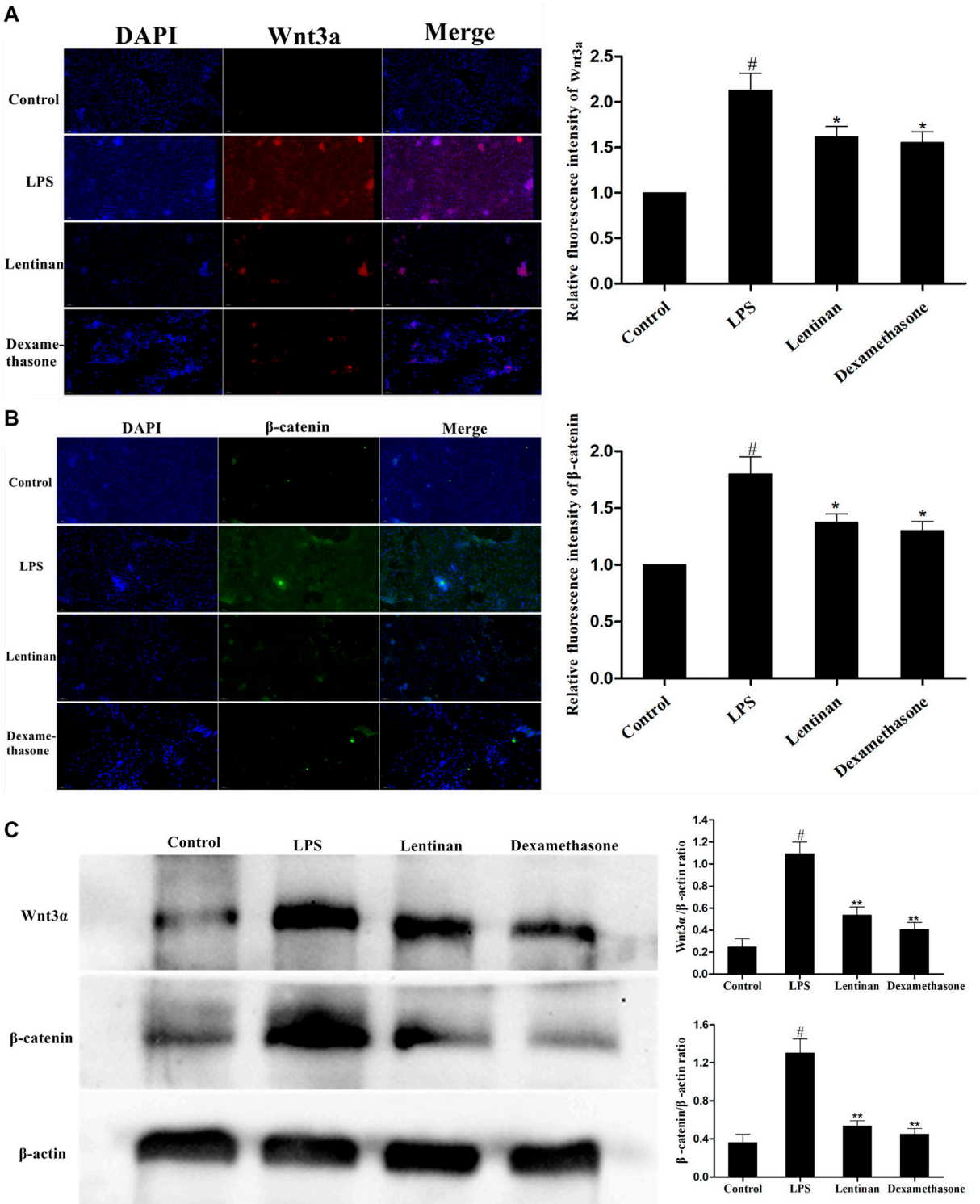


FIGURE 7 | Effects of lentinan on the activation of the Wnt/β-catenin pathway in mMECs. **(A,B)** The activation of the Wnt/β-catenin signaling pathway in LPS-stimulated mMECs was also determined by the immunofluorescence technique. **(C)** The expression of Wnt/β-catenin proteins was detected by western blot. *β*-actin served as an internal control. All data are represented as the mean ± S.E.M. of three replicates.

the proinflammatory functions were recorded in Wnt3a-stimulated several cells. Moreover, it has been found that mutations in genes encoding β-catenin or other Wnt pathway molecules have been verified in several inflammatory diseases, cancers (Castellone et al., 2009). To further explore the anti-inflammatory mechanism of lentinan, we then investigated the activation of the Wnt/β-catenin pathway in LPS-stimulated mMECs. The result showed that lentinan suppressed the activation of the Wnt/β-catenin pathway in LPS-stimulated mMECs. As we had expected, consistent results were obtained in the tissue immunofluorescence test.

In conclusion, the present results suggested that lentinan had a good anti-inflammatory function in LPS-stimulated mastitis through inhibiting the Wnt/β-catenin signaling pathway. Therefore, the results of our study also gave an insight that lentinan may serve as a potential treatment for mastitis.

DATA AVAILABILITY STATEMENT

The original contributions presented in the study are included in the article/**Supplementary Material**, and further inquiries can be directed to the corresponding author.

ETHICS STATEMENT

The animal study was reviewed and approved by the Institutional Animal Care and Use Committee in Zhejiang University.

AUTHOR CONTRIBUTIONS

All the authors listed below were involved in this research, and they have approved the article submission. HY participated in the main experiment and edited the article. GX participated in experiment design and statistical analysis. AD participated in the animal experiment and data collection. HW participated in experiment design and writing.

FUNDING

This research was funded by the special projects for Local Science and Technology Development guided by the Central Government (No. 2019L3011); Key Laboratory of Fujian Universities Preventive Veterinary Medicine and Biotechnology, Longyan University, Longyan 364012, China (No.2020KF02); and Longyan University and Fujian Provincial Key Laboratory for Prevention and Control of Animal Infectious Diseases and Biotechnology, Longyan 364012, China (No.ZDSYS2020001).

SUPPLEMENTARY MATERIAL

The Supplementary Material for this article can be found online at: https://www.frontiersin.org/articles/10.3389/fphar.2021.755768/full#supplementary-material

REFERENCES

Antonelli, M., Donelli, D., and Firenzuoli, F. (2020). "Lentinan for Integrative Cancer Treatment: an Umbrella Review," in 1st International Electronic Conference on Biomolecules: Natural and Bio-Inspired Therapeutics for Human Diseases. doi:10.3390/iecbm2020-08733

Castellone, M. D., De Falco, V., Rao, D. M., Bellelli, R., Muthu, M., Basolo, F., et al. (2009). The Beta-Catenin Axis Integrates Multiple Signals Downstream from RET/papillary Thyroid Carcinoma Leading to Cell Proliferation. *Cancer Res.* 69, 1867–1876. doi:10.1158/0008-5472.CAN-08-1982

Chen, X., Zheng, X., Zhang, M., Yin, H., Jiang, K., Dai, H. A., et al. (2018). Nuciferine Alleviates LPS-Induced Mastitis in Mice via Suppressing the TLR4-NF-Kb Signaling Pathway. *Inflamm. Res.* 67, 903–911. doi:10.1007/s00011-018-1183-2

Chen, X., Zheng, X., Zhang, M., Yin, H., Jiang, K., Wu, H., et al. (2018). Nuciferine Alleviates LPS-Induced Mastitis in Mice via Suppressing the TLR4-NF-Kb Signaling Pathway. *Inflamm. Res.* 67, 903–911. doi:10.1007/s00011-018-1183-2

Dai, H., Coleman, D. N., Hu, L., Martinez-Cortés, I., Wang, M., Parys, C., et al. (2019). Methionine and Arginine Supplementation Alter Inflammatory and Oxidative Stress Responses during Lipopolysaccharide challenge in Bovine Mammary Epithelial Cells *In Vitro*. *J. Dairy Sci.* 103, 676–689. doi:10.3168/jds.2019-16631

Doehring, C., and Sundrum, A. (2019). The Informative Value of an Overview on Antibiotic Consumption, Treatment Efficacy and Cost of Clinical Mastitis at Farm Level. *Prev. Vet. Med.* 165, 63–70. doi:10.1016/j.prevetmed.2019.02.004

Filioussis, G., Kachrimanidou, M., Christodoulopoulos, G., Kyritsi, M., Hadjichristodoulou, C., Adamopoulou, M., et al. (2020). Short Communication: Bovine Mastitis Caused by a Multidrug-Resistant, Mcr-1-Positive (Colistin-resistant), Extended-Spectrum β-Lactamase-Producing *Escherichia coli* Clone on a Greek Dairy Farm. *J. Dairy Sci.* 103 (1), 852–857. doi:10.3168/jds.2019-17320

Guan, X., He, Y., Wei, Z., Shi, C., Li, Y., Zhao, R., et al. (2021). Crosstalk between Wnt/β-Catenin Signaling and NF-Kb Signaling Contributes to Apical Periodontitis. *Int. Immunopharmacol* 98, 107843. doi:10.1016/j.intimp.2021.107843

Hou, C., Chen, L., Yang, L., and Ji, X. (2020). An Insight into Anti-Inflammatory Effects of Natural Polysaccharides. *Int. J. Biol. Macromol* 153, 248–255. doi:10.1016/j.ijbiomac.2020.02.315

Iida, T., Yokoyama, Y., Wagatsuma, K., Hirayama, D., and Nakase, H. (2018). Impact of Autophagy of Innate Immune Cells on Inflammatory Bowel Disease. *Cells* 8, 1–13. doi:10.3390/cells8010007

Jiang, K., Ma, X., Guo, S., Zhang, T., Zhao, G., Wu, H., et al. (2018). Anti-Inflammatory Effects of Rosmarinic Acid in Lipopolysaccharide-Induced Mastitis in Mice. *Inflammation* 41, 437–448. doi:10.1007/s10753-017-0700-8

Krishnamoorthy, P., Goudar, A. L., Suresh, K. P., and Roy, P. (2021). Global and Countrywide Prevalence of Subclinical and Clinical Mastitis in Dairy Cattle and Buffaloes by Systematic Review and Meta-Analysis. *Res. Vet. Sci.* 136, 561–586. doi:10.1016/j.rvsc.2021.04.021

Kumar, V. (2019). The Complement System, Toll-Like Receptors and Inflammasomes in Host Defense: Three Musketeers' One Target. *Int. Rev. Immunol.* 38, 131–156. doi:10.1080/08830185.2019.1609962

Kusebauch, U., Hernández-Castellano, L. E., Bislev, S. L., Moritz, R. L., Røntved, C. M., and Bendixen, E. (2018). Selected Reaction Monitoring Mass Spectrometry of Mastitis Milk Reveals Pathogen-Specific Regulation of Bovine Host Response Proteins. *J. Dairy Sci.* 101, 6532–6541. doi:10.3168/jds.2017-14312

Li, S., Zhou, C., Zhu, Y., Chao, Z., Sheng, Z., Zhang, Y., et al. (2021). Ferrostatin-1 Alleviates Angiotensin II (Ang II)- Induced Inflammation and Ferroptosis in Astrocytes. *Int. Immunopharmacol* 90, 107179. doi:10.1016/j.intimp.2020.107179

Lin, W., Jia, D., Fu, C., Zheng, Y., and Lin, Z. (2020). Electro-Acupuncture on ST36 and SP6 Acupoints Ameliorates Lung Injury via Sciatic Nerve in a Rat Model of Limb Ischemia-Reperfusion. *J. Inflamm. Res.* 13, 465–470. doi:10.2147/JIR.S264093

Lv, Q., Gu, Y., Qi, Y., Liu, Z., Ma, G. E., and Medicine, T. (2020). Effects of Lentinan on NF-Kb Activity in the Liver of Burn Rats with Sepsis. *Exp. Ther. Med.* 20, 2279–2283. doi:10.3892/etm.2020.8955

Meade, E., Savage, M., Garvey, P., Slattery, M. A., and Garvey, M. (2019). Antibiotic Resistant Zoonotic Pathogens of Bovine Mastitis and Possible Agents of Foodborne Disease. *CJMI* 5, 1–11. doi:10.31031/CJMI.2019.02.000550

Mu, Y. R., Zhou, M. Y., Cai, L., Liu, M. M., and Li, R. (2020). Overexpression of Aquaporin 1 in Synovium Aggravates Rat Collagen-Induced Arthritis Through Regulating β-Catenin Signaling: An *In Vivo* and *In Vitro* Study. *J. Inflamm. Res.* 13, 701–712. doi:10.2147/JIR.S271664

Nishitani, Y., Zhang, L., Yoshida, M., Azuma, T., Kanazawa, K., Hashimoto, T., et al. (2013). Intestinal Anti-inflammatory Activity of Lentinan: Influence on IL-8 and TNFR1 Expression in Intestinal Epithelial Cells. *PLoS One* 8, e62441. doi:10.1371/journal.pone.0062441

Nobrega, D. B., Tang, K. L., Caffrey, N. P., De Buck, J., Cork, S. C., Ronksley, P. E., et al. (2020). Prevalence of Antimicrobial Resistance Genes and its Association with Restricted Antimicrobial Use in Food-Producing Animals: A Systematic Review and Meta-Analysis. *J. Antimicrob. Chemother.* 76, 561–575. doi:10.1093/jac/dkaa443

Puggioni, G. M. G., Tedde, V., Uzzau, S., Guccione, J., Ciaramella, P., Pollera, C., et al. (2019). Evaluation of a Bovine Cathelicidin ELISA for Detecting Mastitis in the Dairy Buffalo: Comparison with Milk Somatic Cell Count and Bacteriological Culture. *Res. Vet. Sci.* 128, 129–134. doi:10.1016/j.rvsc.2019.11.009

Quandt, J., Arnovitz, S., Haghi, L., Woehlk, J., Gounari, F., Okoreeh, M., et al. (2021). Wnt–β-Catenin Activation Epigenetically Reprograms Treg Cells in Inflammatory Bowel Disease and Dysplastic Progression. *Nat. Immunol.* 22 (4), 471–484. doi:10.1038/s41590-021-00889-2

Ren, G., Xu, L., Lu, T., Zhang, Y., Wang, Y., Yin, J., et al. (2018). Protective Effects of Lentinan on Lipopolysaccharide Induced Inflammatory Response in Intestine of Juvenile Taimen (Hucho Taimen, Pallas). *Int. J. Biol. Macromol* 121, 317–325. doi:10.1016/j.ijbiomac.2018.09.121

Ruegg, P. L. (2017). A 100-Year Review: Mastitis Detection, Management, and Prevention. *J. Dairy Sci.* 100, 10381–10397. doi:10.3168/jds.2017-13023

Shao, G., Tian, Y., Wang, H., Liu, F., and Xie, G. (2015). Protective Effects of Melatonin on Lipopolysaccharide-Induced Mastitis in Mice. *Int. Immunopharmacol* 29, 263–268. doi:10.1016/j.intimp.2015.11.011

Shin, H. S., Yoo, I. H., Kim, Y. J., Lee, J. Y., Kim, H. B., Jin, S., et al. (2010). MKP1 Regulates the Induction of MCP1 by Streptococcus Pneumoniae Pneumolysin in Human Epithelial Cells. *Mol. Cell* 30, 263–270. doi:10.1007/s10059-010-0113-0

Silva-García, O., Valdez-Alarcón, J., and Izabal-Aguirre, B. A. (2014). The Wnt/β-Catenin Signaling Pathway Controls the Inflammatory Response in Infections Caused by Pathogenic Bacteria. *Mediators Inflamm.* 2014, 310183. doi:10.1155/2014/310183

Stevens, M., Piepers, S., Supré, K., Dewulf, J., and De Vliegher, S. (2016). Quantification of Antimicrobial Consumption in Adult Cattle on Dairy Herds in Flanders, Belgium, and Associations with Udder Health, Milk Quality, and Production Performance. *J. Dairy Sci.* 99, 2118–2130. doi:10.3168/jds.2015-10199

Stokes, B. A., Yadav, S., Shokal, U., Smith, L. C., and Eleftherianos, I. (2015). Bacterial and Fungal Pattern Recognition Receptors in Homologous Innate Signaling Pathways of Insects and Mammals. *Front. Microbiol.* 6, 19. doi:10.3389/fmicb.2015.00019

Umar, S. (2012). Citrobacter Infection and Wnt Signaling. *Curr. Colorectal Cancer Rep.* 8, 298–306. doi:10.1007/s11888-012-0143-4

Wang, J., Gao, Y., Lin, F., Han, K., and Wang, X. (2019a). Omentin-1 attenuates lipopolysaccharide (LPS)-induced U937 macrophages activation by inhibiting the TLR4/MyD88/NF-κB signaling. *Arch. Biochem. Biophys.* 679, 108187. doi:10.1016/j.abb.2019.108187

Wang, X., Wang, W., Wang, L., Yu, C., Zhang, G., Zhu, H., et al. (2019b). Lentinan Modulates Intestinal Microbiota and Enhances Barrier Integrity in a Piglet Model Challenged with Lipopolysaccharide. *Food Funct.* 10, 479–489. doi:10.1039/c8fo02438c

Wu, H., Zhao, G., Jiang, K., Chen, X., Zhu, Z., Qiu, C., et al. (2016). Puerarin Exerts an Antiinflammatory Effect by Inhibiting NF-kB and MAPK Activation in Staphylococcus Aureus-Induced Mastitis. *Phytother Res.* 30, 1658–1664. doi:10.1002/ptr.5666

Wu, H., Jiang, K., Zhang, T., Zhao, G., and Deng, G. (2017). Hydroxytyrosol Exerts an Anti-inflammatory Effect by Suppressing Toll-like Receptor 2 and TLR 2 Downstream Pathways in Staphylococcus Aureus-Induced Mastitis in Mice. *J. Funct. Foods* 35, 595–604. doi:10.1016/j.jff.2017.06.035

Zadoks, R. N., Middleton, J. R., Mcdougall, S., Katholm, J., and Schukken, Y. H. (2011). Molecular Epidemiology of Mastitis Pathogens of Dairy Cattle and Comparative Relevance to Humans. *J. Mammary Gland Biol. Neoplasia* 16, 357–372. doi:10.1007/s10911-011-9236-y

Zhang, S., and Zhao, Y. (2019). Lentinan Protects Cardiomyocytes against Hypoxia-Induced Injury by Regulation of microRNA-22/Sirt1. *Artif. Cell Nanomed Biotechnol* 47, 3938–3946. doi:10.1080/21691401.2019.1666863

Zhou, M. Y., Cai, L., Feng, X. W., Mu, Y. R., Meng, B., Liu, F. Y., et al. (2021). Lentivirus-Mediated Overexpression or Silencing of Aquaporin 1 Affects the Proliferation, Migration and Invasion of TNF-α-Stimulated Rheumatoid Arthritis Fibroblast-Like Synoviocytes by Wnt/β-Catenin Signaling Pathway. *J. Inflamm. Res.* 14, 1945–1957. doi:10.2147/JIR.S312783

Zi, Y., Jiang, B., He, C., and Liu, L. (2020). Lentinan Inhibits Oxidative Stress and Inflammatory Cytokine Production Induced by Benzo(a)pyrene in Human Keratinocytes. *J. Cosmet. Dermatol.* 19, 502–507. doi:10.1111/jocd.13005

Conflict of Interest: The authors declare that the research was conducted in the absence of any commercial or financial relationships that could be construed as a potential conflict of interest.

Publisher's Note: All claims expressed in this article are solely those of the authors and do not necessarily represent those of their affiliated organizations, or those of the publisher, the editors, and the reviewers. Any product that may be evaluated in this article, or claim that may be made by its manufacturer, is not guaranteed or endorsed by the publisher.

Copyright © 2021 Yin, Xue, Dai and Wu. This is an open-access article distributed under the terms of the Creative Commons Attribution License (CC BY). The use, distribution or reproduction in other forums is permitted, provided the original author(s) and the copyright owner(s) are credited and that the original publication in this journal is cited, in accordance with accepted academic practice. No use, distribution or reproduction is permitted which does not comply with these terms.

frontiers in Pharmacology

ORIGINAL RESEARCH
published: 13 October 2021
doi: 10.3389/fphar.2021.754038

Betulin Alleviates the Inflammatory Response in Mouse Chondrocytes and Ameliorates Osteoarthritis via AKT/Nrf2/HO-1/NF-κB Axis

Chenghao Ren[1,2,3], *Jie Jin*[1,2,3], *Wei Hu*[1,2,3], *Qi Chen*[1,2,3], *Jian Yang*[1,2,3], *Yaosen Wu*[1,2,3], *Yifei Zhou*[1,2,3], *Liaojun Sun*[1,2,3], *Weiyang Gao*[1,2,3], *Xiaolei Zhang*[1,2,3,4]* and *Naifeng Tian*[1,2,3]*

[1]Department of Orthopaedics, the Second Affiliated Hospital and Yuying Children's Hospital of Wenzhou Medical University, Wenzhou, China, [2]The Second School of Medicine, Wenzhou Medical University, Wenzhou, China, [3]Zhejiang Provincial Key Laboratory of Orthopaedics, Wenzhou, China, [4]Chinese Orthopaedic Regenerative Medicine Society, Hangzhou, China

OPEN ACCESS

Edited by:
Dahui Liu,
Hubei University of Chinese Medicine, China

Reviewed by:
Naila Rasheed,
Qassim University, Saudi Arabia
Claudio Ferrante,
University of Studies G.d'Annunzio Chieti and Pescara, Italy

***Correspondence:**
Xiaolei Zhang
zhangxiaolei@wmu.edu.cn
Naifeng Tian
naifengtian@wmu.edu.cn

Specialty section:
This article was submitted to Inflammation Pharmacology, a section of the journal Frontiers in Pharmacology

Received: 05 August 2021
Accepted: 06 September 2021
Published: 13 October 2021

Citation:
Ren C, Jin J, Hu W, Chen Q, Yang J, Wu Y, Zhou Y, Sun L, Gao W, Zhang X and Tian N (2021) Betulin Alleviates the Inflammatory Response in Mouse Chondrocytes and Ameliorates Osteoarthritis via AKT/Nrf2/HO-1/NF-κB Axis. Front. Pharmacol. 12:754038. doi: 10.3389/fphar.2021.754038

Osteoarthritis (OA) is a common degenerative joint disease featuring the degeneration, destruction, and ossification of cartilage. Inflammation which may facilitate OA occurrence and development is considered as the main pathological factor. Betulin, a natural product extracted from birch bark, has been commonly used for inflammation treatment; however, its role in OA remains unclear. This study is aimed to explore whether betulin can suppress IL-1β–induced inflammation in chondrocytes and alleviate OA *in vitro* and *in vivo*. In *in vitro* studies, the generation of pro-inflammatory factors, such as interleukin-6 (IL-6), tumor necrosis factor alpha (TNF-α), prostaglandin E2 (PGE2), and nitric oxide (NO), was assessed using the enzyme-linked immunosorbent assay (ELISA) and Griess reaction. As revealed by results, betulin inhibited the expression of pro-inflammatory mediators. In addition, the protein expressions of inducible nitric oxide synthase (iNOS), cyclooxygenase-2 (COX-2), matrix metalloproteinase (MMP-13), thrombospondin motifs 5 (ADAMTS5), Collagen II, and Aggrecan were quantified using Western blot analysis. We found that betulin could inhibit the generation of COX-2 and iNOS induced by IL-1β, indicating that betulin has anti-inflammatory effects in chondrocytes. Furthermore, betulin downregulates the expression of MMP-13 and ADAMTS-5 and upregulates the expression of Collagen II and Aggrecan, indicating that it can inhibit the degradation of the extracellular matrix. In mechanism, betulin activated the AKT/Nrf2 pathway and inhibited the phosphorylation of p65. In *in vivo* studies, administration of betulin *in vivo* could inhibit cartilage destruction and inflammatory progression. Therefore, these findings suggest that betulin may alleviate IL-1β–induced OA via the AKT/Nrf2/HO-1/NF-κB signal axis, and betulin may be a potential drug for the treatment of OA.

Keywords: betulin, osteoarthritis (OA), AKT, NRF, NF-κB, inflammation

Abbreviations: AKT, protein kinase B; Nrf2, nuclear factor erythroid 2-related factor; HO-1, heme oxygenase-1; NF-κB, nuclear transcription factor-κB; SO, safranin O and fast green; HE, hematoxylin and eosinn; OARSI, Osteoarthritis Research Society International

INTRODUCTION

Osteoarthritis (OA) is a long-lasting, chronic, and progressive joint disease characterized by the loss or destruction of joint function and morphological integrity. It is mainly manifested as joint pain with serious impact on daily life (Kean et al., 2004). However, the specific pathogenesis of OA remains unclear (Sun et al., 2017). In addition, due to the insufficient efficacy of current drug therapy, clinical symptoms can be temporarily relieved, urgently requiring drugs with good efficacy and less side effects to reverse the progress of OA (Krustev et al., 2015). According to the increasing evidence, inflammatory mechanisms play a key role in the progression of OA (Bonnet and Walsh, 2005; Scanzello, 2017). A large number of inflammatory cytokines, such as interleukin-6 (IL-6), interleukin-1β (IL-1β), and tumor necrosis factor-α (TNF-α) are involved in OA occurrence and development (Fernandes et al., 2002), among which IL-1β is the main pro-inflammatory cytokine. Previous studies have revealed that IL-1β can induce the activation of nuclear transcription factor B (NF-κB) and promote the secretion of pro-inflammatory mediators (Abramson et al., 2001; Vincenti and Brinckerhoff, 2002; Chabane et al., 2008; Zhang et al., 2018), resulting in the decomposition of the intra-articular matrix above the synthetic level (Dodge and Poole, 1989; Nummenmaa et al., 2015), and finally accelerating the deterioration of OA. Therefore, inhibiting the IL-1β–mediated inflammatory response is an effective therapeutic strategy to suppress the progression of OA.

There is evidence that the NF-κB signal pathway can regulate the expression of inflammatory mediators and participate in the inflammatory process, such as IL-1β–induced inflammation and apoptosis (Wang et al., 2016). The stimulation of IL-1β will lead to the degradation of IκBα, release of the bound NF-κB dimer, and activation of the NF-κB signal pathway, thereby causing inflammation (Kumar et al., 2004; Hayden and Ghosh, 2011). Studies have shown that the nuclear factor–erythroid 2–related factor (Nrf2) and heme oxygenase-1 (HO-1) are important signal mediators in anti-inflammatory defense mechanisms, and the activation of the Nrf2/HO-1 signal can inhibit inflammatory effects (Jiang et al., 2014). In addition, we also found that by activating AKT, the expression of HO-1 can be regulated via the Nrf2 pathway (Lu et al., 2014; Huang et al., 2015; Yeh et al., 2015). According to reports, many natural products with anti-inflammatory activity exert anti-inflammatory protection by inducing HO-1 (Parada et al., 2015; Chan et al., 2017). Therefore, the NF-κB or HO-1 pathway may be a potential therapeutic target.

Betulin is a triterpene natural product extracted from birch bark, with anti-inflammatory activity that can be used to control various inflammatory diseases in folk medicine (Bai et al., 2016). For example, betulin attenuates renal injury in septicemic rats by inhibiting TLR4/NF-κB signal pathway (Zhao et al., 2016). In addition, it has been found that betulin inhibits IL-1β–induced matrix metalloproteinase gene expression and production (Ra et al., 2017), suggesting that betulin may delay the progression of OA, but the mechanism on how exactly it slows down the development of inflammation is unclear; this study specifically elaborated the specific mechanism of betulin in the progress of OA. It is worth noting that the role of the AKT/Nrf2/HO-1/NF-κB signal axis in the progression of OA has not been clarified yet. This study aims to explore whether betulin can reduce the inflammation level of OA by regulating the signal axis of AKT/Nrf2/HO-1/NF-κB, thus alleviating the progression of OA.

MATERIALS AND METHODS

Reagents

Betulin (purity ≥98%) was dissolved in dimethylsulfoxide (DMSO), diluted in PBS, and administered in a culture medium (final concentrations of DMSO were 0.5%), as 0.5% DMSO alone did not affect the proliferation of chondrocytes. Type II collagenase was purchased from Solarbio (Beijing, China). Recombinant IL-1β was obtained from Novoprotein (China). The primary antibodies against Aggrecan (ab3778), Collagen II (ab34712), MMP-13 (ab1010), ADAMTS5 (ab41037), HO-1 (ab13248), Nrf2 (ab92946), AKT (ab8805), Lamin B (ab16048), GAPDH (ab8245), P65 (ab16502), IκBα (ab32518), P-IκBα (ab133462), and P-P65 (ab76302) were purchased from Cambridge ABCAM Company in England. Cell count kit-8 (CCK-8) was purchased from Dojindo (Kumamoto, Japan). 6-diamino-2-phenylindole (DAPI) nuclear staining was obtained from Beyotime, Shanghai, China. Griess reagent is provided by Biomass Life Sciences Co., Ltd. (Shanghai, China). ELISA kits for tumor necrosis factor-α (TNF-α), interleukin-6 (IL-6), and prostaglandin E2 (PGE-2) were provided by the Minneapolis R & D system.

Isolation and Culture of Primary Chondrocytes

10-week-old C57BL/6 male wildtype (WT) mice were purchased from the Animal Center of the Chinese Academy of Sciences (Shanghai). After euthanasia with 10% chloral hydrate, the knee joint and hip cartilage of the mice were washed in phosphate-buffered saline (PBS) and minced into pieces measuring approximately 2 mm. The cartilage tissue was digested for 4 h with 0.2% Type II collagenase at 37°C. The digested cartilage samples were centrifuged at 37°C for 3 min. The supernatant was inoculated in a culture dish (seeding density: 10^5 cells/cm^2). 10% fetal bovine serum (FBS) and 1% antibiotic (penicillin/streptomycin) DMEM/F-12 were incubated at 37 °C, 5% CO_2, and the culture medium was replaced every day. 80 and 90% were mixed and separated with 0.25% trypsin-EDTA solution and then cultured. In this study, only 0–2 generation cells were used to avoid phenotypic loss (Wu et al., 2018) (Zheng et al., 2018).

CCK-8 Assay

To evaluate the potential toxicity of betulin to mouse chondrocytes, the CCK-8 (Dojindo Co, Kumamoto, Japan) test was performed in accordance with the manufacturer's instructions. In short, cartilage cells were seeded at a density of 2×10^5/mL (0.1 mL/well) in a 96-well plate and allowed to attach for 24 h to keep the log phase growth at the time of drug treatment, then treated with betulin under a concentration

gradient of (0, 25, 50, 100, and 200 μM) for 24 h or 48 h, 10 μL CCK-8 solution was added to each well and incubated at 37°C for 4 h. Then the optical density was measured by spectrophotometer (Thermo Fisher) at 450 nm. All the experiments were carried out for three times.

Determination of NO, PGE2, TNF-α, and IL-6

Chondrocytes cultured in culture dishes were exposed to betulin (0, 25, 50, and 100 μM) of different concentrations, incubated at 37°C for 2°h, then incubated with IL-1β (10 ng/ml) for 24 h. The concentration of NO was determined by Griess reaction. The concentrations of PGE2, TNF-α, and IL-6 in each culture were determined by the ELISA method (Au et al., 2007). All the tests were carried out for three times.

Western Blotting

Chondrocytes were incubated for 2 h in growth medium with 25, 50, and 100 μM of betulin followed by incubation in the presence or absence of IL-1β (10 ng/mL) for 24 h. Cells were collected and lysed with Radioimmunoprecipitation Assay (RIPA) lysis buffer [with 1% phenylmethanesulfonyl fluoride (PMSF)], the nucleoproteins of cells were obtained using a nuclear extraction kit. The protein concentration was quantified using a bicinchoninic acid (BCA) protein assay kit. Sodium dodecyl sulfate–polyacrylamide gel electrophoresis (SDS-PAGE) and polyvinylidene fluoride (PVDF) membrane were used to separate and transfer 40 ng proteins, and then sealed with 5% skim milk for 2 h. Then, the primary antibody was used overnight at 4°C. After the primary antibody was incubated, the membrane was washed with Tris-buffered Saline with 0.1% Tween-20 (TBST) for three times for 5 min, and then incubated at room temperature in 5% TBST for 2 h with the corresponding secondary antibody. After being rinsed by TBST, the film was developed with the enhanced chemiluminescence kit, and the gray value of the film was quantitatively determined by Image Lab 3.0 software (Bio-Rad).

Real-Time PCR

Chondrocytes were inoculated into 6-well plates. After 24 h of culture, the cultured chondrocytes were stimulated with different concentrations (25, 50, and 100 μM) of betulin followed by incubation for 24 h with or without IL-1β (10 ng/mL). The total RNA of monolayer chondrocytes was extracted with TRIzol reagent. The concentration of RNA was determined by spectrophotometry at 260 nm, and the quality and purity of RNA were determined by the A260/A280 ratio. The first-strand cDNA was synthesized with 10 ng total RNA and the QuantiTect reverse transcription kit. The CFX96 real-time PCR (RT-PCR) system was used for 10-min reaction at 95°C, 15-min reaction at 95 °C, and 1-min reaction at 60 °C, with a circulation of 40 times, and the total reaction volume was 10 μL (4.5 μL diluted cDNA, 0.25 μL forward primer, 0.25 μL reverse primer, and 5 μL SYBR Green Master Mix). The target mRNA level was normalized to the GAPDH level and compared with the control group. The primers for iNOS, IL-6, COX-2, and TNF-α were designed as follows (Pfaffl, 2001):

iNOS (F)5'GACGAGACGGATAGGCAGAG3' (R) 5'CATGCAAGGAAGGAACT3'

IL-6 (F)5'CCGGAGAGGAGACTTCAG3' (R) 5'TCCACGATTTCCCAGAGAAC3′

COX-2 (F)5'TCCTCACATCCCTGAGAACC3' (R) 5'GTCGCACACTCTGTTGTGCT3′

TNF-α (F)5'ACGGCATGGATCTCAAAGAC3' (R) 5'GTGGGTGAGGAGCACGTAGT3′

Immunofluorescence Analysis

Chondrocytes incubated with or without betulin (50 μM) for 2 h, then co-incubated with IL-1β (10 ng/ml) for 24 h, fixed with 4% paraformaldehyde solution at room temperature for 15 min, rinsed using PBS for three times, and then treated with 0.1% TritonX-100 at room temperature for 5 min. The cover slides were placed in a wet box, sealed at 37°C with 5% bovine serum albumin for 1 h, then diluted with primary antibodies at 4°C for 12°h, rinsed by phosphate buffer, incubated with goat anti-rabbit IgG antibody coupled with fluorescein at room temperature for 1 h, and then stained with DAPI. The fluorescence microscope was used for imaging.

Animal Model

10-weeks-old C57BL/6 male wild-type (WT) mice (n = 18) were selected from the Shanghai Animal Center of Chinese Academy of Sciences. All the experiments were performed in accordance with the regulations of the Animal Protection and Utilization Committee of Wenzhou Medical University (wyde2021-0297). The mouse OA model was established by surgical resection of medial meniscus (DMM). Mice were anesthetized with 1% pentobarbital sodium, then the right knee joint was cut open with microsurgical scissors and the medial meniscus tibial ligament of the right knee joint was transected to protect the lateral meniscus ligament during the operation. As a control, the medial meniscus tibial ligament was not transected, while the left knee arthrotomy was performed as the sham operation group. The mice were randomly divided into three groups: the first group was the Sham group, the second group was the DMM group, and the third group was the DMM+Betulin group (n = 6 mice in each group). After operation, the mice in the third group were injected intraperitoneally with betulin (20 mg/kg/d) (Ma and Long, 2016), and the mice in the other groups were injected with the same amount of inert carrier (DMSO) for 8 weeks under the temperature of 20 ± 2°C, with a relative humidity of 50 ± 10%, and the light/dark cycle of 12 h. All animals were killed 8 weeks after the operation, and the cartilage samples were taken for immunological and histological analyses.

Histopathological Analysis

Cartilage destruction was evaluated using SO and HE staining, and the slides of each joint were stained. Then, the morphological changes of the cartilage and its surrounding tissue were observed using a microscope, and articular cartilage destruction was evaluated using the Osteoarthritis Research Society International (OARSI) medial femoral condyle and medial tibial plateau scoring systems.

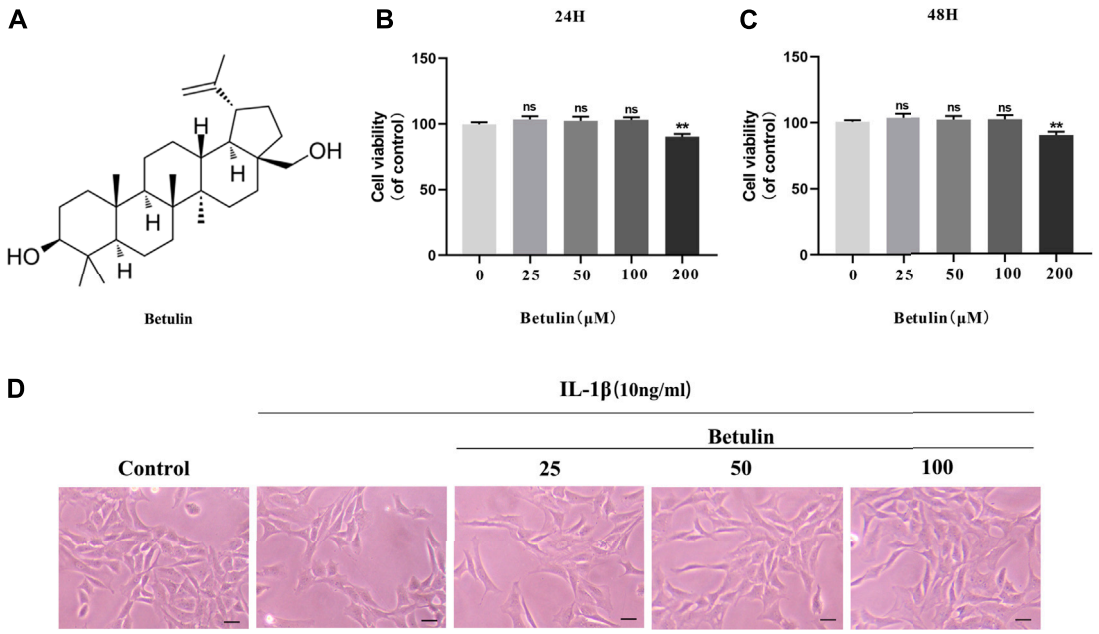


FIGURE 1 | Effect of betulin on the viability of OA chondrocytes. **(A)** The chemical structure of betulin. **(B–C)** The cell was cultured with betulin (0, 25, 50, 100, and 200 μM) different concentrations for 24 and 48 h, and the cell viability was measured using the CCK-8 kit. **(D)** After the chondrocytes were pretreated with different concentrations of betulin, the chondrocytes were imaged with a phase contrast microscope (scale bar: 50 μm). The data in the figure represent the average ± SD, $^{**}p < 0.01$ compared to the control group, n = 3.

Immunohistochemical Analysis

Knee joint tissue was fixed with 4% paraformaldehyde, decalcified, and embedded in paraffin, then it was sliced, dewaxed, and rehydrated, treated with 3% (v/w) hydrogen peroxide and 0.25% trypsin-EDTA solution at 37°C for 30 min. Then, the slices were incubated in 10% bovine serum albumin for 60 min (37°C). The first antibody was treated at 4°C for 24 h. On the second day, the secondary antibody was incubated at 4°C for 1 h. The images were analyzed using Image-ProPlus6.0 version software. Five slices were taken from each group for quantitative analyses.

X-Ray Imaging

X-ray examination was performed on the mice in the three groups at the eighth week after operation. X-ray imaging was performed on all animals using digital X-ray system. The degree of articular cartilage degeneration was evaluated by joint space, cartilage surface calcification, and osteophyte formation.

Molecular Docking Model

The molecular structure of betulin was derived from PubChem database and imported into Chem3D for molecular energy minimization and geometric optimization. The protein structure of AKT (PDBID:4GV1) was from the Protein Data Bank database (http://www.rcsb.org/). The structure of the protein was treated on the Maestro11.9 platform. The Protein Preparation Wizard of Schrodinger was used to treat the protein, remove the crystal water, add the missing hydrogen atom, repair the missing bond information, repair the missing peptide, and finally minimize the energy and optimize the geometric structure of the protein (Rajeswari et al., 2014; Fazi et al., 2015). All molecules were prepared according to the default settings of the Lig Prep module. When screening in the Glide module, the prepared receptor was introduced to specify the appropriate location in the receptor grid generation, the predicted active site of the protein was selected as the centroid of the 12 Å box. Finally, molecular docking and screening were carried out by the standard method.

Statistical Analysis

All experiments were performed at least three times. All data were presented as the mean ± SD and carried out by SPSS 20.0 software. The differences between groups were analyzed by one-way ANOVA with Tukey's multiple comparison test. $p < 0.05$ and $p < 0.01$ were considered to be significant.

RESULTS

The Effect of Betulin on the Viability of Chondrocytes

The chemical structure of betulin is shown in **Figure 1A**. The CCK-8 experiment was performed to determine the cytotoxic effect of betulin on chondrocytes. Chondrocytes were incubated with betulin of different concentrations (0, 25, 50, 100, and 200 μM) for 24 and 48 h. As shown by **Figures 1B–C**, the cell viability of chondrocytes were not significantly affected at the concentration of 0–100 μM but decreased slightly at the

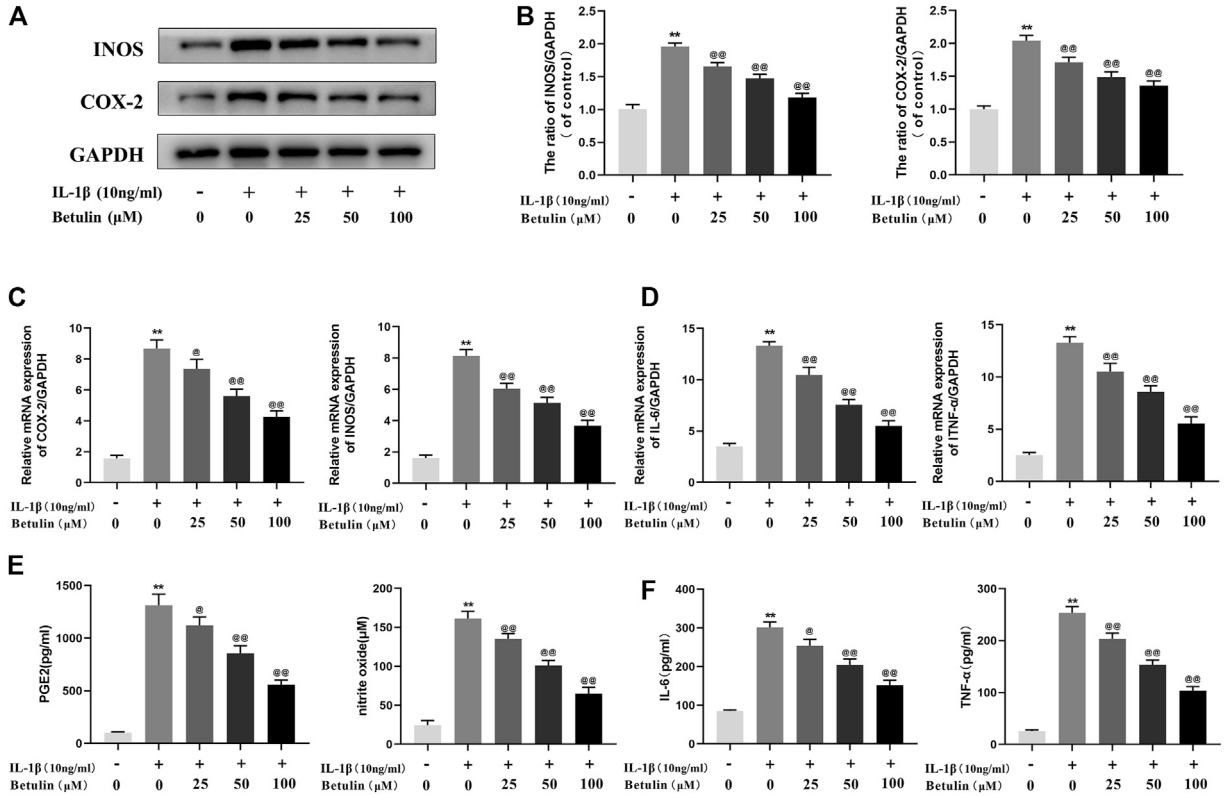


FIGURE 2 | Betulin treatment can inhibit the generation of pro-inflammatory mediators. OA chondrocytes were pretreated with betulin (0, 25, 50, and 100 μM) of different concentrations for 2 h, then stimulated by IL-1β (10 ng/ml) for 24 h. **(A–B)** The protein expression of iNOS and COX-2 was detected by Western blot and quantitatively analyzed. **(C–D)** The mRNA expression levels of iNOS, COX-2, IL-6, and TNF-α were detected by RT-PCR. **(E–F)** The generation of NO, PGE2, TNF-α, and IL-6 was detected by Griess reaction and the ELISA method. The data in the figure are represented as the average ±SD, $^{*}p < 0.05$, $^{**}p < 0.01$ compared with the control group, $^{@@}p < 0.01$ compared with the IL-1β group, n = 3.

concentration of 200 μM ($p < 0.01$). The results of treatment for 48 h were similar ($p < 0.01$). Besides, under IL-1β treatment, the number of chondrocytes decreased and the cells shrank. After betulin treatment, the survival of the chondrocytes increased in a dose-dependent manner. Therefore, betulin with the concentrations of (0, 25, 50, and 100 μM) was used in all subsequent experiments.

Betulin Inhibits the Generation of Pro-inflammatory Mediators

It was speculated that betulin has an anti-inflammatory effect in the OA cell model. To validate this hypothesis, it was first investigated whether betulin inhibits the production of pro-inflammatory mediators. The expression of iNOS and COX-2 was detected by Western blot (**Figures 2A,B**). The generation of iNOS and COX-2 stimulated by IL-1β was significantly higher than that in the control group ($p < 0.01$). Betulin treatment could reduce the expression of iNOS and COX-2 in the chondrocytes in a dose-dependent manner ($p < 0.01$). The cell suspension was collected using TRIzol reagent to analyze the mRNA levels of the pro-inflammatory mediators (IL-6 and TNF-α) and enzymes (iNOS and COX-2) by quantitative RT-PCR. The results further verify this conclusion (**Figures 2C,D**). In addition, released enzymes (iNOS and COX-2) generated NO and PGE2 inflammatory mediators in cells, respectively. Griess reaction was used to detect the concentration of endogenous NO in cell suspensions, and the ELISA kit was used to detect the levels of PGE2, TNF-α, and IL-6. As shown in **Figures 2E,F**, the expression of NO, IL-6, TNF-α, and PGE-2 increased significantly compared with that in the blank control group ($p < 0.01$), while betulin reversed this phenomenon in a dose-dependent manner. This verified that betulin could inhibit the generation of pro-inflammatory mediators.

Betulin Inhibits the Degradation of Extracellular Matrix Induced by IL-1β

In the progress of OA, the extracellular matrix of cartilage cells is continuously degraded, to explore the protective effect of betulin on cartilage extracellular matrix degradation induced by IL-1β. The expression of Aggrecan, Collagen II, ADAMTS-5, and MMP13 in chondrocytes was detected by Western blot with betulin of different concentrations (**Figures 3A,B**). The results showed that the expression of Collagen II and Aggrecan decreased significantly, while the expression of ADAMTS-5

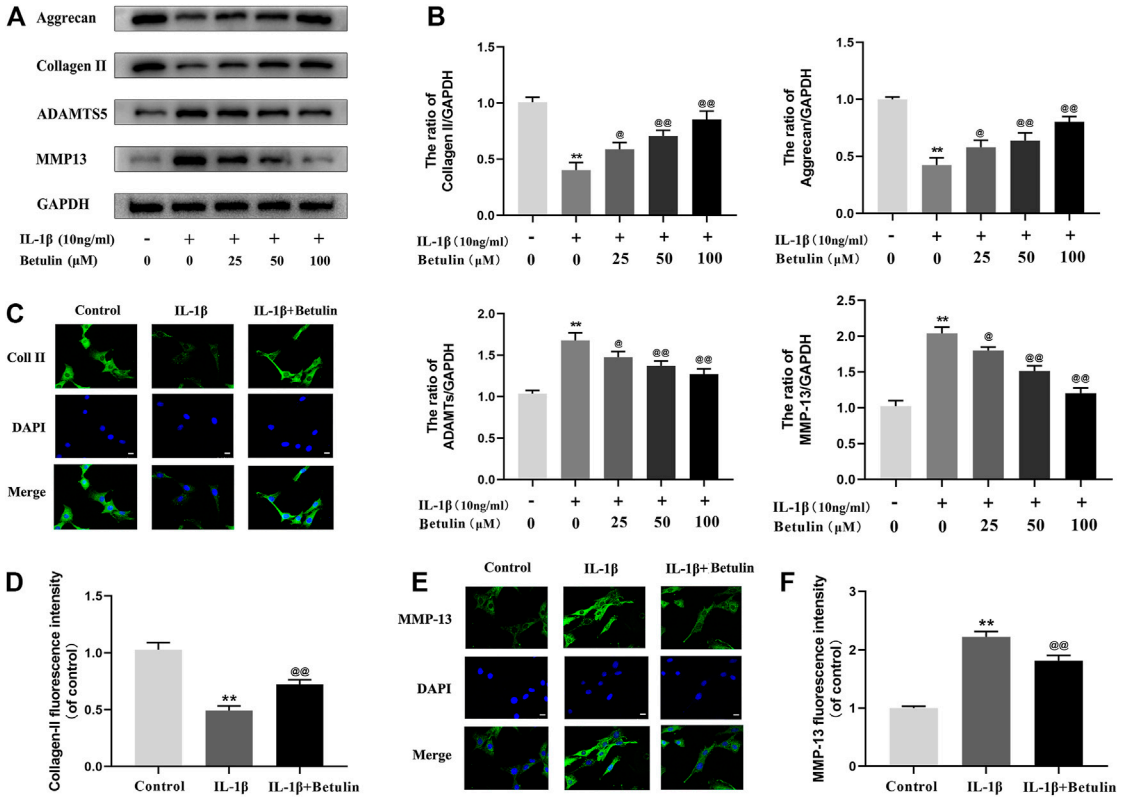


FIGURE 3 | Betulin treatment can inhibit the degradation of extracellular matrix. OA chondrocytes were cultured with betulin (0, 25, 50, and 100 μM) of different concentrations for 2 h, followed by stimulation with or without IL-1β (10 ng/ml) for 24 h. **(A–B)** The protein expression levels of Collagen II, Aggrecan, MMP13, and ADAMTS-5 were detected by Western blot and quantitatively analyzed. **(C–F)** Immunofluorescence staining combined with DAPI staining (scale: 25 μm) was used to detect the fluorescent expression of MMP13.The data in the figure are represented as the mean ± SD, $^{**}p < 0.01$ compared with the control group, $^{@@}p < 0.01$ compared with the IL-1β group, n = 3.

and MMP13 increased significantly after the stimulation of IL-1β ($p < 0.01$). However, betulin reversed the expression of Collagen II and reduced the protein levels of MMP13 and ADAMTS5 in a dose-dependent manner. In addition, we also used the immunofluorescence method. After the treatment of IL-1β, the fluorescence intensity of Collagen II decreased while that of MMP-13 increased ($p < 0.01$). The treatment of betulin reversed this trend (**Figures 3C–F**) ($p < 0.01$), which conformed to that of Western blot, and further verified that betulin could prevent ECM degradation and suppress the development of OA.

Betulin Inhibits NF-κB Signal Activation in OA Chondrocytes

Many molecules involved in inflammatory reaction are regulated by the NF-κB pathway. To further explore the effect of betulin on the NF-κB pathway in chondrocytes, the expression of the target proteins in the NF-κB pathway induced by betulin was observed using Western blot (**Figure 4A,B,C,F**). The phosphorylation of IκBα and p65 increased significantly after IL-1β stimulation ($p < 0.01$). Betulin treatment could inhibit the degradation of IκBα in the cytoplasm and inhibit the phosphorylation of p65. Then, we further observed the effect of betulin on the translocation of p65 to IL-1β induced into the nucleus. As expected, in the control group, the p65 active protein was mainly located in the cytoplasm, while in the IL-1β group, most of the p65 active protein was transferred to the nucleus. The betulin pretreatment significantly inhibited p65 translocation to the nucleus (**Figures 4D,E**) ($p < 0.01$). These results suggest that betulin inhibits the activation of the NF-κB signal pathway in the chondrocytes and plays an anti-inflammatory role.

Molecular Docking Between Betulin and AKT Protein

According to the results of molecular docking obtained by the standard method, the results show that the compound has a good binding to the target protein, and the binding energy is −6.68 (kcal/mol). The lower the energy required for binding, the easier it is to bind to the target protein. In addition, the complex formed by the docking compound and protein was visualized by Pymol2.1 software, and the binding mode of the compound and protein was obtained (**Figures 5A–C**). According to the binding mode, we can clearly see that betulin and AKT protein bind to VAL-164, ALA-177, PHE-442, GLU-234, MET-227,

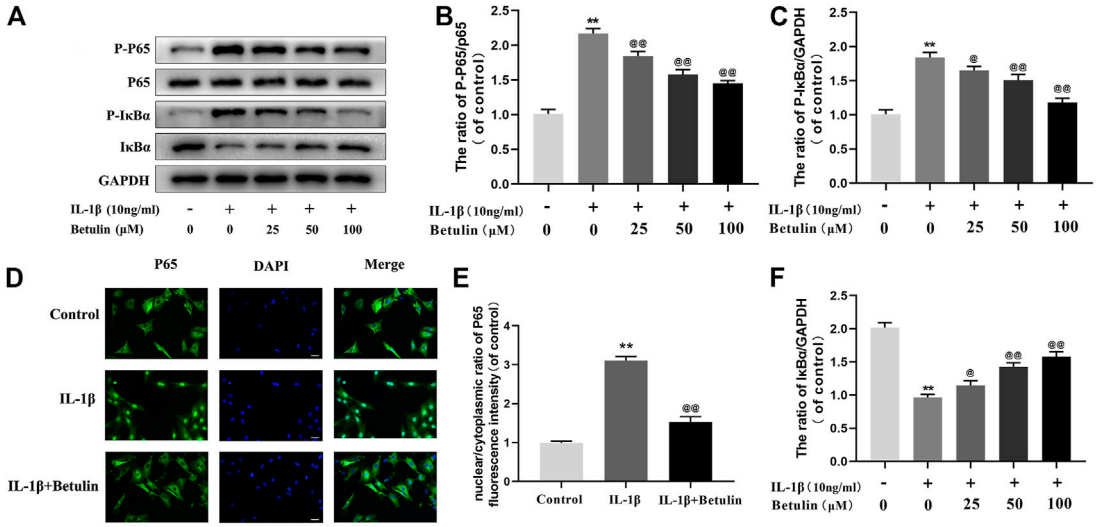


FIGURE 4 | Betulin treatment inhibited the activation of NF-κB signal. OA chondrocytes were cultured with betulin (0, 25, 50, and 100 μM) of different concentrations for 2 h, and then stimulated by IL-1β (10 ng/ml) for 24 h. **(A–C,F)** The protein expression levels of p-p65, p65, IκBα, and p-IκBα were detected by Western blot and quantitatively analyzed. **(D,E)** Immunofluorescence staining combined with DAPI staining (scale: 25 μm) were used to detect the entry of characteristic index p65 into the nucleus and quantitative analysis of fluorescence intensity. The data in the figure are represented as the mean ± SD, $^{**}p < 0.01$ compared with the control group, $^{@@}p < 0.01$ compared with the IL-1β group, n = 3.

ASP-292, and other amino acid residues. We also found that betulin can form strong hydrogen bonds with amino acid active groups such as GLU-234 and ASP-292, and the distances of 1.8 Å and 2.9 Å are much smaller than 3.5 Å of the traditional hydrogen bonds, which plays an important role in the stability of both. In addition, betulin can also form hydrophobic interactions with hydrophobic residues (**Figures 5D,E**). These interactions can improve the stability of betulin in AKT protein, indicating that betulin and AKT protein have a high affinity. Betulin is a potentially active small molecule that can be used to activate AKT.

Betulin Promotes the Phosphorylation of AKT, Enhances the Nuclear Expression of Nrf2, and Upregulates the Expression of HO-1

Studies have shown that AKT, Nrf2, and HO-1 are involved in inflammation. In order to explore the influence of betulin on AKT, Nrf2, and HO-1 signaling pathways, the chondrocytes were treated with betulin at different time gradients. It was found that betulin promoted the phosphorylation of AKT and reached the highest at 60 min but decreased at 120 min. Furthermore, betulin activated Nrf2, and the expression of Nrf2 reached the highest in the nucleus of 60 min. There was a time delay in the activation of HO-1, which reached peak in 120 min (**Figures 5F,G**) ($p < 0.01$).

Betulin Promotes Nuclear Translocation of Nrf2 via AKT Signal Pathway

Previous studies have revealed that the activation of Nrf2 is regulated by upstream kinases. To confirm that betulin regulates Nrf2 nuclear translocation via the AKT pathway, chondrocytes were pretreated with AKT inhibitor (MK2206, 10 μM), and then treated with betulin (50 μM). The expression of phosphorylated AKT, nuclear Nrf2 (Nu-Nrf2), and cytoplasmic Nrf2 (Cy-Nrf2) was detected by Western blot. The results showed that although betulin promoted the nuclear translocation of Nrf2 ($p < 0.01$), MK2206 inhibited the nuclear expression of Nrf2 ($p < 0.05$), indicating that betulin's promotion of Nrf2 nuclear translocation is mediated by the AKT pathway (**Figures 6A–D**).

Betulin Upregulates the Expression of HO-1 via Activating Nrf2 Pathway

To illustrate the relationship between Nrf2 and HO-1, Chondrocytes were pretreated with Nrf2 inhibitor (RA, 5 μM), then treated with betulin (50 μM), and the protein levels of HO-1 and Nu-Nrf2 were detected by Western blot. The results showed that the protein levels of HO-1 and Nu-Nrf2 increased significantly after betulin treatment compared to the control group ($p < 0.01$) and Nrf2 transfer to the nucleus (**Figures 7A–D**) ($p < 0.01$). The inhibition of Nrf2 by RA abolished the upregulation of HO-1 protein induced by betulin and inhibited the nuclear translocation of Nrf2. These results indicate that betulin promotes HO-1 expression by activating the Nrf2 pathway. Furthermore, it was observed whether MK2206 and RA treatment affect the anti-inflammatory effect of betulin. The results showed that treatment with RA and MK2206 partially reversed the inhibitory effect of betulin on pro-inflammatory mediators (**Figures 7E–H**). These results indicate that betulin exerts anti-inflammatory effects through the AKT/Nrf2/HO-1 pathway.

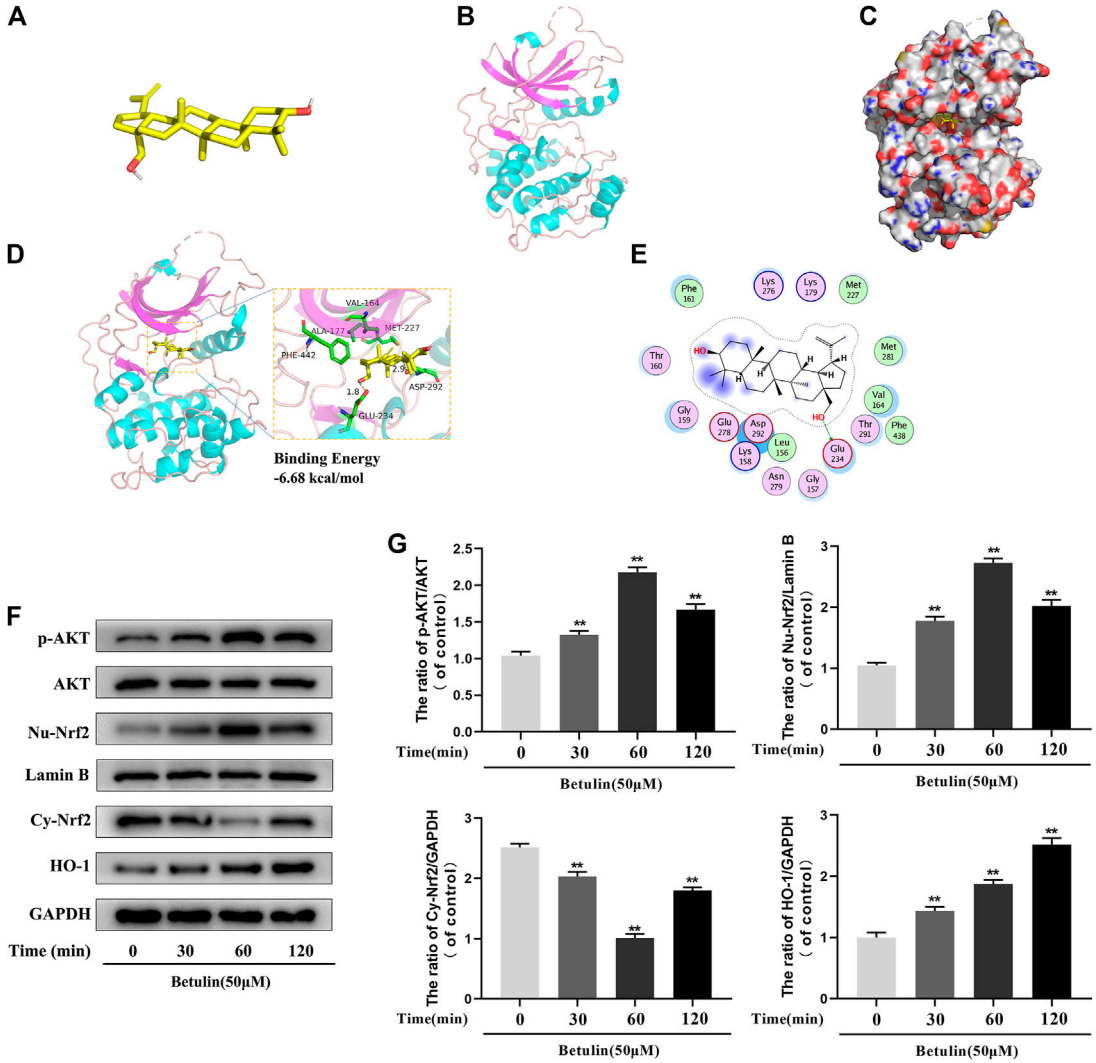


FIGURE 5 | The molecular docking model shows the affinity between Betulin and AKT. Betulin promotes the phosphorylation of AKT, enhances the nuclear expression of Nrf2, and upregulates the expression of HO-1. **(A)** The model of Betulin. **(B)** The ribbon model of AKT. **(C)** The space filling model of the binding of Betulin and AKT protein. **(D)** Three-dimensional (3D) binding model between Betulin and AKT protein. The backbone of the protein was rendered in tube and appears bright blue; Betulin is rendered yellow; the yellow dash represents the hydrogen bond distance, and the binding energy of the two is −6.68 kcal/mol. **(E)** Two-dimensional binding model between Betulin and AKT protein. The chondrocytes were treated with betulin (50 μM) for 0, 30, 60, and 120 min. **(F–G)** The protein levels of nuclear Nrf2 (Nu-Nrf2), p-AKT, HO-1, and cytoplasmic Nrf2 (Cy-Nrf2) were detected by Western blotting and quantitatively analyzed. The data in the figure are represented as the mean ± SD, $^{**}p < 0.01$ compared with the control group, n = 3.

Betulin Inhibits the Activation of NF-κB Pathway and the Generation of Pro-inflammatory Mediators Through HO-1 Pathway

Studies have shown that HO-1 can regulate the NF-κB pathway. The chondrocytes were pretreated with HO-1 inhibitor SnPP-IX (40 μM) and then treated with betulin (50 μM). The results of Western blot showed that SnPP-IX pretreatment abolished the inhibitory effect of betulin on p65 phosphorylation (**Figures 8A–D**) ($p < 0.01$). In addition, we also observed whether the HO-1 inhibitor SnPP-IX affected the anti-inflammatory effect of betulin. The results showed that SnPP-IX treatment reversed the inhibitory effect of betulin on pro-inflammatory mediators (**Figure 8E**) ($p < 0.01$). These results suggest that betulin plays an anti-inflammatory role by inhibiting the activation of the NF-κB pathway in chondrocytes through the HO-1 pathway.

Betulin Plays a Protective Role in the DMM OA Model

We used the mouse DMM model induced by surgery. X-ray analysis, SO staining, HE staining, and the OARSI score were used to evaluate the severity of OA at 8 weeks after surgery. X-ray analysis showed that the joint space became narrower, and there

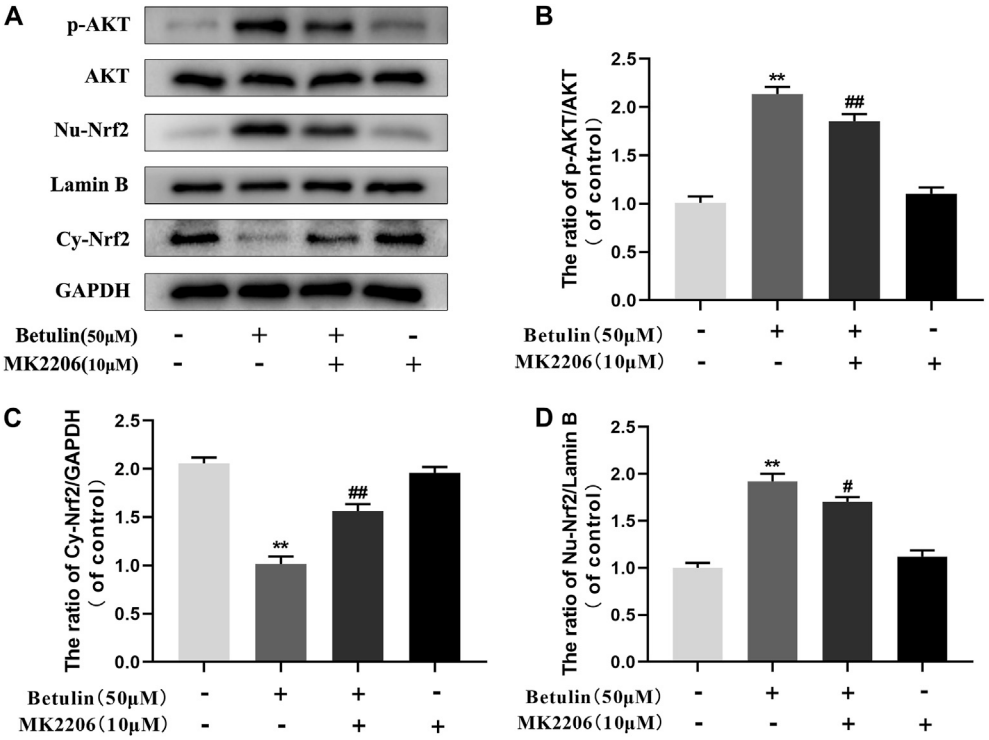


FIGURE 6 | Betulin promotes nuclear translocation of Nrf2 via the AKT signal pathway. The chondrocytes were pretreated with AKT inhibitor MK2206 (10 μM) for 2 h and then treated with betulin (50 μM) for 2 h. **(A–D)** The protein levels of Nu-Nrf2, Cy-Nrf2, and p-AKT were detected by Western blotting and quantitatively analyzed. The results showed that the AKT signal participated in the inflammatory process induced by IL-1β. The data in the figure show that the average value is ±SD, $^{**}p < 0.01$ compared with the control group, $^{\#\#}p < 0.01$ compared with the Betulin-treated group, n = 3.

existed hyperosteogeny in the DMM group, but this symptom was alleviated after the treatment of betulin (**Figure 9A**) ($p < 0.01$). SO staining and HE staining showed that there were more signs of destructive cartilage erosion on the articular cartilage surface in the DMM group than in the sham operation group ($p < 0.05$). The articular cartilage matrix was lost and a large amount of proteoglycan was degraded in the operation group. After betulin treatment, the cartilage matrix and cartilage thickness were alleviated, indicating that betulin thickened the articular cartilage and repaired the destruction of the articular cartilage (**Figure 9C**). The OARSI score was consistent with the above SO staining results (**Figure 9B**). Compared with the DMM group, the OARSI score decreased after betulin treatment ($p < 0.01$). The immunohistochemical staining of Nrf2 and p-AKT was used to further verify the effect of betulin on OA. As shown in the figure, the positive expression points of Nrf2 and p-AKT in the chondrocytes increased after betulin treatment (**Figures 9D,F**) ($p < 0.01$). In addition, we also performed immunohistochemical staining of inflammatory factors IL-6 and TNF-α. The results showed that the positive expression points of IL-6 and TNF-α in the chondrocytes decreased after betulin treatment, indicating that betulin inhibited the progression of inflammation in OA (**Figure 9G**) ($p < 0.01$). To sum up, Betulin inhibits the progression of OA in mice by activating the AKT/Nrf2/HO-1 signal axis *in vivo*.

DISCUSSION

The current research results show that betulin plays an anti-inflammatory role in the chondrocytes by activating the AKT/NRF-2/HO-1 pathway and inhibits the generation of pro-inflammatory cytokines (IL-6 and TNF-α) and enzymes (iNOS and COX-2) by inhibiting the NF-κB pathway, indicating that betulin is a potential candidate drug for the treatment of OA.

OA is one of world's most common degenerative diseases, especially among the elderly (Thysen et al., 2015). Existing evidence shows that inflammatory mechanism plays an important role in regulating biomechanical disorders of the joint tissue, resulting in OA occurrence and development (Wojdasiewicz et al., 2014). The subchondral bone as the source of inflammatory mediators participates in the pain process of OA. However, there is no effective drug treatment for OA (da Costa et al., 2017). Despite the wide application of nonsteroidal anti-inflammatory drugs in clinics (Sun et al., 2017), these can only temporarily relieve clinical symptoms, while their overuse will lead to serious adverse reactions. Therefore, a safe and effective drug with few side effects is needed. In recent years, plant-derived compounds have been provided to have good anti-inflammatory effects with less side reactions. They have attracted researchers' interest as drugs for the treatment of OA, among which betulin is one. It has biological activity including anti-

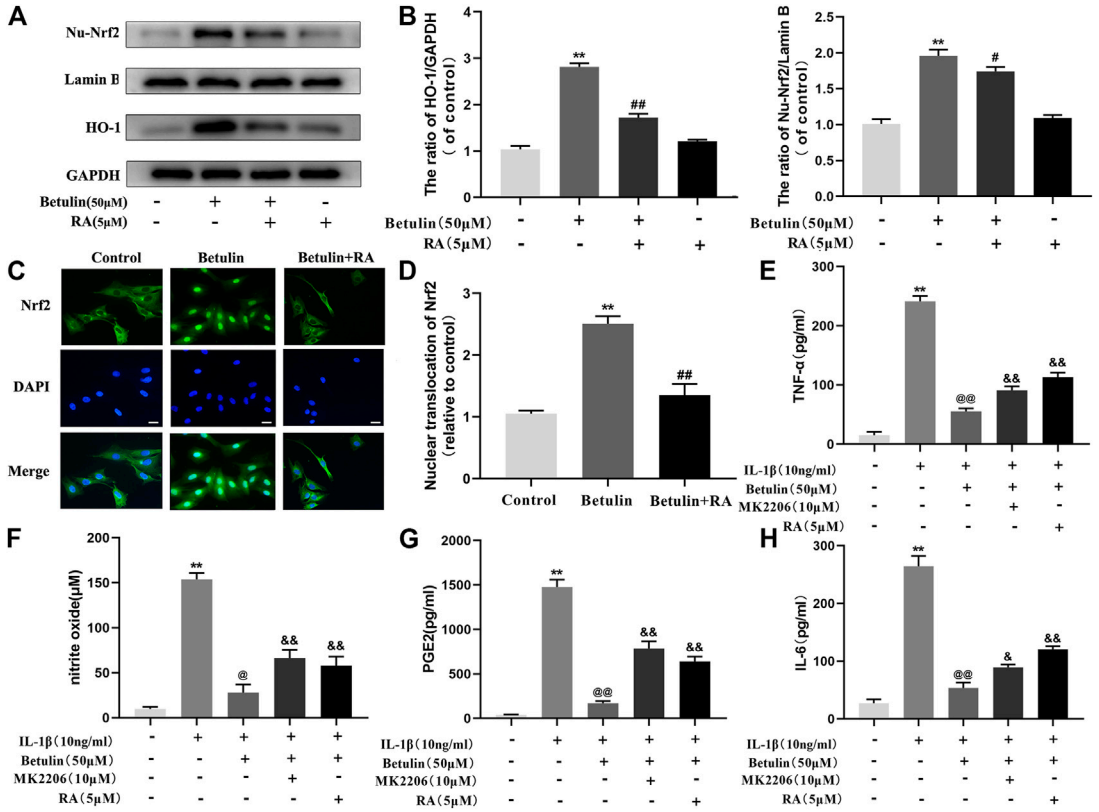


FIGURE 7 | Betulin upregulates the expression of HO-1 via activating the Nrf2 pathway. The chondrocytes were treated with retinoic acid (RA, 5 μM), an inhibitor of Nrf2, for 2 h and then treated with betulin (50 μM) for 2 h. **(A–B)** The expression levels of Nu-Nrf2 and HO-1 in chondrocytes were detected by Western blotting and quantitatively analyzed. **(C–D)** Immunofluorescence staining combined with DAPI staining (scale: 25 μm) were used to detect the entry of Nrf2 into the nucleus and quantitatively analyzed. **(E–H)** The protein levels of TNF-α, IL-6, and PGE2 were measured by the commercial ELISA kits, and the generation of NO was measured by Griess reaction. The data in the figure show that the average value is ±SD, $^{**}p < 0.01$ compared with the control group, $^{\#\#}p < 0.01$ compared with the Betulin-treated group, $^{\&\&}p < 0.01$ compared with the Betulin + IL-1β–treated group, $^{@}p < 0.05$ compared with the IL-1β group, n = 3.

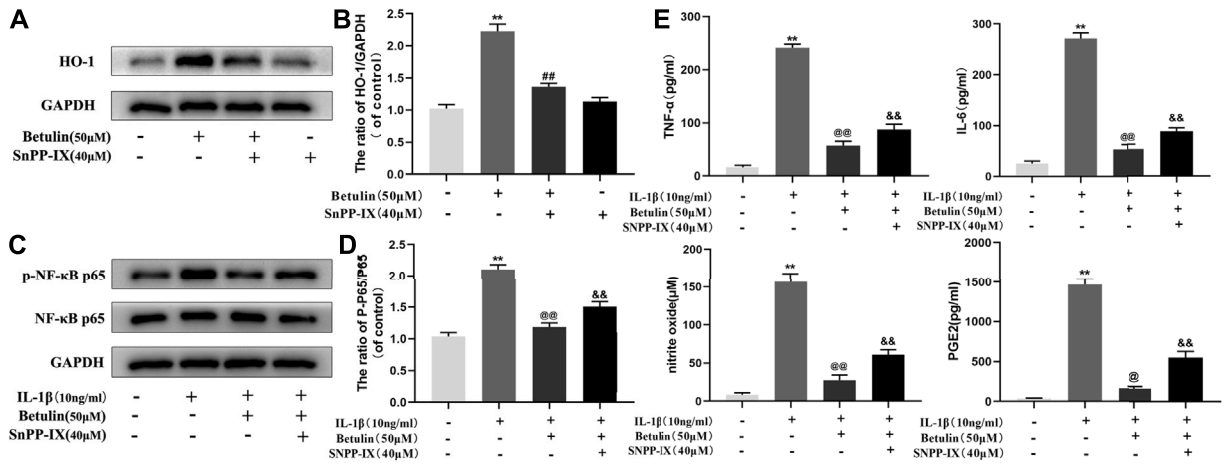


FIGURE 8 | Betulin inhibits the activation of the NF-κB pathway and the generation of pro-inflammatory mediators through the HO-1 pathway. The chondrocytes were pretreated with HO-1 inhibitor SnPP-IX (40 μM) for 2 h and treated with betulin (50 μM) for 2 h. **(A–D)** The protein levels of p-p65 and HO-1 were detected by Western blotting and quantitatively analyzed. **(E)** The protein levels of TNF-α, IL-6, and PGE2 were measured by the commercial ELISA kits and the generation of NO was measured by Griess reaction. The data in the figure show that the average value is ±SD, $^{**}p < 0.01$ compared with the control group, $^{\#\#}p < 0.01$ compared with the Betulin-treated group, $^{\&\&}p < 0.01$ compared with the Betulin + IL-1β–treated group, $^{@}p < 0.05$, $^{@@}p < 0.01$ compared with the IL-1β group, n = 3.

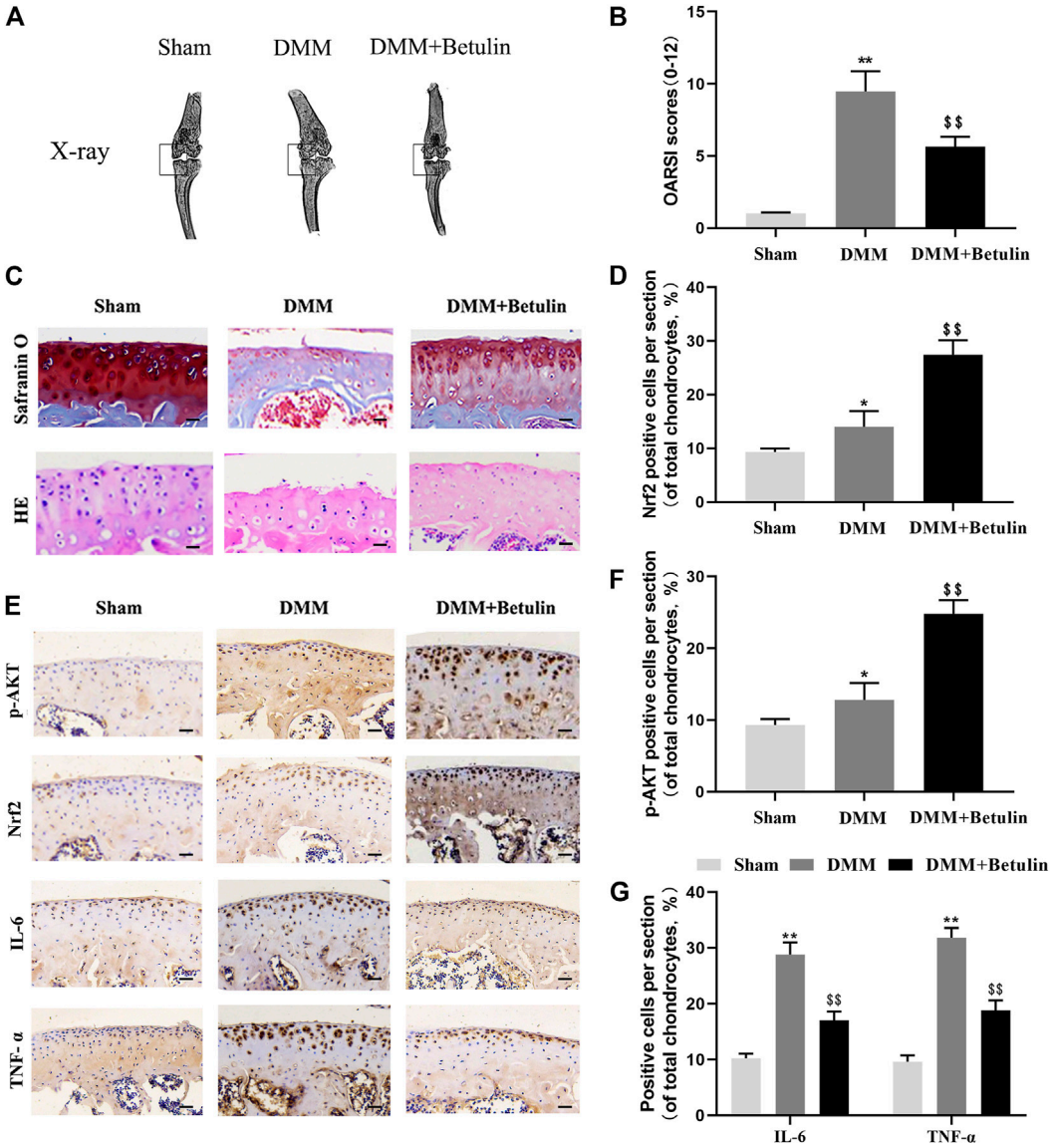


FIGURE 9 | Betulin inhibits the progression of DMM-induced OA in mice. The mice were randomly divided into three groups: the Sham group, DMM group, and DMM + Betulin group. The sham operation was performed in the Sham group, and the OA model was established in the DMM and DMM + Betulin groups. Eight weeks after operation, **(A)** X-ray imaging of the knee joints of the mice in the different experimental groups were performed, and betulin processing alleviated the stenosis of the joint space. **(B–C)** The knee joints of the mice in the different experimental groups were stained with SO staining and HE staining (scale: 50 μm), and the histological changes of OA were evaluated by the score of the OARSI. **(E)** Immunohistochemical staining of p-AKT, Nrf2, IL-6, and TNF-α expression in the cartilage specimens (scale: 50 μm). **(D–G)** The percentage of p-AKT, Nrf2, IL-6, and TNF-α positive cells in each section was quantitatively analyzed by Image-Pro Plus software. The data in the figure show that the average value is ±SD, $^{**}p < 0.01$ compared with the control group, $^{\$\$}p < 0.01$ compared with the DMM group, n = 6.

inflammation (Ci et al., 2017; Ra et al., 2017). Therefore, this experiment mainly verifies whether betulin has a protective effect on OA. Through this experiment, we have discovered that betulin can inhibit the release of pro-inflammatory factors and inhibit the degradation of extracellular matrix of chondrocytes. In addition, we have also explored the mechanism of betulin in OA. Betulin inhibits the development of inflammation mainly by activating the AKT/Nrf2/HO-1 pathway and inhibiting the NF-κB pathway. To sum up, betulin can improve the injury of the articular cartilage and inhibit the progression of OA.

NF-κB is a nuclear transcription activator under research in recent years, with significant effect on the generation of inflammatory cytokines (Chun et al., 2014; Srinivasan and Lahiri, 2015). As it regulates the expression of inflammatory mediators, it is a target for the treatment of inflammatory diseases. Under physiological conditions, the NF-κB dimer binds to IκBα (inhibitor protein) in a state of inactivation. When stimulated, IκBα is degraded by phosphorylation, and p65 phosphorylation is transferred to the nucleus, inducing the overexpression of various inflammatory factors and

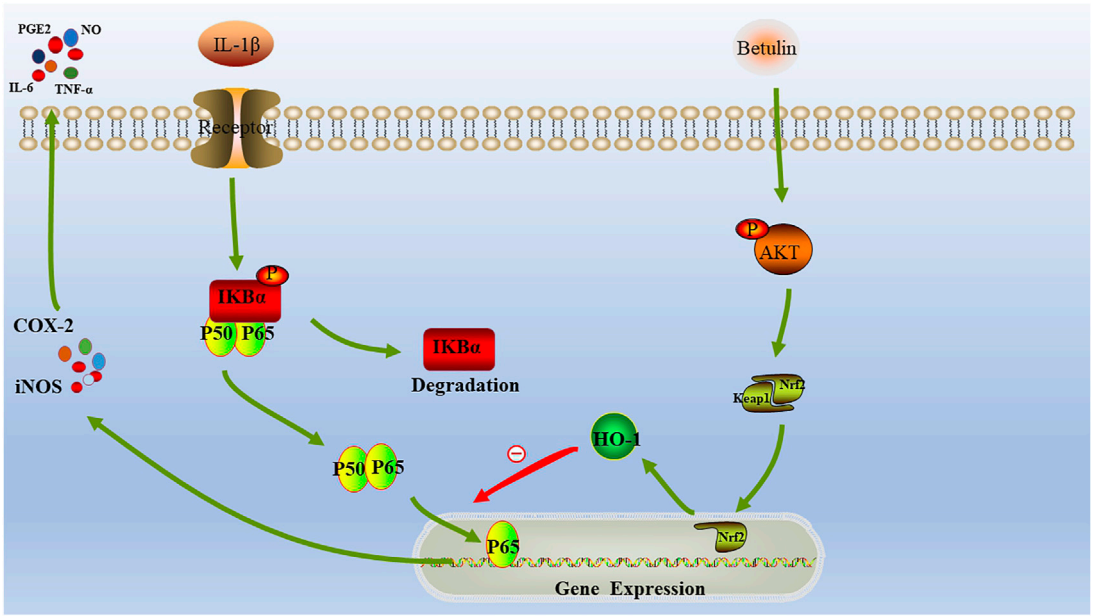


FIGURE 10 | Schematic diagram: The molecular mechanism of betulin involved in the progress of OA.

aggravating the development of inflammation. It is reported that inhibiting the expression of p65 can block the expression of inflammatory mediators in chondrocytes stimulated by IL-1β (Hou et al., 2017). Therefore, in this experiment, we discussed the relationship between betulin and NF-κB signaling, betulin could inhibit the phosphorylation of NF-κB p65 and its translocation to the nucleus, thereby downregulating the expression and secretion of pro-inflammatory cytokines to play an anti-inflammatory effect.

AKT is a serine/threonine kinase and a downstream signal molecule of PI3K, activated by it (Zhang et al., 2015; Li et al., 2017; Ouyang et al., 2017). It regulates the release of inflammatory cytokines and plays an important role in various disease models as verified by studies (Yan et al., 2018). Thus, we speculate whether betulin also inhibits the progression of OA by activating AKT phosphorylation. As we expected, the phosphorylated expression of AKT was enhanced and the expression of Nrf2 in the nucleus was activated under the effect of betulin, indicating that AKT participated in the anti-inflammatory process of betulin. In addition, a large number of studies have shown that Nrf2 is a redox transcription factor and a major participant in antioxidant response (Motohashi and Yamamoto, 2004). PI3K can also promote neuronal survival by activating Akt phosphorylation and Nrf2 nuclear translocation as reported (de Oliveira et al., 2016). This experiment also proved that betulin-induced Nrf2 nuclear translocation was inhibited after being pretreated with MK2206 (AKT inhibitor), suggesting that the activation of the AKT pathway can increase Nrf2 nuclear translocation and enhance Nrf2 expression of antioxidant and anti-inflammatory genes in the nucleus, thus playing an anti-inflammatory role. To sum up, betulin exerts its anti-inflammatory effect by activating the AKT pathway to promote nuclear transfer of Nrf2.

HO-1 is the most important antioxidant enzyme *in vivo* with anti-inflammatory effects (Poss and Tonegawa, 1997; Yachie et al., 1999). Some studies have revealed that HO-1 is regulated by the Nrf2 signal pathway (Chen et al., 2003; Pittalà et al., 2013). Under physiological conditions, Nrf2 maintains its stability through the combining with Keap1 (Jaiswal, 2004). When stimulated, after dissociation from Keap1, Nrf2 enters the nucleus and binds to antioxidant response elements, resulting in the upregulation of downstream genes, such as HO-1 (Nguyen et al., 2009). In this study, we found that betulin activated the AKT/Nrf2/HO-1 signaling pathway. In addition, we also found that the pretreatment with HO-1 inhibitors (SnPP-IX) could inhibit the activation of NF-κB signal induced by IL-1β and could reverse betulin's anti-inflammatory effect, indicating that betulin plays an anti-inflammatory effect by activating the AKT/Nrf2/HO-1/NF-κB signal pathway. In addition, this conclusion was further confirmed by *in vivo* experiments. In short, Betulin may serve as therapeutic target for OA (**Figure 10**).

In summary, these results suggest that betulin significantly inhibits the inflammatory reaction of OA induced by IL-1β by activating the AKT/Nrf2/HO-1/NF-κB signal axis, further indicating that betulin, with significant anti-inflammatory effects, can serve as a safe and effective natural medicine for the treatment of OA.

DATA AVAILABILITY STATEMENT

The original contributions presented in the study are included in the article/**Supplementary Files**; further inquiries can be directed to the corresponding authors.

ETHICS STATEMENT

The animal study was reviewed and approved by the Animal Protection and Utilization Committee of Wenzhou Medical University.

AUTHOR CONTRIBUTIONS

XZ, CR, and JJ carried out the experiments, analyzed the results, and wrote the manuscript. QC, JY, and NT provided assistance for data acquisition and data analyses. YW, YZ, LS, and WG carried out the literature search and manuscript editing. XZ, CR, WH reviewed and revised the manuscript. All authors have read and approved the content of the manuscript.

FUNDING

National Natural Science Foundation of China (81972094); Lin He's New Medicine and Clinical Translation Academician Workstation Research Fund (18331213) and Zhejiang Provincial Natural Science Foundation of China (LY18H060012).

SUPPLEMENTARY MATERIAL

The Supplementary Material for this article can be found online at: https://www.frontiersin.org/articles/10.3389/fphar.2021.754038/full#supplementary-material

REFERENCES

Abramson, S. B., Attur, M., Amin, A. R., and Clancy, R. (2001). Nitric Oxide and Inflammatory Mediators in the Perpetuation of Osteoarthritis. *Curr. Rheumatol. Rep.* 3 (6), 535–541. doi:10.1007/s11926-001-0069-3

Au, R. Y., Al-Talib, T. K., Au, A. Y., Phan, P. V., and Frondoza, C. G. (2007). Avocado Soybean Unsaponifiables (ASU) Suppress TNF-Alpha, IL-1beta, COX-2, iNOS Gene Expression, and Prostaglandin E2 and Nitric Oxide Production in Articular Chondrocytes and Monocyte/macrophages. *Osteoarthritis Cartilage.* 15 (11), 1249–1255. doi:10.1016/j.joca.2007.07.009

Bai, T., Yang, Y., Yao, Y. L., Sun, P., Lian, L. H., Wu, Y. L., et al. (2016). Betulin Alleviated Ethanol-Induced Alcoholic Liver Injury via SIRT1/AMPK Signaling Pathway. *Pharmacol. Res.* 105, 1–12. doi:10.1016/j.phrs.2015.12.022

Bonnet, C. S., and Walsh, D. A. (2005). Osteoarthritis, Angiogenesis and Inflammation. *Rheumatology (Oxford)* 44 (1), 7–16. doi:10.1093/rheumatology/keh344

Chabane, N., Zayed, N., Afif, H., Mfuna-Endam, L., Benderdour, M., Boileau, C., et al. (2008). Histone Deacetylase Inhibitors Suppress Interleukin-1beta-Induced Nitric Oxide and Prostaglandin E2 Production in Human Chondrocytes. *Osteoarthritis Cartilage.* 16 (10), 1267–1274. doi:10.1016/j.joca.2008.03.009

Chan, C. K., Tan, L. T., Andy, S. N., Kamarudin, M. N. A., Goh, B. H., and Kadir, H. A. (2017). Anti-neuroinflammatory Activity of Elephantopus Scaber L. Via Activation of Nrf2/HO-1 Signaling and Inhibition of P38 MAPK Pathway in LPS-Induced Microglia BV-2 Cells. *Front. Pharmacol.* 8, 397. doi:10.3389/fphar.2017.00397

Chen, Y. H., Yet, S. F., and Perrella, M. A. (2003). Role of Heme Oxygenase-1 in the Regulation of Blood Pressure and Cardiac Function. *Exp. Biol. Med. (Maywood)* 228 (5), 447–453. doi:10.1177/15353702-0322805-03

Chun, J. M., Nho, K. J., Kim, H. S., Lee, A. Y., Moon, B. C., and Kim, H. K. (2014). An Ethyl Acetate Fraction Derived from Houttuynia Cordata Extract Inhibits the Production of Inflammatory Markers by Suppressing NF-Kb and MAPK Activation in Lipopolysaccharide-Stimulated RAW 264.7 Macrophages. *BMC Complement. Altern. Med.* 14, 234. doi:10.1186/1472-6882-14-234

Ci, X., Zhou, J., Lv, H., Yu, Q., Peng, L., and Hua, S. (2017). Betulin Exhibits Anti-inflammatory Activity in LPS-Stimulated Macrophages and Endotoxin-Shocked Mice through an AMPK/AKT/Nrf2-dependent Mechanism. *Cell Death Dis.* 8 (5), e2798. doi:10.1038/cddis.2017.39

da Costa, B. R., Reichenbach, S., Keller, N., Nartey, L., Wandel, S., Jüni, P., et al. (2017). Effectiveness of Non-steroidal Anti-inflammatory Drugs for the Treatment of Pain in Knee and Hip Osteoarthritis: a Network Meta-Analysis. *Lancet* 390 (10090), e21–e33. doi:10.1016/s0140-6736(17)31744-0

de Oliveira, M. R., Peres, A., Ferreira, G. C., Schuck, P. F., and Bosco, S. M. (2016). Carnosic Acid Affords Mitochondrial Protection in Chlorpyrifos-Treated Sh-Sy5y Cells. *Neurotox Res.* 30 (3), 367–379. doi:10.1007/s12640-016-9620-x

Dodge, G. R., and Poole, A. R. (1989). Immunohistochemical Detection and Immunochemical Analysis of Type II Collagen Degradation in Human normal, Rheumatoid, and Osteoarthritic Articular Cartilages and in Explants of Bovine Articular Cartilage Cultured with Interleukin 1. *J. Clin. Invest.* 83 (2), 647–661. doi:10.1172/jci113929

Fazi, R., Tintori, C., Brai, A., Botta, L., Selvaraj, M., Garbelli, A., et al. (2015). Homology Model-Based Virtual Screening for the Identification of Human Helicase DDX3 Inhibitors. *J. Chem. Inf. Model.* 55 (11), 2443–2454. doi:10.1021/acs.jcim.5b00419

Fernandes, J. C., Martel-Pelletier, J., and Pelletier, J. P. (2002). The Role of Cytokines in Osteoarthritis Pathophysiology. *Biorheology* 39 (1-2), 237–246.

Hayden, M. S., and Ghosh, S. (2011). NF-κB in Immunobiology. *Cell Res.* 21 (2), 223–244. doi:10.1038/cr.2011.13

Hou, S. M., Hou, C. H., and Liu, J. F. (2017). CX3CL1 Promotes MMP-3 Production via the CX3CR1, C-Raf, MEK, ERK, and NF-Kb Signaling Pathway in Osteoarthritis Synovial Fibroblasts. *Arthritis Res. Ther.* 19 (1), 282. doi:10.1186/s13075-017-1487-6

Huang, C. S., Lin, A. H., Yang, T. C., Liu, K. L., Chen, H. W., and Lii, C. K. (2015). Shikonin Inhibits Oxidized LDL-Induced Monocyte Adhesion by Suppressing NFκB Activation via Up-Regulation of PI3K/Akt/Nrf2-dependent Antioxidation in EA.Hy926 Endothelial Cells. *Biochem. Pharmacol.* 93 (3), 352–361. doi:10.1016/j.bcp.2014.12.005

Jaiswal, A. K. (2004). Nrf2 Signaling in Coordinated Activation of Antioxidant Gene Expression. *Free Radic. Biol. Med.* 36 (10), 1199–1207. doi:10.1016/j.freeradbiomed.2004.02.074

Jiang, T., Tian, F., Zheng, H., Whitman, S. A., Lin, Y., Zhang, Z., et al. (2014). Nrf2 Suppresses Lupus Nephritis through Inhibition of Oxidative Injury and the NF-Kb-Mediated Inflammatory Response. *Kidney Int.* 85 (2), 333–343. doi:10.1038/ki.2013.343

Kean, W. F., Kean, R., and Buchanan, W. W. (2004). Osteoarthritis: Symptoms, Signs and Source of Pain. *Inflammopharmacology* 12 (1), 3–31. doi:10.1163/156856004773121347

Krustev, E., Rioux, D., and McDougall, J. J. (2015). Mechanisms and Mediators that Drive Arthritis Pain. *Curr. Osteoporos. Rep.* 13 (4), 216–224. doi:10.1007/s11914-015-0275-y

Kumar, A., Takada, Y., Boriek, A. M., and Aggarwal, B. B. (2004). Nuclear Factor-kappaB: its Role in Health and Disease. *J. Mol. Med. (Berl)* 82 (7), 434–448. doi:10.1007/s00109-004-0555-y

Li, T., Mo, H., Chen, W., Li, L., Xiao, Y., Zhang, J., et al. (2017). Role of the PI3K-Akt Signaling Pathway in the Pathogenesis of Polycystic Ovary Syndrome. *Reprod. Sci.* 24 (5), 646–655. doi:10.1177/1933719116667606

Lu, C. Y., Yang, Y. C., Li, C. C., Liu, K. L., Lii, C. K., and Chen, H. W. (2014). Andrographolide Inhibits TNFα-Induced ICAM-1 Expression via Suppression of NADPH Oxidase Activation and Induction of HO-1 and GCLM Expression through the PI3K/Akt/Nrf2 and PI3K/Akt/AP-1 Pathways in Human Endothelial Cells. *Biochem. Pharmacol.* 91 (1), 40–50. doi:10.1016/j.bcp.2014.06.024

Ma, C., and Long, H. (2016). Protective Effect of Betulin on Cognitive Decline in Streptozotocin (STZ)-induced Diabetic Rats. *Neurotoxicology* 57, 104–111. doi:10.1016/j.neuro.2016.09.009

Motohashi, H., and Yamamoto, M. (2004). Nrf2-Keap1 Defines a Physiologically Important Stress Response Mechanism. *Trends Mol. Med.* 10 (11), 549–557. doi:10.1016/j.molmed.2004.09.003

Nguyen, T., Nioi, P., and Pickett, C. B. (2009). The Nrf2-Antioxidant Response Element Signaling Pathway and its Activation by Oxidative Stress. *J. Biol. Chem.* 284 (20), 13291–13295. doi:10.1074/jbc.R900010200

Nummenmaa, E., Hämäläinen, M., Moilanen, T., Vuolteenaho, K., and Moilanen, E. (2015). Effects of FGF-2 and FGF Receptor Antagonists on MMP Enzymes, Aggrecan, and Type II Collagen in Primary Human OA Chondrocytes. *Scand. J. Rheumatol.* 44 (4), 321–330. doi:10.3109/03009742.2014.1000372

Ouyang, Z. H., Wang, W. J., Yan, Y. G., Wang, B., and Lv, G. H. (2017). The PI3K/Akt Pathway: a Critical Player in Intervertebral Disc Degeneration. *Oncotarget* 8 (34), 57870–57881. doi:10.18632/oncotarget.18628

Parada, E., Buendia, I., Navarro, E., Avendaño, C., Egea, J., and López, M. G. (2015). Microglial HO-1 Induction by Curcumin Provides Antioxidant, Antineuroinflammatory, and Glioprotective Effects. *Mol. Nutr. Food Res.* 59 (9), 1690–1700. doi:10.1002/mnfr.201500279

Pfaffl, M. W. (2001). A New Mathematical Model for Relative Quantification in Real-Time RT-PCR. *Nucleic Acids Res.* 29 (9), e45. doi:10.1093/nar/29.9.e45

Pittalà, V., Salerno, L., Romeo, G., Modica, M. N., and Siracusa, M. A. (2013). A Focus on Heme Oxygenase-1 (HO-1) Inhibitors. *Curr. Med. Chem.* 20 (30), 3711–3732. doi:10.2174/09298673113203000003

Poss, K. D., and Tonegawa, S. (1997). Reduced Stress Defense in Heme Oxygenase 1-deficient Cells. *Proc. Natl. Acad. Sci. U S A.* 94 (20), 10925–10930. doi:10.1073/pnas.94.20.10925

Ra, H. J., Lee, H. J., Jo, H. S., Nam, D. C., Lee, Y. B., Kang, B. H., et al. (2017). Betulin Suppressed Interleukin-1β-Induced Gene Expression, Secretion and Proteolytic Activity of Matrix Metalloproteinase in Cultured Articular Chondrocytes and Production of Matrix Metalloproteinase in the Knee Joint of Rat. *Korean J. Physiol. Pharmacol.* 21 (1), 19–26. doi:10.4196/kjpp.2017.21.1.19

Rajeswari, M., Santhi, N., and Bhuvaneswari, V. (2014). Pharmacophore and Virtual Screening of JAK3 Inhibitors. *Bioinformation* 10 (3), 157–163. doi:10.6026/97320630010157

Scanzello, C. R. (2017). Chemokines and Inflammation in Osteoarthritis: Insights from Patients and Animal Models. *J. Orthop. Res.* 35 (4), 735–739. doi:10.1002/jor.23471

Srinivasan, M., and Lahiri, D. K. (2015). Significance of NF-Kb as a Pivotal Therapeutic Target in the Neurodegenerative Pathologies of Alzheimer's Disease and Multiple Sclerosis. *Expert Opin. Ther. Targets.* 19 (4), 471–487. doi:10.1517/14728222.2014.989834

Sun, M. M., Beier, F., and Pest, M. A. (2017). Recent Developments in Emerging Therapeutic Targets of Osteoarthritis. *Curr. Opin. Rheumatol.* 29 (1), 96–102. doi:10.1097/bor.0000000000000351

Thysen, S., Luyten, F. P., and Lories, R. J. (2015). Targets, Models and Challenges in Osteoarthritis Research. *Dis. Model. Mech.* 8 (1), 17–30. doi:10.1242/dmm.016881

Vincenti, M. P., and Brinckerhoff, C. E. (2002). Transcriptional Regulation of Collagenase (MMP-1, MMP-13) Genes in Arthritis: Integration of Complex Signaling Pathways for the Recruitment of Gene-specific Transcription Factors. *Arthritis Res.* 4 (3), 157–164. doi:10.1186/ar401

Wang, C., Zeng, L., Zhang, T., Liu, J., and Wang, W. (2016). Tenuigenin Prevents IL-1β-induced Inflammation in Human Osteoarthritis Chondrocytes by Suppressing PI3K/AKT/NF-κB Signaling Pathway. *Inflammation* 39 (2), 807–812. doi:10.1007/s10753-016-0309-3

Wojdasiewicz, P., Poniatowski, Ł. A., and Szukiewicz, D. (2014). The Role of Inflammatory and Anti-inflammatory Cytokines in the Pathogenesis of Osteoarthritis. *Mediators Inflamm.* 2014, 561459. doi:10.1155/2014/561459

Wu, D., Jin, S., Lin, Z., Chen, R., Pan, T., Kang, X., et al. (2018). Sauchinone Inhibits IL-1β Induced Catabolism and Hypertrophy in Mouse Chondrocytes to Attenuate Osteoarthritis via Nrf2/HO-1 and NF-Kb Pathways. *Int. Immunopharmacol.* 62, 181–190. doi:10.1016/j.intimp.2018.06.041

Yachie, A., Niida, Y., Wada, T., Igarashi, N., Kaneda, H., Toma, T., et al. (1999). Oxidative Stress Causes Enhanced Endothelial Cell Injury in Human Heme Oxygenase-1 Deficiency. *J. Clin. Invest.* 103 (1), 129–135. doi:10.1172/jci4165

Yan, J., Li, J., Zhang, L., Sun, Y., Jiang, J., Huang, Y., et al. (2018). Nrf2 Protects against Acute Lung Injury and Inflammation by Modulating TLR4 and Akt Signaling. *Free Radic. Biol. Med.* 121, 78–85. doi:10.1016/j.freeradbiomed.2018.04.557

Yeh, Y. H., Kuo, C. T., Chang, G. J., Chen, Y. H., Lai, Y. J., Cheng, M. L., et al. (2015). Rosuvastatin Suppresses Atrial Tachycardia-Induced Cellular Remodeling via Akt/Nrf2/heme Oxygenase-1 Pathway. *J. Mol. Cell Cardiol.* 82, 84–92. doi:10.1016/j.yjmcc.2015.03.004

Zhang, J., Yu, X. H., Yan, Y. G., Wang, C., and Wang, W. J. (2015). PI3K/Akt Signaling in Osteosarcoma. *Clin. Chim. Acta.* 444, 182–192. doi:10.1016/j.cca.2014.12.041

Zhang, L., Ma, S., Su, H., and Cheng, J. (2018). Isoliquiritigenin Inhibits IL-1β-Induced Production of Matrix Metalloproteinase in Articular Chondrocytes. *Mol. Ther. Methods Clin. Dev.* 9, 153–159. doi:10.1016/j.omtm.2018.02.006

Zhao, H., Zheng, Q., Hu, X., Shen, H., and Li, F. (2016). Betulin Attenuates Kidney Injury in Septic Rats through Inhibiting TLR4/NF-Kb Signaling Pathway. *Life Sci.* 144, 185–193. doi:10.1016/j.lfs.2015.12.003

Zheng, G., Zhan, Y., Tang, Q., Chen, T., Zheng, F., Wang, H., et al. (2018). Monascin Inhibits IL-1β Induced Catabolism in Mouse Chondrocytes and Ameliorates Murine Osteoarthritis. *Food Funct.* 9 (3), 1454–1464. doi:10.1039/c7fo01892d

Conflict of Interest: The authors declare that the research was conducted in the absence of any commercial or financial relationships that could be construed as a potential conflict of interest.

Publisher's Note: All claims expressed in this article are solely those of the authors and do not necessarily represent those of their affiliated organizations, or those of the publisher, the editors, and the reviewers. Any product that may be evaluated in this article, or claim that may be made by its manufacturer, is not guaranteed or endorsed by the publisher.

Copyright © 2021 Ren, Jin, Hu, Chen, Yang, Wu, Zhou, Sun, Gao, Zhang and Tian. This is an open-access article distributed under the terms of the Creative Commons Attribution License (CC BY). The use, distribution or reproduction in other forums is permitted, provided the original author(s) and the copyright owner(s) are credited and that the original publication in this journal is cited, in accordance with accepted academic practice. No use, distribution or reproduction is permitted which does not comply with these terms.

frontiers in Pharmacology

ORIGINAL RESEARCH
published: 21 October 2021
doi: 10.3389/fphar.2021.735079

Saikosaponin D Attenuates Pancreatic Injury Through Suppressing the Apoptosis of Acinar Cell via Modulation of the MAPK Signaling Pathway

*Caixia Li[1†], Lihua Cui[1†], Lanqiu Zhang[1], Lei Yang[1], Yuzhen Zhuo[1], Jialin Cui[2], Naiqiang Cui[1] and Shukun Zhang[1]**

[1]Tianjin Key Laboratory of Acute Abdomen Disease Associated Organ Injury and ITCWM Repair, Institute of Acute Abdominal Diseases of Integrated Traditional Chinese and Western Medicine, Tianjin Nankai Hospital, Nankai Clinical College, Tianjin Medical University, Tianjin, China, [2]The Clinical Medicine, Tianjin Medical University, Tianjin, China

OPEN ACCESS

Edited by:
Dahui Liu,
Hubei University of Chinese Medicine, China

Reviewed by:
Chenghai Liu,
Shanghai University of Traditional Chinese Medicine, China
Jean Lu,
Academia Sinica, Taiwan

***Correspondence:**
Shukun Zhang
shu1971@163.com

[†]These authors have contributed equally to this work

Specialty section:
This article was submitted to Ethnopharmacology, a section of the journal Frontiers in Pharmacology

Received: 12 July 2021
Accepted: 15 September 2021
Published: 21 October 2021

Citation:
Li C, Cui L, Zhang L, Yang L, Zhuo Y, Cui J, Cui N and Zhang S (2021) Saikosaponin D Attenuates Pancreatic Injury Through Suppressing the Apoptosis of Acinar Cell via Modulation of the MAPK Signaling Pathway. Front. Pharmacol. 12:735079. doi: 10.3389/fphar.2021.735079

Chronic pancreatitis (CP) is a progressive fibro-inflammatory syndrome. The damage of acinar cells is the main cause of inflammation and the activation of pancreatic stellate cells (PSCs), which can thereby possibly further aggravate the apoptosis of more acinar cells. Saikosaponind (SSd), a major active ingredient derived from Chinese medicinal herb bupleurum falcatum, which exerted multiple pharmacological effects. However, it is not clear whether SSd protects pancreatic injury of CP via regulating the apoptosis of pancreatic acinar cells. This study systematically investigated the effect of SSd on pancreatic injury of CP *in vivo* and *in vitro*. The results revealed that SSd attenuate pancreatic damage, decrease the apoptosis and suppress the phosphorylation level of MAPK family proteins (JNK1/2, ERK1/2, and p38 MAPK) significantly in the pancreas of CP rats. In addition, SSd markedly reduced the apoptosis and inflammation of pancreatic acinar AR42J cells induced by cerulein, a drug induced CP, or Conditioned Medium from PSCs (PSCs-CM) or the combination of PSCs-CM and cerulein. Moreover, SSd significantly inhibited the activated phosphorylation of JNK1/2, ERK1/2, and p38 MAPK induced by cerulein or the combination of PSCs-CM and cerulein in AR42J cells. Furthermore, SSd treatment markedly decreased the protein levels of p-JNK and p-p38 MAPK caused by PSCs-CM alone. In conclusion, SSd ameliorated pancreatic injury, suppressed AR42J inflammation and apoptosis induced by cerulein, interrupted the effect of PSCs-CM on AR42J cells inflammation and apoptosis, possibly through MAPK pathway.

Keywords: chronic pancreatitis, saikosaponin d, AR42J acini cell, apoptosis, MAPK pathway

INTRODUCTION

Pancreatitis is an inflammatory disease of the pancreas and divided into acute and chronic pancreatitis. Chronic pancreatitis (CP) is characterized by irreversible inflammatory disorders that leading to fibrotic destruction of pancreatic parenchyma, endocrine, and exocrine dysfunction (Sheth et al., 2017). CP develops due to repeated episodes of acute pancreatitis (AP)

resulting in the activation of pancreatic stellate cells (PSCs); thus fibrosis (Beyer et al., 2020). There is no specific treatment for CP. Elucidation to the new targets of the injured pancreas and the interplay with the cells will help identify potential therapies.

Previous studies on CP focuses on pancreatic stellate cells (PSCs), which majorly involved in the process of fibrosis. Acinar cell injury is the central to AP. However, the role of acinar cells in CP was less studied. It was well accepted that the process of cellular apoptosis of acinar cells was observed during the course of CP and the acinar cell apoptosis index was higher in CP than controls (Su et al., 2001; Bateman et al., 2002). In the early stage of CP, acinar cells were firstly damaged and initiated a cascade of pancreatic autodigestion and inflammation. The acinar cell injury involves acinar cell release of inflammatory mediators, activation of PSCs and recruitment of various immune cells (Patel Fine., 2005). The activated PSCs ultimately produce excessive extracellular matrix (ECM), manifested as pancreatic fibrosis (Chen et al., 2012; Erkan et al., 2012). In turn, the activated PSCs secret kinds of cytokines and chemokines that further facilitate the apoptosis of acinar cells (Xia et al., 2018). Therefore, preventing or suppressing the injury of acinar cells might be an efficacious therapeutic strategy for CP.

Matsushita et al. found that the apoptosis of pancreatic acinar cells was increased in a dibutyltin dichloride (DBTC) induced CP model (Matsushita et al., 2012). Apoptosis refers to a programmed form of cell death after being subjected to various stimuli (D'Arcy 2019). The role of the pro-apoptotic protein Bax and the anti-apoptotic protein Bcl-2 in regulating apoptosis are mainly to change the mitochondria Permeation of the outer membrane and regulate the release of cytochrome C. Then cytochrome C activates Caspase-9 and effector apoptotic protease Caspase-3. Afterwards, activated Caspase-3 trigger the cascade of apoptosis, and eventually lead to apoptosis (Jia et al., 2012). The MAPK family includes three members: p38 MAPK, c-Jun N-terminal kinase (JNK) and extracellular signal-regulated kinase 1 and 2 (ERK1/2). ERK, JNK, and p38 MAPK have been reported increased in mice CP model (Xu et al., 2018). Moreover, growing evidence demonstrated that the activation of MAPK cascades promoting cell apoptosis (Liu et al., 2018; Zakki et al., 2018).

Saikosaponin d (SSd) is a triterpenoid saponin compound derived from the plant *Bupleurum falcatum*. SSd has been reported to exert multiple pharmacological effects, including anti-inflammation activity (Wang et al., 2015). Recently, our previous study suggested that SSd inhibited autophagy of PSCs through PI3K/Akt/mTOR pathway, thus ameliorated pancreatic fibrosis (Cui et al., 2019), However, it is not clear whether SSd protect pancreatic injury of CP via regulating the apoptosis of pancreatic acinar cells.

In the present study, we measured the effects of SSd on DBTC induced pancreatic injury *in vivo*, and investigated the regulation of SSd on the cell apoptosis in AR42J cells *in vitro*. We found that SSd notably ameliorated pancreatic injury through reduced the number of apoptotic pancreatic acinar cells via inhibiting MAPK pathway. Furthermore, SSd protected the cerulein-induced injury of AR42J cells through suppressing MAPK pathway. Meanwhile, further exploration suggested that SSd interrupted the effects of PSCs-CM and the combination of PSCs-CM and cerulein on AR42J cells apoptosis through MAPK pathway. Thus, our findings might help to comprehensively elucidate the role of SSd in protecting pancreatic injury in CP.

METHODS

Materials and Reagents

Saikosaponin d (SSd) was purchased from Beijing Shenzhou Kechuang chemical technology research institute (purity>98%; Beijing, China). Its chemical structure is shown in the **Figure 1A**. GAPDH (#5174), Bax (#2772), Bcl-2 (#2876), Caspase-3 (#14220), Cleaved-caspase-3 (#9664), Caspase-9 (#9508), Phospho-p38 MAPK (#9211), p-JNK (#9255), JNK (#9252), and p-ERK1/2 (#8544) antibodies were obtained from Cell Signalling Technologies (Beverly, MA, United States). Cerulein (HY-A0190) were purchased from Med Chem Express (Shanghai, China).

Animals and CP Model

Male Wistar rats (weighting, 150–170 g) were purchased from Beijing Huafukang Biotechnology Co., Ltd (Beijing, China). All experiments were conducted in accordance with the Chinese Guide for the Care and Use of Laboratory Animals as well as the methods for the management of experimental animals. All experiments were approved by the Medicine Ethical Committee of Tianjin Nankai hospital. All animals were randomly assigned into three groups including the control group, the CP group and the CP treated with SSd group (eight mice for each group) according to the experimental design outlined in **Figure 1B**.

The rat model of CP was induced by caudal vein injection of 7 mg/kg DBTC (Sigma Aldrich, United States) (Cui et al., 2019). Briefly, DBTC (Sigma-Aldrich, China) was dissolved in 100% ethanol first (one part), mixed with glycerol (two parts) and finally mixed with DMSO (two parts). The proportion of three solutions was 1:2:2. The CP group and SSd group were injected DBTC solution (7 mg/kg body weight) into the caudal vein. (Inoue et al., 2002). For the control group, the rats were injected with vehicle (ethanol:glycerol:DMSO, 1:2:2) only. The day after DBTC induction, the rats were orally administered with normal saline (with 0.5% carboxymethyl cellulose, (Na-CMC)) or 1 mg/kg/d SSd in 1.0 ml saline (with 0.5% Na-CMC). Rats were euthanized and analyzed after 4 weeks.

Histological Examinations

Haematoxylin and eosin (H and E) staining was used to explore the changes of histology in the pancreas. Pancreas was rapidly removed and immediately fixed in 4% paraformaldehyde solution. Fixed tissues were cut into 5 μm sections and used for H and E staining. The pancreatic histopathology scores were calculated by evaluating the following criteria: edema, acinar vacuolization and necrosis, and proinflammatory cell infiltration, in accordance with previous reports (Niina, et al., 2014) (0 is normal and 4 is severe).

Serum Parameters

Serum amylase and lipase activities were measured by using assay kits (C016-1, A054-2, Nanjing Jiancheng Bioengineering Institute,

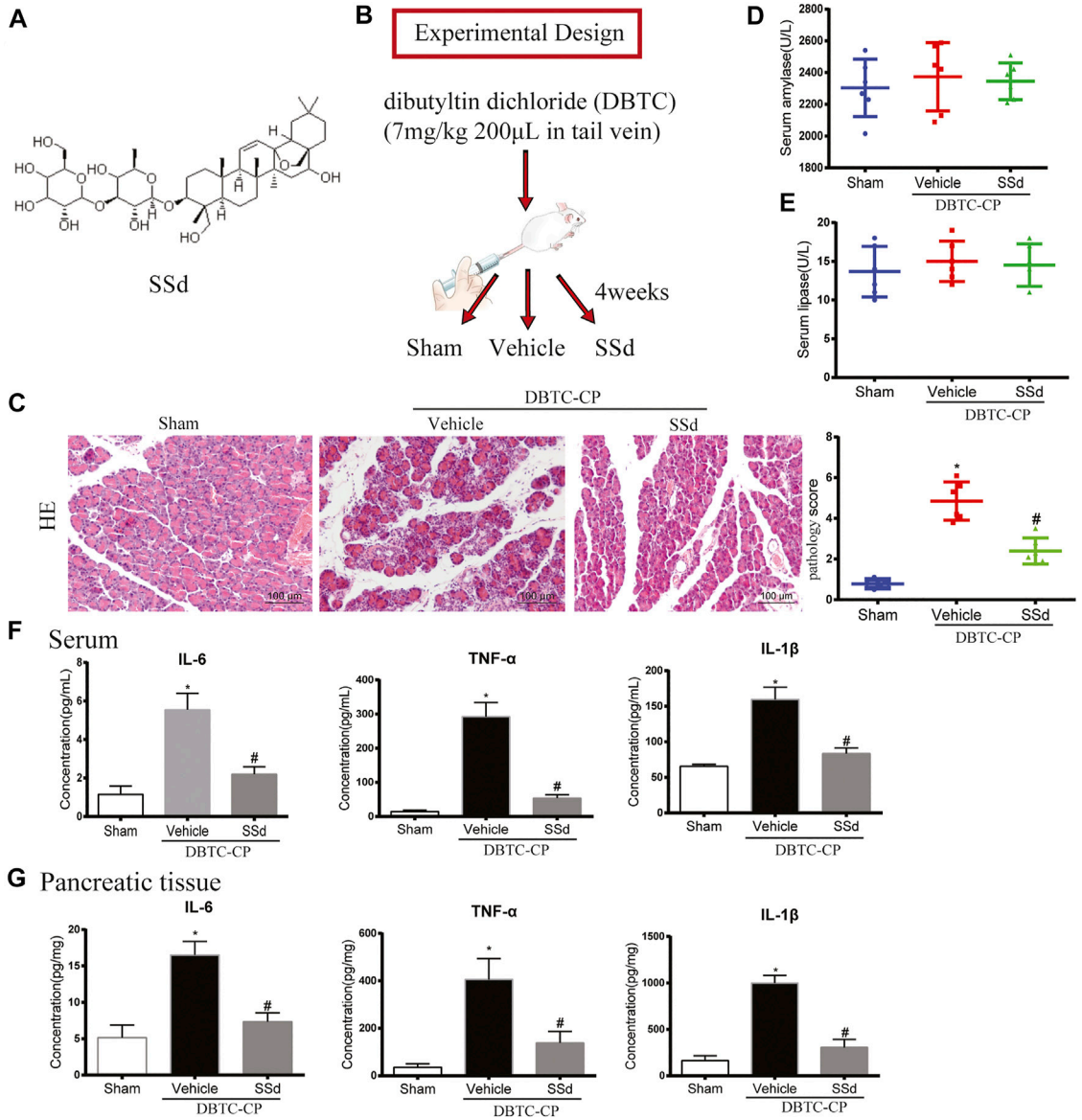


FIGURE 1 | Effects of SSd on the histological changes, serum amylase and lipase in DBTC-induced CP **(A)** The chemical structure of SSd **(B)** Schematic of *in vivo* experiment design. **(C)** The pathological score of H and E staining (original magnification, ×200). **(D)** Serum amylase levels. **(E)** Serum lipase levels. **(F)** The levels of IL-6, TNF-α, and IL-1β in serum. **(G)** The levels of IL-6, TNF-α, and IL-1β in pancreatic tissue. (n = 6–8, $*p < 0.05$ vs. Sham group; $\#p < 0.05$ vs. CP group).

Nanjing, China) with spectrophotometric determination according to the manufacturer's protocols.

ELISA

The inflammatory factors IL-6, TNFα, and IL-1β in serum and pancreatic tissue were estimated by using assay kits (CSB-E04640r, CSB-E11987r, CSB-E08055r, CusaBio, Wuhan, China) according to the manufacturer's protocols.

In Situ TUNEL Fluorescence Staining Assay

A TdT-mediated dUTP nick-end labeling (TUNEL) assay (Promega, Wisconsin, United States) was performed to identify the apoptotic cell *in situ*. Briefly, the paraffined pancreatic sections were dewaxed to hydrate, covered with protease K for 30 min at 37°C. The slides were washed by PBS and then incubated with TUNEL reaction mixed solution at 37°C for 1 h. For analysis, the images were captured with fluorescence microscope (Leica, German) and the apoptotic cells were stained green. To avoid histological differences between the samples, five visual fields were randomly selected for each slice (six rats per group, n = 6). The Image Pro Plus 6.0 software were used to analyzed the percentage of TUNEL-positive cells (%) in the pancreas.

Cell Lines and Culture Conditions

Rat pancreatic acinar AR42J cells were obtained from ProCell (CL-0025, Wuhan, Hubei, China) and cultured in Ham's Fe12 K

TABLE 1 | Primers used for RT-qPCR analysis.

Primers	Forward sequence 5′-3′	Reverse sequence 5′-3′
Bax	TTGCTACAGGGTTTCATCCAG	TGTTGTTGTCCAGTTCATCG
Bcl-2	GGGGCTACGAGTGGGATACT	GACGGTAGCGACGAGAGAAG
IL-6	GTTGCCTTCTTGGGACTGATG	TATATACTGGTCTGTTGTGGGTGGT
TNF-α	CTTCTCATTCCCGCTCGTG	CAGCTGCTCCTCTGCTTGGTGGTTT
IL-1β	AGGCTGACAGACCCCAAAAG	CTCCACGGGCAAGACATAGG
GAPDH	AGATGGTGAAGGTCGGTGTG	CTGGAAGATGGTGATGGGTT

medium containing 20% fetal bovine serum and 1% penicillin/streptomycin.

Cell Viability Assay

AR42J were seeded in 96-well plate with 5×10^3 cells/well. Cells were treated with different concentrations of SSd (0, 1, 10, 20, 30, 40 or 50 μM) for 24 h, then added 10 μl Cell Counting Kit-8 solution (Beyotime, Shanghai, China) to each well. After incubation for another 4 h, the absorbance at 450 nm was determined by microplate reader. The percentage of viable cells was calculated using the following formula: Cell viability (%) = [(A450 treated-A450blank)/(A450 control-A450blank)] × 100.

Isolation, Identification and Culture of Rat PSCs

The primary PSCs were isolated from rat pancreas using Nycodenz (Axis-Shield, Norway) density gradient centrifugation as reported previously (Li, et al., 2018). Then PSCs were cultured in DMEM (Gibco) supplemented with 10% fetal bovine serum and 1% antibiotics (penicillin/streptomycin). The third to fifth generation of PSCs were used for experiments.

Preparation of Conditioned Medium From PSCs (PSCs-CM)

PSCs (passage 3) were seeded at 5×10^5 cells per 10-cm plate in DMEM medium. PSCs reached 80% confluence and then placed in serum-free medium for 24 h. The medium was then collected for *in vitro* experiments.

Reverse Transcription Quantitative Polymerase Chain Reaction (RT-qPCR)

Total RNA was isolated by Trizol (Takara, China) according to the manufacturer's protocol. Total RNA (1 μg) of each sample was reverse-transcribed into cDNA using Revert Aid First Strand cDNA Synthesis Kit (K1622, Thermo, United States). qPCR was performed to quantify gene expression levels by using Go Taq® Qpcr Master Mix Kit (cat.no. A6001, Promega, Wisconsin, United States). Primer sequences are listed in **Table 1**. The results were quantified as $2^{-\triangle\triangle Ct}$. The relative mRNA expression data are shown as the relative fold change normalized to GAPDH.

Western Blot Analysis

Rat pancreas tissue samples and cell were lysed using Protein lysates RIPA buffer (Solarbio, Beijing, China). BCA protein assay Kit (Thermo, United States) was used to measure the protein concentrations. Protein samples were separated by SDS-PAGE and subsequently transferred to the PVDF membrane (Millipore, United States). After blocking with 5% non-fat milk, the membranes were probed with primary antibodies at 4°C overnight, followed by incubation with secondary antibodies (1:50,000) for 2 h at room temperature. The proteins were visualized using the Chemiluminescent Substrate Kit (Affinity Biosciences, United States) and calculated using the Chemidoc XRS System (Bio-Rad, United States).

Apoptosis Analysis

Annexin V-FITC/PI apoptosis detection kit (Sungene Biotech, Tianjin, China) was used to detect the effect of SSd on AR42J apoptosis according to the manufacturer's instruction. The samples were measured by a FACScan flow cytometer (Beckman, CA, United States) as previously described (Cui, et al., 2020).

Statistical Analyses

Results were presented as Mean ± SD. Data were analyzed via one-way ANOVA (multiple groups) and GraphPad Prism software 6. p value <0.05 was considered as statistically significant.

RESULTS

SSd Attenuates Pancreatic Injury in DBTC-Induced CP

In CP, due to the long-term injury of acinar cells resulting the atrophy of acinar cells and dysfunction of pancreas. To investigate the protective effect of SSd on pancreatic injury of CP, we comprehensively evaluated the pancreatic function of each group. As shown in **Figure 1C**, H and E staining indicated that SSd alleviated pancreatic injury in DBTC-induced CP rats. Pancreatic pathology score revealed that SSd effectively reduced pancreatic injury of CP ($p < 0.05$, **Figure 1B**). However, as shown in **Figures 1D,E**, the activities of serum amylase and lipase were no statistical significance in DBTC-induced rats. Additionally, we detected the expression of several key inflammatory factors in the CP model. We observed a gradual increase of the levels of IL-6, TNF-α, and IL-1β in serum and pancreatic tissues in DBTC-

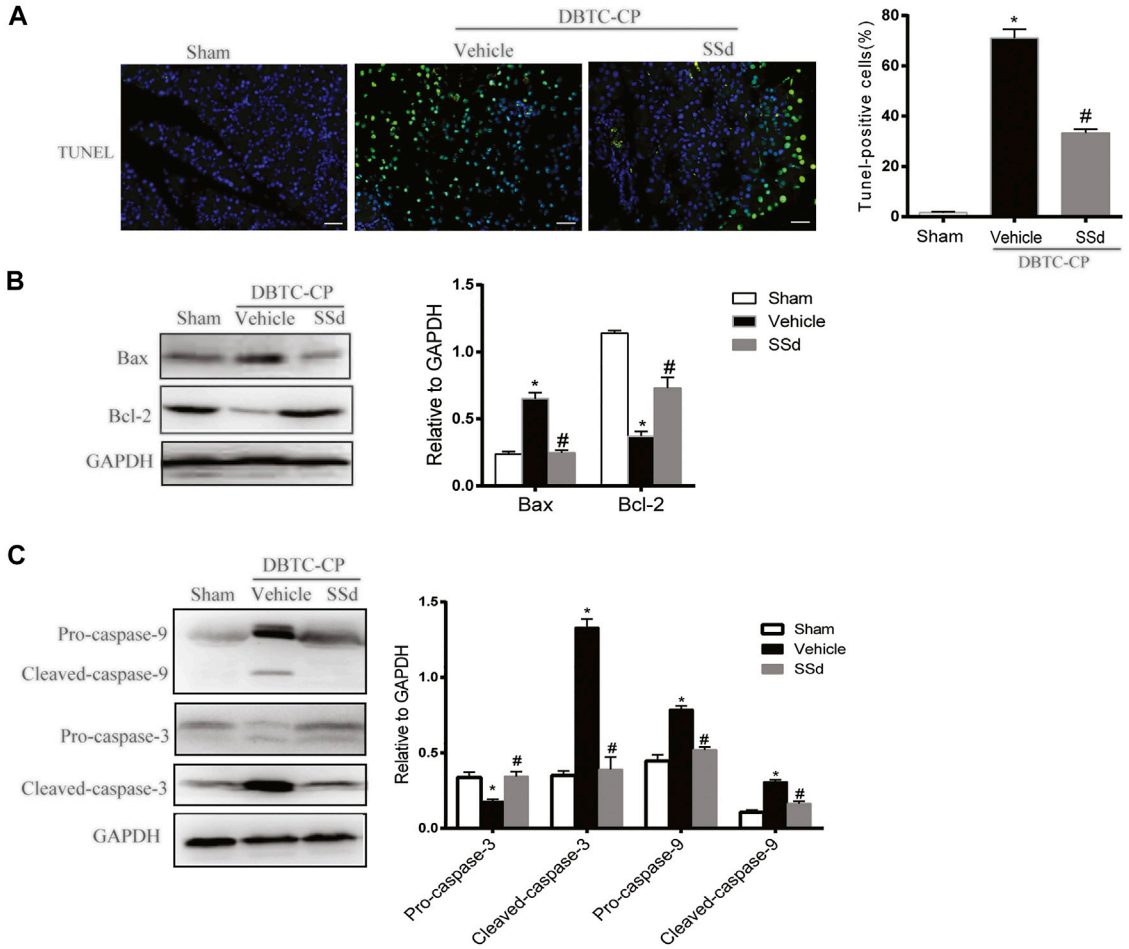


FIGURE 2 | SSd alleviates pancreatic injury in DBTC-induced CP. **(A)** Apoptosis of pancreatic cells were detected by TUNEL staining. **(B)** Western blot analysis of BAX, Bcl-2 in the pancreas. **(C)** Western blot analysis of apoptotic proteins Pro-caspase-3, Cleaved-caspase-3, Pro-caspase-9, and Cleaved-caspase-9 in the pancreas. Data are shown as the mean ± SEM of at least three independent experiments. (n = 6–8, $*p < 0.05$ vs. Sham group; $\#p < 0.05$ vs. CP group).

induced CP rats. Importantly, SSd treatment substantially decreased the expression of these inflammatory factors (**Figures 1F,G**).

SSd Alleviates the Apoptosis of Pancreatic Cells in DBTC-Induced CP

The development of CP was also accompanied by apoptosis and necrosis of pancreatic cells and it is a strategy to mitigate the pancreatic tissue damage by suppressing excessive apoptosis and necrosis (Erkan et al., 2012). TUNEL staining and western blot were used to investigate whether SSd can alleviate the apoptosis of pancreatic cells in CP rats. As shown in **Figure 2A**, the number of TUNEL-positive pancreatic cells was markedly elevated in DBTC-induced CP rats, While SSd notably decreased the number of TUNEL-positive pancreatic cells. Subsequently, western blot results suggested that the protein levels of pro-apoptotic protein Bax, cleaved caspase-9, and the cleaved caspase-3 were significantly increased whereas the expression of anti-apoptotic protein Bcl-2, Pro-caspase-9, and Pro-cspase-3 were reduced in DBTC-induced CP rats ($p < 0.05$). SSd treatment significantly inhibited the protein levels of Bax, Cleaved-caspase-9, and Cleaved-caspase-3, while increased the expression of Bcl-2, Pro-caspase-9 and Pro-caspase-3 (**Figures 2B,C**). These observations suggested that SSd administration suppressed the apoptosis of pancreatic cells caused by CP.

SSd Treatment Suppressed MAPK Cascades in DBTC-Induced CP

We analyzed the expression of the MAPK pathway in pancreatic tissues. The expression of p-JNK, p-ERK1/2, and p-p38 MAPK were significantly increased in the DBTC-induced CP group compared with the normal control group while SSd treatment notably decreased the levels of the p-JNK, p-ERK1/2 and p-p38 MAPK compared with the DBTC-induced CP group (**Figure 3**). Therefore, SSd could alleviate the pancreatic injury and inflammation *in vivo* maybe through suppressing the phosphorylation of MAPK pathway.

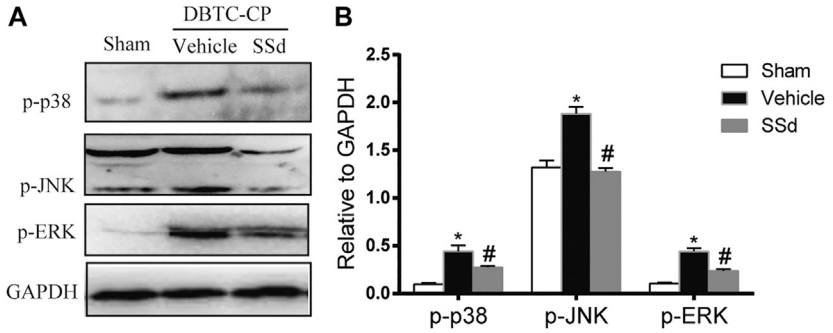


FIGURE 3 | SSd inhibited the phosphorylation activation of MAPK family proteins in DBTC-induced CP. Western blot analysis of p-JNK, p-ERK 1/2, and p-p38 MAPK. (n = 6–8, $* p < 0.05$ vs. Sham group; $\#p < 0.05$ vs. CP group).

SSd Attenuated Apoptosis and Inflammation of AR42J Cells Induced by Cerulein

Firstly, Cell viability of AR42J treated with different doses of SSd for 24 h was detected by CCK8. As shown in **Figure 4A**, the viability of AR42J gradually decreased in a dose-dependent manner with SSd administrated. Therefore, we choose 2.5 and 5 μM SSd (relevant cell viability was not affected) in following experiments. We next detected the protective role of SSd against cerulein-induced AR42J cells apoptosis, we measured cell apoptosis by staining the cells with Annexin V-FITC/PI. As shown in **Figure 4B**, cerulein (10 nM) significantly induced both early and late apoptosis of AR42J cells. Meanwhile, the mRNA transcription and protein levels of the Bax was significantly increased while Bcl-2 was markedly decreased induced by cerulein (**Figure 4C**). Western blot results indicated that cerulein significantly decreased the protein levels of the Pro-caspase-9 and the Pro-caspase-3 and increased the levels of the Cleaved-caspase-9 and the Cleaved-caspase-3 (**Figures 4D,E**). On the contrary, SSd treatment markedly suppressed the apoptotic events in AR42J cells pre-incubated with cerulein. Besides, we also found that SSd treatment notably decreased the levels of IL-6, TNF-α, and IL-1β in AR42J cells induced by cerulein (**Figure 4C**). Taken together, these findings suggested that SSd administration protected AR42J cells from apoptosis and inflammation induced by cerulein.

SSd Reduced Apoptosis and Inflammation of AR42J Cells Induced by PSCs-CM or PSCs-CM and Cerulein Combination

In a previous study, Xia et al. found that the CM from LTC-14 PSCs instigated apoptosis in the AR42J cells (Xia, et al., 2018). In our co-culturing experiments, we detected the co-culturing effects of the CM from PSCs on the apoptosis and inflammation of AR42J cells. Consistent with previous finding, we found that the PSCs-CM could also induce the apoptosis and inflammation of AR42J. As shown in **Figure 5A**, PSCs-CM significantly promoted the apoptotic ratio of AR42J. PSCs-CM also markedly increased the mRNA levels of IL-6, TNF-α, IL-1β, and Bax while decreased the level of Bcl-2 (**Figure 5B**). Moreover, Western blotting result showed that the protein levels of Bax, Cleaved-caspase-3, and Cleaved-caspase-9 were significantly increased whereas the expression of Bcl-2 and Pro-caspase-9 decreased with PSCs-CM treatment (**Figures 5C,D**). But such detrimental effects of PSCs-CM were markedly declined by SSd treatment at 5 μM (**Figures 5A–D**).

Then, to analyze whether PSCs-CM and cerulein combination enhance the apoptosis of AR42J, AR42J was pretreated with cerulein for 1 h prior of PSCs-CM treatment. As expected, we observed that PSCs-CM and cerulein combination greatly induced the apoptosis ratio and the inflammation of AR42J compared with PSCs-CM treatment alone (**Figures 5A,B**). Additionally, PSCs-CM and cerulein combination substantially decreased the expression of Pro-caspase-3 while increased the protein level of Cleaved-caspase-3 compared with PSCs-CM treatment alone, but there was no significant difference in the Bax, Bcl-2, Pro-caspase-9, and Cleaved-caspase-9 between the PSCs-CM and cerulein combination group and the PSCs-CM treatment alone group. (**Figures 5C,D**). However, such apoptotic events were inhibited by the SSd administration at 5 μM (**Figures 5A–D**). In summary, these *in vitro* results showed that the inflammation and acinar cell apoptosis caused by PSCs-CM alone or PSCs-CM and cerulein combination were substantially supressed by SSd treatment.

SSd Inhibited the Activity of MAPK Cascades in AR42J

To further explore mechanism of the protective effects of SSd on the cerulein-induced apoptosis of AR42J, we detected the expression of MAPK pathway. As shown in **Figure 6A**, the increase in p-JNK, p-ERK1/2, and p-p38 MAPK expressions in AR42J cells induced by cerulein were greatly suppressed by SSd administration.

Moreover, the western blot results also showed that PSCs-CM significantly increased the expression of p-JNK and p-p38 MAPK, but had no effect on the expression of p-ERK while SSd treatment markedly decreased the protein levels of p-JNK and p-p38 MAPK (**Figure 6B**). Additionally, PSCs-CM and cerulein combination notably increased the phosphorylation of JNK1/2, ERK1/2, and

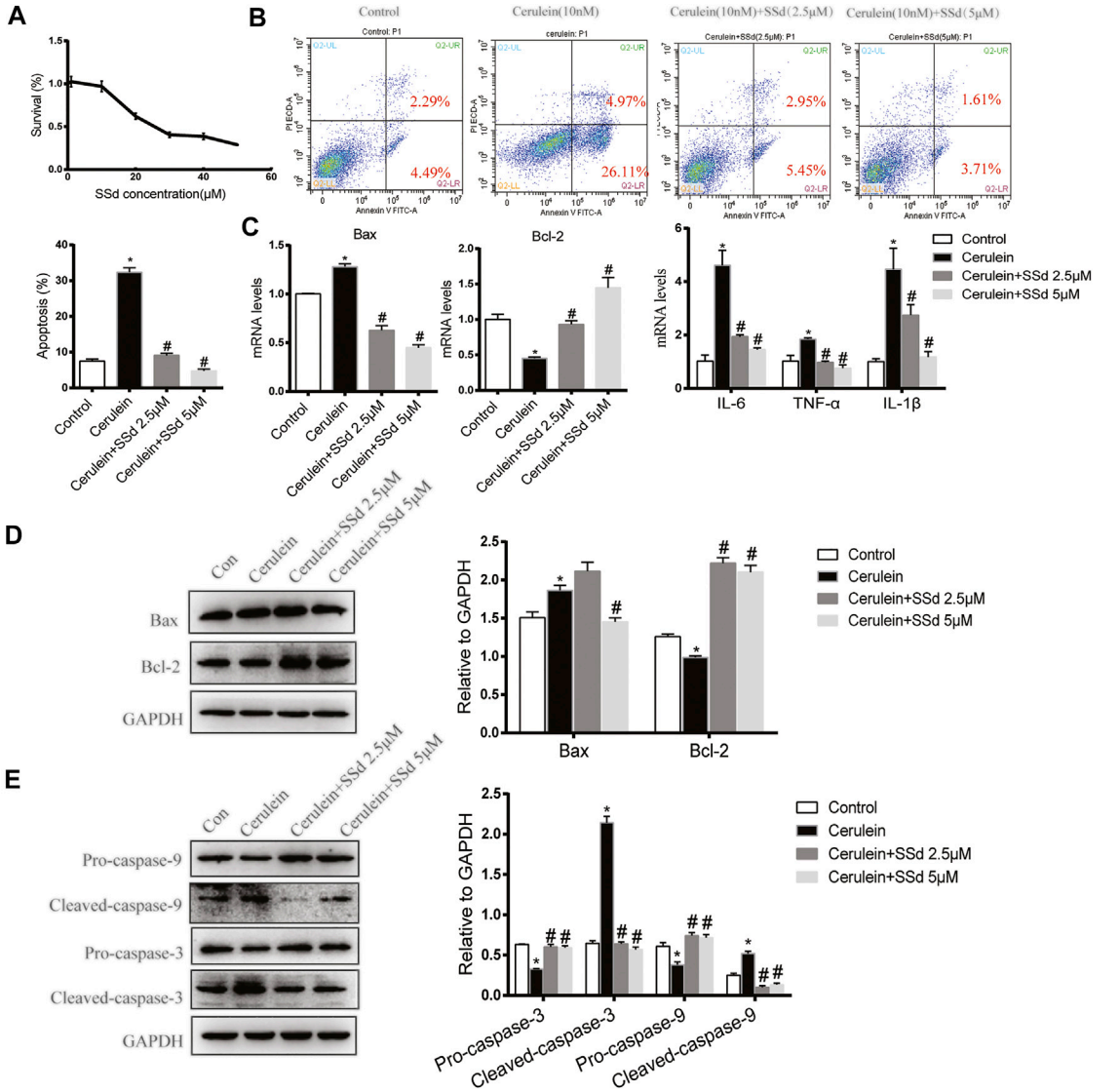


FIGURE 4 | SSd attenuated apoptosis and inflammation of AR42J cells induced by cerulein. **(A)** CCK8 assay detected the cell viability of AR42J after SSd treatment. **(B)** Flow cytometry analysis of apoptosis of AR42J. AR42J were pre-treated with cerulein 10 nM for 1 h, then incubated with or without 2.5 μM or 5 μM SSd for 24 h. **(C)** RT-PCR analysis of Bax, Bcl-2, IL-6, TNF-α, and IL-1β. **(D)** Western blot analysis of Bax and Bcl-2. **(E)** Western blot analysis of C Pro-caspase-3, Cleaved-caspase-3, Pro-caspase-9, and Cleaved-caspase-9. Data are shown as the mean ± SEM of at least three independent experiments (*$p < 0.05$ compared with the control group, #$p < 0.05$ compared with the cerulein induced group).

p38 MAPK compared with PSCs-CM treatment alone, and SSd could significantly inhibit their phosphorylation levels (**Figure 6B**). These data demonstrated that the protection of SSd on the apoptosis and inflammation of AR42J cells is through down-regulated the phosphorylation of JNK1/2, ERK1/2, and p38 MAPK. Although exact molecular mechanisms of such an interplay remain to be investigated.

DISCUSSION

In the present study, to further confirm whether SSd could alleviate pancreatic injury during the development of CP, we using a DBTC-induced CP model. The results revealed that SSd attenuate pancreatic damage, decrease the apoptosis and suppress the phosphorylation level of MAPK family proteins (JNK1/2, ERK1/2, and p38 MAPK) significantly in the pancreas of CP rats. The *in vitro* studies have shown that SSd attenuated the apoptosis of AR42J induced by cerulein or PSCs-CM or the combination of PSCs-CM and cerulein through significantly inhibited the activated phosphorylation of JNK1/2 and p38 MAPK.

CP is characterized by inflammation and fibrosis. The injury of pancreatic acinar cells caused the inflammation and the excessive activation of PSCs induced the fibrosis. Recently, our previous study demonstrated that SSd inhibited autophagy of PSCs, thus ameliorated pancreatic fibrosis (Cui et al., 2019). The current

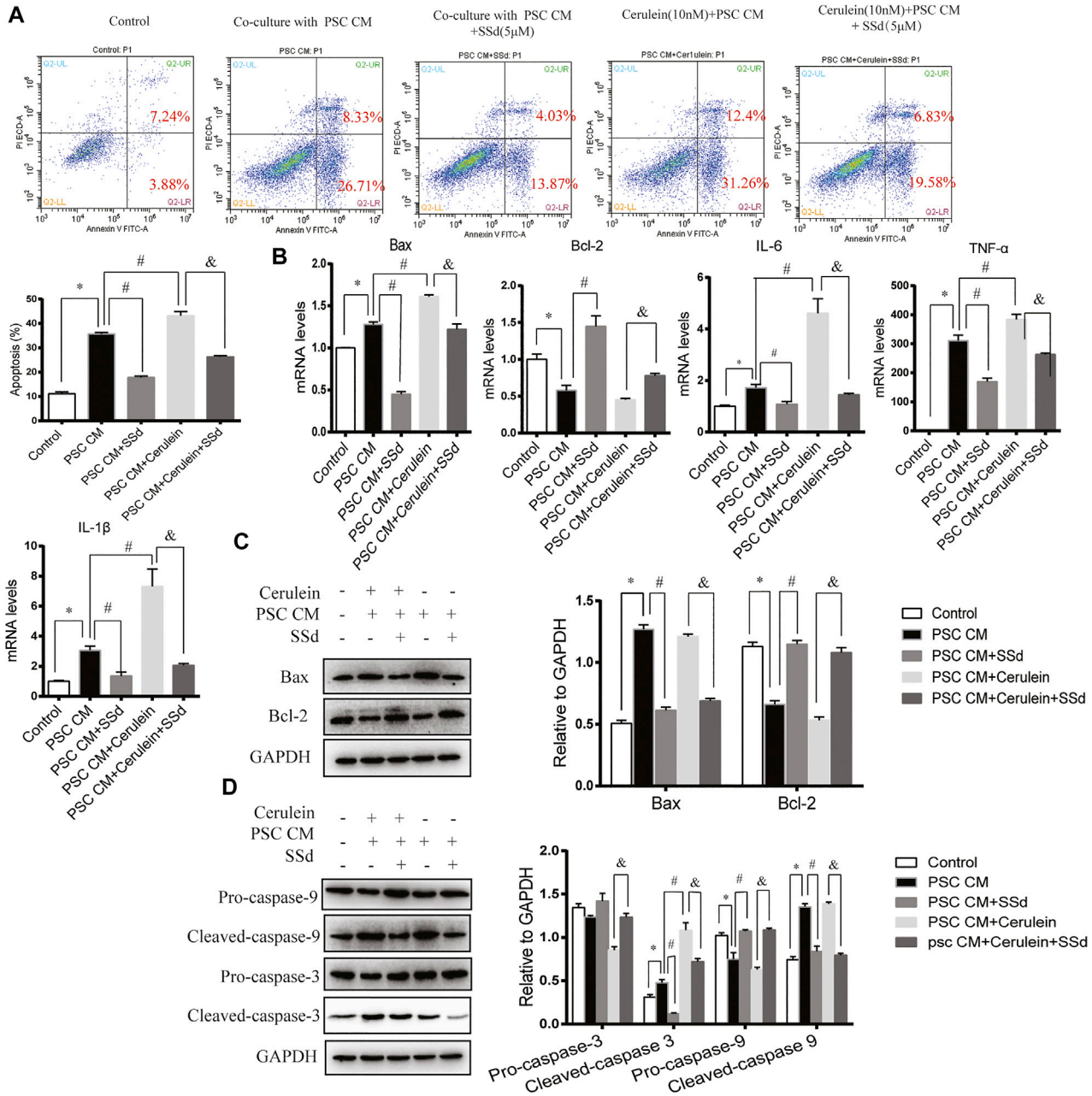


FIGURE 5 | SSd reduced apoptosis and inflammation of AR42J cells induced by PSCs-CM or PSCs-CM and cerulein combination. AR42J cells were pre-treated with PSCs-CM with 5 μM SSd or 10 nM cerulein or 10 nM cerulein and 5 μM SSd for 24 h. **(A)** Flow cytometry analysis of apoptosis of AR42J. **(B)** RT-PCR analysis of Bax, Bcl-2, IL-6, TNF-α, and IL-1β. **(C)** Western blot analysis of Bax and Bcl-2. **(D)** Western blot analysis of Pro-caspase-3, Cleaved-caspase-3, Pro-caspase-9, and Cleaved-caspase-9. Data are shown as the mean ± SEM of at least three independent experiments. (*$p < 0.05$ compared with the control group, #$p < 0.05$ compared with the PSCs-CM group, and $p < 0.05$ compared with PSCs-CM + cerulein group).

study is the first study to investigate the effects of SSd treatment on the pancreatic injury and inflammation of CP via regulating the apoptosis of pancreatic acinar cells. Pancreatic acinar cells play a key role in the initiation of pancreatitis. Brigitte *et al.* reported that during the development of DBTC-induced CP in rats, there were distinct parenchymal cell damage, which characterized by a significant increase in serum amylase and lipase activities during the early period upon DBTC exposure. however, the activities returned to normal levels at days 28 (Glawe et al., 2005). In the present study, we used a rat experimental DBTC-induced CP model and also found that the activities of serum amylase and lipase were no statistical significance in DBTC-induced rats at days 28. Furthermore, Norio et al. reported that the apoptotic index of pancreatic

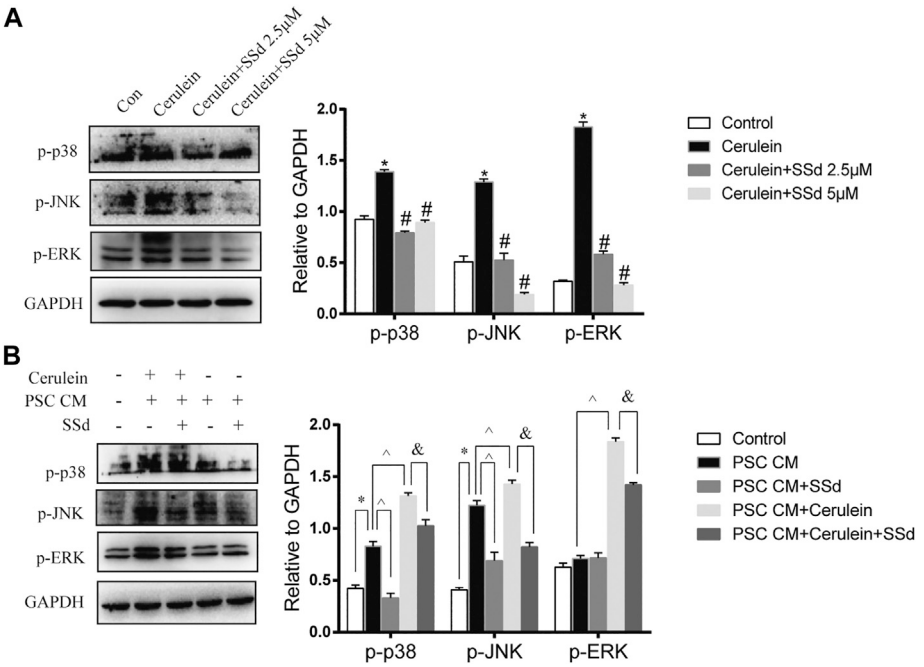


FIGURE 6 | Effect of SSd on AR42J apoptosis and inflammation through the MAPK pathway. **(A)** Western blot analysis of p-JNK, p-ERK 1/2, and p-p38 MAPK. AR42J were pre-treated with cerulein 10 nM for 1h, then incubated with or without 5 μM or 10 μM SSd for 24 h. **(B)** Western blot analysis of p-JNK, p-ERK 1/2, and p-p38 MAPK. AR42J cells were pre-treated with PSCs-CM with 5 μM SSd or 10 nM cerulein or 10 nM cerulein and 5 μM SSd for 24 h. Data are shown as the mean ± SEM of at least three independent experiments. (*$p < 0.05$ compared with the control group, #$p < 0.05$ compared with the cerulein induced group, ^$p < 0.05$ compared with the PSCs-CM group, and $p < 0.05$ compared with PSCs-CM + cerulein group).

acinar cells in DBTC administered rats were significantly increased (Matsushita et al., 2012). In this study, the results indicated that DBTC strikingly increased the number of apoptotic pancreatic acinar cells and the Western blot results of apoptotic-related protein levels of Bax, Bcl-2, Pro-caspase-9, Cleaved-caspase-9, Pro-caspase-3, and Cleaved-caspase-3 further confirmed this. Whereas SSd administration significantly reduced the apoptosis of acinar cells. MAPKs regulate many cellular processes, including growth, differentiation, survival, and apoptosis, as well as cytokine production, and have been reported increased in mice CP model (Lee et al., 2003). Our study indicated that SSd markedly inhibited the phosphorylation of JNK, ERK1/2, and p38 MAPK in DBTC-induced CP model.

Previous studies revealed that cerulein-stimulated apoptosis of AR42J cells via up-regulation of IL-6 (Yu et al., 2005). It is worth mentioning that SSd possesses anti-inflammatory activity. SSd suppresses pro-inflammatory cytokines including TNF-α, IL-6 (Lu, et al., 2012). In this study, we treated AR42J cells with 10 nM cerulein for 24 h *in vitro*. Similar to these aforementioned findings, our results showed that cerulein increased cytokines expression (including IL-6,TNF-α and IL-1β) and the apoptosis of AR42J cells. Whereas SSd could protect the pancreatic acinar cells from injury not only by decreased the expressions of IL-6 and TNF-α but also inhibited the apoptosis of AR42J cells. An increasing evidence demonstrated that initial damage to the acinar cells induced the activation of PSCs, which can thereby possibly further aggravate the destruction and apoptosis of more acinar cells, generating a vicious circle (Gryshchenko et al., 2018; Xia et al., 2018). Therefore, we also evaluated the impact of SSd on the inflammation and apoptosis induced by PSCs-CM or the combination of PSCs-CM and cerulein in AR42J cells. The results indicated that the CM from primary PSCs, is similar to cerulein, could also increase the mRNA levels of IL-6,TNF-α and IL-1β, and promote the apoptosis of AR42J cells. Then, SSd treatment reduced the apoptosis of AR42J cells induced by PSCs-CM. Furthermore, PSCs-CM and cerulein combination greatly induced the apoptosis and inflammation of AR42J compared with PSCs-CM treatment alone, but such detrimental effects were also markedly reduced by SSd administration. However, we don't know that how many pro-inflammatory cytokines are contained in PSCs-CM and which cytokines of PSCs-CM are essential for inducing the apoptosis of AR42J. Interestingly, activation of PSCs can occur by both autocrine and paracrine mechanisms. Among them, autocrine cytokines include IL-1, IL-6, interleukin-8 (IL-8), TNF-α, transforming growth factor-beta1 (TGF-β1), platelet derived growth factor (PDGF), monocyte chemoattractant protein-1 (MCP-1) and so on (Bynigeri et al., 2017). Several studies showed SSd decreased the expression of pro-inflammatory cytokines including IL-6, TNF-α, and IL-1β (Wang et al., 2015; Ma et al., 2015). Therefore, we speculated that SSd exerts its anti-inflammatory effect by neutralizing the proinflammatory cytokines IL-6, TNF-α, and IL-1β contained in PSCs-CM. We will perform a large-scale cytokine analysis (or

transcriptome analysis) to seek the essential cytokines in our future work.

We further investigated molecules that regulate apoptosis and inflammation after treatment with SSd. Cerulein induces cytokine expression and apoptotic cell death may be regulated by MAPK in pancreatic acinar cells (Lee et al., 2003). Lin, et al. reported SSd reduces HO-induced PC12 cell apoptosis by blocking MAPK-dependent oxidative damage (Lin et al., 2016). In order to explore the mechanisms, we detected the expression of the phosphorylation of JNK, ERK1/2, and p38 MAPK upon SSd treatment *in vitro*. The results indicated that SSd could reduce cerulein induced AR42J apoptosis via suppressing the MAPK signaling pathways. Moreover, we also found that PSCs-CM could significantly increase the protein levels of p-p38 and p-JNK, but there was no obvious alteration of p-ERK1/2. Additionally, PSCs-CM and cerulein combination notably increased the phosphorylation of JNK1/2, ERK1/2, and p38 MAPK compared with PSCs-CM treatment alone. Our study also demonstrated SSd strikingly suppressed the phosphorylation of JNK and p38 MAPK in both PSCs-CM alone and the combination of PSCs-CM and cerulein treatment in AR42J cells. A diverse set of transcription factors implicated in MAPK-induced apoptosis have been identified and validated (Cuenda et al., 2007; Zeke et al., 2016). Activator protein 1 (AP-1) and p53 were regulated by JNK and p38, which result in increased expression of pro-apoptotic proteins and decreased expression of anti-apoptotic proteins (Wang et al., 2021; Lu et al., 2020) and have been reported to be elevated in the apoptosis of pancreatic acinar cells (Lee et al., 2003; Tan et al., 2020). Therefore, we suspect that SSd regulate the apoptosis of AR42J cells induced by cerulein or PSCs-CM through AP-1 or p53 pathway. We need to verify it in our future work.

Of course, there are still several limitations exist in this study. Although we have shown the protective role of SSd from the pancreatic injury in DBTC-induced rats CP, we only measured the effect of a single dose of SSd. The dose-response effect of SSd in experimental CP remains unknown. So, we will confirm the optimal dosage of SSd in our future works. More importantly, we only measure the effects of PSCs-CM on the apoptosis of AR42J cells, but the effects of AR42J cells on the activation and apoptosis of PSCs were not detected. Besides, detailed mechanism of SSd on the effects of a crosstalk between PSCs and AR42J cells were not fully explain, which deserves further investigation.

In conclusion, the current study systematically explored the role of SSd in alleviating pancreatic injury *in vivo* and *in vitro*. Mechanistically, SSd exerted a marked protective effect on the inflammation and apoptosis of AR42J cells induced by cerulein via MAPK pathway. Furthermore, SSd interrupted the effects of PSCs-CM alone and the combination of PSCs-CM and cerulein on AR42J cells inflammation and apoptosis through MAPK pathway. Collectively, these results suggested that SSd could be a potential therapeutic agent for the clinical management of CP.

DATA AVAILABILITY STATEMENT

The raw data supporting the conclusions of this article will be made available by the authors, without undue reservation.

ETHICS STATEMENT

The animal study was reviewed and approved by the Medicine Ethical Committee of Tianjin Nankai hospital.

AUTHOR CONTRIBUTIONS

C-XL: data curation and analyzed, methodology, and writing the original draft. C-XL, L-HC, and S-KZ participated in experimental design. L-QZ, LY, Y-ZZ, and JC performed the experiments. All authors gave final approval for the submitted version.

FUNDING

This work was supported by the Scientific Research Project of Integrated Traditional Chinese and Western Medicine of Tianjin Municipal Health Committee (2019037), the Scientific Research Projects in Key Areas of Traditional Chinese Medicine of Tianjin Municipal Health Committee (2019004), the National Natural Science Foundation of China (82004147), the Scientific and Technological Personnel Training Project of Tianjin Municipal Health Committee (RC20142), and the Chen Xiao-ping Foundation for the Development of Science and Technology of Hubei Province (CXPJJH12000001-2020335).

SUPPLEMENTARY MATERIAL

The Supplementary Material for this article can be found online at: https://www.frontiersin.org/articles/10.3389/fphar.2021.735079/full#supplementary-material

REFERENCES

Bateman, A. C., Turner, S. M., Thomas, K. S., McCrudden, P. R., Fine, D. R., and Johnson, P. A. (2002). Apoptosis and Proliferation of Acinar and Islet Cells in Chronic Pancreatitis: Evidence for Differential Cell Loss Mediating Preservation of Islet Function. *Gut* 50, 542–548. doi:10.1136/gut.50.4.542

Beyer, G., Habtezion, A., Werner, J., Lerch, M. M., and Mayerle, J. (2020). Chronic Pancreatitis. *The Lancet* 396, 499–512. doi:10.1016/s0140-6736(20)31318-0

Bynigeri, R. R., Jakkampudi, A., Jangala, R., Subramanyam, C., Sasikala, M., Rao, G. V., et al. (2017). Pancreatic Stellate Cell: Pandora's Box for Pancreatic Disease Biology. *World J. Gastroenterol.* 23 (3), 382–405. doi:10.3748/wjg.v23.i3.382

Chen, J. M., and Férec, C. (2012). Genetics and Pathogenesis of Chronic Pancreatitis: The 2012 Update. *Clin. Res. Hepatol. Gastroenterol.* 36, 334–340. doi:10.1016/j.clinre.2012.05.003

Cuenda, A., and Rousseau, S. (2007). p38 MAP-Kinases Pathway Regulation, Function and Role in Human Diseases. *Biochim. Biophys. Acta.* 1773 (8), 1358–1375. doi:10.1016/j.bbamcr.2007.03.010

Cui, L. H., Li, C. X., Zhuo, Y. Z., Yang, L., Cui, N. Q., and Zhang, S. K. (2019). Saikosaponin D Ameliorates Pancreatic Fibrosis by Inhibiting Autophagy of Pancreatic Stellate Cells via PI3K/Akt/mTOR Pathway. *Chem. Biol. Interact.* Chemico-biological *Interactions*. 300, 18–26. doi:10.1016/j.cbi.2019.01.005

D'Arcy, M. S. (2019). Cell Death: a Review of the Major Forms of Apoptosis, Necrosis and Autophagy. *Cell Biol Int.* 43 (6), 582–592. doi:10.1002/cbin.11137

Erkan, M., Adler, G., Apte, M. V., Bachem, M. G., Buchholz, M., Detlefsen, S., et al. (2012). StellaTUM: Current Consensus and Discussion on Pancreatic Stellate Cell Research. *Gut* 61, 172–178. doi:10.1136/gutjnl-2011-301220

Glawe, C., Emmrich, J., Sparmann, G., and Vollmar, B. (2005). *In Vivo* characterization of Developing Chronic Pancreatitis in Rats. *Lab. Invest.* 85 (2), 193–204. doi:10.1038/labinvest.3700212

Gryshchenko, O., Gerasimenko, J. V., Peng, S., Gerasimenko, O. V., and Petersen, O. H. (2018). Calcium Signalling in the Acinar Environment of the Exocrine Pancreas: Physiology and Pathophysiology. *J. Physiol.* 596 (14), 2663–2678. doi:10.1113/JP275395

Inoue, M., Ino, Y., Gibo, J., Ito, T., Hisano, T., and Arita, Y. (2002). The Role of Monocyte Chemoattractant Protein-1 in Experimental Chronic Pancreatitis Model Induced by Dibutyltin Dichloride in Rats. *Pancreas* 25 (4), e64–e70. doi:10.1097/00006676-200211000-00023

Jia, L. T., Chen, S. Y., and Yang, A. G. (2012). Cancer Gene Therapy Targeting Cellular Apoptosis Machinery. *Cancer Treat. Rev.* 38 (7), 868–876. doi:10.1016/j.ctrv.2012.06.008

Lee, J., Seo, J., Kim, H., Chung, J. B., and Kim, K. H. (2003). Signal Transduction of Cerulein Induced Cytokine Expression and Apoptosis Pancreatic Acinar Cells. *Ann. NY Acad. Sci.* 1010, 104–108. doi:10.1196/annals.1299.017

Li, C. X., Cui, L. H., Zhuo, Y. Z., Hu, J. G., Cui, N. Q., and Zhang, S. K. (2018). Inhibiting Autophagy Promotes Collagen Degradation by Regulating Matrix Metalloproteinases in Pancreatic Stellate Cells. *Life Sci.* 208, 276–283. doi:10.1016/j.lfs.2018.07.049

Lin, X., Wu, S., Wang, Q., Shi, Y., Liu, G., Zhi, J., et al. (2016). Saikosaponin-D Reduces H2O2-Induced PC12 Cell Apoptosis by Removing ROS and Blocking MAPK-dependent Oxidative Damage. *Cell Mol Neurobiol.* 36 (8), 1365–1375. doi:10.1007/s10571-016-0336-5

Liu, W., Xu, C., Ran, D., Wang, Y., Zhao, H., Gu, J., et al. (2018). CaMKII Mediates Cadmium Induced Apoptosis in Rat Primary Osteoblasts through MAPK Activation and Endoplasmic Reticulum Stress. *Toxicology* 406-407, 70–80. doi:10.1016/j.tox.2018.06.002

Lu, C. N., Yuan, Z. G., Zhang, X. L., Yan, R., Zhao, Y. Q., Liao, M., et al. (2012). Saikosaponin a and its Epimer Saikosaponin D Exhibit Anti-inflammatory Activity by Suppressing Activation of NF-Kb Signaling Pathway. *Int. Immunopharmacol.* 14 (1), 121–126. doi:10.1016/j.intimp.2012.06.010

Lu, L., Ma, J., Sun, M., Wang, X., Gao, E., Lu, L., et al. (2020). Melatonin Ameliorates MI-Induced Cardiac Remodeling and Apoptosis through a JNK/p53-Dependent Mechanism in Diabetes Mellitus. *Oxid Med. Cel Longev.* 2020, 1535201. doi:10.1155/2020/1535201

Ma, X., Dang, C., Kang, H., Dai, Z., Lin, S., Guan, H., et al. (2015). Saikosaponin-D Reduces Cisplatin-Induced Nephrotoxicity by Repressing ROS-Mediated Activation of MAPK and NF-Kb Signalling Pathways. *Int. Immunopharmacol.* 28 (1), 399–408. doi:10.1016/j.intimp.2015.06.020

Matsushita, K., Mizushima, T., Shirahige, A., Tanioka, H., Sawa, K., Ochi, K., et al. (2012). Effect of Taurine on Acinar Cell Apoptosis and Pancreatic Fibrosis in Dibutyltin Dichloride-Induced Chronic Pancreatitis. *Acta Med. Okayama.* 66 (4), 329–334. doi:10.18926/AMO/48687

Niina, Y., Ito, T., Oono, T., Nakamura, T., Fujimori, N., Igarashi, H., et al. (2014). A Sustained Prostacyclin Analog, ONO-1301, Attenuates Pancreatic Fibrosis in Experimental Chronic Pancreatitis Induced by Dibutyltin Dichloride in Rats. *Pancreatology.* 14 (3), 201–210. doi:10.1016/j.pan.2014.02.009

Patel, M., and Fine, D. R. (2005). Fibrogenesis in the Pancreas after Acinar Cell Injury. *Scand. J. Surg.* 94 (2), 108–111. doi:10.1177/145749690509400205

Sheth, S. G., Conwell, D. L., Whitcomb, D. C., Alsante, M., Anderson, M. A., Barkin, J., et al. (2017). Academic Pancreas Centers of Excellence: Guidance from a Multidisciplinary Chronic Pancreatitis Working Group at PancreasFest. *Pancreatology* 17 (3), 419–430. doi:10.1016/j.pan.2017.02.015

Su, S. B., Motoo, Y., Xie, M. J., and Sawabu, N. (2001). Apoptosis in Rat Spontaneous Chronic Pancreatitis: Role of the Fas and Fas Ligand System. *Dig. Dis. Sci.* 46, 166–175. doi:10.1023/a:1005537218459

Tan, J. H., Cao, R. C., Zhou, L., Zhou, Z. T., Chen, H. J., Xu, J., et al. (2020). ATF6 Aggravates Acinar Cell Apoptosis and Injury by Regulating p53/AIFM2 Transcription in Severe Acute Pancreatitis. *Theranostics* 10 (18), 8298–8314. doi:10.7150/thno.46934

Wang, H. W., Liu, M., Zhong, T. D., and Fang, X. M. (2015). Saikosaponin-d Attenuates Ventilator-Induced Lung Injury in Rats. *Int. J. Clin. Exp. Med.* 8 (9), 15137–15145. PMID: 26628997; PMCID: PMC4658886.

Wang, L., Yang, Y. F., Chen, L., He, Z. Q., Bi, D. Y., Zhang, L., et al. (2021). Compound Dihuang Granule Inhibits Nigrostriatal Pathway Apoptosis in Parkinson's Disease by Suppressing the JNK/AP-1 Pathway. *Front. Pharmacol.* 12, 621359. doi:10.3389/fphar.2021.621359

Xia, Y., Xiao, H. T., Liu, K., Zhang, H. J., and Tsang, S. W. (2018). Resveratrol Ameliorates the Severity of Fibrogenesis in Mice with Experimental Chronic Pancreatitis. *Mol. Nutr. Food Res.* 62 (16), e1700561. doi:10.1002/mnfr.201700561

Xu, X. F., Liu, F., Xin, J. Q., Fan, J. W., Wu, N., Zhu, L. J., et al. (2018). Respective Roles of the Mitogen-Activated Protein Kinase (MAPK) Family Members in Pancreatic Stellate Cell Activation Induced by Transforming Growth Factor-Beta1 (TGF-Beta1). *Biochem. Biophys. Res. Commun.* 501 (2), 365–373. doi:10.1016/j.bbrc.2018.04.176

Yu, J. H., Lim, J. W., Kim, H., and Kim, K. H. (2005). NADPH Oxidase Mediates Interleukin-6 Expression in Cerulein-Stimulated Pancreatic Acinar Cells. *Int. J. Biochem. Cel Biol.* 37 (7), 1458–1469. doi:10.1016/j.biocel.2005.02.004

Zakki, S. A., Cui, Z. G., Sun, L., Feng, Q. W., Li, M. L., and Inadera, H. (2018). Baicalin Augments Hyperthermia-Induced Apoptosis in U937 Cells and Modulates the MAPK Pathway via ROS Generation. *Cell Physiol Biochem.* 45 (6), 2444–2460. doi:10.1159/000488263

Zeke, A., Misheva, M., Reményi, A., and Bogoyevitch, M. A. (2016). JNK Signaling: Regulation and Functions Based on Complex Protein-Protein Partnerships. *Microbiol. Mol. Biol. Rev.* 80 (3), 793–835. doi:10.1128/MMBR.00043-14

Conflict of Interest: The authors declare that the research was conducted in the absence of any commercial or financial relationships that could be construed as a potential conflict of interest.

Publisher's Note: All claims expressed in this article are solely those of the authors and do not necessarily represent those of their affiliated organizations, or those of the publisher, the editors and the reviewers. Any product that may be evaluated in this article, or claim that may be made by its manufacturer, is not guaranteed or endorsed by the publisher.

Copyright © 2021 Li, Cui, Zhang, Yang, Zhuo, Cui, Cui and Zhang. This is an open-access article distributed under the terms of the Creative Commons Attribution License (CC BY). The use, distribution or reproduction in other forums is permitted, provided the original author(s) and the copyright owner(s) are credited and that the original publication in this journal is cited, in accordance with accepted academic practice. No use, distribution or reproduction is permitted which does not comply with these terms.

frontiers in Pharmacology

ORIGINAL RESEARCH
published: 25 October 2021
doi: 10.3389/fphar.2021.749189

Exploring Multifunctional Bioactive Components from *Podophyllum sinense* Using Multi-Target Ultrafiltration

Huixia Feng[1,2,3,4], *Guilin Chen*[1,3,4], *Yongli Zhang*[1,3,4] *and Mingquan Guo*[1,2,3,4]*

[1]*Key Laboratory of Plant Germplasm Enhancement and Specialty Agriculture, Wuhan Botanical Garden, Chinese Academy of Sciences, Wuhan, China,* [2]*College of Life Sciences, University of Chinese Academy of Sciences, Beijing, China,* [3]*Sino-Africa Joint Research Center, Chinese Academy of Sciences, Wuhan, China,* [4]*Innovation Academy for Drug Discovery and Development, Chinese Academy of Sciences, Shanghai, China*

Podophyllum sinense (*P. sinense*) has been used as a traditional herbal medicine for ages due to its extensive pharmaceutical activities, including antiproliferative, anti-inflammatory, antiviral, insecticidal effects, etc. Nevertheless, the specific bioactive constituents responsible for its antiproliferative, anti-inflammatory, and antiviral activities remain elusive, owing to its complicated and diversified chemical components. In order to explore these specific bioactive components and their potential interaction targets, affinity ultrafiltration with multiple drug targets coupled with high performance liquid chromatography/mass spectrometry (UF–HPLC/MS) strategy was developed to rapidly screen out and identify bioactive compounds against four well-known drug targets that are correlated to the application of *P. sinense* as a traditional medicine, namely, Topo I, Topo II, COX-2, and ACE2. As a result, 7, 10, 6, and 7 phytochemicals were screened out as the potential Topo I, Topo II, COX-2, and ACE2 ligands, respectively. Further confirmation of these potential bioactive components with antiproliferative and COX-2 inhibitory assays *in vitro* was also implemented. Herein, diphyllin and podophyllotoxin with higher EF values demonstrated higher inhibitory rates against A549 and HT-29 cells as compared with those of 5-FU and etoposide. The IC_{50} values of diphyllin were calculated at 6.46 ± 1.79 and 30.73 ± 0.56 μM on A549 and HT-29 cells, respectively. Moreover, diphyllin exhibited good COX-2 inhibitory activity with the IC_{50} value at 1.29 ± 0.14 μM, whereas indomethacin was 1.22 ± 0.08 μM. In addition, those representative constituents with good affinity on Topo I, Topo II, COX-2, or ACE2, such as diphyllin, podophyllotoxin, and diphyllin *O*-glucoside, were further validated with molecular docking analysis. Above all, the integrated method of UF–HPLC/MS with multiple drug targets rapidly singled out multi-target bioactive components and partly elucidated their action mechanisms regarding its multiple pharmacological effects from *P. sinense*, which could provide valuable information about its further development for the new multi-target drug discovery from natural medicines.

Keywords: *Podophyllum sinense*, ultrafiltration-LC/MS, antiproliferative, anti-inflammatory, multi-target

OPEN ACCESS

Edited by:
Hongzhi Du,
Hubei University of Chinese Medicine, China

Reviewed by:
Sajjad Gharaghani,
University of Tehran, Iran
Changxing Qi,
Huazhong University of Science and Technology, China

***Correspondence:**
Mingquan Guo
guomq@wbgcas.cn

Specialty section:
This article was submitted to Ethnopharmacology, a section of the journal Frontiers in Pharmacology

Received: *30 July 2021*
Accepted: *20 September 2021*
Published: *25 October 2021*

Citation:
Feng H, Chen G, Zhang Y and Guo M (2021) Exploring Multifunctional Bioactive Components from Podophyllum sinense *Using Multi-Target Ultrafiltration. Front. Pharmacol. 12:749189. doi: 10.3389/fphar.2021.749189*

INTRODUCTION

The majority of drugs introduced into the body exert pharmacological effects through interaction with various corresponding biological target molecules. For instance, enzymes which play key roles in the pathogenicity and progression of certain disease with specific physiological functions have exerted great potentials in drug discovery and development as drug targets (Yao et al., 2013; Zhu et al., 2013). Recent studies demonstrated that enzyme inhibitors can inhibit the activity of specific enzymes related to certain diseases, thereby possessing huge potentials for the development of therapeutic drugs (Rengasamy et al., 2014; Orhan, 2019). Natural products have long been evolved to exhibit a wide range of chemical and functional diversities (Zhang et al., 2020), and thus play a crucial role in the field of new drug development as valuable biological resources (Chang et al., 2016). On the one hand, however, the chemical components from natural products, such as medicinal plants, are complicated and often act in a multi-target manner; on the other hand, these phytochemicals bring varied biological activities but also pose huge challenges to screen and identify the specific bioactive compounds, and further elucidate their corresponding mechanisms of action (Chen et al., 2018). In this context, it is pivotal to develop an efficient strategy to correlate their complex chemical ingredients with diverse pharmacological activities in order to decipher the chemical basis of the drug effects. Traditional herbal medicine has been proposed to prevent or cure diseases in a multi-component and multi-target way, but little or no direct evidence was provided so far. In order to meet this tough challenge, the present work aims to develop an affinity ultrafiltration LC/MS based multi-drug target strategy by taking *Podophyllum sinense* as an example.

P. sinense (H.L. Li) (Christenh. & Byng) belongs to *Podophyllum*, Berberidaceae. It has been regarded as a traditional Chinese folk medicine for many years and is widely distributed in Hubei, Sichuan, and Shaanxi provinces (Terabayashi et al., 1984). As the medicinal part, its rhizomes have been traditionally used for the treatment of contusions, fractures, snake bites, traumatic swelling, tracheitis, rheumatic pain, etc. (Zhao et al., 2014). Phytochemical studies indicate that *P. sinense* contains multitudinous bioactive ingredients, such as lignans, flavonoids, anthraquinones, and volatile oils (Ma et al., 1993). Among these ingredients, lignans are reported as the primary bioactive components and demonstrate remarkable antiproliferative, anti-inflammatory, antiviral, insecticidal activities (Castro et al., 2003; Yuan et al., 2011; Liu et al., 2015). However, the specific bioactive compounds responsible for its antiproliferative, anti-inflammatory, and antiviral activities remain unknown till date.

The first step to solve this puzzle is to explore the phytochemical basis of the pharmacological effects of *P. sinense* for some specific drug targets that are used in order to elucidate the potential mechanism of action. In this way, it is very urgent to develop an effective and comprehensive approach to correlate its holistic bioactivity to its multi-purpose chemical components. Especially, the UF–LC/MS strategy could fill this gap, since it can simultaneously screen out and identify the bioactive components correlated to specific drug targets, which is especially applicable to the complex extracts of natural products (Zhao et al., 2009; Cieśla and Moaddel, 2016). Affinity ultrafiltration can facilitate the rapid separation of small molecule ligands bound with large molecular receptors (drug targets) from unbound molecules, and LC–MS can enable the quick identification of potential bioactive ligands after they are released from the targets (Qin et al., 2015). In this regard, the combination of the two techniques is not only vital to reveal the effective phytochemicals of natural products, such as medicinal plants, but also conducive to drug discovery (Qin et al., 2015; Ma et al., 2020). To date, UF–LC/MS technology has been successfully applied to screen bioactive ingredients in natural products by employing various disease-related drug targets (Mulabagal and Calderón, 2010; Lavecchia et al., 2013; Li et al., 2015; Chen et al., 2020; Zhang et al., 2021).

In light of these inspiring research ideas and the research progress in both phytochemicals and pharmacology on *P. sinense*, Topo I, Topo II, COX-2, and ACE2 were chosen as the potential drug targets to synchronously screen for their correlated bioactive components. Among these drug targets, DNA topoisomerase (Topo) catalyzes the DNA topological changes by breaking DNA strands transiently and plays a fundamental role in cell life (You and Gao, 2019). Generally, DNA topos are divided into type I and type II, therein Topo I fractures a single strand of duplex DNA to alter the topological structure, while Topo II breaks double strands to transform the topological structure (Delgado et al., 2018). These two enzymes, belonging to ribozymes, maintain the normal topological heterogeneity of the double-stranded DNA and are highly expressed in tumor cells (Liang et al., 2019). Consequently, they have become pivotal therapeutic targets for anticancer drugs currently, and their novel inhibitors are being actively sought (Sinha, 1995; Liang et al., 2019). With regard to cyclooxygenase 2 (COX-2), it is known as a key rate-limiting enzyme in the biosynthesis of the prostaglandins (PGs), which plays a dominant role in the pathophysiological process of chronic inflammation and cancer (Regulski et al., 2016; Mahboubi Rabbani and Zarghi, 2019). That is to say, the synthesis of PGs could be blocked by inhibiting the activity of COX-2, which further induces tumor cell apoptosis and inhibit tumor angiogenesis, invasion, and metastasis (Peng et al., 2018). Meanwhile, COX-2 inhibitors are a new generation of antitumor drugs with fewer side effects and high curative powers, which can be used as auxiliary drugs for the treatment of cancer, and their design and synthesis have been the hot spots for researchers (Mahboubi Rabbani and Zarghi, 2019). As for angiotensin-converting enzyme II (ACE2), it is a type I transmembrane metal carboxypeptidase, a homolog of carboxypeptidase ACE, which generates angiotensin II, the main active peptide of the renin–angiotensin system (RAS) (Hooper et al., 2020). ACE2 is widely expressed in the human lungs, heart, liver, kidney, and gastrointestinal mucosa (Leung et al., 2020). Meanwhile, ACE2 also plays an extremely critical role in the whole process of SARS-CoV-2 infection and disease (Shahid et al., 2020). The first point is that ACE2 can act as a receptor and bind to the viral S protein to mediate viral infection. Several studies have indicated that the viral infection could

upregulate the ACE2 receptor, which is the main binding receptor used by the SARS-CoV-2 virus to enter host cells, and then exert an essential impact on the pathogenesis of severe lung failure (Gheblawi et al., 2020). Moreover, ACE2 can also participate in the process of acute lung injury and can be used as a key regulator to protect against acute lung injury (Kuba et al., 2010). In addition, ACE2, a powerful negative regulator, can regulate the RAS and participate in the process of lowering blood pressure (Garvin et al., 2020). Finally, as an essential biomolecule for the expression of neutral amino acid transporters on the surface of epithelial cells, ACE2 can bind to amino acid transporters and affect the process of amino acid absorption by the intestines and kidneys (Kuba et al., 2010). To the best of our knowledge, we, for the first time combine the UF–LC/MS method with the above-mentioned four drug targets that are closely correlated to the reported pharmacological effects of *P. sinense*, aiming to simultaneously explore the correlations between its bioactive chemical components and the underlying mechanisms of antitumor, anti-inflammation, and antivirus, which could provide the first piece of evidence to show that it acts in a multi-target and multi-component manner. In addition, this work would also provide a sufficient theoretical basis for further drug research and development efforts and rational clinical use of *P. sinense* in the near future.

MATERIALS AND METHODS

Plant Materials

The medicinal material was the dried rhizome of *P. sinense*, and it was collected from the Shennongjia forest area in Hubei province. Afterward, the identification of the specimen was enthusiastically assisted by Professor Guangwan Hu, a senior taxonomist of the Key Laboratory of Plant Germplasm Enhancement and Specialty Agriculture (Wuhan Botanical Garden), Chinese Academy of Sciences. This material was packed in sealed polyethylene bags and then stored in the refrigerator at 4°C until further use.

Chemicals and Reagents

The chemical standards of diphyllin, diphyllin *O*-glucoside, podophyllotoxin, kaempferol, kaempferol 3-*O*-glucoside, and quercetin 3-*O*-glucoside (Purity ≥98.0%) were bought from Chengdu Alfa Biotechnology Co., Ltd. (Chengdu, China), Shanghai Aladdin Bio-Chem Technology Co., Ltd. (Shanghai, China), and Shanghai Tauto Biotech Co., Ltd. (Shanghai, China), respectively. 5-Fluorouracil (5-FU), indomethacin, and etoposide were purchased from Shanghai Aladdin Bio-Chem Technology Co., Ltd. (Shanghai, China) and Shanghai Yuanye Bio-technology Co., Ltd. (Shanghai, China). Topo I, Topo II, COX-2, and ACE2 were provided by New England Biolabs (Ipswich, MA, United States), Sigma-Aldrich (St Louis, MO, United States), and Novoprotein (Shanghai, China), respectively. The protein-staining sulforhodamine B (SRB) cell proliferation and cytotoxicity detection kits were purchased from Shanghai BestBio Biotechnology Co., Ltd. (Shanghai, China). The COX-2 inhibitor screening assay kits were obtained from Shanghai Beyotime Biotechnology Co., Ltd. (Shanghai, China). The 30 kDa cut-off centrifugal ultrafiltration filters (YM-30) were bought from Millipore Co., Ltd. (Bedford, MA, United States). The Millipore membranes (0.22 μm) were purchased from Tianjin Jinteng Experiment Equipment Co., Ltd. (Tianjin, China). The HPLC grade solvents of formic acid (FA) and acetonitrile (ACN) were purchased from TEDIA Company Inc. (Fairfield, OH, United States). The pure water for the HPLC–ESI–MS was prepared by the EPED water system (Yeap Esselte Tech. Co., Nanjing, China). All other analytical grade chemicals and solvents were obtained from Shanghai Chemical Reagent Corp. (Shanghai, China).

Preparation of the Extracts from *P. sinense*

For the sample preparation, the rhizome of *P. sinense* was first crushed with a high-speed disintegrator. An aliquot of 200 g raw powders was weighed accurately and then was soaked in 90% ethanol overnight with the material-to-liquid ratio of 1:10. Next, ultrasonic extraction was performed at room temperature for 30 min. Then, the filtrate was obtained by vacuum filtration. And, the above extraction process was repeated two times. Finally, the three filtrates were combined and concentrated under reduced pressure to obtain ethanol extracts of *P. sinense*.

Affinity Ultrafiltration Procedures

The present affinity ultrafiltration screening procedures were carried out based on our previous methods with slight modifications (Chen et al., 2020). In brief, the crude extracts of *P. sinense* were accurately weighed and fully dissolved in tri (hydroxymethyl) aminomethane hydrochloride (Tris-HCl, pH 7.80) or phosphate buffer saline (PBS, pH 6.87) to prepare the sample solutions for ultrafiltration screening. One hundred microliters of tested sample solution (at a final concentration of 2 mg/ml) was incubated with 10 μl of Topo I (5 U), Topo II (2 U), COX-2 (4 U), or ACE2 (0.5 μg) in a constant temperature shaking incubator at 37°C for 40 min. After incubation, the mixtures were transferred to a 30 KD ultrafiltration tube and then centrifuged at 10,000 rpm for 10 min. Then, the filtrates were eluted by 200 μl of Tris-HCl or PBS three times to eliminate unbound ligands. Subsequently, the ligands specifically bound to Topo I, Topo II, COX-2, or ACE2 were released from the complexes by cultivating 10 min at room temperature with 200 μl of 90% methanol, and after that they were centrifuged at 10,000 rpm for 10 min with three times. Ultimately, all the residues above were collected and reestablished in 50 μl of methanol after lyophilizing, and then analyzed using the HPLC–ESI–MS/MS. Meanwhile, the inactivated enzyme solution, which was placed in boiling water for 10 min, was regarded as the control group adopting the same procedure as above.

HPLC–ESI–MS/MS Conditions

The crude extracts of *P. sinense* were dissolved in methanol ahead of schedule. The two filtrates mentioned above were analyzed straight away employing the HPLC–ESI–MS/MS system with a TSQ Quantum Access MAX mass spectrometer (Thermo Fisher Scientific, San Jose, CA, United States), which is coupled to a Thermo Access 600 HPLC system. Chromatographic separations

were performed on a Waters Symmetry RP-C18 column (4.6 mm × 250 mm, 5 μm) and connected with a guard column at 30°C. The mobile phase consisted of 0.1% FA-H_2O (A) and ACN (B), and the optimized gradient chromatographic conditions were carried out as follows: 0 min, 5% (B); 40 min, 95% (B). The injection volume was adjusted to 10 μl, the flow rate was set as 0.8 ml/min, and the UV chromatograms were monitored at a wavelength of 292 nm.

Considering the ESI-MS/MS analysis, the triple quadrupole mass spectrometer electrospray ionization (ESI) was adopted to obtain various fragment ions in the positive ion mode. The optimized instrument conditions were implemented as follows: the spray voltage, vaporizer temperature and capillary temperature were 3,000 V, 350 and 250°C, respectively; the cone voltage, sheath gas pressure, and aux gas pressure were 40.0 V, 40, and 10 psi, respectively; the acquisition data of *m/z* ranging from 150 to 1,000 were gained in the full-scan mode; the collision energy varied from 30 to 45 eV for the MS/MS analysis in the data-dependent scanning mode. Eventually, all the above data available were acquired from the professional software of Thermo Xcalibur ChemStation (Thermo Fisher Scientific).

Anti-Proliferative Assay *in vitro*

Cell proliferation was determined by SRB assay according to the manufacturer's instructions (Vichai and Kirtikara, 2006). Non-small lung cell cancer (A549) and colon cancer (HT-29) cell lines were maintained in Dulbecco's Modified Eagle's Medium (DMEM) replenished with 1% penicillin–streptomycin and 10% fetal bovine serum (FBS), and further incubated in 5% CO_2 and 90% relative humidity at 37°C. In brief, these two cell lines were seeded into 96-well plates with a density of 1.0×10^4 per well and grown overnight. Next, the cells were treated with various concentrations of samples and incubated for 48 h. The medium with less than 0.1% DMSO was used as the blank control in this assay, and 5-FU as well as etoposide was regarded as the positive controls. The optical density (OD) value of each well was recorded at 540 nm with a multifunctional microplate reader (Tecan Infinite M200 PRO, TECAN, Männedorf, Switzerland). The inhibition rate was estimated and calculated, as shown in the formula:

$$\textbf{Inhibition rate}\ (\%) = \frac{(\mathbf{OD_C} - \mathbf{OD_S})}{\mathbf{OD_C}} \times 100\%,$$

where OD_C is the absorbance value of the blank control, and OD_S is the absorbance value of the tested sample or positive control. The data were expressed as means ± standard deviation (SD) of three replicates.

COX-2 Inhibitory Assay *in vitro*

The COX-2 inhibitory assay was performed utilizing a COX-2 inhibitor screening kit to detect the *in vitro* anti-inflammatory activity of these screened compounds as previously described, with slight modifications (Fan et al., 2015). In brief, COX-2 probe (50 X), COX-2 cofactor (50 X), and COX-2 substrate (50 X) were placed in DMSO at 37°C for 2 min to promote melting, and all the above solutions were diluted 10 times with the COX-2 assay buffer. Next, Tris-HCl (150 μl, pH 7.90), COX-2 cofactor (10 μl), and COX-2 (10 μl) solutions were mixed in a 96-well blackboard. An aliquot of 10 μl sample solution with the tested concentrations of 0.625–20 μM was added into mixtures and incubated at 37°C for 10 min. Subsequently, 10 μl of COX-2 probe was added to each well, and the reaction mixture was initiated by adding 10 μl of COX-2 substrate quickly. Finally, fluorescence measurement was performed after incubation in the dark at 37°C for 5–20 min. The excitation wavelength of the reaction mixtures was set at 560 nm, and the emission wavelength was monitored at 590 nm. The calculation of inhibition rate using the formula was as follows:

$$\textbf{Inhibition rate}\ (\%) = \frac{(\mathbf{RFU_1} - \mathbf{RFU_2})}{(\mathbf{RFU_3} - \mathbf{RFU_4})} \times 100\%.$$

Here, RFU_1, RFU_2, and RFU_3 represented the relative fluorescence unit of 100% enzyme activity control group, tested sample, and the blank control group, respectively. Meanwhile, indomethacin, a kind of non-steroidal anti-inflammatory drug (NSAID) (Lucas, 2016), was regarded as the positive control. COX-2 assay buffer without COX-2 and the tested sample were served as the blank control. Each sample solution was tested in three parallels, and the final experimental results were expressed in the form of means ± SD.

Molecular Docking Analysis

Molecular docking assay was applied to simulate and analyze the binding energy, binding site, and the mode of action between screened potential phytochemicals and Topo I, Topo II, COX-2 or ACE2 by employing the computational program AutoDock Vina 1.5.6 and Discovery Studio 4.5 Client (Towler et al., 2004). The analytical procedures were primarily comprised of the determination of the interaction sites between the receptor and the ligand, generation of the scoring system, and the calculation of docking results. Firstly, the 3D structure of Topo I (PDB ID: 1T8I), Topo II (PDB ID: 3QX3), COX-2 (PDB ID: 1CX2), and ACE2 (PDB ID: 1R42) was downloaded from the PDB databases (www.rcsb.org). The structure of the ligand was processed by ChemBioDraw Ultra 14.0, and the file was modified to PDB format. After that, the receptor and ligand were processed by hydrogenating, calculating the charge, and confirming the protonation state using AutodockTools software. The receptor and the ligand were converted to readable file format (pdbqt). Subsequently, AutoGrid processing was performed to set the box size (60 × 60 × 60), spacing (0.375), and the docking active site of Topo I (*X*: 21.474; *Y*: −2.226; *Z*: 27.863), Topo II (*X*: 33.026; *Y*: 95.765; *Z*: 51.567), COX-2 (*X*: 24.263; *Y*: 21.528; *Z*: 16.497), or ACE2 (*X*: 52.874; *Y*: 68.399; *Z*: 33.501). Finally, after setting the relevant parameters, AutoDock calculations on the genetic algorithm (run 50 times) were conducted for the structure of small molecule receptors in a flexible way. In addition, 5-FU and camptothecin were considered as the positive control against Topo I. MLN-4760 and chloroquine were regarded as the positive control against ACE2. Etoposide and indomethacin were deeded as the positive control against Topo II and COX-2, respectively.

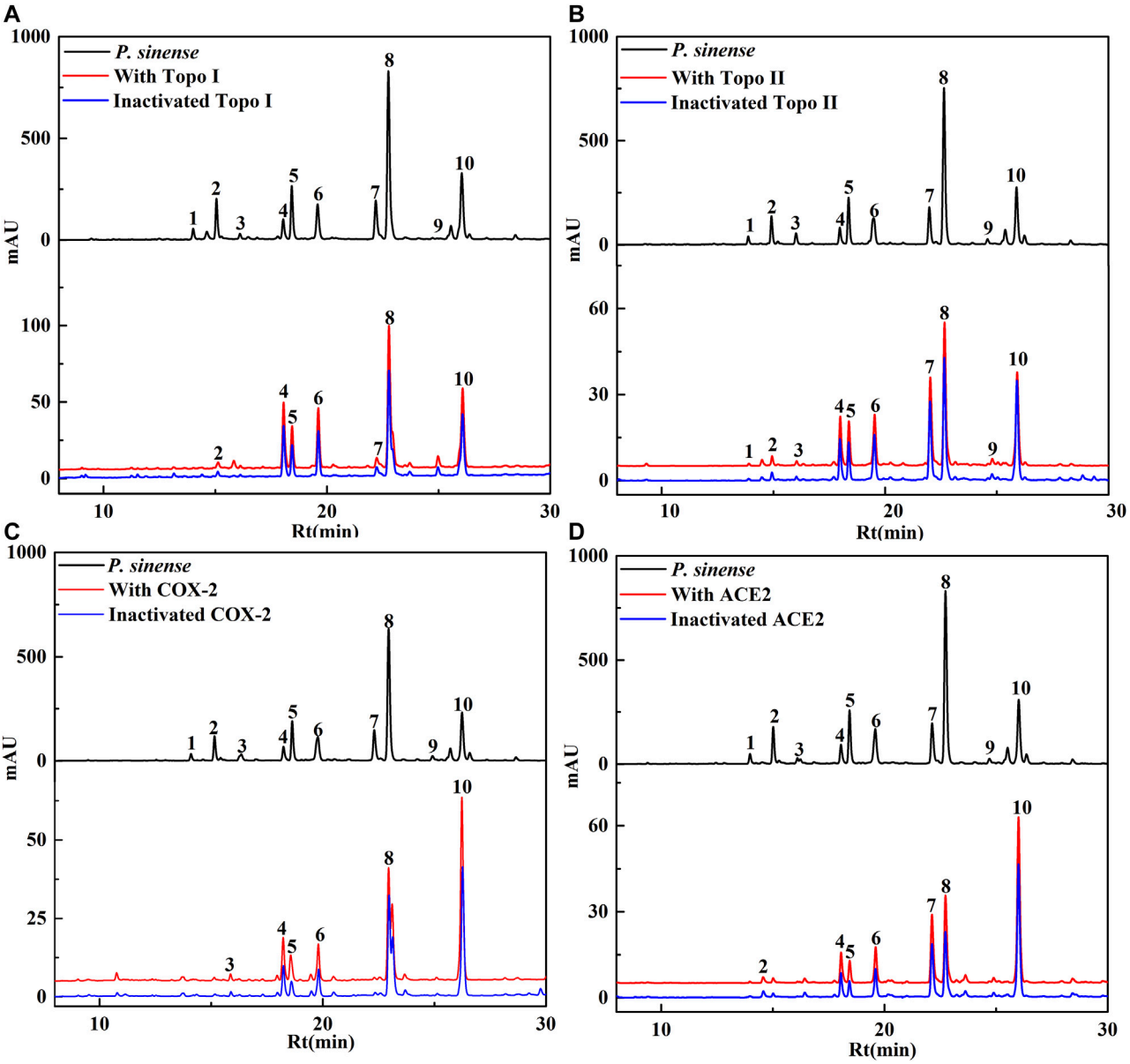


FIGURE 1 | HPLC chromatograms of the chemical constituents in *P. sinense* were obtained after ultrafiltration at 292 nm. The black solid line represents HPLC profiles of the crude extracts of *P. sinense* without ultrafiltration; the red line and blue line represent the total extract of *P. sinense* with activated and inactivated Topo I **(A)**, Topo II **(B)**, COX-2 **(C)**, and ACE2 **(D)**, respectively.

Statistical Analysis

All the resulted values were expressed as means ± SD in triplicate, and the differences were regarded to be significant at $p < 0.05$ for all analyses. The half maximal inhibitory concentration (IC_{50}) values were obtained by means of plotting the inhibitory rates against tested sample concentrations with a series of different concentration gradients. Statistical data analysis in the present study was performed by applying the GraphPad Prism 8 Software (GraphPad Software Corp., Sam Diego, CA, United States), the Origin 2019 Software (OriginLab Corp., Northampton, MA, United States), the ChemBioOffice 14.0 Software (CambridgeSoft Corp., Cambridge, MA, United States), and the SPSS 16.0 Software (SPSS Inc., Chicago, IL, United States).

RESULTS

Ultrafiltration Analysis of Topo I, Topo II, COX-2, and ACE2 Ligands in *P. sinense*

P. sinense has been utilized as a folk medicine for centuries in China. Numerous studies have shown that *P. sinense* possesses significant antiproliferative, anti-inflammatory, and antiviral

TABLE 1 | EFs and the UF–LC/MS data of the bioactive compounds bound to Topo I, Topo II, COX-2, and ACE2 from the crude extracts of *P. sinense*.

Peak No.	Rt[a] (min)	EFs[b] (%)				[M+H]$^+$	Characteristic fragment (*m/z*)	Identification
		Topo I	Topo II	COX-2	ACE2			
1	13.88	—	0.20	—	—	465	465, 303, 85	Quercetin 3-*O*-glucoside[c]
2	14.92	0.37	0.18	—	0.22	449	449, 287	Kaempferol 3-*O*-glucoside[c]
3	16.02	—	0.49	1.49	—	415	313, 298, 282, 229	Podophyllotoxin isomer[d]
4	17.98	9.36	2.86	4.40	2.76	543	381, 363, 351, 333, 305	Cleistanthin B isomer[d]
5	18.37	2.38	1.15	1.39	0.65	397	397, 313, 282, 229	*β*-Apopicropodophyllin[d]
6	19.49	3.07	0.90	1.14	1.37	543	381, 363, 351, 333, 305	Diphyllin *O*-glucoside[c]
7	21.98	0.48	1.04	—	3.10	287	287, 241, 213, 165, 153	Kaempferol[c]
8	22.64	3.89	1.17	1.61	1.31	415	397, 313, 282, 247, 229	Podophyllotoxin[c]
9	24.59	—	1.08	—	—	395	395, 380, 351, 336, 320	Chinensinaphthol methyl ether[d]
10	25.88	4.41	0.26	5.25	3.68	381	381, 363, 351, 333, 305	Diphyllin[c]

[a]*Rt, retention time.*
[b]*EFs, enrichment factors.*
[c]*Compared with the corresponding standards.*
[d]*Identified based on the published literature.*

activities (Castro et al., 2003; Yousefzadi et al., 2010). In order to further offer a new theoretical basis for the clinical use of the *P. sinense*, this study took advantage of the UF–LC/MS strategy with four drug targets (Topo I, Topo II, COX-2, and ACE2) to rapidly screen out and identify active constituents corresponding to its antiproliferative, anti-inflammatory, and antiviral activities as reported. After incubation with Topo I, Topo II, COX-2 or ACE2 for affinity ultrafiltration, the bound ligands in *P. sinense* were released and further characterized by HPLC–MS analysis. **Figure 1** displayed that the HPLC chromatograms of the chemical components from *P. sinense* exhibited obvious differences after the interaction with Topo I, Topo II, COX-2, and ACE2, respectively.

Based on the variations in the chromatographic peaks of the components from the crude extracts of *P. sinense* before and after incubated with Topo I, Topo II, COX-2, and ACE2, the enrichment factor (EF) values will be applied to evaluate the degree of affinities between the potential bioactive components from *P. sinense* and the target enzymes. The EF value was computed, as shown in the following formula:

$$\mathbf{EF}\ (\%) = \frac{(\mathbf{A}_1 - \mathbf{A}_2)}{\mathbf{A}_0} \times 100\%.$$

Here, A_1, A_2, and A_0 represent the peak area of each chromatographic peak from the crude extracts of *P. sinense* that is treated with activated, inactivated, and without Topo I, Topo II, COX-2, and ACE2, respectively (Chen et al., 2020). When employed to evaluate the affinity between the active constituents and the enzyme, the EF value implies the ability of diverse components to bind to the target enzyme. These components were further identified based on the MS/MS data in comparison with the spectra of corresponding standards or related references, and the results were revealed in **Table 1**. As expected, the EF values of each constituent listed in the table deviated from each other. It was observed that 7, 10, 6, and 7 chemical components in the HPLC chromatograms incubated with active Topo I, Topo II, COX-2, and ACE2 in *P. sinense* were provided with higher peak areas than that of the inactivated control group, respectively. The results indicated these constituents exerted specific binding towards Topo I, Topo II, COX-2, or ACE2, and thus were considered as primary potential ligands for Topo I, Topo II, COX-2, and ACE2, respectively. Notably, it is the first time to clearly describe the primary Topo I, Topo II, COX-2, and ACE2 ligands in *P. sinense*.

Structural Identification of Topo I, Topo II, COX-2, and ACE2 Ligands in *P. sinense*

The samples after affinity ultrafiltration screening were subsequently analyzed by HPLC–ESI–MS/MS to exploit the ligands corresponding to Topo I, Topo II, COX-2, and ACE2, respectively. The HPLC–ESI–MS/MS analysis was carried out in the positive ion mode. The retention time (Rt), quasi-molecular ([M+H]$^+$), and the characteristic MS/MS fragments of each component were shown in **Table 1**. By comparing with the MS/MS fragments of the chemical composition reported in the literature, as well as the spectrum of the corresponding standards, 10 potential bioactive compounds screened from the crude extracts of *P. sinense* were identified in total, and their chemical structures were presented in **Figure 2**.

Peak 1 exhibited the [M+H]$^+$ ion at *m/z* 465, and the aglycon ion [M+H-$C_6H_{10}O_5$]$^+$ was further generated at *m/z* 303 by losing a hexose moiety, which was speculated to be quercetin monoglycoside. By comparison with the ion fragments of the existing standards, thus the peak 1 was identified as quercetin 3-*O*-glucoside (isoquercitrin, calculated for $C_{21}H_{20}O_{12}$, 464 Da). Peak 2 presented the [M+H]$^+$ ion at *m/z* 449, and the aglycone fragment ions at *m/z* 287 indicated the loss of a hexose moiety [M+H-$C_6H_{10}O_5$]$^+$. Comparing the retention time and the MS/MS spectra with the ion fragments of the corresponding standards, peak 2 was determined to be kaempferol 3-*O*-glucoside (astragalin, calculated for $C_{21}H_{20}O_{11}$, 448 Da). Peak 7 ([M+H]$^+$ at *m/z* 287) was considered to be kaempferol (calculated for $C_{15}H_{10}O_6$, 286 Da) by comparing its LC–MS/MS with the standard compound. Peak 8 showed the [M+H]$^+$ ion at *m/z* 415 and further suffered a neutral loss of the water molecular moiety to produce the fragment ion of the [M+H-H_2O]$^+$ ion at *m/z* 397. Typically, the ions at *m/z* 313 and *m/z* 282

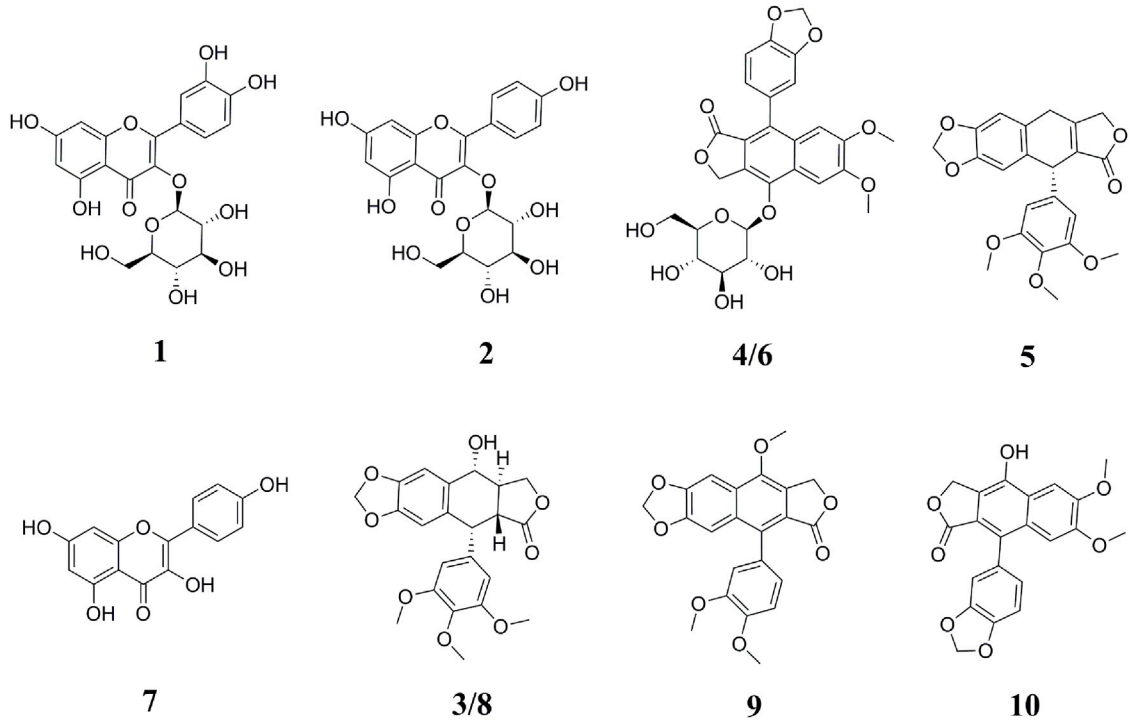


FIGURE 2 | Chemical structures of bioactive compounds identified from *P. sinense* based on the MS/MS spectra or the corresponding standards. The peak numbers in this figure correspond to those listed in **Table 1**.

were accorded with the characteristic retro Diels–Alder (RDA) cleavage ($[M+H-H_2O-C_4H_4O_2]^+$) and the neutral loss of the methomyl moiety ($[M+H-H_2O-C_4H_4O_2-OCH_3]^+$), respectively. In addition, the fragment ions of $[M+H-C_6H_3(OCH_3)_3]^+$ at *m/z* 247 and $[M+H-C_6H_3(OCH_3)_3-H_2O]^+$ at *m/z* 229 were regarded as the successive neutral losses of the trimethoxyphenyl moiety and the water molecular moiety, respectively. Based on the comparison of the LC–MS/MS analysis to the corresponding standards, peak 8 was thus identified as podophyllotoxin (calculated for $C_{22}H_{22}O_8$, 414 Da). Similarly, peak 3 ($[M+H]^+$ at *m/z* 415) and peak 5 ($[M+H]^+$ at *m/z* 397) generated the parallel characteristic fragment ions in contrast to peak 8 (Lautié et al., 2008). Hence, peak 3 was tentatively identified as the isomers of peak 8. As for peak 5, it was tentatively suggested as *β*-apopicropodophyllin (calculated for $C_{22}H_{20}O_7$, 396 Da) when compared with those of the ESI–MS/MS spectra and the corresponding fragmentation pathways. For the sake of further elucidating the structures of those lignans, the ESI–MS/MS spectra and representative fragmentation pathways of Peak 8 were revealed in **Figure 3**. Tentatively, comparing their MS/MS spectra with the corresponding standards and the related literature reported previously, peaks 6 and 10 were deduced as diphyllin *O*-glucoside (cleistanthin B, calculated for $C_{27}H_{26}O_{12}$, 542 Da) and diphyllin (calculated for $C_{21}H_{16}O_7$, 380 Da) (Jullian-Pawlicki et al., 2015), respectively. Peaks 4 and 6 displayed the identical $[M+H]^+$ ion at *m/z* 543 and the MS/MS spectra at *m/z* 381, 363, 351, 333, and 305, implying that they were structural isomers. Fragment ions at *m/z* 381, 363 and 333 were obtained by the losses of a hexose moiety, the methyl moiety and CO_2 moiety, respectively. For Peak 9 ($[M+H]^+$ at *m/z* 395), fragment ions of $[M+H-CH_3]^+$ at *m/z* 380 and $[M+H-CO_2]^+$ at *m/z* 351 were produced by the losses of the methyl moiety and CO_2 moiety, respectively. Based on the comparison of the conceivable fragmentation pathways and the MS/MS spectra of the published literature, peak 9 was deduced as chinensinaphthol methyl ether (calculated for $C_{22}H_{18}O_7$, 394 Da) (Qin et al., 2016).

Anti-Proliferative and COX-2 Inhibitory Assays on Ligands Screened from *P. sinense*

In order to associate pharmacological effects with potential active phytochemicals, antiproliferative and COX-2 inhibitory assays *in vitro* were performed to assess and verify the inhibitory effects of several screened ligands on Topo and COX-2. Herein, 5-FU and etoposide were considered as the positive controls for antiproliferative assay *in vitro*. Indomethacin was used as the positive control for COX-2 inhibitory assays *in vitro*. For antiproliferative assay *in vitro*, **Figure 4** showed the inhibitory effects of these selected components and two positive drugs on A549 and HT-29 cells. Among these compounds, diphyllin (Peak 10) and podophyllotoxin (Peak 8) exhibited higher inhibitory rates against A549 and HT-29 cells at a concentration of 100 μM in contrast to 5-FU and etoposide, thereinto, the IC_{50} values of diphyllin were computed at 6.46 ± 1.79 and 30.73 ± 0.56 μM on A549 and HT-29 cells, respectively. As for COX-2 inhibitory

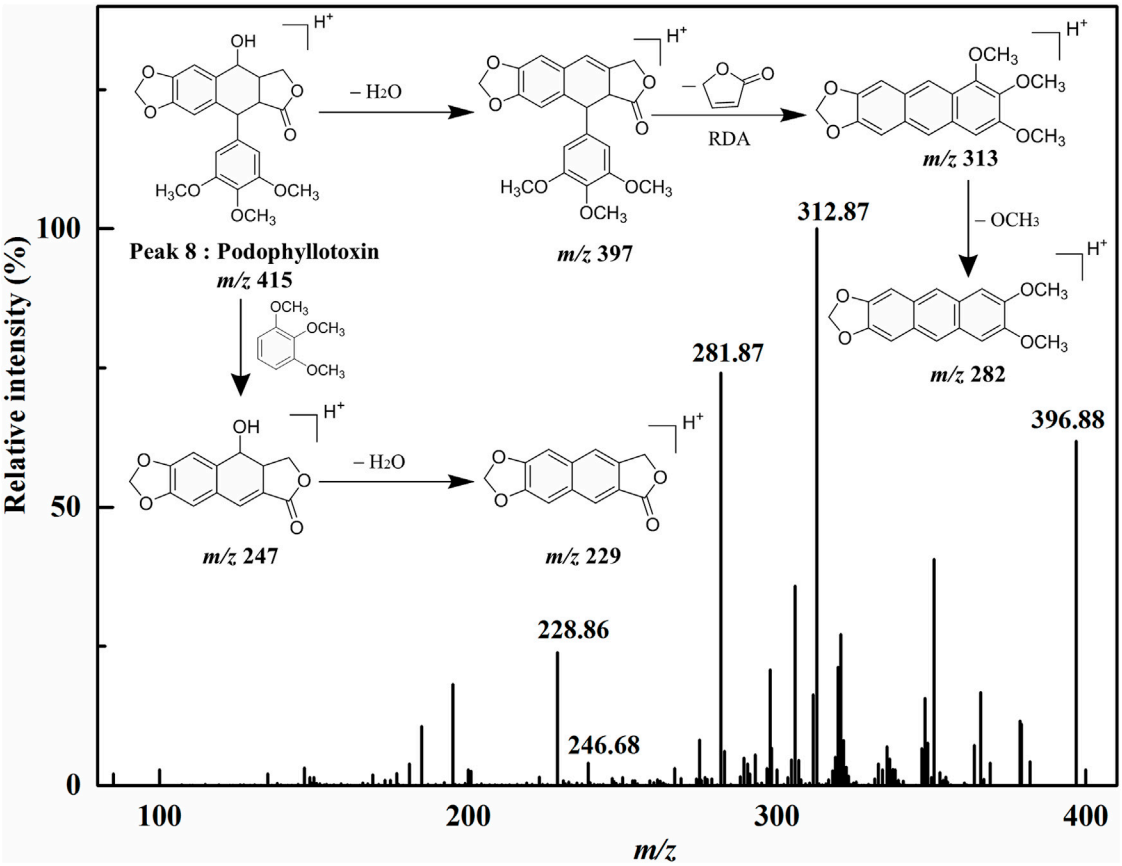


FIGURE 3 | ESI-MS/MS spectra and the proposed fragmentation pathways of Peak 8.

assays *in vitro*, **Table 2** enumerated the IC_{50} values of the representative compounds screened from *P. sinense*. Diphyllin, as the representative potentially anti-inflammatory component with the highest EF value, displayed good inhibition with the IC_{50} value at 1.29 ± 0.14 μM, compared to indomethacin at 1.22 ± 0.08 μM. Furthermore, podophyllotoxin and diphyllin *O*-glucoside (Peak 6) with the lower EF values exhibited relatively low inhibition with the IC_{50} values at 10.49 ± 0.61 μM and greater than 20 μM in comparison to diphyllin and indomethacin, respectively. Consequently, it was worthwhile to screen out and identify these potentially active components from *P. sinense*.

Molecular Docking Analysis

Molecular docking is a crucial approach to predict and study the interactions between receptors and ligands. In order to further explore and comprehend the possible mechanism of action, molecular docking studies were carried out to simulate the interactions between Topo I, Topo II, COX-2, and ACE2 as well as several bioactive compounds screened from *P. sinense*. **Table 3** displayed the molecular docking results of potential bioactive ligands screened from *P. sinense* and positive drugs against Topo I, Topo II, COX-2, and ACE2. Therein, the results of the 2D and 3D ligand-to-target interactions between ACE2 and diphyllin, diphyllin *O*-glucoside or chloroquine were shown in **Figure 5**.

As shown in **Table 3**, diphyllin exhibited higher affinity to Topo I with the binding energy (BE) of -6.72 kcal/mol, and the theoretical IC_{50} value of 11.95 μM, lower than the positive control 5-FU (−3.70 kcal/mol and 1.95 mM), and slightly higher than Topo I inhibitor camptothecin (−7.57 kcal/mol and 2.85 μM). Kaempferol 3-*O*-glucoside displayed lower affinity to Topo I, and the BE as well as its theoretical IC_{50} value, was computed as −3.59 kcal/mol and 2.35 mM, higher than 5-FU, camptothecin, and diphyllin. With regard to Topo II, podophyllotoxin showed a strong affinity, which its BE and the theoretical IC_{50} value were calculated as −9.45 kcal/mol and 117.98 nM, lower than Topo II inhibitor etoposide (−7.62 kcal/mol and 2.59 μM), and kaempferol 3-*O*-glucoside (−5.28 kcal/mol and 134.95 μM). As for COX-2, the data of docking simulation unveiled that diphyllin expressed a high binding affinity value of −9.95 kcal/mol, and the theoretical IC_{50} value was 51.12 nM, which was relatively lower than the positive control indomethacin (−9.18 kcal/mol and 186.44 nM). Furthermore, diphyllin *O*-glucoside manifested a relatively low affinity to COX-2 with the BE of -4.4 kcal/mol and the theoretical IC_{50} value of 568.94 μM, higher than diphyllin. With respect to ACE2, diphyllin was discovered with a high binding affinity of −7.07 kcal/mol and the

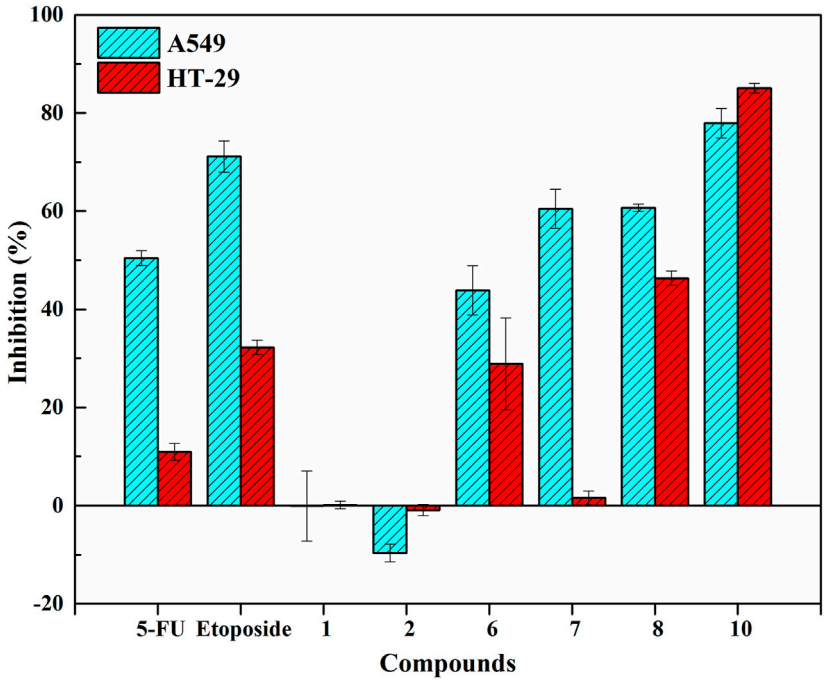


FIGURE 4 | Inhibitory effects of these selected components and two positive drugs on A549 and HT-29 cells.

TABLE 2 | The IC_{50} values of representative compounds screened from *P. sinense* against COX-2 *in vitro*.

No.	Compounds	IC_{50} (μM)[a]
1	Diphyllin	1.29 ± 0.14
2	Podophyllotoxin	10.49 ± 0.61
3	Diphyllin *O*-glucoside	>20
4	Indomethacin[b]	1.22 ± 0.08

[a]*IC_{50}, half-maximal inhibitory concentrations.*
[b]*Positive control.*

theoretical IC_{50} value at 6.52 μM, whereas chloroquine (as the positive control) and MLN-4760 (as the ACE2 inhibitor) were 1.01 and 738.62 μM with the BE of −8.18 and −4.27 kcal/mol, respectively. Similarly, diphyllin *O*-glucoside exerted a relatively strong binding efficiency and indicated the BE of −6.59 kcal/mol with ACE2 from the docking process with the theoretical IC_{50} value at 14.87 μM, respectively. Most importantly, several bioactive ligands screened and identified with the larger EF values possessed lower binding energies and inhibitory effects compared with the same group by molecular docking analysis based on ultrafiltration screening and other *in vitro* bioactivity assays. For instance, diphyllin with large EF values exerted high affinities to Topo I and COX-2, possessing antiproliferative and anti-inflammatory effects confirmed by *in vitro* bioactivity assays and molecular docking analysis. Podophyllotoxin with a relatively large EF value displayed a good affinity to Topo II, which indicated this compound was provided with good antiproliferative activity. The molecular docking results were in full compliance with the ultrafiltration screening and *in vitro* bioactivity verification results, thus further validating the feasibility of the molecular docking method.

DISCUSSION

Screening for Topo I, Topo II, COX-2, and ACE2 Ligands in *P. sinense*

Generally, the conventional strategy for the characterization of bioactive components from the medicinal plant is to extract, separate, and identify its chemical constituents by employing traditional phytochemical methods, and then to conduct various biological activity tests combined with pharmacological models to screen each chemical compound obtained (Zhang et al., 2013; Wang et al., 2019). However, the entire operation process was very time-consuming and labor-intensive. In addition, due to the inherent chemical complexity of herbal medicine and its diversified action targets of natural medicines corresponding to a wide range of medicinal uses for various disease indications, the traditional screening method cannot fully reflect the chemical basis of its medicinal effects (Wang et al., 2019).

As a consequence, in order to address the above limitations and challenges, biological activity-oriented research on the interactions between target enzymes and the small active

TABLE 3 | The molecular docking results of potential bioactive ligands screened from *P. sinense* and positive drugs against Topo I, Topo II, COX-2 and ACE2.

No.	Compounds	Drug targets	BE[a] (kcal/mol)	IC_{50} (μM)	H-bond atoms[b]
1	Diphyllin	Topo I	−6.72	11.95	Da113, Dc112, Asp533, Arg364
		COX-2	−9.95	0.05	Ala527, Arg120, His90, and Tyr355
		ACE2	−7.07	6.52	Asp350, Asp382
2	Diphyllin *O*-glucoside	COX-2	−4.43	568.94	Arg120, Gly526, Ser530, Tyr355, Tyr385
		ACE2	−6.59	14.87	Ala348, Arg514, Asn394, His378, Glu375, Pro346
3	Podophyllotoxin	Topo II	−9.45	0.12	Da12, Dt9, Gln778
4	Kaempferol 3-*O*-glucoside	Topo I	−3.57	2,350.00	Arg364, Arg488, Dg12, Thr718
		Topo II	−5.28	134.95	Dt9, Arg503
5	Camptothecin[c]	Topo I	−7.57	2.85	Da113, Dc112, Glu356, Lys425
6	5-FU[d]	Topo I	−3.70	1,950.00	Met428, Tyr426
7	Etoposide[e]	Topo II	−7.62	2.59	Da12, Gln778
8	Indomethacin[f]	COX-2	−9.18	0.19	Glu524
9	MLN-4760[g]	ACE2	−4.27	738.62	Glu375, Glu402, Thr371
10	Chloroquine[h]	ACE2	−8.18	1.01	His374, His378, Glu402

[a]*BE, binding energy.*
[b]*H-bond, hydrogen bond.*
[c]*Positive control.*
[d]*Positive control.*
[e]*Positive control.*
[f]*Positive control.*
[g]*Positive control.*
[h]*Positive control.*
Ala, alanine; Asp, aspartic acid; Arg, arginine; Gln, glutamine; Glu, glutamic acid; Gly, glycine; His, histidine; Lys, lysine; Met, methionine; Ser, serine; Thr, threonine; Tyr, tyrosine.

molecules integrated with the UF–LC/MS approach may provide a good solution. A schematic diagram of the UF–LC/MS screening assay is illustrated in **Figure 6**. Compared with conventional phytochemical methods, such as thin-layer chromatography (TLC), repeated column chromatography, and low throughput screening tests with purified individual compounds, this strategy can not only rapidly screen out the potential active components against specific targets for certain diseases from crude mixtures without tedious separation process, but also contribute partly to the elaboration of the mechanisms of action for the traditional herbal medicine of interest at the cellular and molecular levels; thereby would offer new tactics for the better use or improving the therapeutic efficacy of diseases (Qin et al., 2015). In light of that, the UF–LC/MS approach was applied to rapidly screen and identify 7, 10, 6, and 7 potential active ligands against Topo I, Topo II, COX-2, and ACE2 from *P. sinense*, respectively.

According to the EF values of each component screened from the crude extracts of *P. sinense*, peaks 4, 6, 8, and 10 exhibited relatively higher affinity with Topo I or Topo II, and they were preliminarily inferred to be primary antiproliferative active compounds; in addition, peak 10 exerted stronger binding affinity with COX-2 compared with other peaks, and it was presumed to be the dominating anti-inflammatory active component; and there are several compounds, such as peaks 4, 6, 7, 8, and 10, revealing better binding affinities to the ACE2, which may be its prime antiviral active ingredients. On the one hand, peak 8 associated with Topo I and Topo II exhibited relatively good affinity, which was speculated that this composition may act on these three enzymes so as to exert potential antitumor effects. And the same components like peak 4 binding to Topo I, Topo II, COX-2, and ACE2 exerted relatively good affinity. Similarly, peak 10 presented good affinity to Topo I, COX-2, and ACE2. These results indicated that there existed in the alike bioactive components in *P. sinense* for the multipurpose pharmacological effects. On the other hand, the compounds with larger EF values were more strongly bound to the target enzyme, and more ingredients can be retained during their reactions with the drug targets. In the meantime, due to a large number of active components screened out, there existed synergistic effects among these compounds, jointly exerting multiple effects in clinical practice. Theoretically, the discrepant EF values may be ascribed to their competitively differential interactions with Topo I, Topo II, COX-2, and ACE2. In order to further explore the mechanisms of action underlying the multifunctional use of *P. sinense* in the multi-component and multi-target manner, the potential bioactive compounds screened out from *P. sinense* with multiple drug targets including Topo I, Topo II, COX-2 and ACE2 were then reconstructed as interaction network diagrams to better demonstrate the correlations between the diverse chemical components and their corresponding targets, as shown in **Figure 7**.

In vitro Bioactive Validation of the Representative Bioactive Compounds

Considering the above screening results listed in **Table 1**, lignans accounted for the primary bioactive constituents, which was consistent with the results revealed by the previous phytochemical studies (Ma et al., 1993). Furthermore, lignans also exerted various and striking pharmacological activities, including antiproliferative, anti-inflammatory, antiviral and insecticidal effects (Yuan et al., 2011; Liu et al., 2015). Subsequently, further functional assays were carried out to validate their activities so as to better correlate the

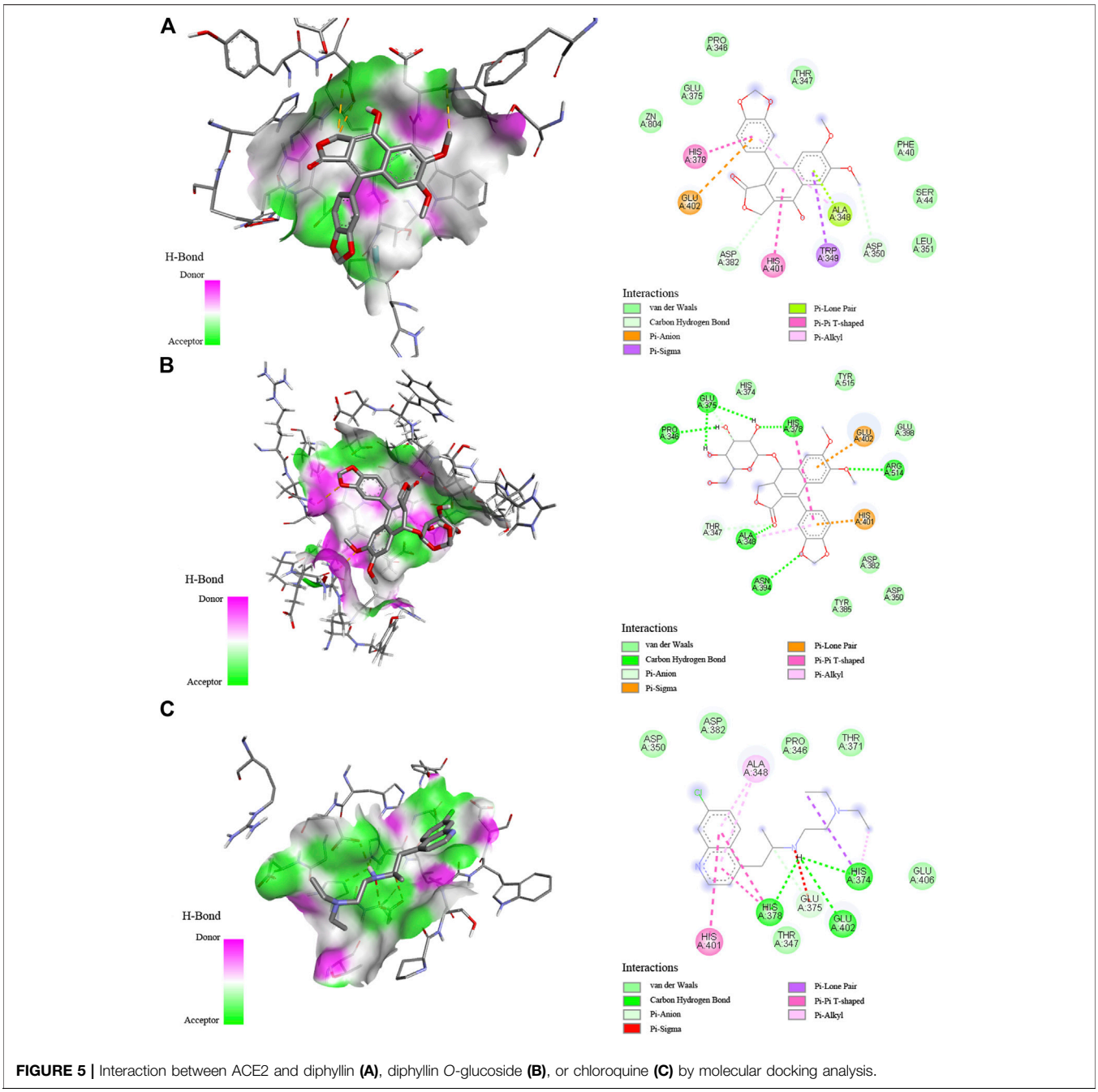


FIGURE 5 | Interaction between ACE2 and diphyllin **(A)**, diphyllin *O*-glucoside **(B)**, or chloroquine **(C)** by molecular docking analysis.

phytochemical components with pharmacological activities. For the underlying antiproliferative effects, diphyllin and podophyllotoxin with the higher specific binding to Topo I or Topo II in view of our screening experiments and the verification results reported in the literature, we preliminarily inferred that these compounds were considered as the potential Topo I or Topo II ligands and possessed remarkable anti-tumor activity. It was assumed that these components could exert cytotoxic activity on multifarious cancer cell lines by interfering with cell cycle progression, giving rise to DNA damage and inducing apoptosis. As shown in **Figure 4**, it could be observed that the inhibitory rates of these selected compounds were consistent with the results of ultrafiltration screening based on their EF values. Among these verified components, diphyllin and podophyllotoxin with larger EF values displayed good inhibitory effects on A549 and HT-29 cells compared with the positive controls of 5-FU and etoposide for antiproliferative assay *in vitro*. Compared with the positive control indomethacin, podophyllotoxin and diphyllin with higher EF values showed favorable inhibitory activities for COX-2 inhibitory assay *in vitro*. Thus, it could be seen that the above successful *in vitro* verification experiments of bioactive components screened from *P. sinense* comprehensively

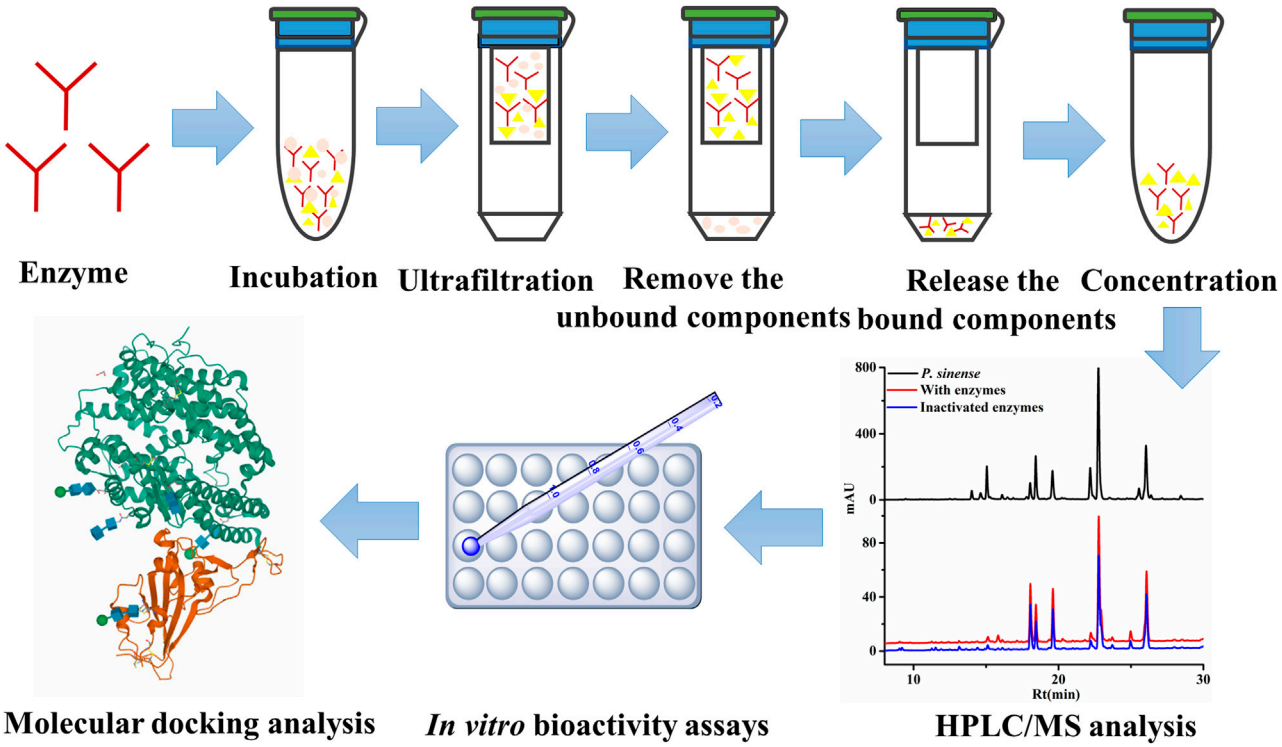


FIGURE 6 | Schematic diagram of UF–HPLC/MS assay to screen and identify the ligands against different drug targets.

clarified the feasibility of the UF-LC/MS approach. Meanwhile, this technology can be employed efficiently to guide further research on the correlation between bioactive constituents and multi-pharmacological activities linked to multiple drug targets, which can provide new opportunities for discovering more therapeutic agents from natural products.

Molecular Docking Studies

Several component groups had been rapidly screened from the crude extract of *P. sinense* and preliminarily considered to possess potentially promising antiproliferative, anti-inflammatory, and antiviral effects as shown in **Table 1**. Therein, diphyllin displayed a high affinity to Topo I, COX-2, and ACE2 with large EF values of 4.41, 5.25, and 3.68, respectively. Diphyllin *O*-glucoside exhibited relatively low and moderate affinity to COX-2 and ACE2 with the EF values of 1.14 and 1.37 compared with the corresponding drug targets in the same group, respectively. Podophyllotoxin with a relatively large EF value of 1.17 exerted a good affinity to Topo II. Kaempferol 3-*O*-glucoside with the EF values of 0.37 and 0.18 indicated a relatively low affinity to Topo I and Topo II, respectively. The molecular docking simulation exhibited that these bioactive ligands screened were chiefly docked within the active sites of four drug targets of interest. Meanwhile, the docking analysis could further elaborate the interactions and the underlying mechanisms of action between these potentially bioactive compounds and multiple drug targets including Topo I, Topo II, COX-2, and ACE2.

The docking results verified that the chemical structures of the bioactive ligands significantly affected the interaction sites and binding affinities with Topo I, Topo II, COX-2, and ACE2. More importantly, the active sites and hydrogen bonds (H-bonds) played very crucial roles in the catalytic ability of Topo I, Topo II, COX-2, and ACE2. When several compounds and their respective positive controls were docked with Topo I, Topo II, COX-2, and ACE2, the BE and the theoretical IC_{50} values were ordered as camptothecin > diphyllin > 5-FU; podophyllotoxin > etoposide; diphyllin > indomethacin; chloroquine > diphyllin > diphyllin *O*-glucoside > MLN-4760; the amount of formed H-bonds was ranked as follows: diphyllin = camptothecin > 5-FU; podophyllotoxin > etoposide; diphyllin > indomethacin; and diphyllin *O*-glucoside > chloroquine = MLN-4760 > diphyllin. The results indicated that these compounds exerted good inhibitory activities against Topo I, Topo II, COX-2 and ACE2.

Among these compounds, diphyllin was lodged into the active pocket of the Topo I-DNA complex by forming H-bonds between the hydroxyl groups of B ring and the key amino acid residue Asp533. In the meantime, H-bonds with DNA residue Dc112 enhanced their interaction to DNA strands. Furthermore, the lactone ring 5-oxo of its C ring shaped H-bonds with the residues Arg364 and Da113. In addition, it could also be clearly found that this top active ligand was provided with a strong binding with COX-2. The lactone ring 5-oxo group of C ring of diphyllin interacted with the key residues of COX-2 including Arg120 and Tyr355 (Kurumbail et al., 1996). Moreover, it built one H-bond between the hydroxyl groups of B ring and the residue Ala527 to enhance the binding forces. It also formed one H-bond between

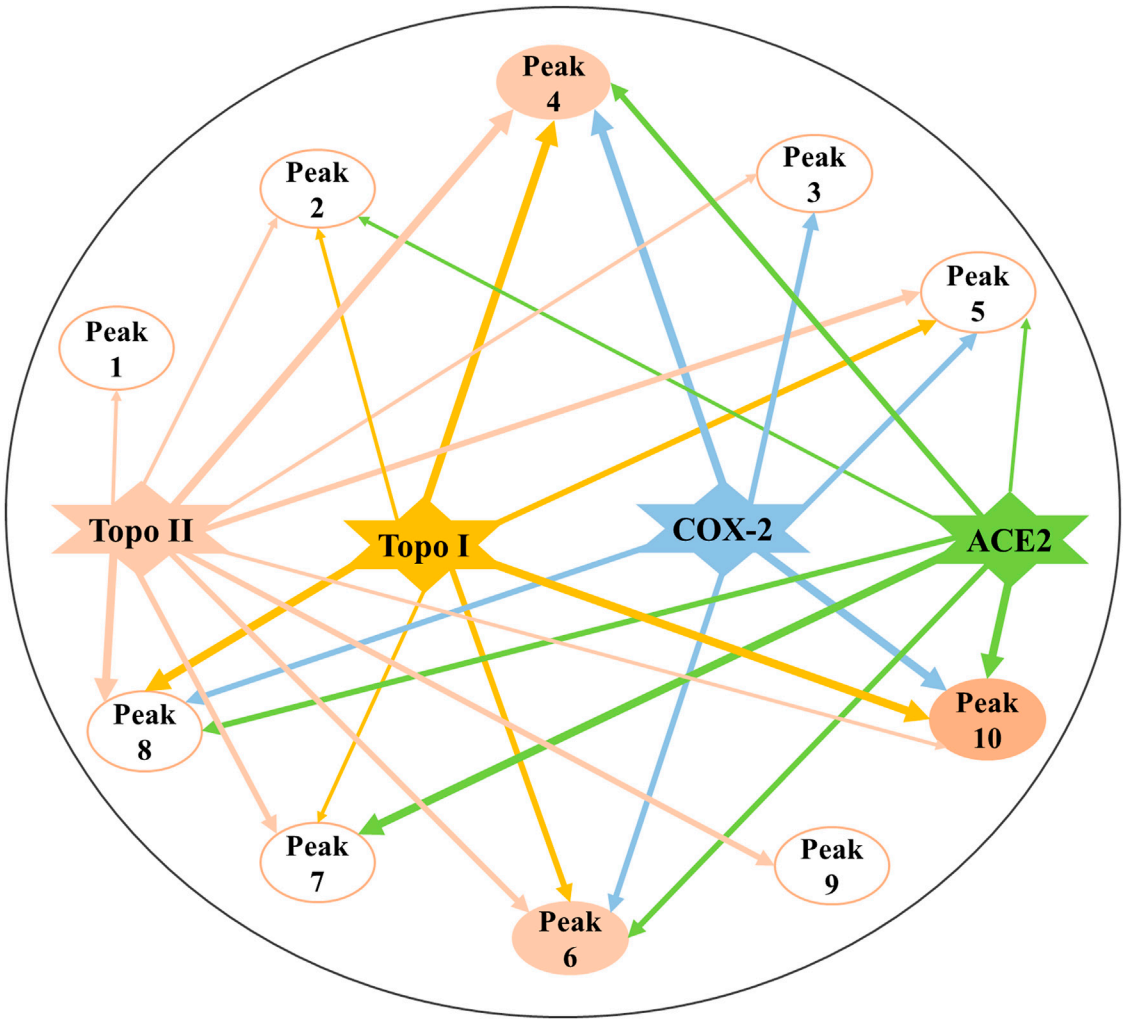


FIGURE 7 | Constructed multi-component and multi-target network incorporating the potential bioactive components screened out with multiple drug targets. The line thicknesses roughly represent the binding or action intensity for their corresponding interactions.

the oxygen-containing groups of the methylenedioxybenzene ring and the residue His90. Additionally, the side chains of Val349 and Val523 amino acid residues displayed Pi-Alkyl and Pi-sigma forces to its B ring, while on the other side, some residues such as Ala516, Gly526, Tyr385 and so forth surrounded the compound through van der Waals' forces. There were also some reports stating that diphyllin inhibited the activity of vacuolar-type H^+-ATPase (V-ATPase) with the effective test concentration (EC) of 0.3 μM using cell-based assays targeting the viral entry previously (Prasansuklab et al., 2021). In the present study, diphyllin with a high binding affinity to ACE2 was shortlisted as prominent ligands by applying molecular docking analysis. It was observed that the lactone ring of diphyllin formed one H-bond with the amino acid residue Asp382. Meanwhile, the methoxybenzene groups of A ring of this compound also shaped one H-bond with the residue Asp350 on ACE2 to further enhance the affinity. The key amino acid residues His378 and His401 exhibited Pi-Pi T-shaped force to the phenyl-containing groups of the methylenedioxybenzene ring and the hydroxyl groups of B ring of this compound. Likewise, the lactone ring 5-oxo group of C ring of diphyllin *O*-glucoside formed H-bonds with the residue Ala348. Moreover, the residues Arg514 and Asn394 built H-bonds to the methoxybenzene groups of the A ring and the oxygen-containing groups of the methylenedioxybenzene ring of this compound, respectively. Furthermore, the hydroxyl group of the arabinosyl moiety of this compound formed three stable H-bonds with different types of amino acid residues His378, Glu375, Pro346 attached to ACE2. Additionally, the residues Glu402 and His401 shared Pi-Sigma and Pi-Lone Pair forces to the phenyl groups of A and D rings of this compound. The docking result was similar to chloroquine and MLN-4760 (as the positive controls) which formed several stable H-bonds such as His374, His378 or Glu375, indicating these H-bonds formed with residues on ACE2 played a pivotal role in the targeted binding process. With regard to Topo II, the trimethoxyphenyl

group of E ring of podophyllotoxin shared H-bonds with the residue Gln778, serving as an H-donor to the ring. At the same time, podophyllotoxin intercalated into the DNA complex through H-bonds with the residues Da12 and Dt9. It was observed to form three conventional H-bonds with the residues Da12, Dt9, and Gln778, of which interacted with Topo II inhibitor etoposide as well. Moreover, there were related literature reports that podophyllotoxin could be applied as a cell division inhibitor possessing antitumor activity in the metaphase of cell division, which inhibited the polymerization of microtubules and mitosis of the nucleus, and thus was suspended in the metaphase (Liu et al., 2015). Furthermore, there existed other essential driven forces such as the Van der Waals force, hydrophobic and electrostatic effects between those potential active ingredients and Topo I, Topo II, COX-2, or ACE2 in the process of molecular docking simulation. Above all, the molecular docking analysis was consistent with the results of affinity ultrafiltration screening. Therefore, these components were promising to be developed as potential antiproliferative, anti-inflammatory, and antiviral lead candidates for the discovery of target-specific therapeutic drugs.

CONCLUSION

The therapeutic effects of medicinal plants are mainly on account of the integral complex chemical properties of multiple secondary metabolites, which could interact on multiple drug targets or synergistically interact with various biochemical pathways to conduct its holistic curative effects. This study aimed to comprehensively explore the underlying pharmacological mechanisms of action for *P. sinense* in a multi-target and multi-component way using Topo I, Topo II, COX-2, and ACE2 as potential target enzymes. Besides, combined these drug targets with the UF–LC/MS screening strategy, we were able to quickly screen out multi-functional components responsible for the antiproliferative, anti-inflammatory, and antiviral activities from the crude extracts of *P. sinense* for the first time. In total, 7, 10, 6, and 7 components were fished out as the potential Topo I, Topo II, COX-2, and ACE2 ligands, respectively. It is obviously that these components could act synergistically on the corresponding drug targets in a multi-component manner to take their effects. On the other side, among these active components, the individual compound that bound well to diverse target enzymes, such as Topo I and Topo II, had been detected as the single bioactive ingredient in *P. sinense* to simultaneously exert its intricate action mechanisms in a multi-target way. The activity verification of representative components, such as diphyllin and podophyllotoxin, further confirmed the feasibility of our screening method, and their potential pharmacological effects with *in vitro* assays. Meanwhile, the molecular docking simulation further indicated and validated the inhibitory mechanisms between Topo I, Topo II, COX-2 or ACE2 and those representative constituents such as diphyllin, podophyllotoxin and diphyllin *O*-glucoside. To the best of our knowledge, this is the first report to systematically investigate the antiproliferative, anti-inflammatory and antiviral activities, their potentially responsible chemical components and mechanisms by employing bio-affinity ultrafiltration with the multiple drug targets combined with LC/MS. This work will not only facilitate and elucidate the correlations between potential bioactive components and their biological targets including the underlying mechanisms of action, but also lay a further solid foundation for discovering more novel and curative agents from *P. sinense* or other medicinal plants.

DATA AVAILABILITY STATEMENT

The raw data supporting the conclusion of this article will be made available by the authors, without undue reservation.

AUTHOR CONTRIBUTIONS

MG designed the research and superintended the whole study. GC supervised the study and revised the manuscript. YZ designed and performed the antiproliferative assay *in vitro*. HF carried out the experiments and wrote the manuscript. All the authors have read and approved the final manuscript.

FUNDING

This work was jointly supported by the National Natural Science Foundation of China (Grant No. 81673580 to MG) and the Youth Innovation Promotion Association of the Chinese Academy of Sciences (Grant No. 2020337 to GC).

ACKNOWLEDGMENTS

The authors would like to thank Prof. GH for his assistance in identifying the plant material and thank Mr. RT for his help with molecular docking analysis.

REFERENCES

Castro, M. A., Del Corral, J. M., Gordaliza, M., Grande, C., Gómez-Zurita, A., García-Grávalos, D., et al. (2003). Synthesis and Cytotoxicity of Podophyllotoxin Analogues Modified in the A Ring. *Eur. J. Med. Chem.* 38, 65–74. doi:10.1016/s0223-5234(02)00007-7

Chang, J., Kim, Y., and Kwon, H. J. (2016). Advances in Identification and Validation of Protein Targets of Natural Products without Chemical Modification. *Nat. Prod. Rep.* 33, 719–730. doi:10.1039/c5np00107b

Chen, G., Wu, J., Li, N., and Guo, M. (2018). Screening for Antiproliferative and Anti-inflammatory Components from *Rhamnus davurica* Pall. Using Bio-Affinity Ultrafiltration with Multiple Drug Targets. *Anal. Bioanal. Chem.* 410, 3587–3595. doi:10.1007/s00216-018-0953-6

Chen, G. L., Xu, Y. B., Wu, J. L., Li, N., and Guo, M. Q. (2020). Hypoglycemic and Hypolipidemic Effects of *Moringa oleifera* Leaves and Their Functional Chemical Constituents. *Food Chem.* 333, 127478. doi:10.1016/j.foodchem.2020.127478

Cieśla, Ł., and Moaddel, R. (2016). Comparison of Analytical Techniques for the Identification of Bioactive Compounds from Natural Products. *Nat. Prod. Rep.* 33, 1131–1145. doi:10.1039/c6np00016a

Delgado, J. L., Hsieh, C. M., Chan, N. L., and Hiasa, H. (2018). Topoisomerases as Anticancer Targets. *Biochem. J.* 475, 373–398. doi:10.1042/BCJ20160583

Fan, H. W., Liu, G. Y., Zhao, C. F., Li, X. F., and Yang, X. Y. (2015). Differential Expression of COX-2 in Osteoarthritis and Rheumatoid Arthritis. *Genet. Mol. Res.* 14, 12872–12879. doi:10.4238/2015.October.21.7

Garvin, M. R., Alvarez, C., Miller, J. I., Prates, E. T., Walker, A. M., Amos, B. K., et al. (2020). A Mechanistic Model and Therapeutic Interventions for COVID-19 Involving a RAS-Mediated Bradykinin Storm. *ELife* 9, e59177. doi:10.7554/eLife.59177

Gheblawi, M., Wang, K., Viveiros, A., Nguyen, Q., Zhong, J. C., Turner, A. J., et al. (2020). Angiotensin-Converting Enzyme 2: SARS-CoV-2 Receptor and Regulator of the Renin-Angiotensin System: Celebrating the 20th Anniversary of the Discovery of ACE2. *Circ. Res.* 126, 1456–1474. doi:10.1161/CIRCRESAHA.120.317015

Hooper, N. M., Lambert, D. W., and Turner, A. J. (2020). Discovery and Characterization of ACE2 - a 20-year Journey of Surprises from Vasopeptidase to COVID-19. *Clin. Sci.* 134, 2489–2501. doi:10.1042/CS20200476

Jullian-Pawlicki, N., Lequart-Pillon, M., Huynh-Cong, L., Lesur, D., Cailleu, D., Mesnard, F., et al. (2015). Arylnaphthalene and Aryltetralin-type Lignans in Hairy Root Cultures of *Linum perenne*, and the Stereochemistry of 6-Methoxypodophyllotoxin and One Diastereoisomer by HPLC-MS and NMR Spectroscopy. *Phytochem. Anal.* 26, 310–319. doi:10.1002/pca.2565

Kuba, K., Imai, Y., Ohto-Nakanishi, T., and Penninger, J. M. (2010). Trilogy of ACE2: A Peptidase in the Renin-Angiotensin System, a SARS Receptor, and a Partner for Amino Acid Transporters. *Pharmacol. Ther.* 128, 119–128. doi:10.1016/j.pharmthera.2010.06.003

Kurumbail, R. G., Stevens, A. M., Gierse, J. K., McDonald, J. J., Stegeman, R. A., Pak, J. Y., et al. (1996). Structural Basis for Selective Inhibition of Cyclooxygenase-2 by Anti-inflammatory Agents. *Nature* 384, 644–648. doi:10.1038/384644a0

Lautié, E., Quintero, R., Fliniaux, M. A., and Villarreal, M. L. (2008). Selection Methodology with Scoring System: Application to Mexican Plants Producing Podophyllotoxin Related Lignans. *J. Ethnopharmacol.* 120, 402–412. doi:10.1016/j.jep.2008.09.014

Lavecchia, A., Di Giovanni, C., Cerchia, C., Russo, A., Russo, G., and Novellino, E. (2013). Discovery of a Novel Small Molecule Inhibitor Targeting the Frataxin/Ubiquitin Interaction via Structure-Based Virtual Screening and Bioassays. *J. Med. Chem.* 56, 2861–2873. doi:10.1021/jm3017199

Leung, J. M., Yang, C. X., Tam, A., Shaipanich, T., Hackett, T. L., Singhera, G. K., et al. (2020). ACE-2 Expression in the Small Airway Epithelia of Smokers and COPD Patients: Implications for COVID-19. *Eur. Respir. J.* 55, 2000688. doi:10.1183/13993003.00688-2020

Li, S., Tang, Y., Liu, C., Li, J., Guo, L., and Zhang, Y. (2015). Development of a Method to Screen and Isolate Potential Xanthine Oxidase Inhibitors from *Panax Japlcus Var* via Ultrafiltration Liquid Chromatography Combined with Counter-current Chromatography. *Talanta* 134, 665–673. doi:10.1016/j.talanta.2014.12.005

Liang, X., Wu, Q., Luan, S., Yin, Z., He, C., Yin, L., et al. (2019). A Comprehensive Review of Topoisomerase Inhibitors as Anticancer Agents in the Past Decade. *Eur. J. Med. Chem.* 171, 129–168. doi:10.1016/j.ejmech.2019.03.034

Liu, Y. Q., Tian, J., Qian, K., Zhao, X. B., Morris-Natschke, S. L., Yang, L., et al. (2015). Recent Progress on C-4-Modified Podophyllotoxin Analogs as Potent Antitumor Agents. *Med. Res. Rev.* 35, 1–62. doi:10.1002/med.21319

Lucas, S. (2016). The Pharmacology of Indomethacin. *Headache* 56, 436–446. doi:10.1111/head.12769

Ma, C., Yang, J. S., and Luo, S. R. (1993). Study on Lignans from *Diphylleia Sinensis*. *Yao Xue Xue Bao* 28, 690–694. doi:10.16438/j.0513-4870.1993.09.010

Ma, H., Liang, H., Cai, S., O'keefe, B. R., Mooberry, S. L., and Cichewicz, R. H. (2020). An Integrated Strategy for the Detection, Dereplication, and Identification of DNA-Binding Biomolecules from Complex Natural Product Mixtures. *J. Nat. Prod.* 84, 750–761. doi:10.1021/acs.jnatprod.0c00946

Mahboubi Rabbani, S. M. I., and Zarghi, A. (2019). Selective COX-2 Inhibitors as Anticancer Agents: A Patent Review (2014-2018). *Expert Opin. Ther. Pat.* 29, 407–427. doi:10.1080/13543776.2019.1623880

Mulabagal, V., and Calderón, A. I. (2010). Development of an Ultrafiltration-Liquid Chromatography/Mass Spectrometry (UF-LC/MS) Based Ligand-Binding Assay and an LC/MS Based Functional Assay for *Mycobacterium tuberculosis* Shikimate Kinase. *Anal. Chem.* 82, 3616–3621. doi:10.1021/ac902849g

Orhan, I. E. (2019). Enzyme Inhibitors as the Attractive Targets for the Treatment of Various Diseases. *Curr. Med. Chem.* 26, 3206–3207. doi:10.2174/0929867326181908211156 41

Peng, Y., Wang, Y., Tang, N., Sun, D., Lan, Y., Yu, Z., et al. (2018). Andrographolide Inhibits Breast Cancer through Suppressing COX-2 Expression and Angiogenesis via Inactivation of P300 Signaling and VEGF Pathway. *J. Exp. Clin. Cancer Res.* 37, 248. doi:10.1186/s13046-018-0926-9

Prasansuklab, A., Theerasri, A., Rangsinth, P., Sillapachaiyaporn, C., Chuchawankul, S., and Tencomnao, T. (2021). Anti-COVID-19 Drug Candidates: A Review on Potential Biological Activities of Natural Products in the Management of New Coronavirus Infection. *J. Tradit. Complement. Med.* 11, 144–157. doi:10.1016/j.jtcme.2020.12.001

Qin, S., Ren, Y., Fu, X., Shen, J., Chen, X., Wang, Q., et al. (2015). Multiple Ligand Detection and Affinity Measurement by Ultrafiltration and Mass Spectrometry Analysis Applied to Fragment Mixture Screening. *Anal. Chim. Acta* 886, 98–106. doi:10.1016/j.aca.2015.06.017

Qin, J., Luo, J., Zhao, H., Zhang, S., Zhang, X., and Yang, M. (2016). Determination and Pharmacokinetics of Chinensinaphthol Methyl Ether in Rat Urine by a Sensitive and Specific UFLC-ESI-MS/MS Method. *J. Chromatogr. B Analyt. Technol. Biomed. Life Sci.* 1033-1034, 311–316. doi:10.1016/j.jchromb.2016.08.041

Regulski, M., Regulska, K., Prukała, W., Piotrowska, H., Stanisz, B., and Murias, M. (2016). COX-2 Inhibitors: A Novel Strategy in the Management of Breast Cancer. *Drug Discov. Todaytoday* 21, 598–615. doi:10.1016/j.drudis.2015.12.003

Rengasamy, K. R., Kulkarni, M. G., Stirk, W. A., and Van Staden, J. (2014). Advances in Algal Drug Research with Emphasis on Enzyme Inhibitors. *Biotechnol. Adv.* 32, 1364–1381. doi:10.1016/j.biotechadv.2014.08.005

Shahid, Z., Kalayanamitra, R., Mcclafferty, B., Kepko, D., Ramgobin, D., Patel, R., et al. (2020). COVID-19 and Older Adults: What We Know. *J. Am. Geriatr. Soc.* 68, 926–929. doi:10.1111/jgs.16472

Sinha, B. K. (1995). Topoisomerase Inhibitors. A Review of Their Therapeutic Potential in Cancer. *Drugs* 49, 11–19. doi:10.2165/00003495-199549010-00002

Terabayashi, S., Wofford, D. E., and Ying, T. S. (1984). A Monograph of *Diphylleia* (Berberidaceae). *J. Arnold Arbor.* 65, 57–94.

Towler, P., Staker, B., Prasad, S. G., Menon, S., Tang, J., Parsons, T., et al. (2004). ACE2 X-ray Structures Reveal a Large Hinge-Bending Motion Important for Inhibitor Binding and Catalysis. *J. Biol. Chem.* 279, 17996–18007. doi:10.1074/jbc.M311191200

Vichai, V., and Kirtikara, K. (2006). Sulforhodamine B Colorimetric Assay for Cytotoxicity Screening. *Nat. Protoc.* 1, 1112–1116. doi:10.1038/nprot.2006.179

Wang, Z., Liang, H., Cao, H., Zhang, B., Li, J., Wang, W., et al. (2019). Efficient Ligand Discovery from Natural Herbs by Integrating Virtual Screening, Affinity Mass Spectrometry and Targeted Metabolomics. *Analyst* 144, 2881–2890. doi:10.1039/c8an02482k

Yao, C., Na, N., Huang, L., He, D., and Ouyang, J. (2013). High-throughput Detection of Drugs Binding to Proteins Using Desorption Electrospray Ionization Mass Spectrometry. *Anal. Chim. Acta* 794, 60–66. doi:10.1016/j.aca.2013.07.016

You, F., and Gao, C. (2019). Topoisomerase Inhibitors and Targeted Delivery in Cancer Therapy. *Curr. Top. Med. Chem.* 19, 713–729. doi:10.2174/1568026619666190401112948

Yousefzadi, M. S., Sharifi, M., Behmanesh, M., Moyano, E., Bonfill, M., Cusido, R. M., et al. (2010). Podophyllotoxin: Current Approaches to its Biotechnological Production and Future Challenges. *Eng. Life Sci.* 10, 281–292. doi:10.1002/elsc.201000027

Yuan, Y., Wang, Y., Huang, M., Xu, R., Zeng, H., Nie, C., et al. (2011). Development and Characterization of Molecularly Imprinted Polymers for the Selective Enrichment of Podophyllotoxin from Traditional Chinese Medicines. *Anal. Chim. Acta* 695, 63–72. doi:10.1016/j.aca.2011.04.007

Zhang, Y., Xiao, S., Sun, L., Ge, Z., Fang, F., Zhang, W., et al. (2013). Rapid Screening of Bioactive Compounds from Natural Products by Integrating

5-Channel Parallel Chromatography Coupled with on-Line Mass Spectrometry and Microplate Based Assays. *Anal. Chim. Acta* 777, 49–56. doi:10.1016/j.aca.2013.03.028

Zhang, L., Song, J., Kong, L., Yuan, T., Li, W., Zhang, W., et al. (2020). The Strategies and Techniques of Drug Discovery from Natural Products. *Pharmacol. Ther.* 216, 107686. doi:10.1016/J.PHARMTHERA.2020.107686

Zhang, H., Xu, C., Tian, Q., Zhang, Y., Zhang, G., Guan, Y., et al. (2021). Screening and Characterization of Aldose Reductase Inhibitors from Traditional Chinese Medicine Based on Ultrafiltration-Liquid Chromatography Mass Spectrometry and *In Silico* Molecular Docking. *J. Ethnopharmacol.* 264, 113282. doi:10.1016/j.jep.2020.113282

Zhao, H. Y., Zhang, Y. Z., and Xiao, C. L. (2009). Advances in the Study of Affinity Selection-Ultrafiltration/HPLC-MS. *Yao Xue Xue Bao* 44, 1084–1088. doi:10.16438/j.0513-4870.2009.10.012

Zhao, C., Zhang, N., He, W., Li, R., Shi, D., Pang, L., et al. (2014). Simultaneous Determination of Three Major Lignans in Rat Plasma by LC-MS/MS and its Application to a Pharmacokinetic Study after Oral Administration of *Diphylleia Sinensis* Extract. *Biomed. Chromatogr.* 28, 463–467. doi:10.1002/bmc.3066

Zhu, H., Liu, S., Li, X., Song, F., Liu, Z., and Liu, S. (2013). Bioactivity Fingerprint Analysis of Cyclooxygenase-2 Ligands from Radix Aconiti by Ultrafiltration-UPLC-MS^n. *Anal. Bioanal. Chem.* 405, 7437–7445. doi:10.1007/s00216-013-7153-1

Conflict of Interest: The authors declare that the research was conducted in the absence of any commercial or financial relationships that could be construed as a potential conflict of interest.

Publisher's Note: All claims expressed in this article are solely those of the authors and do not necessarily represent those of their affiliated organizations, or those of the publisher, the editors and the reviewers. Any product that may be evaluated in this article, or claim that may be made by its manufacturer, is not guaranteed or endorsed by the publisher.

Copyright © 2021 Feng, Chen, Zhang and Guo. This is an open-access article distributed under the terms of the Creative Commons Attribution License (CC BY). The use, distribution or reproduction in other forums is permitted, provided the original author(s) and the copyright owner(s) are credited and that the original publication in this journal is cited, in accordance with accepted academic practice. No use, distribution or reproduction is permitted which does not comply with these terms.

frontiers in Pharmacology

ORIGINAL RESEARCH
published: 26 October 2021
doi: 10.3389/fphar.2021.775730

Total C-21 Steroidal Glycosides From *Baishouwu* Ameliorate Hepatic and Renal Fibrosis by Regulating IL-1β/MyD88 Inflammation Signaling

Tingting Qin[1,2†], Mingliang Wang[1,2†], Ting Zhang[1,2], Yingyu Wang[1,2], Yunyun Zhang[1,2], Muhammad Hasnat[3], Zirui Zhuang[1,2], Yongfang Ding[1,2] and Yunru Peng[1,2*]*

[1]Affiliated Hospital of Integrated Traditional Chinese and Western Medicine, Nanjing University of Chinese Medicine, Nanjing, China, [2]Department of Pharmacology and Toxicology, Jiangsu Province Academy of Traditional Chinese Medicine, Nanjing, China, [3]Institute of Pharmaceutical Sciences, University of Veterinary and Animal Sciences, Lahore, Pakistan

OPEN ACCESS

Edited by:
Dahui Liu,
Hubei University of Chinese Medicine, China

Reviewed by:
Puyang Gong,
Southwest Minzu University, China
Xiaoqi Jing,
Shanghai Institute of Materia Medica (CAS), China

***Correspondence:**
Yunru Peng
pengyunru@126.com
Yongfang Ding
Yongfangding@gmail.com

[†]These authors have contributed equally to this work

Specialty section:
This article was submitted to Ethnopharmacology, a section of the journal Frontiers in Pharmacology

Received: 14 September 2021
Accepted: 12 October 2021
Published: 26 October 2021

Citation:
Qin T, Wang M, Zhang T, Wang Y, Zhang Y, Hasnat M, Zhuang Z, Ding Y and Peng Y (2021) Total C-21 Steroidal Glycosides From Baishouwu Ameliorate Hepatic and Renal Fibrosis by Regulating IL-1β/MyD88 Inflammation Signaling. Front. Pharmacol. 12:775730. doi: 10.3389/fphar.2021.775730

Fibrosis is a worldwide public health problem, which typically results from chronic diseases and often leads to organ malfunction. Chronic inflammation has been suggested to be the major trigger for fibrogenesis, yet mechanisms by which inflammatory signals drive fibrogenesis have not been fully elucidated. Total C-21 steroidal glycosides (TCSG) from *Baishouwu* are the main active components of the root of *Cynanchum auriculatum* Royle ex Wight, which exert hepatoprotective and anti-inflammation properties. In this study, we established a mouse model with the coexistence of hepatic and renal fibrosis and aimed to investigate the effects of TCSG from *Baishouwu* on fibrosis and explored the potential mechanisms. The results of biochemical and pathological examinations showed that TCSG from *Baishouwu* improved liver and kidney function and alleviated hepatic and renal fibrosis by reducing collagen and extracellular matrix deposition in bile duct ligation and unilateral ureteral occlusion (BDL&UUO) mice. According to network pharmacology analysis, the mechanisms underlying the effects of TCSG from *Baishouwu* on hepatic and renal fibrosis were associated with inflammatory response pathways, including "Signaling by interleukins", "MAP kinase activation", "MyD88 cascade initiated on plasma membrane", and "Interleukin-1 family signaling". Regression analysis and western blot results revealed that IL-1β/MyD88 inflammation signaling played an essential role in the anti-fibrotic effects of TCSG from *Baishouwu*. Further data displayed that TCSG from *Baishouwu* affected inflammatory response and extracellular matrix deposition via suppressing the activation of p38 MAPK/JNK and NF-κB p65 signaling cascades both in the liver and kidney of BDL&UUO mice. Thus, our findings suggest TCSG from *Baishouwu* as a natural regimen against hepatic and renal fibrosis and provide direct evidence that IL-1β/MyD88 signaling crucially contributes to hepatic and renal fibrosis and modulates liver-kidney crosstalk by maintaining tight control over inflammatory responses.

Keywords: hepatic fibrosis, renal fibrosis, inflammation, total C-21 steroidal glycosides, IL-1β/MyD88 signaling

INTRODUCTION

Fibrosis is a pathological response characterized by abnormal hyperplasia and excessive deposition of extracellular matrix (ECM) during the process of repair after tissue damage, which has been considered to account for up to 45% of all deaths in the industrialized world (Distler and Györfi, 2019; Henderson et al., 2020). During the pathological process of a variety of chronic diseases, excessively accumulated ECM results in fibrogenesis and increases tissue hardness, which subsequently blocks the diffusion of oxygen and nutrients, further damaging the organs, particularly, hepatic and renal fibrosis are commonly detected in clinical practice (Weiskirchen et al., 2019; Zhao et al., 2020). Emerging studies demonstrate that hepatic and renal fibrosis share similar pathogenesis and pathological characteristics, showing a potential interaction in the pathogenesis, although they occur in different organs. Liver cirrhosis and non-alcoholic fatty liver disease are suggested as independent risk factors for the incidence of chronic kidney disease (Targher et al., 2011; Bernardi et al., 2015). Alternatively, increasing pieces of evidence establish that chronic kidney disease can lead to liver dysfunction, contribute to the development of non-alcoholic fatty liver disease, and associate metabolic disturbances (Musso et al., 2015; Marcuccilli and Chonchol, 2016). These findings drove a popular area of scientific interest in liver-kidney organ crosstalk during the last decade. However, the related pathogenetic mechanisms are not fully known that it is necessary to elucidate the complex and intertwined mechanisms linking hepatic and renal fibrosis and develop effective antifibrotic therapeutic strategies.

Many distinct factors have been revealed to participate in the progression of fibrotic diseases, among which chronic inflammation is thought to be the major contributing factor. It is now clear that persistent inflammation resulting in a chronic wound-healing response can facilitate an increase in the deposition of ECM and sustained tissue damage both in the liver and kidney, ultimately leading to fibrosis (Heymann and Tacke, 2016; Tecklenborg et al., 2018). Consequently, focusing on the cellular mechanisms involved in the stimulation of inflammation and identifying the key mediators have been considered as the targets to alleviate hepatic and renal fibrosis. Traditional Chinese medicine (TCM), widely used in Asian countries for thousands of years, possesses a dual role in immunological regulation, as well as anti-fibrotic actions in the liver and kidney (Ma et al., 2013; Zhang and Schuppan, 2014; Shen et al., 2018; Wang et al., 2020). The root of *Cynanchum auriculatum* Royle ex Wight is a famous TCM known as *Baishouwu*, which has been used as a tonic medicine or healthy food for centuries. Based on the theory of TCM, this herb exhibits medicinal properties, including nourishing the liver and kidney and enhancing immune function. Pharmacological studies reveal that *Baishouwu* shows remarkable hepatoprotective, anti-inflammatory, and antitumor bioactivities (Jang et al., 2016; Li et al., 2018; Chen et al., 2019). The total C-21 steroidal glycosides (TCSG) are commonly accepted as one of the most bioactive ingredients separated from *Baishouwu* (Chen et al., 2019). Previously, we reported that TCSG from *Baishouwu* protected the liver against the damage of oxidative toxicity and inflammatory reactions (Cui et al., 2019; Zhang et al., 2021). We also found that TCSG from *Baishouwu* inhibited the development of hepatocellular carcinoma by suppressing the hepatic inflammation-fibrosis axis induced by diethylnitrosamine (Ding et al., 2017; Ding et al., 2019). Moreover, our recent research demonstrated that TCSG from *Baishouwu* relieved renal fibrosis by regulating the process of renal tubular epithelial-mesenchymal transformation (Yin and Peng, 2020). However, it is not yet clear whether TCSG from *Baishouwu* can regulate hepatic and renal fibrosis, or the involved regulation procession and molecular mechanisms.

In the present study, we aimed to evaluate whether TCSG from *Baishouwu* had therapeutic effects on hepatic and renal fibrosis in the mouse model of bile duct ligation and unilateral ureteral occlusion (BDL&UUO) with a parallel focus on the role of inflammation in the liver-kidney axis. To further explore the underlying mechanism, system network pharmacology analysis was applied to predict the potential mechanism network and then validation experiments were carried out.

MATERIALS AND METHODS

Animals

Adult male C57BL/6 mice weighing 20–22 g were purchased from Shanghai Slack Laboratory Animal Co., Ltd (Shanghai, China). Animal experiments were performed in accordance with the Guidelines for the Care and Use of Laboratory Animals published by the US National Institutes of Health (Publication No.85-23, revised 1996). The care, handling, and experimental procedures of animals were approved by the Ethics Committee of Jiangsu Integrated Traditional Chinese and Western Medicine Hospital (NO. AEWC-20180712-37). Mice were housed under a 12 h light/dark cycle at 22–25°C with 50–60% humidity and provided access to food and water *ad libitum*. All mice were subjected to a 1-week acclimatization period prior to the experimental protocol.

Animal Surgery and Experimental Design

Mice were randomly allocated into the sham group (n = 10) and model group (n = 45). The mouse model of hepatic and renal fibrosis was established by BDL and UUO surgical operation under sterile conditions according to previous research (Chevalier et al., 2009; Yokota et al., 2018). Briefly, experimental mice were anesthetized with isoflurane. The experimental area was disinfected with 75% alcohol. After the application of antiseptic on the skin, a 2–3 cm incision was made just below the xiphoid process. The common bile duct was identified, ligated, and two surgical knots were fixed. Then a second bile duct ligation was added in the same manner without division to avoid any interference caused by the loose end. Meanwhile, the ureter was identified, ligated, but not divided as described in the bile duct surgery. The sham group underwent a sham procedure, in which the bile duct and ureter were identified and exposed without ligation. 24 hours after surgery, animals subjected to the model group were randomly divided into

TABLE 1 | PCR primer sequences.

Target gene	Forward primer (5–3′)	Reverse primer (5–3′)
GAPDH	TGC ACC ACC AAC TGC TTA G	GGA TGC AGG GAT GAT GTT C
TGF-β1	CTT CAA TAC GTC AGA CAT TCG GG	GTA ACG CCA GGA ATT GTT GCT A
α-SMA	TCC CTG GAG AAG AGC TAC GAA CT	AAG CGT TCG TTT CCA ATG GT
IL-1β	TGGACCTTCCAGGATGAGGACA	GTTCATCTCGGAGCCTGTAGTG
Col 1a1	CCT GGC AAA GAC GGA CTC AAC	GCT GAA GTC ATA ACC GCC ACT G
Col 3a1	CTG TAA CAT GGA AAC TGG GGA AA	CCA TAG CTG AAC TGA AAA CCA CC

three groups (n = 15 per group): the model group, the TCSG low-dose group (180 mg/kg/day, TCSG-L), and the TCSG high-dose group (360 mg/kg/day, TCSG-H), and received intragastric drug treatment every other day for 14 days. The extract of TCSG from *Baishouwu* was performed as described in our previous study (Ding et al., 2019). The sham group and model group were received the same volume of vehicles. At the end of the experiment, blood samples were collected from the retroorbital venous plexus. Then animals were sacrificed under isoflurane anesthesia, followed by liver and kidney samples collected for further analysis.

Serum and Urine Biochemistry

Blood samples were centrifuged (3,000 g, 10 min, 4°C) to prepare serum. Urine samples were diluted using ice-cooled normal saline and centrifuged (5,000 g, 5 min, 4°C) to prepare the clear supernatant. An automatic analyzer (C8000 Roche, Hoffmann-La Roche Inc, Switzerland) and commercial kits (Nanjing Jiancheng Bioengineering Institute, Nanjing, China) were employed to analyze serum and urine biochemistry, including serum levels of alanine transaminase (ALT), aspartate transaminase (AST), total bilirubin (T-Bil), alkaline phosphatase (ALP), total cholesterol (T-CHO), albumin and globulin ratio (A/G), blood urea nitrogen (BUN), and creatinine (Cre), as well as the content of urine protein and urine Cre.

Histological Analysis

Liver and kidney tissues were fixed in paraformaldehyde solution followed by paraffin embedding. Tissue sections with 5 μm thickness were stained with hematoxylin and eosin (HE) to assess inflammation and necrosis. The Masson trichrome staining was used to evaluate liver and kidney fibrotic alterations. Immunohistochemistry was applied using paraffin sections incubated with primary antibodies: α-SMA (1:100, #19245, Cell Signaling Technology) and TGF-β1 (1:100, #92486, Abcam). Images were observed using a Leica microsystem (DMi8, Leica Microsystems, German, Weztlar). The percentage of the stained positive area was quantified by ImageJ software.

The Level of Tissue Hydroxyproline

Tissue hydroxyproline (Hyp) was assessed to investigate the level of collagen deposition, which is an index of liver and kidney fibrosis (García et al., 2002). The content of Hyp in tissues was determined using commercial kits (Nanjing Jiancheng Bioengineering Institute) according to the instructions. Generally, the tissue slices were digested in 1 ml hydrochloric acid (6 mol/l) for 5 h under 100°C. After cooling, a 10 μl indicator was added following the addition of solutions A and B for making the solution PH = 6. Then the mixture was centrifugated (3,500 g, 10 min) and the supernatant was incubated with the other test solutions at 60°C for 15 min. Centrifugation was performed (3,500 g, 10 min) and the absorbance of samples was measure at 550 nm using the microplate reader (NanoQuant, Switzerland).

Network Pharmacology

The network pharmacology technique was used to explore the underlying mechanisms of TCSG in the treatment of hepatic and renal fibrosis. There are 12 active ingredients identified in TCSG from *Baishouwu* according to the literature and our previous study by LC-Q/TOF-MS (Wang et al., 2017; Chen et al., 2019). The details of the twelve active ingredients were shown in **Supplementary Figure S1**. The targets of TCSG active ingredients were identified by searching the genes database of Swiss Target Prediction database (http://www.swisstargetprediction.ch/index.php) and Pubmed (https://pubmed.ncbi.nlm.nih.gov/). The proven targets for hepatic fibrosis and renal fibrosis were identified by searching DisGeNet database (https://www.disgenet.org/). There were 1,179 target genes related to hepatic fibrosis and 570 target genes associated with renal fibrosis which were consolidated in Excel. The potential therapeutic targets were collected from the interactions of target genes and the networks were constructed by using Cytoscape 3.8.0. The STRING database (https://www.string-db.org/) was used to obtain the interaction relationship between target genes.

Protein-Protein (PPI) Interaction Network

PPI networks were constructed to investigate the molecular mechanisms of TCSG intervening hepatic and renal fibrosis. TCSG-disease PPI networks were constructed by merging the TCSG network and the disease network. The Network Analyzer plug-in was used to calculate the networks node parameters and the module analysis was carried out by the MCODE plug-in to screen potential therapeutic targets.

Pathway and Functional Enrichment Analysis

The underlying pathways associated with TCSG against fibrosis of the liver and kidney were analyzed by the ClueGO plug-in. The gene ontology (GO) database (http://geneontology.org/) was applied for function enrichment analysis and the Reactome Pathway database (https://reactome.org/) was used for pathway enrichment analysis.

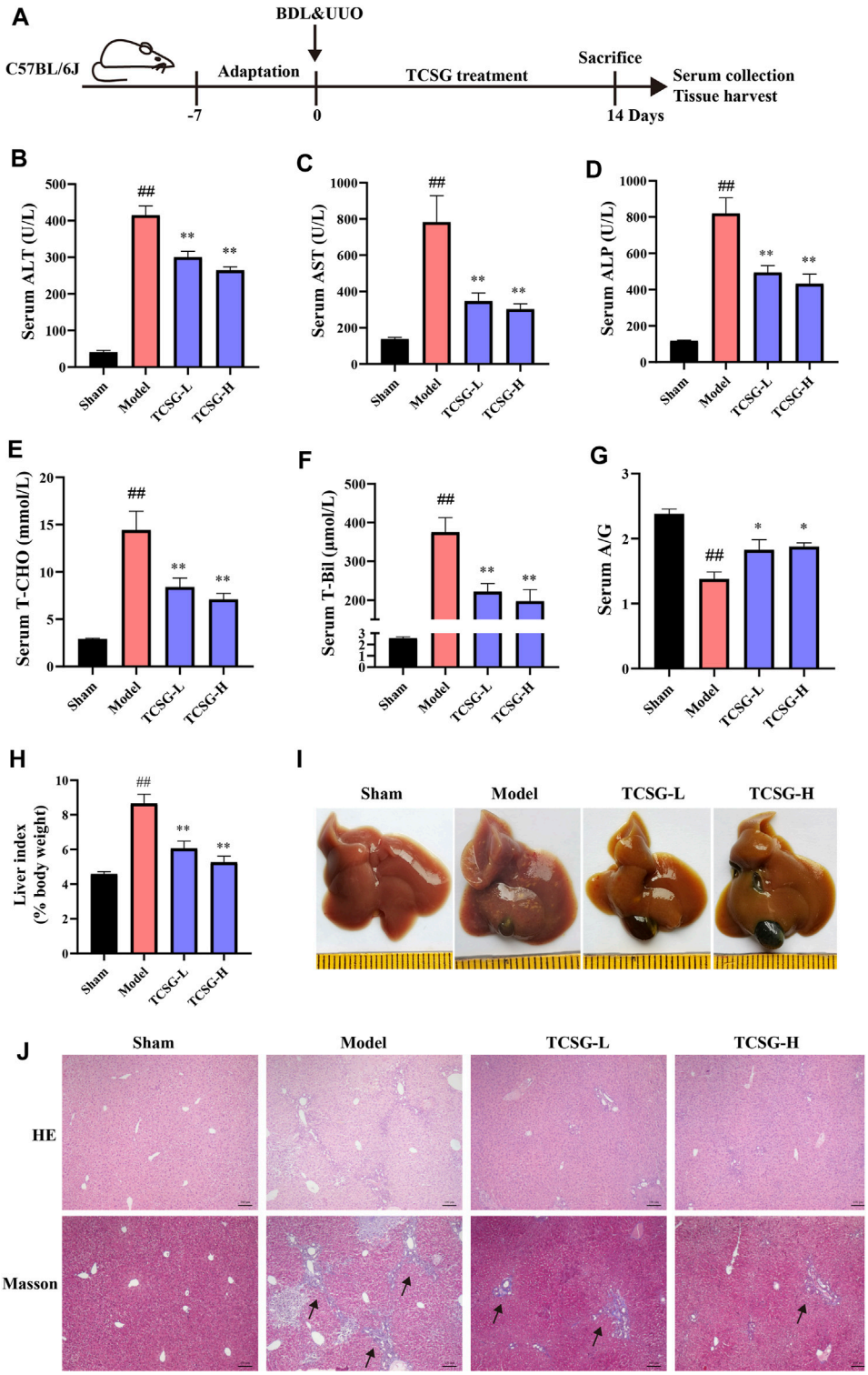


FIGURE 1 | TCSG from *Baishouwu* ameliorated liver damage in BDL&UUO mice. **(A)** Schematic diagram of hepatic and renal fibrosis model with TCSG treatment. After BDL&UUO operation, mice were treated with TCSG for consecutive 14 days, followed by sacrifice and tissues collection. **(B–G)** The effects of TCSG on serum biochemical measurements of liver injury. **(H)** The effects of TCSG on the liver index. **(G)** The effects of TCSG on the morphologic changes of the liver. **(J)** The effects of TCSG on liver pathological changes detected by HE staining and liver collagen accumulation determined by Masson staining (scale bar 100 μm). Data are shown as means ± SEM (n = 10–12), $^{\#\#}p < 0.01$, significantly different from sham group; $^{*}p < 0.05$, $^{**}p < 0.01$, significantly different from model group.

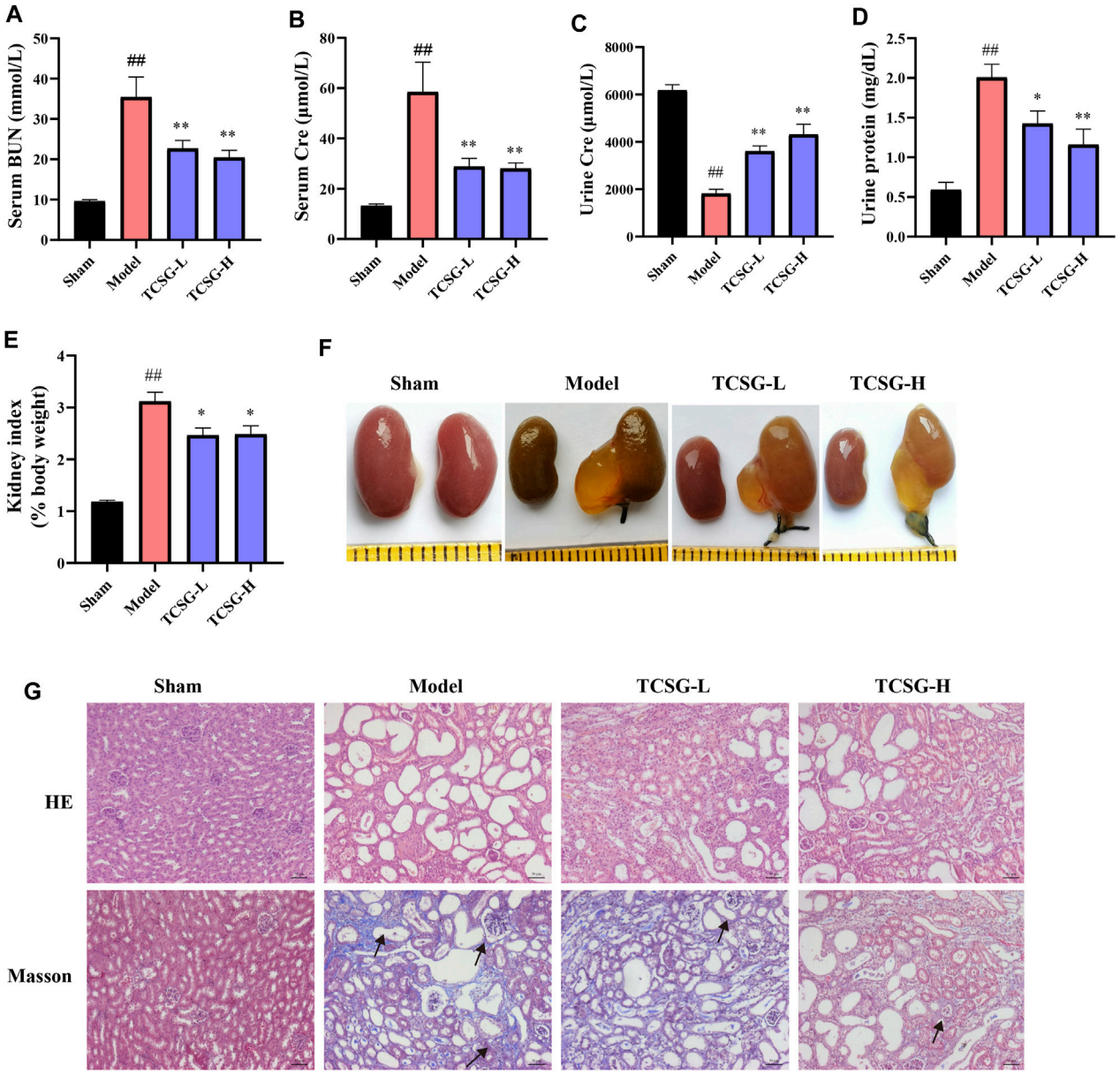


FIGURE 2 | TCSG from *Baishouwu* relieved kidney injury in BDL&UUO mice. **(A,B)** The effects of TCSG on serum biochemical measurements of kidney injury. **(C,D)** The effects of TCSG on urine biochemical measurements of kidney injury. **(E)** The effects of TCSG on the kidney index. **(F)** The effects of TCSG on the morphologic changes of the kidney. **(G)** The effects of TCSG on kidney pathological changes detected by HE staining and kidney collagen accumulation determined by Masson staining (scale bar 50 μm). Data are shown as means ± SEM (n = 10–12), $^{\#\#}p < 0.01$, significantly different from sham group; $^{*}p < 0.05$, $^{**}p < 0.01$, significantly different from model group.

Quantitative Real-Time PCR

Total RNA of liver and kidney tissues was extracted with TRIzol (Thermo Fisher Scientific, Shanghai, China) according to the manufacture's protocol. RNA was reversely transcribed into cDNA and quantitative real-time PCR (qRT-PCR) was performed on the detection systems (Bio-Rad, United States). Primer sequences used in the study were shown in **Table 1**. Samples were initially denaturized at 95°C for 15 min and processed under 40 consecutive thermal cycles (94°C, 15 s; 60°C, 30 s; 72°C, 30 s) followed by the final melting-curve cycle. The relative abundance was calculated by the ΔΔCt method. The transcript levels of genes were normalized to GAPDH in the corresponding sample.

Western Blot Analysis

The total proteins from liver and kidney tissues were lysed by RIPA buffer (Beyotime Biotechnology, Shanghai, China) containing 1% PMSF. Protein concentrations were determined using a BCA protein

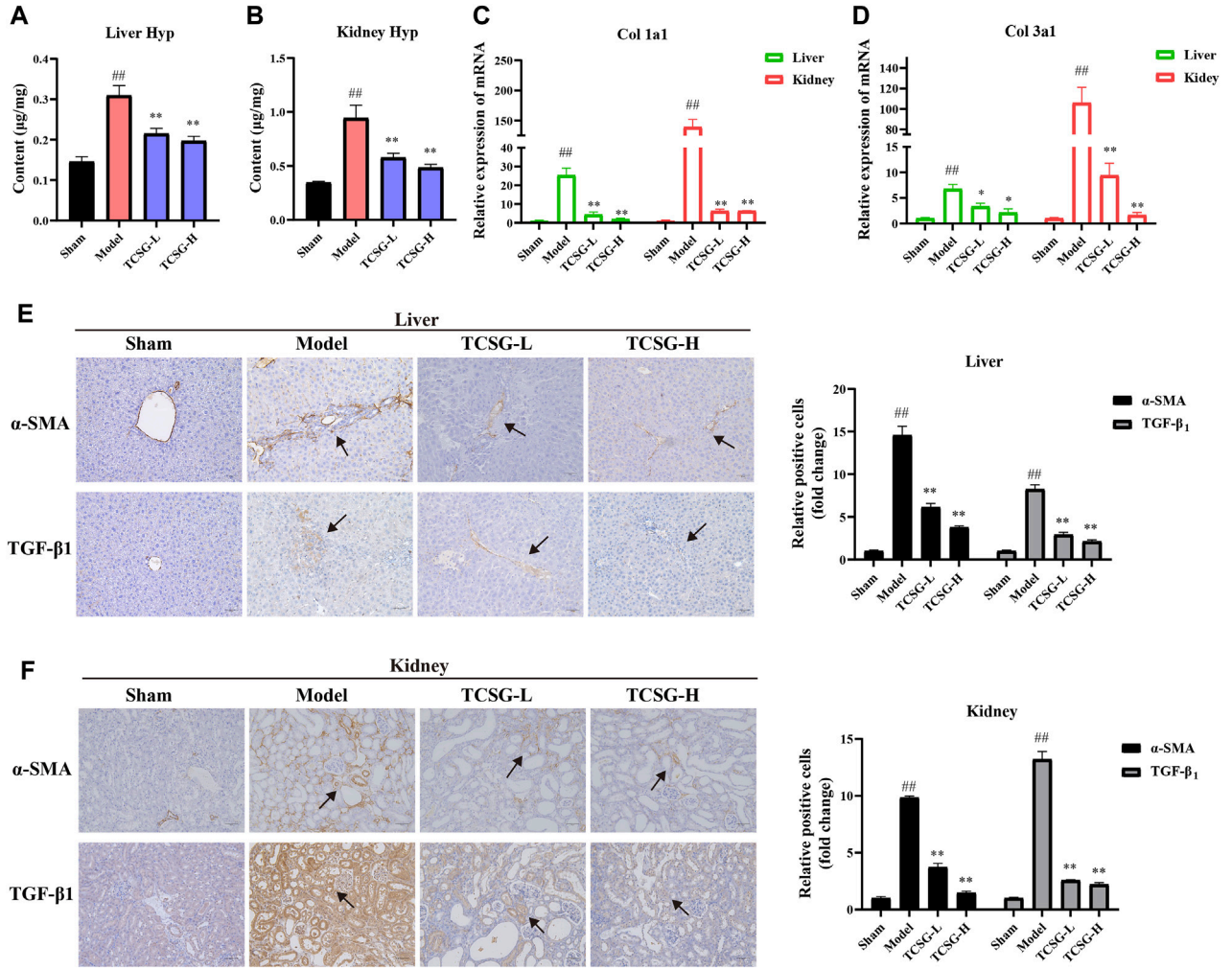


FIGURE 3 | TCSG from *Baishouwu* inhibited hepatic and renal fibrosis in BDL&UUO mice. **(A)** Liver hydroxyproline concentration assays. **(B)** Kidney hydroxyproline concentration assays. **(C,D)** mRNA expressions of Col 1a1 and Col 3a1 in mice liver and kidney samples. **(E)** Immunohistochemistry and quantitative analysis of the levels of α-SMA and TGF-β1 in the liver. **(F)** Immunohistochemistry and quantitative analysis of the levels of α-SMA and TGF-β1 in the kidney. Data are shown as means ± SEM (n = 6), $^{\#\#}p < 0.01$, significantly different from sham group; $^{*}p < 0.05$, $^{**}p < 0.01$, significantly different from model group.

assay kit (KeyGEN Biotech, Nanjing, China). The equal amount of lysates (30 μg) were separated by SDS-PAGE and then electrophoretically transferred to PVDF membranes (Millipore Billerica, MA, United States). Membranes were blocked with 5% skim milk in TBST at room temperature for 1 h and then incubated with primary antibodies, MyD88 (1:500, ab2064, Abcam), TRAF6 (1:2000, ab33915, Abcam), IKKα (1:1,000, ab32518, Abcam), p-IKKα (1:1,000, #2859, Cell Signaling Technology), NF-kB p65 (1:1,000, #8242, Cell Signaling Technology), p38 (1:1,000, #8690, Cell Signaling Technology), p-p38 (1:1,000, #4511, Cell Signaling Technology), JNK (1:1,000, #9252, Cell Signaling Technology), p-JNK (1:1,000, #4668, Cell Signaling Technology), Lamin B (1:1,000, ab133741, Abcam), and GAPDH (1:1,000, #2118, Cell Signaling Technology), overnight at 4°C. HRP-conjugated anti-rabbit/mouse IgG was then incubated with membranes for 1 h at room temperature. The blots were imaged using electrochemiluminescence with Tanon Automatic Chemiluminescence Image analysis system. The quantitative analysis was determined using Image J software.

Statistical Analysis

All data were expressed as mean ± SEM. GraphPad Prism 8 software was used for statistical analysis. Statistical significance was determined by using one-way analysis of variance (ANOVA) with Turkey's post hoc test. The significant difference was considered at $p < 0.05$.

RESULTS

TCSG From *Baishouwu* Ameliorated Liver Damage in BDL&UUO Mice

To evaluate the effects of TCSG from *Baishouwu* on liver damage in the BDL&UUO mice model, the liver biochemical parameters were

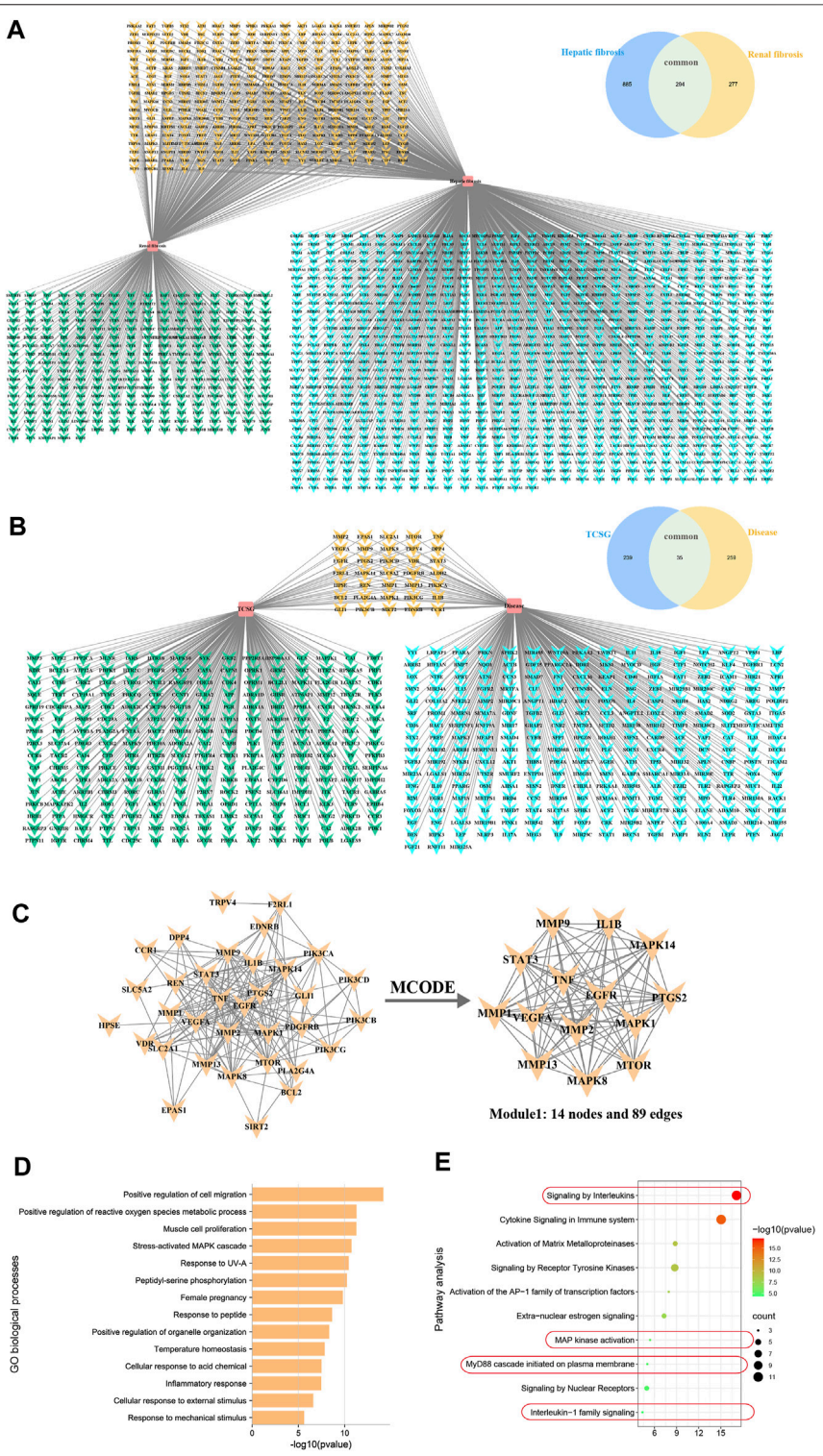


FIGURE 4 | Network pharmacology analyzed potential mechanisms for antifibrotic effects of TCSG from *Baishouwu*. **(A)** Unique and shared disease targets for hepatic fibrosis and renal fibrosis. **(B)** Common targets of TCSG in treating hepatic and renal fibrosis. **(C)** Construction of PPI network for TCSG therapeutic targets and the core genes analyzed by plug-in MCODE. **(D)** GO enrichment analysis of core targets for TCSG in treating hepatic and renal fibrosis. **(E)** Reactome pathways enrichment analysis of core targets for TCSG in treating hepatic and renal fibrosis.

firstly detected. Results showed that the levels of serum ALT and AST were significantly higher indicating liver injury in the model mice (**Figures 1B,C**). Significant elevation in the serum levels of ALP suggested cholestasis in the model mice (**Figure 1D**). On the other hand, the changes in serum levels of liver function biomarkers were also evident. Serum T-CHO and T-Bil were increased and serum A/G was decreased (**Figures 1E–G**). It was worth noting that these changes of biochemical markers were improved after the administration of TCSG. Liver tissue histopathological changes were also assessed in the BDL&UUO mice model. Results of the liver index indicated significant hepatomegaly in the model mice (**Figure 1H**). The liver morphology showed apparent changes in the group of model mice, the surface of which contained many visible white particles (**Figure 1I**). Further, HE staining and Masson staining revealed the evident inflammation, tissue necrosis, and collagen deposition in the model group (**Figure 1J**). Nevertheless, treatment with TCSG positively affected the liver index of the model mice, and TCSG administration also improved the liver pathological changes. Together, these data indicated that TCSG from *Baishouwu* attenuated liver damage in the BDL&UUO mice model.

TCSG From *Baishouwu* Relieved Kidney Injury in BDL&UUO Mice

Next, the kidney biochemical parameters were investigated to assess the effects of TCSG from *Baishouwu* on kidney injury in the BDL&UUO mice model. As shown in **Figure 2**, serum BUN and Cre were significantly upregulated in the model group (**Figures 2A,B**). Urinalysis of biomarkers also revealed an increase in urine protein and Cre (**Figures 2C,D**). TCSG treatment, both at low and high doses, markedly decreased serum and urine biomarkers, suggesting the alleviated kidney injury in BDL&UUO mice. Moreover, organ weight indices exhibited an abnormal weight of the kidney in the model mice (**Figure 2E**), and kidney morphology showed partial renal tubular dilatation and vacuolar deformation in the model mice (**Figure 2F**). HE staining of the model mice presented interstitial inflammation, tubular atrophy, and necrosis meanwhile, Masson staining revealed the obvious collagen deposition (**Figure 2G**). It was found that not only the organ weight indices but also pathological changes of the kidney showed a corresponding improvement after treatment with TCSG in BDL&UUO mice. These findings suggested that TCSG from *Baishouwu* relieved kidney injury in the BDL&UUO mice model.

TCSG From *Baishouwu* Inhibited Hepatic and Renal Fibrosis in BDL&UUO Mice

The visible collagen formation in the liver and kidney was associated with the progression of fibrosis, thus we further estimated the effects of TCSG on hepatic and renal fibrosis. The severity of fibrosis was determined biochemically by measuring Hyp content in the liver and kidney. Results showed the distinct upregulation of Hyp content in the liver and kidney of model mice, however, TCSG remarkably downregulated Hyp content (**Figures 3A,B**). The levels of fibrogenic markers in the liver and kidney, including Col 1a1 and Col 3a1, were significantly elevated in the model mice but decreased after treatment with TCSG (**Figures 3C,D**). Immunohistochemistry assays also validated that the expressions of TGF-β1 and α-SMA were increased in the liver and kidney of model mice, whereas TCSG treatment reduced the expression of these fibrogenic genes (**Figures 3E,F**). Accordingly, these data suggested that TCSG from *Baishouwu* exerted beneficial effects to inhibit the progression of hepatic fibrosis and renal fibrosis in BDL&UUO mice.

Network Pharmacology Analyzed Potential Mechanisms for Antifibrotic Effects of TCSG From *Baishouwu*

To explore the molecular mechanism associated with the anti-fibrotic effects of TCSG from *Baishouwu*, the network pharmacology technique was applied, which provided directions to illustrate the related potential targets and the hub for signaling pathways. As for 12 bioactive components in TCSG from *Baishouwu*, 274 targets were retrieved from databases and counted to construct the composition-target network (**Supplementary Table S1** and **Supplementary Figure S2**). Meanwhile, a total of 1,456 targets were identified from 1,179 hepatic fibrosis-related targets and 571 renal fibrosis-related targets (**Supplementary Table S2**). Among them, 294 targets were shared by hepatic and renal fibrosis, which accounted for 24.94% of the hepatic fibrosis-related targets and 51.49% of the renal fibrosis-related targets (**Figure 4A**). The compound-disease network was constructed and 35 common targets were identified as potential therapeutic targets for TCSG against hepatic and renal fibrosis (**Figure 4B**). Then the PPI networks of potential therapeutic targets were built in the STRING database, which was subsequently imported in Cytoscape3.8.0 for analysis. The MCODE plug-in was used to calculate the modules involved in special functions. Module 1 got the best score of 13.69 and consisted of 14 hub target genes (**Figure 4C**). Furthermore, candidate targets of the core PPI network were subjected to GO biological processes and pathway enrichment analysis in the Reactome database. The relevant biological processes of TCSG against fibrosis of the liver and kidney were shown in **Figure 4D** and the significantly enriched pathways showed that the core targets were strongly associated with "Signaling by interleukins", "MAP kinase activation", "MyD88 cascade initiated on plasma membrane", and "Interleukin-1 family signaling" (**Figure 4E**). Combined with the enrichment analysis results and the annotation of the Reactome database, it can be seen that TCSG from *Baishouwu* may affect inflammatory cascade through IL-1β/MyD88 signaling (**Supplementary Figure S3**).

TCSG From *Baishouwu* Ameliorated Hepatic and Renal Fibrosis by Suppressing IL-1β/MyD88 Inflammation Signaling

Although the signals driving fibrogenesis have not been fully elucidated, several lines of evidence suggest that IL-1 signals play a vital role in triggering fibrotic liver and kidney disease (Kamari

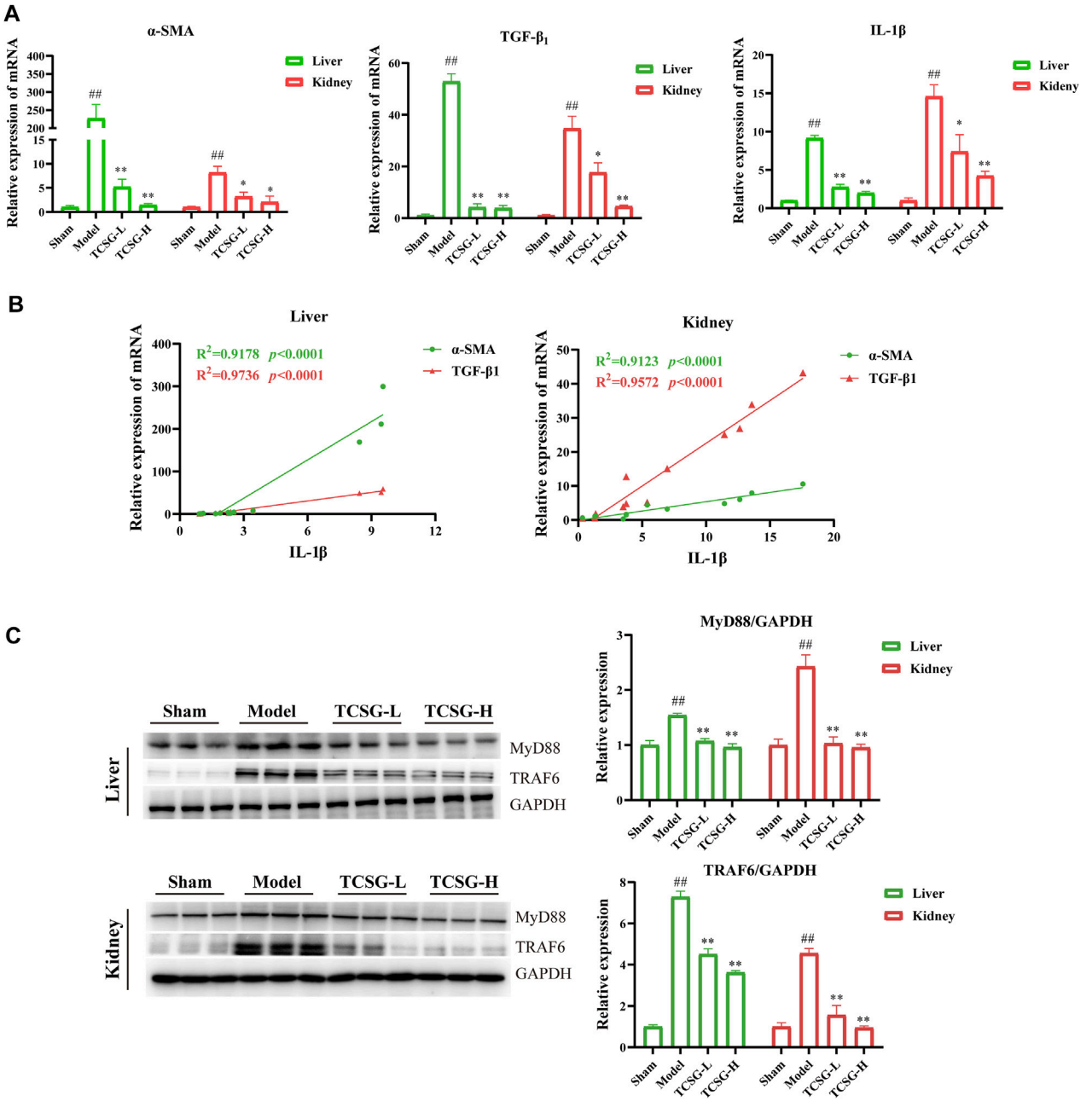


FIGURE 5 | TCSG from *Baishouwu* ameliorated hepatic and renal fibrosis by suppressing IL-1β/MyD88 inflammation signaling. **(A)** mRNA expressions of α-SMA, TGF-β1, and IL-1β in the liver and kidney. **(B)** Correlation of IL-1β levels with α-SMA and TGF-β1 levels in the liver and kidney. R = Spearman's rank correlation coefficient. **(C)** Western blot and quantitative analysis of MyD88 and TRAF6 expression in the liver and kidney. Data are shown as means ± SEM (n = 3), $^{\#\#}p < 0.01$, significantly different from sham group; $^{*}p < 0.05$, $^{**}p < 0.01$, significantly different from model group.

et al., 2011; Lemos et al., 2018). According to the results of comprehensive informatics analysis, TCSG may exhibit the antifibrotic effect by affecting inflammatory cascade through IL-1β/MyD88 signaling. Thus, we validated the related mechanism in the BDL&UUO mice model. Results of qRT-PCR showed that the levels of α-SMA, TGF-β1, and IL-1β were significantly increased both in the liver and kidney of model mice, however, TCSG treatment reversed these changes (**Figure 5A**). Notably, regression analysis revealed that the levels of IL-1β were positively associated with the expression of α-SMA and TGF-β1 (**Figures 5B,C**), which suggested the possibility that TCSG-antifibrotic effects were tightly correlated with IL-1β signal transduction. Western bolt analysis displayed that the expression of MyD88 and TRAF6 was high, but was significantly reduced after treatment with TCSG in the liver and kidney of BDL&UUO mice (**Figure 5D**). To sum up, these data demonstrated that

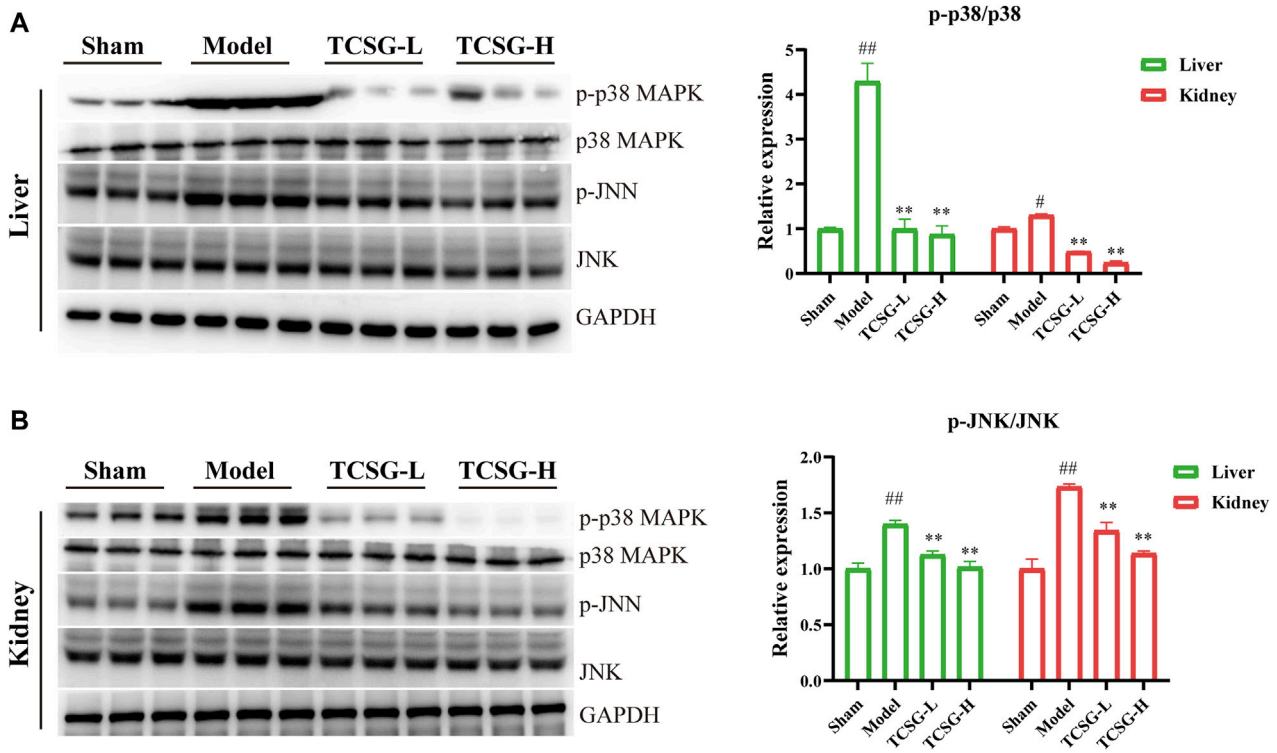


FIGURE 6 | TCSG from *Baishouwu* repressed p38 MAPK/JNK signaling in the liver and kidney. **(A)** Western blot and quantitative analysis of p38 MAPK and p-JNK expression in the liver. **(B)** Western blot and quantitative analysis of p38 MAPK and p-JNK expression in the kidney. Data are shown as means ± SEM ($n = 3$), $^{\#}p < 0.05$, $^{\#\#}p < 0.01$, significantly different from sham group; $^{**}p < 0.01$, significantly different from model group.

TCSG from *Baishouwu* could affect the IL-1β/MyD88 signaling in the BDL&UUO mice model, yet the downstream biological pathways needed further study.

TCSG From *Baishouwu* Repressed p38 MAPK/JNK Signaling and Blocked the Nuclear Localization of NF-κB p65 in the Liver and Kidney

MAPK cascade and NF-κB family members act as essential components of the MyD88/TRIF6-dependent inflammation signal transduction pathway (Lim and Staudt, 2013; Liu and Ding, 2016). Results of enrichment analysis revealed that TCSG-related core targets were significantly enriched in MAP kinase (MAPK) activation and the hub target genes of TCSG against fibrosis contained MAPK14, one of the p38 MAPKs which plays an important role in response to inflammatory stimuli. Accordingly, we examined the effects of TCSG on p38 MAPK activation. As shown in **Figure 6A**, the levels of p-p38 MAPK and p-JNK were remarkably up-regulated in the liver of model mice compared to the control, whereas TCSG treatment alleviated these changes. Similarly, the levels of p-p38 MAPK and p-JNK were increased in the kidney of model mice but decreased after TCSG administration (**Figure 6B**). Furthermore, western blot results showed that TCSG treatment reduced the levels of p-IκB in the liver and kidney, the phosphorylation of which could subsequently liberate the active NF-κB, and the elevated levels of nuclear NF-κB p65 were also reversed by TCSG administration (**Figures 7A,B**). Together, these data demonstrated that p38 MAPK/JNK and NF-κB p65 signaling participated in antifibrotic effects of TCSG from *Baishouwu* in the BDL&UUO mice model.

DISCUSSION

In the current study, a mouse model of hepatic and renal fibrosis was employed to evaluate the protective effects of TCSG from *Baishouwu* on liver and kidney injury and to explore the correlation between hepatic and renal fibrosis. We found that TCSG from *Baishouwu* alleviated the dysfunction of the liver and kidney and reduced the degree of fibrosis both in the liver and kidney by inhibiting the generation of collagen in BDL&UUO mice. Network pharmacology analysis showed that inflammation response was a major contributing factor to the anti-fibrotic effects of TCSG from *Baishouwu* on the liver and kidney. Further studies demonstrated that TCSG from *Baishouwu* suppressed the development of hepatic and renal fibrosis through inhibiting MyD88 signal transduction activated by IL-1β and subsequent p38 MAPK and NF-κB p65 downstream signaling. Taken together, these findings suggest a potential

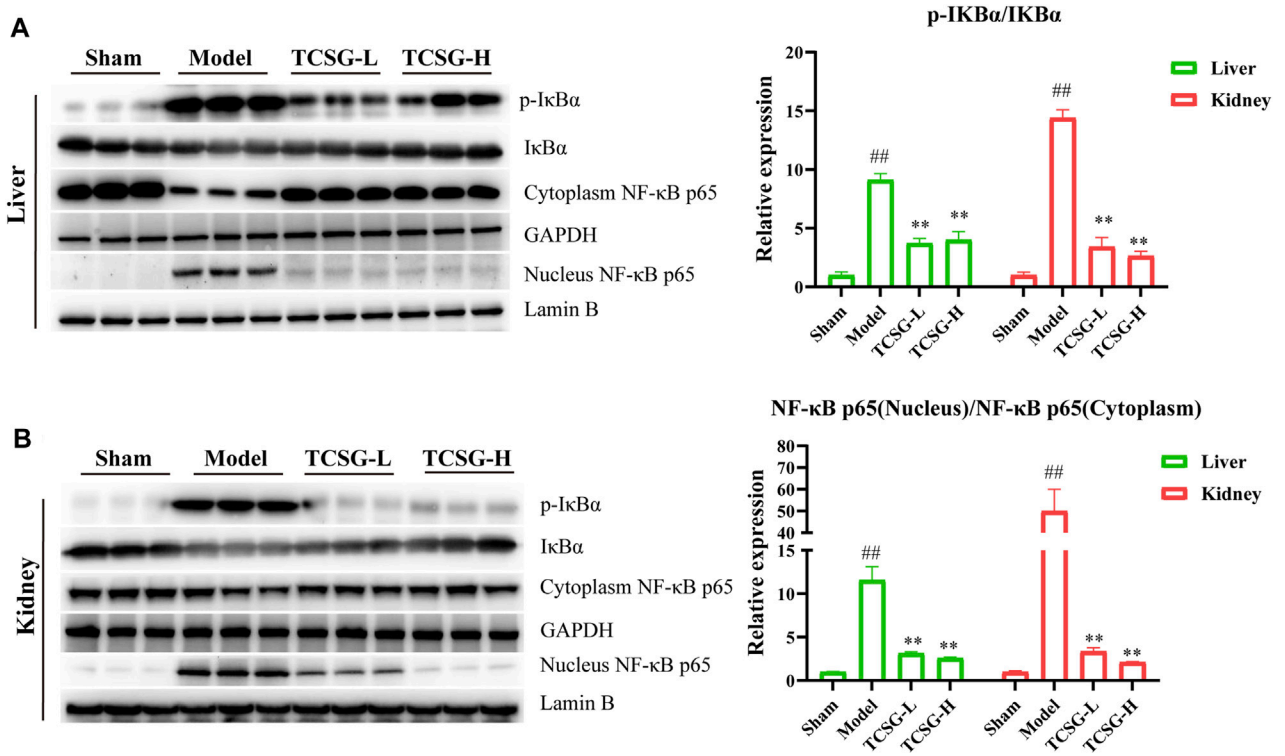


FIGURE 7 | TCSG from *Baishouwu* blocked the nuclear localization of NF-κB p65 in the liver and kidney. **(A)** Western blot and quantitative analysis of p-IκBα and nucleus NF-κB p65 expression in the liver. **(B)** Western blot and quantitative analysis of p-IκBα and nucleus NF-κB p65 expression in the kidney. Data are shown as means ± SEM (n = 3), $^{\#\#}p < 0.01$, significantly different from sham group; $^{**}p < 0.01$, significantly different from model group.

correlation between hepatic and renal fibrosis and provide a new therapeutic approach to treat hepatic and renal fibrosis.

Emerging evidence reveals the crosstalk between organs which can affect their function. According to the clinical data, hepatic failure often leads to renal failure, and respectively, kidney dysfunction can result in dysregulated lipid metabolism and dyslipidemia (Wadei, 2012; Agrawal et al., 2018). As more studies demonstrate the strong correlation between chronic liver disease and kidney disease recently, there is an increased interest in understanding the liver-kidney axis (Raj et al., 2020; Heda et al., 2021). The previous study had developed a rodent model of BDL followed by lipopolysaccharide (LPS) injection to generate acute kidney injury and determine the pathophysiology of renal failure in cirrhosis, however, the development of renal fibrosis was not observed in the BDL&LPS model (Shah et al., 2012). We used to establish a model of hepatic and renal fibrosis by thioacetamide and UUO in SD rats, nevertheless, the low survival rate of the model group brought worry about the experimental animal amount (Zhuang et al., 2021). In the present study, we optimized the selection the coexistence of the hepatic and renal fibrosis model and explored the effects of medicine on the prevention and treatment of the disease. For the classical hepatic fibrosis model and renal interstitial fibrosis model, the combination of BDL and UUO can quickly establish a rodent model with the coexistence of hepatic and renal fibrosis. Our results showed that there was significant dysfunction of the liver and kidney in BDL&UUO mice, as well as well-characterized fibrosis both in the liver and kidney, which suggested that the BDL&UUO model could be employed to investigate the relationship between hepatic fibrosis and renal fibrosis.

Baishouwu is a traditional tonic that can boost the liver and kidney, enrich vital essence and blood, strengthen the bones and muscles, and benefit life essence based on the theory of TCM (Chen et al., 2019). According to the phytochemical studies, acetophenones and C-21 steroidal glycosides are the major bioactive constituents of *Baishouwu*. Moreover, it has been considered that the medicinal value of C-21 steroidal glycosides is more prominent. Pharmacological research reported that TCSG from *Baishouwu* could be used to treat chronic hepatitis and hepatic fibrosis and our previous study demonstrated that TCSG from *Baishouwu* had therapeutic effects on liver cancer and hepatic inflammation (Peng et al., 2008; Ding et al., 2019). In this study, we found that TCSG from *Baishouwu* remarkably improved the function of the liver and kidney and alleviated the degree of hepatic and renal fibrosis in BDL&UUO mice. Our data not only provided a potential therapeutic approach for hepatic and renal fibrosis therapy but also verified TCM theory "boost liver and kidney". Furthermore, network pharmacological analysis was applied to assess the related biological system networks. Our previous research has determined the 12 bioactive components in TCSG from *Baishouwu* and the associated targets were obtained from the

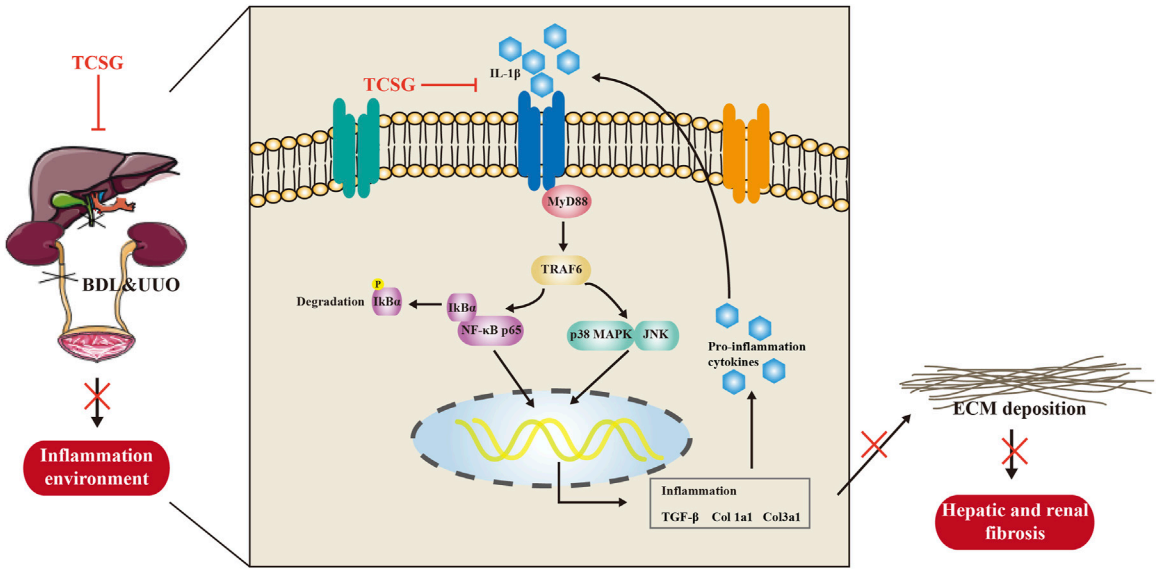


FIGURE 8 | The schematic diagram of the potential mechanism of TCSG from Baishouwu against hepatic and renal fibrosis.

database. Finally, 35 corresponding targets were found to be therapeutic targets against hepatic and renal fibrosis, among which the most critical targets were IL-1β, MAPK14, PTGS2, mTOR, MAPK8, MMP13, MMP1, MMP9, MAPK1, STAT3, TNF, EGFR, VEGFA, and MMP2. The core targets were further subjected to function and pathway enrichment analysis, the result of which showed that TCSG might regulate inflammatory response through the cascade of events by Interleukins signaling, MAP kinase activation, MyD88 cascade initiated on plasma membrane, and Interleukin-1 family signaling pathways. In conclusion, these data provided the direction of underlying mechanisms for TCSG from *Baishouwu* against hepatic and renal fibrosis.

Chronic systemic inflammation is thought to have a pivotal role in the pathogenesis of hepatic fibrosis and renal fibrosis. It has become increasingly evident that excessive release of pro-inflammatory cytokines contributes to promoting the progression of fibrosis. In hepatic fibrosis, pro-inflammatory cytokines, including IL-1, IL-6, and TNF-α, generated by Kupffer, hepatocytes, and infiltrating inflammatory cells promote liver damage (Poniachik et al., 2006; Rock et al., 2010; Stienstra et al., 2010). Similarly, during kidney injury, pro-inflammatory cytokines trigger cell stress and drive secondary inflammatory mediators in the renal epithelium and interstitial stroma contributing to the renal fibrogenic process (Anders, 2014; Cao et al., 2015). More specifically, mounting evidence indicates that IL-1β can accelerate TGF-β1 expression and collagen production in the absence of Smad signaling (Cáceres et al., 2019), the reason of which lies in the fact that IL-1β exerts its effects by binding to IL-1 receptor and signal transduction adaptor MyD88, regulating fibrosis both in the liver and kidney (Kamari et al., 2011; Lemos et al., 2018). Our data showed the expression of α-SMA and TGF-β1 were positively correlated with the levels of IL-1β, indicating that the anti-fibrotic effects of TCSG from *Baishouwu* were closely related to IL-1β inflammatory response. Combined with the results of network pharmacological analysis, we further detected the MyD88 signaling and found that the current model of fibrogenesis activated MyD88/TRAF6 signal transduction in the liver and kidney, whereas TCSG from *Baishouwu* reversed the activation. This observation was consistent with previous studies pointing out that the IL-1β/MyD88-dependent mechanism could amplify inflammation and exacerbate fibrosis in the response to tissue injury (Gasse et al., 2007; Leaf et al., 2017). Our findings added further information in the understanding of inflammatory response in tissue injury and implicated the IL-1β/MyD88 signaling in the liver-kidney axis in the fibrogenic process.

The p38 MAPK and JNK signaling is an important intracellular signaling pathway associated with the production of profibrotic mediators. Inhibition of the activation of p38 MAPK or JNK can protect against inflammation and fibrosis (Sugiyama et al., 2012). Our study represented that TCSG from *Baishouwu* inhibited the phosphorylation of p38 MAPK and JNK induced by BDL&UUO surgery in the liver and kidney, indicating that p38 MAPK/JNK signaling was a downstream effector signal of inflammatory response affected by TCSG from *Baishouwu*. In addition, we have observed that TCSG from *Baishouwu* has affected the activation of NF-κB p65, which is a key transcriptional regulator of inflammatory signals and appears to regulate fibrosis via multiple mechanisms, including direct fibrogenic responses and antiapoptotic effects (Luedde and Schwabe, 2011). In the canonical pathway, IκBα is the most prominent inhibitor of NF-κB p65 activity, the phosphorylation of which can subsequently be degraded and liberates NF-κB p65 for nuclear entry. The current study demonstrated that inhibition of the activation of p38 MAPK/JNK and NF-κB p65 signaling cascade exerted protective effects against hepatic and renal fibrosis, nevertheless, previous research had pointed out that

NF-κB p65 could collaborate with p38 MAPK and resist hepatocyte apoptosis induced by TNF or LPS (Heinrichsdorff et al., 2008). These contradictory conclusions show an interesting finding that NF-κB mediates both pro-inflammatory and anti-apoptotic responses among different models of liver injury, and a very weak or a very strong NF-κB activation may cause negative effects on the liver. Complete blockage of TNF-induced NF-κB activation in conditional deletion animals resulted in massive hepatocyte apoptosis after LPS injection (Luedde et al., 2007; Inokuchi et al., 2010), while inhibition of NF-κB in Kupffer cells or hepatic stellate cells led to a decrease in the severity of liver fibrosis both in chronically injured animals and patients with hepatitis C virus (Son et al., 2007; Oakley et al., 2009). It is noted that excessive stimulation of IL-1β promoted NF-κB activation to exceed its threshold and thereby accentuated hepatic inflammation and fibrosis in the BDL&UUO mice model. Accordingly, NF-κB p65 signaling was also a downstream effector of TCSG against fibrosis.

Although the current data suggested the role of IL-1β/MyD88 inflammation signaling in the liver-kidney axis to a certain extent, there are still some limitations to be further solved. Whether the pathological changes in the model of BDL&UUO were the direct toxicity of organs at the same time or the injury based on the interaction of liver and kidney function was unclear. As a result, it needs to systematically explore the changes in the model of BDL&UUO using omics technology in future research. Moreover, the establishment of co-culture of hepatic stellate cells and renal tubular epithelial cells to examine the relationship of liver and kidney under the influence of inflammatory factors can also contribute to enhancing the understanding of the crosstalk between the liver and kidney.

CONCLUSION

Our results demonstrate strong evidence for the anti-inflammatory effect of TCSG from *Baishouwu* on hepatic and renal fibrosis in the BDL&UUO mice model. The present study highlights the importance of the IL-1β/MyD88-induced inflammation signaling in the development of hepatic and renal fibrosis (**Figure 8**). The insights obtained from this study have important implications for the development of novel therapies for hepatic and renal fibrosis.

DATA AVAILABILITY STATEMENT

The original contributions presented in the study are included in the article/**Supplementary Material**, further inquiries can be directed to the corresponding authors.

ETHICS STATEMENT

The animal study was reviewed and approved by Ethics Committee of Jiangsu Integrated Traditional Chinese and Western Medicine Hospital (Affiliated Hospital of Integrated Traditional Chinese and Western Medicine, Nanjing University of Chinese Medicine).

AUTHOR CONTRIBUTIONS

TQ, MW, and MH designed the study and drafted the original manuscript. MW, TZ, and YW carried out the animal experiment. TQ conducted the network pharmacology analysis. YZ and ZZ assisted in biochemical tests and molecular mechanism research. YD and YP contributed to the data analysis and revised the manuscript. All the authors approved the final manuscript.

FUNDING

This study was funded by the National Natural Science Fund of China (Nos. 81774178, 81378888).

SUPPLEMENTARY MATERIAL

The Supplementary Material for this article can be found online at: https://www.frontiersin.org/articles/10.3389/fphar.2021.775730/full#supplementary-material

REFERENCES

Agrawal, S., Zaritsky, J. J., Fornoni, A., and Smoyer, W. E. (2018). Dyslipidaemia in Nephrotic Syndrome: Mechanisms and Treatment. *Nat. Rev. Nephrol.* 14 (1), 57–70. doi:10.1038/nrneph.2017.155

Anders, H. J. (2014). Immune System Modulation of Kidney Regeneration-Mmechanisms and Implications. *Nat. Rev. Nephrol.* 10 (6), 347–358. doi:10.1038/nrneph.2014.68

Bernardi, M., Moreau, R., Angeli, P., Schnabl, B., and Arroyo, V. (2015). Mechanisms of Decompensation and Organ Failure in Cirrhosis: From Peripheral Arterial Vasodilation to Systemic Inflammation Hypothesis. *J. Hepatol.* 63 (5), 1272–1284. doi:10.1016/j.jhep.2015.07.004

Cáceres, F. T., Gaspari, T. A., Samuel, C. S., and Pinar, A. A. (2019). Serelaxin Inhibits the Profibrotic TGF-β1/IL-1β Axis by Targeting TLR-4 and the NLRP3 Inflammasome in Cardiac Myofibroblasts. *Faseb j* 33 (12), 14717–14733. doi:10.1096/fj.201901079RR

Cao, Q., Harris, D. C., and Wang, Y. (2015). Macrophages in Kidney Injury, Inflammation, and Fibrosis. *Physiology (Bethesda)* 30 (3), 183–194. doi:10.1152/physiol.00046.2014

Chen, W. H., Zhang, Z. Z., Ban, Y. F., Rahman, K., Ye, B. Z., Sun, X. L., et al. (2019). Cynanchum Bungei Decne and its Two Related Species for "Baishouwu": A Review on Traditional Uses, Phytochemistry, and Pharmacological Activities. *J. Ethnopharmacol* 243, 112110. doi:10.1016/j.jep.2019.112110

Chevalier, R. L., Forbes, M. S., and Thornhill, B. A. (2009). Ureteral Obstruction as a Model of Renal Interstitial Fibrosis and Obstructive Nephropathy. *Kidney Int.* 75 (11), 1145–1152. doi:10.1038/ki.2009.86

Cui, W. W., Peng, Y. R., and Ding, Y. F. (2019). Effects of Total C-21 Steroidal Glucosides from Cynanchum Auriculatum on Oxidative Stress Pathway in Mice with Liver Injury. *Zhongguo Zhong Yao Za Zhi* 44 (14), 2960–2965. doi:10.19540/j.cnki.cjcmm.20190426.401

Ding, Y. F., Wu, Z. H., Wei, Y. J., Shu, L., and Peng, Y. R. (2017). Hepatic Inflammation-Fibrosis-Cancer Axis in the Rat Hepatocellular Carcinoma Induced by Diethylnitrosamine. *J. Cancer Res. Clin. Oncol.* 143 (5), 821–834. doi:10.1007/s00432-017-2364-z

Ding, Y. F., Peng, Z. X., Ding, L., and Peng, Y. R. (2019). Baishouwu Extract Suppresses the Development of Hepatocellular Carcinoma via TLR4/MyD88/NF-Kb Pathway. *Front. Pharmacol.* 10, 389. doi:10.3389/fphar.2019.00389

Distler, J. H. W., Györfi, A. H., Ramanujam, M., Whitfield, M. L., Königshoff, M., and Lafyatis, R. (2019). Shared and Distinct Mechanisms of Fibrosis. *Nat. Rev. Rheumatol.* 15 (12), 705–730. doi:10.1038/s41584-019-0322-7

García, L., Hernández, I., Sandoval, A., Salazar, A., Garcia, J., Vera, J., et al. (2002). Pirfenidone Effectively Reverses Experimental Liver Fibrosis. *J. Hepatol.* 37 (6), 797–805. doi:10.1016/s0168-8278(02)00272-6

Gasse, P., Mary, C., Guenon, I., Noulin, N., Charron, S., Schnyder-Candrian, S., et al. (2007). IL-1R1/MyD88 Signaling and the Inflammasome Are Essential in Pulmonary Inflammation and Fibrosis in Mice. *J. Clin. Invest.* 117 (12), 3786–3799. doi:10.1172/jci32285

Heda, R., Yazawa, M., Shi, M., Bhaskaran, M., Aloor, F. Z., Thuluvath, P. J., et al. (2021). Non-Alcoholic Fatty Liver and Chronic Kidney Disease: Retrospect, Introspect, and Prospect. *World J. Gastroenterol.* 27 (17), 1864–1882. doi:10.3748/wjg.v27.i17.1864

Heinrichsdorff, J., Luedde, T., Perdiguero, E., Nebreda, A. R., and Pasparakis, M. (2008). p38 Alpha MAPK Inhibits JNK Activation and Collaborates with IkappaB Kinase 2 to Prevent Endotoxin-Induced Liver Failure. *EMBO Rep.* 9 (10), 1048–1054. doi:10.1038/embor.2008.149

Henderson, N. C., Rieder, F., and Wynn, T. A. (2020). Fibrosis: from Mechanisms to Medicines. *Nature* 587 (7835), 555–566. doi:10.1038/s41586-020-2938-9

Heymann, F., and Tacke, F. (2016). Immunology in the Liver-From Homeostasis to Disease. *Nat. Rev. Gastroenterol. Hepatol.* 13 (2), 88–110. doi:10.1038/nrgastro.2015.200

Inokuchi, S., Aoyama, T., Miura, K., Osterreicher, C. H., Kodama, Y., Miyai, K., et al. (2010). Disruption of TAK1 in Hepatocytes Causes Hepatic Injury, Inflammation, Fibrosis, and Carcinogenesis. *Proc. Natl. Acad. Sci. U S A.* 107 (2), 844–849. doi:10.1073/pnas.0909781107

Jang, S. A., Lee, S., Sohn, E. H., Yang, J., Park, D. W., Jeong, Y. J., et al. (2016). Cynanchum Wilfordii Radix Attenuates Liver Fat Accumulation and Damage by Suppressing Hepatic Cyclooxygenase-2 and Mitogen-Activated Protein Kinase in Mice Fed with a High-Fat and High-Fructose Diet. *Nutr. Res.* 36 (9), 914–924. doi:10.1016/j.nutres.2016.06.007

Kamari, Y., Shaish, A., Vax, E., Shemesh, S., Kandel-Kfir, M., Arbel, Y., et al. (2011). Lack of Interleukin-1α or Interleukin-1β Inhibits Transformation of Steatosis to Steatohepatitis and Liver Fibrosis in Hypercholesterolemic Mice. *J. Hepatol.* 55 (5), 1086–1094. doi:10.1016/j.jhep.2011.01.048

Leaf, I. A., Nakagawa, S., Johnson, B. G., Cha, J. J., Mittelsteadt, K., Guckian, K. M., et al. (2017). Pericyte MyD88 and IRAK4 Control Inflammatory and Fibrotic Responses to Tissue Injury. *J. Clin. Invest.* 127 (1), 321–334. doi:10.1172/jci87532

Lemos, D. R., McMurdo, M., Karaca, G., Wilflingseder, J., Leaf, I. A., Gupta, N., et al. (2018). Interleukin-1β Activates a MYC-Dependent Metabolic Switch in Kidney Stromal Cells Necessary for Progressive Tubulointerstitial Fibrosis. *J. Am. Soc. Nephrol.* 29 (6), 1690–1705. doi:10.1681/asn.2017121283

Li, X. Y., Zhou, L. F., Gao, L. J., Wei, Y., Xu, S. F., Chen, F. Y., et al. (2018). Cynanbungeigenin C and D, a Pair of Novel Epimers from Cynanchum Bungei, Suppress Hedgehog Pathway-Dependent Medulloblastoma by Blocking Signaling at the Level of Gli. *Cancer Lett.* 420, 195–207. doi:10.1016/j.canlet.2018.02.005

Lim, K. H., and Staudt, L. M. (2013). Toll-Like Receptor Signaling. *Cold Spring Harb Perspect. Biol.* 5 (1), a011247. doi:10.1101/cshperspect.a011247

Liu, Q., and Ding, J. L. (2016). The Molecular Mechanisms of TLR-Signaling Cooperation in Cytokine Regulation. *Immunol. Cel Biol* 94 (6), 538–542. doi:10.1038/icb.2016.18

Luedde, T., and Schwabe, R. F. (2011). NF-κB in the Liver-Llinking Injury, Fibrosis and Hepatocellular Carcinoma. *Nat. Rev. Gastroenterol. Hepatol.* 8 (2), 108–118. doi:10.1038/nrgastro.2010.213

Luedde, T., Beraza, N., Kotsikoris, V., van Loo, G., Nenci, A., De Vos, R., et al. (2007). Deletion of NEMO/IKKgamma in Liver Parenchymal Cells Causes Steatohepatitis and Hepatocellular Carcinoma. *Cancer Cell* 11 (2), 119–132. doi:10.1016/j.ccr.2006.12.016

Ma, H. D., Deng, Y. R., Tian, Z., and Lian, Z. X. (2013). Traditional Chinese Medicine and Immune Regulation. *Clin. Rev. Allergy Immunol.* 44 (3), 229–241. doi:10.1007/s12016-012-8332-0

Marcuccilli, M., and Chonchol, M. (2016). NAFLD and Chronic Kidney Disease. *Int. J. Mol. Sci.* 17 (4), 562. doi:10.3390/ijms17040562

Musso, G., Cassader, M., Cohney, S., Pinach, S., Saba, F., and Gambino, R. (2015). Emerging Liver-Kidney Interactions in Nonalcoholic Fatty Liver Disease. *Trends Mol. Med.* 21 (10), 645–662. doi:10.1016/j.molmed.2015.08.005

Oakley, F., Teoh, V., Ching-A-Sue, G., Bataller, R., Colmenero, J., Jonsson, J. R., et al. (2009). Angiotensin II Activates I kappaB Kinase Phosphorylation of RelA at Ser 536 to Promote Myofibroblast Survival and Liver Fibrosis. *Gastroenterology* 136 (7), 2334–2344. doi:10.1053/j.gastro.2009.02.081

Peng, Y. R., Li, Y. B., Liu, X. D., Zhang, J. F., and Duan, J. A. (2008). Antitumor Activity of C-21 Steroidal Glycosides from Cynanchum Auriculatum Royle Ex Wight. *Phytomedicine* 15 (11), 1016–1020. doi:10.1016/j.phymed.2008.02.021

Poniachik, J., Csendes, A., Díaz, J. C., Rojas, J., Burdiles, P., Maluenda, F., et al. (2006). Increased Production of IL-1alpha and TNF-Alpha in Lipopolysaccharide-Stimulated Blood from Obese Patients with Non-Alcoholic Fatty Liver Disease. *Cytokine* 33 (5), 252–257. doi:10.1016/j.cyto.2006.02.006

Raj, D., Tomar, B., Lahiri, A., and Mulay, S. R. (2020). The Gut-Liver-Kidney Axis: Novel Regulator of Fatty Liver Associated Chronic Kidney Disease. *Pharmacol. Res.* 152, 104617. doi:10.1016/j.phrs.2019.104617

Rock, K. L., Latz, E., Ontiveros, F., and Kono, H. (2010). The Sterile Inflammatory Response. *Annu. Rev. Immunol.* 28, 321–342. doi:10.1146/annurev-immunol-030409-101311

Shah, N., Dhar, D., El Zahraa Mohammed, F., Habtesion, A., Davies, N. A., Jover-Cobos, M., et al. (2012). Prevention of Acute Kidney Injury in a Rodent Model of Cirrhosis Following Selective Gut Decontamination Is Associated with Reduced Renal TLR4 Expression. *J. Hepatol.* 56 (5), 1047–1053. doi:10.1016/j.jhep.2011.11.024

Shen, Y. L., Wang, S. J., Rahman, K., Zhang, L. J., and Zhang, H. (2018). Chinese Herbal Formulas and Renal Fibrosis: An Overview. *Curr. Pharm. Des.* 24 (24), 2774–2781. doi:10.2174/1381612824666180829103355

Son, G., Iimuro, Y., Seki, E., Hirano, T., Kaneda, Y., and Fujimoto, J. (2007). Selective Inactivation of NF-kappaB in the Liver Using NF-kappaB Decoy Suppresses CCl4-Induced Liver Injury and Fibrosis. *Am. J. Physiol. Gastrointest. Liver Physiol.* 293 (3), G631–G639. doi:10.1152/ajpgi.00185.2007

Stienstra, R., Saudale, F., Duval, C., Keshtkar, S., Groener, J. E., van Rooijen, N., et al. (2010). Kupffer Cells Promote Hepatic Steatosis via Interleukin-1beta-dependent Suppression of Peroxisome Proliferator-Activated Receptor Alpha Activity. *Hepatology* 51 (2), 511–522. doi:10.1002/hep.23337

Sugiyama, N., Kohno, M., and Yokoyama, T. (2012). Inhibition of the P38 MAPK Pathway Ameliorates Renal Fibrosis in an NPHP2 Mouse Model. *Nephrol. Dial. Transpl.* 27 (4), 1351–1358. doi:10.1093/ndt/gfr550

Targher, G., Chonchol, M., Zoppini, G., Abaterusso, C., and Bonora, E. (2011). Risk of Chronic Kidney Disease in Patients with Non-Alcoholic Fatty Liver Disease: Is There a Link. *J. Hepatol.* 54 (5), 1020–1029. doi:10.1016/j.jhep.2010.11.007

Tecklenborg, J., Clayton, D., Siebert, S., and Coley, S. M. (2018). The Role of the Immune System in Kidney Disease. *Clin. Exp. Immunol.* 192 (2), 142–150. doi:10.1111/cei.13119

Wadei, H. M. (2012). Hepatorenal Syndrome: A Critical Update. *Semin. Respir. Crit. Care Med.* 33 (1), 55–69. doi:10.1055/s-0032-1301735

Wang, X. J., Li, Z. L., Lv, X. H., Zuo, Q. Y., Zhao, Y. M., Ding, Y. F., et al. (2017). Antitumor Evaluation and Multiple Analysis on Different Extracted Fractions of the Root of Cynanchum Auriculatum Royle Ex Wight. *J. Sep. Sci.* 40 (15), 3054–3063. doi:10.1002/jssc.201601415

Wang, H. N., Shen, Z., Liu, Q., Hou, X. Y., Cao, Y., Liu, D. H., et al. (2020). Isochlorogenic Acid (ICGA): Natural Medicine with Potentials in Pharmaceutical Developments. *Chin. J. Nat. Med.* 18 (11), 860–871. doi:10.1016/s1875-5364(20)60029-2

Weiskirchen, R., Weiskirchen, S., and Tacke, F. (2019). Organ and Tissue Fibrosis: Molecular Signals, Cellular Mechanisms and Translational Implications. *Mol. Aspects Med.* 65, 2–15. doi:10.1016/j.mam.2018.06.003

Yin, X., and Peng, Y. (2020). Effects of Total C-21 Steroidal Glucosides from Cynanchum Auriculatum on Renal Fibrosis in Rats and Mechanisms Involved.

Chin. Traditional Herbal Drugs 51 (11), 3021–3028. doi:10.7501/j.issn.0253-2670.2020.11.021

Yokota, S., Ono, Y., Nakao, T., Zhang, P., Michalopoulos, G. K., and Khan, Z. (2018). Partial Bile Duct Ligation in the Mouse: A Controlled Model of Localized Obstructive Cholestasis. *J. Vis. Exp.* 133, 56930. doi:10.3791/56930

Zhang, L., and Schuppan, D. (2014). Traditional Chinese Medicine (TCM) for Fibrotic Liver Disease: Hope and Hype. *J. Hepatol.* 61 (1), 166–168. doi:10.1016/j.jhep.2014.03.009

Zhang, T., Ding, Y., and Peng, Y. (2021). Mechanism of Total C-21 Steroidal Glucosides from Root of Cynanchum Auriculatum in Activation of Human Hepatic Stellate Cells via TGF-β1/Smad Signaling Pathway. *Chin. Pharmacol. Bull.* 37 (9), 1231–1236. doi:10.3969/j.issn.1001-1978.2021.09.009

Zhao, X., Kwan, J. Y. Y., Yip, K., Liu, P. P., and Liu, F. F. (2020). Targeting Metabolic Dysregulation for Fibrosis Therapy. *Nat. Rev. Drug Discov.* 19 (1), 57–75. doi:10.1038/s41573-019-0040-5

Zhuang, Z. R., Wang, M. L., Peng, Y. R., and Shen, M. Q. (2021). Effect of C21 Steroidal Glycoside of Cynanchum Auriculatum on Liver and Kidney Fibrosis through TLR4 Pathway. *Zhongguo Zhong Yao Za Zhi* 46 (11), 2857–2864. doi:10.19540/j.cnki.cjcmm.20200105.401

Conflict of Interest: The authors declare that the research was conducted in the absence of any commercial or financial relationships that could be construed as a potential conflict of interest.

Publisher's Note: All claims expressed in this article are solely those of the authors and do not necessarily represent those of their affiliated organizations, or those of the publisher, the editors and the reviewers. Any product that may be evaluated in this article, or claim that may be made by its manufacturer, is not guaranteed or endorsed by the publisher.

Copyright © 2021 Qin, Wang, Zhang, Wang, Zhang, Hasnat, Zhuang, Ding and Peng. This is an open-access article distributed under the terms of the Creative Commons Attribution License (CC BY). The use, distribution or reproduction in other forums is permitted, provided the original author(s) and the copyright owner(s) are credited and that the original publication in this journal is cited, in accordance with accepted academic practice. No use, distribution or reproduction is permitted which does not comply with these terms.

frontiers in Pharmacology

ORIGINAL RESEARCH
published: 28 October 2021
doi: 10.3389/fphar.2021.764904

Metabolomics Study of Guizhi Fuling Capsules in Rats With Cold Coagulation Dysmenorrhea

Yu Zhang†, Na Su†, Weiyi Liu, Qingqing Wang, Jianguo Sun and Ying Peng**

Key Lab of Drug Metabolism and Pharmacokinetics, State Key Laboratory of Natural Medicines, China Pharmaceutical University, Nanjing, China

OPEN ACCESS

Edited by:
Zhaocheng Ma, Huazhong Agricultural University, China

Reviewed by:
Shih-Min Hsia, Taipei Medical University, Taiwan
Longshan Zhao, Shenyang Pharmaceutical University, China

***Correspondence:**
Jianguo Sun
jgsun@cpu.edu.cn
Ying Peng
1020162518@cpu.edu.cn

†Yu Zhang and Na Su contributed equally to this research.

Specialty section:
This article was submitted to Inflammation Pharmacology, a section of the journal Frontiers in Pharmacology

Received: *26 August 2021*
Accepted: *14 October 2021*
Published: *28 October 2021*

Citation:
Zhang Y, Su N, Liu W, Wang Q, Sun J and Peng Y (2021) Metabolomics Study of Guizhi Fuling Capsules in Rats With Cold Coagulation Dysmenorrhea. Front. Pharmacol. 12:764904. doi: 10.3389/fphar.2021.764904

Dysmenorrhea refers to a kind of uterine cramping pain that occurs in women during the period of menstrual. Guizhi Fuling Capsules are mainly used for the treatment of various pain syndromes and especially effective in treating primary dysmenorrhea. However, the research on its modern pharmacology and mechanism of action have not been thoroughly carried out. It is not clear about the main active ingredients, potential targets and metabolic pathways involved in its efficacy. Therefore, this research project employed estradiol benzoate sensitization combined with oxytocin pain to construct the cold coagulation syndrome dysmenorrhea model, observed the anti-dysmenorrhea effect of Guizhi Fuling Capsules, and used the metabolomics to explore its mechanism. The results showed that Guizhi Fuling Capsules could considerably reduce the number of writhing times in dysmenorrhea rats, increasing the level of PGE2 and β-EP and reducing the contents of PGF2α in rat serum. Pathological sections of uterus and ovaries also showed that Guizhi Fuling Capsules could significantly relieve endometrial hyperplasia and improve ovarian function. The LC/MS-based metabolomics of rat uterine indicated that the model group has a great deviation from the control group. Compared with the model group, the Guizhi Fuling Capsules group had a tendency to shift to the control group, and the main metabolic changes was mainly concentrated on saturated and unsaturated fatty acids. Among them, arachidonic acid is in a pivotal position, and the expression of its rate-limiting enzyme (COX-2) involved in its cyclooxygenase metabolic pathway was significantly up-regulated in the model group, but significantly decreased after the intervention of Guizhi Fuling Capsules. In conclusion, Guizhi Fuling Capsules can effectively relieve primary dysmenorrhea, and this effect may be attributed to the regulation effects of Guizhi Fuling Capsules on endogenous metabolism, such as inhibiting arachidonic acid converted to prostaglandins through downregulate the expression of COX-2, which plays an anti-inflammatory effect.

Keywords: cold coagulation dysmenorrhea, guizhi fuling capsules, metabolomics, traditional Chinese medicine, arachidonic acid

INTRODUCTION

Dysmenorrhea refers to a kind of uterine cramping pain that occurs in women before or after the menstrual period (Shirvani et al., 2015). In recent years, with the increasement of social pressure, the incidence rate of dysmenorrhea is gradually growing. According to epidemiological statistics, about 50% of women suffered from dysmenorrhea, 10% of which had endured more severe menstrual cramps. This kind of pain not only affects individual's quality of life, but also lower the level of happiness (Lefebvre et al., 2005). The treatment of dysmenorrhea in western medicine is mainly the application of non-steroidal anti-inflammatory drugs, which could merely provide temporary pain relief instead of fundamental treatment and additionally cause drug resistance, gastrointestinal adverse as well as liver and kidney damage. On the contrast, traditional Chinese medication focus on curing dysmenorrhea itself, where patients are diagnosed and treated based on the overall analysis of the disease and physical condition (Xiu-Hong et al., 2015).

Generally, dysmenorrhea could be categorized as primary dysmenorrhea and secondary dysmenorrhea, in which the primary one accounts for more than 90% (Meirong et al., 2020). Caused by excessive pathological uterine contraction, primary dysmenorrhea mainly occurs in women during their teenage years without any organic pelvic lesions, which pathogenesis is not clear. Syndrome of cold coagulation and blood stasis is one of the most common clinical classification of it. There are a variety of methods to establish the cold coagulation syndrome dysmenorrhea model: whole body freezing method (Shujing et al., 2018; Shujing et al., 2020), local frostbite method (Wang and Feng, 2000), wind cold environment method (Tang et al., 2000), ice water immersion method (Cheng et al., 2005), ice water immersion joint drug method (Yan et al., 2014; Xihong et al., 2017; Meng, 2018) and surgery plus drug method (Lu et al., 2010). However, the ice-water immersion method uses short-term overstimulation to build the model, and the local frostbite method ignores the overall concept, which both cannot fit well with the disease. Therefore, the cold coagulation dysmenorrhea model used in this experiment is established on the basis of the traditional dysmenorrhea model using the method of whole body freezing. This model comes from the dysmenorrhea animal model preparation specifications issued by the Chinese Society of Traditional Chinese Medicine and the Professional Committee of Experimental Pharmacology of Traditional Chinese Medicine in 2018 (medicine and Medicine., 2018). It conforms to the modeling ideas and characteristics of the TCM syndrome model and has been adopted by a large number of researchers.

Guizhi Fuling Capsules evolved from Guizhi Fuling Pills in "The Synopsis of the Golden Chamber" by Zhang Zhongjing in the Eastern Han Dynasty (Yunxi et al., 2016). It is mainly composed of Chinese medicinal materials such as Guizhi, Poria, White Peony, Peony Bark, and Peach Kernel. Jiangsu Kangyuan Pharmaceutical Co., Ltd. (Nanjing, Jiangsu, China) has continuously improves the production process of Guizhi Fuling Capsules, and now its production of Guizhi Fuling Capsules has successfully overcomes the unstable characteristics of traditional Chinese medicine preparations (Qingli et al., 2019). Guizhi Fuling Capsules have a variety of pharmacological effects such as anti-inflammatory, analgesic, anti-tumor, smooth muscle regulation, endocrine regulation and immunity enhancement. It is mainly used for gynecological indications, such as the treatment of dysmenorrhea, uterine fibroids, dysfunctional uterine bleeding, menorrhagia, amenorrhea, endometriosis, and some symptoms related to ovarian cysts (Yan et al., 2014). Meanwhile, studies have shown that the extract of Guizhi Fuling Capsules can inhibit the activity of protein tyrosine kinases and exert anti-tumor effects (Lianhua et al., 2012). Guizhi Fuling Capsules has definite curative effect, less side effects and adverse reactions, and is the preferred drug for the treatment of gynecological related diseases. However, the main active ingredients of Guizhi Fuling Capsules for anti-dysmenorrhea, the metabolic pathways involved and the target of the drug effect are not clear. Due to the complexity of the traditional Chinese medicine compound, it has not carried out in-depth modern pharmacology and the mechanism of action.

The objects of metabolomics research are small molecular compounds in biological samples, systems, tissues or cells in the body. Metabolomics is an emerging discipline that uses modern analytical methods such as chromatography and mass spectrometry to determine qualitative/quantitative information of endogenous compounds. The changes from these endogenous substances can reflect the interaction between the inside and outside of the organ or system, which is to reflect the physiological changes in a certain pathological process as a whole. In recent years, with the advancement of analytical methods such as HPLC and GC-MS, metabolomics research has developed rapidly, especially in the interpretation of traditional Chinese medicine prescriptions, pharmacological effects of traditional Chinese medicine and pharmacological effects of active ingredients in natural medicine. Metabolomics is also an important method on the road of Chinese medicine going abroad and being recognized and accepted by the world. Metabolomics can reflect the changes of small molecule metabolites in the body at an overall level. Therefore, this research will explore the possible mechanism of Guizhi Fuling Capsules's anti-dysmenorrhea effect by using metabolomics technology.

METHODS

Materials and Reagents

Estradiol benzoate was purchased from Aladdin. Oxytocin injection and soybean oil was purchased from Maclean. Guizhi Fuling Capsules are provided by Kangyuan Pharmaceutical. 5-13C-glutamine (Cambridge Isotope Laboratories, Andover, MA, United States); PGF2α kit, PGE2 kit and β-EP kit were purchased from Nanjing Jiancheng Bioengineering Research Institute.

Experimental Animals

Three-months-old female SD rats (SPF grade) were purchased from Shanghai SIPPR-BK Laboratory Animal Co., Ltd.

(Shanghai, China). The rats were fed with standard food with 12/12 h light/dark cycle and drink freely. Animal experiments were approved by the Ethics Committee of China Pharmaceutical University. We did our best to reduce animal suffering and reduce the number of animals used.

SD rats were divided into control group, model group, Guizhi Fuling administration group, six in each group. Except for the blank group, in the 10-day modeling cycle, the others were injected subcutaneously with estradiol benzoate at a dose of 2.5 mg/kg on the first and last days and at a dose of 1 mg/kg from day 2 to day 9. After disassembling the capsule shell of the Guizhi Fuling Capsule, grind the content and suspend it with 0.5% CMC-Na to prepare a suspension with a concentration of 1 g/kg, which is equivalent to 10 times the human dosage. Guizhi Fuling Capsules were administered orally for 10 days, and the time of each administration was half an hour after the injection of estradiol benzoate. After the administration, the rats were placed in an ultra-low temperature refrigerator (−20°C) for 2 h, and it was opened for ventilation for 5 s at 1 h. On the 10th day, 1 h after subcutaneous injection of estradiol benzoate, oxytocin was injected intraperitoneally at a dose of 2 U/kg. Observe the number of twists in the next 30 min.

Sample Preparation

After successful modeling, the rats were bled from the femoral vein and sacrificed. Serum was collected for kit detection, while the uterine tissue was collected for related determinations. Accurately weigh and pulverize 30 mg of uterine tissue, add 900 μl of precipitant (15 μg/ml C13-glutamine in 80% methanol water) and two zirconium beads to prepare a homogenate. The mixture was centrifuged at 20,000 g at 4°C for 10 min. Transfer 200 μl of supernatant to a 1.5 ml EP tube, evaporate to dryness, reconstitute the residue with 100 μl of 80% methanol water, centrifuge at 18,000 rpm at 4°C for 5 min, transfer 80 μl of supernatant to a sample bottle. Then inject 10 μl for HPLC-QTOF/MS analysis.

HPLC-Q/TOF-MS-Based Metabolomics Assay

Chromatographic Conditions

Column: Waters XB ridge Amide 3.5 μm, 4.6 × 100 mm Column, column temperature: 40°C, water phase (A): 5 mM ammonium acetate ultrapure water, adjust pH to 9.0 (containing 5% acetonitrile) with ammonia, organic phase (B): Acetonitrile, flow rate: 0.4 ml/min, analysis time: 26.0 min, gradient elution: 0 ~ 3.0 min (85% B), 3.0 ~ 6.0 min (85 ~ 30% B), 6.0 ~ 15.0 min (30 ~ 2% B), 15.0 ~ 18.0 min (2% B), 18.0 ~ 19.0 min (2 ~ 85% B), 19.0 ~ 26.0 min (85% B).

Mass Spectrometry Conditions

The HPLC system consisted of a LC-30A binary pump, a SIL-30AC autosampler and a CTO-30AC column oven (Shimadzu, Japan) coupled with a hybrid quadrupole time-of-fight tandem mass spectrometer (AB SCIEX Triple TOF 5600, Foster City, CA). Electrospray ionization (ESI) is used for MS detection in negative ion mode. The parameter settings are as follows: TOF MS scan, m/z: 50–1000Da; product ion scan, m/z 50–900 Da; Gas 1, 50 psi; Gas 2, 30 psi, CUR, 30 psi; TEM,500; ISVF, −4500 V; DP, −100 V; CE, −10 V; and CE in product ion scan (IDA), -35 V.

Data Acquisition and Data Analysis

The accurate mass was calibrated by the calibration delivery system (CDS), and automatic calibration was carried out every eight samples. Data exploration and peak area integration were performed with PeakView and MultiQuant 2.0 from AB SCIEX. All uterine tissue samples were mixed as quality control (QC) samples, and the QC samples were injected every ten samples to monitor the stability of the analysis. All detected compounds were identified by comparing the retention times and mass spectra (both the MS and MS/MS spectra) of the detected compound with a reference database established in our laboratory (Wang et al., 2018) and with other free online databases, such as MASSBANK (http://www.massbank.jp/index-e.html), METLIN (http://metlin.scripps.edu) and MS2T (http://prime.psc.riken.jp/lcms/ms2tview/ms2tview.htm). The raw data is the peak area of each compound, which is used to represent its content in the sample.

Statistical Analysis

The metabolites detected by metabolomics analysis were relatively quantitative and needed to be normalized by internal standard to weight the peak area. In order to compare the differences of each group, the data was analyzed using SIMCA-P13.0 bit software, which mainly included data pre-processing, data correction, PCA analysis, PLS-DA analysis and screening of differential compounds. Thus, further processing of spectra, analysis of metabolic pathway, analysis of physiological and biochemical significance can be taken. Principal component analysis (PCA) is an unsupervised method used to illustrate the overall distribution of all samples. Partial least squares discriminant analysis (PLS-DA) is a supervised method used to confirm the general separation of groups. Orthogonal partial least squares discriminant analysis (OPLS-DA) is an extension of PLS-DA and is used to distinguish two groups and identify different metabolites. In addition, MetaboAnalyst (http://www.metaboanalyst.ca) was used for metabolomic pathway analysis based on differential metabolites.

The results were expressed as mean ± S.D. All data were analyzed using Graph Pad Prism software (Graph Pad, United States). Statistical levels were calculated using one-way analysis of variance (ANOVA). A p-value of less than 0.05 was considered significantly different.

RESULTS

Evaluation of the Therapeutic Effect of Dysmenorrhea Model

Behavioral Indicators

The Behavioral indicators is an important criterion for clinical diagnosis and judgment of female dysmenorrhea, it is an important technical indicator for the success of the design and preparation of dysmenorrhea models. The manifestations of

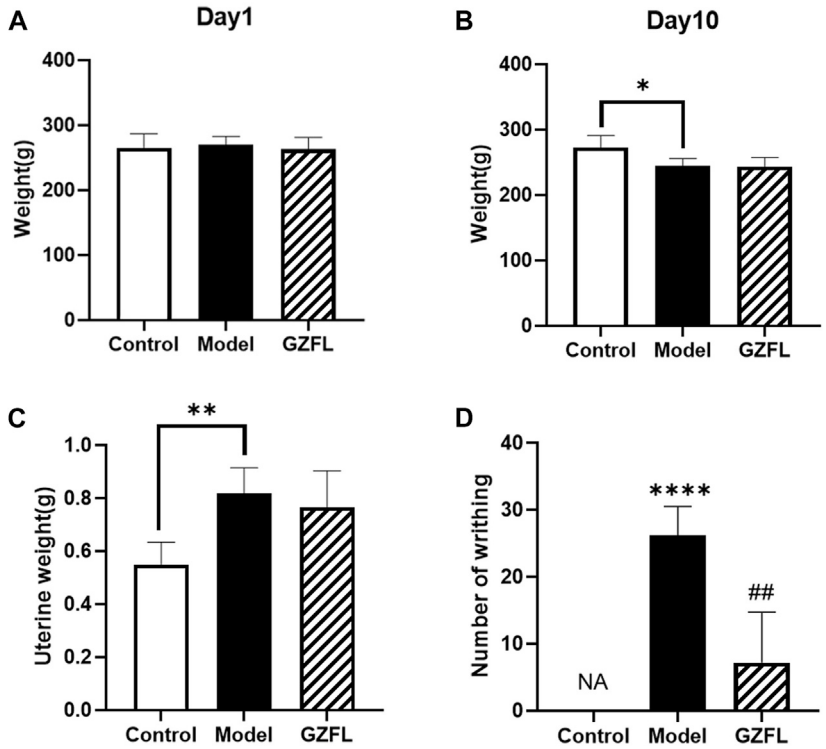


FIGURE 1 | (A) The weight of the rat on day 1 of the experiment **(B)** The weight of the rat on day 10 **(C)** the weight of the uterus on day 10 of the experiment **(D)** the number of writhings recorded on day 10 of the experiment. ($\bar{x}\pm s$, n = 6, compared with Control group: $^{*}p < 0.05$ $^{**}p < 0.01$ $^{***}p < 0.001$ $^{****}p < 0.0001$; compared with Model group: $^{\#}p < 0.05$ $^{\#\#}p < 0.01$ $^{\#\#\#}p < 0.001$ $^{\#\#\#\#}p < 0.0001$).

writhing mainly include indentation on both sides of the abdomen, abdominal wall sticking down, buttocks raised, twisted body or hind limb extension. Each time the rat exhibits the above-mentioned writhing performance, it is considered that there is a writhing and recorded. In this experiment, rats in each group had basically the same body weight before administration while after 10 days of modeling, all rats in the experimental group except the control one lost weight (**Figures 1A,B**). Compared with the control group, the weight of the rat's uterus increased after the administration of estradiol benzoate. (**Figure 1C**). The rats in the blank control group did not show any writhing symptoms, while that in the model group showed strong symptoms. As shown in **Figure 1D**, compared with the model group, the writhing frequency of the medical intervention groups was significantly reduced.

Biochemical Indicators

As shown in **Figure 2**, the level of PGE2 in the serum of rats in the model group was significantly reduced, while that in the model group was significantly increased after administration. However, the level of PGF2α showed an opposite trend to that of PGE2. The content of PGE2α in the serum of rats in the model group was abundant, and it was significantly reduced after administration. Therefore, the ratio of PGF2α/PGE2 in the model group increased significantly, and decreased significantly after administration. The trends of β-EP and PGE2 are basically the same. Compared with the control group, the β-EP content of the model group reduced significantly, while that of the Guizhi Fuling group increased significantly.

Pathological Indicators

Figure 3 shows histopathological sections of the uterus. In the control group, endometrial epithelial cells are complete, the thickness of endometrium and myometrium is normal, and uterine cavity is smooth. However, in the model group, the uterine structure is out of order, uterine cavity is not smooth and the endometrial hyperplasia is obvious. The uterine cavity of the Guizhi Fuling group tends to be smooth. **Figure 4** shows typical pathological sections of the rat ovary. For ovarian tissue, the follicles of the control group are arranged in an orderly manner. While in the model group, the number of atresia follicles increases, the arrangement of follicles is disordered, after the treatment of Guizhi Fuling, the symptoms above are relieved. As shown in **Figure 4D**, compared with the control group, the corpus luteum radius of the model group increased by about 1.5 times, and the corpus luteum radius decreased by about 1.2 times after administration of Guizhi Fuling.

Metabolomics Analysis

Analyze the uterine sample data by PLS-DA. By observing its distribution in the mathematical model space, it was found that

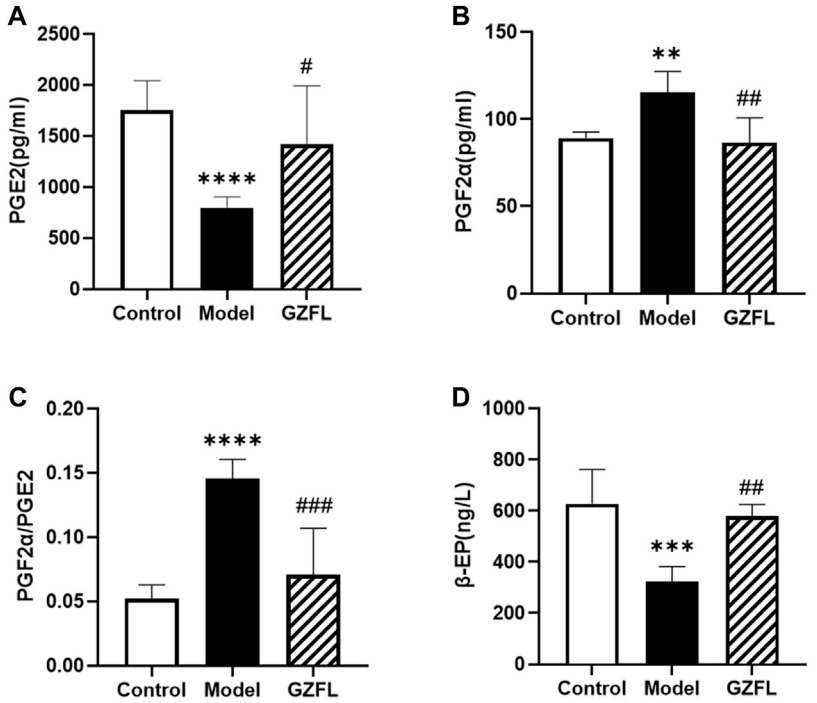


FIGURE 2 | Serum biochemical indexes **(A)** PGE_2 level **(B)** $PGF_{2\alpha}$ level **(C)** $PGF_{2\alpha}/PGE_2$ ratio **(D)** β-EP level ($\bar{x}\pm s$, n = 6, compared with control group: $^{*}p < 0.05$ $^{**}p < 0.01$ $^{***}p < 0.001$ $^{****}p < 0.0001$; compared with model group: $^{\#}p < 0.05$ $^{\#\#}p < 0.01$ $^{\#\#\#}p < 0.001$ $^{\#\#\#\#}p < 0.0001$).

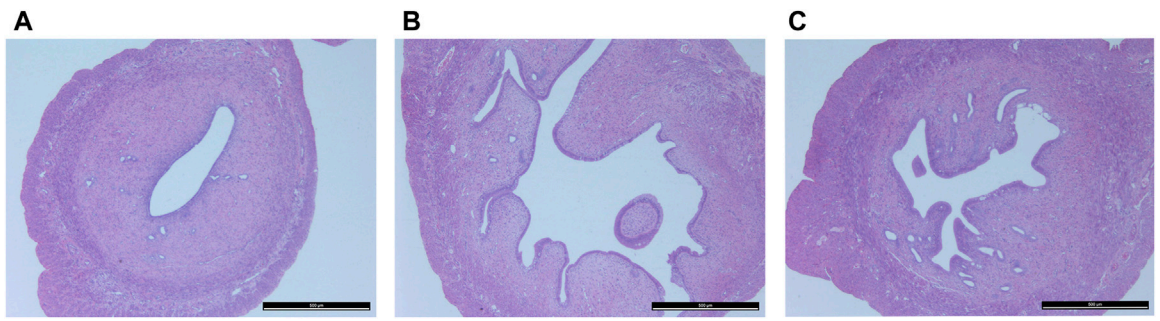


FIGURE 3 | Histopathological section of uterus**(A)** Control group **(B)** Model group **(C)** GZFL group.

the PLS-DA (**Figure 5**) score charts have better inter-group differences and intra-group aggregation. The uterine samples of the control group, model group and Guizhi Fuling group are distinguished significantly, and there is a big difference in metabolism of each group. The results of the substitution test showed that the model has good reliability (**Supplementary Figure S1**). Firstly, the difference compounds are initially screened out through the condition of VIP>1, and then the ones that meet the condition of $p < 0.05$ are screened out through the *t* test. The differential compounds were analyzed on MetaboAnalyst website. The results of metabolic pathways are shown in **Figure 6**. The metabolic pathways mainly focus on fatty acid production, arachidonic acid and taurine metabolism. **Figure 7** is a comparison diagram of the content of compounds detected in the uterine tissue of the dysmenorrhea model group and the normal control group, the Guizhi Fuling Capsule administration group and the dysmenorrhea model group. It can be found that most of the differential compounds are significantly down-regulated in primary dysmenorrhea, but after Guizhi Fuling Capsule interferes with dysmenorrhea, most of the differential compounds are significantly up-regulated. Similarly, the heat map (**Figure 8**) also clearly show the obvious metabolic changes between the three investigated groups. Combined with **Figure 9**, it can be seen that the differential compounds in uterine tissue are mainly concentrated on some saturated and unsaturated fatty acids, and this change could be reversed after drug intervention.

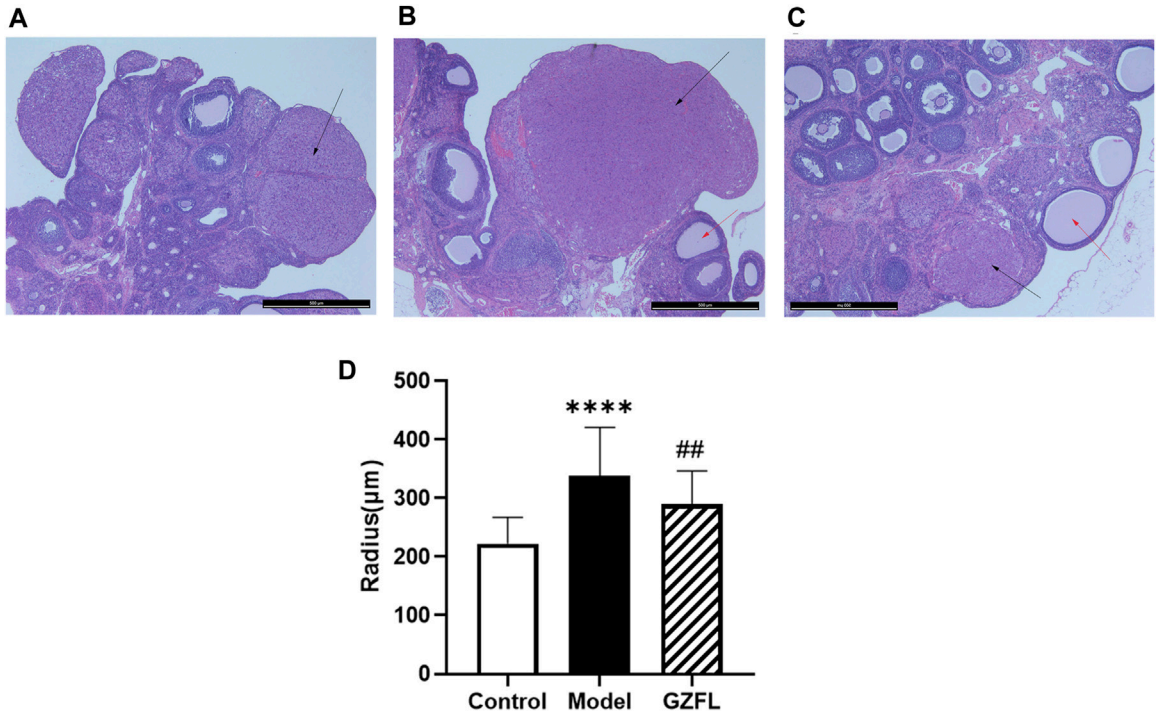


FIGURE 4 | Typical ovarian histopathology section, The black arrow represents the corpus luteum, the red arrow represents atretic follicles **(A)** Control group **(B)** Model control group **(C)** GZFL group **(D)** Rat corpus luteum radius ($\bar{x}\pm s$, n = 6, compared with control group: $^{*}p < 0.05$ $^{**}p < 0.01$ $^{***}p < 0.001$ $^{****}p < 0.0001$; compared with model group: $^{\#}p < 0.05$ $^{\#\#}p < 0.01$ $^{\#\#\#}p < 0.001$ $^{\#\#\#\#}p < 0.0001$).

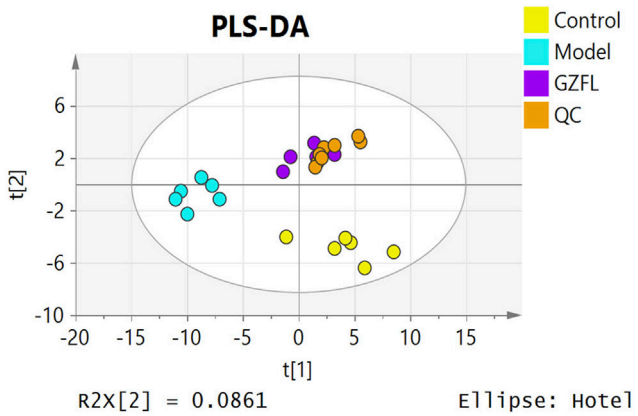


FIGURE 5 | PLS-DA score plot of uterine tissue samples from three test groups (Control, Model, GZFL) and quality control (QC).

Regulation in COX-2 Expression

From metabolomics analysis results, Guizhi Fuling Capsule may exert anti-dysmenorrhea effects by affecting the metabolism of fatty acids *in vivo*, such as oleic acid, stearic acid, palmitic acid, and arachidonic acid. Among them, cyclooxygenase-2(COX-2) is a rate-limiting enzyme involved in the cyclooxygenase metabolism pathway of arachidonic acid, which can catalyze the conversion of arachidonic acid to prostaglandins (PGs) and induce inflammation. Our results have found that the expression of COX-2 both in liver and uterus happened to increase significantly (about a 4-fold increase) after dysmenorrhea modeling. However, after the intervention of Guizhi Fuling Capsules, its expression was significantly reduced (about 2 times lower) (**Figure 10**). Therefore, we speculate that Guizhi Fuling Capsule may inhibit the conversion of arachidonic acid to *p*Gs by down-regulating the expression of COX-2, thereby inhibiting the occurrence and development of inflammation. .

DISCUSSION

We choose female rats to establish primary dysmenorrhea model, because female rats have a short estrus cycle, leading them suitable to study the changes in the reproductive cycle (Marcondes et al., 2002). Then, dysmenorrhea itself is a physiological phenomenon that mostly occurs within a certain age group of human beings, especially primary dysmenorrhea, which is caused by non-pelvic organic diseases. Primary dysmenorrhea is mostly caused by mental factors, and most of them occur in menarche. The average age at which Eastern women experience menarche is 12–16 years old. The three-month-old rat is equivalent to a human being 12–14 years old. Therefore, we finally chose three-month-old female rats as our model animals.

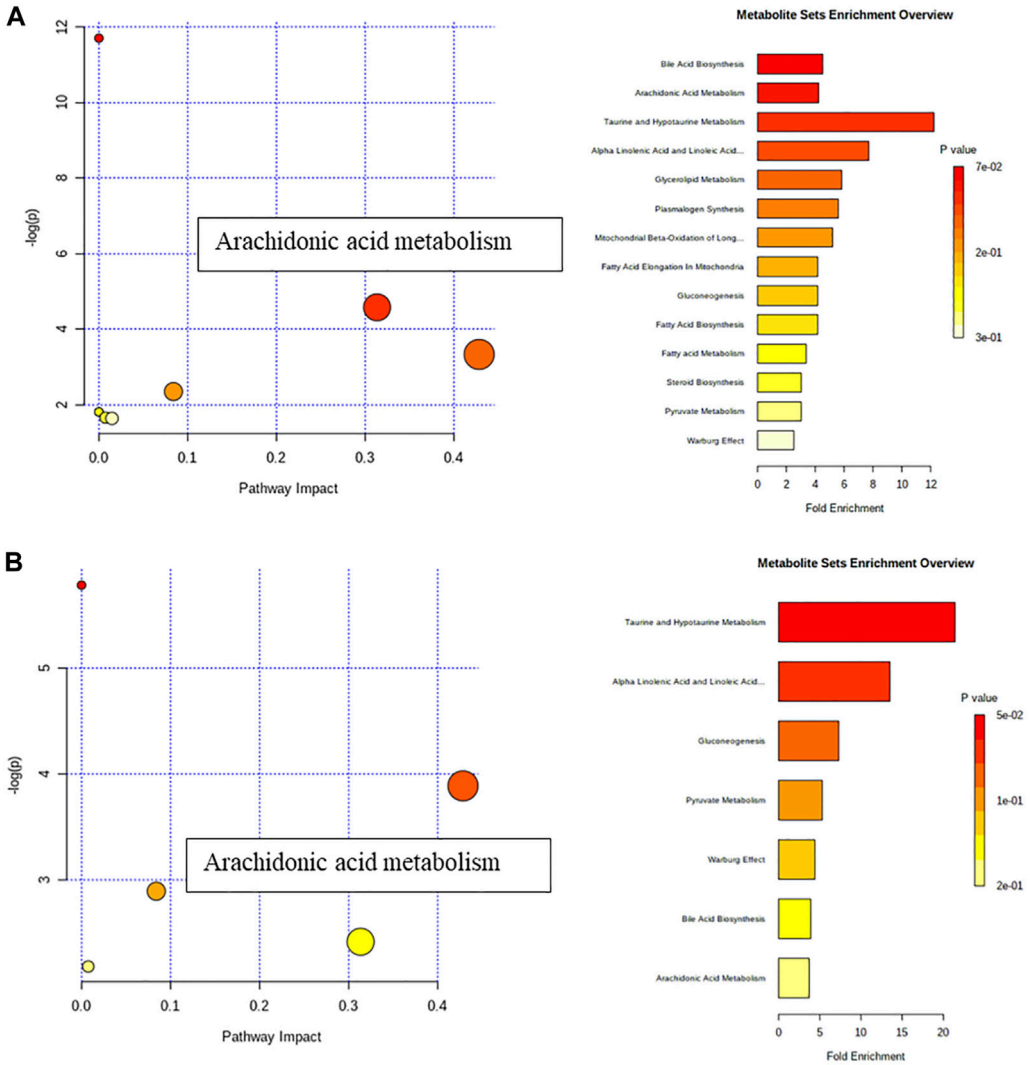


FIGURE 6 | Metabolic pathway analysis **(A)** Metabolic pathway analysis between Control and Model group **(B)** Metabolic pathway analysis between Model and GZFL group.

The model of experimental dysmenorrhea could be established by using estradiol benzoate and oxytocin, in order to synchronize the uterine cycle and cause artificial estrus, animals were given estrogen for 10 consecutive days to increase uterine sensitivity. After artificial estrus, oxytocin was injected to the animals to induce contraction of uterine smooth muscle and cause pain, which was manifested as writhing response. Writhing response is the most direct expression of dysmenorrhea in rats, so it is the most widely used behavioral index for the overall evaluation of visceral pain response. Studies have shown that the occurrence of dysmenorrhea is mainly related to the abnormal synthesis and release of prostaglandins in the endometrium of the menstrual period. The increased ratio of PGF2α/PGE2 leads to enhanced spastic contraction of uterine smooth muscle and dysmenorrhea (Yoshino and Ellis, 1987). PGE2 is one of the most important endogenous substances for inhibiting the inflammatory response. It has the effects of dilating blood vessels, increasing blood flow to organs throughout the body, reducing peripheral resistance of blood vessels, immunosuppression and anti-inflammatory. In the pharmacodynamics experiment, PGF2α/PGE2 in the serum of the model group rats was significantly increased, and significantly decreased after administration. β-EP has a powerful endogenous analgesic effect. It is affected by sex hormones, and participates in the regulation of reproductive endocrine. In the rat pharmacodynamics experiment, β-EP and PGE2 showed the same trend. Compared with the control group, the concentration of β-EP in the serum of the model group was significantly reduced; compared with the model group, that of the Guizhi Fuling Capsules group was significantly higher. This is the same as the results of previous studies (Sun et al., 2014).

The uterine tissue samples of dysmenorrhea rats were analyzed by metabolomics. It was found that many fatty acids had significant changes in the dysmenorrhea model, but Guizhi

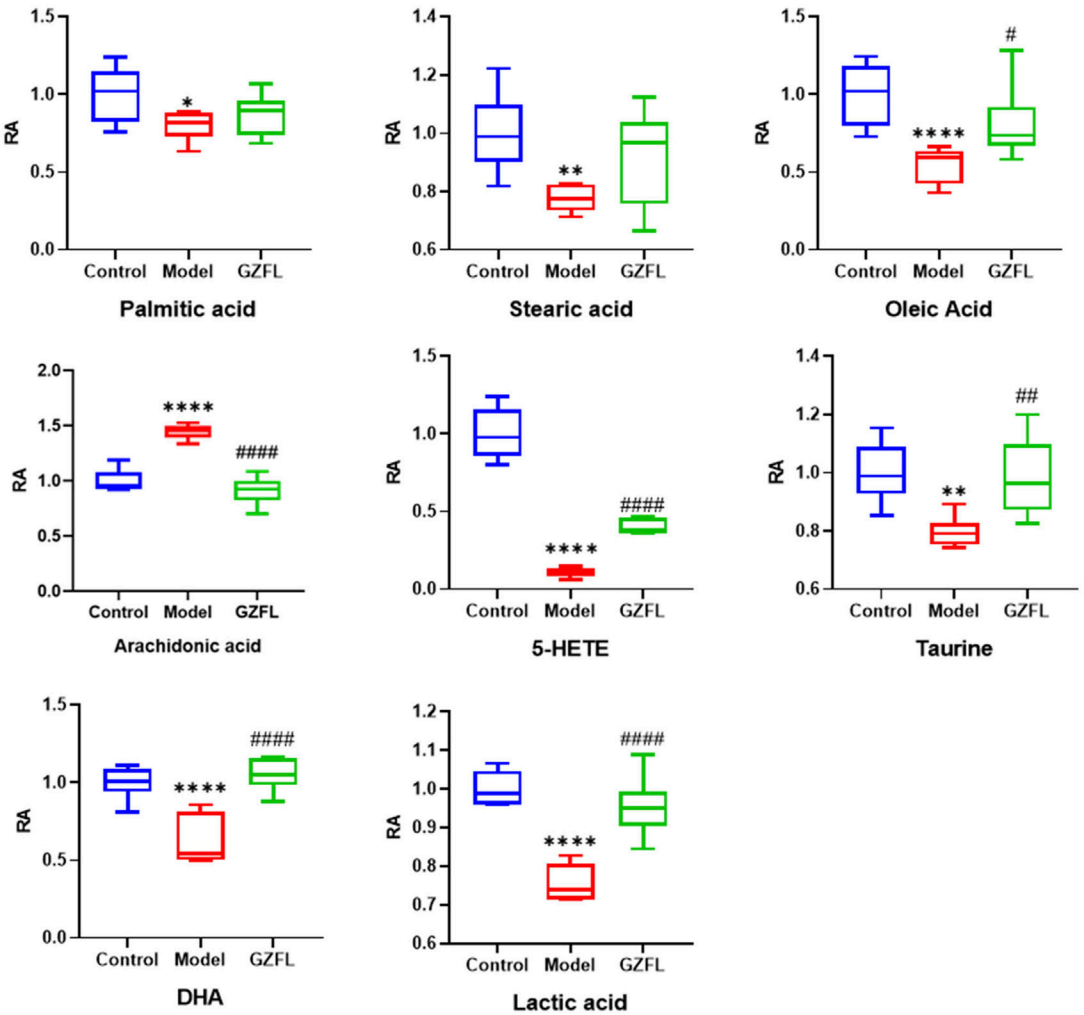


FIGURE 7 | Relative abundance (RA) of the differential metabolites ($\bar{x}\pm s$, n = 6, compared with blank control group: $^{*}p < 0.05$ $^{**}p < 0.01$ $^{***}p < 0.001$ $^{****}p < 0.0001$; compared with the model group: $^{\#}p < 0.05$ $^{\#\#}p < 0.01$ $^{\#\#\#}p < 0.001$ $^{\#\#\#\#}p < 0.0001$).

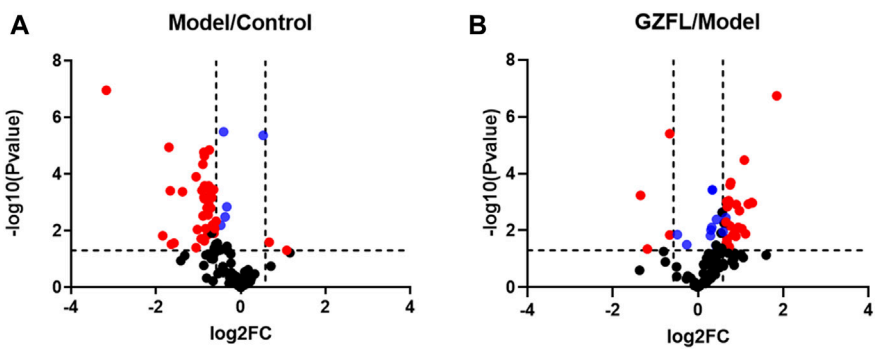


FIGURE 8 | Volcano plots of compounds detected in uterine tissue for metabolomics analysis (A) Volcano plot for Model group versus Control group (B) Volcano plot for Guizhi Fuling Capsules administration group (GZFL) versus Model group. Take |FC| = 1.5 and *p*-value = 0.05 as the truncation standard. The black dots represent compounds with no significant difference, the red dots are compounds with a differential expression fold greater than 1.5 times, and the blue dots represent compounds with a significant difference but a fold change of less than 1.5 times.

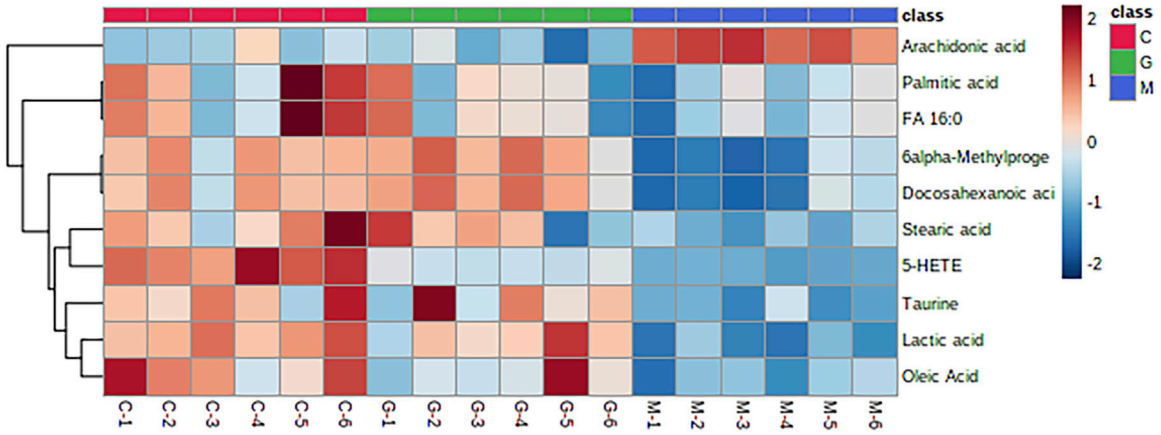


FIGURE 9 | Heatmap of hierarchical clustering analysis for three test groups of Control rats (group C), Model rats (group M) and Guizhi Fuling Capsules administration rats (group G), the abscissa represents different experimental groups, the ordinate represents the differential metabolites investigated, the color represents the relative content of the corresponding metabolite in the corresponding sample, red represents the higher content in the sample, and blue represents the lower content.

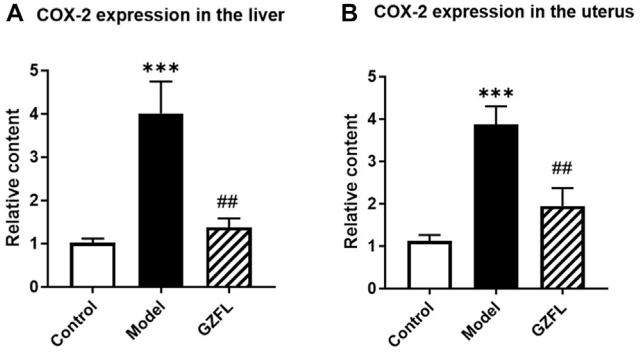


FIGURE 10 | COX-2 gene expression changes in rats **(A)** COX-2 expression in liver **(B)** COX-2 expression in uterine tissue ($\bar{x}\pm s$, n = 6, compared with Control group: $^{***}p < 0.001$; compared with Model group: $^{\#\#}p < 0.01$).

Fuling Capsules can reverse this change to varying degrees after intervention. Among them, arachidonic acid metabolic pathway is in a pivotal position. Arachidonic acid has many metabolic pathways, one of which is to generate prostaglandin and thromboxane through cyclooxygenase metabolism (Wang et al., 2014). Prostaglandin endoperoxidase (PTGS), also known as cyclooxygenase (COX), is the key enzyme that regulates the release of prostaglandins, including two isoforms: structural cyclooxygenase-1 (COX-1) and inducible cyclooxygenase-2 (COX-2), in which COX-2 is an inducible form only existing in inflammation. After being stimulated by inflammatory mediators, endotoxin, hypoxia factor, epidermal growth factor (EGF), COX-2 gene is induced to be highly expressed, resulting in the increase of PGI2, PGE1, PGE2 content, which could participate in inflammatory reaction. This is considered as the main source of inflammatory prostaglandins (Mitchell and Kirkby, 2019). In dysmenorrhea model rats, the expression of COX-2 in liver and uterus of rats increased significantly, and the expression of mRNA in rats from Guizhi Fuling group decreased significantly compared with the model group (**Figure 10**). The results suggested that Guizhi Fuling Capsules could reduce the production of prostaglandin by regulating the expression of COX-2.

Moreover, docosahexaenoic acid (DHA) is a type of n-3 unsaturated fatty acid. Recent studies have shown that when metabolized by cyclooxygenase and lipoxygenase, DHA is transformed into powerful anti-inflammatory molecules, and DHA may produce anti-inflammatory effects by inhibiting the arachidonic acid cascade (Tokuyama and Nakamoto, 2011). Lactic acid is closely related to the metabolism and polarization of macrophages. Lactic acid is a regulator of macrophage metabolism and can prevent excessive inflammation. Studies have revealed a new connection between lactic acid and the control of uterine inflammation, and found that high levels of lactic acid act on uterine GPR81 and down-regulate pro-inflammatory genes (Zhou et al., 2021). Taurine is an endogenous anti-injury substance in humans. Studies have shown that taurine has a protective effect on nonylphenol-induced uterine pathological damage in mice (Ding et al., 2018).

In summary, we speculate that Guizhi Fuling Capsules may partially reduce the synthesis of arachidonic acid through the arachidonic acid metabolic pathway, and regulate the expression of COX-2 to reduce the production of downstream prostaglandins, thereby reducing the production of inflammatory mediators release to achieve the purpose of alleviating dysmenorrhea.

CONCLUSION

In a word, we have proved that Guizhi Fuling Capsules has a good effect on cold coagulation dysmenorrhea model rats,

can significantly reduce the number of writhing, regulate the level of serum PGE2, PGF2α, β-EP, improve endometrial hyperplasia and ovarian function. The uterine tissue samples of dysmenorrhea rats were analyzed by metabolomics. It was found that Guizhi Fuling Capsules could reduce the interference of estradiol benzoate and oxytocin on the metabolism products of rats. Guizhi Fuling Capsules mainly played an anti-dysmenorrhea role by regulating the metabolism of arachidonic acid. More results suggest that Guizhi Fuling Capsules may inhibit the conversion of arachidonic acid into prostaglandins by down-regulating the expression of COX-2. Further experiments are needed to study the effect of Guizhi Fuling Capsules on other substances in arachidonic acid metabolism pathway.

DATA AVAILABILITY STATEMENT

The original contributions presented in the study are included in the article/**Supplementary Material**, further inquiries can be directed to the corresponding authors.

ETHICS STATEMENT

The animal study was reviewed and approved by Ethics Committee of China Pharmaceutical University.

AUTHOR CONTRIBUTIONS

YZ and NS performed the majority of the experiment and wrote manuscript; WL and QW supported several experiments; JS and YP supervised the research and revised the manuscript.

FUNDING

This work was supported by grants from National Natural Science Foundation (No. 81773987) and "Double First-Class" University project (CPU2018GF07).

SUPPLEMENTARY MATERIAL

The Supplementary Material for this article can be found online at: https://www.frontiersin.org/articles/10.3389/fphar.2021.764904/full#supplementary-material.

REFERENCES

Cheng, X., Du, H., and Li, D. (2005). Establishment of Syndrome Model of Blood Stasis Due to Cold Accumulation in Rats. *Chin. J. Basic Med. Traditional Chin. Med.* 11, 604–605. doi:10.3969/j.issn.1006-3250.2005.08.019

Ding, X., Han, P., and Wang, H. (2018). Effect of Taurine on the Pathological Damage of Mouse Uterus Induced by Nonylphenol. *Dig. world's latest Med. Inf.* 18, 192–193. doi:10.19613/j.cnki.1671-3141.2018.86.113

Lefebvre, G., Pinsonneault, O., Antao, V., Black, A., Burnett, M., Feldman, K., et al. (2005). Primary Dysmenorrhea Consensus Guideline. *J. Obstet. Gynaecol. Can.* 27, 1117–1146. doi:10.1016/s1701-2163(16)30395-4

Lianhua, F., Ruoyun, C., Jing, G., Haiguang, Y., Hongqing, W., Jiachun, L., et al. (2012). Guizhi Fuling Capsule Extracts *In Vitro* Anti-tumor Activity and Mechanism. *Chin. Pharm. J.* 47, 813–817. CNKI:SUN:ZGYX.0.2012-10-024.

Lu, A. N., Cai, Y. Y., Song, M., Zhang, W. T., and Cai, D. Y. (2010). A Pharmacodynamic Model for Cold-Pain Evaluation in Rats with Primary Dysmenorrhea. *Chin. Pharmacol. Bull.* 26, 1242–1245. CNKI:SUN:YAOL.0.2010-09-033.

Marcondes, F. K., Bianchi, F. J., and Tanno, A. P. (2002). Determination of the Estrous Cycle Phases of Rats: Some Helpful Considerations. *Braz. J. Biol.* 62, 609–614. doi:10.1590/s1519-69842002000400008

medicine, C. s. o. t. C., and Medicine., p. c. o. e. p. o. t. C. (2018). Specifications for Preparation of Dysmenorrhea Animal Models (Draft). *Chin. J. Exp. Traditional Med. Formulae* 24, 20–24. doi:10.13422/j.cnki.syfjx.20183005

Meirong, D., Xiumin, L., Tian, Y., Jieli, G., Fengchao, D., and Xiuling, X. (2020). Research Status and Treatment Progress of Primary Dysmenorrhea. *Chin. folk remedies* 28, 113–117. doi:10.19621/j.cnki.11-3555/r.2020.1055

Meng, T. (2018). Study on the Intervention of Shaofu Zhuyu Decoction Plus Jianfang on Dysmenorrhea Model Rats of Cold Coagulation and Stasis Type. *Biped and Health* 027, 181–182. CNKI:SUN:SZBJ.0.2018-06-115.

Mitchell, J. A., and Kirkby, N. S. (2019). Eicosanoids, Prostacyclin and Cyclooxygenase in the Cardiovascular System. *Br. J. Pharmacol.* 176, 1038–1050. doi:10.1111/bph.14167

Qingli, W., Runbin, S., Jiye, A., and Yuan, X. (2019). Metabolomics Study of Curcumin in Mice with Nonalcoholic Fatty Liver Disease. *Drug Eval. Res.* 042, 402–411. doi:10.7501/j.issn.1674-6376.2019.03.005

Shirvani, M. A., Motahari-Tabari, N., and Alipour, A. (2015). The Effect of Mefenamic Acid and Ginger on Pain Relief in Primary Dysmenorrhea: a Randomized Clinical Trial. *Arch. Gynecology&Obstetrics.* 291, 1277–81. doi:10.1007/s00404-014-3548-2

Shujing, L. I., Xiaoning, Z., Mingsheng, S., Zhaofeng, L. I., Shuzhong, G., and Yuxia, M. A. (2018). Effect of Navel Therapy on Behavior of Dysmenorrhea Rats with Cold Coagulation and Blood Stasis. *Liaoning J. Traditional Chin. Med.* 45, 390–393+446. doi:10.13192/j.issn.1000-1719.2018.02.056

Shujing, L., Yuning, M., Chen, C., Yahui, P., and Yuxia, M. (2020). Effect of Moxibustion on Transient Receptor Potential Vanilloid Type 1 of Uterus in Rats with Dysmenorrhea of Cold Coagulation and Blood Stasis Type. *Chin. Arch. Traditional Chin. Med.* 38, 41–44+260. doi:10.13193/j.issn.1673-7717.2020.01.010

Sun, L., Nan, L., and Li, J. (2014). Experimental Study of Guizhi Fuling Capsule on Primary Dysmenorrhea. *Chin. Med. Herald* 020, 15–17. CNKI:SUN:HNZB.0.2014-03-006.

Tang, Z., Song, X., Yuan, J., and Hou, Z. (2000). Experimental Study on the Effect of Moxibustion on Promoting Blood Circulation and Removing Blood Stasis in Rats with Cold Blood Coagulation and Stasis Syndrome. *Chin. J. Basic Med. Traditional Chin. Med.* 06, 43–46. CNKI:SUN:ZYJC.0.2000-04-016.

Tokuyama, S., and Nakamoto, K. (2011). Unsaturated Fatty Acids and Pain. *Biol. Pharm. Bull.* 34, 1174–1178. doi:10.1248/bpb.34.1174

Wang, W., Cai, Q., Zhou, F., Liu, J., Jin, X., Ni, P., et al. (2018). Impaired Pentose Phosphate Pathway in the Development of 3D MCF-7 Cells Mediated Intracellular Redox Disturbance and Multi-Cellular Resistance without Drug Induction. *Redox Biol.* 15, 253–265. doi:10.1016/j.redox.2017.12.009

Wang, X., and Feng, P. (2000). Experimental Observation on Animal Model of Cold Coagulation and Blood Stasis Syndrome. *Beijing J. Traditional Chin. Med.* 05, 44–45. doi:10.16025/j.1674-1307.2000.05.021

Wang, Y., Armando, A. M., Quehenberger, O., Yan, C., and Dennis, E. A. (2014). Comprehensive Ultra-performance Liquid Chromatographic Separation and Mass Spectrometric Analysis of Eicosanoid Metabolites in Human Samples. *J. Chromatogr. A.* 1359, 60–69. doi:10.1016/j.chroma.2014.07.006

Xihong, M., Xiaojing, F., Yang, X., and Bai, Y. (2017). Foxiangyin on the Model Rats with Cold Coagulation and Blood Stasis Dysmenorrhea Pain Reaction and Blood Rheology. *Heb Med.* 23, 1791–1794. doi:10.3969/j.issn.1006-6233.2017.11.009

Xiu-Hong, W. U., En-Long, Y., Ze, S., Cheng-Yu, P., Lu-Wen, H. E., and Shu-Xiang, Z. (2015). Experimental Research of "Guizhi Fuling Pills " for the

Treatment of Dysmenorrhea of Blood Stasis Type. *shanghai J. Traditional Chin. Med.* 49, 102–105. doi:10.16305/j.1007-1334.2015.05.032

Yan, W., Wei-Ping, Y., Tian-Qi, C., Fang, P., Heng-Mao, C., Yun-Hua, Z., et al. (2014). Effect of Evodia Rutaecarpa Decoction on Model Rat of Dysmenorrhea in the Type of Cold Retention and Blood Stasis. *Guizhou Sci.* 32, 71–74. CNKI: SUN:GZKX.0.2014-04-011.

Yoshino, S., and Ellis, E. F. (1987). Effect of a Fish-Oil-Supplemented Diet on Inflammation and Immunological Processes in Rats. *Int. Arch. Allergy Appl. Immunol.* 84, 233–240. doi:10.1159/000234429

Yunxi, Z., Xiaoliang, J., Shiyin, G. U., Ying, P., Wei, X., Zhenzhong, W., et al. (2016). Anti-dysmenorrhea Mechanism of Guizhifuling Capsule Based on its Anti-inflammation Effect. *Chin. J. Clin. Pharmacol. Ther.* 21, 1095–1102.

Zhou, H. C., Yan, X. Y., Yu, W., Yu, W. W., Liang, X. Q., Du, X. Y., et al. (2021). Lactic Acid in Macrophage Polarization: The Significant Role in Inflammation and Cancer. *Int. Rev. Immunol.* 25, 1–15. doi:10.1080/08830185.2021.1955876

Conflict of Interest: The authors declare that the research was conducted in the absence of any commercial or financial relationships that could be construed as a potential conflict of interest.

Publisher's Note: All claims expressed in this article are solely those of the authors and do not necessarily represent those of their affiliated organizations, or those of the publisher, the editors and the reviewers. Any product that may be evaluated in this article, or claim that may be made by its manufacturer, is not guaranteed or endorsed by the publisher.

Copyright © 2021 Zhang, Su, Liu, Wang, Sun and Peng. This is an open-access article distributed under the terms of the Creative Commons Attribution License (CC BY). The use, distribution or reproduction in other forums is permitted, provided the original author(s) and the copyright owner(s) are credited and that the original publication in this journal is cited, in accordance with accepted academic practice. No use, distribution or reproduction is permitted which does not comply with these terms.

frontiers in Pharmacology

ORIGINAL RESEARCH
published: 03 December 2021
doi: 10.3389/fphar.2021.773592

Euphorbia Factor L2 ameliorates the Progression of K/BxN Serum-Induced Arthritis by Blocking TLR7 Mediated IRAK4/IKKβ/IRF5 and NF-kB Signaling Pathways

*Jing Tang[1,2†], Xiaolan Cheng[3†], Shiyu Yi[4†], Yuanyuan Zhang[5], Zhigang Tang[1], Yutong Zhong[1], Qiuping Zhang[1], Bin Pan[6] and Yubin Luo[1]**

[1]*Laboratory of Rheumatology and Immunology, West China Hospital, Sichuan University, Sichuan, China,* [2]*Department of Rheumatology and Immunology, Luzhou's People's Hospital, Luzhou, China,* [3]*Affiliated Hospital of Integrated Traditional Chinese and Western Medicine, Nanjing University of Chinese Medicine, Nanjing, China,* [4]*Department of Rheumatology and Immunology, The General Hospital of Western Theater Command PLA, Chengdu, China,* [5]*Sichuan Food and Drug Inspection and Testing Institute, Chengdu, China,* [6]*Shandong Peninsula Engineering Research Center of Comprehensive Brine Utilization, Weifang University of Science and Technology, Shouguang, China*

OPEN ACCESS

Edited by:
Dahui Liu,
Hubei University of Chinese Medicine, China

Reviewed by:
Sheikh Fayaz Ahmad,
King Saud University, Saudi Arabia
Raffaele Strippoli,
Sapienza University of Rome, Italy

***Correspondence:**
Yubin Luo
luoyubin2016@163.com

†These authors have contributed equally to this work and share first authorship

Specialty section:
This article was submitted to Inflammation Pharmacology, a section of the journal Frontiers in Pharmacology

Received: *10 September 2021*
Accepted: *03 November 2021*
Published: *03 December 2021*

Citation:
Tang J, Cheng X, Yi S, Zhang Y, Tang Z, Zhong Y, Zhang Q, Pan B and Luo Y (2021) Euphorbia *Factor L2 ameliorates the Progression of K/BxN Serum-Induced Arthritis by Blocking TLR7 Mediated IRAK4/IKKβ/IRF5 and NF-kB Signaling Pathways. Front. Pharmacol. 12:773592. doi: 10.3389/fphar.2021.773592*

Toll like receptor (TLR)s have a central role in regulating innate immunity and their activation have been highlighted in the pathogenesis of rheumatoid arthritis (RA). EFL2, one of diterpenoids derived from *Euphorbia* seeds, is nearly unknown expect for its improving effect on acute lung injury. Our present study aimed to investigate EFL2's pharmacokinetic features, its therapeutic effect on rheumatoid arthritis, and explored the potential anti-arthritic mechanisms. K/BxN serum transfer arthritis (STA) murine model was used to assess EFL2's anti-arthritic effects. We also applied UPLC-MS method to measure the concentrations of EFL2 in plasma. The inhibitory effects of this compound on inflammatory cells infiltration and activation were determined by flow cytometry analysis and quantitative real-time polymerase chain reaction (qRT-PCR) *in vivo*, and immunochemistry staining and ELISA in murine macrophages and human PBMCs *in vitro*, respectively. The mechanism of EFL2 on TLRs mediated signaling pathway was evaluated by PCR array, Western blot, plasmid transfection and confocal observation. Intraperitoneal (i.p.) injection of EFL2, instead of oral administration, could effectively ameliorate arthritis severity of STA mice. The inflammatory cells migration and infiltration into ankles were also significantly blocked by EFL2, accompanied with dramatically reduction of chemokines mRNA expression and pro-inflammatory cytokines production. *In vivo* PCR microarray indicated that EFL2 exerted anti-arthritis bioactivity by suppressing TLR7 mediated signaling pathway. *In vitro* study confirmed the inhibitory effects of EFL2 on TLR7 or TLR3/7 synergistically induced inflammatory cytokines secretion in murine macrophages and human PBMCs. In terms of molecular mechanism, we further verified that EFL2 robustly downregulated TLR7 mediated IRAK4-IKKβ-IRF5 and NF-κB signaling pathways activation, and blocked IRF5 and p65 phosphorylation and translocation activity. Taken together, our data indicate EFL2's therapeutic potential as a candidate for rheumatoid arthritis and other TLR7-dependent diseases.

Keywords: euphorbia factor L2, serum-induced arthritis, TLR7, IRF5, rheumatoid arthritis

INTRODUCTION

Rheumatoid arthritis (RA) is a chronic inflammatory autoimmune disease characterized with synovitis, cartilage erosion and joints damage (Orr et al., 2018). Although the precise etiology of RA is still unclear, the acknowledged critical step in the process of RA initiation and development is the immune break including the innate and adaptive immune cells activation, followed by excessive pro-inflammatory cytokines, chemokines and different antibodies production (Orr et al., 2018). The hallmark of RA is the chronic synovitis associated with massive amounts of innate immune cells infiltration (e.g., mast cells, neutrophils, monocytes, dentritic cells, and macrophages) as well as small proportions of T and B lymphocytes (Orr et al., 2018). Antigen-activated CD4+T cells can stimulate myeloid cells, especially neutrophils and macrophages. These activated cells then interact with synovial fibroblasts, osteoclasts and chondrocytes to release matrix metalloproteinases (MMPs), RANK ligand (RANKL), cyclooxygenase 2 (Cox2), and prostaglandins generation which contribute to sustained synovitis, cartilage erosion, and joint damage (Choy, 2012; Lee et al., 2013; You et al., 2014).

TNF-α and IL-1β, the well-known cytokines which play a critical role in etiology of RA, are produced mainly by monocytes and macrophages. TNF-α receptors are expressed on a variety of target cells. Their activation can trigger production of other cytokines, induce endothelial adhesion molecules, and stimulates collagenase and osteoclast differentiation (Weinblatt, 1992; Lee et al., 2013). Therefore, TNF-α was previously investigated as a target in RA treatment (Yamanaka, 2015). IL-1β displays activity in RA that is similar to TNF-α. They activate intra-cellular signal-transduction pathways that go through a series of kinases, leading to the activation of nuclear-factor kappa B (NF-κB) (Weinblatt, 1992). Previous reports have showed that blockage of IL-1 was significantly effective in RA, reducing inflammation, bone destruction and disease progression (Joosten et al., 1999; Pascual et al., 2005). IL-6 is another pro-inflammatory cytokine produced by T cells, monocytes, macrophages, and synovial fibroblasts (Hunter and Jones, 2015). It is reported that RA patients have elevated serum levels of both IL-6 and IL-6R in serum and synovial fluid (Santos Savio et al., 2015). IL-6 has a crucial role in the inflammatory processes once at the joint, including osteoclast-mediated bone resorption and pannus development (Srirangan and Choy, 2010). In the treatment of RA, IL-6 blockade has proven to be very useful for those patients who are refractory to conventional therapy or TNF inhibitors (Narazaki et al., 2017). Chemokines also play an important role in the recruitment of leucocyte subset in inflamed joints in RA. Blocking CXC chemokine receptor 3(CXCR3) or C-C chemokine receptor 5 (CCR5) have the potent anti-arthritic effects on collagen-induced arthritis (CIA) in DBA/1J mice, which was mainly due to the NF-κB expression suppression in immune cells (Bakheet et al., 2020; Ansari et al., 2021). Due to the importance of inflammatory cytokines/chemokines in RA pathogenesis, targeting the key cytokines or upstream signaling activation will be useful strategy to control clinic symptoms and alleviate disease severity.

Toll-like receptors (TLRs), a family of innate pattern recognition receptors, are widely involved in the regulation of innate immunity. So far, 10 TLRs substypes have been identified (Kawai and Akira, 2010). Among TLRs, the impact of TLR 2, 3, 4, seven and 9 on arthritis development has been investigated in STA model in details. TLR2 exhibits an inhibitory role in STA model by controlling the inhibitory FcrRIIB receptor on macrophages (Abdollahi-Roodsaz et al., 2013). TLR9 activation facilitates the binding of unmethylated DNA CpG motifs (CpGs) to dentritic cells (DCs) and the subsequent crosstalk with natural kill cells (NKs), leading to a significant reduction of neutrophil migration into the joint (Wu et al., 2007). Though TLR4 is normally thought to play a pathogenic role in diseases, the impacts of TLR4 on the progression of arthritis in STA model are inconsistent in different studies (Choe et al., 2003; Kim and Chung, 2012). On the contrast, it is clear that TLR3 and seven play a pivotal role in arthritis progression. Moreover, they also have a synergy effect on IL-1β production, which is mostly dependent on the interferon regulatory factor (IRF5) function (Duffau et al., 2015). In addition, NF-κB signaling pathways, involved into inflammatory responses in the pathogenesis of RA (Bondeson et al., 1999; Tak et al., 2001), can also be activated in myeloid cells when TLR7/8 agonists bind to their receptors, and the subsequent cytokines production are cell-type dependent (Eng et al., 2018).

IRF5 is known as a key transcription factor involved in the control of the expression of pro-inflammatory cytokines responses to microbial infection and type I interferon responses to virus (Krausgruber et al., 2010). Recently, polymorphisms in the IRF5 gene have been found to associate with an increased risk of developing rheumatoid arthritis, lupus erythematosus and inflammatory bowel diseases (Demirci et al., 2007; Balasa et al., 2010; Dawidowicz et al., 2011). As a central transcription factor of TLR7 signaling, IRF5 can affect neutrophil influx to the inflammatioin sites, define the inflammatory macrophages phenotype and impact cytokines production (Schoenemeyer et al., 2005; Weiss et al., 2015). TLR7 induced IL-1β production in synovial fibroblasts and M1-type macrophage from rheumatoid arthritis patients was also in an IRF5-dependent manner (Guo et al., 2018). In addition, IRF5 also has the species-invariant role in controlling the inflammatory macrophage phenotype (Weiss et al., 2013). Depletion of IRF5 is able to protected mice from methylated BSA-induced acute arthritis or K/BxN serum transfer arthritis, suggesting that IRF5 could be an attractive therapeutic target in arthritis.

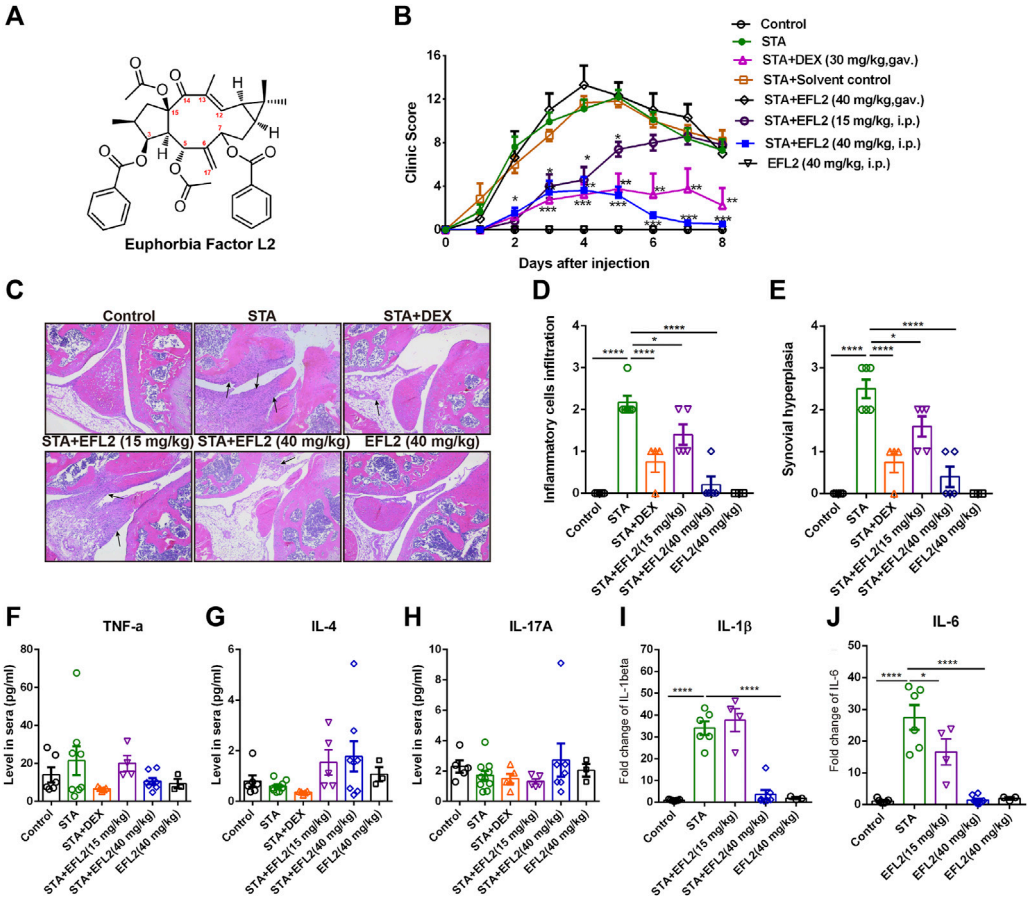


FIGURE 1 | Euphorbia factor L2 effectively alleviates K/BxN serum transfer arthritis (STA) in mice **(A)** Chemical structure of EFL2 ($C_{38}H_{42}O_9$, molecular weight = 642.735) **(B)** Arthritic index in each group was recorded every day after serum injection (day 0) **(C)** Representative hematoxylin and eosin (H.E.) staining images of the knee joints. Assessment of inflammatory cell infiltration **(D)** and synovial hyperplasia **(E)** in the knee joints from the control (n = 6), STA (n = 8), STA mice treated with DEX (n = 5) or EFL2 (15 or 40 mg/kg) (n = 5–8) and mice solely treated with EFL2 (40 mg/kg) (n = 3) **(F–J)** TNF-α **(F)**, IL-4 **(G)**, IL-17A **(H)**, IL-1β **(I)** and IL-6 **(J)** levels in the blood of control, STA and STA mice treated with DEX or EFL2. Data represent the mean values ±SEM. $^*p < 0.05$, $^{**}p < 0.01$, $^{***}p < 0.001$ were considered as significant.

Euphorbia L. are traditional medicine for folk medicine practice (Li et al., 2003). They are reported to have many pharmacological effects and be used in the treatment of ascites syndrome, abscess, arthralgia syndrome and hemorrhage syndrome (Li et al., 2003). A previous study reported that supplementation with *Euphorbia hirta* (*E. hirta*) extract significantly alleviated the adjuvant induced arthritis (AIA) in mice by decreasing the levels of inflammatory-mediators (Ahmad et al., 2014). The seeds of *Euphorbia lathyris L.* are the most typical and traditionally used herbs. Due to the mupltiple pharmacological effects, they have been added in chinese herbal compound preparation such as Zijingding and the traditional Chinese medicine prescription "Tongguansan" (Mei, 1989; Fan and Zhang, 1991). In a series of latheyran editerpenes extracted from *Euphorbia lathyris L.* seeds, known as *Euphorbia* factor L1-L11 (EFL1-11), EFL2 has been reported to have anti-cancer ability. It induced the apoptosis of lung cancer cell line A549 in a dose-dependent manner *in vitro* (Lin et al., 2017). A separate study also indicated its inhibitory effect tumor growth by suppressing SMMC-7721 and Hep G2 cells proliferation and migration via STAT3 phosphorylation (Fan et al., 2019). Our recent study identified EFL2's robust improving effect on LPS-induced lung injury in mice (Zhang et al., 2018). In the present study, we assessed the pharmaceutic and pharmacokinetic features of EFL2, and evaluated its protective effect on K/BxN serum-transfer arthritis in mice. Moreover, we determined its inhibitory role on TLR7 mediated signaling pathways and elucidated its anti-arthritis mechanisms both *in vivo* and *in vitro*.

MATERIALS AND METHODS

Preparation of EFL2

Isolation and identification of EFL2 ($C_{38}H_{42}O_9$, **Figure 1A**) were performed as described before (Zhang et al., 2018). The purity of up to over 98% was determined by HPLC. EFL2 was dissolved in DMSO as a stock solution. The stock solution was diluted (1:100) with sterile PBS supplemented with 3% tween 20 before administrated to mice (the final concentration of DMSO is 1%).

Establishment of K/BxN Serum-Transfer Arthritis Model and Animal Treatment

K/BxN serum was collected from K/BxN mice at 8 weeks of age, pooled, aliquoted and stored at -20 °C. K/BxN serum-transfer arthritis (STA) model was induced by intraperitoneal (i.p.) application of 150 μL of serum at day 0. Clinical score for arthritis severity was assessed using a 0–4 point scale for each paw at various time points (0–16 total score) as described previously (Luo et al., 2011). 8-week old male C57BL/6 mice were purchased from Dashuo Animal Center (China, Chengdu), maintained at 25°C, and exposed to 12-h light and dark cycles. Mice were fed with standard laboratory chow and water with 1 week of acclimatization. Naive mice were used as the control group. Except the control mice, all mice were i. p. injected with 150 μL of serum, then randomly divided into the following groups and treated with different compounds daily for the consecutive 8 days: 1) STA group; 2) Solvent control group, mice were gavaged with the solvent; 3) Dexamethasone (DEX) group, mice were gavaged with 30 mg/kg DEX; 4) EFL2 group 1, mice were gavaged with 40 mg/kg EFL2; 5) EFL2 group 2, mice were intraperitoneally injected with 15 mg/kg EFL2; 6) EFL2 group 3, the control mice were intraperitoneally injected with 40 mg/kg EFL2. In addition, the control mice were intraperitoneally injected with 40 mg/kg EFL2. All animal experiments were conducted in accordance with ethical regulation for animal care and use in China.

In vivo Pharmacokinetic Study

Prior to the pharmacokinetic study, 12 male C57BL/6 mice were fasted for 12 h with free access to water, and then treated by intraperitoneal injection of EFL2 at a dose of 40 mg/kg. About 50 μL blood samples were collected via the oculi chorioideae vein at 0.5, 1, 2, 4, 8, 12, 24, 72, 96, and 168 h, respectively. After centrifugation at 5,000 rpm for 10 min, plasma samples were obtained and frozen at −80°C until analysis. The pharmacokinetic parameters of EFL2 were calculated using WinNolin 4.0.1 software.

Preparation of Plasma Sample

20 μL plasma samples were spiked with 340 μL acetonitrile by vortex mixing for 30 s. The mixture was then centrifuged at 10,000 rpm for 5 min at 4°C to separate the precipitated protein. An aliquot of 50 μL supernatant was transferred to a fresh tube and spiked with 450 μL mobile phase (acetonitrile containing 0.1% formic acid). After centrifugation at 13,000 rpm for 5 min, 3 μL supernatant was injected into Agilent 6,495 Triple Quadrupole LC/MS/MS system for each time. Then, the concentration of EFL2 was determined.

Instrumentation and UPLC-MS Method

An Agilent 1,200 series UPLC system (Agilent Technologies, Waldbronn, Germany) equipped with an 6,495 quadruple mass spectrometer (Agilent Technologies, Santa Clara, CA, United States) were used for pharmacokinetic study. The separation was carried out with Waters Acquity UPLC BEH C18 column (2.1 × 50 mm, 1.7 μm) at a constant temperature of 30 °C. The mobile phase was composed of aqueous solution (0.1% formic acid, A) and acetonitrile (containing 0.1% formic acid, B) and the program of the mobile phase was as follows: 0 min, 40% B; 1 min, 40% B; 1.5 min, 80% B; 2.5 min, 90% B; 4 min, 90% B; 4.1 min, 40% B; 6 min, 40% B, at a flow rate of 0.3 ml/min. The mass spectra were acquired using a triple quadrupole mass spectrometer with ESI ion source in positive mode. The ionization conditions were as follows: drying gas temperature (N2), 300°C; gas flow, 11 L/min (N2); nebulizer pressure, 35 psi (N2). An Agilent Mass Hunter workstation was used for data processing.

Histological Assessment

The left knee joints were removed on day 13 post STA and fixed in 4% formaldehyde overnight at 4°C. The tissues were decalcified in EDTA and sectioned after embedding in paraffin. 5 μm sections were deparaffinized with xylene, re-hydrated with 100, 95 and 80% ethanol and then stained with hematoxylin and eosin (H&E). Histopathological changes in the knee joints were measured using a semiquantitative scoring system (0–4 scale) to assess synovial hyperplasia and articular inflammatory cells infiltration as previously described (Yamanishi et al., 2002).

Flow Cytometry Analysis

150 μL peripheral blood and the hind ankles were collected on day 5 and 13 post KBx/N serum transfer, respectively. For the peripheral blood samples, red blood cells were lysed and cells were prepared as single cell solution. The hind ankles were cut into 1 mm^2 pieces, and then digested in 10% DMEM containing Collagen IV (1 mg/ml) for 1 h at 37°C. Single cell solution was then prepared after passing through 40 μm cell strainer. 1×10^6 cells were stained with FITC-conjugated CD11b (BD, United States, 1:500), PE-conjugated F4/80 (BD, United States, 1:400), PerCP-Cy5.5-conjugated Ly6G (BD, United States, 1:400) and APC-conjugated Ly6C (BD, United States, 1:200) to detect macrophage, neutrophil and monocyte. Data were acquired using a BD FACSCalibur flow cytometer (BD Biosciences) and were analyzed by using FlowJo software (Version 7.6.1).

Cell Preparation and Culture

RAW264.7 cells, a mouse macrophage cell line, were cultured in DMEM medium containing 10% fetal bovine serum (FBS), 1% penicillin-streptomycin and maintained at 37 °C in 5% CO_2 humidified air. Bone marrow-derived macrophages (BMDMs) generation was performed as following description. In brief, bone marrow cells were harvested from tibias and femurs of C57BL/6 mice and differentiated for 7 days in DMEM medium supplemented with 10% FBS, 1% penicillin-streptomycin and 50 ng/ml M-CSF. For human peripheral blood mononuclear cells (PBMCs) preparation, 5 ml peripheral venous blood was obtained from healthy donors in West China Hospital. PBMCs were isolated with Human Lymphocyte Separation Medium (LTS1077, Tian Jing, China) according to the manufacturer's instructions. The experimental protocols were performed according to the approved guidelines established by the Institutional Human Research Subject Protection Committee

of the Ethics Committee of West China Hospital, Sichuan University, China.

Cell Viability Measurement

The effects of EFL2 on RAW264.7 cells, BMDMs and PBMCs viability were evaluated by Cell Counting Kit-8 (CCK8) assay (Dojindo, Japan). Briefly, RAW264.7 cells (1×10^5 cells/well), BMDMs (1×10^5 cells/well) and PBMCs (1×10^6 cells/well) were plated into 96-well plates and then incubated at 37 °C in 5% CO_2 incubator overnight. The medium was disposed next day and cells were incubated with different concentrations of EFL2 (0.1, 0.5, 1, 5, 10, 25, 50 and 100 μM) for 20 h. After disposing the supernatant, 100 μL of culture medium supplemented with 10 μL of CCK8 were added into wells and incubated for an additional 4 h. The optical absorbance at 450 nm was read with a Biotek Eon™ microplate reader (Biotek, Vermont, United States).

ELISA Assay for Cytokines Measurement

RAW264.7 cells (5×10^5/ml), BMDMs (5×10^5/ml) and PBMCs (2×10^6/ml) were plated in 96-well plates and incubated overnight. RAW264.7 cells (5×10^5/ml) or BMDMs were either solely stimulated by poly:IC (1 μg/ml) (InvivoGen, United States), R837 (20 μg/ml) (Invegen, United States) and the combination of poly:IC and R837, or pretreated with EFL2 (1, 5 and 10 μM) 30 min prior to poly:IC and/or R837 stimulation for 24 h. For the anti-inflammatory molecular mechanism study, RAW264.7 cells (5×10^5/ml) were plated in 96-well plates and stimulated with R837 (20 μg/ml) with or without the addition of NF-κB inhibitor (JSH-23, 10 μM/ml) for 24 h. After 24 h, the culture supernatant was collected for cytokines measurements.

IL-4, IL-17A and TNF-α in sera from different group mice were measured using CBA Multiplex kit (BD, United States). The concentrations of IL-1β and IL-6 in serum or supernatant were detected by ELISA Kit (MULTI SCIENCES, China) according to the manufacturers' instructions.

Western Blot Assay

RAW264.7 cells (2×10^6 cells/well) were plated into 6-well plates and then incubated at 37°C in 5% CO_2 for 24 h. After incubated with various concentrations of EFL2 (1, 5 and 10 μM) for 1 h, cells were then stimulated by R837 (20 μg/ml) for 30 min. Cell lysates were prepared by direct lysis in 20 μL IP buffer (Beyotime Biotechnology, Shanghai, China). After obtaining the whole cell extracts, the cytosolic and nuclear were seperated using Nuclear and Cytoplasmic Protein Extraction Kit (Beyotime Biotechnology, Shanghai, China). BCA Protein Assay Kit (Beyotime Biotechnology, Nantong, China) was applied to determine the protein concentrations. The bands corresponding to p- IKKα/β, IKKα/β, *p*-IκBα, IκBα, p-p65, p65, *p*-IRAK4, IRAK4, *p*-IKKβ, IKKβ, *p*-IRF5, IRF5, β-actin and Lamin B were visualized using a Western Blot Detection Chemiluminescence Kit (Merck). Protein extracted from the total lysates/cytoplasm and nucleus was quantified in relation to β-actin and Lamin B bands, respectively.

The antibodies used in the experiments were as follows: rabbit anti-mouse IKKα/β polyclonal antibody (1:1,000, Abways, China), rabbit anti-mouse IκBα polyclonal antibody (1:1,000, Abgent, China), rabbit anti-mouse p65 polyclonal antibody (1:1,000, Abgent, China), rabbit anti-mouse phosphorylated IKKα (Ser176)/β (Ser177) (1:1,000, Abways, China), rabbit anti-mouse phosphorylated IκBα (1:1,000, Abcam, United States), rabbit anti-mouse phosphorylated p65 (1:1,000, Abcam, United States), rabbit anti-mouse IRAK4 polyclonal antibody (1:1,000, Proteintech, United States), rabbit anti-mouse phosphorylated IRAK4 (Thr345/Ser346) (1:1,000, Affinity, United States), rabbit anti-mouse IKKβ polyclonal antibody (1:1,000, Abbkine, United States), rabbit anti-mouse phosphorylated IKKβ (Ser177) (1:1,000, Abways, China), rabbit anti-mouse IRF5 polyclonal antibody (1:1,000, Immunoway, United States), rabbit anti-mouse phosphorylated IRF5 (Ser437) (1:1,000, Affinity, United States), anti-mouse actin monoclonal antibody (1:20,000, Transgen, China) and rabbit anti-mouse LaminB monoclonal antibody (1:5,000, Abways, China).

Transfection of IRF5 Plasmid

RAW264.7 cells (4×10^5 cells/well) were seeded into 6-well plates before transfection with the plasmid. When cells confluency reached 60%, RAW264.7 cells were transfected with plasmid IRF5-mouse vector (Origene, United States) using TransEasy™ Transfection Reagent (FOREGENE, China). IRF5 plasmid was suspended with transfection reagent as 1:1.5. Cells were incubated at 37°C for 24 h, then treated with EFL2 and R837 for another 24 h. The supernatant was collected for IL-1β and IL-6 measurements using ELISA kits as described above. For western blot detection, RAW264.7 cells were pretreated with EFL2 (10 μM) for 1 h and stimulated with R837 (20 μg/ml) for 40 min after IRF5 plasmid transfection. Cell lysates were prepared as described above.

Confocal Microscopy

P65 and IRF5 translocation activity was analyzed by confocal microscopy. Briefly, 1×10^5 RAW264.7 cells were plated on coverslips overnight. Cells were pretreated with various concentrations of EFL2 (1, 5 and 10 μM) for 1 h and then stimulated by R837 (20 μg/ml) for 30 min. After washed with ice-cold PBS, RAW264.7 cells were fixed with 4% paraformaldehyde for 20 min at room temperature. The coverslips were washed with PBS with 0.2% tween 20 and blocked with 5% goat serum. Primary antibodies were applied to coverslips overnight at 4°C, followed by secondary antibodies incubation for 1 h at room temperature. After three times wash, coverslips were mounted with Fluoroshield™ with DAPI (Solarbio, China) and images were acquired by confocal microscopy (ZEISS, Germany). Primary antibody: rabbit anti-mouse IRF5 (1:800, Abcam, China); rabbit anti-mouse p65 (1:1,000, Abcam, China). Secondary antibody: Alexa eFluor® 488 conjugated goat anti-rabbit IgG (1:2000, Thermo Fisher Scientific, Carlsbad, United States).

Immunochemistry Staining

The dissected left ankles were fixed in 4% formaldehyde overnight. Embedding, de-paraffinization, and re-hydration of

the ankle sections were the same as described for H&E staining. After treated with 3% hydrogen peroxidase for 10 min, the tissue sections were immersed in a 10 mM sodium citrate buffer (pH 6.0) for 15 min at 95°C, and washed with PBS. The sections were then blocked with 5% goat serum in PBS, and incubated with primary antibodies overnight at 4°C. Primary antibodies were as follows: rabbit anti-mouse IL-1β (1:600, Abcam, China); rabbit anti-mouse IL-6 (1:50, Abcam, China). The signal was visualized using an Envision System (DAKO, United States). The images were then acquired by microscopy (Leica DMil).

PCR Array Analysis

Total RNA was isolated from the right ankles using the TRIzol Reagent (Invitrogen) and purified with RNeasy Mini Kit and RNase-Free DNase Set (Qiagen). RNA quality was determined using a spectrophotometer and was reversely transcribed using Wcgene® mRNA cDNA kit. The complementary DNA was used on the Toll-like Receptor Pathway PCR Array plate (Wcgene® biotech, China).

Quantitative RT-PCR

Frozen right ankles were pulverized with liquid nitrogen and total RNA was extracted using Trizol reagent (Invitrogen). RNA was reverse transcribed into cDNA using an oligo d(T) primer. The obtained cDNA was applied for quantitative RT-PCR using SYBR Green I-dTTP (Eurogentec). Samples were analyzed in triplicate, and β-actin was used as endogenous controls. Data was analyzed using the $2^{-\Delta\Delta Ct}$ method and is expressed as "Fold change" (expression relative to housekeeping gene and normalized to reference sample).

Statistical Analysis

Data are presented as the mean ± SEM. Statistical analysis for multiple comparisons was performed by one-way ANOVA followed by Bonferroni's post-hoc comparisons test using GraphPad Prism 8.0 software. $^{*}p < 0.05$, $^{**}p < 0.01$, $^{***}p < 0.001$, $^{****}p < 0.0001$ were considered as significant difference.

RESULTS

EFL2 Effectively Alleviates Arthritis Severity in STA Mice

Developing anti-arthritic drugs and verifying therapeutic effect can be achieved by taking advantage of animal arthritis models. Although many murine models of arthritis have inflammation effector features, the injection of K/BxN mice serum containing antibodies against glucose-6-phosphate isomerase (G6PI) mainly induce inflammatory arthritis by initiating innate immune system. Unlike collagen-induced arthritis, myeloid cells exert a central role in K/BxN serum-transfer model, but T and B cells are not required (Christensen et al., 2016). Macrophages, neutrophils and $Ly6C^{-}$ nonclassical monocytes are major pivotal cell types which play an essential role in the initiation, progression and resolution of sterile joint inflammation in K/BxN serum-transfer arthritis (STA) model (Solomon et al., 2005; Misharin et al., 2014).

TABLE 1 | Pharmacokinetic parameters of ELF2 in mice after intraperitoneal injection of EFL2 (n = 6 for each time points).

Parameter	Unit	EFL2
T_{max}	h	2.5 ± 1.73
C_{max}	ng/ml	4,525.12 ± 1,630.01
*t*1/2	h	21.17 ± 7.11
AUC_{0-t}	h*ng/ml	374.10 ± 163.96
$AUC_{0-\infty}$	h*ng/ml	379.43 ± 165.88
MRT_{0-t}	H	59.16 ± 2.75
$MRT_{0-\infty}$	H	61.38 ± 3.70

In this study, we evaluate the inhibitory effect of EFL2 on inflammatory arthritis, and also test the therapeutic efficiency of EFL2's gavage and intraperitoneal (i.p.) injection in STA mice. The clinic scores in STA mice showed a rapidly increased clinic score following with slow remission from day 5–8 (**Figure 1B**). Meanwhile, histological assessment of the joints demonstrated abundant infiltrated inflammatory cells in the knee of STA mice, accompanied with obvious synovial hyperplasia (**Figures 1C–E**).

In contrast, DEX administration significantly lowered arthritis clinical scores, and reduced infiltrated cells in the joints of STA mice (**Figures 1B–E**). In EFL2-treated groups, EFL2 oral administration did not affect the arthritis severity of STA mice at all (**Figure 1B**). Whereas, i. p. injection with the same dose of EFL2 (40 mg/kg) dramatically improved joint swelling and redness in STA mice (**Figure 1B**). 15 mg/kg of EFL2, to a moderate extent, alleviated arthritis symptoms, particularly in the acute phase of arthritis (**Figure 1B**). Mice were sacrificed on day 8 and there were abundant inflammatory cells infiltrating into the joint in STA mice, accompanied with obvious synovial hyperplasia (**Figures 1C–E**). As shown in **Figure 1C**, 15 mg/kg of EFL2 only partially reduced the excessive inflammatory cells infiltration and synovium hyperplasia in STA mice. In contrast, high dose of EFL2 (40 mg/kg) or DEX treatment significantly inhibited inflammatory status and inflamed synovium in joints of STA mice (**Figures 1C–E**).

Inflammatory cytokines (e.g. TNF-α, IL-17, IL-1β and IL-6) are known to be pathogenic factors triggering joint diseases and established synovitis (Martin et al., 2017). The impact of EFL2 on a series of pro-inflammatory cytokines production was also assessed. Interestingly, no significant changes in TNF-α, IL-4 and IL-17A levels were observed among different groups (**Figures 1F–H**). Unlike TNF-α, IL-1β is absolutely required for disease development in K/BxN serum transfer arthritis (Ji et al., 2002). Meanwhile, IL-6 is also considered as a key inflammatory mediator in the pathogenesis of rheumatoid arthritis (Calabrese and Rose-John, 2014). Over 2-fold levels of IL-1β and IL-6 were detected in the sera of STA mice, which were significantly reduced by EFL2 (40 mg/kg, i. p.) or DEX treatment (**Figures 1I,J**). In contrast, 15 mg/kg of EFL2 only effectively inhibited IL-6 level of STA mice on day 8 (**Figure 1J**). Taken together, above results indicate that the intraperitoneal administration of EFL2 is able to ameliorate the disease severity of STA, which might due to the decrease of pro-inflammatory cytokines production in serum.

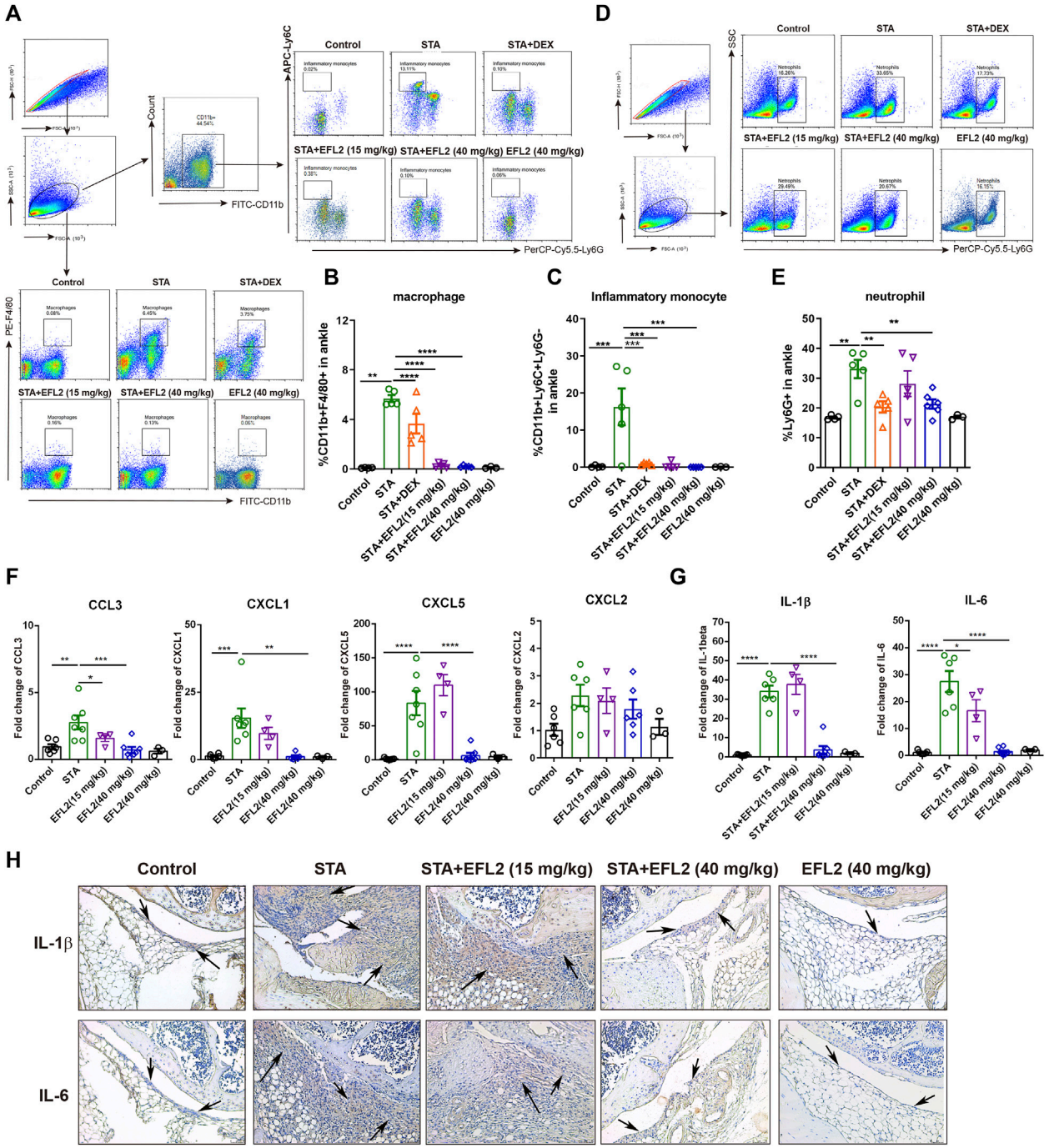


FIGURE 2 | Euphorbia factor L2 suppresses inflammatory cells infiltration into the ankle. Flow cytometry gating strategy and quantification for macrophages ($CD11b^+F4/80^+$) **(A, B)**, inflammatory monocytes ($CD11b^+Ly6C^+Ly6G^-$) (A, C) and neutrophils ($Ly6G^+$) **(D, E)** in the ankles from the control, STA, STA mice treated with DEX or EFL2 (15 or 40 mg/kg) and mice solely treated with EFL2 (40 mg/kg) (n = 3-7 per group) **(G, H)** mRNA expressions of chemokine CCL3, CXCL-1, CXCL-5, CXCL2 **(G)** and inflammatory cytokine IL-1β and IL-6 **(H)** in the ankles from each group **(I)** Immunohistochemical staining for IL-1β and IL-6 in the ankle from the control, STA, STA mice treated with EFL2 (15 or 40 mg/kg) and mice solely treated with EFL2 (40 mg/kg). Arrows represent the synovium with numbers of infiltrated inflammatory cells. Data represent the mean values ±SEM. $^*p < 0.05$, $^{**}p < 0.01$, $^{***}p < 0.001$, $^{****}p < 0.0001$ were considered as significant.

Pharmacokinetic Study of EFL2

An UPLC-MS/MS method was successfully developed and applied to a pharmacokinetic study of EFL2 in the plasma after intraperitoneal injection. The main pharmacokinetic parameters of EFL2 were shown in **Table 1**. After 40 mg/kg intraperitoneal injection, the concentration of EFL2 reached a

maximum plasma concentration (C_{max}) of 4,525.12 ± 1,630.01 ng/ml, and the time to reach the maximum concentration (T_{max}) was 2.50 ± 1.73 h. The short T max indicated that EFL2 was rapidly absorbed *in vivo* and produced quick therapeutic effects. The area under the plasma concentration versus time curve from zero to time t (AUC_{0-t}) was (374.10 ± 163.96) h·ng/ml for EFL2. Besides, EFL2's half time ($t_{1/2}$) value was 21.17 ± 7.11 h, which suggested that EFL2 was slowly eliminated *in vivo*.

EFL2 Suppresses the Inflammatory Cells Infiltration and Activation in Ankles of STA Mice

The infiltration of myeloid cells, especially macrophages and neutrophils, is a prominent feature of synovium lesions, and is also positively correlated with the degree of joint erosion (Choy, 2012; Orr et al., 2018). Next, we performed flow cytometry to analyze different myeloid cells in blood and ankle of mice, respectively. Compared with control mice, STA mice showed dramatic increases in the proportions of neutrophil ($Ly6G^+$) and inflammatory monocyte ($CD11b^+Ly6C^+Ly6G^-$) in the circulation (**Supplementary Figure S1**). In addition, we detected predominant neutrophils infiltration in the ankles of STA mice (**Figures 2D,E**), accompanied with significantly increased percentages of macrophages and inflammatory monocytes (**Figures 2A–C**). 30 mg/kg DEX significantly inhibited the increases of these myeloid cells subsets in the ankles of STA mice (**Figures 2A–E**). While, EFL2, at the dose of 15 mg/kg, remarkably reduced macrophage and inflammatory monocyte influx into the ankles but not neutrophil (**Figures 2B,C**). 40 mg/kg of EFL2 treatment displayed a more robust suppressive effect on the expansions of these three myeloid cells subsets both in the blood and ankles of STA mice (**Supplementary Figure S1**, **Figures 2A–E**).

To assess whereby EFL2 administration prevents the infiltration of these myeloid cells in the ankles, we analyzed the mRNA expressions of known neutrophil chemoattractant, such as CXCL1, CXCL2, CXCL5, and chemokine (C-C motif) ligand CCL3, CCL4 and CCL5 in the ankles of mice. CCL4 and CCL5 mRNA expressions were undetectable in our study. No significantly changes were observed in CXCL2 gene expression among different groups (**Figure 2F**). In contrast, CXCL1 and CXCL5 mRNA expressions were significantly up-regulated in the ankles of STA mice on day 5, which were remarkably down-regulated by 40 mg/kg EFL2 i. p. treatment (**Figure 2F**). Meanwhile, this compound also significantly reduced the gene expression of CCL3, known as macrophage trafficking, in STA mice (**Figure 2F**). In contrast, EFL2, at the dose of 15 mg/kg, only significantly decreased chemoattractant CCL3 mRNA expression (**Figure 2F**).

Since the infiltration of myeloid cells contributes to increased inflammatory cytokines levels in inflamed joints, we next detected mRNA expression of inflammatory cytokines in the ankles. Compared with control mice, IL-1β and IL-6 mRNA expression increased to 35- and 27-fold in the ankles of STA mice, respectively, which were robustly inhibited by EFL2 i. p. treatment (**Figure 2G**). Immunohistochemical staining for IL-1β and IL-6 further confirmed EFL2 could inhibit these two cytokines production in the local inflamed joints (**Figure 2H**). Collectively, these data indicate that EFL2 i. p. administration is able to inhibit inflammatory cells infiltration by suppressing neutrophil and macrophage chemoattractants and suppress their activation to reduce local inflammatory cytokines production.

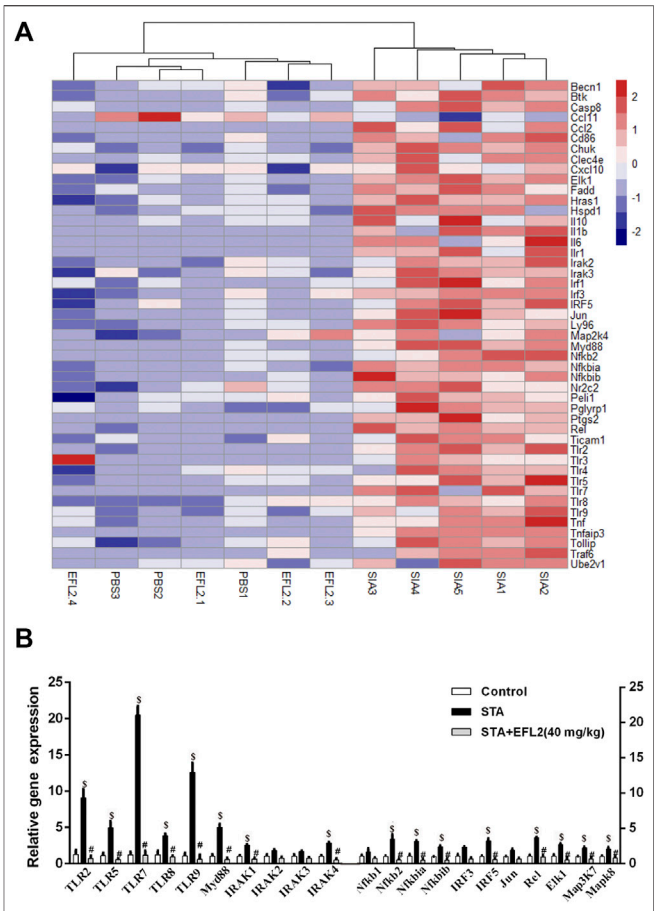


FIGURE 3 | Euphorbia factor L2 suppresses TLR signaling pathway activation **(A)** Heat map showing the log(fold-changes) in TLR signalling pathway genome in the ankles of mice. Color scale ranges from red to blue which respectively denotes the up- or down-regulated of the genes **(B)** RT-PCR verified the changes in the transcriptional regulators mRNA expression among control, STA and STA mice i. p. injected with EFL2 (40 mg/kg) (n = 3 in control, n = 5 in STA and EFL2 treated groups). Data represent the mean values ±SEM. $^*p < 0.05$, $^{**}p < 0.01$, $^{***}p < 0.001$ were considered as significant. **$**: STA versus Control, $p < 0.05$; #: STA + EFL2 treatment versus STA, $p < 0.05$.

The Suppressive Role of EFL2 on TLR Signaling Pathway in Ankles of STA Mice

Toll-Like Receptors (TLRs) are reported to implicate into the initiation, progagation and remission phases of STA (Guo et al., 2018). To identify the most relevant TLR signaling pathway which is implicated into EFL2's suppressive effect on STA and

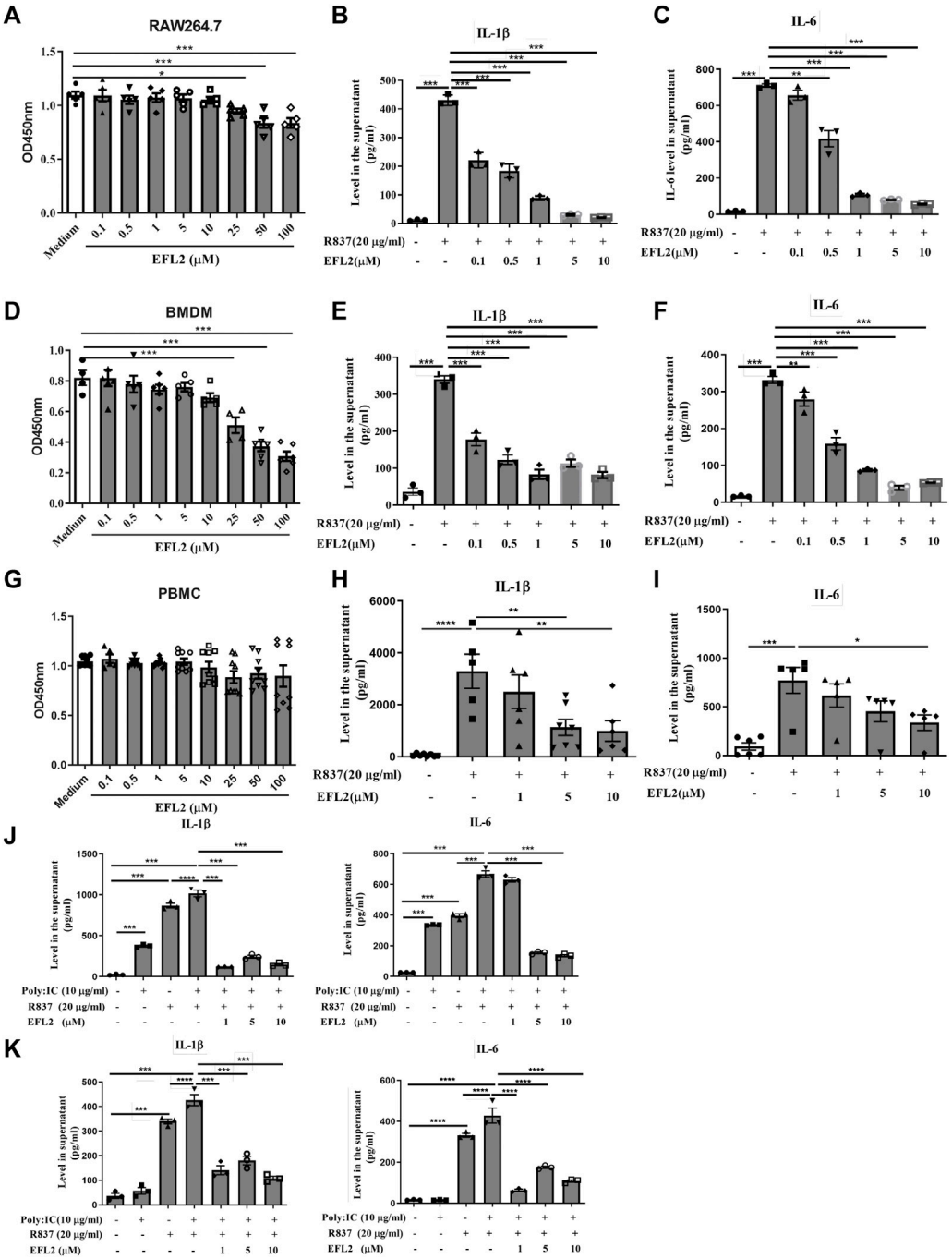


FIGURE 4 | Euphorbia factor L2 reduces IL-1β and IL-6 production in R837-stimulated macrophages in vitro **(A, D, G)** Cytotoxicity effect of different concentrations of EFL2 (0.1, 0.5, 1, 5, 10, 25, 50 and 100 μM) on RAW264.7 cell **(A)** bone marrow-derived macrophages (BMDMs) **(D)** or PBMCs **(B, E, H)** Effect of different concentrations of EFL2 (0.1, 0.5, 1, 5, 10 μM) on IL-1β production in R837-stimulated RAW264.7, BMDMs and PBMCs **(C, F, I)** Effect of different concentrations of EFL2 on IL-6 production in R837-stimulated RAW264.7, BMDMs and PBMCs **(J, K)** The inhibitory effect of EFL2 on IL-1β and IL-6 secreted by RAW264.7**(J)** or BMDMs **(K)** under the co-stimulation of poly:IC and R837. n = 3 for each group in an independent experiment. Data represent the mean values ±SEM of three independent experiments. *$p < 0.05$, **$p < 0.01$, ***$p < 0.001$ were considered statistically significant.

inflammatory cytokines production, PCR array was performed in this study. As shown in **Figure 3A**, 44 gene expressions were increased in ankle of STA mice compared with control mice. Recently, emerging newer data indicate the role of TLR7 in the pathogenicity of RA, particular in the aspect of rhematoid synovitis (Kim et al., 2016) and bone erosion (Kim et al., 2019). A recent study showed that TLR7 deficiency alleviated K/BxN serum-induced arthritis by imparing interferon

regulatory factor 5 (IRF5) mediated IL-1β and IL-6 produced by macrophages and synovial fibroblasts, respectively (Duffau et al., 2015). We found a 16-fold increase in TLR7 expression at the transcriptional level in STA mice compared with control mice (**Figures 3A,B**). In addition, mRNA expressions of TLR2 and 9 which mediate an inhibitory role in STA model (Abdollahi-Roodsaz et al., 2013) were also significantly increased in STA mice. Consistently, STA mice displayed up-regulated mRNA expressions of other downstream genes including Myd88, IRAK1/4, Nfkbia/ib, IRF5, Rel, Map3K7 and Mapk8 (**Figure 3B**). While, 40 mg/kg EFL2 i. p. injection exerted a robust inhibitory effect on above up-regulated genes expression (**Figure 3B**). The inhibitory effects of TLR2 and TLR9 in STA pathogenesis can not explain the EFL2's anti-inflammatory role in arthritis. Considering TLR7 mediated-downstream has a promoting role in inflammatory arthritis (Guo et al., 2018), we hypothesized that EFL2 may mainly interfere with TLR7-mediated signaling pathway in STA model to alleviate the inflammatory status in mice.

EFL2 Strongly Inhibits TLR7-Induced Cytokine Production *in vitro*

EFL2 is a latheyran editerpene extracted from *Euphorbia lathyris L*. seeds with toxicity. We noticed that the peak concontration of EFL2 in sera was equal to 7.03 μM based on Cmax (4.52 ± 1.63 μg/ml) and its molecular weight ($C_{38}H_{42}O_9$, MW = 642.6). Therefore, we set up the concentrations (from 0.1 to 100 μM) to test the toxicity of EFL2 on these cell lines. As shown in **Figure 4**. A and D, EFL2, did not display significant cytotoxicity in RAW264.7 cells or primary murine bone marrow-derived macrophages (BMDMs) until its concentration reached 25 μM (**Figures 4A,D**). In contrast, EFL2 did not affect PBMCs viability even at the high concentration of 100 μM (**Figure 4G**), suggesting that PBMCs are not sensitive to EFL2 treatment than murine macrophages.

Next, we test EFL2's anti-inflammatory ability in murine macrophages and human PBMCs *in vitro*. R837, also known as imiquimod, is a strong TLR7 ligand agonist. It robustly induced IL-1β and IL-6 release in the supernatant of RAW264.7 cells, BMDMs and PBMCs (**Figure 4**). Notably, EFL2, even at the lower concentration of 0.1 μM, was able to effectively inhibit IL-1β secretion in RAW64.7 or BMDMs (**Figures 4B,E**). This compound also dose-dependently reduced IL-6 production in murine macrophages (**Figures 4C,F**). By comparison, the suppressive effect of EFL2 on IL-1β production was prior to that on IL-6 in human PBMCs (**Figures 4B,C**).

It is shown that TLR3 has a marked synergy role with TLR7 ligand for IL-1β production in BMDMs (Guo et al., 2018). In this study, we applied poly (I:C), a strong TLR3 agonist, to stimulate murine macrophages solely or together with R837. Poly (I:C) itself did not affect IL-1β and IL-6 production in BMDMs, but it significantly increased these two cytokines secretion in RAW264.7 cells. The addition of poly (I:C) did enhance IL-1β and IL-6 production in either R837-stimulated RAW264.7 cells or BMDMs (**Figures 4J,K**). Various concentrations of EFL2 to different expent decreased the levels of IL-1β and IL-6 in the supernatant of these two murine macrophages co-stimulated by poly (I:C) and R837 (**Figures 4J,K**). Overall these data demonstrate that EFL2 exerts effective anti-inflammatory role via inhibiting TLR7-induced proinflammatory cytokines production in murine macrophages.

EFL2 Suppresses TLR7-Mediated IRAK4/IKKβ/IRF5 Signaling Pathway Activation

Following TLR7/8 activation, IRAK4 kinase can act with TAK1 to cause IKKβ phosphorylation, subsequently inducing IRF5 phosphorylation and translocation in human monocytes (Cushing et al., 2017). Based on above data, we hypothesize that TLR7-mediated IRF5 signaling pathway is implicated into the molecular mechanisms of EFL2's anti-inflammatory effect. Similar to the previous findings in human monocyte (Cushing et al., 2017), R837 rapidly triggered the phosphorylation of IRAK4 and IKKβ in RAW264.7 cells (**Figures 5A–C**), followed with IRF5 phosphorylation at ser437 (**Figures 5D,E**). Additionally, R837 enhanced IRF5 translocational activity in 1 h, evidenced by the decreased expression in cytoplasm but increased expression in nucleus (**Figures 5D,F**). Immunofluorescence staining further confirmed that R837 dramatically induced IRF5 translocation from cytoplasm to nucleus (**Figure 5G**). While, EFL2 pretreatment significantly suppressed the phosphorylation of IRAK4, IKKβ and IRF5 in R837-stimulated RAW264.7 cells (**Figures 5A–F**). Meanwhile, IRF5 translocation was also effectively blocked by EFL2 at the concentrations of 5 and 10 μM (**Figures 5D,F**), which was also represented by less IRF5 positive staining in nucleus (**Figure 5G**).

To further confirm if the blockage of IRF5 activation is an essential process whereby EFL2 decreases pro-inflammatory cytokines reduction, IRF5 plasmid was transfected into RAW264.7 cells. As shown in **Supplementary Figure S2**, there was a significant upregulation of IRF5 expression in RAW264.7 transfected with IRF5, accompanied with IRF5 expression increase both in cytoplasm and nucleus (**Figure 5H**). Meanwhile, overexpression of IRF5 significantly reversed the suppressive effect of EFL2 on nuclear translocation of IRF5 (**Figures 5H,I**). Moreover, EFL2-induced reduction of IL-1β and IL-6 was effectively reversed with overexpression of IRF5 (**Figures 5J,K**). Overall, above data demonstrate that EFL2 is able to robustly block IRAK4-IKKβ-IRF5 signaling pathway activation, leading to pro-inflammatory cytokines IL-1β and IL-6 reduction.

NF-κB Signaling Pathway is Implicated into EFL2 Caused Pro-Inflammatory Cytokines Reduction

TLR7 agonist is reported to induce NF-κB activation in myeloid cells (Eng et al., 2018). Considering that IRF5 plasmid transfection did not completely reverse the reduced IL-1β production, we detected the impact of EFL2 on NF-κB activation in R837-stimulated RAW264.7 cells. As shown in **Figure 6A**, the phosphorylation of IKKα/β and IκB-α rapidly

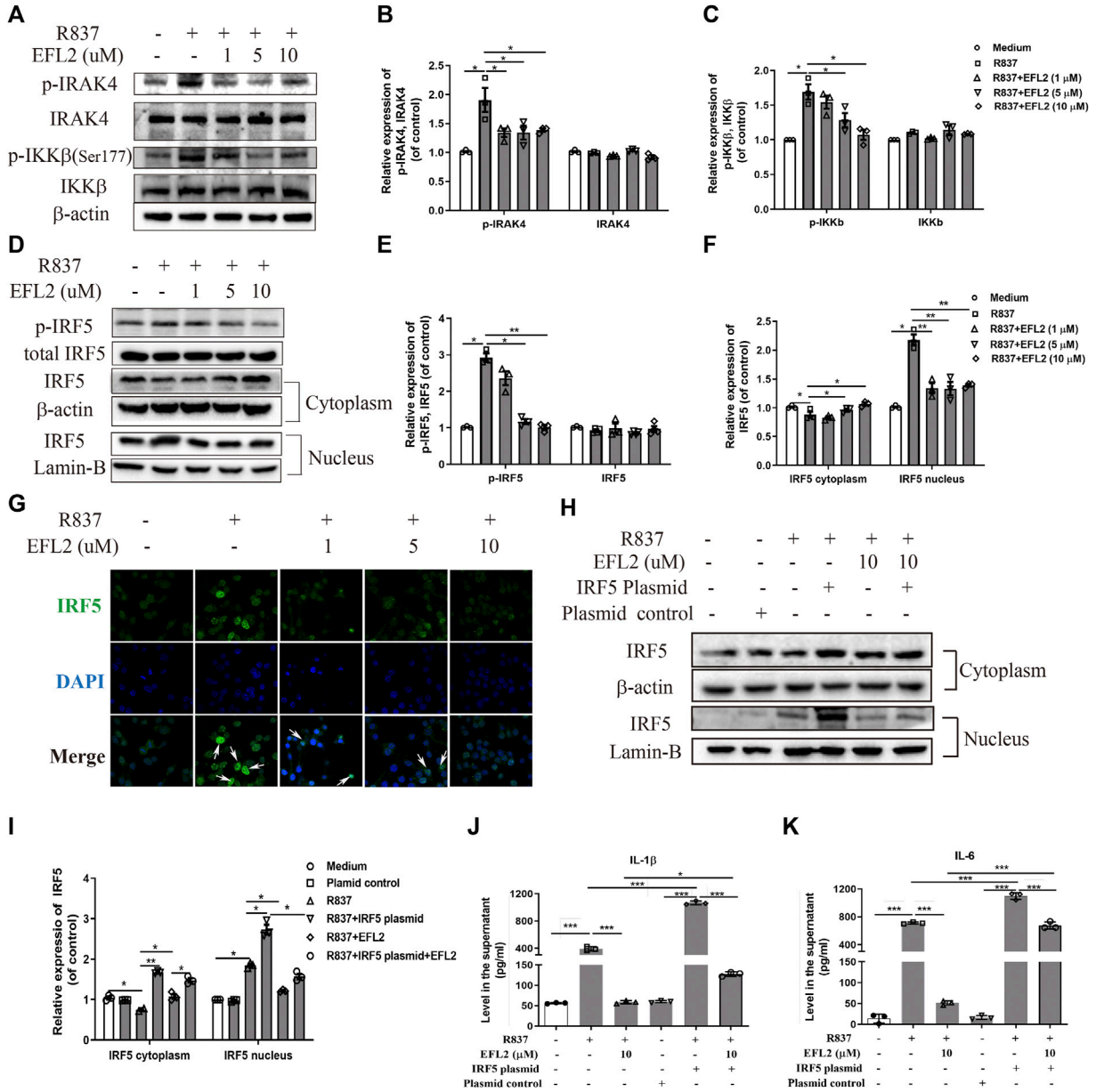


FIGURE 5 | EFL2 reduced IL-1β and IL-6 production via robustly inhibiting TLR7-IKKβ-IRF5 signalling pathway **(A-C)** Western blot bands **(A)** and quantification of *p*-IRAK4, IRAK4 **(B)**, *p*-IKKβ and IKKβ expression **(C)** in RAW264.7 cells **(D-F)** Western blot bands **(D)** and effects of EFL2 on R837-induced IRF5 phosphorylation **(E)** and IRF5 expression in cytoplasm and nucleus **(F) (G)** IRF5 localization determined by immunofluorescence staining (Magnification: ×40) **(H)** IRF5 expression in cytoplasm and nucleus after IRF5 overexpression **(I)** Quantification of IRF5 expression after transfection **(J, K)** The levels of IL-1β **(J)** and IL-6 **(K)** produced by RAW264.7 cells before and after IRF5 overexpression (n = 3 for each group in an independent experiment). Data represent the mean values ±SEM of three independent experiments. $^{*}p < 0.05$, $^{**}p < 0.01$, $^{***}p < 0.001$ were considered as significant.

occurs in R837-stimulated RAW264.7 cells (**Figures 6A–C**), followed by NF-κB subunit p65 phosphorylation and translocation from cytoplasm to nucleus (**Figures 6D–G**). In TLR7-mediated NF-κB signaling activation, EFL2 effectively inhibited IKKα/β, IκB-α and p65 phosphorylation (**Figures 6A,D**). In addition, NF-κB subunit p65 translocation activity was also significantly suppressed by this compound (**Figures 6D,G**), which was further represented by less p65 positive staining in nucleus (**Figure 6G**). To further confirm if EFL2-induced IL-1β and IL-6 reduction was also NF-κB-dependent in our cell system, we test the effect of JSH-23, a NF-κB inhibitor, on these two cytokines production. Interestingly, JSH-23, to a large extent, blocked R837-induced IL-1β production but only partially reduced IL-6 secretion in RAW 264.7 cells (**Figure 6H**), suggesting that NF-kB activation was indeed involved into TLR7 activation induced-IL-1β and IL-6 secretion in

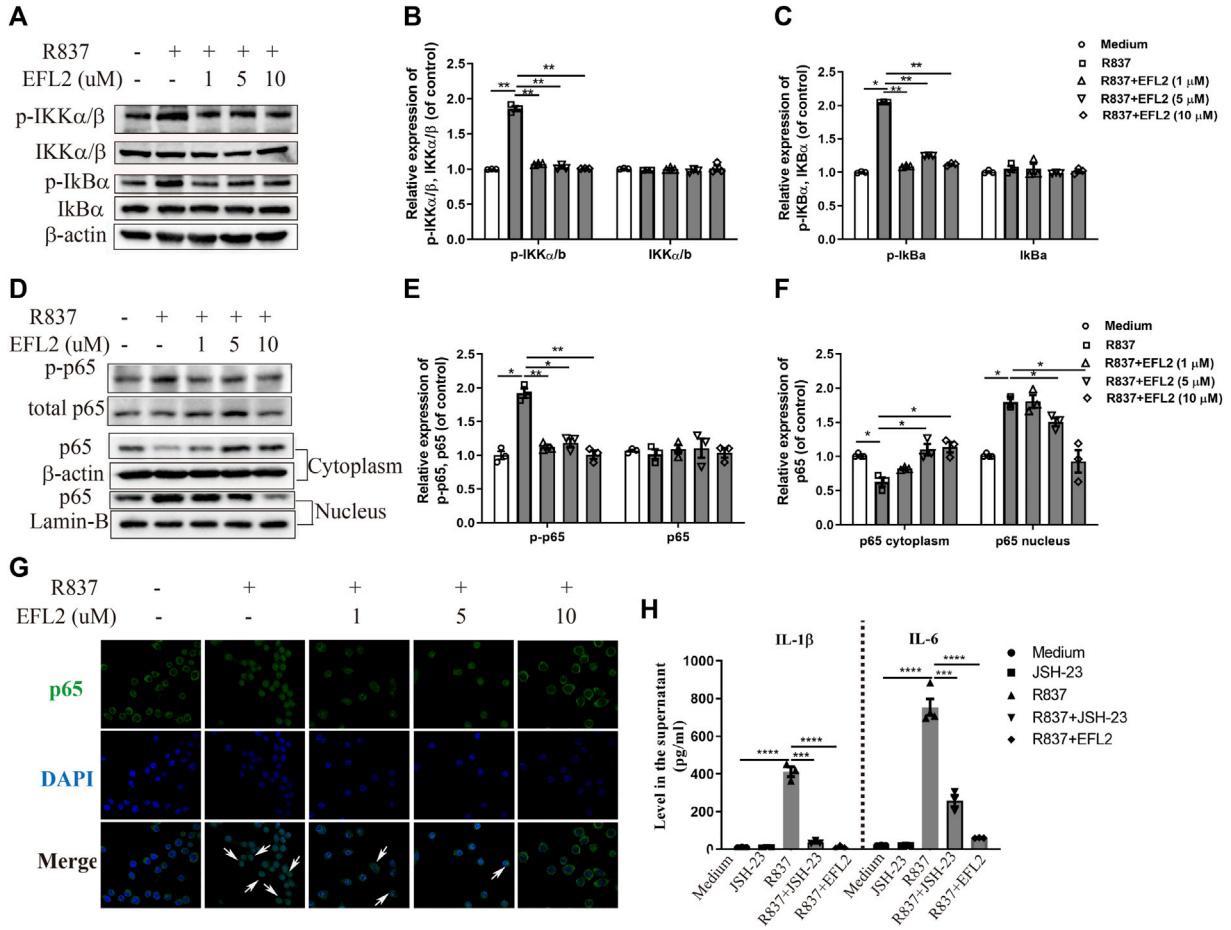


FIGURE 6 | EFL2 inhibited the NF-κB signaling pathway activation. RAW264.7 cells were incubated with different concentrations of EFL2 (1, 5 and 10 μM) for 1 h, followed by R837 (20 μg/ml) stimulation for 30 min, then harvested for western blotting analysis **(A–C)** Western blot bands **(A)** and quantification of *p*-IKKα/β, IKKα/β **(B)**, *p*-IkBα and IkBα **(C)** in RAW 264.7 cells **(D–F)** Western blot bands **(D)** and quantification of p-p65 **(E)** and p65 expression in cytoplasm and nucleus **(F)** in RAW 264.7 cells **(G)** p65 localization determined by immunofluorescence staining (Magnification: ×40) **(H)** Effect of NF-κB inhibitor on R837-induced IL-1β and IL-6 production (n = 3 for each group in an independent experiment). Data represent the mean values ±SEM of three independent experiments. $^{*}p < 0.05$, $^{**}p < 0.01$, $^{***}p < 0.01$, $^{***}p < 0.01$ were considered as significant.

RAW264.7 cells. Meanwhile, we noticed that EFL2, at the 10 μM, showed a stronger inhibitory ability on IL-1β and IL-6 production compared to JSH-23 (**Figure 6H**), suggesting NF-kB signaling pathway activation partially contributes to EFL2's inhibitory effect on inflammatory cytokines release in macrophages.

DISCUSSION

Although etiopathology of RA is not fully understood, the central roles of TLRs in RA pathogenesis have been gradually uncovered in preclinical models. In this study, we identified a strong anti-arthritic effect of EFL2 in K/BxN serum transfer arthritis, where myeloid cells infiltration and inflammatory cytokines levels were significantly suppressed by EFL2. In addition, the molecular mechnism study explored that EFL2 exerted anti-IL-1β and IL-6 production role by suppressing TLR7-induced IRAK4-IKKβ-IRF5 and NF-κB signaling pathway activation.

In the current study, one interesting finding is the therapeutic difference of EFL2 on STA between gavage and intraperitoneal administration. Unlike i. p. administration, treatment of STA mice with equal dose of EFL2 by gavage hardly improved ankle redness or swelling in mice. There are many potential functional groups in the structure of EFL2, such as α, β-unsaturated ketone (at 14C position), terminal alkene (at 6C position) and four ester groups (two acetate groups at 5C and 15C position, two benzoate groups at 3C and 7C position). We speculate that the four ester groups are less stable than other functional groups in gastrointestinal environment because the pH in the gastrointestinal tract is beneficial for hydrolyzation of ester, and the different types of protease may accelerate this trend. This hydrolysis degradation of EFL2 is probably the crucial reason for the difference of pharmacological activity between the oral and intraperitoneal injection. Another reason which may lead to the low oral activity is that too many ester groups reduce the solubility of EFL2 and make it difficult to oral absorption.

Unlike TNF-α, IL-1β is absolutely required for disease development in K/BxN serum transfer arthritis (Ji et al., 2002). Although one study indicated that IL-6 did not play a major role in the inflammatory response in this model (Ji et al., 2002), it is still considered as a key inflammatory mediator in the pathogenesis of rheumatoid arthritis (Narazaki et al., 2017). In the measurement of a series of cytokines, we observed that EFL2 significantly reduced the levels of IL-1β and IL-6 in serum, but surpringly did not affect other cytokines. Given the pathologic manifestations in the K/BxN serum-transfer model are joint-specific (Ji et al., 2002), we also determined the effect of EFL2 on pro-inflammatory cytokines gene expression in the inflamed ankles. Similar to the trend in the circulation, IL-1β and IL-6 gene expression in STA mice was also significantly reduced by EFL2 treatment. One explanation is due to the EFL2-depended decrease in the levels of these two cytokines in the circulation. Another possibility is the reduction of infiltrated myeloid cells which are the important resources of IL-1β and IL-6 production in the ankles of STA mice.

Among TLRs, the implication of TLR2 and 4 in RA pathogenesis gained most attention in the earlier studies (Radstake et al., 2004; Huang et al., 2007; Davis et al., 2015). Recently, emerging newer data indicate the role of TLR7 in the pathogenicity of RA, particular in the aspect of rhematoid synovitis (Kim et al., 2016) and bone erosion (Kim et al., 2019). Potential TLR7 ligands, a GUUGUGU rich miR-Let7b, is found in human synovial fluid from RA patients (Kim et al., 2016). miR-Let7b can drive RA naive myeloid cell into M1 macrophages and promote inflammatory response in myeloid cells through TLR7 ligation (Kim et al., 2016). Besides the evidence in RA patients, TLR7 is also reported to implicate in the pathogenicity of both collagen-induced arthritis and STA model (Alzabin et al., 2012; Chen et al., 2012). Based on these reports and our PCR array data, we speculate EFL2 may inhibit the inflammaotry status in STA mice by interferring with TLR7 mediated-signaling pathway activation. Although TLR2 and TLR9 mRNA expressions were also significantly altered among the control, STA and EFL2 treatment groups (**Figure 3B**), the changes of TLR2 and TLR9 mRNA expressions can not explain the anti-inflammatory role of EFL2 in STA model because the inhibitory effects of TLR2 and TLR9 on STA (Abdollahi-Roodsaz et al., 2013). In fact, our *in vitro* experiments confirmed that EFL2 did have strong inhibitory effect on TLR7 activation-mediated inflammatory cytokines release in macrophages. Interestingly, in this study, we observed the dually inhibitory ability of EFL2 on TLR7-mediated NF-κB and IRAK4-IKKβ-IRF5 signaling pathway activation *in vitro*.

The transcription factor NF-κB plays a critical role in inflammation, cell proliferation, and apoptosis (Baeuerle and Baltimore, 1996; Vishva and Mak, 2002). Once the cell is stimulated by agents, the IκB is phosphorylated by IκB kinase (IKK) complex containning catalytic subunits IKKα and IKKβ(Mercurio et al., 1997; Ghosh and Karin, 2002). This phosphorylation targets IκB for degradation via the ubiquitin-proteasome pathway and allows nuclear translocation of classical NF-κB complexes, mostly p65 and p50 (Brown et al., 1995; Chen et al., 1995). Following TLR7/8 activation, a recent study uncovers that IRAK4 kinase acts with TAK1 to phosphorylate IKKβ, which subsequently induces IRF5 phosphorylation and translocation in human monocytes (Cushing et al., 2017). Importantly, IRAK4-IKKβ–IRF5 axis is independent of NF-κB (Cushing et al., 2017). IRF5 activation, involved in TLR7 downstream signaling pathways, can mediate the induction of pro-inflammatory cytokines down stream of TLRs, affect neutrophil influx to the inflammatioin sites (Weiss et al., 2015), and define the inflammatory macrophages phenotype and effective Th1 and Th17 cells generation (Krausgruber et al., 2011). A recent study also showed that TLR7 deficiency led to K/BxN serum-induced arthritis reduction by imparing interferon regulatory factor 5 (IRF5) mediated IL-1β and IL-6 generation in macrophages and synovial fibroblasts, respectively. Therefore, it is possible that EFL2 may exhibit anti-inflammation effect by suppressing these two signaling pathways. The findings that the phosphorylation of IKKα/β, an upstream activator, was significantly inhibited by EFL2 supported the above hypothesis. On the other hand, the production of IL-1β in RAW264.7 cells was only partially rescued after IRF5 plasmid transfection, suggesting that there are other pathways that may also contribute to this cytokine production. In fact, EFL2 did inhibit NF-κB signaling pathway activation (**Figure 6**). More importantly, we also showed that NF-κB signaling activation is important to TLR7-mediated IL-1β production. Taken together, our data suggest that EFL2 exerts anti-inflammatory effect by suppressing TLR7-induced IRAK4-IKKβ-IRF5 and NF-κB signaling pathways activation.

Targeting TLRs ligands or the relevant signaling pathways is a promising strategy for rheumatoid arthritis therapy. Here, we demonstrate that EFL2 exerts the robust anti-arthritic effect by inhibiting myeloid cells infiltration and IL-1β and IL-6 production whereby TLR7-mediated IRAK4-IKKβ signaling activation were significantly blocked. Moreover, we identified EFL2 as an effective IRF5 inhibitor to block the inflammatory responses during arthritis development. This novel information indicates the new opportunity for further investigation of EFL2 as a potential candidate in TLR7 or IRF5-dependent inflammatory diseases.

DATA AVAILABILITY STATEMENT

The original contributions presented in the study are included in the article/**Supplementary Material**, further inquiries can be directed to the corresponding author.

ETHICS STATEMENT

The animal study was reviewed and approved by Ethics Committee at West China Hospital, Sichuan University.

AUTHOR CONTRIBUTIONS

JT, QZ and YTZ performed the *in vitro* study, XC and YYZ carried out the pharmacokinetic studies. SY and ZT performed the *in vivo* pharmacological studies. JT, XC and SY collected and

analyzed the data. BP isolated and identified the chemical structure of EFL2. YL designed this study, wrote and revised the article.

FUNDING

This work was carried out under the sponsor of National Natural Science Foundation of China (Grant: 81403041, 81770101 and 81501412) and Outstanding interdisciplinary project of West china Hospital, Sichuan University (Grant Nr: ZYJC18024), Science and Technology Research and Development Plan of Sichuan province (2020YFS0266).

ACKNOWLEDGMENTS

We would like to thanks Qiaorong Huang for insisting the flow cytometry measurement and data analysis.

SUPPLEMENTARY MATERIAL

The Supplementary Material for this article can be found online at: https://www.frontiersin.org/articles/10.3389/fphar.2021.773592/full#supplementary-material.

Supplementary Figure S1 | Euphorbia factor L2 suppresses inflammatory cells expansion in the peripheral blood. Representative flow cytometry plots and quantification of the percentages of neutrophils (Ly6G+) **(A,B)**, macrophages (CD11b+F4/80+) **(C,D)**, and inflammatory monocytes (CD11b+Ly6C+Ly6G−) **(E,F)** in the blood from the control, STA, STA mice treated with DEX or EFL2 (15 or 40 mg/kg) and mice solely treated with EFL2 (40 mg/kg) (n = 3–7 for each group). Data represent the mean values ± SEM of three independent experiments. $^{**}p<0.05$, $^{**}p<0.01$ were considered statistically significant.

Supplementary Figure S2 | IRF5 expression in RAW 264.7 cells after transfected with IRF5 plasmid. **(A)** Western blot bands **(B)** Quantification of IRF5 expression in R837-stimulated RAW264.7 cells before and after IRF5 overexpression. Data represent the mean values ± SEM of three independent experiments. *p<0.05, **p<0.01, ***p<0.001 were considered as significant.

REFERENCES

Abdollahi-Roodsaz, S., Koenders, M. I., Walgreen, B., Bolscher, J., Helsen, M. M., van den Bersselaar, L. A., et al. (2013). Toll-like Receptor 2 Controls Acute Immune Complex-Driven Arthritis in Mice by Regulating the Inhibitory Fcγ Receptor IIB. *Arthritis Rheum.* 65 (10), 2583–2593. doi:10.1002/art.38087

Ahmad, S. F., Attia, S. M., Bakheet, S. A., Ashour, A. E., Zoheir, K. M., and Abd-Allah, A. R. (2014). Anti-inflammatory Effect of Euphorbia Hirta in an Adjuvant-Induced Arthritic Murine Model. *Immunol. Invest.* 43 (3), 197–211. doi:10.3109/08820139.2013.857350

Alzabin, S., Kong, P., Medghalchi, M., Palfreeman, A., Williams, R., and Sacre, S. (2012). Investigation of the Role of Endosomal Toll-like Receptors in Murine Collagen-Induced Arthritis Reveals a Potential Role for TLR7 in Disease Maintenance. *Arthritis Res. Ther.* 14 (3), R142. doi:10.1186/ar3875

Ansari, M. A., Nadeem, A., Bakheet, S. A., Attia, S. M., Shahid, M., Alyousef, F. S., et al. (2021). Chemokine Receptor 5 Antagonism Causes Reduction in Joint Inflammation in a Collagen-Induced Arthritis Mouse Model. *Molecules* 26 (7), 1839. doi:10.3390/molecules26071839

Baeuerle, P. A., and Baltimore, D. (1996). NF-kappa B: Ten Years after. *Cell* 87 (1), 13–20. doi:10.1016/s0092-8674(00)81318-5

Bakheet, S. A., Alrwashied, B. S., Ansari, M. A., Nadeem, A., Attia, S. M., Alanazi, M. M., et al. (2020). CXC Chemokine Receptor 3 Antagonist AMG487 Shows Potent Anti-arthritic Effects on Collagen-Induced Arthritis by Modifying B Cell Inflammatory Profile. *Immunol. Lett.* 225, 74–81. doi:10.1016/j.imlet.2020.06.014

Balasa, A., Gathungu, G., Kisfali, P., Smith, E. O., Cho, J. H., Melegh, B., et al. (2010). Assessment of DNA Methylation at the Interferon Regulatory Factor 5 (IRF5) Promoter Region in Inflammatory Bowel Diseases. *Int. J. Colorectal Dis.* 25 (5), 553–556. doi:10.1007/s00384-010-0874-0

Bondeson, J., Foxwell, B., Brennan, F., and Feldmann, M. (1999). Defining Therapeutic Targets by Using Adenovirus: Blocking NF-kappaB Inhibits Both Inflammatory and Destructive Mechanisms in Rheumatoid Synovium but Spares Anti-inflammatory Mediators. *Proc. Natl. Acad. Sci. U S A.* 96 (10), 5668–5673. doi:10.1073/pnas.96.10.5668

Brown, K., Gerstberger, S., Carlson, L., Franzoso, G., and Siebenlist, U. (1995). Control of I Kappa B-Alpha Proteolysis by Site-specific, Signal-Induced Phosphorylation. *Science* 267 (5203), 1485–1488. doi:10.1126/science.7878466

Calabrese, L. H., and Rose-John, S. (2014). IL-6 Biology: Implications for Clinical Targeting in Rheumatic Disease. *Nat. Rev. Rheumatol.* 10 (12), 720–727. doi:10.1038/nrrheum.2014.127

Chen, S. Y., Shiau, A. L., Li, Y. T., Lin, Y. S., Lee, C. H., Wu, C. L., et al. (2012). Suppression of Collagen-Induced Arthritis by Intra-articular Lentiviral Vector-Mediated Delivery of Toll-like Receptor 7 Short Hairpin RNA Gene. *Gene Ther.* 19 (7), 752–760. doi:10.1038/gt.2011.173

Chen, Z., Hagler, J., Palombella, V. J., Melandri, F., Scherer, D., Ballard, D., et al. (1995). Signal-induced Site-specific Phosphorylation Targets I Kappa B Alpha to the Ubiquitin-Proteasome Pathway. *Genes Dev.* 9 (13), 1586–1597. doi:10.1101/gad.9.13.1586

Choe, J. Y., Crain, B., Wu, S. R., and Corr, M. (2003). Interleukin 1 Receptor Dependence of Serum Transferred Arthritis Can Be Circumvented by Toll-like Receptor 4 Signaling. *J. Exp. Med.* 197 (4), 537–542. doi:10.1084/jem.20021850

Choy, E. (2012). Understanding the Dynamics: Pathways Involved in the Pathogenesis of Rheumatoid Arthritis. *Rheumatology (Oxford)* 51 (Suppl. 5), V3–V11. doi:10.1093/rheumatology/kes113

Christensen, A. D., Haase, C., Cook, A. D., and Hamilton, J. A. (2016). K/BxN Serum-Transfer Arthritis as a Model for Human Inflammatory Arthritis. *Front. Immunol.* 7, 213. doi:10.3389/fimmu.2016.00213

Cushing, L., Winkler, A., Jelinsky, S. A., Lee, K., Korver, W., Hawtin, R., et al. (2017). IRAK4 Kinase Activity Controls Toll-like Receptor-Induced Inflammation through the Transcription Factor IRF5 in Primary Human Monocytes. *J. Biol. Chem.* 292 (45), 18689–18698. doi:10.1074/jbc.M117.796912

Davis, M. L. R., LeVan, T. D., Yu, F., Sayles, H., Sokolove, J., Robinson, W., et al. (2015). Associations of Toll-like Receptor (TLR)-4 Single Nucleotide Polymorphisms and Rheumatoid Arthritis Disease Progression: an Observational Cohort Study. *Int. Immunopharmacol* 24 (2), 346–352. doi:10.1016/j.intimp.2014.12.030

Dawidowicz, K., Allanore, Y., Guedj, M., Pierlot, C., Bombardieri, S., Balsa, A., et al. (2011). The Interferon Regulatory Factor 5 Gene Confers Susceptibility to Rheumatoid Arthritis and Influences its Erosive Phenotype. *Ann. Rheum. Dis.* 70 (1), 117–121. doi:10.1136/ard.2010.129171

Demirci, F. Y., Manzi, S., Ramsey-Goldman, R., Minster, R. L., Kenney, M., Shaw, P. S., et al. (2007). Association of a Common Interferon Regulatory Factor 5 (IRF5) Variant with Increased Risk of Systemic Lupus Erythematosus (SLE). *Ann. Hum. Genet.* 71 (Pt 3), 308–311. doi:10.1111/j.1469-1809.2006.00336.x

Duffau, P., Menn-Josephy, H., Cuda, C. M., Dominguez, S., Aprahamian, T. R., Watkins, A. A., et al. (2015). Promotion of Inflammatory Arthritis by Interferon Regulatory Factor 5 in a Mouse Model. *Arthritis Rheumatol.* 67 (12), 3146–3157. doi:10.1002/art.39321

Eng, H. L., Hsu, Y. Y., and Lin, T. M. (2018). Differences in TLR7/8 Activation between Monocytes and Macrophages. *Biochem. Biophys. Res. Commun.* 497 (1), 319–325. doi:10.1016/j.bbrc.2018.02.079

Fan, L., Zhu, H., Tao, W., Liu, L., Shan, X., Zhao, M., et al. (2019). Euphorbia Factor L2 Inhibits TGF-β-Induced Cell Growth and Migration of Hepatocellular Carcinoma through AKT/STAT3. *Phytomedicine* 62, 152931. doi:10.1016/j.phymed.2019.152931

Fan, R. L., and Zhang, Q. W. (1991). Clinical Application of Zijin Troches (In Chinese). *Chin. Traditional Patent Med.* 11, 22–23.

Ghosh, S., and Karin, M. (2002). Missing Pieces in the NF-kappaB Puzzle. *Cell* 109 (Suppl. l), S81–S96. doi:10.1016/s0092-8674(02)00703-1

Guo, L., Hao, R., Tian, F., An, N., and Wang, K. (2018). Interferon Regulatory Factor 5 (IRF5) Regulates the Expression of Matrix Metalloproteinase-3 (MMP-3) in Human Chondrocytes. *Int. Immunopharmacol* 55, 231–236. doi:10.1016/j.intimp.2017.11.035

Huang, Q., Ma, Y., Adebayo, A., and Pope, R. M. (2007). Increased Macrophage Activation Mediated through Toll-like Receptors in Rheumatoid Arthritis. *Arthritis Rheum.* 56 (7), 2192–2201. doi:10.1002/art.22707

Hunter, C. A., and Jones, S. A. (2015). IL-6 as a keystone Cytokine in Health and Disease. *Nat. Immunol.* 16 (5), 448–457. doi:10.1038/ni.3153

Ji, H., Pettit, A., Ohmura, K., Ortiz-Lopez, A., Duchatelle, V., Degott, C., et al. (2002). Critical Roles for Interleukin 1 and Tumor Necrosis Factor Alpha in Antibody-Induced Arthritis. *J. Exp. Med.* 196 (1), 77–85. doi:10.1084/jem.20020439

Joosten, L. A., Helsen, M. M., Saxne, T., van de Loo, F. A., Heinegard, D., and van den Berg, W. B. (1999). IL-1 Alpha Beta Blockade Prevents Cartilage and Bone Destruction in Murine Type II Collagen-Induced Arthritis, whereas TNF-Alpha Blockade Only Ameliorates Joint Inflammation. *J. Immunol.* 163 (9), 5049–5055.

Kawai, T., and Akira, S. (2010). The Role of Pattern-Recognition Receptors in Innate Immunity: Update on Toll-like Receptors. *Nat. Immunol.* 11 (5), 373–384. doi:10.1038/ni.1863

Kim, H., and Chung, D. (2012). TLR4-mediated IL-12 Production Enhances IFN-γ and IL-1β Production, Which Inhibits TGF-β Production and Promotes Antibody-Induced Joint Inflammation. *Arthritis Res. Ther.* 14 (5), R210. doi:10.1186/ar4048

Kim, K. W., Kim, B. M., Won, J. Y., Lee, K. A., Kim, H. R., and Lee, S. H. (2019). Toll-like Receptor 7 Regulates Osteoclastogenesis in Rheumatoid Arthritis. *J. Biochem.* 166 (3), 259–270. doi:10.1093/jb/mvz033

Kim, S. J., Chen, Z., Essani, A. B., Elshabrawy, H. A., Volin, M. V., Volkov, S., et al. (2016). Identification of a Novel Toll-like Receptor 7 Endogenous Ligand in Rheumatoid Arthritis Synovial Fluid that Can Provoke Arthritic Joint Inflammation. *Arthritis Rheumatol.* 68 (5), 1099–1110. doi:10.1002/art.39544

Krausgruber, T., Blazek, K., Smallie, T., Alzabin, S., Lockstone, H., Sahgal, N., et al. (2011). IRF5 Promotes Inflammatory Macrophage Polarization and TH1-TH17 Responses. *Nat. Immunol.* 12 (3), 231–238. doi:10.1038/ni.1990

Krausgruber, T., Saliba, D., Ryzhakov, G., Lanfrancotti, A., Blazek, K., and Udalova, I. A. (2010). IRF5 Is Required for Late-phase TNF Secretion by Human Dendritic Cells. *Blood* 115 (22), 4421–4430. doi:10.1182/blood-2010-01-263020

Lee, A., Qiao, Y., Grigoriev, G., Chen, J., Park-Min, K. H., Park, S. H., et al. (2013). Tumor Necrosis Factor α Induces Sustained Signaling and a Prolonged and Unremitting Inflammatory Response in Rheumatoid Arthritis Synovial Fibroblasts. *Arthritis Rheum.* 65 (4), 928–938. doi:10.1002/art.37853

Li, T. Q., Guo, Q. H., and Tian, Z. F. (2003). The Study on the Medicinal Value of Peking euphorbia Family Planks(in Chinese). *Chin. Arch. Traditional Chin. Med.* 21 (8), 1349–1350. doi:10.3969/j.issn.1673-7717.2003.08.078

Lin, M., Tang, S., Zhang, C., Chen, H., Huang, W., Liu, Y., et al. (2017). Euphorbia Factor L2 Induces Apoptosis in A549 Cells through the Mitochondrial Pathway. *Acta Pharm. Sin B* 7 (1), 59–64. doi:10.1016/j.apsb.2016.06.008

Luo, Y., Boyle, D. L., Hammaker, D., Edgar, M., Franzoso, G., and Firestein, G. S. (2011). Suppression of Collagen-Induced Arthritis in Growth Arrest and DNA Damage-Inducible Protein 45β-Deficient Mice. *Arthritis Rheum.* 63 (10), 2949–2955. doi:10.1002/art.30497

Martin, P., Palmer, G., Rodriguez, E., Seemayer, C. A., Palomo, J., Talabot-Ayer, D., et al. (2017). Deficiency in IL-1 Receptor Type 2 Aggravates K/BxN Serum Transfer-Induced Arthritis in Mice but Has No Impact on Systemic Inflammatory Responses. *J. Immunol.* 198 (7), 2916–2926. doi:10.4049/jimmunol.1600855

Mei, J. R. (1989). Example of Application Experience of Ancestral Prescription "tong Guan Li Niao San" (In Chinese). *Jiangsu J. Traditional Chin. Med.* 05, 14–15.

Mercurio, F., Zhu, H., Murray, B. W., Shevchenko, A., Bennett, B. L., Li, J., et al. (1997). IKK-1 and IKK-2: Cytokine-Activated IkappaB Kinases Essential for NF-kappaB Activation. *Science* 278 (5339), 860–866. doi:10.1126/science.278.5339.860

Misharin, A. V., Cuda, C. M., Saber, R., Turner, J. D., Gierut, A. K., Haines, G. K., 3rd, et al. (2014). Nonclassical Ly6C(-) Monocytes Drive the Development of Inflammatory Arthritis in Mice. *Cell Rep* 9 (2), 591–604. doi:10.1016/j.celrep.2014.09.032

Narazaki, M., Tanaka, T., and Kishimoto, T. (2017). The Role and Therapeutic Targeting of IL-6 in Rheumatoid Arthritis. *Expert Rev. Clin. Immunol.* 13 (6), 535–551. doi:10.1080/1744666x.2017.1295850

Orr, C., Vieira-Sousa, E., Boyle, D. L., Buch, M. H., Buckley, C. D., Cañete, J. D., et al. (2018). Corrigendum: Synovial Tissue Research: a State-Of-The-Art Review. *Nat. Rev. Rheumatol.* 14 (1), 60. doi:10.1038/nrrheum.2017.206

Pascual, V., Allantaz, F., Arce, E., Punaro, M., and Banchereau, J. (2005). Role of Interleukin-1 (IL-1) in the Pathogenesis of Systemic Onset Juvenile Idiopathic Arthritis and Clinical Response to IL-1 Blockade. *J. Exp. Med.* 201 (9), 1479–1486. doi:10.1084/jem.20050473

Radstake, T. R., Roelofs, M. F., Jenniskens, Y. M., Oppers-Walgreen, B., van Riel, P. L., Barrera, P., et al. (2004). Expression of Toll-like Receptors 2 and 4 in Rheumatoid Synovial Tissue and Regulation by Proinflammatory Cytokines Interleukin-12 and Interleukin-18 via Interferon-Gamma. *Arthritis Rheum.* 50 (12), 3856–3865. doi:10.1002/art.20678

Santos Savio, A., Machado Diaz, A. C., Chico Capote, A., Miranda Navarro, J., Rodríguez Alvarez, Y., Bringas Pérez, R., et al. (2015). Differential Expression of Pro-inflammatory Cytokines IL-15Ralpha, IL-15, IL-6 and TNFalpha in Synovial Fluid from Rheumatoid Arthritis Patients. *BMC Musculoskelet. Disord.* 16, 51. doi:10.1186/s12891-015-0516-3

Schoenemeyer, A., Barnes, B. J., Mancl, M. E., Latz, E., Goutagny, N., Pitha, P. M., et al. (2005). The Interferon Regulatory Factor, IRF5, Is a central Mediator of Toll-like Receptor 7 Signaling. *J. Biol. Chem.* 280 (17), 17005–17012. doi:10.1074/jbc.M412584200

Solomon, S., Rajasekaran, N., Jeisy-Walder, E., Snapper, S. B., and Illges, H. (2005). A Crucial Role for Macrophages in the Pathology of K/B X N Serum-Induced Arthritis. *Eur. J. Immunol.* 35 (10), 3064–3073. doi:10.1002/eji.200526167

Srirangan, S., and Choy, E. H. (2010). The Role of Interleukin 6 in the Pathophysiology of Rheumatoid Arthritis. *Ther. Adv. Musculoskelet. Dis.* 2 (5), 247–256. doi:10.1177/1759720x10378372

Tak, P. P., Gerlag, D. M., Aupperle, K. R., van de Geest, D. A., Overbeek, M., Bennett, B. L., et al. (2001). Inhibitor of Nuclear Factor kappaB Kinase Beta Is a Key Regulator of Synovial Inflammation. *Arthritis Rheum.* 44 (8), 1897–1907. doi:10.1002/1529-0131(200108)44:8<1897:AID-ART328>3.0.CO;2-4

Vishva, D., and Mak, T. W. (2002). NF-κB Signaling: Many Roads Lead to Madrid. *Cell* 111, 615. doi:10.1016/s0092-8674(02)01166-2

Weinblatt, M. E. (1992). Biological Agents in Rheumatoid Arthritis. *J. Rheumatol. Suppl.* 32, 85–91.

Weiss, M., Blazek, K., Byrne, A. J., Perocheau, D. P., and Udalova, I. A. (2013). IRF5 Is a Specific Marker of Inflammatory Macrophages *In Vivo*. *Mediators Inflamm.* 2013, 245804. doi:10.1155/2013/245804

Weiss, M., Byrne, A. J., Blazek, K., Saliba, D. G., Pease, J. E., Perocheau, D., et al. (2015). IRF5 Controls Both Acute and Chronic Inflammation. *Proc. Natl. Acad. Sci. U S A.* 112 (35), 11001–11006. doi:10.1073/pnas.1506254112

Wu, H. J., Sawaya, H., Binstadt, B., Brickelmaier, M., Blasius, A., Gorelik, L., et al. (2007). Inflammatory Arthritis Can Be Reined in by CpG-Induced DC-NK Cell Cross Talk. *J. Exp. Med.* 204 (8), 1911–1922. doi:10.1084/jem.20070285

Yamanaka, H. (2015). TNF as a Target of Inflammation in Rheumatoid Arthritis. *Endocr. Metab. Immune Disord. Drug Targets* 15 (2), 129–134. doi:10.2174/1871530315666150316121808

Yamanishi, Y., Boyle, D. L., Pinkoski, M. J., Mahboubi, A., Lin, T., Han, Z., et al. (2002). Regulation of Joint Destruction and Inflammation by P53 in Collagen-Induced Arthritis. *Am. J. Pathol.* 160 (1), 123–130. doi:10.1016/s0002-9440(10)64356-8

You, S., Yoo, S. A., Choi, S., Kim, J. Y., Park, S. J., Ji, J. D., et al. (2014). Identification of Key Regulators for the Migration and Invasion of Rheumatoid Synoviocytes through a Systems Approach. *Proc. Natl. Acad. Sci. U S A.* 111 (1), 550–555. doi:10.1073/pnas.1311239111

Zhang, Q., Zhu, S., Cheng, X., Lu, C., Tao, W., Zhang, Y., et al. (2018). Euphorbia Factor L2 Alleviates Lipopolysaccharide-Induced Acute Lung Injury and Inflammation in Mice through the Suppression of NF-Kb Activation. *Biochem. Pharmacol.* 155, 444–454. doi:10.1016/j.bcp.2018.07.025

Conflict of Interest: The authors declare that the research was conducted in the absence of any commercial or financial relationships that could be construed as a potential conflict of interest.

Publisher's Note: All claims expressed in this article are solely those of the authors and do not necessarily represent those of their affiliated organizations, or those of the publisher, the editors and the reviewers. Any product that may be evaluated in this article, or claim that may be made by its manufacturer, is not guaranteed or endorsed by the publisher.

Copyright © 2021 Tang, Cheng, Yi, Zhang, Tang, Zhong, Zhang, Pan and Luo. This is an open-access article distributed under the terms of the Creative Commons Attribution License (CC BY). The use, distribution or reproduction in other forums is permitted, provided the original author(s) and the copyright owner(s) are credited and that the original publication in this journal is cited, in accordance with accepted academic practice. No use, distribution or reproduction is permitted which does not comply with these terms.

frontiers in Pharmacology

ORIGINAL RESEARCH
published: 14 December 2021
doi: 10.3389/fphar.2021.746786

Yi Shen Juan Bi Pill Regulates the Bone Immune Microenvironment *via* the JAK2/STAT3 Signaling Pathway *in Vitro*

Ya Xia[1†], Danping Fan[2,3,4†], Xiaoya Li[5†], Xiangchen Lu[1,4,6†], Qinbin Ye[4], Xiaoyu Xi[4], Qiong Wang[4], Hongyan Zhao[7] and Cheng Xiao[2,3,4]**

[1]School of Traditional Chinese Medicine, Beijing University of Chinese Medicine, Beijing, China, [2]Department of Emergency, China-Japan Friendship Hospital, Beijing, China, [3]Graduate School of Peking Union Medical College, Chinese Academy of Medical Sciences/Peking Union Medical College, Beijing, China, [4]Institute of Clinical Medicine, China-Japan Friendship Hospital, Beijing, China, [5]The Institute of Medicinal Plant Development, Chinese Academy of Medical Sciences/Peking Union Medical College, Beijing, China, [6]Pinggu Hospital, Beijing Traditional Chinese Medicine Hospital, Beijing, China, [7]Beijing Key Laboratory of Research of Chinese Medicine on Prevention and Treatment for Major Diseases, Experimental Research Center, China Academy of Chinese Medical Sciences, Beijing, China

OPEN ACCESS

Edited by:
Dahui Liu,
Hubei University of Chinese Medicine, China

Reviewed by:
Junqing Liang,
Hebei Provincial Center for Clinical Laboratory, China
Quan Xingping,
University of Macau, China

***Correspondence:**
Hongyan Zhao
zhaohongyan1997@163.com
Cheng Xiao
xc2002812@126.com

[†]These authors have contributed equally to this work

Specialty section:
This article was submitted to Inflammation Pharmacology, a section of the journal Frontiers in Pharmacology

Received: 24 July 2021
Accepted: 15 November 2021
Published: 14 December 2021

Citation:
Xia Y, Fan D, Li X, Lu X, Ye Q, Xi X, Wang Q, Zhao H and Xiao C (2021) Yi Shen Juan Bi Pill Regulates the Bone Immune Microenvironment via the JAK2/STAT3 Signaling Pathway in Vitro. Front. Pharmacol. 12:746786. doi: 10.3389/fphar.2021.746786

Rheumatoid arthritis (RA) is characterized by an impaired articular bone immune microenvironment, which is associated with regulatory T cells (Tregs) hypofunction and osteoclasts (OCs) hyperfunction and leads to articular bone erosion and systemic bone loss. Studies have shown that Tregs slow bone loss in RA by regulating the bone resorption function of OCs and the JAK/STAT signaling pathway can regulate the immunosuppressive function of Tregs and reduce the bone erosion function of OCs. Yi Shen Juan Bi Pill (YSJB) is a classic Chinese herbal compound for the treatment of RA. However, whether YSJB regulates bone immune microenvironment homeostasis through JAK/STAT signaling pathway remains unclear. Based on *in vitro* OC single culture, Treg single culture and OC-Treg coculture systems, treatments were performed using drug-containing serum, AG490 and JAK2 siRNA to explore whether YSJB-containing serum regulates the homeostasis of the bone immune microenvironment through the JAK/STAT signaling pathway. *In vitro*, YSJB treatment decreased the number of $TRAP^+$ cells and the areas of bone resorption and inhibited the expression of RANK, NFATc1, c-fos, JAK2, and STAT3 in both the OC single culture system and the OC-Treg coculture system. Tregs further reduced the number of $TRAP^+$ cells and the areas of bone resorption in the coculture system. YSJB promoted the secretion of IL-10 while inhibiting the expression of JAK2 and STAT3 in Tregs. Moreover, inhibiting the expression of JAK2 with the JAK2 inhibitor AG490 and JAK2 siRNA improved the immunosuppressive functions of Treg, inhibited OC differentiation and bone resorption. Our study demonstrates that YSJB can regulate OC-mediated bone resorption and Treg-mediated bone immunity through the JAK2/STAT3 signaling pathway. This study provides a new strategy for regulating the bone immune microenvironment in RA with traditional Chinese medicine.

Keywords: rheumatoid arthritis, Yi Shen Juan Bi Pill, osteoclast, regulatory T cell, JAK2/STAT3 signaling pathway

INTRODUCTION

Rheumatoid arthritis (RA) is a chronic autoimmune inflammatory disease that is characterized by irreversible cartilage injury and secondary bone erosion. Most RA patients develop into disability following bone destruction and bone loss (Smolen et al., 2016; Rotta et al., 2020). Bone damage and bone loss are closely associated with abnormal bone resorption mediated by osteoclasts (OCs) (Zhao et al., 2017). In addition, overactivation of the immune system disrupts bone homeostasis. As negative immunoregulatory cells, regulatory T cells (Tregs) are particularly important for regulating bone balance in RA. Our previous study also showed that Tregs inhibited the differentiation and bone resorption of OCs by secreting interleukin (IL)-10 and transforming growth factor (TGF)-β, which regulated bone immune microenvironment homeostasis (Xu et al., 2016).

The Janus kinase/signal transduction and activator of transcription (JAK/STAT) signaling pathway, which acts as a downstream element of more than 50 cytokines, not only regulates embryonic formation and the immune response but also affects biological processes such as cell proliferation, differentiation, and apoptosis, including those of OCs and Tregs (Villarino et al., 2017). As a specific JAK2 kinase inhibitor, AG490 blocks RANKL-mediated OC differentiation by inhibiting the expression of NFATc1 *via* the STAT3 pathway (Li et al., 2013). Moreover, AG490 inhibits OC differentiation by downregulating the number of $CD4^+IL^-17A^+$ T helper 17 (Th17) cells and upregulating the number of $CD4^+CD25^+$forkhead box P3 $(Foxp3)^+$ Tregs (Park et al., 2014), as well as several molecules that favor Treg functions, such as Foxp3 and programmed cell death protein 1 (ICOS) (Park et al., 2014; Chen et al., 2018; Li and Xiong, 2020).

In traditional Chinese medicine, kidney deficiency syndrome is the most common syndrome of RA. Yi Shen Juan Bi Pill (YSJB), a classic herbal compound in traditional Chinese medicine, has been widely used to treat RA with kidney deficiency patterns in clinical settings in China. We have previously shown that YSJB significantly alleviated bone damage in collagen-induced arthritis (CIA) rats with kidney deficiency and inhibited local joint inflammation and OC differentiation in CIA rats (Zhao et al., 2012). Interestingly, YSJB also regulates the balance of T cell phenotypes (Zhao et al., 2018). In addition, YSJB regulates the levels of IL-6, IL-17A, IL-10, TGF-β1, Th17, Tregs and OCs in CIA rats. These factors and cells are important regulatory factors and effector cells in the JAK2/STAT3 pathway and mediate bone resorption. However, it has not been reported whether the mechanism by which YSJB can treat RA is associated with the JAK2/STAT3 signaling pathway. The present study used CIA rats with castration and obtained YSJB-containing serum. By blocking the JAK2/STAT3 signaling pathway, the mechanism by which YSJB regulates the JAK2/STAT3 signaling pathway to alleviate bone resorption was further explored based on an OC-Treg coculture system. This study provides a new experimental basis for the treatment of RA with YSJB.

METHODS

Animals

Female Sprague-Dawley (SD) rats (180–200 g) and male C57BL/6 mice (6 weeks old) were purchased from the National Institutes for Food and Drug Control [animal license number: SCXK (Beijing) 2014-0013]. All animals were housed in the Experimental Animal Center of the Institute of Clinical Medical Sciences, China-Japan Friendship Hospital (Experimental Animal Center license number: SCXK (Beijing) 2016-0043). All experiments received ethic approval by the Institute of Clinical Medical Sciences, China-Japan Friendship Hospital, Beijing, China and were conducted within ethical limits. The animals were maintained in a specific pathogen-free environment with a temperature of 23°C (±2°C) and were subjected to a 12 h light/dark cycle.

Preparation of Drug-Containing Sera

The 40 female rats were randomly divided into two groups according to weight. Then, 32 of the rats were anesthetized, and their ovaries were removed according to standard surgical procedures. The other 8 rats were treated as the control group, in which fat tissue near the ovaries on both sides were removed. Twenty-eight days after castration, the 32 castrated rats were immunized intradermally at the tail root with 100 μl of a fully emulsified mixture of bovine type II collagen (Chondrex, Redmond, United States) and isopycnic incomplete Freund's adjuvant (IFA; Chondrex) and received booster injections in the same way on day 7 after the initial immunization. Meanwhile, control group rats underwent the same method of injection with an equal volume of saline water.

On the 14th day after immunization, rats that successfully developed arthritis were divided into three groups as follows: 1) castrated CIA, 2) castrated CIA plus methotrexate (MTX; Shanghai Sine Pharmaceutical, Shanghai, China) treatment, and 3) castrated CIA plus YSJB (Jiangsu Zhengda Qingjiang Pharmaceutical, Jiangsu, China) treatment. The rats in the MTX group and YSJB group were treated with MTX (1.02 mg/kg body weight) and YSJB (3.87 g/kg body weight), respectively, by gavage twice a day. Meanwhile, rats in the control group and CIA group received an equal volume of distilled water (10 ml/kg). Rats in each group were given the treatments for 3 days. One hour after the last dose, all rats were anesthetized. Blood samples were collected from the abdominal aorta and centrifuged to obtain serum (quality control data are shown in **Supplementary Material S1** and **Supplementary Material S2**).

OC Isolation and Culture

OC progenitor cells (OPCs) were isolated and cultured as previously reported (Xu et al., 2016). The mice were sacrificed by cervical dislocation. Femurs and tibias were isolated, and the ends were trimmed. The bone marrow cavity was rinsed with alpha-modified Eagle's medium (α-MEM; HyClone, Logan, United States), and bone marrow cells (BMCs) were collected by centrifuging the medium containing bone marrow. Subsequently, cells were cultured in α-MEM supplemented

with 10% fetal bovine serum (FBS; PAN Biotech GmbH, Aidenbach, Germany), 1% penicillin-streptomycin (PS; Gibco BRL, Grand Island, NY, United States) and recombinant murine M-CSF (20 ng/ml; PeproTech, Rocky Hill, United States) after red blood cell (RBC) lysis buffer (Solarbio, Beijing, China) was used to deplete RBCs. Twenty-four hours later, nonadherent cells were collected and cultured in tissue culture plates at an appropriate density in α-MEM containing 10% FBS and M-CSF (20 ng/ml). Three days later, adherent cells were considered OPCs. To induce OPCs to differentiate into OCs, the cells were cultured for an additional 5 days in fresh differentiation α-MEM containing 10% FBS, 1% PS, M-CSF (20 ng/ml), and RANKL (50 ng/ml; PeproTech). Complete fresh differentiation medium was used every couple of days, and the concentration of each factor remained constant.

$CD4^+CD25^+$ Treg Purification and Culture

Suspensions of splenic cells were obtained by passing spleen tissue isolated from C57BL/6 mice through a 200-mesh metal mesh grid in RPMI-1640 (Gibco) medium, followed by filtration with a 70 mm cell strainer (BD Biosciences, San Jose, United States). Spleen cells were sorted using an EasySep™ Mouse CD4 Positive T Cell Pre-Enrichment Kit (STEMCELL Technologies, Vancouver, Canada) to obtain $CD4^+$ T cells, and then negative selection was used to obtain $CD4^+CD25^-$ Tregs using an EasySep® Mouse CD25 Positive Selection Kit (STEMCELL). $CD4^+CD25^-$ Tregs were resuspended in differentiation RPMI-1640 medium containing 10% FBS, 1% PS, recombinant murine IL-2 (1,000 U/mL; PeproTech), TGF-β1 (10 ng/ml; PeproTech) and anti-CD28 (2 μg/ml; BD Biosciences) and cultured in a round-bottom 96-well plate with anti-murine CD3 (10 μg/ml; BD Biosciences) at a density of 5×10^5 cells/well (200 μl per well). Half of the differentiation medium was refreshed every couple of days and the concentration of each factor remained constant. $CD4^+CD25^+$ Tregs were successfully positively selected with an EasySep® Mouse CD25 Positive Selection Kit after 7 days and were used for subsequent experiments. We explored the method during the early stage. Flow cytometry was used to identify the phenotype of Tregs (Xu et al., 2016).

Coculture of OCs With $CD4^+CD25^+$ Tregs

Nonadherent BMCs were seeded in 24-well culture plates at a density of 5×10^5 cells/well. Three days later, Tregs (2×10^4) were added to each well. Cells were then maintained in differentiation α-MEM with a 1:25 ratio of Tregs: OPCs. Every 2 days, half of the medium was replaced with fresh differentiation α-MEM. The bottom was not touched when changing medium.

Groups and the Addition of Drug-Containing Serum

Each culture system was divided into four groups: DMSO, AG490, MOCK and siRNA. DMSO was used as a control for AG490, and MOCK was used as a control for siRNA. Each group was further divided into four subgroups as follows: 1) control, 2) CIA, 3) CIA+MTX, and 4) CIA+YSJB. OPCs and Tregs were cultured in the absence or presence of AG490 (MedChemExpress, New Jersey, United States) and siRNA (SyngenTech, Beijing, China). Twenty-four hours later, 10% drug-containing serum that had been previously obtained from rats was added to the differentiation medium.

The Cytotoxicity of AG490 Against OCs

The effect of AG490 on cell viability was measured using a CCK-8 assay. OPCs were cultured in 96-well plates at a density of 4×10^4 cells/well in differentiation α-MEM (20 ng/mL M-CSF, 50 ng/ml RANKL, 10% FBS, 1% PS) with AG490 (0, 2.5, 5, 10, 20, 50 μM). The concentration of each factor was kept constant when adding fresh medium. Five days later, fresh α-MEM containing 10% CCK-8 was used to replace the differentiation α-MEM. The absorbance was measured at a wavelength of 450 nm.

siRNA Interference

siRNA was purchased from SyngenTech. All sequences are shown in **Supplementary Material S3**. Cells were transfected with siRNA using a Lipofectamine® 3,000 transfection kit (Thermo Fisher Scientific, Waltham, United States) according to the manufacturer's protocol. qRT-PCR was used to confirm the transfection efficiency.

Tartrate-Resistant Acid Phosphatase Staining

Nonadherent BMCs were seeded in 96-well culture plates at a density of 1×10^5 cells/well (200 μl per well). After the OPCs were cultured for 5 days, TRAP staining was performed according to the instructions of the TRAP staining kit (Sigma-Aldrich, Louis, United States) to assess osteoclastogenesis. OC formation was scored by the number of $TRAP^+$ cells that contained 3 or more nuclei. OCs in the whole well were counted.

Bone Resorption Pit Formation Assay

Bone slices (Immunodiagnostic Systems Limited, Boldon, United Kingdom) were placed in 96-well culture plates containing nonadherent BMCs at a density of 4×10^5 cells/well (200 μL per well), incubated for 3 days and cultured with OPCs for 10 days. Then, the bone slices were fixed in 2.5% glutaraldehyde for 5 min and washed in 0.25 mol/L ammonium hydroxide for 10 min to remove the cells from the bone slices. The bone slices were sequentially dehydrated with 40, 75, 95, and 100% ethanol. After drying naturally, the bone slices were dyed with 1% toluidine blue (Sigma-Aldrich) at room temperature for 5 min. Using a Leica Qwin image analysis system (Leica Microsystem, Germany), the areas of the bone resorption pits were analyzed.

Enzyme-Linked Immunosorbent Assay

Culture supernatant was collected on day 5. According to the instructions of the ELISA kit (Diaclone, France), the levels of IL-10 and TGF-β1 were measured.

Quantitative Real-Time PCR

Total RNA was isolated using TRIzol reagent (Invitrogen, Carlsbad, CA, United States). A PrimeScript RT reagent kit

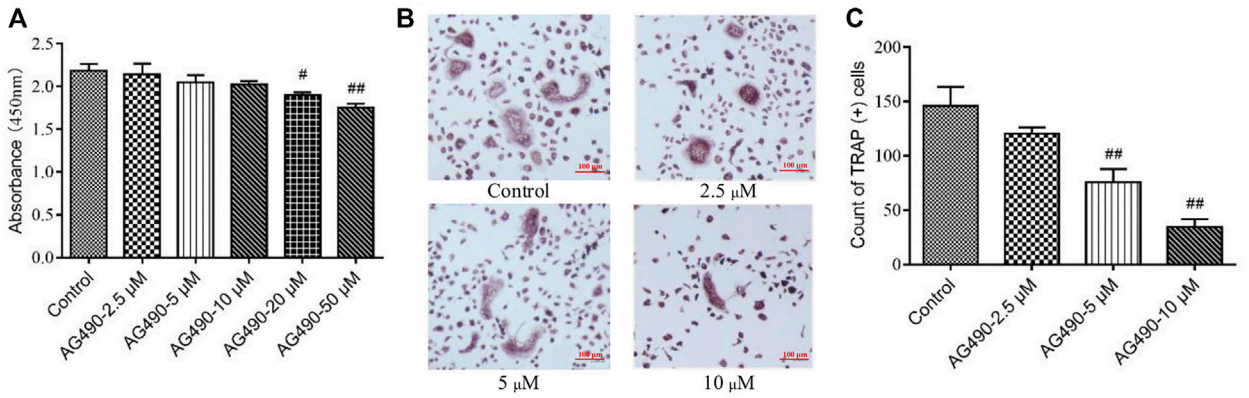


FIGURE 1 | Effect of AG490 on cells viability and osteoclastogenesis in the OC single culture system. **(A)** Cells (OPCs and OCs) viability was assessed by CCK-8 assays after treatment with AG490 (0, 2.5, 5, 10, 20, or 50 μM). **(B,C)** TRAP staining in OCs after treatment with AG490 (0, 2.5, 5 or 10 μM). Scale bars = 100 μm. The data are shown as the mean ± SEM (n ≥ 2). $^{\#}p < 0.05$, $^{\#\#}p < 0.01$ compared with the control group.

(TaKaRa, Tokyo, Japan) was used to reverse transcribe RNA into cDNA. The levels of mRNA were analyzed using SYBR Premix Ex Taq (TliRNaseH Plus; TaKaRa) in a Quant Studio 5 real-time PCR instrument (Thermo Fisher Scientific). The thermocycling conditions were as follows: incubation at 95°C for 30 s, followed by 40 cycles of 95°C for 5 s, 60°C for 34 s, then dissociation stage. The results were normalized to β-actin and calculated using the $2^{-\Delta\Delta Ct}$ method. Primer sequences are shown in **Supplementary Material S4**.

Western Blot

Proteins of OCs and Tregs were harvested using RIPA Lysis Buffer (Beyotime Biotechnology, Shanghai, China) that was supplied with protease and phosphatase inhibitor cocktails (Beijing ComWin Biotech Co., Ltd. Beijing, China). The protein concentration was measured using bicinchoninic acid (BCA; Solarbio) protein assay. Then, the proteins were mixed with loading buffer and denatured in metal bath (100°C, 5 min). Following, the target proteins were divided *via* sodium dodecyl sulfate–polyacrylamide gel electrophoresis with constant voltage of 100 V and transferred onto a polyvinylidene fluoride membrane (Millipore, Billerica, United States) with constant current of 300 mA in 1 h. In order to eliminate nonspecific protein binding, membranes were blocked at room temperature for 2 h with 5% skim milk (BD Biosciences) in 1 × TBST (Beyotime). And then, membranes were incubated overnight at 4°C with primary antibodies followed: phosphorylated (p-) JAK2 (1:1,000), p-STAT3 (1:2000), JAK2 (1:1,000), STAT3 (1:1,000) (Cell Signaling Technology, MA, United States). Appropriate secondary antibodies were incubated for 2 h and protein bands were detected using eECL western blot kit (Beijing ComWin Biotech Co., Ltd.). Band densities were quantified using Image Lab 3.0 software (Bio-Rad Laboratories, CA, United States).

Statistical Analysis

Statistical analysis was carried out using SPSS 20.0 software. One-way analysis of variance (ANOVA) and Dunnett's T3 test were used to determine significant differences. Nonparametric tests were used if the data were abnormally distributed. All data are expressed as the mean ± SEM. The significance level was set at $p < 0.05$.

RESULTS

Cytotoxicity of AG490 on OPCs

As we all know, OPCs can differentiate into OCs under the stimulation of M-CSF and RANKL (Xu et al., 2016). That's how we get OCs in this study. Since a paucity of evidence has been found on the toxicity of AG490 in OPCs, we first determined the dose with CCK-8 assays and TRAP staining. OPCs might have differentiated into OCs during CCK-8 assay, so the experiment reflected the effect of AG490 on the viability of overall cells, including OPCs and OCs. The results showed that the absorbance decreased with increasing AG490 concentrations. AG490 had almost no effect on the viability of cells at doses ranging from 2.5 to 10 μM (**Figure 1A**), which indicated that AG490 was not cytotoxic to cells (OPCs and OCs) at concentrations below 10 μM. Moreover, when the concentration of AG490 was greater than 5 μM, the number of $TRAP^{+}$ cells decreased significantly (**Figures 1B,C**). The TRAP staining revealed a situation how many OPCs differentiated into OCs. It suggested that AG490 could inhibit the differentiation of OPCs into OCs at concentrations greater than 5 μM. Based on these results, 10 μM AG490 was used for subsequent experiments.

YSJB Blocked the JAK2/STAT3 Signaling Pathway in Tregs and OCs

To determine the regulatory effect of YSJB on OCs differentiation whether *via* the JAK2/STAT3 pathway, we performed loss-of-function studies in OPCs. OPCs were treated with JAK2 siRNA (#1, #2, and #3) to decrease JAK2 expression. JAK2 mRNA levels were significantly reduced after gene knockdown (**Figure 2A**).

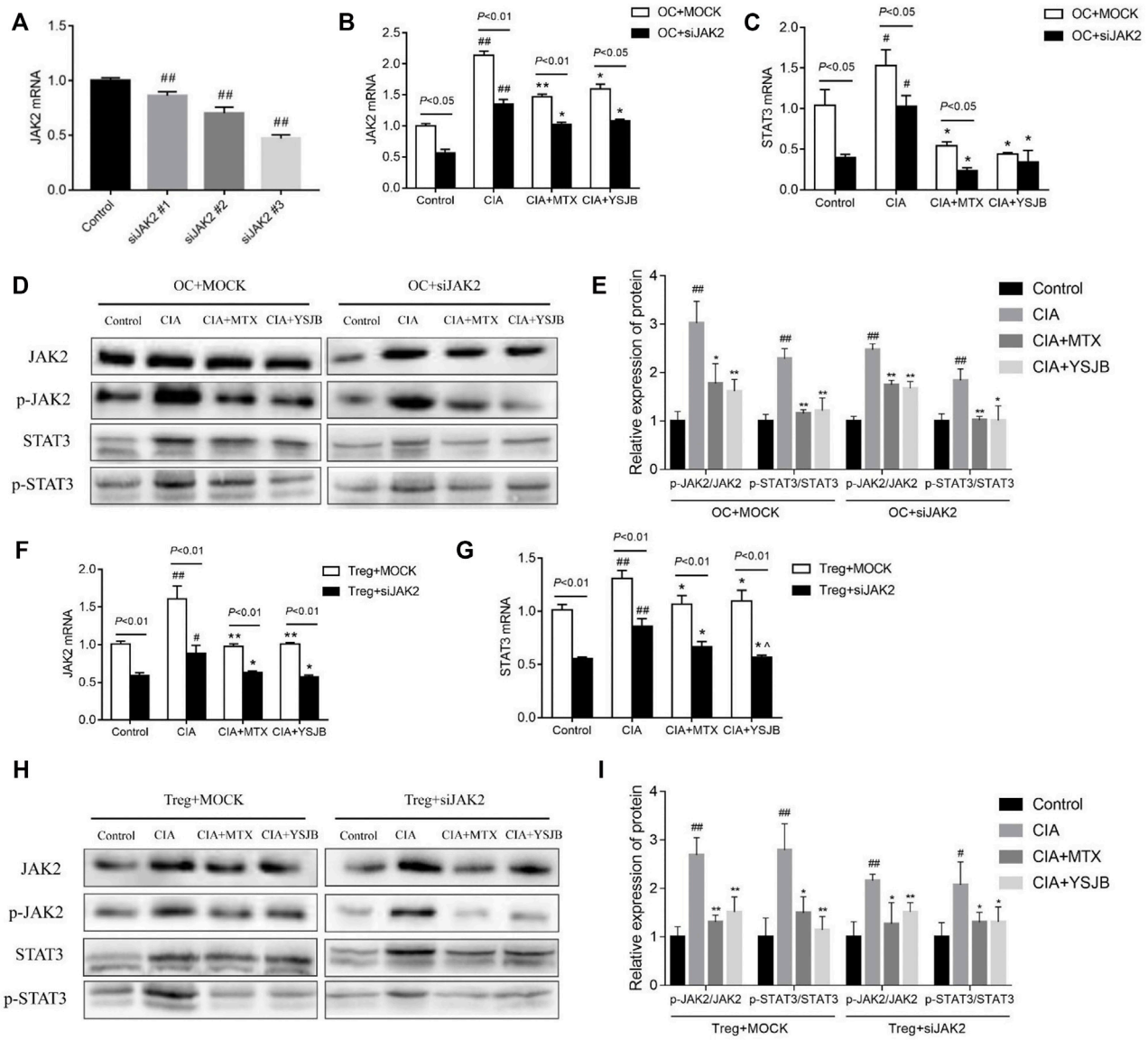


FIGURE 2 | Effect of YSJB and JAK2 siRNA on the JAK2/STAT3 signaling pathway. **(A)** Confirmation of JAK2 knockdown in OCs. **(B)** The relative mRNA levels of JAK2 in OCs. **(C)** The relative mRNA levels of STAT3 in OCs. **(D)** Representative bands of JAK2, p-JAK2, STAT3, and p-STAT3 protein detected by western blot assay in OCs. **(E)** Protein expression levels of p-JAK2/JAK2 and p-STAT3/STAT3 in OCs. **(F)** The relative mRNA levels of JAK2 in Tregs. **(G)** The relative mRNA levels of STAT3 in Tregs. **(H)** Representative bands of JAK2, p-JAK2, STAT3, and p-STAT3 protein detected by western blot assay in Tregs. **(I)** Protein expression levels of p-JAK2/JAK2 and p-STAT3/STAT3 in Tregs. Cells were treated with drug-containing serum and JAK2 siRNA. $^{\#}p < 0.05$, $^{\#\#}p < 0.01$ compared with the control group; $^{*}p < 0.05$, $^{**}p < 0.01$ compared with the CIA group.

JAK2 siRNA #3 showed the highest knockdown efficiency and was used in subsequent experiments.

The mRNA levels of JAK2 and STAT3 as well as the protein levels of p-JAK2/JAK2 and p-STAT3/STAT3 were measured in single culture systems of OC and Treg respectively (**Figures 2B–I**), following intervention with YSJB and other reagents. The results showed that the mRNA levels of JAK2 and STAT3 in the CIA group were significantly increased compared with control group in OCs and Tregs. These results suggested that CIA-containing serum promoted the activation of JAK2/STAT3 signaling pathway in OCs and Tregs. However, after treatment with MTX or YSJB, their expression levels were reduced compared with those in the CIA group (**Figures 2B,C** and **Figures 2F,G**). Western blot assay showed similar trends in protein expressions of JAK2, STAT3 in OCs and Tregs after treatment with JAK2 siRNA and YSJB (**Figures 2D,H**). As we all know that, JAK2/STAT3 signaling pathway plays the role mainly by phosphorylation, so the levels of p-JAK2/JAK2 and p-STAT3/STAT3 were used to illustrate the degree of JAK2/STAT3 signal pathway activation. The levels of p-JAK2/JAK2, p-STAT3/STAT3

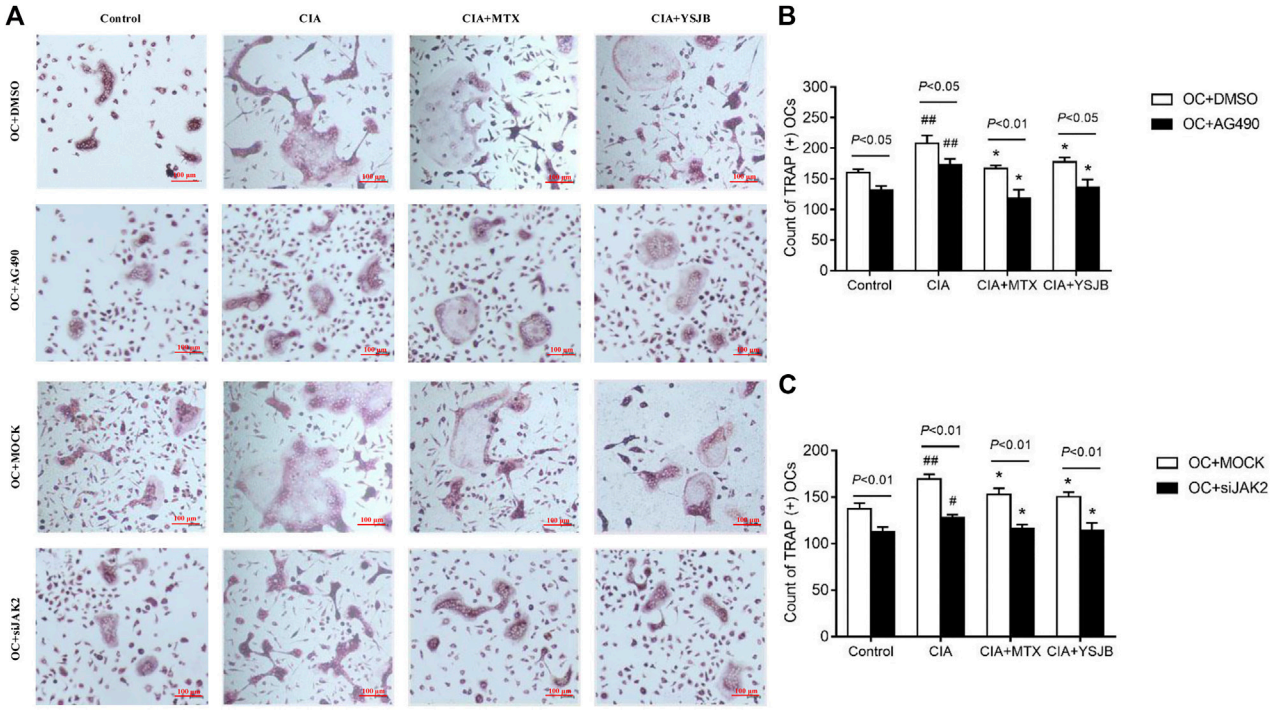


FIGURE 3 | Effect of YSJB, AG490 and JAK2 siRNA on osteoclastogenesis in the OC single culture system. **(A)** Images of TRAP staining in OPCs treated with drug-containing serum (Control, CIA, CIA + MTX, CIA + YSJB), AG490 and JAK2 siRNA. Scale bar = 100 μm. **(B,C)** The number of TRAP$^+$ cells. The data are shown as the mean ± SEM (n ≥ 2). $^{\#}p < 0.05$, $^{\#\#}p < 0.01$ compared with the control group; $^{*}p < 0.05$; $^{**}p < 0.01$ compared with the CIA group.

were significantly higher in the CIA group compared with the control group. In contrast, the relative expression levels of p-JAK2/JAK2, p-STAT3/STAT3 were significantly lower in the MTX and YSJB groups compared with the CIA group. JAK2 siRNA treatments resulted in significantly lower protein levels of p-JAK2, JAK2, p-STAT3, and STAT3 compared with the Mock groups. Furthermore, after treated with the JAK2 siRNA, the relative expression levels of P-JAK2/JAK2 and P-STAT3/STAT3 in CIA group did not increase as much as treated with the Mock, and additional YSJB treatment didn't exert strong inhibitory effect on p-JAK2/JAK2, p-STAT3/STAT3 as before (**Figures 2E–I**). These results illustrated that YSJB could block the JAK2/STAT3 signaling pathway in both Tregs and OCs, indicating the role of JAK2/STAT3 pathway in the protection of YSJB regulate bone immune microenvironment.

YSJB Inhibited Osteoclastogenesis, Perhaps Through JAK2/STAT3 Signaling Pathway

In order to explore the effect of JAK2/STAT3 signaling pathway on OC differentiation, AG490 or JAK2 siRNA was used in the process of inducing OPCs differentiation into OC. Osteoclastogenesis was evaluated by TRAP staining (**Figure 3A** and **Figure 4A**). Interestingly, the number of TRAP$^+$ cells was significantly downregulated after treatment with AG490 or JAK2 siRNA in both the OC single culture system and the coculture system. These results suggested that blocking or knocking down JAK2 could inhibit osteoclastogenesis. As shown in **Figures 3B,C** and **Figures 4B,C**, the number of TRAP$^+$ cells in the CIA group was significantly increased compared with that in the control group in the absence or presence of AG490 and JAK2 siRNA. Compared with that in the CIA group, the number of TRAP$^+$ cells in the MTX group and YSJB group decreased. These results suggested that CIA-containing serum promoted osteoclastogenesis, while YSJB and MTX could inhibit the osteoclastogenesis. The combination of YSJB and AG490/JAK2 siRNA did not enhance the inhibitory effect of YSJB on OC differentiation. It might suggest that YSJB could inhibit the differentiation of OCs through CIA-induced JAK pathway. In addition, we found that the number of TRAP$^+$ cells was lower in the coculture systems than in the single OC culture system (**Figures 4D–G**). The results showed that Tregs increased suppression of YSJB in OC formation. This might be related to the fact that YSJB inhibited JAK2/STAT3 signaling pathway in OCs and Tregs.

YSJB Inhibited OC-Mediated Bone Resorption, Perhaps Through JAK2/STAT3 Signaling Pathway

After OPCs were cultured for 10 days, the bone slices were stained with toluidine blue. The absorbed surfaces of the bone slices were measured in each group to elucidate the effect of YSJB on bone resorption (**Figure 5A** and **Figure 6A**). Consistent with the TRAP

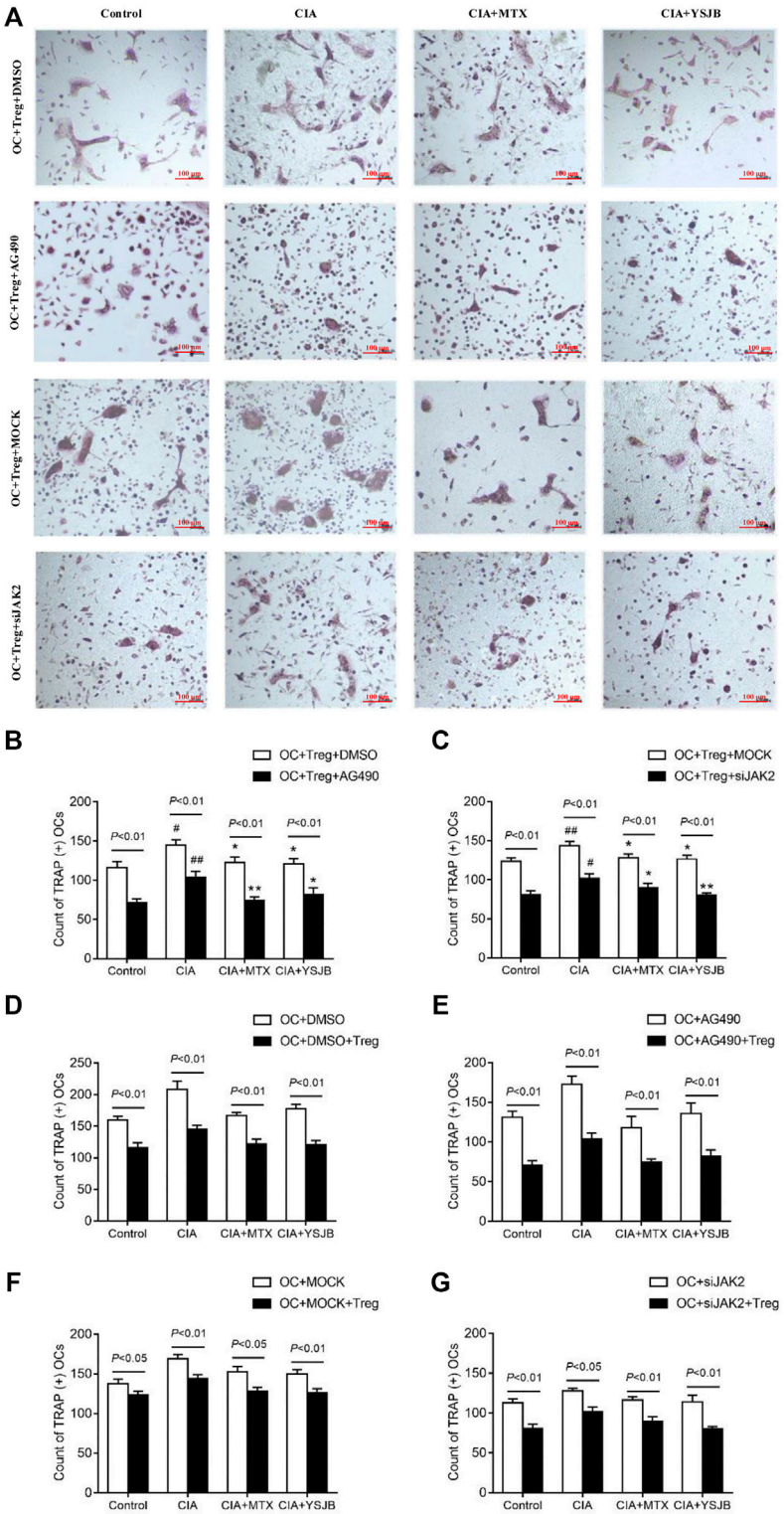


FIGURE 4 | Effect of YSJB, AG490 and JAK2 siRNA on osteoclastogenesis in the OC-Treg coculture system (25:1). **(A)** Images of TRAP staining in the coculture system after treatment with drug-containing serum (Control, CIA, CIA + MTX, CIA + YSJB), AG490 and JAK2 siRNA. Scale bar = 100 μm. **(B,C)** The number of TRAP$^+$ cells in the coculture system treated as described in **(A)**. **(D–G)** The number of TRAP$^+$ OCs after the addition of Tregs. The data are shown as the mean ± SEM (n ≥ 2). $^{\#}p <$ 0.05, $^{\#\#}p < 0.01$ compared with the control group; $^{*}p < 0.05$, $^{**}p < 0.01$ compared with the CIA group.

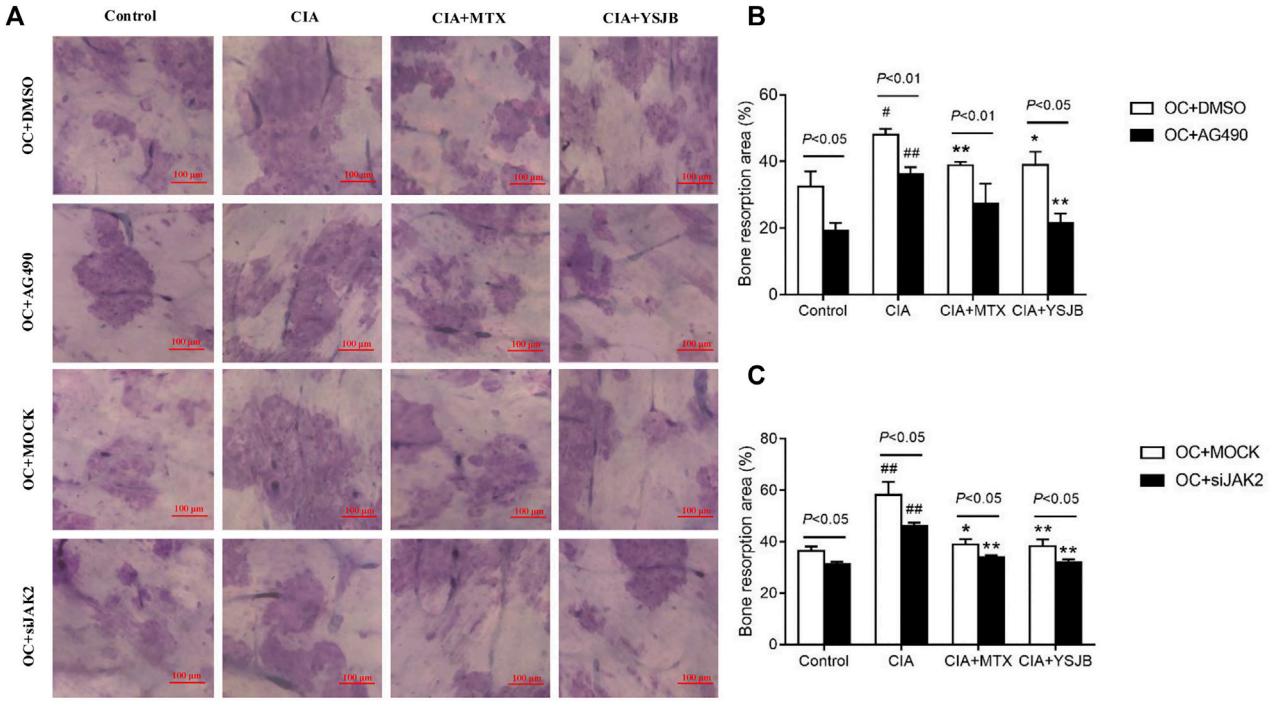


FIGURE 5 | Effect of YSJB, AG490 and JAK2 siRNA on bone resorption in the OC single culture system. **(A)** Images of bone resorption pits. Scale bar = 100 μm. **(B,C)** The areas of the bone resorption pits were measured by the image analysis program. The data are shown as the mean ± SEM (n ≥ 2). $^{\#}p < 0.05$, $^{\#\#}p < 0.01$ compared with the control group; $^{*}p < 0.05$, $^{**}p < 0.01$ compared with the CIA group.

staining results, the adsorbed surface was smaller in the presence of AG490 and JAK2 siRNA than in the absence of these factors. It suggested that blocking JAK2/STAT3 signaling pathway could inhibit bone resorption. In addition, in the absence or presence of AG490 and JAK2 siRNA, bone resorption was obviously increased in the CIA group compared with the control group. In the presence of MTX or YSJB, the areas of bone lacunae were significantly reduced. The results illustrated that MTX and YSJB inhibited bone resorption. (**Figures 5B,C** and **Figures 6B,C**). Moreover, the presence of Tregs also reduced bone resorption (**Figures 6D–G**). Perhaps, these due to the inhibitory effect of YSJB on JAK2/STAT3 signaling pathway.

Blocking the JAK2/STAT3 Signaling Pathway Downregulated RANK, NFATc1, and C-fos mRNA Levels in OCs

As shown previously, OC differentiation and bone resorption were significantly inhibited in the groups with low JAK2 expression. As specific genes associated with OC differentiation, RANK, NFATc1 and c-fos reflect the activity of OCs. To investigate the molecular mechanism by which YSJB, AG490 and JAK2 siRNA regulate the activity of OCs, the mRNA levels of RANK, NFATc1 and c-fos in the OC single culture system and coculture system were measured. We showed that YSJB and MTX significantly suppressed the mRNA expression of RANK, NFATc1 and c-fos both in OC single cultures and in the coculture system compared with those in the CIA group. JAK2 inhibitors and JAK2 knockdown inhibited the expression of these three genes (**Figures 7A–L**). Collectively, we demonstrated that YSJB restrained the JAK2/STAT3 signaling pathway to inhibit the expression of certain genes associated with OC differentiation.

Blocking the JAK2/STAT3 Signaling Pathway Promoted Treg Secretion of IL-10

In previous studies, we demonstrated that IL-10 and TGF-β1 secreted by Tregs inhibited osteoclastogenesis (Xu et al., 2016). In this study, the expression levels of IL-10 and TGF-β1 were measured in a Treg single culture system. As shown in **Figures 8A,B**, **Figurse 8E,F**, IL-10 was expressed at low levels in the CIA group compared with the control group. MTX and YSJB reversed this reduction. However, there was no marked difference in TGF-β1 (**Figures 8C,D**, **Figures 8G,H**). Consistent with these results, we also showed that AG490 or JAK2 siRNA promoted IL-10 expression (**Figures 8A,B**, **Figures 8E,F**). These results indicated that blocking the JAK2/STAT3 signaling pathway upregulated the expression of IL-10. Perhaps the Treg-mediated reduction in the differentiation and bone resorption of OCs is associated with this signaling pathway.

DISCUSSION

RA is a common autoimmune disease that leads to joint malformation and even loss of joint function. Under normal

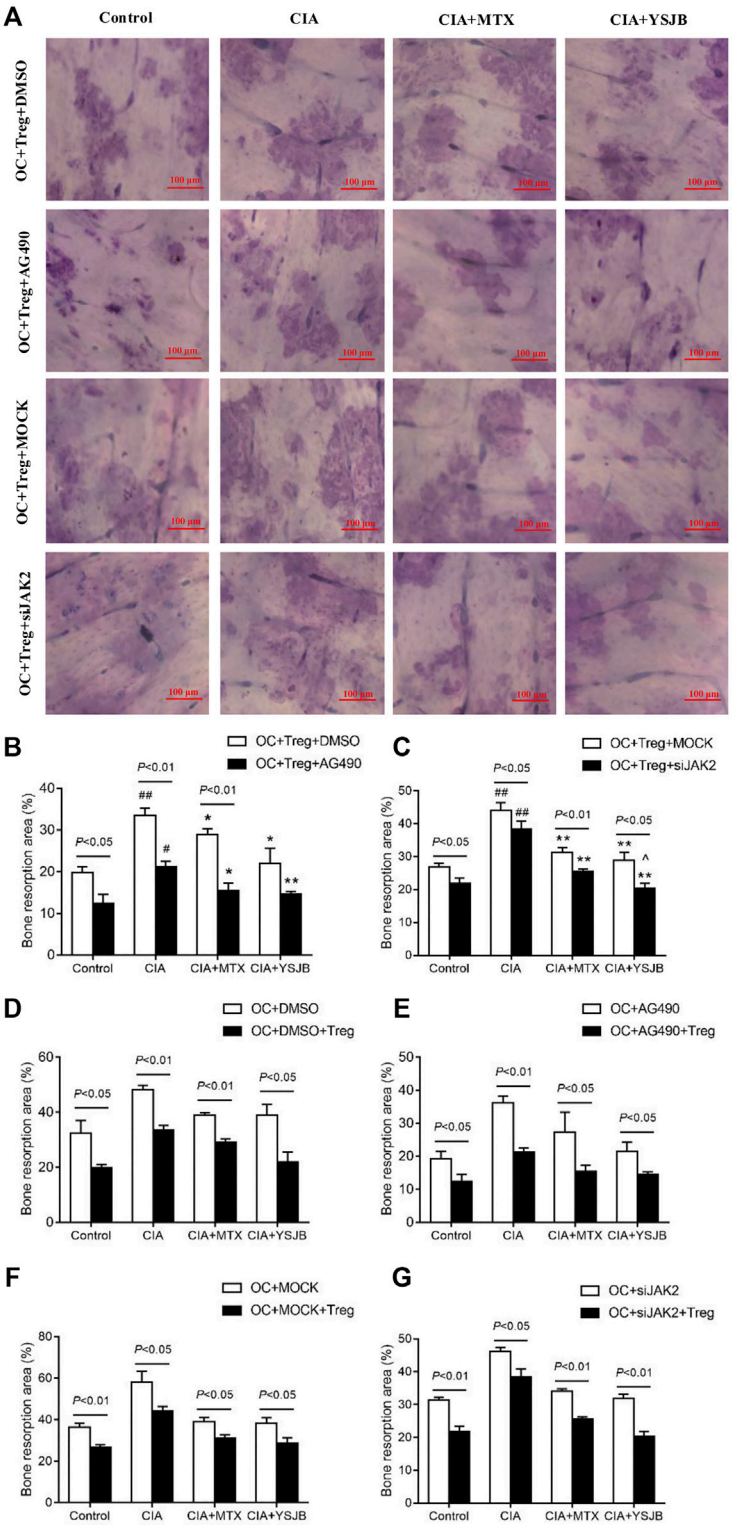


FIGURE 6 | Effect of YSJB, AG490 and JAK2 siRNA on bone resorption in the coculture system. **(A)** Images of bone resorption pits. Scale bar = 100 μm. **(B,C)** The areas of the bone resorption pits were measured by the image analysis program. **(D–G)** The areas of the bone resorption pits after the addition of Tregs. The data are shown as the mean ± SEM (n ≥ 2). $^{\#}p < 0.05$, $^{\#\#}p < 0.01$ compared with the control group; $^{*}p < 0.05$, $^{**}p < 0.01$ compared with the CIA group; $\hat{}p < 0.05$, $\hat{}\hat{}p < 0.01$ compared with the CIA+MTX group.

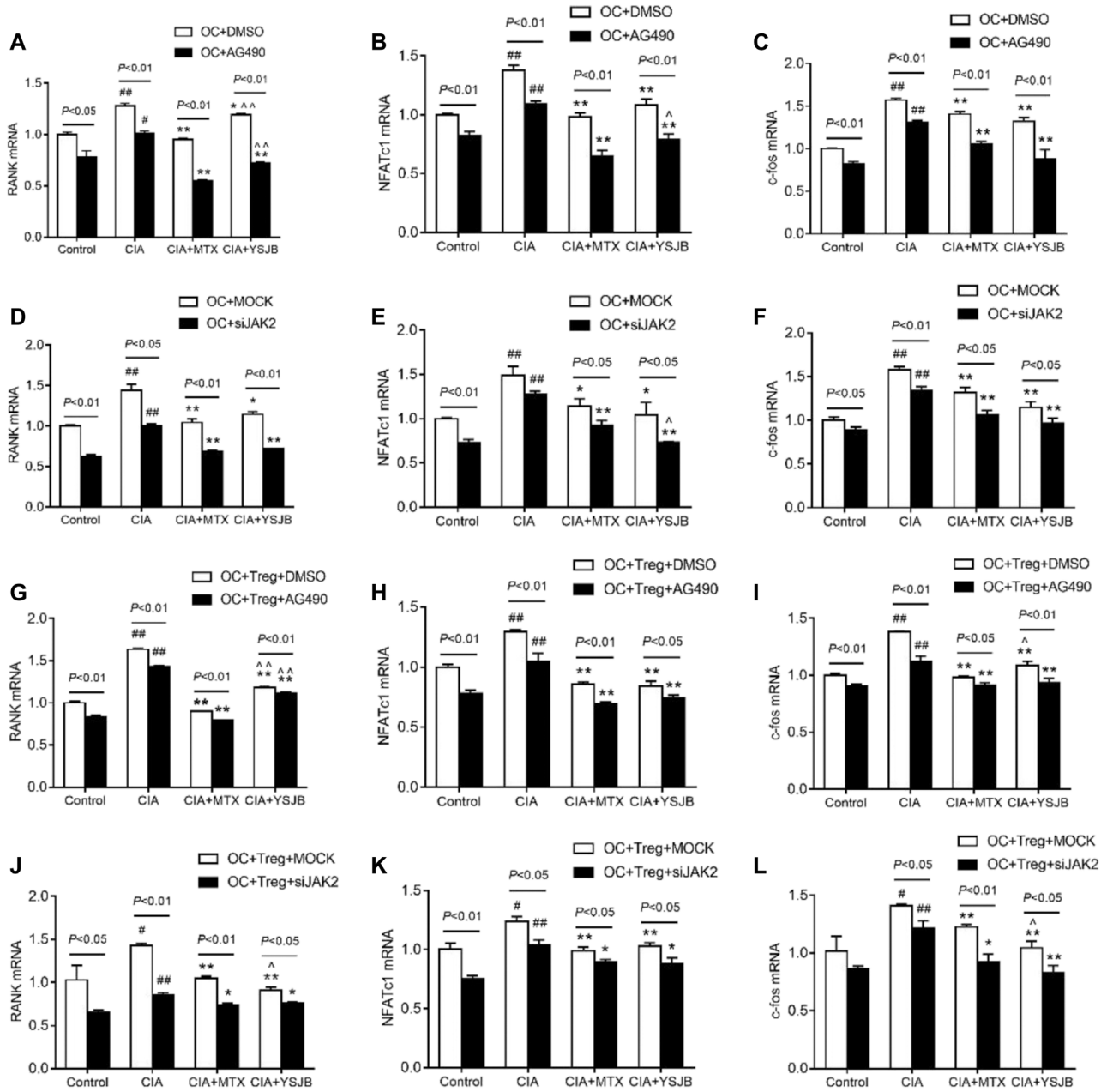


FIGURE 7 | YSJB**,** AG490 and JAK2 siRNA decreased the mRNA levels of RANK, NFATc1, and c-fos, which were associated with the differentiation and maturation of OCs. **(A–F)** The mRNA levels of RANK, NFATc1, and c-fos in the OC single culture system. **(G–L)** The mRNA levels of RANK, NFATc1, and c-fos in the coculture system. Cells were treated with drug-containing serum, AG490 or JAK2 siRNA. $^{\#}p < 0.05$, $^{\#\#}p < 0.01$ compared with the control group; $^{*}p < 0.05$, $^{**}p < 0.01$ compared with the CIA group; $\hat{}p < 0.05$, $\hat{}\hat{}p < 0.01$ compared with the CIA+MTX group.

circumstances, osteoblasts (OBs) and OCs interact to maintain bone homeostasis. However, OCs are overactivated in RA, shifting bone homeostasis toward bone resorption. Therefore, inhibiting OC differentiation in RA patients is of great importance in the treatment of RA. In addition, it has been reported that the immune system interacts with bone tissue (Walsh et al., 2018).

T cells are crucial in regulating the pathogenesis and progression of RA, especially in the initial stage of the autoimmune response and during local inflammatory responses in the joints (Sakaguchi et al., 2003; Komatsu and Takayanagi, 2012; Zerbini et al., 2017). T cells can differentiate into $CD8^+$ T cells and $CD4^+$ T cells. The latter can differentiate into Th17, Tregs and other subtypes (Srivastava et al., 2018). Both Th17 cells and Tregs are involved in regulating OC differentiation and jointly maintain bone homeostasis. Th17 cells regulate bone mass in two main ways. On the one hand, RANKL is highly

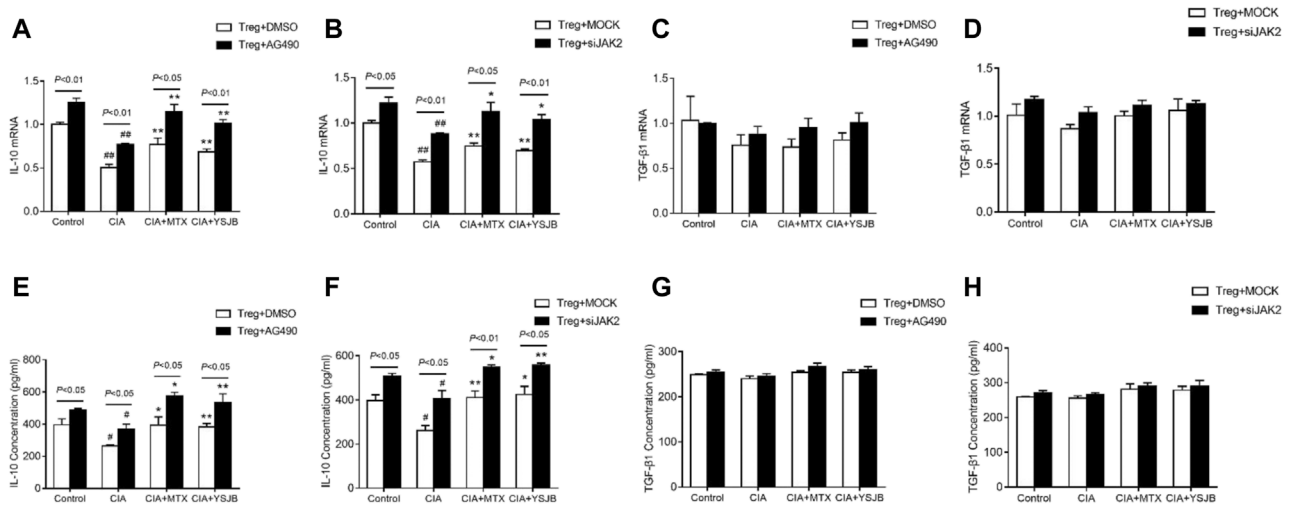


FIGURE 8 | YSJB, AG490 and JAK2 siRNA promoted the secretion of IL-10 by Tregs. The mRNA levels of IL-10 and TGF-β1 were measured by qRT-PCR **(A–D)** and ELISA **(E–H)** in Tregs treated with drug-containing serum, AG490 or JAK2 siRNA. $^{\#}p < 0.05$, $^{\#\#}p < 0.01$ compared with the control group; $^{*}p < 0.05$, $^{**}p < 0.01$ compared with the CIA group.

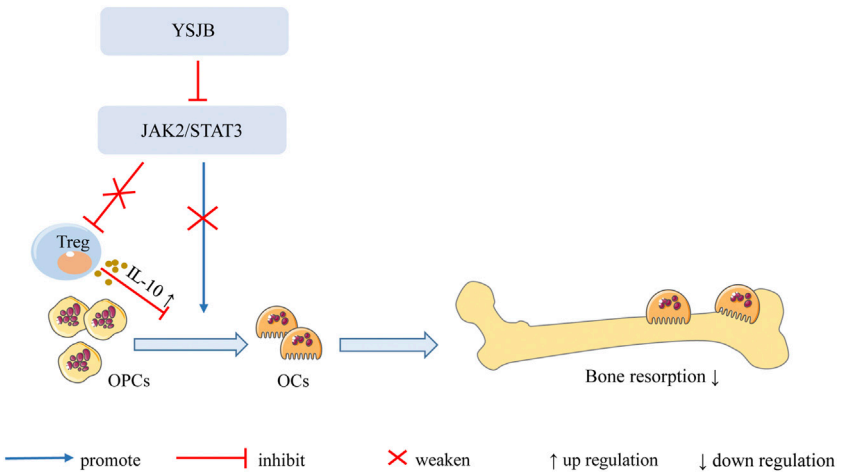


FIGURE 9 | Mechanism of YSJB regulates the bone immune microenvironment. YSJB directly regulates the JAK2/STAT3 signaling pathway in OCs, thereby inhibiting OC differentiation and bone loss. Moreover, YSJB regulates the JAK2/STAT3 signaling pathway in Tregs and upregulates the expression of IL-10. YSJB enhances the immunosuppressive function of Tregs and indirectly inhibits OC differentiation and bone loss.

expressed in Th17 cells. RANKL binds to RANK on the surface of OPCs to promote OC generation. On the other hand, Th17 cells secrete IL-17, which directly enhances RANKL expression in OBs and synovial fibroblasts, thereby promoting the formation of OCs (Ono and Takayanagi, 2017). The RANKL-RANK signaling pathway is known to be important for OC development. RANKL can be expressed on the surface of stromal cells, OBs and T cells. The binding of RANKL and RANK activates the NF-κB signaling pathway, affecting the function of the immune system and adjusting bone remodeling (Theill et al., 2002; Hanada et al., 2011; Liu and Zhang, 2015). In contrast to Th17 cells, Tregs inhibit the production of OCs by blocking RANKL production. A study showed that the binding of Tregs expressing cytotoxic T lymphocyte-associated antigen-4 (CTLA-4) with CD80/CD86 on the surface of OPCs induces OPC apoptosis (Fischer et al., 2019). Moreover, Tregs can also secrete cytokines with immunosuppressive activity, such as IL-10, which inhibits the differentiation and maturation of OCs by upregulating the secretion of osteoprotegerin (OPG) and downregulating the expression of RANKL (Taylor et al., 2006; Dar et al., 2018). YSJB is a frequently used Chinese medicine for the clinical treatment of RA. Studies have shown that YSJB has a regulatory effect on the immune system. We established a method in which OCs were cultured with Tregs to explore the relationship between bone and the immune system in RA (Xu

et al., 2016). In the current study, we used this method to evaluate the efficacy and mechanism of YSJB.

In this study, the number of $TRAP^+$ cells and the areas of bone lacunae were elevated in the CIA group. YSJB or MTX significantly diminished these two indicators compared with those in the CIA group. MTX is an anchor drug for RA treatment. Studies have shown that MTX inhibits osteoclastogenesis and inflammation (Ponchel et al., 2014; Kanagawa et al., 2016). Therefore, MTX was used as a positive control drug to explore the therapeutic effect of YSJB. The results showed that MTX and YSJB had similar effects on inhibiting OC differentiation and bone resorption. Moreover, YSJB or MTX inhibited the expression of RANK, NFATc1, and c-fos in OCs and promoted the expression of IL-10 in Tregs. However, YSJB was not as effective in inhibiting RANK as MTX.

Here, we found that the expression of JAK2 and STAT3 was increased in the CIA group, suggesting that the JAK2/STAT3 signaling pathway accelerates osteoclastogenesis. The JAK/STAT pathway, particularly when activated by IL-6/gp130 (Bellido et al., 1997), has been shown to play a role in adjusting osteoclastogenesis (Park et al., 2014; Adam et al., 2020; Sims, 2020). It has been reported that IL-6 can not only stimulate OPCs to transform into OCs but also induce osteoclastogenesis by increasing the expression of RANKL in OBs (Tamura et al., 1993). Currently, some JAK inhibitors have been used to treat RA, such as tofacitinib and baricitinib (Mease et al., 2017; Taylor et al., 2017). Studies have shown that AG490 inhibits the expression of RANK, NFATc1 and TRAP in OCs (Li et al., 2013; Park et al., 2014), which is consistent with our results. In addition, our results suggested that YSJB or MTX could interfere with the expression of JAK2 and STAT3 compared with that in the CIA group, reducing OC differentiation and function. However, in OCs, the expression of STAT3 in the YSJB group showed a downward trend after transfection with JAK2 siRNA, but the effect was not significant, perhaps due to the limited sample size. At the molecular level, blocking the JAK2/STAT3 signaling pathway decreased the expression of critical genes associated with OC formation, including RANK, NFATc1 and c-fos, but increased the secretion of IL-10 by Tregs.

In summary, our findings demonstrate that YSJB directly regulates the JAK2/STAT3 signaling pathway in OCs and downregulates the expression of RANK, NFATc1 and c-fos in OCs, thereby inhibiting OC differentiation and bone loss. Moreover, YSJB regulates the JAK2/STAT3 signaling pathway in Tregs and upregulates the expression of IL-10. YSJB enhances the immunosuppressive function of Tregs and indirectly inhibits OC differentiation and bone loss (**Figure 9**).

DATA AVAILABILITY STATEMENT

The raw data supporting the conclusions of this article will be made available by the authors, without undue reservation.

ETHICS STATEMENT

The animal study was reviewed and approved by the Institute of Clinical Medical Sciences, China-Japan Friendship Hospital.

AUTHOR CONTRIBUTIONS

YX, DPF, XYL, and XCL contributed equally to this paper. HYZ and CX formulated the concept and designed the study. DPF, YX, XYL, and XCL performed the experiments. YX, DPF, and XYL analyzed the data. YX, DPF, and XYL drafted the paper. QBY, XYX, and QW participated in discussions associated with the paper. HYZ and CX revised the paper. All authors read and approved the final manuscript.

FUNDING

This study was financially supported by the National Natural Science Foundation of China (Grant number 81873223) and the Fundamental Research Funds for the Central Public Welfare Research Institutes (Grant number ZZ2018001).

SUPPLEMENTARY MATERIAL

The Supplementary Material for this article can be found online at: https://www.frontiersin.org/articles/10.3389/fphar.2021.746786/full#supplementary-material

REFERENCES

Adam, S., Simon, N., Steffen, U., Andes, F. T., Scholtysek, C., Müller, D. I. H., et al. (2020). JAK Inhibition Increases Bone Mass in Steady-State Conditions and Ameliorates Pathological Bone Loss by Stimulating Osteoblast Function. *Sci. Transl. Med.* 12 (530), eaay4447. doi:10.1126/scitranslmed.aay4447

Bellido, T., Borba, V. Z., RobersonManolagas, P. S. C., and Manolagas, S. C. (1997). Activation of the Janus Kinase/STAT (Signal Transducer and Activator of Transcription) Signal Transduction Pathway by Interleukin-6-type Cytokines Promotes Osteoblast Differentiation. *Endocrinology* 138 (9), 3666–3676. doi:10.1210/endo.138.9.5364

Chen, Q., Mo, L., Cai, X., Wei, L., Xie, Z., Li, H., et al. (2018). ICOS Signal Facilitates Foxp3 Transcription to Favor Suppressive Function of Regulatory T Cells. *Int. J. Med. Sci.* 15 (7), 666–673. doi:10.7150/ijms.23940

Dar, H. Y., Azam, Z., Anupam, R., Mondal, R. K., and Srivastava, R. K. (2018). Osteoimmunology: The Nexus between Bone and Immune System. *Front. Biosci. (Landmark Ed.)* 23, 464–492. doi:10.2741/4600

Fischer, L., Herkner, C., Kitte, R., Dohnke, S., Riewaldt, J., Kretschmer, K., et al. (2019). Foxp3+ Regulatory T Cells in Bone and Hematopoietic Homeostasis. *Front. Endocrinol. (Lausanne)* 10, 578. doi:10.3389/fendo.2019.00578

Hanada, R., Hanada, T., Sigl, V., Schramek, D., and Penninger, J. M. (2011). RANKL/RANK-beyond Bones. *J. Mol. Med. (Berl)* 89 (7), 647–656. doi:10.1007/s00109-011-0749-z

Kanagawa, H., Masuyama, R., Morita, M., Sato, Y., Niki, Y., Kobayashi, T., et al. (2016). Methotrexate Inhibits Osteoclastogenesis by Decreasing RANKL-Induced Calcium Influx into Osteoclast Progenitors. *J. Bone Miner. Metab.* 34 (5), 526–531. doi:10.1007/s00774-015-0702-2

Komatsu, N., and Takayanagi, H. (2012). Inflammation and Bone Destruction in Arthritis: Synergistic Activity of Immune and Mesenchymal Cells in Joints. *Front. Immunol.* 3, 77. doi:10.3389/fimmu.2012.00077

Li, D. Y., and Xiong, X. Z. (2020). ICOS+ Tregs: A Functional Subset of Tregs in Immune Diseases. *Front. Immunol.* 11, 2104. doi:10.3389/fimmu.2020.02104

Li, C. H., Zhao, J. X., Sun, L., Yao, Z. Q., Deng, X. L., Liu, R., et al. (2013). AG490 Inhibits NFATc1 Expression and STAT3 Activation during RANKL Induced Osteoclastogenesis. *Biochem. Biophys. Res. Commun.* 435 (4), 533–539. doi:10.1016/j.bbrc.2013.04.084

Liu, W., and Zhang, X. (2015). Receptor Activator of Nuclear Factor-κB Ligand (RANKL)/RANK/osteoprotegerin System in Bone and Other Tissues (Review). *Mol. Med. Rep.* 11 (5), 3212–3218. doi:10.3892/mmr.2015.3152

Mease, P., Hall, S., Fitzgerald, O., van der Heijde, D., Merola, J. F., Avila-Zapata, F., et al. (2017). Tofacitinib or Adalimumab versus Placebo for Psoriatic Arthritis. *N. Engl. J. Med.* 377 (16), 1537–1550. doi:10.1056/NEJMoa1615975

Ono, T., and Takayanagi, H. (2017). Osteoimmunology in Bone Fracture Healing. *Curr. Osteoporos. Rep.* 15 (4), 367–375. doi:10.1007/s11914-017-0381-0

Park, J. S., Lee, J., Lim, M. A., Kim, E. K., Kim, S. M., Ryu, J. G., et al. (2014). JAK2-STAT3 Blockade by AG490 Suppresses Autoimmune Arthritis in Mice via Reciprocal Regulation of Regulatory T Cells and Th17 Cells. *J. Immunol.* 192 (9), 4417–4424. doi:10.4049/jimmunol.1300514

Ponchel, F., Goëb, V., Parmar, R., El-Sherbiny, Y., Boissinot, M., El Jawhari, J., et al. (2014). An Immunological Biomarker to Predict MTX Response in Early RA. *Ann. Rheum. Dis.* 73 (11), 2047–2053. doi:10.1136/annrheumdis-2013-203566

Rotta, D., Fassio, A., Rossini, M., Giollo, A., Viapiana, O., Orsolini, G., et al. (2020). Osteoporosis in Inflammatory Arthritides: New Perspective on Pathogenesis and Treatment. *Front. Med. (Lausanne)* 7, 613720. doi:10.3389/fmed.2020.613720

Sakaguchi, N., Takahashi, T., Hata, H., Nomura, T., Tagami, T., Yamazaki, S., et al. (2003). Altered Thymic T-Cell Selection Due to a Mutation of the ZAP-70 Gene Causes Autoimmune Arthritis in Mice. *Nature* 426 (6965), 454–460. doi:10.1038/nature02119

Sims, N. A. (2020). The JAK1/STAT3/SOCS3 axis in Bone Development, Physiology, and Pathology. *Exp. Mol. Med.* 52 (8), 1185–1197. doi:10.1038/s12276-020-0445-6

Smolen, J. S., Aletaha, D., and Mcinnes, I. B. (2016). Rheumatoid Arthritis. *Lancet* 388 (10055), 2023–2038. doi:10.1016/S0140-6736(16)30173-8

Srivastava, R. K., Dar, H. Y., and Mishra, P. K. (2018). Immunoporosis: Immunology of Osteoporosis-Role of T Cells. *Front. Immunol.* 9, 657. doi:10.3389/fimmu.2018.00657

Tamura, T., Udagawa, N., Takahashi, N., Miyaura, C., Tanaka, S., Yamada, Y., et al. (1993). Soluble Interleukin-6 Receptor Triggers Osteoclast Formation by Interleukin 6. *Proc. Natl. Acad. Sci. U S A.* 90 (24), 11924–11928. doi:10.1073/pnas.90.24.11924

Taylor, A., Verhagen, J., Blaser, K., Akdis, M., and Akdis, C. A. (2006). Mechanisms of Immune Suppression by Interleukin-10 and Transforming Growth Factor-Beta: the Role of T Regulatory Cells. *Immunology* 117 (4), 433–442. doi:10.1111/j.1365-2567.2006.02321.x

Taylor, P. C., Keystone, E. C., van der Heijde, D., Weinblatt, M. E., Del Carmen Morales, L., Reyes Gonzaga, J., et al. (2017). Baricitinib versus Placebo or Adalimumab in Rheumatoid Arthritis. *N. Engl. J. Med.* 376 (7), 652–662. doi:10.1056/NEJMoa1608345

Theill, L. E., Boyle, W. J., and Penninger, J. M. (2002). RANK-L and RANK: T Cells, Bone Loss, and Mammalian Evolution. *Annu. Rev. Immunol.* 20, 795–823. doi:10.1146/annurev.immunol.20.100301.064753

Villarino, A. V., Kanno, Y., and O'Shea, J. J. (2017). Mechanisms and Consequences of Jak-STAT Signaling in the Immune System. *Nat. Immunol.* 18 (4), 374–384. doi:10.1038/ni.3691

Walsh, M. C., Takegahara, N., Kim, H., and Choi, Y. (2018). Updating Osteoimmunology: Regulation of Bone Cells by Innate and Adaptive Immunity. *Nat. Rev. Rheumatol.* 14 (3), 146–156. doi:10.1038/nrrheum.2017.213

Xu, H., Zhao, H., Lu, C., Qiu, Q., Wang, G., Huang, J., et al. (2016). Triptolide Inhibits Osteoclast Differentiation and Bone Resorption *In Vitro* via Enhancing the Production of IL-10 and TGF-β1 by Regulatory T Cells. *Mediators Inflamm.* 2016, 8048170. doi:10.1155/2016/8048170

Zerbini, C. A. F., Clark, P., Mendez-Sanchez, L., Pereira, R. M. R., Messina, O. D., Uña, C. R., et al. (2017). Biologic Therapies and Bone Loss in Rheumatoid Arthritis. *Osteoporos. Int.* 28 (2), 429–446. doi:10.1007/s00198-016-3769-2

Zhao, H., Li, J., He, X., Lu, C., Xiao, C., Niu, X., et al. (2012). The Protective Effect of Yi Shen Juan Bi Pill in Arthritic Rats with Castration-Induced Kidney Deficiency. *Evid. Based Complement. Alternat. Med.* 2012, 102641. doi:10.1155/2012/102641

Zhao, H., Xu, H., Qiao, S., Lu, C., Wang, G., Liu, M., et al. (2017). Boldine Isolated from Litsea Cubeba Inhibits Bone Resorption by Suppressing the Osteoclast Differentiation in Collagen-Induced Arthritis. *Int. Immunopharmacol.* 51, 114–123. doi:10.1016/j.intimp.2017.08.013

Zhao, H., Xu, H., Zuo, Z., Wang, G., Liu, M., Guo, M., et al. (2018). Yi Shen Juan Bi Pill Ameliorates Bone Loss and Destruction Induced by Arthritis through Modulating the Balance of Cytokines Released by Different Subpopulations of T Cells. *Front. Pharmacol.* 9, 262. doi:10.3389/fphar.2018.00262

Conflict of Interest: The authors declare that the research was conducted in the absence of any commercial or financial relationships that could be construed as a potential conflict of interest.

Publisher's Note: All claims expressed in this article are solely those of the authors and do not necessarily represent those of their affiliated organizations, or those of the publisher, the editors and the reviewers. Any product that may be evaluated in this article, or claim that may be made by its manufacturer, is not guaranteed or endorsed by the publisher.

Copyright © 2021 Xia, Fan, Li, Lu, Ye, Xi, Wang, Zhao and Xiao. This is an open-access article distributed under the terms of the Creative Commons Attribution License (CC BY). The use, distribution or reproduction in other forums is permitted, provided the original author(s) and the copyright owner(s) are credited and that the original publication in this journal is cited, in accordance with accepted academic practice. No use, distribution or reproduction is permitted which does not comply with these terms.

frontiers in Pharmacology

ORIGINAL RESEARCH
published: 15 December 2021
doi: 10.3389/fphar.2021.767333

Puerarin Alleviates Depression-Like Behavior Induced by High-Fat Diet Combined With Chronic Unpredictable Mild Stress *via* Repairing TLR4-Induced Inflammatory Damages and Phospholipid Metabolism Disorders

Li-Na Gao[1,2]*, *Maocai Yan*[1], *Lirun Zhou*[1,3], *Jian'an Wang*[1], *Chunmei Sai*[1], *Yingjie Fu*[1], *Yang Liu*[1] *and Lin Ding*[1]

[1]College of Pharmacy, Jining Medical University, Rizhao, China, [2]Shandong Collaborative Innovation Center for Diagnosis, Treatment and Behavioral Interventions of Mental Disorders, Institute of Mental Health, Jining Medical University, Jining, China, [3]Institute of Chinese Materia Medica, China Academy of Chinese Medical Sciences, Beijing, China

OPEN ACCESS

Edited by:
Zhaocheng Ma,
Huazhong Agricultural University, China

Reviewed by:
Thangaraj Devadoss,
KVSR Siddhartha College of Pharmaceutical Sciences, India
Hong-Feng Gu,
University of South China, China

***Correspondence:**
Li-Na Gao
linagao228@126.com

Specialty section:
This article was submitted to Neuropharmacology, a section of the journal Frontiers in Pharmacology

Received: *19 September 2021*
Accepted: *23 November 2021*
Published: *15 December 2021*

Citation:
Gao L-N, Yan M, Zhou L, Wang J, Sai C, Fu Y, Liu Y and Ding L (2021) Puerarin Alleviates Depression-Like Behavior Induced by High-Fat Diet Combined With Chronic Unpredictable Mild Stress via Repairing TLR4-Induced Inflammatory Damages and Phospholipid Metabolism Disorders. Front. Pharmacol. 12:767333. doi: 10.3389/fphar.2021.767333

Puerarin has been reported as a potential agent for neuro-inflammatory disorders. However, there have been no reports of using puerarin for the treatment of depression based on Toll-like receptor 4 (TLR4)–mediated inflammatory injury. In this study, we evaluated the protective effects of puerarin on depression-like rats induced by a high-fat diet (HFD) combined with chronic unpredictable mild stress (CUMS). The mechanism was screened by lipidomics and molecular docking and confirmed by *in vivo* tests. Puerarin treatment significantly improved 1% sucrose preference and ameliorated depression-like behavior in the open-field test. The antidepressive effects of puerarin were associated with decreased pro-inflammatory cytokine production, including interleukin-6 (IL-6) and tumor necrosis factor-α (TNF-α), and increased anti-inflammatory cytokine levels (IL-10) in rat hippocampal tissues and plasma. Hematoxylin–eosin (H&E), immunofluorescence staining, and Western blotting results displayed that puerarin alleviated inflammatory injury by suppressing TLR4 expression and by repairing the intestine mucus barrier *via* enhancing the expression of claudin-1 and occludin. Non-targeted lipidomics analysis showed that the most significantly different metabolites modified by puerarin were phospholipids. Puerarin treatment–altered biomarkers were identified as PC (15:1/20:1), PE (15:1/16:1), and PI (18:2/20:1) in comparison with the HFD/CUMS group. Molecular docking modeling revealed that puerarin could bind with cytosolic phospholipase A2 (cPLA2) and cyclooxygenase-2 (COX-2), which play central roles in TLR4-mediated phospholipid metabolism. *In vivo*, puerarin treatment decreased the enzyme activities of cPLA2 and COX-2, resulting in lower production of prostaglandin E_2 (PGE_2) in hippocampal and intestinal tissues. In conclusion, puerarin treatment reverses HFD/CUMS-induced depression-like behavior by inhibiting TLR4-mediated intestine mucus

barrier dysfunction and neuro-inflammatory damages *via* the TLR4/cPLA2/COX-2 pathway.

Keywords: puerarin, depression, Toll-like receptor 4, inflammation, cytosolic phospholipases A2, cyclooxygenase 2

INTRODUCTION

Depression is characterized by long-term depressed mood and loss of interest and pleasure. The phenotype and course of a depressive episode is singular, recurring, or chronic (Gururajan et al., 2019). Thus, depression is highly heterogeneous. Currently, the proportion of the global population suffering from major depression has increased to more than 300 million people (World Health, 2017). In addition to the extraordinary economic burden, the tragedy of suicide contributes to the high mortality of this disorder. Moreover, a major depression-induced reduction in lifespan is due to the significant increase in vulnerability to major medical disorders, such as stroke, diabetes, cancer, and cardiovascular disease (Beurel et al., 2020). Several hypotheses have been developed for the pathologic process of depressive disorder, including the monoamine hypothesis (Hirschfeld, 2000), glutamate hypothesis (Sanacora et al., 2012), and hypothalamic–pituitary–adrenocortical (HPA) axis hypothesis (Holsboer, 2000). A reflection of the 20-year studies indicates that increased inflammation and hyperactivity of the HPA axis are two of the most consistent biological findings in major depression (Pariante, 2017). However, the underlying pathological mechanism is still elusive.

Inflammation plays a vital role in the pathophysiology of depression. In comparison with healthy controls, patients with major depression have higher concentrations of inflammatory cytokines, including tumor necrosis factor (TNF)-α, interleukin (IL)-1β, IL-6, and C-reactive protein (CRP), while lower IL-10 concentration in blood (Euteneuer et al., 2017; Felger et al., 2020). Pro-inflammatory cytokines may be produced in the brain or may enter the brain from the periphery through 1) active transport; 2) "leaky" area across the blood–brain barrier (BBB); and 3) the afferent vagal pathway or activated monocytes, generating second messenger signals to activate glial cells to overproduce cytokines. Abnormally heightened cytokines change the brain structure and function by affecting neurotransmission, HPA axis, hippocampal neurogenesis, etc. (Kempuraj et al., 2017; Cervellati et al., 2020). Moreover, cytokines may dysregulate the levels of serotonin transporter proteins, tryptophan 2,3-dioxygenase (TDO), indoleamine 2,3-dioxygenase (IDO), and endogenous metabolites (Kindler et al., 2020). Toll-like receptors, the innate immune response pattern recognition receptors, have been described along with pro-inflammatory signaling pathways. TLR4 predominantly recognizes lipopolysaccharides (LPS) from Gram-negative bacteria. Changes of TLR4 signaling pathways were found in the peripheral circulation system or the central nervous system (CNS) of patients with major depression and depression-like animal models (Hung et al., 2016; Rahimifard et al., 2017; Fu et al., 2019). Most important is that TLR4 is an independent risk factor related to the severity of depression (Wu et al., 2015). In addition to neuroimmune and neuroendocrine systems, upregulated TLR4 signaling in blood was associated with leakage of damage-related molecular patterns through the gut (Hung et al., 2016). Thus, the link between TLR4 and symptoms of depression should be further investigated, and TLR4 may be a potential therapeutic target for the development of antidepressants.

In chronic stress–induced depressive mice, hippocampal damages are triggered by activating TLR4, glycogen synthase kinase-3 (GSK3), phosphatidylinositol-3/protein kinase B (PI3K/AKT), and downstream inflammatory signal transmission (Cheng et al., 2016). Mice suffering from chronic stress are more likely to show depression-like behavioral phenotypes, and TLR4 knockout can reduce chronic stress–induced cytokine levels in the mice hippocampus (Cheng et al., 2016). In addition, chronic stress–induced animals show heightened intestinal permeability by activating the TLR4-related signal transduction pathways (Gárate et al., 2013; Guo et al., 2019). TLR4 is a key molecule that regulates dietary nutrition, intestinal flora, and metabolic inflammation. A long-term high-fat diet (HFD) damages the intestinal permeability and increases the content of toxins, such as LPS, in intestinal tissues (Velloso et al., 2015). LPS activates immune cells by binding to the CD14–TLR4 complex, leading to the transcription of nuclear factor-κB (NF-κB) to generate large amounts of TNF-α, IL-6, and oxygenase-2 (COX-2) and induce the inflammation cascade (Yiu et al., 2017). Accordingly, both HFD and chronic stress induce the activation of TLR4 in the intestine and central nervous system, resulting in the over-production of cytokines. TLR4-mediated inflammation may be an important node in the molecular network of diseases induced by an HFD and chronic stress.

Chronic unpredictable mild stress (CUMS) simulates the social stress, and an HFD mimics the fast food diet. CUMS and HFD are two of the main factors that induce depression as well as its comorbidities. However, there are no studies which focus on the treatment of depression based on the TLR4-mediated inflammatory damages in HFD/CUMS-induced depression-like animal models. Puerarin (7,4′-dihydroxyisoflavone-8β-glucopyranoside, **Figure 1A**) is the major secondary metabolite obtained from the roots of *Pueraria lobata* (Willd.) Ohwi. Traditionally, it is used for the treatment of splenasthenic diarrhea. Recent studies demonstrated that puerarin exerts a wide-spectrum pharmacological effect, such as anti-inflammation, antioxidation, calcium antagonization, reducing blood viscosity, and improving learning and memory in coronary heart disease, diabetes, and neurodegenerative diseases (Zhou et al., 2014; Qiu et al., 2017; Cai et al., 2018; Liu et al., 2019). The signal pathways regulated by puerarin involve TLR4/p38/MAPK, TLR4/NF-κB, PI3K/AKT, cyclic adenosine monophosphate (cAMP), transforming growth factor (TGF)-β1, and GSK-

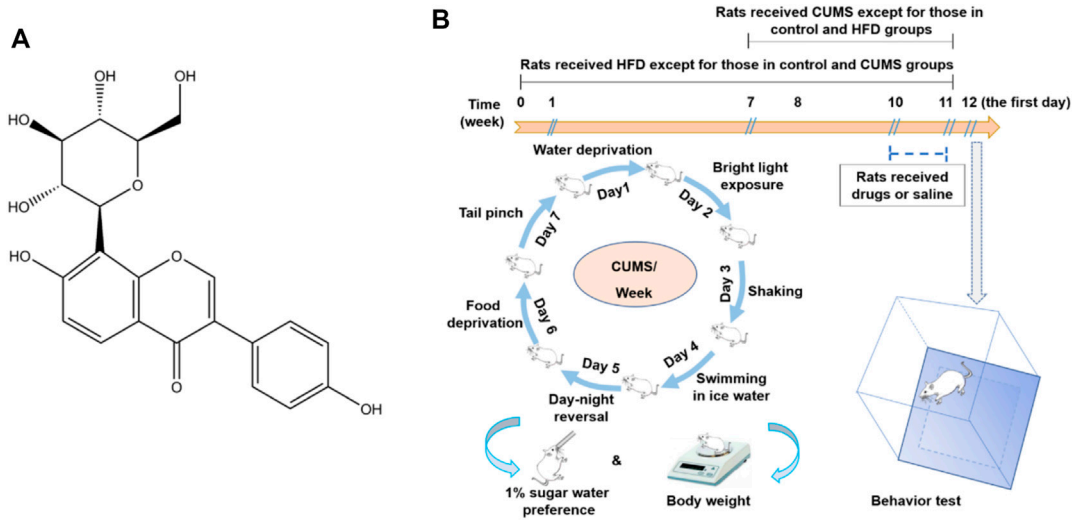


FIGURE 1 | Structure of puerarin **(A)** and a schematic diagram of the HFD/CUMS procedure, drug administration, and behavioral evaluation **(B)**.

3β/Nrf2 (Ji et al., 2016; Hou et al., 2018; Jeon et al., 2020). Puerarin has been described to treat depression-like animals induced by chronic stress and ovariectomy (Zhao et al., 2017; Tantipongpiradet et al., 2019); however, there is no report on the study of puerarin regulating HFD/CUMS-induced depression. Therefore, the current study aims to evaluate the protective effect of puerarin on HFD/CUMS-induced depressive rats and clarify the molecular mechanisms based on the TLR4-mediated inflammatory responses.

MATERIALS AND METHODS

Materials

Puerarin (>98%) was purchased from Jiangsu Yongjian Pharmaceutical Technology Co., Ltd. (Jiangsu, China); fluoxetine hydrochloride (Prozac) was purchased from Eli Lilly and Company; simvastatin was obtained from Dalian Meilun Biotech Co., Ltd. (Dalian, China); rat ELISA kits of IL-6 and TNF-α were purchased from PeproTech (Rocky Hill, United States); the IL-10 rat ELISA kit was purchased from eBioscience (San Diego, United States); the BCA Protein Assay Kit was purchased from Pierce (Rochford,United States); Goat Anti-Mouse IgG H&L (Alexa Fluor® 647) antibodies were purchased from Abcam (Cambridge, MA); anti-TLR4, anti–claudin-1, anti-occludin, anti–β-actin, and HRP-conjugated Goat Anti-Rabbit IgG antibodies were purchased from Servicebio (Wuhan, China); the UNIQ-10 column TRIzol total RNA extraction kit was obtained from Sangon Biological Engineering Technology & Services Co., Ltd. (Shanghai, China). The FastStart Universal SYBR Green Master (ROX) kit was purchased from Roche (Mannheim, Germany); the calcium-dependent cytosolic phospholipases A2 (cPLA2) assay kit and prostaglandin E_2 (PGE_2) Express EIA Monoclonal Kit were purchased from Cayman Chemical (Minneapolis, United States). The COX-2 inhibitor screening kit was obtained from Beyotime Biotechnology (Shanghai, China).

Male Sprague–Dawley (SD) rats (160–180 g) and a high-fat diet containing 4.6 kcal/g (49% fat, 20% protein, and 31% carbohydrate) were purchased from Qingdao Daren Fucheng Animal Husbandry Co., Ltd. [SCXK: (Lu) 2019 0003, Qingdao, China]. The rats were housed in a ventilated, temperature-controlled (22–24°C), and standardized sterile animal room at Jining Medical University. All of the rats were adapted for 1 week with free access to food and water. All animal experiments in the present study were performed according to the National Institutes of Health guidelines for animal care and approved by the Ethics Committee of Jining Medical University (Approval No. 2019-YX-04).

HFD/CUMS Procedure and Drug Administration

The rats were randomly divided into 10 groups with 10 rats per group, including 1) the normal control group, 2) HFD group, 3) CUMS group, 4) HFD/CUMS group, 5) HFD/CUMS + fluoxetine (10 mg/kg) group, 6) HFD/CUMS + simvastatin (10 mg/kg) group, 7) HFD/CUMS + fluoxetine + simvastatin group, (8–10) HFD/CUMS + puerarin (30, 60, and 120 mg/kg) groups. As shown in **Figure 1B**, the rats received a HFD except those which were fed with a normal diet in the control and CUMS groups for 11 weeks. All rats received 1% (w/v) sugar water training since the third day of the seventh week for 4 days: two bottles of 1% sucrose per cage for 24 h; one bottle of water and one bottle of 1% sugar water for another 24 h; and two bottles of water for another two days. Since the eighth week, the rats in the CUMS and HFD/CUMS groups were exposed to one random stressor between 9:00 and 11:00 a.m. per day for 4 weeks. The stressors included noises for 3 h (60 dB), tail clamp for 2 min, swimming in cold water (10°C) for 5 min, inversion of light/dark

cycle for 24 h, food deprivation for 24 h, water deprivation for 24 h, and level shaking for 5 min (1 time/s). Since the 11th week, the rats in various groups were given sterile 0.9% saline, fluoxetine, simvastatin, fluoxetine + simvastatin, puerarin (30, 60, or 120 mg/kg), respectively, once per day for 7 days. Fluoxetine, simvastatin, and puerarin were dissolved in sterile 0.9% saline solution and stored at 4°C for up to 24 h.

Open-Field Test, Body Weight Test, and Sucrose Consumption Test

The open-field test was used to explore the behavior of rats. The open-field apparatus was a 100 × 100 × 40 cm black box equipped with a video tracking system (Ethovision, Netherlands). Each rat was placed into the center of the box and was observed for 6 min. The rearing numbers, time resting, time activity, and total distance traveled during the last 4 min were recorded and statistically analyzed.

The body weight of all rats was recorded at days 0, 7, 14, 21, 28, 35, 42, 49, 56, 63, 70, and 77. The 1% sucrose preference test was carried out at days 50, 57, 64, 71, and 78 to evaluate the anhedonic-like state of rats (Pothion et al., 2004). Before the test, all of the rats were deprived of food and water for 24 h and then fed with one bottle of water and one bottle of 1% sucrose solution for 1 h (8:00–9:00 a.m.). Water and sucrose solution consumption was obtained by weighing the bottles before and after the test. The sucrose preference rate was calculated according to the following formula:

$$\text{Sucrose consumption (\%)} = \frac{\text{Sucrose intake}}{\text{Sucrose water intake} + \text{Water intake}} \times 100.$$

Detection of Inflammatory Cytokines

After the behavior test, blood of anesthetized rats was collected into heparinized anticoagulant tubes and centrifuged at 3,000 rpm for 10 min. Plasma was then obtained and stored at −20°C until use. Simultaneously, the hippocampal tissues of rats were quickly harvested, frozen in lipid nitrogen immediately, and stored at −80°C. The levels of IL-6, TNF-α, and IL-10 in plasma and hippocampal tissues were detected by commercial ELISA kits, according to the manufacturer's instructions. The results of hippocampal tissues were corrected as picogram per milligram protein.

Histological Analysis of Small Intestines

After anesthetization, the rats were killed, and 2 cm of small intestines was dissected and fixed in 10% formalin solution for hematoxylin and eosin (H&E) staining. The histological and pathological changes of each slice were observed by using an optical microscope at a magnification of 100 ×.

Western Blotting Analyses

The small intestines and hippocampal tissues (~50 mg) were quickly harvested, frozen in liquid nitrogen immediately, and stored at −80°C. The protein expression of TLR4, claudin-1, and occludin was determined by Western blotting. Small intestines and hippocampal tissues were homogenized using lysis buffer at a ratio of 1:5 (mg/μl) and quantified by the BCA protein assay kit (Thermo, United States). Samples containing an equal amount of the protein (40 μg) were subjected to 10% SDS-PAGE electrophoresis and blotted on the PVDF membrane. After blocking with 5% bovine serum albumin (BSA) in phosphate-buffered saline-Tween 20 (PBST) for 2 h at room temperature, the PVDF membrane was incubated with respective primary antibodies at 4°C overnight. The dilution of anti-TLR4, anti–claudin-1, anti-occludin, and anti–β-actin antibody was 1: 1000, 1:500, 1:1000, and 1:1500, respectively. After washing with PBST, the membrane was incubated with horseradish peroxidase–conjugated secondary antibody (1:3000) for 2 h at room temperature. Then, the membranes were washed five times using PBST and incubated with the ECL substrate. Finally, the membrane was scanned into a computer, and densitometry was quantified using ImageJ software.

Real-time RT-PCR Analysis for mRNA Expression

Total RNA of hippocampal tissues was extracted using the Sangon UNIQ-10 column TRIzol total RNA extraction kit and reverse-transcribed using the ImProm-II Reverse Transcription System cDNA synthesis kit, according to the manufacturer's instructions. Primer sequences used for TLR4, occludin-1, claudin, and β-actin are shown in **Table 1**. The real-time RT-PCR reactions were performed using the SYBR Green system on an ABI 7500 PCR System (Thermo Fisher, MA, United States). MRNA expression was normalized to β-actin mRNA levels. Relative expression was determined relative to the normal control using the $2^{-\Delta\Delta C_T}$ method (Livak and Schmittgen, 2001).

TLR4 Immunofluorescence Staining

After dissection, the rat brain tissues were immediately fixed in 10% (v/v) neutral formalin solution. Then, the tissues were embedded in paraffin and cut to 5 μm thick. The slides were deparaffinized and rehydrated before immunofluorescence staining using the anti-TLR4 antibody overnight at 4°C. After washing with phosphate-buffered saline (PBS, ph = 7.4), TLR4-positive cell detection was enhanced by using a Goat Anti-Mouse IgG H&L (Alexa Fluor® 647) antibody (Abcam, Cambridge, MA) in the dark. Moreover, the nuclei were stained with 4′,6′-diamidino-2-phenylindole (DAPI, 2 μg/ml). The stained slides were observed on a CRI fluorescence imaging system (Maestro2, CRI, United States) and analyzed using ImageJ software.

Non-Targeted Lipidomic Analysis and Data Processing

Rat hippocampal tissues (~80 mg) were transferred into 2-ml centrifuge tubes. A total of 600 μl chloroform methanol mixed solution (2:1, precooled at −20°C) was added and vortexed for 30 s. After transferring the samples to ice for 40 min, 190 μl H_2O was added and vortexed for 30 s. After transferring the samples on ice for 10 min, the supernatant was centrifuged at 12,000 rpm for 5 min at room temperature. Then, ~300 μl of the lower layer

TABLE 1 | Real-time RT-PCR oligonucleotide primers.

Gene	Primer	Sequence (5′-3′)	PCR product (bp)
β-actin	Forward	TGTTACCAACTGGGACGACA	165
(NM_007393.3)	Reverse	GGGGTGTTGAAGGTCTCAAA	—
TLR4	Forward	GAGCCGGAAAGTTATTGTGG	150
(NM_019178.2)	Reverse	AGCAAGGACTTCTCCACTTTCT	—
Occludin	Forward	GAGGGTACACAGACCCCAGA	161
(NM_031329.3)	Reverse	CAGGATTGCGCTGACTATGA	—
Claudin-1	Forward	CCTCCAATGCCGTTCTGTAT	118
(NM_031699.3)	Reverse	AGGGCCTTTGCTACAGATGA	—

was transferred into a new contribute tube. This cycle was repeated once, and the samples were concentrated and dried in vacuum. Finally, the samples were dissolved with 200 μl isopropanol, and the supernatant was filtered through a 0.22-μm membrane to obtain the prepared samples for LC-MS.

Separation and chromatography of the samples on an Agilent 1290 infinity series UHPLC (Agilent Corporation, CA, United States) coupled to a Triple TOF® 6600 mass spectrometer system (AB SCIEX, United States)were performed. In brief, chromatographic separation was performed on a Phenomenex Kinetex C18 column (100 × 2.1 mm, 1.7 μm) maintained at 55°C. The temperature of the autosampler was 8°C. Gradient elution of the analytes was carried out with acetonitrile: water = 40:60 (10 mM ammonium formate) (A) and isopropanol: acetonitrile = 90:10 (10 mM ammonium formate) (B) at a flow rate of 0.30 ml/min. The injection volume was 2 μl in the positive mode and 6 μl in the negative mode. An increasing linear gradient of solvent B (v/v) was used as follows: 0–1.5 min, 40% B; 1.5–10.5 min, 40–85% B; 10.5–14 min, 85% B; 14–14.1 min, 85–100% B; 14.1–15 min, 100% B; 15–15.2 min, 100%–40% B; and 15.2–18 min, 40% B.

The mass spectrometry parameters were used as follows: ion source gas 1 (GS1), 60 psi; ion source gas 2 (GS2), 60 psi; curtain gas (CUR), 30 psi; temperature, 600°C; and ion spray voltage floating (ISVF), 5,000 V or −4,500 V in positive or negative modes; declustering potential (DP) 100 V. The data-dependent acquisition (DDA) method was used for MS/MS acquisition. Each acquisition cycle consists of one rapid TOF MS survey scan (200 ms) followed by the consecutive acquisition of 11 product ion scans (50 ms each). For the TOF MS survey scan, the mass range is from 200 to 2,000 Da, and collision energy (CE) is set as 10 V. For the product ion scan, the mass ranges are from 100 to 2,000 Da, and collision energy (CE) is set as 45 ± 25 V. Dynamic background subtraction was applied. Dynamic exclusion was implemented to remove some unnecessary information in the MS/MS spectra.

LipidView software (v4.2) was used to annotate the obtained raw data and then peak identification, filtration, and alignment were performed. The data were normalized by MetaboAnalyst 5.0 (https://www.metaboanalyst.ca/). Principal component analysis (PCA) and partial least square analysis (PLS-DA) were carried out. Differentially altered lipid metabolites were screened based on variable importance in projection (VIP) values. Metabolites with VIP >1 and p (corr) < 0.05 were further evaluated with an independent sample t-test. Moreover, the false discovery rate (FDR) was also used to evaluate the significance of differences in each metabolite. An FDR less than 0.05 was considered as significant.

Molecular Docking Simulations

The binding ability and binding mode of puerarin to cPLA2 and COX-2 were investigated through molecular docking studies. The crystallography structure of cPLA2 [PDB ID: 1DB5 (Schevitz et al., 1995)] and COX-2 [PDB ID: 3QH0 (Liang, 2011)] was retrieved from the PDB database and preprocessed in BIOVIA Discovery Studio 2017. Puerarin was then docked to cPLA2 and COX-2 with the CDOCKER module in Discovery Studio 2017. The binding site sphere radius was set to 10 Å for COX-2 and 9 Å for cPLA2. Twenty docked poses were generated for each docking simulation. The top-ranked poses were selected for further analysis. 3D figures were generated by Discovery Studio 2017. 2D diagrams were generated by LigPlot v.1.0 (Wallace et al., 1995).

Enzyme Activity Detection of cPLA2 and COX-2

For the enzyme activity detection of cPLA2, small intestine and hippocampal tissues were perfused with PBS containing 0.16 mg/ml heparin to remove red blood cells and clots. Then, the tissues (50 mg) were homogenized in 1 ml pre-cold buffer (50 mM HEPES, pH 7.4, containing 1 mM EDTA). After being centrifuged, the supernatant was analyzed according to the instructions of the commercial kit (Cayman Chemical, Ann Arbor, MI, United States). The samples were diluted at 1:5 and 1:10, respectively, for hippocampal tissues and small intestines. The absorbance was recorded at 414 nm using a plate reader. To detect the enzyme activity of COX-2, the COX-2 inhibitor screening kit (Beyotime Biotechnology, China) was used. The hippocampal tissues and small intestines were homogenized using lysis buffer at a ratio of 1:5 (mg/μl) and quantified by the BCA protein assay kit (Thermo, United States). The enzyme activity of COX-2 of the samples was analyzed following the instructions of the commercial kit and corrected as Relative Fluorescence Unit (RFU) per gram protein.

Assay of PGE_2 Production

Production of PGE_2 in the hippocampus and small intestine tissues was detected by enzyme-linked immunosorbent assay (ELISA). The hippocampal tissues and small intestines were homogenized using lysis buffer at a ratio of 1:8 (mg/μl) and

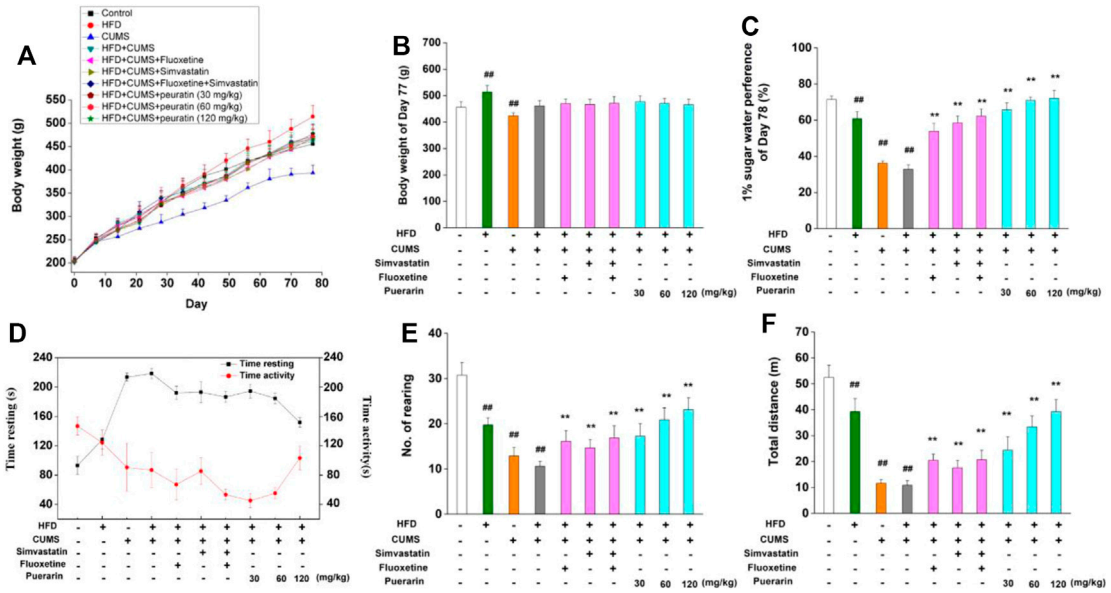


FIGURE 2 | Effect of puerarin on body weight, sucrose preference, and depression-like behavior. **(A)** Body weight of all rats was recorded at days 0, 7, 14, 21, 28, 35, 42, 49, 56, 63, 70, and 77. **(B)** Body weight at the 77th day was statistically analyzed. **(C)** Water and sucrose solution consumption at the 78th day were carried out, and the sucrose preference rate was calculated. The time resting or activity **(D)**, rearing numbers **(E)**, and total distance **(F)** traveled during the last 4 min were recorded and statistically analyzed. Values are expressed as mean ± S.E.M (n = 8). $^{\#\#}p < 0.01$ vs. the normal control group; $^{**}p < 0.01$ vs. the HFD/CUMS group.

quantified by the BCA protein assay kit (Thermo, United States). The concentration of PGE_2 was detected according to the instruction of the commercial PGE_2 EIA monoclonal kit (Minneapolis, United States). The results were corrected as picogram per milligram protein.

Statistical Analysis

All data were represented as mean ± S.E.M. N indicated the number of animal samples in each group. Statistical analyses were performed with Origin Pro 2021 software by Student's t-test (between two groups) or one-way analysis of variance (ANOVA, among multiple groups). The p-value less than 0.05 was considered statistical significant.

RESULTS

Puerarin Improved Sucrose Preference and Depression-Like Behavior in HFD/CUMS-Induced Rats

In order to investigate the protective effect of puerarin on depression, an HFD/CUMS-induced depression-like rat model was used. As shown in **Figures 2A,B**, in comparison with the normal control group, the body weight of rats in the HFD group significantly increased from the 56th day, while significant weight loss was observed in the CUMS-alone group at the 77th day ($p <$ 0.01). However, no significant difference was found among other groups because an HFD and CUMS have opposite effects on weight gain. Anhedonia, the main symptom of depressive disorder, was detected by the 1% sucrose preference test. Compared with the normal control group, rats in the HFD, CUMS, and HFD/CUMS groups showed significantly less sucrose consumption (**Figure 2C**, $p < 0.01$). The drug treatment groups, including simvastatin, fluoxetine, simvastatin + fluoxetine, and puerarin (30, 60, and 120 mg/kg), showed significant higher consumption of sucrose solution than the HFD/CUMS group ($p < 0.01$). In the open-field test (**Figures 2D–F**), HFD, CUMS, and HFD/CUMS stimulation prolonged time resting, while decreasing time activity and number. of rearing and total distance ($p < 0.01$), showing behaviors indicative of depression. In comparison with the HFD/CUMS group, simvastatin, fluoxetine, simvastatin + fluoxetine, and puerarin (30, 60, and 120 mg/kg) treatments significantly alleviated the depression-like behaviors ($p < 0.01$).

Puerarin Antagonized the Abnormal Protein Expression of IL-6, TNF-α, and IL-10 in Hippocampal Tissues and Plasma

To further investigate the protective role of puerarin on HFD/CUMS-induced inflammation in the peripheral and CNS, the protein levels of IL-6, TNF-α, and IL-10 in plasma and hippocampal tissues were detected. The results in **Figure 3** demonstrated that chronic stimulation of HFD, CUMS, and HFD/CUMS significantly induced inflammatory damage by enhancing the protein level of IL-6 and TNF-α and reducing the expression of IL-10 in the hippocampus and plasma ($p <$ 0.01). However, in comparison with the HFD/CUMS group, simvastatin + fluoxetine or puerarin treatment antagonized the abnormal protein expression of IL-6, TNF-α, and IL-10 in hippocampal tissues and plasma ($p < 0.01$ or $p < 0.05$).

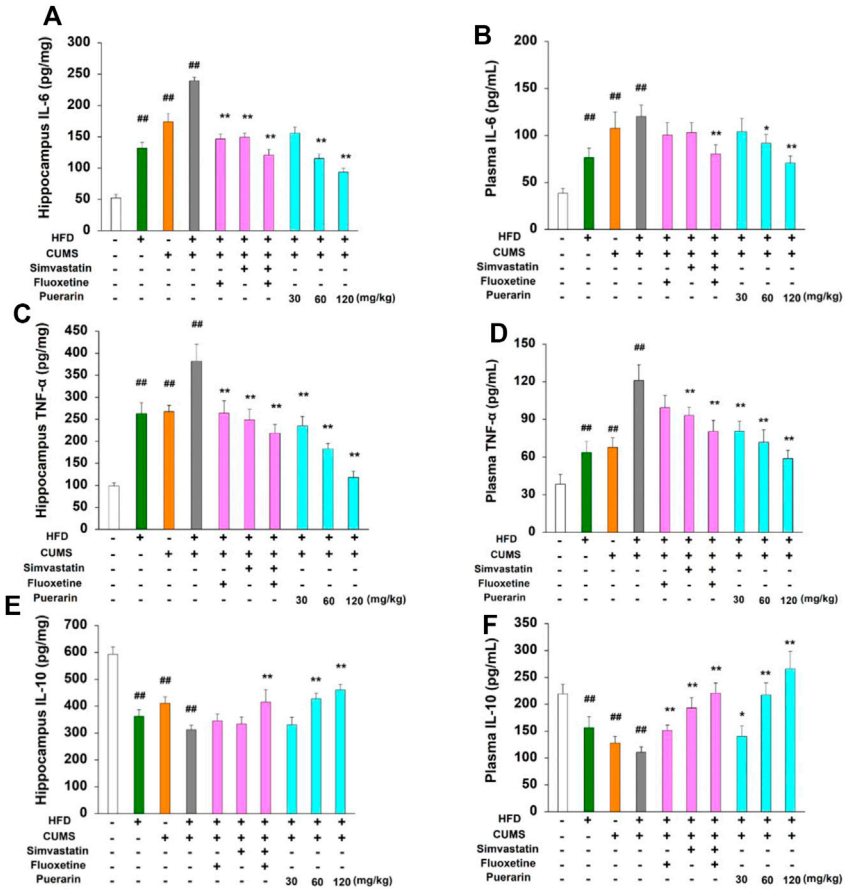


FIGURE 3 | Effect of puerarin on protein expression of IL-6, TNF-α, and IL-10 in hippocampal tissues and plasma. After drug treatment for consecutive 7 days (one time per day), plasma and hippocampal tissues were obtained. The protein levels of IL-6 **(A, B)**, TNF-α **(C, D)**, and IL-10 **(E, F)** in hippocampal tissues and plasma were detected by using commercial ELISA kits, respectively. The results of hippocampal tissues were corrected as picogram per milligram protein. Values are expressed as mean ± S.E.M (n = 8). $^{\#\#}p < 0.01$ vs. the normal control group; $^{*}p < 0.05$ and $^{**}p < 0.01$ vs. the HFD/CUMS group.

Moreover, a dose-dependent manner was observed in puerarin-treated (30, 60, and 120 mg/kg) groups.

Puerarin Repaired Pathological Damage of the Small Intestine of Depression-Like Rats

As shown in **Figure 4A**, in the normal control group, the small intestinal mucosal villi were arranged regularly, and no obvious damage was observed. The small intestinal mucosa of the rats in the HFD, CUMS, and HFD/CUMS groups were severely damaged, including the following characteristics: 1) the thickness from the serosa to muscularis was less; 2) the villi were broad and short and considerably swollen, broken, or necrotic; and 3) the arrangement of the lamina propria cells was completely disordered. Long-term stimulation of CUMS showed that the serosal layer was loosely arranged or fell off from the muscle layer. Among which, the morphological structure of the small intestine mucosa of rats in the HFD/CUMS group was the most severely damaged. Compared with the HFD/CUMS group, the changes of the small intestine mucosa were improved. Moreover, the simvastatin + fluoxetine-treated group and puerarin (120 mg/kg)-treated groups showed that the villi were basically intact, arranged tightly, and the structure of each layer was relatively clear and complete.

The pathological damage of the small intestine may be related to the increase in intestinal permeability mediated by abnormal expression of TLR4. Subsequently, the mRNA and protein expressions of TLR4, occludin, and claudin-1 were determined by real-time RT-PCR and Western blotting, respectively. As displayed in **Figures 4B,E**, HFD, CUMS, and HFD/CUMS stimulations significantly increased the mRNA and protein concentrations of TLR4 in the small intestine ($p < 0.01$). However, simvastatin, fluoxetine, simvastatin + fluoxetine, and puerarin (30, 60, or 120 mg/kg) treatments significantly downregulated the abnormal TLR4 levels ($p < 0.01$). Moreover, rats in the HFD, CUMS, and HFD/CUMS groups increased intestinal permeability by reducing the mRNA and protein expression of occludin (**Figures 4C,F**) and claudin-1 (**Figures 4D,G**, $p < 0.01$ or $p < 0.05$). After the rats received simvastatin, fluoxetine, simvastatin + fluoxetine, or puerarin (30, 60, and 120 mg/kg), the mRNA expressions of occludin and claudin-1 were considerably upregulated ($p < 0.01$ or $p <$

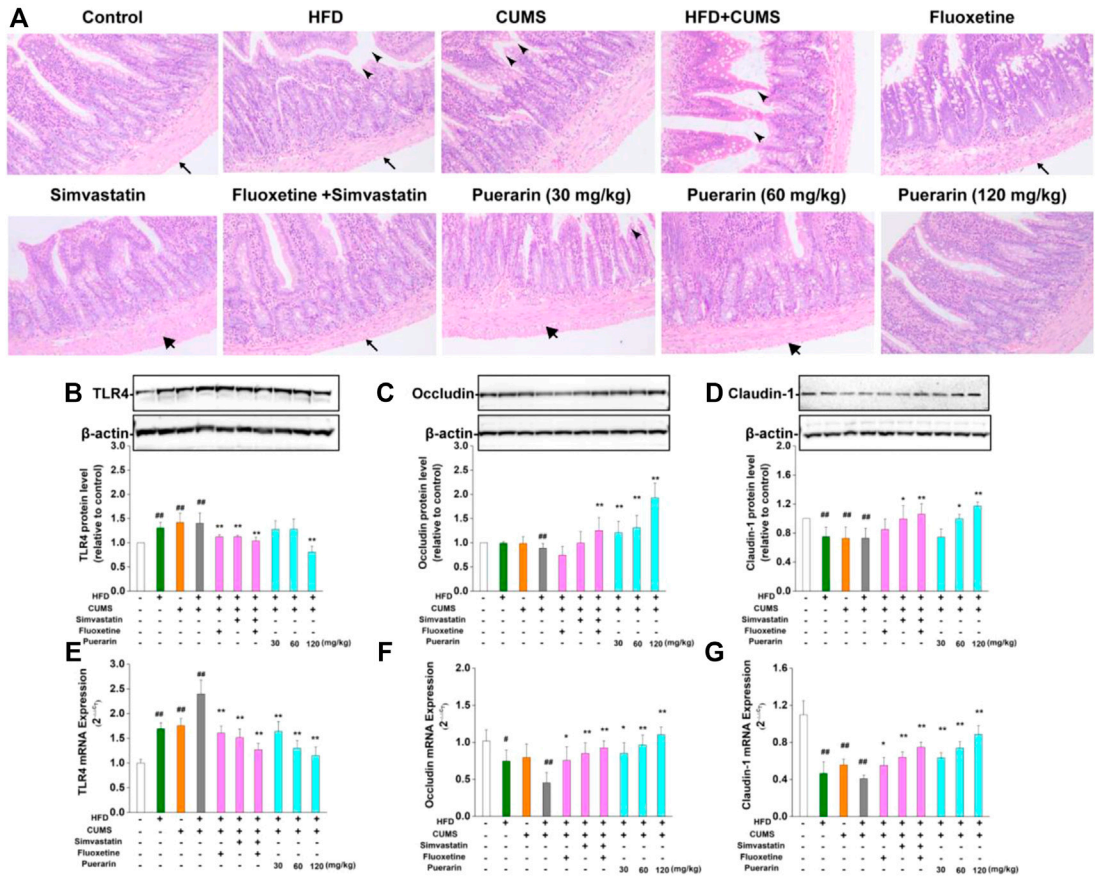


FIGURE 4 | Effect of puerarin on HFD/CUMS-induced small intestine mucosa. **(A)** Pathological damage of the small intestine was detected by H&E staining.↖ indicates the thickness from the serosa to muscularis;↘ shows that the villi were swollen and broken, and the arrangement of the lamina propria cells was completely disordered;↡ indicates that the serosal layer was loosely arranged or fell off from the muscle layer. The magnification was 100 ×. The protein expression of TLR4 **(B)**, occludin **(C)**, and claudin-1 **(D)** was analyzed by Western blotting. β-actin was used as the internal reference. The densitometry was quantified using ImageJ software. The mRNA levels of TLR4 **(E)**, occludin **(F)**, and claudin-1 **(G)** were detected by real-time RT-PCR. β-actin was used as the housekeeping gene. Values are expressed as mean ± S.E.M ($n = 3$ for Western blotting and $n = 4$ for real-time RT-PCR). $^{\#}p < 0.05$ and $^{\#\#}p < 0.01$ vs. the normal control group; $^{*}p < 0.05$ and $^{**}p < 0.01$ vs. the HFD/CUMS group.

0.05). Similarly, the protein expression of occludin and claudin-1 was significantly enhanced by simvastatin + fluoxetine or puerarin (30, 60, and 120 mg/kg) ($p < 0.01$ or $p < 0.05$). These results indicated that the intestinal permeability was restored.

Puerarin Decreased the Number of TLR4-Positive Cells in the Prefrontal Cortex of the HFD/CUMS-Induced Rats

The TLR4 levels in the prefrontal cortex were identified as red, and the nucleus was stained in blue. As displayed in **Table 2** and **Figure 5A**, the number of TLR4-positive cells in the HFD, CUMS, and HFD/CUMS groups was more than that of the normal control group ($p < 0.01$). Moreover, the intensity of red fluorescence in the HFD/CUMS group was stronger than that of the other groups. In comparison with the HFD/CUMS group, the rats that received fluoxetine, simvastatin, simvastatin + fluoxetine, or puerarin (30, 60, and 120 mg/kg) treatments showed that the number of TLR4-positive cells was reduced to 70.35, 37.78, 30.36, 65.20, 29.64, and 17.02% ($p < 0.01$). Moreover, we detected the expression of hippocampal TLR4. As shown in **Figure 5B**, HFD, CUMS, and HFD/CUMS stimulations significantly enhanced the expression of TLR4 ($p < 0.01$ or $p < 0.05$). However, rats in the simvastatin, simvastatin + fluoxetine, or puerarin (30, 60, and 120 mg/kg) groups displayed a remarkably decreased TLR4 level ($p < 0.01$ or $p < 0.05$).

Puerarin Improved Abnormal Lipid Metabolism in Hippocampal Tissues

Lipid metabolites are important signaling molecules in cells. The effect of puerarin on lipid metabolism is shown in **Figure 6**. PLS-DA score plots showed a complete separation between the control and HFD/CUMS groups and HFD/CUMS and PUE groups, indicating that there were different lipid metabolites among the three groups. The top 15 most different metabolites were LacCer (d19:0/12:1), PC (O-22:2/14:1), TG (16:0/22:6/18:1), PC

TABLE 2 | Semi-quantification of TLR4-positive cells.

Group	TLR4-positive cells	Groups	TLR4-positive cells
Normal control	1.83 ± 0.31	Simvastatin	8.5 ± 0.99**
HFD	8.83 ± 0.6##	Simvastatin + fluoxetine	6.83 ± 1.01**
CUMS	17.33 ± 1.12##	Puerarin (30 mg/kg)	14.67 ± 1.20**
HFD/CUMS	22.50 ± 1.31##	Puerarin (60 mg/kg)	6.67 ± 0.84**
Fluoxetine	15.83 ± 0.87**	Puerarin (120 mg/kg)	3.83 ± 0.60**

*The number of TLR4-positive cells was averaged from six random grids. Values are expressed as mean ± S.E.M (n = 6). ##p < 0.01 vs. the normal control group; *p < 0.05 and **p < 0.01 vs. the HFD/CUMS group.*

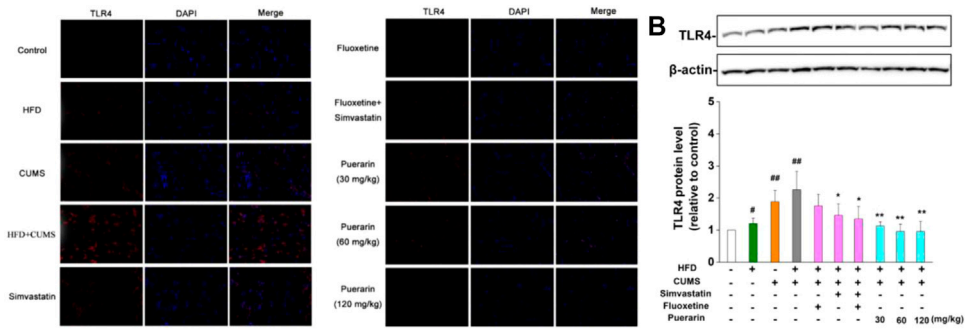


FIGURE 5 | Puerarin decreased the level of CNS TLR4. **(A)** Puerarin decreased the level of TLR4 in the prefrontal cortex of HFD/CUMS-induced depression-like rats (400×magnification). The localization of TLR4 was determined by immunofluorescence. TLR4-positive cells were identified as red, and the nucleus was stained with DAPI in blue. **(B)** Puerarin reduced the expression of TLR4 in the hippocampal tissues of HFD/CUMS-induced depression-like rats. The protein expression of TLR4 was detected by Western blotting. β-actin was used as the internal reference. The densitometry was quantified using ImageJ software. Values are expressed as mean ± S.E.M (n = 3). $^{\#}p < 0.05$ and $^{\#\#}p < 0.01$ vs. the normal control group; $^{*}p < 0.05$ and $^{**}p < 0.01$ vs. the HFD/CUMS group.

(14:0/18:4), Cer (14:0/21:0), PC (16:1/22:2), PE (P-16:0/18:2), PC (P-18:0/18:1), PC (22:5/38:0), Sph (d16:0), DG (16:1/20:3/20:0), PE (16:1/22:6), lyso-PE (20:0/0:0), PC (16:0/18:3), and TG (16:0/18:0/18:0). Among the differently altered metabolites, more than 65% were phospholipids. Therefore, based on the phospholipid metabolism abnormalities, the group heatmap is shown in **Figure 6D**. In comparison with the HFD/CUMS group, the puerarin-modified phospholipid biomarkers were identified as PC (15:1/20:1), PE (15:1/16:1), and PI (18:2/20:1).

Puerarin Inhibited the Enzyme Activity of cPLA2 and COX-2 and Decreased the Production of PGE_2

The docking results revealed that puerarin exhibited moderate binding affinity to cPLA2 and weak binding affinity to COX-2 (**Figure 7A**). The ligand bonded to cPLA2 and COX-2 mainly through hydrogen bonding and hydrophobic interactions. As illustrated in **Figure 7B**, puerarin formed several hydrogen bonds with Ser530, Tyr385, and Phe518 of COX-2, as well as a number of hydrophobic interactions with Val349, Leu352, and Met522. Puerarin formed hydrogen bonds with Gly29, Cys44, Asp48, and His47 of cPLA2 and hydrophobic interactions with Val30, Tyr21, His6, and Ala17.

To confirm the results of molecular docking, the effect of puerarin on enzyme activities of cPLA2 and COX-2 was evaluated. As shown in **Figures 7C–E**, HFD, CUMS, and HFD/CUMS stimulation significantly increased the enzyme activities of cPLA2 and COX-2, resulting in enhanced PGE_2 concentration in hippocampal and small intestinal tissues ($p < 0.01$). In comparison with the HFD/CUMS group, simvastatin, simvastatin + fluoxetine, and puerarin (30, 60, and 120 mg/kg) treatments significantly decreased the enzyme activity of cPLA2 ($p < 0.05$ or $p < 0.01$). Moreover, all drug-treated groups, including fluoxetine, simvastatin, simvastatin + fluoxetine, and puerarin (30, 60, and 120 mg/kg), showed weaker enzyme activities of COX-2 and a lower PGE_2 level than those in the HFD/CUMS group ($p < 0.01$).

DISCUSSION

Depression is one of the most common comorbidities of chronic diseases, including cardiovascular, diabetes, and obesity (Bădescu et al., 2016; Lu et al., 2019; Gold et al., 2020). The differential metabolites in urine and plasma between depressive and healthy subjects indicate that the pathogenesis of depressive disorder is related to lipid metabolism, amino acid metabolism, and energy metabolism (Xu et al., 2012; Huang et al., 2020; Wang et al., 2020). Thus, it is necessary to build a complex model to better simulate the multifactorial nature of depression or depression combined with physical diseases. A study based on a single mechanism of depression has certain limitations. A single inducing factor can only simulate one or more pathogeneses

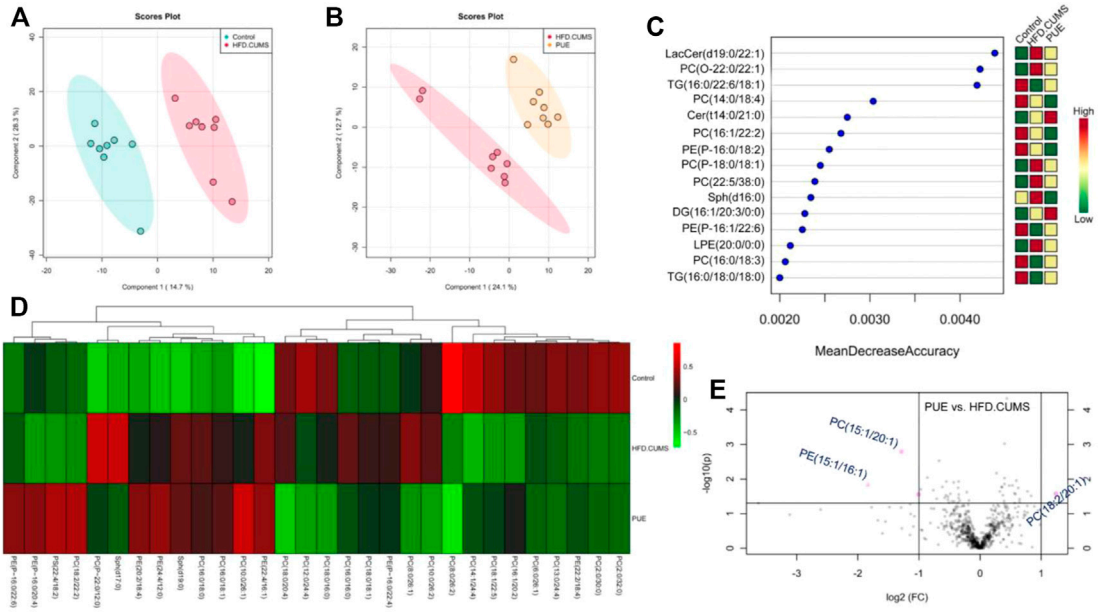


FIGURE 6 | Puerarin-modified lipid metabolism abnormalities in HFD/CUMS-induced rat hippocampal tissues. **(A)** PLS-DA score plot based on the control vs. HFD/CUMS groups. **(B)** PLS-DA score plot based on HFD/CUMS vs. PUE groups. **(C)** Random forest analysis of the top 15 most different metabolites among the control, HFD/CUMS, and PUE groups. "Mean Decrease Accuracy" and "Mean Decrease Gini" were used to measure the importance of a metabolite in discriminating groups in a random forest. The greater the two values, the greater the importance of metabolites in the random forest. **(D)** Heatmap of different phospholipid metabolites. **(E)** Volcano plot based on PUE vs. HFD/CUMS. The identified biomarkers were PC (15:1/20:1), PE (15:1/16:1), and PI (18:2/20:1). LacCer: lactosylceramide, TG: triglyceride, Sph: sphingolipid, PC: phosphatidylcholines, Cer: ceramide, PE: phosphatidylethanolamine, LPE: lyso-PE, DG: diacylglycerols, and PI: phosphatidylinositol. Values are expressed as mean ± S.E.M (n = 8).

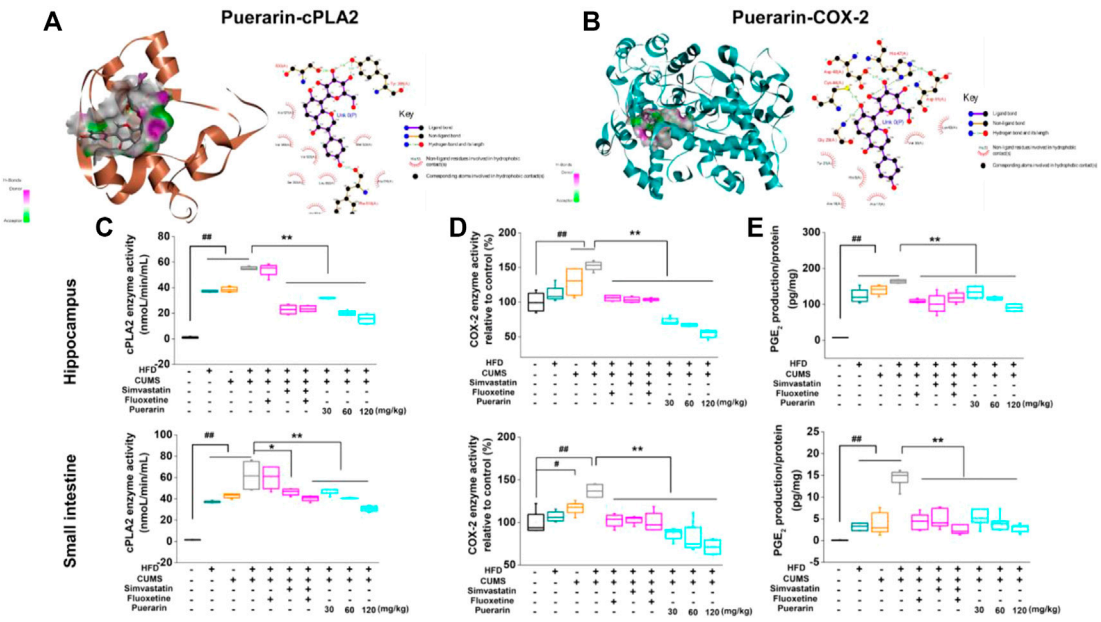


FIGURE 7 | Puerarin inhibited the enzyme activity of cPLA2 and COX-2 and decreased the production of PGE_2. The 3D and 2D diagrams of the interaction of puerarin-cPLA2 **(A)** and puerarin-COX-2 **(B)** by molecular docking. Puerarin inhibited the enzyme activity of cPLA2 and COX-2 in the hippocampus and small intestine. The enzyme activities of cPLA2 **(C)** and COX-2 **(D)**, as well as the downstream PGE_2 **(E)** production, were analyzed by using commercial kits. Values are expressed as mean ± S.E.M (n = 6). $^{\#}p < 0.05$ and $^{\#\#}p < 0.01$ vs. the normal control group; $^{*}p < 0.05$, $^{**}p < 0.01$ vs. the HFD/CUMS group.

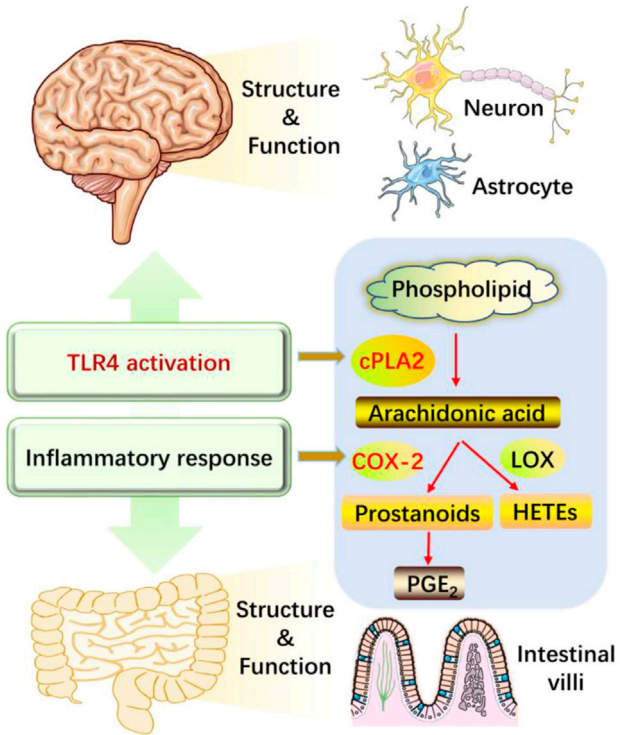


FIGURE 8 | Puerarin protected against HFD/CUMS-induced depression *via* the TLR4/cPLA2/COX-2 pathway. HFD/CUMS stimulation induced depression-like behavior *via* increasing inflammatory damages. Inflammatory response is related to TLR4 activation, inducing the changes of structure and function in the brain and small intestine tissues. Puerarin treatment alleviated the depressive phenotype by suppressing TLR4 activation and cytokine over-production, restoring lipid metabolites, inhibiting enzyme activities of cPLA2 and COX-2, and decreasing downstream PGE_2 production. HFD: high-fat diet; CUMS: chronic unpredictable mild stress; TLR4: Toll-like receptor 4; LOX: lipoxygenase; cPLA2: calcium-dependent cytosolic phospholipases A2; COX-2: cyclooxygenase-2; PGE_2: prostaglandin E_2; HETEs: hydroxyeicosatetraenoic acids.

of depression (Gururajan et al., 2019). To better explore the pathological mechanism of depression and promote the development of new antidepressant drugs, valid animal models are urgently required. CUMS, as a widely used stimulus for inducing depression-like behavior, reasonably simulates the life state of people who are under long-term mental stress. In terms of nutritional intake, the HFD simulates the unhealthy fast food diet. Thus, the depressant-like model induced by CUMS combined with the HFD may better simulate the complexity of the pathogenesis of depression, including neurotransmitter dysfunction, inflammatory response, abnormal metabolism, and brain–gut axis disorders.

The crosstalk between inflammation and neurocircuits drives the development of depression and has been taken as a potential direction for antidepressant therapies (Miller and Raison, 2016). Cytokines, one of the most investigated immuno-components in depression, directly affect cell functions and communication by exerting pro-inflammatory or anti-inflammatory actions. In addition to central cytokines, peripheral cytokines can, indeed, influence behavior. For example, chronic stress disrupts BBB integrity, promoting peripheral IL-6 to enter into brain parenchyma and resulting in depression-like behaviors (Menard et al., 2017). Cytokines have multiple impacts on neurotransmitter systems. However, it remains unclear how cytokines contribute to the development of depression and what is the underlying mechanism.

In the present study, we evaluated the protective effect of puerarin on HFD/CUMS-induced depression-like rats and explored the molecular mechanisms based on TLR4-mediated inflammatory responses. The results demonstrated that puerarin improved the behaviors in HFD/CUMS-induced depressive rats. IL-6 and TNF-α are two of the most studied pro-inflammatory markers in the blood of major depressive patients (Pedraz-Petrozzi et al., 2020). Following this, we detected the expression of peripheral and central cytokines and found that both HFD and CUMS stimulations heightened the protein concentrations of IL-6 and TNF-α, while blocking the expression of IL-10. However, puerarin treatment significantly alleviated inflammatory damages by restoring HFD/CUMS-induced abnormal levels of IL-6, IL-10, and TNF-α in plasma and hippocampal tissues.

The HFD directly modulates intestinal mucus composition and changes gut microflora by enhancing pro-inflammatory signaling cascades (Rohr et al., 2020). It is unclear if CUMS-induced intestinal hyper-permeability is the pathogenesis or consequence of major depression. However, compelling evidence indicates that CUMS action on the gut may exacerbate neuro-inflammation and neurodegeneration (Dodiya et al., 2020). Therefore, we further detected the histological morphology of small intestine mucosa and the related key molecules, including TLR4, occludin, and claudin-1. HFD and CUMS stimulation showed severe injuries on the villi, such as swelling and breakage. Moreover, the arrangement of lamina propria cells was completely disordered. The difference between HFD and CUMS stimulation is that the former one attenuated the thickness from the serosa to muscularis and the latter one induced the arrangement of the serosal layer loosely or fell off from the muscle layer. However, puerarin (120 mg/kg) treatment significantly restored the intestine mucosa morphology. The villi of the rats which received puerarin (120 mg/kg) were basically intact and arranged tightly, and the structure of each layer was relatively clear and complete. The intestinal hyper-permeability leads to leakiness to endotoxins. TLR4 delivers extracellular antigens into cells and induces inflammatory responses. In addition, TLR4 regulates tight junction proteins, such as occludin and claudin-1 *via* protein kinase C (PKC) hyperactivity (Wardill et al., 2014). Real-time RT-PCR and Western blotting results displayed that puerarin downregulated the mRNA and protein expressions of TLR4, resulting in increased concentrations of occludin and claudin-1. Likely, puerarin-treated groups showed a reduction of TLR4 levels in the rats' prefrontal cortex and hippocampal tissues. These data indicated that puerarin alleviated peripheral and central inflammatory damages by restoring intestinal permeability *via* TLR4 signaling pathways. Thus, we hypothesized that puerarin exerted antidepressive actions through TLR4-associated mechanisms.

TLR4 regulates COX-2 and PGE_2, which play an important role in the proliferation and apoptosis in response to intestinal mucosal damage (Fukata et al., 2006). cPLA2 is a key enzyme for membrane phospholipid metabolism. As key enzymes for the metabolism of polyunsaturated fatty acids (PUFAs) and the synthesis of PGE_2, the genetic variation of cPLA2 and COX-2 genes increases the risk of depression (Su et al., 2010). TLR4 accelerates phospholipid metabolism by activating cPLA2 to produce a large amount of arachidonic acid and free fatty acids, which leads to membrane channel activation and hemodynamic changes (Teply et al., 2016). To further explore the underlying mechanism, non-targeted lipidomics of hippocampal tissues was detected. Among the top 15 most different metabolites, 60 % were phospholipid metabolites. Thus, we mainly focused on the effect of puerarin on phospholipid metabolism. Compared with the HFD/CUMS group, three biomarkers were identified, namely, PC (15:1/20:1), PE (15:1/16:1), and PI (18:2/20:1). cPLA2 and COX-2 are two important enzymes in the process of phospholipid metabolism. Furthermore, molecular docking of puerarin-cPLA2 and puerarin-COX-2 was performed. Although the docking results indicated that puerarin exhibited moderate binding affinity to cPLA2 and weaker binding affinity to COX-2, we verified the results *in vivo* and found that puerarin significantly inhibited the enzyme activities of cPLA2 and COX-2 and decreased the production of PGE_2 in the small intestine and hippocampal tissues in a dose-dependent manner.

CONCLUSION

As illustrated in **Figure 8**, long-term HFD/CUMS stimulation evokes peripheral and central inflammation responses and TLR4 activation. The abnormal concentrations of inflammatory cytokines change the structure and function of the brain and small intestine, resulting in a depressive phenotype. The interaction between TLR4 and cytokines is complex and is difficult to evaluate if TLR4 activation is the cause or consequence of cytokine outburst. The main concern of the current study is that both TLR4 and cytokines regulate the metabolism of arachidonic acids. Puerarin treatment alleviated HFD/CUMS-induced depression-like behavior by inhibiting TLR4-associated inflammatory responses. Mechanistically, puerarin treatment restored the lipid metabolism abnormalities. For the phospholipid metabolism, puerarin not only changed the phospholipid metabolites but also inhibited the enzyme activities of cPLA2 and COX-2. In conclusion, puerarin treatment reversed HFD/CUMS-induced depression-like behavior by inhibiting TLR4-mediated inflammatory damages and phospholipid metabolism disorders. Subsequently, we will further detect the effects of puerarin on phospholipid metabolism and intestinal microflora to declare the TLR4 signaling pathway–associated functions of the brain–gut axis or other potential mechanisms.

DATA AVAILABILITY STATEMENT

The original contributions presented in the study are included in the article/Supplementary Material, further inquiries can be directed to the corresponding author.

ETHICS STATEMENT

The animal study was reviewed and approved by the Ethics Committee of Jining Medical University.

AUTHOR CONTRIBUTIONS

Conceptualization, L-NG; methodology, L-NG, MY, LZ, and YL; software, MY; validation, L-NG and JW; formal analysis, L-NG, LZ, and YL; resources, L-NG; data curation, L-NG; original draft preparation, L-NG; reviewing and editing, L-NG, CS, YF, and LD; supervision, L-NG; project administration, L-NG; funding acquisition, L-NG. All authors have read and approved the final version of the manuscript.

FUNDING

This research was funded by the National Natural Science Foundation of China, Grant Number 81903824 and the NSFC cultivation project of Jining Medical University, Grant Number JYP2018KJ04.

REFERENCES

Bădescu, S. V., Tătaru, C., Kobylinska, L., Georgescu, E. L., Zahiu, D. M., Zăgrean, A. M., et al. (2016). The Association between Diabetes Mellitus and Depression. *J. Med. Life* 9, 120–125.

Beurel, E., Toups, M., and Nemeroff, C. B. (2020). The Bidirectional Relationship of Depression and Inflammation: Double Trouble. *Neuron* 107, 234–256. doi:10.1016/j.neuron.2020.06.002

Cai, S. A., Hou, N., Zhao, G. J., Liu, X. W., He, Y. Y., Liu, H. L., et al. (2018). Nrf2 Is a Key Regulator on Puerarin Preventing Cardiac Fibrosis and Upregulating Metabolic Enzymes UGT1A1 in Rats. *Front. Pharmacol.* 9, 540. doi:10.3389/fphar.2018.00540

Cervellati, C., Trentini, A., Pecorelli, A., and Valacchi, G. (2020). Inflammation in Neurological Disorders: the Thin Boundary between Brain and Periphery. *Antioxid. Redox Signal.* 33, 191–210. doi:10.1089/ars.2020.8076

Cheng, Y., Pardo, M., Armini, R. S., Martinez, A., Mouhsine, H., Zagury, J. F., et al. (2016). Stress-induced Neuroinflammation Is Mediated by GSK3-dependent TLR4 Signaling that Promotes Susceptibility to Depression-like Behavior. *Brain Behav. Immun.* 53, 207–222. doi:10.1016/j.bbi.2015.12.012

Dodiya, H. B., Forsyth, C. B., Voigt, R. M., Engen, P. A., Patel, J., Shaikh, M., et al. (2020). Chronic Stress-Induced Gut Dysfunction Exacerbates Parkinson's Disease Phenotype and Pathology in a Rotenone-Induced Mouse Model of Parkinson's Disease. *Neurobiol. Dis.* 135, 104352. doi:10.1016/j.nbd.2018.12.012

Dong, L., Vecchio, A. J., Sharma, N. P., Jurban, B. J., Malkowski, M. G., and Smith, W. L. (2011). Human Cyclooxygenase-2 Is a Sequence Homodimer that Functions as a Conformational Heterodimer. *J. Biol. Chem.* 286, 19035–19046. doi:10.1074/jbc.M111.231969

Euteneuer, F., Dannehl, K., del Rey, A., Engler, H., Schedlowski, M., and Rief, W. (2017). Peripheral Immune Alterations in Major Depression: The Role of

Subtypes and Pathogenetic Characteristics. *Front. Psychiatry* 8, 250. doi:10.3389/fpsyt.2017.00250

Felger, J. C., Haroon, E., Patel, T. A., Goldsmith, D. R., Wommack, E. C., Woolwine, B. J., et al. (2020). What Does Plasma CRP Tell Us about Peripheral and central Inflammation in Depression. *Mol. Psychiatry* 25, 1301–1311. doi:10.1038/s41380-018-0096-3

Fu, S., Wang, J., Hao, C., Dang, H., and Jiang, S. (2019). Tetramethylpyrazine Ameliorates Depression by Inhibiting TLR4-NLRP3 Inflammasome Signal Pathway in Mice. *Psychopharmacology (Berl)* 236, 2173–2185. doi:10.1007/s00213-019-05210-6

Fukata, M., Chen, A., Klepper, A., Krishnareddy, S., Vamadevan, A. S., Thomas, L. S., et al. (2006). Cox-2 Is Regulated by Toll-like Receptor-4 (TLR4) Signaling: Role in Proliferation and Apoptosis in the Intestine. *Gastroenterology* 131, 862–877. doi:10.1053/j.gastro.2006.06.017

Gárate, I., Garcia-Bueno, B., Madrigal, J. L., Caso, J. R., Alou, L., Gomez-Lus, M. L., et al. (2013). Stress-induced Neuroinflammation: Role of the Toll-like Receptor-4 Pathway. *Biol. Psychiatry* 73, 32–43. doi:10.1016/j.biopsych.2012.07.005

Gold, S. M., Köhler-Forsberg, O., Moss-Morris, R., Mehnert, A., Miranda, J. J., Bullinger, M., et al. (2020). Comorbid Depression in Medical Diseases. *Nat. Rev. Dis. Primers* 6, 69. doi:10.1038/s41572-020-0200-2

Guo, L. T., Wang, S. Q., Su, J., Xu, L. X., Ji, Z. Y., Zhang, R. Y., et al. (2019). Baicalin Ameliorates Neuroinflammation-Induced Depressive-like Behavior through Inhibition of Toll-like Receptor 4 Expression *via* the PI3K/AKT/FoxO1 Pathway. *J. Neuroinflammation* 16, 95–21. doi:10.1186/s12974-019-1474-8

Gururajan, A., Reif, A., Cryan, J. F., and Slattery, D. A. (2019). The Future of Rodent Models in Depression Research. *Nat. Rev. Neurosci.* 20, 686–701. doi:10.1038/s41583-019-0221-6

Hirschfeld, R. M. (2000). History and Evolution of the Monoamine Hypothesis of Depression. *J. Clin. Psychiatry* 61, 4–6. doi:10.4088/jcp.v61n0405

Holsboer, F. (2000). The Corticosteroid Receptor Hypothesis of Depression. *Neuropsychopharmacology* 23, 477–501. doi:10.1016/S0893-133X(00)00159-7

Hou, B., Zhao, Y., Qiang, G., Yang, X., Xu, C., Chen, X., et al. (20182018). Puerarin Mitigates Diabetic Hepatic Steatosis and Fibrosis by Inhibiting TGF-β Signaling Pathway Activation in Type 2 Diabetic Rats. *Oxidative Med. Cell. longevity* 2018, 1–13. doi:10.1155/2018/4545321

Huang, T., Balasubramanian, R., Yao, Y., Clish, C. B., Shadyab, A. H., Liu, B., et al. (2020). Associations of Depression Status with Plasma Levels of Candidate Lipid and Amino Acid Metabolites: A Meta-Analysis of Individual Data from Three Independent Samples of US Postmenopausal Women. *Mol. Psychiatry* 26, 1–13. doi:10.1038/s41380-020-00870-9

Hung, Y. Y., Huang, K. W., Kang, H. Y., Huang, G. Y., and Huang, T. L. (2016). Antidepressants Normalize Elevated Toll-like Receptor Profile in Major Depressive Disorder. *Psychopharmacology (Berl)* 233, 1707–1714. doi:10.1007/s00213-015-4087-7

Jeon, Y. D., Lee, J. H., Lee, Y. M., and Kim, D. K. (2020). Puerarin Inhibits Inflammation and Oxidative Stress in Dextran Sulfate Sodium-Induced Colitis Mice Model. *Biomed. Pharmacother.* 124, 109847. doi:10.1016/j.biopha.2020.109847

Ji, L., Du, Q., Li, Y., and Hu, W. (2016). Puerarin Inhibits the Inflammatory Response in Atherosclerosis *via* Modulation of the NF-Kb Pathway in a Rabbit Model. *Pharmacol. Rep.* 68, 1054–1059. doi:10.1016/j.pharep.2016.06.007

Kempuraj, D., Thangavel, R., Selvakumar, G. P., Zaheer, S., Ahmed, M. E., Raikwar, S. P., et al. (2017). Brain and Peripheral Atypical Inflammatory Mediators Potentiate Neuroinflammation and Neurodegeneration. *Front Cel Neurosci* 11, 216. doi:10.3389/fncel.2017.00216

Kindler, J., Lim, C. K., Weickert, C. S., Boerrigter, D., Galletly, C., Liu, D., et al. (2020). Dysregulation of Kynurenine Metabolism Is Related to Proinflammatory Cytokines, Attention, and Prefrontal Cortex Volume in Schizophrenia. *Mol. Psychiatry* 25, 2860–2872. doi:10.1038/s41380-019-0401-9

Liu, S., Cao, X. L., Liu, G. Q., Zhou, T., Yang, X. L., and Ma, B. X. (2019). The In Silico and *In Vivo* Evaluation of Puerarin against Alzheimer's Disease. *Food Funct.* 10, 799–813. doi:10.1039/c8fo01696h

Livak, K. J., and Schmittgen, T. D. (2001). Analysis of Relative Gene Expression Data Using Real-Time Quantitative PCR and the 2(-Delta Delta C(T)) Method. *Methods* 25, 402–408. doi:10.1006/meth.2001.1262

Lu, Y., Sareddy, G. R., Wang, J., Wang, R., Li, Y., Dong, Y., et al. (2019). Neuron-Derived Estrogen Regulates Synaptic Plasticity and Memory. *J. Neurosci.* 39, 2792–2809. doi:10.1523/jneurosci.1970-18.2019

Menard, C., Pfau, M. L., Hodes, G. E., Kana, V., Wang, V. X., Bouchard, S., et al. (2017). Social Stress Induces Neurovascular Pathology Promoting Depression. *Nat. Neurosci.* 20, 1752–1760. doi:10.1038/s41593-017-0010-3

Miller, A. H., and Raison, C. L. (2016). The Role of Inflammation in Depression: from Evolutionary Imperative to Modern Treatment Target. *Nat. Rev. Immunol.* 16, 22–34. doi:10.1038/nri.2015.5

Pariante, C. M. (2017). Why Are Depressed Patients Inflamed? A Reflection on 20 Years of Research on Depression, Glucocorticoid Resistance and Inflammation. *Eur. Neuropsychopharmacol.* 27, 554–559. doi:10.1016/j.euroneuro.2017.04.001

Pedraz-Petrozzi, B., Neumann, E., and Sammer, G. (2020). Pro-inflammatory Markers and Fatigue in Patients with Depression: A Case-Control Study. *Sci. Rep.* 10, 1–12. doi:10.1038/s41598-020-66532-6

Pothion, S., Bizot, J. C., Trovero, F., and Belzung, C. (2004). Strain Differences in Sucrose Preference and in the Consequences of Unpredictable Chronic Mild Stress. *Behav. Brain Res.* 155, 135–146. doi:10.1016/j.bbr.2004.04.008

Qiu, Z. K., Zhang, G. H., Zhong, D. S., He, J. L., Liu, X., Chen, J. S., et al. (2017). Puerarin Ameliorated the Behavioral Deficits Induced by Chronic Stress in Rats. *Sci. Rep.* 7, 6266. doi:10.1038/s41598-017-06552-x

Rahimifard, M., Maqbool, F., Moeini-Nodeh, S., Niaz, K., Abdollahi, M., Braidy, N., et al. (2017). Targeting the TLR4 Signaling Pathway by Polyphenols: a Novel Therapeutic Strategy for Neuroinflammation. *Ageing Res. Rev.* 36, 11–19. doi:10.1016/j.arr.2017.02.004

Rohr, M. W., Narasimhulu, C. A., Rudeski-Rohr, T. A., and Parthasarathy, S. (2020). Negative Effects of a High-Fat Diet on Intestinal Permeability: A Review. *Adv. Nutr.* 11, 77–91. doi:10.1093/advances/nmz061

Sanacora, G., Treccani, G., and Popoli, M. (2012). Towards a Glutamate Hypothesis of Depression: an Emerging Frontier of Neuropsychopharmacology for Mood Disorders. *Neuropharmacology* 62, 63–77. doi:10.1016/j.neuropharm.2011.07.036

Schevitz, R. W., Bach, N. J., Carlson, D. G., Chirgadze, N. Y., Clawson, D. K., Dillard, R. D., et al. (1995). Structure-based Design of the First Potent and Selective Inhibitor of Human Non-pancreatic Secretory Phospholipase A2. *Nat. Struct. Biol.* 2, 458–465. doi:10.1038/nsb0695-458

Su, K. P., Huang, S. Y., Peng, C. Y., Lai, H. C., Huang, C. L., Chen, Y. C., et al. (2010). Phospholipase A2 and Cyclooxygenase 2 Genes Influence the Risk of Interferon-Alpha-Induced Depression by Regulating Polyunsaturated Fatty Acids Levels. *Biol. Psychiatry* 67, 550–557. doi:10.1016/j.biopsych.2009.11.005

Tantipongpiradet, A., Monthakantirat, O., Vipatpakpaiboon, O., Khampukdee, C., Umehara, K., Noguchi, H., et al. (2019). Effects of Puerarin on the Ovariectomy-Induced Depressive-like Behavior in ICR Mice and its Possible Mechanism of Action. *Molecules* 24, 4569. doi:10.3390/molecules24244569

Teply, R. M., Packard, K. A., White, N. D., Hilleman, D. E., and DiNicolantonio, J. J. (2016). Treatment of Depression in Patients with Concomitant Cardiac Disease. *Prog. Cardiovasc. Dis.* 58, 514–528. doi:10.1016/j.pcad.2015.11.003

Velloso, L. A., Folli, F., and Saad, M. J. (2015). TLR4 at the Crossroads of Nutrients, Gut Microbiota, and Metabolic Inflammation. *Endocr. Rev.* 36, 245–271. doi:10.1210/er.2014-1100

Wallace, A. C., Laskowski, R. A., and Thornton, J. M. (1995). LIGPLOT: a Program to Generate Schematic Diagrams of Protein-Ligand Interactions. *Protein Eng.* 8, 127–134. doi:10.1093/protein/8.2.127

Wang, M., Gui, X., Wu, L., Tian, S., Wang, H., Xie, L., et al. (2020). Amino Acid Metabolism, Lipid Metabolism, and Oxidative Stress Are Associated with post-stroke Depression: a Metabonomics Study. *BMC Neurol.* 20, 1–10. doi:10.1186/s12883-020-01780-7

Wardill, H. R., Gibson, R. J., Logan, R. M., and Bowen, J. M. (2014). TLR4/PKC-mediated Tight junction Modulation: a Clinical Marker of Chemotherapy-Induced Gut Toxicity. *Int. J. Cancer* 135, 2483–2492. doi:10.1002/ijc.28656

World Health, O. (2017). *Depression and Other Common Mental Disorders: Global Health Estimates*. Geneva: World Health Organization.

Wu, M. K., Huang, T. L., Huang, K. W., Huang, Y. L., and Hung, Y. Y. (2015). Association between Toll-like Receptor 4 Expression and Symptoms of Major Depressive Disorder. *Neuropsychiatr. Dis. Treat.* 11, 1853–1857. doi:10.2147/NDT.S88430

Xu, H. B., Zhang, R. F., Luo, D., Zhou, Y., Wang, Y., Fang, L., et al. (2012). Comparative Proteomic Analysis of Plasma from Major Depressive Patients: Identification of Proteins Associated with Lipid Metabolism and Immunoregulation. *Int. J. Neuropsychopharmacol.* 15, 1413–1425. doi:10.1017/S1461145712000302

Yiu, J. H., Dorweiler, B., and Woo, C. W. (2017). Interaction between Gut Microbiota and Toll-like Receptor: from Immunity to Metabolism. *J. Mol. Med. (Berl)* 95, 13–20. doi:10.1007/s00109-016-1474-4

Zhao, J., Luo, D., Liang, Z., Lao, L., and Rong, J. (2017). Plant Natural Product Puerarin Ameliorates Depressive Behaviors and Chronic Pain in Mice with Spared Nerve Injury (SNI). *Mol. Neurobiol.* 54, 2801–2812. doi:10.1007/s12035-016-9870-x

Zhou, Y. X., Zhang, H., and Peng, C. (2014). Puerarin: a Review of Pharmacological Effects. *Phytother Res.* 28, 961–975. doi:10.1002/ptr.5083

Conflict of Interest: The authors declare that the research was conducted in the absence of any commercial or financial relationships that could be construed as a potential conflict of interest.

Publisher's Note: All claims expressed in this article are solely those of the authors and do not necessarily represent those of their affiliated organizations, or those of the publisher, the editors, and the reviewers. Any product that may be evaluated in this article, or claim that may be made by its manufacturer, is not guaranteed or endorsed by the publisher.

Copyright © 2021 Gao, Yan, Zhou, Wang, Sai, Fu, Liu and Ding. This is an open-access article distributed under the terms of the Creative Commons Attribution License (CC BY). The use, distribution or reproduction in other forums is permitted, provided the original author(s) and the copyright owner(s) are credited and that the original publication in this journal is cited, in accordance with accepted academic practice. No use, distribution or reproduction is permitted which does not comply with these terms.

frontiers in Pharmacology

ORIGINAL RESEARCH
published: 20 December 2021
doi: 10.3389/fphar.2021.766474

Shugan Hewei Decoction Alleviates Cecum Mucosal Injury and Improves Depressive- and Anxiety-Like Behaviors in Chronic Stress Model Rats by Regulating Cecal Microbiota and Inhibiting NLRP3 Inflammasome

Yingying Yue[1,2], Yu Chen[1,2], Hao Liu[1], Lesi Xu[1,2], Xian Zhou[1], Hao Ming[3], Xin Chen[1], Miaoqi Chen[1], Yunya Lin[1], Lin Liu[1], Yingqian Zhao[1] and Songlin Liu[1]**

[1]College of Traditional Chinese Medicine, Hubei University of Chinese Medicine, Wuhan, China, [2]Institute of Classical Prescription Applications, Hubei University of Chinese Medicine, Wuhan, China, [3]School of Medicine, Jianghan University, Wuhan, China

OPEN ACCESS

Edited by:
Zhaocheng Ma,
Huazhong Agricultural University, China

Reviewed by:
Wenzhi Hao,
Jinan University, China
Bing Li,
Fudan University, China

***Correspondence:**
Yingqian Zhao
zhaoyingqian2000@163.com
Songlin Liu
newforest@163.com

Specialty section:
This article was submitted to Ethnopharmacology, a section of the journal Frontiers in Pharmacology

Received: 29 August 2021
Accepted: 08 November 2021
Published: 20 December 2021

Citation:
Yue Y, Chen Y, Liu H, Xu L, Zhou X, Ming H, Chen X, Chen M, Lin Y, Liu L, Zhao Y and Liu S (2021) Shugan Hewei Decoction Alleviates Cecum Mucosal Injury and Improves Depressive- and Anxiety-Like Behaviors in Chronic Stress Model Rats by Regulating Cecal Microbiota and Inhibiting NLRP3 Inflammasome. Front. Pharmacol. 12:766474. doi: 10.3389/fphar.2021.766474

Chronic stress is a significant cause of depression, anxiety, and intestinal mucosal injury. Gut microbiota disturbances are also associated with these disorders. Shugan Hewei Decoction (SHD), which is a traditional Chinese medicine formula developed by our team, has shown superior therapeutic effects in the treatment of depression, anxiety, and functional gastrointestinal diseases caused by chronic stress. In this study, we investigated the modulatory effect of SHD on the cecal microbiota and cecum mucosal NOD-like receptor protein 3 (NLRP3) inflammasome in a chronic unpredictable stress (CUS)/social isolation rat model. After the SHD intervention, the CUS model rats showed improvements in their depressive- and anxiety-like behaviors, as well as sustained body weight growth and improved fecal characteristics. SHD improved the cecal microbiota diversity and changed the abundance of six microbial genera. A Spearman's correlation analysis showed a strong correlation between the NLRP3 inflammasome and CUS-perturbed cecal biomarker microbiota. SHD regulated the excessive expression of NLRP3, ASC, caspase-1, interleukin-1β (IL-1β), and IL-18 in the serum and cecum mucosa induced by CUS, as well as the activation of the Toll-like receptor 4/nuclear factor-κB signaling cascades. Our results reveal the pharmacological mechanisms of SHD and provide a validated therapeutic method for the treatment of depression, anxiety, and cecum mucosal injury.

Keywords: chronic stress, cecal microbiota, NLRP3 inflammasome, Shugan Hewei Decoction, traditional Chinese medicine

INTRODUCTION

Chronic stress due to social pressure or negative emotional stimulation can lead to psychological and somatic manifestations, such as anxiety, depression, and functional gastrointestinal disorders (Qin et al., 2014; Stefanaki et al., 2018), all of which endanger public physical and psychological health (Baxter et al., 2013). Depression and anxiety are the most common psychiatric disorders, and they are

currently recognized by WHO as the fourth most prevalent contributors to the global burden of disease (Liang et al., 2016). Depression and anxiety can disturb the homeostasis of the gastrointestinal tract, resulting in loss of appetite, abdominal distension, abdominal pain, abnormal bowel habits, changes in fecal traits, and other symptoms (Bhatia and Tandon, 2005). Chronic stress-induced gastrointestinal symptoms are associated with intestinal mucosal injury, which further exacerbates inflammatory reactions (Wei et al., 2019). Moreover, the intestinal microbiome plays an important role in the incidence of gastrointestinal diseases induced by mental and psychological factors (Karl et al., 2018). Intestinal microbiome disturbances have been reported in both chronic stress primate (Zheng et al., 2020) and rodent models (Ding et al., 2020), and these disturbances are related to NOD-like receptor protein 3 (NLRP3) inflammasome activation in the intestinal mucosa (Inserra et al., 2018; Hao et al., 2021). The NLRP3 inflammasome acts as a bridge between stress and the intestinal immune response, and it plays a dual role in promoting inflammation and maintaining intestinal homeostasis, both of which affect gastrointestinal function (Lamkanfi and Dixit, 2014). The intestinal microbiota and NLRP3 inflammasome are involved in the development of depression, anxiety, and functional gastrointestinal disorders that are induced by chronic stress; thus, they are recognized as potential targets for managing stress-related diseases.

The NLRP3 inflammasome, which is a multimeric protein complex consisting of a cytoplasmic innate receptor (NLRP3), an apoptosis-associated speck-like protein containing a CARD domain (ASC), and a cysteinyl aspartate specific proteinase (caspase-1) (Kim and Jo, 2013), is responsible for activating inflammatory responses upon infection and cellular damage. NLRP3 inflammasome activation correlates with stress responses (Fleshner et al., 2017), depressive- and anxiety-like behaviors, and gut microbiota composition (Wong et al., 2016). It also plays a major role in regulating chronic intestinal inflammation and the maturation of interleukin-1β (IL-1β) and IL-18, both of which are associated with an increased risk of colitis development (Perera et al., 2017). The NLRP3 inflammasome is closely related to the intestinal microbiota, which plays an important role in maintaining gastrointestinal and mental health along the brain–gut axis that connects the central nervous system and the human gastrointestinal tract. There is mounting data indicating that cumulative stress resulting from psychological, environmental, and physical stressors has a consistent and meaningful impact on the intestinal microbiota (Karl et al., 2018), and intestinal microbiota participate in the pathogenesis of gastrointestinal dysfunction mediated by chronic stress.

Shugan Hewei Decoction (SHD), which is a traditional Chinese medicine formula developed by our team, is used clinically to treat various stomach disorders, including functional gastrointestinal diseases induced by chronic stress. It was developed based on the formula for Sini San (SNS) in *Treatise on Febrile Diseases*, which is an ancient Chinese medicine book that was written about 1,800 years ago. SNS is composed of four herbs: *Bupleurum chinense* DC. (Apiaceae; Bupleuri Radix), *Paeonia lactiflora* Pall. (Paeoniaceae; Paeoniae Radix Alba), *Citrus* × *aurantium* L. (Rutaceae; Aurantii Fructus Immaturus), and *Glycyrrhiza uralensis* Fisch. ex DC. (Fabaceae; Glycyrrhizae Radix et Rhizoma). It has been applied clinically for the treatment of mental and gastrointestinal disorders, including depression and functional gastrointestinal disorders (Shen et al., 2016). SNS can improve depressive behaviors by inhibiting inflammation (Zong et al., 2019). SHD, which is an advanced version of SNS that has six additional Chinese herbs, provides improved therapeutic effects and longer efficacy for managing depression and gastrointestinal disorders. SHD is composed of the following commonly used Chinese herbs: *Bupleurum chinense* DC. (Apiaceae; Bupleuri Radix), *Paeonia lactiflora* Pall. (Paeoniaceae; Paeoniae Radix Alba), *Citrus* × *aurantium* L. (Rutaceae; Aurantii Fructus Immaturus), *Curcuma aromatica* Salisb. (Zingiberaceae; Curcumae Radix), *Wurfbainia villosa* (Lour.) Skornick. and A.D.Poulsen (Zingiberaceae; Amomi Fructus), *Atractylodes macrocephala* Koidz.(Asteraceae; Atractylodis Macrocephalae Rhizoma), *Aucklandia costus* Falc. (Asteraceae; Aucklandiae Radix), *Coptis chinensis* Franch. (Ranunculaceae, Coptidis Rhizoma), *Tetradium ruticarpum* (A.Juss.) T.G.Hartley (Rutaceae; Euodiae Fructus), and *Glycyrrhiza uralensis* Fisch. ex DC. (Fabaceae; Glycyrrhizae Radix et Rhizoma) (**Figure 1**). Our previous studies have shown that the SHD formulation and its active substance fractions can improve depressive-like behaviors in a chronic unpredictable stress (CUS)–induced rat model by regulating the release of neurotransmitters (Glu and GABA) in the hypothalamus and inducing the synergistic effects of several neurotransmitters (DA, 5-HT, NA, 5-HIAA) in the PFC-NAc-VTA neural circuit (Mou et al., 2019; Chen et al., 2021). However, the mechanism by which SHD improves gastrointestinal disorders and whether cecal microbiota, intestinal inflammation, and the NLRP3 inflammasome are related to the SHD antidepressant mechanism remain unclear.

In this study, we identified the chemical constituents of SHD and analyzed the active compounds in medicated rat serum using HPLC-TOF-MS/MS. We demonstrated that SHD may alleviate cecum mucosal injury by maintaining intestinal microbiota homeostasis and inhibiting the excessive activation of the NLRP3 inflammasome and Toll-like receptor 4 (TLR4)/nuclear factor (NF)-κB signaling pathway, which also improves depressive-like behaviors and the ability of SHD to regulate neurotransmitter release. Our study provides an advanced therapeutic method for the treatment of chronic stress-related diseases.

MATERIALS AND METHODS

Animal Care and Use

A total of 84 healthy male Sprague–Dawley SPF rats (SYXK (E) 2017-0067) weighing 160–200 g were purchased from the Chinese Center for Disease Control and Prevention (Wuhan, Hubei, China), and subjected to a 7-day adaptive feeding process prior to starting the formal experiment. The rats were housed in the SPF Animal Lab at the Hubei University of Chinese Medicine

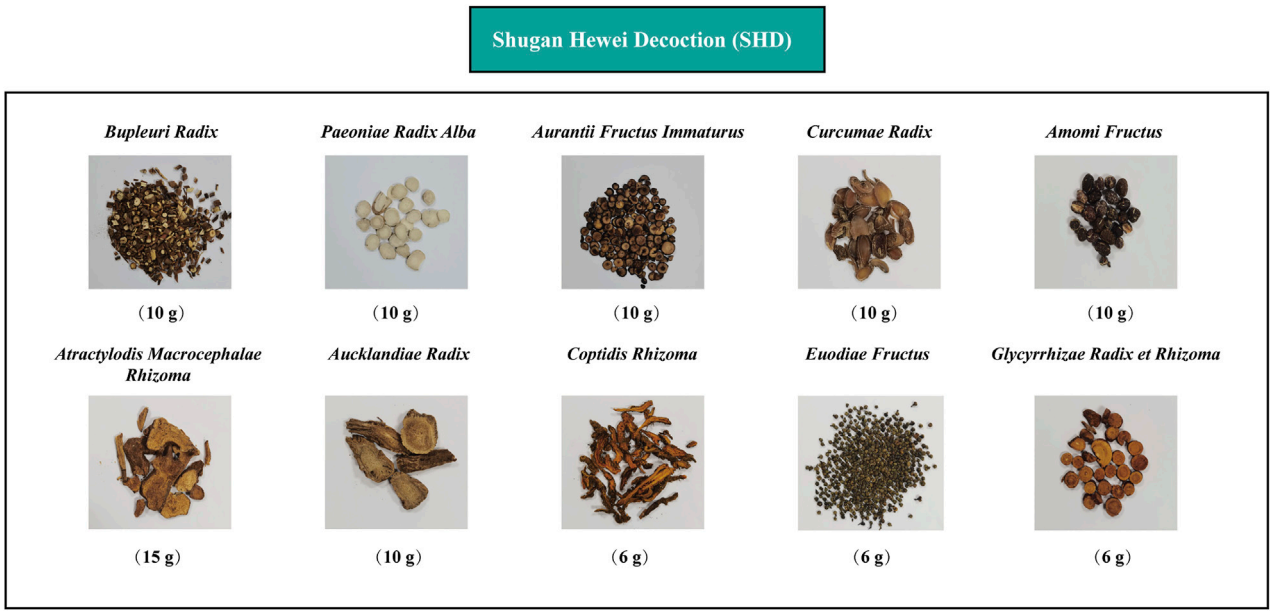


FIGURE 1 | Chinese herbs formula of Shugan Hewei Decoction (SHD).

under a 12-h light/dark cycle at a constant temperature (25 ± 1°C) and humidity (55–65% relative humidity) with *ad libitum* access to food and water. After 7 days of acclimatization to the environment, 80 rats with similar body weights were selected and randomly divided into a control group (12 rats) and a model group (68 rats), and all the model group rats were housed independently. The model rats were subjected to seven different chronic unpredictable stress (CUS) for 21 days. The 8 CUS-resistant rats were screened out using the sucrose preference test (SPT), open field test (OFT), and forced swimming test (FST) after 3 weeks of exposure to CUS. The remaining 60 rats were randomly divided into the following five groups: a model group, a low SHD dosage (SHD-L) group, a high SHD dosage (SHD-H) group, a SNS group, and a fructooligosaccharide (FOS) group, with 12 rats in each group (**Figure 2A**). The animal experiments were reviewed and approved by the Animal Ethics Committee (HUCMS 201903009), and all the experiments complied with current animal welfare guidelines.

Drug Preparation and Intervention

The SHD consists of 10 herbs, containing *Bupleurum chinense* DC. (Apiaceae; Bupleuri Radix), 10 g; *Paeonia lactiflora* Pall. (Paeoniaceae; Paeoniae Radix Alba), 10 g; *Citrus* × *aurantium* L. (Rutaceae; Aurantii Fructus Immaturus), 10 g; *Curcuma aromatica* Salisb. (Zingiberaceae; Curcumae Radix), 10 g; *Wurfbainia villosa* (Lour.) Skornick. and A.D.Poulsen (Zingiberaceae; Amomi Fructus), 10 g; *Atractylodes macrocephala* Koidz. (Asteraceae; Atractylodis Macrocephalae Rhizoma), 15 g; *Aucklandia costus* Falc. (Asteraceae; Aucklandiae Radix), 10 g; *Coptis chinensis* Franch. (Ranunculaceae, Coptidis Rhizoma), 6 g; *Tetradium ruticarpum* (A.Juss.) T.G.Hartley (Rutaceae; Euodiae Fructus), 6 g; and *Glycyrrhiza uralensis* Fisch. ex DC. (Fabaceae; Glycyrrhizae Radix et Rhizoma), 6 g (**Figure 1**, **Supplementary Table S1**). The SNS consists of four herbs, containing *Bupleurum chinense* DC. (Apiaceae; Bupleuri Radix), 10 g; *Paeonia lactiflora* Pall. (Paeoniaceae; Paeoniae Radix Alba), 10 g; *Citrus* × *aurantium* L. (Rutaceae; Aurantii Fructus Immaturus), 10 g; and *Glycyrrhiza uralensis* Fisch. ex DC. (Fabaceae; Glycyrrhizae Radix et Rhizoma), 10 g. All the raw herbs were provided by Tianji Pharmaceutical Co., Ltd (Hubei, China) and produced based on the procedure described in the Chinese Pharmacopoeia 2015 Edition (National Pharmacopoeia Commission, 2015). The weights of each herb were determined according to the clinical dose. Dry FOS powder (Batch No. 1903303301, purity ≥95.0%) was prepared by the Quantum Hi-Tech Biological Co. Ltd. (Guangzhou City, China) in accordance with the process described in the PRC National Standard GB/T 23528-2009.

Briefly, SHD raw herb weights in total of 930 g (10 doses of raw herbs of SHD) was soaked and then extracted with 10-fold mass of water (9,300 ml). First, 1.38 g of volatile oil (yield of 0.15%) and 23.7 g of aromatic water (yield of 2.55%) were extracted by steam distillation and then stored at −20°C; then by water extraction and alcohol precipitation method, the raw herb was boiled for 3 times, 2 h each, the water exact from each time were retrieved and mixed, then concentrated down to 930 ml (equal to 1 g crude herb/ml) by water bath method. The water extract was filtrated and 74.20 g of polysaccharides was obtained (yield of 7.98%), and the remaining liquid supernatant was concentrated by rotary evaporator and 242.20 g of extractum was obtained (yield of 26.0%); the polysaccharides and extractum were kept in a desiccator before use. The SHD total extract was obtained with

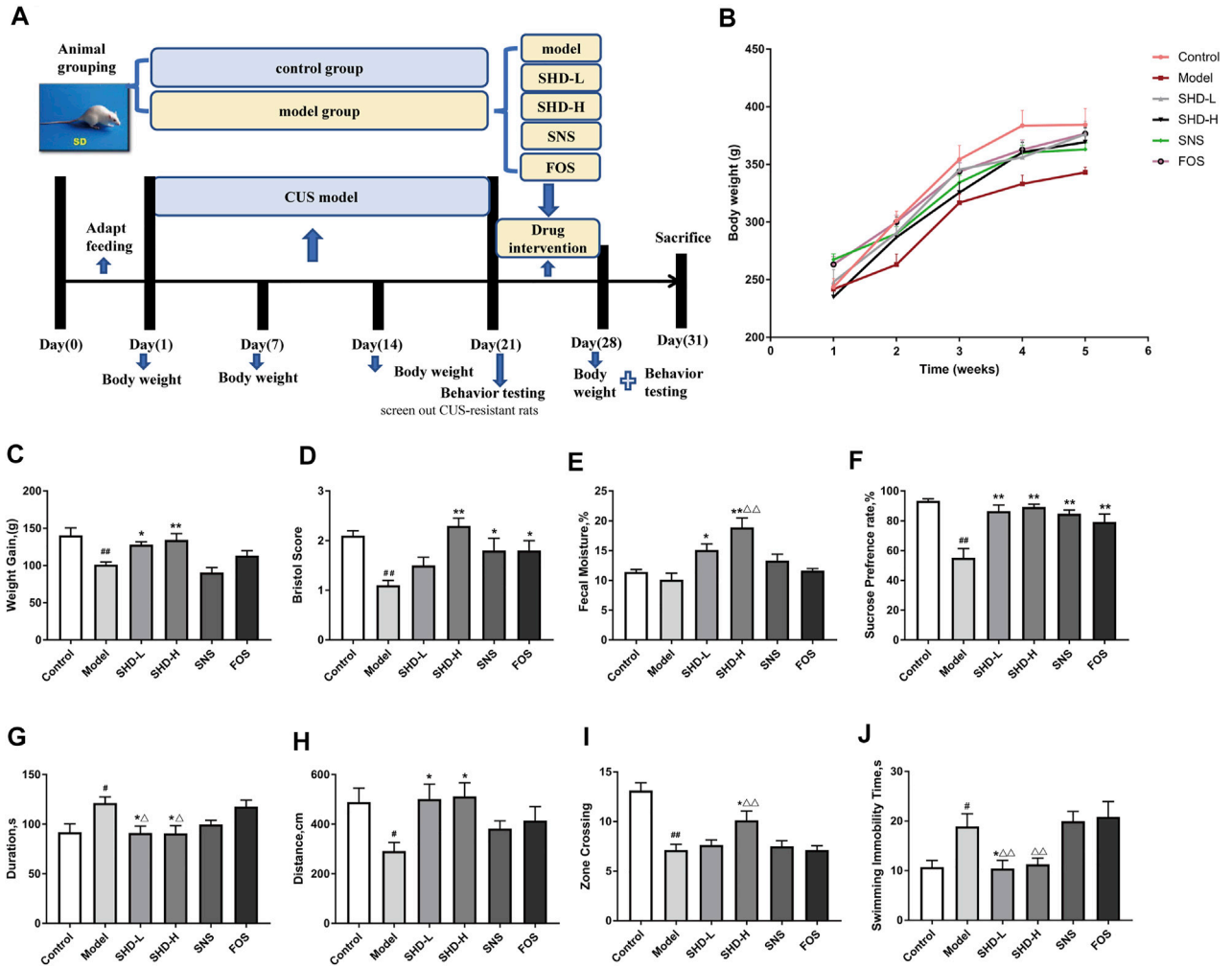


FIGURE 2 | Schematic diagram of the experimental procedures used in this study and the effects of SHD on the weight, fecal traits, and depressive-like behaviors of chronic unpredictable stress (CUS) model rats. **(A)** An experimental flowchart detailing the feeding, grouping, drug interventions, and measuring of the rats. **(B)** Changes in the body weights of the CUS model rats (n = 8). **(C)** Effect of SHD on the weight gains experienced by the CUS model rats (n = 8–9). **(D)** Effect of SHD on the Bristol evaluation scores for the CUS model rats (n = 10). **(E)** Effect of SHD on the fecal moisture content in the CUS model rats (n = 5). **(F)** The sucrose preference rate from the sucrose preference test (SPT) (n = 8). **(G)** The stationary time observed during the open field test (OFT) (n = 8). **(H)** The total movement distance observed during the OFT (n = 8). **(I)** The number of central areas crossing the lattice during the OFT (n = 8). **(J)** The immobility time observed during the forced swimming test (FST) (n = 8). The data are expressed as the mean ± SEM. $^{\#}p < 0.05$, $^{\#\#}p < 0.01$ *vs.* the control group. $^{*}p < 0.05$, $^{**}p < 0.01$ *vs.* the model group. $^{\Delta}p<0.05$, $^{\Delta\Delta}p<0.01$ *vs.* the FOS group. SHD-L, the low dosage of the Shugan Hewei Decoction; SHD-H, the high dosage of the Shugan Hewei Decoction; SNS, Sini San; FOS, fructooligosaccharide.

a yield of 36.7% (341.48 g: 930 g). Distilled water was used to solve SHD total extract into liquid with the concentration of 0.56 g crude drug/ml (the SHD low dose) and 1.12 g crude drug/ml (the SHD high dose). The SNS preparation method is the same as that of SHD. The SNS total extract was obtained with a yield of 38.4% (153.6 g: 400 g) and SNS liquid with the concentration of 0.48 g crude drug/ml. The FOS solution is prepared according to the relevant literature (Chi et al., 2020), with the concentration of 0.315 g/ml. After completion, all the solution was divided and sterilized, and then stored at 4°C for later. The intragastric administration dosage was calculated based on the clinical equivalent dosage for an adult. The FOS was administered intragastrically (3.15 g/kg/day). The SHD-L dosage was 1.34 g/kg/day (3.67 g crude drug/kg/d), and the SHD-H dosage was 2.68 g/kg/day (7.34 g crude drug/kg/day). The high dose was the clinical equivalent. The SNS dosage was 1.21 g/kg/day (3.15 g crude drug/kg/day) (Zhu et al., 2020). The control group rats were given free access to food and water, and five rats were housed in each cage. The model group rats received an equal volume of distilled water, while the other four groups received the corresponding drug interventions for 7 days, twice a day.

HPLC-TOF-MS/MS Analysis of SHD

An HPLC-TOF-MS/MS analysis was conducted to identify the main chemical components of the SHD preparation. The SHD concentration was 1 g/ml (a 1-ml solution containing 1 g of the original herbs). The standards for paeoniflorin (Lot X12A8C33672) and palmatine chloride (Lot Z12J7X15968)

were provided by Shanghai Yuanye Bio-Technology Co., Ltd. (purity ≥98%, Chengdu, China). Saikosaponin A (Lot 110,777–201,711, purity ≥91.3%), naringin (Lot 110,722–201,815, purity ≥91.3%), neohesperidin (Lot 111,857–201,703, purity ≥99.2%), hesperidin (Lot 10,721–201,818, purity ≥96.2%), liquiritin (Lot 111,610–201,607, purity ≥93.1%), and glycyrrhetinic acid (Lot 110,723–201,715, purity ≥99.6%) were provided by the National Institutes for Food and Drug Control (Beijing, China). The HPLC was performed on an Agilent 1260 Infinity HPLC system (Agilent Technologies, Santa Clara, California, USA) equipped with an Agilent ZorBax Eclipse Plus C18 RRHD (2.1 × 50 mm, 1.8 μm). The mobile phase was eluted with 0.1% formic acid ultra-pure water (A) and acetonitrile (B) in gradient mode. The acetonitrile proportion varied according to the gradient elution program: 0–3 min, 90% A; 3–8 min, 90–65% A; 8–10 min, 65–40% A; 10–16 min, 40–20% A at a flow rate of 0.4 ml/min. An electrospray ion source was used to collect the data under the positive and negative ion modes. The full-mass scanning range was 150–1,500 m/z. The column temperature was 30°C, and the detection wavelength was set at 275 nm.

Preparation of SHD-Containing Serum

Briefly, to collect the SHD-containing serum and the control serum, 20 Sprague–Dawley rats were randomly divided into two groups: one group was treated with SHD (14.68 g/kg), and the other group was treated with normal saline (10 ml/kg). Blood samples from each of the rats were then centrifuged at 3,500×*g* for 10 min at 4°C, and the serum was filtered through a 0.22-μm microporous membrane.

Chronic Unpredictable Stress

The CUS procedure was performed as previously described (Willner et al., 1987), although with slight modifications. In brief, the rats were exposed to a randomly selected stressor daily for 21 days. The stressors included food deprivation for 24 h, water deprivation for 24 h, tail squeezing for 1 min, swimming in 4°C water for 5 min, shaking 1 time/s for 5 min, reversal of the light/dark cycle, and shocking the plantar surface (50 mV, stimulation once every 5 s, intermittent 5 s, 10 times in total; **Supplementary Table S2**). Food and water were freely available to the control group rats, which remained undisturbed on another shelf, except for the 12-h deprivation period prior to each sucrose test.

Body Weight and Feces Traits

The body weight of each of the rats was recorded 1 day prior to the initiation of the experiments (day 0), as well as on days 7 and 21 of the interventions and 7 days (day 28) after the interventions. The body weight growth was calculated using the formula (Wn – W28)/W28 × 100%, in which W28 is the body weight on the last day of the intervention and W0 is the body weight on the last acclimation day. Changes in the general conditions and fecal characteristics between the groups and at different time points were recorded. The fecal Bristol scores and moisture contents were measured 12 h after the end of the last administration and before the sample collection. Rats in each group were placed in metabolic cages and fed in single cages lined with white paper. Centrifuge tubes (50 ml) were placed at the bottom of the cages to separate urine, avoiding the influence on the feces traits. The fecal traits of the rats were observed for 12 h, after which fecal samples were collected in centrifuge tubes. The average score of Bristol was calculated for each group according to the Bristol stool form scale (**Supplementary Table S3**) (Lewis and Heaton, 1997). The weight of the wet fecal samples was measured, and the average value was recorded as "A". The centrifuge tubes were then placed in a drying box for 2 h, after which they were weighed again, with the average value recorded as "B". The fecal moisture content was calculated using the following formula: fecal moisture content = (A − B)/A × 100%.

Behavioral Testing

Behavioral testing was performed as previously described (Moretti et al., 2019) in 7 days after the interventions (day 28).

For the SPT, the rats were given two bottles of 1% sucrose solution on the first training day. After 24 h, one of the 1% sucrose bottles was replaced with sterile water. After the adaptation phase, the rats were deprived of water and food for 23 h. The rats were then given free access to both water and 1% sucrose solution for 2 h, after which the remaining amounts of water and sucrose solution were measured. The sucrose preference ratio was determined using the following formula: sucrose preference ratio (%) = sucrose intake (ml) × 100%/[sucrose intake (ml) + water intake (ml)].

The OFT was performed at the end of the SPT. The OFT device included a field reaction box (90 cm × 90 cm×45 cm) and an automatic data acquisition system. The color of the inner wall of the reaction box was black, and the bottom surface was divided into small squares (5 cm × 5 cm). A digital camera was secured 2 m above the device, and its field-of-view covered the entire interior of the box. During the experiment, a rat was placed in the center of the reaction box, which was in a dark and quiet room. A SMART 3.0 animal behavior video acquisition system (Panlab, Barcelona, Spain) was used to record images of the rats for 5 min during the OFT, and the total movement distance, stationary time, and number of times that the rats crossed the central areas were analyzed over a 3-min span. The OFT was scheduled to take place between 8 and 12 a.m. To minimize cross-contamination, the experimental area was cleaned using 75% ethanol after each rat completed the test. To avoid subjectivity errors, both anxiety-like behavior tests were independently evaluated by two trained observers.

The FST was used to detect depressive-like behavior as characterized by immobility during a forced swim, as we described previously (Brenes et al., 2006). A pre-forced swim was conducted for 15 min 1 day before the actual test. During the test, each rat was placed inside a cylinder filled with water (the water temperature was controlled at 25 ± 1°C). During the FST, there is a period of vigorous activity during which the rat tries to escape, followed by a characteristic immobility, in which the rat only moves to maintain its head above water. In the current study, the immobility time was defined as the time during which the rat stopped struggling and floated in the water or only made small body movements to keep its head afloat. In the FST, this physical

immobility is used as an indicator of behavioral despair. The immobility time for each rat was recorded and measured independently by two trained observers within a test period of 6 min.

Sample Collection and Preparation

The rats were anesthetized using an intraperitoneal injection of pentobarbital sodium (50 mg/kg), after which different sample materials were collected from the rats in each group. For the rats numbered 1–6 in each group: first, a 6-ml sample of blood was taken from the abdominal aorta and placed in a coagulation tube at room temperature for 1 h, after which the tubes were placed at 4°C overnight. The blood was then centrifuged at 3,000 rpm at 4°C for 10 min, and the serum was collected from each tube and stored at −20°C for later use. The cecal contents (2 ml) were collected from each rat using a sterile tube under sterile environmental conditions, and approximately 1–2 cm of cecal tissue was also collected. The aforementioned samples were immediately stored at −80°C. The serum samples were analyzed using ELISA to detect the expression of the NLRP3 inflammasome and related inflammatory cytokines. The cecal contents were sequenced using the 16S rRNA high-throughput method to detect the structure of and changes in the cecal microbiota. The cecal tissues were detected using RT-PCR and western blotting to observe the expression of related mRNAs and proteins.

A 4% paraformaldehyde aortic perfusion and fixation was performed for the rats numbered 7–12 in each group. The cecal contents (2 ml) were collected from each of these rats using sterile tubes under sterile environmental conditions, and the cecal samples were immersed in liquid nitrogen and ultimately transferred to −80°C. In addition, cecal tissues (1–2 cm) were separated and fixed in 4% paraformaldehyde at 4°C for 4–6 h. The cecal tissues were then embedded in paraffin and sagittal sections were removed. The pathological morphology of the fixed cecal tissues was observed using H&E staining. An immunofluorescence (IF) co-localization analysis was used to detect the NLRP3 inflammasome in the cecal tissues. The cecal content detection method for these samples was the same as described previously.

H&E Staining of Cecal Tissue

After the cecal tissues were fixed in 4% paraformaldehyde, they were dehydrated using gradient ethanol and embedded in paraffin. The paraffin sections were then deparaffinized, and the tissues were cut into 4-μm-thick sections and stained with H&E (hematoxylin stained the nucleus and eosin stained, dehydrated, and sealed the cytoplasm). Finally, images of the cecum mucosal tissues were captured using an optical microscope (Nikon Eclipse CI, Tokyo, Japan) and analyzed using an image acquisition system (Nikon DS-U3, Tokyo, Japan) to evaluate their histopathology.

16S rRNA Gene Sequencing of Cecal Contents

DNA Extraction and PCR Amplification

Microbial community genomic DNA was extracted from the cecal contents samples using the E.Z.N.A.® soil DNA Kit (Omega Bio-tek, Norcross, GA, USA) according to the manufacturer's instructions. The DNA extract was checked on a 1% agarose gel, and DNA concentration and purity were determined using a NanoDrop 2000 UV–vis spectrophotometer (Thermo Scientific, Wilmington, DE, USA).

The V3–V4 hypervariable region of the bacterial 16S rRNA gene was amplified with primer pairs 338 F (5′-ACTCCTACG GGAGGCAGCAG-3′) and 806 R (5′-GGACTACHVGGGTWTCTAAT-3′) using an ABI GeneAmp 9700 PCR thermocycler (ABI, Foster City, CA, USA). The PCR amplification was performed as follows: initial denaturation at 95°C for 3 min, followed by 27 cycles of denaturing at 95°C for 30 s, annealing at 55°C for 30 s and extension at 72°C for 45 s, and single extension at 72°C for 10 min, and end at 4°C. The PCR mixtures contained 5× TransStart FastPfu buffer (4 μl), 2.5 mM dNTPs (2 μl), 5 μM forward primer (0.8 μl), 5 μM reverse primer (0.8 μl), TransStart FastPfu DNA polymerase (0.4 μl), template DNA (10 ng), and ddH_2O (up to 20 μl). The PCR reactions were performed in triplicate, and the PCR product was extracted from a 2% agarose gel and purified using an AxyPrep DNA Gel Extraction Kit (Axygen Biosciences, Union City, CA, USA) according to the manufacturer's instructions. The purified product was then quantified using a Quantus Fluorometer (Promega, Madison, WI, USA).

Illumina MiSeq Sequencing

The purified amplicons were pooled in equimolar amounts and paired-end sequenced on an Illumina MiSeq PE300/NovaSeq PE250 platform (Illumina, San Diego, CA, USA) according to the standard protocols developed by Majorbio Bio-Pharm Technology Co. Ltd. (Shanghai, China). The raw reads were deposited in the NCBI Sequence Read Archive database (accession number: SRP324274).

Processing of Sequencing Data

The raw 16S rRNA gene sequencing reads were demultiplexed, quality-filtered by fastp version 0.20.0 (Chen et al., 2018), and merged using FLASH version 1.2.7 (Magoč and Salzberg, 2011) with the following criteria: 1) the 300-bp reads were truncated at any site receiving an average quality score <20 over a 50-bp sliding window, and the truncated reads shorter than 50 bp were discarded, reads containing ambiguous characters were also discarded; 2) only overlapping sequences longer than 10 bp were assembled according to their overlapped sequence. The maximum mismatch ratio of overlap region is 0.2. Reads that could not be assembled were discarded; 3) samples were distinguished according to the barcode and primers, and the sequence direction was adjusted, exact barcode matching, two nucleotide mismatches in primer matching. Operational taxonomic units (OTUs) with a 97% similarity cutoff (Stackebrandt and Goebel, 1994; Edgar, 2013) were clustered using UPARSE version 7.1 (Edgar, 2013), and chimeric sequences were identified and removed. The taxonomy of each OTU representative sequence was analyzed against the 16S rRNA database (e.g., Silva v138) by RDP Classifier version 2.2 (Wang et al., 2007) using confidence threshold of 0.7.

ELISA of Serum

The NLRP3 expression levels in the serum were measured using ELISA kits (Wuhao Inc., Shanghai, China) according to the manufacturer's instructions. The expression levels of caspase-1, IL-1β, IL-10, and IL-18 in the serum were also measured using ELISA kits (Cusabio Inc., Wuhan, Hubei, China) according to the manufacturer's instructions.

RT-PCR of Cecal Tissues

Total RNA was extracted from the rat tissues using Trizol reagent, and the RNA integrity was confirmed using agarose gel electrophoresis. CDNA was reverse transcribed from the mRNA using a reverse transcription kit, and RT-qPCR was performed using SYBR green assays. The sequences of the target genes were identified using the NCBI database, and primer5 software was used to design the primers. The sequences of the primer pair were as follows: NLRP3: 5′-CAG AAGCTGGGGTTGGTGAA-3′ (forward) and 5′-CAGCAGGAG TGTGAGGTGAG-3′ (reverse), product length 218 bp; caspase-1: 5′-AGCTTCAGTCAGGTCCATCAG-3′ (forward) and 5′-AAG ACGTGTACGAGTGGGTG-3′ (reverse), product length 227 bp; IL-1β: 5′-TGTGATGTTCCCATTAGAC-3′ (forward) and 5′-AATACCACTTGTTGGCTTA-3′ (reverse), product length 139 bp; ASC: 5′-GGACAGTACCAGGCAGTTCG-3′ (forward) and 5′-GTCACCAAGTAGGGCTGTGT-3′ (reverse), product length 140 bp; IL-18: 5′-ACAGCCAACGAATCCCAGAC-3′ (forward) and 5′-TCCATTTTGTTGTGTCCTGGC-3′ (reverse), product length 224 bp; actin: 5′-TCCTCTGTGACTCGTGGGAT-3′ (forward) and 5′-TGGAGAATACCACTTGTTGGCT-3′ (reverse), product length 174 bp. The $2^{-\Delta\Delta Ct}$ method was used to analyze the relative gene expression levels.

Immunofluorescence of Cecal Tissues

All the sections were analyzed by an investigator blinded to the diagnosis data. Positive staining results for NLRP3, caspase-1, and ASC were counted in each of the three different microscopic fields. The cell densities are expressed as the mean numbers of positively stained cells per field. The results of the double-staining for NLRP3 (green) and caspase-1 (red) and for NLRP3 (green) and ASC (red) were analyzed in a similar manner.

Western Blot of Cecal Tissues

Proteins were extracted from the cecal tissues by adding RIPA lysis buffer to the samples, followed by repeated grinding, incubation on ice for 10 min, and centrifugation at 16,000×*g* for 15 min at 4°C to obtain the supernatant. For the western blot analysis, 240 μl of the protein supernatant was mixed with 60 μl of 5× loading buffer, after which the mixture was boiled for 10 min then cooled on ice. Tissue lysate samples were resolved using SDS-PAGE and transferred to nitrocellulose membranes. The membranes were then immersed in 5% defatted milk powder (prepared using 1× PBST) at room temperature for 90 min, after which they were incubated at 4°C overnight with the following primary antibodies diluted in 1× PBST: anti-TLR4, anti-NF-κB, anti-p-NF-κB, anti-myeloid differentiation factor 88 (MyD88) (1: 1,000 dilution); and β-actin (1:3,000 dilution). The next day, the membranes were incubated at room temperature for 60 min with HRP goat anti-mouse IgG and HRP goat anti-rabbit IgG secondary antibodies, both of which were diluted 1:3,000 in 1× PBST. The membranes were then incubated at room temperature for 90 min, followed by five washes with ECL chemiluminescent solution for color development. The exposed films were scanned and analyzed using Quantity One software.

Correlation Analysis

To explore the functional relationship between the cecal microbiota, the NLRP3 inflammasome (NLRP3, ASC, caspase-1), and the downstream inflammatory factors (IL-1β and IL-18) in the serum and cecal tissues, we formulated a correlation matrix based on Spearman's correlation coefficient ($|R|\geq 0.5$, $p < 0.05$). A Spearman's correlation was calculated and plotted using R (version 3.5.0, corrplot package).

Statistical Analysis

The quantitative data were analyzed using GraphPad Prism 6 software (GraphPad Software, Inc., San Diego, CA, USA) and are presented as the mean ± SEM. The differences between the groups were compared using a two-way ANOVA and the Tukey–Kramer test. The significance of the comparisons between the groups for the non-parametric and parametric data with abnormal distributions was determined using the Kruskal–Wallis test, followed by the Mann–Whitney test (SPSS 11.5; IBM Corporation, Armonk, NY, USA). The results of the alpha diversity analysis of the cecal microbiota abundance and composition are expressed as the mean ± SD. A linear discriminant analysis (LDA) coupled with effect size measurement (LEfSe) of the cecal microbiota abundance and composition was based on the Kruskal–Wallis and Wilcoxon tests, and the LDA score threshold was 4.0–5.0. Statistical significance was set at $p < 0.05$.

RESULTS

HPLC-TOF-MS/MS Analysis of SHD

The main components of SHD, the SHD-containing serum, and the pure standard substances are presented in **Figure 3**. The following seven major components were identified in the SHD extract: 1) paeoniflorin, 2) liquiritin, 3) naringin, 4) hesperidin, 5) neohesperidin, 6) palmatine chloride, and 7) Saikosaponin A (**Table 1**). In addition, we identified naringin, neohesperidin, and palmatine chloride in the SHD-containing serum.

SHD Maintains Weight Gain and Improves the Fecal Disorder of CUS Model Rats

The body weight changes in the rats mainly reflected the food intake level, metabolic status, gastrointestinal digestion, and absorption function of each of the rats. After inducing chronic stress, the feeding behavior of rats often changes, and this behavioral change was manifested as a reduction in body weight gain (Keser et al., 2020). The body weights of the rats in all the groups showed an increasing trend during the interventions (**Figure 2B**). The weight gain for the model

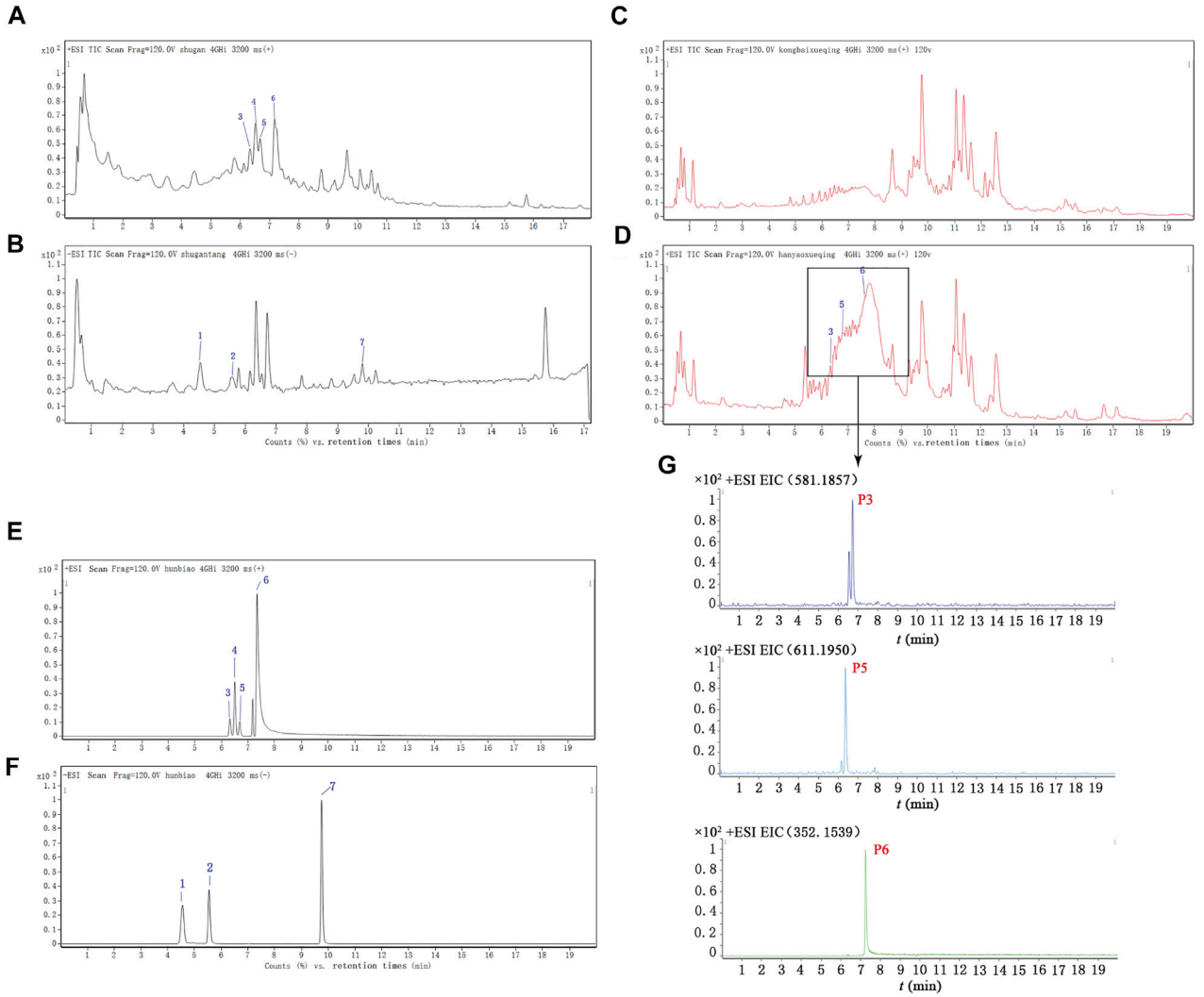


FIGURE 3 | Total ion chromatograms (TICs) for SHD, the SHD-containing serum, and the standard substances. **(A)** The TIC for SHD in the positive mode. **(B)** The TIC for SHD in the negative mode. **(C)** The TIC for the control serum in the positive mode. **(D)** The TIC for the SHD-containing serum in the positive mode. **(E)** The TIC for the standard substances in the positive mode. **(F)** The TIC for the standard substances in the negative mode. **(G)** The ion intensity of the three prototype components identified in the SHD-containing serum. The numbers marked in the figure correspond to (1) paeoniflorin, (2) liquiritin, (3) naringin, (4) hesperidin, (5) neohesperidin, (6) palmatine chloride, and (7) Saikosaponin A.

TABLE 1 | Herbal sources and retention times of seven components in SHD

Peak number	Retention times/min	Quasi-molecular ion (m/z)	Formula	Error range (10^{-6})	Fragment ion (m/z)	Ion detection mode	Constituents	Source
1	4.464	525.1624	$C_{23}H_{28}O_{11}$	1.90	479.15, 449.15	–	Paeoniflorin	*Paeonia lactiflora* Pall.
2	5.530	419.1339	$C_{21}H_{22}O_9$	0.48	257.08, 149.02	+	Liquiritin	*Glycyrrhiza uralensis* Fisch.
3	6.309	581.1854	$C_{27}H_{32}O_{14}$	−1.89	419.13, 273.07	+	Naringin[a]	*Citrus aurantium* L.
4	6.513	611.1946	$C_{28}H_{34}O_{15}$	−3.93	303.08, 153.01	+	Hesperidin	*Citrus aurantium* L.
5	6.684	611.1946	$C_{28}H_{34}O_{15}$	−3.93	303.08, 153.01	+	Neohesperidin[a]	*Citrus aurantium* L.
6	7.139	352.1566	$C_{21}H_{22}ClNO_4$	4.83	337.13, 322.11	+	Palmatine chloride[a]	*Coptis chinensis* Franch.
7	9.814	825.4623	$C_{42}H_{68}O_{13}$	2.30	779.5	–	Saikosaponin A	*Bupleurum chinense* DC.

[a]*Three prototype components were detected in the SHD-containing serum.*

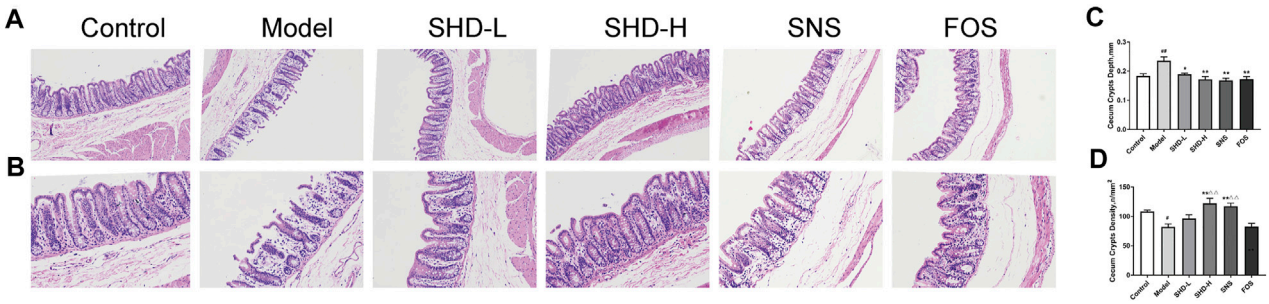


FIGURE 4 | SHD alleviates cecum mucosal histopathology and improves cecum mucosal injury in CUS model rats. **(A)** Sections stained with H&E staining to assess the cecum mucosal injury (×100). Scale bar = 50 μm. **(B)** Sections stained with H&E to assess the cecum mucosal injury (×200). Scale bar = 50 μm. **(C)** Quantification of the mean cecum crypt depths (mm). **(D)** Quantification of the mean cecum crypt densities (n/mm^2). The data are expressed as the mean ± SEM, $n = 5$. $^{\#}p < 0.05$, $^{\#\#}p < 0.01$ *vs.* the control group. $^{*}p < 0.05$, $^{**}p < 0.01$ *vs.* the model group. $^{\Delta}p<0.05$, $^{\Delta\Delta}p<0.01$ *vs.* the FOS group.

group decreased from day 1 to day 28 compared with that of the control group ($p < 0.01$, **Supplementary Table S4**). However, the weight gain for the SHD-L and SHD-H groups increased significantly compared with the model group ($p < 0.05$ or $p < 0.01$), whereas the SNS group exhibited a slight reduction in body weight gain compared with the model group. Although there was not a significant difference between the FOS group and the model group, the FOS group still showed an upward trend in weight gain. On the other hand, both SHD-L and SHD-H alleviated the CUS-induced reduction in body weight gain, and SHD-H had a better effect on maintaining a healthy body weight gain (**Figure 2C**).

The Bristol stool scale divides stool samples into seven categories: types 1 and 2 indicate constipation (score 1); types 3 and 4 are ideal (score 2); type 4 is the easiest shape to defecate. Types 5–7 indicate possible diarrhea (score 3). The fecal Bristol score and fecal moisture content can reflect the frequency of defecation, fecal pattern, and intestinal function in rats (Li et al., 2012). As shown in **Supplementary Table S4**, decreased Bristol scores were observed for the CUS model rats compared with those for the control group ($p < 0.01$). Following the SHD-H treatment, the Bristol score and fecal moisture content for the rats were elevated compared with those of the model group ($p < 0.01$) (**Figures 2D,E**). There was not a significant difference in the fecal moisture content for the SNS and FOS groups compared with the model group; however, there was still an increasing trend. In short, these results indicate that SHD-H can improve fecal disorders and maintain weight gains in CUS model rats.

SHD Improves Cecum Mucosal Injury in CUS Model Rats

To assess whether SHD can ameliorate cecum mucosal injury, we used H&E staining to determine the changes in the pathophysiological characteristics of the rats (Kolacz et al., 2019). As shown in **Figures 4A,B**, the cecal structure of the rats in the control group was intact, and the cecum mucosal folds were well arranged. In the CUS group, the epithelial structure was destroyed, the intestinal villi were ruptured, and the cross-sectional area of the cecum crypts was reduced. Moreover, inflammatory cell infiltration was observed in the cecum mucosa and muscular layer. Compared with the CUS group, the inflammatory cell infiltration and degree of cecum mucosa damage were both reduced in the SHD, SNS, and FOS groups to varying degrees. The cross-sectional area of the intestinal crypts in the SHD-H group was enlarged. A small amount of inflammatory cell infiltration can also be seen in the submucosa, and the intestinal villi remain continuous. Partial mucosal epithelial rupture and mucosal and submucosal infiltration of a small number of inflammatory cells were observed in the SNS group. The cecum mucosa folds continuously in the FOS group, and a small number of inflammatory cells are invading the cavity. As shown in **Figure 4C**, after 3 weeks of exposure to CUS, the cecum crypt depth increased significantly compared with that of the control group ($p < 0.01$), while the SHD-L, SHD-H, SNS, and FOS treatments markedly reversed the cecum crypt depth increase ($p < 0.05$ or $p < 0.01$). In addition, the cecum crypt density decreased significantly ($p < 0.05$) in the CUS model compared with the control group, but the SHD-H treatment completely reversed the reduction ($p < 0.01$) (**Figure 4D**). These results indicate that SHD can ameliorate cecum mucosal injury in CUS model rats.

SHD Reverses CUS-Induced Depressive and Anxiety-Like Behaviors in CUS Model Rats

We compared the alterations in the depressive- and anxiety-like behaviors of the six rat groups using SPT, OFT, and FST. The SPT is an effective quantitative index for evaluating anhedonia (Liu et al., 2018). The effects of SHD on the sucrose preference of the CUS rats during the SPF are shown in **Figure 2F** (**Supplementary Table S5**). The 21-day stress procedure with separation caused a significant decrease in the sucrose preference of the CUS model group compared with the control group ($p < 0.01$), indicating that the CUS model was successfully created. The sucrose preferences increased ($p < 0.01$) in the SHD-L, SHD-H, FOS, and SNS groups compared with the model group. SHD-H showed the strongest effect on restoring the sucrose preference of the CUS rats.

The OFT is a method that is used to evaluate the autonomous and exploratory behaviors exhibited by experimental animals, as well as the stress they experience, when they are placed in a new environment; the test is based on the frequency and duration of certain behaviors (Roth and Katz, 1979). As shown in **Figures 2G,H**, and I (**Supplementary Table S6**), the model group exhibited a shorter total movement distance ($p < 0.05$), longer stationary time ($p < 0.05$), and fewer central areas crossing the lattice ($p < 0.01$) compared with the control group. After the SHD-H intervention, we observed a longer total movement distance, shortened stationary time, and increased number of central areas crossing the lattice ($p < 0.05$) for the rats compared with the model group. There was no significant difference in the OFT results among the SNS, FOS, and model groups.

The FST is a negative stress experiment designed to make use of the inability of animals to escape from harsh environments, which leads to desperation behaviors (Fitzgerald et al., 2019). As shown in **Figure 2J** (**Supplementary Table S5**), the model group showed a much longer immobility time ($p < 0.05$) compared with the control group. The SHD-L group ($p < 0.05$) showed a marked reduction in the total immobility time compared with the model group, while the SNS and FOS groups showed no differences. There was not a significant difference in the immobility time for the SHD-H group compared with the model group, although there was still a markedly decreasing trend. These results indicate that SHD can reverse depressive- and anxiety-like behaviors in CUS model rats with a better efficacy compared with SNS.

SHD Remodels Cecal Microbiota Dysbiosis of CUS Model Rats

We sequenced the V3–V4 region of the 16S rRNA gene of 49 samples from the six groups of rats, which yielded 2,888,146 high-quality reads for subsequent analysis, as an average of 20,351 sequences per sample (**Supplementary Table S7**). A total of 1,326 OTUs were generated through direct denoising, and 1,318 OTUs were obtained by drawing out the sample sequence according to the minimum number of sample sequences. A rank–abundance curve showed that the OTU classification level of the cecal contents from the rats in each group was higher in species richness and uniformity, and the proportion of some of the dominant microbiota was higher (**Supplementary Figure S1**). A pan-analysis indicated that the sample was sufficient, and the total bacterial species richness was high (**Supplementary Figure S2**). A core analysis indicated that the numbers of core microbiota in the cecal contents from the rats in each group was different (**Supplementary Figure S3**). The alpha diversity, as calculated using the Simpson and Chao indices, indicated that the CUS model led to greatly reduced microbiota populations and diversity relative to the control group, while the SHD-H and SNS treatments reversed this imbalance to varying degrees (**Figures 5A,B** and **Supplementary Table S8**). FOS promotes the proliferation and activity of beneficial bacteria in the intestine, although excessive FOS intake will disturb the original balance of the intestinal microbiota and reduce diversity. This may explain the poor results for the FOS group in this part of the analysis (Ten et al., 2003).

To understand the impact of SHD on the cecal microbiota, we further analyzed two different cecal microbiota taxonomic levels. At the phylum level, the CUS model rats showed a reduction in the relative abundance of *Bacteroidetes* and *Proteobacteria* and an increase in the abundance of *Firmicutes*. In contrast, SHD-H, SNS, and FOS significantly increased the levels of *Bacteroidetes* and decreased the levels of *Firmicutes* in the CUS model rats (**Table 2** and **Figure 5C**). At the genus level, the distribution of microbiota among the different samples showed both similarity and distinctiveness. The CUS model rats showed an increase in the relative abundance of *Lactobacillus* and *Lachnospiraceae_NK4A136_group* and a reduction in the abundance *of Prevotellae_9*, *Roseburia*, *Blautia,* and *Prevotella_1*. In contrast, SHD-H and FOS significantly decreased the relative abundance of *Lactobacillus* and *Lachnospiraceae_NK4A136_group* and increased the abundance of *Prevotellae_9*, *Roseburia*, *Blautia*, and *Prevotella*_1 (**Table 3** and **Figure 5D**).

A principal coordinates analysis revealed a distinct shift in the cecal microbiota composition in the CUS model rats treated with SHD-H, SNS, and FOS compared with the CUS rats (**Figure 5E**). The analysis of similarities ($R = 0.4050$, $p = 0.0010$) shows that the differences between the groups are more significant than the differences within the groups (**Figure 5F**). A LEfSe analysis was applied at the phylum and genus levels to determine the key microbial taxa that were differentially represented in the CUS model rats and the rats exposed to the various treatments. Ten key phyla and ten key genera were identified in the six groups (**Figures 5G,H**). As shown in **Figure 5I**, the cecal microbiota, such as *Firmicutes*, *Lactobacillaceae*, and *Bacteroides*, are taking part in distinguishing control from CUS model rats. Notably, *Roseburia*, *Tenericutes*, and *Fusicatenibacter* play vital roles in the SHD-treated groups, while the specific bacterial taxa in the SNS- and FOS-treatment groups were *Bacteroides_S24_7_group* and *Prevotella_1*.

To investigate the cecal microbiota functions associated with the SHD treatment, we used the PICRUSt software package to analyze the 16S rRNA gene profiles. When the data were analyzed using the COG database (**Supplementary Figure S4**), the microbiota functions were found to be mainly related to carbohydrate transport and metabolism, transcription, and amino acid transport and metabolism. When the Tax4Fun software package was used (**Supplementary Figure S5**), a KEGG pathway analysis showed that the predicted function of the microbiota was associated with carbohydrate metabolism, membrane transport, and the immune system. Collectively, these results indicate that CUS is associated with cecal microbiota disturbances, while SHD, SNS, and FOS remodel cecal microbiota dysbiosis *in vivo*. Notably, the abundance and proportion of the cecal microbiota in the SHD-H group were the closest to those of the control group.

SHD Regulates NLRP3 Inflammasome Expression in CUS Model Rats

Disturbances in the intestinal microbiota and immune function of the intestinal mucosa are associated with the development of

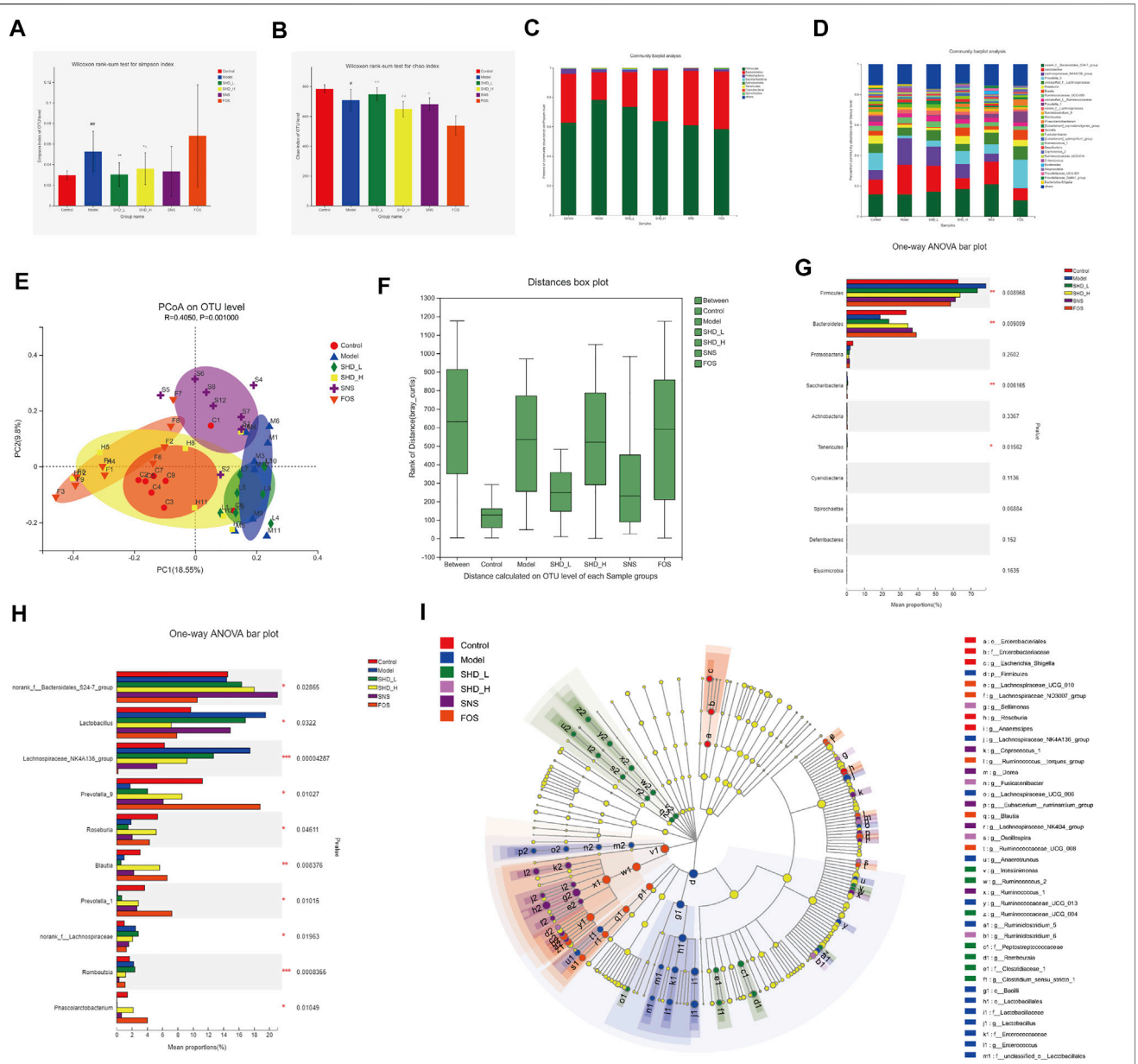


FIGURE 5 | SHD remodels the cecal microbiota dysbiosis of CUS model rats. **(A)** Effect of SHD on the alpha diversity of the cecal contents from the rats in each group (n = 7–8), the Simpson index of the operational taxonomic unit (OTU) level. **(B)** Effect of SHD on the alpha diversity of the cecal contents from the rats in each group (n = 7–8), the Chao index of the OTU level. **(C)** Effect of SHD on the microbiota abundance (phylum level) in the rats in each group (n = 7–8). **(D)** Effect of SHD on the microbiota abundance (genus level) in the rats in each group (n = 7–8). **(E)** A principal coordinates analysis (PCoA) map based on the unweighted Unifrac matrix and Bray–Curtis dissimilarity. **(F)** An analysis of similarities of the distance calculated at the OTU level for each group. **(G)** Comparison of the relative microbiota abundance (phylum level) in the cecal contents from the rats in each group (n = 7–8). **(H)** Comparison of the relative microbiota abundance (genus level) in the cecal contents from the rats in each group (n = 7–8). **(I)** A linear discriminant analysis (LDA) coupled with effect size measurement (LEfSe) of the different microbiota in the cecal contents from the rats in each group, from the phylum level to the genus level (LDA score 3). The data are expressed as the mean ± SD. *Indicates statistical significance (*$0.01 < p \leq 0.05$, **$0.001 < p \leq 0.01$, ***$p \leq 0.001$).

gastrointestinal dysfunction (Weiss and Hennet, 2017). When the intestinal microbiota is disturbed, the intestinal mucosal barrier can be damaged. This causes the bacteria to come into contact with the submucosal immune cells, which leads to intestinal mucosal NLRP3 inflammation activation (Inserra et al., 2018). We investigated the expression of the NLRP3 inflammasome in the serum using ELISA to determine whether SHD could inhibit NLRP3 inflammation in the rats. As shown in **Figures 6A,B** (**Supplementary Table S9**), the serum NLRP3 and caspase-1 levels in the CUS model group were significantly higher than those in the control group ($p < 0.01$). However, after treatment with SHD-L, SHD-H, or SNS, the serum NLRP3 and caspase-1

TABLE 2 | Effect of SHD on bacterial abundance (by phylum) in each group of rats (%, n = 7–8)

Phylum level	Control	Model	SHD-L	SHD-H	SNS	FOS
Firmicutes	62.71	78.22	73.56	63.73	61.03	58.46
Bacteroidetes	33.30	18.84	23.60	34.52	36.97	39.05
Proteobacteria	3.44	1.93	1.52	1.13	1.63	1.52
Saccharibacteria	0.17	0.46	0.61	0.20	0.03	0.31
Actinobacteria	0.17	0.23	0.25	0.27	0.13	0.40
Tenericutes	0.18	0.27	0.38	0.08	0.04	0.10
Cyanobacteria	0.01	0.03	0.02	0.01	0.11	0.03
Spirochaetae	0.01	0.00	0.02	0.03	0.00	0.12
Others	0.02	0.01	0.03	0.01	0.05	0.01

levels were significantly decreased compared with the model group ($p < 0.01$ and $p < 0.05$, respectively). As shown in **Figure 6C** (**Supplementary Table S9**), the serum IL-1β level in the model group was also higher than that of the control group ($p < 0.01$). As shown in **Figure 6D**, the serum IL-18 level in the model group was lower than that of the control group ($p < 0.01$). After the SHD-H, SNS, and FOS treatments, we observed lower IL-1β levels and higher IL-18 levels in the rats ($p < 0.01$ and $p < 0.05$, respectively). Compared with the FOS group, the SHD-H group showed significantly better efficacy for regulating the release of the NLRP3 inflammasome ($p < 0.01$). Our results are consistent with the findings that cecal microbiota disturbances caused by CUS are related to the NLRP3 inflammasome (Hao et al., 2021), and SHD can regulate the expression of the serum NLRP3 inflammasome, as well as that of the downstream IL-1β and IL-18 in serum.

To evaluate whether SHD influences the NLRP3 inflammasome and exerts its therapeutic effects in cecal tissue, we tested the mRNA levels of the NLRP3 inflammasome and its associated inflammatory cytokines (IL-1β and IL-18) in the cecal tissues using RT-PCR. **Figures 6E,G–I** (**Supplementary Table S10**) illustrate that the NLRP3, caspase-1, IL-1β, and IL-18 mRNA levels were significantly increased in the CUS model rats ($p < 0.01$ or $p < 0.05$), but they were downregulated after treatment with SHD-H and SNS. There was not a significant difference in the ASC mRNA levels between either the SHD-H group or the SNS group and the model group (**Figure 6F**). Furthermore, we determined the protein expression levels of the NLRP3 inflammasome using an immunofluorescence co-localization analysis of the cecal mucosa. As shown in **Figures 6J,K** (**Supplementary Tables S11 and S12**), the NLRP3, ASC, and caspase-1 positive areas in the cecal mucosa of the model group were increased compared with the control group ($p < 0.05$). After the SHD-H treatment, the NLRP3 and caspase-1 positive areas were decreased compared with those detected in the model group ($p < 0.05$). However, there was not a significant difference in the NLRP3 and ASC positive areas between the FOS and model groups. These results indicate that SHD-H can inhibit cecal tissue inflammation by regulating the abnormal expression of the NLRP3 inflammasome, as well as that of the downstream inflammatory factors IL-1β and IL-18.

NLRP3 inflammasome activation is closely related to TLR signaling (Jo et al., 2016), which is altered by the host intestinal microbiota during chronic intestinal inflammation (Burgueño and Abreu, 2020). TLR4 activates the transcription factor NF-κB through MyD88, which is critical for the expression of cytokines, chemokines, and costimulatory molecules, such as TNF-α, IL-1β, and IL-18 (Kawai and Akira, 2011; Kawasaki and Kawai, 2014). We examined the expression of proteins associated with the NLRP3 inflammasome in the TLR4 signaling pathway, including TLR4, p-NF-κB, NF-κB, and MyD88, using western blotting. As shown in **Figure 6M**, the TLR4 expression level in the cecal tissue of the model group was significantly decreased ($p < 0.05$) compared with that of the control group and increased in the SHD-L and SNS groups ($p < 0.01$). Notably, there was not a significant increase in the TLR4 expression after the SHD-H intervention compared with that of the model group. The p-NF-κB/NF-κB and MyD88 protein expression levels were increased in the model group in comparison with the control group ($p < 0.01$ and $p < 0.05$, respectively), and they were further upregulated by the SHD-L and SHD-H interventions ($p < 0.01$ and $p < 0.05$, respectively), while they were downregulated by FOS ($p < 0.01$ and $p < 0.05$, respectively) in comparison with the model group (**Figures 6N,O**). These results indicate that SHD can modulate the TLR4/NF-κB signaling pathway, which is involved in NLRP3 inflammasome expression and the downstream production of IL-1β and IL-18 in serum and cecal tissue.

Relationship Between the Cecal Microbiota and NLRP3 Inflammasomes in Cecal Tissue and Serum

To understand whether SHD affects the NLRP3 inflammasome and the release of downstream IL-1β and IL-18 through

TABLE 3 | Effect of SHD on bacterial abundance (by genus) in each group of rats (%, n = 7–8)

Genus level	Control	Model	SHD-L	SHD-H	SNS	FOS
norank_f_Bacteroidales_S24-7_group	14.47	14.44	16.29	17.99	21.09	10.55
Lactobacillus	9.67	19.50	16.88	7.13	14.87	7.86
Lachnospiraceae_NK4A136_group	6.27	17.41	12.66	9.15	5.22	0.15
Prevotella_9	11.21	1.72	3.95	8.59	6.08	18.67
unclassified_f_Lachnospiraceae	6.18	5.20	6.89	4.73	7.68	8.81
Roseburia	5.34	1.88	1.49	5.14	2.03	4.24
Blautia	3.06	0.96	0.57	5.56	2.23	6.61
Ruminococcaceae_UCG-005	3.26	3.91	3.64	2.60	2.77	2.31
unclassified_f_Ruminococcaceae	2.75	2.54	3.64	2.92	2.83	2.45
Prevotella_1	3.63	0.10	0.63	2.86	2.62	7.22
Others	34.15	32.33	33.36	33.32	32.59	31.12

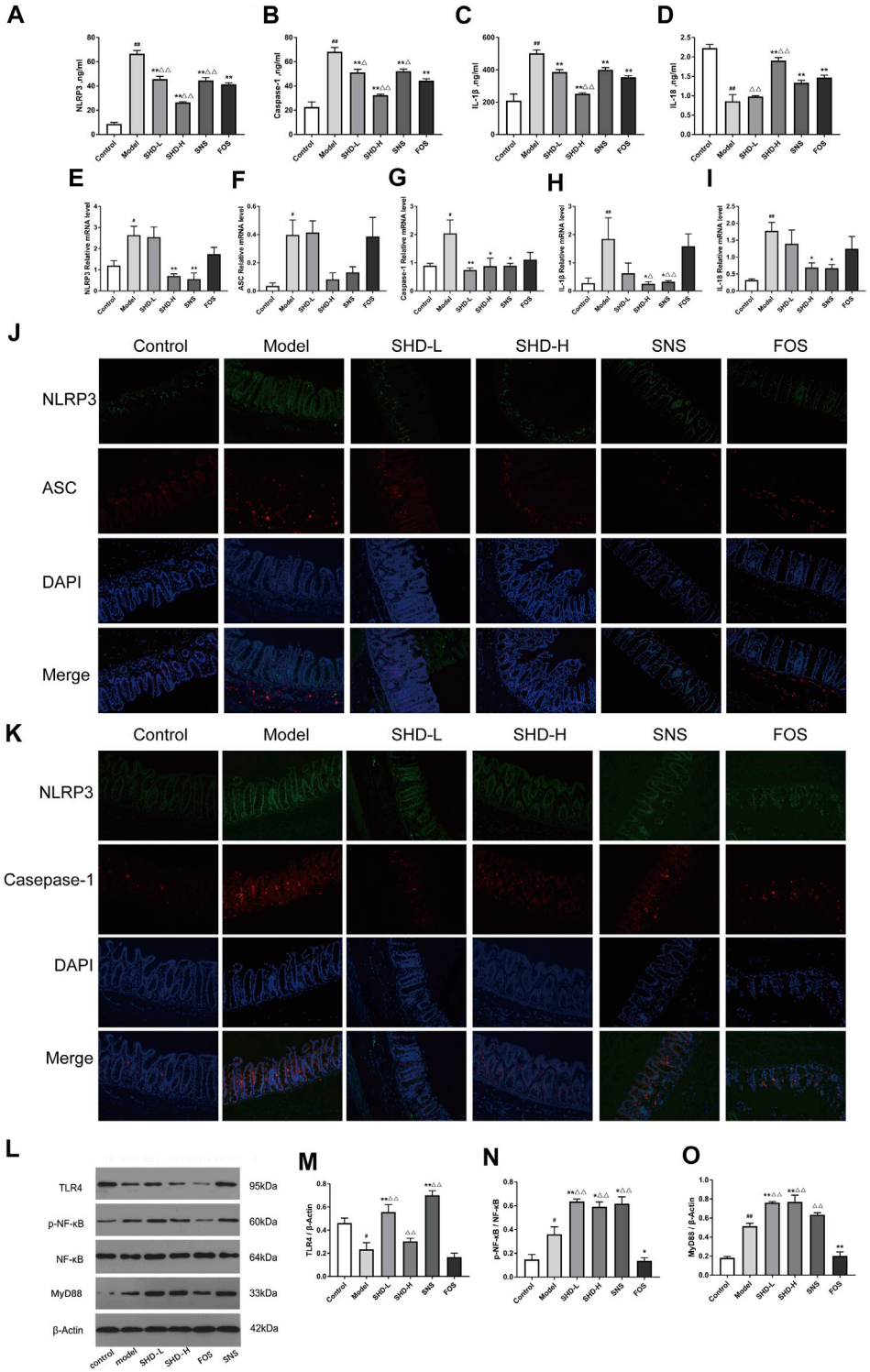


FIGURE 6 | SHD reduces the CUS-induced expression of NOD-like receptor protein 3 (NLRP3), apoptosis-associated speck-like protein containing a CARD domain (ASC), caspase-1, interleukin-1β (IL-1β), and IL-18 in the serum and cecum mucosa and the activation of the Toll-like receptor 4 (TLR4)/nuclear factor (NF)-κB signaling cascades. **(A)** Serum levels of NLRP3 in each group. **(B)** Serum levels of caspase-1 in each group. **(C)** Serum levels of IL-1β in each group. **(D)** Serum levels of IL-18 in each group ($n = 5$). **(E)** Relative mRNA expression levels of NLRP3 in the cecal tissue. **(F)** Relative mRNA expression levels of ASC in the cecal tissue. **(G)** Relative mRNA expression levels of caspase-1 in the cecal tissue. **(H)** Relative mRNA expression levels of IL-1β in the cecal tissue. **(I)** Relative mRNA expression levels of IL-18 in the cecal tissue. The $2^{-\Delta\Delta Ct}$ method was used to analyze the relative gene expression ($n = 4$–5). **(J)** Positive area expression levels of NLRP3 and ASC in the cecal

(*Continued*)

FIGURE 6 | tissue. **(K)** Positive area expression levels of NLRP3 and caspase-1 in the cecal tissue (×200) using immunofluorescence. Scale bar: 50 μm (n = 4–6). **(L)** Western blot assays were performed to evaluate the expression levels of TLR4, p-NF-κB, NF-κB, and myeloid differentiation factor 88 (MyD88) in the cecal tissue of the control, model, SHD-L, SHD-H, SNS, and FOS group rats. β-Actin was used as the loading control. **(M)** Quantitative analysis of the relative expression levels of TLR4 in the cecal tissue. **(N)** Quantitative analysis of the relative expression levels of p-NF-κB/NF-κB in the cecal tissue. **(O)** Quantitative analysis of the relative expression levels of MyD88 in the cecal tissue (n = 3). The data are expressed as the mean ± SEM. $^{*}p < 0.05$, $^{**}p < 0.01$ *vs*. the control group; $^{\#}p < 0.05$, $^{\#\#}p < 0.05$, *vs*. the CUS model group; $^{\triangle}p < 0.05$, $^{\triangle\triangle}p < 0.05$, *vs*. the FOS group.

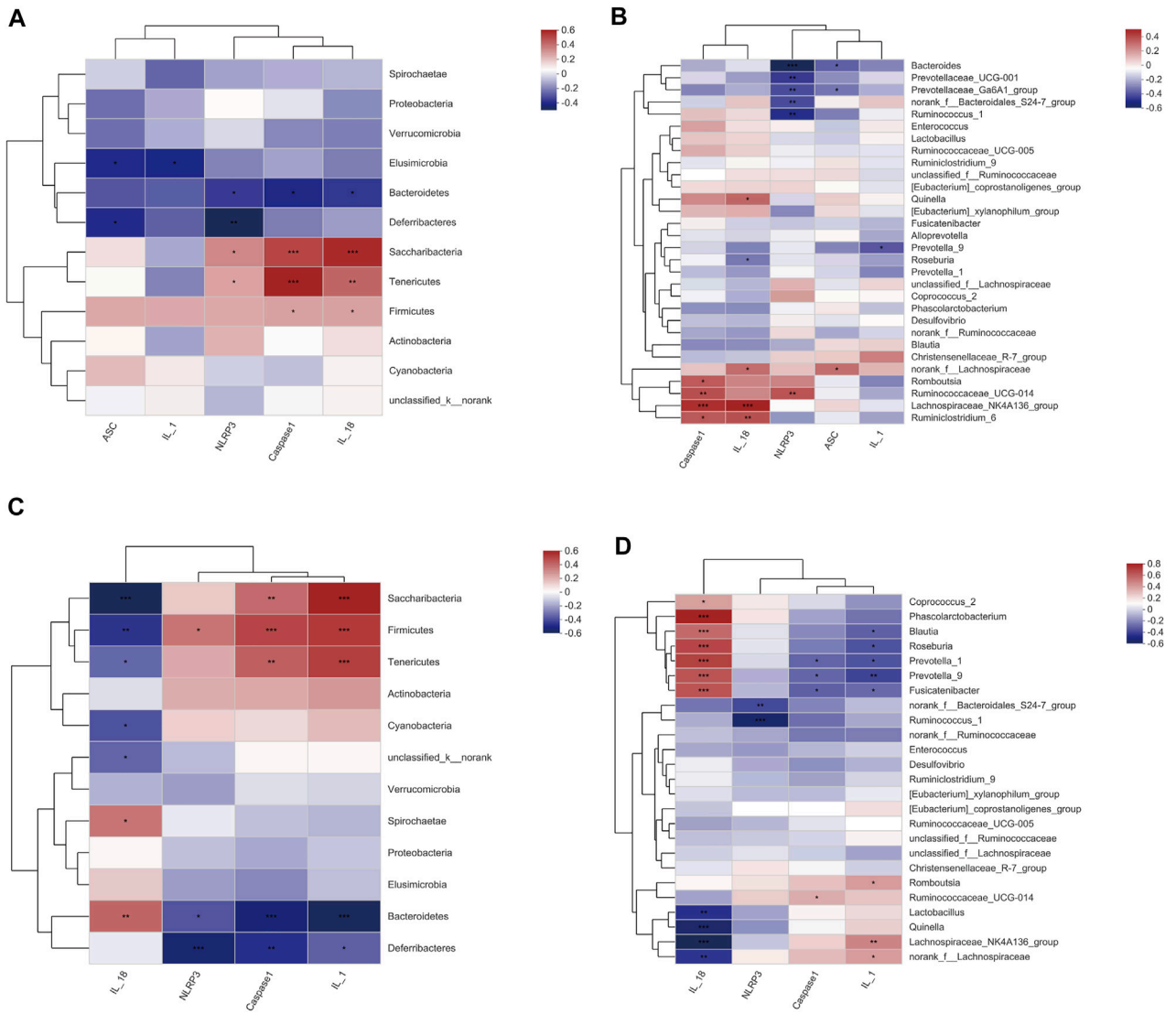


FIGURE 7 | A Spearman's correlation between the cecal microbiota and NLRP3 inflammasome in the cecum tissue and serum. **(A)** Correlations between the cecal microbiota (phylum level) and NLRP3 inflammasome mRNA in the cecum tissue. **(B)** Correlations between the cecal microbiota (genus level) and NLRP3 inflammasome mRNA in the cecum tissue. **(C)** Correlations between the cecal microbiota (phylum level) and NLRP3 inflammasome in the serum. **(D)** Correlations between the cecal microbiota (genus level) and NLRP3 inflammasome in the serum. *R* value, the closer this value is to 1, the more positive the correlation, while the closer it is to −1, the more negative the correlation. ($p \leq 0.001$) indicates an extremely significant correlation, ($0.001 < p \leq 0.01$) indicates a very significant correlation, ($0.01 < p \leq 0.05$) indicates a significant correlation. The data are expressed as the mean ± SEM, (n = 6).

regulation of the cecal microbiota, we analyzed the correlations between the biomarker microbiota and the NLRP3 inflammasome in the cecal tissue and serum of the CUS rats. A Spearman's correlation test was performed on the pooled data set, and the results are shown in **Supplementary Table S13**. As shown in **Figure 7A**, at the phylum level, the abundance of *Firmicutes* was positively correlated with the expression of both caspase-1 and IL-18 mRNA (R = 0.289, 0.288, p = 0.044, 0.045,

respectively). The *Bacteroidetes* abundance was negatively correlated with the expression of NLRP3, caspase-1, and IL-18 mRNA (R = −0.287, −0.333, −0.289, p = 0.045, 0.019, 0.037, respectively). Other phyla, such as *Saccharobacter*, were positively correlated with the expression of NLRP3, caspase-1, and IL-1β mRNA (R = 0.346, 0.496, 0.562, p = 0.047, 0.00001, 0.0003, respectively); *Tenericutes* was positively correlated with the expression of NLRP3, caspase-1, and IL-1β mRNA (R = 0.285, 0.587, 0.424, p = 0.015, 0.0003, 0.002, respectively). At genus level (**Supplementary Table S14**, and **Figure 7B**), *norank_f_Bacteroidales_S24-7_group* was negatively correlated with the expression of NLRP3 mRNA (R = -0.384, p = 0.00648), while *Prevotella_9* was negatively correlated with IL-1β mRNA expression (R = −0.355, p = 0.012). *Lachnospiraceae_NK4A136_group* was positively correlated with the expression of both caspase-1 and IL-18 mRNA (R = 0.456, 0.494, respectively, $p < 0.001$ for both), and *Roseburia* was negatively correlated with IL-18 mRNA expression (R = −0.289, p = 0.0436).

Interestingly, we observed different correlations between the NLRP3 inflammasome expression and the microbiota in the serum; this was particularly true for *Firmicutes*, which was positively associated with NLRP3, caspase-1, and IL-1β (R = 0.353, 0.471, 0.505, p = 0.01275, 0.00064, 0.00021, respectively), but inversely related to the IL-18 expression (R = −0.408, p = 0.00362) (**Supplementary Tables S15 and S16** and **Figures 7C,D**). This analysis revealed that the inflammasomes and the inflammation markers IL-1β and IL-18 seem to be strongly influenced by the cecal microbiota, as we observed significant correlations with most of the bacterial groups (i.e., *Firmicutes*, *Bacteroidetes*, *Saccharobacter*, and *Tenericutes*) investigated. However, part of the cecal microbiota was not correlated with the inflammasome, suggesting that some of the bacterial groups in the cecum have different functions that are unlikely to influence inflammation. In summary, these results suggest that SHD regulates cecal microbiota disturbances and inhibits NLRP3 inflammasomes in CUS model rats to ameliorate cecum mucosal injury.

DISCUSSION

The adaptive stress response can improve an individual's adaptability and survivability when they are exposed to an onerous situation; however, excessive or chronic stress can markedly disrupt body homeostasis, leading to varying degrees of physiological, psychological, and gastrointestinal dysfunction (Molina-Torres et al., 2019). In this study, we found that the weight gains experienced by the chronic stress model rats were significantly decreased, and they were accompanied by a fecal trait disorder, which is consistent with previous reports (González-Torres and Dos, 2019; Li et al., 2019). In addition, we found that the higher cecum crypt depths and lower cecum crypt densities that we observed under light microscopy might explain the fecal trait disorders. However, physical and psychological comorbidities are often characteristic of chronic stress-related diseases (Averous et al., 2020). In our investigation, after 21 days, the CUS model rats showed various depressive- and anxiety-like behavior changes, as assessed through the SPT, FST, and OFT. We determined that these behavioral changes, which are similar to those that accompany the liver-stomach disharmony syndrome described in traditional Chinese medicine, are characteristics that are inherent to the CUS model rats, suggesting that the model development was successful. We observed that the weight gains, fecal disorders, cecum mucosal injuries, and depressive- and anxiety-like behaviors in the CUS model rats improved significantly with the SHD-H and SNS treatments. Our pharmacodynamic observations revealed that SHD-H could maintain weight gains, improve fecal disorders, and reverse depressive-like behaviors, and these benefits may be associated with the effects of relieving cecum mucosal injury.

Differences in anxiety-related behaviors are commonly reported in mice with altered gut microbiomes, which implicate the gut microbiota in stress (Park et al., 2013). The gut microbiota is mainly dominated by *Firmicutes* and *Bacteroidetes*, although *Proteobacteria*, *Actinobacteria*, *Verrucomicrobia*, and *Fusobacteria* are also present in the colon and cecum (Averous et al., 2020). Subtle alterations in the *Firmicutes*/*Bacteroidetes* ratio have been described in studies of patients with irritable bowel syndrome (correlated with clinical depression and anxiety) (Jeffery et al., 2012); irritable bowel syndrome is also associated with chronic low-grade inflammation (Akiho et al., 2010). Furthermore, in a previous study, a noteworthy decrease in the abundance of *Bacteroidetes* and increase in *Firmicutes* were detected in a chronic unpredictable mild stress model group, and these results were reversed with FOS treatment (Li et al., 2019). Such gut microbiome alterations may be indicators of drug therapy effectiveness (Zhu et al., 2019). The main function of *Firmicutes* in the intestine is to hydrolyze carbohydrates and proteins (Bäckhed et al., 2005). *Bacteroides* mainly act on steroids, polysaccharides, and bile acids, which contribute to protein synthesis and the absorption of polysaccharides (Xu et al., 2003). Commensal *Lactobacillus* species can restore homeostasis in intestinal disorders; thus, they play a protective role against inflammatory diseases. A recent study showed that *L. acidophilus* suppressed proinflammatory cytokines, such as IL-6, TNFα, and IL-1β in colon tissues (Park et al., 2018). The *Lachnospiraceae_NK4A136_group*, *unclassified_f_Lachnospiraceae* belongs to the *Lachnospiraceae* family. *Lachnospiraceae* is one of the most abundant families within the *Firmicutes* phylum, and it is most often associated with the beneficial production of short-chain fatty acids (SCFAs) from complex polysaccharides (Vacca et al., 2020). *Prevotella_9* and *Prevotella_1* both belong to the *Prevotellaceae* family, which is also known to produce SCFAs. SCFA receptors regulate gut primarily through gene expression (e.g., inhibition of the nuclear transcription factor NF-κB, downregulation of pro-inflammatory factors, and inhibition of intestinal inflammation) (Duncan et al., 2009). *Blautia* and *Roseburia* represent the genera most involved in the control of gut inflammatory processes and immune system maturation (La Rosa et al., 2019; Liu et al., 2021). In the present investigation, our findings concerning the gut microbiota are consistent with these reports. We found that the species diversity and richness of the

cecal microbiota in the CUS model rats were significantly decreased, while SHD-H increased this diversity and richness, and it did so with better efficacy compared with SNS. We also found that the *Firmicutes*, *Bacteroidetes*, and *Proteobacteria* abundance ratio balance at the phylum level was restored in the CUS model rats after the SHD-H treatment. Specifically, *Lactobacillus* and *Lachnospiraceae_NK4A136_group* in the *Firmicutes* phylum were decreased, while *Roseburia* and *Blautia* were increased; in addition, *Prevotella_9* and *Prevotella_1* were increased in *the Bacteroidetes* phylum. Furthermore, SHD-H had a better effect on regulating the abundance ratio balance of the cecal microbiota than did FOS. We concluded that the CUS-induced cecal microbiota imbalance can be reversed by treatment with SHD-H. This effect may be related to the reduction of intestinal inflammation and release of inflammatory factors.

Dysbiosis of the gut microbiota increases intestinal permeability, leading bacterial metabolites, such as endotoxin (lipopolysaccharide, LPS), to stimulate intestinal mucosal TLRs (Larabi et al., 2020). LPS activates the NLRP3 inflammasome *via* recognition by TLRs, resulting in the production of proinflammatory factors, such as IL-1β and IL-18 (Kelley et al., 2019), and acceleration of the gastrointestinal dysfunction process (Hirota et al., 2011). Caspase-1 is a cysteine protease that cleaves pro-IL-1β and pro-IL-18 into their mature isoforms in response to stressful stimuli such as psychosocial and microbial stress (Lamkanfi et al., 2007). IL-1β and IL-18 are involved in maintaining intestinal integrity and epithelial repair, while aberrant IL-1β and IL-18 signaling can be detrimental to gut function (Nowarski et al., 2015). However, deregulation of pro-inflammatory cytokine production can lead to immunopathology and immune responses. In our investigation, we found that the serum levels of NLRP3, caspase-1, and IL-1β were significantly decreased in the CUS model rats after the SHD, SNS, or FOS treatments, while the IL-18 levels were significantly increased. IL-18, which is a member of the IL-1 family of cytokines, has pro-inflammatory and immune defense enhancing properties (Kaplanski, 2018). The IL-18 level in the model group was lower than that of the control group, suggesting that chronic stress can reduce IL-18 levels, which may be related to declines in immune defense properties. However, the IL-18 levels of the SHD-H, SNS, and FOS groups increased, indicating that these drug treatments can enhance the anti-stress and immune responses. Activation of hypothalamic–pituitary–adrenal axis (HPA axis) and stress-induced changes in the levels of corticosteroids and corticosterone may regulate the inflammatory response (Shuei and Bruno, 2008), making the IL-1β and IL-18 serum level change trends inconsistent. SHD-H and FOS had a significant effect on reversing these changes. However, in the cecal tissue, the relative expression of the NLRP3, ASC, caspase-1, IL-1β, and IL-18 mRNAs was significantly decreased by treatment with either SHD-H or SNS, and both treatment groups showed consistent results in the expression of the positive area. Therefore, we determined that SHD-H may exert its effects on gastrointestinal function regulation by adjusting the intestinal inflammation imbalance, inhibiting the activation of the NLRP3 inflammasome-driven pathways (including ASC and caspase-1), and regulating the abnormal expression of IL-1β and IL-18 in the serum and cecum.

The TLR4 signaling pathway is a crucial upstream regulator of NLRP3 inflammasomes (Silk et al., 2017). The NLRP3 inflammasome activation pathway includes two stages: initiation and activation. The pathogen-associated molecular patterns and damage-associated molecular patterns are mainly identified by TLR4 during the initiation phase. NF-κB is activated by the downstream signaling molecule MyD88. Finally, the expression of NLRP3 and pro-IL-1β is induced. During the activation stage, multiple stimuli promote the assembly of the NLRP3 inflammasome complex and activate the TLR4 signaling pathway (Wang and Hauenstein, 2020). Indeed, our results showed that the TLR4 protein expression level in the cecal tissue of the CUS model rats was markedly downregulated, while the p-NF-κB/NF-κB and MyD88 protein expression levels were upregulated. In addition, the TLR4 protein expression levels in the cecal tissue were increased after treatment with SHD-L, SHD-H, and SNS, and the p-NF-κB/NF-κB and MyD88 proteins were still increased. However, an opposite trend was observed for the FOS. The reason for these results may be that the CUS model is different from the acute inflammatory injury model, and the SHD mechanism may be partially different from that of FOS. In addition, TLR4-related mechanisms can mediate stress-induced adaptations through multi-directional communication between the immune, neural, and endocrine systems during stress (Liu et al., 2014). We can assume that SHD and SNS can increase the protein expression of TLR4 in the cecal tissue to enhance the adaptations to chronic stress. At the chronic stress stage, the sustained activation of the HPA axis demonstrates cortisol resistance, which upregulates NF-κB signaling. NF-κB increases the proinflammation cytokines, which in turn reduce the inflammatory responses (Tian et al., 2014). There is the bidirectional communication between the gut microbiota and the HPA axis, which controls various body processes in response to stress (Farzi et al., 2018). This may explain the continued increases in the p-NF-κB/NF-κB and MyD88 protein levels after the SHD and SNS treatments, both of which may modulate the network regulation of the cecal microbiota and HPA axis to affect the TLR4/NF-κB signaling pathway. Therefore, we determined that NLRP3 inflammasome can be adjusted by treatment with SHD or SNS through multiple pathways and targets, both in the serum and cecal tissue, and the TLR4/NF-κB signaling pathway may be one of those pathways.

Moreover, the extent to which the NLRP3 inflammasome is activated appears to be greatly influenced by the composition and function of the gut microbiome (Wong et al., 2016). Interestingly, upregulation of the NLRP3 inflammasome pathway disrupts the gut microbiota by influencing pro-inflammatory signaling, which modulates the gut microbiota composition by increasing the representation of bacterial clades conducive to pro-inflammatory signaling (e.g., *Proteobacteria*, *Allistipes*, *Prevotella*, *Oscillibacter*, *Actinobacteria*) and decreasing the representation of bacterial clades conducive to anti-inflammatory signaling (e.g., *Firmicutes*, *Faecalibacterium*, *Lachnospiraceae*, and *Bacteroidetes*) (Inserra et al., 2018). In addition, *Proteus mirabilis* (a *Proteobacteria* phylum member) triggers NLRP3 activation and IL-1β production (Seo et al., 2015). Conversely, the abundance of *Lactobacillus*, a genus

involved in inflammasome activation via caspase-1-mediated IL-1β production, was increased (Zheng et al., 2016).

FOS can regulate intestinal microbiota disturbances, inhibit the expression of the NLRP3 inflammasome and the intestinal mucosal pre-inflammatory cytokines IL-1α and IL-1β to affect gastrointestinal function (Ferenczi et al., 2016), and improve mental and emotional abnormalities (Savignac et al., 2016). This is why FOS was used in the positive control group in this experiment, as these FOS characteristics aided in clarifying the SHD mechanism. Li et al. reported that moxibustion and probiotic treatments elicited similar effects by regulating intestinal host-microbial homeostasis and the expression of NLRP3 inflammasome-related factors (Li et al., 2021). However, little is known about how SHD regulates the intestinal microbiota and NLRP3 inflammasome signaling. In this study, our correlation analysis showed that *Firmicutes*, *Bacteroidetes*, *Saccharobacter*, *Tenericutes* (phylum level), *norank_f_Bacteroidales_S24-7_group*, *Prevotella_9*, *Lachnospiraceae_NK4A136_group*, and *Roseburia* (genus level) are biomarker microbiota, which are highly correlated with the NLRP3 inflammasome and downstream inflammatory factors (IL-1β, IL-18) in CUS model rats. We considered that SHD could regulate cecal microbiota and that they are highly correlated with the NLRP3 inflammasome and downstream inflammatory factors (IL-1β and IL-18) in CUS model rats. Therefore, we determined that SHD could regulate cecal microbiota to inhibit CUS-induced NLRP3 inflammasome activation.

Notably, compared with SNS, SHD-H provided superior efficacy in terms of maintaining weight gain, improving fecal traits, alleviating cecum mucosal injury, inhibiting NLRP3 inflammasome expression, and regulating the diversity, abundance, and proportion of the cecal microbiota. Although both SHD-H and FOS can remodel cecal microbiota dysbiosis, SHD-H has more obvious advantages in maintaining weight gain, improving cecum mucosal injury, reversing depressive- and anxiety-like behaviors, and regulating NLRP3 inflammasome expression in CUS model rats. Therefore, SHD-H provides an advanced therapeutic effect for the treatment of depression and gastrointestinal dysfunction caused by chronic stress.

CONCLUSION

The results of our study suggest that SHD can alleviate cecum mucosal injury and improve depressive- and anxiety-like behaviors by regulating the cecal microbiota and inhibiting the excessive activation of the NLRP3 inflammasome in the cecum and serum. Our work reveals the pharmacological mechanisms of SHD and provides a new therapeutic method for the prevention and treatment of psychosomatic comorbidities related to intestinal function disorders and depressive- and anxiety-like behaviors. SHD contains 10 traditional Chinese herbs, each of which contains complex chemical compounds. Therefore, it will be necessary to clarify which compounds in the SHD formulation have beneficial effects on stress-related diseases and what their precise targets are. In addition, because SHD metabolism *in vivo* is complicated, further studies are needed to identify the gut-derived metabolites and other metabolomic products that are involved in the relationship between gut microbiota dysbiosis and inflammasomes. Nevertheless, this study is far from sufficient, more investigations are needed, and a series of follow-up studies are underway in our laboratory.

DATA AVAILABILITY STATEMENT

The data presented in the study are deposited in the (online) repository, accession number NCBI SRP324274.

ETHICS STATEMENT

The animal study was reviewed and approved by Animal Ethics Committee of Hubei University of Chinese Medicine (Approval number: HUCMS 201903009).

AUTHOR CONTRIBUTIONS

SL, YZ, and YY conceived the hypothesis, designed the experiments, and revised the article. YY, YC, and HL performed the experiments and drafted the article. HM, XC, LX, XZ, and MC performed part of experiments. YL, LL, and YC revised the article. All authors read and approved the final article.

FUNDING

This work was supported by the National Natural Science Foundation of China (81904076), Innovation Team Project of Education Department of Hubei Province (T201808).

ACKNOWLEDGMENTS

We are grateful for the support from the team and National Natural Science Fund, China.

SUPPLEMENTARY MATERIAL

The Supplementary Material for this article can be found online at: https://www.frontiersin.org/articles/10.3389/fphar.2021.766474/full#supplementary-material

REFERENCES

Akiho, H., Ihara, E., and Nakamura, K. (2010). Low-grade Inflammation Plays a Pivotal Role in Gastrointestinal Dysfunction in Irritable Bowel Syndrome. *World J. Gastrointest. Pathophysiol* 1 (3), 97–105. doi:10.4291/wjgp.v1.i3.97

Averous, P., Charbonnier, E., and Dany, L. (2020). Relationship between Illness Representations, Psychosocial Adjustment, and Treatment Outcomes in Mental Disorders: A Mini Review. *Front. Psychol.* 11, 1167. doi:10.3389/fpsyg.2020.01167

Bäckhed, F., Ley, R. E., Sonnenburg, J. L., Peterson, D. A., and Gordon, J. I. (2005). Host-bacterial Mutualism in the Human Intestine. *Science* 307 (5717), 1915–1920. doi:10.1126/science.1104816

Baxter, A. J., Patton, G., Scott, K. M., Degenhardt, L., and Whiteford, H. A. (2013). Global Epidemiology of Mental Disorders: what Are We Missing? *PLoS One* 8 (6), e65514. doi:10.1371/journal.pone.0065514

Bhatia, V., and Tandon, R. K. (2005). Stress and the Gastrointestinal Tract. *J. Gastroenterol. Hepatol.* 20 (3), 332–339. doi:10.1111/j.1440-1746.2004.03508.x

Brenes Sáenz, J. C., Villagra, O. R., and Fornaguera Trías, J. (2006). Factor Analysis of Forced Swimming Test, Sucrose Preference Test and Open Field Test on Enriched, Social and Isolated Reared Rats. *Behav. Brain Res.* 169 (1), 57–65. doi:10.1016/j.bbr.2005.12.001

Burgueño, J. F., and Abreu, M. T. (2020). Epithelial Toll-like Receptors and Their Role in Gut Homeostasis and Disease. *Nat. Rev. Gastroenterol. Hepatol.* 17 (5), 263–278. doi:10.1038/s41575-019-0261-4

Chen, S., Zhou, Y., Chen, Y., and Gu, J. (2018). Fastp: an Ultra-fast All-In-One FASTQ Preprocessor. *Bioinformatics* 34 (17), i884–i890. doi:10.1093/bioinformatics/bty560

Chen, X., Ma, Y., Mou, X., Liu, H., Ming, H., Chen, Y., et al. (2021). Synergistic Effect of Several Neurotransmitters in PFC-NAc-VTA Neural Circuit for the Anti-depression Effect of Shuganheweitang in a Chronic Unpredictable Mild Stress Model. *Nat. Product. Commun.* 16 (3), 1934578X2110024. doi:10.1177/1934578X211002415

Chi, L., Khan, I., Lin, Z., Zhang, J., Lee, M. Y. S., Leong, W., et al. (2020). Fructo-oligosaccharides from Morinda Officinalis Remodeled Gut Microbiota and Alleviated Depression Features in a Stress Rat Model. *Phytomedicine* 67, 153157. doi:10.1016/j.phymed.2019.153157

Ding, F., Wu, J., Liu, C., Bian, Q., Qiu, W., Ma, Q., et al. (2020). Effect of Xiaoyaosan on Colon Morphology and Intestinal Permeability in Rats with Chronic Unpredictable Mild Stress. *Front. Pharmacol.* 11, 1069. doi:10.3389/fphar.2020.01069

Duncan, S. H., Louis, P., Thomson, J. M., and Flint, H. J. (2009). The Role of pH in Determining the Species Composition of the Human Colonic Microbiota. *Environ. Microbiol.* 11 (8), 2112–2122. doi:10.1111/j.1462-2920.2009.01931.x

Edgar, R. C. (2013). UPARSE: Highly Accurate OTU Sequences from Microbial Amplicon Reads. *Nat. Methods* 10 (10), 996–998. doi:10.1038/nmeth.2604

Farzi, A., Fröhlich, E. E., and Holzer, P. (2018). Gut Microbiota and the Neuroendocrine System. *Neurotherapeutics* 15 (1), 5–22. doi:10.1007/s13311-017-0600-5

Ferenczi, S., Szegi, K., Winkler, Z., Barna, T., and Kovács, K. J. (2016). Oligomannan Prebiotic Attenuates Immunological, Clinical and Behavioral Symptoms in Mouse Model of Inflammatory Bowel Disease. *Sci. Rep.* 6, 34132. doi:10.1038/srep34132

Fitzgerald, P. J., Yen, J. Y., and Watson, B. O. (2019). Stress-sensitive Antidepressant-like Effects of Ketamine in the Mouse Forced Swim Test. *PLoS One* 14 (4), e0215554. doi:10.1371/journal.pone.0215554

Fleshner, M., Frank, M., and Maier, S. F. (2017). Danger Signals and Inflammasomes: Stress-Evoked Sterile Inflammation in Mood Disorders. *Neuropsychopharmacology* 42 (1), 36–45. doi:10.1038/npp.2016.125

González-Torres, M. L., and Dos Santos, C. V. (2019). Uncontrollable Chronic Stress Affects Eating Behavior in Rats. *Stress* 22 (4), 501–508. doi:10.1080/10253890.2019.1596079

Hao, W., Wu, J., Yuan, N., Gong, L., Huang, J., Ma, Q., et al. (2021). Xiaoyaosan Improves Antibiotic-Induced Depressive-like and Anxiety-like Behavior in Mice through Modulating the Gut Microbiota and Regulating the NLRP3 Inflammasome in the Colon. *Front. Pharmacol.* 12, 619103. doi:10.3389/fphar.2021.619103

Hirota, S. A., Ng, J., Lueng, A., Khajah, M., Parhar, K., Li, Y., et al. (2011). NLRP3 Inflammasome Plays a Key Role in the Regulation of Intestinal Homeostasis. *Inflamm. Bowel Dis.* 17 (6), 1359–1372. doi:10.1002/ibd.21478

Inserra, A., Rogers, G. B., Licinio, J., and Wong, M. L. (2018). The Microbiota-Inflammasome Hypothesis of Major Depression. *Bioessays* 40 (9), e1800027. doi:10.1002/bies.201800027

Jeffery, I. B., O'Toole, P. W., Öhman, L., Claesson, M. J., Deane, J., Quigley, E. M., et al. (2012). An Irritable Bowel Syndrome Subtype Defined by Species-specific Alterations in Faecal Microbiota. *Gut* 61 (7), 997–1006. doi:10.1136/gutjnl-2011-301501

Jo, E. K., Kim, J. K., Shin, D. M., and Sasakawa, C. (2016). Molecular Mechanisms Regulating NLRP3 Inflammasome Activation. *Cell. Mol. Immunol.* 13 (2), 148–159. doi:10.1038/cmi.2015.95

Kaplanski, G. (2018). Interleukin-18: Biological Properties and Role in Disease Pathogenesis. *Immunol. Rev.* 281 (1), 138–153. doi:10.1111/imr.12616

Karl, J. P., Hatch, A. M., Arcidiacono, S. M., Pearce, S. C., Pantoja-Feliciano, I. G., Doherty, L. A., et al. (2018). Effects of Psychological, Environmental and Physical Stressors on the Gut Microbiota. *Front. Microbiol.* 9, 2013. doi:10.3389/fmicb.2018.02013

Kawai, T., and Akira, S. (2011). Toll-like Receptors and Their Crosstalk with Other Innate Receptors in Infection and Immunity. *Immunity* 34 (5), 637–650. doi:10.1016/j.immuni.2011.05.006

Kawasaki, T., and Kawai, T. (2014). Toll-like Receptor Signaling Pathways. *Front. Immunol.* 5, 461. doi:10.3389/fimmu.2014.00461

Kelley, N., Jeltema, D., Duan, Y., and He, Y. (2019). The NLRP3 Inflammasome: An Overview of Mechanisms of Activation and Regulation. *Int. J. Mol. Sci.* 20 (13), 3328. doi:10.3390/ijms20133328

Keser, I., Cvijetić, S., Jurasović, J., Barić, I. C., Kauzlarić, M., Aimunić, K., et al. (2020). Association of Chronic Stress, Inflammation, Body Composition and Dietary Intake in Croatian university Students. *P. Nutr. Soc.* 79 (OCE2), E192. doi:10.1017/s0029665120001408

Kim, J. J., and Jo, E. K. (2013). NLRP3 Inflammasome and Host protection against Bacterial Infection. *J. Korean Med. Sci.* 28 (10), 1415–1423. doi:10.3346/jkms.2013.28.10.1415

Kolacz, J., Kovacic, K. K., and Porges, S. W. (2019). Traumatic Stress and the Autonomic Brain-Gut Connection in Development: Polyvagal Theory as an Integrative Framework for Psychosocial and Gastrointestinal Pathology. *Dev. Psychobiol.* 61 (5), 796–809. doi:10.1002/dev.21852

La Rosa, S. L., Leth, M. L., Michalak, L., Hansen, M. E., Pudlo, N. A., Glowacki, R., et al. (2019). The Human Gut Firmicute Roseburia Intestinalis Is a Primary Degrader of Dietary β-mannans. *Nat. Commun.* 10 (1), 905. doi:10.1038/s41467-019-08812-y

Lamkanfi, M., and Dixit, V. M. (2014). Mechanisms and Functions of Inflammasomes. *Cell* 157 (5), 1013–1022. doi:10.1016/j.cell.2014.04.007

Lamkanfi, M., Kanneganti, T. D., Franchi, L., and Núñez, G. (2007). Caspase-1 Inflammasomes in Infection and Inflammation. *J. Leukoc. Biol.* 82 (2), 220–225. doi:10.1189/jlb.1206756

Larabi, A., Barnich, N., and Nguyen, H. T. T. (2020). New Insights into the Interplay between Autophagy, Gut Microbiota and Inflammatory Responses in IBD. *Autophagy* 16 (1), 38–51. doi:10.1080/15548627.2019.1635384

Lewis, S. J., and Heaton, K. W. (1997). Stool Form Scale as a Useful Guide to Intestinal Transit Time. *Scand. J. Gastroenterol.* 32 (9), 920–924. doi:10.3109/00365529709011203

Li, B.-r., Shao, S.-y., Yuan, L., Jia, R., Sun, J., Ji, Q., et al. (2021). Effects of Mild Moxibustion on Intestinal Microbiome and NLRP3 Inflammasome in Rats with 5-Fluorouracil-Induced Intestinal Mucositis. *J. Integr. Med.* 19 (2), 144–157. doi:10.1016/j.joim.2020.12.004

Li, H., Wang, P., Huang, L., Li, P., and Zhang, D. (2019a). Effects of Regulating Gut Microbiota on the Serotonin Metabolism in the Chronic Unpredictable Mild Stress Rat Model. *Neurogastroenterol Motil.* 31 (10), e13677. doi:10.1111/nmo.13677

Li, N., Wang, Q., Wang, Y., Sun, A., Lin, Y., Jin, Y., et al. (2019b). Fecal Microbiota Transplantation from Chronic Unpredictable Mild Stress Mice Donors Affects Anxiety-like and Depression-like Behavior in Recipient Mice via the Gut Microbiota-Inflammation-Brain axis. *Stress* 22 (5), 592–602. doi:10.1080/10253890.2019.1617267

Li, Y., Zheng, H., Zeng, F., Zhou, S. Y., Zhong, F., Zheng, H. B., et al. (2012). Use Acupuncture to Treat Functional Constipation: Study Protocol for a Randomized Controlled Trial. *Trials* 13, 104. doi:10.1186/1745-6215-13-104

Liang, Y., Yang, X., Zhang, X., Duan, H., Jin, M., Sun, Y., et al. (2016). Antidepressant-like Effect of the Saponins Part of Ethanol Extract from SHF. *J. Ethnopharmacol.* 191, 307–314. doi:10.1016/j.jep.2016.06.044

Liu, J., Buisman-Pijlman, F., and Hutchinson, M. R. (2014). Toll-like Receptor 4: Innate Immune Regulator of Neuroimmune and Neuroendocrine Interactions in Stress and Major Depressive Disorder. *Front. Neurosci.* 8, 309. doi:10.3389/fnins.2014.00309

Liu, M. Y., Yin, C. Y., Zhu, L. J., Zhu, X. H., Xu, C., Luo, C. X., et al. (2018). Sucrose Preference Test for Measurement of Stress-Induced Anhedonia in Mice. *Nat. Protoc.* 13 (7), 1686–1698. doi:10.1038/s41596-018-0011-z

Liu, X., Mao, B., Gu, J., Wu, J., Cui, S., Wang, G., et al. (2021). Blautia-a New Functional Genus with Potential Probiotic Properties? *Gut Microbes* 13 (1), 1–21. doi:10.1080/19490976.2021.1875796

Magoč, T., and Salzberg, S. L. (2011). FLASH: Fast Length Adjustment of Short Reads to Improve Genome Assemblies. *Bioinformatics* 27 (21), 2957–2963. doi:10.1093/bioinformatics/btr507

Molina-Torres, G., Rodriguez-Arrastia, M., Roman, P., Sanchez-Labraca, N., and Cardona, D. (2019). Stress and the Gut Microbiota-Brain axis. *Behav. Pharmacol.* 30 (2 3-Spec Issue), 187–200. doi:10.1097/FBP.0000000000000478

Moretti, M., Werle, I., da Rosa, P. B., Neis, V. B., Platt, N., Souza, S. V. S., et al. (2019). A Single Coadministration of Subeffective Doses of Ascorbic Acid and Ketamine Reverses the Depressive-like Behavior Induced by Chronic Unpredictable Stress in Mice. *Pharmacol. Biochem. Behav.* 187, 172800. doi:10.1016/j.pbb.2019.172800

Mou, X. J., Liu, H., Lin, N., Chen, X., and Liu, S. L. (2019). Effects of Shugan Hewei Decoction and Active Substance Fractions on Behavior and Neurotransmitter Levels in Hypothalamus of Depression Model Rats. *Zhongguo Zhong Yao Za Zhi* 44 (15), 3343–3348. doi:10.19540/j.cnki.cjcmm.20190515.301

Nowarski, R., Jackson, R., Gagliani, N., de Zoete, M. R., Palm, N. W., Bailis, W., et al. (2015). Epithelial IL-18 Equilibrium Controls Barrier Function in Colitis. *Cell* 163 (6), 1444–1456. doi:10.1016/j.cell.2015.10.072

Park, A. J., Collins, J., Blennerhassett, P. A., Ghia, J. E., Verdu, E. F., Bercik, P., et al. (2013). Altered Colonic Function and Microbiota Profile in a Mouse Model of Chronic Depression. *Neurogastroenterol Motil.* 25 (9), 733–e575. doi:10.1111/nmo.12153

Park, J. S., Choi, J. W., Jhun, J., Kwon, J. Y., Lee, B. I., Yang, C. W., et al. (2018). Lactobacillus Acidophilus Improves Intestinal Inflammation in an Acute Colitis Mouse Model by Regulation of Th17 and Treg Cell Balance and Fibrosis Development. *J. Med. Food* 21 (3), 215–224. doi:10.1089/jmf.2017.3990

Qin, H. Y., Cheng, C. W., Tang, X. D., and Bian, Z. X. (2014). Impact of Psychological Stress on Irritable Bowel Syndrome. *World J. Gastroenterol.* 20 (39), 14126–14131. doi:10.3748/wjg.v20.i39.14126

Roth, K. A., and Katz, R. J. (1979). Stress, Behavioral Arousal, and Open Field Activity-Aa Reexamination of Emotionality in the Rat. *Neurosci. Biobehav Rev.* 3 (4), 247–263. doi:10.1016/0149-7634(79)90012-5

Savignac, H. M., Couch, Y., Stratford, M., Bannerman, D. M., Tzortzis, G., Anthony, D. C., et al. (2016). Prebiotic Administration Normalizes Lipopolysaccharide (LPS)-induced Anxiety and Cortical 5-HT2A Receptor and IL1-β Levels in Male Mice. *Brain Behav. Immun.* 52, 120–131. doi:10.1016/j.bbi.2015.10.007

Seo, S. U., Kamada, N., Muñoz-Planillo, R., Kim, Y. G., Kim, D., Koizumi, Y., et al. (2015). Distinct Commensals Induce Interleukin-1β via NLRP3 Inflammasome in Inflammatory Monocytes to Promote Intestinal Inflammation in Response to Injury. *Immunity* 42 (4), 744–755. doi:10.1016/j.immuni.2015.03.004

Shen, X., Zhao, Z., Luo, X., Wang, H., Hu, B., and Guo, Z. (20162016). Systems Pharmacology Based Study of the Molecular Mechanism of SiNiSan Formula for Application in Nervous and Mental Diseases. *Evid. Based Complement. Alternat Med.* 2016, 9146378. doi:10.1155/2016/9146378

Shuei, S., and Bruno, C. (2008). Interleukin-18 and Stress. *Brain Res. Rev.* 58 (1).

Silk, E., Zhao, H., Weng, H., and Ma, D. (2017). The Role of Extracellular Histone in Organ Injury. *Cell Death Dis* 8 (5), e2812. doi:10.1038/cddis.2017.52

Stackebrandt, E., and Goebel, B. M. (1994). Taxonomic Note: A Place for DNA-DNA Reassociation and 16S rRNA Sequence Analysis in the Present Species Definition in Bacteriology. *Int. J. Syst. Bacteriol.* 44 (4), 846–849. doi:10.1099/00207713-44-4-846

Stefanaki, C., Pervanidou, P., Boschiero, D., and Chrousos, G. P. (2018). Chronic Stress and Body Composition Disorders: Implications for Health and Disease. *Hormones (Athens)* 17 (1), 33–43. doi:10.1007/s42000-018-0023-7

Ten Bruggencate, S. J., Bovee-Oudenhoven, I. M., Lettink-Wissink, M. L., and Van der Meer, R. (2003). Dietary Fructo-Oligosaccharides Dose-Dependently Increase Translocation of salmonella in Rats. *J. Nutr.* 133 (7), 2313–2318. doi:10.1093/jn/133.7.2313

Tian, R., Hou, G., Li, D., and Yuan, T. F. (2014). A Possible Change Process of Inflammatory Cytokines in the Prolonged Chronic Stress and its Ultimate Implications for Health. *ScientificWorldJournal* 2014, 780616. doi:10.1155/2014/780616

Vacca, M., Celano, G., Calabrese, F. M., Portincasa, P., Gobbetti, M., and De Angelis, M. (2020). The Controversial Role of Human Gut Lachnospiraceae. *Microorganisms* 8 (4), 573. doi:10.3390/microorganisms8040573

Wang, L., and Hauenstein, A. V. (2020). The NLRP3 Inflammasome: Mechanism of Action, Role in Disease and Therapies. *Mol. Aspects Med.* 76, 100889. doi:10.1016/j.mam.2020.100889

Wang, Q., Garrity, G. M., Tiedje, J. M., and Cole, J. R. (2007). Naive Bayesian Classifier for Rapid Assignment of rRNA Sequences into the New Bacterial Taxonomy. *Appl. Environ. Microbiol.* 73 (16), 5261–5267. doi:10.1128/AEM.00062-07

Wei, L., Li, Y., Tang, W., Sun, Q., Chen, L., Wang, X., et al. (2019). Chronic Unpredictable Mild Stress in Rats Induces Colonic Inflammation. *Front. Physiol.* 10, 1228. doi:10.3389/fphys.2019.01228

Weiss, G. A., and Hennet, T. (2017). Mechanisms and Consequences of Intestinal Dysbiosis. *Cell. Mol. Life Sci.* 74 (16), 2959–2977. doi:10.1007/s00018-017-2509-x

Willner, P., Towell, A., Sampson, D., Sophokleous, S., and Muscat, R. (1987). Reduction of Sucrose Preference by Chronic Unpredictable Mild Stress, and its Restoration by a Tricyclic Antidepressant. *Psychopharmacology (Berl)* 93 (3), 358–364. doi:10.1007/BF00187257

Wong, M. L., Inserra, A., Lewis, M. D., Mastronardi, C. A., Leong, L., Choo, J., et al. (2016). Inflammasome Signaling Affects Anxiety- and Depressive-like Behavior and Gut Microbiome Composition. *Mol. Psychiatry* 21 (6), 797–805. doi:10.1038/mp.2016.46

Xu, J., Bjursell, M. K., Himrod, J., Deng, S., Carmichael, L. K., Chiang, H. C., et al. (2003). A Genomic View of the Human-Bacteroides Thetaiotaomicron Symbiosis. *Science* 299 (5615), 2074–2076. doi:10.1126/science.1080029

Zheng, P., Zeng, B., Zhou, C., Liu, M., Fang, Z., Xu, X., et al. (2016). Gut Microbiome Remodeling Induces Depressive-like Behaviors through a Pathway Mediated by the Host's Metabolism. *Mol. Psychiatry* 21 (6), 786–796. doi:10.1038/mp.2016.44

Zheng, P., Wu, J., Zhang, H., Perry, S. W., Yin, B., Tan, X., et al. (2020). The Gut Microbiome Modulates Gut-Brain axis Glycerophospholipid Metabolism in a Region-specific Manner in a Nonhuman Primate Model of Depression. *Mol. Psychiatry* 26, 2380–2392. doi:10.1038/s41380-020-0744-2

Zhu, C., Zhao, L., Zhao, J., and Zhang, S. (2020). Sini San Ameliorates Duodenal Mucosal Barrier Injury and Low-grade Inflammation via the CRF Pathway in a Rat Model of Functional Dyspepsia. *Int. J. Mol. Med.* 45 (1), 53–60. doi:10.3892/ijmm.2019.4394

Zhu, H. Z., Liang, Y. D., Ma, Q. Y., Hao, W. Z., Li, X. J., Wu, M. S., et al. (2019). Xiaoyaosan Improves Depressive-like Behavior in Rats with Chronic Immobilization Stress through Modulation of the Gut Microbiota. *Biomed. Pharmacother.* 112, 108621. doi:10.1016/j.biopha.2019.108621

Zong, Y., Chen, T., Dong, H., Zhu, L., and Ju, W. (2019). Si-Ni-San Prevents Reserpine-Induced Depression by Inhibiting Inflammation and Regulating CYP450 Enzymatic Activity. *Front. Pharmacol.* 10, 1518. doi:10.3389/fphar.2019.01518

Conflict of Interest: The authors declare that the research was conducted in the absence of any commercial or financial relationships that could be construed as a potential conflict of interest.

Publisher's Note: All claims expressed in this article are solely those of the authors and do not necessarily represent those of their affiliated organizations, or those of the publisher, the editors, and the reviewers. Any product that may be evaluated in this article, or claim that may be made by its manufacturer, is not guaranteed or endorsed by the publisher.

Copyright © 2021 Yue, Chen, Liu, Xu, Zhou, Ming, Chen, Chen, Lin, Liu, Zhao and Liu. This is an open-access article distributed under the terms of the Creative Commons Attribution License (CC BY). The use, distribution or reproduction in other forums is permitted, provided the original author(s) and the copyright owner(s) are credited and that the original publication in this journal is cited, in accordance with accepted academic practice. No use, distribution or reproduction is permitted which does not comply with these terms.

frontiers in Pharmacology

ORIGINAL RESEARCH
published: 24 December 2021
doi: 10.3389/fphar.2021.797605

Amelioration of AOM/DSS-Induced Murine Colitis-Associated Cancer by Evodiamine Intervention is Primarily Associated with Gut Microbiota-Metabolism-Inflammatory Signaling Axis

Mengxia Wang[1,2,3†], Biqiang Zhou[2†], Weihong Cong[4], Miao Zhang[2], Ziwen Li[2,3], Yan Li[2,3], Shaoyu Liang[2,3], Keji Chen[4], Depo Yang[1*] and Zhengzhi Wu[2*]*

[1]School of Pharmaceutical Sciences, Sun Yat-sen University, Guangzhou, China, [2]The First Affiliated Hospital of Shenzhen University, Shenzhen Second People's Hospital, Shenzhen, China, [3]Shenzhen Institute of Geriatrics, Shenzhen, China, [4]National Clinical Research Center for Chinese Medicine Cardiology, Xiyuan Hospital, China Academy of Chinese Medical Sciences, Beijing, China

Evodiamine (EVO), an indole alkaloid derived from Rutaceae plants *Evodia rutaecarpa* (Juss.) Benth.、*Evodia rutaecarpa* (Juss.) Benth. Var. bodinieri (Dode) Huang or *Evodia rutaecarpa* (Juss.) Benth. Var. officinalis (Dode) Huang, has anti-inflammatory and anti-tumor activities. Our previous study found that EVO attenuates colitis by regulating gut microbiota and metabolites. However, little is known about its effect on colitis-associated cancer (CAC). In this study, the protective effects of EVO on azoxymethane (AOM)/dextran sulfate sodium (DSS)-induced colitis and tumor mice were observed, and the underlying potential mechanism was clarified. The results suggested that EVO ameliorated AOM/DSS-induced colitis by inhibiting the intestinal inflammation and improving mucosal barrier function. And EVO significantly reduced the number and size of AOM/DSS-induced colorectal tumors along with promoted apoptosis and inhibited proliferation of epithelial cell. Moreover, EVO promoted the enrichment of SCFAs-producing bacteria and reduced the levels of the pro-inflammatory bacteria, which contributes to the changes of microbiota metabolism, especially tryptophan metabolism. Furthermore, inflammatory response (like Wnt signaling pathway、Hippo signaling pathway and IL-17 signaling pathway) were effectively alleviated by EVO. Our study demonstrated that the protective therapeutic action of EVO on CAC is to inhibit the development of intestinal inflammation-cancer by regulating gut microbiota metabolites and signaling pathways of colon intestinal epithelial, which may represent a novel agent for colon cancer prevention via manipulation of gut microbiota.

Keywords: colitis-associated cancer, Evodiamine, gut microbiota, tryptophan metabolism, inflammatory signaling pathway

OPEN ACCESS

Edited by:
Dahui Liu,
Hubei University of Chinese Medicine, China

Reviewed by:
Tao Su,
Guangzhou University of Chinese Medicine, China
Jose A. Uranga,
Rey Juan Carlos University, Spain

***Correspondence:**
Keji Chen
kjchenvip@163.com
Depo Yang
lssydp@mail.sysu.edu.cn
Zhengzhi Wu
szwzz001@163.com

†These authors have contributed equally to this work

Specialty section:
This article was submitted to Ethnopharmacology, a section of the journal Frontiers in Pharmacology

Received: *19 October 2021*
Accepted: *08 December 2021*
Published: *24 December 2021*

Citation:
Wang M, Zhou B, Cong W, Zhang M, Li Z, Li Y, Liang S, Chen K, Yang D and Wu Z (2021) Amelioration of AOM/DSS-Induced Murine Colitis-Associated Cancer by Evodiamine Intervention is Primarily Associated with Gut Microbiota-Metabolism-Inflammatory Signaling Axis. Front. Pharmacol. 12:797605. doi: 10.3389/fphar.2021.797605

INTRODUCTION

Colorectal cancer (CRC) is the third most commonly diagnosed cancer worldwide, with high morbidity and mortality rates (Siegel et al., 2020). Studies have found that CRC may be affected by environmental factors (e.g., diet, smoking, alcohol), heredity (e.g. genetic mutations, microRNAs expression) and immune system (Chen et al., 2017). Accumulating evidences indicate that chronic inflammation of the colon may have a closely linked to the pathogenesis of CRC. Inflammatory bowel diseases (IBD), including ulcerative colitis (UC) and Crohn's disease (CD), which is associated with an increased risk of CRC, may progress to colitis-associated colorectal cancer (CAC) (Rieder et al., 2017). While CAC is known to be related to inflammation, the specific mechanism of inflammation involved in the pathogenesis of CAC have not been clarified.

In recent years, new lines of evidence have shown that gut microbiota play a key role in the development of IBD and CRC (Drewes et al., 2016; Li et al., 2020). Studies have also shown that changes in microbial composition and diversity are associated with the progression of CAC. An analysis of five different IBD patient cohorts form five different countries revealed that there are major differences in the diversity and abundance of the gut microbiota between healthy individuals and IBD patients (Sankarasubramanian et al., 2020). Interestingly, similar to IBD patients, the microbiota composition of CRC patients had also similar changes, characterized by increased abundance of Proteobacteria and decreased Firmicutes (Gagniere et al., 2016). The adherent/invasive strains of *Escherichia coli* were highly abundant in the colonic mucosa of patients with colorectal carcinoma and adenoma (Wang Z. et al., 2019). Recently, an interesting study showed that a purified membrane protein derived from the probiotics *Akkermansia muciniphila* could blunt the occurrence of colitis associated tumors (Wang L. et al., 2020). A longitudinal study of a CAC mouse model has also showed a significant change in microbiota composition in the presence of chemically induced chronic intestinal inflammation (Liang et al., 2014). These findings suggest that the gut microbiota may serve as a pivotal mediator for the progression of intestinal diseases and regulate the composition of gut microbiota has emerged in the prevention of CAC.

CAC is a progressive process from inflammation to cancer, so the prevention of CAC is of vital importance. At present, one of the most prevalent treatments for IBD in clinical is administration of some agents, including 5-aminosalicylic acid, corticosteroids, biological agents and immunosuppressants (Gao et al., 2020). However, treatment with these drugs tends to increase the patient's susceptibility to infection and leads to different adverse drug reactions (Gong et al., 2018). Once a malignant tumor is detected, total colectomy should be considered, but prophylactic surgery (proctocolectomy) does not always eliminate the risk of carcinogenesis (Sokol et al., 2014; Wang X. et al., 2019). Due to the limited efficacy and side effects of these therapies, alternative drugs that have the potential to treat both early inflammatory and late oncogenic stages should be developed; at the same time, the development from IBD to CRC is a long process, which provides an opportunity for intervention to inhibit the development of CRC.

Evodiamine (EVO), a quinolone alkaloid from the traditional botanical drug *Evodia rutaecarpa* (Juss.) Benth., *Evodia rutaecarpa* (Juss.) Benth. Var. bodinieri (Dode) Huang or *Evodia rutaecarpa* (Juss.) Benth. Var. officinalis (Dode) Huang (Chinese name: Wu-Zhu-Yu; Rutaceae), has been reported to have beneficial pharmacological properties, such as anti-obesity, anti-inflammation, anti-thrombotic and anti-cancer (Yu et al., 2016). It has been reported that the EVO inhibited high-fat diet-induced colitis-associated cancer in mice through regulating the gut microbiota (Zhu et al., 2020). And we have previously demonstrated that EVO can be effectively used to prevent and treat UC rats by regulating the gut microbiota and metabolism (Wang L. et al., 2020). Moreover, EVO could induce apoptosis and inhibit migration of colorectal cancer cells (Zhao et al., 2015). However, whether EVO inhibits the occurrence of colon cancer by inhibiting intestinal inflammation is still unclear, and the underlying mechanism has not yet been elucidated. The complex interaction between gut microbiota and anti-inflammatory and anti-tumor activities during CAC are also not fully understood.

Therefore, in this study with a mouse azomethanze (AOM)/sodium dextran sulfate (DSS)-induced colitis model and AOM/DSS-induced tumor model, we demonstrated that EVO treatment significantly protected against colitis, colon carcinogenesis and tumor growth. We want to know whether EVO affects the gut microbiota of CAC mice. Moreover, we also want to investigate if EVO changes metabolic activities and pathways after regulating the gut microbiota composition. On the other hand, we want to understand whether EVO impacts the gene-gene interaction of colonic epithelial cells after changing the composition of gut microbiota. This study can be considered as a reference for EVO to further study the mechanism of CAC, which is a promising agent for the prevention and treatment of CAC.

MATERIALS AND METHODS

Mice and AOM/DSS-Induced Colitis-Associated Colorectal Cancer

Specific pathogen-free (SPF) male C57BL/6 mice (6–8 weeks old, obtained from the Center of Laboratory Animal Science of Guangdong) were maintained in a specific sterile colony under a complete controlled condition (temperature 23 ± 2°C; humidity 50–70%; 12 h-light dark cycle and lighting at 8:00 am) and were allowed access to a commercial diet and water ad libitum.

For the early enteritis model, after a seven-day adaptation period, mice were randomly allocated to three groups (n = 12): Control group, AOM/DSS group and EVO group. AOM/DSS and EVO groups mice were intraperitoneally (i.p.) injected with 10 mg/ kg AOM (Sigma-Aldrich) at the start point of Week 1 and then received 2.5%DSS (MP Biomedical, 36,000–50000 MW) for 7 days. From the first day of the model induction, the mice of EVO group were gavaged with 40 mg/ kg Evodiamine (Meilunbio, MB5729), Control group and AOM/DSS group received orally 0.5%CMC-Na respectively daily for 18 days (**Figure 1A**), the dose of EVO was determined by the previous dose-effect relationship study in our research group (Wang MX. et al., 2020). Body weights were monitored daily and disease

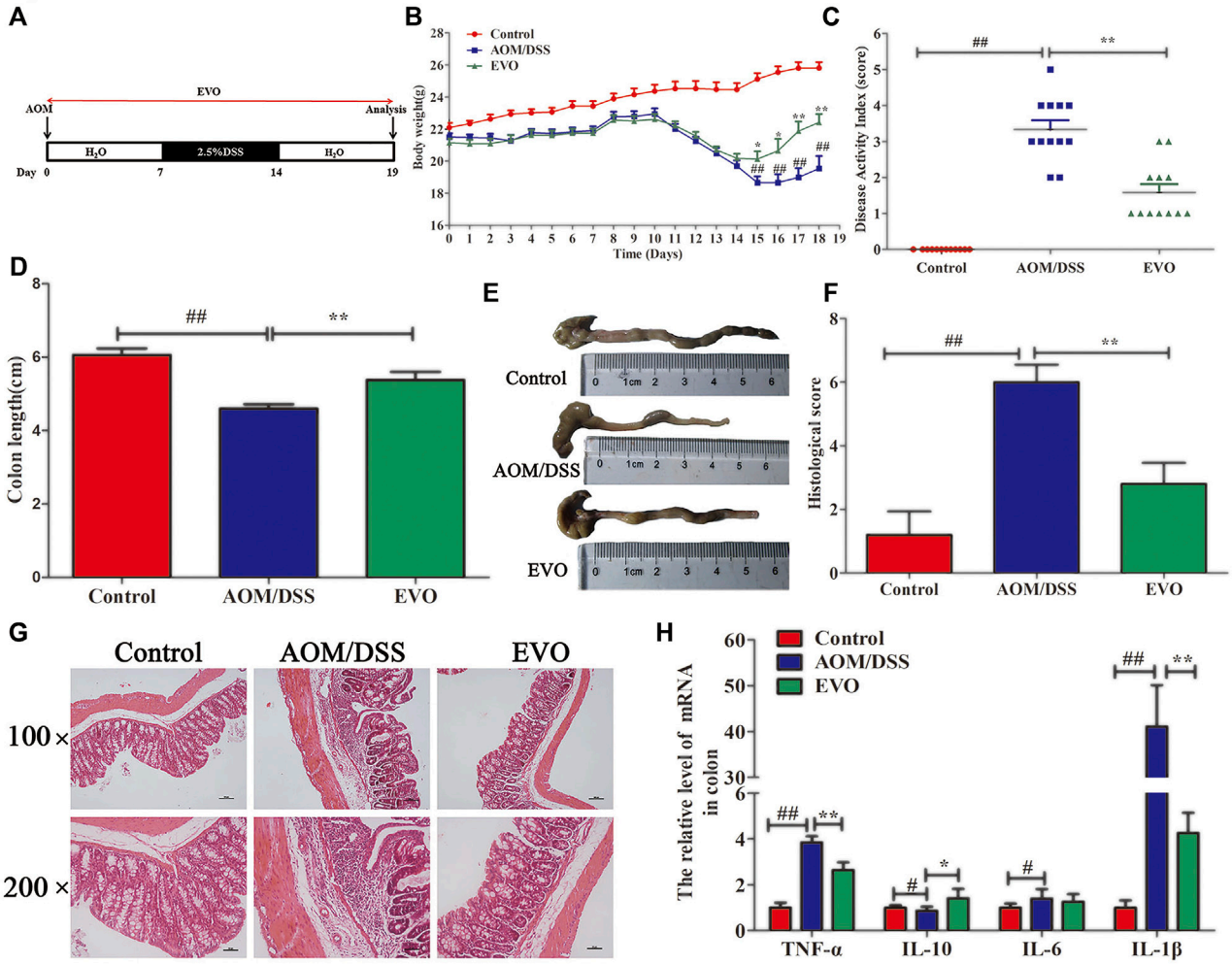


FIGURE 1 | EVO alleviates colitis at the early stage of CAC. **(A)** Experimental protocol for model. **(B)** Body weight change. **(C)** Disease activity index score. **(D–E)** Colon length. **(F)** Histological scores. **(G)** H&E staining. **(H)** Inflammatory cytokines in colon. The results are presented as mean ± SD. $^{\#}p < 0.05$, $^{\#\#}p < 0.01$, Control *vs*. AOM/DSS; $^{*}p < 0.05$, $^{**}p < 0.01$, EVO *vs*. AOM/DSS.

activity index (including weight loss, intestinal bleeding and stool consistency) (**Supplementary Table S1**) (Cooper et al., 1993). Feces samples were collected on 18th days and stored at -80°C for further analysis.

For advanced tumor model, after a seven-day adaptation period, mice were randomly allocated to three groups (n = 12): Control group, AOM/DSS group and EVO group. AOM/DSS and EVO groups mice were received a i.p. injection of 10 mg/ kg AOM and 7 days later, 2.5%DSS administration was repeated three times for whole test periods (Weeks 2, 5, and 8). From the first day of the model induction, the mice of EVO group were gavaged with 40 mg/ kg Evodiamine, Control group and AOM/DSS group received orally 0.5%CMC-Na respectively daily for 12 weeks (**Figure 3A**). During the study, body weights were measured every 3 days. Feces samples were collected on 84th days and stored at −80°C for further analysis.

The mice were euthanized, their colons were measured and quantified the gross tumors (Tumor size (mm) = diameter of tumor). 1.0–2.0 cm sections were dissected from distal-colon and either snap-forzen in liquid N_2 for futher analysis, stored in RNA later for RNA extraction, or fixed in 4%paraformaldehyde for histology assessment. All animal experiments were approved by the institutional animal care and use committee and conducted in accordance with Care and Use of Laboratory Animals guidelines.

Histopathological Analysis

After fixation for 48 h by 4%paraformaldehyde, the formalin-fixed colon samples were buried in paraffin wax and 3-μm thick paraffin sections were stained with hematoxylin-eosin (HE) for histological analysis. Tissue pathology was scoring using previously described systems (Ranganathan et al., 2013). And images were measured under the microscope (Leica DM5000B, Leica, Germany).

Alcian Blue-Periodic Acid Sthiff Staining

To analyze goblet cells (GCs), the fixed colons were then stained using Alcian blue and periodic acid-Schiff (AB-PAS).

Observation and taking photos were performed under standing microscope (BX53, Olympus, Japan). GCs were quantified using the Cell counter Image-Pro Plus 6.0 software and normalized to crypt numbers, the analysis was performed on 10 crypts per animal.Frontiers requires figures to be submitted individually, in the same order as they are referred to in the manuscript.

Terminal Deoxynucleotidyl Transferase dUTP Nick End Labeling Staining

Apoptosis was detected by a terminal deoxynucleotidyl transferase dUTP nick end labeling (TUNEL) according to the manufacturer's protocol (Wanleibio). Images were visualized by Confocal Scanning Laser Microscope (ZEISS, Germany). We randomly selected five tumor sections for TUNEL detection, and TUNEL-positive cells were counted in images by Image-Pro Plus 6.0.

Immunohistochemistry Staining

Paraffin-embedded tissues were used for analyzing the expression of Ki-67. Tissue sections were deparaffinised and rehydrated using a graded ethanol series and distilled water, and then treated with 3%H_2O_2 in methanol for 30 min then washed with PBS, 10%normal goat serum incubated for 30 min. After washing, primary antibody Ki-67 (ab16667, 1:300) was applied to tissue overnight at 4°C. Sections were then washed in PBS three times and incubated with secondary antibodies. Following washing, sections were developed with DAB using a commercial kit (CoWin Biosciences), counterstained with hematoxylin, coverslipped. Finally, observation and taking photos were performed under standing microscope (BX53, Olympus, Japan). The proportion of Ki-67 positive cells was determined by counting immunostain positive cells, as a percentage to the total number of nuclei in the field. At least 1,000 cells were counted in five random microscopic fields, which was analysed by Image-Pro Plus 6.0.

Colon RNA Extraction and Real-Time PCR

Total RNA was extracted from colon tissues using Trizol reagent (TaKaRa) and quantified for cDNA synthesis. Quantitative real-time PCR reactions were performed using the CFX96 detection system (Bio-Plex) and SYBR Green (TIANGEN). The primers are listed in **Supplementary Table S2**. The expression levels were calculated with the $2^{-\Delta\Delta Ct}$ method, and the Ct values were normalized using GAPDH as a reference gene.

16S rRNA Amplicon Sequencing

Feces on day 18 and 84 were used to detect changes in the gut microbiota of the mice. Bacterial DNA in feces was extracted by the Stool Genomic DNA Kit (QIAGEN, Germany) then amplified by qPCR using the primers: 338F (5′-ACTCCTACGGGAGGC AGCAG-3′) and 806R (5′-GGACTACHVGGGTWTCTAAT-3′). All samples were sequenced using the 250-base pair paired-end strategy on the Illumina HiSeq 2,500 platform according to the manufacturer's instruction. High-quality sequence reads were then analyzed using the Quantitative Insights Into Microbial Ecology (QIIME, 1.9.1, http://qiime.org/scripts/assign_taxonomy.html) software package and visualized using R software (Version 3.4.1). Functional contributions of the microbial communities were predicted based on OUT using R package Tax4Fun with the Kyoto Encyclopedia of Genes and Genomes (KEGG) database (Asshauer et al., 2015).

Liquid Chromatography-Mass Spectrometry-Based Non-targeted Metabolomics Analyses

50 mg of feces was collected into a tube and added methanol-water (4:1, v/v), crushed by a high-throughput tissue crusher at low temperatures; vortexing and three cycles of ultrasound (10 min); placed at −20°C for 30 min; and centrifuged at 13,000 × g and 4°C for 15 min. The supernatants were subjected to metabolomics profiling. A quality control (QC) sample, made by mixing and blending equal volumes (10 μL) of each sample, was used to examine the entire analysis process instrument stability and ensure the reliability of the results.

LC-MS was performed on a Thermo UHPLC system equipped with a binary solvent delivery manager and a sample manger, coupled with a Thermo Q Exactive Mass Spectrometer equipped with an electrospray interface. LC conditions: Column: Acquity BEH C18 column (100 mm × 2.1 mm i.d., 1.7 μm; Waters, Milford, United States). Solvent: Solvent A was aqueous formic acid (0.1% (v/v) formic acid) and Solvent B was acetonitrile/isopropanol (1/1) (0.1% (v/v) formic acid). The gradient was set as follows: 0–3 min, 5% B; 3–9 min, 20%B; 9–13 min, 95%B; 13.0–13.1 min, 95%B; 13.1–16 min, 5%B. Injection volume was 10 μL, flow rate was 0.4 ml/ min, and column temperature was set at 40°C. The mass spectrometric data was collected using a Thermo UHPLC-Q Exactive Mass Spectrometer equipped with electrospray ionization (ESI) source operating in either positive or negative ion mode.

The total ion chromatograms were collected and the ion selection, peak alignment, peak matching and filtering was carried out by Progenesis QI (Waters Corporation, Milford, United States). The online METLIN database (https://metlin.scripps.edu/) and HMDB database (http://www.hmdb.ca/) were used to identify metabolites. After normalization, data were exported to SIMCA V13.0 (Umetrics, Sweden) for multivariate data analysis. The differential compounds were screened by q value (p value adjusted by false discovery rate (FDR))≥0.05 and variable importance in the projection (VIP)≥1 from the cross-validated PLS-DA model. Finally, the biomarkers were analyzed by Metabolomics Pathway Analysis (MetPA) to describe the involved potential metabolic pathways.

Colon Transcriptomics

Total RNA was extracted from colon tissue using TRIzol® Reagent according the manufacturer's instructions (Invitrogen) and genomic DNA was removed using DNase I (TaKara). Extract RNA, gene expression and data analysis was performed as our previous study (Wang MX. et al., 2020).

Statistical Analysis

The correlation between microbes and physiological index was calculated by Spearman correlation with SPSS (version 21.0). All

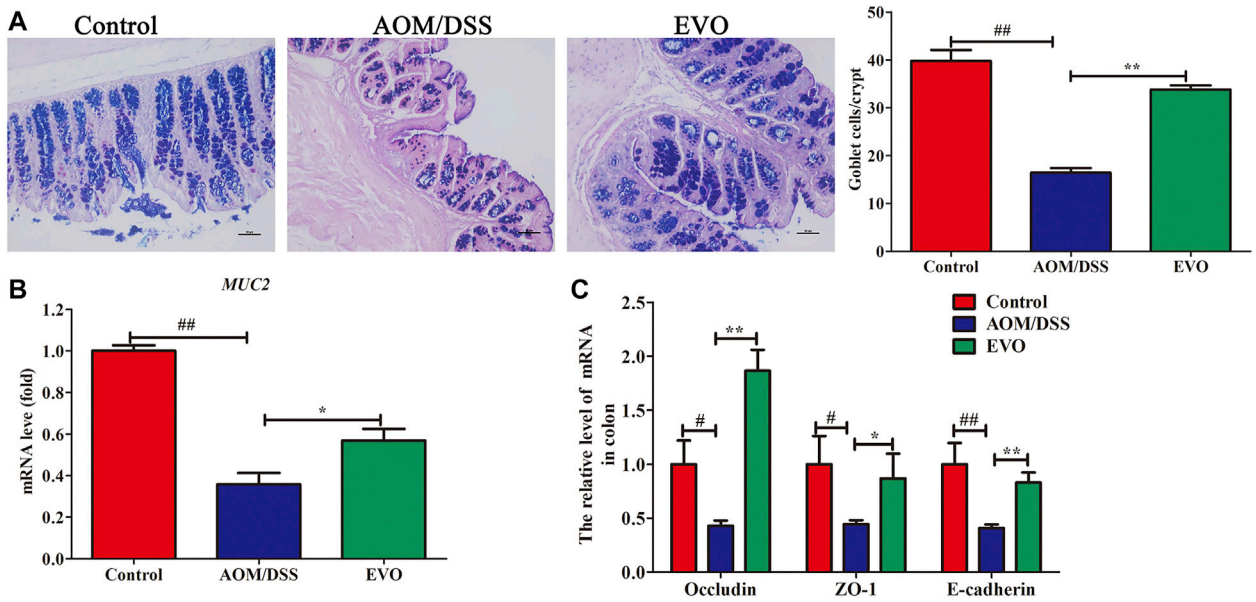


FIGURE 2 | EVO improves damage to the colonic mucosal barrier in AOM/DSS-induced colitis mice. **(A)** AB-PAS staining and the number of goblet cells. **(B)** The relative expression of *MUC2*. **(C)** Changes in colon mucosal barrier molecule mRNA levels. The results are presented as mean ± SD. $^{\#}p < 0.05$, $^{\#\#}p < 0.01$, Control *vs*. AOM/DSS; $^{*}p < 0.05$, $^{**}p < 0.01$, EVO *vs*. AOM/DSS.

the values in the tables and figures are expressed as the mean ± SD. Statistical analyses were carried out using t-test between two groups and one-way ANOVA followed by Tukey-Kramer post-hoc test among multiple groups using SPSS software. A difference of $p < 0.05$ was considered as statistical significance.

RESULTS

EVO Suppressed AOM/DSS-Induced Colitis in Mice

To determine whether EVO could attenuate the acute colitis of CAC, AOM-induced mice were challenged with 2.5%DSS for 7 days, and EVO was gavaged throughout the experiment (**Figure 1A**). Disease activity index (DAI) score, including body weight loss, presence of blood in stool and diarrhea, were observed after the DSS challenge (**Figure 1C**). Treatment with EVO relieved the body weight loss and decreased the DAI score (**Figures 1B,C**). In addition, the shortened colon length induced by DSS was significantly increased by EVO administration (**Figures 1D,E**). HE staining showed that AOM/DSS induced the destruction of intestinal epithelial structure, massive infiltration of inflammatory cells, crypt loss and large area edema (**Figure 1G**), accompanied by an increase in pathological score (**Figure 1F**). However, these pathological changes were remarkably reversed by EVO treatment (**Figures 1F,G**). EVO treatment also significantly inhibited the concentration of pro-inflammatory cytokines TNF-α and IL-1β, increased the expression of anti-inflammatory cytokine IL-10 (**Figure 1H**). Collectively, these results suggested that EVO ameliorated the acute colitis of CAC mice.

EVO Restored Intestinal Barrier Function in AOM/DSS-Induce Colitis in Mice

We measured AB-PAS staining, MUC2 and tight junction molecules (Occludin, ZO-1 and E-cadherin) in the colon as parameters for the integrity of intestinal barrier. AB-PAS staining of the gut tissues of representative mice in each group showed that the quantity of goblet cells in AOM/DSS group was significantly reduced (**Figure 2A**). EVO supplementation significantly increased the number of goblet cells, promoted the secretion of MUC2 and the expression of Occludin, ZO-1 and E-cadherin (**Figures 2A–C**). These results indicated that EVO could rescue these AOM/DSS-induced damage to the gut barrier and increase gut permeability.

EVO Attenuated AOM/DSS-Induced Colon Tumorigenesis in CAC Mice

To investigate the impact of EVO on the intestinal tumor, we established AOM/DSS recurring inflammation-driven colorectal cancer (**Figure 3A**). AOM/DSS administration reduced the body weight, however, EVO group showed a protective effect on weight loss (**Figure 3B**). Expectedly, EVO treatment could significantly increase the colon length and the length-weight ratio of colon, and relieved splenomegaly (**Figures 3C–E**). All mice in the AOM/DSS group had colon tumors, but administration with EVO suppressed tumor cells development and decreased the tumors size (**Figures 3F,G**). In the AOM/DSS group, high-grade dysplasia of intestinal epithelium and heavily infiltrated with inflammatory cells were observed, indicating the existence of inflammation and highly differentiated adenocarcinoma of the

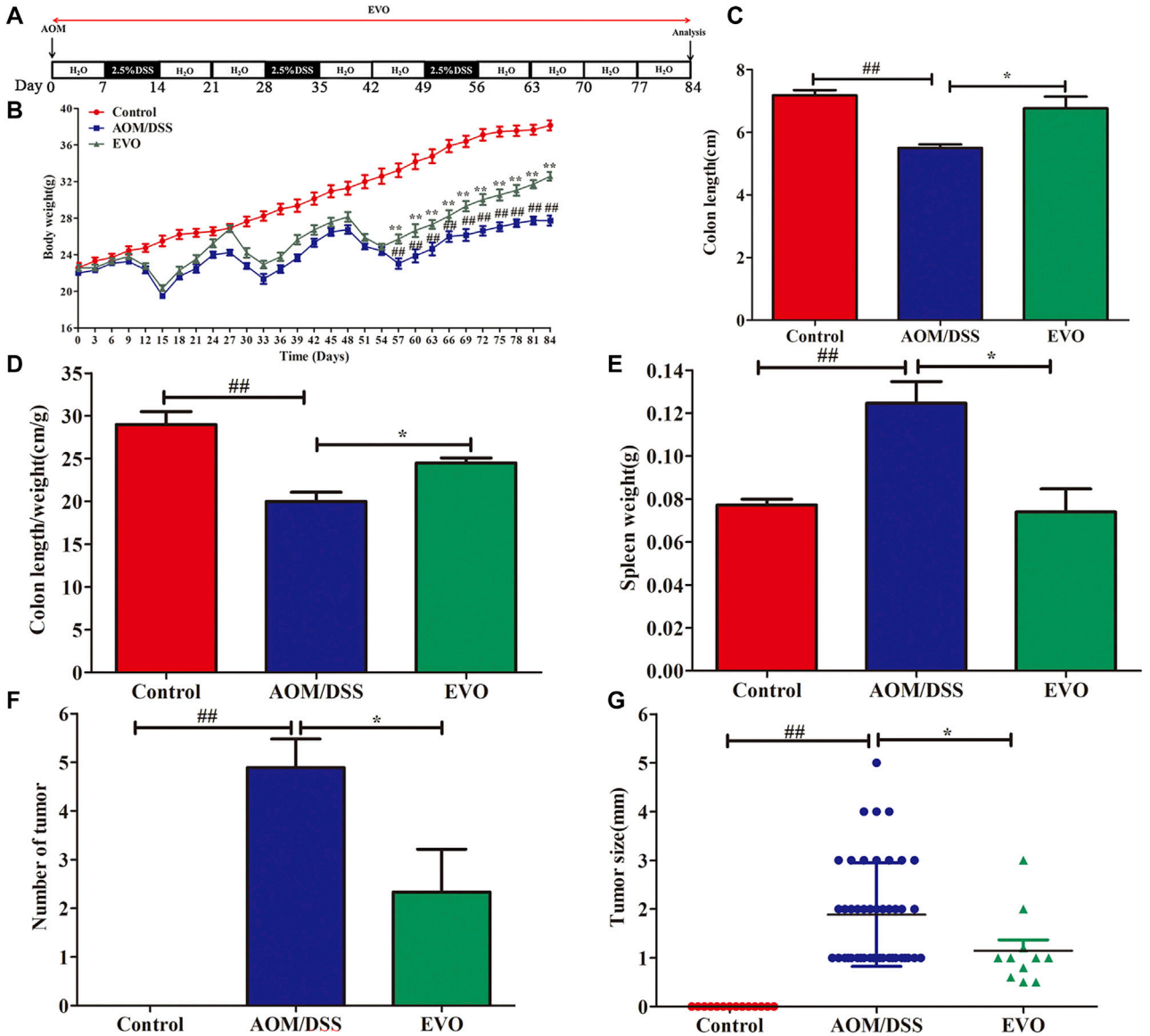


FIGURE 3 | EVO prevents tumorigenesis and growth at a late stage of CAC. **(A)** Protocol of EVO and AOM/DSS treatments used in this study. **(B)** Body weight change. **(C)** Colon length. **(D)** Colon length/weight ratio. **(E)** Spleen weight. **(F)** Tumor number. **(G)** Tumor size. The results are presented as mean ± SD. $^{\#}p < 0.05$, $^{\#\#}p < 0.01$, Control *vs*. AOM/DSS; $^{*}p < 0.05$, $^{**}p < 0.01$, EVO *vs*. AOM/DSS.

colon (**Figure 4A**). Treatment with EVO could inhibit inflammatory cells infiltration and tumorigenesis, and maintain the intestinal epithelial structure. To investigate the effect of EVO on tumor cells, we examined the proliferation and apoptosis in colon tumor tissues. The rate of Ki-67 positive cells in AOM/DSS was significantly increased than that in EVO group (**Figures 4A,B**). Compared with the AOM/DSS group, the number of apoptotic cells increased in the EVO group (**Figure 4C**). These results suggested that EVO inhibited the proliferation of colon tumor cells and promoted their apoptosis. Finally, we used AB/PAS staining to detect the goblet cells quantity. The results showed that the numbers of mucin granule-containing goblet cells were markedly lower after exposure to AOM/DSS than in the EVO group (**Figure 4D**). The result indicated that EVO protected the mucous layer and thus inhibited the tumorigenesis.

EVO Treatment Modulated the Composition of Gut Microbiota in AOM/DSS-Induced Colitis Mice

To investigate the impact of EVO on gut microbiota composition in AOM/DSS-induced colitis mice, we performed 16S rRNA gene sequencing of feces in three groups. The α-diversity indices, richness indices (Ace and Chao) and diversity indices (PD whole tree, Shannon and Simpson) were declined in AOM/

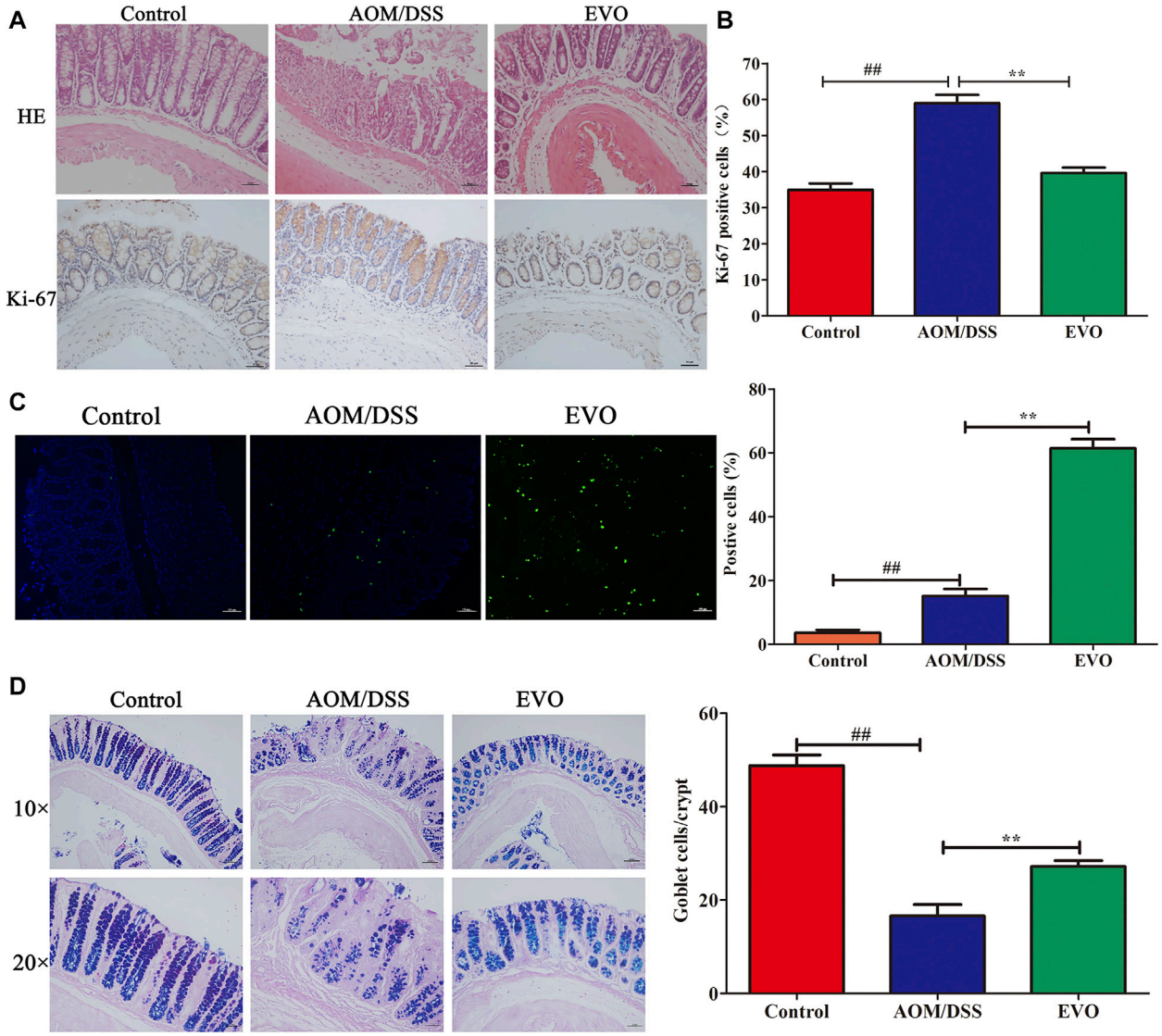


FIGURE 4 | | Effect of EVO treatment on cell proliferation and apoptosis in CAC model. **(A)** HE staining and Ki-67 analysis. **(B)** The proportion of Ki-67 positive cells in the colon of CAC mice. **(C)** Representative photo for TUNEL staining and assessment of the apoptotic cells. **(D)** AB-PAS staining and the number of goblet cells. The results are presented as mean ± SD. $^{\#\#}p < 0.01$, Control *vs*. AOM/DSS; $^{**}p < 0.01$, EVO *vs*. AOM/DSS.

DSS group compared with Control group, and EVO treatment could impact on the α-diversity of microbiota (**Figures 5A,B**; **Supplementary Figure S1A–C**; **Supplementary Table S3**). To characterize the global differences in feces microbial communities among groups, a principal coordinates analysis (PCoA) was performed on bray_curtis. The PCoA plots showed a distinct clustering of the microbiota composition among the three groups (analysis of similarity [ANOSIM]; between Control group and AOM/DSS group, $p = 0.003$; between AOM/DSS group and EVO group, $p = 0.007$), indicating EVO could modulate the structure of gut microbiota in AOM/DSS-induced colitis mice (**Figure 5C**; **Supplementary Figure S1D–E**).

To investigate the abundance and distribution of gut microbiota in the Control group, AOM/DSS group and EVO group, we analyzed the variation of microbiota at the phylum level. Six primary phyla (Bacteroidetes, Firmicutes, Campilobacterota, Desulfobacterota, Proteobacteria and Verrucomicrobiota) were shown in the bacterial communities (**Supplementary Table S4**). Compared with Control group, AOM/DSS-induced the relative abundance of Firmicutes and Campilobacterota were decreased, and the levels of Bacteroidetes, Desulfobacterota, Proteobacteria and Verrucomicrobiota were elevated, while it was restored by EVO treatment (**Figure 5D**; **Supplementary Figure S1F**). Moreover, the Firmicutes/Bacteroidetes ratio increased from 0.72 to 0.81 by EVO supplementation (**Supplementary Figure S1G**). To further explore the changes of gut microbiota community in each group, an analysis of the genus level was performed

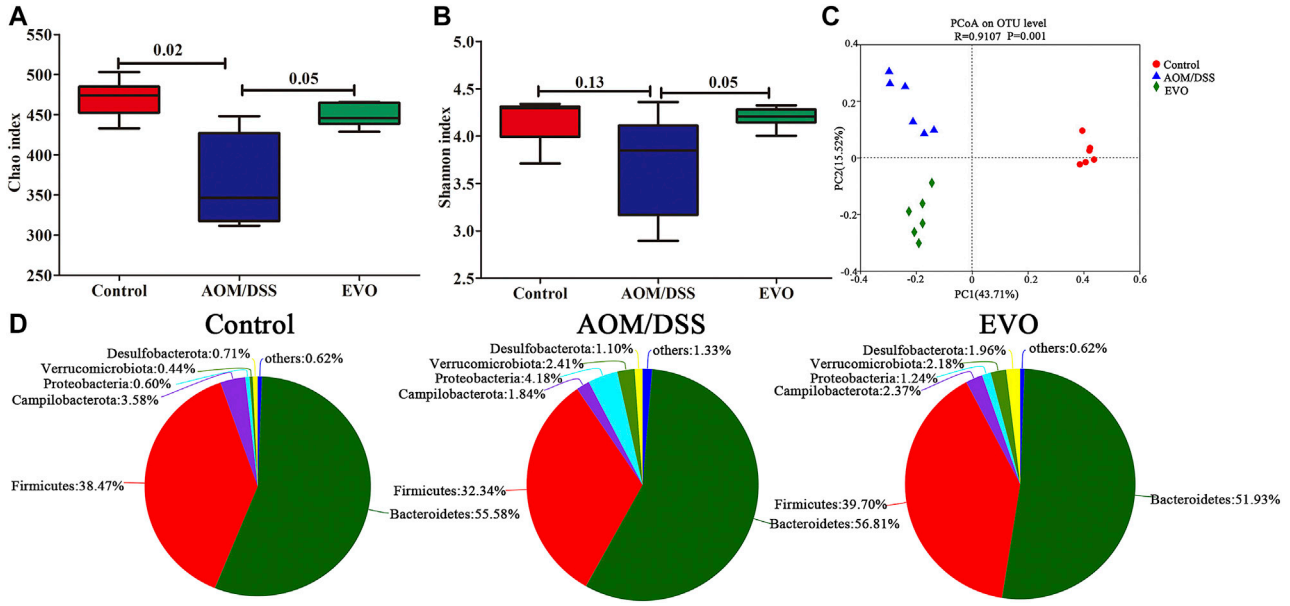


FIGURE 5 | | EVO alters AOM/DSS-induced colitis mice fecal microbiota composition. **(A)** Chao index. **(B)** Shannon index. **(C)** UniFrac-based PCoA plot. **(D)** Phylum levels pie chart.

(**Figure 6A**). Based on a 97% species similarity, a total of 135 genera were identified from the three groups, of which 34 genera with relative abundance made up at least more than 0.5% in one group were analyzed. Compared with the Control group, the relative abundance of *ASF356*, *Alistipes*, *Alloprevotella*, *Anaerotruncus*, *Candidatus_Saccharimonas*, *Colidextrribacter*, *GCA-900066575*, *Helicobacter*, *Lachoclostridium*, *Lachnospiraceae_NK4A136_group*, *Oscillibacter*, *Roseburia*, *norank_f_*Muribaculaceae, *norank_f_Oscillospiraceae*, *norank_f_Ruminococcaceae*, *unclassified_f_Lachnospiracease*, *unclassified_f_Oscillospiraceae*, and *unclassified_o_Bacteroidales* were decreased, and the levels of *Akkermansia*, *Bacteroides*, *Bifidobacterium*, *Desulfovibrio*, *Escherichia-Shigella*, *Eubacterium_fissicatena_group*, *Lactobacillus*, *Parabacteroides*, *Parasutterella*, *Prevotellaceae_UCG-001*, *Rikenella*, *Ruminococcus_torques_group*, *Turicibacter*, *norank_f__norank_o__Clostridia_UCG-014*, *unclassified_f__Ruminococcaceae* were increased (**Figures 6B,C**). However, EVO treatment could significantly increase the relative abundance of *Alloprevotella*, *Lachnoclostridium*, *Oscillibacter*, *unclassified_f_Lachnospiraceae*, *unclassified_f_Ruminococcaceae*, *unclassified_o_Bacteroidales*, and decrease the levels of *Bacteroides*, *Parasutterella*, *Turicibacter*. Taken together, our results showed that EVO treatment changed the composition of gut microbiota after AOM/DSS-induced colitis mice.

Association Between Gut Microbiota and Colitis-Related Pathophysiological Traits

To further investigate whether changes in gut microbiota are correlated with the remission of colitis symptoms, the Spearman correlation between the top 20 genus and related physiological indicators among three groups (**Figure 6D**, **Supplementary Table S5**). We found that the feces microbiota (*Bacteroides*, *Lactobacillus*, *Parasutterella* and *Eubacterium_fissicatena_group*; $p < 0.05$) were negative correlation with body weight, goblet cells, colon length and MUC2, and were positive correlation with TNF-α, pathological score and IL-1β, while the correlation between *Alloprevotella* and indicators were just opposite to the above results. Interestingly, we also found that *Akkermansia* was negative associated with MUC2、colon length、ZO-1 and E-cadherin, was positive associated with TNF-α ($p < 0.05$), *Lachnospiraceae_NK4A136_group* was positive correlation with colon length and E-cadherin, was negative correlation with TNF-α and IL-1β ($p < 0.05$).

The Effect of EVO on Gut Microbiota in CAC Mice

To further investigate whether EVO attenuated AOM/DSS-induced colon tumorigenesis is related to gut microbiota, 16S rRNA analysis was performed on feces samples collected at 84th days. Common microbial α-diversity indices, richness indices (Chao and Ace) and diversity indices (Shannon, Simpson and PD whole tree) were declined in AOM/DSS group, and EVO treatment could increase the diversity indices and not change the richness indices, indicating that EVO can increase microbial community diversity (**Figure 7A**; **Supplementary Figure S2A–E**; **Supplementary Table S6**). PCoA based on the Unweighted UniFrac algorithm clearly revealed that the microbial community changed among three groups (**Figure 7B**). To further understand the result of PCoA, the Hierarchical clustering analysis was conducted, the Hierarchical clustering

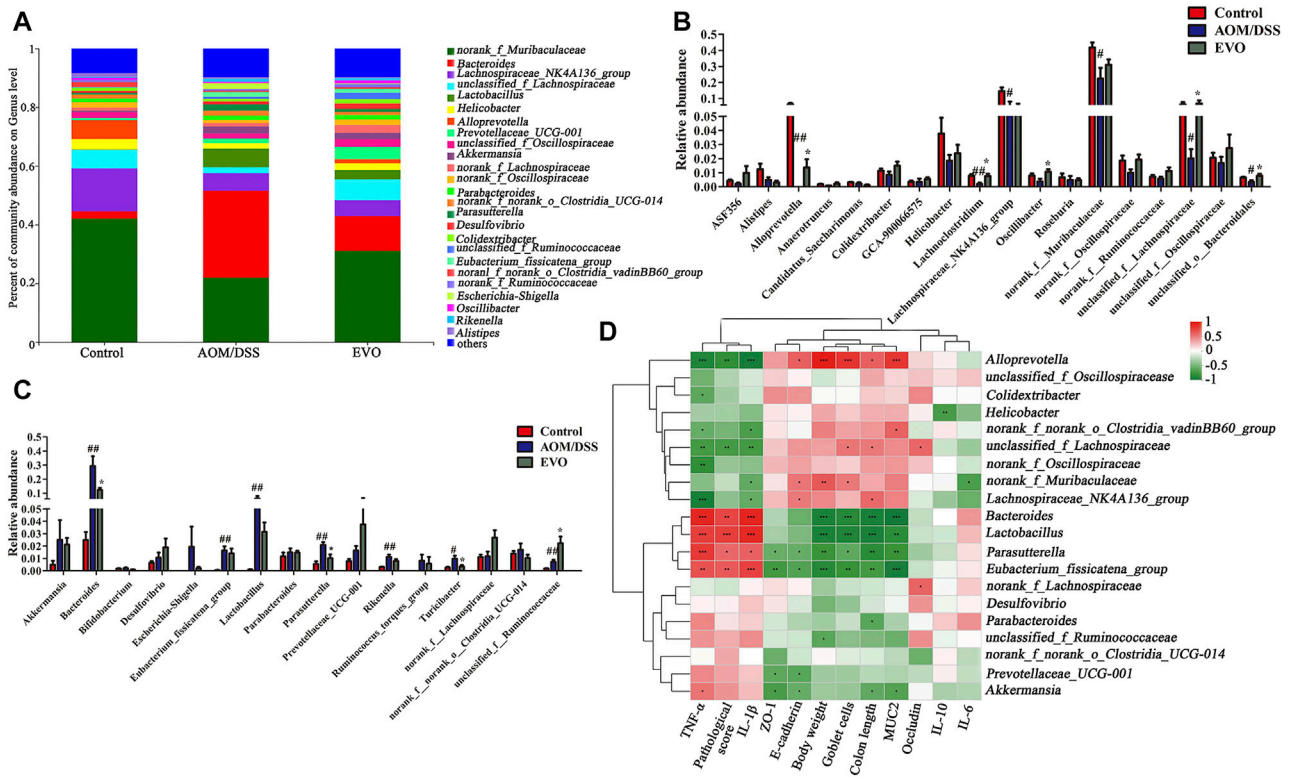


FIGURE 6 | | Analysis of gut microbiota following EVO treatment in AOM/DSS-induced colitis mice. **(A)** The intestinal microbiota distribution at the family level. The up-regulated gut microbiota **(B)** and the down-regulated gut microbiota **(C)** at the genus level. **(D)** Spearman's correlation analysis of microbiota and physiological indexes. $^{*}p < 0.05$, $^{**}p < 0.01$, $^{***}p < 0.001$.

tree showed an obvious separation among three groups (**Supplementary Figure S2F**).

Based on the average abundance analysis, at the phylum level, Bacteroidetes, Firmicutes, Actinobacteria, Campilobacterota, Desulfobacterota and Proteobacteria were the major phyla in the three groups. Compared with Control group, the relative abundance of Bacteroidetes, Actinobacteria and Proteobacteria were increased, and Firmicutes, Campilobacterota and Desulfobacterota were decreased in AOM/DSS group (**Figure 7C**). However, there was no significant difference in the relative abundance at the phylum level between EVO group and AOM/DSS group. At the family level, a total of 16 families with a relative abundance of more than 1% in at least one group were identified from the three groups (**Figure 7D**). AOM/DSS increased the relative abundance of *Bacteroidaceae*, Marinifilaceae and Rikenellaceae, and decreased the level of Desulfovibrionaceae ($p < 0.05$). Further, we observed that EVO markedly increased the relative abundance of Sutterellaceae ($p < 0.05$) and Lactobacillaceae ($p > 0.05$). To analyze the changes of gut microbiota at the genus level, we selected the ten must abundant microbial genera and their abundance was analyzed (**Figure 7E**). The most abundant genera were *norank_f_*Muribaculaceae, *Bacteroides*, *Lactobacillus*, *Lachnosirpacear_NK4A136_group* and *Prevotellacear_UCG-001*. The abundance of *Bacteroides*, *Alistipes* and *Odoribacter* were higher in the AOM/DSS group than in the Control group (**Figure 7F**). Compared with AOM/DSS group, the abundance of *Bacteroides*, *Lactobacillus*, Lachospiraceae*_NK4A136_group* and *Prevotellaceae_UCG-001* were higher in the EVO group ($p > 0.05$). It's worth noting that EVO could significantly decrease the abundance of *Alistipes* (**Figure 7F**).

Key Bacteria Responding to EVO Supplementation From Colitis to Tumors in CAC Mice

We jointly analyzed the microbiota evolution of CAC mice at 18 and 84 days by using LEfSe to identify the specific bacterial phylotypes that were changed by EVO. On the basis of taxa with linear discriminant analysis (LDA) scores greater than three and $p < 0.05$, we concluded that CAC model mice, compared with Control group altered 68 (50 increased and 18 decreased), and 42 (19 increased and 23 decreased), at 18 and 84 days respectively (**Supplementary Figures S3A, S3C**). We can see that the harmful bacteria (e.g., *g_Rikenella,* *g_*Streptococcaceae、*g_*Erysipelatoclostridiaceae and *g_Mucisirillum*) increased significantly in the early stage of colitis, while the beneficial bacteria (e.g., *g_Lachnoclostridium, g_Prevotellaceae_NK3B31_group, g_Candidatus_Arthromitus*

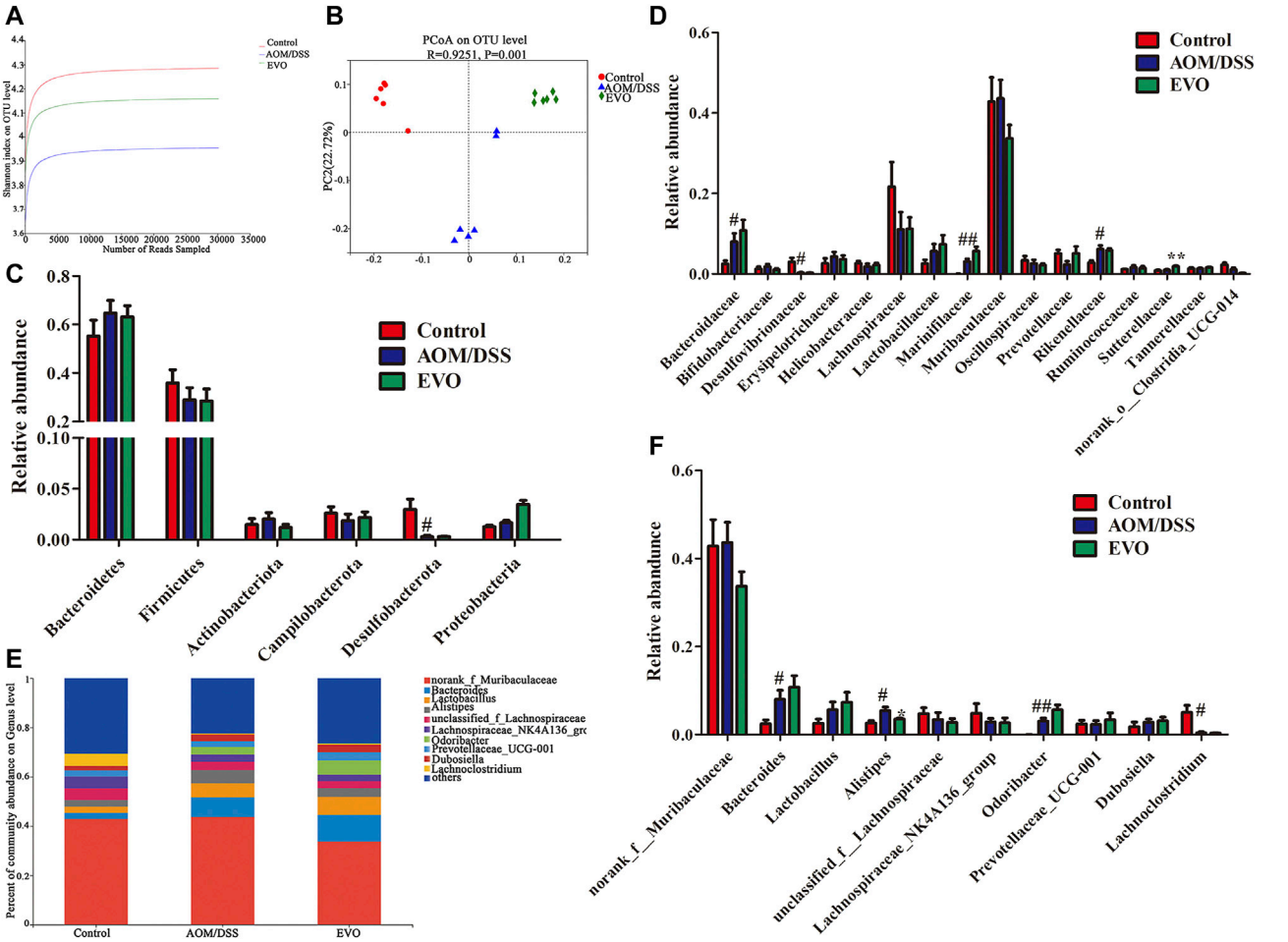


FIGURE 7 | | EVO changes the gut microbiota of AOM/DSS-induced colon cancer mice. **(A)** Shannon index. **(B)** UniFrac-based PCoA plot. The relative abundance of gut microbiota at Phylum level **(C)** and at the family level **(D)**. **(E–F)** The relative abundance of gut microbiota at genus level. $^{\#}p < 0.05$, $^{\#\#}p < 0.01$, Control *vs*. AOM/DSS; $^{*}p < 0.05$, $^{**}p < 0.01$, EVO *vs*. AOM/DSS.

and *g_Alloprevotella*) decreased significantly in the later stage of tumor. Among the 69 increased bacterial genera, CAC model mice altered 7 shared genera from colitis to tumor, and while in 41 reduced genera, CAC model mice altered 4 shared genera (**Figure 8A**). Levels of *o__Peptostreptococcales-Tissierellales, f__Bacteroidaceae, f__*Peptostreptococcaceae*, g__Bacteroides*、*g__Rikenella, g__Romboutsia* and *g__Turicibacter* were significantly enriched in CAC mice, whereas *f__Prevotellaceae, g__Alloprevotella, g__Lachnoclostridium* and *g__Tuzzerella* were reduced observably in the AOM/DSS group compared with Control group.

And treatment with EVO, compared with CAC model mice altered 28 (9 increased and 19 decreased), and 27 (20 increased and 7 decreased), at 18 and 84 days respectively (**Supplementary Figures S3B, S3D**). We also can see that treatment with EVO could decrease significantly the harmful bacteria (e.g., *f_*Erysipelotrichaceae*, f_*Deferribacteraceae*, g_Mucispirillum* and *g_Streptococcus*) in the early stage of colitis, while increase the beneficial bacteria (e.g. *f__*Sutterellaceae、*g__unclassified_f__Prevotellaceae, g__Parasutterella* and *g__Anaeroplasma*) in the later stage of tumor. Among the 26 reduced bacterial genera, EVO treatment altered three shared genera from colitis to tumor (**Figure 8B**). Levels of *o__Clostridiales, f__Clostridiaceae* and *g__Clostridium_sensu_stricto_1* were significantly reduced in EVO group compared with AOM/DSS group. And while in 29 increased genera, EVO treatment altered 0 shared genera, indicating that different probiotics may play a role in different stages of CAC. In the early stage of colitis, EVO could increase the levels of *f__Ruminococcaceae*、*g__Alloprevotella, g__Oscillibacter* and *g__Lachnoclostridium* (**Figure 8C**). Levels of *f__*Sutterellaceae、*g__unclassified_f__Prevotellaceae, g__Parasutterella* and *g__Anaeroplasma* were enriched significantly in EVO group at the late stage of CAC(**Figure 8D**).

Predictive Microbiota Functional Profiling in CAC Mice

Tax4Fun based on OTUs was used to predict the functional contribution of the microbiota. We identified 4975 Kyoto

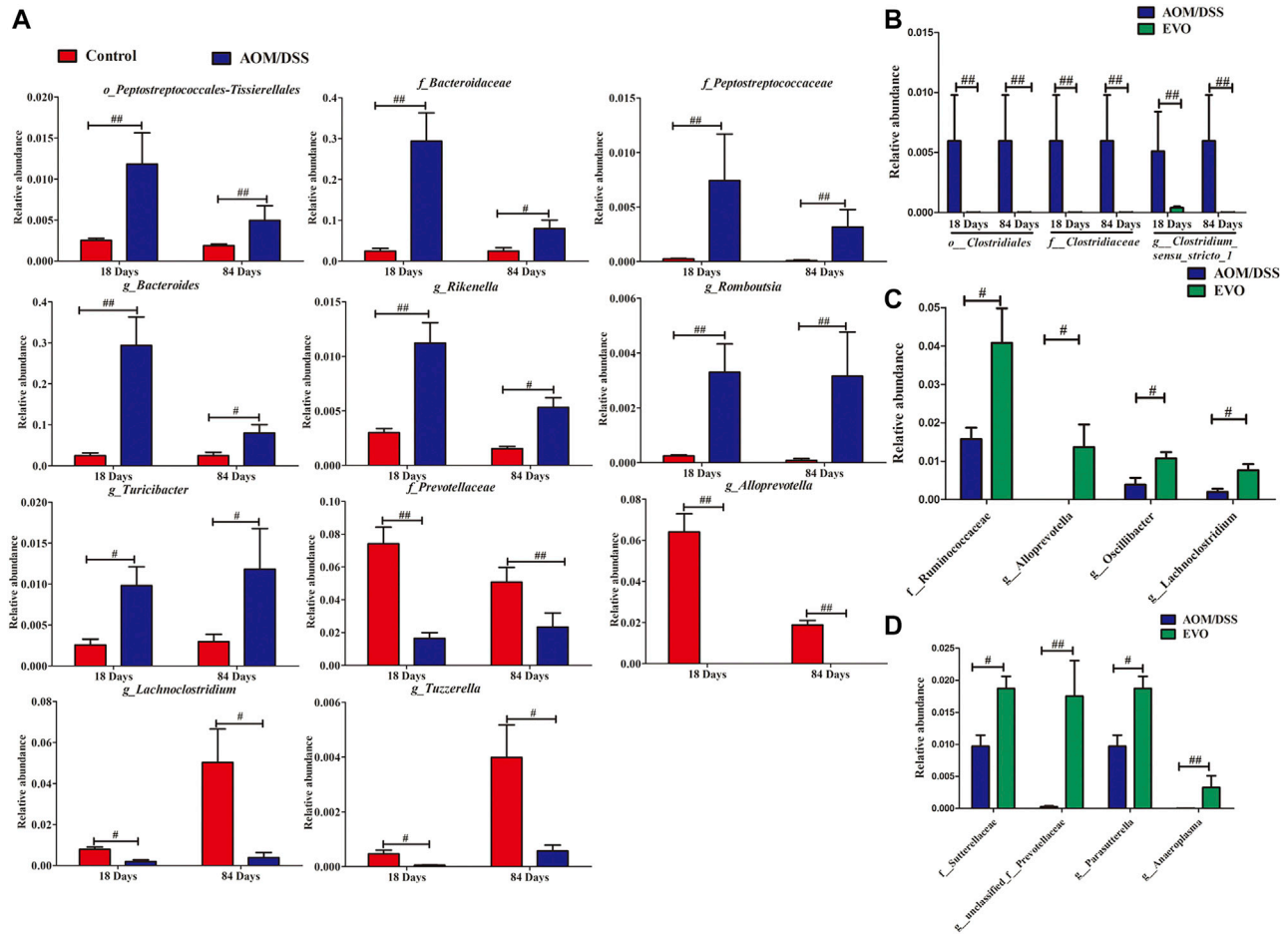


FIGURE 8 | Taxonomic differences of gut microbiota among Control, AOM/DSS and EVO groups from colitis to tumorigenesis. **(A)** Comparison of the bacterial community in 18- and 84-days CAC mice in the Control group and AOM/DSS group. **(B)** Comparison of the bacterial community in 18- and 84-days CAC mice in the EVO group and AOM/DSS group. Comparison of the bacterial community in 18-days **(C)** and 84-days **(D)** CAC mice in the EVO group and AOM/DSS group. $^{\#}p < 0.05$, $^{\#\#}p < 0.01$.

Encyclopedia of Genes and Genomes (KEGG) orthologs (KOs), mainly belonging to the pathway Metabolism, Environmental Information Processing and Genetic Information Processing. A total of 2,796 KOs were identified with significantly different abundances between AOM/DSS group and Control group, and 3592 KOs differed in abundance between EVO group and AOM/DSS group (false-discovery rate [FDR], $p < 0.05$). In the level 3 KEGG pathways, the microbial gene functions, including those associated with lipid metabolism (ko00120、ko00121), nucleotide metabolism (ko00230, ko00240), replication and repair (ko03030, ko03410, ko03420, ko03430, ko03440) and Glycan biosynthesis and metabolism (ko00540), were decreased significantly in EVO group, while those carbohydrate metabolism (ko00020, ko00040, ko00053, ko00562, ko00620, ko00630, ko00640, ko00650), amino acid metabolism (ko00280, ko00310, ko00330, ko00340, ko00360, ko00380), metabolism of cofactors and vitamins (ko00130, ko00730, ko00860), energy metabolism (ko00910、ko00920) and cell motility (ko02030, ko02040) were increased (FDR, $p < 0.05$, **Figures 9A,B**).

EVO Regulated Metabolites in AOM/DSS-Induced Colon Cancer Mice

To investigate the effects of EVO on metabolite profiles CAC mice, we examined metabolites in the fecal in a non-targeted manner. The heat map of sample correlation showed a high similarity of metabolites expression in the samples within the group (**Supplementary Figure S4A–B**). PCA and PLS-DA were performed to identify the changes in metabolite profiles on positive and negative ESI data. PCA of metabolites showed a clear separation between AOM/DSS and Control groups, and overlaps existed between EVO and Control groups (**Supplementary Figure S4C–D**). The resulting score plot from PLS-DA in the positive (for the first four components, $R^2Y = 0.977$ and $Q^2 = 0.836$) and negative mode (for the first four components, $R^2Y = 0.978$ and $Q^2 = 0.881$) indicated a clear separation among the three groups (**Figures 10A,B**). In order to test the validity of the PLS-DA model, a permutation test (200 times) for PLS-DA was applied (**Supplementary Figure S4E–F**).

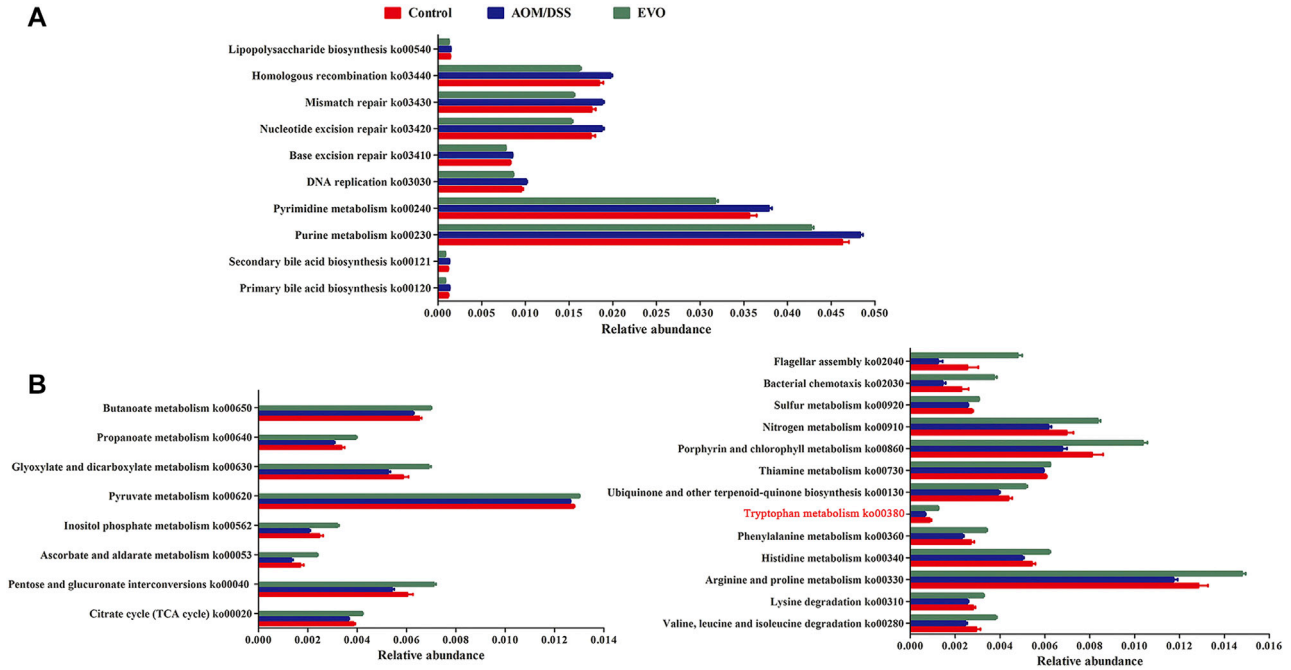


FIGURE 9 | Interred gut microbiota functions by Tax4Fun from 16S rRNA gene sequences among Control, AOM/DSS and EVO groups in AOM/DSS-induced colon cancer mice. **(A)** Up-regulated metabolism and down-regulated metabolism **(B)** in EVO group.

The R^2Y and Q^2 values derived from the permuted data were lower than the original points to the right, indicating the validation of the PLS-DA model.

Multivariate statistics (VIP_OPLS-DA>1) and unit statistics (p_value < 0.05) were used to screen differential metabolites, a total of 355 differential metabolites were identified between AOM/DSS and Control groups, and 370 differential metabolites in abundance between EVO and AOM/DSS groups (**Supplementary Tables S7, S8**). Among these, 242 differential metabolites disturbed by AOM/DSS could be restored by EVO, we further analyzed 242 differential metabolites on the KEGG pathways and found that differential metabolites were mainly involved in biosynthesis of other secondary metabolites, lipid metabolism, chemical structure transformation maps and amino acid metabolism (**Figure 10C**). KEGG metabolic pathway enrichment analysis showed that the differential metabolites were mapped to about 41 pathways (**Supplementary Table S9**). The metabolites were significantly enriched in 12 KEGG pathways (p_value < 0.05), and biosynthesis of phenylpropanoids, isoflavonoid biosynthesis, choline metabolism in cancer, retrograde endocannabinoid signaling, sphingolipid metabolism and tryptophan metabolism were the six pathways with the most significant enrichment (**Figure 10D**). Based on the Tax4Fun function prediction and non-target metabolomics studies, tryptophan metabolism was found to be co-metabolism pathway, indicating that tryptophan metabolism may play an important role in the effect of EVO on intestinal inflammation and carcinogenesis.

EVO Regulated the Gene Expressions of Colon Epithelial Cells in CAC Mice

The data above clearly showed that EVO could regulate the gut microbiota and metabolism of CAC mice. We performed RNA-Seq analysis to investigate the influence of EVO on gene expressions of colon epithelial cells in CAC mice. Compared with Control group, we obtained 863 up-regulated and 1421 down-regulated genes in the AOM/DSS group (P_adjust < 0.05, FC ≥ 2 or FC ≤ 0.5, **Supplementary Table S10**). However, 376 genes that were highly expressed and 280 genes that were lowly expressed in the EVO-treated group compared with AOM/DSS group (P_adjust < 0.05, FC ≥ 2 or FC ≤ 0.5, **Supplementary Table S11**). Furthermore, we identified 274 common genes in Control vs AOM/DSS and AOM/DSS vs EVO two data sets. Interestingly, 236 common genes showed an opposite trend of gene expression in AOM/DSS and EVO groups, indicating the involvement of these molecular targets in EVO-mediated prevention of CAC (**Supplementary Table S12**). Two clusters were obtained by clustering analysis of 236 differentially expressed genes according to their gene expression patterns in the three groups (**Figure 11A**). Then, GO enrichment analysis was performed on 236 genes belonging to two different clusters, and found that genes in Cluster 1 mainly enriched many GO terms related to immune response, such as "mucosal immune response" (*Defa2*, *Defa2*, 、*Defa30* etc.) and response to organism, such as "defense response to Gram-negative bacterium" (*Lyz1*, *Mmp7*, *Defa21* etc.) (**Figure 11B**). We found that differently genes in Cluster 1 were composed of significantly downregulated genes in the EVO group,

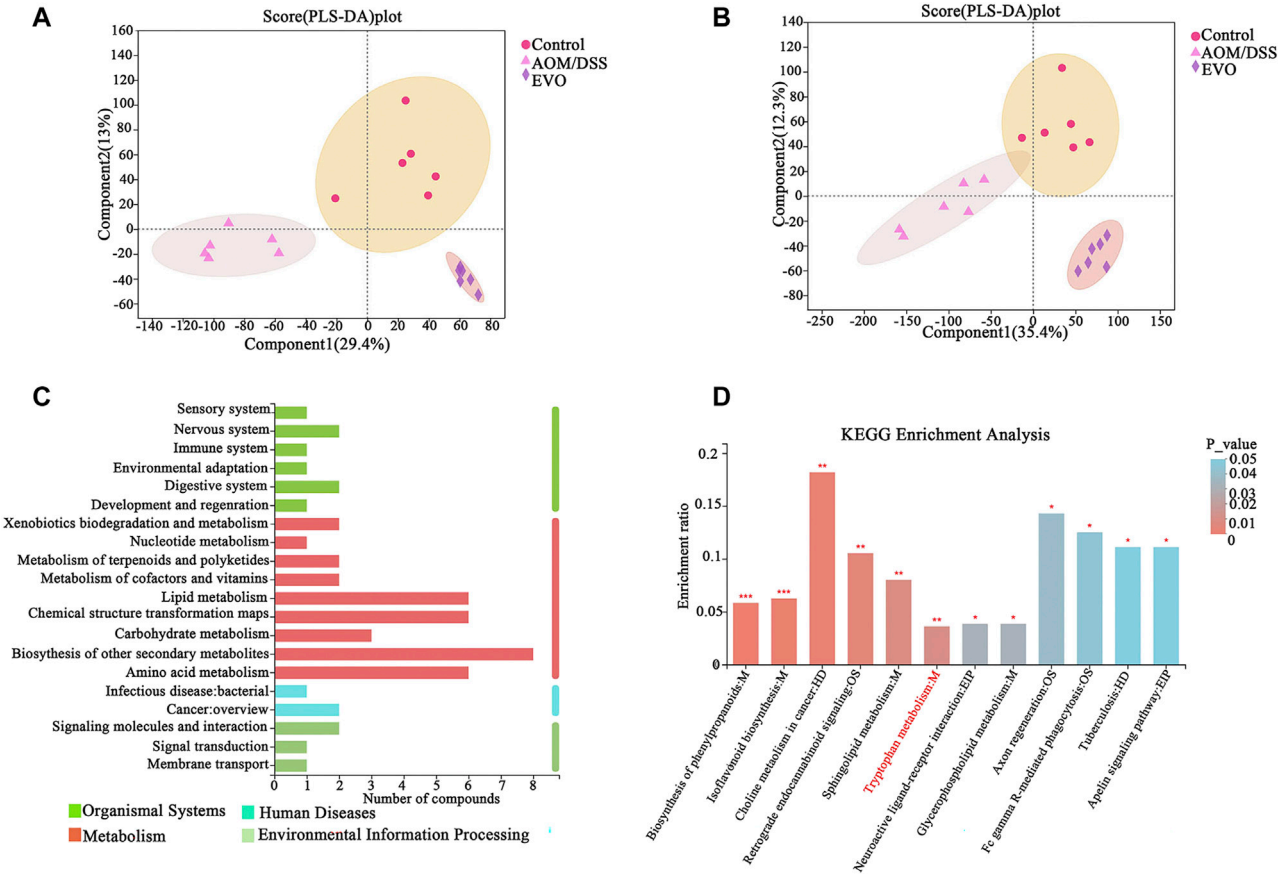


FIGURE 10 | The difference of fecal metabolites among Control, AOM/DSS and EVO groups in AOM/DSS-induced colon cancer mice. PLS-DA map in positive ion model **(A)** and in negative ion model **(B)**. **(C)** KEGG pathway on level 1 and level 2 related to differential metabolites. **(D)** KEGG pathway enrichment column chart.

suggesting a potential role of EVO therapy in reducing gut inflammation. In cluster 2, genes enriched some GO terms related to signal transduction, such as "methyl indole-3-acetate esterase activity" (*Ces1e*, *Ces1g*) and "G protein-coupled peptide receptor activity" (*Vipr2*, *Sstr1*, *Tacr2*, *Nlrp6*), and protein metabolism, such as "peptide catabolic process" (*Enpep*, *Cpe*, *Naaladl1*) and "peptide receptor activity" (*Vipr2*, *Sstr1*, *Tacr2*, *Nlrp6*) (**Figure 11B**). In view of the relatively high expression of genes in cluster two in EVO group, indicating that signal transduction and protein metabolism were significantly improved after EVO treatment. In the KEGG analysis, the downregulated genes were mainly concentrated in inflammatory signaling pathway (Wnt signaling pathway、Hippo signaling pathway、L-17 signaling pathway and Cytokine-cytokine receptor interaction), Pancreatic secretion and NOD-like receptor signaling pathway (**Figure 11C**). The upregulated genes were mainly enriched in Drug metabolism and Calcium signaling pathway (**Figure 11D**). Significant enrichment of functions and pathways may help us further investigate the role of differently genes in CAC. Together, our RNA-seq data reveal that EVO treatment significantly alleviates the inflammation of the CAC mice colon, potentially through the alteration in the gut microbiota.

DISCUSSION

Wu-Zhu-Yu, a longstanding Chinese botanical drug, is traditionally used for the treatment of digestive system disease, so it is important to understand how EVO inhibits intestinal inflammation and tumors. In this study, we evaluated the mechanism by which EVO relieved inflammation and inhibited the tumors in CAC mice through the gut microbiota, metabolic activity and transcription molecules. Collectively, according to the 16S rRNA sequencing, non-targeted metabolomics analyses and colon transcriptomics results, we revealed the mechanism of the effect of EVO on CAC mice from inflammation to colorectal tumors.

From the results above, we can see that EVO could significantly reduce the inflammation of AOM/DSS-induced colitis, which may be related to the maintenance of intestinal barrier function. The intestinal mucosal layer is the first line of defense against both commensal microbes and invading pathogens, the integrity of which is critical for health (Desai et al., 2016). The colonic mucus layer is a dynamic and chemically complex barrier, mainly composed of MUC2 secreted by GC, which forms the protective mucus barrier atop the intestinal epithelium (Allaire et al., 2018). Defects in the mucus layer

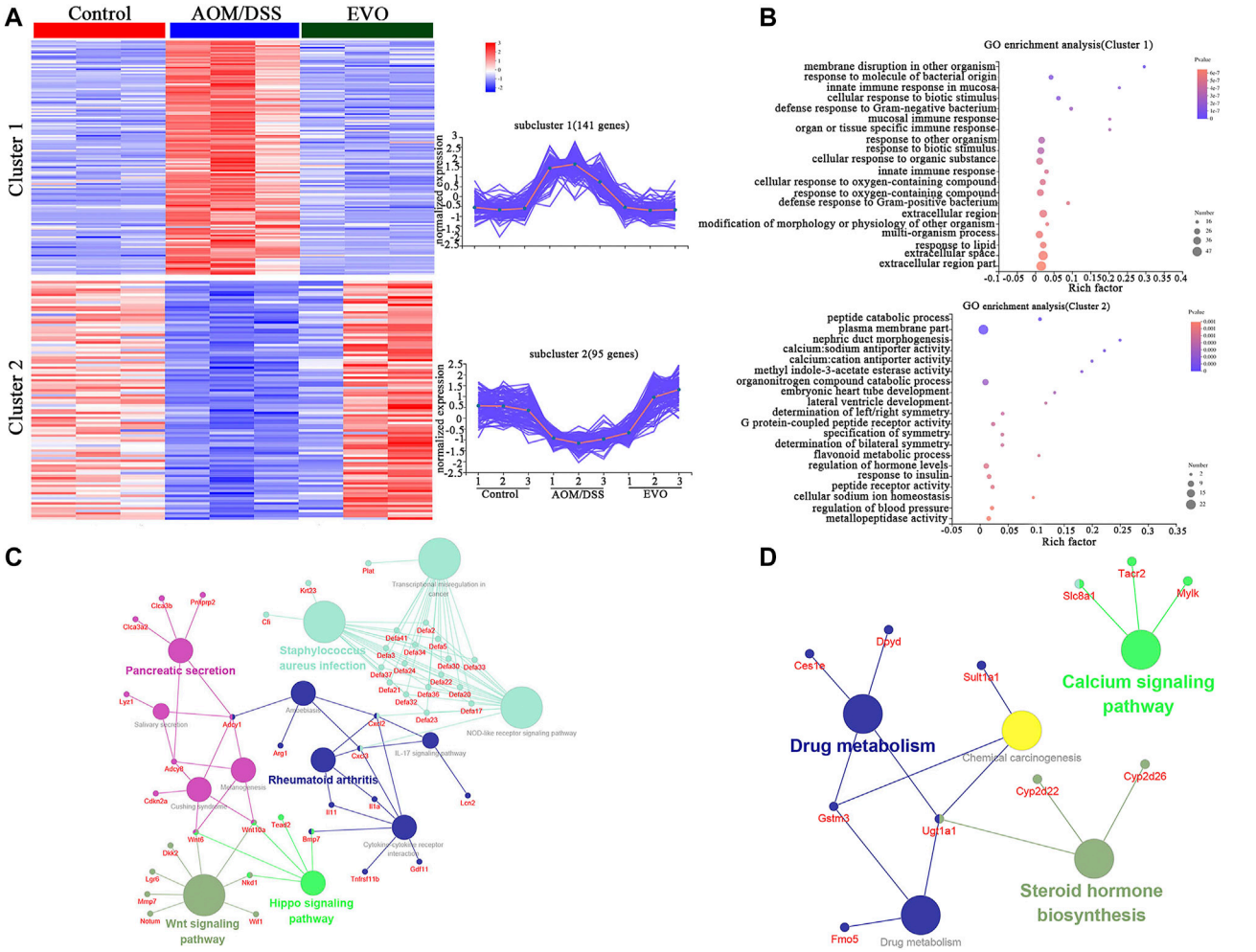


FIGURE 11 | Comparisons of gene expression profiles by RNA-seq among Control, AOM/DSS and EVO groups in AOM/DSS-induced colon cancer mice in the colon. **(A)** Genewise clustering heatmap of all 236 differentially expressed genes according to the gene expression patterns, showing segregation into two clusters. **(B)** Doptplot of GO terms enriched for the two clusters. Down-regulating the genes **(C)** and up-regulating the genes **(D)** enrichment KEGG pathways.

increase susceptibility to pathogens, leading to low-grade inflammation and dysbiosis (Desai et al., 2016). The TJ plays an important role in maintaining the integrity of the intestinal barrier. The loss of barrier integrity increases the translocation of bacterial antigens and stimulates the inflammatory response of intestinal mucosa (Jin et al., 2021). In our results, the number of GC, the expression of MUC2 and tight junction protein in the gut tissues of CAC mice were increased by EVO. Inflammation is a critical link between IBD and CRC (Svrcek et al., 2018). We speculate that EVO significantly decreased the number and size of AOM/DSS-induced colorectal tumors, promoted cell apoptosis and inhibited the proliferation of intestinal epithelial cell, which was related to the early inhibitory effect of EVO on gut inflammation.

Several studies have suggested that gut microbiota play an important role in maintaining intestinal homeostasis, which is closely associated with the pathogenesis of IBD and CRC (Wong and Yu, 2019; Caruso et al., 2020). For example, there are differences in microbiota composition between the inflamed and non-inflamed colonic segments in CD and UC. The transfer of feces from CRC patients to mice enhanced intestinal cell proliferation in germ-free mice and promoted tumorigenesis in conventional mice given AOM to induce colon neoplasia (Wong et al., 2017; Ryan et al., 2020). In view of these, we hypothesize that gut microbiota play a critical role in EVO's inhibition of enteritis-intestinal cancer. In the present study, we found that EVO could regulate the composition of gut microbiota in AOM/DSS-induced colitis. At the phylum level, the abundance of Proteobacteria was significantly increased in AOM/DSS group. Proteobacteria is enriched in intestinal pathogens, which can cause inflammation and change intestinal microbiota, and promote the development of IBD (Mukhopadhya et al., 2012). Genus of *Alloprevotella*, *Lachnoclostridium* and *Oscillibacter* levels were obviously increased by EVO treatment. *Alloprevotella* is a SCFAs-producing bacteria that plays a key role in maintaining intestinal homeostasis and is

believed to confer benefits upon host well-being (Shang et al., 2018; Liu YJ. et al., 2020). *Lachnoclostridium* is involved in the production of propionate, and *Oscillibacter*, which has previously negatively correlated with CD, expresses acetyl-CoA acetyltransferase and enzymes necessary for butyrate production (Mondot et al., 2011; Polansky et al., 2015; Xiang et al., 2021). In the present study, we found that EVO significantly suppressed the increase in the abundance of *Bacteroides*, *Parasutterella* and *Turicibacter* in AOM/DSS-treated colitis mice. It has been reported that the concentration of *Bacteroides* in UC is significantly higher than that in healthy controls, which plays an important role in triggering colitis (Ohkusa and Koido, 2015). The pathogenic Gram-negative bacteria *Parasutterella* was found to be higher in IBD patients with CD and CRC patients (Ibrahim et al., 2019; Sobhani et al., 2019). *Turicibacter* is an opportunistic pathogen or pro-inflammatory bacteria, which was observed an increased in the abundance in AOM/DSS-induced CRC, while some reported that *Turicibacter* was considered an anti-inflammatory taxon as studies proved as depletion of *Turicibacter* in animal models of IBD (Wu et al., 2019; Liu M. et al., 2020). Thus, the role of *Turicibacter* in the development of CRC needs to be further investigated. Moreover, correlation analysis revealed that *Bacteroides* and *Parasutterella* were positively correlated with inflammatory factors and negatively correlated with intestinal barrier integrity, while *Alloprevotella* was the opposite. Microbial dysbiosis and intestinal barrier dysfunction are considered to be two important pathogenic factors that trigger colitis (Jin et al., 2021). Our study showed that EVO inhibited the AOM/DSS-induced colitis through regulating the gut microbiota.

Considering the important role of gut microbiota in CAC development, we further analyzed the changes of gut microbiota in AOM/DSS-induced colon tumor. Notably, EVO could increase the microbial community diversity and change the composition of microbiota. *Prevotellaceae* (the family and the genus *Prevotellaceae_UCG-001*), were induced to decrease by AOM/DSS, which is consistent with our results (Wu et al., 2019). *Prevotellaceae* is identified as a probiotic that is highly coated by secretory IgA, and butyrate could protect the host against colitis-associated colon cancer by enriching its abundance (Zhang Y. et al., 2018). Sutterellaceae, which is very commom and abundant in intestinal mucosa, was significantly increased by EVO treatment, and its role largely unexplored with being partly controversial for published reports. Some studies have reported that Sutterellaceae has a mild pro-inflammatory capacity in gastrointestinal tract but not contributing to be disrupted epithelial homeostasis, and the ability of Sutterellaceae to adhere to epithelial mucosa indicate that they may have an immunonodulatory role (Hiippala et al., 2016). The role of Sutterellaceae in the development of CAC deserves further study. *Alistipes* was found to be associated with CRC in a previous study and exhibited increased tumor development (Dai et al., 2018). In the comparison of key bacteria changes between enteritis-intestinal cancer mice treated with EVO, *Ruminococcaceae*, *Alloprevotella*, *Oscillibacter* and *Lachoclostridium* were four beneficial bacteria with the most significant increase from AOM/DSS-induced colitis mice treated EVO, and Sutterellaceae, *unclassified_f_Prevotellaceae*, *Parasutterella* and *Anaeroplasma* were four beneficial bacteria with the most significant increase from AOM/DSS-induced colon tumor mice treated EVO. *Ruminococcaceae*, *Alloprevotella*, *Oscillibacter* and *Lachoclostridium* were considered an anti-inflammatory factor due to their production of SCFAs, which a major source of energy for colonic epithelial cells and exhibits anti-inflammatory properties (Ohkusa and Koido, 2015; Bian et al., 2019). This result indicated that EVO inhibited AOM/DSS-induced colitis by promoting the enrichment of SCFAs producing bacteria to relieve gut inflammation and maintain intestinal barrier. Although some studies have shown an increase in the abundance of *Parasutterella* in CRC, our understanding of the function of *Parasutterella* remains limited. *Parasutterella* isolates successfully colonized the mature mouse gut without causing significant shifts in bacterial composition and host innate immune response, but significantly altered the cecal metabolome, including multiple biological processes and pathways, which may exert potential beneficial effects on the intestinal mucosal homeostasis (Ju et al., 2019). The level of *Anaeroplasma* (phylum Tenericutes) was significantly decreased in obese mice, while the increased abundance is related to a reduction expression of inflammatory factors (Terzo et al., 2020). At the same time, the relative abundance of *Anaeroplasma* was reduced in DSS-induced mice (Zhang XJ. et al., 2018). Sutterellaceae, *unclassified_f_Prevotellaceae*, *Parasutterella* and *Anaeroplasma* forms a beneficial core bacteria set that promotes EVO's mitigation of AOM/DSS-induced colon cancer. Notable, the relative abundance of *Clostridiales*, *Clostridiaceae* and *Clostridium_sensu_stricto_1* (belong to Firmicutes) were significantly increased from colitis to cancer by EVO treatment, which are associated with inflammation and disease and decreased during inflammation, indicating that it may be the core bacteria of EVO that inhibit CAC development (Zijlmans et al., 2015; Busbee et al., 2020).

The functional capabilities of the microbial communities were analyzed by Tax4fun. We found that EVO treatment may have an impact on a wide range of biological functions. Abnormal lipid metabolism plays a critical role in the progression of adenomas, EVO could significantly decrease lipid accumulation by affecting bile acid biosynthesis and improving bile metabolism to prevent colon cancer (Li et al., 2019). To satisfy the higher requirements of purine and pyrimidine metabolism for tumor growth, nucleotide metabolism is over-transcribed (Chen et al., 2020). *S.cerevisiae* enhances host purine metabolism in colitis mice, and rhein could change purine metabolism to alleviate colitis, which was consistent with our results. Accurate duplication of DNA prior to cell division is essential to suppress mutagenesis and tumor development, while increased DNA replication stress plays a positive role in the proliferation of CRC (Church et al., 2013). It is known that the biosynthesis of lipopolysaccharide, a pathogen-associated pathway, is harmful for the maintenance of the physiological homeostasis, which was inhibited in EVO group (Yao et al., 2017). Additionally, EVO treatment could promote the functional maturation of gut microbiota, which is characterized by increased basic metabolism (carbohydrate metabolism, amino acid metabolism, metabolism of cofactors

and vitamins, energy metabolism and cell motility). The metabolism associated with SCFAs (e.g. Butanoate metabolism and Propanoate metabolism) is consistent with the increase of SCFAs-producing bacteria. Reduced levels of amino acid metabolism, such as tryptophan metabolism, are associated with a compromised epithelial barrier in IBD and tumour progression in CRC, indicating that changes in intestinal amino acids metabolism mediated by microbiota may be involved in the pathogenesis of CAC development (Crotti et al., 2019). These data indicate that EVO may mitigate the development of CAC through regulating the function of gut microbiota.

A total of 242 differential metabolites were detected in the three groups through untargeted metabolomics, and these metabolites were involved in KEGG metabolic pathways and mainly belong to the four KEGG modules: metabolism, organismal systems, environmental information processing and human diseases. KEGG pathway enrichment analysis found 12 significant pathways. Biosythesis of other secondary metabolites (Biosythesis of phenylpropanoids and Isoflavonoid biosynthesis) were significantly changed by EVO. Flavonoids are commonly ingested diet-derived compounds that are metabolized by gut microbiota, which have been widely demonstrated to have multiple pharmacological properties in intestinal pathology (Braune and Blaut, 2016; Gong et al., 2019). The microbiome contribution to intestinal flavonoid levels was evident from the elevated levels of naringenin and apigenin in EVO-treated CAC mice. Choline metabolism has been shown to be sensitive to changes in gut microbiota, and is closely connection with colorectal cancer development (Saeedi et al., 2020). Sphingolipids are a class of plasma-associated lipids produced by the host and specific bacteria, which have important biologic functions in metabolic, apoptotic and inflammatory pathways of host cells (Schirmer et al., 2019). Many studies have shown that the abnormalities of sphingolipid metabolism may be involved in inflammation and carcinogenesis, and EVO interferes with changes in sphingolipid metabolism, suggesting that sphingolipid metabolism plays an important role in EVO inhibiting the development of CAC (Ohnishi et al., 2017). EVO treatment also changed the tryptophan metabolism, which is consistent with the prediction of the metabolite function of Tax4Fu, and regulating tryptophan metabolism is also an attractive strategy for the treatment of intestinal diseases.

Based on the results of transcriptomic analysis, we found CAC mice had distinct gene expression profiles compared to Control mice, which may be related to host genetic differences or microbiome differences. Treatment with EVO significantly altered colon gene expression by upregulating and downregulating specific sets of genes. Among the GO terms and KEGG pathways that were significantly enriched by EVO treatment, those involved in tumor-specific immune responses were downregulated. NOD-like receptor proteins have been shown to be associated with various autoimmune or inflammatory diseases, and NOD-like receptor signaling pathways are strongly enriched in colonic tumor tissues (Zhang et al., 2017). Wnt signaling pathway plays a key role in cell development, differentiation and tissue homeostasis, abnormal activation of Wnt signaling pathway is related to the progression of tumorigenesis and tumor metastasis (Zhao et al., 2018). EVO reduced tumor-specific immune responses and may help alleviated CAC. In addition, EVO treatment upregulated pathways involved in signal transduction and Calcium signaling pathway. G protein-coupled receptor ligands, that are encoded by the microbiota and are agonists to receptors (e.g. SCFAs) that have important implications for gastrointestinal and metabolic physiology, has been shown to function as a tumor suppressor in the colon (e.g. GPR109A) (Cani and Jordan, 2018; Lavelle and Sokoi, 2020). In sum, during the procession of intestinal inflammation to carcinogenesis, a variety of immunological and inflammatory signaling events, were inhibited, and a variety of signal transduction and metabolism were activated by EVO and involved in a complex biological process.

In conclusion, we have confirmed that EVO treatment effectively attenuated AOM/DSS-induced colitis and colon cancer in mice by inhibiting the intestinal inflammation and improving mucosal barrier functions. In addition, EVO promoted the enrichment of SCFAs-producing bacteria and reduced the pro-inflammatory bacteria levels, which contributes to the changes of microbiota metabolism, especially tryptophan metabolism. Finally, our results indicated that inflammatory response and tumor-specific immune responses were effectively alleviated by EVO. Collectively, our results highlight that EVO, as a compound with properties in modulating gut microbiota and metabolism, in treating intestinal disorders in the future.

DATA AVAILABILITY STATEMENT

The original contributions presented in the study are publicly available. This data can be found here: National Center for Biotechnology Information (NCBI) BioProject database under accession number PRJNA770849.

ETHICS STATEMENT

The animal study was reviewed and approved by The First Affiliated Hospital of Shenzhen University, Shenzhen Second People's Hospital.

AUTHOR CONTRIBUTIONS

MW, BZ, KC, DY, and ZW conceived and designed the experiments. MW and BZ carried out the experiments and drafted the manuscript. MZ, ZL, and YL assisted with the animal experiments. WC and SL assisted with the data analyzed.

FUNDING

This study was financially supported by The Sanming Project of Medicine in Shenzhen (SZSM201612049)-the Chen-Keji

Academician's Geriatrics Team of Integrated Traditional Chinese and Western Medicine, China Academy of Chinese Medical Sciences, The China Postdoctoral Science Foundation (2021M693696), The Shenzhen Science and Technology Planning Program (No. JCYJ20180227175929767), National Natural Science Foundation of China (No. 81803867), The Scientific Research Project of Guangdong Provincial Bureau of Traditional Chinese Medicine (20201319), National Key R&D Program of Ministry of Science and Technology (2017YFC1703304), GuangDong Basic and Applied Basic Research Foundation (2020A1515011427), Shenzhen Municipal Science and Technology Project (JCYJ20190812171005713).

SUPPLEMENTARY MATERIAL

The Supplementary Material for this article can be found online at: https://www.frontiersin.org/articles/10.3389/fphar.2021.797605/full#supplementary-material

REFERENCES

Allaire, J. M., Crowley, S. M., Law, H. T., Chang, S.-Y., Ko, H.-J., Vallance, B. A., et al. (2018). The Intestinal Epithelium: central Coordinator of Mucosal Immunity. *Trends Immunol.* 39, 677–696. doi:10.1016/j.it.2018.04.002

Asshauer, K. P., Wemheuer, B., Daniel, R., and Meinicke, P. (2015). Tax4Fun: Predicting Functional Profiles from Metagenomic 16S rRNA Data. *Bioinformatics* 31, 2882–2884. doi:10.1093/bioinformatics/btv287

Bian, X., Wu, W., Yang, L., Lv, L., Wang, Q., Li, Y., et al. (2019). Administration of Akkermansia Muciniphila Ameliorates Dextran Sulfate Sodium-Induced Ulcerative Colitis in Mice. *Front. Microbiol.* 10, 2259. doi:10.3389/fmicb.2019.02259

Braune, A., and Blaut, M. (2016). Bacterial Species Involved in the Conversion of Dietary Flavonoids in the Human Gut. *Gut. Microbes* 7, 216–234. doi:10.1080/19490976.2016.1158395

Busbee, P. B., Menzel, L., Alrafas, H. R., Dopkins, N., Becker, W., Miranda, K., et al. (2020). Indole-3-carbinol Prevents Colitis and Associated Microbial Dysbiosis in an IL-22-dependent Manner. *JCI. Insight.* 5, e127551. doi:10.1172/jci.insight.127551

Cani, P. D., and Jordan, B. F. (2018). Gut Microbiota-Mediated Inflammation in Obesity: a Link with Gastrointestinal Cancer. *Nat. Rev. Gastroenterol. Hepatol.* 15, 671–682. doi:10.1038/s41575-018-0025-6

Caruso, R., Lo, B. C., and Núñez, G. (2020). Host-microbiota Interactions in Inflammatory Bowel Disease. *Nat. Rev. Immunol.* 20, 411–426. doi:10.1038/s41577-019-0268-7

Chen, J., Pitmon, E., and Wang, K. (2017). Microbiome, Inflammation and Colorectal Cancer. *Semin. Immunol.* 32, 43–53. doi:10.1016/j.smim.2017.09.006

Chen, Y., Ni, J., Gao, Y., Zhang, J., Liu, X., Chen, Y., et al. (2020). Integrated Proteomics and Metabolomics Reveals the Comprehensive Characterization of Antitumor Mechanism Underlying Shikonin on colon Cancer Patient-Derived Xenograft Model. *Sci. Rep.* 10, 14092. doi:10.1038/s41598-020-71116-5

Church, D. N., Briggs, S. E., Palles, C., Domingo, E., Kearsey, S. J., Grimes, J. M., et al. (2013). DNA Polymerase ε and δ Exonuclease Domain Mutations in Endometrial Cancer. *Hum. Mol. Genet.* 22, 2820–2828. doi:10.1093/hmg/ddt131

Cooper, H. S., Murthy, S. N., Shah, R. S., and Sedergran, D. J. (1993). Clinicopathologic Study of Dextran Sulfate Sodium Experimental Murine Colitis. *Lab. Invest.* 69, 238–249.

Crotti, S., Bedin, C., Bertazzo, A., Digito, M., Zuin, M., Urso, E. D., et al. (2019). Tryptophan Metabolism as Source of New Prognostic Biomarkers for FAP Patients. *Int. J. Tryptophan. Res.* 12, 1178646919890293. doi:10.1177/1178646919890293

Dai, Z., Coker, O. O., Nakatsu, G., Wu, W. K. K., Zhao, L., Chen, Z., et al. (2018). Multi-cohort Analysis of Colorectal Cancer Metagenome Identified Altered Bacteria across Populations and Universal Bacterial Markers. *Microbiome* 6, 70. doi:10.1186/s40168-018-0451-2

Desai, M. S., Seekatz, A. M., Koropatkin, N. M., Kamada, N., Hickey, C. A., Wolter, M., et al. (2016). A Dietary Fiber-Deprived Gut Microbiota Degrades the Colonic Mucus Barrier and Enhances Pathogen Susceptibility. *Cell* 167, 1339–e21. doi:10.1016/j.cell.2016.10.043

Drewes, J. L., Housseau, F., and Sears, C. L. (2016). Sporadic Colorectal Cancer: Microbial Contributors to Disease Prevention, Development and Therapy. *Br. J. Cancer* 115, 273–280. doi:10.1038/bjc.2016.189

Gagnière, J., Raisch, J., Veziant, J., Barnich, N., Bonnet, R., Buc, E., et al. (2016). Gut Microbiota Imbalance and Colorectal Cancer. *World J. Gastroenterol.* 22, 501–518. doi:10.3748/wjg.v22.i2.501

Gao, X., Fan, W., Tan, L., Shi, Y., Ding, C., Liu, S., et al. (2020). Soy Isoflavones Ameliorate Experimental Colitis by Targeting ERα/NLRP3 Inflammasome Pathways. *J. Nutr. Biochem.* 83, 108438. doi:10.1016/j.jnutbio.2020.108438

Gong, Y., Dong, R., Gao, X., Li, J., Jiang, L., Zheng, J., et al. (2019). Neohesperidin Prevents Colorectal Tumorigenesis by Altering the Gut Microbiota. *Pharmacol. Res.* 148, 104460. doi:10.1016/j.phrs.2019.104460

Gong, Z., Zhao, S., Zhou, J., Yan, J., Wang, L., Du, X., et al. (2018). Curcumin Alleviates DSS-Induced Colitis via Inhibiting NLRP3 Inflammsome Activation and IL-1β Production. *Mol. Immunol.* 104, 11–19. doi:10.1016/j.molimm.2018.09.004

Hiippala, K., Kainulainen, V., Kalliomäki, M., Arkkila, P., and Satokari, R. (2016). Mucosal Prevalence and Interactions with the Epithelium Indicate Commensalism of Sutterella Spp. *Front. Microbiol.* 7, 1706. doi:10.3389/fmicb.2016.01706

Ibrahim, A., Hugerth, L. W., Hases, L., Saxena, A., Seifert, M., Thomas, Q., et al. (2019). Colitis-induced Colorectal Cancer and Intestinal Epithelial Estrogen Receptor Beta Impact Gut Microbiota Diversity. *Int. J. Cancer* 144, 3086–3098. doi:10.1002/ijc.32037

Jin, G., Tang, Q., Ma, J., Liu, X., Zhou, B., Sun, Y., et al. (2021). Maternal Emulsifier P80 Intake Induces Gut Dysbiosis in Offspring and Increases Their Susceptibility to Colitis in Adulthood. *mSystems* 6, e01337–20. doi:10.1128/mSystems.01337-20

Ju, T., Kong, J. Y., Stothard, P., and Willing, B. P. (2019). Defining the Role of Parasutterella, a Previously Uncharacterized Member of the Core Gut Microbiota. *ISME. J.* 13, 1520–1534. doi:10.1038/s41396-019-0364-5

Lavelle, A., and Sokol, H. (2020). Gut Microbiota-Derived Metabolites as Key Actors in Inflammatory Bowel Disease. *Nat. Rev. Gastroenterol. Hepatol.* 17, 223–237. doi:10.1038/s41575-019-0258-z

Li, L., Li, X., Zhong, W., Yang, M., Xu, M., Sun, Y., et al. (2019). Gut Microbiota from Colorectal Cancer Patients Enhances the Progression of Intestinal Adenoma in Apcmin/+ Mice. *EBioMedicine* 48, 301–315. doi:10.1016/j.ebiom.2019.09.021

Li, X., Liu, Y., Wang, Y., Li, X., Liu, X., Guo, M., et al. (2020). Sucralose Promotes Colitis-Associated Colorectal Cancer Risk in a Murine Model along with Changes in Microbiota. *Front. Oncol.* 10, 710. doi:10.3389/fonc.2020.00710

Liang, X., Li, H., Tian, G., and Li, S. (2014). Dynamic Microbe and Molecule Networks in a Mouse Model of Colitis-Associated Colorectal Cancer. *Sci. Rep.* 4, 4985. doi:10.1038/srep04985

Liu, M., Xie, W., Wan, X., and Deng, T. (2020b). Clostridium Butyricum Modulates Gut Microbiota and Reduces Colitis Associated colon Cancer in Mice. *Int. Immunopharmacol.* 88, 106862. doi:10.1016/j.intimp.2020.106862

Liu, Y. J., Tang, B., Wang, F. C., Tang, L., Lei, Y. Y., Luo, Y., et al. (2020a). Parthenolide Ameliorates colon Inflammation through Regulating Treg/Th17 Balance in a Gut Microbiota-dependent Manner. *Theranostics* 10, 5225–5241. doi:10.7150/thno.43716

Mondot, S., Kang, S., Furet, J. P., Aguirre de Carcer, D., McSweeney, C., Morrison, M., et al. (2011). Highlighting New Phylogenetic Specificities of Crohn's Disease Microbiota. *Inflamm. Bowel Dis.* 17, 185–192. doi:10.1002/ibd.21436

Mukhopadhya, I., Hansen, R., El-Omar, E. M., and Hold, G. L. (2012). IBD-what Role Do Proteobacteria Play? *Nat. Rev. Gastroenterol. Hepatol.* 9, 219–230. doi:10.1038/nrgastro.2012.14

Ohkusa, T., and Koido, S. (2015). Intestinal Microbiota and Ulcerative Colitis. *J. Infect. Chemother.* 21, 761–768. doi:10.1016/j.jiac.2015.07.010

Ohnishi, T., Hashizume, C., Taniguchi, M., Furumoto, H., Han, J., Gao, R., et al. (2017). Sphingomyelin Synthase 2 Deficiency Inhibits the Induction of Murine Colitis-Associated colon Cancer. *FASEB. J.* 31, 3816–3830. doi:10.1096/fj.201601225RR

Polansky, O., Sekelova, Z., Faldynova, M., Sebkova, A., Sisak, F., and Rychlik, I. (2015). Important Metabolic Pathways and Biological Processes Expressed by Chicken Cecal Microbiota. *Appl. Environ. Microbiol.* 82, 1569–1576. doi:10.1128/AEM.03473-15

Ranganathan, P., Jayakumar, C., Manicassamy, S., and Ramesh, G. (2013). CXCR2 Knockout Mice Are Protected against DSS-Colitis-Induced Acute Kidney Injury and Inflammation. *Am. J. Physiol. Ren. Physiol* 305, F1422–F1427. doi:10.1152/ajprenal.00319.2013

Rieder, F., Fiocchi, C., and Rogler, G. (2017). Mechanisms, Management, and Treatment of Fibrosis in Patients with Inflammatory Bowel Diseases. *Gastroenterology* 152, 340–e6. doi:10.1053/j.gastro.2016.09.047

Ryan, F. J., Ahern, A. M., Fitzgerald, R. S., Laserna-Mendieta, E. J., Power, E. M., Clooney, A. G., et al. (2020). Colonic Microbiota Is Associated with Inflammation and Host Epigenomic Alterations in Inflammatory Bowel Disease. *Nat. Commun.* 11, 1512. doi:10.1038/s41467-020-15342-5

Saeedi, B. J., Liu, K. H., Owens, J. A., Hunter-Chang, S., Camacho, M. C., Eboka, R. U., et al. (2020). Gut-resident Lactobacilli Activate Hepatic Nrf2 and Protect against Oxidative Liver Injury. *Cell. Metab.* 31, 956–e5. doi:10.1016/j.cmet.2020.03.006

Sankarasubramanian, J., Ahmad, R., Avuthu, N., Singh, A. B., and Guda, C. (2020). Gut Microbiota and Metabolic Specificity in Ulcerative Colitis and Crohn's Disease. *Front. Med.* 7, 606298. doi:10.3389/fmed.2020.606298

Schirmer, M., Garner, A., Vlamakis, H., and Xavier, R. J. (2019). Microbial Genes and Pathways in Inflammatory Bowel Disease. *Nat. Rev. Microbiol.* 17, 497–511. doi:10.1038/s41579-019-0213-6

Shang, Q., Jiang, H., Cai, C., Hao, J., Li, G., and Yu, G. (2018). Gut Microbiota Fermentation of marine Polysaccharides and its Effects on Intestinal Ecology: An Overview. *Carbohydr. Polym.* 179, 173–185. doi:10.1016/j.carbpol.2017.09.059

Siegel, R. L., Miller, K. D., Goding Sauer, A., Fedewa, S. A., Butterly, L. F., Anderson, J. C., et al. (2020). Colorectal Cancer Statistics, 2020. *CA. Cancer J. Clin.* 70, 145–164. doi:10.3322/caac.21601

Sobhani, I., Bergsten, E., Couffin, S., Amiot, A., Nebbad, B., Barau, C., et al. (2019). Colorectal Cancer-Associated Microbiota Contributes to Oncogenic Epigenetic Signatures. *Proc. Natl. Acad. Sci. U S A.* 116, 24285–24295. doi:10.1073/pnas.1912129116

Sokol, H., Seksik, P., and Cosnes, J. (2014). Complications and Surgery in the Inflammatory Bowel Diseases Biological Era. *Curr. Opin. Gastroenterol.* 30, 378–384. doi:10.1097/MOG.0000000000000078

Svrcek, M., Borralho Nunes, P., Villanacci, V., Beaugerie, L., Rogler, G., De Hertogh, G., et al. (2018). Clinicopathological and Molecular Specificities of Inflammatory Bowel Disease-Related Colorectal Neoplastic Lesions: the Role of Inflammation. *J. Crohns. Colitis.* 12, 1486–1498. doi:10.1093/ecco-jcc/jjy132

Terzo, S., Mulè, F., Caldara, G. F., Baldassano, S., Puleio, R., Vitale, M., et al. (2020). Pistachio Consumption Alleviates Inflammation and Improves Gut Microbiota Composition in Mice Fed a High-Fat Diet. *Int. J. Mol. Sci.* 21, 365. doi:10.3390/ijms21010365

Wang, L., Tang, L., Feng, Y., Zhao, S., Han, M., Zhang, C., et al. (2020a). A Purified Membrane Protein from Akkermansia Muciniphila or the Pasteurised Bacterium Blunts Colitis Associated Tumourigenesis by Modulation of CD8+ T Cells in Mice. *Gut* 69, 1988–1997. doi:10.1136/gutjnl-2019-320105

Wang, M. X., Lin, L., Chen, Y. D., Zhong, Y. P., Lin, Y. X., Li, P., et al. (2020b). Evodiamine Has Therapeutic Efficacy in Ulcerative Colitis by Increasing Lactobacillus Acidophilus Levels and Acetate Production. *Pharmacol. Res.* 159, 104978. doi:10.1016/j.phrs.2020.104978

Wang, X., Saud, S. M., Zhang, X., Li, W., and Hua, B. (2019b). Protective Effect of Shaoyao Decoction against Colorectal Cancer via the Keap1-Nrf2-ARE Signaling Pathway. *J. Ethnopharmacol.* 241, 111981. doi:10.1016/j.jep.2020.113532

Wang, Z., Hua, W., Li, C., Chang, H., Liu, R., Ni, Y., et al. (2019a). Protective Role of Fecal Microbiota Transplantation on Colitis and Colitis-Associated colon Cancer in Mice Is Associated with Treg Cells. *Front. Microbiol.* 10, 2498. doi:10.3389/fmicb.2019.02498

Wong, S. H., and Yu, J. (2019). Gut Microbiota in Colorectal Cancer: Mechanisms of Action and Clinical Applications. *Nat. Rev. Gastroenterol. Hepatol.* 16, 690–704. doi:10.1038/s41575-019-0209-8

Wong, S. H., Zhao, L., Zhang, X., Nakatsu, G., Han, J., Xu, W., et al. (2017). Gavage of Fecal Samples from Patients with Colorectal Cancer Promotes Intestinal Carcinogenesis in Germ-free and Conventional Mice. *Gastroenterology* 153, 1621–e6. doi:10.1053/j.gastro.2017.08.022

Wu, M., Li, J., An, Y., Li, P., Xiong, W., Li, J., et al. (2019). Chitooligosaccharides Prevents the Development of Colitis-Associated Colorectal Cancer by Modulating the Intestinal Microbiota and Mycobiota. *Front. Microbiol.* 10, 2101. doi:10.3389/fmicb.2019.02101

Xiang, S., Ye, K., Li, M., Ying, J., Wang, H., Han, J., et al. (2021). Xylitol Enhances Synthesis of Propionate in the colon via Cross-Feeding of Gut Microbiota. *Microbiome* 9, 62. doi:10.1186/s40168-021-01029-6

Yao, X., Zhang, C., Xing, Y., Xue, G., Zhang, Q., Pan, F., et al. (2017). Remodelling of the Gut Microbiota by Hyperactive NLRP3 Induces Regulatory T Cells to Maintain Homeostasis. *Nat. Commun.* 8, 1896. doi:10.1038/s41467-017-01917-2

Yu, L., Wang, Z., Huang, M., Li, Y., Zeng, K., Lei, J., et al. (2016). Evodia Alkaloids Suppress Gluconeogenesis and Lipogenesis by Activating the Constitutive Androstane Receptor. *Biochim. Biophys. Acta* 1859, 1100–1111. doi:10.1016/j.bbagrm.2015.10.001

Zhang, X., Wei, L., Wang, J., Qin, Z., Wang, J., Lu, Y., et al. (2017). Suppression Colitis and Colitis-Associated colon Cancer by Anti-s100a9 Antibody in Mice. *Front. Immunol.* 8, 1774. doi:10.3389/fimmu.2017.01774

Zhang, X. J., Yuan, Z. W., Qu, C., Yu, X. T., Huang, T., Chen, P. V., et al. (2018b). Palmatine Ameliorated Murine Colitis by Suppressing Tryptophan Metabolism and Regulating Gut Microbiota. *Pharmacol. Res.* 137, 34–46. doi:10.1016/j.phrs.2018.09.010

Zhang, Y., Kang, C., Wang, X. L., Zhou, M., Chen, M. T., Zhu, X. H., et al. (2018a). Dietary Factors Modulate Colonic Tumorigenesis through the Interaction of Gut Microbiota and Host Chloride Channels. *Mol. Nutr. Food Res.* 62. doi:10.1002/mnfr.201700554

Zhao, L. C., Li, J., Liao, K., Luo, N., Shi, Q. Q., Feng, Z. Q., et al. (2015). Evodiamine Induces Apoptosis and Inhibits Migration of HCT-116 Human Colorectal Cancer Cells. *Int. J. Mol. Sci.* 16, 27411–27421. doi:10.3390/ijms161126031

Zhao, Q., Bi, Y., Zhong, J., Ren, Z., Liu, Y., Jia, J., et al. (2018). Pristimerin Suppresses Colorectal Cancer through Inhibiting Inflammatory Responses and Wnt/β-Catenin Signaling. *Toxicol. Appl. Pharmacol.* 386, 114813. doi:10.1016/j.taap.2019.114813

Zhu, L. Q., Zhang, L., Zhang, J., Chang, G. L., Liu, G., Yu, D. D., et al. (2020). Evodiamine Inhibits High-Fat Diet-Induced Colitis-Associated Cancer in Mice through Regulating the Gut Microbiota. *J. Integr. Med.* 19, 56–65. doi:10.1016/j.joim.2020.11.001

Zijlmans, M. A., Korpela, K., Riksen-Walraven, J. M., de Vos, W. M., and de Weerth, C. (2015). Maternal Prenatal Stress Is Associated with the Infant Intestinal Microbiota. *Psychoneuroendocrinology* 53, 233–245. doi:10.1016/j.psyneuen.2015.01.006

Conflict of Interest: The authors declare that the research was conducted in the absence of any commercial or financial relationships that could be construed as a potential conflict of interest.

Publisher's Note: All claims expressed in this article are solely those of the authors and do not necessarily represent those of their affiliated organizations, or those of the publisher, the editors and the reviewers. Any product that may be evaluated in this article, or claim that may be made by its manufacturer, is not guaranteed or endorsed by the publisher.

Copyright © 2021 Wang, Zhou, Cong, Zhang, Li, Li, Liang, Chen, Yang and Wu. This is an open-access article distributed under the terms of the Creative Commons Attribution License (CC BY). The use, distribution or reproduction in other forums is permitted, provided the original author(s) and the copyright owner(s) are credited and that the original publication in this journal is cited, in accordance with accepted academic practice. No use, distribution or reproduction is permitted which does not comply with these terms.

frontiers in Pharmacology

ORIGINAL RESEARCH
published: 23 February 2022
doi: 10.3389/fphar.2022.783506

Bilobalide Exerts Anti-Inflammatory Effects on Chondrocytes Through the AMPK/SIRT1/mTOR Pathway to Attenuate ACLT-Induced Post-Traumatic Osteoarthritis in Rats

*Tianwen Ma[1,2†], Liangyu Lv[1,2†], Yue Yu[1,2†], Lina Jia[1,2], Xiaopeng Song[1,2], XinYu Xu[1,2], Ting Li[1,2], Xuanbo Sheng[1,2], Haoran Wang[1,2], Jiantao Zhang[1,2] and Li Gao[1,2]**

[1]College of Veterinary Medicine, Northeast Agricultural University, Harbin, China, [2]Heilongjiang Key Laboratory of Animals Disease Pathogenesis and Comparative Medicine, Harbin, China

OPEN ACCESS

Edited by:
Hongzhi Du,
Hubei University of Chinese Medicine, China

Reviewed by:
Wei Dong Chen,
Anhui University of Chinese Medicine, China
Ziqiao Yuan,
Zhengzhou University, China

***Correspondence:**
Li Gao
gaoli43450@163.com

†These authors have contributed equally to this work and share first authorship

Specialty section:
This article was submitted to Ethnopharmacology, a section of the journal Frontiers in Pharmacology

Received: 26 September 2021
Accepted: 21 January 2022
Published: 23 February 2022

Citation:
Ma T, Lv L, Yu Y, Jia L, Song X, Xu X, Li T, Sheng X, Wang H, Zhang J and Gao L (2022) Bilobalide Exerts Anti-Inflammatory Effects on Chondrocytes Through the AMPK/SIRT1/mTOR Pathway to Attenuate ACLT-Induced Post-Traumatic Osteoarthritis in Rats. Front. Pharmacol. 13:783506. doi: 10.3389/fphar.2022.783506

Although osteoarthritis (OA) significantly affects the quality of life of the elderly, there is still no effective treatment strategy. The standardized *Ginkgo biloba* L. extract preparation has been shown to have a wide range of therapeutic effects. Bilobalide, a unique ingredient of *Ginkgo biloba*, has anti-inflammatory and antioxidant pharmacological properties, but its mechanism of action on OA remains unknown. In this study, we investigated the effects of bilobalide on the development of OA through *in vivo* and *in vitro* experiments, as well as its potential anti-inflammatory mechanisms. The *in vitro* experiments demonstrated that bilobalide significantly inhibited the production of inducible nitric oxide synthase (iNOS), cyclooxygenase-2 (COX-2), and matrix metalloproteinase 13 (MMP13) in ATDC5 chondrocytes induced by Interleukin-1β (IL-1β). At the molecular level, bilobalide induced chondrocyte autophagy by activating the AMPK/SIRT1/mTOR signaling pathway, which increased the expression of autophagy-related Atg genes, up-regulated the expression of LC3 protein, and reduced the expression of the p62 protein. *In vivo*, bilobalide exerted significant anti-inflammatory and anti-extracellular matrix (ECM) degradation effects in a rat model of post-traumatic OA (PTOA) induced by anterior cruciate ligament transection (ACLT). Bilobalide could relieve joint pain in PTOA rats, inhibit the expression of iNOS and COX-2 protein in cartilage via the AMPK/SIRT1/mTOR pathway, and reduce the level of ECM degradation biomarkers in serum. In conclusion, bilobalide exhibits vigorous anti-inflammatory activity, presenting it as an interesting potential therapeutic agent for OA.

Keywords: bilobalide, autophagy, AMPK/SIRT1/mTOR, inflammation, osteoarthritis, ACLT

1 INTRODUCTION

Osteoarthritis (OA) is an age-related, painful, and disabling disease. Around 35% of the global population over the age of 60 suffers from symptomatic (painful, disabling) OA (Grassel et al., 2021). OA may develop in any joint, such as the shoulders, hands, feet, spine, knees, and hip joints (Katz et al., 2021). Currently, Non-steroidal anti-inflammatory drugs (NSAIDs) and tramadol are recommended for the clinical treatment of OA. However, NSAIDs have gastrointestinal and

cardiovascular side effects, are commonly used in clinical practice for the short-term treatment of OA (Chen et al., 2008). Safe and effective drugs for preventing or reversing the progression of OA are therefore still lacking (Pérez-Lozano et al., 2021).

Notably, plant extracts have attracted a lot of attention due to their safe and diverse biological activities (Sukhikh et al., 2021) (Henrotin and Mobasheri, 2018). *Ginkgo biloba* L. extract is one of the most widely used botanical drugs in the world (Achete de Souza et al., 2020). Various biological preparations made from *Ginkgo biloba* L. extract as raw materials are commonly used in medicines, dietary supplements, food additives, cosmetics, and functional beverages (Mahadevan and Park, 2008; dal Belo et al., 2009; Aziz et al., 2018; Palacios et al., 2019). Bilobalide is a sesquiterpene compound extracted from *Ginkgo biloba* L. that has received widespread interest due to its anti-inflammatory (Jiang et al., 2014), anti-oxidative (Achete de Souza et al., 2020), and neuroprotective properties (Feng et al., 2019). Bilobalide has been shown to inhibit the production of pro-inflammatory mediators, improve mitochondrial function, and prevent damage caused by cerebral ischemia (Jiang et al., 2014). Recent studies indicate that bilobalide inhibits IL-17-induced inflammatory damage in ATDC5 cells by down-regulating microRNA-125a *via* the JNK and NF-kB signaling pathways (Mao et al., 2019), demonstrating that bilobalide has anti-inflammatory effects on chondrocytes. However, further studies on its molecular mechanism are required.

Autophagy is a widely occurring cell self-protection mechanism that acts as an intracellular scavenger to maintain intracellular balance in eukaryotic cells (Kang and Elledge, 2016; Vinatier et al., 2018). The activation of autophagy has positive significance for the survival of chondrocytes in the early stage of OA (Duan et al., 2020). During the development of OA, decreased chondrocyte autophagy leads to impaired cellular function, resulting in joint aging and dysfunction (Netea-Maier et al., 2016), indicating that autophagy plays an important role in the development of OA and is expected to be an important target for OA treatment. Several studies have reported that bilobalide can interfere with certain diseases by regulating autophagy. Bilobalide inhibits LPS-induced neuroinflammation and promotes autophagy (Qin et al., 2021). After cerebral ischemia/reperfusion injury in rats, treatment with bilobalide can significantly reduce cell apoptosis and autophagy, while promoting angiogenesis (Zheng et al., 2018). These findings indicated that the dynamic process of regulating autophagy and anti-inflammatory can delay the development of certain diseases, although it remains unclear whether bilobalide inhibits the inflammatory response of OA via the autophagy pathway.

Adenosine Monophosphate Activated Protein Kinas (AMPK) is an energy sensor that monitors and responds to changes of AMP/ATP ratio in the intracellular (Asby et al., 2015). Sirtuin 1 (SIRT1), a downstream signaling molecule of AMPK, has been shown to trigger the formation of autophagosomes by inducing the expression of autophagy-related proteins (Lee et al., 2008; Mengqi Zhang et al., 2020). The activity of SIRT1 can be positively regulated by AMPK (Wang et al., 2020). Recent studies have found that abnormal AMPK/SIRT1 activity is linked to the development of OA (Mei et al., 2020; Jiang et al., 2021; Zheng et al., 2021). It has been demonstrated that AMPK serves as a potent activator of autophagy to protect chondrocytes from cellular stress. In the nutrient-poor context, active AMPK phosphorylates, an essential component for mTOR activation, and then directly inhibits mTOR, which induces autophagy (Holczer et al., 2019). Moreover, the AMPK/SIRT1/mTOR pathway is known to be associated with autophagy and may be a potential pharmacological target for OA.

In this study, we focused on 1) the anti-inflammatory and anti-ECM degradation effects of bilobalide in IL-1β-induced ADTC5 chondrocytes, and 2) its protective effects in an anterior cruciate ligament transection (ACLT)-induced rat model of post-traumatic OA (PTOA) and its underlying mechanism. This study aimed to provide new insights for the treatment of OA and lay the foundation for future clinical applications of bilobalide.

2 MATERIALS AND METHODS

2.1 Cell Culture and Treatment

ATDC5 cells were purchased from Shanghai Zhong Qiao Xin Zhou Biotechnology Co., Ltd. (Shanghai, China). The cells were cultured in Dulbecco's Modified Eagle Medium/Nutrient Mixture F-12 (DMEM/F12) medium (Gibco, Gaithersburg, MD, United States) containing 10% fetal bovine serum (FBS) (BI, Israel) and 1% penicillin-streptomycin (Beyotime, Nantong, China) at 37°C and 5% CO_2. Insulin-transferrin-sodium selenite media supplement (ITS) (Sigma, St. Louis, MO, United States) was added to the culture medium for 14 days after cell attachment to induce differentiation into chondrogenic ATDC5 cells according to a previous method (Mengqi Zhang et al., 2020).

2.2 Cell Counting Kit-8 Assay

Bilobalide (purity ≥ 98%) was purchased from Chengdu Must Bio-technology Co., Ltd. (Chengdu, China). Requirements considered to be relevant in guidelines for best practice in natural products pharmacological research have been taken into account (Heinrich et al., 2020). Viable cell proliferation was determined using CCK-8 (APExBIO, Houston, TX, United States). Cells were seeded in 96-well plates and treated with 10 ng/ml IL-1β (Novoprotein, China) and bilobalide (0, 7.5, 15, 30, 60, and 120 μM) for 12 or 24 h. Different concentrations of bilobalide dissolved in dimethylsulfoxide (DMSO) were added to the medium, with the final concentration of DMSO not exceeding 0.05%. Following that, 10 μl of CCK-8 solution was added. After 30 min, a multi-function microplate reader (BioTEK, Winooski, VT, United States) was used to measure the absorbance at 450 nm.

2.3 Dansylcadaverine Staining

Dansylcadaverine (MDC) staining (Solarbio, China) was used to observe the formation of autophagosomes as a marker of autophagy. The MDC staining procedure was based on a previous study (Ma et al., 2021). Briefly, cells were cultured in

a 6-well plate with 10 ng/ml IL-1β and 60 μM bilobalide for 24 h before being fixed with 4% paraformaldehyde for 15 min. After removing the fixative, the cells were washed with PBS and incubated with MDC dye for 60 min. Autophagosomes were observed using a fluorescence microscope (Leica, Germany).

2.4 Transmission Electron Microscopy

Autophagic vesicles were observed using transmission electron microscopy. Chondrocytes treated with 10 ng/ml IL-1β and 60 μM bilobalide were collected. The chondrocytes were fixed with 2.5% glutaraldehyde at 4°C for 24 h, then dehydrated step by step using ethanol. Following that, the samples were washed thoroughly with PBS and embedded in resin. The samples were then sectioned and stained with 2% uranyl acetate aqueous solution for 1 h in the dark. Images were captured using an H-7650 electron microscope (Hitachi, Japan).

2.5 Immunofluorescence Staining

Cells were seeded in a confocal Petri dish (35 mm), then chondrocytes were cultured with or without 10 ng/ml IL-1β and 60 μM bilobalide for 24 h. The cells were then fixed with 4% paraformaldehyde for 15 min, washed with PBS, and permeabilized with .5% Triton X-100 for 15 min. Following that, the chondrocytes were blocked with 3% BSA for 30 min before being incubated with the SIRT1 antibody (ABclonal, Wuhan, China) (1:200) at 4°C overnight. Next, the cells were incubated with the Alexa 488 Goat Anti-Rabbit IgG (H+L) antibody (APExBIO) at room temperature for 1 h. The cell nuclei were counter-stained with DAPI (Beyotime) for 10 min. Images were captured using a fluorescence microscope (Leica).

2.6 Western Blotting

Total protein was extracted from rat cartilage and ATDC5 chondrocytes using Radio Immunoprecipitation Assay (RIPA) (Beyotime) containing protease and phosphatase inhibitors (MedChemExpress, New Jersey, United States). Protein concentrations were determined using a Bicinchoninic acid (BCA) protein assay kit (Beyotime). Equal quantities of total proteins were separated by Sodium Dodecyl Sulfate Polyacrylamide Gel Electrophoresis (SDS-PAGE) and transferred to a polyvinylidene difluoride membrane. After blocking with 5% bovine serum albumin (BSA) for 1 h, the membrane was incubated with the following primary antibodies overnight at 4°C: iNOS (1:1,500, ABclonal), COX-2 (1:2,000, ABclonal), MMP13 (1:2,000, ABclonal), GAPDH (1: 2,000, ABclonal), p-mTOR (1:500, Wanleibio, China), mTOR (1: 2,000, ABclonal), LC3 (1:2,000, Proteintech, China), p62 (1:2,000, ABclonal), p-AMPK (1:2,000, ABclonal), AMPK (1:2,000, ABclonal), and SIRT1 (1:1,000, ABclonal). Following that, the membrane was incubated with secondary antibodies (1:3,000, ZSGB-BIO, China) for 1 h. The ECL buffer (Vazyme, China) was added onto the membrane, and protein bands were visualized using the Tannon automatic gel image analysis system (China). The relative expression level of the protein was analyzed using the ImageJ software. The inhibitors, autophagy inhibitor chloroquine (CQ), AMPK inhibitor compound C, and SIRT inhibitor Selisistat (EX-527), were all purchased from MedChemExpress (United States).

2.7 Quantitative Real-Time Polymerase Chain Reaction Analysis

Total RNA was extracted using the RNA simple total RNA kit (Tiangen, China) according to the manufacturer's instructions. Reverse transcription was performed using the ReverTra Ace qPCR RT Master Mix with gDNA Remover (TOYOBO, Japan). Complementary DNA (cDNA) was amplified using the ChamQ Universal SYBR qPCR Master Mix (Vazyme). The expression levels of the target genes were evaluated using a relative quantification approach ($2^{-\Delta\Delta CT}$ method) against β-actin levels. The forward and reverse primer sequences of all genes are listed in **Table 1**.

2.8 ACLT-Induced Rat Model of Post-Traumatic OA

Forty male Sprague-Dawley rats (12-weeks-old, 300–350 g) were purchased from Changchun Yisi Experimental Animal Technology Co., Ltd. (License number: SCXK-2018-007) (Changchun, China) and kept in a controlled environment (light/dark, 12/12 h; temperature 23 ± 1°C). The rats were acclimated for 1 week before experiments were carried out. The rats were randomly divided into five groups: control (sham operation and treated with a salt solution), OA (ACLT surgery to induce OA), celecoxib (2.86 mg/kg/day celecoxib [Pfizer Pharmaceutical, New York, United States] (Panahifar et al., 2014) was administered as a positive control), 5 mg/kg + Bilobalide (the OA rats treated with 5 mg/kg/day of bilobalide), and 10 mg/kg + Bilobalide (the OA rats treated with 10 mg/kg/day of bilobalide), with eight rats in each group. The ACLT-induced PTOA models for rats and animal postoperative care were established according to previous studies (Ma et al., 2020). Rats in the 5 mg/kg + Bilobalide and 10 mg/kg + Bilobalide groups received oral bilobalide daily for 6 weeks. The bilobalide dosage was based on previous studies (Heng Zhang et al., 2020; Zhao et al., 2021). After 6 weeks of treatment, the rats in each group were euthanized by intraperitoneal injection of a lethal dose of ether, and their knee joints and blood samples were taken. The blood was centrifuged at 1,000 g for 20 min at room temperature. The supernatant was collected and stored at −80°C for further analysis. The animal surgery procedure and treatments used in this study were approved by The Laboratory Animal Welfare and Ethics Committee of Northeast Agricultural University (#NEAU-2021-03-1157-6). Every effort was made to minimize animal suffering and reduce the number of animals used.

2.9 Animal Behavior Tests

2.9.1 Mechanical Sensitivity

After ACLT surgery, rats were subjected to weekly behavioral tests. Mechanical sensitivity was assessed by measuring the withdrawal thresholds of both hind paws in response to the application of von Frey filaments using the up-down method, as previously described (Katri et al., 2019).

TABLE 1 | The primer sequences used in qPCR assay.

Gene	Forward primer (5′-3′)	Reverse primer (5′-3′)
β-actin	5′-GTGACGTTGACATCCGTAAAGA-3′	5′-GCCGGACTCATCGTACTCC-3′
Atg3	5′-ACACGGTGAAGGGAAAGGC-3′	5′-TGGTGGACTAAGTGATCTCCAG-3′
Atg4	5′-GCTGGTATGGATTCTGGGGAA-3′	5′-TGGGTTGTTCTTTTTGTCTCTCC-3′
Atg5	5′-TGTGCTTCGAGATGTGTGGTT-3′	5′-ACCAACGTCAAATAGCTGACTC-3′
Atg6	5′-ATGGAGGGGTCTAAGGCGTC-3′	5′-TGGGCTGTGGTAAGTAATGGA-3′
Atg7	5′-TCTGGGAAGCCATAAAGTCAGG-3′	5′-GCGAAGGTCAGGAGCAGAA-3′
Atg9	5′-CCGAGGGGAGCAAATCACC-3′	5′-TAGTCCACACAGCTAACCAGG-3′
Atg12	5′-TGAATCAGTCCTTTGCCCCT-3′	5′-CATGCCTGGGATTTGCAGT-3′
Atg13	5′-CCAGGCTCGACTTGGAGAAAA-3′	5′-AGATTTCCACACACATAGATCGC-3′
Atg16	5′-GCCCAGTTGAGGATCAAACAC-3′	5′-CTGCTGCATTTGGTTGTTCAG-3′

2.9.2 Vocalizations Evoked by Extension of the Knee

The knee extension test was performed for the right leg by starting with the knee in the resting position (slightly flexed). The knee was extended while the thigh was held. The number of vocalizations that occurred during the five extensions was recorded (Im et al., 2010; Piel et al., 2014). After the habituation procedure, mechanical sensitivity and vocalizations evoked by extension of the knee were assessed before surgery and up to 6 weeks post-surgery. The behavioral tests were evaluated by two independent researchers (LL and YY). Any disagreements between the researchers were resolved by a third researcher (LG.).

2.10 Histological Assessments

All rats were killed 6 weeks after ACLT. Knee joint samples were collected, fixed in 4% paraformaldehyde for 24 h, decalcified in 10% EDTA at 4°C for several days, embedded in paraffin then sectioned into 4-lm-thick sections. For further histological analyses, hematoxylin-eosin (HE) and toluidine blue (TB) staining were performed on the sections. Histopathological features were semi-quantitatively scored according to the Osteoarthritis Research Society International (OARSI) grading system (Pritzker et al., 2006).

2.11 ELISA Detection of Rat Osteoarthritis Biomarkers

The levels of C-telopeptides of type II collagen (CTX-II), Cartilage oligomeric matrix protein (COMP), and Collagenase cleavage neopeptide (C2C) in rat serum were determined with ELISA. The ELISA kit was purchased from Shanghai Enzyme-linked Biotechnology Co., Ltd. (Mlbio, China). ELISA was performed according to the manufacturer's instructions. Three replicate wells were used for each set of samples and the average OD value was obtained. The OD values at 450 nm were measured using a multi-function microplate reader (BioTEK). All experiments were conducted in the Heilongjiang Key Laboratory of Animals Disease Pathogenesis and Comparative Medicine.

2.12 Statistical Analysis

All statistical analyses were performed using the SPSS software (version 19.0 for Windows, Chicago, IL, United States). Results were presented as mean ± standard (SD) deviation. The data were evaluated for Gaussian distribution using the Kolmogorov–Smirnov test. All data had normal distribution and were analyzed with parametric statistics (one-way ANOVA, two-way ANOVA, paired two-tailed Student's t-test, and unpaired two-tailed Student's t-test). $p < .05$ was considered statistically significant.

3 RESULTS

3.1 Effect of Bilobalide on ATDC5 Chondrocyte Viability

The molecular structure of bilobalide is shown in **Figure 1A**. Bilobalide intervention for 12 h had limited cytotoxicity on ATDC5 chondrocytes (**Figure 1B**). However, after 24 h of intervention, bilobalide at a concentration of 120 mM significantly reduced ATDC5 chondrocytes viability (**Figure 1C**). When cells were stimulated with bilobalide for 24 h, the activity of the cells increased at a concentration of 7.5–60 μM. Therefore, bilobalide was used at 15, 30, and 60 μM in subsequent experiments, with a treatment time of 24 h.

3.2 Bilobalide Inhibited IL-1β-Induced Pro-inflammatory Cytokines and MMP13 Production in ATDC5 Chondrocytes

Chondrocytes were treated with 10 ng/ml IL-1β in the presence or absence of bilobalide for 24 h. In chondrocytes, 10 ng/ml IL-1β stimulation caused an abnormal increase in inducible nitric oxide synthase (iNOS) and cyclooxygenase-2 (COX-2) inflammatory factors (**Figures 2A,B**). However, bilobalide could antagonize those effects. In addition, bilobalide significantly inhibited the expression of the MMP13 protein ($p < .05$). In ATDC5 chondrocytes induced by IL-1β, 60 μM bilobalide intervention had the greatest inhibitory effect on iNOS and COX-2. The above results indicated that bilobalide could protect ATDC5 chondrocytes from IL-1β-induced inflammation by down-regulating the expression of iNOS, COX-2, and MMP13.

3.3 Bilobalide Initiates Autophagy in IL-1β-Induced ATDC5 Chondrocytes

In order to exclude autophagy induced by serum starvation (Rong et al., 2021), the DMEM/F12 medium containing 10% fetal bovine serum was consistently used in this study. Because IL-1β induction may also affect autophagy (Ge et al., 2018), the

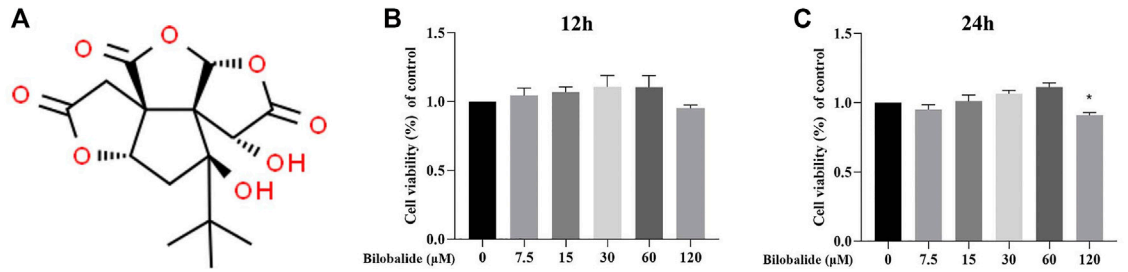


FIGURE 1 | The effect of bilobalide on the viability of ATDC5 chondrocytes. **(A)** Chemical structure of bilobalide. **(B,C)** Bilobalide cytotoxicity on chondrocytes at 12 and 24 h. All data were presented as mean ± SD ($n = 5$). $^{*}p < .05$ indicates significant differences between different groups compared to the control group (Statistical analysis using one-way ANOVA and paired two-tailed Student's t-test).

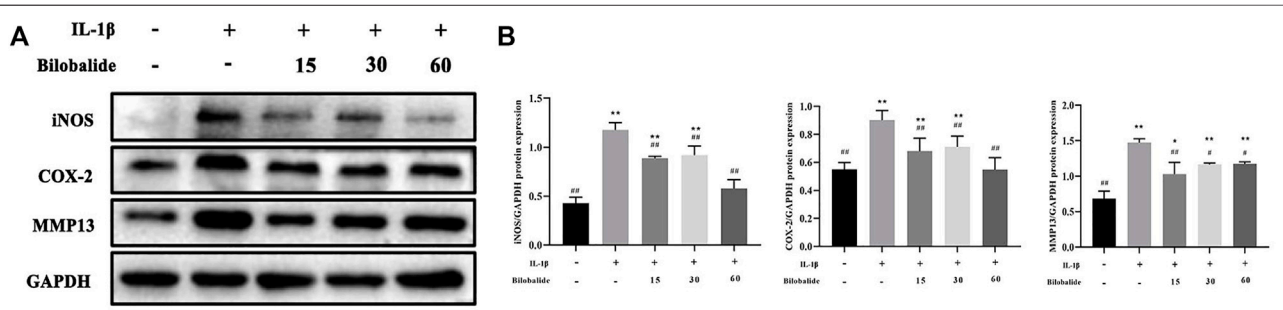


FIGURE 2 | Influence of bilobalide on the IL-1β-induced inflammatory reaction in ATDC5 chondrocytes. **(A,B)** Western blot analysis of iNOS, COX-2, and MMP13 protein levels in chondrocytes. All data were presented as mean ± SD ($n = 3$). $^{*}p < .05$ and $^{**}p < .01$ compared to the control group; $^{\#}p < .05$ and $^{\#\#}p < .01$ compared to the IL-1β group (Statistical analysis using one-way ANOVA and paired two-tailed Student's t-test).

expression of the autophagy marker protein LC3II was examined at different 10 ng/ml IL-1β induction times. The results showed that after chondrocytes were exposed to 10 ng/ml IL-1β for 24 h, the expression of LC3II protein was significantly reduced ($p < .05$) and there was a decrease in chondrocyte autophagy (**Figures 3A,B**). Therefore, based on the above experimental results and combined with the previous CCK-8 results, 10 ng/ml IL-1β was selected to treat cells for 24 h in subsequent experiments.

The results of MDC staining showed that the number of autophagosomes in the IL-1β + bilobalide group increased in a dose-dependent manner compared to the control group ($p < .05$) (**Figures 3C,D**). In order to verify the initiation of autophagy, transmission electron microscopy was used to observe autophagic vesicles (**Figure 3E**). When IL-1β and bilobalide were both added, autophagic vesicles were abundant, including autophagosome with double-layer membranes and autophagolysosome with single-layer membranes, compared to treatment with 10 ng/ml IL-1β alone.

3.4 Bilobalide Inhibited IL-1β-Induced ATDC5 Chondrocyte Inflammation by Restoring Autophagy

Next, the expression of p-mTOR, mTOR, LC3II, and p62 in ATDC5 chondrocytes was evaluated (**Figure 4A**). Compared to the control group, the expression of p-mTOR and p62 increased after IL-1β stimulation ($p < .05$), while the expression of LC3II significantly decreased ($p < .05$). However, after the addition of bilobalide, the expression of p-mTOR and p62 decreased in a dose-dependent manner, while LC3II expression displayed a dose-dependent increase. These findings demonstrated that bilobalide promoted autophagy in a dose-dependent manner.

Following that, a kinetic experiment was performed (**Figure 4B**). Chondrocytes were treated with 10 ng/ml IL-1β and 60 μM bilobalide at the same time for 6–48 h to determine the expression of LC3II. The expression of LC3II significantly increased after 24 h of treatment ($p < .05$). Autophagy induced by IL-1β in the presence of bilobalide was most prominent within 24 h. In addition, qPCR results showed that the relative level of the Atg genes significantly increased compared to the IL-1β group after treatment with 10 ng/ml IL-1β and 60 μM bilobalide for 24 h ($p < .05$) (**Figure 4C**).

3.5 Autophagy is Required for Bilobalide's Anti-Inflammation Activity

In order to better understand the mechanism of autophagy and inflammation induced by bilobalide in ATDC5 chondrocytes, we analyzed the expression of LC3II, p62, iNOS, COX-2, and MMP13 of the 60 μM bilobalide treated group after intervention with 30 μM

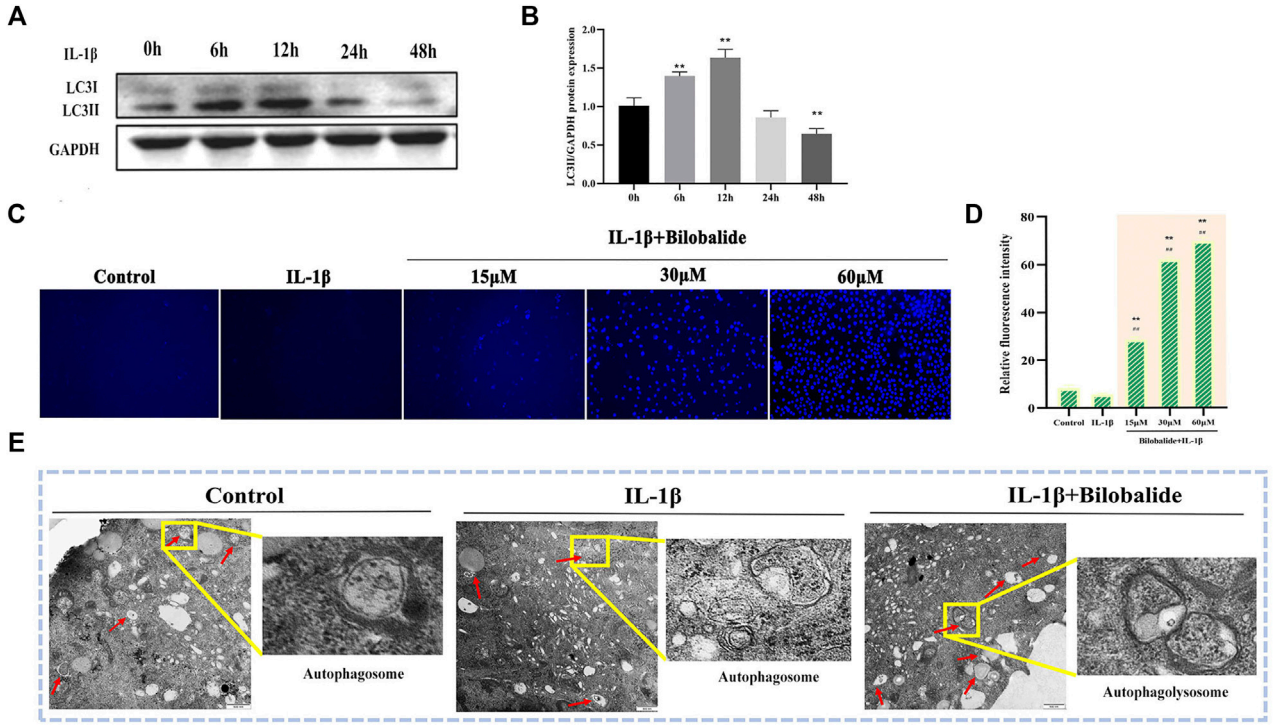


FIGURE 3 | Bilobalide induces autophagy in IL-1β-induced ATDC5 chondrocytes. **(A,B)** Western blot analysis of LC3II protein expression after IL-1β induced cartilage for different periods. **(C,D)** The number of autophagosomes was observed using MDC dye under a fluorescence microscope. Magnification ×10. **(E)** Autophagic vesicles were observed using transmission electron microscopy. Magnification ×3000. All data were presented as mean ± SD ($n = 3$). ** $p < 0.01$ compared to the control group; #$p < 0.05$ and ##$p < 0.01$ compared to the IL-1β group (Statistical analysis using one-way ANOVA and paired two-tailed Student's t-test).

CQ (**Figures 4D,E**). The chondrocytes were divided into five groups: (I) control, (II) IL-1β, (III) Bilobalide + IL-1β, (IV) CQ, and (V) Bilobalide + IL-1β + CQ. Groups IV and V were pretreated with CQ for 1 h, then incubated with bilobalide for 24 h. The combined action of IL-1β and bilobalide resulted in significantly increased expression of the LC3II protein ($p < .05$), while the expression of the p62 protein was significantly inhibited ($p < .05$). After adding the CQ inhibitor alone, the expression of the LC3II protein was significantly reduced ($p < .05$), while the expression of the p62 protein was significantly increased ($p < 0.05$). Interestingly, the expression of LC3II and p62 in the bilobalide + IL-1β + CQ group increased compared to the bilobalide + IL-1β group. We hypothesized that CQ blocked the fusion of autophagic vesicles and lysosomes, thereby inhibiting the degradation of the LC3II and the p62 protein. In addition, bilobalide significantly inhibited the up-regulation of iNOS, COX-2, and MMP3 expression in chondrocytes induced by IL-1β, while the addition of CQ reversed the decrease in iNOS, COX-2, and MMP3 proteins caused by bilobalide.

3.6 Bilobalide Promotes Chondrocyte Autophagy by Regulating AMPK/SIRT1/mTOR Pathway

The expression of the SIRT1 protein was detected by immunofluorescence. Compared to the control group, SIRT1 expression was significantly increased after 10 ng/ml IL-1β and 60 μM bilobalide treatment ($p < .05$) (**Figures 5A,B**). Western blot analysis revealed that the expression of p-AMPK and SIRT1 increased in a dose-dependent manner compared to the control group ($p < .05$) (**Figures 5C,D**). Chondrocytes were pretreated with compound C and EX-527 to verify the activation of AMPK and SIRT1 (**Figures 5E,F**). In the presence of 60 μM bilobalide and 10 ng/ml IL-1β, pretreatment with compound C significantly reduced phosphorylation of AMPK ($p < .05$), while EX-527 significantly inhibited the expression of SIRT1 ($p < .05$). After 60 μM bilobalide was added, the expression of p-AMPK and SIRT1 in chondrocytes significantly increased ($p < .05$), but the degree of increase was decreased by the addition of compound C or EX-527, respectively. This suggested that bilobalide activated the AMPK/SIRT1 signaling pathway. In order to further explore the role of AMPK/SIRT1 in autophagy signaling, compound C or EX-527 were used to determine the protein levels of mTOR, p-mTOR, iNOS, COX-2, and MMP13 (**Figures 5G,H**). The results revealed that in the presence of bilobalide and IL-1β, the expression of p-mTOR, iNOS, COX-2, and MMP13 were significantly reduced ($p < .05$). However, the addition of compound C or EX-527 improved the reduction of p-mTOR, iNOS, COX-2, and MMP13 ($p < .05$). These results suggested that the AMPK/SIRT1 pathway regulates

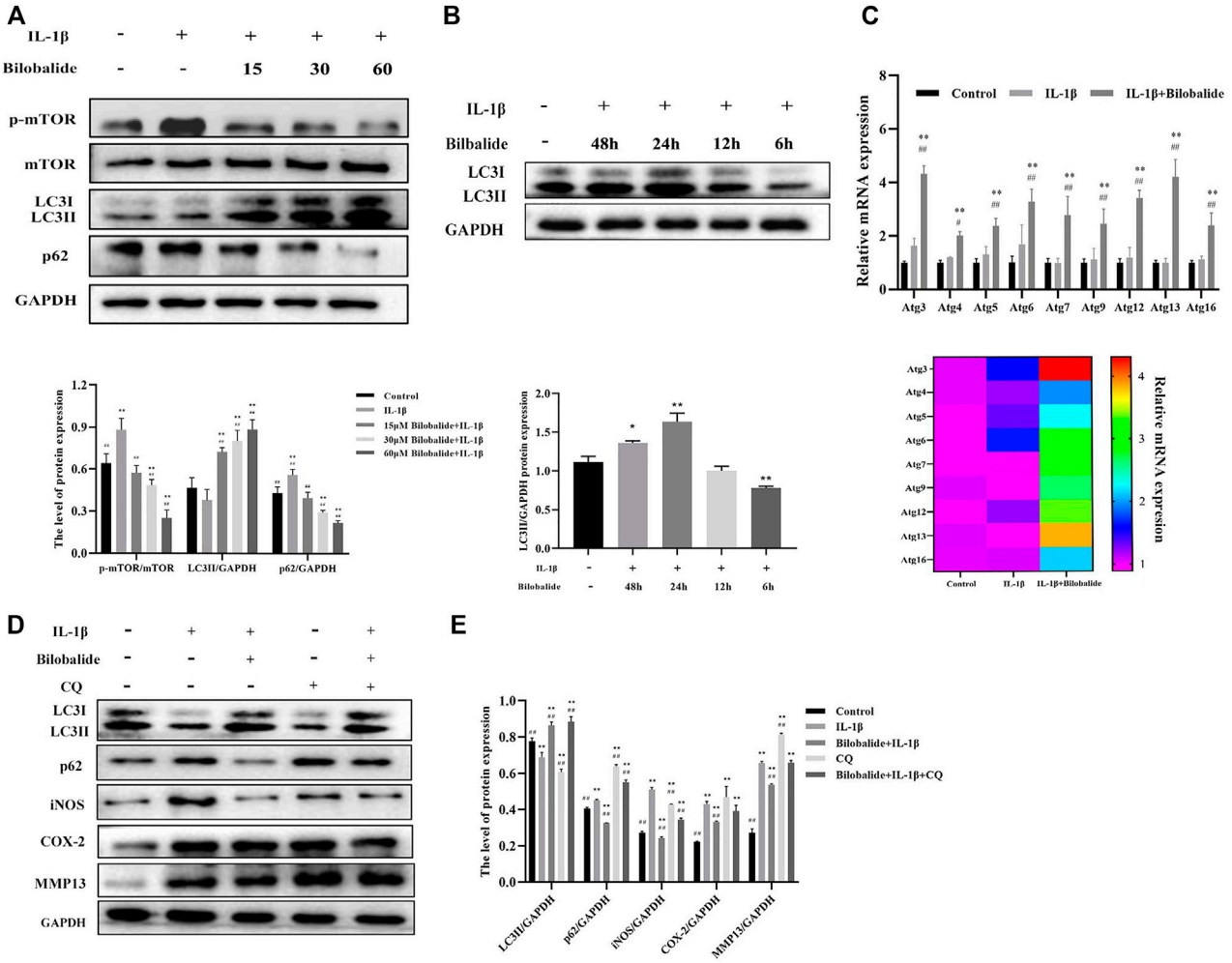


FIGURE 4 | The effect of bilobalide on autophagy in ATDC5 chondrocytes induced by IL-1β. **(A)** Western blot analysis of mTOR, p-mTOR, LC3II, and p62 protein expression after treatment with 10 ng/ml IL-1β and different concentrations bilobalide for 24 h. **(B)** The effect of 60 μM bilobalide with different incubation periods in the presence of 10 ng/ml IL-1β on autophagy was determined through the LC3II protein using western blot. **(C)** The expression levels of certain autophagy-related genes (Atg genes) were evaluated using qPCR. **(D,E)** Chondrocytes were pretreated with 30 μM CQ. The protein levels of LC3II, p62, COX-2, and MMP13 were examined by Western blot. All data were presented as mean ± SD ($n = 3$). $^{*}p < .05$ and $^{**}p < .01$ compared to the control group; $^{\#}p < .05$ and $^{\#\#}p < .01$ compared to the IL-1β group (Statistical analysis using one-way ANOVA, two-way ANOVA, paired two-tailed Student's t-test, and unpaired two-tailed Student's t-test).

the level of phosphorylation of mTOR, thereby modulating downstream cascades related to autophagy.

3.7 Bilobalide Attenuates ACLT-Induced Post-Traumatic OA in Rats *via* AMPK/SIRT1/mTOR Pathway

Compared to the control group, the mechanical sensitivity of the rats was significantly reduced within 6 weeks of establishing the model, as seen in **Figure 6A**. In comparison to the OA group, the mechanical sensitivity of rats was significantly increased after the administration of 5 mg/kg and 10 mg/kg bilobalide. In the knee extension test, the number of vocalizations was also significantly reduced in rats after 6 weeks of bilobalide administration (**Figure 6B**).

The representative HE and TB images and OARSI scores of the knee joints of each group are shown in **Figure 6C**. The cartilage structure and layers of the control group were clear and complete, the chondrocytes were arranged neatly, and TB was evenly stained. The articular cartilage in the OA group was severely damaged, with obvious cracks appearing in the tibia and femur. Furthermore, the chondrocytes were vacuolated and arranged in clusters, and the intensity of TB staining was reduced. In the celecoxib group, the cartilage surface was rough, the surface of the femur was slightly rough, the surface chondrocytes were destroyed, the surface of the tibia was severely damaged, the inflammatory cells infiltrated to the middle layer, and the cell arrangement was disordered. Compared to the OA group, the OARSI score of the celecoxib group was significantly lower ($p <$ .05). After treatment with bilobalide, the cartilage of the knee joint of rats was protected; the surface roughness of the femur was significantly reduced and the cell arrangement was relatively in order. In the 5 mg/kg + Bilobalide group a part of the tibia was

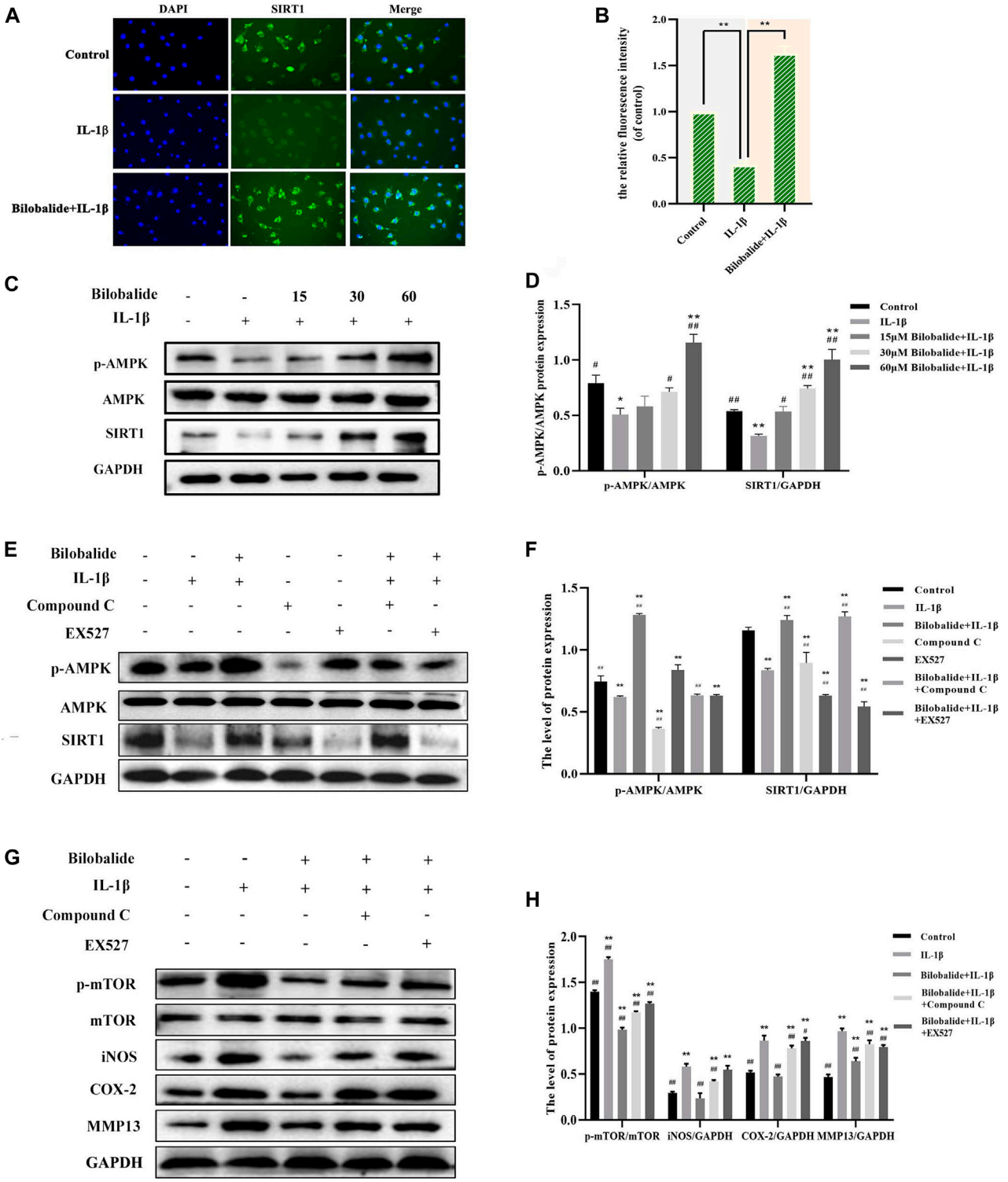


FIGURE 5 | The effect of bilobalide on the AMPK/SIRT1/mTOR signaling pathway in ATDC5 chondrocytes induced by IL-1β. **(A,B)** The fluorescence intensity of the Sitr1 protein was detected by immunofluorescence. **(C,D)** Western blot analysis of AMPK, p-AMPK, and SIRT1 protein expression after treating the cells with IL-1β and different concentrations bilobalide for 24 h **(E,F)** Western blot analysis of AMPK, p-AMPK, and SIRT1 protein expression after chondrocytes were pretreated with the AMPK inhibitor compound C and the SIRT1 inhibitor EX-527. **(G,H)** Western blot analysis of mTOR, p-mTOR,iNOS, COX-2, and MMP13 protein expression after the addition of compound C or EX-527. All data were presented as mean ± SD ($n = 3$). $^{*}p < .05$ and $^{**}p < .01$ compared to the control group; $^{\#}p < .05$ and $^{\#\#}p < .01$ compared to the IL-1β group (Statistical analysis using one-way ANOVA, two-way ANOVA, paired two-tailed Student's t-test, and unpaired two-tailed Student's t-test).

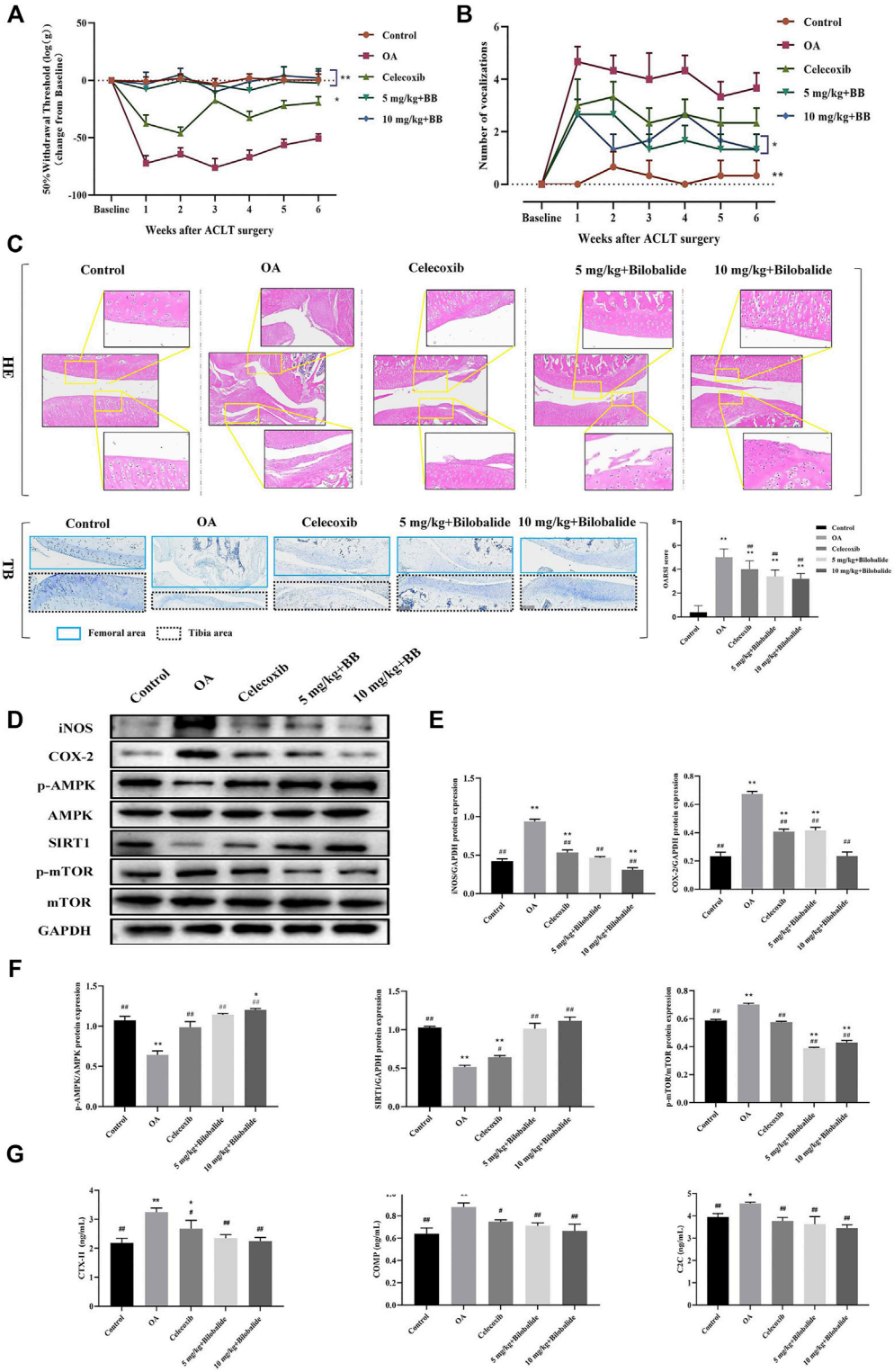


FIGURE 6 | Bilobalide attenuates ACLT-induced PTOA in rats via AMPK/SIRT1/mTOR pathway. **(A)** Mechanical sensitivity. **(B)** Vocalizations evoked by extension of the knee. **(C)** Representative images of the knee joint stained with hematoxylin-eosin (HE) and toluidine blue (TB) and OARSI scores after 6 weeks of treatment. Magnification ×10. **(D–F)** Western blot analysis of AMPK/SIRT1/mTOR pathway related proteins expression in rat cartilage. **(G)** The levels of ECM degradation biomarkers CTX-II, COMP, and C2C in the serum of rats after bilobalide intervention were determined using ELISA. All data were presented as mean ± SD ($n = 3$). $^{*}p < .05$ and $^{**}p < .01$ compared to the control group; $^{\#}p < .05$ and $^{\#\#}p < .01$ compared to the IL-1β group (Statistical analysis using one-way ANOVA and paired two-tailed Student's t-test).

still infiltrated by inflammation; the chondrocytes were disordered; however, the intensity of TB staining was stronger than the OA group. In the 10 mg/kg + Bilobalide group, chondrocyte hypertrophy and vacuolization were observed in the femoral area, and there was no obvious loss of chondrocytes; compared to the OA group, the OARSI score of rats after bilobalide administration was significantly reduced ($p < .05$).

As shown in **Figures 6D,E**, 6 weeks after ACLT surgery, the expression of inflammatory factors iNOS and COX-2 in the OA group was significantly increased ($p < .05$), while bilobalide inhibited the expression of iNOS and COX-2. Notably, 10 mg/kg bilobalide had the most significant therapeutic effect. We observed that compared with the OA group, the expression of p-AMPK and SIRT1 was significantly increased ($p < .05$) after bilobalide administration, while the expression of p-mTOR was inhibited by bilobalide (**Figures 6D,F**). This indicates that Bilobalide attenuates cartilage iNOS and COX-2 levels in PTOA rats through the AMPK/SIRT1/mTOR pathway.

The type II collagen degradation products CTX-II and C2C, and non-collagen COMP in ECM are OA biomarkers for evaluating cartilage damage. As shown in **Figure 6G**, the levels of CTX-II, COMP, and C2C in the serum of rats in the OA group were significantly increased compared to the control group ($p < .05$). The celecoxib group, as a positive control, effectively reduced the expression of three biomarkers in the serum compared to the OA group ($p < .05$). After 6 weeks of bilobalide intervention, the levels of CTX-II, C2C, and COMP in the serum of rats were significantly reduced ($p < .05$). Furthermore, 10 mg/kg bilobalide had a better effect than other groups. These findings demonstrated that bilobalide could effectively reduce the degradation of ECM in rats, thereby protecting the joints.

4 DISCUSSION

Ginkgo biloba L. extract has anti-inflammatory properties (Ilieva et al., 2004; Ye et al., 2019) and its sesquiterpene lactone compound bilobalide may have significant pharmacological effects (Goldie and Dolan, 2013). A large number of studies have confirmed that IL-1β is a pro-inflammatory factor that plays a key role in the pathological process of OA (Wang and He, 2018; Jenei-Lanzl et al., 2019). IL-1β induced increased OA-related protein expressions in a time and concentration dependent manner (Tu et al., 2019). The stimulation of IL-1β (10 ng/ml) for 24 h could induce inflammation in chondrocytes (Wang et al., 2019; Pei et al., 2021). IL-1β has been shown to induce the overproduction of iNOS and COX-2, which is directly relevant to the secretion of nitric oxide (NO) and prostaglandin E2 (PGE2) (Sheu et al., 2015). In our study, the expression of iNOS, COX-2 and MMP13 increased after 10 ng/ml IL-1β induced chondrocytes, which proved that 10 ng/ml IL-1β successfully induced chondrocyte inflammation model *in vitro*. In addition, bilobalide inhibited the expression of the iNOS, COX-2, and MMP13 proteins. In the rat PTOA model established by ACLT, bilobalide induced and inhibited the expression of iNOS and COX-2 in rat cartilage tissue. These results indicated that bilobalide inhibited inflammation and slowed down the degradation of chondrocyte ECM.

Pro-inflammatory cytokines and autophagy play a key role in the pathophysiology of diseases, and there is evidence to prove the cross-talk effect between autophagy and pro-inflammatory cytokines (Ge et al., 2018). IL-1β was demonstrated to trigger autophagosome formation, and they may induce autophagy as part of a negative feedback loop to limit the inflammatory response, and promote cytokine-mediated anti-microbial defense (Zhang et al., 2015). Autophagic processes can orchestrate the transcription, processing, and production of proinflammatory cytokines, serving as a negative feedback loop for the modulation of inflammatory as well as immune responses. Therefore, in order to clarify the optimal conditions under which IL-1β-induced chondrocyte autophagy cannot be detected, we set different IL-1β induction time under the premise of determining the concentration of 10 ng/ml IL-1β, and observe the influence of IL-1β time gradient on autophagy. Similarly, Rong et al. used LPS (0.5 μg/ml) to induce the RAW264.7 cell inflammation model, and detected the autophagy induced by LPS at different times (0–48 h) by Western blot, and found that the expression of LC3/p62 protein was reduced after 24 h of induction (Rong et al., 2021). It has been reported that compared with normal chondrocytes, rat chondrocytes treated with 10 ng/ml IL-1β for 24 h have observed a reduction in autophagy levels (Yan et al., 2021). Interestingly, we found that IL-1β (10 ng/ml) induced ATDC5 chondrocytes for 24 h, and the autophagy level was significantly reduced, which is consistent with previous studies (Zhou et al., 2021). We determined that 10 ng/ml IL-1β induced a significant decrease in the autophagy intensity of chondrocytes for 24 h.

Recent studies believe that autophagy is a key regulator of OA and a potential therapeutic target (Valenti et al., 2021; Tian et al., 2021). The production of LC3II is a common sign of autophagy maturation, and the scaffold protein p62 is the substrate protein of autophagy, which mainly accumulates substances that need to be degraded in the cell, reflecting the degree of autophagy degradation (Tanida, 2011). We found that the autophagosomes after the co-treatment of IL-1β and bilobalide increased significantly, indicating that chondrocyte autophagy was initiated. LC3II protein expression was significantly increased after bilobalide treatment, and phosphorylated mTOR and p62 proteins were significantly reduced, indicating that bilobalide induced chondrocyte autophagy by inhibiting the mTOR pathway, and the substances in autophagy were successfully degraded. Our results showed that the co-treatment of bilobalide and IL-1β significantly up-regulated the expression of autophagy-related genes (Atg genes). These results indicate that after mTOR phosphorylation is inhibited by upstream signals, the activated ULK1-Atg13-FIP200 complex participates in the formation of autophagic vesicles by activating Atg6, class III phosphatidylinositol 3-kinase and Atg14 complex (Yang and Klionsky, 2010). After autophagy is induced, LC3-I is bound to the highly lipophilic phosphatidylethanolamine (PE) by Atg7, Atg3, and Atg12-Atg5-Atg16L complex to produce LC3-II. Finally, PE

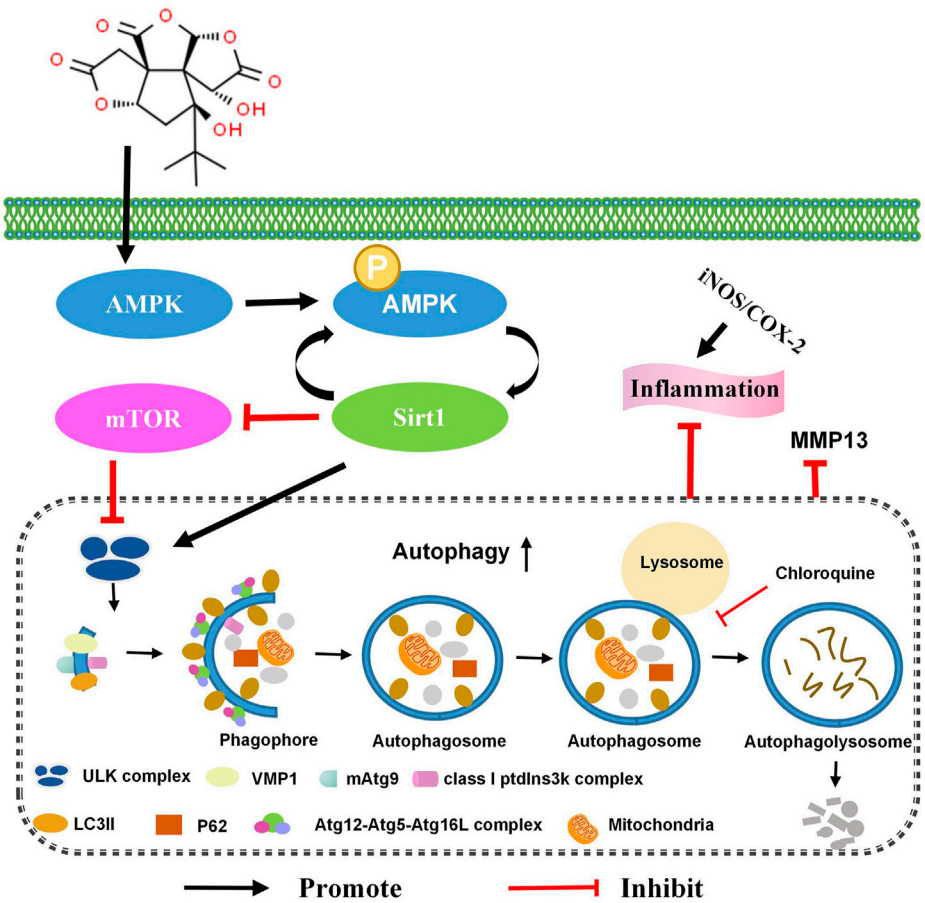


FIGURE 7 | Bilobalide reduces IL-1β-induced ATDC5 chondrocyte inflammation by activating the AMPK/SIRT/mTOR pathway, leading to chondrocyte autophagy.

promotes the integration of LC3-II into the lipid membrane to form autophagosomes. Among them, Atg9 played a key role in promoting the lipidation of Atg8 (Sawa-Makarska et al., 2020). Interestingly, We found that CQ effectively inhibited bilobalide-induced chondrocyte autophagy by inhibiting the degradation of LC3II and P62 protein. After CQ inhibited autophagy, the down-regulation of iNOS, COX-2 and MMP3 proteins induced by bilobalide was weakened. These findings indicated that autophagy is required for the protective effect of bilobalide in ATDC5 chondrocytes. This study discovered that the co-treatment with bilobalide and IL-1β increased the expression of p-AMPK and Srit1. However, the addition of compound C or EX-527 resulted in a lower increase in p-AMPK and Srit1. In the presence of bilobalide and IL-1β, the expression of p-mTOR, iNOS, COX-2, and MMP13 were significantly reduced, and the reduction of p-mTOR, iNOS, COX-2, and MMP13 were attenuated after the addition of compound C or EX-527. Previous studies have revealed that metformin has been shown to increase the phosphorylation level of AMPK and up-regulate SIRT1 protein expression, leading to increased chondrocyte autophagy and decreased catabolism (Wang et al., 2020), which is consistent with our findings. Furthermore, we validated that bilobalide regulates the AMPK/SIRT1 signaling pathway and reduces the expression of mTOR to activate autophagy and protect chondrocytes from damages.

The use of NSAIDs places a greater physical and financial burden on patients (Cooper et al., 2019). Therefore, it is particularly important to study natural compounds that have significant efficacy, few side effects, and can treat OA. Previous studies have shown that L-theanine can reduce the level of C2C in the serum of rats with OA induced by ACLT (Bai et al., 2020). Isorhamnetin inhibits the expression of COMP and CTX-II in MIA-induced OA rats and prevents cartilage damage (Tsai et al., 2019). In this study, we discovered that bilobalide had obvious health effects on OA. In the rat model of PTOA induced by ACLT, the pathological changes of cartilage were weakened after 6 weeks of oral administration of bilobalide, especially the protective effect on the femur. The serum levels of CTX-II, COMP, and C2C in the model group were significantly higher than the control group, indicating that degradation of type II collagen and proteoglycan in the cartilage ECM of PTOA rats led to the aggravation of OA. After bilobalide was administered, the levels of CTX-II, COMP, and C2C in the rat serum were significantly reduced, indicating that bilobalide inhibited

ECM degradation and exerted chondroprotective effects. Furthermore, it was able to reduce joint pain in PTOA rats, reducing the symptoms of OA; this discovery is critical for future clinical studies.

The long-term safety of *Ginkgo biloba* L. extract is unclear, which limits its clinical application (Mahadevan and Park, 2008). In addition, excessive consumption of Ginkgo leaf extracts has been reported to cause occasional adverse effects, including gastrointestinal disturbances, dizziness, allergic skin reactions, headaches, excessive bleeding, and anaphylaxis-like reactions (only with intravenous administration) (Vale, 1998; Benjamin et al., 2001; De Smet, 2002; Mahadevan and Park, 2008). We discovered that bilobalide, a unique constituent of *Ginkgo biloba* L., up-regulates chondrocyte autophagy flux and autophagy-related genes via the AMPK/SIRT1/mTOR signaling pathway. Furthermore, it reduces the levels of iNOS, COX-2, and MMP13, and has a protective effect on ATDC5 chondrocytes (**Figure 7**).

This study revealed that bilobalide has significant anti-inflammatory and anti-ECM degradation effects in ACLT-induced rat PTOA, suggesting that it could delay the progression of OA caused by cartilage pathology and damage. However, the study only focused on cartilage degeneration. More studies are therefore needed to clarify the effects of bilobalide on synovial inflammation and subchondral bone remodeling. Moreover, further *in vivo* research is required to establish the effectiveness bilobalide in the treatment of OA. Importantly, extensive pharmacological and toxicity studies are required for the treatment of OA with bilobalide before investigating the possibility of its clinical application. Nonetheless, Our results could provide new insights regarding the protective mechanism of bilobalide on articular cartilage.

DATA AVAILABILITY STATEMENT

The original contributions presented in the study are included in the article/Supplementary Material, further inquiries can be directed to the corresponding author.

ETHICS STATEMENT

The animal study was reviewed and approved by the Laboratory Animal Welfare and Ethics Committee of Northeast Agricultural University (#NEAU-2021-03-1157-6).

AUTHOR CONTRIBUTIONS

TM and LG conceived and designed the experiments. LL, YY, LJ, XPS, XX, and TL performed the experiments. TM, XBS, HW, and JZ analyzed the data and prepared figures. TM, LL and YY wrote the manuscript. All the authors read and approved the final manuscript.

FUNDING

This work was supported by the National Key R&D Program of China (2017YFD0502200) and the Applied Technology Research and Development Plan of Heilongjiang (GX18B023 and GA18B203).

ACKNOWLEDGMENTS

Thanks to Wuhan Servicebio Technology Co., Ltd. for the technical support of the pathological section of this study.

REFERENCES

Achete de Souza, G., de Marqui, S. V., Matias, J. N., Guiguer, E. L., and Barbalho, S. M. (2020). Effects of Ginkgo Biloba on Diseases Related to Oxidative Stress. *Planta Med.* 86 (6), 376–386. doi:10.1055/a-1109-3405

Asby, D. J., Cuda, F., Beyaert, M., Houghton, F. D., Cagampang, F. R., and Tavassoli, A. (2015). AMPK Activation via Modulation of De Novo Purine Biosynthesis with an Inhibitor of ATIC Homodimerization. *Chem. Biol.* 22 (7), 838–848. doi:10.1016/j.chembiol.2015.06.008

Aziz, T. A., Hussain, S. A., Mahwi, T. O., Ahmed, Z. A., Rahman, H. S., and Rasedee, A. (2018). The Efficacy and Safety of Ginkgo Biloba Extract as an Adjuvant in Type 2 Diabetes Mellitus Patients Ineffectively Managed with Metformin: a Double-Blind, Randomized, Placebo-Controlled Trial. *Drug Des. Devel Ther.* 12, 735–742. doi:10.2147/DDDT.S157113

Bai, H., Zhang, Z., Li, Y., Song, X., Ma, T., Liu, C., et al. (2020). L-theanine Reduced the Development of Knee Osteoarthritis in Rats via its Anti-inflammation and Anti-matrix Degradation Actions: *In Vivo* and *In Vitro* Study. *Nutrients* 12 (7). doi:10.3390/nu12071988

Benjamin, J., Muir, T., Briggs, K., and Pentland, B. (2001). A Case of Cerebral Haemorrhage-Can Ginkgo Biloba Be Implicated? *Postgrad. Med. J.* 77 (904), 112–113. doi:10.1136/pmj.77.904.112

Chen, Y. F., Jobanputra, P., Barton, P., Bryan, S., Fry-Smith, A., Harris, G., et al. (2008). Cyclooxygenase-2 Selective Non-steroidal Anti-inflammatory Drugs (Etodolac, Meloxicam, Celecoxib, Rofecoxib, Etoricoxib, Valdecoxib and Lumiracoxib) for Osteoarthritis and Rheumatoid Arthritis: a Systematic Review and Economic Evaluation. *Health Technol. Assess.* 12 (11), 1–iii. doi:10.3310/hta12110

Cooper, C., Chapurlat, R., Al-Daghri, N., Herrero-Beaumont, G., Bruyère, O., Rannou, F., et al. (2019). Safety of Oral Non-selective Non-steroidal Anti-inflammatory Drugs in Osteoarthritis: What Does the Literature Say? *Drugs Aging* 36 (Suppl. 1), 15–24. doi:10.1007/s40266-019-00660-1

dal Belo, S. E., Gaspar, L. R., Maia Campos, P. M., and Marty, J. P. (2009). Skin Penetration of Epigallocatechin-3-Gallate and Quercetin from green tea and Ginkgo Biloba Extracts Vehiculated in Cosmetic Formulations. *Skin Pharmacol. Physiol.* 22 (6), 299–304. doi:10.1159/000241299

De Smet, P. A. (2002). Herbal Remedies. *N. Engl. J. Med.* 347 (25), 2046–2056. doi:10.1056/NEJMra020398

Duan, R., Xie, H., and Liu, Z. Z. (2020). The Role of Autophagy in Osteoarthritis. *Front Cell Dev Biol* 8, 608388. doi:10.3389/fcell.2020.608388

Feng, Z., Sun, Q., Chen, W., Bai, Y., Hu, D., and Xie, X. (2019). The Neuroprotective Mechanisms of Ginkgolides and Bilobalide in Cerebral Ischemic Injury: a Literature Review. *Mol. Med.* 25 (1), 57. doi:10.1186/s10020-019-0125-y

Ge, Y., Huang, M., and Yao, Y. M. (2018). Autophagy and Proinflammatory Cytokines: Interactions and Clinical Implications. *Cytokine Growth Factor. Rev.* 43, 38–46. doi:10.1016/j.cytogfr.2018.07.001

Goldie, M., and Dolan, S. (2013). Bilobalide, a Unique Constituent of Ginkgo Biloba, Inhibits Inflammatory Pain in Rats. *Behav. Pharmacol.* 24 (4), 298–306. doi:10.1097/FBP.0b013e32836360ab

Grässel, S., Zaucke, F., and Madry, H. (2021). Osteoarthritis: Novel Molecular Mechanisms Increase Our Understanding of the Disease Pathology. *J. Clin. Med.* 10 (9). doi:10.3390/jcm10091938

Heinrich, M., Appendino, G., Efferth, T., Fürst, R., Izzo, A. A., Kayser, O., et al. (2020). Best Practice in Research - Overcoming Common Challenges in Phytopharmacological Research. *J. Ethnopharmacol* 246, 112230. doi:10.1016/j.jep.2019.112230

Henrotin, Y., and Mobasheri, A. (2018). Natural Products for Promoting Joint Health and Managing Osteoarthritis. *Curr. Rheumatol. Rep.* 20 (11), 72. doi:10.1007/s11926-018-0782-9

Holczer, M., Hajdú, B., Lőrincz, T., Szarka, A., Bánhegyi, G., and Kapuy, O. (2019). A Double Negative Feedback Loop between mTORC1 and AMPK Kinases Guarantees Precise Autophagy Induction upon Cellular Stress. *Int. J. Mol. Sci.* 20 (22). doi:10.3390/ijms20225543

Ilieva, I., Ohgami, K., Shiratori, K., Koyama, Y., Yoshida, K., Kase, S., et al. (2004). The Effects of Ginkgo Biloba Extract on Lipopolysaccharide-Induced Inflammation *In Vitro* and *In Vivo*. *Exp. Eye Res.* 79 (2), 181–187. doi:10.1016/j.exer.2004.03.009

Im, H. J., Kim, J. S., Li, X., Kotwal, N., Sumner, D. R., van Wijnen, A. J., et al. (2010). Alteration of Sensory Neurons and Spinal Response to an Experimental Osteoarthritis Pain Model. *Arthritis Rheum.* 62 (10), 2995–3005. doi:10.1002/art.27608

Jenei-Lanzl, Z., Meurer, A., and Zaucke, F. (2019). Interleukin-1β Signaling in Osteoarthritis - Chondrocytes in Focus. *Cell Signal* 53, 212–223. doi:10.1016/j.cellsig.2018.10.005

Jiang, M., Li, J., Peng, Q., Liu, Y., Liu, W., Luo, C., et al. (2014). Neuroprotective Effects of Bilobalide on Cerebral Ischemia and Reperfusion Injury Are Associated with Inhibition of Pro-inflammatory Mediator Production and Down-Regulation of JNK1/2 and P38 MAPK Activation. *J. Neuroinflammation* 11, 167. doi:10.1186/s12974-014-0167-6

Jiang, W., Liu, H., Wan, R., Wu, Y., Shi, Z., and Huang, W. (2021). Mechanisms Linking Mitochondrial Mechanotransduction and Chondrocyte Biology in the Pathogenesis of Osteoarthritis. *Ageing Res. Rev.* 67, 101315. doi:10.1016/j.arr.2021.101315

Kang, C., and Elledge, S. J. (2016). How Autophagy Both Activates and Inhibits Cellular Senescence. *Autophagy* 12 (5), 898–899. doi:10.1080/15548627.2015.1121361

Katri, A., Dąbrowska, A., Löfvall, H., Karsdal, M. A., Andreassen, K. V., Thudium, C. S., et al. (2019). A Dual Amylin and Calcitonin Receptor Agonist Inhibits Pain Behavior and Reduces Cartilage Pathology in an Osteoarthritis Rat Model. *Osteoarthritis Cartilage* 27 (9), 1339–1346. doi:10.1016/j.joca.2019.05.016

Katz, J. N., Arant, K. R., and Loeser, R. F. (2021). Diagnosis and Treatment of Hip and Knee Osteoarthritis: A Review. *JAMA* 325 (6), 568–578. doi:10.1001/jama.2020.22171

Lee, I. H., Cao, L., Mostoslavsky, R., Lombard, D. B., Liu, J., Bruns, N. E., et al. (2008). A Role for the NAD-dependent Deacetylase Sirt1 in the Regulation of Autophagy. *Proc. Natl. Acad. Sci. U S A.* 105 (9), 3374–3379. doi:10.1073/pnas.0712145105

Ma, T. w., Wen, Y. j., Song, X. p., Hu, H. l., Li, Y., Bai, H., et al. (2020). Puerarin Inhibits the Development of Osteoarthritis through Antiinflammatory and Antimatrix-degrading Pathways in Osteoarthritis-induced Rat Model. *Phytotherapy Res.* 35, 2579–2593. doi:10.1002/ptr.6988

Ma, Y., Liu, H., Du, X., Petlulu, P., Chen, X., Wang, R., et al. (2021). IRE1 and CaMKKβ Pathways to Reveal the Mechanism Involved in Microcystin-LR-Induced Autophagy in Mouse Ovarian Cells. *Food Chem. Toxicol.* 147, 111911. doi:10.1016/j.fct.2020.111911

Mahadevan, S., and Park, Y. (2008). Multifaceted Therapeutic Benefits of Ginkgo Biloba L.: Chemistry, Efficacy, Safety, and Uses. *J. Food Sci.* 73 (1), R14–R19. doi:10.1111/j.1750-3841.2007.00597.x

Mao, D., Li, H., Zhang, L., Xu, J., Yu, C., and Zhang, Q. (2019). Bilobalide Alleviates IL-17-induced Inflammatory Injury in ATDC5 Cells by Downregulation of microRNA-125a. *J. Biochem. Mol. Toxicol.* 33 (12), e22405. doi:10.1002/jbt.22405

Mei, R., Lou, P., You, G., Jiang, T., Yu, X., and Guo, L. (2020). 17β-Estradiol Induces Mitophagy Upregulation to Protect Chondrocytes via the SIRT1-Mediated AMPK/mTOR Signaling Pathway. *Front. Endocrinol.* 11, 615250. doi:10.3389/fendo.2020.615250

Netea-Maier, R. T., Plantinga, T. S., van de Veerdonk, F. L., Smit, J. W., and Netea, M. G. (2016). Modulation of Inflammation by Autophagy: Consequences for Human Disease. *Autophagy* 12 (2), 245–260. doi:10.1080/15548627.2015.1071759

Palacios, S., Soler, E., Ramírez, M., Lilue, M., Khorsandi, D., and Losa, F. (2019). Effect of a Multi-Ingredient Based Food Supplement on Sexual Function in Women with Low Sexual Desire. *BMC Womens Health* 19 (1), 58. doi:10.1186/s12905-019-0755-9

Panahifar, A., Jaremko, J. L., Tessier, A. G., Lambert, R. G., Maksymowych, W. P., Fallone, B. G., et al. (2014). Development and Reliability of a Multi-Modality Scoring System for Evaluation of Disease Progression in Pre-clinical Models of Osteoarthritis: Celecoxib May Possess Disease-Modifying Properties. *Osteoarthritis Cartilage* 22 (10), 1639–1650. doi:10.1016/j.joca.2014.06.013

Pei, W., Huang, X., Ni, B., Zhang, R., Niu, G., and You, H. (2021). Selective STAT3 Inhibitor Alantolactone Ameliorates Osteoarthritis via Regulating Chondrocyte Autophagy and Cartilage Homeostasis. *Front. Pharmacol.* 12, 730312. doi:10.3389/fphar.2021.730312

Pérez-Lozano, M. L., Cesaro, A., Mazor, M., Esteve, E., Berteina-Raboin, S., Best, T. M., et al. (2021). Emerging Natural-Product-Based Treatments for the Management of Osteoarthritis. *Antioxidants (Basel)* 10 (2). doi:10.3390/antiox10020265

Piel, M. J., Kroin, J. S., van Wijnen, A. J., Kc, R., and Im, H. J. (2014). Pain Assessment in Animal Models of Osteoarthritis. *Gene* 537 (2), 184–188. doi:10.1016/j.gene.2013.11.091

Pritzker, K. P., Gay, S., Jimenez, S. A., Ostergaard, K., Pelletier, J. P., Revell, P. A., et al. (2006). Osteoarthritis Cartilage Histopathology: Grading and Staging. *Osteoarthritis Cartilage* 14 (1), 13–29. doi:10.1016/j.joca.2005.07.014

Qin, Y. R., Ma, C. Q., Wang, D. P., Zhang, Q. Q., Liu, M. R., Zhao, H. R., et al. (2021). Bilobalide Alleviates Neuroinflammation and Promotes Autophagy in Alzheimer's Disease by Upregulating lincRNA-P21. *Am. J. Transl Res.* 13 (4), 2021–2040.

Rong, X., Xu, J., Jiang, Y., Li, F., Chen, Y., Dou, Q. P., et al. (2021). Citrus Peel Flavonoid Nobiletin Alleviates Lipopolysaccharide-Induced Inflammation by Activating IL-6/STAT3/FOXO3a-mediated Autophagy. *Food Funct.* 12 (3), 1305–1317. doi:10.1039/d0fo02141e

Sawa-Makarska, J., Baumann, V., Coudevylle, N., von Bülow, S., Nogellova, V., Abert, C., et al. (2020). Reconstitution of Autophagosome Nucleation Defines Atg9 Vesicles as Seeds for Membrane Formation. *Science* 369 (6508). doi:10.1126/science.aaz7714

Sheu, S. Y., Ho, S. R., Sun, J. S., Chen, C. Y., and Ke, C. J. (2015). Arthropod Steroid Hormone (20-Hydroxyecdysone) Suppresses IL-1β-induced Catabolic Gene Expression in Cartilage. *BMC Complement. Altern. Med.* 15, 1. doi:10.1186/s12906-015-0520-z

Sukhikh, S., Noskova, S., Ivanova, S., Ulrikh, E., Izgaryshev, A., and Babich, O. (2021). Chondroprotection and Molecular Mechanism of Action of Phytonutraceuticals on Osteoarthritis. *Molecules* 26 (8), 2391. doi:10.3390/molecules26082391

Tanida, I. (2011). Autophagosome Formation and Molecular Mechanism of Autophagy. *Antioxid. Redox Signal.* 14 (11), 2201–2214. doi:10.1089/ars.2010.3482

Tian, Z., Zhang, X., and Sun, M. (2021). Phytochemicals Mediate Autophagy against Osteoarthritis by Maintaining Cartilage Homeostasis. *Front. Pharmacol.* 12, 795058. doi:10.3389/fphar.2021.795058

Tsai, S. W., Lin, C. C., Lin, S. C., Wang, S. P., and Yang, D. H. (2019). Isorhamnetin Ameliorates Inflammatory Responses and Articular Cartilage Damage in the Rats of Monosodium Iodoacetate-Induced Osteoarthritis. *Immunopharmacol Immunotoxicol* 41 (4), 504–512. doi:10.1080/08923973.2019.1641723

Tu, C., Huang, X., Xiao, Y., Song, M., Ma, Y., Yan, J., et al. (2019). Schisandrin A Inhibits the IL-1β-Induced Inflammation and Cartilage Degradation via Suppression of MAPK and NF-Kb Signal Pathways in Rat Chondrocytes. *Front. Pharmacol.* 10, 41. doi:10.3389/fphar.2019.00041

Vale, S. (1998). Subarachnoid Haemorrhage Associated with Ginkgo Biloba. *Lancet* 352 (9121), 36. doi:10.1016/S0140-6736(05)79516-7

Valenti, M. T., Dalle Carbonare, L., Zipeto, D., and Mottes, M. (2021). Control of the Autophagy Pathway in Osteoarthritis: Key Regulators, Therapeutic Targets and Therapeutic Strategies. *Ijms* 22 (5), 2700. doi:10.3390/ijms22052700

Vinatier, C., Domínguez, E., Guicheux, J., and Caramés, B. (2018). Role of the Inflammation-Autophagy-Senescence Integrative Network in Osteoarthritis. *Front. Physiol.* 9, 706. doi:10.3389/fphys.2018.00706

Wang, C., Yao, Z., Zhang, Y., Yang, Y., Liu, J., Shi, Y., et al. (2020). Metformin Mitigates Cartilage Degradation by Activating AMPK/SIRT1-Mediated Autophagy in a Mouse Osteoarthritis Model. *Front. Pharmacol.* 11, 1114. doi:10.3389/fphar.2020.01114

Wang, F., Liu, J., Chen, X., Zheng, X., Qu, N., Zhang, B., et al. (2019). IL-1β Receptor Antagonist (IL-1Ra) Combined with Autophagy Inducer (TAT-Beclin1) Is an Effective Alternative for Attenuating Extracellular Matrix Degradation in Rat and Human Osteoarthritis Chondrocytes. *Arthritis Res. Ther.* 21 (1), 171. doi:10.1186/s13075-019-1952-5

Wang, T., and He, C. (2018). Pro-inflammatory Cytokines: The Link between Obesity and Osteoarthritis. *Cytokine Growth Factor. Rev.* 44, 38–50. doi:10.1016/j.cytogfr.2018.10.002

Yan, J., Ni, B., Sheng, G., Zhang, Y., Xiao, Y., Ma, Y., et al. (2021). Rhoifolin Ameliorates Osteoarthritis via Regulating Autophagy. *Front. Pharmacol.* 12, 661072. doi:10.3389/fphar.2021.661072

Yang, Z., and Klionsky, D. J. (2010). Mammalian Autophagy: Core Molecular Machinery and Signaling Regulation. *Curr. Opin. Cell Biol* 22 (2), 124–131. doi:10.1016/j.ceb.2009.11.014

Ye, J., Ye, C., Huang, Y., Zhang, N., Zhang, X., and Xiao, M. (2019). Ginkgo Biloba Sarcotesta Polysaccharide Inhibits Inflammatory Responses through Suppressing Both NF-Kb and MAPK Signaling Pathway. *J. Sci. Food Agric.* 99 (5), 2329–2339. doi:10.1002/jsfa.9431

Zhang, H., Cao, N., Yang, Z., Fang, X., Yang, X., Li, H., et al. (2020a). Bilobalide Alleviated Dextran Sulfate Sodium-Induced Experimental Colitis by Inhibiting M1 Macrophage Polarization through the NF-Kb Signaling Pathway. *Front. Pharmacol.* 11, 718. doi:10.3389/fphar.2020.00718

Zhang, M., Kenny, S. J., Ge, L., Xu, K., and Schekman, R. (2015). Translocation of Interleukin-1β into a Vesicle Intermediate in Autophagy-Mediated Secretion. *Elife* 4. doi:10.7554/eLife.11205

Zhang, M., Liu, Y., Huan, Z., Wang, Y., and Xu, J. (2020b). Metformin Protects Chondrocytes against IL-1β Induced Injury by Regulation of the AMPK/NF-κ B Signaling Pathway. *Pharmazie* 75 (12), 632–636. doi:10.1691/ph.2020.0762

Zhao, M., Qin, J., Shen, W., and Wu, A. (2021). Bilobalide Enhances AMPK Activity to Improve Liver Injury and Metabolic Disorders in STZ-Induced Diabetes in Immature Rats via Regulating HMGB1/TLR4/NF-Kb Signaling Pathway. *Biomed. Res. Int.* 2021, 8835408. doi:10.1155/2021/8835408

Zheng, L., Zhang, Z., Sheng, P., and Mobasheri, A. (2021). The Role of Metabolism in Chondrocyte Dysfunction and the Progression of Osteoarthritis. *Ageing Res. Rev.* 66, 101249. doi:10.1016/j.arr.2020.101249

Zheng, Y., Wu, Z., Yi, F., Orange, M., Yao, M., Yang, B., et al. (2018). By Activating Akt/eNOS Bilobalide B Inhibits Autophagy and Promotes Angiogenesis Following Focal Cerebral Ischemia Reperfusion. *Cell Physiol Biochem* 47 (2), 604–616. doi:10.1159/000490016

Zhou, H., Li, G., Wang, Y., Jiang, R., Li, Y., Wang, H., et al. (2021). Microbial Metabolite Sodium Butyrate Attenuates Cartilage Degradation by Restoring Impaired Autophagy and Autophagic Flux in Osteoarthritis Development. *Front. Pharmacol.* 12, 659597. doi:10.3389/fphar.2021.659597

Conflict of Interest: The authors declare that the research was conducted in the absence of any commercial or financial relationships that could be construed as a potential conflict of interest.

Publisher's Note: All claims expressed in this article are solely those of the authors and do not necessarily represent those of their affiliated organizations, or those of the publisher, the editors and the reviewers. Any product that may be evaluated in this article, or claim that may be made by its manufacturer, is not guaranteed or endorsed by the publisher.

Copyright © 2022 Ma, Lv, Yu, Jia, Song, Xu, Li, Sheng, Wang, Zhang and Gao. This is an open-access article distributed under the terms of the Creative Commons Attribution License (CC BY). The use, distribution or reproduction in other forums is permitted, provided the original author(s) and the copyright owner(s) are credited and that the original publication in this journal is cited, in accordance with accepted academic practice. No use, distribution or reproduction is permitted which does not comply with these terms.

frontiers in Pharmacology

ORIGINAL RESEARCH
published: 24 February 2022
doi: 10.3389/fphar.2021.730579

Notoginsenoside R1 (NG-R1) Promoted Lymphatic Drainage Function to Ameliorating Rheumatoid Arthritis in TNF-Tg Mice by Suppressing NF-κB Signaling Pathway

Danli Jiao[1,2,3,4†], *Yang Liu*[1,3,4†], *Tong Hou*[1,3,4], *Hao Xu*[1,3,4], *Xiaoyun Wang*[1,3,4,5], *Qi Shi*[1,3,4], *Yongjun Wang*[1,3,4,5], *Qiujuan Xing*[2*] *and Qianqian Liang*[1,3,4*]

[1]*Longhua Hospital, Shanghai University of Traditional Chinese Medicine, Shanghai, China,* [2]*Shanghai Changning Tianshan Traditional Chinese Medicine Hospital, Shanghai, China,* [3]*Spine Institute, Shanghai University of Traditional Chinese Medicine, Shanghai, China,* [4]*Key Laboratory of Theory and Therapy of Muscles and Bones, Ministry of Education (Shanghai University of Traditional Chinese Medicine), Shanghai, China,* [5]*Shanghai Research Institute of Acupuncture and Meridian, Shanghai University of Traditional Chinese Medicine, Shanghai, China*

Rheumatoid arthritis (RA) is a chronic autoimmune disease that is primarily characterized by synovial inflammation. Our previous studies demonstrated that the lymphatic system is critical for the development and maintenance of RA disease, and sufficient lymph drainage helps to improve joint inflammation. In this study, we found that NG-R1, the main active component in the traditional Chinese medicinal herb Sanchi, activating lymphatic function can attenuate synovial inflammation. According to histopathological staining of ankle sections, NG-R1 significantly decreased the area of inflammation and reduced bone destruction of ankle joints in TNF-Tg mice. Near infrared-indocyanine green (NIR-ICG) lymphatic imaging system has shown that NG-R1 significantly improved the lymphatic drainage function. However, the molecular mechanism of its activity is not properly understood. Our in-depth study demonstrates that NG-R1 reduced the inflammatory cytokine production of lymphatic endothelial cells (LECs) stimulated by TNF-α, and the mechanism ameliorated the phosphorylation of IKKα/β and p65, and the translocation of p65 into the nucleus. In summary, this study proved that NG-R1 promoted lymphatic drainage function to ameliorating rheumatoid arthritis in TNF-Tg mice by suppressing NF-κB signaling pathway.

Keywords: notoginsenoside R1, rheumatoid arthritis, lymphatic drainage function, NF-κB signaling pathway, inflammation, TNF-Tg mice

OPEN ACCESS

Edited by:
Zhaocheng Ma,
Huazhong Agricultural University, China

Reviewed by:
Yaozu Xiang,
Tongji University, China
Xihai Li,
Fujian University of Traditional Chinese Medicine, China
Hongting Jin,
Zhejiang Chinese Medical University, China

***Correspondence:**
Qiujuan Xing
xqjcyzw0808@163.com
Qianqian Liang
liangqianqiantcm@126.com

†These authors have contributed equally to this work and share first authorship

Specialty section:
This article was submitted to Inflammation Pharmacology, a section of the journal Frontiers in Pharmacology

Received: *28 July 2021*
Accepted: *15 December 2021*
Published: *24 February 2022*

Citation:
Jiao D, Liu Y, Hou T, Xu H, Wang X, Shi Q, Wang Y, Xing Q and Liang Q (2022) Notoginsenoside R1 (NG-R1) Promoted Lymphatic Drainage Function to Ameliorating Rheumatoid Arthritis in TNF-Tg Mice by Suppressing NF-κB Signaling Pathway. Front. Pharmacol. 12:730579. doi: 10.3389/fphar.2021.730579

INTRODUCTION

Rheumatoid arthritis is a chronic systemic disease with autoimmune pathogenesis and systemic involvement, which is associated with the overexpression profile of many proinflammatory cytokines (Petrovska et al., 2021, 102797; Hosseinikhah et al., 2021). This autoimmune disorder affects nearly 1% of the total adult population and remains a cause of high rates of morbidity and mortality in humans (Zhao and Zhang, 2018, 123). NF-κB activation contributes to the inflammatory pathogenesis of RA, resulting in synovium hyperplasia and cartilage and bone erosion (Wang

et al., 2016; Zhang et al., 2018; Yang et al., 2019; Acimovic et al., 2018). Thus, the potential treatment of RA by blocking NF-κB activation interactions can be highlighted. Current RA therapies mainly target immune inflammation and the efficacy is subject to ceiling effects (Pratt et al., 2021, e337–e346).

The lymphatic system plays a key role in the pathogenesis and treatment of inflammatory and invasive arthritis, and it has been proved that improving lymphatic drainage function effectively reduced RA joint inflammation (Bouta et al., 2018, 94–106; Hou et al., 2020, 526–534; Liu et al., 2021, 541–553). The lymphatic system is involved in the pathologic development of rheumatoid arthritis by redistributing cytokines, chemical factors, and other inflammation-related factors around the inflamed joint into the lymphatic vessels, thereby reducing the inflammatory factors in the joint cavity aggravated by accumulated joint lesions (Liang et al., 2015a, 648–55). Specifically, long-term chronic inflammation will stimulate lymphatic endothelial cells (LECs) to release proinflammatory cytokines, which will accelerate the apoptosis of lymphatic smooth muscle cells (LSMCs) and inhibit their proliferation (Telinius and Hjortdal, 2019, 1777–1784, Liang et al., 2021, 58). This persistent inflammation leads to structural and functional of lymphatics abnormalities, lymphatic drainage dysfunction, and further aggravates the inflammation of the joints (Deng et al., 2021, 2174; Liang et al., 2020, e12876). Most importantly, targeting lymphatics represents an innovative strategy for therapeutic intervention in RA.

Panax notoginsen (Burk) F. H. Chen (Sanqi in Chinese) is a traditional Chinese medical drug which has the effect of promoting blood circulation and removing blood stasis (Wang et al., 2016, 234–58). Notoginsenoside R1 (NG-R1) is one of the major bioactive ingredients of Panax notoginsen. Modern pharmacological studies have indicated that NG-R1 possesses anti-tumor, anti-aging, antioxidative, and anti-inflammation effects (Sun et al., 2013, 1758–70, Yu et al., 2016, 21730; Liu et al., 2020, 551–565). However, it is not clear whether NG-R1 can alleviate arthritis inflammation in RA and whether it has beneficial effects on lymphatic function. We in a preliminary experiment found that NG-R1 had anti-inflammatory and anti-rheumatic effects. Therefore, we conducted *in vivo* and *in vitro* experiments to verify that NG-R1 reduces articular inflammatory injury and alleviates RA progression by promoting lymphatic drainage function.

MATERIALS AND METHODS

Animals

Three-month-old female TNF-Tg (TNF-Tg line 3,647) mice were provided by the Shanghai Southern Model Animal Laboratory Center (Shanghai, China). The TNF-Tg mice were bred as heterozygotes on a C57BL/6 background, and their wild-type (WT) littermates were used as normal controls. Mice were housed in a temperature (25°C) and humidity (45–55%)-controlled environment and provided libitum access to maintenance diet and water. All animal procedures were performed according to the Guiding Principles for the Care and Use of Laboratory Animals approved by the Animal Regulations of the National Science and Technology Committee of China under the approval of the Longhua Hospital Animal Ethics Committee (Shanghai, China).

Drug Intervention

TNF-Tg mice were randomly divided into two groups: TNF-Tg group and NG-R1 group (10 mice/group). A batch of littermates of wild type (WT) mice were used as the WT group (10 mice/group). The TNF-Tg group and WT group were treated with the same volume of 0.5% CMC-Na (0.5 g CMC-Na + 99.5 ml aqueous solution + 500 μl tween). NG-R1 group mice were treated with 20 mg/kg NG-R1 (2 mg NG-R1 + 1 ml 0.5% CMC-Na) by daily intraperitoneal injection and continuously for 8 weeks.

Arthritis Symptoms Assessment

We conducted the measurements of arthritis index, ankle circumference, and weight. Arthritis disease malformation grade assessment: arthritis grade 0, normal (no swelling or malformation); grade 1, mild, but marked redness of the ankle joint or wrist swelling, or significant redness and swelling or malformation limited to individual figures, regardless of the number of affected numbers; grade 2, moderate redness and swelling or malformation of the ankle or wrist; grade 3, severe redness and swelling or malformation of the entire paw, including number; grade 4, the limbs are most inflamed and multiple joints. Body weight: an electronic body weight scale will measure weight once a week. Ankle circumference: the degree of ankle joint swelling was measured with a vernier caliper. The counts and grades recorded by two independent blinded examiners once a week.

Near-Infrared Indocyanine Green Lymphatic Imaging

Mice were anesthetised with isoflurane and treated with local depilation, then ICG (0.1 μg/ml, dissolved in distilled water and stored at 4°C in the dark) was injected into footpads. After the ICG signal was stable, the fluorescence signal was observed for 600 s continuously, and the pulse number was obtained according to the fluctuation times of the signal intensity of lymphatic vessels. The ImageJ software (National Institutes of Health, Bethesda, Maryland) was used to determine the region of interest (ROI) during the lymph flow in the leg of mice, and the fluorescence signal intensity within the ROI was recorded at 1 and 24 h. Lymphatic clearance was calculated according to the following formula: clearance = ((ROI1h−ROI1hbg)-(ROI24h−ROI24hbg))/(ROI1 h − ROI1 hbg)*100% (bg = background).

Histologic and Histomorphometric Analyses

After ending treatments, the mice were sacrificed, and the ankle joints were excised to prepare paraffin sections. Four-micrometer consecutive tissue sections were cut from each arrayed paraffin block and prepared on pathological slides. The slices were stained by alcian blue/orange G (ABOG) or tartrate-resistant acid

phosphatase (TRAP) for histologic analysis. The inflamation area, cartilage area, osteoclast number at ankle joints, and astragalus bone area of the ankle joint of mice in 3 groups were statistically analyzed. Slides were scanned using the Olympus VS120-S5-E whole-slide imaging system (Olympus, Japan). All images were analyzed using the Olympus OlyVIA software (Olympus, Japan).

Immunofluorescence and Immunohistochemistry

The number of lymphatic vessels was counted by immunofluorescence staining. The tissue sections were added with trypsin and repaired in 37°C incubators for 15 min, blocked by 4% Bovine Serum Albumin (BSA) for another 1 h. Primary FITCα-SMA antibody (Sigma, F3777) and hamster monoclonal antimouse podoplanin antibody (Abcam, cat. #ab11936) incubate overnight at 4°C. The second Goat anti-hamster podoplanin (1:400, diluted by 0.4%BSA/PBS reagent) was incubated for another 1 h and immunofluorescence staining slides were scanned using an Olympus VS-120 whole-slide imaging system.

Whole-mount staining of the back skin of the foot was stained to analyze the percentage of smooth muscle cell (SMC) coverage. The skin of the back of the foot was obtained when mice were sacrificed. We removed fat and other connective tissue, and then soaked the kin in 10% formalin at 4°C overnight and then permeated with 0.5% Triton X. After blocking with 4% Bovine Serum Albumin (BSA) for another 1 h, the skin tissues were incubated with 1: 1,000 dilution of Podoplanin antibody (Abcam, cat. #ab11936) and 1:400 dilution of fluorescein isothiocyanate labeled anti-SMA antibody at 4°C overnight. The images were recorded by Olympus VS-120 software. The whole operation should avoid light. The calculation formula is as follows: SMC coverage percentage = (SMC coverage area/whole lymphatic vessel area) × 100%.

Micro-Computed Tomography

The tight ankle joints were obtained when mice were sacrificed and then fixed in 10% formalin for 48 h, washed in phosphate-buffered saline (PBS) for 2 h, and then soaked in 75% ethanol, scanned by micro-CT system (Scanco VIVA CT80, SCANCO Medical AG, Switzerland). The X-ray tube voltage was 55 kV and tube current 72 μA, with a voxel size of 10 μm. The cross-section images were realigned in 3D using the SCANCO proprietary software to observe the morphology of astragalus.

Serum Biochemical Parameters Determination

Peripheral blood samples were collected from mice when they were sacrificed. Blood samples (1 ml each) were collected from mouse eyeballs and then centrifuged to extract the upper serum. The serum level of Inflammatory cytokines TNF-α (NeoBioScience, China. cat.# EMC102a) and IL-6 (NeoBioScience, China. cat. #EMC004) were detected in strict accordance with the instructions of the kit.

Cell Culture

Mouse Primary Lymphatic Endothelial Cells/C57-6092 (Catalog Number: C57-6092) were cultured in α-MEM (Hyclone, Logan, UT, United States) supplemented with 100 IU/ml of penicillin/streptomycin (Sigma-Aldrich, United States) and 10% heat-inactivated fetal bovine serum (Gibco, United States) and maintained at 37°C in a humidified atmosphere with 5% CO_2.

Cytotoxicity Assay

Cytotoxicity assay was measured by Cell Counting Kit-8 (Dojindo. Japan. cat. #CK04) assay according to the manufacturer's instructions. LECs were adjusted at a density of 1×10^4 cells/ml seeded in a 96-well plate, then exposed at various concentrations of NG-R1 for 24 h. A total of 10 μl CCK-8 solution was added into each well for another 1 h at 37°C. The resulting optical density was detected at 450 nm by a microplate reader (Biotek).

Co-Culture of LECs and LSMCs

Co-culture was performed with Transwell (0.4 μm pore size, Corning). LECs were seeded on chambers in 6-well plates for 24 h, and then pretreated with NG-R1 (5, 10, and 50 μM) for 2 h, stimulated and then pretreated with NG-R1 (5, 10, 50 μM) for 2 h and stimulated with TNF-α, culture chambers with LECs were then transferred into another 6-well plate, which had already been coated with LSMCs for 2 days. After 24 h of co-culture, LSMCs were harvested for analysis of the expression level of functional muscle genes h1-calponin, smα22, SM myosin heavy chain, and smα2 mRNA.

Real-Time Polymerase Chain Reaction

Total RNA was extracted using Trizol (Thermo.United States. cat. #15596018) reagent according to the manufacturer's instructions and the cDNA obtained by using the PrimeScript TM RT kit (Taraka. Japan. cat. #RR037A) according to the manufacturer's protocol. Real-time PCR analysis was performed using Hieff TM qPCR SYBR Green Master Mix (Taraka. Japan. cat. #1 1201ES08) reagents on q-PCR CFX96 machine (Bio-rad). The primers for qRT-PCR were shown in **Table 1**.

Western Blot

The protein was collected, and 30 μg of protein from each sample was separated by 15% SDSPAGE and transferred to polyvinylidene flfluoride membrane and then separated by sodium dodecyl sulfate polyacrylamide gel electrophoresis (SDSPAGE) and transferred to a Polyvinylidene flfluoride (PVDF) membrane. After blocking with 5% bovine serum albumin in TBST at room temperature for 2 h, the membranes were incubated with the Phospho-IKKα (Ser176)/IKKβ (Ser177) Antibody (cat. # 2688), Phospho-NF-κB p65 (Ser536) (93H1) Rabbit mAb (cat. #3033) overnight at 4°C. After washing with TBST for three times, the membranes were incubated with the corresponding horseradish peroxidase-labeled secondary antibodies (cat. #7074). Proteins were scanned using the ECL detection system. All the antibodies were purchased from Cell SignalingTechnology (Beverly, NJ, United States).

TABLE 1 | Sequence of primers used in the real time polymerase chain reaction.

Genes	Sequence of primers	Gen bank accession number	Annealing (°C)	Product size (bp)
h1-calponin	F: 5′ TGGCCCAGA AATACGACCAC3′ R: 5′ CCGGCTGGAGCTTGTTGATA3′	NM 031747.1	60	144
SM α22-actin	F: 5′ TCTCCTTCCAGCCCACAAAC3′ R: 5′ TTCACGGCTCATGCCATAGG3′	NM_031549.2	60	82
Smooth muscle myoxln, heavy chain 11	F: 5′ TCCGGTGTTCTCCTGCTAGT 3′ R: 5′ GGGCCATTGGGCTGTTTATG 3′	NM_001170600.1	60	134
SM α2-action	F: 5′ TATTCTGTCTGGATCGGCGG 3′ R: 5′ ACATTCACAGTTGTGTGCTAGAG 3′	NM_031004.2	60	196
TNF- α	F: 5′ AGTGACAAGCCTGTA GCCC 3′ R: 5′ GAGGTTGACTTTCTCCTGGTAT 3′	NM_013693.3	57	252
IL-1β	F: 5′ CTGCTACATCA GCACCTCAC 3′ R: 5′ AGAAACAGTCCA GGCCATAC 3′	NM_008361.4	55	124
IL-6	F: 5′ TGTATGAACAACGATGATGCACTT 3′ R: 5′ ACTCTGGCTTTG TCTTTCTTGTTATCT3′	NM_001314054.1	60	197
iNOS	F: 5′ AACGGA GAAC GTTGGATTTG 3′ R: 5′CAGCACAAGGGGTTTTCTTC3′	NM_010927.3	54	151
β-Actin	F: 5′ TTGCTGACA GGATGCA GAAGGAGA 3′ R: 5′ ACTCCTGCTTGCTGATCCACATCT 3′	NM_031144.3	60	159

Statistical Analysis

Statistical analysis was performed by Graphpad Prism (Version 8.0). Data are presented as means ± standard error of mean (SEM). One-way ANOVA followed by Dunnett's t-test was used to determine differences between groups. As to 3 groups with different time points, we applied two-way ANOVA (or nonparametric) comparison. $p < 0.05$ were considered statistically significant.

RESULTS

NG-R1 Alleviates the Symptoms of Articular Inflammation in TNF-Tg Mice

To establish whether NG-R1 reduced inflammation, we used TNF-Tg mice model and treated with NG-R1 for 8 weeks (**Figure 1**). As for arthritis symptoms assessment, we found that NG-R1 treatment group did significantly attenuate the degree of joint malformation and ankle circumference in TNF-Tg mice compared to the model group (**Figures 1B,C**). Body weight is an important index to reflect body development, and showed that NG-R1 treatment group did effectively improved the trend of weight loss in TNF-Tg mice (**Figure 1D**). To further confirm the anti-inflammatory effect of NG-R1 in TNF-Tg mice, we tested the expression of serum inflammatory factors in mice by ELISA Kit and found that NG-R1 could effectively inhibit the expression of serum inflammatory factors IL-6 and TNF-α (**Figures 1E,F**). These results indicated that NG-R1 alleviates the symptoms of articular inflammation in TNF-Tg mice.

NG-R1 Attenuated the Synovial Inflammation, Hyperplasia, and the Cartilage and Bone Destruction of the Joint

A histopathological evaluation of the ankle joints was performed to examine the degrees of inflammatory damage. Histological examination and histomorphometric analysis showed that ankle joints from the model group had severe synovial inflammatory hyperplasia, cartilage loss, bone destruction, and greater osteoclasts numbers around the astragalus. ABOG staining analysis showed that NG-R1 treatment group had conspicuous reduced synovial inflammation, bone erosion, and cartilage destruction (**Figures 2A–C,E**). TRAP staining found that the NG-R1 treatment group had fewer osteoclasts around the astragalus in the ankle joints than the model group (**Figures 2A,D**). Three-dimensional micro-CT results indicated that the ankle joints in the model group was obviously eroded, while the NG-R1 treatment group remained intact (**Figure 2A**). These results indicated that NG-R1 effectively attenuated the inflammatory symptoms of ankle joints and inhibited the development of rheumatoid arthritis in TNF-Tg Mice.

NG-R1 Promotes Lymphatic Drainage Function in TNF-Tg Mice

Our previous studies demonstrated that sufficient lymph drainage helps to improve joint inflammation (Liang et al., 2015). We next sought to investigate if NG-R1 attenuated inflammation in TNF-Tg mice was somehow due to promoted lymphatic drainage function. The lymphatic vessel function was related to the contraction frequency of lymphatic vessels and lymphatic pulse frequency. At 24 h after mice were injected with ICG in the left footpad, we found that the fluorescence intensities of TNF-Tg mice were higher, and this prompted us that TNF-Tg mice display impaired lymphatic function. However, after NG-R1 treatment the mice showed more rapid clearance of ICG, and this results indicates an enhanced lymphatic clearance function (**Figures 3A,B**). Lymphatic pulse frequency is proven to be another important indicator of lymphatic drainage function. The lymphatic pulse frequency of TNF-Tg mice was about 0.7 beats per minute, and then after NG-R1 treatment, the frequency was able to reach 1.0 beats per minute (**Figures 3C,D**). These data

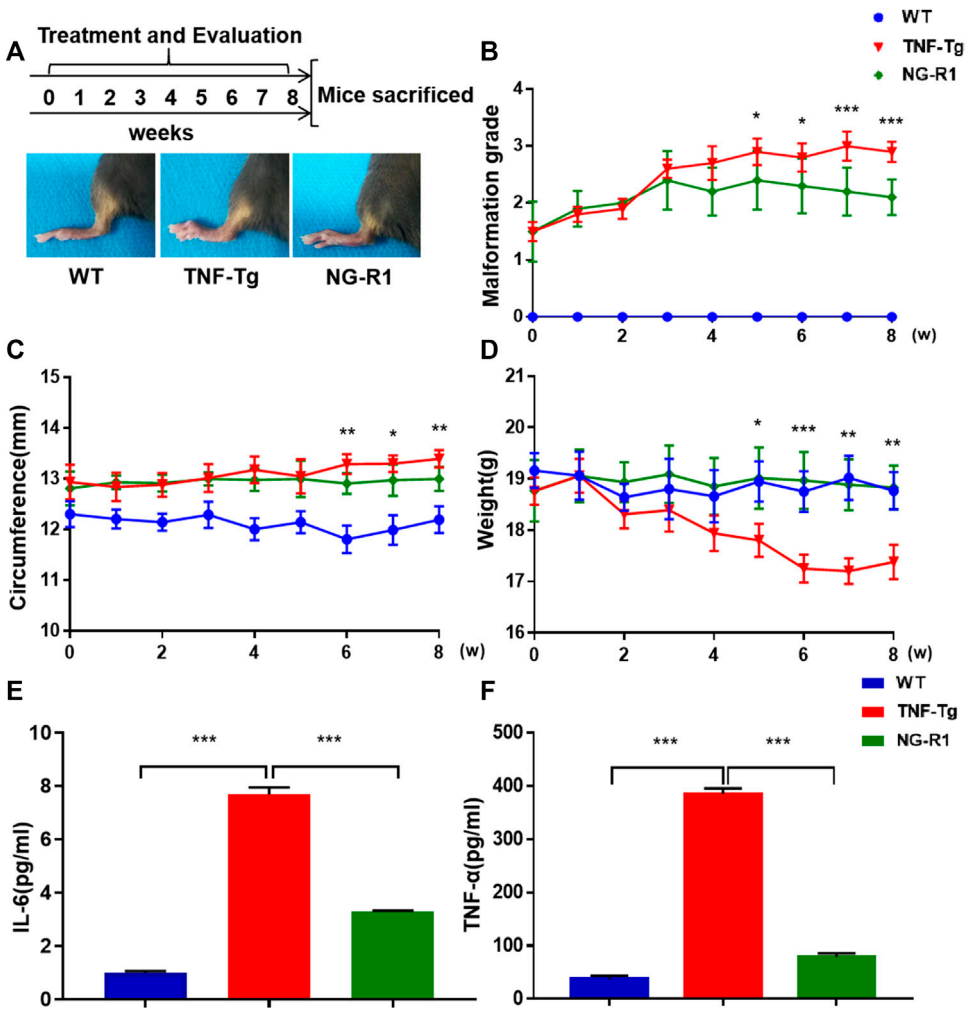


FIGURE 1 | TNF-Tg mice exhibited ameliorated inflammation after 8 weeks of NG-R1 treatment. **(A)** Schematic flow of mice treatment strategy and experimental procedure. The representative pictures of the paws of mice after treatment. **(B–D)** The arthritis malformation grades,circumference and weight in TNF-Tg mice were evaluated weekly. **(E,F)** ELISA Kit was performed on serum for IL-6 and TNF-α. Data represent mean ± SEM, (n = 10 per group). $^{*}p < 0.05$, $^{**}p < 0.01$, $^{***}p < 0.001$, two-way ANOVA.

suggested that NG-R1 promotes lymphatic drainage function in TNF-Tg mice.

NG-R1 Improves Lymphatic Vessels Structure Recovery

To prove whether the mechanism of NG-R1 improving lymphatic function is related to promoting lymphatic structural recovery and increasing the number of lymphatic vessels, we performed Whole Mount staining and immunofluorescence staining. Whole Mount staining revealed that the structure of the lymphatic vessel was significant destruction and the area covered by lymphatic smooth muscle was reduced in the model group (**Figure 4A**). The area covered by lymphatic smooth muscle was increased in the NG-R1 treatment group compared with the TNF-Tg mice group (**Figure 4B**). In addition, we conducted podoplanin/α-SMA immunofluorescence staining to examine the numbers of the lymphatic vessel. Immunofluorescence staining is visible in yellow indicating the collecting lymphatic vessels (**Figure 4C**). We performed statistical experiments on the number of collecting lymphatic vessels. However, NG-R1 did not affect the lymphatic vessel numbers in TNF-Tg mice (**Figure 4D**). These data indicate that NG-R1 improves lymphatic vessel structure recovery but not increase the number of lymphatic vessels.

To further verify the effect of NG-R1 on lymphatic smooth muscle cell function, we simulated the lymphatic structure and established a coculture system. LECs with or without NG-R1 pretreatment were stimulated with TNF-α and then co-cultured with LSMCs via transwell for 24 h. The results demonstrated that paracrine factors from the TNF-α stimulated LECs reduced the

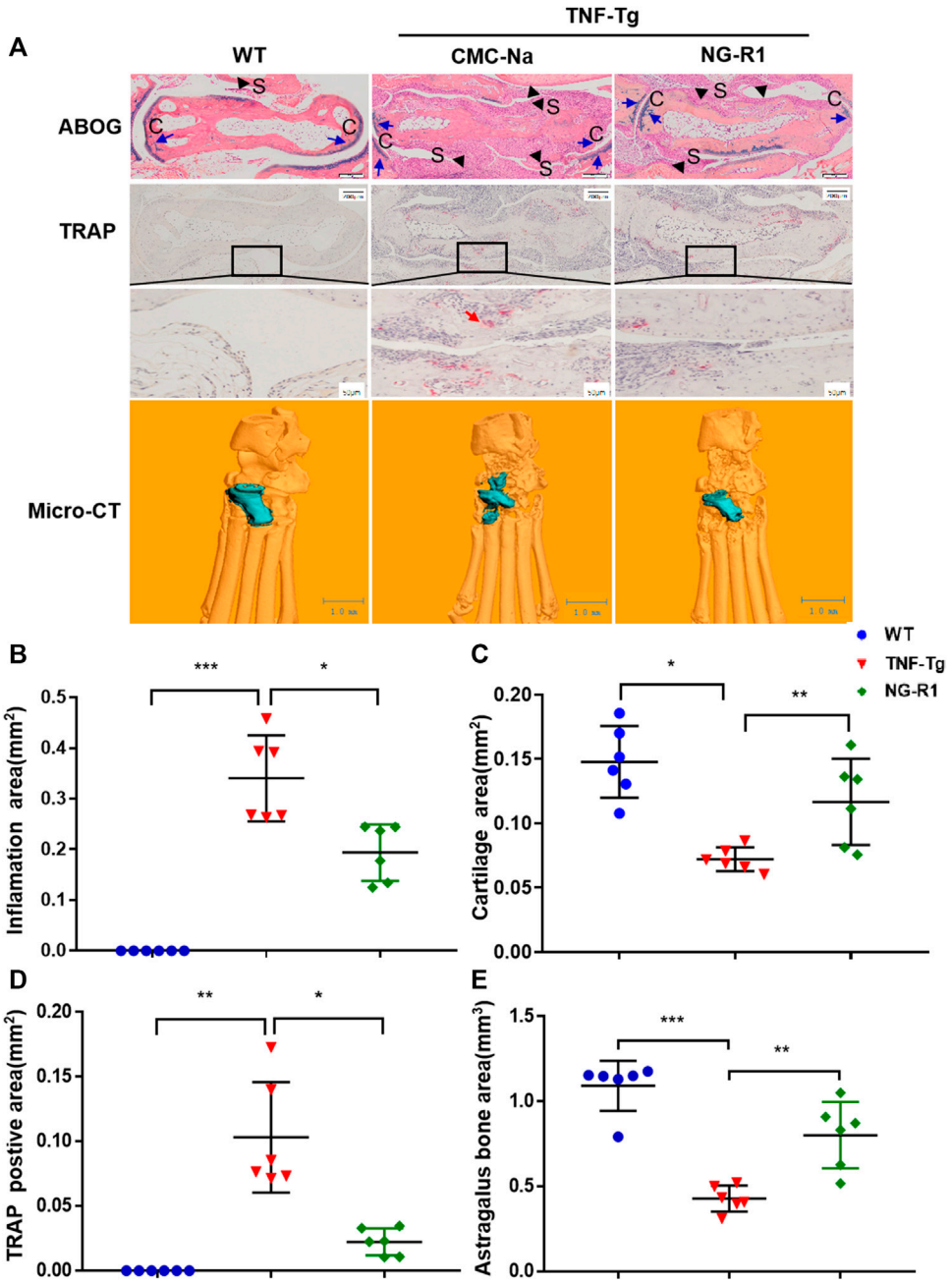


FIGURE 2 | NG-R1 protects TNF-Tg mice from synovial inflammation and inflammatory bone loss. **(A)** Representative images stained for ABOG and TRAP at ankle joint sections. Black arrows indicate synovial tissue (S). Blue arrows indicate cartilage (C). Red arrows indicate the TRAP-positive mature osteoclasts. Longitudinal sections of 3-dimensional reconstructed ankle joints by micro-CT. ABOG staining: Magnification, ×80; scale bars per column, 200 μm. TRAP staining: Magnification, ×80; scale bars per column, 200 μm. Locally large graph: Magnification, ×200; scale bars per column, 50 μm. **(B–E)** Quantification of inflamation area, cartilage area, trap postive area, and astragalus bone area. Data represent mean ± SEM (n = 6 per group). *p < 0.05, **p < 0.01, ***p < 0.001, one-way ANOVA.

expression levels of muscle-related genes, including h1-calponin, smα22, smooth muscle myosin heavy chain, and smα2 in the LSMCs, which is prevented by NG-R1 (**Figures 5A–D**). NG-R1 increased the expression of the lymphatic smooth muscle cell function marker gene and promoted the recovery of the lymphatic vessel structure.

NG-R1 Reduces the Production of Pro-Inflammatory Cytokines by TNF-α Treated LECs

We investigated the CCK-8 kit to assess the potential cytotoxicity of NG-R1, and we found that NG-R1 did not affect cell viability on LECs after incubation 24 h even at a concentration of 100 μM

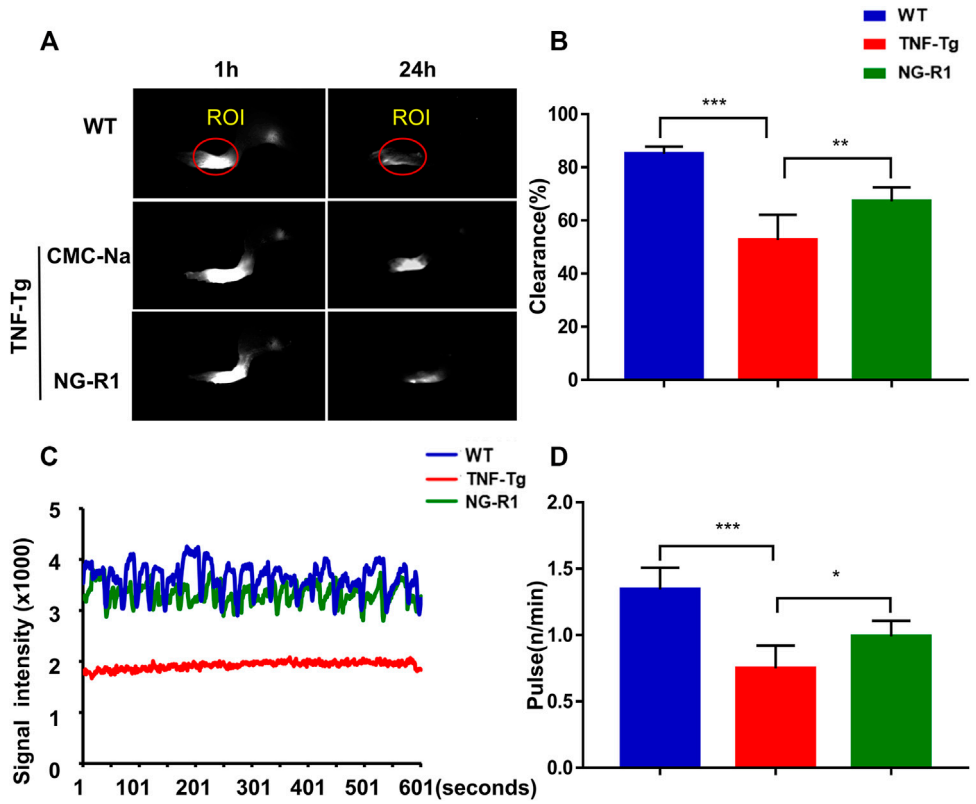


FIGURE 3 | NG-R1 improved the lymphatic drainage function by increasing the pulse and clearance rate of TNF-Tg mice lymphatic vessels. Lymphatic vessels of the left footpad were examined using near-infrared ICG imaging immediately and at 1 and 24 h post-ICG administration. The ICG fluorescence signal intensity at the footpads (outlined by the red circles) was recorded and used the software ImageJ analyzes the marked area and obtains within 600 s fluctuates. **(A,B)** A representative ICG signal of footpads and the percentage of ICG clearance. **(C,D)** Detection and analysis of lower limb lymphatic contraction pulse in TNF-Tg mice. Data represent mean ± SEM (n = 6 per group). $^{*}p < 0.05$, $^{**}p < 0.01$, $^{***}p < 0.001$, one-way ANOVA.

(**Figure 6A**). Therefore, we decided to set the highest concentration of NG-R1 at 100 μM for the following experiments. LECs were pretreated with NG-R1 (5, 10, and 50 μM) for 2 h, then stimulated with TNF-α (20 ng/ml) for another 12 h. It has been shown that TNF-α significantly increased crucial pro-inflammatory cytokines TNF-α, IL-1β, IL-6, and iNOS mRNA expression levels. We found that NG-R1 dose-dependently decreased the mRNA expression of TNF-α, IL-1β, IL-6, and iNOS induced by TNF-α activated LECs (**Figures 6B–E**).

NG-R1 Suppressed the Phosphorylation of p65 and p65 Nuclear Accumulation in TNF-α-Induced LECs

It has been demonstrated that the NF-κB signaling pathway is a crucial inflammatory pathway involved in the development of rheumatoid arthritis. Thus, we examined whether NG-R1 regulates the activation of NF-κB signaling in LECs cells stimulated with TNF-α. We found that the phosphorylation of IKKα/β and p65 was markedly increased after being stimulated with TNF-α (20 ng/ml) for 15 min and 30 min. The phosphorylation of p65 was significantly inhibited in TNF-α-induced cells by treatment of NG-R1 (50 μM). However, it did not affect the phosphorylation of IKKα/β (**Figures 7A–C**). In addition, an immunofluorescence assay revealed that NG-R1 significantly reduced the level of p65 in the nucleus of LECs induced TNF-α-stimulated (**Figures 7D–E**). Thus, NG-R1 inhibited TNF-α-induced activation of the NF-κB signaling pathway.

DISCUSSION

NG-R1 exhibits a pharmacological activity against excessive inflammation, but its mechanism of action has not been studied in RA. Here, our study is the first time to investigate the anti-inflammatory effect of NG-R1 in RA as well as elucidate its possible mechanism by which NG-R1 alleviates RA symptoms. Our current study demonstrated NG-R1 as a potential effective therapeutic medicine for the treatment of RA. We found that NG-R1 effectively improved inflammatory symptoms in the ankle joint of TNF-Tg mice by promoting the lymphatic drainage function while suppressing NF-κB signaling pathway-mediated production of proinflammatory effectors in LECs.

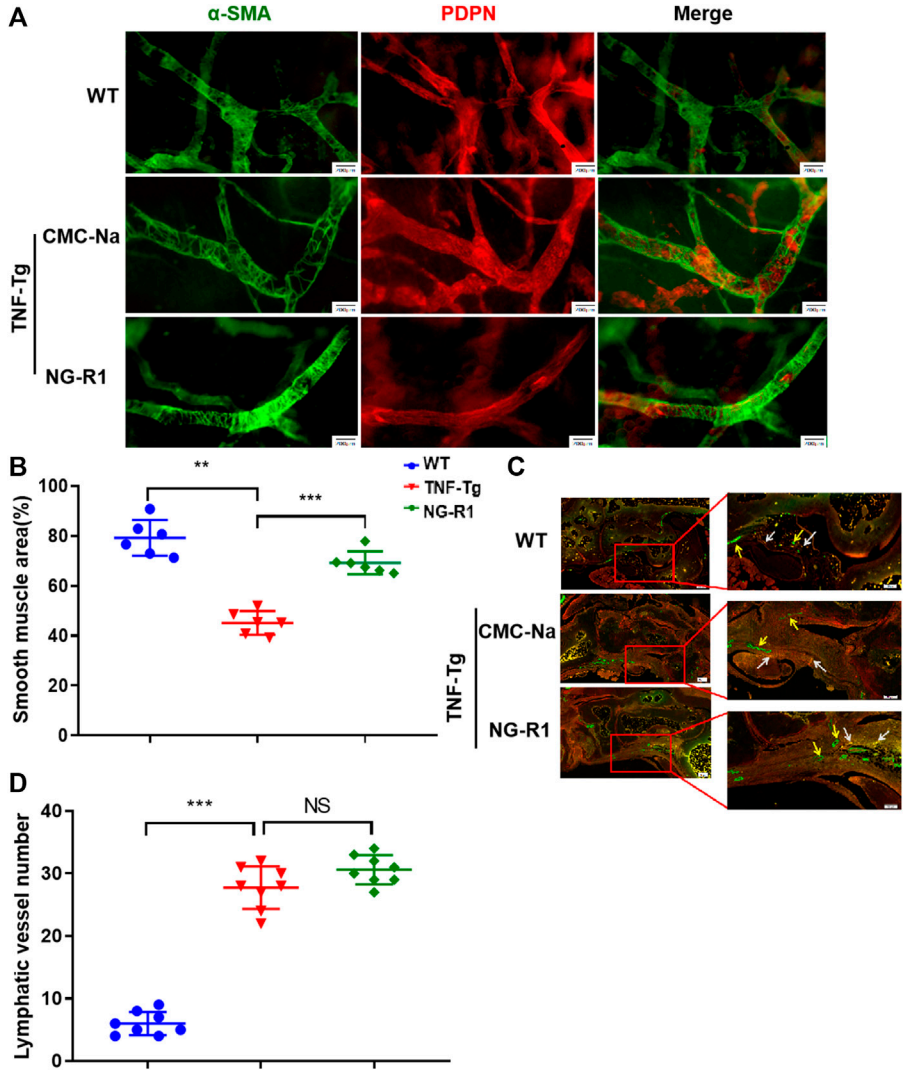


FIGURE 4 | NG-R1 improves lymphatic vessels structure recovery. **(A)** Whole Mount Immunofluorescence Staining of Lymphatic capillaries. α-SMA (green)and PDPN (red). Bar, 200 μm. **(B)** Proportion of lymphatic smooth muscle region were counted ($n = 6$ per group). **(C)** Immunofluorescence Staining showed that yellow arrow was indicated blood vessels (Podoplanin−/α-SMA+), white arrow indicates collecting lymphatic vessels (Podoplanin+/SMA+). **(D)** The number of lymphatic vessels was statistically analyzed ($n = 8$ per group). Immunofluorescence staining: Magnification, ×80; scale bars per column, 200 μm. Locally largegraph: Magnification, ×80; 100; scale bars per column, 100 μm. Data represents mean ± SEM, NS > 0.05, $^{*}p < 0.05$, $^{**}p < 0.01$, $^{***}p < 0.001$, One-way ANOVA.

Notoginsenoside (NG-R1) is a novel triterpene saponin compound, one of the main bioactive ingredients from Panax notoginseng (PN) root, which is commonly used to treat cardiovascular diseases (Zhu et al., 2020), neurodegenerative disease (Liu et al., 2020), diabetic nephropathy (Zhang et al., 2019), and cancer (Li et al.,2020). NG-R1 improved the imbalance between iNOS and eNOS and blockaded activation of NF-κB and the subsequent myocardial inflammatory and apoptotic responses in endotoxemic mice (Sun et al., 2013). NG-R1 relived LPS-elicited inflammatory damages via blocking NF-κB in a miR-301a-silenced manner (Dong et al., 2020). NG-R1 protected neuron cells from inflammatory damage by decreasing pro-inflammatory cytok IL-2, IL-6, and TNF-α expression, and inactivating the JNK pathway (Sun et al., 2019). Inflammation plays a key role in its pathogenesis, and they can aggravate persistent pain, structural change within the joint, bone destruction, and disability. TNF-Tg mice as a mature model of RA with TNF-α overexpression, which spontaneously develop mild ankle joint inflammation and bone erosion (Wang et al., 2020). Therefore, we chose 3-month-old TNF-Tg mice and WT littermates, and our current study proved that NG-R1 significantly attenuated the degree of joint malformation and ankle swelling in TNF-Tg mice, and improved the gradual emaciation of mice. The pathological changes of rheumatoid arthritis usually include synovial hyperplasia (Nygaard and Firestein et al., 2020),

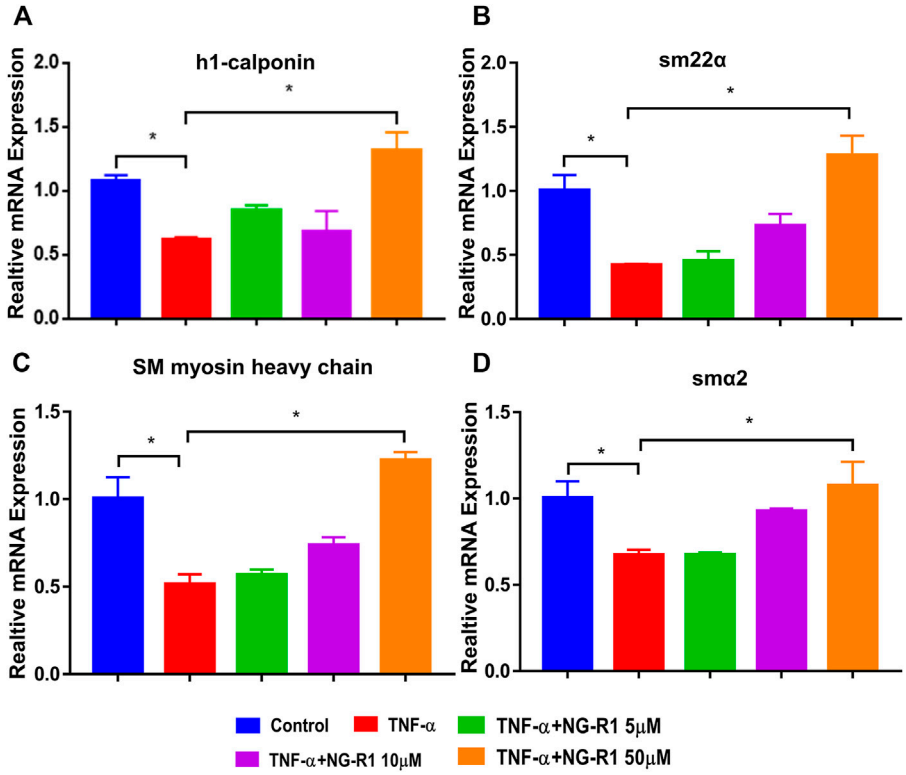


FIGURE 5 | NG-R1 improved the function of lymphatic smooth muscle cells (LSMCs) in the inflammatory state induced by TNF-α. **(A–D)** The coculture model of LECs and LSMCs was used to detect the effect of NG-R1 (5, 10, and 50 μM) on the expression level of functional muscle genes h1-calponin, smα22, SM myosin heavy chain, smα2 mRNA of LSMCs in inflammatory environment induced by TNF-α (20 ng/ml). Data represents mean ± SEM. The experiment was repeated at least three times. *$p < 0.05$, One-way ANOVA.

pannus formation (Huh et al., 2015), degeneration of cartilage, and bone destruction (Hardy et al., 2018). histopathological evaluation of the ankle joints and three-dimensional micro-CT further confirmed that synovial hyperplasia, cartilage loss, and bone destruction were effectively relieved after the treatment of NG-R1. Evidence suggests that cytokines such as IL-1, IL-6, and TNF-α contribute to the induction and maintenance of inflammation during the pathological process of RA (Noack and Miossec et al., 2017). Meanwhile, our study confirmed that NG-R1 inhibited the expression of inflammatory factors IL-6 and TNF-α in serum and reduced the inflammatory response *in vivo*.

The lymphatic system plays an integral role in the development and progression of a range of disease conditions (Abdallah et al., 2020), which maintains extracellular fluid homeostasis as favorable, promotes metabolism, regulates immunity, and this also proves that it is possible to study the pathology and mechanism of the disease from the perspective of the lymphatic system (Breslin et al., 2018). We have shown previously that TNF-Tg mice with severe arthritis typically have reduced or loss of lymphatic vessel contractions and decreased lymphatic flow from inflamed joints, but the mechanisms involved are unknown. Our previous studies showed that sufficient lymph drainage helps to improve joint inflammation, and drugs activating lymphatic function can attenuate synovial inflammation (Guo et al., 2009). In this study, we showed NG-R1 promoted lymphatic drainage function in TNF-Tg mice by accelerating lymphatic pulse frequency and lymphatic clearance. Next, we investigated the effect of NG-R1 on the structure and number of lymphatic vessels. Immunofluorescence staining results confirmed that NG-R1 did not affect the lymphatic vessel numbers in TNF-Tg mice, but it improved the destruction of lymphatic structures in the inflammatory state and increased the area covered by lymphatic smooth muscle.

Our previous studies have confirmed the importance of lymphatic system in arthritis inflammation. In this study, as a common inflammatory inducer, TNF-α was applied to evoke extreme inflammation in LECs. TNF promoted the production of nitric oxide (NO) by LECs and caused LSMCs apoptosis, reduced expression of muscle functional genes, and LSMCs contribute to the dysfunction of synovial lymphatic vessels in inflammatory arthritis. Thus, we conducted the coculture system of LECs and LSMCs.The results demonstrated that NG-R1 increased the expression of lymphatic smooth muscle cell function marker geneh1-

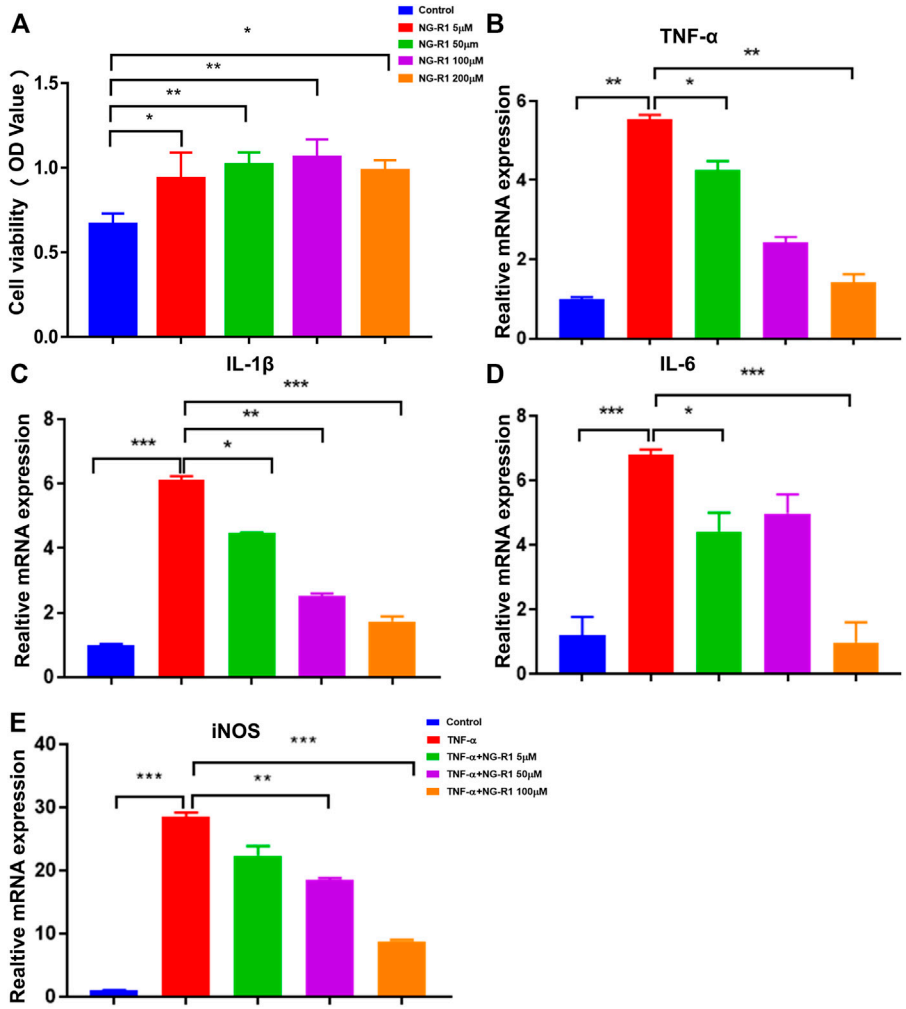


FIGURE 6 | NG-R1 ameliorated the inflammatory cytokines production of LECs stimulated by TNF-α. **(A)** Cytotoxicity assay used Cell Counting Kit-8 to determine the effective concentration of NG-R1. LECs was treated with different concentrations of NG-R1 (5, 50, 100, and 200 μM) for 24 h. **(B–E)** LECs were also pretreated for 2 h with NG-R1 (5, 50, and 100 μM) prior to stimulation with TNF-α (20 ng/ml) for another 12 h. The mRNA levels of TNF-α,IL-1β, IL-6, and iNOS were determined using qPCR. Data represents mean ± SEM. The experiment was repeated at least three times. *$p < 0.05$, **$p < 0.01$, ***$p < 0.001$, One-way ANOVA.

calponin, smα22, SM myosin heavy chain, and smα2 and promoted the contractile function of LSMCs and accelerated lymphatic drainage. NF-κB signaling pathway is one of the important transcriptional pathways in RA, which mainly regulates the level of pro-inflammatory mediators and induces the expression of IL-1, IL-6, and TNF-α and promotes the phosphorylation of p65 and IKKα/β in LECs. Our results show that NG-R1 dose-dependently inhibits TNF-α induced inflammatory cytokines TNF-α, IL-1β, IL-6, and iNOS production in LECs. NG-R1 repressed the phosphorylation of p65, and p65 nuclear accumulation relieved TNF-α-elicited inflammatory damages. However, NG-R1 without any effect on the phosphorylation of IKKα/β under the stimulation of TNF-α. Furthermore, inhibiting NF-κB signaling pathway in TNF-TG mice also inhibited the expression of serum inflammatory factors and improved synovial inflammation, cartilage erosion, and bone destruction of the ankle joint. These have led us to speculate that NG-R1 may play an anti-inflammatory role in RA. In future work, we also plan to continue to conduct experiments to explore NF-κB signal pathways by adding inhibitors or activators.

CONCLUSION

In summary, using TNF-Tg mice as a model of chronic inflammatory arthritis, we reported for the first time that NG-R1 promoted lymphatic drainage function to ameliorate rheumatoid arthritis by suppressing the NF-κB signaling pathway. Thus, inhibiting inflammatory cytokines production and improvement of the lymphatic vessel draining function together represent a potential therapeutic strategy for RA. Meanwhile, it also represents that NG-R1 is a new potential treatment for rheumatoid arthritis.

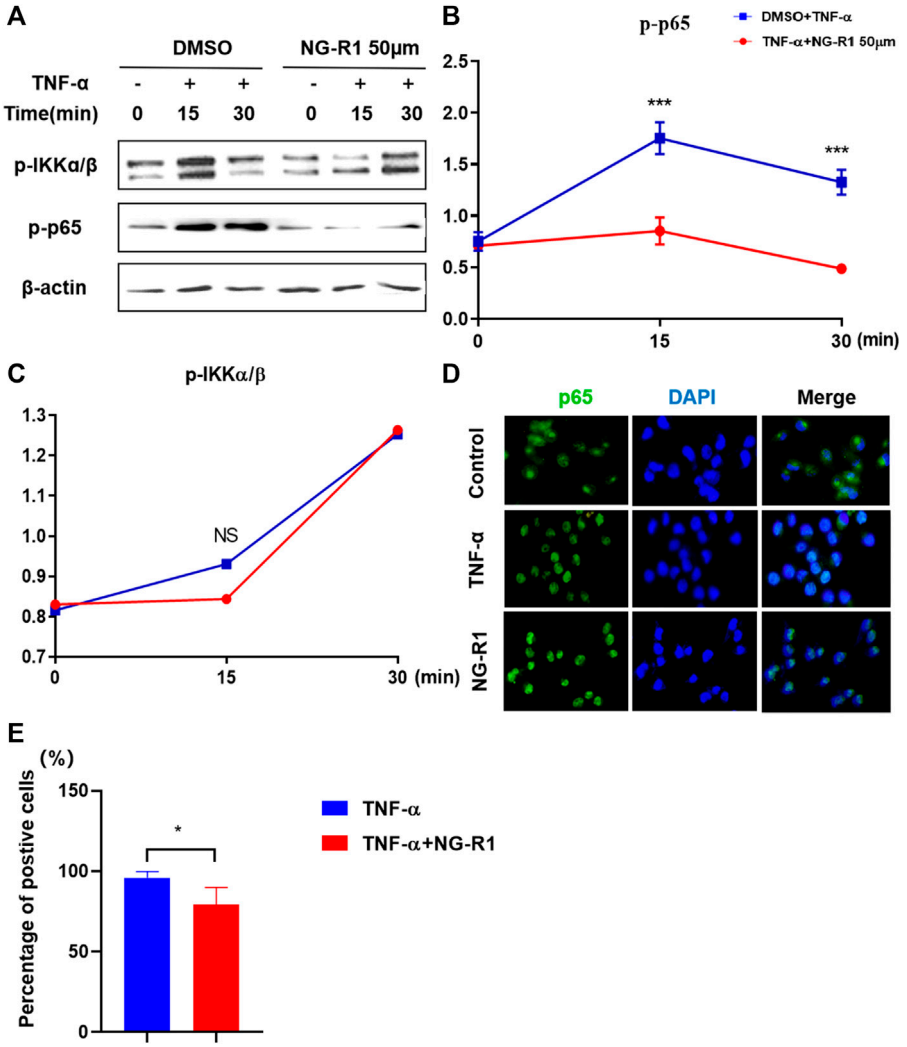


FIGURE 7 | NG-R1 inhibited NF-κB activation by impairing p65 phosphorylation. **(A–C)** Immunoblots for phos-phorylation of IKKα/β, p65, protein level in LECs stimulated with TNF-α (20 ng/ml) for 0, 15, and 30 min in the presence of NG-R1 (50 μM). The experiment was repeated at least three times. **(D)** The cells were stained with anti-p65 (green) and DAPI (blue) for 30 min. **(E)** LECs were stimulated with TNF-α for 30 min in the presence or absence of NG-R1 pretreatment for 2 h. Data represent mean ± SEM. The experiment was repeated at least three times. *$p < 0.05$, one-way ANOVA.

DATA AVAILABILITY STATEMENT

The original contributions presented in the study are included in the article/**Supplementary Material**, and further inquiries can be directed to the corresponding authors.

ETHICS STATEMENT

The animal study was reviewed and approved and all animal procedures were performed according to the Guiding Principles for the Care and Use of Laboratory Animals approved by the Animal Regulations of the National Science and Technology Committee of China under the approval of the Longhua Hospital Animal Ethics Committee (Shanghai, China).

AUTHOR CONTRIBUTIONS

DJ, YL, and TH conceived the study, TH, HX, and XW performed electronic literature searches, DJ and YL performed study selection and data extraction, QL and QX performed quality check. DJ and YL undertook the analyses with YW, QS, and QL. QL, QX, and HX critically revised the manuscript. All authors have read and approved the final manuscript.

FUNDING

This work was sponsored by National Key R&D Program of China (2018YFC1704300 to WYJ), National Natural Science Foundation (81822050 and 81920108032 to LQQ, 81930116 to WYJ, 81904227 to WXY), Shanghai Natural Science Foundation of China

(18ZR1436200 to XQJ), 2021 Changning district, Shanghai medical doctor innovation talent base project (RCJD2021B07 to XQJ), Qihuang Young Scholar of National Administration of Traditional Chinese Medicine to LQQ, Leading medical talents in Shanghai (2019LJ02 to LQQ), Dawn plan of Shanghai Municipal Education Commission (19SG39 to LQQ), the program for innovative research team of ministry of Science and Technology of China (2015RA4002 to WYJ), "Innovation Team" development projects (IRT1270 to WYJ), Shanghai TCM Medical Center of Chronic Disease (2017ZZ01010 to WYJ), Three Years Action to Accelerate the Development of Traditional Chinese Medicine Plan (ZY (2018-2020)-CCCX-3003 to WYJ).

SUPPLEMENTARY MATERIAL

The Supplementary Material for this article can be found online at: https://www.frontiersin.org/articles/10.3389/fphar.2021.730579/full#supplementary-material

REFERENCES

Acimovic, I. (2018). The Influence of Health Qigong on the Subjectively Expressed Psychophysical State of Patients with Rheumatoid Arthritis, Rheum, Osteoporosis, Osteopenia. *CASE REPORT* 1, 150–154. doi:10.4103/CMAC.CMAC_33_18

Bouta, E. M., Bell, R. D., Rahimi, H., Xing, L., Wood, R. W., Bingham, C. O., et al. (2018). Targeting Lymphatic Function as a Novel Therapeutic Intervention for Rheumatoid Arthritis. *Nat. Rev. Rheumatol.* 14 (2), 94–106. doi:10.1038/nrrheum.2017.205

Deng, C., Zhang, Q., He, P., Zhou, B., He, K., Sun, X., et al. (2021). Targeted Apoptosis of Macrophages and Osteoclasts in Arthritic Joints Is Effective against Advanced Inflammatory Arthritis. *Nat. Commun.* 12 (1), 2174. doi:10.1038/s41467-021-22454-z

Hosseinikhah, S. M., Barani, M., Rahdar, A., Madry, H., Arshad, R., Mohammadzadeh, V., et al. (2021). Nanomaterials for the Diagnosis and Treatment of Inflammatory Arthritis. *Ijms* 22 (6), 3092. doi:10.3390/ijms22063092

Hou, T., Liu, Y., Wang, X., Jiao, D., Xu, H., Shi, Q., et al. (2020). Ginsenoside Rg1 Promotes Lymphatic Drainage and Improves Chronic Inflammatory Arthritis. *J. Musculoskelet. Neuronal Interact* 20 (4), 526–534.

Liang, Q. Q., Shi, Q., Wood, R. W., Xing, L. P., and Wang, Y. J. (2015). Peri-articular Lymphatic System and "Bi" Theory of Chinese Medicine in the Pathogenesis and Treatment of Arthritis. *Chin. J. Integr. Med.* 21 (9), 648–655. doi:10.1007/s11655-015-2305-0

Liang, Q., Zhang, L., Xu, H., Li, J., Chen, Y., Schwarz, E. M., et al. (2021). Lymphatic Muscle Cells Contribute to Dysfunction of the Synovial Lymphatic System in Inflammatory Arthritis in Mice. *Arthritis Res. Ther.* 23 (1), 58. doi:10.1186/s13075-021-02438-6

Liang, T., Song, M., Xu, K., Guo, C., Xu, H., Zhang, H., et al. (2020). TRIM32 Promotes Inflammatory Responses in Rheumatoid Arthritis Fibroblast-like Synoviocytes. *Scand. J. Immunol.* 91 (6), e12876. doi:10.1111/sji.12876

Liu, H., Yang, J., Yang, W., Hu, S., Wu, Y., Zhao, B., et al. (2020). Focus on Notoginsenoside R1 in Metabolism and Prevention against Human Diseases. *Drug Des. Devel Ther.* 14, 551–565. doi:10.2147/DDDT.S240511

Liu, Y., Jin, J., Xu, H., Wang, C., Yang, Y., Zhao, Y., et al. (2021). Construction of a pH-Responsive, Ultralow-Dose Triptolide Nanomedicine for Safe Rheumatoid Arthritis Therapy. *Acta Biomater.* 121, 541–553. doi:10.1016/j.actbio.2020.11.027

Petrovská, N., Prajzlerová, K., Vencovský, J., Šenolt, L., and Filková, M. (2021). The Pre-clinical Phase of Rheumatoid Arthritis: From Risk Factors to Prevention of Arthritis. *Autoimmun. Rev.* 20 (5), 102797. doi:10.1016/j.autrev.2021.102797

Pratt, A. G., Siebert, S., Cole, M., Stocken, D. D., Yap, C., Kelly, S., et al. (2021). Targeting Synovial Fibroblast Proliferation in Rheumatoid Arthritis (TRAFIC): an Open-Label, Dose-Finding, Phase 1b Trial. *Lancet Rheumatol.* 3 (5), e337–e346. doi:10.1016/S2665-9913(21)00061-8

Sun, B., Xiao, J., Sun, X. B., and Wu, Y. (2013). Notoginsenoside R1 Attenuates Cardiac Dysfunction in Endotoxemic Mice: an Insight into Oestrogen Receptor Activation and PI3K/Akt Signalling. *Br. J. Pharmacol.* 168 (7), 1758–1770. doi:10.1111/bph.12063

Telinius, N., and Hjortdal, V. E. (2019). Role of the Lymphatic Vasculature in Cardiovascular Medicine. *Heart* 105 (23), 1777–1784. doi:10.1136/heartjnl-2018-314461

Wang, T., Guo, R., Zhou, G., Zhou, X., Kou, Z., Sui, F., et al. (2016). Traditional Uses, Botany, Phytochemistry, Pharmacology and Toxicology of Panax Notoginseng (Burk.) F.H. Chen: A Review. *J. Ethnopharmacol* 188, 234–258. doi:10.1016/j.jep.2016.05.005

Yu, Y., Sun, G., Luo, Y., Wang, M., Chen, R., Zhang, J., et al. (2016). Cardioprotective Effects of Notoginsenoside R1 against Ischemia/reperfusion Injuries by Regulating Oxidative Stress- and Endoplasmic Reticulum Stress- Related Signaling Pathways. *Sci. Rep.* 6, 21730. doi:10.1038/srep21730

Zhang, B., Zhang, X., Zhang, C., Shen, Q., Sun, G., and Sun, X. (2019). Notoginsenoside R1 Protects Db/db Mice against Diabetic Nephropathy via Upregulation of Nrf2-Mediated HO-1 Expression. *Molecules* 24 (2), 247. doi:10.3390/molecules24020247

Zhao, G., and Zhang, H. (2018). Notch-1 siRNA and Methotrexate towards a Multifunctional Approach in Rhematoid Arthritis Management: a Nanomedicine Approach. *Pharm. Res.* 35 (6), 123. doi:10.1007/s11095-018-2401-x

Conflict of Interest: The authors declare that the research was conducted in the absence of any commercial or financial relationships that could be construed as a potential conflict of interest.

Publisher's Note: All claims expressed in this article are solely those of the authors and do not necessarily represent those of their affiliated organizations, or those of the publisher, the editors and the reviewers. Any product that may be evaluated in this article, or claim that may be made by its manufacturer, is not guaranteed or endorsed by the publisher.

Copyright © 2022 Jiao, Liu, Hou, Xu, Wang, Shi, Wang, Xing and Liang. This is an open-access article distributed under the terms of the Creative Commons Attribution License (CC BY). The use, distribution or reproduction in other forums is permitted, provided the original author(s) and the copyright owner(s) are credited and that the original publication in this journal is cited, in accordance with accepted academic practice. No use, distribution or reproduction is permitted which does not comply with these terms.

Advantages of publishing in Frontiers

OPEN ACCESS
Articles are free to read for greatest visibility and readership

FAST PUBLICATION
Around 90 days from submission to decision

HIGH QUALITY PEER-REVIEW
Rigorous, collaborative, and constructive peer-review

TRANSPARENT PEER-REVIEW
Editors and reviewers acknowledged by name on published articles

Frontiers
Avenue du Tribunal-Fédéral 34
1005 Lausanne | Switzerland

Visit us: www.frontiersin.org
Contact us: frontiersin.org/about/contact

REPRODUCIBILITY OF RESEARCH
Support open data and methods to enhance research reproducibility

DIGITAL PUBLISHING
Articles designed for optimal readership across devices

FOLLOW US
@frontiersin

IMPACT METRICS
Advanced article metrics track visibility across digital media

EXTENSIVE PROMOTION
Marketing and promotion of impactful research

LOOP RESEARCH NETWORK
Our network increases your article's readership